AD-A113 907 ADVISORY GROUP FOR AEROSPACE RESEARCH AND DEVELOPMENT--ETC F/G 20/4
FLUID DYNAMICS OF JETS WITH APPLICATIONS TO V/STOL.(U)
JAN 82
UNCLASSIFIED AGARD-CP-308 NL

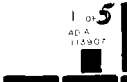

AGARD-CP-308

AD A113907

CP 308

FLUID DYNAMICS OF JETS WITH APPLICATIONS TO V/STOL

FDP

DTIC FILE COPY

AGARD

ADVISORY GROUP FOR AEROSPACE RESEARCH & DEVELOPMENT

7 RUE ANCELLE 92200 NEUILLY SUR SEINE FRANCE

AGARD CONFERENCE PROCEEDINGS No. 308

Fluid Dynamics of Jets with Applications to V/STOL

DTIC
ELECTE
APR 27 1982
S D

NORTH ATLANTIC TREATY ORGANIZATION

DISTRIBUTION AND AVAILABILITY
ON BACK COVER

This document has been approved for public release and sale; its distribution is unlimited.

82 04 27 151

AGARD-CP-308

NORTH ATLANTIC TREATY ORGANIZATION

ADVISORY GROUP FOR AEROSPACE RESEARCH AND DEVELOPMENT

(ORGANISATION DU TRAITE DE L'ATLANTIQUE NORD)

AGARD Conference Proceedings No.308

FLUID DYNAMICS OF JETS WITH APPLICATIONS TO V/STOL

Papers presented and discussions held at the Fluid Dynamics Panel Symposium held at the Fundaçao Calouste Gulbenkian, Lisbon, Portugal, 2–5 November 1981.

THE MISSION OF AGARD

The mission of AGARD is to bring together the leading personalities of the NATO nations in the fields of science and technology relating to aerospace for the following purposes:

- Exchanging of scientific and technical information;
- Continuously stimulating advances in the aerospace sciences relevant to strengthening the common defence posture;
- Improving the co-operation among member nations in aerospace research and development;
- Providing scientific and technical advice and assistance to the North Atlantic Military Committee in the field of aerospace research and development;
- Rendering scientific and technical assistance, as requested, to other NATO bodies and to member nations in connection with research and development problems in the aerospace field;
- Providing assistance to member nations for the purpose of increasing their scientific and technical potential;
- Recommending effective ways for the member nations to use their research and development capabilities for the common benefit of the NATO community.

The highest authority within AGARD is the National Delegates Board consisting of officially appointed senior representatives from each member nation. The mission of AGARD is carried out through the Panels which are composed of experts appointed by the National Delegates, the Consultant and Exchange Programme and the Aerospace Applications Studies Programme. The results of AGARD work are reported to the member nations and the NATO Authorities through the AGARD series of publications of which this is one.

Participation in AGARD activities is by invitation only and is normally limited to citizens of the NATO nations.

The content of this publication has been reproduced
directly from material supplied by AGARD or the authors.

Published January 1982

Copyright © AGARD 1982
All Rights Reserved

ISBN 92-835-0308-2

Printed by Technical Editing and Reproduction Ltd
Harford House, 7–9 Charlotte St, London, W1P 1HD

FOREWORD

The Symposium on Fluid Dynamics of Jets with Applications to V/STOL was planned in response to current aeronautical developments which highlight the need for improvements in the understanding of jets and the fundamentals of mixing. The most important of these developments are vertical and short take-off and landing aircraft which employ thrust vectoring or lift augmentation. Sessions on Jet Interactions with Neighbouring Surfaces, Jet Structure and Development, Wind Tunnel Simulation, Injection and Thrust Augmentation, and Theoretical Models provided a comprehensive overview of the state of art in the field.

This volume includes the thirty-one papers presented at the Symposium sponsored by the AGARD Fluid Dynamics Panel in Lisbon, Portugal, on 2–5 November 1981. In addition, a summary of important features of the meeting made by Dr Ir. B.M.Spee is included following the papers. A more comprehensive Technical Evaluation Report will be prepared for publication early in 1982.

DTIC COPY INSPECTED 2

Accession For
NTIS GRA&I [X]
DTIC TAB [ ]
Unannounced [ ]
Justification
By
Distribution/
Availability Codes
Dist | Avail and/or Special
A

AGARD FLUID DYNAMICS PANEL

Dr K.J.Orlik-Rückemann
National Aeronautical Establishment
National Research Council
Montreal Road
Ottawa, Ontario K1A OR6, Canada

M.l'Ing. en Chef B.Monnerie
Chef de la Division d'Aérodynamique Appliquée
ONERA
29 Avenue de la Division Leclerc
92320 Châtillon, France

PROGRAM COMMITTEE MEMBERS

Dr B.Quinn (co-Chairman)
President
Aeronautical Research Assoc-Princeton
50 Washington Road
Princeton, N.J. 08540, USA

M.l'Ing. Général P.CARRIERE
Senior Scientific Advisor
ONERA
29 Avenue de la Division Leclerc
92320 Châtillon, France

Professor Dr Ing.K.Gersten
Institut für Thermo und Fluiddynamik
Ruhr-Universität Bochum
Postfach 10 21 48
D-4630 Bochum 1, FRG

Mr D.S.Siegel
Project Manager, Materials Technology
Office of Naval Research
Attn: Code 260
800 N.Quincy St.
Arlington
VA 22217, USA

Professor A.D.Young (Co-Chairman)
Queen Mary College
Aeronautics Dept
Mile End Road
London E1 4N6, UK

Professor A.F. de O.Falcao
Pavilhao de Maquinas
Istituto Superior Tecnico
1096 Lisboa Codex, Portugal

Dr Ing.U.Sacerdote
v. Direttore
Gruppo Attivita' Spaziali
ED Energie Alternative
Aeritalia S.P.A.
Corso Marche 41
10146 Torino, Italy

Dr Ir.B.M.Spee
Deputy Director
National Aerospace Laboratory NLR
Anthony Fokkerweg 2
1059 CM Amsterdam, Netherlands

PANEL EXECUTIVE

Robert H.Rollins II

CONTENTS

	Page
FOREWORD	iii
PANEL AND PROGRAMME COMMITTEE MEMBERS	iv
	Reference
GENERAL REVIEW: SOME ASPECTS OF JET DYNAMICS AND THEIR IMPLICATIONS FOR VTOL RESEARCH by L.J.S.Bradbury	1
SESSION I – JET INTERACTIONS WITH NEIGHBOURING SURFACES	
JET INTERACTIONS WITH NEIGHBOURING SURFACES by J.Barche	2
INTERACTION OF SIMPLE AND MULTIPLE JETS WITH A PLANE SURFACE by A.R.Janeiro Borges and D.X.Viegas	3
RECOLLEMENT DE DEUX JETS SUR EUX-MEMES par C.Bourque	4
JETS IMPINGING NORMALLY AND OBLIQUELY TO A WALL by S.R.B.Araujo, D.F.G.Durao and F.J.C.Firmino	5
AN INVESTIGATION OF INCLINED JETS IN A CROSSWIND by P.Taylor and D.J.Watkins	6
AN EXPERIMENTAL INVESTIGATION OF AN UPPER SURFACE BLOWING CONFIGURATION by G.D.Catalano, J.B.Morton and R.R.Humphris	7
AN EXPERIMENTAL AND THEORETICAL INVESTIGATION OF THE INTERACTION BETWEEN THE ENGINE JET AND THE SURROUNDING FLOW FIELD WITH REGARD TO THE PRESSURE DRAG ON AFTERBODIES by A.Zacharias	8
SESSION II – JET STRUCTURE AND DEVELOPMENT	
STRUCTURE AND DEVELOPMENT OF TURBULENT JETS by J.Mathieu and G.Charnay	9
A ROW OF JETS IN A CROSS FLOW by Z.A.Khan, J.J.McGuirk and J.H.Whitelaw	10
EXPERIMENTAL INVESTIGATION OF INITIALLY PLANAR JETS INCLINED TO AN EXTERNAL FLOW by Y.Pontikis, R.A.Feik and A.D.Young	11
RESONANT ENTRAINMENT OF A CONFINED PULSED JET by P.G.Parikh	12
FLOW FIELD AND NOISE SOURCES OF JET IMPINGEMENT ON FLAPS AND GROUND SURFACE by G.Neuwerth	13
THE NEAR FIELD OF A PLANE TURBULENT JET by L.N.Persen	14

Reference

SESSION III – WINDTUNNEL SIMULATION OF FLOW FIELD, FORCES MOMENTS

SURVEY PAPER: JET V/STOL WIND-TUNNEL SIMULATION AND GROUNDPLANE EFFECTS
by R.J.Margason 15

THE MODELLING AND PREDICTION OF MULTIPLE JET V/TOL AIRCRAFT FLOW FIELDS IN GROUND EFFECT
by *D.R.Kotansky* *16*

EVALUATION OF THE EFEECTS OF MODEL SCALE AND TEST TECHNIQUE ON JET-INDUCED EFFECTS
by S.G.Kalemaris 17

JET EFFECTS ON FORCES AND MOMENTS OF A V/STOL FIGHTER TYPE AIRCRAFT
by B.Haftmann 18

SESSION IV – INJECTION AND THRUST AUGMENTATION

THRUST AUGMENTING EJECTORS: A REVIEW OF THE APPLICATION OF JET MECHANICS TO V/STOL AIRCRAFT PROPULSION
by B.Quinn 19

OPTIMISATION THEORIQUE ET CONTROLE EXPERIMENTAL D'UN INJECTEUR
par A.Mignosi 20

UNSTEADY EJECTORS
by H.Viets 21

IMPROVEMENT OF EJECTOR THRUST AUGMENTATION BY PULSATING OR FLAPPING JETS
by G.Binder and H.Didelle 22

ETUDE EXPERIMENTALE D'UN DEVIATEUR DE JET
par M.Lepretre et C.Portier 23

TURBOPROP AND TURBOJET EJECTOR OPTIMISATION
by V.P.Riviello, A.Murolo and G.Torella 24

SESSION V – THEORETICAL MODELS AND THEIR ASSESSMENT

ON THE INCLUSION OF INFORMATION ON EDDY STRUCTURE IN SECOND-ORDER-CLOSURE MODELS OF TURBULENT FLOWS
by *C.duP.Donaldson and G.Sandri* 25

A THREE DIMENSIONAL FINITE ELEMENT ALGORITHM FOR PREDICTION OF V/STOL JET-INDUCED FLOWFIELDS
by A.J.Baker, P.D.Manhardt, J.A.Orzechowski and K.T.Yen 26

PREDICTION OF PROPULSION INDUCED EFFECTS IN TRANSITION USING A MODIFIED JET WAKE MODEL
by M.M.Walters and K.T.Yen 27

SESSION VI – INVITED BRIEF CONTRIBUTIONS

EFFECTS OF BUOYANCY AND ENTRAINMENT ON HOT FREE JETS AND WALL JETS
by K.Gersten, F.v.Schulz-Hausmann and S.Schilawa 28

V/STOL AIRCRAFT AND FLUID DYNAMICS
by L.Roberts and S.B.Anderson 29

INVESTIGATION OF WALL JETS
by E.Krause, *D.Hänel* and N.I.I.Hewedy 30

Reference

THE CALCULATION OF JET INTERFERENCE PRESSURE DISTRIBUTION USING INTEGRAL AND NUMERICAL METHODS BASED ON ACTUAL MEASUREMENTS OF ENTRAINMENT
by P.E.C.Ransom and J.H.Barnes 31

SUMMARY REMARKS
by B.M.Spee S

CLOSING REMARKS C
by B.Quinn and K.J.Orlik-Rückemann

SOME ASPECTS OF JET DYNAMICS AND THEIR IMPLICATIONS FOR VTOL RESEARCH.

by
L.J.S. Bradbury
Mechanical Engineering Department
University of Surrey, Guildford, Surrey GU2 5XH, U.K.

SUMMARY

This paper discusses some of the problems associated with jet interference on VTOL aircraft. The jet interference that arises in hovering both in and out of ground effect is considered first and the factors that influence the entrainment that is responsible for the interference are discussed. In particular, it is shown that the flow in the initial region of a jet is strongly affected by circumferential variations in the jet nozzle flow angle and that this might account for some of the anomolous results for the decay of jets issuing from VTOL models. The possible use of Reichardt's method for studying the behaviour of non-uniform jets is also discussed. The problem of jet interference in transition is next examined and the basis on which model tests are currently carried out is briefly reviewed. The dynamics of jet interference in transition are then considered in more detail and it is suggested that unlike interference in hovering, transition interference might well be accounted for on the basis of a potential flow model of the jet in a cross-flow. Some experimental evidence in support of this notion is examined and a few examples of comparisons between predicted and experimental pressure distributions around a single jet issuing from a flat plate are given.

1. Introduction.

The attractiveness of an aircraft with conventional aerodynamic performance in normal flight but with an ability to take off and land vertically is so obvious for both civil and military applications that it is quite unnecessary to discuss the virtues of such a craft. However, until the advent of the jet engine, the possibility of developing a VTOL aircraft of this type did not really exist and, even then, it was only in the 1950's that the specific thrust and overall thrust of jet engines reached a stage where VTOL development could begin to be contemplated as a real possibility. In the intervening years, an enormous amount of effort has been devoted to research in this field and this has included the development of many VTOL research aircraft. The first of these - the so-called Rolls Royce "flying bedstead" flew in 1953 and since then, about a further twenty VTOL aircraft of one sort or another have flown. However, in spite of these intensive efforts, there exists only one military VTOL aircraft in use in any numbers in the West - the Harrier and its various derivatives - and no civil VTOL aircraft at all is in service.

Although it is by no means the only reason, it has certainly been an important contributory factor to this situation that the aerodynamic design of VTOL aircraft in the take-off phase of flight has posed many difficult problems which we are not yet in a position to resolve. One of these is that, unlike the conventional aircraft, the angle that the incident flow vector makes with the axis of the aircraft can take any value during the take-off and transition phases of flight so that it is necessary to consider the aerodynamic characteristics of the aircraft over a far more extensive range of conditions than is normally the case. In many of these situations, the aircraft is a far from slender shape and the flow around it is characterised by large scale separations of the sort more typical of bluff body flows than of "slender" aircraft flows. However, the principle problem is that there are very extensive aerodynamic interactions between the lifting jets and the flow around the aircraft. At take-off, the lifting jets strike the ground and produce complex flows around the aircraft resulting often in substantial and unfavourable aerodynamic forces on the airframe. There is also the possibility of recirculation of hot exhaust gases into the engine intakes with a consequent loss of thrust and engine performance. Damage due to the ingestion of debris thrown up by the impacting jets is also a problem. During the transition phase of flight from vertical lift off to conventional horizontal flight, it is also found that the lifting jets produce significant aerodynamic interference with the flow over the aircraft producing both a loss of aerodynamic lift and significant pitching moment changes. From the point of view of this conference, it is these jet interference effects that are the subject of major interest.

For present purposes, it is convenient to group problems of jet interference into three flow regimes, namely (i) hovering in ground effect, (ii) hovering out of ground effect and (iii) transition from hovering to forward flight out of ground effect. There are some circumstances such as a rolling take-off where ground effects occur in conjunction with forward movement of the aircraft but these will not be considered here.

As illustrations of the type of jet interference effects that may develop, figures 1,2 and 3 show a range of results of model tests corresponding to the three flow regimes (Williams and Wood (1966)). Figure 1 shows the unfavourable interference that occurs in hovering close to the ground for a delta wing model with a range of lifting jet configurations and for two positions of the wing. It is possible under some circumstances to produce favourable ground effects but, in these tests, there was always a loss of lift. It should be noted that the lift losses are strongly dependent on aircraft and lifting jet geometries. As far as hovering out of ground effect is concerned, figure 2 shows results for a very simple circular planform model with a single lifting jet as a function of the ratio of the planform diameter to jet diameter. The lift losses in this case are typically a few percent of the thrust whereas the ground effect losses can be significantly higher and they are therefore generally a more serious problem. Finally, figure 3 shows some lift loss results for a model in the transition phase of flight out of ground effect. The results show a lift loss as a function of the ratio of the model forward speed to the jet exit velocity for a similar range of aircraft and jet nozzle geometries as was used in the ground effect tests. This figure again illustrates the substantial lift losses that can occur and these may be accompanied by pitching moment changes whose magnitudes may be such as to give rise to stability problems.

It has to be acknowledged that the flows leading to these interference effects are often so complex that there seems little prospect of developing methods for predicting their effects although the more audacious of those working on numerical solutions of model equations for turbulent flows are beginning to address themselves to flows of ever increasing complexity. Nevertheless, for sometime to come, it is almost certainly the case that the development of VTOL aircraft will rest far more heavily on model tests than is the case with conventional aircraft. Unfortunately, wind tunnel tests on VTOL models are themselves much more difficult than those on conventional aircraft models because of the need to simulate the lifting jets and also because wind tunnel interference effects are more complex than those usually encountered in conventional model tests. The need to simulate the lifting jets creates a series of practical problems with overall force and moment measurements on models to which are connected compressed air supplies feeding the plenum chambers within the models. The development of techniques to accomplish this task has been a major undertaking in its own right but the problem of interest in the present context is to try and understand those features of the lifting jets which it is important include in model tests. Along with the wind tunnel blockage problem, this has been and remains one of the most important topics of research into jet aerodynamics relevant to VTOL aircraft and this paper will attempt to discuss some aspects of this problem. In section 2, the factors affecting entrainment into jets issuing into still air in or out of ground effect are considered. The importance of the initial region close to the jet nozzle is emphasised and guidelines for establishing the important characteristics of a jet nozzle flow are put forward. In addition, some comments are made on the possibility of using the largely discarded Reichardt's method for examining the effect on entrainment of non-uniform jet nozzle velocity profiles. Section 3 then discusses jet interference in transition out of ground effect and the effects on the interference of jet Mach number, temperature and velocity profile are briefly examined. The detailed discussion is centred almost entirely on the simple case of a single jet issuing normally from a plane wall into a mainstream flow because this is the flow for which there is most experimental information. It is suggested that in contrast to the interference effects discussed in section 2, the flow around jets in cross flow is probably dominated by potential flow effects and some evidence to support this notion is presented.Some suggestions are then put forward for future theoretical and experimental work which might lead to a better understanding of jet interference in transition.

2. Jets in still air - entrainment dominated flows.

We will consider first the problem of jet simulation in studies of jet interference in hovering both in and out of ground effect. Although it is a rather obvious point, it is important to note that, in both cases, the potential flow solutions for the jet flows would not lead to any interference effects at all. The potential flow of a jet issuing into still air is a trivial flow and consists simply of a tubular vortex sheet of strength $\gamma = U_J/2$ where U_J is the jet nozzle velocity. The sheet moves with a velocity of $U_J/2$ and produces a uniform internal jet stream of velocity U_J and no external velocity field at all. In the case of jets impinging on the ground, the potential flow solutions are not so trivial but they would also produce no external flow to the vortex sheets separating the jet from the ambient air. Thus, the hovering lift losses both in and out of ground effect occur entirely as a result of entrainment due to turbulent mixing and. therefore, if we are either to predict or measure accurately these interference effects, it is important that the mixing is properly modelled in either theoretical or experimental work on the hovering lift losses.

2.1 Entrainment into non-impacting jets in still air.

The simplest jet configuration involving entrainment is the flow of a single jet issuing into still air. Figure (4) shows sketches of the structure of such a jet for a subsonic case and for a supersonic jet. The purpose of this figure is to emphasise in an extreme way that the flow in the region near the nozzle is dependent on the precise nozzle conditions such as jet Mach number, temperature, the species of the gas and possibly many other parameters like the turbulence level, velocity profile and so on. However, some way downstream, the flow will be well subsonic and the mass flow in the jet will be largely composed of air entrained from the surroundings. Under these circumstances, it can be argued that the only conserved property on which the jet structure will depend is the overall thrust, T, and the structure of the jet will be independent of other nozzle conditions. It is well established that turbulent free jet flows are almost entirely Reynolds number independent and, on the basis of simple dimensional arguments, the spread of some appropriately defined jet width δ and the decay of the jet centre-line velocity U_o will then take the following forms, namely

$$\frac{\delta}{x-x_o} = C_1 \qquad (2.1.1(a))$$

$$\frac{U_o(x-x_o)}{\sqrt{T/\rho_a}} = C_2 \qquad (2.1.1(b))$$

where C_1 and C_2 are constants and x_o is an apparent origin of the downstream jet flow and its position is the only influence that the precise nozzle conditions will have on the jet development. ρ_a is the ambient air density.It is interesting to note that these conditions can also be obtained in an apparently independent manner by looking for the circumstances under which a self-preserving jet flow can develop where the shape of the mean velocity profiles and the distributions of the turbulent stresses are similar at all downstream stations. In such a flow,

$$\frac{U}{U_o} = F\left(\frac{r}{\delta}\right)$$

$$\frac{\overline{uv}}{U_o^2} = g\left(\frac{r}{\delta}\right) \text{ and so on for the normal stresses.}$$

U is the mean velocity at radius r, $\overline{uv}$ is the turbulent shear stress and f and g are functions of r/δ only. By substituting these expressions into the momentum equation, an ordinary differential equation in f and g is obtained which shows that an axisymmetric self-preserving solution is only possible if $\delta \sim x$, $U_o \sim x^{-1}$. These conditions are equivalent to equations (2.1.1(a)) and (2.1.1(b)). There is abundant experimental evidence to show that a flow of this sort develops some way downstream of the nozzle and, although there is

some uncertainty over the precise values of the constants, values of C_1=0.089 and C_2=7.7 in equations (2.1.1(a)) and (2.1.1(b)) give reasonable agreement with most sets of experimental data if the jet width is defined as the radius at which the mean velocity U= $U_o/2$.

From the point of view of the irrotational external flow induced by entrainment into the jet, this may be represented in the far field not too close to the jet by the flow into a distribution of sinks along the axis of the jet whose strength per unit length is given by the rate of change along the axis of the volume flow contained within the jet. From dimensional arguments alone, the mass flow M in the downstream region will be given by

$$\frac{M}{\sqrt{\rho_a T (x-x_0)^2}} = \text{a constant.} \qquad (2.1.2)$$

or, for the sink strength,

$$m = \frac{1}{\rho_a}\frac{dM}{dx} \propto \sqrt{T/\rho_a}$$

A direct and convincing demonstration of the validity of this relationship can be found in the work of Ricou and Spalding (1961) on entrainment into jets consisting of gases of a number of different species. They found that the ratio of mass flow in the jet to the nozzle mass flow was well represented by the expression

$$\frac{M}{M_J} = 0.32\,\frac{x}{d}\left(\frac{\rho_a}{\rho_J}\right)^{1/2} \qquad (2.1.3)$$

where M_J is the nozzle mass flow, d is the nozzle diameter and ρ_a, ρ_J are the densities of the ambient air and jet nozzle gas respectively. It is simple to recast this to give

$$M = 0.32\sqrt{\frac{\pi \rho_a T x^2}{4}} \qquad (2.1.4)$$

which is consistent with equation (2.1.2) and does not contain details of the nozzle flow apart from the overall thrust T.

From the above arguments, it would seem that the development of the flow some way downstream of the nozzle is comparatively well understood and the magnitude of the sink strength representing the effects of entrainment reasonably well established. Near the nozzle, the situation is more complicated and some anomolous experimental results have been obtained for this region of the flow. In classical experiments on axisymmetric jets, it is conventional to produce the jet from a plenum chamber with a large contraction ratio to a short parallel nozzle. From such an arrangement, it is possible to produce a very uniform nozzle velocity profile with a low turbulence level and only thin boundary layers on the nozzle walls. Figure (5) shows a sketch of such an arrangement and the structure of the flow resulting from it. Mixing layers develop at the edge of the jet and these spread in an approximately linear manner until they coalesce. Thereafter, the flow is fully turbulent across the entire width of the jet and the flow soon develops the self-preserving characteristics given by equations (2.1.1(a)) and (2.1.1(b)). The region near the nozzle is often referred to as the potential core region because the total head on the centre-line remains constant until the mixing layers merge with one another.

Figure (6) shows some measurements of the variation of mean velocity and the u-component turbulent intensity along the centre-line of a jet produced in the manner described. The potential core length is about five diameters in length and, thereafter, the mean velocity variation rapidly assumes the form given by equation (2.1.1(b)). Although it is not particularly significant from a jet interference point of view, it should be noted that although the mean velocity field rapidly appears to be self-preserving, the turbulent intensity distributions show that a proper self-preserving structure does not develop until about 20 or 30 diameters downstream. For mixing layers which spread linearly and which have similar velocity profiles, it is not difficult to show that the rate of change of mass flow in the potential core region also grows in a linear manner so that

$$\frac{dM}{dx} = \frac{M_J}{d}\left(A + B\frac{x}{d}\right)$$

where A and B are constants. By assuming that the mixing layers have a Gaussian velocity profile and that momentum is conserved at the end of the potential core region*, one obtains

$$\frac{dM}{dx} = \frac{M_J}{d}\left[\frac{0.661}{x_c/d} + \frac{1.186}{(x_c/d)^2}\frac{x}{d}\right] \qquad (2.1.5)$$

where x_c is the length of the potential core region.

As a measure of the relative importance to entrainment of the initial region of the jet to the downstream self-preserving region, figures 7(a) and 7(b) show the u-component velocities induced in the plane of the nozzle by a distribution of sinks given by equation (2.1.5) compared to the velocities induced by a semi-infinite line of constant strength sinks given by differentiating equation (2.1.3) and starting at $x=x_c$. The calculations have been carried out for x_c/d = 6 and x_c/d = 3. These induced velocities can be thought of as downwash velocities due to entrainment into a single lifting jet. As one might expect at a radial distance from the nozzle up to about two diameters, the contributions

---

* Momentum flux cannot be conserved in the potential core by linearly growing mixing layers with similar velocity profiles. However, an expression for the entrainment that is accurate enough for present purposes can be obtained by ensuring conservation of momentum between the nozzle and the end of the potential core.

from the potential core region are the larger of the two but they still continue to be significant even at a radius ratio r/d of about 5 which is roughly typical of the equivalent planform to nozzle area encountered in VTOL models. Also, the induced velocities are significantly affected by the assumed length of the potential core. Since it might be argued that the lift losses in hover out of ground effect would be roughly proportional to the square of some typical downwash velocity, it is apparent that the potential core region makes a significant contribution to the lift loss and this lift loss will be strongly affected by anything that changes the length of the potential core to any great extent.

The above discussion on jet entrainment presupposed a particular type of well controlled nozzle geometry. However, in the case of VTOL models, space restrictions often create severe difficulties in producing acceptable jet nozzle conditions. For subsonic jets, "acceptable" is usually taken to mean that the final nozzle flow has a velocity distribution that is constant within, say, a few percent of the mean value. Developing nozzle flows of this sort can be a time consuming operation involving manipulating the internal air supply arrangements and the use of gauzes at or near the nozzle exits to try and achieve reasonably uniform exit conditions. However, even when an apparently acceptable nozzle flow has been produced, it is well known that marked variations in the subsequent jet development can occur. This is most easily seen in the decay of the centre-line velocity and figure (8) shows results of Gentry and Margason (1966) showing apparently the effect of different plenum chamber geometries on the velocity decay rate. As another example, figure (9) shows results of Hargreaves (1970) which seem to demonstrate a large and very surprising effect of either Reynolds number or Mach number on the jet development. From the previous discussion on the sensitivity of entrainment to the initial region of the jet, it is clear that the lift losses due to entrainment would be strongly influenced by these differing nozzle conditions. In an attempt to explain this type of anomolous behaviour, a series of experiments were carried out on a comparatively large 8 inch diameter jet at the University of Surrey in which it was the intention to study the effect on the jet development of nozzle boundary layer thickness, nozzle turbulence level and convergence of the nozzle flow. As reported by Bradbury and Khadem (1975), no very significant effect of the tested variation of these parameters on jet development was found and certainly no effects remotely comparable to those shown in figures (8) and (9). Coincidentally at the time of these tests, some investigations were being carried out at RAE Farnborough on the working section flow of a closed return open jet wind tunnel. To suppress vortex the rings which are thought to be shed from an open jet, it is conventional to mount a ring of "teeth" or "tabs" on the circumference of the jet and which intrude into the jet. To check on the possible effect of these tabs, a series of experiments were carried out with a range of tabs mounted on the circumference of the 8 inch diameter jet and figure (10) shows the effect of these tabs on the decay of the jet centre-line velocity. The surprising result is that the largest effect on the decay rate was obtained with only two tabs and it is worth emphasising that these tabs are really quite small in comparison with the diameter of the nozzle. After some investigation, it transpired that the effect of the tabs is to produce a circumferential variation in the flow direction (Bradbury and Khadem(1975)) and these flow angle variations cause gross distortions of the jet cross-section. The effect can almost certainly be accounted for on the basis of potential flow arguments. Figure (11) shows a sketch of a potential flow jet with circumferential variations in flow angle. The surface of the jet is a constant pressure surface and, as a result, it is difficult to imagine any significant restoring pressure forces developing within the jet to reduce the flow inclinations. The jet will therefore tend to split in two as shown in figure (11). In a real flow, this effect would almost certainly encourage turbulent mixing although, at the same time, this will tend to smear out the flow angle variations. Nonetheless,the effect can certainly be seen in velocity profile measurements downstream of the nozzle. Figure (12) shows iso-velocity contours at two and four diameters downstream and the tendency for the jet to split in two is apparent. In the plane of the nozzle, the velocity distribution was constant to within one percent of the mean value apart from the comparatively thin boundary layer region on the nozzle walls.

In view of the failure to explain the anomolies in jet centre-line velocity decay rates due to the more obvious parameters like turbulence level and so on, it seemed that flow angle variations might be responsible at least in some of the cases. A model similar to the one used by Gentry And Margason (1966) was constructed to test this idea and figure (13) shows the decay of centre-line velocity obtained from this model. Although not identical with Gentry and Margason's results, it did exhibit a rapid decay of centre-line velocity similar to that shown in their original report. Figure (14) shows the flow angle variations measured in the plane of the nozzle. They are larger than those induced by the tabs and this provides powerful evidence that flow angle variations might be the cause of some of the anomolous results reported in VTOL model tests. The flow angle variations in VTOL models could, of course, arise in many ways due to the internal plenum chamber geometries of the models which are almost inevitably far from axisymmetric. It is also very possible that the internal flows could be Reynolds number sensitive since separation of "small-scale" components may be involved and this might produce the apparent Reynolds number effects reported by Hargreaves and shown in figure (9).

The outcome of the above investigations suggests that measurements of jet nozzle conditions should be more extensive than has tended to be the case in many VTOL model tests. In addition to measuring the nozzle velocity profile, it is clearly important to measure the centre-line velocity variation and, if this shows unusual characteristics, it is then recommended that measurements of flow angle be made at the jet nozzle exit. Alternatively, a few velocity traverses across the jet could be made at one or two diameters downstream at several azimuthal angles to check if gross distortions of the jet are occurring.

Although it is usual in VTOL model tests to try and obtain a uniform velocity profile at the nozzle exits, the velocity profiles occurring in full scale lifting jets are hardly likely to be uniform. There seems to be a surprising lack of information about the structure of full scale jet engine flows and, apart from many other factors, this creates some uncertainties about the likely accuracy that can be attached to model test results. Nevertheless, non-uniformity in velocity profile seems likely to be a factor of some importance and, at the moment, there is little experimental data on its effect on jet development although some experiments have been carried out involving overall force measurements by Mayson, Ogilvie and Harris (1971).It is now possible to calculate the development of non-uniform jets using a number of modern turbulent flow prediction methods but the accuracy of the results is uncertain and the computing time would be considerable if an extensive range of parameters were to be studied. Although it has long ceased to be a seriously considered turbulence model, the aged Reichardt's method still provides a comparatively simple means of studying not only non-uniform jets but also non-circular jet nozzles and multi-jet

development. For example, Kynstautus (1964) showed that the spread of a row of circular jets and their transition to a quasi-two-dimensional jet was quite reasonably predicted using Reichardt's method.

For a distribution of jets with arbitrary velocity distributions and cross-sections, the velocity at a point P using Reichardt's method is given by

$$U^2(P) = \frac{1}{\pi c^2 x^2} \iint U_J^2 e^{-c^2 \frac{r^2}{x^2}} dA \qquad (2.1.6)$$

where dA is an elementary area over which the jet velocity is U_J. r is the radial distance from this area to the point P (see figure (15)) and c is a constant. The integration would be carried out over all the jet nozzle areas. For the velocity on the centre-line of a uniform circular jet, Reichardt's method gives

$$\frac{U_o^2}{U_J^2} = 1 - e^{-\frac{1}{4c^2(x/d)^2}} \qquad (2.1.7)$$

and when $x/d \gg 1$, this gives

$$\frac{U_o^2}{U_J^2} \sim \frac{1}{4c^2(x/d)^2}$$

so that by comparison with equation (2.1.1(b)) with $C_2 = 7.7$, a value of c=0.073 is suggested. Figure (6) shows a comparison between equation (2.1.7) and experimental data for the decay of the centre-line velocity. The agreement is fair except in the transition region from the potential core to the fully turbulent jet.

As an example of its use in the case of non-circular jets, it is straightforward to show that for a rectangular jet of span s and depth h, the velocity on the axis of the jet is given by

$$\frac{U_o^2}{U_J^2} = \operatorname{erf}\left(\frac{h}{2cx}\right)\operatorname{erf}\left(\frac{s}{2cx}\right) \qquad (2.1.8)$$

For a two-dimensional jet, this becomes

$$\frac{U_o^2}{U_J^2} = \operatorname{erf}\left(\frac{h}{2cx}\right)$$

and when $x/h \gg 1$, this gives

$$\frac{U_o^2}{U_J^2} \sim \frac{1}{c\sqrt{\pi}} \cdot \frac{1}{x/h} = \frac{7.73}{x/h} \qquad \text{with } c=0.073.$$

Experimental data for two-dimensional jets is well fitted by an expression

$$\frac{U_o^2}{U_J^2} = \frac{6.25}{x/h}$$

which is not too different from Reichardt's value and would result in an estimate of entrainment which would differ by only about 10%.

For the decay of the centre-line velocity of a rectangular jet, figure (16) shows a comparison between equation (2.1.7) and some recent experimental data of Krothapalli, Baganoff and Karamcheti (1981) for rectangular jets of aspect ratio 16.7 and 5.5.

Whilst the agreement is not particularly close, it is comparable to that achieved using far more complex calculation methods using k-ε type turbulence models (McGuirk and Rodi(1977) although obviously Reichardt's method is far more restricted in its overall area of application.

Returning to the effect of a non-uniform velocity profile,it is quite simple to use Reichardt's method to compute the velocity profile development with non-uniform nozzle velocity profiles. For a jet consisting of a circular core jet surrounded by an annular jet with a different velocity (see figure (17)), the particular result for the velocity on the centre-line of such a jet is given by

$$U_o^2 = U_{J_c}^2\left[1 - e^{-\left(\frac{D_i}{D_o}\right)^2 \frac{1}{4c^2(x/D_o)^2}}\right] + U_{J_a}^2\left[e^{-\left(\frac{D_i}{D_o}\right)^2 \frac{1}{4c^2(x/d)^2}} - e^{-\frac{1}{4c^2(x/D_o)^2}}\right] \qquad (2.1.9)$$

where U_{J_c}, U_{J_a} are the core and annular jet velocities respectively and D_i and D_o are the core jet and annular jet diameters respectively. There are a few results for the centre-line velocity decay given by Mayson et al and these are compared with equation (2.1.9) in figure (17). Again,the agreement is not particularly close but it is sufficiently good to probably enable Reichardt's method to be used in a parametric study of velocity profile variation on jet entrainment. For example, it would be interesting to compute entrainment rates for non-uniform jets using Reichardt's method and then calculate downwash velocities from the appropriate sink strengths. This might usefully serve to indicate the likely influence of velocity profile variations on the hovering lift losses. It might even be possible to correlate the lift loss measurements of Mayson et al on circular planform models with, say, the square of the calculated downwash velocities induced at the edge of the circular models.

2.2 Entrainment into impacting jets in still air.

In the case of VTOL models hovering in ground effect, the jet flows are more complicated than those encountered in hovering out of ground effect. However, for a single jet impinging on the ground, it is well known that a fully turbulent radial wall jet develops in which the wall jet thickness δ approximately varies like r and the peak velocity varies like r^{-1} where r is the radial distance from the point of impact. In consequence, the mass flow in a wall jet also varies approximately like r so that the rate of change of mass flow with radius is constant. The analogy with the far downstream behaviour of the axisymmetric free jet is clear although it should be stressed that the above behaviour of the radial wall jet is only

approximately satisfied due to the influence of the wall shear stress. An expression for the mass flow in a wall jet that is strictly analogous to that of Ricou and Spalding for the axisymmetric free jet has been given by Skifstad(1970) and, in recast form, this expression is

$$\frac{M}{\sqrt{\rho_a T}(r-r_o)^2} = 0.603$$

where r_o is an origin shift which makes allowance for the different initial conditions of the jet at the impact point. Since the lift losses in ground effect almost certainly arise mainly from the entrainment into the wall jet flow rather than from the entrainment into the jet flow prior to impact, there is a good prospect that the lift losses should not show much sensitivity to the precise nozzle conditions including Mach number, jet temperature and gas species. In the case of more complicated jet and airframe geometries, this is even more likely but, of course, this does not preclude experimental difficulties arising from, say, Reynolds number effects from the flow of the entrained air around the model.

3. Jet interference in transition - jets in cross-flow.

As in the case of hovering jet interference, the problem associated with representing the lifting jets on VTOL models in the transition phase of flight is of central importance in VTOL research. It is perhaps worth mentioning that intake interference effects are generally not sufficiently important to warrant modelling the intake flows. As far as the jets are concerned, the general practice is to ensure the correct scaling of the nozzle areas and then, for a given aircraft configuration, to assume that the jet interference effects are dependent only on an effective jet to free-stream velocity ratio defined as

$$m = \sqrt{\left(\int \rho_J U_J^2 \, dA_J\right)/(\rho_1 U_1^2)}$$

where ρ_1, ρ_J are the densities of the mainstream and jet nozzle flows respectively and U_1, U_J are the corresponding velocities. A_J is the jet nozzle area. For jets with uniform exit velocity profiles, there are a few experiments with hot gas jets up to 300°C which seem to show that this is an acceptable idea to allow for jet temperature effects (Williams and Wood(1966), Martin (1963)). Similarly, Mach number effects up to choking and Reynolds number effects do not seem significant. A more important effect might be the influence of non-uniform velocity profiles and recently Phipps (1981) has completed an investigation of the pressure distribution around a single jet issuing from a wall into a cross-flow in which the jet consisted of an annular/core jet combination of the sort shown in figure (17). The definition of an equivalent uniform jet having the same mass flow and thrust as the annular/core jet nozzle did not apparently prove a satisfactory means of collapsing the data and a better collapse was obtained using the radius of the outer annular jet and an effective velocity ratio defined as

$$m_E = \sqrt{\frac{A_c U_{J_c}^2 + A_A U_{J_a}^2}{(A_c + A_a) U_1^2}}$$

where A_A, A_c are the areas of the annular and core jets respectively and U_{J_a}, U_{J_c} are the corresponding jet velocities. Unfortunately, as Phipps acknowledges, this definition breaks down as the annular velocity is reduced to zero and it also did prove to be adequate in dealing with the purely annular jet.

Before attempting a more detailed discussion of the mechanism of jet interference in transition, some further general points need to be made. Figure (18) shows a sketch of a VTOL aircraft in transition to forward flight. As far as calculating the interference effects are concerned, the lifting jets can be surrounded by a surface which contains entirely the rotational jet flows. If the normal components of velocity to the surface are known, the surface may be replaced by a distribution of sources or sinks with a strength proportional to the normal velocity components and this singularity representation would produce the correct potential flow external to the jets. In general, the distance from the jet plumes to the aircraft are significantly greater than the cross-sectional dimensions of the jet and, in this far field, the velocity field induced by the surface singularities around the jet will tend to that produced by a line of singularities distributed along an appropriately defined jet path. The singularities may be sinks if there is a net inflow across the surface but they might also consist of doublets, quadrapoles and so on whose strength would be obtained by taking higher moments of the surface singularities.

If an appropriate singularity distribution could be determined either theoretically or experimentally, one might hope that the interference effects could be calculated using existing methods for calculating the load distributions on wings. Thus, the problem of jet interference in transition really reduces to determining an appropriate singularity distribution to represent the lifting jets. In order to make some progress with this fundamental problem, a great deal of experimental work has been carried out on the much simpler problem of a single jet issuing normally from a wall into a cross-flow and the remainder of this section will be devoted to this flow to try and highlight the mechanisms of jet interference in transition.

3.1 A single jet issuing into a cross-flow.

When a jet issues into a cross-flow, it is deflected downstream and its boundaries spread as a result of turbulent mixing in much the same way as occurs with a jet issuing into still air. In addition, there are a pair of contra-rotating vortex structures which develop on either side of the jet as it spreads downstream and these are certainly the most striking characteristic of the flow (see figure (19).There have been many theories developed for predicting the deflection of a jet in cross-flow and they fall into two broad categories. In the first type, the assumption is that the deflection results from the turbulent entrainment of air and they have usually been based on arguments of the "mixing of streams of ping-pong balls" variety in which the resultant jet direction is taken to be the vector sum of the jet momentum flux and the momentum flux of the entrained mainstream flow. The difficulty with these theories is that the entrainment is adjusted to give good agreement with experimental data for the jet paths and they result in entrainment rates which are very much larger than those that occur in jets in still air and in parallel moving streams. Snel's work(1974) is typical of these theories. The appropriate singularity distribution arising from models of this sort would be a distribution of sinks whose strength per unit length is proportional to the rate of entrainment. However, there is nothing in these models that can account for the vortex motions in the jet. The other class of theories for predicting jet paths make use of a cross-flow

drag on the jet analogous to the drag on a solid bluff body. However, it is necessary to use drag coefficients which seem very high in order to obtain good agreement with experiments and it is not easy with theories of this type to establish the singularity distributions necessary to calculate the external flow field. These two types of theory have also been presented in combination (for example Wooler, Burghart and Gallagher (1967)) but neither the mixing or cross-flow drag mechanisms of jet deflection seem very convincing. In the previous sections on jets issuing into still air, it was argued that the interference effects in hovering arose solely from turbulent mixing since, in this case, the potential flow would not give rise to any external flow. However, in the case of a jet in cross-flow, there is the possibility that a non-trivial potential flow solution exists in which the jet is deformed and deflected by the mainstream. Indeed, all our experience of high Reynolds number flows would suggest that where it is possible for significant pressure and inertia forces to develop, the main features of a flow can be accounted for on the basis of potential flow solutions with the possibility of having to involve real flow effects through boundary conditions. Figure (20) is a sketch of the type of potential flow solution one might obtain in which the vortex sheet separating the the mainstream from the jet flow is deformed and forces on the jet develop in much the same way as they develop as a result of the bound vorticity of a wing. Such a solution would naturally include "trailing" vorticity to ensure continuity of vortex lines with the "cross-flow" vortex lines. The highest order singularity distribution representing this flow in the far field would consist of a doublet distribution since no entrainment into the jet occurs. In fact, the effect of turbulent mixing would probably only serve to smear out the vortex sheets but one would not expect either the path of the jet or the doublet distribution to be significantly affected.

Whilst it is a simple matter to discuss the possibility of a potential flow solution, it is unfortunately difficult even to set-up the potential flow problem with the appropriate boundary conditions and there has been no significant progress in obtaining closed solutions of this type. However, a semi-empirical model can be developed which emphasises the potential flow approach to the problem and, whilst opinions about the validity of some of the arguments involved are unlikely to be universal, it serves to illustrate that the problem can be considered in a different light.

The first interesting observation that can be made is that the doublet strength at infinity downstream of a three-dimensional body in potential flow on which there is a lift L can be shown to be (see, for example, Küchemann (1978)),

$$\mu(\infty) = \frac{L}{\rho_1 U_1} \tag{3.1.1}$$

where $\mu(\infty)$ is the doublet strength of the trailing vortex sheet at infinity downstream and U_1 is the free-stream velocity. The doublet strength is given by

$$\mu = \iint y\,\omega\,dy\,dz \tag{3.1.2}$$

where the streamwise vorticity, $\omega = \left(\frac{\partial w}{\partial y} - \frac{\partial v}{\partial z}\right)$ and the integration is carried out over the entire cross-stream plane. The y and z-directions are shown in figure (20).

In the case of a jet in cross-flow, it will experience a force normal to the mainstream direction equal to the jet thrust if it is deflected through 90°. For a uniform jet, equation (3.1.1) then gives

$$\frac{\mu(\infty)}{a^2 U_1} = \pi m^2 \tag{3.1.3}$$

where $m = U_j/U_1$ is the jet to free-stream velocity ratio and a is the jet radius. As can be seen from equation (3.1.2), the direct measurement of doublet strength is a difficult and tedious exercise but a few measurements have been made by Endo and Nakamura (1965) and Thompson (1971) using five hole pitch and yaw tubes. The measurements were made at various positions along the jet path and at various values of jet to free-stream velocity ratio, m. Their results for the flow far downstream of the jet nozzle are shown in figure (21) and compared with equation (3.1.3). In all the circumstances, the agreement is remarkably good and it seems that this simple argument can account both qualitatively and quantitatively for the trailing vortex motions that can be observed in the jet.

To calculate the external flow field, the doublet distribution along the path of the jet is required. If the jet has been deflected through an angle θ, we may assume that the lift force acting on it is T(1-cos θ) where T is the jet thrust and the obvious assumption can then be made that the doublet strength at this position will still be given approximately by equation (3.1.1) so that

$$\mu(\ell) = \frac{T(1-\cos\theta)}{\rho U_1}$$

where ℓ is the distance along the jet path at which the jet has been deflected through an angle θ. In non-dimensional form,

$$\frac{\mu(\ell)}{a^2 U_1} = \pi m^2 (1-\cos\theta) \tag{3.1.4}$$

Now, in order to apply this expression to the calculation of the induced velocity field around the jet, it is necessary to know the jet path on which the place the doublet distribution. It is the most serious weakness of the present approach that it does not easily lead to a prediction of the path and, in the absence of any better guide, experimental results of jet path measurements have been used. There have been numerous measurements of jet path by Brown (1976), Chassaing et al (1974), Endo and Nakamura (1965), Graefe (1975), Thompson (1971), Jordinson (1956) and others and results have generally been obtained for the path of the maximum total head. The agreement between the path measurements from all these various

investigators is only fair but a reasonable fit to most of the data can be made by the expression

$$\frac{X_o}{m^{1.36}a} = 0.27\left(\frac{Z_o}{m^{1.36}a}\right)^3 \qquad (3.1.5)$$

where X_o and Z_o are the co-ordinates of the maximum total head jet path. Z_o is the co-ordinate normal to the wall and X_o is the co-ordinate in the downstream direction. Figure (22) shows a comparison between this expression and Thompson's data as a typical example. Also shown in figure (22) are a few results for the vortex centre paths with an expression similar to equation (3.1.5) fitted to the data. It is clear from this figure that the scale of the plume is substantial and not really small in comparison to the distance from the plume to the wall region where we are attempting to predict the pressure distribution. There is also obviously some ambiguity as to the appropriate definition of the jet path. However, using the expressions for the peak total head paths and the vortex centre paths enables the angle θ and the distance ℓ along the jet path in equation (3.1.4) to be calculated and figure (23) shows equation (3.1.4) compared with experimental data for doublet strengths at different positions along the jet paths. The use of the vortex centre paths gives marginally better agreement with equation (3.1.4) than using the peak total head paths but it would be unwise to attach too much significance to this. The important point is the the doublet strenghts measured are clearly close to those given by the simple argument behind equation (3.1.4).

Using equation (3.1.4) and the empirical expression for the vortex centre paths, it is now possible to calculate the pressure distributions on the wall around the jet. Figures (24) and (25) show a comparison between the experimental distributions of Bradbury and Wood (1964) and these calculated distributions for velocity ratios m of 4 and 8 respectively. There is a reasonable measure of agreement between the experimental and calculated distributions and it provides further evidence that however deficient the prsent model might be, the doublet strength along the jet cannot be too different from that predicted by equation (3.1.4). Further, if it is assumed that the entrainment due to turbulent mixing is not very different from that of a jet issuing into still, some allowance for entrainment can be made by including a distribution of sinks along the jet path with a constant strength given by Ricou and Spalding's expression - equation (2.1.4). Figures (26) and (27) show the effect of the addition of these sinks to the predicted distributions. As might be expected, they swing the isobars upstream but they do not particularly improve the overall agreement with the experimental distributions. Moreover, their effect on the overall force on the wall is very small which is consistent with the assumption that turbulent mixing is not the dominant factor in this problem.

An interesting feature of these results is that if the jet paths are of the general form

$$\frac{X_o}{g(m)a} = \text{Function of}\left(\frac{Z_o}{g(m)a}\right)\text{only} \qquad (3.1.6)$$

where g(m) is a function of m only, then it is easy to demonstrate that the induced velocity components arising from the doublet distribution given by equation (3.1.4) will have a similarity form which gives on the wall

$$\frac{u_i}{U_1}\left(\frac{g(m)}{m}\right)^2 = \text{Function of}\left(\frac{r}{g(m)a}, \psi\right)\text{only} \qquad (3.1.7)$$

where r and ψ are the polar co-ordinates of a point on the wall. u_i is a particular velocity component induced at that point. . This may be taken one stage further because the bulk of the force on the wall arises from regions where the pressure coefficient based on the free-stream velocity is small. Under these circumstances,

$$C_p \approx \frac{2u}{U_1}$$

where u is the x-component of the induced velocity. The force on circular regions around the jet can be presented in the form of a suction force coefficient defined as

$$C_s = \frac{\text{Suction force}}{\frac{1}{2}\rho U_1^2 \pi a^2} = -\frac{1}{\pi}\int_1^{r/a}\int_0^{2\pi} C_p \frac{r}{a}\, d\left(\frac{r}{a}\right) d\psi \qquad (3.1.8)$$

In terms of the similarity variables, this may be written

$$C_s = \frac{2m^2}{\pi}\left[\int_0^{2\pi}\int_0^{r/(g(m)a)}\left(\frac{g(m)}{m}\right)^2\frac{u}{U_1}\cdot\frac{r}{g(m)a}\, d\left(\frac{r}{g(m)a}\right)d\psi - \int_0^{2\pi}\int_0^{1/g(m)}\left(\frac{g(m)}{m}\right)^2\frac{u}{U_1}\frac{r}{g(m)a}\, d\left(\frac{r}{g(m)a}\right)d\psi\right]$$

Over the range of velocity ratios m of normal interest (say from 2 to 20) and radius ratios r/a greater than 5, say, the second term on the right hand side turns out to be small compared to the first term so that

$$C_s \approx \frac{2m^2}{\pi}\int_0^{2\pi}\int_0^{r/(g(m)a)}\left(\frac{g(m)}{m}\right)^2\frac{u}{U_1}\frac{r}{g(m)a}\, d\left(\frac{r}{g(m)a}\right)d\psi \qquad (3.1.9)$$

or

$$\frac{C_s}{m^2} = \text{Function of}\left(\frac{r}{g(m)a}\right)\text{only} \qquad (3.1.10)$$

If an expression of the form of equation (3.1.5) is taken for the jet path, $g(m) = m^{1.35}$ and we obtain

$$m C_p = \text{Function of} \left(\frac{r}{m^{1.35} a}, \psi \right) \text{only} \tag{3.1.11}$$

$$\frac{C_s}{m^2} = \text{Function of} \left(\frac{r}{m^{1.35} a} \right) \text{only} \tag{3.1.12}$$

The importance of these similarity results is that, if they have any validity, the induced velocity field and the suction force on the wall will depend not on the jet velocity and jet radius as separate parameters but only on them in the combination given in equations (3.1.11) and (3.1.12). Thus, the flow field around a jet of some particular radius or velocity ratio can be made equivalent to a jet of some other radius and some other suitably scaled velocity ratio. An analogous result to the present similarity expressions can be found in the theory of jet flaps where it can be shown that provided the thickness of the jet sheet is small, the only parameter of the jet that appears in the theory is the jet momentum flux and neither the jet thickness or its velocity appear as separate parameters. However, the physical arguments leading to the similarity result in jet flap theory is more soundly based than those presented here for a circular jet. In this latter case, the form of the similarity result arises simply from the form of the empirical jet path expression used and this has no obvious physical significance. Nevertheless, the concept is interesting and, from experience of similar problems, it seems not unlikely that in the event of jet interference being more clearly understood, similarity laws similar to the present relationships may still be found to apply.

Figure (28) shows a wide range of experimental suction force coefficients for different velocity and radius ratios plotted in the form suggested by equation (3.1.12). Also shown is the theoretical result obtained from using the vortex centre path expression and the doublet strength equation (3.1.4) in equation (3.1.9). The experimental results are not obviously inconsistent either with the general form of the similarity result or with the predicted curve but it should be noted that there is a good deal of scatter particularly in the results of Fearn and Weston (1975). In working out these results, it appears that insufficient care has sometimes been taken in the definition of the reference static pressure so that the integration of the loads at large distances from the nozzle are subject to a good deal of uncertainty. Thus, the agreement between the results of different authors in this apparently straightforward experiment is less than one might expect and, indeed, it is found that in some cases, there is apparently no limit to the force experienced on the wall as the limits of integration are extended further from the jet nozzle!

As far as the detailed pressure coefficients are concerned, they collapse less well on the basis of the similarity argument. But, it can be shown that although the sinks representing entrainment (which do not conform to the same similarity argument) only contribute a few percent to the overall force, they do influence the pressure coefficient distributions sufficiently to prevent close agreement with the similarity result. It is possible to make some crude allowance for this effect and Bradbury (1968) has shown that if this is done, the pressure coefficient distributions collapse on the basis of the similarity argument to about the same extent as the overall suction force coefficents.

Of course, the object of the present exercise was to produce a singularity distribution that could be used in calculations on finite wings. The assumption would need to be made that the jet paths obtained from experiments on flat plates could be used for jets issuing from wings. The problem of multi-jet geometries creates even more difficulties. However, Wooler et al (1967) and Ziegler and Wooler (1971) have applied their singularity representation of jets to finite wings including multi-jet arrangements and the fact that their approach is conceptually different from the present one should not obscure the point that they are demonstrating the possibility of jet interference calculations on more practical geometries.

The final point to note in this section is that the similarity argument can be applied directly to finite wings. For a given planform geometry but with different diameter jet nozzles, the equivalent similarity result is

$$\frac{\Delta L}{T} = \text{Function of} \left(\frac{1}{m^{1.35}} \sqrt{\frac{A_p}{A_J}} \right) \text{only} \tag{3.1.13}$$

where ΔL is the interference lift loss and A_p, A_J are the planform areas and jet nozzle areas respectively. The final figure (29) shows results from Williams and Wood (1966) for a delta wing model with two different diameter single jets plotted in this way. It cannot be claimed that the collapse is particularly good but it would at least enable test results on a model with one diameter of jet nozzles to be used to estimate the lift losses on a similar planform model but with different nozzle areas.

4. Concluding remarks.

In this paper, some attempt has been made to discuss various aspects of jet dynamics relevant to VTOL aircraft. It will be noted that some emphasis has been put on potential flow arguments wherever they seem appropriate. In part, this has been a deliberate ploy to offset the tendency by some to assume that in all situations where there is a turbulent shear layer, the flow must be treated as if the turbulence is always the dominant phenomenon. The discussion has also centred on those topics which the author has had some direct experience of and the neglect of other topics must not be taken as an assumption that they are considered less important than those covered in this paper. In particular, there is a great need for work on wind tunnel interference effects on VTOL models. Although much has been published on this topic, a reliable method of correcting VTOL model results for wind tunnel blockage is still not available. It is known that in tests in which the lifting jets impinge on the tunnel walls, a complete breakdown of the working section flow can occur due to the forward flow and the subsequent separation from the tunnel walls of the impinging jets. Some progress with establishing a criterion for when this occurs has been made (see, for example, Owen (1970) but serious interference effects occur well before this situation is

reached. There is now some work on comparative tests on VTOL models in different wind tunnel working sections (e.g. Trebble (1978)) but careful comparative tests with some standard model in a range of wind tunnels equipped for VTOL testing would still be a useful exercise.

As far as topics covered in this paper are concerned, there are some recommendations for future work that can be made particularly in the area of jet interference effects in transition. There are an increasing number of wind tunnels equipped with computer controlled traversing gears and on-line data processing systems and the possibility of making detailed flow surveys is not as daunting as it once was. Therefore, a most interesting experiment would be to extend the type of work carried out by Endo and Nakamura (1965) and Thompson (1971) in which the complete vector mean flow field in a deflecting jet is measured. These results would provide further direct experimental data on the singularity distribution and, for all its deficiences, the experiments are probably best carried out still with a conventional five hole pitch and yaw tube.

The final recommendation is directed at those who are working in the field of turbulent flow prediction methods. Having implied that possibly too much emphasis is sometimes placed on the contributions of turbulence to many aerodynamic problems, it has to be acknowledged in contradistinction to this that workers in this field are attempting solutions to flows of ever increasing complexity. In the present context, it should be noted that Patankar, Basu and Alpay (1977) and Jones and McGuirk (1980) have obtained numerical solutions for jets in a crossflow using k-ϵ turbulence model equations. Whatever criticisms may be levelled at the turbulence models used by these authors, it is nevertheless the case that they are numerically solving the full three-dimensional equations of motion. If the emphasis of this present paper is correct, the turbulent mixing is not an important characteristic in the VTOL jet interference in transition so that it may be that their solutions are giving singularity distributions and indeed the external flow field that are largely independent of the turbulence model used.The above authors have been aiming their work at problems rather different from jet interference and, therefore, they have not computed quantities like the doublet strengths or the pressure distributions around the jet nozzles. These would be interesting calculations to carry out.

Acknowledgements.

The author would like to acknowledge the many helpful discussions on jet interference with E.C. Maskell and P.B. Earnshaw at R.A.E. Farnborough. I would also like to acknowledge the contributions made by members of various ARC committees. In every case, I am very grateful for their help whilst exonerating them from responsibility for any of the more bizarre opinions expressed in this paper.

References.

Bradbury,L.J.S. & Wood, M.N.	1964	Static pressure distribution around a circular jet exhausting normally from a plane wall into an airstream. RAE TN Aero 2978.
Bradbury,L.J.S.	1968	Similarity laws in jet interference. ARC 30572, FM 3991.
Bradbury,L.J.S. & Khadem, H.	1975	The distortion of a jet by tabs. Journal of Fluid Mechanics, Vol.77, pp.473-497.
Brown, D.	1968	The circular jet in a uniformly sheared flow. Ph.D. thesis, University of Bristol.
Chassaing,P, George,J Clavia,A & Sananes, F.	1974	Physical characteristics of subsonic jets in a cross-stream. Journal of Fluid Mechanics, Vol62, pp.41-64
Endo,H & Nakamura,M.	1965	Bending and development of three-dimensional jets in crosswind. Technical Report of the National Aerospace Lab. TR-216
Fearn, R.L. & Weston, R.P.	1975	Induced pressure distributions of a jet in crossflow. NASA TN D-7916
Gentry,G.L. & Margason, R.J.	1966	Jet induced lift losses on VTOL configurations hovering in and out of ground effect. NASA TN D-3166.
Graefe,H.J.	1974	Analyse des strömungsfeldes von querangeblaseren freistrahlen nach strömungsfeldmessungen. DLR-Forsehungsbericht 75-14
Hargreaves, J.J.	1970	Design, development and calibration of a jet efflux plenum chamber model for use in V/STOL research models. British Aircraft Corporation Report AXR-23
Jordinson, J	1956	Flow in a jet directed normal to the wind. ARC R & M 3074.
Jones, W.P. & McGuirk, J.J.	1980	Computation of a round turbulent jet discharging into a confined crossflow. Turbulent Shear Flows 2, Springer-Verlag, Berlin.
Keffer, J.F. & Baines, W.D.	1963	The round jet in a crossflow. Journal of Fluid Mechanics, Vol.15, pp.481-496.
Krothapalli,A Baganoff,D & Karamcheti,K.	1981	On the mixing of a rectangular jet. Journal of Fluid Mechanics, Vol.107,pp.201-220.
Küchemann, D.	1978	The aerodynamic design of aircraft. Pergammon Press.

Kynstautus, R.	1964	The turbulent jet from a series of holes in a line. Aeronautical Quarterly Vol.15,pp.1-28.
Martin, L.	1963	An investigation into some of the parameters involved in simulating a hot jet blowing at 90° to a two-dimensional wing undersurface. ARC paper 38141.
Mayson,I Ogilvie,F.B. & Harris, K.D.	1971	An investigation under static external flow conditions of the axial force induced on a circular flat plate surrounding simple uniform and co-axial jets exhausting normally to the plates. H.S.A. Hatfield Research Report 1010.
McGuirk, J.J. & Rodi, W.	1977	The calculation of three-dimensional turbulent free jets. 1st Symposium on Turbulent Shear Flows. University of Pennsylvania.
Owen, T.B.	1970	Wind tunnel and other facilities required for V/STOL model testing. RAE TM 1198.
Patankar, S.V. Besu,D.K. & Alpay, S.A.	1977	Prediction of the three-dimensional velocity field of a deflected jet. Journal of Fluids Engineering, December, pp.758-762.
Phipps, R.S.B.	1981	The behaviour of jets with a variable velocity profile in crossflow. Ph.D. thesis, University of Bristol.
Ricou,F.P. & Spalding, D.B.	1961	Measurements of entrainment by axisymmetric turbulent jets. Journal of Fluid Mechanics, Vol.2,pp.21-32.
Skifstad, J.G.	1970	Aerodynamics of jets pertinent to VTOL aircraft. Journal of Aircraft, Vol.7, No.3,pp.193-204
Snel, H.	1974	A model for the calculation of the properties of a jet in crossflow. NLR TR 74080, Netherlands.
Taylor, P.	1977	An investigation of an inclined jet in a crosswind. Aeronautical Quarterly, February, pp.51-58.
Thompson, A.M.	1971	The flow induced by jets exhausting normally from a plane wall in a cross-stream. Ph.D. thesis, Imperial College.
Trebble, W.J.G.	1978	Investigation of the effect of tunnel walls on the flow near a model containing a lifting jet. RAE TM Aero 1781
Williams, J. & Wood, M.N.	1966	Aerodynamic interference effects with jet-lift V/STOL aircraft under static and forward speed conditions. RAE TR 66403.
Wooler, P.T. Burghart, G.H. & Gallagher, J.T.	1967	The pressure distribution on a rectangular wing with a jet exhausting normally into an airstream. AIAA Paper 67-1, 5th Aerospace Sciences Meeting, New York.
Ziegler,H & Wooler, P.T.	1971	Multiple jets exhausting into a crossflow. Journal of Aircraft, June, pp.414-420.

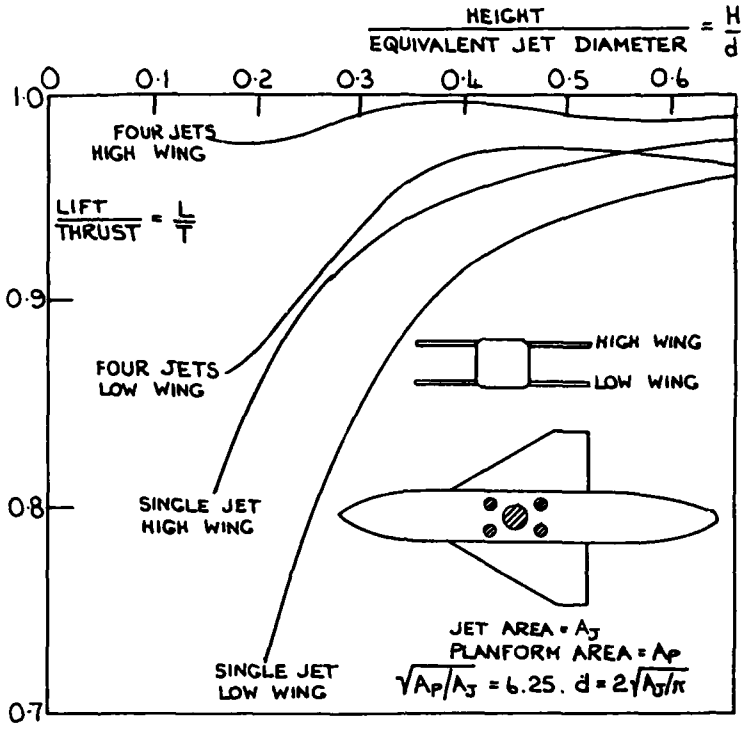

FIG.1 LIFT LOSSES HOVERING IN GROUND EFFECT

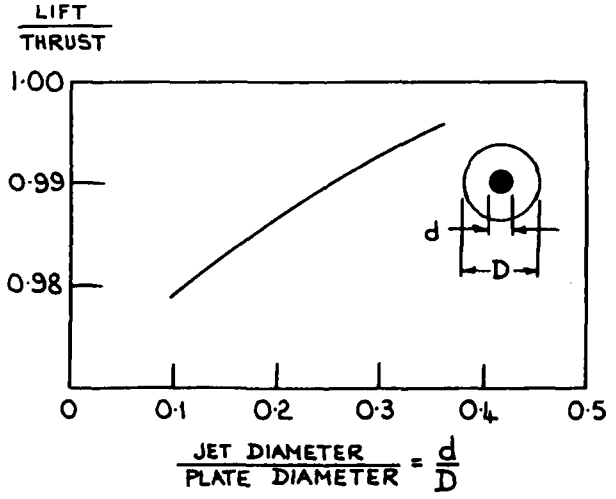

FIG. 2 LIFT LOSSES HOVERING OUT OF GROUND EFFECT.

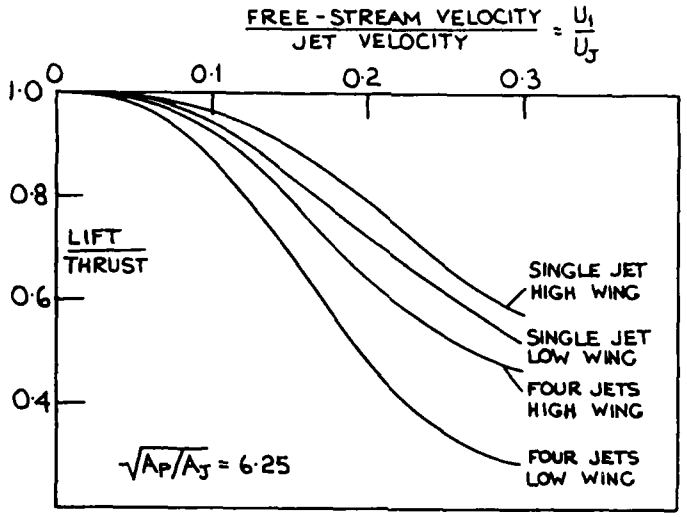

FIG.3 LIFT LOSSES IN TRANSITION

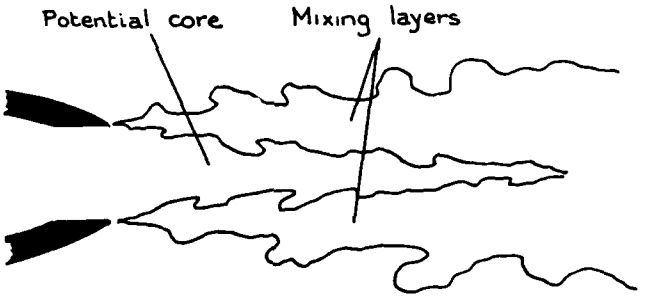

(a) Subsonic

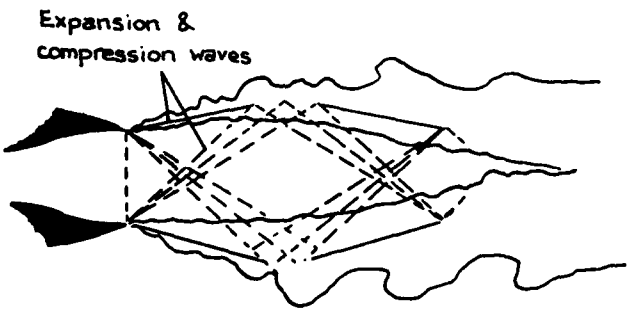

(b) Supersonic.

FIG.4 SKETCH OF A SUBSONIC AND A SUPERSONIC JET.

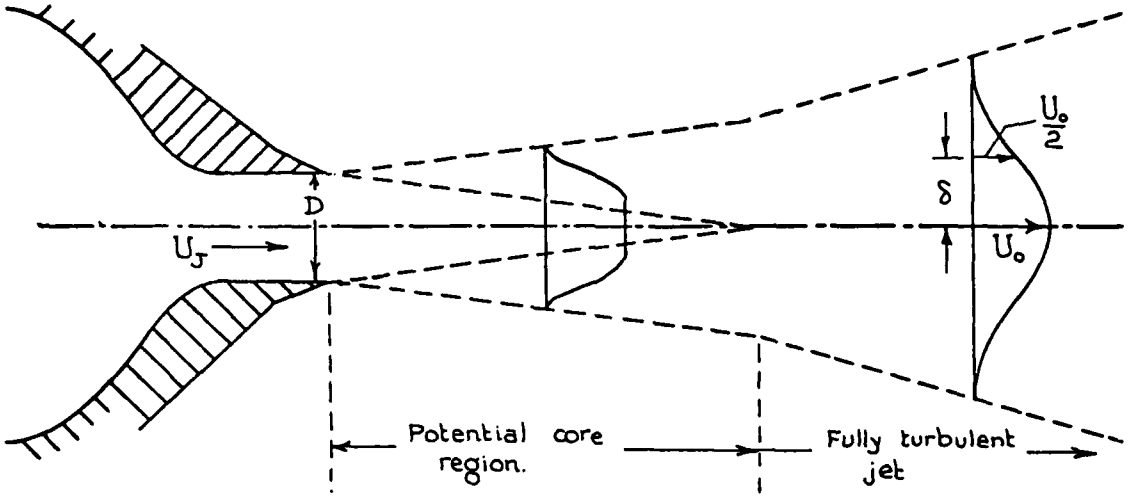

FIG.5 THE DEVELOPMENT OF A 'CLEAN' JET.

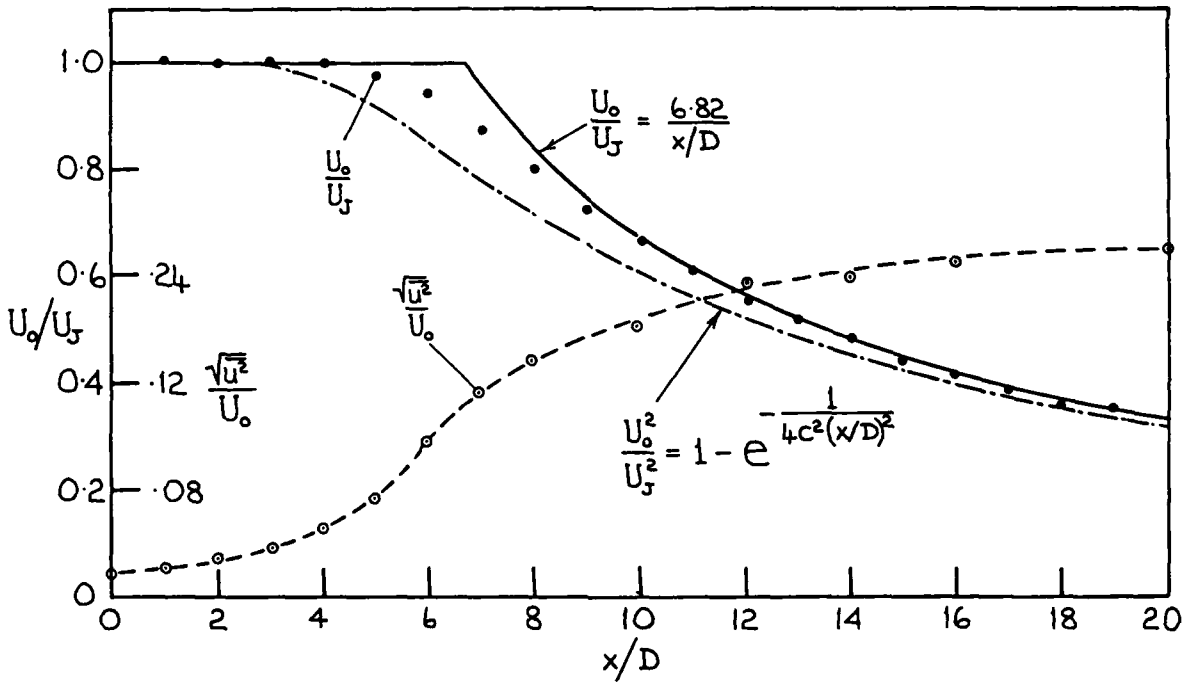

FIG. 6 MEAN VELOCITY AND TURBULENT INTENSITY VARIATION ON THE CENTRE-LINE OF A JET.

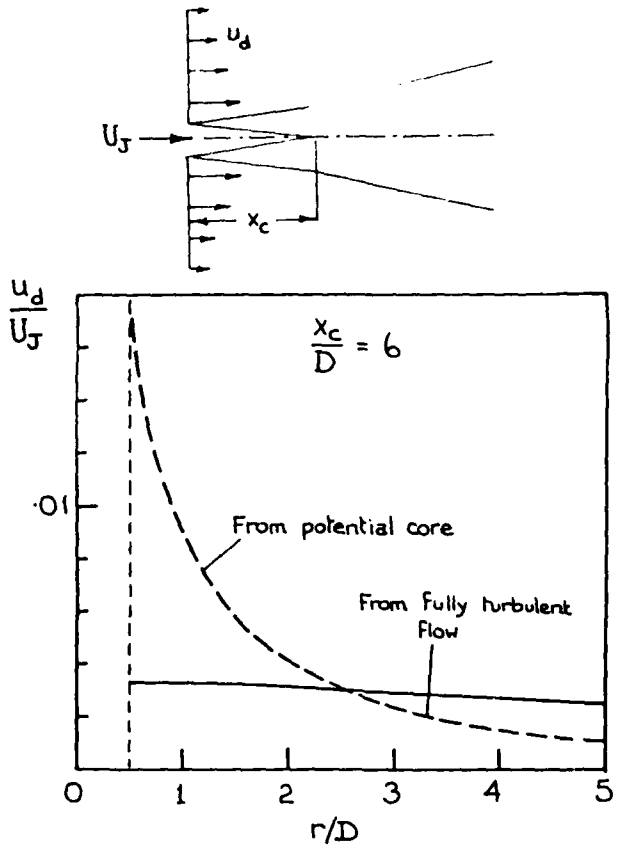

FIG. 7(a) DOWNWASH DUE TO ENTRAINMENT INTO A JET – $x_c/D = 6$.

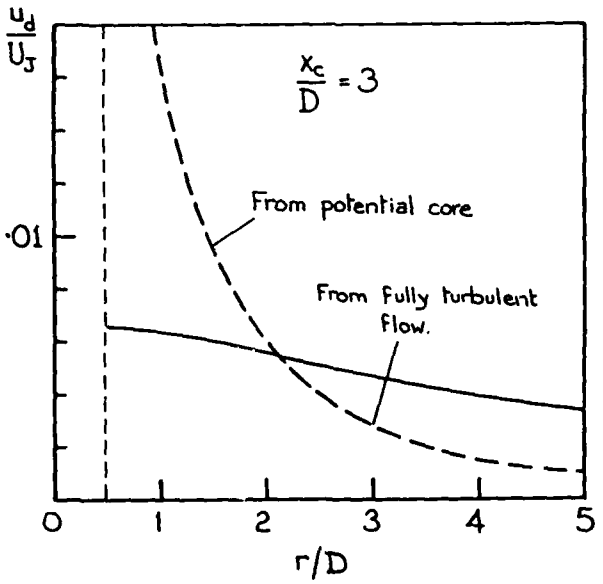

FIG. 7(b) DOWNWASH DUE TO ENTRAINMENT INTO A JET – $x_c/D = 3$.

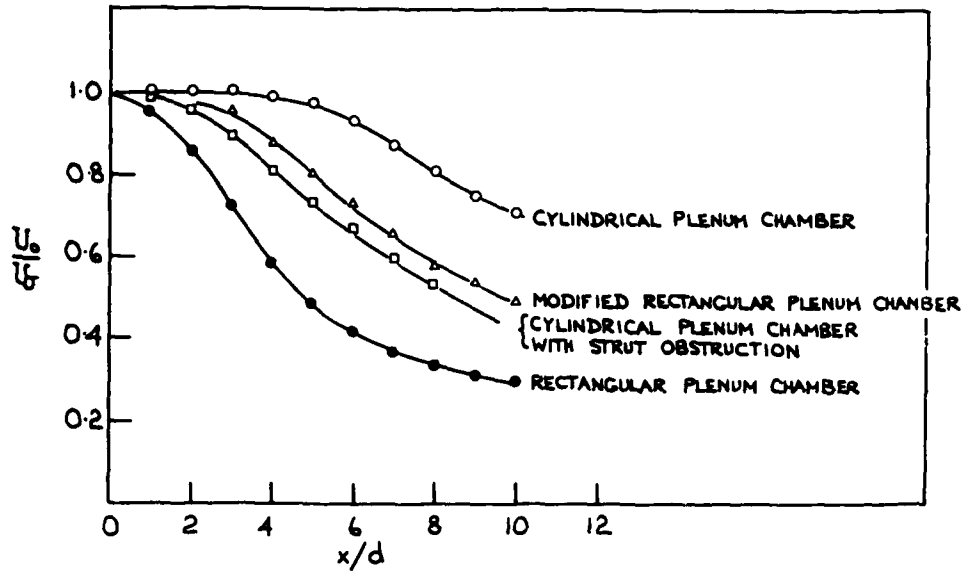

FIG.8 THE DECAY OF THE JET CENTRE-LINE MEAN VELOCITY FROM GENTRY & MARGASON (1966)

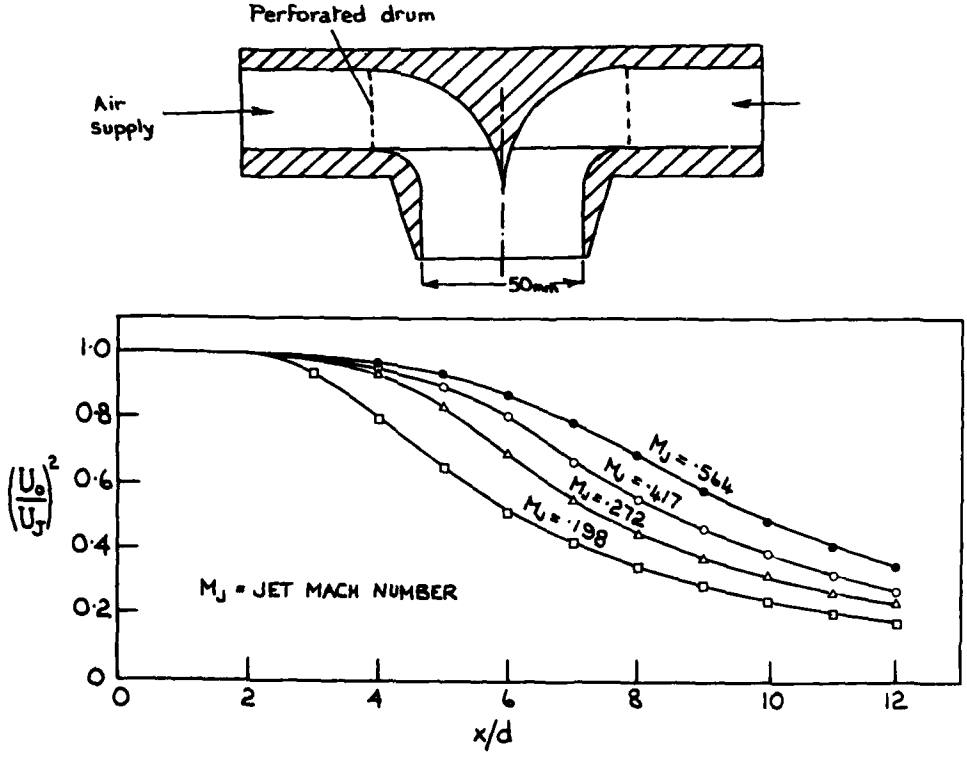

FIG.9 THE DECAY OF JET CENTRE-LINE MEAN VELOCITY FROM HARGREAVES (1970)

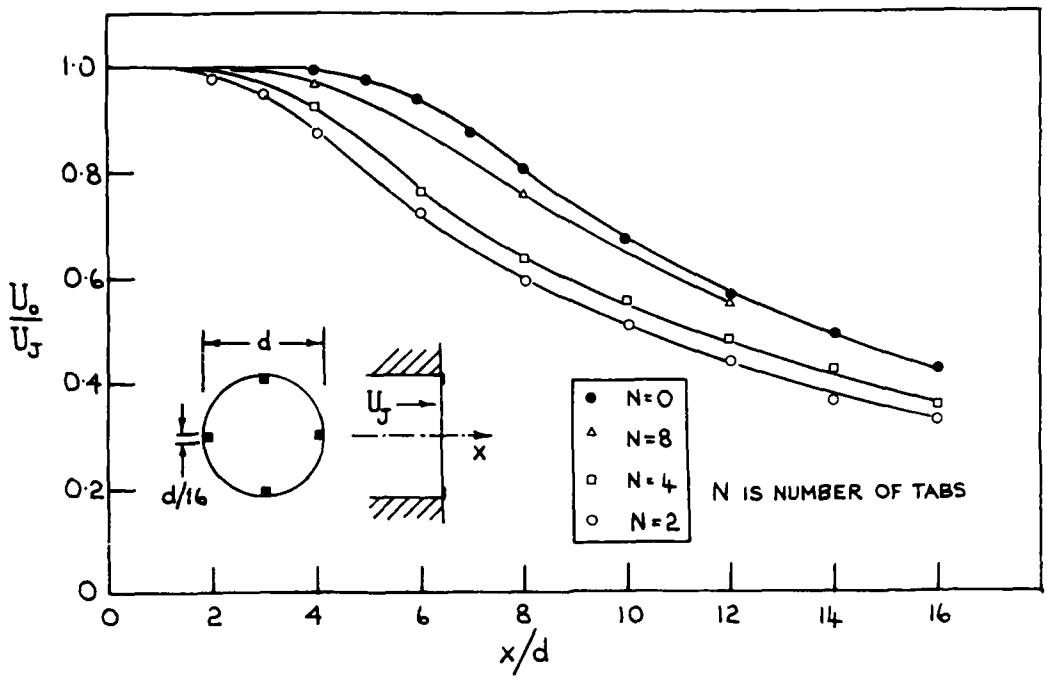

FIG. 10 THE EFFECT OF SQUARE TABS ON THE DECAY OF THE JET CENTRE-LINE MEAN VELOCITY.

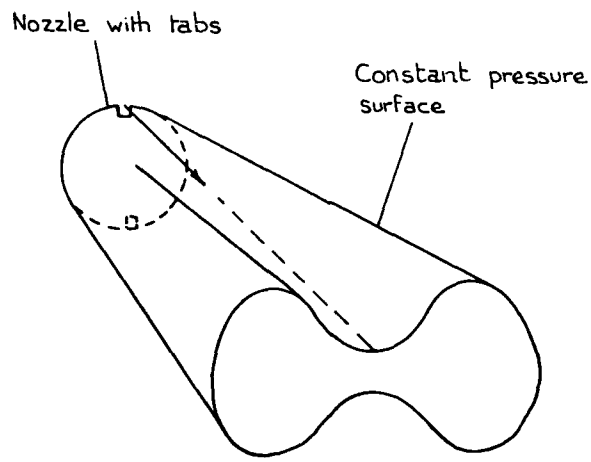

FIG. 11 DISTORTION OF A POTENTIAL FLOW JET DUE TO CIRCUMFERENTIAL VARIATIONS IN NOZZLE FLOW ANGLE.

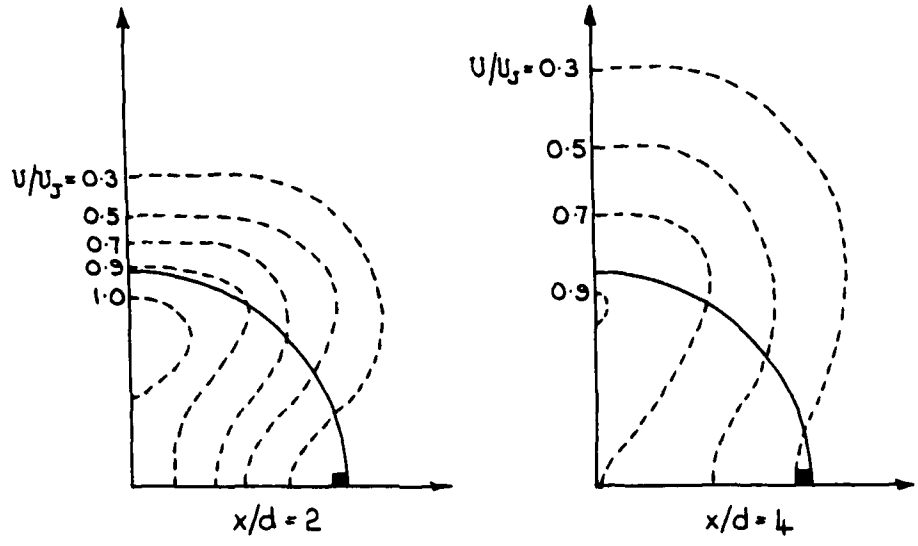

FIG. 12 CONSTANT VELOCITY CONTOURS DOWNSTREAM OF A JET WITH TWO TABS

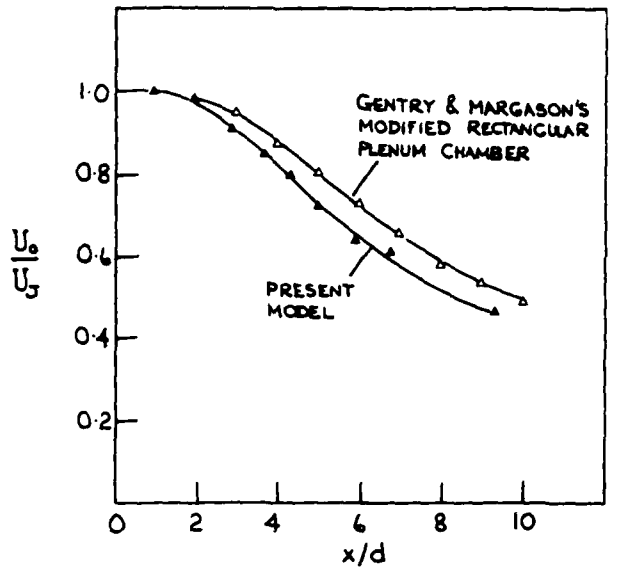

FIG. 13 JET CENTRE-LINE VELOCITY DECAY ON RECONSTRUCTED GENTRY & MARGASON MODEL.

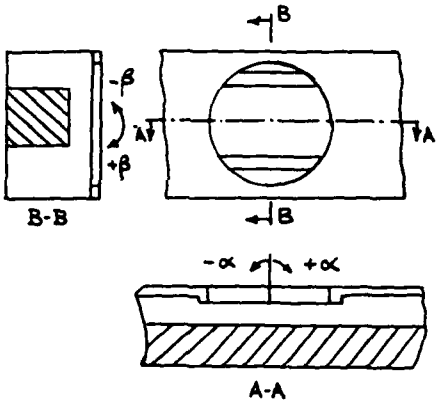

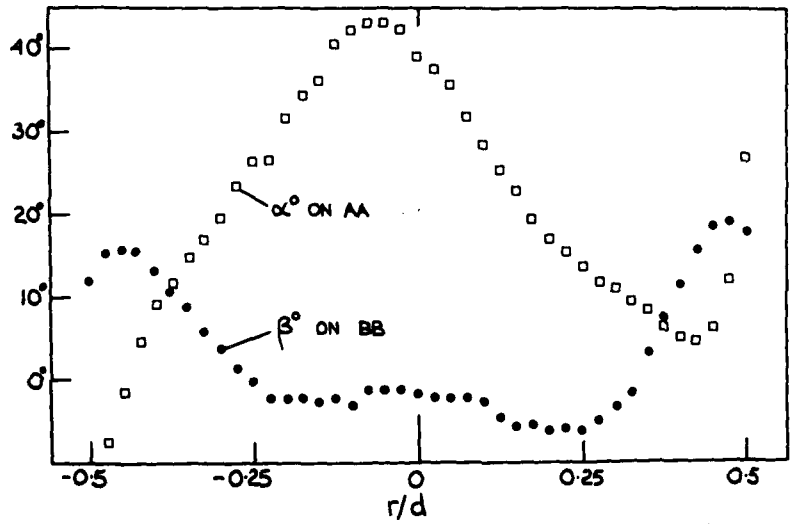

FIG. 14 FLOW ANGLES IN A JET NOZZLE OF THE GENTRY & MARGASON TYPE (x/d = 0.1)

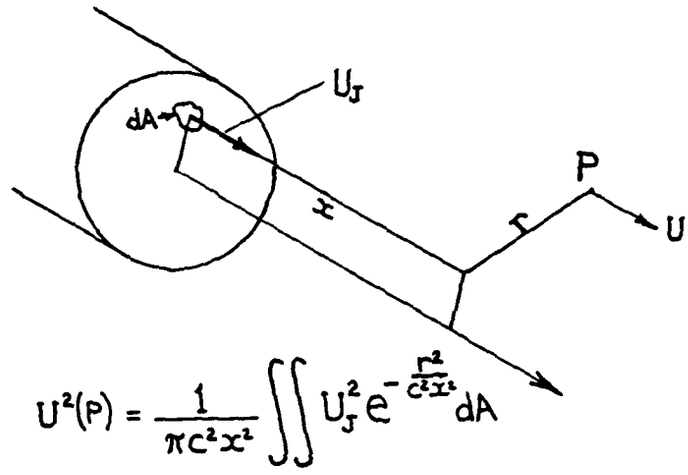

FIG. 15 REICHARDT'S METHOD FOR JETS.

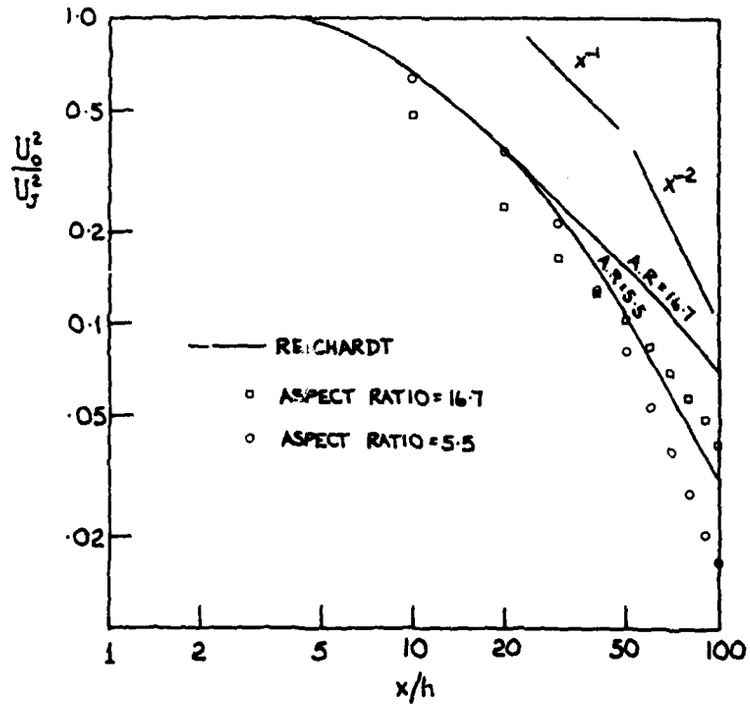

FIG. 16 DECAY OF CENTRE-LINE VELOCITY IN A RECTANGULAR JET.

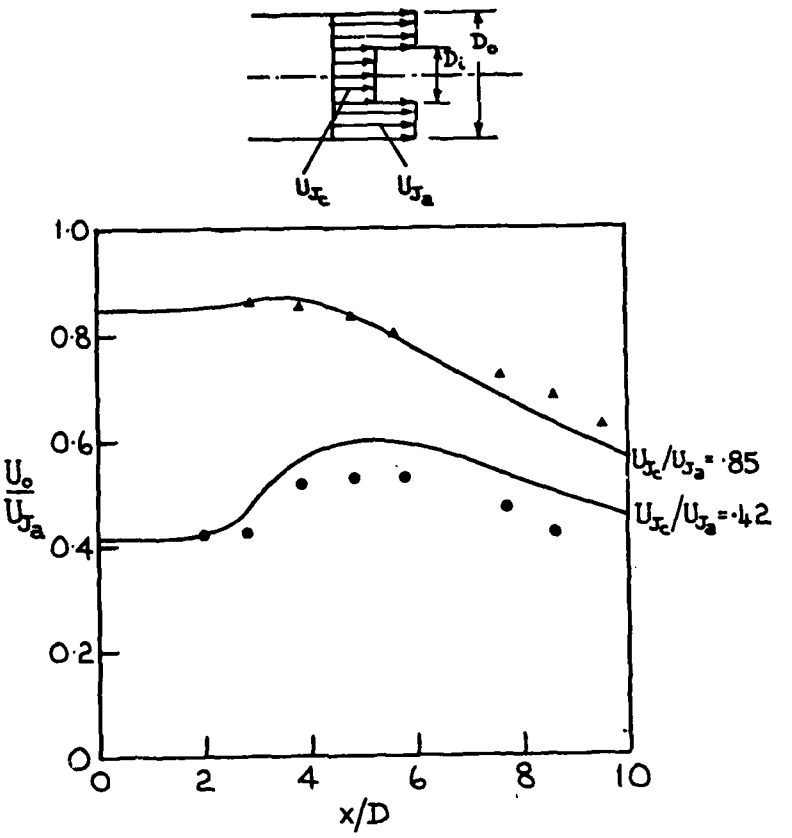

FIG.17 MEAN VELOCITY VARIATION ON THE CENTRE-LINE OF NON-UNIFORM JETS.

● — U_{J_c}/U_{J_a} = 0.42
▲ — U_{J_c}/U_{J_a} = 0·85
} Mayson, Ogilvie, Harris

——— Reichardt's method.

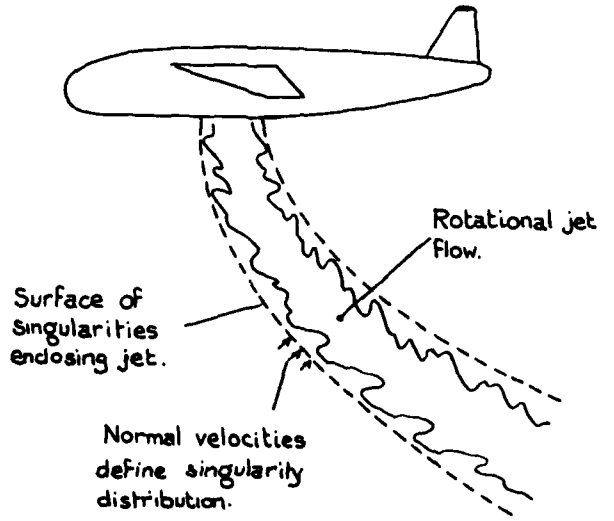

FIG. 18 VTOL AIRCRAFT RANSITION

FIG. 19 FLOW VISUALISATION OF A JET IN CROSSFLOW
(Due to Poisson-Quinton)

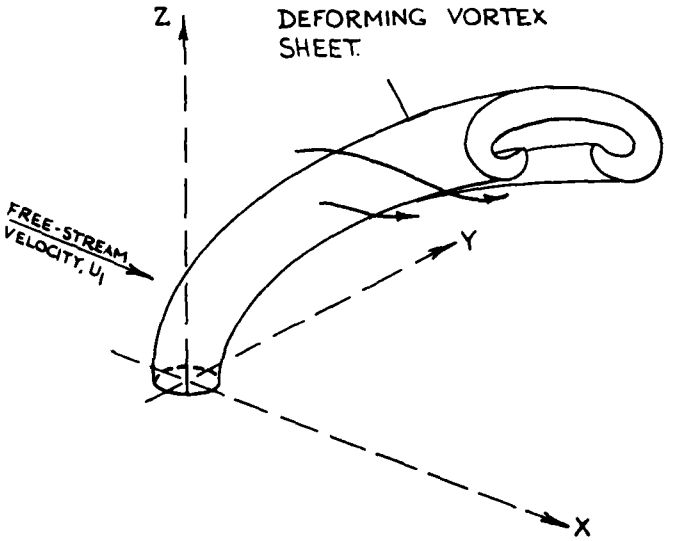

FIG. 20 POTENTIAL FLOW JET IN A CROSS-FLOW

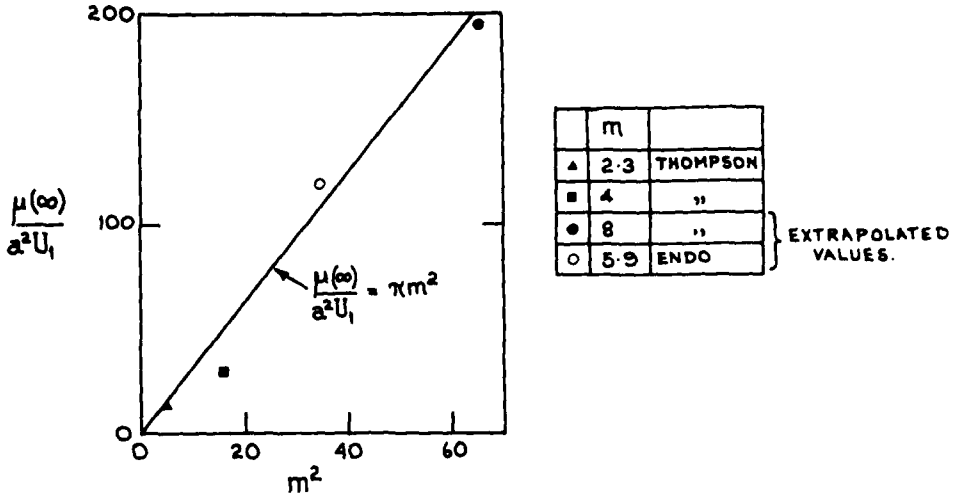

FIG. 21 ASYMPTOTIC DOUBLET STRENGTH DOWNSTREAM OF THE JET NOZZLE.

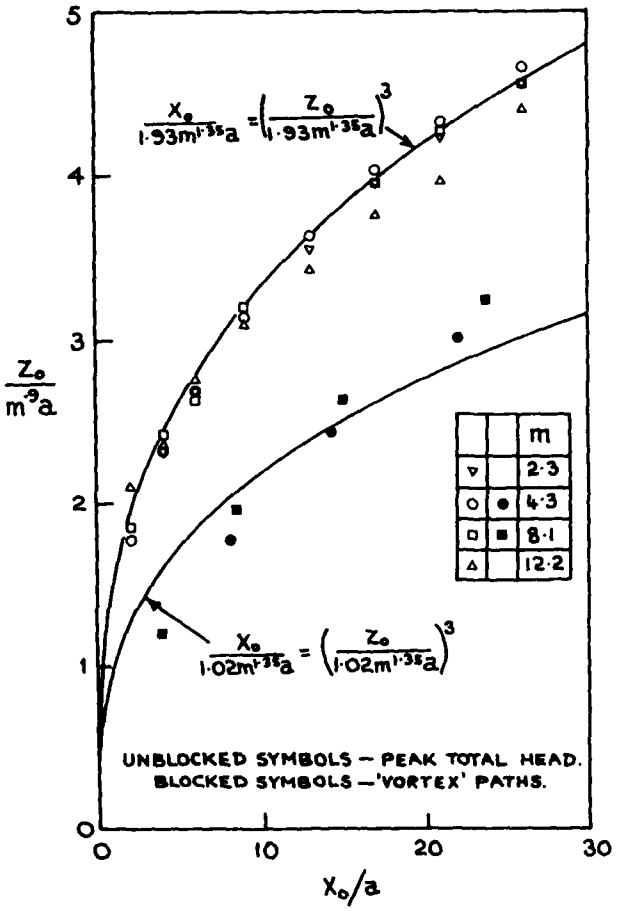

FIG. 22 JET PATHS FOR CIRCULAR NOZZLES. (THOMPSON'S DATA).

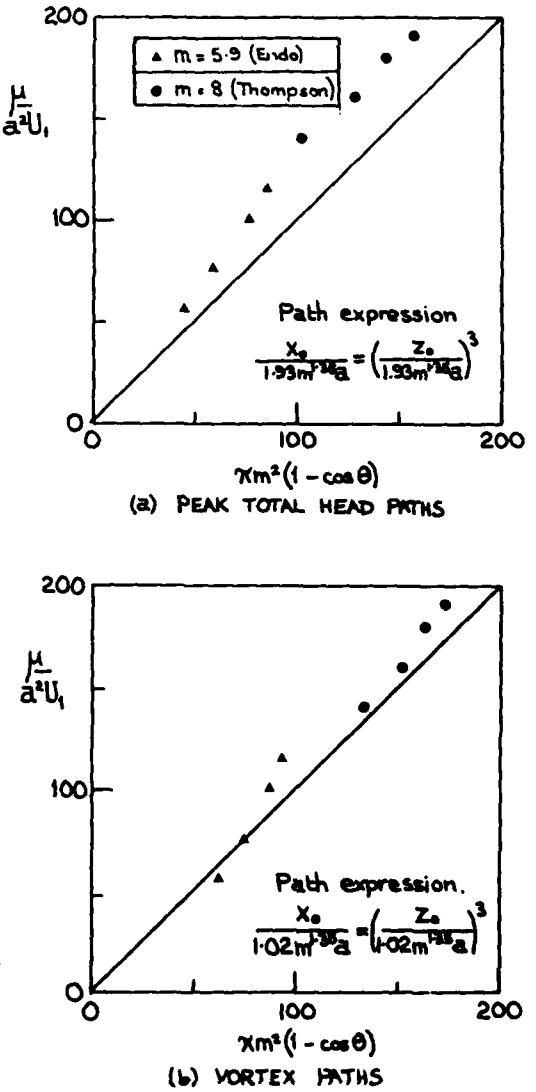

FIG. 23 DOUBLET DISTRIBUTION ALONG JET PATHS.

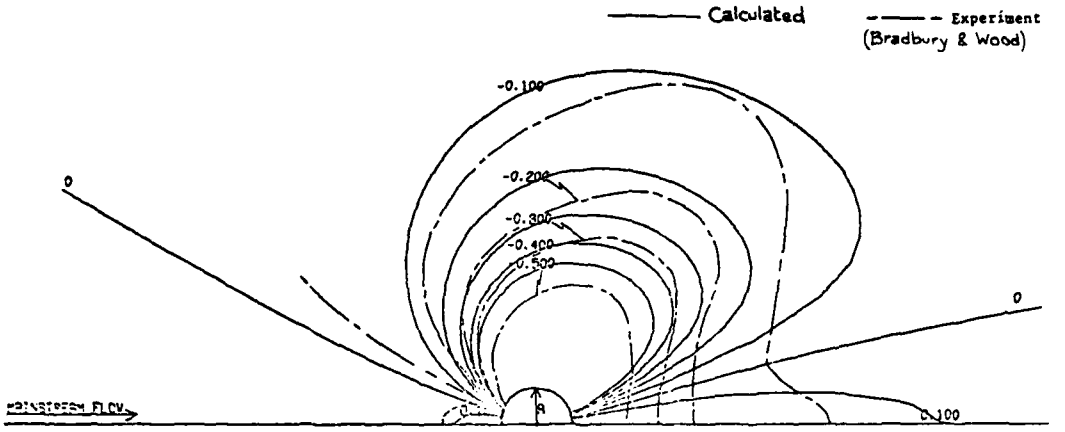

FIG. 24 COMPARISON BETWEEN CALCULATED AND EXPERIMENTAL PRESSURE DISTRIBUTIONS AROUND A JET. (m = 4. VORTEX PATHS)

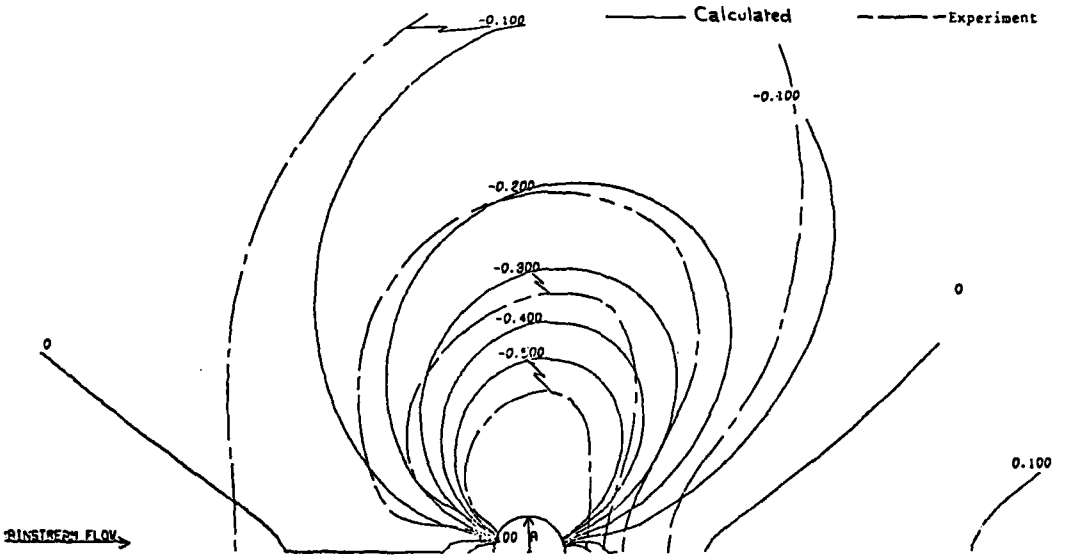

FIG. 25 COMPARISON BETWEEN CALCULATED AND EXPERIMENTAL PRESSURE DISTRIBUTIONS AROUND A JET. (m = 8 VORTEX PATHS)

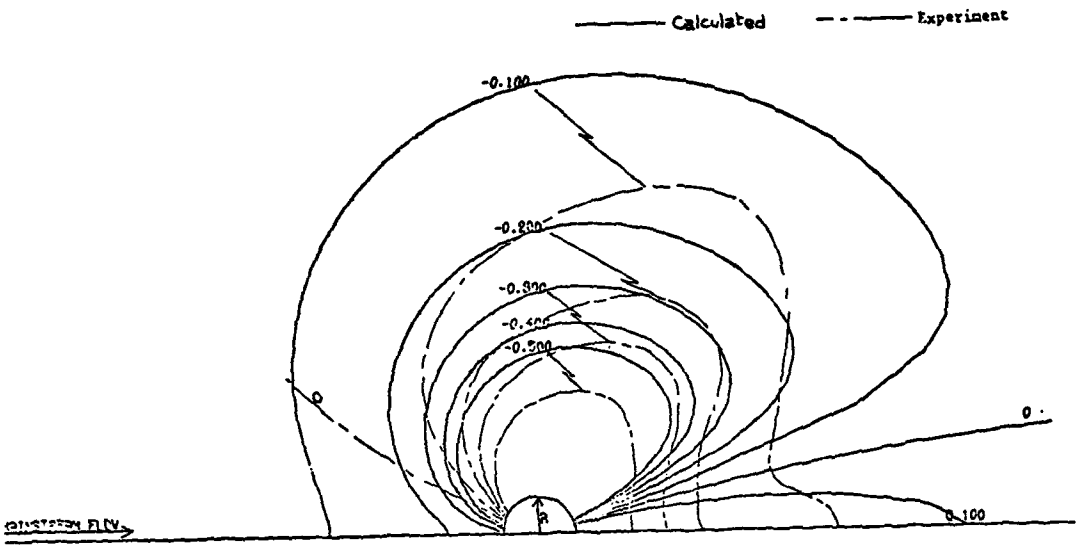

FIG. 26 COMPARISON BETWEEN CALCULATED AND EXPERIMENTAL PRESSURE DISTRIBUTIONS AROUND A JET (m=4 VORTEX PATHS WITH SINKS)

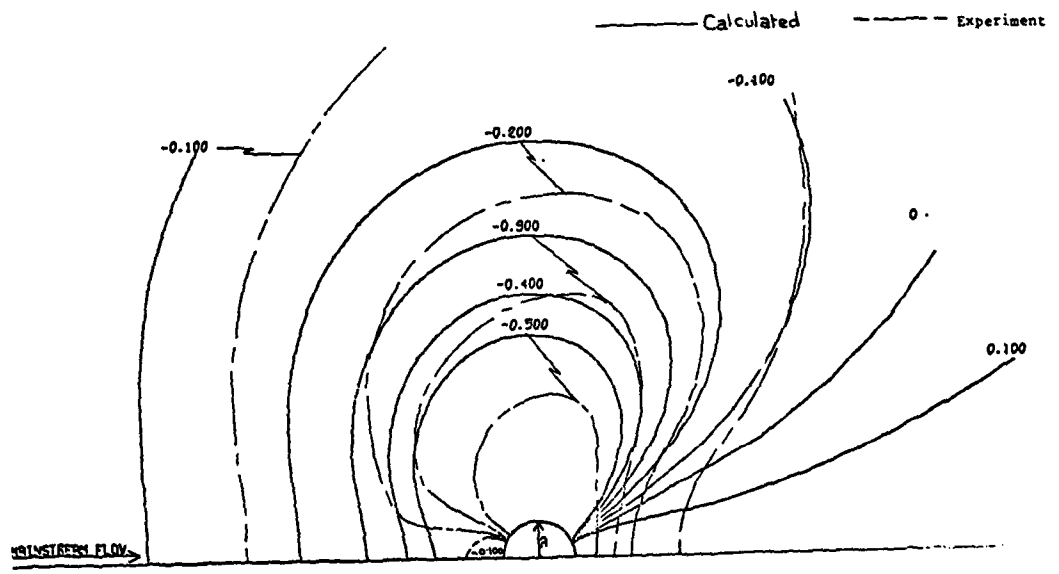

FIG. 27 COMPARISON BETWEEN CALCULATED AND EXPERIMENTAL PRESSURE DISTRIBUTIONS AROUND A JET (m=8 VORTEX PATHS WITH SINKS)

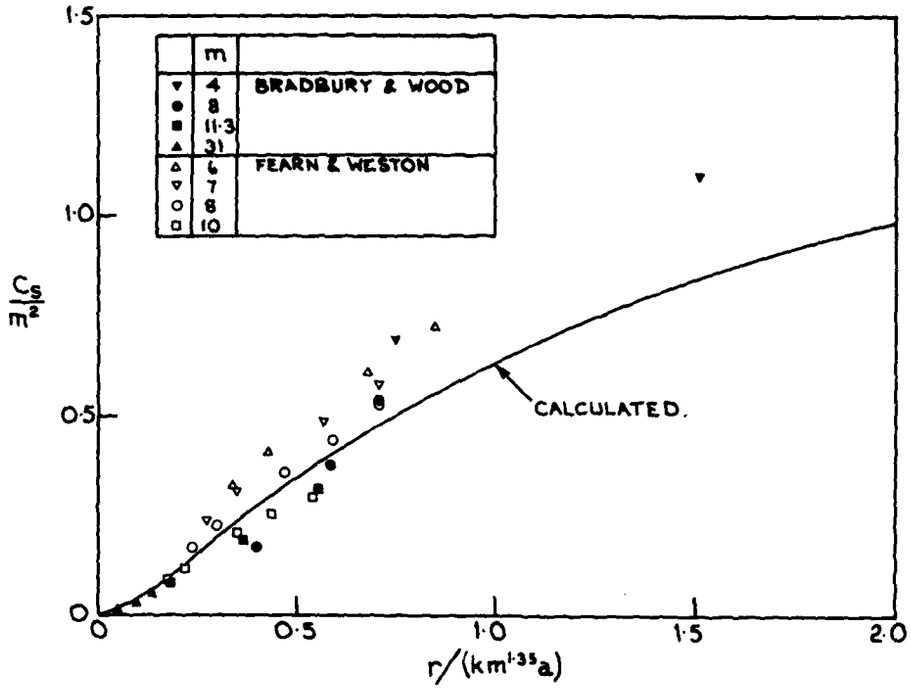

FIG. 28 SUCTION FORCE COEFFICIENTS IN SIMILARITY FORM.
(USING VORTEX PATHS WITH k = 1·02)

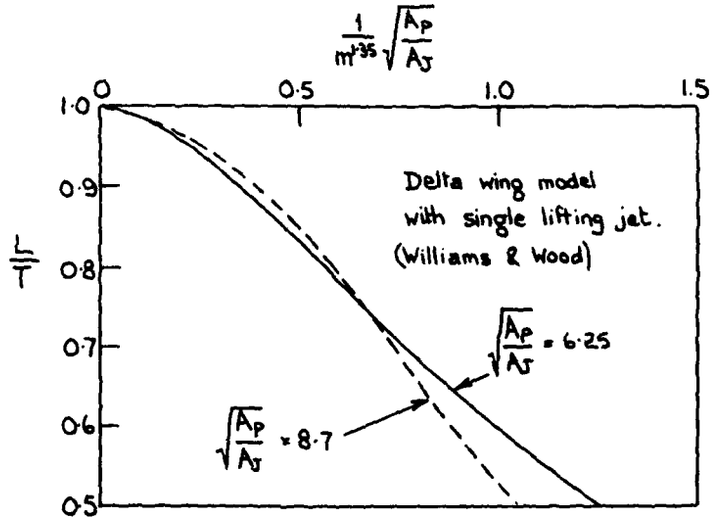

FIG. 29 LIFT LOSS ON A VTOL MODEL IN SIMILARITY CO-ORDINATES

JET INTERACTIONS WITH NEIGHBOURING SURFACES

by Prof. Dr Ing. J.Barche
D.M.V., Voorstenweg 31
8316 PR Marknessee, P.O. Box 175
8300 AD Emmeloord, The Netherlands.

SUMMARY

The present understanding and prediction methods on jet interactions with neighbouring surfaces are briefly reviewed with special attention on transport and V/STOL aircraft.

1. INTRODUCTION

About 40 years ago the first jet aircraft appeared at the sky. Since that time an outstanding progress in aircraft and engine design has been made. In military as well as in civil aviation the jet engine in its different variations has become the standard powerplant and will be the standard powerplant of the aircraft of tomorrow.
Having that 40 years worldwide experience in mind, the basic questions of jet interaction should be understood in the meantime. With few exceptions of special applications the jet interaction phenomena of present aircraft designs are quite well understood, indeed. The understanding of the phenomena, however, is generally not always succeeded by an accurate prediction methodology, needed to meet the high standards in aircraft technology.
The reasons for such a situation are not only to be traced in the turbulent nature of jets or in the complexity of jet-induced flow fields. The restrictions of experimental model testing with respect to a realistic jet simulation as well as the low research on full-scale engines certainly contribute to the still existing lacks of knowledge in this field.
On the basis of a few examples of practical interest it is shown, which type of subsonic jet interaction seems to be in hands with the present knowledge, and which other informations are missed to improve the range of applications.

2. CLASSIFICATION OF JET INTERACTION PHENOMENA

To simplify the discussion on jet interactions it is proposed to distinguish between primary and secondary phenomena, as sketched in figure 1. Hereby it is understood that

- PRIMARY JET FORCE INTERACTIONS
  are direct actions of the JET MOMENTUM on solid surfaces, e.g.
  - the development of engine gross thrust by means of nozzles or afterbodies;
  - the generation of ground erosion due to the jet impact during take-off and landing of VTOL-aircraft;
  - the deceleration of an aircraft by means of a thrust-reverser or
  - the generation of extra forces on wings or bodies as a follow-up of fountain-like autodeflected wall jets.

Of equal or even more importance for modern aircraft are the

- SECONDARY JET FORCE INTERACTIONS,
  defined as interference effects due to the JET-INDUCED FLOW FIELD as a consequence of the jet entrainment, blockage and wake actions.
  In general they result in a
  - modified pressure and friction field past the aircraft and may change the aerodynamic loads in the same order of magnitude as the thrust forces are.

The distinction made on force interactions is also applicable for

- RECIRCULATION EFFECTS,
  defined as consequences of the TEMPERATURE FIELD of/or generated by a jet. Here the
  - primary or nearfield interactions are mainly combined with the fountain or thrust reverser problems and the
  - secondary or farfield interactions are caused by the up-heating of the ambient air in connection with the natural wind or the forward speed of the aircraft.

Recirculation problems are mostly concerned with V/STOL-aircraft and extremely sensitive to the individual configurations. Therefore, they are not discussed within this paper, which is concentrated on force effects and especially on secondary jet interaction phenomena.

3. PRIMARY JET INTERACTIONS

As defined above, primary jet interactions are understood as direct actions of jets on solid surfaces. Typical examples of such types of flow are the jet-afterbody interference as well as the impingement problems of jets or fountain flows. Both interaction phenomena are briefly discussed below.

3.1 Jet-Afterbody Interaction

In the development of jet aircraft the jet-afterbody interaction certainly was the first interference problem to be investigated in the past. A considerable amount of informations has been published - see e.g. (1, 2, 3) - and will be published in the future. However, the existing knowledge could not prevent that in an early design stage of a twin-engine fighter the afterbody contributed 40% of the total drag at transonic speed. Hence, an expensive investigation had to be started to reduce the parasite drag to an acceptable limit.

To discuss the jet-afterbody interference, figure 2 shows the subsonic flow past a circular nozzle. The upper part of the sketch describes the flow around an afterbody in presence of a jet with a high pressure ratio p_{tj}/p_{∞}. On the lower part the corresponding pressure distribution and a typical boundary layer profile are shown.
Due to its turbulent mixing with the ambient air flow

- the jet entrains air from the ambient flow, such increasing its mass rate steadily,
  - induces supervelocities, which correspond to negative pressures on tne body, and
  - increases the drag of that part of an aircraft.

If the jet exit pressure ratio is well above its critical value,

- the jet blocks the flow at the afterbody due to its expansion - in a first order proportional to the so-called plume angle -, hence,
  - decreases the flow past the body, and
  - reduces its drag contribution, consequently.

The favourable effects of the blocking action of a jet are limited, however. As shown in figure 2

- the adverse pressures induced by a jet with a too high pressure ratio lead to a local separation, which
  - increase the drag contribution again, and
  - can lead to an unsteady exit flow.

The relatively simple example of a subsonic flow past a circular afterbody at zero angle of attack clearly demonstrates the sensitivity of the flow problems. Unfortunately, the correlation between the sucking or blocking action of a jet and the afterbody geometry, the jet and ambient flow properties are still far from being completely understood.
Nevertheless, the evaluation of numerous experiments made in the past - see (1, 2, 3) - indicate some general tendencies, namely:

- The influence of the FLIGHT MACH NUMBER M_{∞} up to transonic speeds is approximately given by the Prandtl-Glauert rule, i.e.
  - an increasing Mach number generally reduces the pressures on the afterbody and
  - increases the local drag, therefore.

- The influence of the REYNOLDS NUMBER Re follows the well-known laws, i.e.
  - an increasing Re-number reduces the probability of flow separations, but
  - increases specifically the base pressure.

- The JET EXIT VELOCITY V_j is primarily responsible for the sucking action of a jet, hence
  - an increasing velocity or Mach number M_j increases the jet entrainment, i.e. the drag.

- The JET PRESSURE RATIO p_{tj}/p_{∞} is of major importance with respect to the drag built-up:
  - at low pressure ratios corresponding to subsonic jet velocities the displacement effect "straightens" the flow and reduces the drag compared with a bluff afterbody,
  - at medium pressure ratios the increase in jet speed dominates and consequently the drag increases,
  - at high pressure ratios the blocking action of the jet increases the afterbody pressures and reduces the drag or generates even a thrust force, as long as no separation occurs.

- The JET TEMPERATURE RATIO T_j/T_{∞} seems to interact with the external flow in two different ways, i.e.
  - as long as the outer contour of the afterbody is insulated against the internal flow an increased temperature reduces the drag, but
  - at non-insulated nozzles the coupling between flow and thermal boundary layer results in an increased drag.

Concerning the afterbody geometry it is well-known that

- the BOAT TAIL ANGLE β
  - has its optimun value between 10 and 12°,
  - a smaller angle increases the local friction and consequently the drag, and
  - a steeper gradient generally leads to separation

and

- the BASE SURFACE ratio A_b/A should be as small as possible for low or medium jet pressure ratios.

In summarizing the effects discussed above and especially the effect of the jet pressure ratio, in figure 2 a typical axial force built-up at transonic speeds has been plotted against the pressure ratio. The tests are made with a cold as well as with a hot jet. External and internal flow are carefully insulated from each other to avoid a thermal coupling of both flows.

3.2 Jet Impingements on Solid Surfaces

As mentioned above the jet impingement problems are another type of primary jet interactions. A typical example of application is the

- THRUST REVERSER
  - designed to decelerate the aircraft by turning the jet exit flow approximately against free stream direction,
  - without damaging the aircraft or provoking an engine surge due to recirculation, and
  - resulting in structural loads at the reverser up to twice the jet exit momentum.

In VTOL aircraft design another impingement problem has to be solved, namely the

- GROUND EROSION problem,
  - being a destructive effect of jets on the ground
  - which magnitude depends upon jet exit temperature, dynamic head, impact time as well as on the properties of the ground.

Also in designing VTOL aircraft the jet impingement forces on bodies have to be investigated. Hereby it is understood, that

- JET IMPINGEMENT FORCES are forces on a body resulting from a jet which dimensions are small compared with the dimensions of the body, being mostly
  - a consequence of the so-called FOUNTAIN FLOW - see section 4.2 -, and
  - causing an additional lift but also heat transfer and even surge problems.

The latter flow phenomena are of special importance for future VTOL designs in order to increase their maximum take-off weight MTOW and their specific range R_s. They strongly depend upon the body shape relative to the impinging jet. As a rough indication, in figure 3 some principal results are shown, see (4). Here a jet was blown against a cylindrical cup, a convex and a concave hemisphere. All obstacles had a diameter of about 12 nozzle diameters. The left part of the figure shows some normalized pressure distributions along the obstacle walls. For convenience the free jet velocity distribution has also been indicated. From such pressure distributions the momentum could be calculated. The results, relative to the momentum acting on a flat plate of infinite diameter, are shown on the right part of the same figure. They do not have the desired accuracy for design purposes but indicate, nevertheless, the usable potential of such types of flow.

4. SECONDARY JET INTERACTIONS

Secondary jet interactions have been defined above as interference effects of the jet-induced flow field with the free stream flow past an aircraft.
The study of such problems became essential with the design of VTOL aircraft. But also for the design of modern transport aeroplanes with high by-pass engines this type of interference needs careful consideration.
Therefore, both types of flow interactions are discussed below.

4.1 Jet-Wing Interactions of Transport Aircraft

Most of the transport aircraft are designed for podded engines, which are generally installed at wing or fuselage stations. As a consequence of the high by-pass ratio the engine diameter is rather large compared with the dimensions of the fuselage or wing. Hence, the interference problems between the engine's displacement, intake or exit flow and the wing/body combination or the tail have been considerably enlarged. This has to be taken into account because of the reduced fuel consumption of such type of engines and will be followed by increased efforts on aeroplane drag minimization research. Furthermore, at low speeds the lifting capability of the powerplant is sometimes part of the high lift system of an aircraft.
In general, the interference effects mentioned are problems of the complete powerplant rather than purely jet effects. However, the jet interactions can contribute to a large extent and need a careful examination, therefore.

4.1.1 Jet-Wing Interactions at Low Speeds

To illustrate the jet interaction with a wing some test results on lift and drag are shown in figure 4, see also (5, 6). The tests had been made with a wing/body combination of a transport aircraft; the jets being simulated by calibrated blown nacelles, supported on a separate sting system.
At take-off conditions lift and drag are shown for engines either in underwing- or upperwing position. In both cases the jet exit has the same distance from the wing leading edge. Also the absolute height above the centre line has been maintained.
With reference to the engine-off tests the jet clearly results in a Δc_L-shift, which is positive for the upperwing and negative for the underwing position of the engine.
Furthermore, the maximum lift of the upper-wing engine configuration has been considerably enlarged, but it remains practically unchanged for the under-wing engine.
The induced drag due to the upper-wing jet has equally been improved, but almost no change has been tested for the under-wing case. In addition, a remarkable zero-lift drag for the latter configuration has been measured, which was due to the jet's touching the wing lower surface.
Not shown in figure 4 are results of an increased forward speed up to cruise flight, see (6). These supplementary tests indicate a continuous reduction of the favourable or unfavourable effects; approaching approximately the engine-off case for a velocity ratio of unity.
The analysis of the results clearly underlines the role of the

- JET ENTRAINMENT
  - being a sucking action of the jet
  - which is in a first order linear proportional to the jet exit/free stream velocity ratio.

To check this, some informations on the sucking action of a subsonic jet are necessary. Because of the linear proportionality the problem can be reduced to the jet characteristics at zero free stream velocity. In figure 5 such a

- SUBSONIC JET with its
  - initial or potential core region,
  - a transition region and finally
  - the main region

has been sketched, see e.g. (5, 7). With the assumptions of

- unmixed jet exit velocity inside the core,
- similar velocity profiles outside the core as well as in the main region,
- momentum conservation in the entire jet, and
- linear jet spreadings

the relative mass flow increase can be calculated. Defining the

- ENTRAINMENT as the GRADIENT of mass flow change $d(\dot{m}/\dot{m}_j)/d(x/R_j)$,

its value can be easily obtained within the initial or main region and can be interpolated within the transition region. A typical result is shown in the lower part of figure 5 - see (5, 9, 10) - which is in good agreement with tests (8). Here instead of the entrainment E the equivalent

- ENTRAINMENT VELOCITY V_E resp. V_E^*

has been plotted against the jet path, where V_E defines the in-flow velocity at the jet boundary, and V_E^* the relevant velocity at a fictive cylinder, whose diameter is equivalent to the nozzle diameter. The results shown are valid for

- IDEAL circular NOZZLES, having no flow disturbances at the jet exit and, therefore,
  - a relative in-flow velocity V_E of about 3% in the initial region only, or
  - about 2,5% relative in-flow velocity V_E^* at the nozzle, which steadily increases up to about 8% at the begin of the main region, and remains constant throughout the main region.

It should be noted, however, that

- NON-OPTIMUM NOZZLES have a much stronger jet decay, which
  - reduces the potential core length, and
  - shifts the maximum entrainment V_E^* closer to the nozzle exit.

The results of the entrainment evaluation can be applied to jet-wing/body interaction calculations, provided that the distance between the jet boundary and the obstacle is large enough to prevent deformations of the jet shape. As an example in figure 6 the pressures on a wing with a jet in upper-wing position are shown. The calculation was performed with the help of a panel model which corresponds to the test set-up in figure 4. At all solid surfaces the condition of zero normal flow, at the jet boundary, however, the estimated in-flow velocities had been prescribed. The calculation is in good agreement with the test results as long as the distance between the jet axis and the wing chord is about one nozzle diameter or even more.

Basically, the panel model can also be applied for the calculation of the complete engine interference, taking into account the intake and displacement flow in addition. Hereby special attention has to be paid to simulate the correct mass-flow through the engine, which generally needs some modifications of the conventional panel model singularity distribution, see e.g. (11).

For other applications, e.g. such as upper surface blowing the simple model shown above is no longer useful because of the strong interactions between the jet and the wing/body flow. To calculate such flows a matching procedure has recently been proposed, coupling an inviscid panel code with a viscous code representing the jet (12). As sketched in figure 7 the complete flow field has been divided into zones which are either viscous or inviscid. Both zones are overlapping, the operlapping region being the zone to match the boundary conditions of both flows. The calculation is repeated as long as the viscous and inviscid solutions is the overlapping regions have sufficiently converged to common values.
Such types of calculation procedures seem to become a powerful instrument in the prediction of jet interactions with solid surfaces for the future.
As an example of the results obtained, on top of the right part of figure 7 the lift increase due to overwing blowing has been given. The values are in good agreement with test results as well as with the panel calculations mentioned above.
At the lower part of the same figure the pressure changes due to upper surface blowing are shown. The pressures calculated outside the nozzle are equally in rather good agreement with experimental results: The blocking action of jet and nozzle reduce the lifting pressures on the forward part of the wing, the sucking action of the jet increases the lift on the rear.

4.1.2 Jet Interaction at High Speeds

At high speeds the jet interaction is almost entirely considered as only one of the components within the complete powerplant interaction problem to be solved for engine systems of rather large dimensions installed in close neighbourhood of wings and fuselages. Especially with respect to the drag built-up the

intake as well as the displacement flow of engines and pylons are considered to be of equal or even higher importance compared with the contribution of jets.
Hence, in general a simulation of the complete powerplant rather than a jet alone has been tried in most investigations, see (13, 14, 15, 16). This was done with so-called through-flow nacelles (TFN) as a starting point, blown nacelles and turbo-powered simulators (TPS); the latter are the most representative experimental devices existing at present.
To check the influence of a jet on the pressures induced on a wing, a comparison of the results obtained in use of turbo-powered simulators and through-flow nacelles seems to be helpful. In figure 8 such a comparison is shown for a transport aircraft with conventionally fitted engines, cruising at high speed, see (13). Pressures have been measured at inboard and outboard pylon stations both on the upper and lower surface. The engine-off case as the datum test has also been shown.
Assuming that the TFN represents the intake as well the displacement flow accurately enough, the pressure difference between both tests may be identified as the influence of the jet, as marked in figure 8.
This leads to the conclusion that

- the sucking action of a jet basically
  - reduces the negative pressures at the upper surface of the wing, but
  - increases the negative pressures at the lower surface such that even shocks are generated.

With the help of figure 8 the general importance of a jet representation corresponding to the full-scale jet as well as special studies on the jet influence may be derived. However, this has to be measured against the contribution of the other components of a powerplant, which are equally or even more sensitive with respect to the drag.
To demonstrate this, figure 9 - see (17) - gives some results of the relative drag change obtained from model tests with a through-flow nacelle at different x-, z- and toe-in positions. Bearing in mind the importance of a 1% drag increase or reduction in the profit of an airline, the figure drastically underlines the special care to be taken with respect to the powerplant positioning.

4.2 Jet Interaction on V/STOL-Aircraft

4.2.1 General Jet Properties

To develop jet-lifted V/STOL aircraft the research on jets in ground effect (IGE) as well as out of ground effect (OGE) has required much attention in the past. In many respects such jets are quite different from jets discussed so far. Basically

- VTOL-JETS are understood as a combination of
  - FREE JETS swivelled against the free stream flow up to 90° or more,
  - WALL JETS, developed on the ground as a consequence of the free jet's impingement, and
  - JET FOUNTAINS, caused by the upward self-deflection of more than two wall jets.

A principal sketch of the three components has already been shown in figure 1.
In general the properties of such jets are defined by

- a SUCKING ACTION of free and especially wall jets - due to turbulent mixing with the ambient air - in a cross flow, which speed is small with respect to the jet exhaust velocity,
- a DISPLACEMENT or BLOCKAGE EFFECT, similar in some respect to the flow past solid bodies, and finally
- a WAKE EFFECT, again similar in some respect to the flow past solid bodies and especially important for the multi-jet treatment.

The entrainment of a free or wall jet at zero forward speed can be estimated on the basis of simple momentum conservation and geometrical assumptions, see e.g. (9, 10). For a free jet this already has been discussed in section 4.1.1. For the other properties mostly empirical relations or semi-empirical formulas have to be used. The dependency on numerous empirical constants is still the major problem in predicting such flows.

One of the basic questions still somewhat open is the

- deformation of the JET SHAPE and CENTER LINE in a cross flow,

shown in figure 10. Here the deformation from an initially circular shape via horse-shoe sections into a pair of counter-rotating vortices has been sketched from experimental data. In addition the jet axis, defined by points of local maximum total head, and the vortex axis, defined by points of maximum vorticity are shown in this figure. Both lines differ distinctly from each other. In absence of a more refined theory the question, which line represents which effect best, cannot accurately be answered. From experiments, however, it is proved that force effects on wing/body combinations are quite reasonable represented by the jet total head center line, but for downwash problems on the tail the vortex axis should be taken into account.
Since most of the prediction problems of V/STOL aircraft are lift loss problems, research on total head center line deformations in a cross flow has widely been experienced, see e.g. (10). An empirical formula which was successfully used in practical applications is shown in figure 11. The most important flow parameter in that equation is the

- EQUIVALENT VELOCITY RATIO,
  - being the square root of the dynamic head ratio $(\rho_\infty U_\infty^2 / \rho_j V_j^2)^{\frac{1}{2}}$
  - or simply the velocity ratio U_∞ / V_j in incompressible flow.

It should be noted, however, that the relation only holds for almost ideal circular jets. Rectangular jets with the small side perpendicular to the free stream flow are much stiffer and consequently, jets with the long side perpendicular to the wind direction are considerably weaker with respect to crosswing deformation.

The single jet evaluations discussed so far are primarily important for the general understanding of jet properties, but V/STOL aircraft normally have more than one engine or jet. This automatically leads to a mutual interference of the exhausting jets. From tests it is well-known, that

- the MUTUAL INTERFERENCE EFFECTS
  - are small for jets positioned side by side to the free stream, but
  - highly magnified for jets positioned in line.

Hence, only the latter case needs major attention, see (10). To estimate the mutual interference of two in-line jets, as sketched in figure 12, it is assumed that

- the front jet is to be treated as single jet with negligible interference by the rear jet;
- the rear jet also acts as a single jet, but in a reduced free stream velocity;
- the reduction in velocity is a consequence of the wake behind the front jet, following the properties of wakes past three-dimensional solid bodies;
- the slope of the merged jet axis is mainly determined by the rear characteristics, and
- finally the momentum of the merged jet is the sum of the front and rear jet's momentum.

As shown on the right part of figure 12, the comparison between experiments and approximation method is apparently good.

4.2.2 Jet Interactions out of Ground Effect (OGE)

One of the most critical phases during the flight of a V/STOL aircraft is the so-called

- TRANSITION PHASE, defined as that period in which the wing lift is not yet or any longer sufficiently developed, and the aircraft needs jet lift support.

As mentioned in the preceding sections, the

- SUCKING ACTION of a jet in a cross flow - modified by displacement/wake and jet deformation effects - remarkably reduces the lifting force of the jets.

This is demonstrated on the right part of figure 13, see also e.g. (9, 10, 18, 19). Here the relative lift loss $\Delta L/T$ has been plotted against the equivalent velocity ratio $(u_\infty/v_j)_e$ with the nozzle swivelling angle σ as paramter. It can be easily seen that for jets with an axis perpendicularly to the free stream almost the complete jet lift will be cancelled by its suction at higher speed ranges. However, not shown in the figure 13 is the parabolic development of wing lift working against the adverse effects - see (18) -, such that the nozzles can be continuously swivelled backwards to reduce the lift loss and accelerate the aircraft to wing-borne flight.

It is of fundamental interest for any designer of V/STOL aircraft to predict the lift losses at an early design stage already. Hence, quite a number of engineers and scientists have established prediction methods in the past, see e.g. (9, 10, 19, 20). In principle they all use panel models for the basic aircraft but differ with respect to the implementation of the jets as well as on the assumptions made for its properties.
To illustrate the general prediction approach, in the left part of figure 13 a procedure which correlates sufficiently good with experimental results has been sketched:
The fighter-type aircraft has been represented as a half-model using about 800 panels. The jet center lines are calculated as in-line jets according to section 4.2.1 and figure 12. The jet diameters are assumed to be constant for each jet, corresponding to the individual nozzle diameters and the merged jet section respectively.
On the jet surface the in-flow velocity V_e^* - see figure 5 - has been prescribed. A semi-empirical cross flow correction for both the entrainment and the blockage - see (10) - was introduced to modify the ideal boundary conditions at zero forward speed and to establish a final jet panel model of about 800 panels.
The results obtained with such prediction model are in agreement with the set of curves shown at the right hand side of figure 13, i.e. with experimental work. They also agree fairly well with flight test results. However, it should be noted that prediction models which need some empirical informations from model testing automatically implement any divergence between model and full-scale testing. E.g., if the model jets had been cleaned up to almost ideal jets, its decay is less strong with respect to the aircraft jets, and consequently the full-scale lift losses exceed the predicted values.

4.2.3 Jet Interaction in Ground Effect (IGE)

From practical experience it is known, that an aircraft is considered to be in ground effect as long as its ground clearance is less than about one wing span. The jet interactions which occur during the time period from "Engine Ingnition" to "Out of Ground Effects" strongly depend upon the take-off or landing procedure, see (18).
In principle two different techniques are applied, namely:

- TRUE VERTICAL TAKE-OFF (TVTO) and ROLLING VERTICAL TAKE-OFF (RVTO)

The RVTO technique is mostly used to avoid severe engine recirculation or ground erosion effects as well as to perform over-load take-offs.
Since recirculation and ground erosion effects are beyond the scope of this paper, the discussion of jet interaction effects is concentrated on TVTO, and especially on its worst case, which is

- HOVERING in ground effect

This is because of the fact that a rather small loss in the predicted lift-off potential is directly proportional to a considerable decrease in the range of an aircraft.

As mentioned above and shown in figure 14 the

- JET SYSTEM in HOVERING generally consists of three parts, namely
  - the FREE JETS
  - the WALL JETS and finally
  - the JET FOUNTAINS

In absence of any forward speed the

- SUCKING ACTION of free and wall jets due to the entrained ambient air is responsible for a severe SUCK-DOWN EFFECT on the aircraft

This is shown in figure 14 by the dotted line at the right hand side. The lift-loss is mainly caused by the wall jet entrainment. At small ground clearances it can easily be in the order of the total installed thrust, provided that the engines are concentrated in the middle of a wing and the vertical distance between wing and nozzle exit is small enough. Hence, an aircraft designed in such a manner could never take-off vertically. But even for an aircraft with well-spaced nozzles the lift loss due to the suck-down effects at small ground distances will be in the order of 10% to 20% of the total installed thrust. As shown in figure 14 it decreases continuously with increasing height h above ground, generally related to the wing span b.

At heights above ground in the order of about a wing span the aircraft is considered to be out of ground effect. The remaining suction loss is still in the order of about 1 or 2% of the installed thrust. This is the sucking action of the free jets alone at zero forward speed. Compared with the sucking action of wall jets their amount is evidently much smaller. However, the final loss again depends upon the jet exit properties, as discussed before.

Since most aircraft have more than one exit nozzle, and the distance between the nozzles usually is of the order of some diameters, the free jets impinge the ground independently from each other as single jets. On the ground any free jet is transformed into a wall jet. The individual wall jets meet together at the so-called

- STAGNATION LINE, which is understood as a line on which the normal momentum components of the wall jets cancel each other and only a tangential in- or out-flow exit, therefore.

This is also shown in figure 14. Of special interest are the

- STAGNATION POINTS, which divide the in-flowing from the out-flowing momentum along such lines;

If the impingement points of the single jets as well as the stagnation points are known, the total in-flowing wall jet momentum can be evaluated. It can easily be seen that such a flow must separate from the ground in a point on which the total inner momentum flows meet together. This point is called fountain origin whereas the

- FOUNTAIN JET MOMENTUM is the sum of the in-flowing momentum parts of all contributing wall jets, and
  - three jets are at least necessary to form such a flow.

As shown in figure 14

- a FOUNTAIN JET can considerably reduce the lift loss and even result in a positive lift, however, it should be equally noted that
  - it can contribute to severe recirculation problems.

Furthermore, the fountain jet may not be compared with a steady up-flow. There is always a more or less strong vortex flow superposed; oscillating with rather low frequencies on the ground and consequently on the aircraft, too.

The prediction of IGE-qnteractions is still troublesome with respect to the fountain flows.
The calculation of the suck-down interaction can be done with the help of conventional panel codes, as sketched in figure 15. In a similar way as described for the transition effects both the aircraft as well as the free and wall jets are to be simulated by a panel network with a cutout of all regions of fountain flows. Along the solid surfaces the conventional boundary condition of zero normal velocities exists, but on the jet boundaries the local in-flow velocities have to be prescribed.
The result of such a calculation for a fighter-type aircraft is shown in figure 15. To obtain the suck-down effects the aircraft was treated as a half model, represented by about 800 panels. For the free jet simulation about 150 and for the wall jets only about 100 panels have been used. The predicted suck-down effects are in rather good agreement with experimental results.
To estimate the fountain lift effects, the jet foot-prints and especially the stagnation lines have firstly to be predicted - see (10, 19) -, giving the total fountain momentum and its origin on the ground. The conversion of the fountain jet into a lift force belongs to the problems of primary jet interactions as discussed in section 3.2. Unfortunately, up to now no appropriate method is known and, hence, the conversion has to be done with a rather limited experimental information.
The output of such a fountain lift estimate is equally shown in figure 15, indicating a rather significant lifting action of the fountain jet.
The superposition of both the suck-down and the fountain lift estimate is indicated in figure 15 below, together with some experimental data. The agreement is quite good, but the position of the maximum lift

gain could not be accurately predicted. It is assumed that this is mainly the consequence of the open problems in fountain flow prediction and especially in converting a jet momentum into a lifting force.

4.3 Unsteady Jet Interactions at Low Speeds

The jet interactions discussed so far are exclusively related on steady state interference problems. In order to solve such problems the description of a jet by its mean values was quite successful, as shown in the previous sections, although the turbulent mixing between jet flows and ambient air is an unsteady process by nature.
However, especially at low speeds jet induced buffet-like interactions have sometimes been observed, which are only to be explained from the unsteadiness of a jet. The effects have to do with the installation of large high by-pass engines in close proximity of wings, fuselages or tails. For such types of installation the jet boundary is also in close proximity to the solid surfaces, and the jet velocities in the outer part are of the same order of magnitude the free steam velocities are. In addition, the jet spreading has its maximum at zero forward speed.
To review the situation in figure 16 some simple test informations have been compared. Hereby it is assumed that the steady flow measurements are done with pitot probes, but the unsteady information was obtained from hot-wire anemometers or lasers. In both cases the static pressure inside the jet should be equal to the ambient. As it is well known, for the

- STEADY JET FLOW a velocity profile - as shown on top of figure 16 - will be measured,
  - which is similar for all other axial stations downstream, and
  - indicates a linear jet spreading $\bar{R}(x)$, whereby the spreading angle depends upon the definition of the jet boundary as well as upon the test equipment resolution.

Repeating the tests e.g. with a hot-wire anemometer or laser the

- UNSTEADY JET FLOW tests naturally result in the same mean values,
  - the time history indicates turbulent mixing signals at the inner part of the jet, but furthermore
  - stochastically distributed periods of unmixed laminar flow well inside the jet, as well as
  - periods of turbulent mixing well outside the steady jet boundary.

The latter results obviously demonstrate, that the

- REAL JET BOUNDARY $R(x)$ fluctuates at any axial station across the steady jet boundary $\bar{R}(x)$.

This fluctuation is a normal property of the turbulent mixing process, but it also depends upon the jet exit flow conditions. Hence,

- the FLUCTUATIONS of a JET BOUNDARY are also controlled by the individual jet exit properties as well as by the matching of the fan and generator flow of a by-pass engine.

Unfortunately, little information about such fluctuations obtained from testing engine or aircraft models can be used to predict full-scale problems.
To get a better insight, in figure 17 a procedure has been sketched, which allows the evaluation of the intermittency of a jet. Hereby

- INTERMITTENCY is defined as the time period of turbulent mixing, compared with the total testing time,
  - giving a first information of the fluctuating nature of a jet at any point of the associated flow field.

To obtain the intermittency factor a triggering device can be used, separating turbulent from laminar events, and counting the turbulent time periods as well as the total time.
As a result of such tests the right hand part of figure 17 shows a typical result obtained from experiments on rather clean nozzles:
Based upon the steady state jet boundary, temporarily the unsteady boundary can be well inside to about 0.6 $\bar{R}$, but it also can be well outside up to about 1.5% of the steady state jet radius. Since within the mixing layer large eddies exist, these eddies can impinge the aircraft and sometimes result in dynamic problems as mentioned before.
Such potential problems have been observed on powerplant installations in close proximity to wings, fuselages or tails. They are generally restricted to low speeds and are not a serious problem in cruise flight. Nevertheless, for future design work and aircraft optimization a more detailed information seems to be of high value.

5. CONCLUSION

Since about 40 years an outstanding progress in aircraft and engine design has been made. This includes the optimization of positive as well as the minimization of negative aspects on jet interactions with respect to neighbouring surfaces.
To illustrate the broad field of such interactions some examples of primary and secondary interference phenomena have been reviewed, concerning subsonic/sonic jets within the range from zero forward speed up to the transonic flight regime. This has been done specifically with respect to actual problems of modern transport aircraft design as well as with respect to the renewed interest in military Jet-V/STOL aircraft.
The discussion of the described interaction problems shows, that the phenomena are principally quite well understood, in spite of the complex nature of such flows. The prediction, however, is still somewhat limited.

This is due to the still existing difficulties in the theoretical modelling of three-dimensional turbulent flows, which will be a permanent challenge for the future. But, as it has been shown, some specific problems can be handled on the basis of potential-theoretical flow, provided that the boundary conditions are properly given. Unfortunately, such informations are missed very often, also because of the lack of full-scale engine test data to replace the simplified model test results.
With respect to the progress made in the past, however, it is assumed, that the open questions discussed above will be answered in the near future already.

6. REFERENCES

(1) "Airframe/Propulsion Interference"
AGARD-CP-150, 1974.

(2) "Interferenzwiderstand bei der Zellen-/Triebwerksintegration von Kampfflugzeugen"
BMVg-FBWT 79-20, 1979.

(3) "Aerodynamics of Power Plant Installation"
AGARD-CP-301, 1981.

(4) Donaldson, D.D., Snedeler, R.S. "A Study of Jet Impingement"
J. Fluid Mech., Vol. 45, 1971.

(5) Barche, J. "Beiträge zur Flugphysikalischen Technologie"
VFW-Kurzbericht Ex1-478, 1974 (Internal Report).

(6) Krenz, G., Ewald, B. "Airframe Engine Interaction for Engine Configurations Mounted above the Wing"
AGARD-CP-150, 1974.

(7) Abramovich, G.N. "The Theory of Turbulent Jet"

(8) Hill, B.J. "Measurement of Local Entrainment Rate in the Initial Region of Axisymmetric Turbulent Air Jets"
J. Fluid Mech., Vol. 51, 1972.

(9) Barche, J. "Developing a Prediction Method for Jet-Induced Effects of Arbitrary Jet-Lift V/STOL Configuration"
VFW-Kurzbericht Ef-526, 1975.
(GAC-Contract No.: N 00140-74C-0113)

(10) Siclari, M.J., Barche, J., Migdal, D. "V/STOL Aircraft Prediction Technique Development for Jet-Induced Effects"
Grumman Aerospace Cooperation PDR-623-18, 1975.

(11) Haberland, C., Göde, E. Sauer, G. "Calculation of the Flow Field Around Engine-Wing Configurations"
ICAS-80-4.1, Munich, 1980.

(12) Roberts, D.W. "Prediction of Subsonic Aircraft Flows with Jet Exhaust Interactions"
AGARD-CP-301, 1981.

(13) Harris, A.E., Carter, E.C. "Wind Tunnel Test and Analysis Techniques Using Powered Simulators for Civil Installation Drag Assessment"
AGARD-CP-301, 1981.

(14) Van Engelen, J.A.J. Munniksma, B., Elsenaar, A. "Evaluation of an Experimental Technique to Investigate the Effects of the Engine Position on Engine/Pylon/Wing Interference"
AGARD-CP-301, 1981.

(15) Becle, J.P., Perin, R. "Essais en Soufflerie de maquettes motorisées. Comparison de deux methodes de simulation des sets des reacteurs"
AGARD-CP-301, 1981.

(16) Ewald, B., Smyth, R. "The Role and Implementation of Different Nacelle/Engine Simulation Concepts for Wind Tunnel Testing in Research and Development Work on Transport Aircraft"
AGARD-CP-301, 1981.

(17) Carter, E.C. "The Use of a Large Transonic Wind Tunnel for the Development of Engine Installation on New Civil Transports"
Lecture at Technische Universität Berlin, 1981.

(18) Barche, J. "Jet Lift Problems of V/STOL Aircraft"
AGARD-CP-143, 1974.

(19) Siclari, M.J. Migdal, D. Luzzi, T.W. Barche, J. Palcza, J.L. "Development of Theoretical Models for Jet-Induced Effects on V/STOL Aircraft"
Journal of Aircraft, Vol. 13, No. 12, 1976.

(20) Wooler, P.T.
Kao, H.C.
Schwendemann, M.F.
Wesson, H.R.
Ziegler, H.

"V/STOL Aircraft Aerodynamic Prediction Methods Investigation"
AFFDL-TR-72-26, 1972.

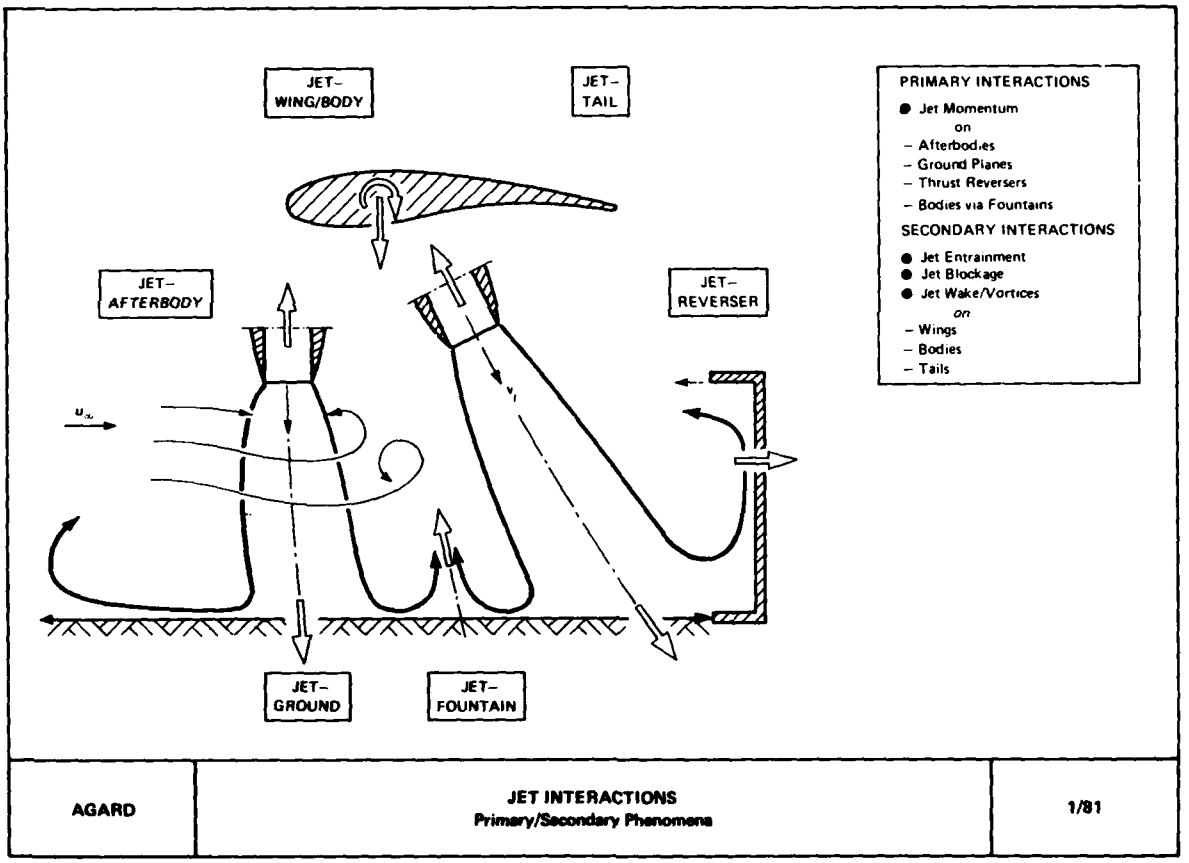

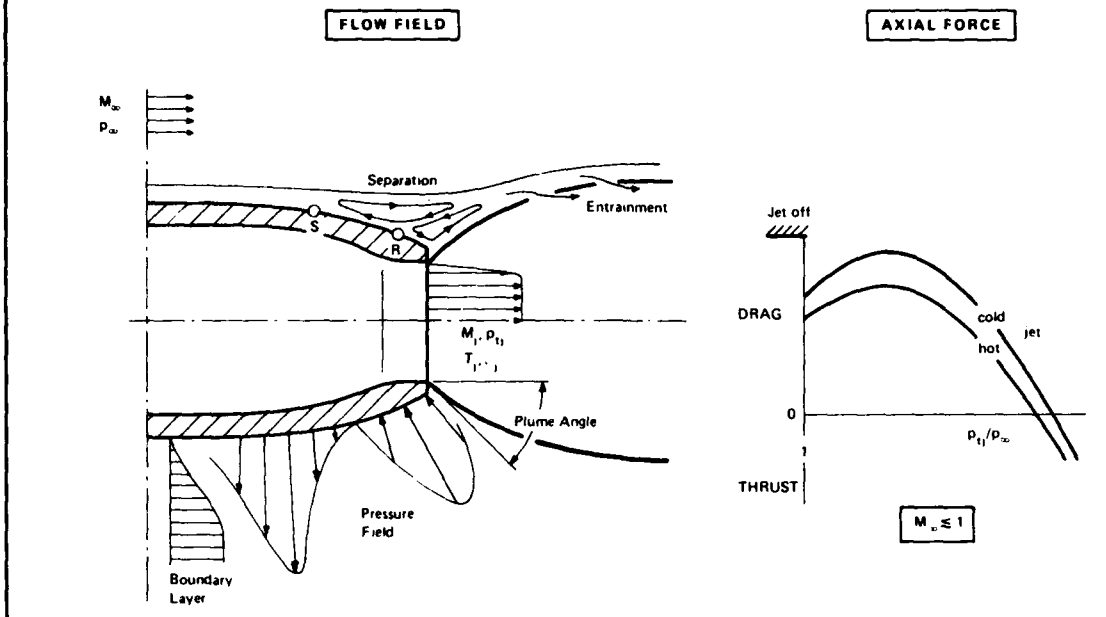

AGARD	JET - AFTERBODY INTERACTION Flow Field, Axial Force	2/81

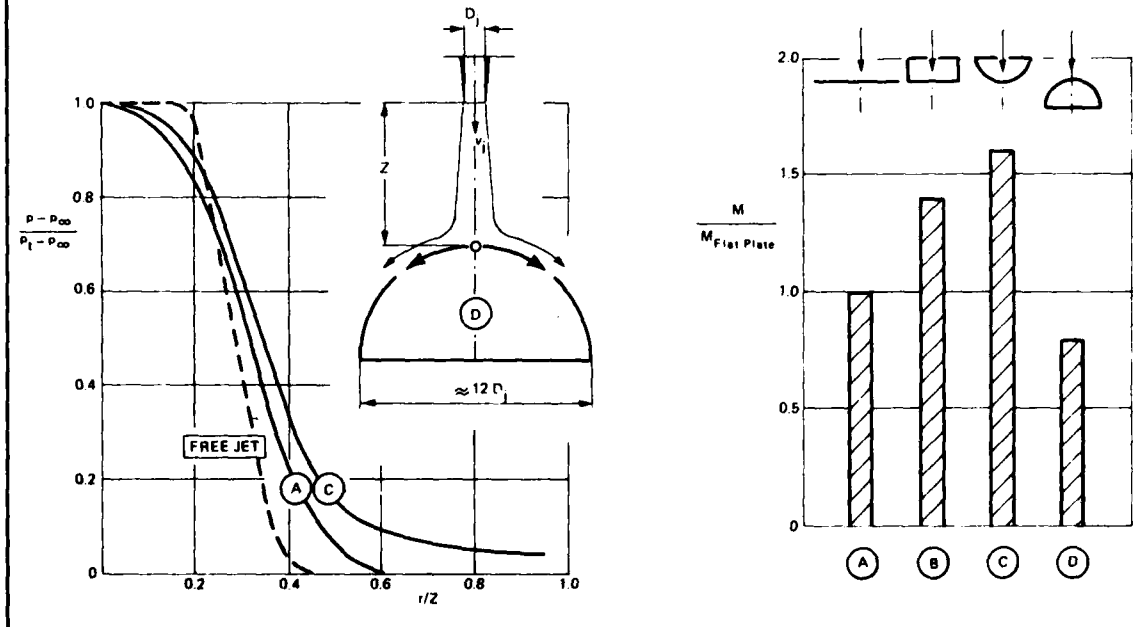

AGARD	JET IMPINGEMENT Effect of Surface Shapes	3/81

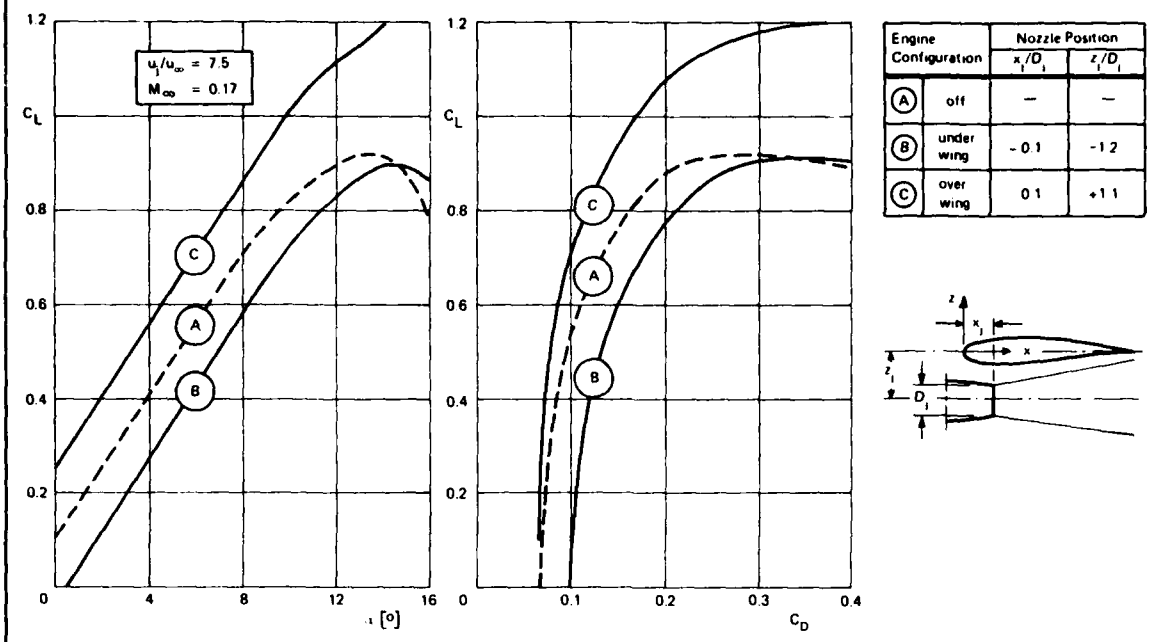

Engine Configuration		Nozzle Position x_j/D_j	Nozzle Position z_j/D_j
A	off	—	—
B	under wing	- 0.1	-1.2
C	over wing	0.1	+1.1

AGARD	JET - WING LOW SPEED INTERACTION Lift/Drag, Take-off Speed	4/81

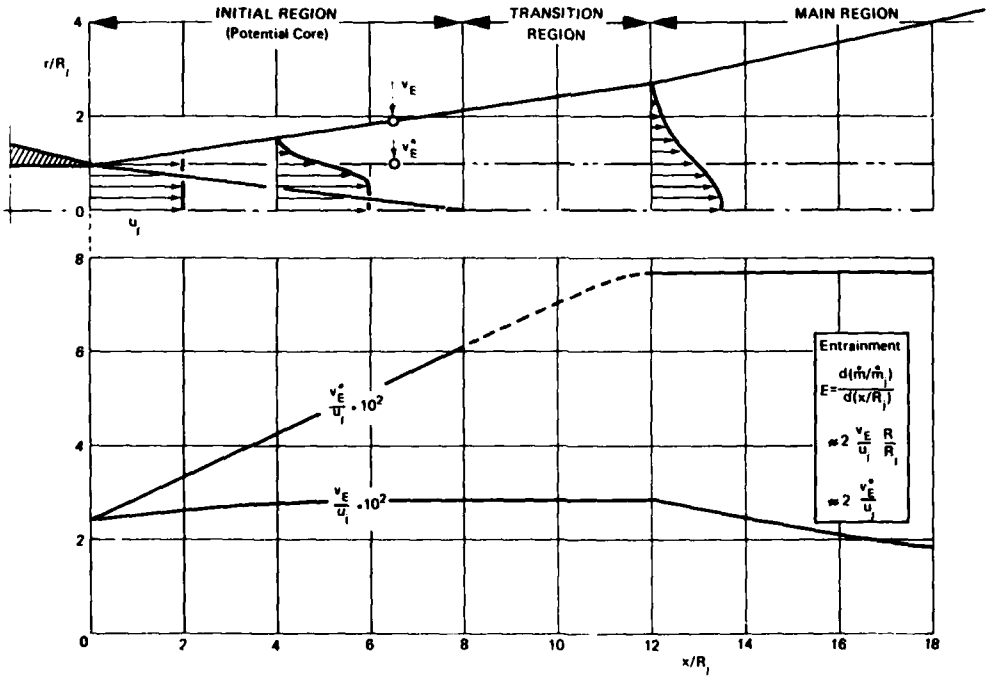

AGARD	SUBSONIC JET Geometry/Entrainment $M_\infty \rightarrow 0$	5/81

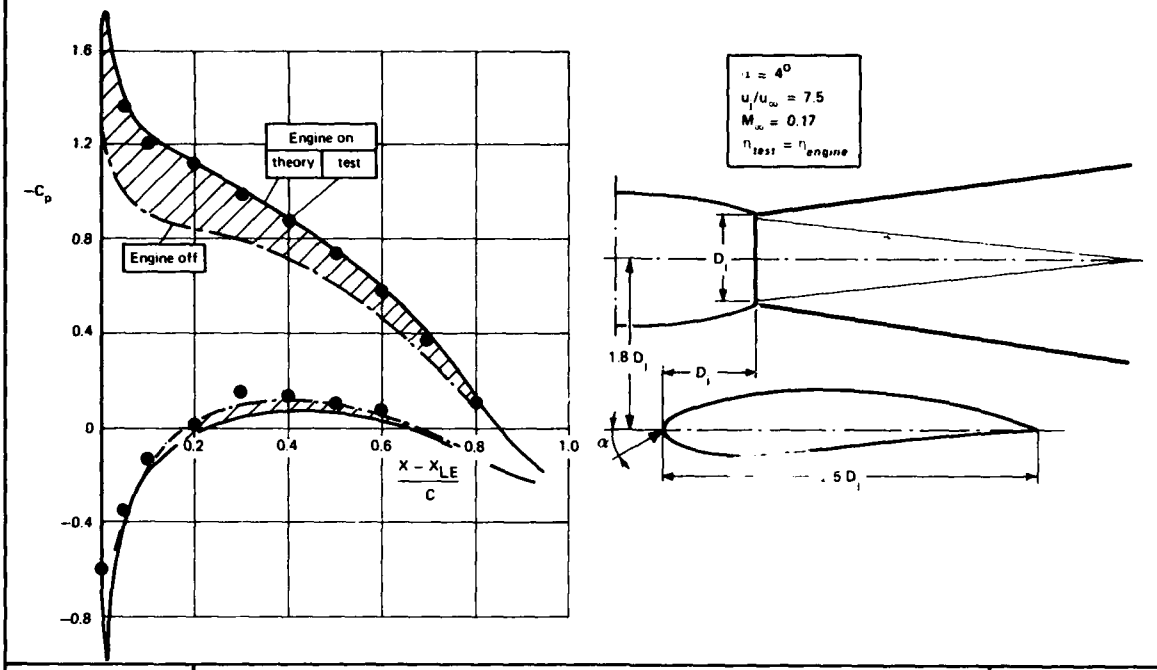

AGARD	JET ENTRAINMENT Upper Wing Engine	6/81

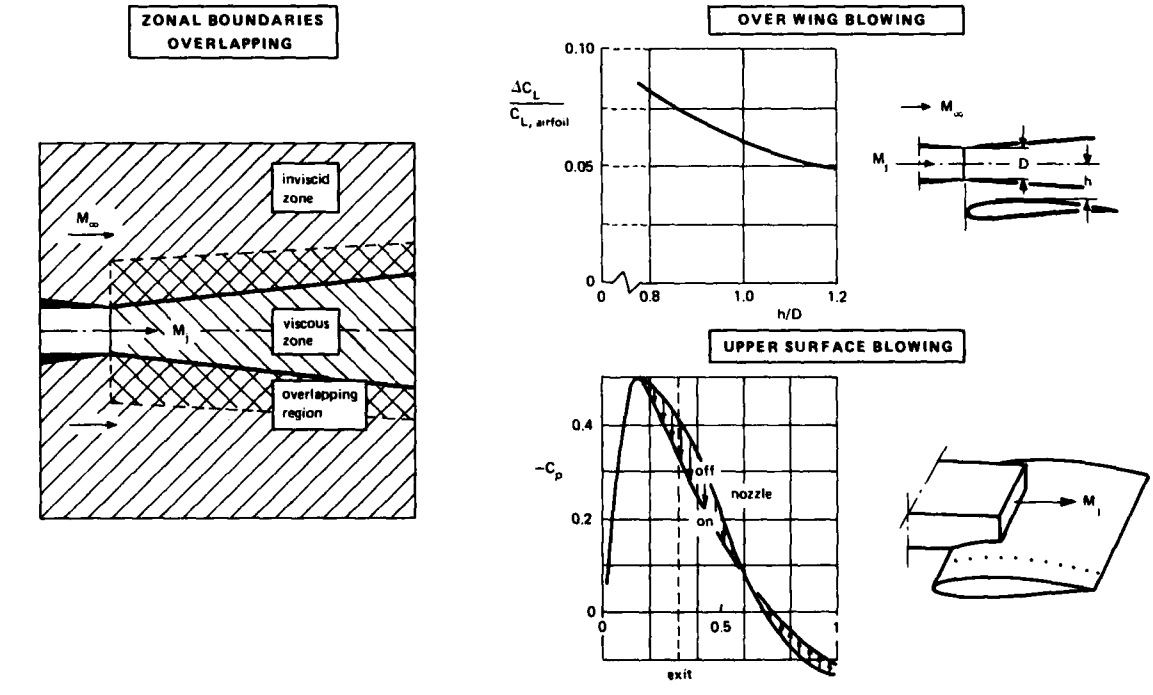

AGARD	VISCOUS/ INVISCID COUPLED ANALYSIS Procedure/Results	7/81

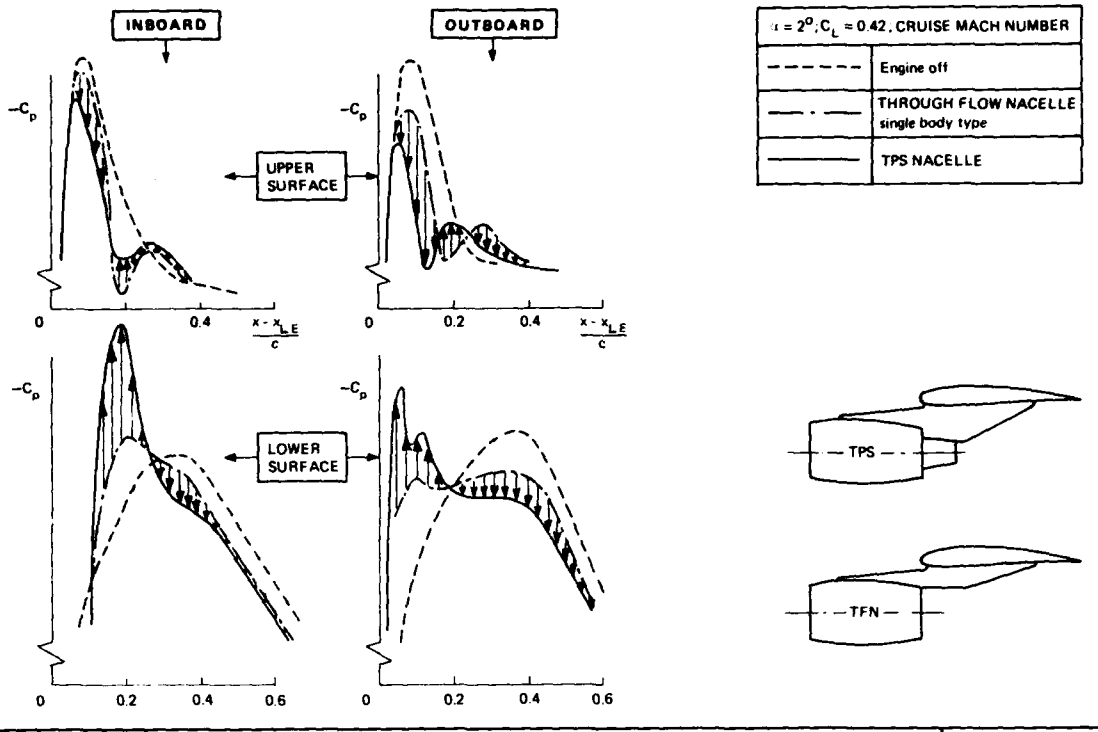

AGARD	ENGINE - WING INTERACTION ① Cruise Speed Pressure Distribution	8/81

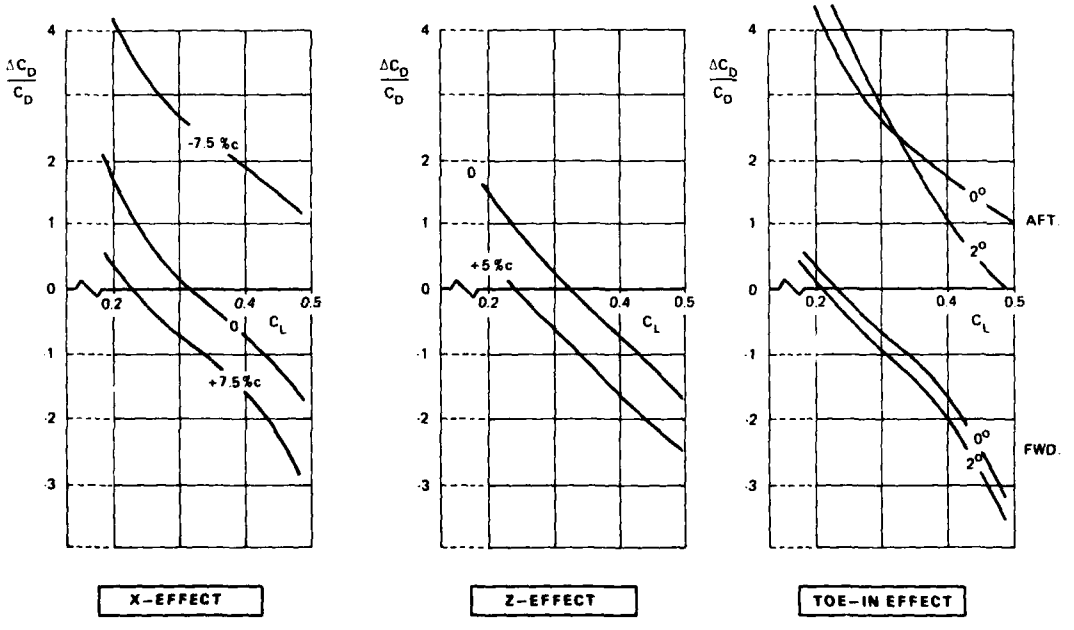

AGARD	ENGINE - WING INTERACTION ② Cruise Speed Engine Position Effects	9/81

JET DEFORMATION

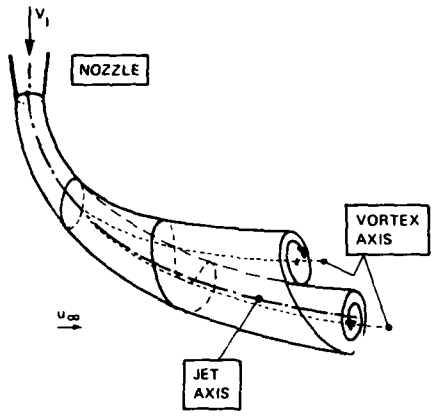

CENTER LINES

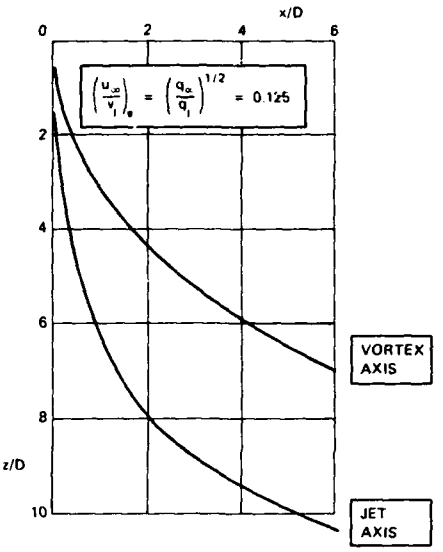

AGARD	JET IN CROSS - FLOW	10/81

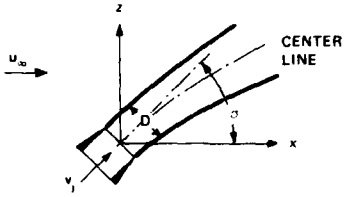

$$\frac{x}{D} \approx 2.3\left(\frac{u_\infty}{v_j}\right)_e^3 \left(\frac{z}{D}\right)^3 + \left(\frac{z}{D}\right)\cot\sigma$$

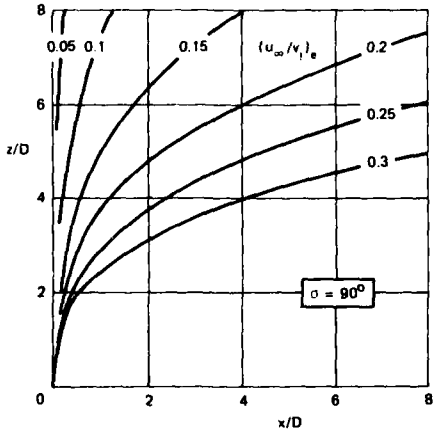

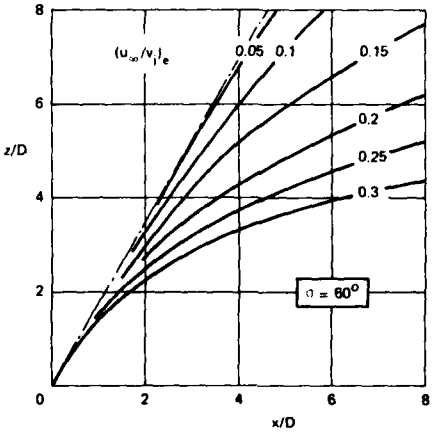

AGARD	JET - CENTERLINE DEFORMATION	11/81

ASSUMPTIONS

- Jet 0 as single jet
- Jet 1 in wake flow
  $u'_\infty / u_\infty = 1 - \Delta\xi^{-2/3}$
- Jet 2 · momentum
  = (Jet 0 + Jet 1) · momentum
- Jet 2 · direction
  = Jet 1 · direction

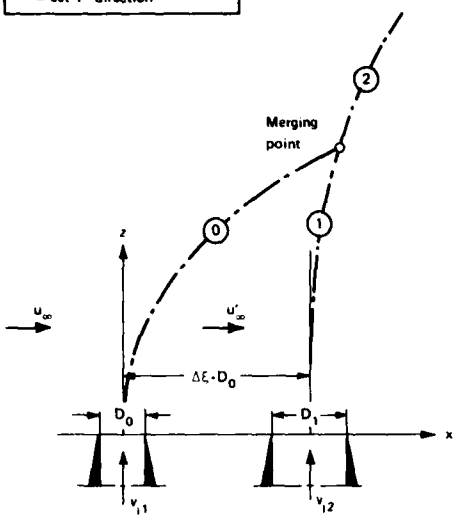

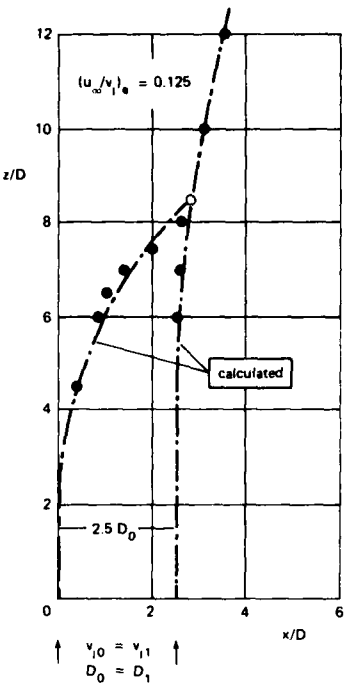

AGARD	IN - LINE JETS Mutual Interference	12/81

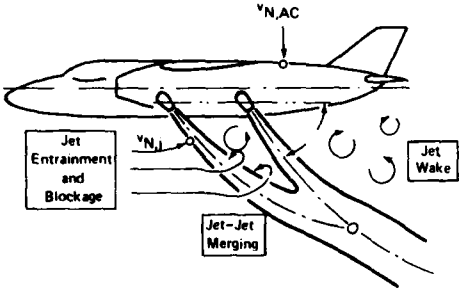

PANEL CODE PREDICTION

- AIRCRAFT (767 panels)
  $v_{N,AC} = 0$
- JETS (810 panels)
  $v_{N,j} \neq 0$
  - free jet entrainment
  - cross flow correction
  - blockage correction
- JET–JET MERGING
  - semi - empirical

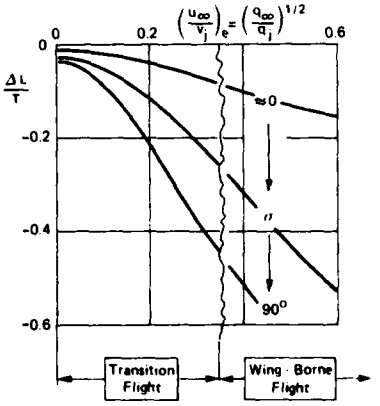

AGARD	JET - AIRCRAFT INTERACTION Out Of Ground Effect (OGE)	13/81

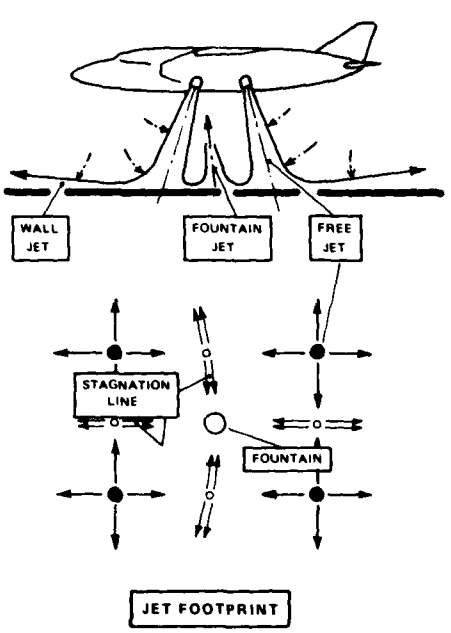

JET FOOTPRINT

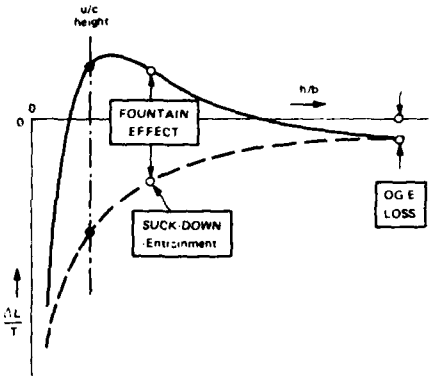

LIFT LOSS BREAK-DOWN

AGARD	JET - AIRCRAFT INTERACTION ① *In Ground Effect (IGE)*	14/81

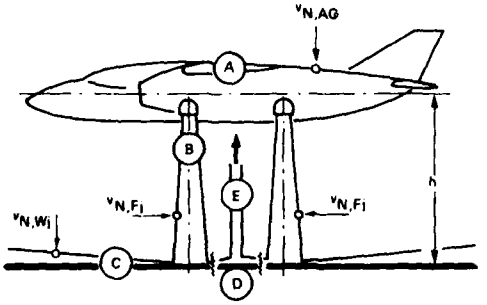

PREDICTION METHOD			
PANEL CODE		"FOUNTAIN"-CODE	
A	AIRCRAFT (767 panels) $v_{N'AC} = 0$	D	STAGNAT. LINES momentum equilibrium
B	FREE JETS (144 panels) $v_{N'Fj} \neq 0$; F. J. – Entrainment	E	FOUNTAIN–LIFT empirical momentum–transformation
C	WALL JETS (108 panels) $v_{N,Wi} \neq 0$; W.J. –Entrainment		

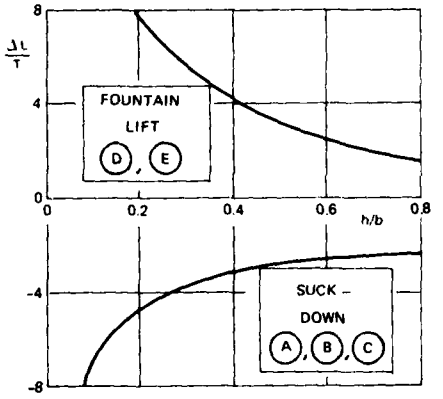

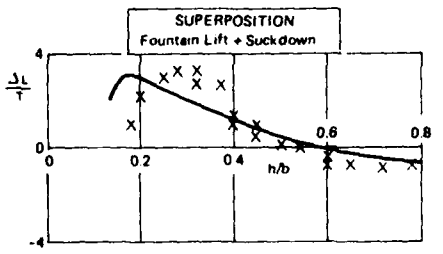

AGARD	JET - AIRCRAFT INTERACTION ② *In Ground Effect (IGE)*	15/81

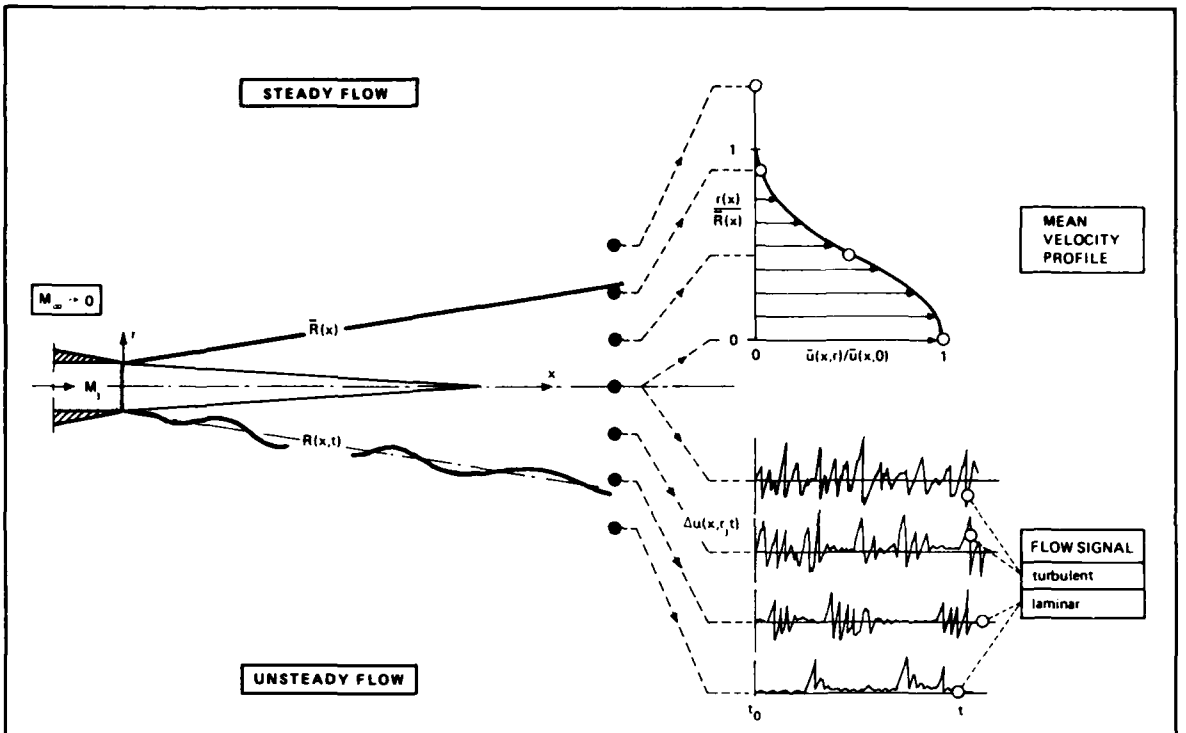

AGARD	STEADY/UNSTEADY VELOCITY SIGNALS Subsonic Jet, $M_\infty \to 0$	16/81

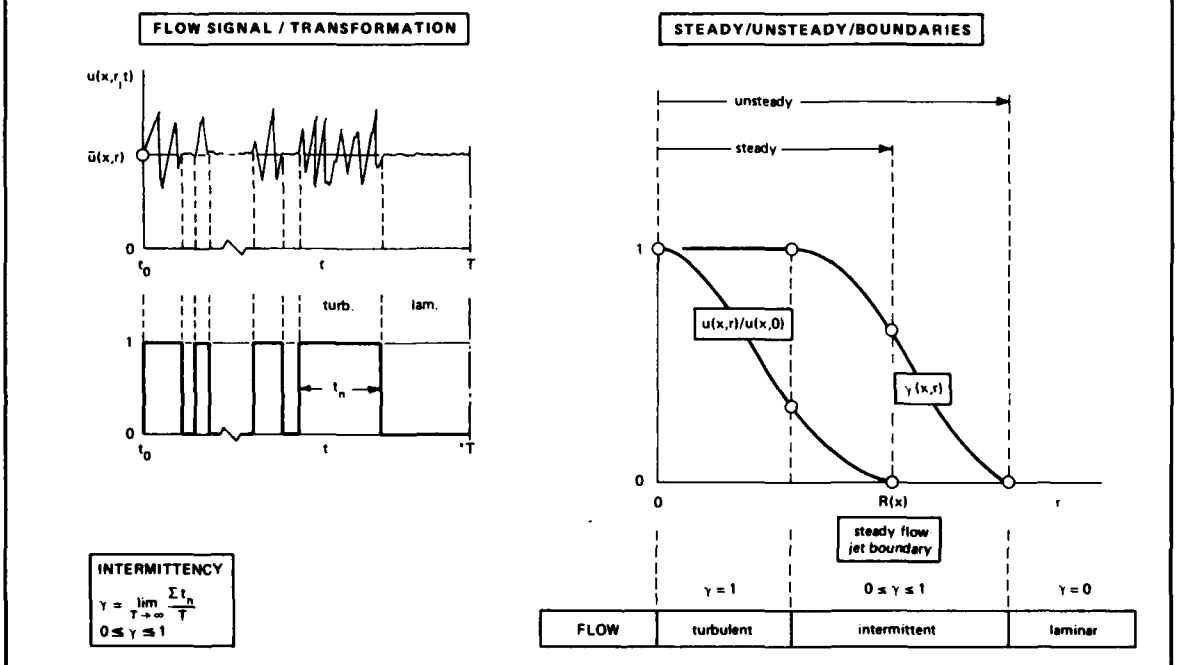

AGARD	JET BOUNDARY FLUCTUATION Evaluation Principle	17/81

INTERACTION OF SIMPLE AND MULTIPLE JETS WITH A PLANE SURFACE

by
A. R. Janeiro Borges
Professor,Faculty of Science and Technology,Universidade Nova de Lisboa,1899LISBOA
and D. X. Viegas
Assistant,Faculty of Science and Technology,Universidade de Coimbra,3000COIMBRA
Portugal

SUMMARY

The scope of the present paper is the study of the shear-stress field produced by simple and multiple circular jets impinging on a plane surface with either normal, oblique or parallel incidence.

The mean shear-stress distribution produced by a single normal jet was measured with a Preston tube and a law for the radial variation of τ_w is proposed for the wall jet region. Measurements of the shear-stress fluctuations with a hot-film sensor showed that the intensity of the fluctuations is small compared with the shear-stress mean value.

An erosion technique was employed to evaluate the shear-stress field. The calibration of the technique for sand particles was done in the flow produced by a normal jet. The variation of τ_w and lines of constant shear-stress were obtained for oblique and parallel impingement. In the latter case a dual jet arrangement was also considered.

An analytical model, based on Reichardt's inductive theory of free turbulence, is developed for the description of the mean properties of the flow produced by single and dual jets parallel to the plane.

SYMBOLS

D	Nozzle diameter	u_τ	Friction velocity
H	Height of the jet	x,y,z	Cartesian coordinates
R_o	Jet's Reynolds number	μ	Velocity coefficient
R_r	Local Reynolds number	ν	Cinematic viscosity
R	Particle's Reynolds number	ξ_1,ξ_2	Non dimensional coordinates
U_o	Jet exit velocity	ρ	Density of the air
d	Mean size of the particles	τ_w	Shear-stress on the wall
$k.k_o$	Free jet constants	τ_c	Critical shear-stress
k',k_o'	Parallel jet constants	ϕ_o	Angle of incidence of the jet
r	Radial cilindrical coordinate	ψ	Shear-stress coefficient
u,v,w	Velocity components		

1.- INTRODUCTION

The interaction of single and multiple jets with a solid surface arises in many practical applications, namely in connection with V/STOL aircraft when operating near or on the ground. One of the effects of this interaction is the projection of solid particles or even the actual erosion of the terrain. This effect is closely related to the shear-stress field produced by the flow on the surface.

The complexity of the flow makes it difficult to predict the shear-stress distribution entirely by analytical means, therefore recourse is had to experimental data. Most of the available techniques require tedious point by point measurements in order to obtain a detailed description of the shear-stress field. Some other techniques are qualitative in nature, giving only a visual description of the flow, that may be useful but not sufficient in many cases. In the present paper use is made of an erosion technique that gives an immediate quantified description of the shear-stress distribution on the surface.

The study was carried out with circular turbulent jets set either at normal, oblique or parallel incidence on a smooth flat plate. In the latter case a dual jet configuration was considered in order to test the applicability of the experimental technique and analytical model used for multijet situations. The main objective of the study was the characterization of the mean shear-stress field on the surface.

The flow produced by the normal jet was employed to calibrate the erosion technique which was then applied to the study of oblique and parallel jets for several configurations. An analytical model, based on Reichardt's theory of free turbulence,was developed for the case of a single and a dual jet parallel do the surface. The agreement found between experimental results and the model predictions validate the assumptions made in its derivation and gives an indication that it should be equally applicable to more complex flow situations.

2.- EXPERIMENTAL SETUP

In the experiments use was made of a set of different nozzles fed with compressed air. Most of the single jet experiments were made with nozzles of internal diameter D=3.91 mm and 8.74mm. The nozzles that were used in the dual jet experiments had D=3.0 and 4.0mm.

The jet exit velocity U_o was always subsonic. The value of U_o was calculated from the nozzle total pressure and ambient condition values, assuming isentropic flow conditions.

The nozzle unit was mounted on a structure which could be set at different angles and distances from the solid boundary. This consisted of a plate of plastic laminated material of the type currently used in the manufacture of blackboards. Its surface was smooth, though not polished.

Mean values of the velocity and shear-stress were obtained with a round total pressure tube used either as a pitot tube or a Preston tube. As the static pressure was equal to the ambient pressure almost everywhere for the flows that were studied, the total pressure reading was a direct measure of the dynamic pressure. Some measurements made with a pitot-static probe checked this assumption. The Preston tube was calibrated using the results of Head & Ram [1] and its validity was verified in a fully developed smooth pipe flow.

Some turbulent characteristics were determined using constant temperature hot-wire probes and a Disa anemometer unit. Measurements of shear-stress fluctuations were also made with a hot-film flush mounted probe, operated at constant temperature with the same electronic equipment. The calibration of this probe was performed directly on the jet flow using the results obtained with the Preston tube.

A detailed description of the experimental equipment is to be found in Viegas [2].

3.- NORMAL JET

The flow produced by a circular turbulent jet impinging normally on a flat plate is sketched in figure 1, together with the main symbols used.

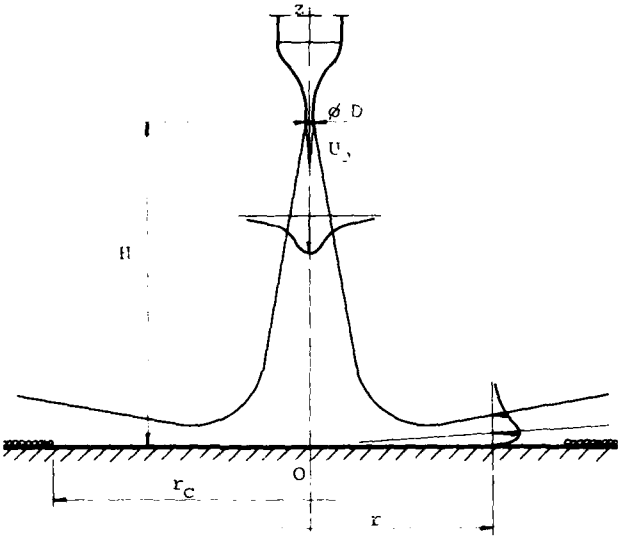

Figure 1 - Normal jet Flow

This flow has been described and studied by several authors (Ref.[3]to[8]). Most of these authors studied the mean pressure and velocity fields, as well as their turbulent caracteristics, either in the impact region or in the radial wall jet. However, as already mentioned, the main purpose of the present paper is the shear-stress distribution on the plane surface. In the case of the normal jet stress fluctuations were also studied in order to evaluate the magnitude of the error involved in the erosion technique.

The shear-stress τ_w at the wall can be represented by the non dimensional paramete

$$\psi = \frac{2\,\tau_w}{\rho\,U_o^2}\left(\frac{H}{D}\right)^2 \qquad (1)$$

which is a function of r/H and of the jet's Reynolds number

$$R_o = \frac{U_o\,D}{\nu} \qquad (2)$$

For the impact region (r/H < 0.2) ref. [6] presents the following expression:

$$\psi = 0.0576\left\{1-\exp\left(-114\left(\frac{r}{H}\right)^2\right)\frac{H}{r}\right\} - 3.02\,\frac{r}{H}\left\{\exp\left(-114\left(\frac{r}{H}\right)^2\right)\right\} \qquad (3)$$

which represents the experimental results quite well for r/H<0.3, as is shown in figure 2. For the wall jet region ψ can be expressed by:

$$\psi = s \left(\frac{r}{H}\right)^{t} \tag{4}$$

where both s and t are slowly varying functions of R_o. The present measurements, together with those of {3},{5} and {6}, showed that:

$$s = 0.214\ R_o^{-0.256} \tag{5}$$

$$t = -\ 0.878\ R_o^{0.078} \tag{6}$$

Substituting Eq. (5) and (6) in (4) one obtains:

$$\psi = 0.214\ R_o^{-0.256} \left(\frac{r}{H}\right)^{-0.878\ R_o^{0.078}} \tag{7}$$

The experimental results are shown in figure 2, in comparison with the curves given by Eq. (3) and (7) for several values of R_o.

	H/D	$R_o \times 10^{-4}$	Ref.
◆	20.5	0.78	Pres.
●	38	1.08	res.
◆	20.5	1.87	
○	38	3.34	
◇	20.5	3.34	
▲	38	6.75	
△	20.5	8	
▽	65.7	6.2	{6}
▼	21.2	8.0	
×	18	18	{3}
◑		9.22	{5}
◐		24.5	
◒		41.5	

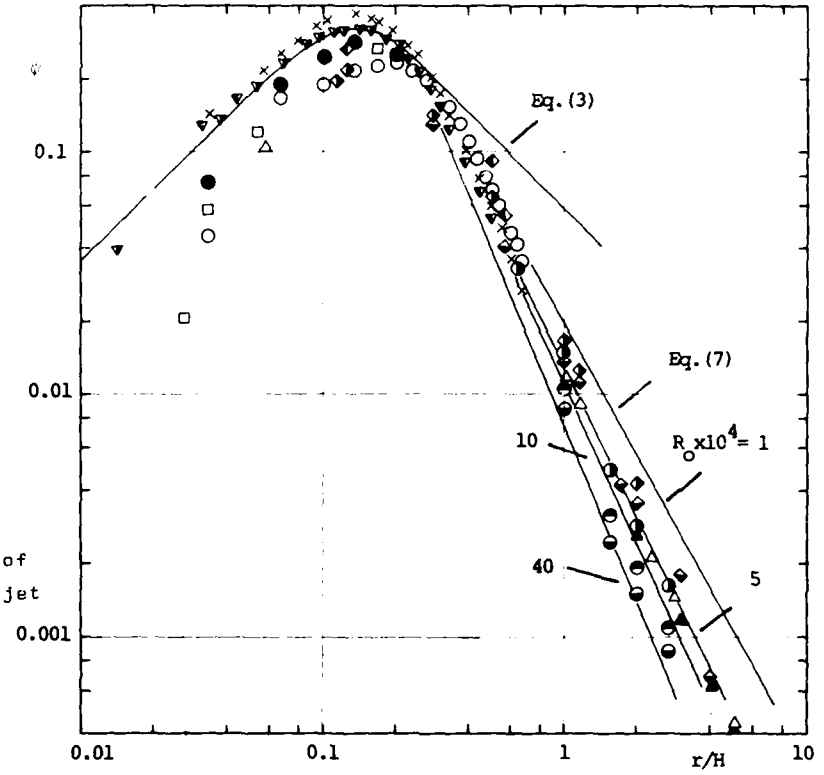

Figure 2 - Radial variation of ψ for the normal jet

Shear stress fluctuations were studied for different values of U_o and at different radial locations. It was found that in the close vicinity of the stagnation point the hot film probe had an anomalous behaviour, as was also noticed in ref.{9},{10} and {11}. The intensity of the fluctuations was found to be small compared with the mean value $\overline{\tau}_w$. The relative intensity is shown in figure 3, as a function of $\overline{\tau}_w$; it decreases from about 25%

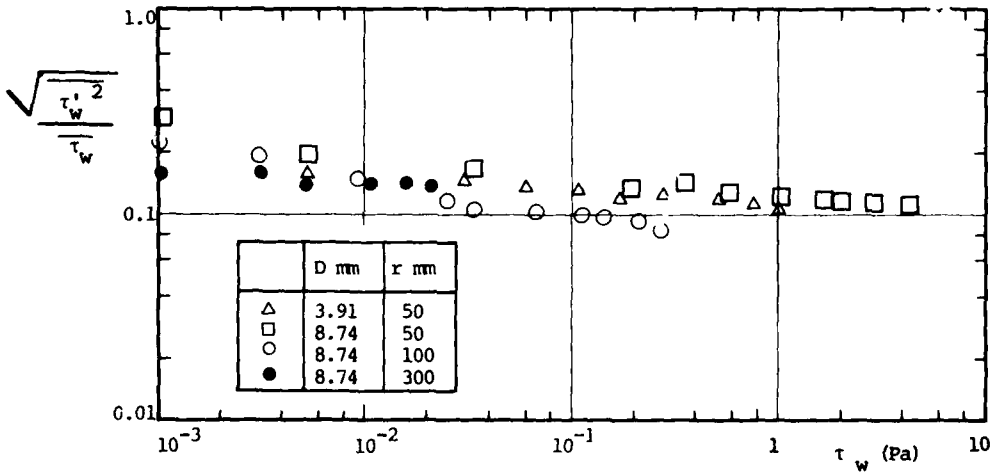

Figure 3 - Intensity of the shear-stress fluctuations as a function of its mean value

to 10% in the range of the present measurements. In turbulent fully developed pipe flow the same behaviour and values of the same order were found by others, namely [12] and [13].

4.- EROSION TECHNIQUE

When a jet impinges on a plate covered by a thin layer of uniform particles, they can be entrained by the flow and an erosion figure thereby formed. Its shape and size depend on the flow configuration and velocity, and on the characteristics of the particles. If the velocity of the jet is raised the size of the figure will increase until an equilibrium state is attained in which the particles do not move.

The erosion technique is based on the fact that the critical shear-stress τ_c that is necessary to initiate the movement of particles of a definite size, shape and density is practically constant, provided the particles are small enough to be well embeded in the constant shear-stress layer.

Sand particles were used in the present experiments. They were carefully sifted and samples of relatively uniform size were used. The samples that were most commonly used had mean sizes d=0.30mm and 0.42mm. For each size the value of τ_c was found to depend on the density of distribution of the sand over the plate. A density parameter γ defined by

$$\gamma = \frac{P}{P_o} \tag{8}$$

was introduced. P is the weight of a sample of sand distributed on a unit area, and P_o is the weight of a compact distribution on the same area of spheres of the same size and density.

The measurement of τ_c was done using the flow produced by the normal jet. Given the axisymmetry of this flow, the erosion figures are aproximately circular, as can be seen in the sample photos shown in figure 4.

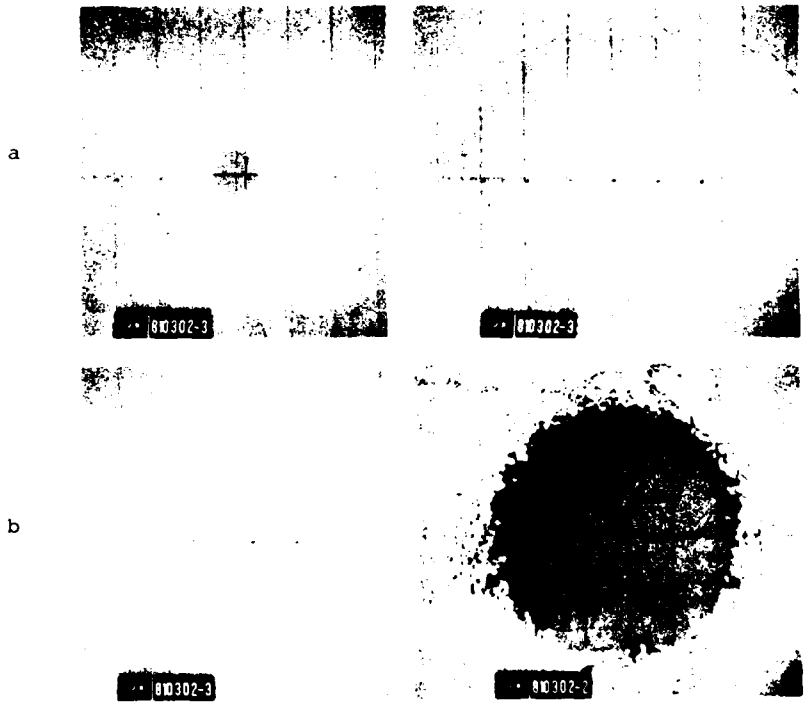

Figure 4 - Some typical erosion figures produced by the normal jet. Sand d=[illegible] mm.
γ=0.25: (a)-$R_r \times 10^{-3}$=0.98; τ_c=0.085Pa; (b)-2.92; [illegible]; (c)-5.45; [illegible].
γ=0.63: (d)-5.48;0.108.

The value of τ_w at the edge of each figure was computed using Eq. (3) or (7). The results of this calibration are represented in figure 5 for the sand with d=0.30mm, for different values of γ. The abcissa of this figure is the local Reynolds number

$$R_r = \frac{u_\tau \, r}{\nu} \tag{9}$$

As can be seen, for R_r greater than about 10^3, the value of τ_c is practically constant. Therefore a value $\overline{\tau}_c$ can be assumed for this regime, which is independent of the large scale properties of the flow and depends mainly on the local properties of the boundary layer, as was stated before. The dipersion of the experimental points is less than ±4%, which is consistent with the order of magnitude of the shear-stress fluctuations and the errors involved in the evaluation of the erosion figure contour. This results in an overall precision that is comparable with that of other techniques.

The particle's Reynolds number R_τ defined by:

$$R_\tau = \frac{u_\tau d}{\nu} \qquad (10)$$

varied between 1 and 7, which shows that the size of the particles is of the same order of magnitude as the width of the viscous sublayer of the flow.

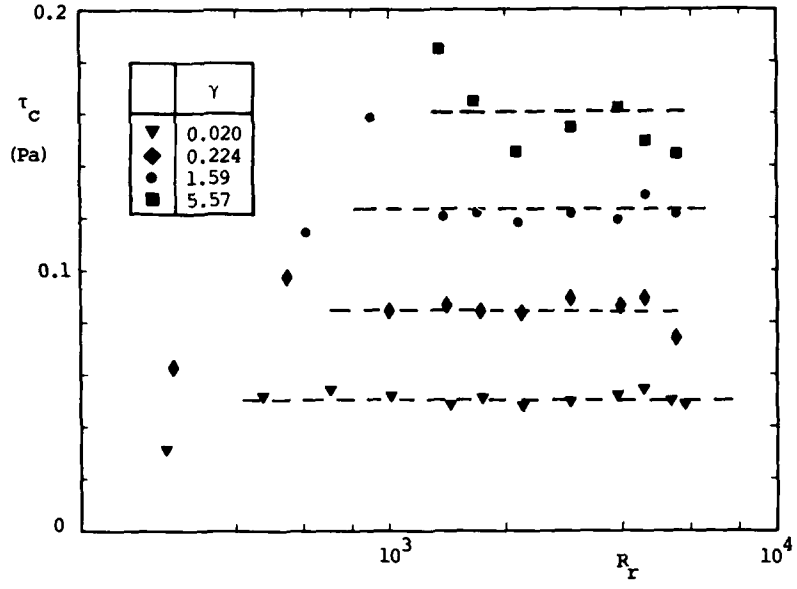

Figure 5 - Critical shear-stresses at the edge of the erosion figure for d=0.30 mm

Tests with different mean sizes and densities of distribution gave the following dependence of τ_c on d and γ:

$$\tau_c = 0.234\ d^{\,0.538}\ \gamma^{\,0.207} \qquad (11)$$

where d is expressed in mm and τ_c in Pa.

The results obtained by this technique were found to be quite repeatable and consistent for different flow geometries and densities of distribution.

5.- OBLIQUE JET

The flow produced by an oblique jet impinging with an angle ϕ_o on the plate is sketched in figure 6. A detailed description of this flow can be found elsewhere ([14] and [15]).

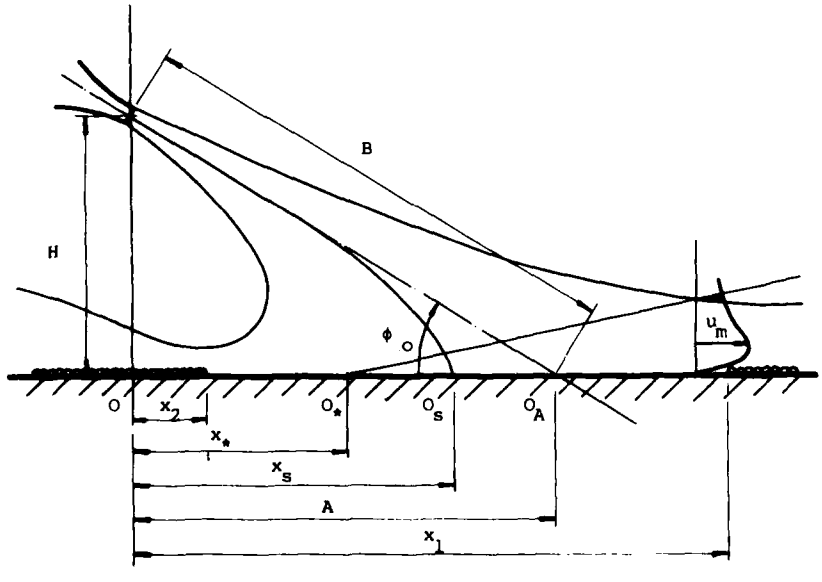

Figure 6 - Oblique jet flow

Erosion tests were made for several configurations, varying the parameter H/D between 15 and 80. The angles of incidence were 15,30,45 and 60°. The validity of the previous calibration was checked for the oblique and parallel jet (ϕ_o=60 and 0° respectively). The results of the erosion tests for these cases showed a good agreement with direct measurements of τ_w using the Preston tube, thus confirming the assumptions that were made about the independence of τ_c on the large scale flow properties.

The maximum value of τ_w on the plane is associated to the most severe interaction between the jet and the surface, which makes its knowledge of great practical importance. Some tests with the normal jet showed that this maximum value ψ_m depends on R_o and H. Using the erosion technique aproximate values of ψ_m were obtained for different angles of incidence. These are shown in figure 7.

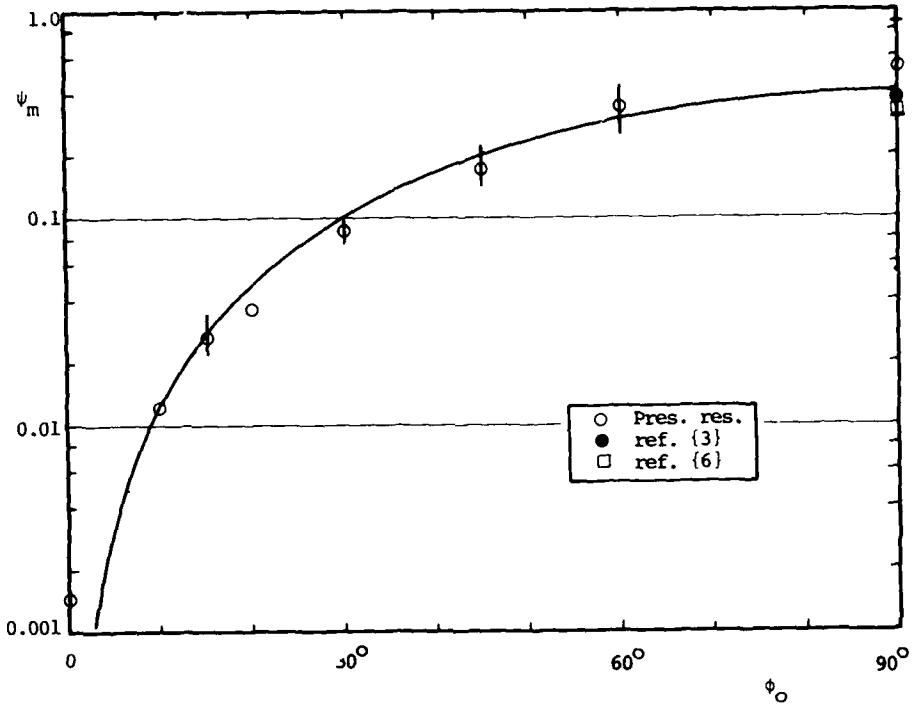

Figure 7 - Maximum shear-stress coefficient for different angles of incidence

It was found that ψ_m varies aproximately with:

$$\psi_m = 0.46 \sin^2 \phi_o \qquad (12)$$

as is shown in the figure. Noting that $B=H/\sin\phi_o$ is the distance along the jet axis from the nozzle to the plate and using the definition of ψ, one gets:

$$\tau_m \propto B^2 \frac{1}{2} \rho U_o^2 D^2 \qquad (13)$$

This result means that the maximum value of the shear-stress is related to the distance of development of the jet before impingement, wathever the angle of impingement may be. The same behaviour was observed for the stagnation pressure by {4} and {14}.

Outside the impact region τ_w decreases also according to a power law similar to that of Eq. (4). Representing by x_1 and x_2 the abcissæ of the edges of the erosion figure, located respectively at the right and at the left of the stagnation point (cf. figure 6), one can define the non dimensional coordinates ξ_1 and ξ_2 by:

$$\xi_1 = \frac{x_1 - x_A}{H} \qquad (14)$$

$$\xi_2 = \frac{x_A - x_2}{H} \qquad (15)$$

The results obtained for different angles of incidence are shown in figure 8 (a) and (b) respectively for ξ_1 and ξ_2.

The values of $\underline{s}$ and $\underline{t}$ in Eq. (4) for the oblique jet are shown in figure 9. In this figure the values of ϕ and ϕ_o are related by:

$$\phi < 90° \qquad \phi = \phi_o$$
$$\phi > 90° \qquad \phi = 180 - \phi_o \qquad (16)$$

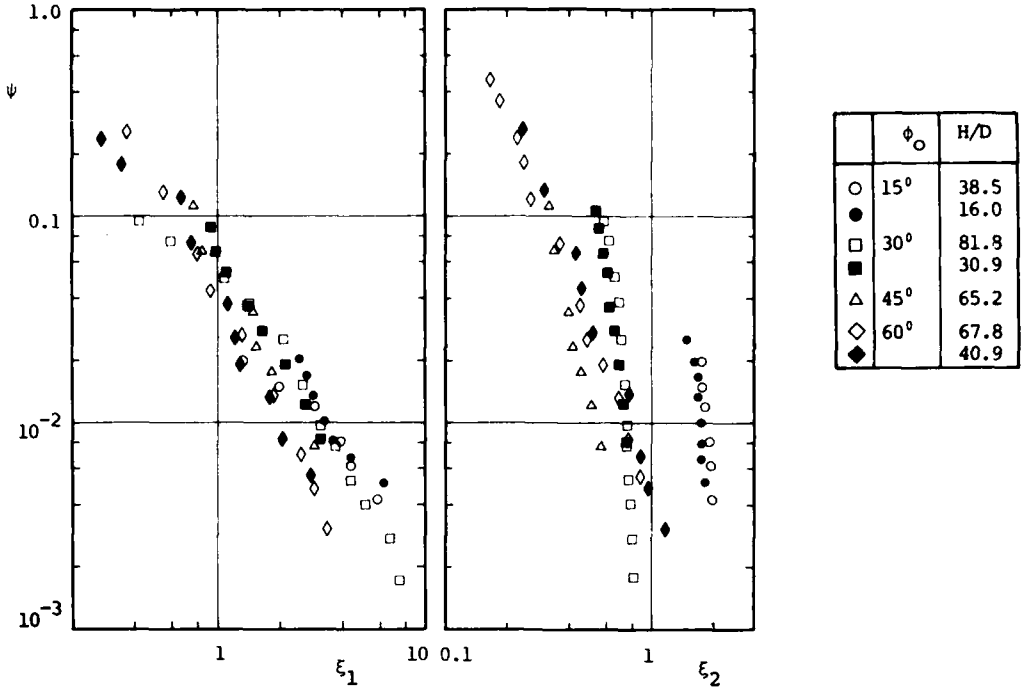

Figure 8 - Shear-stress variation along OX axis for the oblique jet

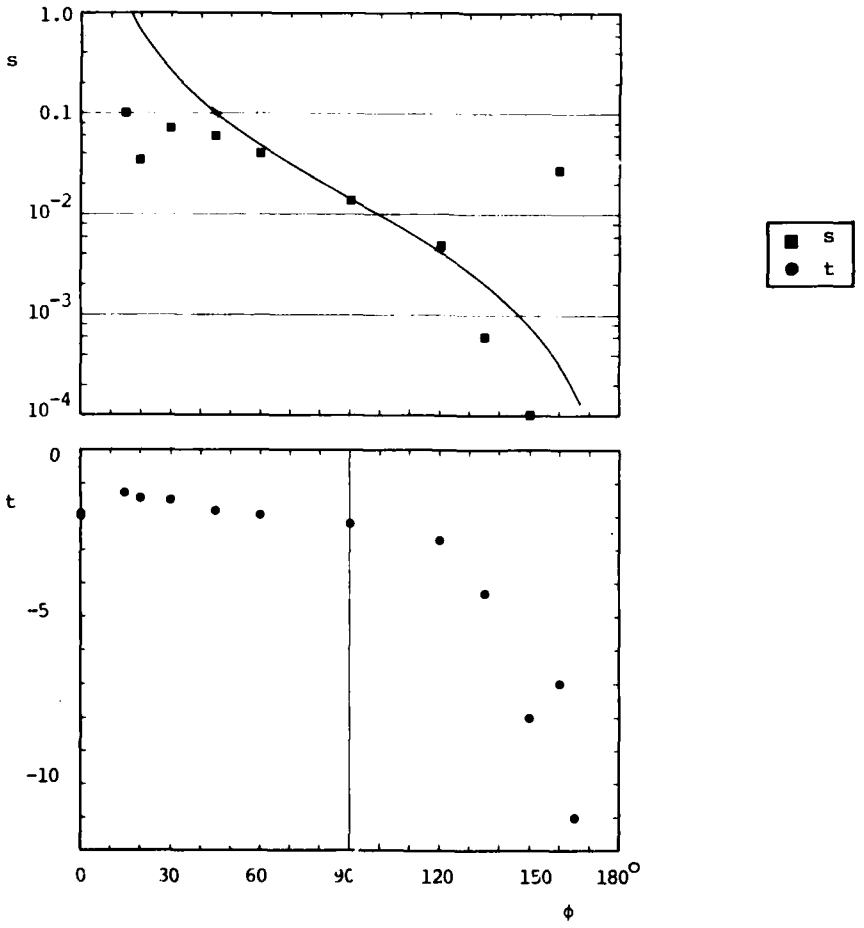

Figure 9 - Experimental values of s and t

The contour of the erosion figures can be assumed to be lines of constant shear-stress values on the plane. As for the oblique jet the flow is no longer axisymmetric it could be expected some variation of τ_c ocurring along the erosion contour. However bearing in mind the results shown in figure 5 it is reasonable to neglect this variation as it must be very small.

From the photos obtained during the erosion tests, lines of constant shear-stress were drawn for the different cases that were studied. These are shown in figure 10.

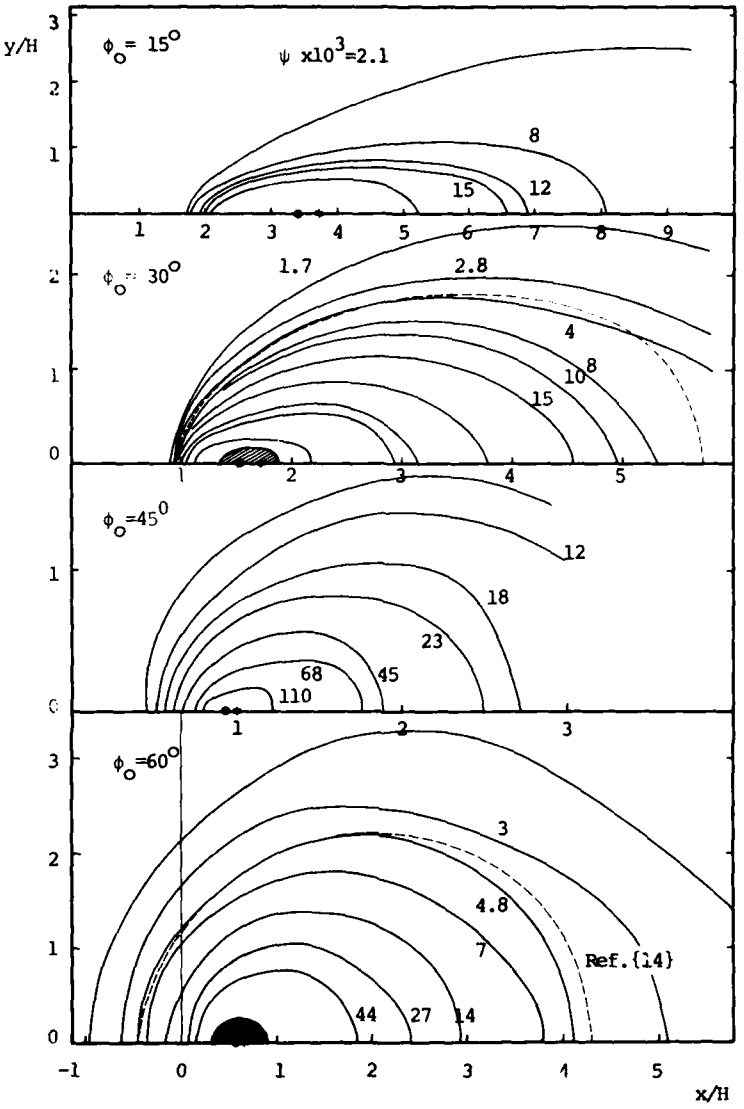

Figure 10 - Lines of constant shear-stress

An interesting property of these lines is that they are similar for each angle of incidence. This was found by reducing them to the same lenght. The collapse of the lines, although presenting some scatter, allows the definition of mean lines for each value of ϕ_o. These are shown in figure 11.

The shape of constant shear-stress lines is very similar to the constant pressure lines presented by {14}. Two of these lines for ϕ_o=30 and 60° are represented in figure 10. Their actual size is that shown by the shaded area. They have been magnified to facilitate comparison with the constant τ_w lines.

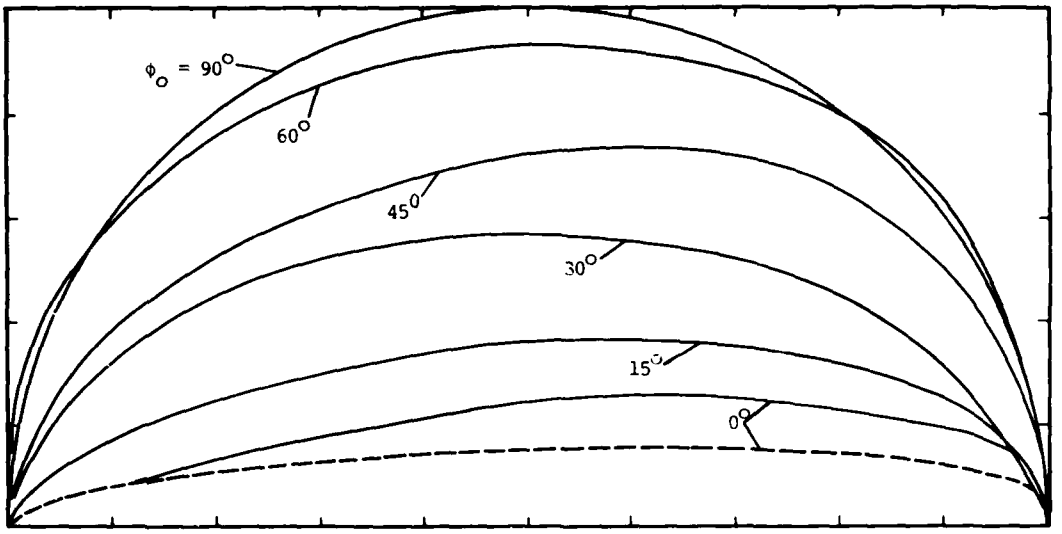

Figure 11 - Shapes of constant shear-stress lines for different angles of incidence

6.- PARALLEL JETS

Considering two parallel jets with the same characteristics, located on the OZ axis, figure 12, following {16},{17} and {2} it is found that the dynamic pressure at a point Q(x,y,z) is given by:

$$\left(\frac{u}{U_o}\cdot\frac{H}{D}\right)^2 = 2\left(\frac{k_o}{x'}\right)^2 \exp\left(-\frac{y'^2+z'^2+1}{(kx')^2}\right)\cosh\frac{2z'}{(kx')^2} \qquad (17)$$

where k and k_o are characteristic constants of the jets and:

$$x' = x/H \; ; \quad y' = y/H \; ; \quad z' = z/H \qquad (18)$$

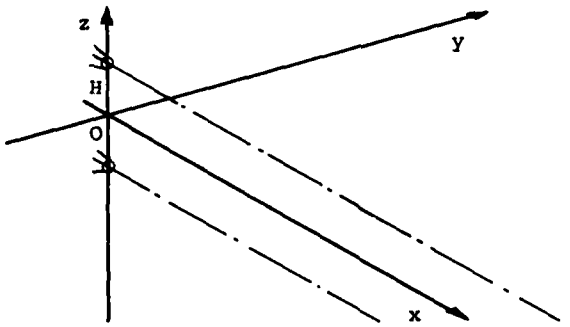

Figure 12 - Geometry definition

Introducing the velocity coefficient

$$\mu = \frac{u}{U_o}\cdot\frac{H}{D} \qquad (19)$$

Eq. (17) shows that for two free jets μ does not depend explicitely on H/D.

Making z=0 and y=0 in (17) one gets respectively:

$$\mu_y = \sqrt{2}\,\frac{k_o}{x'}\exp\left(-\frac{1+y'^2}{2(kx')^2}\right) \qquad (20)$$

$$\mu_z = \sqrt{2}\,\frac{k_o}{x'}\exp\left\{-\left(\frac{z'+1}{2(kx')^2}\right)\right\}\cosh\frac{2z'}{(kx')^2} \qquad (21)$$

These equations give the velocity profiles on XY and XZ planes respectively.

The present analytical model predicts the atachment of the two jets, which after some distance (x 40H) behave like a single circular jet with characteristics similar to the original ones. A detailed analysis of this model and its agreement with experimental results can be found in {2}.

Considering only non negative values of $\underline{z}$ in Eq. (17), this model can be used to study the interaction of a single jet parallel to the plane XY.

Velocity profiles given by Eq. (21) are compared with experimental curves in figure 13. The agreement is quite good except in a small region close to the surface, as could be expected because of the no-slip condition at the wall.

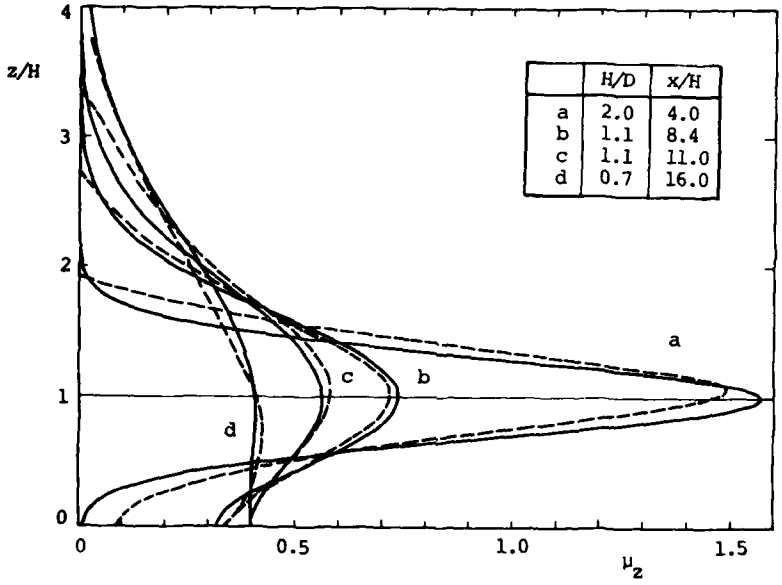

	H/D	x/H
a	2.0	4.0
b	1.1	8.4
c	1.1	11.0
d	0.7	16.0

Figure 13 - Velocity profiles in the symmetry plane for a single parallel jet.

---- Experimental curves
—— Model prediction

As the shear-stress distribution is related to the velocity field close to the surface, the same model will be used to predict the variation of τ_w on the plane XY where $\underline{u}$ shall be replaced by u_τ and it can be written:

$$\psi = \frac{2u_\tau^2}{U_o^2}\left(\frac{H}{D}\right)^2 = ? \frac{k_o'^2}{x'^2}\exp\left(-\frac{1+y'^2}{(k'x')^2}\right) \qquad (22)$$

In this equation k and k_o were replaced by k' and k_o'. Their values were determined experimentally by comparison of the curve of Eq. (22) with direct measurements of τ_w. The best correlation was obtained with $k_o'=0.46$ and $k'=0.11$.

Solving Eq. (22) in order to y' one obtains:

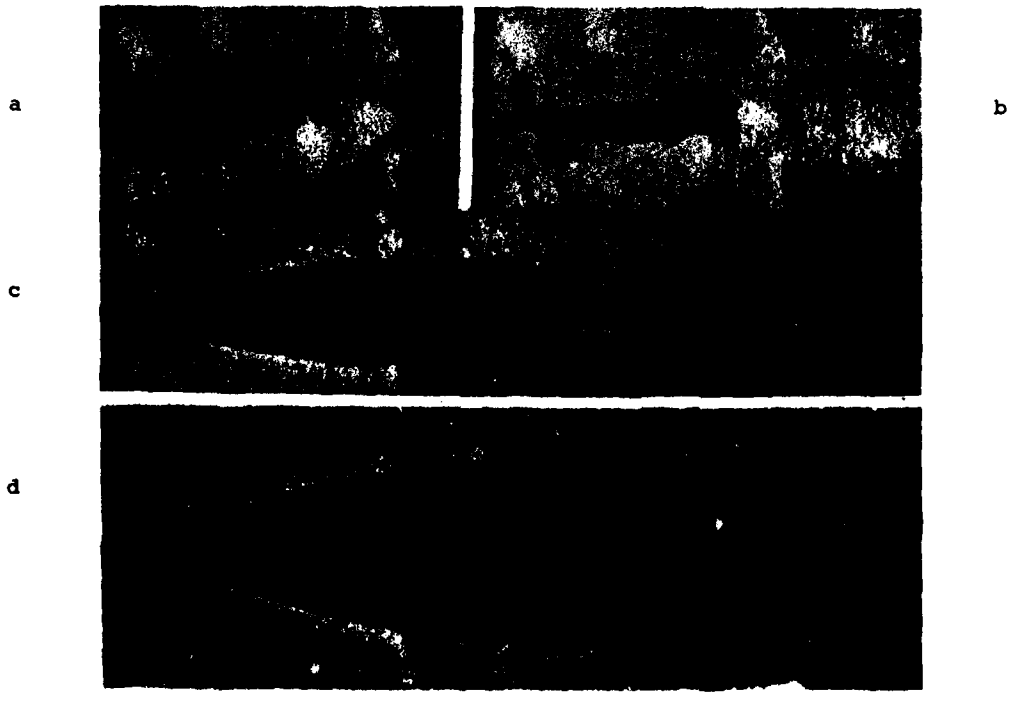

Figure 14 - Some erosion figures produced by a single parallel jet H/D=1.0. (a)-U_o=15.5m/s; $\psi x10^4$=4.2; (b)-21.9;2.8; (c)-43.8;0.60; (d)-68.1;0.30.

$$y' = \sqrt{(k'x')^2 \ln\left(\frac{2k_o'^2}{\psi x'^2}\right) - 1} \qquad (23)$$

that represents a family of lines whose parameter is ψ.

Constant shear-stress lines obtained by erosion tests (figure 14) are compared with those given by the present model in figure 15 and the agreement is found to be good. For the smaller values of ψ an empirical variation of k' between 0.11 and 0.24 was adopted to allow for the efect of boundary layer transition. For details see {2}.

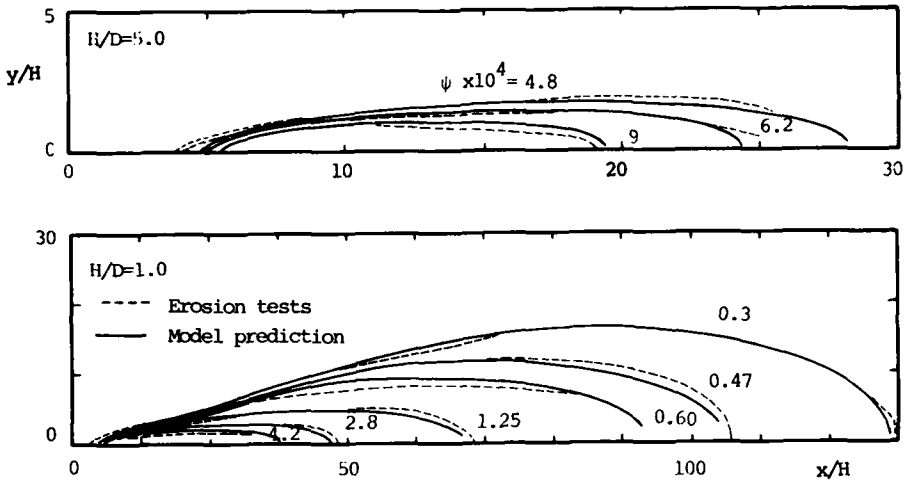

Figure 15 - Lines of constant shear-stress for the single jet

In the case of two equal jets parallel to the plane XY the same procedure used above leads to:

$$\psi = 4\left(\frac{k_o'}{x'}\right)^2 \exp\left(-\frac{1+y'+S'}{(k'x')^2}\right) \cosh\frac{2S'y'}{(k'x')^2} \qquad (24)$$

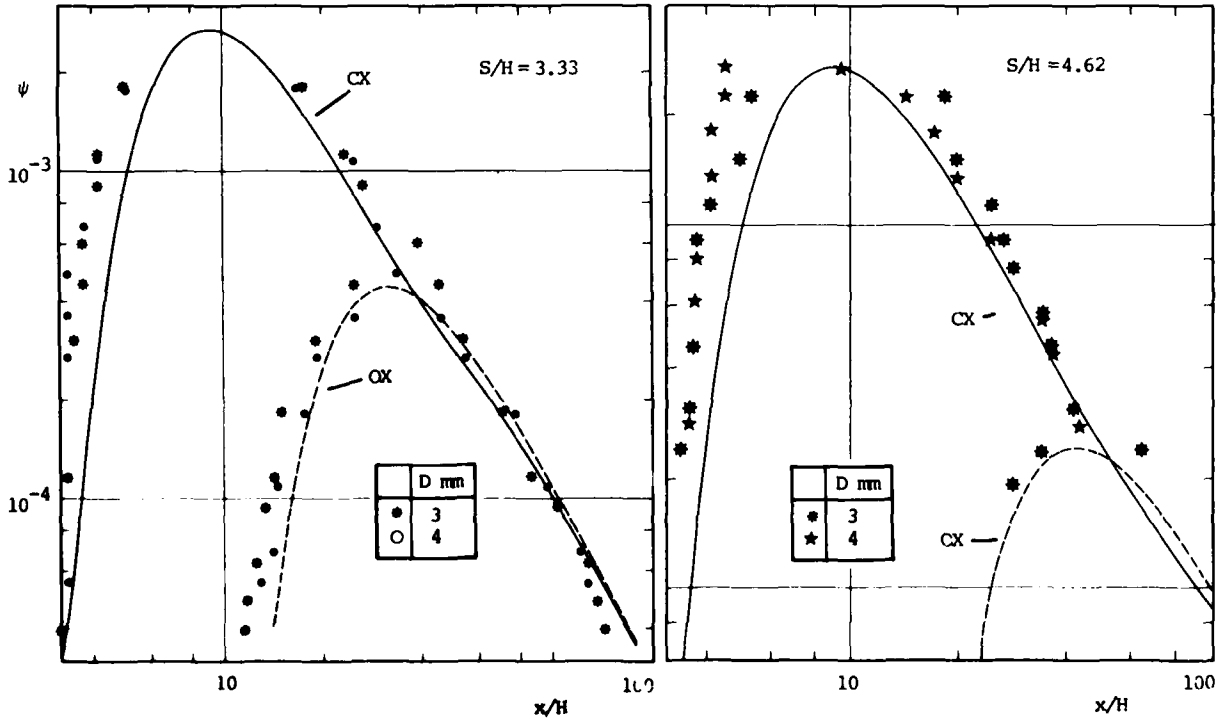

Figure 16 - Variation of the shear-stress coefficient along OX and CX axis for the dual jet

This equation represents the shear-stress distribution on plane XY. The experimental values of the constants are $k'=0.12$ and $k'_o=0.55$. The slight deviation in relation to the previous ones is certainly due to differences in the internal geometry of the nozzles used in both experiments. A configuration parameter $S'=S/H$ is present in Eq. (24) ($2S$ is the distance between the two nozzles). It is easily recognized that the most relevant range of variation of S' is between 1 and 10. The following values were considered in the present study: 1.54, 3.33, 4.62 and 10.0.

The variation of ψ along the OX axis (y=0) and CX axis (y=S) is shown in figure 16 for two of the cases that were studied.

Lines of constant τ_w obtained both by erosion tests and by the analytical model are shown in figure 17.

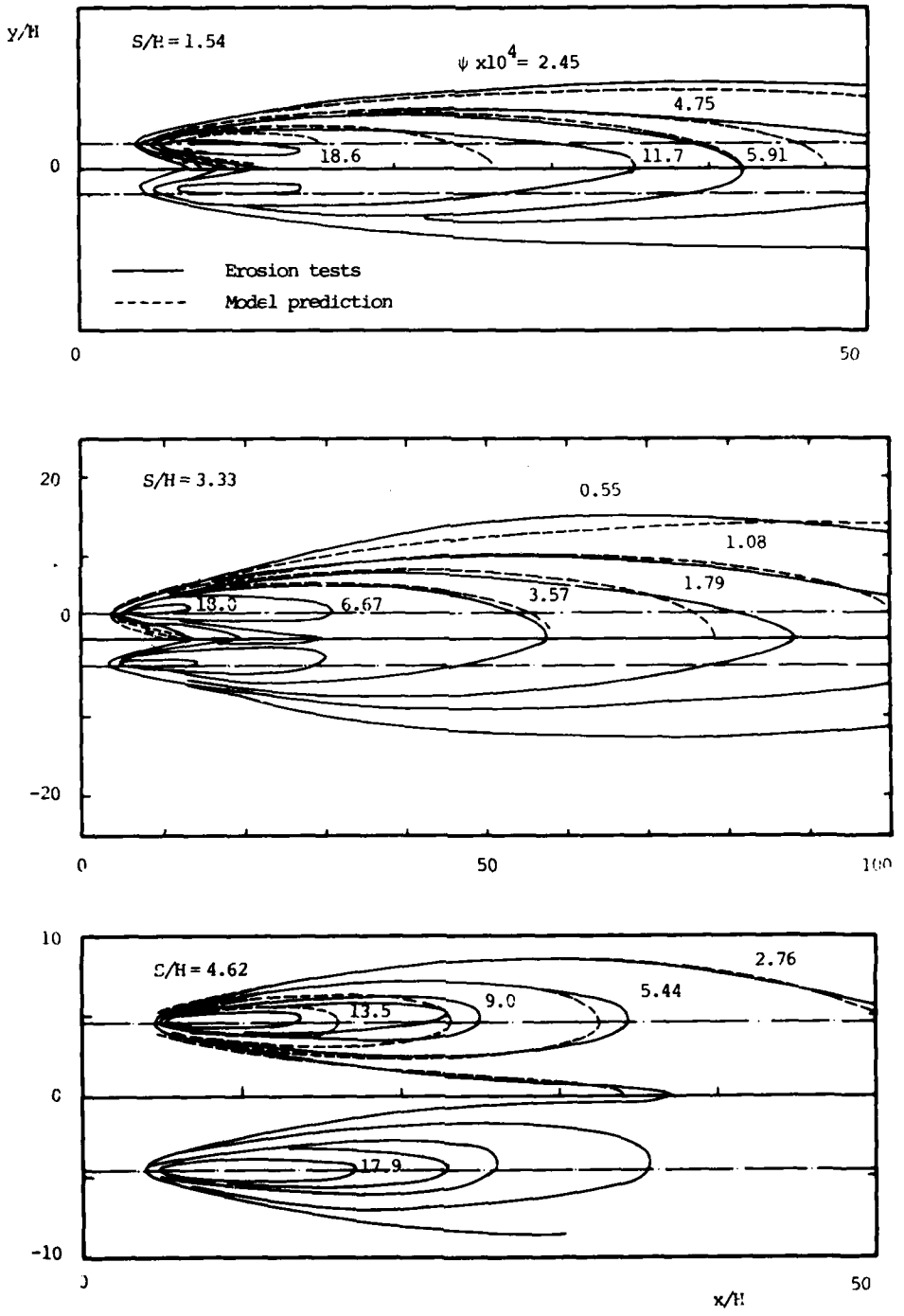

Figure 17 - Lines of constant shear-stress for the dual jet

7.- CONCLUSION

The present paper showed that it is possible to study the shear-stress field produced by a complex flow — such as that of turbulent jets impinging on a plane surface— by means of the erosion technique.

Mean shear-stress measurements for the normal jet agreed with previous results and a more general law for the radial τ_w decaying, including Reynolds number effect, was proposed. The constant shear-stress lines obtained in the oblique jet showed a similarity for each value of the angle of incidence.

The experimental results obtained with parallel single and dual jets were quite consistant with the analytical model proposed, both for mean velocity and shear-stress fields. The application of the present model and technique to more complex flow situations — asymmetrical or multiple jets — is staightforward and is expected to have sufficient accuracy for many engineering applications.

8.- REFERENCES

1 - M. R. Head & V. V. Ram - Simplified presentation of Preston tube calibration - *Aero. Quart., Vol.22, pp 295-300, 1971.*

2 - D. X. Viegas - Uma técnica de erosão aplicada ao estudo da interacção de jactos turbulentos com uma superfície plana - *Ph. D. Thesis, University of Coimbra, 1981.*

3 - P. Bradshaw & E. M. Love - The normal impingement of a circular jet on a flat surface *Aero. Research C., R&M 3205, 1961.*

4 - L. J. S. Bradbury - The normal impingement of an axisymmetric jet onto a normal ground *Aero. Quart., May 1972, pp 141-147.*

5 - M. Poreh, Y. G. Tsuei & J. E. Cermak - Investigation of a turbulent radial wall jet *J. Appl. Mech. (Trans. ASME), Paper nº 67-APM-10, 1967.*

6 - S. Beltaos & N. Rajaratnam - Impinging circular turbulent jets - *J. Hyd. Div., ASCE, Vol. 100, nº HY100, Oct. 1967, pp. 1313-1328.*

7 - Y. G. Tsuei - Axisymmetric boundary layer of a jet impinging on a smooth plate - *Ph. D. Thesis, Colorado State University, Fort Collins, Aug. 1962.*

8 - Y. Era & A. Saima - An investigation of impinging jet - *Bull. JSME, Vol. 19, nº 133, July 1976, pp. 800-807.*

9 - W. D. Baines & J. F. Keffer - Shear-stress and heat transfer at a stagnation point *Int. J. Heat & Mass Transfer, Vol. 14, nº 1, Jan. 1976, pp. 21-26.*

10 - W. D. Baines & J. F. Keffer - Measurement of shear-stress near a stagnation point *Review of Sci. Inst., Vol. 47, nº 4, Apr. 1976, pp. 440-442.*

11 - G. L. Brown - Theory and application of heated films for skin-friction measurement *Proc. of 1967 Heat Transfer and F. M. Institute, pp. 362-381.*

12 - K. R. Sreenivasan & R. A. Antonia - Properties of wall shear-stress in a turbulent duct flow - *J. Appl. Mech. (Trans. ASME), Sept. 1977, pp. 389-395.*

13 - O. Yucel & W. H. Graf - Wall-shear measurements in sand-water mixture flows - *J. Hyd. Div., ASCE, Vol. 103, 1977, pp. 947-963.*

14 - S. Beltaos - Oblique impingement of circular turbulent jets - *J. Hyd. Research, Vol. 14, 1976, pp. 17-36.*

15 - N. Rajaratnam - Turbulent jets - *Elsevier Publ. C., Amsterdam, 1976.*

16 - H. Reichardt - On a new theory of free turbulence - *J. of Aero. Soc., Vol. 47, June 1943, pp. 167-176 (Transl. from ZAMM, Vol. 21, nº 5, Oct. 1941).*

17 - R. Knystautas - The turbulent jet from a series of holes in line - *Aero. Quart., Vol. 15, Feb. 1964, pp. 1-28.*

RECOLLEMENT DE DEUX JETS SUR EUX-MÊMES

Claude Bourque, professeur titulaire
Département de génie mécanique
Université Laval, Québec, Canada
G1K 7P4

RESUME

Une étude expérimentale et théorique du recollement sur eux-mêmes de deux jets turbulents incompressibles a été effectuée. Ces jets de quantité de mouvement différente sont issus de tuyères de directions initiales quelconques séparées par une paroi solide. Ils entourent donc avant de se rencontrer une zone morte en dépression ou en pression suivant les directions initiales relatives des jets.

Expérimentalement, la position du point mort correspondant au recollement a été déterminée pour différentes valeurs des paramètres géométriques. Des mesures de profils des vitesses dans le jet résultant ont été faites et la direction ainsi que la position de ce jet ont été déterminées.

La théorie donne la position du point de recollement, la pression dans l'eau morte entre les jets initiaux et le développement du jet résultant.

NOTATIONS

b	:	largeur de la tuyère
C_p	:	coefficient de pression
d	:	position du jet résultant
D	:	distance entre les deux tuyères
J	:	quantité de mouvement
p	:	pression statique
Q	:	débit volumique
R	:	rayon de courbure de la trajectoire d'un jet
S	:	distance le long du jet
t	:	variable définie par l'équation (8a)
u	:	vitesse en un point du jet
U	:	vitesse à la sortie des tuyères
X	:	distance normale au plan contenant les sorties des tuyères
y	:	distance normale à S
$\bar{y}$	:	valeur de y à la ligne de courant de séparation
Y	:	distance dans la direction du plan de sortie des tuyères
α	:	direction du jet résultant
β	:	direction des jets
Δp	:	différence de pression statique
ρ	:	masse spécifique
σ	:	constante
θ	:	angle de recollement des jets

INDICES

e	:	entraîné de l'eau morte
∞	:	loin des jets
o	:	dans le plan de sortie des tuyères
r	:	retour dans l'eau morte
R	:	au point de recollement
1	:	jet principal
2	:	jet secondaire
3	:	jet résultant
X	:	dans la direction X
Y	:	dans la direction Y

Depuis l'avènement de la fluidique en 1960 de nombreux travaux sur la déviation d'un jet principal par un jet de contrôle plus faible ont été publiés. Il s'agit généralement d'un jet de contrôle perpendiculaire au jet principal et adjacent à ce dernier tel que rencontré dans les amplificateurs proportionnels ou les éléments à bascule. Par ailleurs lorsque l'on veut comparer deux jets dont la quantité de mouvement est du même ordre de grandeur, on utilise un modulateur de deux jets en sens inverse sur le même axe.

On peut concevoir un élément qui peut servir soit d'amplificateur proportionnel, soit de modulateur et qui est constitué de deux jets parallèles ou divergents éloignés au départ d'une certaine distance. L'avantage de cet arrangement est que le jet résultant est déplacé ou dévié entre des limites finies et bien définies lorsque le rapport des quantités de mouvement des deux jets varie de zéro à l'infini. Ce problème de recollement de deux jets a été abordé par Marsters (Ref 1) qui s'est limité à la détermination du recollement de deux jets parallèles identiques. Une étude plus générale théorique et expérimentale avec des jets de directions et de quantités de mouvement différentes et incluant la direction du jet résultant a donc été entreprise.

THEORIE

La formulation des équations conduisant à la détermination du point de recollement (Ref 2) est basée sur le modèle utilisé à la référence 3 avec les hypothèses suivantes:

1) le fluide est incompressible et le même partout
2) l'écoulement est bidimensionnel
3) la vitesse à la sortie des tuyères est uniforme
4) la pression dans la bulle est uniforme
5) les jets sont minces
6) les trajectoires des jets avant le recollement sont des arcs de cercle
7) les profils des vitesses des jets sont donnés par la théorie bidimensionnelle de Görtler

Le modèle de l'écoulement résultant de ces hypothèses est présenté à la figure 1.

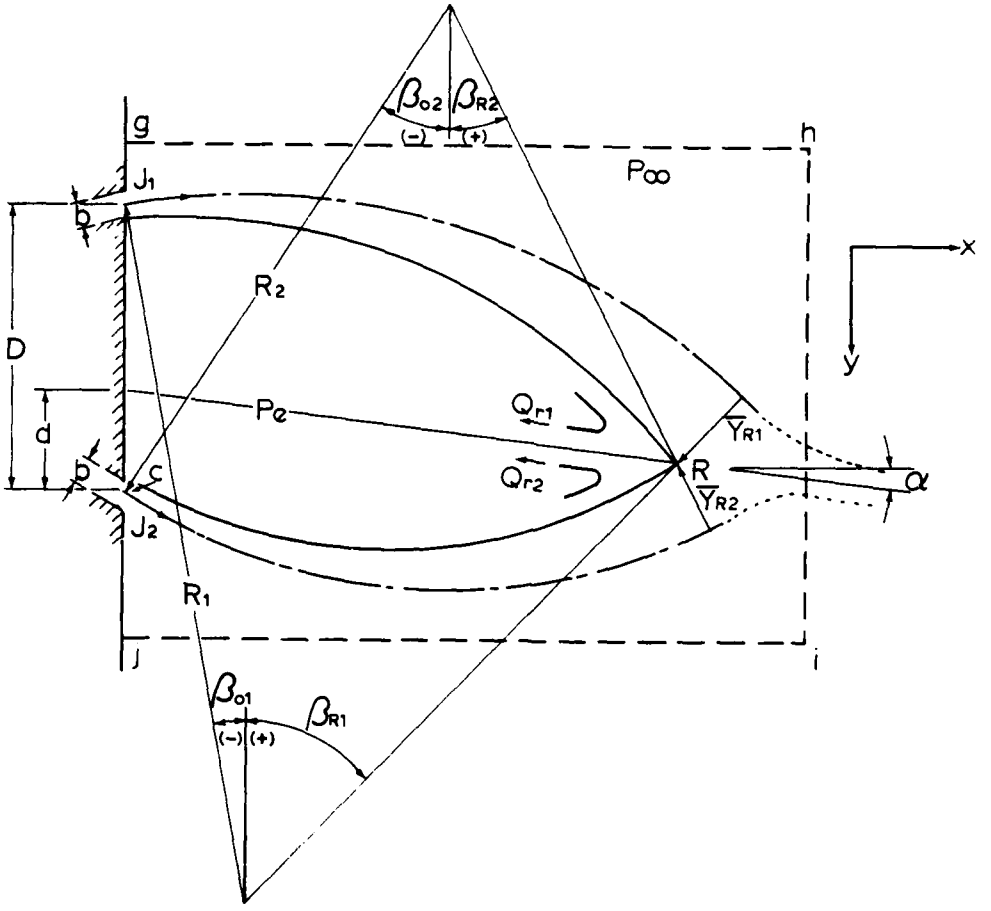

Figure 1: Modèle de l'écoulement

Pour chaque jet, le coefficient de pression dans l'eau morte est

$$c_p = \frac{\Delta p}{\frac{1}{2}\rho U_o^2} \tag{1}$$

où

$$\Delta p = p_e - p_\infty = -\frac{J}{R} \tag{2}$$

ce qui permet d'écrire

$$\frac{R}{b} = -\frac{2}{c_p} \tag{3}$$

Intégrant selon y le profil des vitesses de Görtler

$$u = \frac{\sqrt{3}}{2}\sqrt{\frac{J}{\rho\sigma}}\,\operatorname{sech}^2\,\frac{\sigma y}{S} \tag{4}$$

on obtient le débit volumique en fonction de la distance S mesurée à partir de l'origine théorique du jet située à une distance $\frac{\sigma b}{3}$ en amont de la tuyère.

$$\frac{Q}{Q_o} = \sqrt{\frac{3}{\sigma}} \left(\frac{S}{b}\right)^{\frac{1}{2}} \tag{5}$$

Cette équation multipliée par sa dérivée donne

$$\frac{Q}{Q_o} \frac{dQ}{Q_o} = \frac{3}{2\sigma} d\left(\frac{S}{b}\right) \tag{6}$$

Pour une trajectoire en arc de cercle

$$d\left(\frac{S}{b}\right) = \frac{R}{b} d\beta$$

et l'équation (6) devient

$$\frac{Q}{Q_o} \frac{dQ}{Q_o} = -\frac{3}{\sigma} \frac{d\beta}{c_p}$$

qui peut être intégrée à partir de la tuyère

où $\frac{Q}{Q_o} = 1$ et $\beta = \beta_o$

pour donner le débit en fonction de l'angle β

$$\left(\frac{Q}{Q_o}\right)^2 - 1 = -\frac{6}{c_p} (\beta - \beta_o) \tag{7}$$

Pour qu'il y ait conservation de la masse il faut que la somme des débits de retour dans la bulle des deux jets au point de recollement soit égale à la somme des débits entraînés par les deux jets du côté de la bulle entre les tuyères et le point de recollement.

Le débit Q_r qui revient dans la bulle est obtenu pour chaque jet en intégrant le profil des vitesses de $\bar{y}$ à ∞ au point de recollement

$$Q_r = \frac{1}{2} Q_R (1 - t_R) \tag{8}$$

où

$$t_R = \tanh \frac{\sigma \bar{y}}{S_R} \tag{8a}$$

D'autre part le débit entraîné par un jet du côté de la bulle est

$$Q_e = \frac{1}{2} (Q_R - Q_o) \tag{9}$$

L'équation de conservation de la masse dans la bulle peut donc s'écrire avec les équations (8) et (9).

$$\frac{Q_{R1}}{2} (1 - t_{R1}) + \frac{Q_{R2}}{2} (1 - t_{R2}) = \frac{Q_{o1}}{2}\left(\frac{Q_{R1}}{Q_{o1}} - 1\right) + \frac{Q_{o2}}{2}\left(\frac{Q_{R2}}{Q_{o2}} - 1\right)$$

Introduisant

$$c_{p2} = c_{p1} \frac{J_2}{J_1} \tag{10}$$

$$\frac{Q_{o2}}{Q_{o1}} = \sqrt{\frac{J_2}{J_1}}$$

et avec l'équation (7) on obtient

$$1 - t_{R1} \sqrt{1 - \frac{6}{\sigma c_{p_1}} (\beta_{R1} - \beta_{o1})} + \sqrt{\frac{J_2}{J_1}} \left[1 - t_{R2} \sqrt{1 - \frac{6}{\sigma c_{p_1}} \frac{J_2}{J_1} (\beta_{R2} - \beta_{o2})}\right] = 0 \tag{11}$$

Les valeurs de t donnant les débits de retour sont déterminées à l'aide d'équations de quantité de mouvement. Comme pour le recollement d'un jet (Ref 4) des équations locales autour du recollement donnent de meilleurs résultats que des équations autour d'un volume de contrôle englobant toute la bulle. Pour poser ces équations il faut imaginer autour du point de recollement un plan dans la direction α du jet résultant (fig. 2).

Pour chaque jet dans la direction de ce plan

$$\int_{-\infty}^{\infty} \rho u^2 dy \cos\theta = \int_{-\infty}^{\bar{y}} \rho u^2 dy - \int_{\bar{y}}^{\infty} \rho u^2 dy$$

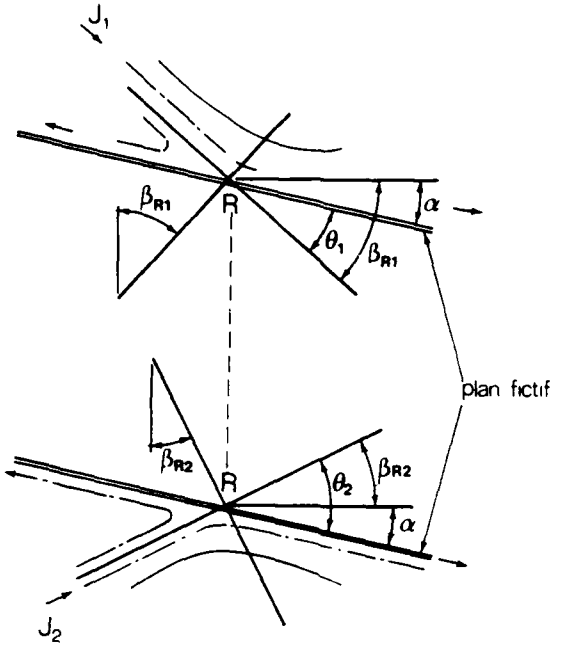

Figure 2: Plan fictif pour les équations de quantité de mouvement

Avec le profil de Görtler cette équation intégrée au recollement donne

$$\cos\theta = \frac{3}{2} t_R - \frac{t^3_R}{2}$$

En terme de β et α on a pour le premier jet

$$\cos(\beta_{R1} - \alpha) = \frac{3}{2} t_{R1} - \frac{t^3_{R1}}{2} \qquad (12)$$

et pour le deuxième

$$\cos(\beta_{R2} + \alpha) = \frac{3}{2} t_{R2} - \frac{t^3_{R2}}{2} \qquad (13)$$

L'angle α donnant la direction du jet résultant est obtenu à l'aide de deux équations de quantité de mouvement autour d'un volume de référence g h i j englobant toute la bulle. (fig. 1)

Dans la direction horizontale

$$J_{X3} = J_1 \cos\beta_{01} + J_2 \cos\beta_{02} + \Delta pD \qquad (14)$$

et dans la direction verticale

$$J_{Y3} = J_1 \sin\beta_{01} - J_2 \sin\beta_{02} \qquad (15)$$

La tangente de la direction résultante est donc

$$\operatorname{tg}\alpha = \frac{J_{y3}}{J_{x3}}$$

et l'angle est donné par

$$\alpha = \operatorname{arctg} \frac{\sin\beta_{01} - \left(\frac{J_2}{J_1}\right) \sin\beta_{02}}{\cos\beta_{01} + \left(\frac{J_2}{J_1}\right) \cos\beta_{02} + \frac{1}{2} c_{p_1} \frac{D}{b}} \qquad (16)$$

Les distances $\bar{y}$ entre les plans de symétrie et les lignes de séparation des jets sont obtenues à partir de la définition déjà introduite

$$t = \tanh \frac{\sigma \bar{y}}{S}$$

qui donne

$$\frac{\bar{y}}{b} = \frac{1}{\sigma} \frac{S}{b} \tanh^{-1} t$$

Avec les équations (5) et (7) ceci devient

$$\frac{\bar{y}}{b} = \frac{1}{3}\left[1 - \frac{6}{\sigma c_p}(\beta - \beta_o)\tanh^{-1} t\right]$$

On a donc pour le premier jet au recollement

$$\bar{y}_{R1} = \frac{1}{3}\left[1 - \frac{6}{\sigma c_{p_1}}(\beta_{R1} - \beta_{01})\right]\tanh^{-1} t_{R1} \tag{17}$$

et pour le deuxième

$$\bar{y}_{R2} = \frac{1}{3}\left[1 - \frac{6}{\sigma c_{p_1}}\frac{J_2}{J_1}(\beta_{R2} - \beta_{02})\right]\tanh^{-1} t_{R2} \tag{18}$$

A ceci il faut ajouter quelques relations géométriques en rapport avec la figure 3.

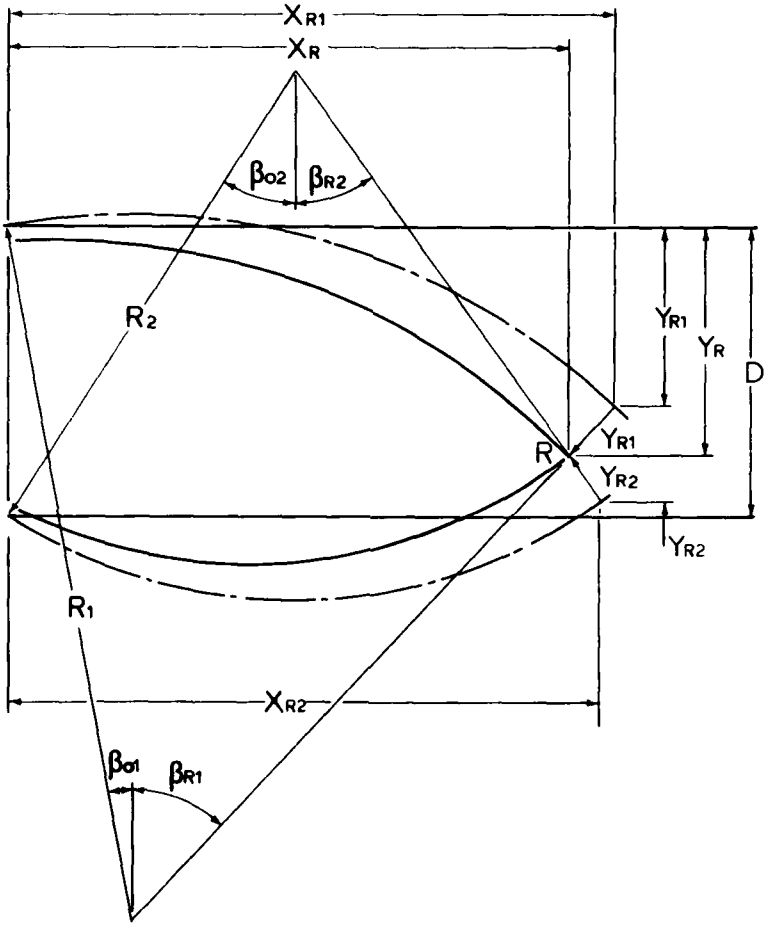

Figure 3: Dimensions relatives au modèle de l'écoulement

$$\frac{D}{b} \quad \frac{Y_{R1}}{b} + \frac{\bar{y}_{R1}}{b}\cos\beta_{R1} + \frac{Y_{R2}}{b} + \frac{\bar{y}_{R2}}{b}\cos\beta_{R2} \tag{19}$$

$$\frac{X_{R1}}{b} - \frac{\bar{y}_{R1}}{b}\sin\beta_{R1} = \frac{X_{R2}}{b} - \frac{\bar{y}_{R2}}{b}\sin\beta_{R2} \tag{20}$$

où

$$\frac{Y_{R1}}{b} = \frac{R_1}{b}(\cos\beta_{01} - \cos\beta_{R1}) \tag{21}$$

$$\frac{Y_{R2}}{b} = \frac{R_2}{b}(\cos\beta_{02} - \cos\beta_{R2}) \tag{22}$$

$$\frac{X_{R1}}{b} = \frac{R_1}{b}(\sin\beta_{R1} - \sin\beta_{01}) \tag{23}$$

$$\frac{X_{R2}}{b} = \frac{R_2}{b} (\sin\beta_{R2} - \sin\beta_{02}) \qquad (24)$$

les angles β_{01} et β_{02} étant négatifs.

On a donc un système de 14 équations qui sont 3, 10, 11, 12, 13, 16, 17, 18, 19, 20, 21, 22, 23 et 24 pour les 14 inconnues t_1, t_2. c_{p1}, α , β_{R1}, β_{R2}, $\bar{y}_{R1}$, $\bar{y}_{R2}$, Y_{R1}. Y_{R2}. X_{R1}, X_{R2}, R_1 et R_2.

Ce système étant non linéaire et plusieurs des variables ne pouvant varier que dans des gammes données de valeurs toute méthode classique de solution n'a que peu de chance de converger. On arrive assez rapidement à la solution en itérant suivant le diagramme donné à la figure 4.

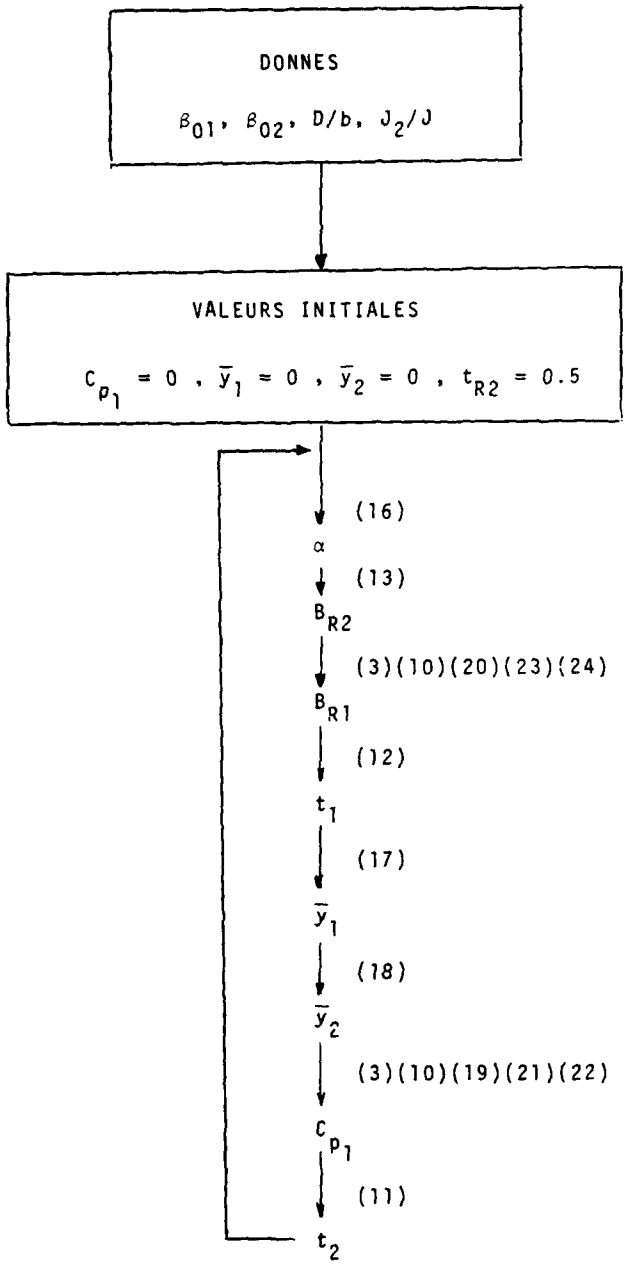

Figure 4: Marche à suivre pour la solution des équations

Les coordonnées du point de recollement sont par rapport à la tuyère supérieure

$$\frac{X_R}{b} = \frac{X_{R1}}{b} - \frac{\bar{Y}_{R1}}{b} \sin\beta_{R1}$$

et

$$\frac{Y_R}{b} = \frac{Y_{R1}}{b} + \frac{\bar{Y}_{R1}}{b} \cos\beta_{R1}$$

La position du point de recollement et la direction α du jet résultant étant déterminées le développement de ce dernier peut être calculé en faisant l'hypothèse qu'il se comporte comme un jet libre issu d'une origine localisée par rapport au point de recollement. Cette origine est déterminée en posant que le débit volumique Q_{03} et la quantité de mouvement J_3 du jet résultant à une distance S_{03} de son origine sont égaux aux débits et aux quantités de mouvement des jets 1 et 2 qui continuent en aval du recollement.

Le débit masse qui continue en aval au recollement est

$$Q_{03} = \int_{-\infty}^{\bar{y}_{R1}} u_1 dy + \int_{-\infty}^{\bar{y}_{R2}} u_2 dy$$

qui devient avec les profils de Görtler

$$\frac{Q_{03}}{Q_{01}} = \frac{1}{2} \frac{\sqrt{3}}{\sigma} \left[\sqrt{\frac{S_{R1}}{b}} (1 + t_{R1}) + \sqrt{\frac{J_2}{J_1} \frac{S_{R2}}{b}} (1 + t_{R2}) \right] \qquad (25)$$

La quantité de mouvement dans le jet résultant est

$$J_3 = \sqrt{J_{X3}^2 + J_{Y3}^2}$$

où J_{X3} et J_{Y3} sont donnés par les équations (14) et (15).

En intégrant le profil des vitesses de Görtler selon y à une distance S_{03} de l'origine on obtient

$$Q_{03} = \sqrt{3} \sqrt{\frac{J_3}{\rho\sigma}} S_{03}^{\frac{1}{2}}$$

d'où on tire la position de l'origine du jet résultant à une distance S_{03} en amont du recollement.

A une courte distance en aval du recollement le profil du jet résultant devient symétrique et il reste à déterminer la position du plan de symétrie dont la direction α est connue mais qui ne passe pas par le point de recollement. Une équation des moments de quantité de mouvement autour d'un point c situé à la sortie de la tuyère secondaire va nous donner la distance d (fig. 1).

On a par rapport au point c

$$J_1 D \cos\beta_{01} + \Delta p D \frac{D}{2} = J_3 d \cos\alpha$$

d'où on tire

$$\frac{d}{D} = \frac{J_1}{J_2} \frac{\cos\beta_0 + \frac{1}{4} cp_1 D/b}{\cos\alpha} \qquad (28)$$

MESURES EXPERIMENTALES

Toutes les mesures ont été effectuées avec le montage illustré à la figure 5. Les profils, facilement modifiables, ont été taillés dans du contraplaqué de 18 mm et sont maintenus entre deux plaques de plastique. Il est ainsi possible de faire varier la direction initiale des jets, leur largeur et la distance qui les sépare. Les débits sont ajustés à l'aide de vannes dans les conduites d'alimentation. Il a été vérifié expérimentalement qu'il n'y avait pas d'effet tridimensionnel sur la position de recollement en autant que les largeurs des tuyères n'étaient pas supérieures à 6 mm. Toutes les mesures, ont donc été effectuées avec ces largeurs maximum.

Le système de traverse peut être orienté à volonté pour être perpendiculaire à la direction du jet résultant.

Les positions des points de recollement ont été déterminées visuellement à l'aide d'une laine montée sur le bout d'une fine tige métallique. Cette méthode n'a pas permis d'obtenir des résultats satisfaisants pour les décrochements D/b plus petit que 7 et pour les rapports de quantité de mouvement J_2/J_1 inférieur à 0,2. La figure 6 présente quelques uns des points obtenus en comparaison avec les prévisions théoriques calculées avec σ égal à 10. On constate que l'accord est bon sauf pour les petites valeurs du rapport des quantités de mouvement. Pour ces petites valeurs, le deuxième jet est fortement incurvé et l'hypothèse de jet mince ne tient plus.

Les directions des jets résultants ont été déterminées à l'aide d'une sonde directionnelle placée à l'endroit de vitesse maximum dans les profils de vitesse. Pour chaque cas,

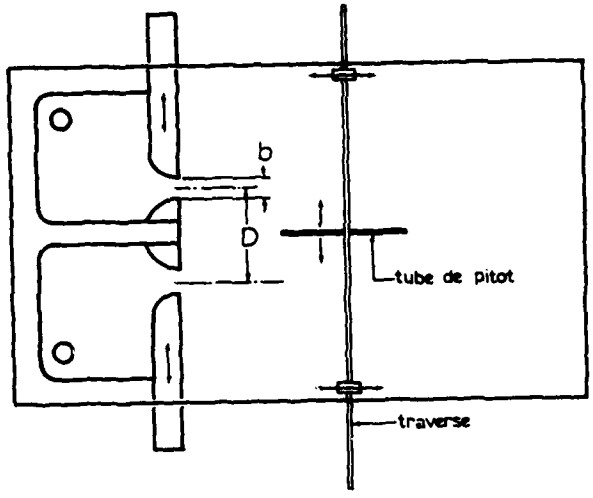

Figure 5: Montage expérimental

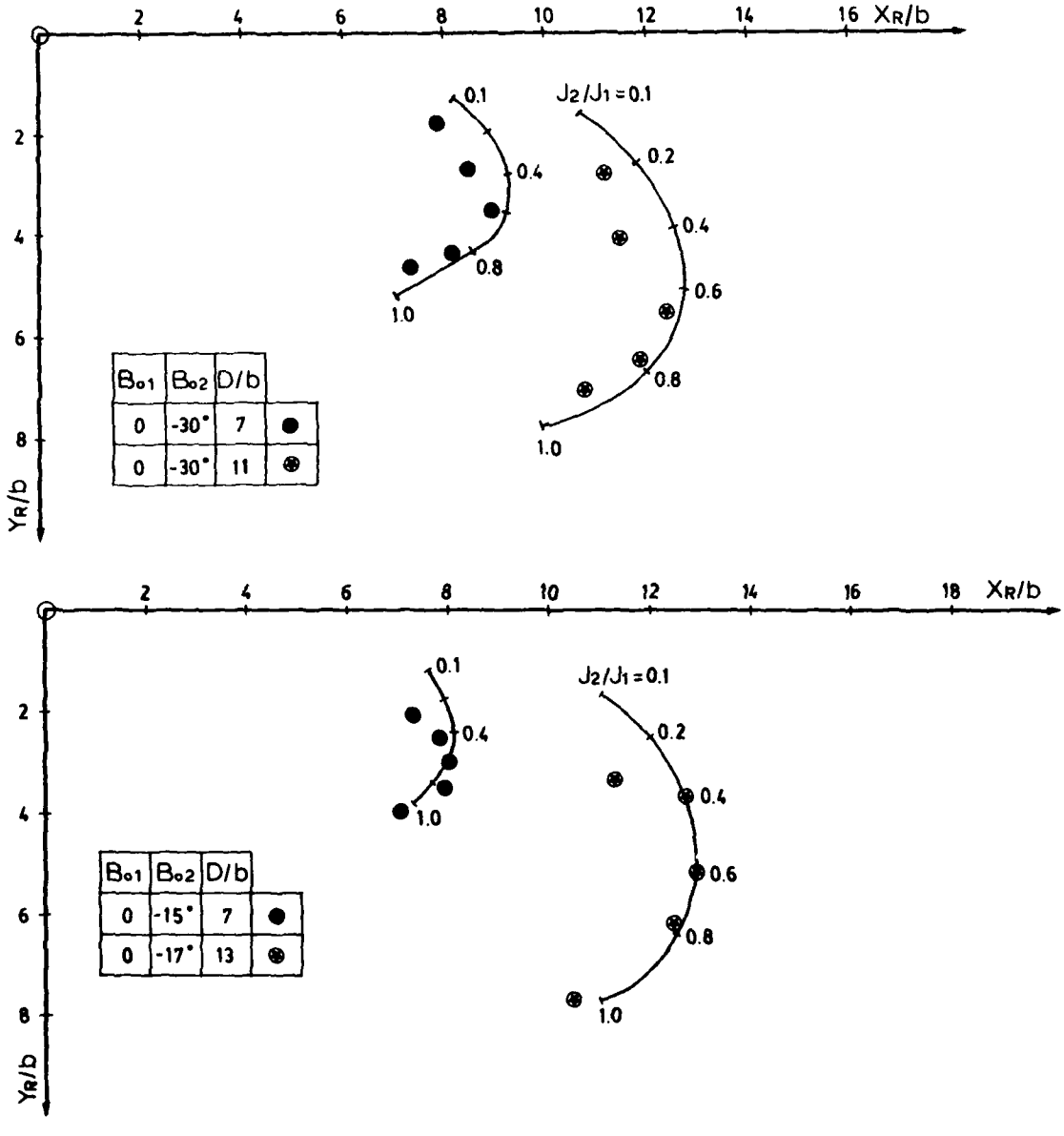

Figure 6: Position du point de recollement

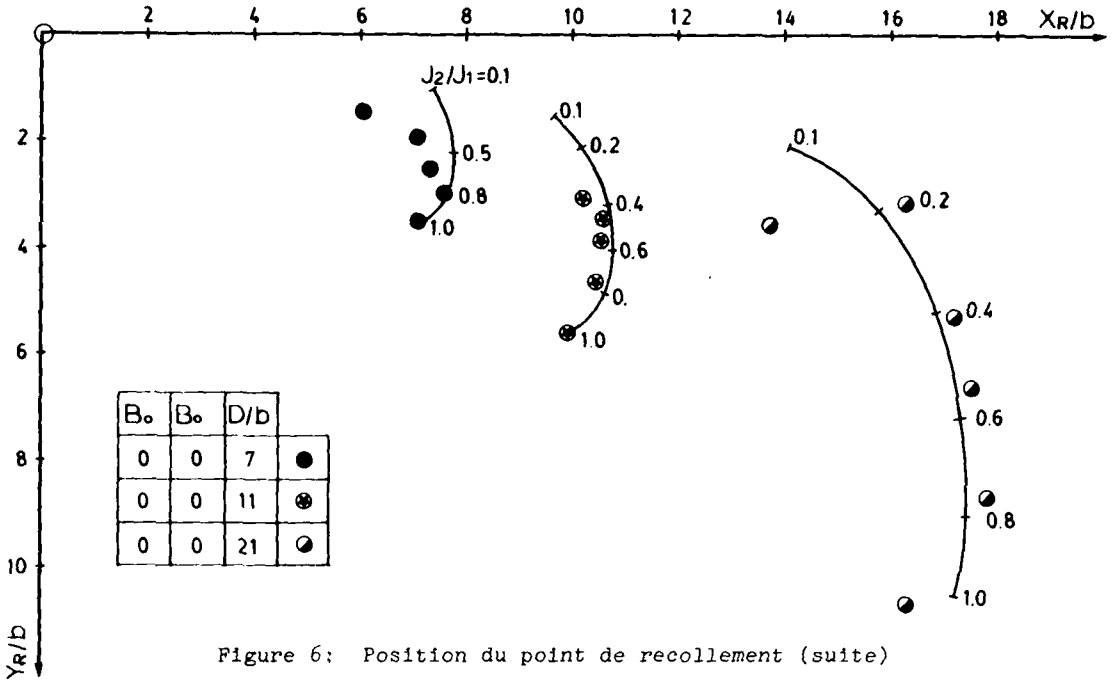

Figure 6: Position du point de recollement (suite)

les valeurs obtenues à différentes distances des tuyères étaient les mêmes. Ces résultats sont présentés à la figure 7 et l'accord avec la théorie est satisfaisant. Lorsque les deux tuyères sont parallèles, l'angle α est toujours égal à zéro et ces résultats ne sont pas présentés.

Les profils de vitesse dans les jets résultants ont été obtenus avec un tube de pitot monté sur le mécanisme de traverse placé perpendiculairement à la direction des jets. La figure 8 présente quelques uns des profils obtenus avec les profils théoriques correspondants. Ces profils ont été obtenus suffisamment loin des tuyères pour être de enus symétriques. L'accord entre la théorie et l'expérience qui est bon aux distances D/b inférieure à 11 devient mauvais aux grandes valeurs de cette distance et du rapport des quantités de mouvement. Ceci est attribuable aux effets du frottement sur les parois étant donné le faible allongement des tuyères et les grandes distances en aval où ont été faites les mesures.

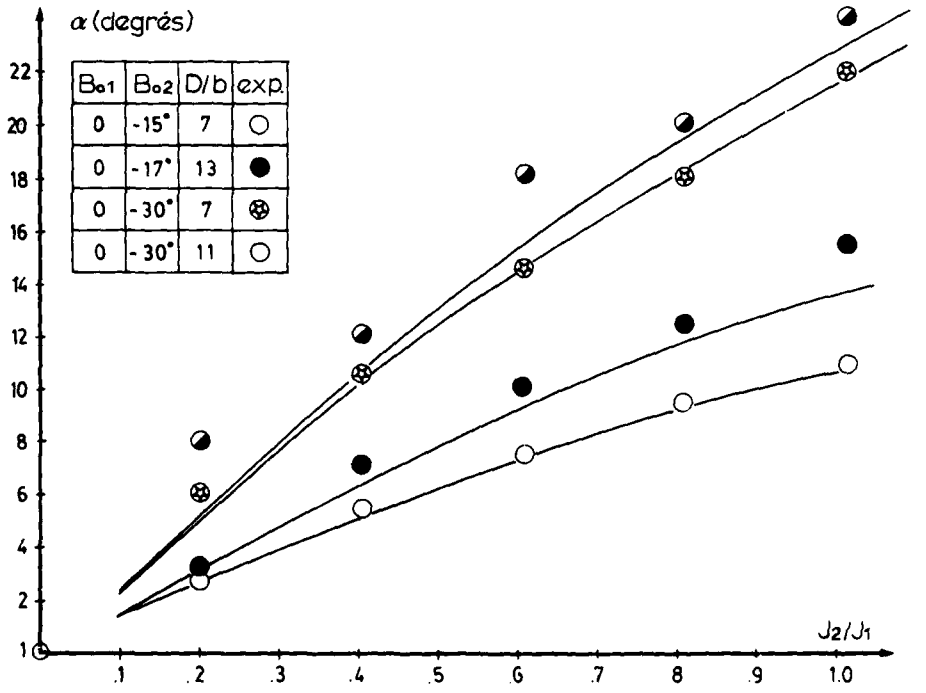

Figure 7: Direction du jet résultant

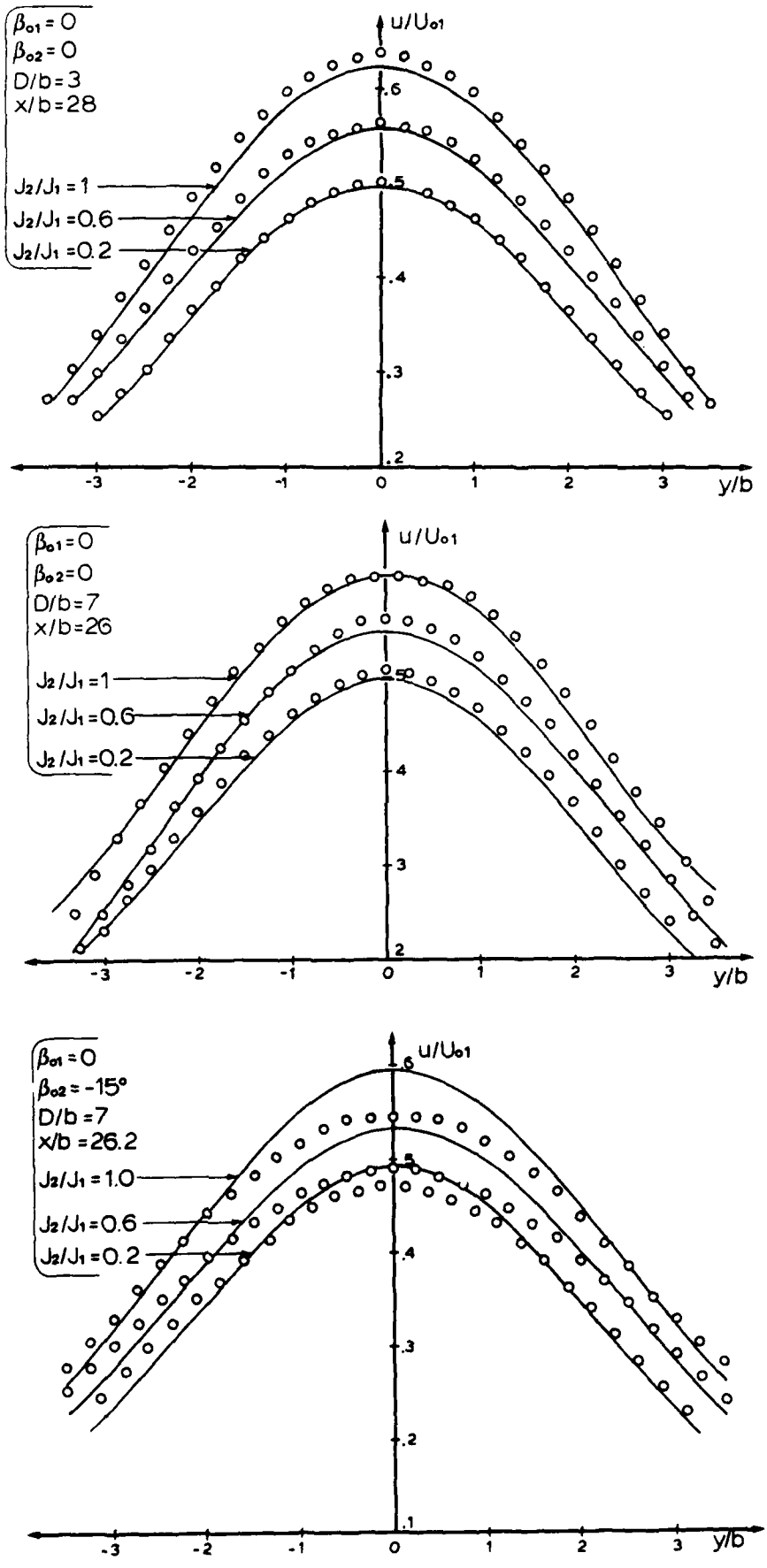

Figure 8: Profils des vitesses dans le jet résultant

La distance d/D du point d'intersection du plan de symétrie des jets résultants avec le plan des tuyères a été déterminée à l'aide de la position des profils de vitesse. La figure 9 présente ces résultats ainsi que les courbes théoriques. On constate que pour deux jets parallèles l'accord est bon sauf pour D/b égal à 3. Lorsque les jets divergent au départ, l'accord devient moins bon à mesure que J_2/J_1 augmente. Les recollements étant alors plus loin des tuyères, il y a probablement ici encore un effet de frottement sur les parois.

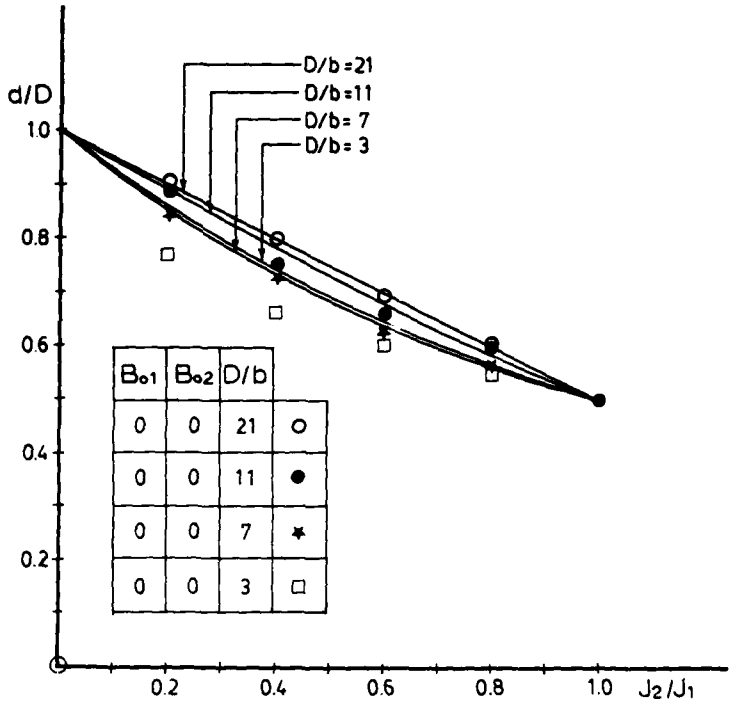

B_{o1}	B_{o2}	D/b	
0	0	21	○
0	0	11	●
0	0	7	★
0	0	3	□

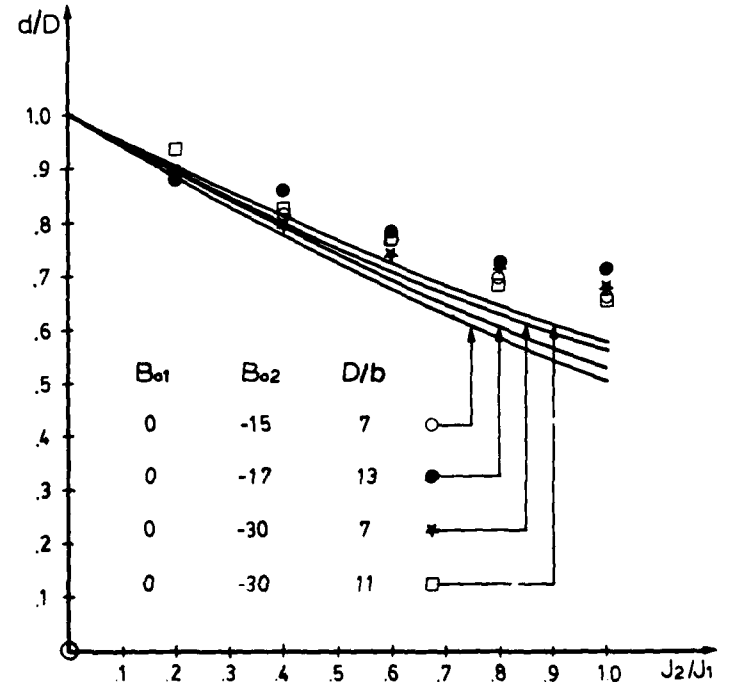

B_{o1}	B_{o2}	D/b
0	-15	7
0	-17	13
0	-30	7
0	-30	11

Figure 9: Position du jet résultant

CONCLUSION

La théorie proposée, malgré des hypothèses assez grossières, donne avec une assez bonne précision la position du recollement et le développement du jet résultant du recollement de deux jets l'un sur l'autre.

REFERENCES

1. Marsters, G.F., The Interaction of Two Plane Parallel Jets, Report 1/77, Dept. of Mech. Eng., Queen's University, Ontario, Canada, June 1977.

2. Thua, D.H., Recollement de deux jets bidimensionnels, Thèse de maîtrise, Université Laval, Québec, Canada, 1981.

3. Bourque, C., Rougier, P., Annular Jet Reattachment, C.S.M.E. Transactions, Vol. 2, No. 2, 1973-74.

4. Bourque, C., Newman, B., Reattachment of a Two-Dimensinal Incompressible Jet to an Adjacent Flat Plate. The Aeronautical Quarterly, Vol. XI, Aug. 1960.

Jets Impinging Normally and Obliquely to a wall

by

S.R.B.Araújo, D.F.G.Durão, F.J.C.Firmino

Instituto Superior Tecnico
Mechanical Engineering Department
Av. Rovisco Pais
1096 Lisbon. Portugal

ABSTRACT

An experimental study of developing jet impinging normally and obliquely on a smooth wall, is presented. A laser Doppler anemometer incorporating a frequency shift device was used to measure the mean and fluctuating velocity components in the free jet and wall jet regions.

12 nozzle diameters downstream of a 14.0 mm diameter nozzle, the jet had mean velocity profiles which were found to have reached similarity with a centre-line turbulence intensity of around 20%. At this location a circular plate was placed and the radial and circumferential development of the wall jet was analysed for impinging angles from 0 to 20 degrees. The values of the maximum velocity and of the distance from the wall to the location where the velocity is half the maximum velocity depend on radial distance and impinging and circumferential angles. The opposite is true for the non-dimensionalized mean velocity profiles which are independent from those parameters. In the fully developed wall jet, the turbulence intensity was always in excess of 30%, and the location of minimum normal stress coincided with that of maximum mean velocity.The velocity probability distributions show the large influence that the outer layer of free turbulent mixing has on the boundary-layer-type region adjacent to the plate. The rate of growth of radial wall jets is, however, smaller than that of radial free jets.

NOMENCLATURE

- b - wall jet: value of R for which $U = U_m/2$
- d - nozzle diameter
- h - distance from the nozzle to the wall, measured along jet axis
- r - free jet: radial coordinate
- $r_{1/2}$ - free jet: value of r for which $U = U_{cl}/2$
- R - wall jet: radial coordinate
- Re_o - Reynolds number at jet exit
- R_v - wall jet: radial distance from the virtual origin
- u - fluctuating velocity
- U - mean velocity
- U_o - mean velocity at nozzle exit
- U_{cl} - free jet: centre line mean velocity
- U_m - wall jet: maximum mean velocity
- x - free jet: longitudinal coordinate
- y - wall jet: coordinate perpendicular to the wall
- y_m - wall jet: value of y for which $U = U_m$
- α - impinging angle: normal impingement, $\alpha = 0$
- θ - circumferential coordinate

1. INTRODUCTION

Laser Doppler anemometry (LDA) has been used to study the flow characteristics of a single round free jet impinging perpendicularly and obliquely on a large plate. This flow finds direct practical application in a large number of engineering problems, affecting spraying, cooling, heating, drying and leaching of solids. Such a flow configuration is also produced by a downwords directed jet from VTOL or STOL aircraft spreading out over the ground.

The flow exhibits three distinct regions:

a- a "free turbulent jet region" where the flow characteristics are identical to those of a free jet,

b- an "impingement region" where the jet undergoes considerable deflection, from quasi-perpendicular to quasi-parallel to the plate, and

c- a "wall jet region" where the jet becomes almost parallel to the wall assuming a flow pattern similar to that of a radial wall jet where the effects of interaction due to the impingement are no longer important.

This hybrid structure , consisting of a free jet, deflecting flow and wall boundary layer with a free upper boundary, is ideal to test the universality of turbulence models together with predicting numerical methods, provided accurate experimental results exist.

The normal impingement of a jet on a flat surface has been studied by several investigators, see references 1 to 11. Hrycak, Lee and Gaunter |1| and Beltaos and Rajaratnam |2|, |3|, used pitot tubes to study the influence of jet Reynolds number and jet distance from the wall on the mean velocity profiles of regions a) and b). Bradshaw and Love |4| reported experimental results, mainly concerning static pressure and skin friction in the impingement region. Bradbury |5| shows a dimensional analysis to correlate velocity and pressure measurements. Glauert |6| was the first to use the eddy viscosity model to study theoretically the turbulent wall jet. Poreh, Tsuei and Cermak |7| using hot-wire anemometry, have shown that the shear stress does not vanish where the velocity gradient is zero, as required by the eddy viscosity model; the measured turbulence intensities were always in excess of 30%.

Donaldson, Snedeker and Margolis |8| studied the heat transfer near the stagnation point and with hot films and hot wires, thermocouples and microphones obtained velocity, temperature and pressure distributions. Ho and Nosseir |9| present extensive pressure measurements to provide experimental evidence and explain an instability process and feedback mechanism on the pressure fluctuations. Gutmark, Wolfshtein and Wygnanski |11| investigated a plain jet impinging on a flat plate.

For the oblique impingement of a round jet on a plane surface the documentation is not extensive. Donaldson and Snedeker |12| present measurements of wall pressure and mean velocities obtained with pitot tubes for impinging angles α, of 15, 30, 45 and 60 degrees, i.e. large deviations from perpendicularity. The jet of Foss and Kleis |13| was almost tangencial to the wall, α = 81 degrees.

The present report aims to extend through experimental investigation the physical understanding of the obliquely impinging jet. LDA was used to measure the mean and fluctuating velocities for two jet Reynolds numbers, four impinging angles and five radii. The nozzle to wall distance was enough to guarantee that the impinging distance did not influence the development of the wall jet. The inaccuracies associated with measurements in highly turbulent flows and due to directional ambiguity of the instantaneous velocity vector, were removed using a LDA frequency-shift device, see reference 14.

The experimental set up and measuring procedure are described on next section, and on section three the results are presented and discussed. On section four conclusions are summarized.

2. EXPERIMENTAL SET UP AND MEASURING PROCEDURE

The jet was produced by a suitably designed nozzle of 14.0 mm diameter, d, and air was supplied by a compressor through a plenum chamber, producing velocities up to 50 m/s. A 50 cm diameter flat and smooth plate was used to provide an impinging surface. The present results were obtained with a nozzle to wall distance, h, of 12 d.

For the alignement of the jet with respect to the wall, the nozzle could be rotated around two perpendicular axis parallel to the plate and translated in two normal directions also parallel to the plate; the surface could rotate around an axis perpendicular to the jet and move along and perpendicularly to the same jet. 0.8 mm diameter pressure tappings drilled on the plate allowed the measurement of the pressure distribution on the plate surface.

Mean and rms values of velocity were obtained for jet Reynolds numbers of 42500 and 32000 and, with the jet perpendicular to the plate, i.e. impinging angle $\alpha = 0^o$, and also with α equal to 10^o, 15^o and 20^o. For the oblique impingement, the measurements were done with values of the circumferential coordinate, θ, of 0, 45, 90, 135 and 180 degrees. On the wall jet flow configuration, $\theta = 0$ corresponds to the radial direction where the values of velocity are larger.

The laser Doppler anemometer used to measure the mean and rms velocities, was of the forward scattering type and comprised a He-Ne 5 mW Spectra-Physics laser, a 150 mm focal length lens to focus the beam on a variable speed TNO rotating diffraction grating used to split and frequency-shift the laser beams, and a focussing arrangement of two 100 mm diameter lenses. The light collecting optics included a RCA photomultiplier, model 4836. In most of the measurements the distance between two consecutive fringes was 4.62 μm. The measuring control volume could be moved with respect to the fixed flow rig since the LDA optical bench was mounted on a three-dimensional traversing mechanism. The photomultiplier signal was band-pass filtered with a Krohn-Hite filter and subsequently analysed by a frequency counter interfaced to an Apple microcomputer. The signal to noise ratio of Doppler bursts was on average in excess of 20 db and the 8/16 cycles frequency comparator circuit of the counter was used with the narrowest validation interval (frequency differences less than 1%) guaranteeing the absence of significant errors in the frequency measurement within each burst. The mean and rms frequencies were calculated from 4000 samples, implying errors of around 1% and 2% respectively. A slow data acquisition rate of around 10 measurements per second, was imposed by the microcomputer to the counter, which is a fast sampling rate instrument, in order to diminish the velocity bias reported in references 14 to 18. The calculated values of the mean, rms, skewness and flatness and the velocity probability distributions were stored on floppy discs and subsequently plotted with a Hewllet-Packard digital plotter It was estimated, see references 14 and 18, that the error associated to the mean and rms values of the profiles shown in the present work is respectively 2% and 4% of the maximum value measured in the profile.

Total pressure probes of 0.8 mm O.D. were also used mounted on a traversing carriage so that they could be moved in three normal directions or rotated.

A smoke generator was used to achieve a visual picture of the flow and cinematography was employed to assist physical interpretation of the measurements.

3. RESULTS AND DISCUSSION

This section is sub-divided in three: impinging jet, wall jet with normal impingement and wall jet with oblique impingement. The figures are based on the results obtained with Reynolds number of 42500, since no significant variations were found with Re = 32000.

3.1. Impinging jet

Figure 1 presents profiles of non-dimensionalized mean velocity measured across the jet at different longitudinal distances, x, and shows that similarity is reached at approximately 8 diameters from the

nozzle. In fact,other slidly different values are also refered on the literature, since, as reported on references 1 and 19, the turbulence intensity and Reynolds number at the jet exit have influence on the initial spreading of the jet. The figure also gives the values of centre-line velocity decay, U_{c1}/U_o, and radial distance from the central axis to the location where the velocity is half the value of centre-line velocity, $r_{1/2}$. They may be evaluated by the equations:

$$U_{c1}/U_o = 6.72\ d/x \qquad \text{and} \qquad 2r_{1/2}/d = 0.172\ x/d$$

The plate was located 12 diameters downstream the nozzle and at this distance, the turbulence intensity at the centre-line of the free jet rounds 20%. Reference 3 shows that for plate to nozzle distances larger than 8.3 nozzle diameters, the development of the impinging region and wall jet is independent of h/d.

3.2. Wall jet with normal impingement

Figure 2 shows non-dimensional mean velocity distributions measured at different radii. For R/d of 9, 12 and 15, the profiles are identical indicating that before R/d = 9 the flow has reached similarity. The values of maximum velocity, U_m, and of the distance from the plate to the location where the velocity is $U_m/2$, b, are also given on the figure; for R larger than 6d, they can be determined using the following equations:

$$b/d = 0.096\ (R/d)^{0.95} \qquad U_m/U_o = 1.4\ (R_v/d)^{-1.12}$$

where R_v is the radial distance measured from the virtual wall jet origin. Plotting $1/U_m$ varying with R, the virtual origin was found equal to -1.5 d, i.e., $R_v = R - 1.5\ d$.

Considering the wall jet as an inner boundary-layer-like region adjacent to the plate with an outer layer of free turbulent mixing, the mean velocities in the outer region can be calculated by the equation

$$\frac{U}{U_m} = \left| 1 - 0.293 \left(\frac{y - y_m}{b - y_m} \right)^{3/2} \right|^2$$

where y_m is the distance from the wall to the location of maximum velocity. However, the velocity variation in the inner region is not well predicted by an equation of the type $U/U_m = K\ (y/y_m)^{1/7}$, as it could be expected from a wall boundary layer flow. This is certainly due to the large influence that the outer flow has on the inner flow. Comparing equations for $r_{1/2}$ and b, it can be seen that the rate of growth of the radial free jet is much larger than that of the radial wall jet.

Turbulence intensity distributions at different radial distances are plotted on figure 3 where large variations can be seen from R/d = 3 to R/d = 6. On the contrary, between 6 and 9 the variations are small indicating approach to the self-preserving region. In this region the rms values are almost independent of y, showing a slowly decrease closer to the outer free boundary. These rms profiles with those of mean velocity, imply a turbulence intensity variation with a minimum corresponding to the location of maximum mean velocity; the magnitude of the minimum rounds 35%. At R/d of 3 and close to the wall, large fluctuations were detected, probably a reminiscence of those existing around the stagnation point; they are complitely smeared at R/d = 6. The high values of the measured normal stress is an indication of the large mixing process existing in all regions of the flow.

Velocity probability distributions (v.p.d.) measured in a region of self-preservation, R/d = 9, are given on figure 4 and show the presence of negative instantaneous velocities from y = 9 mm upwards. Since this distance from the wall is below the point where the mean velocity decreases to half the maximum velocity, (y/b = 0.825 and U/U_m = 0.635) it illustrates how deep inside the flow occurs the entrainment of quiet fluid. It also suggests that problems associated with directional ambiguity and finite velocity fluctuations at locations of near zero mean velocity have been precluding precise measurements of velocity; they were overcome in the present work by the use of a LDA system incorporating a frequency shift device.

The values of skewness and flatness are given on the figure and they indicate that the closest to Gaussian distribution occurs at the location of maximum mean velocity. Case a) shows a v.p.d. on the boundary layer region close to the wall and the skewness value shows that the accelerating effect due to the close presence of fast moving flow, is larger than that of retardation by frictional resistence due to the surface. On the outer edge, the v.p.d. have large values of skewness and flatness as should be expected in entrainment regions where the slower and quiet flows are dragged by the fast moving flow. The turbulence intensities are large particularly on case c) where almost half of the detected velocities have negative sign revealing the presence of eddy structures.

3.3. Wall jet with oblique impingement

Figures 5,6 and 7 report mean velocity measurements obtained with impinging angles, α, of 0, 10, 15 and 20 degrees, at radial planes of θ equal to 0, 45, 90, 135 and 180 degrees and radial distances, R/d, of 3, 6, 9, 12 and 15. θ = 0 and 180 correspond respectively to the direction of maximum and minimum velocities and y is measured perpendicularly to the plate. Figure 5 presents, for θ = 0 and 180, the influence of the impinging angle on the mean velocity profiles. It can be seen that from α = 0 to 20 the profiles have the same general configuration, with the velocity amplitude varying almost linearly with α. The jet rate of growth and the distance from the wall to the location of maximum velocity do not seem significantly influenced by α.

For α = 10 degrees and different radii, figure 6 introduces the influence of the circumferential angle on the velocity profiles. Between θ = 0 to 45 and θ = 135 to 180 degrees, the profile variations are small comparing with those occuring between θ = 45 to 90 and 90 to 135 degrees. However the profiles are similar and it is confirmed that y_m is independent of θ. Figure 7 shows that, for $\alpha = 15^o$, the non-dimensionalized velocity distributions are independent of R/d and θ; the same is true for α = 10 and 20 degrees. The profiles are identical to those of figure 2 measured with normal impingement; for the oblique impingement, proper values of b and U_m have to be considered. Those values and their dependence on R/d, θ and α are given on figures 8, 9 and 10.

For an impinging angle of 10 degrees and different values of θ, figure 8 indicates the variation of U_m and b with radial distance. Figure 9 illustrates the effect of the impinging angle and figure 10 gives

the influence of the circumferential coordinate for different values of α. Figure 8 shows that, as for the normal impingement case, $1/U_m$ changes almost linearly with R. Also the virtual origin does not show significant variation from that obtained with α = 0. Therefore, to evaluate U_m from R, it continues to be valid the use of an equation similar to that obtained for the normal impingement,

$$\frac{U_m}{U_o} = C(\theta, \alpha) \left(\frac{R_v}{d} \right)^{-1.12}$$

where the variation of C with θ and α may be calculated from figures 8 and 9 respectively. The values of $C(\theta, \alpha)$ are given on table 1.

α \ θ	0	45	90	135	180
0	1.4	1.4	1.4	1.4	1..
10	1.6	1.5	1.3	1.1	1.1
15	1.7	1.6	1.3	1.0	.92
20	1.8	1.6	1.1	.89	.76

Table 1. Values of $C(\theta, \alpha)$

For non zero values of α, figure 9 demonstrates that the velocity decay verified when $\theta = 180^o$ is larger than the increase at $\theta = 0$. Also at $\theta = 90^o$, U_m decreases when α increases indicating a non-symmetric growth of the wall jet. Figure 10 confirms the non-linear variation of U_m with θ.

Figures 8 and 10 show that b is not significantly dependent on θ and figure 9 also demonstrates a relative invariance of b with α. Therefore, for the present range of values α, the equation indicated to calculate the values of b for the case of normal impingement, is still valid and can continue to be used for the oblique impingement.

Values of turbulence intensities are shown on figure 11 and in general, the agreement with the measurements presented on figure 3 is good. From R/d = 3 to R/d = 6 a large variation is again detected, but downstream only little differences are noticeable, indicating self-preservation. The variation between the profiles measured at θ = 0 and 180 is smaller than that standing from differences in the mean velocity distributions. The turbulence intensities are high, having a minimum value of around 35% coexisting with the maximum mean velocity.

The velocity probability distributions of figure 12 were measured at the same radial distance as those of figure 4, but for an impinging angle of 10 degrees. The distributions corresponding to θ = 0 and 180 are clearly distinguishable since the velocity ranges are different, however, the main pictures, for instance those concerning entrainment, wall presence, skewness and flatness, are the same and equal to those reported in connection with figure 4.

4. CONCLUSIONS

The following more important conclusions may be extracted from the present work:

a- A laser Doppler anemometer was successfully used to study the mean velocity and turbulent fields of a round free jet impinging normally and obliquely to a wall.

b- At a distance of 12 nozzle diameters downstream the jet exit, and in the absence of the impinging wall, the mean velocity radial profiles have reached similarity and the centre-line turbulence intensity was of 20%. This distance guaranteed that the development of the wall jet was not dependent on nozzle to wall distance.

c- In the wall jet region, the turbulence intensities were high, influenced by the impinging angle and with a minimum value approaching 35% located around the point of maximum mean velocity. In this location the velocity probability distribution was near Gaussian; away from it, the v.p.d. become progressively more positively skewed and with larger flatness values. The outer shear layer was demonstrated to have an important role on the turbulent mixing process.

d- The non-dimensionalized mean velocity profiles measured in the wall jet, are independent of radial distance, circumferential coordinate and impinging angle. The values of b are also independent of α and θ and can be calculated by the equation introduced for the normal impingement case. The values of U_m are dependent on α and θ, as well as on R, and the equation revealed for normal impingement has been modified to include the case of oblique impingement.

REFERENCES

[1] P. Hrycak, D. T. Lee and J. W. Gauntner. Experimental flow characteristics of a single turbulent jet impinging on a flat plate. NASA TN D-5690, 1970.

[2] S. Beltaos and N. Rajaratnam. Impinging circular turbulent jets. J. Hydraulics Division, 100, HY10, 1313, 1974.

[3] S. Beltaos and N. Rajaratnam. Impingement of axisymmetric developing jets. J. Hydraulic Res., 15, 311, 1977.

[4] P. Bradshaw and E. M. Love. The normal impingement of a circular air jet on a flat surface. Aeron. Res. Council, R. & M., 3205, 1959.

[5] L. J. S. Bradbury. The impact of an axisymmetric jet onto a normal ground. Aeron. Quarterly, 23, 141, 1972.

[6] M. B. Glauert. The wall jet. J. Fluid Mech., 1, 625, 1956.

[7] M. Poreh, Y. G. Tsuei and J. E. Cermak. Investigation of a turbulent radial wall jet. J.Applied Mech., 457, 1967.

[8] C. D. Donaldson, R. S. Snedeker and D. P. Margolis. A study of free jet impingement: free jet turbulent structure and impingement heat transfer. J. Fluid Mech., 45, 477, 1971.

[9] C. M. Ho and N. S. Nosseir. Dynamics of an impinging jet: the feedback phenomenon. J. Fluid Mech., 105, 119, 1981.

[10] P. Bakke. An experimental investigation of a wall jet. J. Fluid Mech., 2, 467, 1957.

[11] E. Gutmark, M. Wolfshtein and I. Wygnanski. The plane turbulent impinging jet. J. Fluid Mech., 88, 737, 1978.

[12] C. D. Donaldson and R. S. Snedeker. A study of free jet impingement: mean properties of free and impinging jets. J. Fluid Mech., 45, 281, 1971.

[13] J. F. Foss and S. J. Kleis. Mean flow characteristics for the oblique impingement of an axisymmetric jet. A.I.A.A. Journal, 14, 705, 1976.

[14] D. F. G. Durão and J. H. Whitelaw. Measurements in the region of recirculation behind a disc. Proc. 2nd. Int. Workshop on laser velocimetry, Purdue Univ., 2, 413, 1974.

[15] D. K. McLaughlin and W. G. Tiederman. Biasing correction for individual realization of laser anemometer measurements in turbulent flows. Physics Fluids, 16, 2082, 1973.

[16] D. F. G. Durão and J. H. Whitelaw. Relationship between velocity and signal quality in laser Doppler anemometry. J. Phys. E: Sci. Instrum., 12, 47, 1979.

[17] R. J. Baker. The influence of particle seeding on laser anemometer measurements. A.E.R.E., England, rep.7713, 1974.

[18] D. F. G. Durão and J. H. Whitelaw. Bias in LDA due to velocity-signal amplitude correlation. Proc. Symp. Long range & short range opt. veloc. meas., Saint-Louis, France, 1980.

[19] D. F. G. Durão and J. H. Whitelaw. Performance characteristics of two frequency-tracking demodulators and a counting system: measurements in an air jet. Proc. 2nd. Int. Workshop on laser veloc., Purdue Univ., 1974.

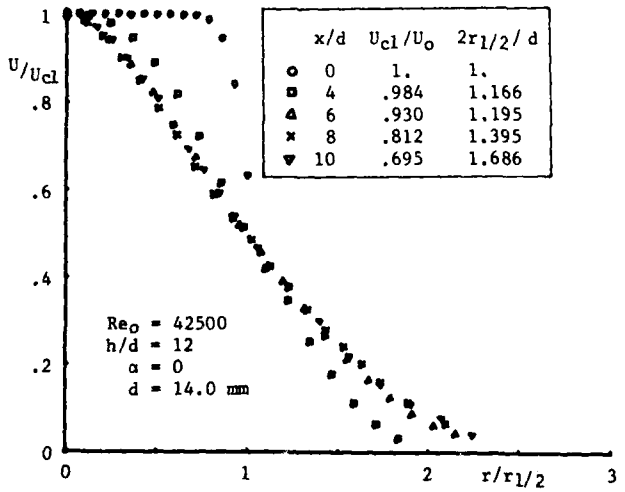

Figure 1 - Impinging jet: radial velocity profiles.

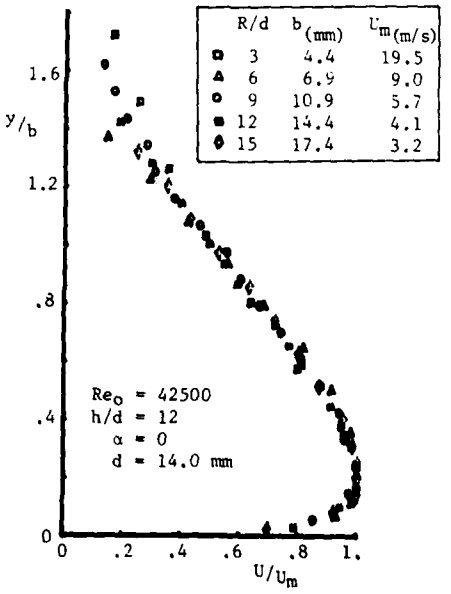

Figure 2 - Wall jet with normal impingement: mean velocity profiles.

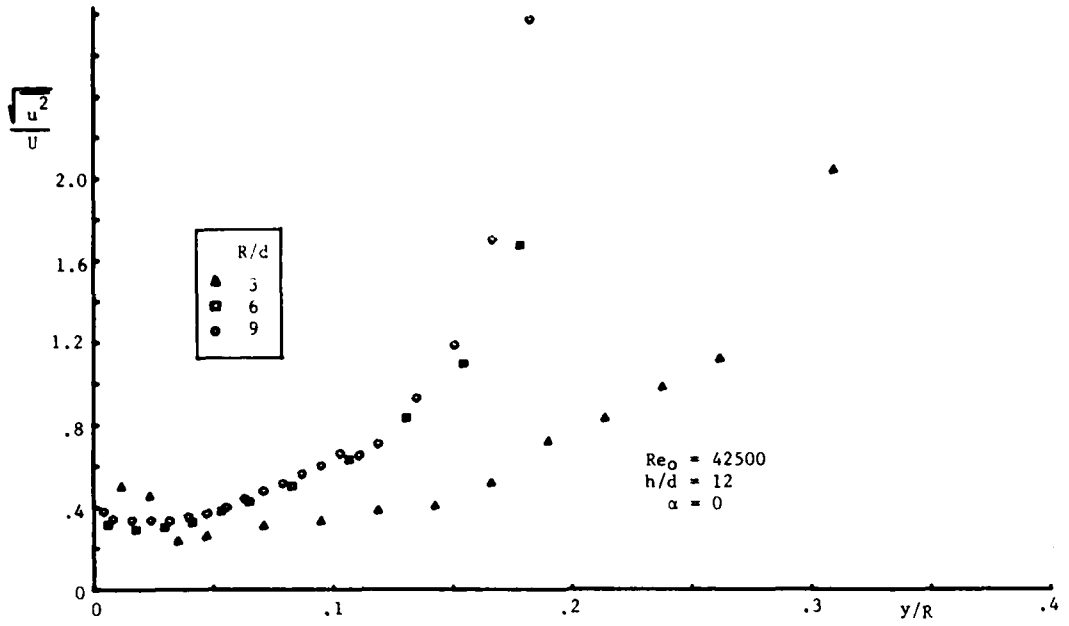

Figure 3 - Wall jet with normal impingement: turbulence intensity profiles at different radii.

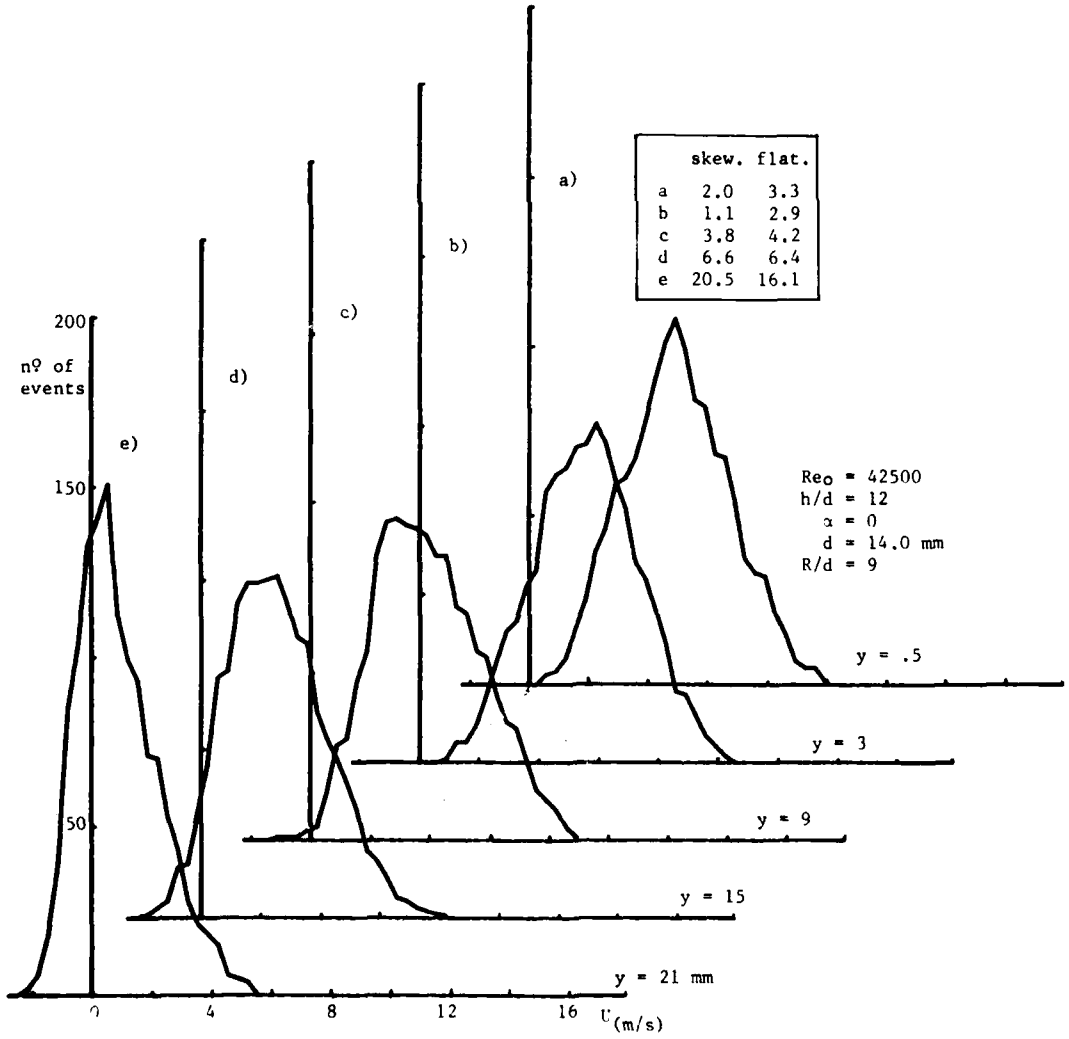

Figure 4 - Wall jet with normal impingement: velocity probability distributions.

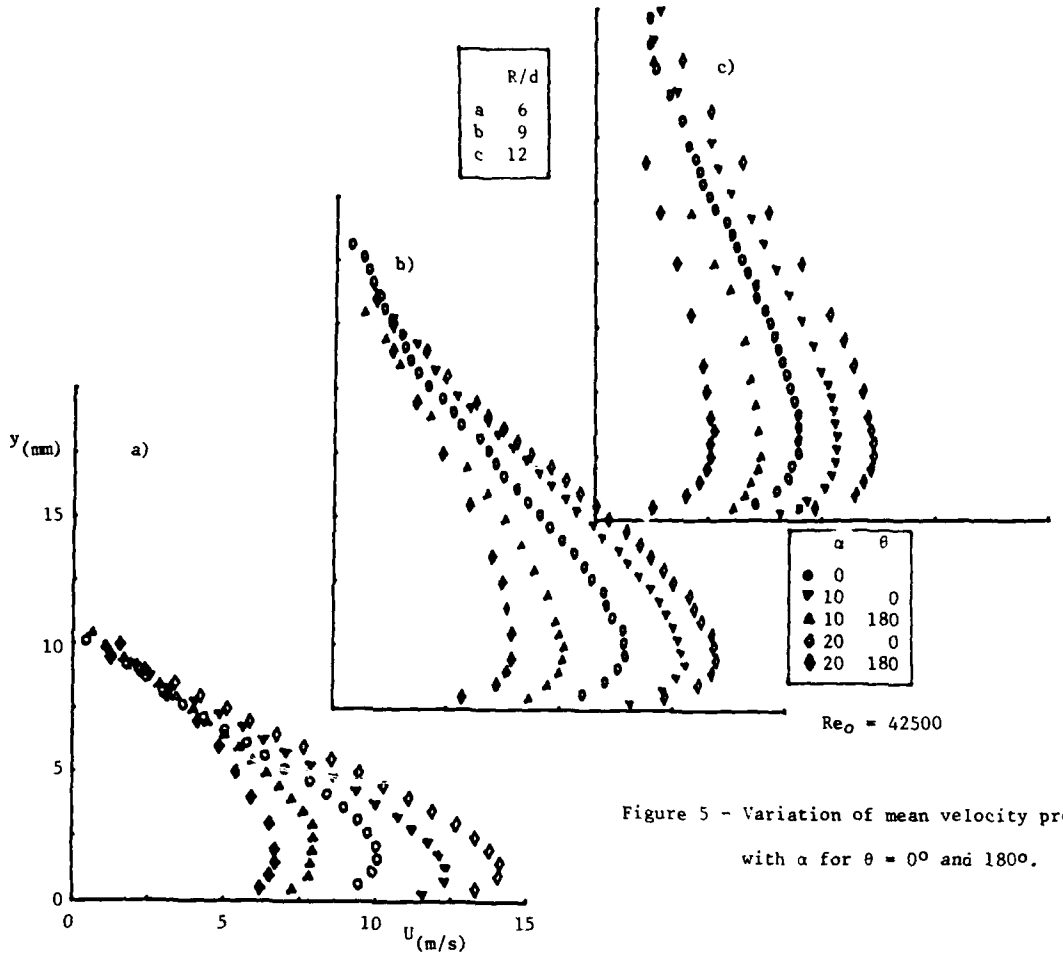

Figure 5 - Variation of mean velocity profiles with α for θ = 0° and 180°.

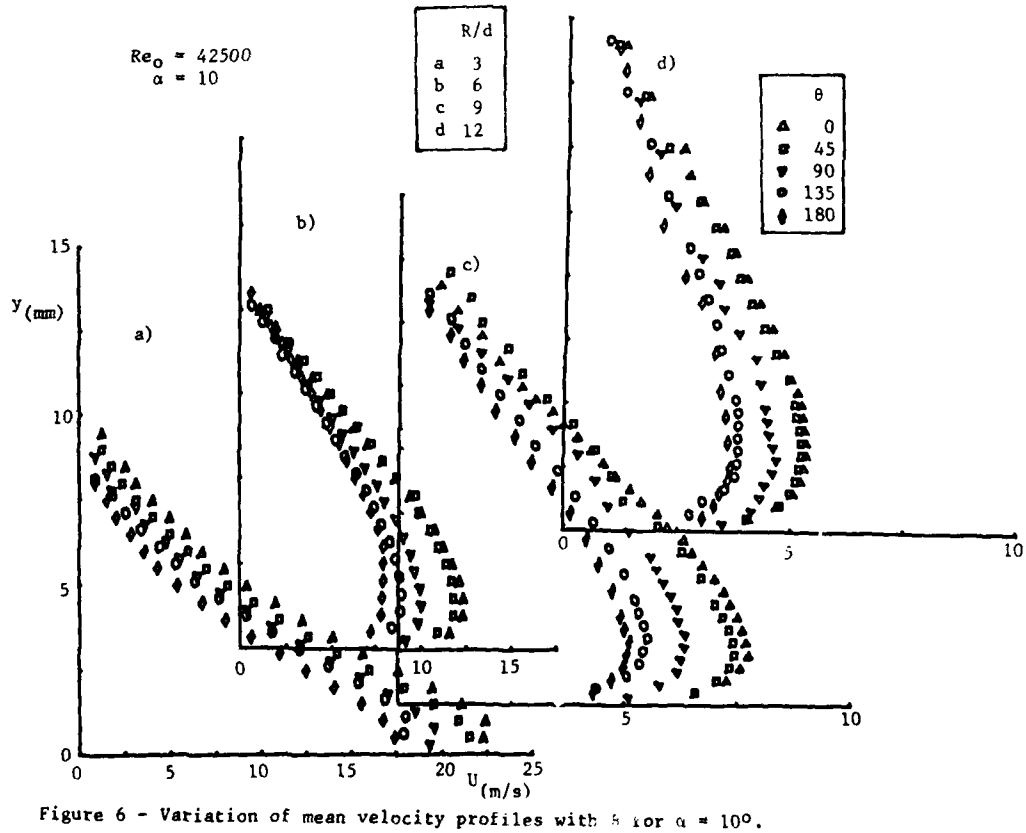

Figure 6 - Variation of mean velocity profiles with θ for α = 10°.

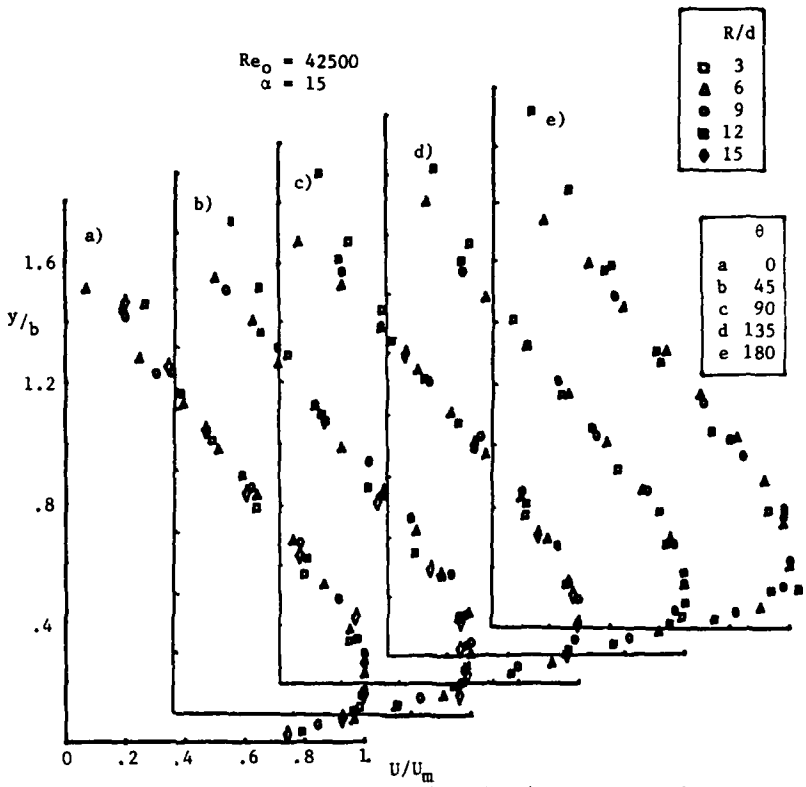

Figure 7 - Dimensionless mean velocity distributions for different θ and radii.

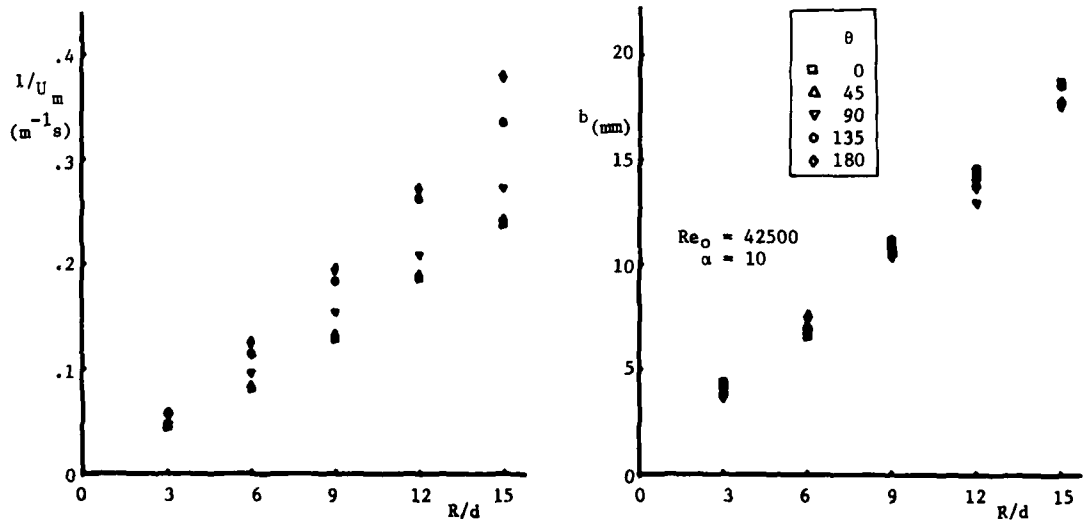

Figure 8 - Variation of U_m and b with radial distance for different values of θ.

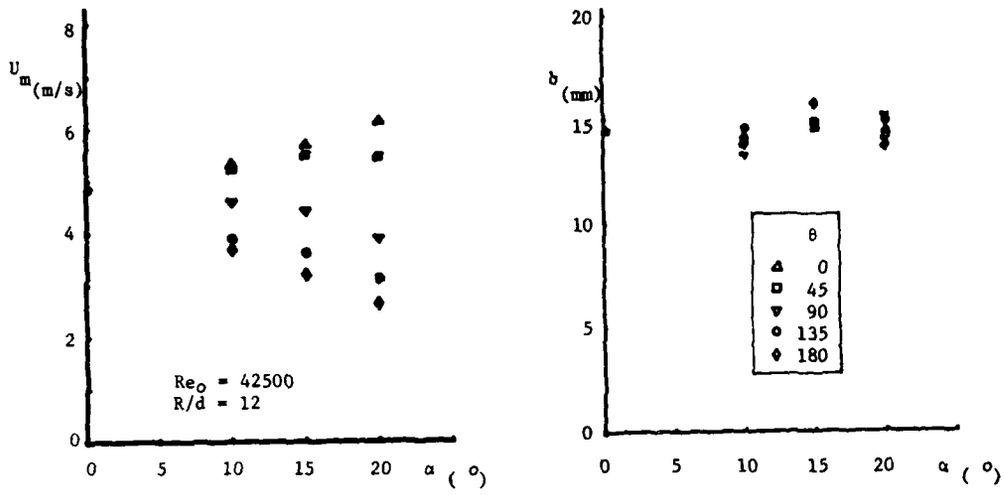

Figure 9 - Variation of U_m and b with impinging angle for different values of θ.

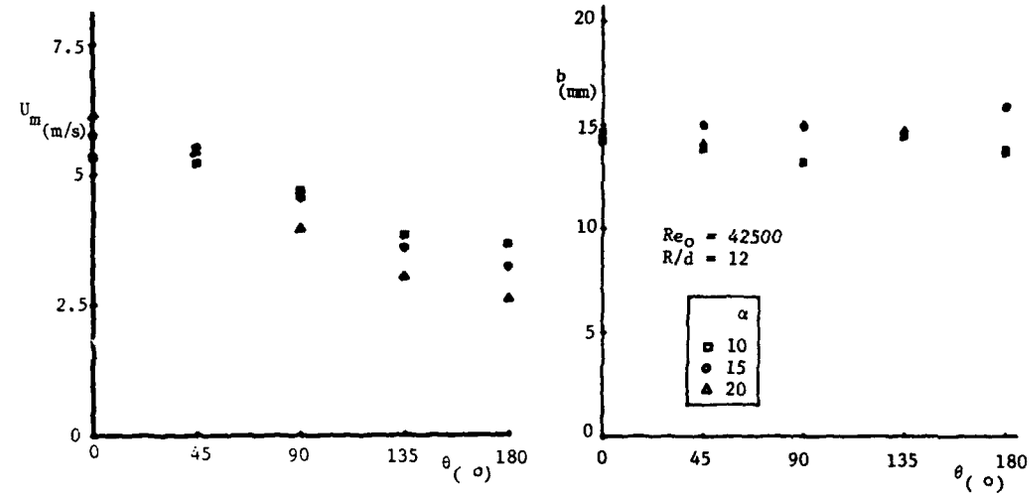

Figure 10 - Variation of U_m and b with θ for different impinging angles.

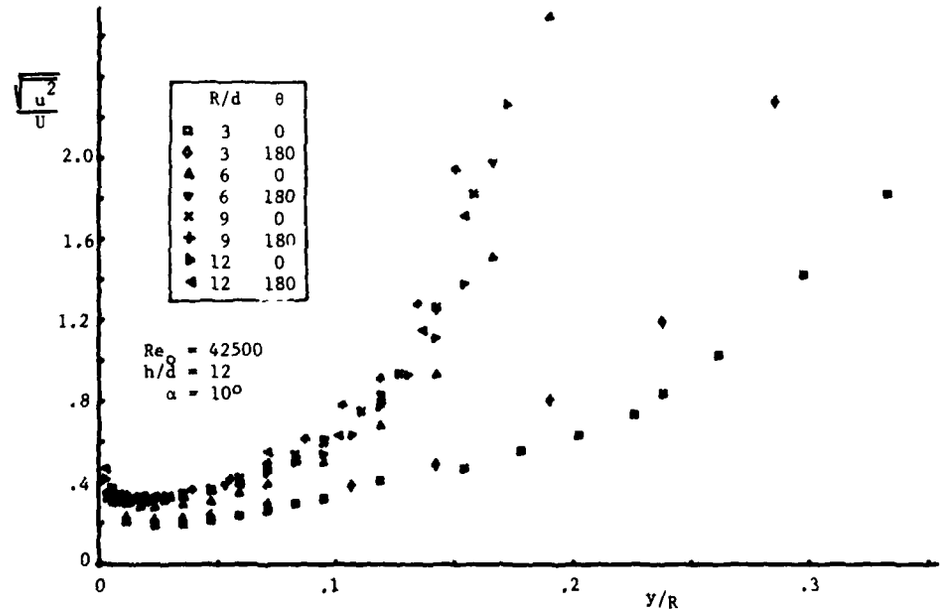

Figure 11 - Turbulence intensity profiles at different radii.

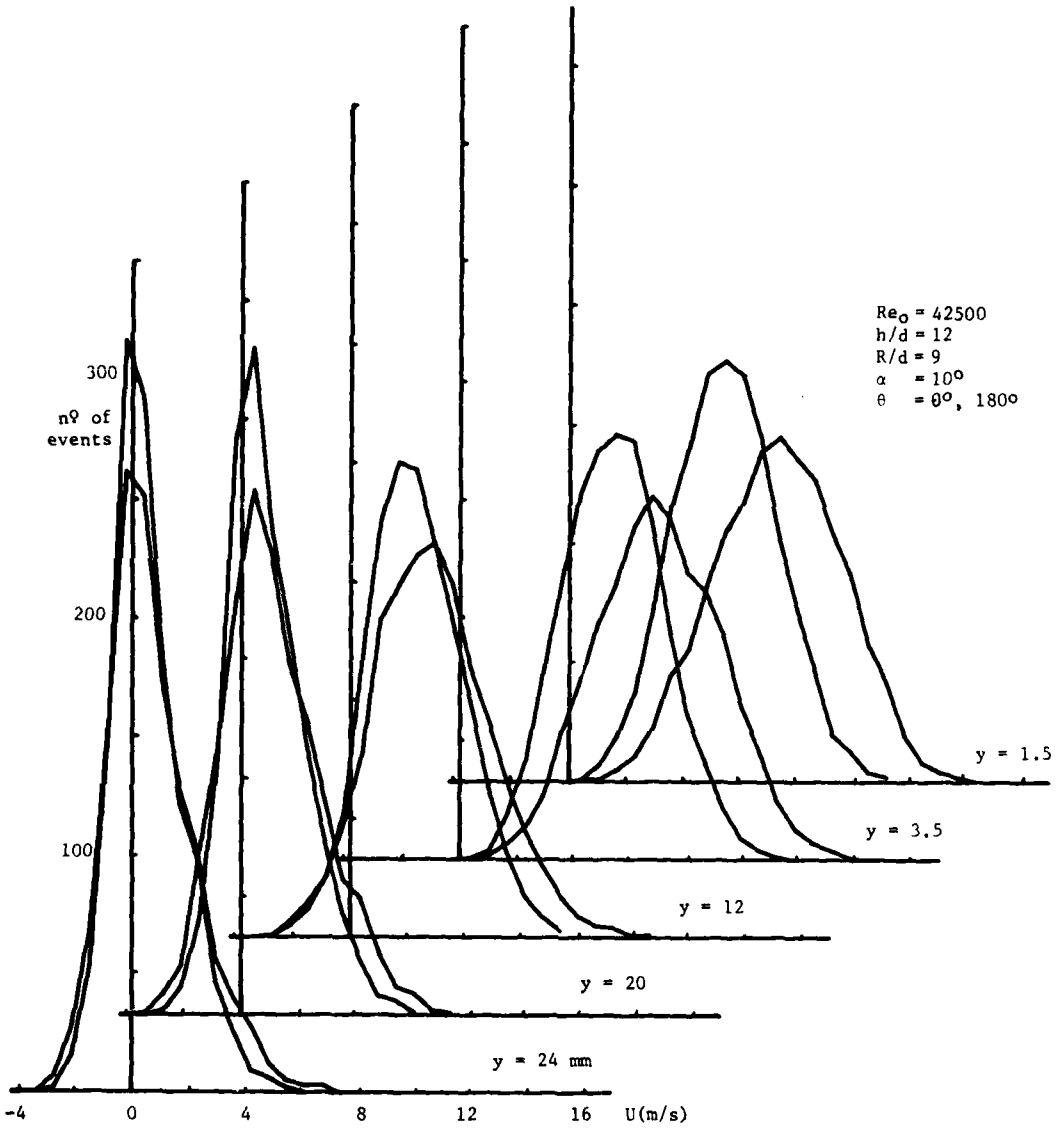

Figure 12 - Velocity probability distributions: α = 10°.

AN INVESTIGATION OF INCLINED JETS IN A CROSSWIND*

P. Taylor
D.J. Watkins

Department of Aeronautics and Astronautics
University of Southampton
Southampton
Hampshire, SO9 5NH
U.K.

SUMMARY

During the last few years, a research programme at the University of Southampton has been investigating the interference characteristics of a turbulent inclined jet exhausting into a turbulent subsonic crosswind. Results are presented of the variation in jet paths (based on the maximum total pressure), the lift loss and the pressure distribution on a flat plate through which the jet exhausts. The angle of inclination of the jet to the crosswind direction has varied from 90° to 15°.

In general, it has been found that the lift loss, the jet deflection, the jet penetration and the rate of total pressure decay along the jet path decreased as the jet inclination was reduced from the position normal to the crosswind. The centre of pressure moved downstream.

A jet exhausting at an angle of 15° to the crosswind has received considerable attention recently and results are presented of the variation with increasing momentum ratio of the pressure distribution on the flat plate through which the jet exhausts, the lift loss, the jet paths and surface oil flow.

To summarise these results, similarity laws have been applied to the lift loss, jet path and centre of pressure as a function of momentum ratio, geometry and angle of inclination.

LIST OF SYMBOLS

A_J Equivalent area of the jet exit ($A_J = \pi r_J^2$)

C_F *Surface force coefficient, defined by equation (2)*

C_p Interference pressure coefficient, defined by equation (1)

C_{p_T} Total pressure coefficient, defined by equation (6)

C_s Suction force coefficient, defined by equation (4)

m Momentum ratio ($m = \sqrt{\frac{\rho_J V_J^2}{\rho_\infty V_\infty^2}}$)

p Pressure

q Dynamic pressure

r_J *Radius of the jet exit*

R Non-dimensional radial distance from the origin to any point in the XY-plane

R_1 Non-dimensional lower limit of integration representing the jet periphery

R_2 Non-dimensional upper limit of integration

V Velocity

S Non-dimensional distance along the jet centreline from the origin

$\bar{x}$ Centre of pressure, defined in equation (5)

X,Y,Z Non-dimensional Cartesian co-ordinate system with origin at the geometrical centre of the nozzle exit plane

θ Angle between the radial from the origin to any point in the XY-plane and the positive X-axis

ξ Non-dimensional distance along the path of maximum total pressure from the origin

ξ_o Non-dimensional length of the potential core

ρ Density

ϕ Jet inclination angle given by the angle between the nozzle centreline and the positive X-axis

Suffixes

A Ambient conditions

E Jet-exit conditions

*This work is supported by SERC Research Contract No.GR/A68271.

J Jet conditions or quantities

O Stagnation conditions

∞ Crosswind conditions

(All linear dimensions, where appropriate, have been non-dimensionalised with respect to the jet radius, r_J).

1. INTRODUCTION

During the last few years, a research programme at the University of Southampton has been investigating the interference characteristics of a turbulent inclined jet exhausting into a turbulent subsonic crosswind. Initial attention has been focussed on measuring the experimental variation in jet paths (based on the maximum total pressure), the lift loss and the surface pressure distribution on a flat plate through which the jet exhausts. The angle of inclination of the jet to the crosswind direction has varied from 15° to 90°. Of recent interest has been the case of jets exhausting at small angles to the crosswind. In particular, a jet exhausting at an angle of 15° to the crosswind has received considerable attention.

To summarize these results, similarity laws have been applied to the lift loss, jet path and centre of pressure as a function of momentum ratio and jet inclination. These laws have provided a useful data base in the absence of a reliable theoretical model.

The above experimental programme has contributed greatly to the broad understanding of the nature of the interference between the jet and crosswind. To gain a more detailed insight and to be able to formulate a fundamental numerical model, experimental information concerning the induced velocity field around the jet is currently being acquired. This should enable the variation in strength and direction of the vorticity in the sheet representing the jet to be determined and to allow standard applications of free wake analysis and panel methods to the problem. This general jet model can then be coupled to existing fuselage/lifting surface computational methods.

The variation in surface pressure distribution, surface force distribution, suction force or lift loss, the path of maximum total pressure and total pressure decay along the centreline of the jet as the jet inclination is reduced from the normal position are presented. The variation in the same quantities as the momentum ratio is increased for the case of the jet inclined at a small angle to the crosswind is also presented. Finally, the application of similarity laws to the variation of the suction force coefficient or lift loss, centre of pressure and jet path with momentum ratio and jet inclination is presented. In each case the angle of jet inclination varied in increments of 15° from 15° to 90° and the momentum ratio varied from 4 to 12 in increments of 2.

2. EXPERIMENTAL ARRANGEMENT

The experimental apparatus consisted of a flat plate through which a circular jet exhausted into a crosswind. The results presented here are derived from two series of tests. In the first set of tests the jet inclination angle varied from 90° to 30° to the crosswind in increments of 15°. In the second set the jet inclination angle was 15°. The experimental apparatus used in the former has been described elsewhere[1] whilst that of the latter is described here. The jet radius was 0.4 in. and all dimensions, where appropriate, are non-dimensionalised by this value.

The crosswind was provided by a closed return wind tunnel of section 164 jet radii high by 210 jet radii wide. The crosswind dynamic pressure for the tests, described here, was 0.572 in water and the crosswind velocity was 15.2 ms^{-1}. The jet was supplied through a nozzle from compressor storage tanks via a plenum chamber. The change in mass flow was negligible during the tests. The nozzle was designed to give a uniform total pressure distribution across the exit plane. All profiles thus obtained were uniform to within ± 8% of the centreline total pressure over 90% of the exit diameter (measured in planes normal to the jet centreline).

The flat plate was of dimension 97.5 jet radii spanwise by 75 jet radii chordwise and was mounted in the floor of the working section with its surface 20 jet radii above the floor. The jet exit was positioned on the plate centreline, 37.5 jet radii behind the sharp leading edge. The plate and nozzle block was instrumented with 230 static pressure tappings each of 1/16 in internal diameter. Tests were conducted to ensure that the flow over the plate was uniform within the area of interest. The boundary layer velocity profile on the plate was measured 42.5 jet radii from the leading edge and was found to follow the 1/7th power law with a momentum thickness, $\delta_2/r_J = 0.14$. No impingement of the jet onto the tunnel roof occurred.

The jet nozzle block fitted into a circular recess in the flat plate. No leakage was detected through the discontinuity in the plate surface. Care was taken to ensure that the jet pipe centreline was not yawed with respect to the crosswind and that the plate and nozzle block surfaces were flush.

Surface oil flow visualisation was conducted by covering the plate and nozzle block with a sheet of matt black contact paper and applying a mixture of 'dayglo

pigment' and diesel oil. Conditions were set and maintained until the pattern became established.

Figure 1 shows the definitions used for axes and flow regions.

3. DEFINITION OF DERIVED RESULTS

The surface pressure distribution data was presented in the form of isobar plots. The interference pressure coefficient, C_p, was defined as

$$C_p = \frac{p_{jet\ on} - p_{jet\ off}}{q_\infty} \tag{1}$$

The surface force coefficient along a radial was denoted by C_F, where

$$C_F = \int_{R_1}^{10} C_p \, R dR \tag{2}$$

The lower limit of integration, R_1, represented the jet exit periphery and varied with jet inclination angle. The term 'surface force distribution' was used to refer to the variation of C_F with increasing angular displacement, θ.

The suction force coefficient, denoted by C_s, was defined as

$$C_s = \frac{\text{Suction Force}}{\frac{1}{2}\rho_\infty V_\infty^2 A_J} \tag{3}$$

where A_J is the equivalent area of the jet exit. This can be rewritten in terms of the surface force coefficient as

$$C_s = -\frac{2}{\pi} \int_0^\pi C_F \, d\theta \tag{4}$$

The centre of pressure was denoted by $\bar{x}$, where

$$\bar{x} = \frac{\int_0^\pi \int_{R_1}^{R_2} C_p X R dR d\theta}{\int_0^\pi \int_{R_1}^{R_2} C_p R dR d\theta} \tag{5}$$

where $X = R\cos\theta$ and the upper limit of integration, R_2, was chosen to include as large an area of the plate surface as possible in order to obtain a more accurate variation of the centre of pressure with inclination, particularly at high velocity ratios and small inclinations. A positive value of $\bar{x}$ can be thought of as representing nose-down pitching and a negative value as nose-up pitching with the sign convention of Figure 1.

C_F, C_s and $\bar{x}$ were derived from the surface pressure data by numerical integration.

The jet trajectories were determined by locating the position of maximum total pressure in successive Y-Z planes behind the jet exit. The jet centreline decay curves were presented as the variation of a total pressure coefficient, C_{p_T}, with S, where

$$C_{p_T} = \frac{p_o - p_A}{p_{o_E} - p_A} \tag{6}$$

where p_o is the total pressure at the point on the jet centreline being determined.

4. DISCUSSION OF RESULTS

Effect of Jet Inclination Angle

The effect of varying the jet inclination angle on the surface pressure isobars and on the centreline pressure distributions is shown in Figures 2 to 7, 8 and 9.

The extent of the low-pressure field was reduced in the lateral and forward regions of the flow field as the jet inclination decreased except in the case of the 15^o inclination jet which had a similar extent in the lateral region to the 30^o inclination jet. The jet exit dimension in the X-direction increased as the inclination decreased and this will have affected the local position of any isobars very close to the jet exit. The variation of the interference pressure coefficient with distance along the plate centreline upstream of the jet showed that the flow appeared to decelerate less immediately upstream of the jet as the inclination decreased for inclinations $90^o \geq \phi \geq 60^o$. For $\phi < 60^o$ no deceleration was shown by the distribution. A small positive region (maximum $C_p < 0.1$) was evident in the distribution for the 15^o inclination jet (Figure 27) but this was followed by a pressure loss as the jet was approached further. The elements of fluid immediately above the plate surface and approaching the jet were given a vertical

component of velocity by the entrainment effect of the jet. This induced vertical component became less with decreasing inclination, causing a reduction in the deceleration of the crosswind as it approached the jet. The horizontal component of velocity of these elements was increased as the jet inclination decreased.

The low-pressure field became more extensive within the wake region as the jet inclination decreased. Characteristic of the surface pressure isobars at small jet inclination angles was a 'swept back lobe' appearance (Figures 6 and 7) which was created by the more extensive low-pressure field in the wake and the less extensive low-pressure field in the lateral region. Two distinct changes in the pressure recovery within the wake region downstream of the jet exit occurred as the jet inclination decreased (Figure 9). For the 90^{o} and 75^{o} inclination jets, the rate of pressure recovery steadily decreased, being very rapid close to the jet exit. For inclination angles between 60^{o} and 30^{o}, the initial rate of pressure recovery was very rapid but was followed by a pressure loss in the region $3 < x < 6$ and a further pressure recovery at a much lower rate for $x > 6$. In the 15^{o} inclination case, a pressure loss occurred in the region $4 < x < 7$ from a large positive value of the interference pressure coefficient (too large to be plotted on Figure 9) followed by a pressure recovery in the region $7 < x < 8.5$. A slight pressure loss then occurred in the region $8.5 < x < 10$ followed by a further pressure recovery for $x > 10$. These observations regarding the pressure recovery could be the result of a stronger interaction between the induced vorticity behind the jet and the plate boundary layer, the jet becoming closer to the plate as the jet inclination angle decreased. An increasing rate of entrainment of the boundary layer in the wake region close to the jet would be expected as the jet inclination decreases.

Figure 10 shows the distribution of the surface force with angular displacement, θ, for varying jet inclination angle. A minimum point occurred in all the distributions. The minimum surface force decreased in magnitude (i.e. became less negative) as the jet inclination decreased from 90^{o} to 30^{o}. The 15^{o} inclination jet, however, showed a minimum peak of approximately twice the magnitude of the 90^{o} inclination jet but this peak was 'sharp', occurring over a much narrower range of angular displacement. The value of the angular displacement at which the minimum surface force occurred, decreased as the jet inclination angle decreased.

The suction force coefficient decreased as the jet inclination decreased from 90^{o} to 30^{o} (Figure 11) showing that the lift loss was lessened. Reducing the inclination from 30^{o} to 15^{o} resulted in an increase of the suction force coefficient to values slightly less than those for the 45^{o} inclination jet, although the major contribution to this coefficient came from different areas of the plate surface as evidenced by the surface force distribution (Figure 10). The low-pressure field extended beyond the upper limit of integration for high velocity ratios (particularly at large and small inclination angles) resulting in the lift loss being underestimated. It would be expected that the lift loss would show an asymptotic value as ϕ approaches zero because the vorticity-induced entrainment would decrease with decreasing inclination becoming zero at $\phi = 0^{o}$, where the only type of entrainment would be of the free jet type.[2] However, for the 15^{o} inclination the lift loss was actually increased compared to the 30^{o} inclination. This enhancement is thought to be caused by the image effect of the plate indicating that the flow field will not tend towards the coflowing case as the inclination is reduced further.

Generally, the centre of pressure moved downstream as the inclination angle decreased (Figure 12). For the 15^{o} inclination, the centre of pressure moved downstream for $m \geq 8$, following the trend for larger inclination angles but for a momentum ratio of 4, the movement was upstream (Figure 31). This general downstream movement as the inclination angle decreased was to be expected as the extent of the low-pressure field in the wake region increased.

The penetration of the jet into the crosswind and the rate of deflection of the jet decreased as the inclination decreased (Figure 13). The initial portion of the trajectories was almost linear. This linear portion became more extensive as the inclination decreased and the 15^{o} inclination jet showed no deflection over the X distance for which measurements were recorded ($0 < X < 24$).

The total pressure decay rate for varied inclination angle is shown in Figure 14. The potential core is indicated by the portion of the curves for which $C_{PT} = 1$. The scatter in the data in this area arose from the difficulty of locating the position of maximum total pressure. The length of the potential core increased with decreasing inclination angle except for the 15^{o} inclination which was of similar length to the 45^{o} inclination. The total pressure decay rates for inclinations $45^{o} \leq \phi \leq 90^{o}$ were very similar. For inclination angles of 15^{o} and 30^{o}, the rates were again very similar but of a lower rate than for $\phi \geq 45^{o}$ and appeared to be broadly similar to the free jet.

Effect of Momentum Ratio at Small Inclination Angle ($\phi = 15^{o}$)

The effect of increasing the momentum ratio on the surface pressure isobars and on the centreline pressure distributions is shown in Figures 15 to 20, 27 and 28. The isobar plots show the characteristic lobe shape of the small inclination angles. In general, increasing the momentum ratio caused an outwards spreading of the entire low-pressure field.

Considering the forward and lateral regions, the low-pressure field spread to the front and sides of the jet as the momentum ratio increased. The angle between an isobar crossing the plate centreline and the centreline increased generally as the momentum ratio increased. The variation of the interference pressure coefficient with distance along the plate centreline upstream of the jet changed with varied momentum ratio. At a momentum ratio of 2, the pressure increased as the jet was approached and then decreased rapidly. The interference pressure coefficient was positive for all values of X at this momentum ratio. At a momentum ratio of 4, the pressure remained fairly constant and then increased to a small positive peak before decreasing rapidly as the jet was approached. For momentum ratios, $m \geq 6$, a pressure loss was observed before the small positive peak, the pressure then decreasing rapidly to negative values. In all cases, the positive peak occurred at X = -7.5 but the interference pressure coefficient did not exceed 0.1. The value of this maximum was not indicative of a stagnation area. A stagnation point would be expected to be very local and difficult to detect. The fluid approaching the jet near to the plate surface was given a vertical component of velocity by the entrainment effect of the jet.

The entire low-pressure field in the wake region moved downstream and slightly outwards as the momentum ratio was increased. The position of the crossing point on the plate centreline of the -0.05, -0.1 and -0.2 isobars moved downstream as the momentum ratio increased. Figures 21 to 26 show the area around the jet exit in more detail and are the results of tests with more closely spaced pressure tappings in this area. An area of positive interference pressure coefficients was evident on the region $4 < x < 7$ for momentum ratios 4 to 12, the thicker isobar on the plots representing the change from negative to positive interference pressure coefficients. The magnitude of these positive interference pressure coefficients was very high (increasing with increasing momentum ratio) and is thought to be caused by impingement of part of the jet onto the plate in this region which then lifted away from the plate with increasing downstream distance. This was possibly the result of a Coanda type effect followed by a buoyancy effect. Near the rear of the jet exit adjacent to this positive area was a region of relatively high magnitude negative interference pressure coefficients, increasing in magnitude as the momentum ratio increased (Figures 23 to 26). This negative area indicates strong entrainment of the boundary layer in this region. Along the plate centreline the interference pressure coefficient decreased from the positive maximum to a negative value at X = 7 for momentum ratios, $m \geq 4$. A gradual pressure recovery then occurred. For m = 2, there was no positive value but a gradual pressure recovery with increasing downstream distance.

The major effect of increasing the momentum ratio was an outwards spreading of the entire low-pressure field. This was caused by the increasing of the entrainment rate as the momentum ratio was increased.

The effect of increasing the momentum ratio on the distribution of the surface force with angular displacement, θ, is shown in Figure 29. The surface force coefficient became increasingly more negative as the momentum ratio increased as would be expected from the surface pressure distribution. A significant feature of the surface force distribution was the minimum 'peak' which occurred in the region $\theta = 10^{o}$ for all momentum ratios. The magnitude of this minimum surface force increased as the momentum ratio increased and the peak was very pronounced at high momentum ratios.

The suction force coefficient increased as the momentum ratio increased (Figure 30). The rate of change of the suction force coefficient with momentum ratio increased slightly probably due to the increasingly large magnitude of the minimum peak which was indicated in the surface force distribution (Figure 29).

The centre of pressure was positive for the range of momentum ratios considered (Figure 31) and decreased (i.e. moved upstream) with increasing momentum ratio for $m \leq 8$ and then increased slightly for $m > 8$. This movement of the centre of pressure corresponds to the changing wake contribution to the surface force.

The photographs of the oil flow pattern on the plate surface for two momentum ratios are shown in Figures 32 and 33. The crosswind was directed from the top to the bottom of the photographs. The presence of a region of separated flow or wake extending downstream from the jet exit was revealed. The width of this wake increased as the momentum ratio increased. Streamlines over a large area of the plate were bent towards the jet and wake, some streamlines terminating at the jet exit periphery and at the wake edge. This showed entrainment of the crosswind into the jet and wake taking place around the whole jet periphery and the edge of the wake. The angle of the streamlines to the plate centreline was greatest approximately one jet radii behind the downstream edge of the jet and of magnitude approximately 60^{o}, this angle decreasing rapidly with increasing distance downstream.

The jet trajectories for momentum ratios 4 to 12 (Figure 34) showed that no deflection of the jet away from the exit angle by the crosswind occurred for approximately 24 jet radii downstream of the jet exit. The scatter in the data as X increased was due to the difficulty in determining Z as the total pressure excess became small.

The total pressure decay rate for varied momentum ratio is shown in Figure 35. The potential core length showed no variation with momentum ratio and was approximately 6 jet radii. The decay rates for momentum ratios, $6 \leq m \leq 12$ were indistinguishable. However, for a momentum ratio of 4, a greater decay rate occurred.

5. SIMILARITY LAWS

The application of similarity laws to the measurements of the suction force coefficient, the centre of pressure and the jet trajectories for jet inclination angles $90^{\circ} \geq \phi \geq 30^{\circ}$ have been described elsewhere[3]. In the correlations presented here, the data of the 15° inclination jet has been added where appropriate.

The functional form of the equation for the suction force coefficient was found to be (from reference 3)

$$\frac{C_s}{(m\sin\phi)^2} = \text{function of } \left[\frac{R_2}{K(m\sin\phi)^n}\right] \tag{7}$$

The suction force coefficients for all inclination angles and momentum ratios are shown in the logarithmic plot of Figure 36. The values of K and n, which were determined by a least-squares analysis are listed in the Figure for each inclination angle. K and n are clearly dependent on inclination and K is dependent on the nozzle. The value of K was arbitrarily assigned for the 90° inclination jet. The large scatter in the data in the region of $C_s/(m\sin\phi)^2 = 0.5$ can be attributed to an effect of the evaluation of C_s at low values of m. Here the magnitude of the pressure readings far from the jet was very small and the relative error in measuring these pressures was more dominant. This large relative error was weighted by a large value of R.

Ignoring the above mentioned data, the overall correlation shows a scatter of about $\pm 10\%$ on the mean line which is very encouraging considering the wide spectrum of data representing varying jet conditions.

The functional form of the equation for the centre of pressure was found to be (from reference 3)

$$\bar{x} = a\,\frac{R_2}{K(m\sin\phi)^n} + c \tag{8}$$

The centres of pressure for all inclinations and momentum ratios are shown in Figure 37. The values of a and c, determined by a least-squares analysis are listed in the Figure. The values of K and n are those determined from the C_s correlation. The scatter of data, with the exception of 2 points, is contained within the mean error band (± 0.23 on the value of $\bar{x}$) applied to the data. The change in direction of movement of $\bar{x}$ with increasing momentum ratio in the case of the 15° inclination jet resulted in difficulties in determining a and c and the inclusion of this data was not altogether satisfactory.

With the above reservations, the overall correlation is again very encouraging.

The functional form of the equation for the jet trajectories was found to be (from reference 3)

$$\frac{X - Z\cot\phi}{K(m\sin\phi)^n} = \text{function of } \left[\frac{\xi - \xi_o}{K(m\sin\phi)^n}\right]^b \tag{9}$$

where ξ is the non-dimensional distance along the path of maximum total pressure from the origin and ξ_o is the non-dimensional length of the potential core. The jet trajectories for $90^{\circ} \geq \phi \geq 45^{\circ}$ for all momentum ratios are shown in Figure 38. The values of b, determined by a least-squares analysis are listed in the Figure. The values of K and n are those determined from the C_s correlation. No data for the 30° inclination jet or the 15° inclination jet is presented. In the former case, the geometry of the experimental model made it possible to obtain only 1 or 2 data points and in the latter the term X-Z cot ϕ was zero because of the lack of deflection of the jet. The large scatter of data in the lower left hand region can be attributed to the uncertainty in measuring the potential core length (± 0.5). The correlated data in this region represents data points that were very close to the potential core and are extremely sensitive to the value of ξ_o. It was suggested in reference 3 that a Reynolds number, possibly based on the velocity difference between the crosswind and the component from the jet in the crosswind direction (and hence incorporating a dependence on ϕ) may provide a second correlating parameter, in the jet trajectory correlation, which becomes important when the jet is close to the plate.

6. CONCLUSIONS

a) Decrease in the Inclination of the Jet

The general effect of decreasing the inclination of the jet on the surface pressure surrounding a jet exhausting into a crosswind has been determined as

(1) The low-pressure field becomes less extensive to the front and sides of the jet.

(2) The surface force increased (became less negative) in these regions.

(3) The lower pressure field became more extensive to the rear of the jet and the surface force decreased in this region.

(4) The suction force coefficient was reduced and the centre of pressure moved downstream.

(5) The jet penetrated the crosswind less and the jet deflection decreased.

(6) The rate of total pressure decay along the jet centre line was reduced.

(7) For the case of the jet inclined at 15^{o} to the crosswind, the surface force exhibited a smaller minimum value behind the jet, a reversal in trend to that observed in (3). Consequently, the suction force coefficient increased as the inclination decreased below 30^{o}.

b) Increase in the Momentum Ratio for the Small Angle Jet (15^{o})

The general effect of increasing the momentum ratio on the surface pressure surrounding a jet exhausting at an inclination of 15^{o} to the crosswind has been determined as

(1) The low-pressure field spread to the lateral and forward regions of the flowfield.

(2) The surface force became more negative in these regions.

(3) The low pressure field became more extensive to the rear of the jet. The surface force exhibited a minimum value in this region, the magnitude increasing with increasing momentum ratio, but the position remaining unchanged. A small area of large positive pressure was apparent immediately downstream of the jet at high momentum ratios probably due to the jet striking the surface in this area.

(4) The suction force coefficient increased and the centre of pressure moved downstream and showed an asymptotic tendency for momentum ratios greater than 8.

(5) The jet suffered little if any deflection and the decay of total pressure along the jet path showed little change for momentum ratios above 6.

c) Application of Similarity Laws

(1) The suction force coefficient correlates well with momentum ratios, and jet inclination.

(2) The centre of pressure correlates well with momentum ratio and jet inclination.

(3) The correlation of the path of maximum total pressure with momentum ratio and jet inclination exhibits considerable scatter.

The application of the similarity laws presented is not entirely conclusive. In the absence of a complete fundamental theoretical model, these laws can predict more compactly the lift loss, centre of pressure and jet path, i.e. the overall gross effects of the jet/crosswind interaction as well as most of the current analytical models which involve complicated semi-empirical relations between various jet properties and which are difficult to justify fundamentally.

REFERENCES

1. Taylor, P. — An Investigation of an Inclined Jet in a Crosswind. Aeronautical Quarterly, Vol.28, February 1977, pp.51-58.

2. Platten, J.L. and Keffer, J.F. — Entrainment in deflected axisymmetric jets at various angles to the stream. University of Toronto, Mechanical Engineering Department, TP 6808, June 1968.

3. Taylor, P. — A summary of crosswind-jet experiments including jet paths, lift losses and centres of pressures, on a flat plate. Vertica, Vol.3, 1979, pp.145-154.

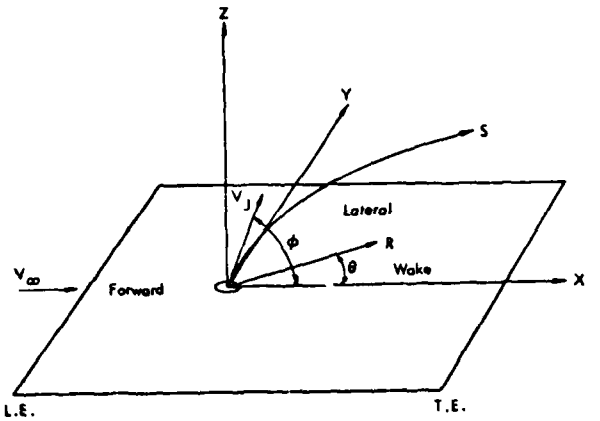

FIGURE 1 DEFINITION OF AXES AND FLOW REGIONS

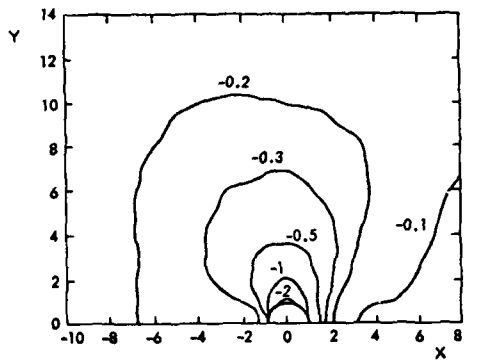

FIGURE 2 SURFACE PRESSURE DISTRIBUTION ($m = 12$, $\phi = 90°$)

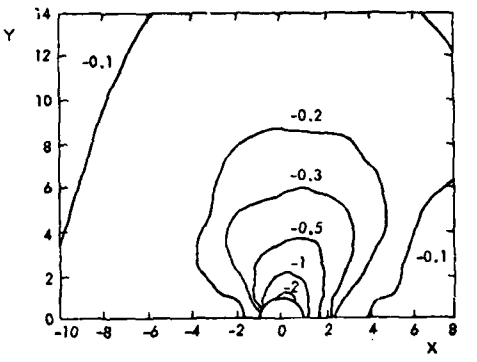

FIGURE 3 SURFACE PRESSURE DISTRIBUTION ($m = 12$, $\phi = 75°$)

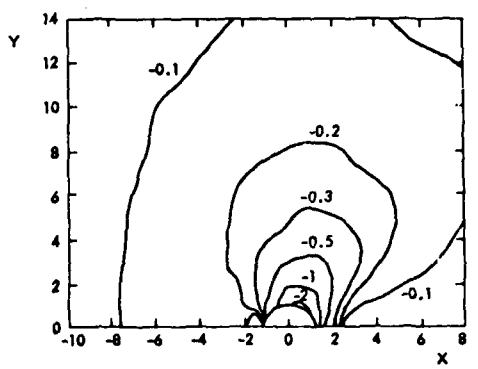

FIGURE 4 SURFACE PRESSURE DISTRIBUTION ($m = 12$, $\phi = 60°$)

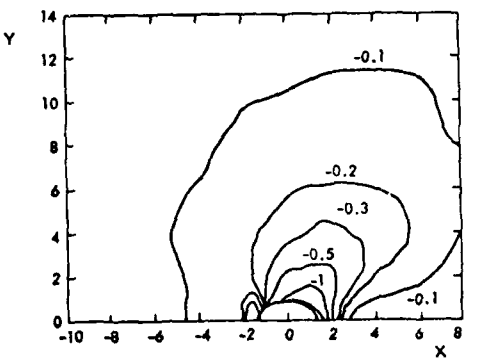

FIGURE 5 SURFACE PRESSURE DISTRIBUTION ($m = 12$, $\phi = 45°$)

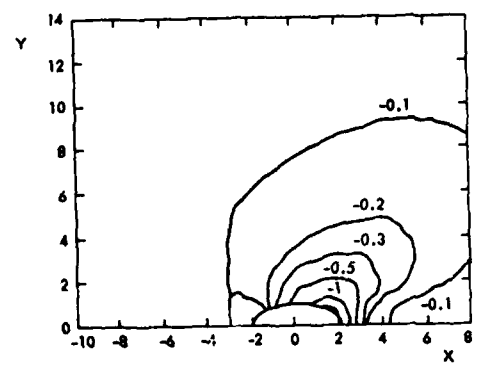

FIGURE 6 SURFACE PRESSURE DISTRIBUTION ($m = 12$, $\phi = 30°$)

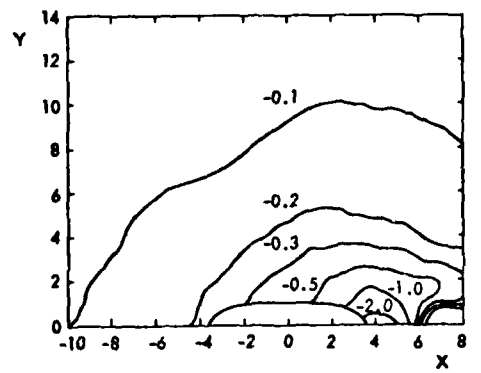

FIGURE 7 SURFACE PRESSURE DISTRIBUTION ($m = 12$, $\phi = 15°$)

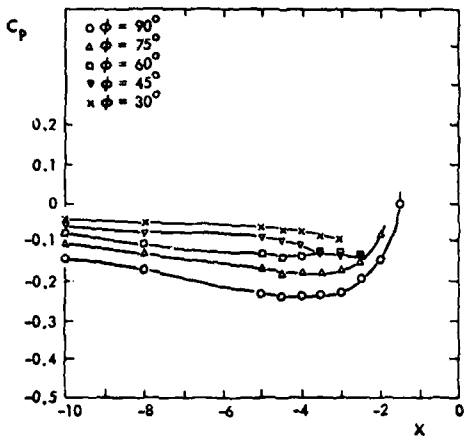

FIGURE 8 UPSTREAM CENTRELINE PRESSURE DISTRIBUTION (m = 12)

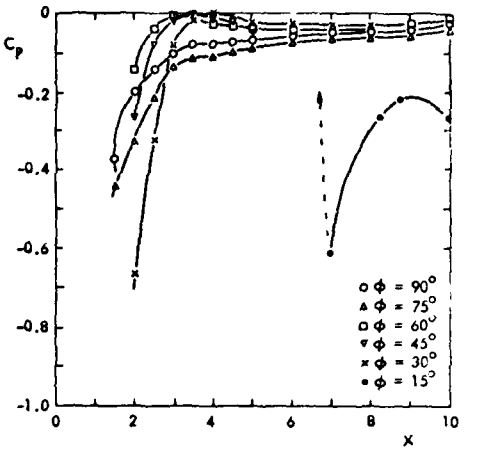

FIGURE 9 DOWNSTREAM CENTRELINE PRESSURE DISTRIBUTION (m = 12)

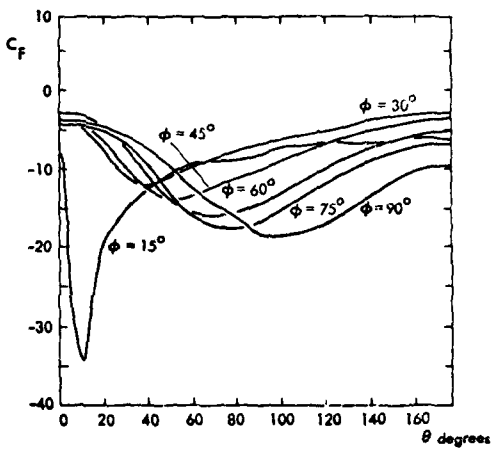

FIGURE 10 VARIATION OF SURFACE FORCE DISTRIBUTION WITH INCLINATION (m = 12)

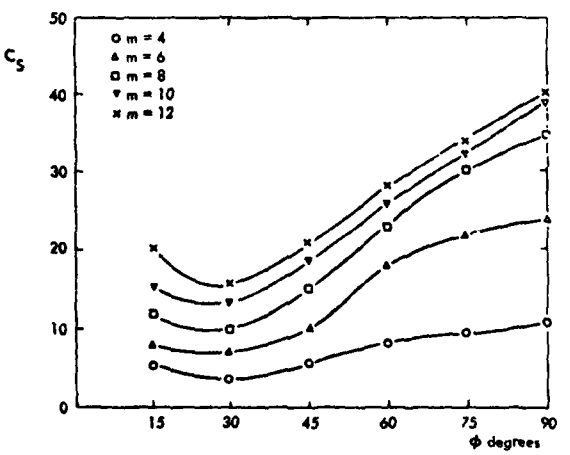

FIGURE 11 VARIATION OF SUCTION FORCE COEFFICIENT WITH INCLINATION

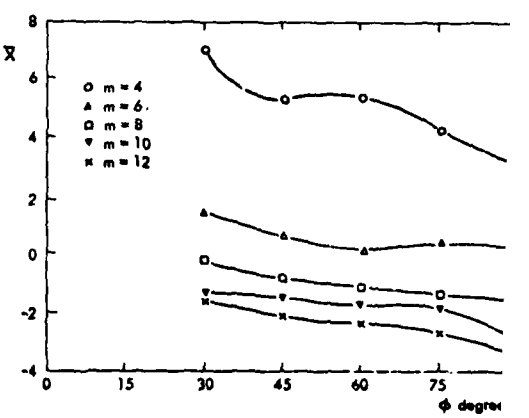

FIGURE 12 VARIATION OF CENTRE OF PRESSURE WITH INCLINATION

AD-A113 907 ADVISORY GROUP FOR AEROSPACE RESEARCH AND DEVELOPMENT--ETC F/G 20/4
FLUID DYNAMICS OF JETS WITH APPLICATIONS TO V/STOL.(U)
JAN 82
UNCLASSIFIED AGARD-CP-308 NL

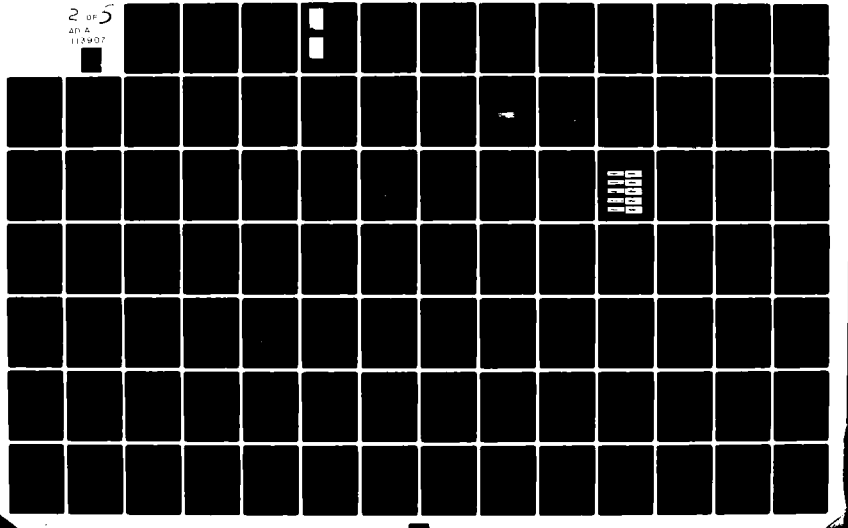

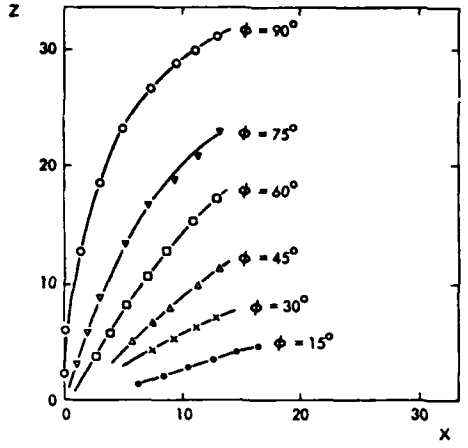

FIGURE 13 JET TRAJECTORIES (m = 12)

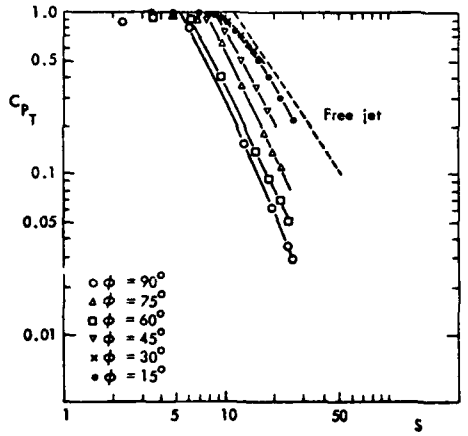

FIGURE 14 TOTAL PRESSURE DECAY RATE
(m = 12)

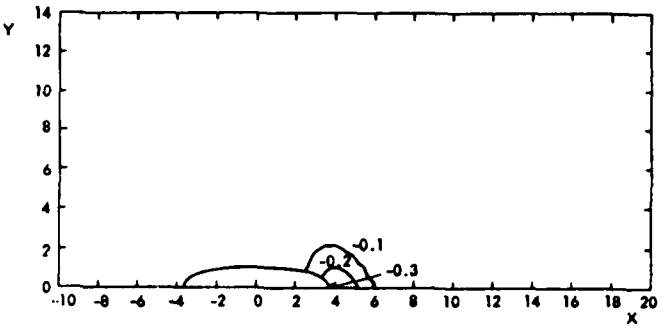

FIGURE 15 SURFACE PRESSURE DISTRIBUTION
(m = 2, ϕ = 15°)

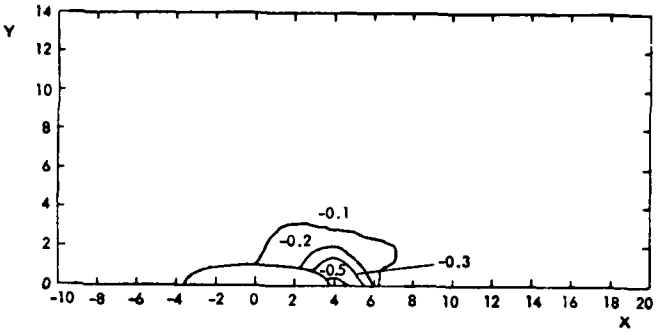

FIGURE 16 SURFACE PRESSURE DISTRIBUTION
(m = 4, ϕ = 15°)

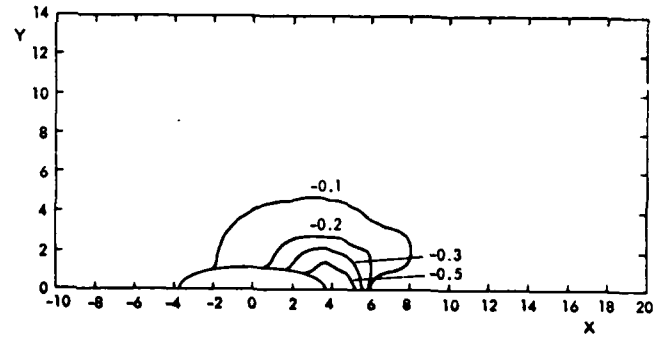

FIGURE 17 SURFACE PRESSURE DISTRIBUTION
(m = 6, ϕ = 15°)

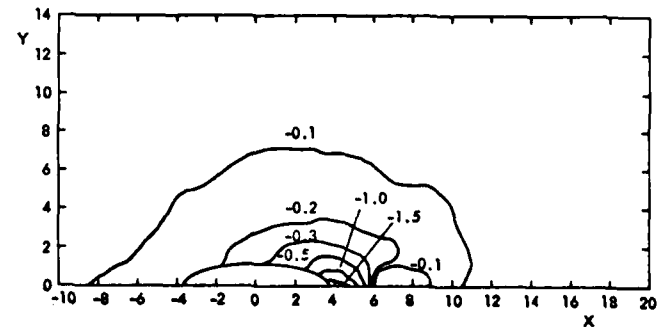

FIGURE 18 SURFACE PRESSURE DISTRIBUTION
(m = 8, ϕ = 15°)

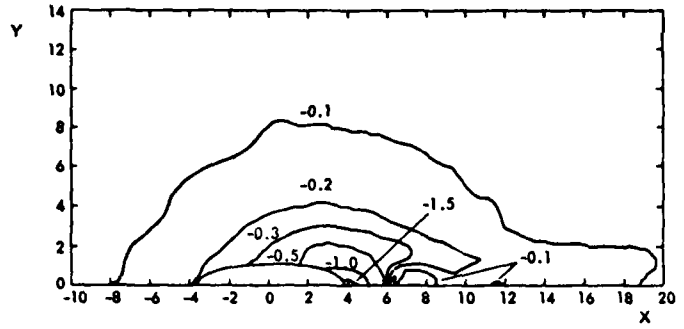

FIGURE 19 SURFACE PRESSURE DISTRIBUTION ($n = 10$, $\phi = 15^{o}$)

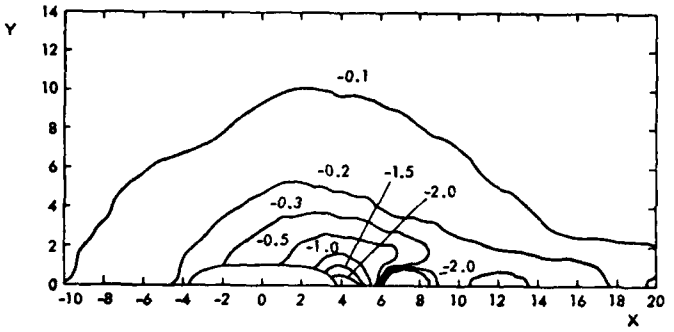

FIGURE 20 SURFACE PRESSURE DISTRIBUTION ($n = 12$, $\phi = 15^{o}$)

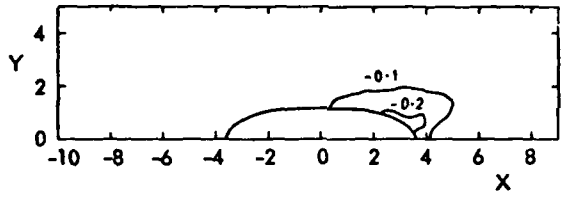

FIGURE 21 SURFACE PRESSURE DISTRIBUTION NEAR THE JET EXIT ($n = 2$, $\phi = 15^{o}$)

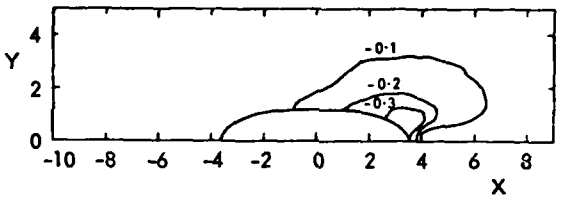

FIGURE 22 SURFACE PRESSURE DISTRIBUTION NEAR THE JET EXIT ($n = 4$, $\phi = 15^{o}$)

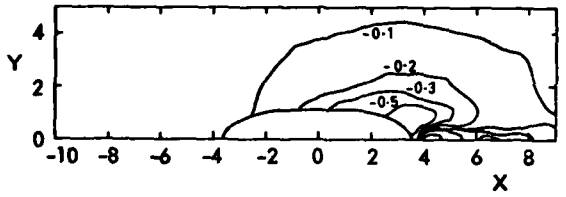

FIGURE 23 SURFACE PRESSURE DISTRIBUTION NEAR THE JET EXIT ($n = 6$, $\phi = 15^{o}$)

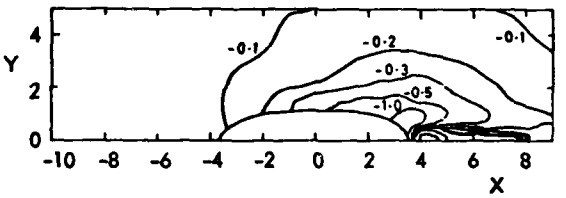

FIGURE 24 SURFACE PRESSURE DISTRIBUTION NEAR THE JET EXIT ($n = 8$, $\phi = 15^{o}$)

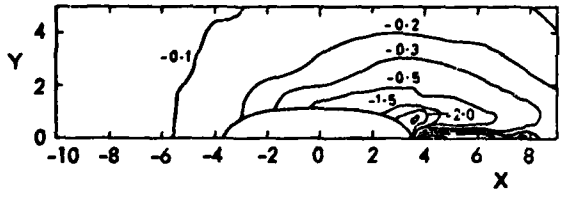

FIGURE 25 SURFACE PRESSURE DISTRIBUTION NEAR THE JET EXIT ($n = 10$, $\phi = 15^{o}$)

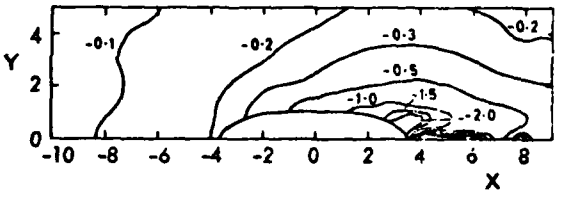

FIGURE 26 SURFACE PRESSURE DISTRIBUTION NEAR THE JET EXIT ($n = 12$, $\phi = 15^{o}$)

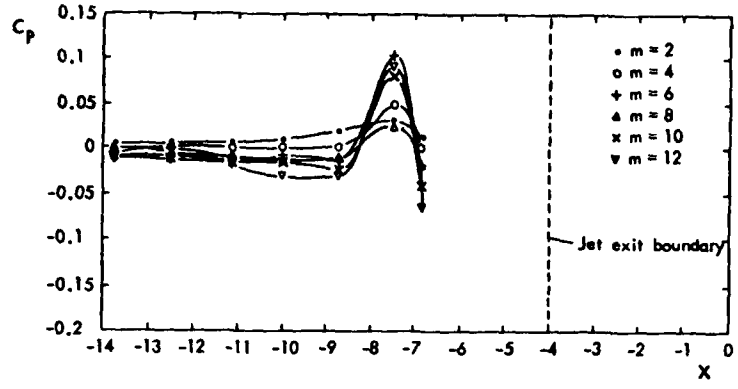

FIGURE 27 UPSTREAM CENTRELINE PRESSURE DISTRIBUTION (ϕ = 15°)

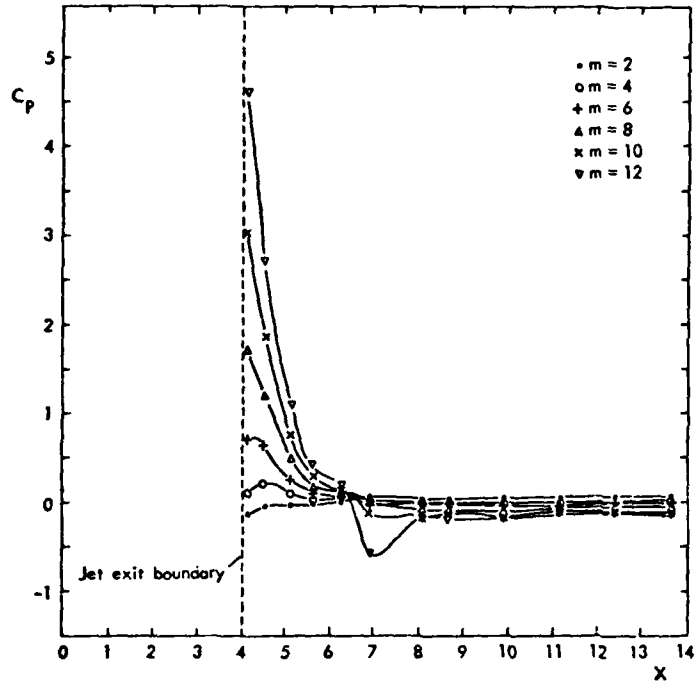

FIGURE 28 DOWNSTREAM CENTRELINE PRESSURE DISTRIBUTION (ϕ = 15°)

FIGURE 29 VARIATION OF SURFACE FORCE DISTRIBUTION WITH MOMENTUM RATIO (ϕ = 15°)

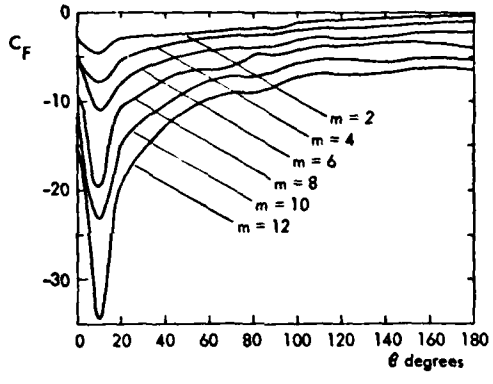

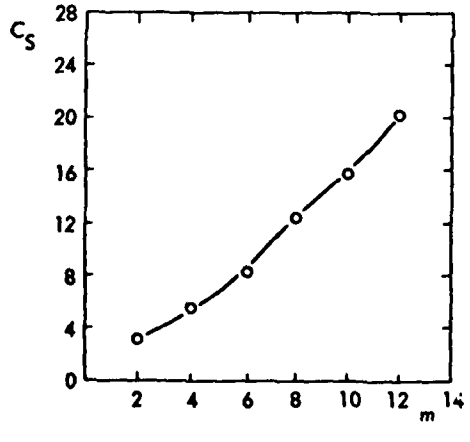

FIGURE 30 VARIATION OF SUCTION FORCE COEFFICIENT WITH MOMENTUM RATIO (ϕ = 15°)

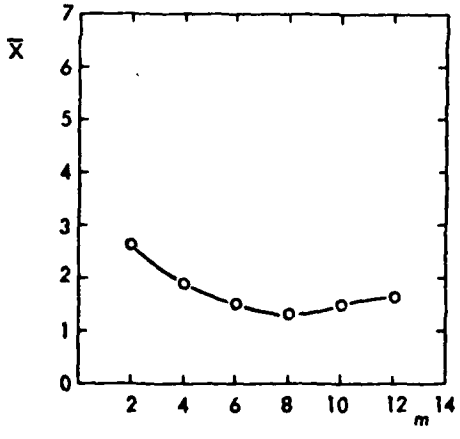

FIGURE 31 VARIATION OF CENTRE OF PRESSURE WITH MOMENTUM RATIO (ϕ = 15°)

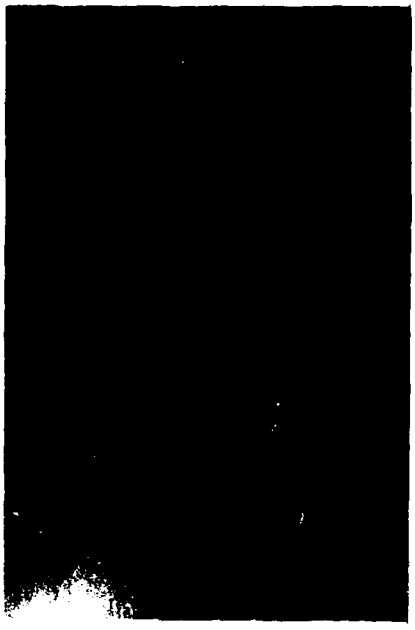

FIGURE 32 OIL FLOW PATTERN ON THE PLATE SURFACE (m = 6, ϕ = 15°)

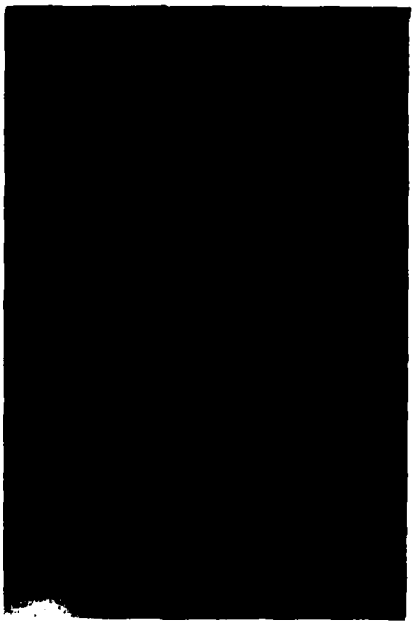

FIGURE 33 OIL FLOW PATTERN ON THE PLATE SURFACE (m = 10, ϕ = 15°)

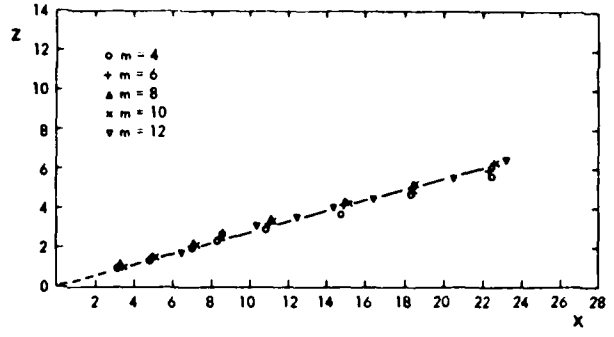

FIGURE 34 JET TRAJECTORIES (ϕ = 15°)

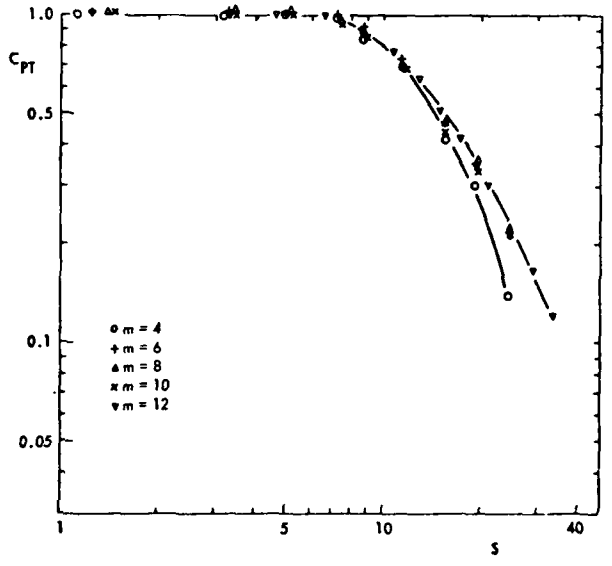

FIGURE 35 TOTAL PRESSURE DECAY RATE (ϕ = 15°)

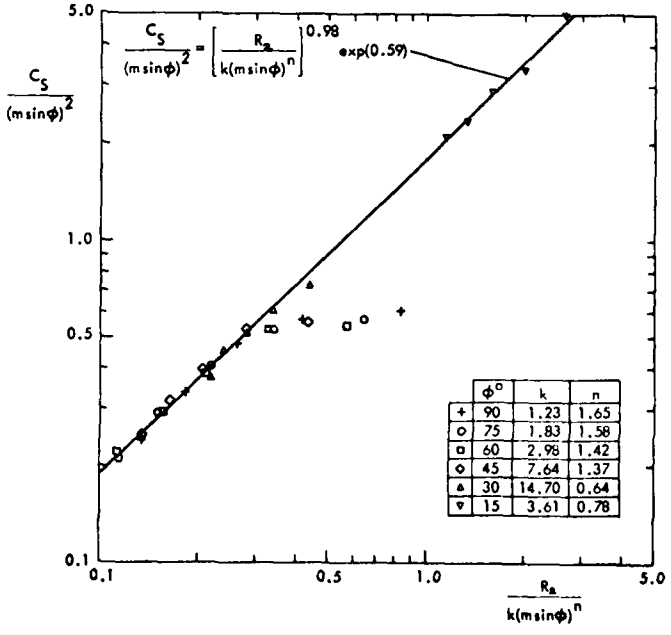

FIGURE 36 CORRELATION OF SUCTION FORCE COEFFICIENT WITH INCLINATION AND MOMENTUM RATIO

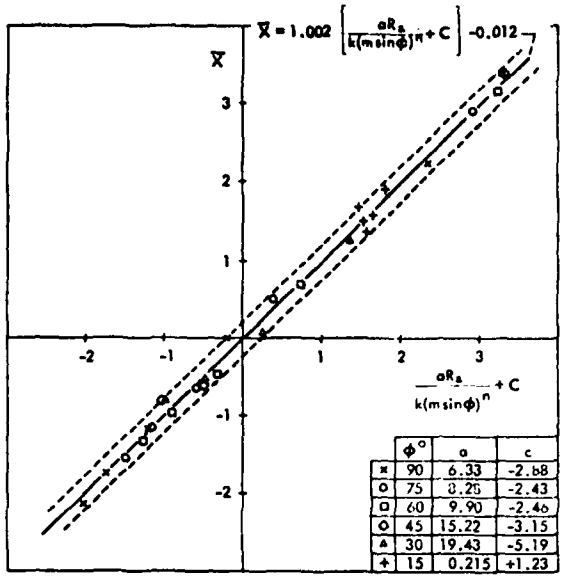

	ϕ°	a	c
×	90	6.33	-2.68
○	75	8.26	-2.43
□	60	9.90	-2.46
◇	45	15.22	-3.15
△	30	19.43	-5.19
+	15	0.215	+1.23

FIGURE 37 CORRELATION OF CENTRE OF PRESSURE WITH INCLINATION AND MOMENTUM RATIO

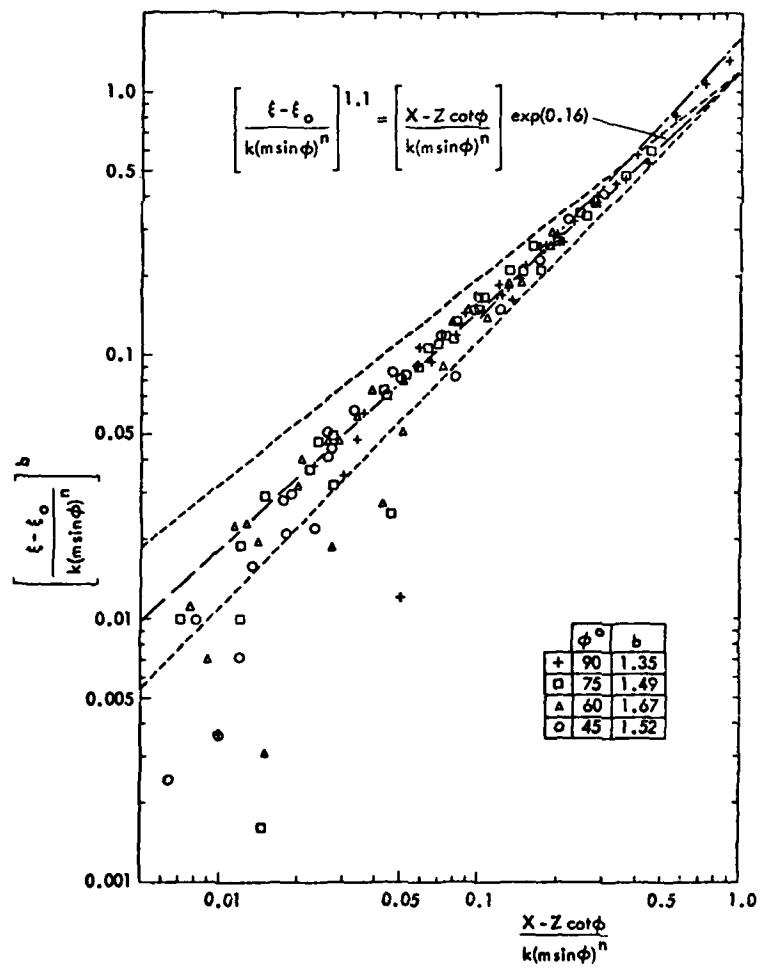

	ϕ°	b
+	90	1.35
□	75	1.49
△	60	1.67
○	45	1.52

FIGURE 38 CORRELATION OF MAXIMUM TOTAL PRESSURE PATH WITH INCLINATION AND MOMENTUM RATIO

An Experimental Investigation of an Upper Surface Blowing Configuration

by

G. D. Catalano
Asst. Prof. of Mechanical Engineering
Louisiana State University
Baton Rouge, Louisiana 70803
U.S.A.

J. B. Morton
Prof. of Mechanical and Aerospace Engineering
University of Virginia
Charlottesville, Virginia 22901
U.S.A.

R. R. Humphris
Senior Sceintist of Nuclear Engineering and Natural Science
University of Virginia
Charlottesville, Virginia 22901
U.S.A.

SUMMARY

The effects of both a flat and a curved wall on the one, two, and three point statistical properties of a coflowing turbulent jet are documented. Mean velocities, turbulent intensities, auto and cross velocity correlation functions, auto and cross velocity spectra, and iso-correlation contours are determined by use of a laser Dappler veloimeter with phase locked loop processor. Pressure field coherence and phase angle function as well as pressure-velocity correlations are made using a condensor type microphone/recorder. The effects of varying ratios of the nozzle exit plane mean velocity to the outer tunnel flow speed is noted. The confining surfaces serve to radically change the flow pattern of the expanding turbulent jet. The curved wall has the effect of rapidly increasing the turbulence in the potential core region and disrupting the jet's large scale turbulent structure. The pressure-velocity correlation functions indicate a strong coupling among the turbulent velocity, species concentration fluctuations, and pressure fluctuations in the jet near field.

INTRODUCTION

Turbulent shear flows can be divided into free shear flows bounded by no walls, flows bounded by one fixed boundary, and flows bounded by two or more fixed boundaries. The present investigation will focus on the class of problems with one fixed boundary, that is, a wall-jet. The motivation for studying the wall jet flow field is derived from its close resemblance to the upper surface blowing (USB) technique which is a possible approach in attempting to increase the short takeoff and landing capability of aircraft (1).

As in an unconfined jet, there exists in a wall jet (Figure 1) two main zones of flow: 1) an initial zone of flow establishment which consists of the growth of the boundary layer on the wall, the potential core, and the mixing region where the flow mechanism is similar to the free shear flow problem and 2) a zone of established flow which consists of a region of free mixing analogous to a free jet and the inner layer which is a class of boundary layer under a turbulent decelerating superstreams (2).

The specific flow field investigated is an axisymmetric nozzle exhauating over a solid boundary with an external uniform flow present.

Consider the classical "black box" approach to studying the wall jet, a methodology first suggested by Clauser (3) for studying turbulent boundary layers. The basic tenets of the approach are that by changing initial conditions and/or boundary conditions of the turbulent flow field, a greater insight into the transport characteristics and processes can be achieved. In this experiment, one initial and one boundary condition are varied. Here, initial condition refers to the ratio of the wall jet exit plane velocity to the outer flow speed boundary condition is changed by varying the curvature of the wall. In fact, two different wall surfaces are chosen with one being flat and other flat initially with a large curvature beginning at four jet diameters downstream.

The importance of varying the ratio of the jet exit plane velocity to the outer tunnel flow speed may be viewed by examining the same effect in ejector type flows. Razinsky and Brighton (4) investigated confined jet mixing in constant area pipes for a range of system parameters. The velocity ratio was found to strongly influence the axial pressure diatubation and the development of the centerline mean velocity.

The effects of wall curvature are dealt with in two quite separate cases: 1) transverse curvature, and 2) longitudinal curvature (5). Only longitudinal curvature will be considered in this investigation. Longitudinal curvature effects on turbulent boundary layers were first investigated by Prandtl (6). The main conclusion was that the flow of a turbulent boundary layer along a convex surface is more stable than along a concave surface. Bradshaw (7) made quantitative use of the analogy between streamline curvature and buoyancy in turbulent shear flow. So and Mellor (8) found that on a convex wall, the Reynolds shear stress and turbulent kinetic energy access the boundary layer are reduced as compared to a plane wall whereas increased for flow along a concave wall.

The strategy of the investigation is as follows: 1) document the statistical properties of the turbulent jet flow in the coflowing stream; 2) examine the effects on the flow field of a solid boundary;

3) vary the longitudinal curvature of the boundary; 4) vary the ratio of the jet exit plane mean velocity to the tunnel speed.

EXPERIMENTAL EQUIPMENT AND TECHNIQUES

A two-color laser Doppler velocimeter in conjunction with a phase locked-loop processor is used to make the velocity measurements (9). The two strongest frequencies of an argon ion laser in the "all lines" mode of operation are selected for use. The two-color LDV system allows the velocity at two different points in the flow fields to be determined with displacement between the probes possible in all three directions. A simple laboratory schematic is shown in Figure 2.

To determine the static and wall surface pressure, the system developed by Schroeder (10) and Herling (11) is used. The essential items include a 1/2 inch condenser-type microphone and a tape recorder. When cross-correlations are made between the fluctuating pressure and velocity fields, both signals are filtered (10Hz - 1000Hz) before being processed in order to achieve a good signal-to-noise ratio.

A computer program is used that enables the spectra of both the pressure and velocity to be obtained as well as the coherence between the two signals. Coherence is essentially the value of the cross-correlation coefficient as a function of frequency. If G_{11} and G_{22} denote the Fourier Transform of the auto-correlation function of pressure and velocity respectively, then the coherence, δ^2_{12}, is defined as follows:

$$\delta^2_{12} = \frac{G_{12}^2}{G_{11}G_{22}}$$

where G_{12} represents the Fourier Transform of the cross-correlation function between the pressure and velocity fluctuations.

A laser light scattering technique developed by Shaughuessy (12) is used to measure the concentration field. The passive admixture data is presented in Reference 9.

EXPERIMENTAL RESULTS

Mean Velocity Profiles

A comparison of the mean velocity profile for the flow over the plate and the flow over the flap to the theoretically predicted classical wall jet profile is presented in Figure 3. The velocity profiles in the center plane ($y/2r_o = 0$) are tested for the fully developed classical wall jet type similarity by plotting $(U - U_{FS})/(U_{max} - U_{FS})$ versus $z/z_{\frac{1}{2}}$. Clearly for the data presented here, the "top hat" profile of the flow leaving the nozzle is still apparent. For any particular profile, Umax and the length scale, $z_{\frac{1}{2}}$, are obtained from the smooth curve drawn through the experimental points. The length scale, $z_{\frac{1}{2}}$, is the vertical distance from the wall surface to the point where $(U - U_{FS}) = 0.5\ (Umax - U_{FS})$ and dU/dy is negative.

The data presented in Figure 3 corresponds to three different downstream locations ($x/2r_o = 3.76$, 4.0, and 4.24). Focussing initially on the mean velocity profile for the flow over the plate, it is clear that these plots are quite different in shape from the classical wall jet model. The is not surprising for it has been theorized that the wall jet actually is slower than the free jet in achieving similarity. Rajaratnam et al. (13) suggested that similarity will not be achieved until approximately ten to fifteen diameters downstream.

Turning next to a discussion of the flow over the flap at $x/2r_o = 3.76$, the mean velocity profile is comparable to the profile for the plate. However at $x/2r_o = 4.0$, the mean velocities plotted are close to the theoretical classical wall jet curve. After the flow has passed the actual curved portion of the flap ($x/2r_o = 4.24$), the closeness to theory is no longer present. In contrast to the flow over the plate, however, the mean velocity profile does lose its "top hat" or flat characteristic much more rapidly. Once again evidence is seen of the earlier breakup of the potential core region of the turbulent jet as it flows over the flap.

To check similarity of the mean velocity profiles in the horizontal planes at any height, $z/2r_o$, from the wall, $(U-U_{FS})/(U_{max}-U_{FS})$ is plotted versus $y/y_{1/2}$ in Figure 4. The quantity $y_{1/2}$ is the length scale in the y or transverse direction and is equal to the lateral displacement from the centerline for which $(U - U_{FS}) = 0.5\ (U_{max} - U_{FS})$.

The mean velocity profiles in the horizontal planes for the unconfined coflowing jet, the flow over the flap and the flow over the plate at a given z location are compared to the curve predicted by Goertler (14) for a free circular jet. The profiles for all three configurations are closer to the theoretical curve in the horizontal plane than is the case for classical wall jet comparison discussed previously. The mean velocity profile for the flap configuration is the closest to the similarity curve while the unconfined jet has the largest discrepancies for the vertical heights $z/2r_o = 0.5$ and $z/2r_o = 0.375$. However, closer to the surface it is the flow over the flap which deviates the most from Goertler's curve.

From this discussion, it is apparent that the flow over the plate tends toward the fully developed turbulent shape in horizontal planes faster than in the vertical plane. Also, the flap seems most effective in transforming the flat velocity profile characteristic of a circular nozzle. With respect to the unconfined coflowing jet the mean velocity profiles are closer to the fully developed turbulent shape in the horizontal planes at $z/2r_o = 0.125$ and 0.25 than is the case at $z/2r_o = 0.375$ and 0.50.

In Fig. 5 mean velocity profiles for the longitudinal component are presented for two downstream locations ($x/2r_o = 2$, 4) and at one vertical position ($z/2r_o = 0.5$) for all three flowfields. The ratio of the local excess velocity, $U-U_{FS}$, to the excess core velocity, U_o-U_{FS}, is plotted vs lateral displacement (non-dimensionalized by twice the radius of the jet) from the centerline of the jet/flap assembly).

Initially, consider the comparison of the width of the three flow configurations. The freely expanding jet and the flow over the plate are quite comparable in width both at two and four diameters downstream. However, the flow over the flap has a large increase in width compared to the previous configurations at both downstream locations. Second, notice the effect of the confining walls on the decay of the centerline velocity. At $x/2r_o = 4$, for example, the excess centerline velocity has decayed to approximately 0.95 $(U_o - U_{FS})$ for the coflowing jet, 0.90 $(U_o - U_{FS})$ for the plate configurations, and 0.55 $(U_o - U_{FS})$ for the flow over the flap. Thus, as the turbulent jet flows over the flap, the velocity field is significantly widened and decelerates much more rapidly.

Mean velocity parallel to the surface of the flap U* vs perpendicular height above the surface of the flap is presented in Fig. 6. An interesting observation that can be made concerning this series of profiles is that U^*/U_o has a greater maximum value at $x/2r_o = 4$ than at $x/2r_o = 2$. This seems to indicate a net transfer of momentum from the core of the jet down toward the surface of the flap.

Mean velocities V were also measured in the lateral (y) direction for the unconfined jet, the flow over the plate, and the flap configuration at the same downstream location ($x/2r_o = 4$ and $z/2r_o = 0.5$). This comparison is presented in Fig. 7. It is interesting to observe that, for the flow over the flap, the maximum value of the ratio $V/(U_o - U_{FS})$ has approximately doubled the maximum value found for the unconfined case.

For the flap configuration, a profile of the mean velocity W in the vertical direction z for the downstream location $x/2r_o = 4$ and $z/2r_o = 0.185$ also is presented in Fig. 7. Comparing this W profile with the one at $z/2r_o = 0.5$ yields the observation that the jet seems to be rotating or rolling up as it spreads out over the surface of the flap. Whereas at $z/2r_o = 0.5$, the maximum value of $W/(U_o - U_{FS})$ is obtained at the centerline of the profile, for $z/2r_o = 0.185$, this velocity ratio remains small and constant in the central region of the velocity field (i.e. $y/2r_o = 0$) and reaches a maximum at approximately $y/2r_o = 0.90$.

In Fig. 8 three vertical and three longitudinal mean velocity profiles are presented for various downstream locations ($x/2r_o = 5.5$, 6.0, and 6.6) at the vertical position, $z/2r_o = -0.57$ for the jet/flap configuration. These profiles indicate, in a quantitative as well as qualitative manner, the effectiveness of the flap in turning the flow. Figure 9 reinforces this by presenting a vectorial diagram of the resultant mean velocities at the centerline ($y/2r_o = 0$) as the flow proceeds downstream.

The effects of the velocity ratio, λ_j, on the width and decay of the centerline velocity for the three respective mean flow fields are presented in Figures 10 and 11. In Figures 10 (a) and (b) for $\lambda_j = 5.1$ and 10.88, the nondimensionalized mixing width, $y_m/2r_o$ is plotted versus $x/2r_o$ for $z/2r_o = 0.5$. The quantity, y_m, is defined as the lateral distance from the centerline to the location where the mean velocity is the arithmetic average of its value on axis and in the secondary stream. The results are compared to a theoretical curve developed by Squire and Trouncer (15).

First, consider the findings for $\lambda_j = 5.1$. While the agreement between the theoretical curve and experimental results for the coflowing jet is quite good, one effect of the confining surfaces can be seen. For the flow over the flap, the value of $y_m/2r_o$ increases much more rapidly than is the case for the other two configurations. With the plate in place, however, the value of $y_m/2r_o$ is somewhat smaller than that for the coflowing jet for the first several diameters downstream but eventually is comparable in magnitude. For $\lambda_j = 10.88$, the results are less clear. However, the rate of increase of $y_m/2r_o$ is considerably less for the flap than is the case for $\lambda_j = 5.1$. It is difficult to draw any strong conclusions, however, since the data is somewhat sketchy. Here, also the mixing widths of the unconfined jet and flow over the plate are comparable in magnitude.

In Figures 11 (a) and (b), the decay of the centerline mean velocity at $z/2r_o = 0.5$ for varying downstream locations is presented. In these Figures, U_o is the center line velocity and U_{FS} is the secondary (wind tunnel) velocity. The meaning of the data for the two jet/confining surface configurations should be discussed. As the flow exits the circular nozzle, the plate and flap tend to transform the "flat top" mean velocity profile, characteristic of an ideal jet, into profiles resembling a wall jet. Thus, the velocity at the nozzle center line would be expected to decrease at a different rate for the jet/plate and jet/flap cases as compared to the unconfined case. For the $z/2r_o$ shown in this figure, the decrease in the mean velocity in x direction is exagerated by the fact that the flow has both changed direction and been "drawn down" toward the flap.

For $\lambda_j = 5.1$, the effectiveness of the flap in decelerating the flow in the x direction is apparent in Figure 11 (a). The more rapid decay of the flow over the plate as compared to the unconfined jet is also noted. When $\lambda_j = 10.88$, the decay of the unconfined jet behaves quite similarly to the case for the smaller value of λ_j. The plate is slightly less effective in decelerating the flow while the effectiveness of the flap is reduced significantly.

The two observations that have been made concerning the relative rates of decay of the centerline mean velocity and the increase in the mixing widths for the flows over the flap with $\lambda_j = 5.1$ and $\lambda_j = 10.88$ are consistent and merit some discussion. The indication seems to be that as the value of λ_j gets larger and approaches the value corresponding to a free jet ($\lambda_j \to \infty$), the flap becomes less effective in both widening and decelerating the flow.

Turbulent Intensities

Measuring turbulent fluctuations with an LDV setup is predicated on the fact that the marking particles can respond to the instantaneous flowfield. For this experiment, particle lag at or near the exit plane of the nozzle is negligible. Also, the rms of the particle response differs from the fluid fluctuations rms by less than 2% up to approximately 2×10^5 Hz (16). In effect, the particle behavior is similar to that of a low-pass filter, with the 3-dB point at 4×10^5 Hz.

The axial and lateral distributions of the turbulence intensities, $(\bar{u}^2)/(U_o-U_{FS})$, are plotted vs lateral displacement from the centerline at the vertical location, $z/2r_o = 0.5$, in Fig. 12.

For the case of the unconfined coflowing jet, the turbulent intensity increases from about 2.5% to 5% at the centerline for the two downstream locations shown. In clear contrast to this case are the two confined flow configurations. Notice that for the flow over the plate, $(\bar{u}^2)^{\frac{1}{2}}/(U_o-U_{FS})$ is greater than either the unconfined or flap cases at $x/2r_o = 2$. At $x/2r_o = 4$, however, the flow over the flap clearly maintains the highest turbulent velocity level. In fact, $(\bar{u}^2)^{\frac{1}{2}}/(U_o-U_{FS})$ for the flow over the flap is more than five times the value it possessed at $x/2r_o = 2$.

Another important observation concerns the relative turbulent intensity value of the three flow configurations in the region $0.5 \leq y/2r_o \leq 1$. Whereas the flap seems to be amplifying the turbulence field in this region as well, the intensities of the plate flow are consistently lower than either of the other two cases. The presence of the confining straight wall seems to be diminishing the momentum transferring process occurring in the outer regions of the flow.

Turbulent intensities in the lateral direction, $(\bar{v}^2)^{\frac{1}{2}}/(U_o-U_{FS})$, are shown in Figs. 13 and 14. In Fig. 13, a comparison of the intensities for the different flow configurations at the same downstream location ($x/2r_o = 4$ and $z/2r_o = 0.5$) is presented. Notice that the turbulent intensity in the lateral direction is much higher in the shearing layer of the unconfined jet than in either of the other two configurations. In Fig. 14 $(\bar{v}^2)^{\frac{1}{2}}/(U_o-U_{FS})$ is presented for the flow over the flap. It indicates the change in the turbulence level as the flow reaches the curved portion of the flap structure.

In Figure 15, the turbulent intensity at $y/2r_o$ and $z/2r_o = 0.5$ is plotted versus downstream location, $x/2r_o$. For both $\lambda_j = 5.1$ and $\lambda_j = 10.88$, the turbulence increases at about the same rate for both the unconfined coflowing jet and the flow over the plate. The magnitude is consistently higher for the plate configuration. In fact, λ_j seems to have very little effect on the experimental data.

For the flow over the flap, however, the value of the parameter, λ_j, is of considerable importance. In the case with $\lambda_j = 10.88$, the increase in turbulence is at a higher rate than is the case for the other two configurations. However, with $\lambda_j = 5.1$, this increase is much more rapid. This fact is quite consistent with the observations made concerning the decay of the mean velocity. At the location in the flow field where the jet is decelerated and widened at the most rapid rate, the turbulence is also amplified greatly giving a strong indication that the flap serves to quickly break-up the potential core flow.

Integral Scales

The longitudinal integral time scale in the x direction is defined in terms of the autocorrelation coefficient as

$$T_1 = \int_o^{t^*} R(t')\, dt'$$

or

$$T_1 = \int_o^{t^*} R(t')\, dt'$$

where t^* is the time at which the coefficient first reaches the value of zero. To obtain the length scale, the integral time scale is multiplied by the local mean velocity, again using the "frozen" turbulence approximation (17).

Thus $L_1 = U \times T_1$

Physically, the integral length scale is approximately the largest turbulent scale in the flow.

The growth of the integral length scale for the unconfined jet for both values of λ_j is addressed in Figures 16 (a) and 16 (b).

Figures 16 (a) deals with the development of the integral scale at the lateral location corresponding to the lip of the nozzle while Figure 16 (b) is concerned with the centerline growth. At the lip of the nozzle, the integral length scale is found to grow linearly downstream as has been predicted by Laurence (18). The scale for the unconfined jet with $\lambda_j = 5.1$ grows somewhat faster than is the case when $\lambda_j = 10.88$. At the centerline of the flow field, the integral scale grows similarly for both values of λ_j. This is not too surprising since the velocity of the outer tunnel flow would not be expected to have a significant effect on the turbulence in this region for the first several diameters downstream.

For the flow over the flap, the development of the integral scale is quite different than is the case for the coflowing jet and is presented in Figure 17. It seems possible that the values measured at both the centerline of the flow field and out at the lateral location of the lip can be plotted on one curve. Also, the value of λ_j does not seem to influence the results. The rapid increase and then decrease of the values of the integral scales are notable in two respects. First, the large jump in the value of L_1 actually takes place before the flow has reached the curved portion of the flap. This is also true with respect to the steep decline. An understanding of this behavior lies in an examination of the definition of the integral length scale. First, since the flow field over the flap grows at the most rapid pace, one would expect the integral length scale, which is an estimate of the largest scale in the flow to reflect this increase. However, as the flow approaches the actual curved portion of the flap, there occurs a turning of the flow direction and also a rapid transforming of the "top hat" mean velocity profile into a profile more typical of a wall jet. Thus, the faster moving fluid particles are closer to the flap surface while out at $z/2r_o = 0.5$, the fluid is moving considerably slower. This large decrease in the mean velocity would cause a decrease in the magnitude of the integral length scale if the integral time scale does not

increase significantly since it is the product of integral time scale and the local mean velocity which are of importance. In fact, the integral time scale is nearly constant between $x/2r_o = 2$ and $x/2r_o = 4$. Secondly, as was noted previously, the integral scale is at best a very weak function of the value of λ_j. Though the presence of the flap amplifies the turbulence in the jet to a lesser extent when λ_j is equal to 10.88, the product of the local mean velocity and the local integral time scale seems independent of the outer tunnel speed. This, however, is difficult to determine precisely since the gradients of the integral scale are very large.

The growth of the integral scales for the flow over the plate is presented in Figures 18 (a) and 18 (b). For both $\lambda_j = 5.1$ and $\lambda_j = 10.88$, the integral scale at the centerline is consistently larger in magnitude than it is at the lip of the nozzle. After roughly four diameters downstream from the exit plane, the growth rate for all four curves shown is approximately the same. In the data presented here, the value of λ_j does effect the magnitude of the integral scale for the first few diameters downstream. However, after that, virtually no influence can be ascertained.

TAYLOR MICROSCALES

Let u' be the fluctuation of the longitudinal velocity in the ambient flow, then the Taylor microscale, λ_T, of turbulence is determined from the following condition.

$$\left(\frac{du'}{dx}\right)^2 = \frac{u'^2}{\lambda_T^2}$$

For isotropic turbulence, the Taylor microscale can be rewritten:

$$\frac{1}{\lambda_T^2} = \frac{1/5 \int_0^\infty k^2 E(d)dk}{\int_0^\infty E(d)\, dk}$$

where k is a wavenumber, and E(k) is the three dimensional energy spectrum function. The integral in the numerator is an indicator of the overall scale of dissipation while the integral in the denominator is an indicator of the overall scale of energy. Thus λ_T may be thought of as the ratio of the dissipation of energy to the total amount of energy in flow.

The Taylor microscale can be determined experimentally by fitting a parabola to the autocorrelation coefficient curve near the origin. The intersection of the parabola with the delay time axis along with the use of Taylor's hypothesis yields the value of the Taylor microscale.

Table 1 shows the value of the Taylor microscale for the three flow configurations with λ_j equal to 5.1 and also equal to 10.88. For each flow field, the Taylor microscale is determined both at the centerline and at the lateral position corresponding to the lip of the nozzle.

Consider initially the microscales determined for the unconfined turbulent jet. The values shown for the centerline position are fairly constant though there does seem to be a slight tendency to increase. Downstream from the lip of the nozzle, that tendency is seemingly stronger. It is interesting to note that the values of λ_T at the centerline with λ_j is equal to 5.1 are consistently lower than corresponding values when λ_j equals 10.88. The opposite is the case, however, downstream from the lip of the nozzle.

Next, the case of the flow of the jet over the plate will be discussed. Here again, a slight increase in the value of the Taylor microscale is noted as the flow progresses downstream. The value of λ_j does seem to have a strong influence on the value of λ_T downstream from the lip of the nozzle. With λ_j equal to 10.88 the values of λ_T out in the shearing layer are almost an order of magnitude different than for the corresponding position for the smaller value of λ_j.

Finally, consider the flow of the turbulent jet over the flap. Here at the centerline and the shearing layer location, the Taylor microscale first increases and then actually decreases in value. This is the case for both ratios of inner jet velocity to outer tunnel flow speed. Since the Taylor microscale may be thought of as the ratio of the dissipation of energy to the total amount in the flow, consider the implication of λ_T decreasing. A decrease in the magnitude of the Taylor microscale represents a decrease in relative magnitudes of the total energy in the flow to the dissipation in the flow. Considering the total energy aspect first, since the turbulence obtains its energy from the mean velocity, a decrease in the mean velocity will eventually show up as a decrease in the total energy of the flow. With respect to the relative increase in the dissipation of energy, recall that the dissipation is dominant at high frequencies. The flap which serves to amplify the turbulence in the flow field quite rapidly enhances the energy cascading process and, thus, could be responsible for the relative increase in the magnitude of the dissipation. Evidence thus points to the fact that the flap has a very strong influence on the turbulent velocity field.

Space-Time Two Point Velocity Correlations

The general space-time correlation coefficient for two points separated in a given flow field is as follows:

$$R_{1,1}(x, y, z, t, \xi_1, \xi_2, \xi_3, \ ) = \frac{u(x, y, z; t)\, u'(x + \xi_1, y + \xi_2, z + \xi_3; t + \ )}{\overline{u^2}^{1/2}\ \overline{u'^2}^{1/2}}$$

where ξ_1, ξ_2, and ξ_3 represent the spatial displacements of one point relative to the other and represents the delay time. Here, the space-time correlations are limited in scope to fluxuating velocities in the x direction only. From these measurements, it is possible to calculate iso-correlation curves for optimum delay, τ_m. Optimum delay time refers to the delay time at which the correlation is a maximum.

Typical results obtained are shown in Figures 19 thru 24. Figures 19 thru 21 deal with the case when ξ_2 is set equal to zero and hence are cross-sectional views of the three flow fields in the x-z plane. Figures 22 and 24 correspond to the iso-correlations curves obtained with ξ_1 set equal to zero and thus represent cross-sectional views in the y-z plane.

The reference point which remains fixed for all the correlation coefficients determined in the three flows has the following coordinates:

$$x/2r_o = 4 \quad y/2r_o = 0 \quad z/2r_o = 0.5$$

This downstream location is chosen for several reasons. First, this is the position at which the flap first begins to curve in a convex manner from the x-direction. Secondly, it has been observed in many of the one point measurements presented earlier in this report that there are significant differences in the three flows at this position,and, also, the statistical properties have been carefully documented.

Before progressing further, a new term must be introduced and it is the line of maximum maximorum of the correlations. Physically what is meant is that a line S is drawn through the point on each correlation level which is separated the farthest amount from the reference point (i.e., $(\xi_1^2 + \xi_2^2)^{\frac{1}{2}}$ or $(\xi_2^2 + \xi_3^2)^{\frac{1}{2}}$ is a maximum). With this line, it is then possible to get an idea of the flow pattern. The pattern of the iso-correlation curves describe, in a qualitative sense, the large scale structure of the various turbulent flow fields. The line S helps in a comparison to the shapes of the curves. If the turbulent flows can be considered as possessing large eddy structures, the line of maximum maximorum yields information about the sense of rotation of the eddies and any deformation.

In Figure 19, the iso-correlation curves in the x-z plane for the case of the unconfined, coflowing jet are shown. The curves are very elongated in the streamwise direction and close to being symmetric with respect to the ξ_1 axis. This is not the case about the ξ_3 axis, which is in contrast with contours presented for a fully developed turbulent boundary layer (5). The difference presumably is due to the fact that part of the flow field lies in the potential core while the rest can be considered a mixing region. The line S, marking the points of maximum maximorum of the correlations is approximately straight which would be the expected behavior.

The iso-correlation curves in the x-z plane for the case of the turbulent jet flowing over the plate are shown in Figure 20. Once again, the curves are elongated in the streamwise direction. There is no axis of symmetry. The pattern formed by the iso-correlation curves is very complex and is composed partly of two different lobes of high correlation value levels. The line S is drawn through the points of maximum maximorum of the correlations as was done in Figure 19. Downstream of the fixed reference point, the line is convex towards the surface of the wall. Upstream of the reference point, it is slightly more difficulty to construct the line, but it also seems to be convex towards the plate's surface. Sternburg (19) has offered a possible explanation of a qualitative nature for the observed shape of the S-lines. He theorizes that this may be caused by the mean shear, deforming the turbulence flow pattern as determined by its vorticity distribution. The maximum correlation will be determined by a point of the vorticity pattern that passes the fixed laser control volume at t equal to zero and is observed at some time, τ, later. The larger eddies which have a longer correlation distance will rotate due to the distortion of the mean shear flow in a clockwise sense and with a center of rotation in x-z plane. As the second, movable control volume approaches the plate, a point of the flow pattern passing the fixed laser "probe" at $\tau = 0$ will be displaced on the average from the wall by this rotation for τ 0, while for τ 0 this point has arrived from a upstream position also at a greater distance from the wall. The rough picture would lead to an S-line convex towards the wall below the center of rotation, a fairly straight line near the center, and it will be curved concave to the wall above the center.

The iso-correlation contours in the x-z plane for the flow of the turbulent jet over the flap are presented in Figure 21. As is the case for the plate configuration, the pattern formed by the isocontours is not symmetric about either the ξ_1 or the ξ_3 axis. Before it has been observed that the previous two controus demonstrated an elongation in the streamwise direction. For the flow over the flap, The elongation exists but the pattern formed is rotated a sizeable amount from the longitudinal direction. Through the points of maximum maximorum of the correlations, the line S is drawn. Before applying Sternburg's approach, it is first necessary to recall the geometry of the flap and the relative position of the reference "probe." In Figure 1, a view of the jet/flap assembly is shown. After a distance of approximately four diameters downstream from the exit plane of the nozzle, the tangent to surface of the flap rotates quickly away from the horizontal direction. Thus, any position for the second "probe" downstream of the $x/2r_o = 4$ plane would be over the curved section of the flap's surface. Now, consider the shape of the line S in Figure 21. Downstream of the reference point, the line heads down towards the wall surface and is also convex relative to the flap. Upstream the line is also inclined with a negative slope from the x-direction, and is essentially straight. Clearly, it is possible to say from observing the iso-correlation contours that the flow is being turned by the flap. Secondly, considering the change in shape of the flap surface and the convex shape of the line S downstream, Sternburg's ideas can be reasonably

applied once again. For the clockwise rotation of the large eddies, a point of the flow pattern passing the reference control volume will tend to both be turned downward by the flap's surface and also be displaced on the average from the wall by this rotation for a positive delay time. The flow pattern upstream of the fixed reference point indicates the direction from which the flow is coming.

In Figure 22, the iso-correlation curves in the y-z plane for the unconfined coflowing turbulent jet flow field are shown. The eccentricity of each of the curves does vary but is essentially zero and thus the iso-correlation levels are close to being circles in shape. Hence, symmetry in the flow exists about the $_2$ and the $_3$ axes. Though Sternburg's ideas cannot be applied in the y-z plane, the line S can be constructed and from its shape, a rough estimate of the flow pattern can be obtained. For the unconfined jet, the line of maximum maximorum can be drawn, starting from the center of the field, off in any radial direction. One line is arbitrarily constructed for the sake of clarity. From observing the line S and the iso-correlation curves, an indication that the jet's flow field is spreading out equally in all direction is apparent. The lower correlation levels farther out from the cneter line represent fluid particles which have been separated from the potential core the longest period of time.

Consider next the iso-correlation curves in the y-z plane for the flow of the turbulent jet over the plate (Figure 23). The change in the shape of the curves caused by the presence of the plate is apparent. The iso-correlation curves are elongated in the lateral direction. Although the flow pattern is clearly not symmetric about the $_2$ axis, symmetry does exist with the respect to the $_3$ axis. As was the case in the x-z plane, the line S is again somewhat more difficult to construct. Allowing some author's discretion, the line S moves out from the center of the flow in a slightly convex manner with respect to the plate's surface. Two impressions can be drawn. Initially, the turbulent jet is drawn downward toward the plate. Secondly, there exists an indication that the flow may be rolling up in the outer regions, or at least some type of canted rotating motion of the larger eddies to the longitudinal downstream is being observed. It is instructive to compare the differing flow patterns displayed in Figures 22 and 23. The width of area enclosed by the iso-correlation curves is significantly smaller for the flow over the plate for $\xi_3 < 0$, about the same for $\xi_3 = 0$ and somewhat larger for the $\xi_3 > 0$. The second observation is reinforced by the measurements made of the mixing widths and the intermittency profiles for the two flows.

Lastly, the iso-correlation curves in the y-z plane for the flow of the turbulent jet over the flap are shown in Figure 24. The iso-correlation curves are markedly elongated in the z direction. The flow pattern is symmetric about the ξ_3 axis, but asymmetric with respect to the ξ_2 axis. The line S is drawn appropriately through the flow field pattern. The first impression is one of noticing the narrowness of the flow pattern. As has been mentioned previously, the flap is much more effective in amplifying the turbulence levels of the turbulent jet. This more rapid and intense mixing action would manifest itself in a decrease in the coherence of the flow field pattern. Thus, in the outer mixing region, the turbulent jet is more apt to have forgotten its previous flow conditions, and correlations between the center of field and a second point farther out in the mixing layer would be weaker. Secondly, consider the direction of the line S. Downstream of the fixed reference point, the line is clearly heading in a negative ξ_3 (i.e. -z) direction. Upstream, there is some arbitrariness involved, but the line also has a negative $_3$ heading. From the flow pattern the impression is made again that flap is quite effective in turning the flow. At a positive delay time, the particles that were at the reference point have moved steadily downward toward the surface of the flap, and thus a stronger correlation level exists. The same type of agreement can also be made for the flow upstream of the reference point.

D. Pressure-Velocity Correlations

Additional information concerning the turbulence structure of the various flow fields can be gained from measurements of the pressure fluctuations at both the wall and in the turbulent jet and correlating those signals with fluctuating turbulent velocities in the potential core and in the shearing region.

Pressures are measured either at surface ports located on the flap or plate or by a pressure probe in the flow. In either case, the following space-time correlation are measured:

$$R_{pu}(\bar{x}, \bar{\xi}, t, \tau) = \frac{p(\bar{x},t)u(\bar{x} + \bar{\xi}, t + \tau)}{[p(\bar{x},t)^2]^{\frac{1}{2}}[u(\bar{x},\bar{\xi}, t + \tau)^2]^{\frac{1}{2}}}$$

where $\bar{\xi}$ is the position of the velocity "probe," measured relative to the pressure probe and p is the static pressure measured at the wall or in the flow field.

The primary focus of this segment of the experimental investigation is to determine the relationship between the pressure and the velocity fields. To show the dependence between the two fields, the coherence is plotted for various pressure and velocity monitoring locations. Coherence, which can be considered a correlation coefficient which varies with frequency, is defined as follows:

$$\delta_{12}^2 = \frac{12}{G_{11}G_{22}}$$

where G_{11}, G_{22} are the Fourier Transforms of the individual autocorrelation functions and G_{12} is the Fourier Transform of the cross-correlation function.

1. Wall Pressure Fluctuations

Cross correlations between fluctuating pressure signals measured at surface ports in the plate and flap and turbulent velocity signals monitored at various locations in the flow field are determined.

Consider first the case of the flow over the plate. To clarify the relationship between pressure and velocity fluctuations, power spectral densities and coherence are determined with the laser "probe" at $\xi_3/2r_o = 0.2, \xi_1/2r_o = \xi_2/2r_o = 0$. Examples of the results for $x/2r_o = 4$ are shown in Figures 25-27.

Here the lateral positioning of the pressure port and laser probe varies from $y/2r_o = 0$ to $y/2r_o = 1$. It is found that inside the lip of the nozzle, $y/2r_o = 0.5$ the velocity spectra and pressure spectra are characterized by large peaks at, in this instance, approximately 300 Hz. The coherence between the pressure and velocity signals is clearly the strongest at this peak frequency. As the pressure and velocity monitoring "probes" are moved outward from $y/2r_o = 0.5$ the spectral peaks are attenuated and the resultant decrease in the coherence is noted.

Coherences are also determined for the flow over the plate with $\xi_2/2r_o$ varying from 0 to 1, $\xi_1/2r_o = 0$ and $\xi_3/2r_o = 0.5$ (Figure 28). Physically, the laser control volume is held fixed at the location $x/2r_o = 4$, $y/2r_o = 0$, and $z/2r_o = 0.5$ with the fluctuating velocity signal being correlated with surface pressures measured at $x/2r_o = 4$, $z/2r_o = 0$, and $y/2r_o = 0$, 0.5 and 1. Though not shown here, it is found that the velocity spectra are not as peaked as is the case at $z/2r_o = 0.2$ and, hence, the coherence between the pressure and velocity signals is diminished. Note that the coherence decreases as the surface probe is moved laterally outward from the jet centerline.

For the flow over the flap, coherences are determined between the pressures monitored at the surface and the velocities at the $y/2r_o = 0$ location. The downstream location is held fixed at $x/2r_o = 4$. In Figure 29, coherences are shown with the laser "probe" held fixed at $\xi_2/2r_o = 0$ and $z/2r_o = 0.2$ while in Figure 30, the laser measuring volume is located at $y/2r_o = 0$ and $z/2r_o = 0.5$. Many of the same observations that were made concerning the flow over the plate can be made once again. The velocity spectra are found to be much more peaked closer to the surface of the flap. The coherence is larger in magnitude between the wall surface pressure and the velocity fluctuations with $\xi_3/2r_o = 0.2$. Also, the coherence is the strongest at approximately 300 Hz.

2. Pressure Fluctuations at Probe

Cross correlations and coherences are determined between the static pressure measured by a static pressure probe and the turbulent velocity fluctuations measured at the jet axis. The pressure is monitored at three lateral locations (i.e., $y/2r_o = 0$, 0.5, 1.0) with the velocity control volume remaining fixed. The vertical location for the pressure probe and LDV volume remains fixed at $z/2r_o = 0.5$.

For the unconfined, coflowing jet, the coherences between the fluctuating pressure and velocity signals are shown in Figures 31-33 for the downstream location, $x/2r_o = 4$. In Figure 31, power spectral densities as well as the coherence between the pressure and velocity field are presented with $\xi_2/2r_o = 0$. Notice that the spectra and the coherence peak at approximately 300 Hz, as was the case for the pressure measured at the wall. In Figures 32 and 33, as the pressure probe is moved radially outward, the coherence decreases.

Next, consider the case of the turbulent jet flowing over the flat plate for the downstream location, $x/2r_o = 4$. The pressure spectrum is again found to be markedly peaked at 300 Hz at $y/2r_o = 0$ and this "bump" is both broadened and attenuated out from the jet axis. The velocity spectrum is not as peaked as it is the case of the unconfined jet. The coherence of the two fluctuating signals (Figure 34) has been significantly reduced with the plate in the flow field, and it decreases with increasing lateral separation of the pressure probe and the laser control volume. The coherences obtained from the turbulent jet/flap configuration for the downstream location $x/2r_o = 4$ are shown in Figure 35. The peak in the velocity spectra has been virtually eliminated. It is interesting to compare the coherence of each $\xi_2/2r_o$ position for this flow with the jet/plate and unconfined jet flow fields. The coherences for the two confined jet flows are quite close in magnitude. The transformation of the turbulent jet into either a classical wall jet or curved wall jet does decrease the relationship between the fluctuating pressure and velocity fields.

Figure 36 shows the change in the value of the correlation coefficient at a given lateral location as the flow progresses downstream in each of the three configurations. The decrease in the correlation coefficient as $x/2r_o$ increases is apparent. Also, the flow of the unconfined, coflowing turbulent jet maintains the highest value of the coefficient at each measurement position.

CONVECTION VELOCITIES

The possibility exists of defining many kinds (20) of convection velocities. Favre, Gaviglio and Dumas (21) showed that convection velocities can be determined from iso-space-time velocity correlation curves $R_{1,1}(\xi,0,0,T)$. Favre et al. then defined the convection velocity as follows:

$$U_{con} = \xi_1/\tau_{max}$$

where τ_{max} is the delay time for which $R_{1,1}$ has a maximum value.

In particular in the case of relatively strong inhomogeniety taking in the dimensionless time $\bar{U}\,t/L$, an average value of $\bar{U}$ across the distance ξ_1, i.e.

$$\bar{U}_1 = \frac{1}{\xi_1}\int_0^{\xi_1} d\,\bar{U}_1(x_1 + \xi_1) = \tfrac{1}{2}[\bar{U}_1(x_1) + \bar{U}_1(x + \xi_1)]$$

where L is any suitable length scale.

The convection velocities determined for the three different flow configurations are shown in Table II. Here for a given longitudinal displacement, nondimensionalized by twice the radius of the jet, between the two measuring laser "probes," the non-
dimensionalized delay time and the ratio fo the convection velocity to the mean velcity are given. Mean velocity here refers to the average value determined using Favre's definition.

Focussing initially on the convection velocity calculated for the unconfined, coflowing turbulent jet, the ratio of the Ucon to $\bar{U}_1$ is very close to unity, and, indeed, remains fairly constant. Thus, in this case, at least, the convection velocity appears to be almost independent of the separation distance. Next,

consider the case of the turbulent jet flowing over the plate. Here something quite interesting happens. As the flow progresses downstream, the convection velocity has approximately the same value as the mean velocity for $\xi_1/2r_o \leq 0$ but for $\xi_1/2r_o$ increasing positively, the ratio $Ucon/\bar{U}_1$ is greater than unity. This phenomenon also occurs in turbulent boundary layers over flat plates (11). To explain the reason for this behavior, recall the vertical height above the surface of the plate at which these measurements are taken and also the shape of the mean velocity profile for this flow in the center vertical plane. Notice that there is a region of faster moving fluid particles closer to the wall surface. Also, as the flow progresses downstream, the profile approaches that found for a classical wall jet. Hence though the ratio of $Ucon/\bar{U}_1$ may be greater than unity, the ratio of Ucon/U max will never be.

Finally, consider the flow of the turbulent jet over the flap. Notice that for $\xi_1/2r_o < 0$, the value of the ratio of $Ucon/\bar{U}_1$ is slightly greater than unity. This can be explained using the same logic that is used in the previous paragraph. The reason that $Ucon/U_1 < 1$ occurs sooner than is the case for the flow over the plate is that the mean velocity profile over the curved surface in the center vertical plane is transformed much more effectively and rapidly from the ideal jet's "flat top" to the wall jet shape. For $\xi_1/2r_o > 0$, the convection velocity has decreased substantially. Presumably this is due to the fact that the flow is undergoing a change in direction.

A summary of the significant results detailed in this experiment will now be given. The presence of the confining surfaces was found to be of importance in the resultant effects on both the mean and fluctuating part of the turbulent velocity field of the jet.

It was found that for the flow over the plate, the mean velocity field tended toward the fully developed turbulent shape in different horizontal planes faster than in the vertical plane at $y/2r_o = 0$. Also, the flap seemed more effective in changing the flat velocity profile characteristic of a circular nozzle into a wall jet profile.

Convection velocities were determined for the three flow configurations. The convection velocity determined for the unconfined jet was found to be approximately equal to the local mean velocity and also to be independent of the separation distance between the "probes." For the cases of the flows over the plate and flap, the convection velocity was greater than the local mean velocity in several instances when the local velocity was considerably less than the maximum velocity at that particular downstream location.

Longitudinal integral length scales and Taylor microscales were determined. The integral scales for the flap were seen to have a rapid increase and then decrease in magnitude as the flow approached the start of the curved portion of the surface. For the unconfined turbulent jet, the growth of the integral scale at $y/2r_o$ was linear, as predicted. At best, the integral scale development for the three different configurations was a weak function of λ_j. The value of λ_j did strongly influence the magnitude of the Taylor microscale, λ_T, at the lateral position corresponding to the lip of the nozzle.

Pressure velocity correlations using both the static pressure probe and the surface ports yielded strong evidence that as the flow progresses downstream, and the flow becomes a fully developed turbulent flow, the relationship between the pressure and velocity fields diminishes. For the first several diameters downstream from the exit plane when the pressure and velocity spectra peak at approximately 300 Hz, the coherence between the two fluctuating fields is the strongest.

Auto and cross correlations were determined for the concentration field at various downstream locations. At $x/2r_o = 4$, the autocorrelation coefficient curve was found to possess a damped sinusoidal nature for the three different flow configurations. The concentration fluctuations at $y = \pm 0.5$ were found to be related both at $x/2r_o = 4$ and $x/2r_o = 8$. The maximum absolute values of the cross correlation coefficient did decrease sizably from four to eight diameters downstream of the exit plane, however. The power spectra for the jet, jet/plate, and jet flap all exhibited a peak at $x/2r_o = 4$ at approximately the same frequency as that found in the core velocity spectra. Here again, evidence exists in reinforcement of the vortex model of the jet. The plate and the flap did seem to diminish the peak and also seemed to cause a shift of energy to lower frequencies in the spectra.

Space-time correlations for the turbulent velocity fields were obtained, and the lines of maximum maximorum were constructed for both the x-z plane and the y-z plane. For the unconfined jet, the iso-correlation levels were symmetric with respect to the ξ_1 axis though very elongated. The line of maximum maximorum was straight and parallel to the ξ_1 axis. In the y-z plane, the iso-correlation levels were circular in shape about the ξ_1 axis. For the flow over the plate, the iso-correlation curves in the x-z plane were very complicated and elongated in the ξ_1 direction and the line of maximum maximorum was cured convex towards the wall both upstream and downstream of the fixed reference "probe." For the flow over the flap the iso-correlation curves were elongated and rotated down towards the surface in the x-z plane, evidence also existed as to confirm the effectiveness of the flap in turning the flow. The iso-correlation contours for the turbulent flow fields demonstrate the existence of large scale structures. Consider the fact that the shape of the contours is significantly different for each of the three flow configurations in both the x-z and the y-z planes. The flow "knows" whether or not a confining surface is present and also "senses" if the wall is curved or flat. This "knowledge" is then seemingly transmitted throughout the flow field.

This experimental investigation has shown that large scale structures do exist in the near field of the turbulent jet. The two point velocity and concentration measurements document this observation. The plate and the flap were found to strongly influence the large scale structure of the jet.

Several conclusions can be reached. First, the flap served to diminish the extent of influence of the large scale structures in the flow field. This should help in reducing the structural loads the flap or wing must endure. Instead of one dominant frequency in the velocity field, the turbulent fluctuations in the entire power spectrum would be amplified. The implication would then be to mount the nozzle as close as possible to the curved portion of the flap. The second conclusion is in reference to comparing the velocity flow field with the two different velocity ratios, λ_j. There exists considerable doubt as to

whether or not the jet flow will even remain attached as the velocity ratio between the inner jet flow and the tunnel flow tends towards infinity. The significance of measurements made in a static testing configuration ($\lambda_j \rightarrow \infty$) is quite questionable.

REFERENCES

1. Schoenster, J. A., Willis, C. M., Schroeder, J. C., and Mixson, J. S., "Acoustic Loads Research for Powered Lift Configurations," Powered Lift Aerodynamics and Acoustics Conference, May 24-26, 1976, Langley Research Center, Hampton, Va., pp 429-444.

2. Hari, V., "A Method to Analyze the Wall Jet Flow," Aeronautical Journal, Vol 77, Oct. 1973, pp 512-515.

3. Clauser, F. H., "The Turbulent Boundary Layer," Advances in Applied Mechanics IV, Academic Press, New York, 1956.

4. Razinsky, E., and Brighton, J. A., Trans ASME 93D, 1971, pp 311.

5. Fernholz, H.-H., "External Flows," Turbulence, ed. P. Bradshaw, Topics in Applied Physics, Vol 12, Springer Verlag, New York, 1978, pp 45-98.

6. Prandtl, L., NACA TM-625 (1929).

7. Bradshaw, P., Journal of Fluid Mechanics, Vol 36, 177, 1969.

8. So, R. M. C. and Mellor, G. L., Journal of Fluid Mechanics, Vol 60, 43, 1973.

9. Catalano, G. D., "An Experimental Investigation of a 3-D Wall Jet," Ph.D. Dissertation, University of Virginia, Charlottesville, Va., 1977.

10. Schroeder, J. C., "Development of Experimental Techniques for Investigation of Unsteady Pressures behind a Cold Model Jet, M.S. Thesis, University of Virginia, Charlottesville, Va., 1976.

11. Herling, W. W., "The Development of an Experimental Facility for the Investigation of Scalery Effects in Prepulsive Lift Configurations," M.S. Thesis, University of Virginia, Charlottesville, Va., 1976.

12. Shanghnessy, E. J., "Measurement of Particle Diffusion in a Turbulent Jet by Laser Light Scattering," Ph.D. Dissertation, University of Virginia, Charlottesville, Va., 1975.

13. Rajaratnam, N., and Paris, B. S., "Three Dimensional Turbulent Wall Jets," Journal of Hydraulics Division, ASME Trans, January 1974.

14. Hari, V., "A Method to Analyze Wall Jet Flow," Aeronautical Journal, October 1973.

15. Pabst, O., Die Ausbiestung Neisser Gasstrahlen in Bewegter Luft II, Teil, UM 8007, 1944.

16. Berricht-Rapport R117/76 Proceeding of the ISL/AGARD Workshop on Laser Auemometry, May 5-7, 1976, Sainte-Louis, France.

17. Tennekes, H. and Lumby, J. L., A First Course in Turbulence, MIT Press, Cambridge, Mass., 1972.

18. Lawrence, J. C., NACA Report 1292, 1955.

19. Sternberg, J., "On the Interpretation of Space Time Correlation Measurements in Shear Flow," The Physics of Fluids, Suppl. 10, Part II, S 146, 1967.

20. Favre, A., "Review on Space Time Correlations in Turbulent Fluids," Journal of Applied Mechanics, ASME Trans., Vol 32E, 1965.

21. Favre, A., Gavigho, J., and Dumas, R., "Structure of Velocity Space Time Correlations in a Boundary Layer," The Physics of Fluids, Suppl 10, Part II, S 138, 1967.

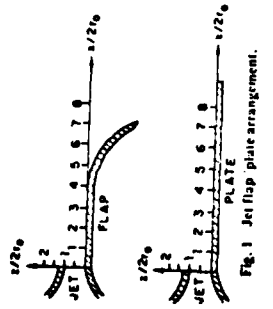

Fig. 1 Jet flap plate arrangement.

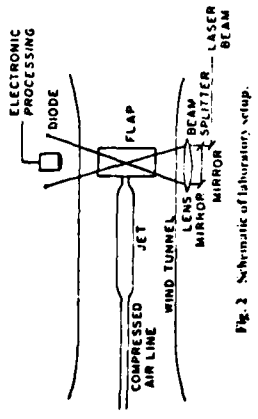

Fig. 2 Schematic of laboratory setup.

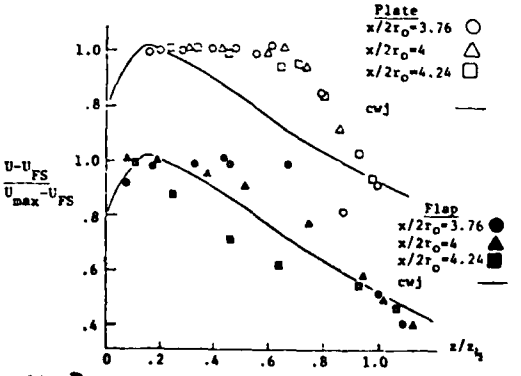

Fig. 3 Comparisons to Classical Wall Jet (cwj), $|y|/2r_o=0$ ($\lambda_j = 5.1$)

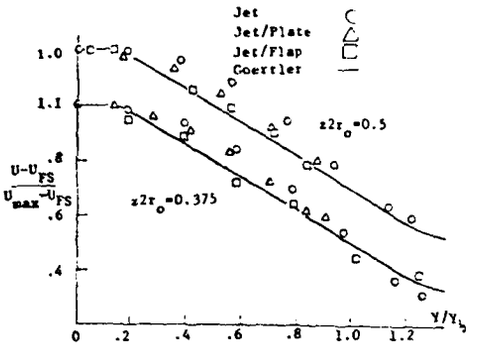

Fig. 4 Mean Velocity Profiles in Horizontal Planes, $x/2r_o$=4 Comparison to Similarity Curve (λ_j= 5.1)

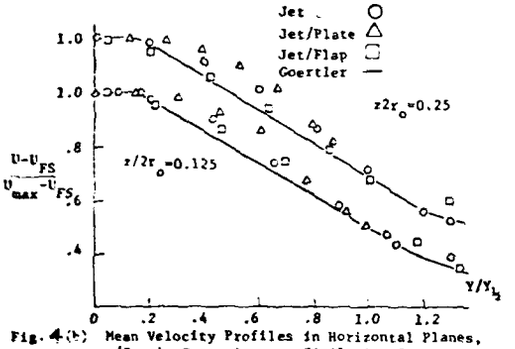

Fig. 4(b) Mean Velocity Profiles in Horizontal Planes, $x/2r_o$=4, Comparison to Similarity Curve (λ_j = 5.1)

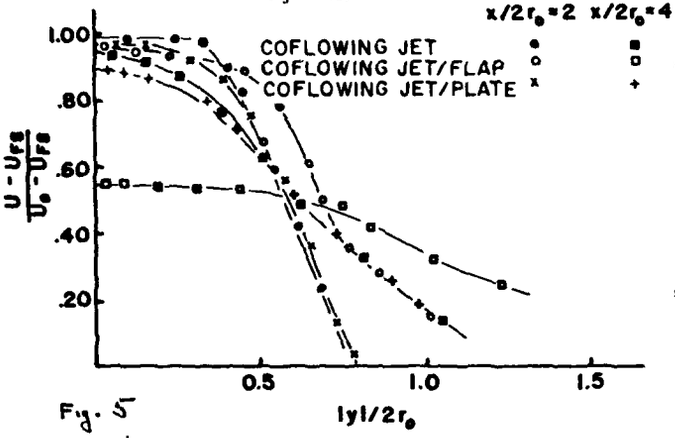

Fig. 5

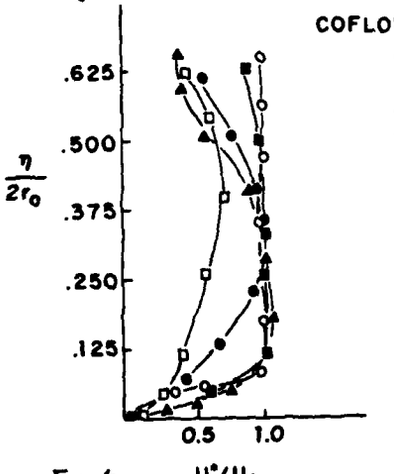

Fig. 6

COFLOW JET ■ $(z/2r_o=0.5, |V|/(U_o-U_f))$
JET/FLAP ▲ $(z/2r_o=0.5, -W/(U_o-U_{fs}))$
JET/FLAP △ $(z/2r_o=.185, -W(U_o-U_f))$
JET/FLAP □ $(z/2r_o=0.5, |V|/U_o-U_f))$
JET/PLATE ○ $(z/2r_o=0.5, |V|/U_o-U_f))$

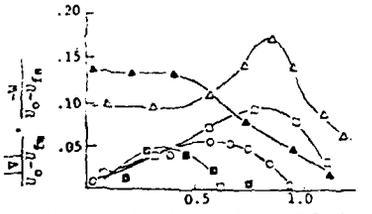

Fig. 7 Vertical and Lateral Mean Velocity Profiles for Flap, $x/2r_o$ = 4 (λ = 5.1)

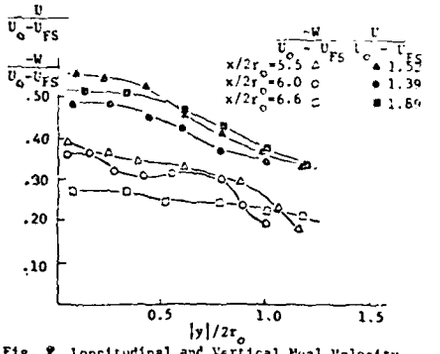

Fig. 8 Longitudinal and Vertical Mean Velocity Profiles for Flap $2/2r_o$=0.57

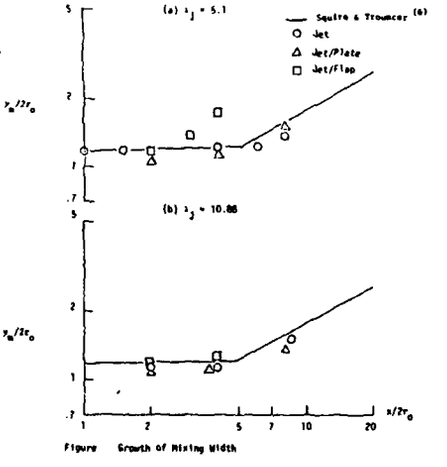

Figure Growth of Mixing Width

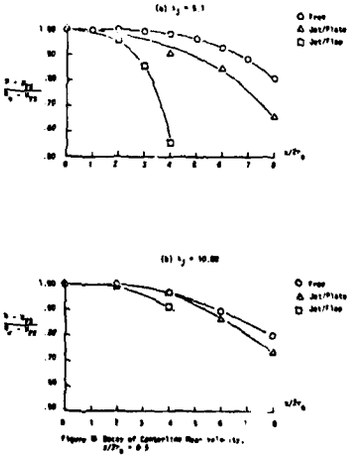

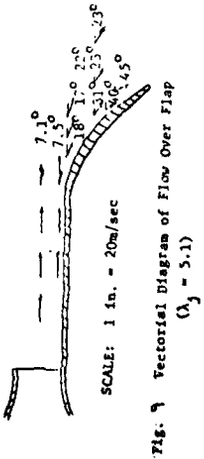

Fig. 9 Vectorial Diagram of Flow Over Flap (λ_j = 5.1)

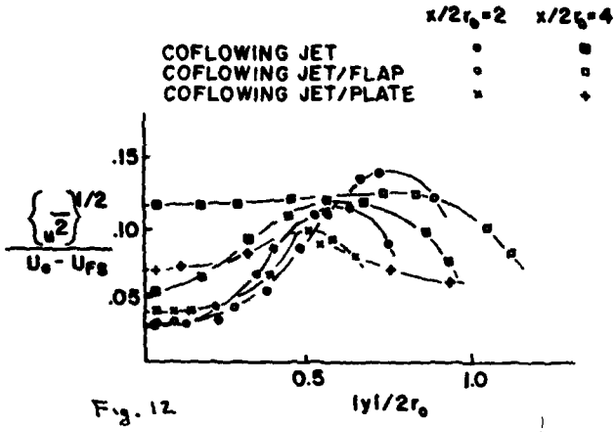

Fig. 12

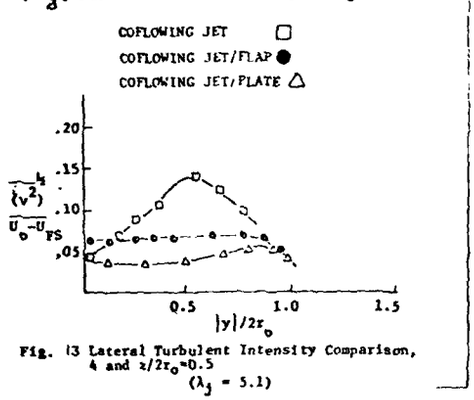

Fig. 13 Lateral Turbulent Intensity Comparison, 4 and $z/2r_0$=0.5
(λ_j = 5.1)

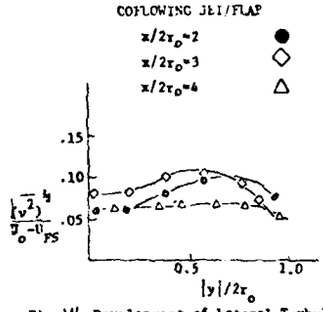

Fig. 14 Development of Lateral Turbulent Intensity Profiles for Flow over Flap, $z/2r_0$=0.5
(λ_j = 5.1)

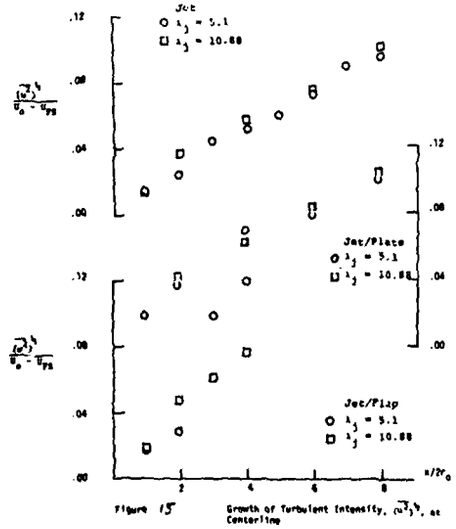

Figure 15 Growth of Turbulent Intensity, $(\overline{u^2})^{1/2}$, at Centerline

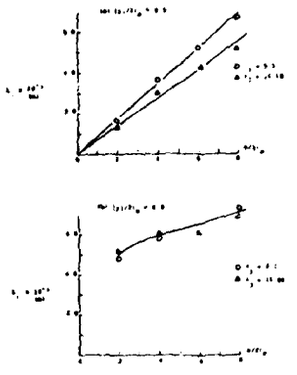

Figure 16 Development of Integral Scale for Jet, $z/2r_0$ = 0.5

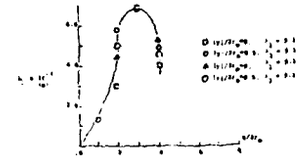

Figure 17 Development of Integral Scale for Jet/Flap, $z/2r_0$ = 0.5 (λ_j = 10.88)

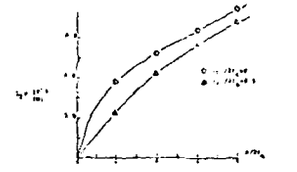

Figure 18(a) Development of Integral Scale for Jet/Plate, $z/2r_0$ = 0.5

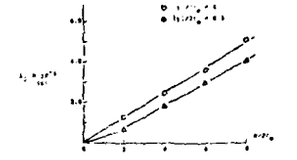

Figure 18(b) Development of Integral Scale for Jet/Plate, $z/2r_0$ = 0.5 (λ_j = 5.1)

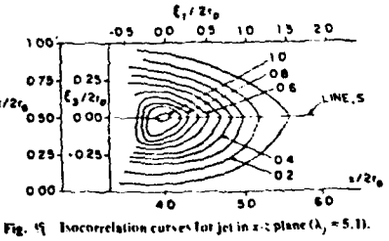

Fig. 19 Isocorrelation curves for jet in x-z plane (λ_j = 5.1).

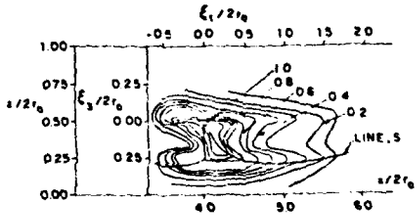

Fig. 20 Isocorrelation curves for jet/plate in x-z plane (λ_j = 5.1).

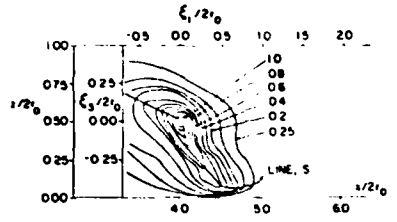

Fig. 21 Isocorrelation curves for jet flap in x-z plane (λ_j = 5.1).

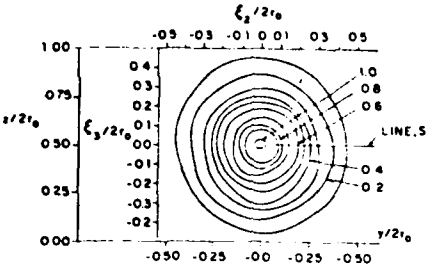

Fig. 22 Isocorrelation curves for jet in y-z plane (λ_j = 5.1).

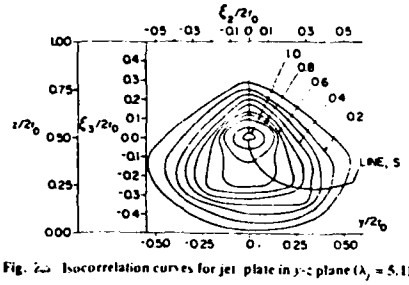

Fig. 23 Isocorrelation curves for jet plate in y-z plane (λ_j = 5.1).

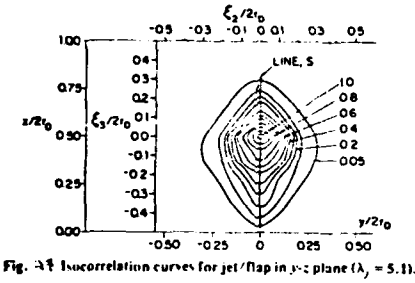

Fig. 24 Isocorrelation curves for jet/flap in y-z plane (λ_j = 5.1).

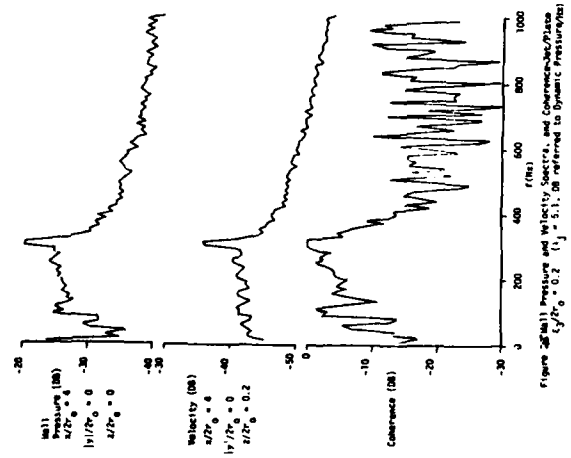

Figure 25 Wall Pressure and Velocity Spectra and Coherence-Jet/Plate
($\xi_3/2r_0$ = 0.2 (λ_j = 5.1), DB referred to Dynamic Pressure/Hz)

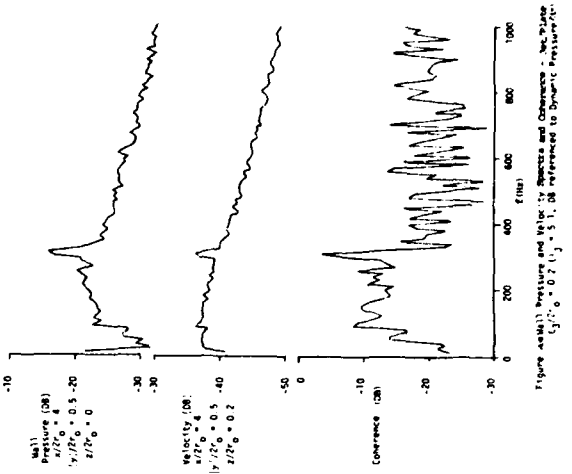

Figure 26 Wall Pressure and Velocity Spectra and Coherence - Jet/Plate
($\xi_3/2r_0$ = 0.2 (λ_j = 5.1), DB referred to Dynamic Pressure/Hz)

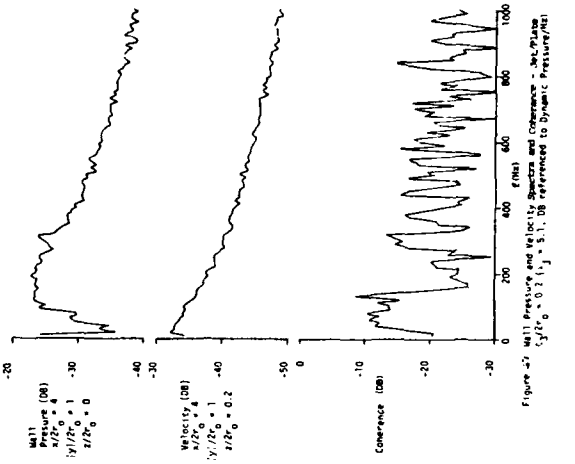

Figure 27 Wall Pressure and Velocity Spectra and Coherence - Jet/Plate
($\xi_3/2r_0$ = 0.2 (λ_j = 5.1), DB referred to Dynamic Pressure/Hz)

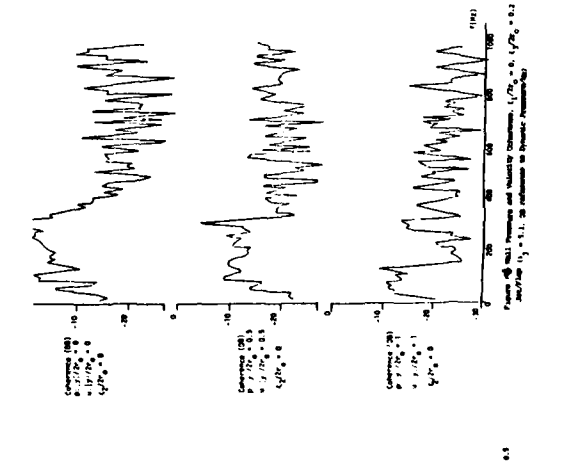

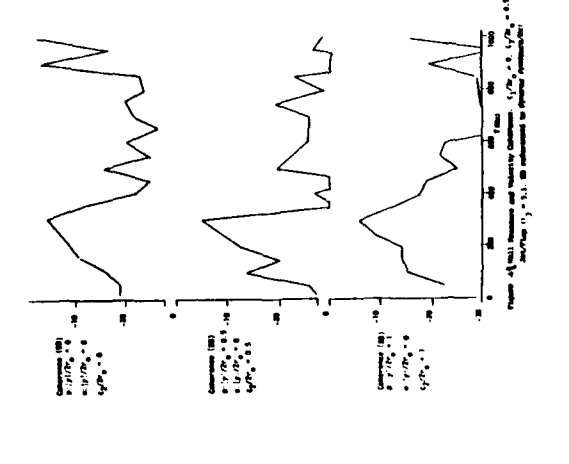

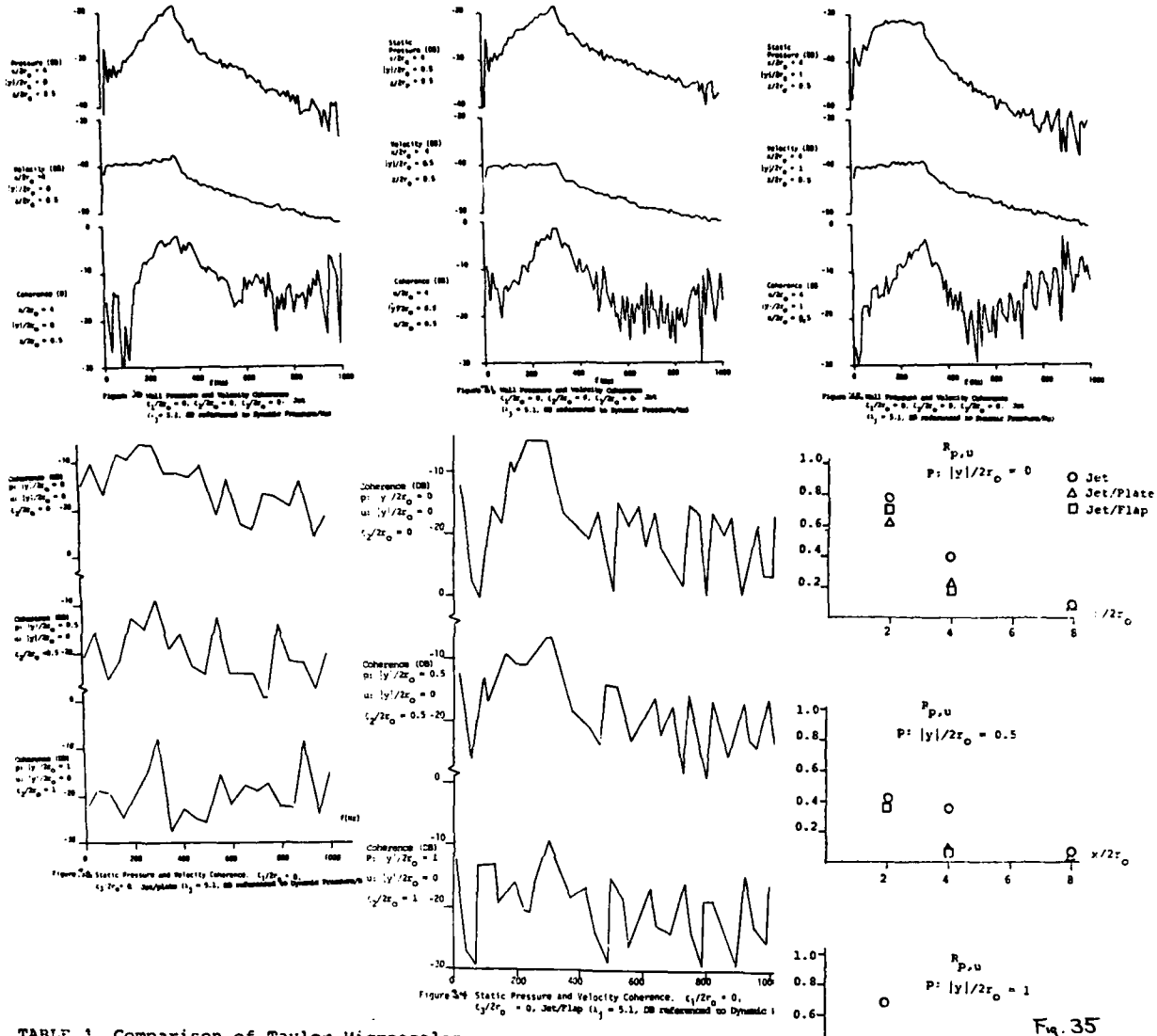

Figure 34 Static Pressure and Velocity Coherence. $\xi_1/2r_o = 0$, $\xi_y/2r_o = 0$, Jet/Flap ($\lambda_j = 5.1$, DB referenced to Dynamic

Fig. 35

TABLE 1 Comparison of Taylor Microscales

	$\lambda_j = 10.88$			$\lambda_j = 5.1$			$\lambda_j = 10.88$		
$x/2r_o$	$\lvert y\rvert/2r_o = 0$	$\lvert y\rvert/2r_o = .5$	$\lvert y\rvert/2r_o = \infty$	$\lvert y'\rvert/2r_c = 0$	$\lvert y'\rvert/2r_c = .5$	$\lvert y'\rvert/2r_c = \infty$	$\lvert y\rvert/2r_o = 0$	$\lvert y\rvert/2r_o = .5$	$\lvert y\rvert/2r_o = \infty$
0				3.52×10^{-3}					
2				1.73×10^{-3}					
4				1.02×10^{-3}					
6				1.08×10^{-3}					
8				1.87×10^{-3}					
	Jet			Jet/Plate			Jet/Flap		
2				3.41×10^{-3}					
3				6.8×10^{-3}					
4				7.3×10^{-3}					
6				7.66×10^{-3}					
8				1.64×10^{-2}					
1							3.96×10^{-3}		
2							1.23×10^{-3}		
3							6.31×10^{-3}		
4							5.1×10^{-3}		

Table 2 Comparison of Convection Velocities

Coflowing Jet

$\frac{\xi_1}{2r_o}$	$\frac{Ucon}{\bar{U}_1}$
-.752	1.34
-.595	1.12
0	1
.177	.843
.610	1.01
.942	1.02
1.22	1.04
1.59	1.05
1.82	1.10
2.73	1.09

Coflowing Jet/Plate

$\frac{\xi_1}{2r_o}$	$\frac{Ucon}{\bar{U}_1}$
-.761	.968
-.595	1.01
0	1
.262	1
.476	1.21
1.14	1.08
1.42	1.11
2.23	1.25
3.06	1.26
5.09	1.66

Coflowing Jet/Flap

$\frac{\xi_1}{2r_o}$	$\frac{\bar{U}\ t_-}{\frac{Ucon}{\bar{U}_1}}$
-1.49	1.16
-1.03	1.11
-.480	1.20
0	1
.426	.242
.770	.258
1.14	.297
1.86	.297
2.55	.300

AN EXPERIMENTAL AND THEORETICAL INVESTIGATION OF THE INTERACTION BETWEEN THE ENGINE JET AND THE SURROUNDING FLOW FIELD WITH REGARD TO THE PRESSURE DRAG ON AFTERBODIES.

by
A. Zacharias
MESSERSCHMITT-BÖLKOW-BLOHM GMBH
Aircraft Division UF FE123
P.O. Box 801160
8000 München 80
West Germany

SUMMARY

In order to clarify the interaction between rotationally symmetric engine jets and afterbody configurations, the dependence of the jet characteristics (i.e. the plume effect and the entrainment) and the afterbody pressure drag on the jet parameters, the free stream Mach number and the afterbody geometry has been analysed. Extensive tests have been carried out in the high subsonic Mach number range on three different afterbodies at Reynolds numbers from 0.5×10^6 to 1.3×10^6. The nozzle pressure ratio and the temperature ratio of the model jets were varied in the range $p_{tj}/p_\infty = (1.0)\ 1.2$ to 2.4 and $T_{tj}/T_\infty = 1.0$ to 2.86 respectively. Measurements were then carried out to determine the static pressure and temperature distribution as well as the boundary-layer profiles over the surface of the models. At the same time, the pressure and temperature profiles in the jet were determined in several planes behind the jet exhaust plane. From the experimental results empirical equations have been set up which show the dependence of the plume effect, the entrainment and the afterbody pressure drag on the jet parameters, the free stream Mach number and the afterbody geometry. With the aid of a finite-element method and theoretical potential flow model for jet simulation, a numerical procedure has been developed which allows the pressure drag on rotationally symmetric afterbodies to be calculated with due allowance for the effects of the engine jets. Comparison of the theoretical and experimental results shows a satisfactory agreement.

LIST OF SYMBOLS

a. Geometrical Symbols

A_o	mm^2	maximum model cross-section
β	°	boattail angle
D	mm	nozzle diameter (= 2R)
D_o	mm	model maximum diameter (= $2R_o$)
L	mm	boattail length
R_s	mm	jet radius
λ_1, λ_2	–	geometrical parameter of the boattail (= L/D_o, D_b/D_o)
x, y, z	–	cartesian coordinates
x, r, ϑ	–	cylindrical coordinates
$\underline{n}$	–	normal vector
$\underline{t}$	–	tangential vector

b. Mathematical Symbols

C_3	constant in eq. (5.2.1)
η	constant in eq. (5.2.1a)
ϕ	velocity potential
∇	nabla-operator = $\left\{\frac{\partial}{\partial x}, \frac{\partial}{\partial y}, \frac{\partial}{\partial z}\right\}$

c. Fluid Mechanical Quantities

α	°	jet spreading angle
b'	–	gradient of the mass flow increase of jet
c_{DP}	–	pressure drag coefficient (= $W_{DP}/q_\infty A_o$)
c_{DF}	–	friction drag coefficient (= $W_{DF}/q_\infty A_o$)
c_p	–	pressure coefficient ($p_{ob} - p_\infty)/q_\infty$)
δ	mm	boundary layer thickness
δ_1	mm	boundary layer displacement thickness, eqs. (6.4) and (6.5)
Ma_∞	–	tunnel free-stream Mach number
$\dot{m}$	kg/s	mass flow
p	bar	static pressure
p_{tj}/p_∞	–	nozzle pressure ratio
q	bar	dynamic pressure
Re	–	Reynolds number (= $\rho_\infty u_\infty D_o/\mu_\infty$)
ρ	kg/m^3	density
t	°	temperature in °C
T	K	absolute temperature
T_{tj}/T_∞	–	jet temperature ratio
u	m/s	velocity

W	kp	drag
w_r^*	m/s	velocity distribution of the jet entrainment, eq. (4.1.6)

d. Indices

∞	free stream
j	jet
j0	settling chamber
jA	jet axis
t	total
i, j, k	indices of the coefficients of the polynomial
n	in normal direction
t	in tangential direction
(e)	related to the element
ik	incompressible
k	compressible

1. INTRODUCTION

To make predictions of both the performance and the aerodynamic properties of an aircraft, a comprehensive knowledge is required as far as the aerodynamics of airframe configurations and engine performance is concerned. On the condition that the flow is attached to the airframe it is nowadays quite possible to make relatively accurate statements about the characteristics of aircraft configurations with nacelles, external stores, etc. However, when a jet engine is installed into the airframe the interaction of the jet on the surrounding flow field must be taken into account. In the case of an aircraft development this means that the jet effects must be understood empirically or theoretically and taken into consideration.

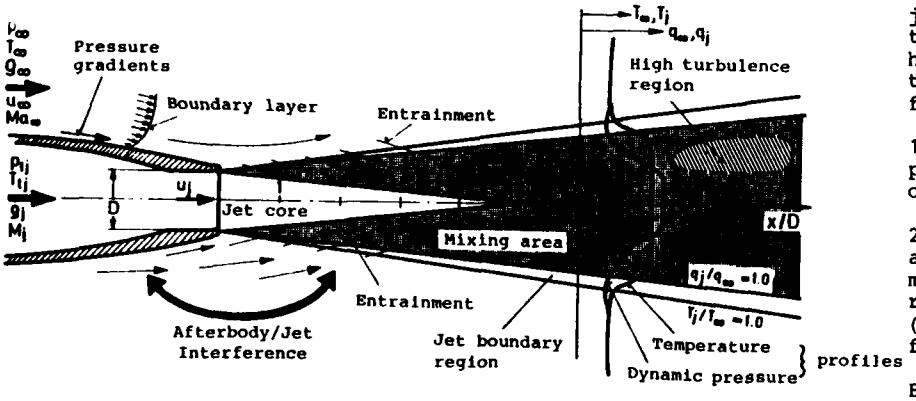

Fig. 1: Schematic drawing of interactive parameters with afterbody jet flow.

Basically, a thrust jet emerging from the engine nozzle has two effects on the surrounding flow field, Fig. 1:

1. The jet has a plume effect acting on the flow.

2. The jet acts as a sink, removing mass from the surrounding flow field (entrainment effect).

Both effects cause the engine jet and the airframe flow to interact.

The development of aircraft with engines installed in the afterbody section has always shown that it is difficult to accurately determine the afterbody pressure drag which on the one hand depends on the afterbody geometry and on the other hand is affected by the plume effect and entrainment of the jet. In turn, the jet effects depend on the parameters of the jet and flow as well as on the afterbody geometry.

Today, numerous studies are found in the literature which deal with the problem of afterbody pressure drag, Ref. 1 to 16 etc. The results obtained from tests on afterbody drag have almost exclusively been discussed from the view of the afterbody geometry, omitting a thorough analysis of the jet effects of the plume and entrainment. However, the spreading behaviour of the jet has not been simultaneously investigated. Important information on spreading angles and entrainment velocity of the jet, which is required for the basic examination of the interaction of the jet and afterbody, is therefore not available. In general, the problem of jet simulation in wind tunnel tests is very difficult, placing exacting requirements on the wind tunnel test technology. The different results obtained from wind tunnel and flight tests emphasize the need to adapt the test conditions to reality, if possible, and to employ exact jet simulation techniques.

Furthermore, numerous studies are found in the literature today dealing experimentally and theoretically with the problems of jet spreading, see Ref. 17 to 35 etc. All studies describe the jet spreading only downstream of the jet exhaust plane. The af-

terbody/nozzle configuration upstream of the jet exhaust plane has not been taken into account or the interest has been limited to the internal nozzle geometry only. However, the afterbody/nozzle geometry is significant for determining the jet spreading behaviour. If the jet effects are to be analyzed with regard to the plume effect and entrainment, general statements will be necessary about the jet spreading angle and the entrainment velocity as a function of the jet pressure and temperature ratio, the free stream Mach number and the afterbody geometry.

In summary it can be said that the flow mechanism of the interaction of the jet and the afterbody is not yet clear. The studies performed until now concentrate on partial problems either in respect of the afterbody drag or the jet spreading behaviour.

The spreading behaviour of rotationally symmetric engine jets and the aerodynamic behaviour of rotationally symmetric afterbodies will be jointly analyzed in this paper. For this purpose, systematic wind tunnel model tests have been carried out on engine jets with different nozzle pressure and temperature ratios with due allowance for the effect on the afterbody pressure distribution and thus on the pressure drag on rotationally symmetric afterbodies with different geometries. Using these results,the jet spreading angle and the entrainment velocity of the jet as a function of the jet parameters, the free stream Mach number and the afterbody geometry are determined. This function has been covered by interpolation polynomials. In addition to this, empirical equations have been set up which represent the afterbody pressure drag as a function of the afterbody geometry, the jet parameters and the free stream Mach number. Based on the experimental results of the jet spreading angle and the entrainment velocity, and with the aid of the finite-method, a procedure has been developed which, for the first time, allows the afterbody pressure distribution and, consequently, the afterbody pressure drag to be calculated with due allowance for the effects of the engine jet. The equations set up and the theoretical results have been checked and verified by the model tests. The final results available in the form of equations can be used by the design engineer as a first estimation of the afterbody pressure drag for single jet/afterbody geometries.

2. EXPERIMENTAL SET-UP AND TECHNIQUE

2.1 Wind Tunnel

The tests have been carried out in the jet induction wind tunnel (SIB) of the DFVLR Institute for Design-Aerodynamics in Braunschweig, Fig. 2, Ref. 36 . The jet induction tunnel is a wind tunnel with a closed test section and an open circuit (Eiffel type tunnel). A J79 jet engine is used to induce the air flow in the test section. The test section has a circular cross section.

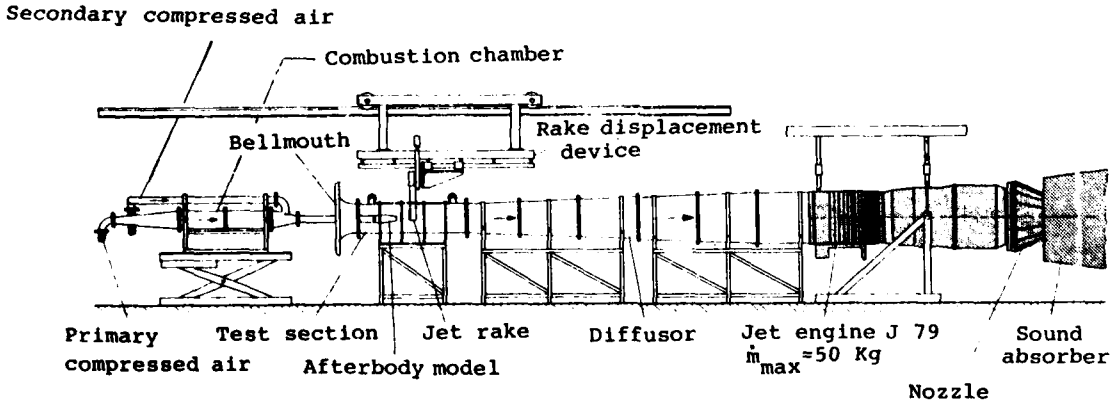

Fig. 2: Jet induction wind tunnel, test set-up

The static pressure on the wall was measured in 8 planes along the test section - 4 static pressure taps per plane symmetrically distributed on the circumference. The pressure and temperature profiles of the model jet and flow were determined using a rake with 30 equidistant test points. The rake was remotely controlled by a probe traversing gear.

The skin temperature distribution was measured by thermocouples which had been carefully embedded in the model surface.

2.2 Models

Fig. 3 shows the outer contours of the three models; the geometrical data are compiled in the table. Configuration 1 represents the 1:7.2 model of the engine nacelle of the HFB-320 test aircraft of the DFVLR. The model is rotationally symmetric and possesses the contour of the upper meridian of the original engine nacelle.

The investigations of the hot gas jet have been exclusively performed with model 1. In order to shield the surface from the thermal radiation of the model jet, extensive constructional measures have been taken to achieve proper insulation. Models 2 and 3 were manufactured at the DFVLR, Porz Wahn, to carry out investigations within the joint AGARD program of "Improved Nozzle Testing Techniques in Transonic Flow", Ref. 38 . Important geometrical parameters of the models used for this test are: the afterbody angles ß of 7°, 10° and 25°; length L of the afterbody, defined as the distance between the maximum cross section and the jet exhaust plane; and the basic diameter in the jet exhaust plane, see Fig. 3. Models 1 and 2 have a circular arc contour while model 3 is cone-shaped with the exception of the shoulder region, which has likewise a circular arc contour. All three models have static pressure orifices distributed on the surface over the entire model length in one plane (z/D = 0). Thermocouples used for recording the surface temperature distribution are embedded in the surface of model 1 in the same plane as the static pressure orifices.

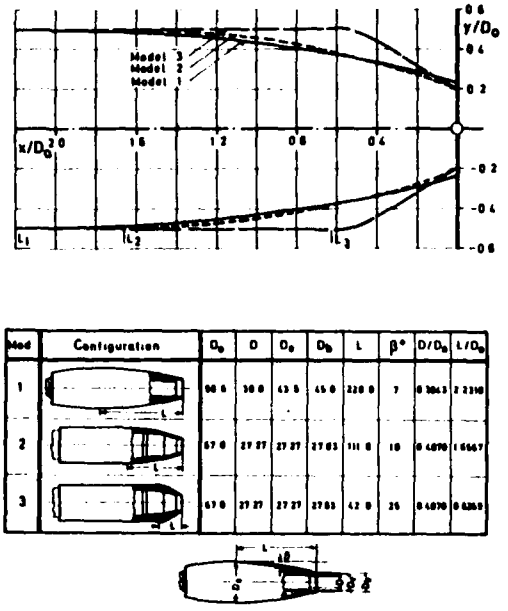

Mod	Configuration	D_0	D	D_0	D_b	L	β°	D/D_0	L/D_0
1		98.6	98.6	43.5	43.5	220.8	7	0.3863	2.2390
2		67.6	27.27	27.27	27.63	111.6	10	0.4070	1.6567
3		67.6	27.27	27.27	27.63	42.8	25	0.4070	0.6268

Fig. 3: Model geometry

2.3 Data Acquisition and Evaluation

The pressure orifices were connected to a data acquisition system via 2 Scanivalves, the thermocouples were connected to reference junctions and a scanner. All test data were recorded fully automatically on paper tape with the aid of the digital data acquisition system scanning the test data at a rate of 5 test points per second. The evaluation took place in the electronic data processing center of the DFVLR, Braunschweig, using a SIEMENS 7.755 data processing system.

In order to establish appropriate mathematical models for the theoretical calculation of the jet spreading it is necessary to gather information on the structure of jet mixing. This requires systematic turbulence measurements of the jet to be carried out. To investigate the influence of the plume and entrainment effects of an engine jet on the surrounding flow field, the jet spreading angle and the entrainment velocity of the jet as a function of the jet and flow parameters as well as the afterbody geometry must be known.

Determining jet profiles is very difficult. Non-intrusive optical measurements (e.g. Laser-Doppler-Anemometry) are very time-consuming and are therefore not developed to be employed for such tests. Measurements of the jet profiles by means of conventional test probes of finite size (e.g. static tubes) are likely to exhibit measuring errors which must be carefully taken into consideration in the evaluation. Pitot probes with long pressure lines and, consequently, low response times are most suitable for measuring the mean values in the turbulent boundary zones of the jet. Thermocouples are similarly slow in behaviour.

The calculation of local velocities in the transonic range is a lengthy procedure and can be made by multiple iterations only. The Pitot probe formula after Rayleigh is used to determine the existence of either subsonic or supersonic speed in the vicinity of the nozzle exit plane, Ref. 23 . Mach number is obtained from the pitot pressure, the static pressure and the local isentropic exponent $\varkappa$. If Ma_∞ is smaller than 1, the velocity is computed using the laws of compressible subsonic aerodynamics. If Ma_∞ is greater than 1, the test values from behind the shock wave are used to determine the undisturbed supersonic flow in front of the normal shock wave. Velocities and temperatures have been computed by means of the precise c_p and $\varkappa$-values which have been determined for each temperature. The gas constant R has always been computed as a function of the air-fuel ratio.

3. TEST PROGRAM DESCRIPTION

The tests carried out with the three models included 5 different free stream Mach numbers (Ma_∞ = 0, 0.4, 0.5, 0.6, 0.7), 6 different nozzle pressure ratios (p_{tj}/p_∞ = 1.0, 1.2, 1.4, 1.6, 1.89, 2.4), and 3 jet temperature ratios (T_{tj}/T_∞ = 1.0, 1.84, 2.86), the latter ones carried out on model 1 only. The boundary layer, surface temperature distribution and afterbody pressure distribution have been surveyed in these tests. Velocity and temperature profiles in the jet have been taken in 13 planes each. Fig. 4, is a summary of the tests carried out.

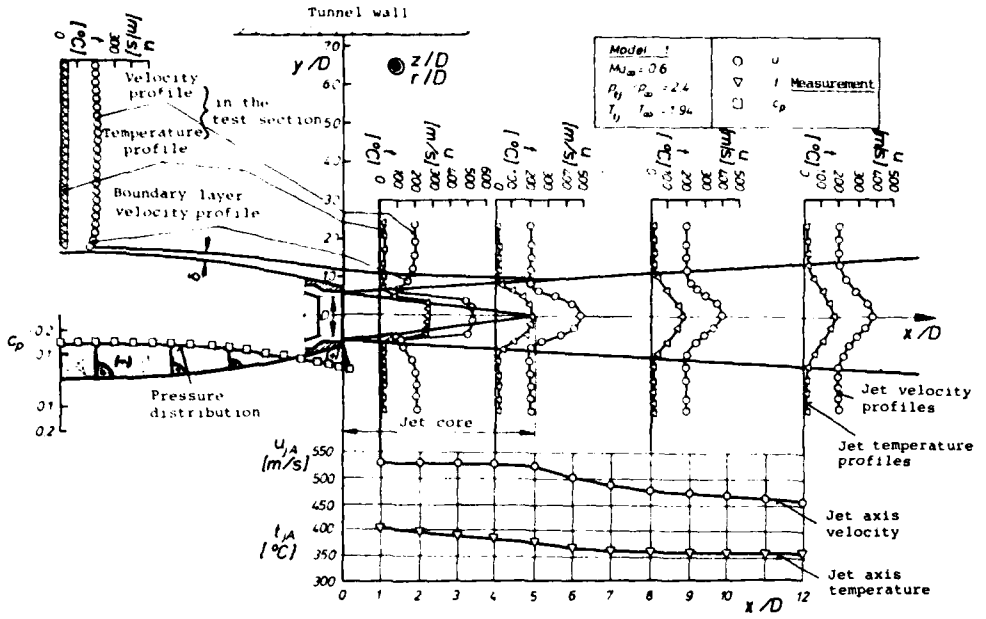

Fig. 4: Measurements of the jet, the boundary layer and the boattail pressure distribtion; results of a test series

4. EXPERIMENTAL RESULTS AND ANALYSIS

4.1 Jet boundaries and entrainment

The velocity profiles indicate that the boundary layer behaviour of the afterbody flow is still maintained far downstream of the jet exhaust plane, Fig. 5. The distance up to the point where complete jet-flow mixing is reached depends on the afterbody geometry, on the free stream Mach number and on the jet parameters. It is between 4 and 10 nozzle diameters in the case of the investigated parameter range. In this range, the radial distance has been assumed for the jet boundary R_S where the velocity profile u = f (r) is a minimum. Further downstream, the well-known condition $u_j = 1.01u_\infty$ was used to determine R_S.

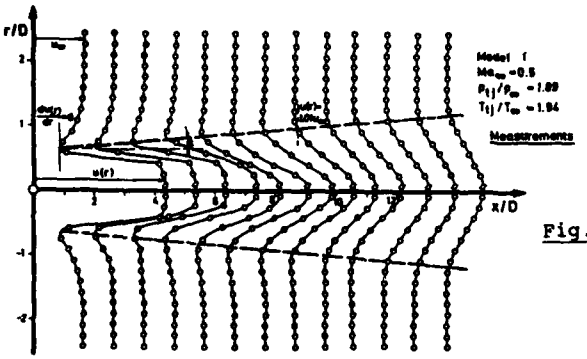

Fig. 5: Velocity profile of the jet and the surrounding flow downstream of the jet exhaust plane

The test results given in Fig. 6 are representative for the entire range of the investigation and show the variation of the jet boundary R_S vs x. The jet boundary is determined as the mean value of four non-consecutive measurements, Fig. 6a. The results obtained from all three models have shown that R_S increases linearly with x and rises continuously with the nozzle pressure ratio. However, the gradient of increase varies between the models, Fig. 6b.

The relation

$$\frac{R_S}{R} = 1 + 2 \cdot \frac{x}{D} \cdot \tan \alpha \qquad (4.1.1)$$

can be derived for jet boundary. Linearity is clearly shown in both the low and the highest nozzle pressure ratio in this investigation. The intermittent structure of the jet boundary is determined as a jet boundary envelope because of the steady character of the measurements and the fact that the mean value is formed. The respective jet spreading angle α has been determined in the relationship 4.1.1.

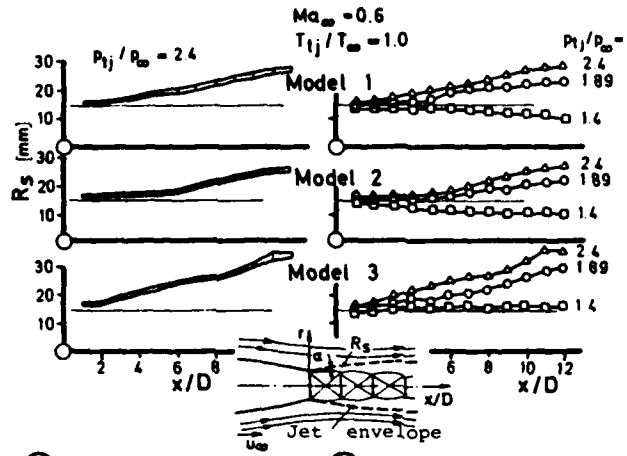

(a) Range of the four test values per plane

(b) Jet boundary radius R_S obtained from one measurement, influence of nozzle pressure ratio p_{tj}/p_∞

Fig. 6: Measured values of the jet radius vs x/D

Fig. 7 shows the influence of the free stream Mach number and the jet parameter on the jet spreading angle for model 1.

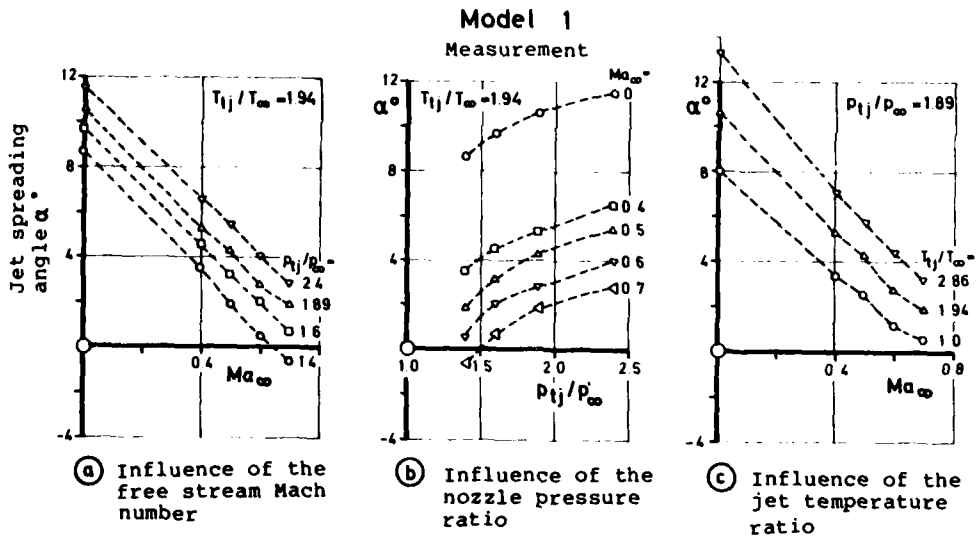

(a) Influence of the free stream Mach number

(b) Influence of the nozzle pressure ratio

(c) Influence of the jet temperature ratio

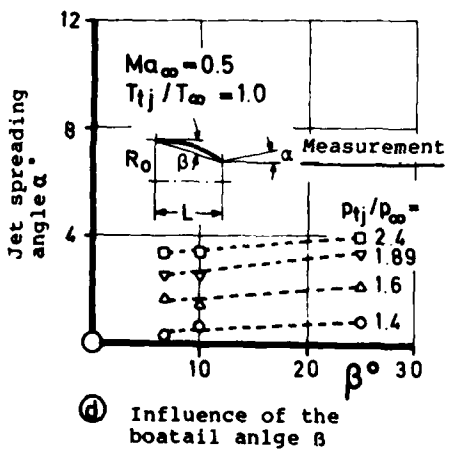

(d) Influence of the boatail anlge β

Fig. 7: Jet spreading angle α, influence of the free stream Mach number, the nozzle pressure ratio, the jet temperature and the afterbody angle

For all nozzle pressure ratios p_{tj}/p_∞ the jet spreading *angle* α *decreases* with the free stream Mach number, Fig. 7a. According to the results, the trend is linear. When plotted versus the *nozzle pressure* ratio p_{tj}/p_∞, the jet spreading angle increases at a higher order than linearly, Fig. 7b. This trend can be noticed for all free stream Mach numbers. Investigations carried out by E.S. LOVE et al. Ref. 34, dealing with the spreading of jets in quiescent air and in the supersonic range yield the same results. A direct comparison between their results and those of the present study is hardly possible because of the low nozzle pressure ratios of the present investigation. A rise of the total jet temperature T_{tj} which, at a constant nozzle pressure ratio, results in a higher jet exhaust velocity u_j, causes a larger jet spreading angle, Fig. 7c.

Increased boattailing, larger afterbody angles ß, yield greater jet spreading angles α, Fig. 7d. These findings clearly show the dependence of the jet spreading behaviour on the afterbody geometry and thus point out the need for a joint investigation of engine jet and afterbody for optimization of the afterbody configuration.

The jet absorbs mass from the external flow field so that, besides the plume effect, an entrainment is produced relative to the jet environment. To obtain clarity about the entrainment effect it is necessary to determine the entrainment velocity. For this purpose, the mass flows of 13 planes (x/D = 0, 1, 2 ... 12) where the pressure and temperature profiles of the jets have been recorded have been calculated by means of the following equation:

$$\dot{m}_{jk} = 2\pi \int_0^{R_{Sk}} \rho(r)_k \cdot u(r)_k \cdot r \cdot dr \qquad (4.1.2)$$

k = 0 to 12

As in the determination of R_S, $\dot{m}_{jk}$ is the mean value obtained from four mass flows.

The results have shown that the mass flow in axial direction has a quadratic pattern with a weak term of 2nd order, Fig. 8, but a linear approximation of

$$\frac{\dot{m}_{jk}}{\dot{m}_{j0}} = 1 + b'\frac{x}{D} \qquad (4.1.3)$$

which is satisfactory. $\dot{m}_{j0}$ is the mass flow calculated from the data obtained in the nozzle settling chamber.

At a *distance* of 12 nozzle diameters behind the jet exhaust plane, the jet heated by 500° C has twice the mass flow of the jet exhaust plane, the jet heated by 250° C has a 1.65-fold mass flow, the cold jet has a 1.2-fold mass flow. In the range of $0 \leq x/D \leq 12$ the gradient

$$\frac{d(\dot{m}_{jk}/\dot{m}_{j0})}{dx} = b' \qquad (4.1.4)$$

increases with the temperature ratio T_{tj}/T_∞.

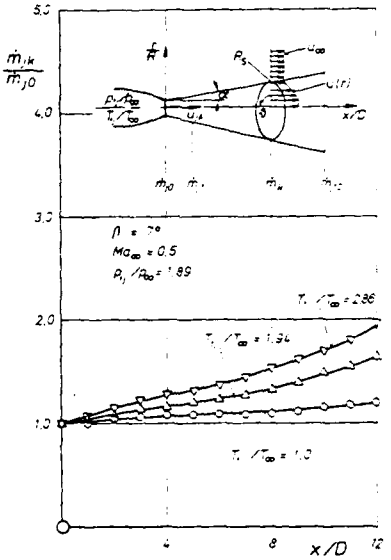

Fig. 8: Mass flow increase of the jet at Ma = 0.5, p_{tj}/p_∞ = 1.89 and ß = 7° (Model 1), temperature influence

The calculation of the entrainment velocity w_r^* vertical to the jet boundary is made according to

$$2\pi \cdot \left[\int_0^{R_{Sk+1}} \rho(r)_{k+1} \cdot u(r)_{k+1} \cdot r \cdot dr - \int_0^{R_{Sk}} \rho(r)_k \cdot u(r)_k \cdot r \cdot dr\right] \qquad (4.1.5)$$

$$= \Delta\dot{m} = \rho_\infty \cdot \Delta F_k \cdot w_r^* \quad .$$

With ΔF_k being the surface of a circular cone segment of the jet, the mass flow increase being $\Delta\dot{m} = \dot{m}_{j0}\, b'\, \Delta x$ and taking into account equation (4.1.1), the result for the entrainment velocity w_r^* in m/s after several transformations is

$$w_r^* = \frac{b' \cos\alpha \, \dot{m}_{j0}}{2\pi \cdot \rho_\infty \{R + (R+x)\tan\alpha\}} \qquad (4.1.6)$$

The mass flow $\dot{m}_{j0}$ in the jet exhaust plane depends on the nozzle geometry and the jet parameters i.e. the operating conditions of the jet engine of the aircraft.

The influence of the jet and flow parameters as well as of the afterbody geometry on the sink intensity of the jet is shown in Fig. 9. The intensity of the jet sink decreases with increasing free stream Mach number. Higher nozzle pressure ratios and jet temperatures, and larger afterbody angles increase the sink intensity.

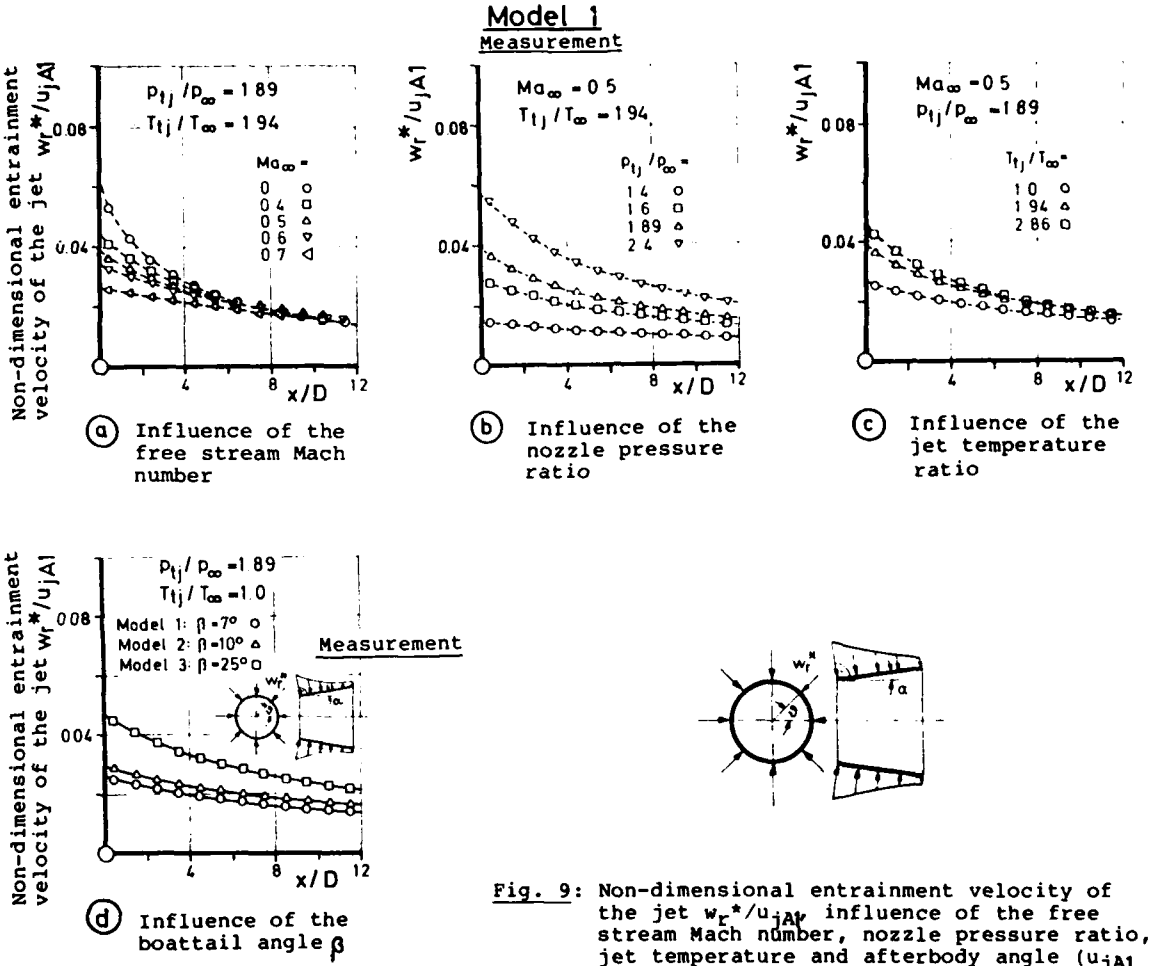

Fig. 9: Non-dimensional entrainment velocity of the jet w_r^*/u_{jA1}, influence of the free stream Mach number, nozzle pressure ratio, jet temperature and afterbody angle (u_{jA1} at x/D = 1).

The entrainment effect of the jet and its spreading angle can be described physically in terms of the molecular viscosity in the case of a laminar jet, and, in the case of a turbulent jet, in addition of the flow turbulence. An air particle with the velocity u_j at the boundary of the jet entrains its adjacent molecule due to the effective viscosity. In this context effective viscosity means that the viscosity under turbulent flow conditions consists of a molecular component and a vortex component. The vortex component to the viscosity does not exist under laminar flow conditions.

At the quiescent environment, the particle of the environment is accelerated and entrains the adjacent outer particle whilst the jet particle decelerates to the same degree as it transmits energy. If the environment is in a state of motion, the mixing region required for the acceleration of the external air particles and for the deceleration of the jet particles is smaller.

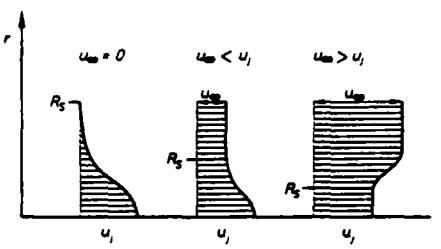

At the same time, the energy transmission of the particles is less because of the smaller velocity dif-

ference relative to the surrounding medium. This results in a smaller jet boundary and consequently a smaller jet spreading angle as well as a retarded decomposition of the jet. The same flow mechanism but in opposite r-direction occurs for $u_j < u_\infty$ including the wake without jet. If the jet is heated, the velocity jump between u_j and u_∞ is larger than that of a cold jet with the other conditions remaining the same (constant p_{tj}/p_∞); the mixing region is correspondingly wider.

If the jet boundary is laid down as defined in the previous chapter, it is physically correct that a static pressure drop in the mixing region is caused by the acceleration of the external air particles. This static depression in the mixing region justifies the assumption of a sink distribution on the jet boundary when establishing potential flow models. These basic physical principles - apart from the existing turbulent flow conditions in the jet - enable a relatively simple explanation to be made of the behaviour of the jet spreading angle as well as that of the entrainment effect.

The behaviour of the jet spreading angle α as a function of the afterbody angle can also be explained by means of the basic physical principles which have been determined. In this context the behaviour of the boundary layer and the conditions of the afterbody external flow in general have a considerable influence. The pressure rise in the afterbody section, which must be overcome by the boundary layer particles, increases with increasing afterbody angle β since the depression at the model shoulder increases with the afterbody angle β due to the greater camber. This will finally result in the separation of the boundary layer when the afterbody angle β has become so great that the extremely slow boundary layer particles cannot proceed into the area of the accordingly steep pressure rise.

The energy which can be transmitted by the jet particles of the boundary zone which is used to accelerate the extremely slow or even backwards drifting particles of the surrounding flow is high and the mixing area between the jet and the flow becomes wider.

These effects cause the jet spreading angle α, Fig. 7d, to increase with an increasing afterbody angle ß, and the sink to become more intense, Fig. 9d. Due to the more vigorous jet mixing, the loss of kinetic energy of the jet particles is greater in the case of a greater afterbody angle ß. This can be proved by the greater deceleration on the longitudinal axis velocity of the jet with increasing afterbody angle ß, Fig. 10.

Here it becomes obvious that the axis-velocity of all three models is similar in close proximity to the jet exhaust plane.

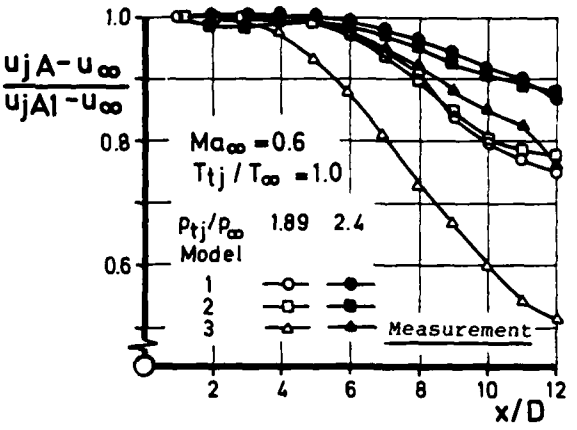

Fig. 10: Velocity of the jet axis downstream of the jet exhaust plane (u_{jA1} at x/D = 1), influence of the afterbody angle ß

4.2 Afterbody Pressure Drag

The pressure drag coefficient of rotationally symmetric afterbodies is calculated by means of the formula:

$$c_{DP} = \frac{W_{DP}}{q_\infty A_0} = \frac{2}{R_0^2} \int c_p \, r \, dr \qquad (4.2.1)$$

and provided that the pressure distribution c_p is rotationally symmetric - this is the case with rotationally symmetric bodies in a flow of zero incidence. c_{DP} is the mean value from 13 pressure drag coefficients which have been determined from 13 successive pressure distribution measurements c_p by means of equation (4.2.1).

To determine the influence of jet temperature on the afterbody pressure drag, it is important that the temperature of the model surface should be kept constant during hot-gas jet tests. Previous investigations, Ref. 37 without a heat insulated model surface have shown that with increasing jet temperature the temperature of the model surface was considerably increased through heat radiation. Thus the boundary layer was additionally heated and consequently the model surface condition changed with the jet temperature. A clear definition of the influence of the jet temperature on the pressure drag can hardly be achieved under such conditions.

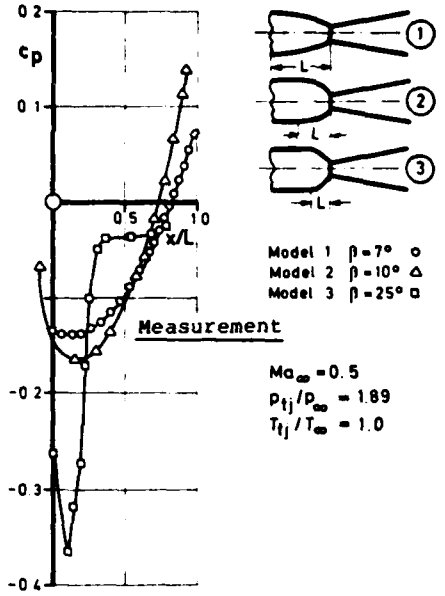

Fig. 11: Influence of the afterbody angle β on the pressure distribution

Fig. 11 gives a general survey of the influence of the afterbody geometry, in particular of the afterbody angle β, on the pressure distribution. For a given free stream Mach number and fixed nozzle pressure/jet temperature ratios, the figure shows the measured distribution values for each model plotted vs x/L.

In close proximity to the shoulder (x/L = 0 ÷ 0.2) a larger afterbody angle β results in large pressure drops because of the accelerated flow and the greater spreading. The larger the afterbody angle β is, the greater is the subsequent pressure rise caused by decelerated flow (diffusor effect). With β = 25°, the flow is separated, from x/L≈0.3 onwards ($dc_p/d(x/L) \approx 0$).

The influence of the free stream Mach number Ma on the afterbody pressure drag is shown in Fig. 12a for model 1 with p_{tj}/p_∞ = 1.89 and for the three jet temperature ratios. The plume effect of the jet is reduced due to the jet spreading angle decreasing with Ma_∞. The entrainment effect is always active in increasing pressure drag although the sink intensity decreases with increasing free stream Mach number. In addition, the reduced static pressure in the area of the model shoulder (x/L = 0) is generally decreased further with Ma which in turn produces a higher pressure drag. It can thus be seen that the pressure drag increases slightly with the free stream Mach number. This trend exists for all three jet temperature ratios.

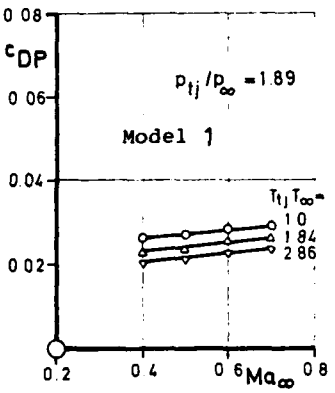

(a) Influence of the free stream Mach number

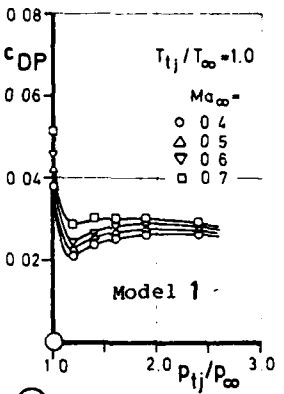

(b) Influence of the nozzle pressure ratio

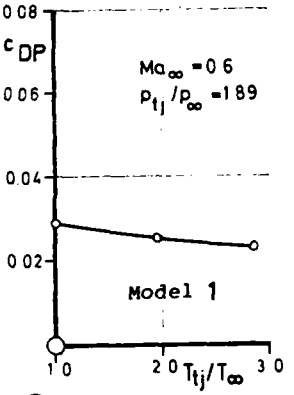

(c) Influence of the jet temperature

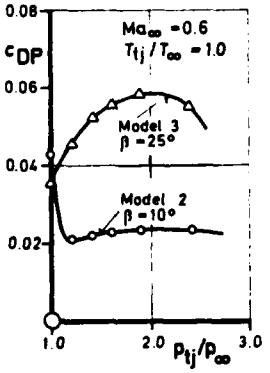

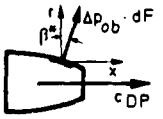

Measurement

Fig. 12: Pressure drag coefficient c_{DP} of model 1, influence of the free stream Mach number, nozzle pressure ratio, jet temperature and boattail angle

The calculated c_{DP} values are plotted in Fig. 12b for the cold jet and four free stream Mach numbers Ma_∞ vs the nozzle pressure ratio p_{tj}/p_∞ for model 1. For the jet-off case (p_{tj}/p_∞ = 1.0) there is no jet displacement effect and therefore the pressure drag coefficient is highest. In case of a jet emerging from the nozzle, c_{DP} first decreases with the increase of the nozzle pressure ratio p_{tj}/p_∞, reaching a minimum value at

p_{tj}/p_∞ = 1.2, and then slowly increases again. This c_{DP} rise starting at $p_{tj}/p_\infty \geq 1.2$ becomes flatter with increasing free stream Mach number Ma_∞ and at Ma_∞ = 0.7 it remains almost constant in the range of $1.2 \leq p_{tj}/p_\infty \leq 2.4$. The same trends have also been found by H. EMUNDS and H. RIEDEL Ref. 37 , W.B. COMPTON III Ref. 39 , 40 , and B. MECHIN and J.M. HARDY Ref. 41 in their investigations of the c_{DP} behaviour as a function of p_{tj}/p_∞ as well as of Ma_∞ . When looking at the variation of the c_{DP} values and considering the behaviour of the jet spreading angle α and the sink intensity w_r^* for the jet as a function of the parameters p_{tj}/p_∞ , T_{tj}/T_∞ and Ma_∞ , as determined in the previous chapter, the variation is relatively easy to explain because of the simultaneous influence of the plume and entrainment effects of the jet.

If a jet emerges from the afterbody nozzle, the external flow field is displaced due to the jet spreading and a recompression of the flow is caused at the afterbody end. For this reason, the course of the c_p distribution towards the afterbody end becomes steeper In this case, the integration of the c_p-values results in a lower afterbody pressure drag as compared with the conditions without jet.

The effect of the nozzle pressure ratio p_{tj}/p_∞ on the pressure drag at constant free stream Mach number is as follows. At p_{tj}/p_∞ = 1.2 the entrainment effect of the jet is small while the plume effect of the jet dominates, which means that low afterbody pressure drags are obtained because of the recompression of the afterbody flow. If p_{tj}/p_∞ is increased, the jet spreading angle and consequently the plume effect are enlarged. If there were only the plume effect of the jet, this would yield even lower coefficients of afterbody presssure drag. However, the sink force of the jet also increases with the nozzle pressure ratio p_{tj}/p_∞ , thus preventing the recompression at the afterbody end more than it is favoured by the larger jet spreading angle α . c_{DP} is therefore increased again with increasing p_{tj}/p_∞ ($p_{tj}/p_\infty \geq 1.2$). In the range of $1.5 < p_{tj}/p_\infty < 2.4$ and with slim afterbody boattailing the plume effect counterbalances the entrainment effect of the jet. In the range of $p_{tj}/p_\infty > 2.4$ the plume effect of the jet dominates more and more and results in a continuous decrease of the afterbody pressure drag coefficient according to the p_{tj}/p_∞ increase, Ref. 38 , 42 .

The jet spreading angle α and the sink intensity increase along with the rising temperature as described in chapter 4.1. The influence of the entrainment effect, however, is less important as compared with that of the plume effect because of the enlarged jet spreading angle α .

A jet temperature rise of 250 °C results in a 11.6% reduction of the afterbody pressure drag coefficient. This is brought about by the intense recompression which, in turn, is due to the dominating plume effect. Fig. 12c shows the afterbody pressure drag coefficients c_{DP} plotted vs the jet temperature ratio T_{tj}/T_∞ for model 1 at Ma_∞ = 0.6 and p_{tj}/p_∞ = 1.89. A jet temperature rise of 500 °C reduces the c_{DP} as compared with the cold jet and, as a consequence, reduces the afterbody pressure drag by 14.5%.

The results of the investigations performed by W.B. COMPTON III Ref. 40 indicate the same trend, while the tests on a heated model surface, Ref. 37 , shows a pressure drag coefficient which is increased by 17.4% at the same jet temperature.

The influence of the free stream Mach number and of the nozzle pressure ratio on the pressure drag coefficient, as shown in the previous chapter for model 1, have also been determined for model 2 whereas differences have been obvious in model 3.

Fig. 12d is a comparison between the pressure drag coefficients of models 2 and 3 plotted vs the nozzle pressure ratio. At a nozzle pressure ratio $p_{tj}/p_\infty \geq 1.0$, model 3 (β = 25°) also shows a c_{DP} variation which is similar to the trend for model 2 (and model 1). The level of the pressure drag coefficient of model 3 is higher. The gradient of increase ($p_{tj}/p_\infty < 2$) or decrease ($p_{tj}/p_\infty \geq 2$) , that is $dc_{DP}/d(p_{tj}/p_\infty)$, is steeper. This is due to the influence of the jet sink whose intensity is greater for this afterbody angle β, see Fig. 9d. Contrary to models 1 and 2, the plume effect of the jet does not become effective until $p_{tj}/p_\infty \approx 2.0$.

5. EMPIRICAL EVALUATION AND COMPARISON

5.1 Jet spreading angle and entrainment velocity of the jet

The important parameters which have a decisive influence on the plume and entrainment effects of the jet, and which therefore assume the function of boundary conditions when setting up a theoretical method to compute the aerodynamic coefficients of afterbodies subjected to jet influences, are summarized in this chapter from the experimental results in the form of closed polynomials. For the purpose of this study the following functions:

jet spreading angle α :

$$\alpha = f(Ma_\infty, p_{tj}/p_\infty, T_{tj}/T_\infty) \qquad \beta = 7^0$$

$$\alpha = f(Ma_\infty, p_{tj}/p_\infty, \beta) \qquad T_{tj}/T_\infty = 1{,}0$$

gradient of mass flow increase of jet b':

$$b' = f(Ma_\infty, p_{tj}/p_\infty, T_{tj}/T_\infty) \qquad \beta = 7^\circ$$

$$b' = f(Ma_\infty, p_{tj}/p_\infty, \beta) \qquad T_{tj}/T_\infty = 1{,}0$$

have been established in this chapter for the investigated range of

$$0{,}0;\ 0{,}4 \le Ma_\infty \le 0{,}7$$
$$1{,}0;\ 1{,}2 \le p_{tj}/p_\infty \le 2{,}4$$
$$1{,}0 \le T_{tj}/T_\infty \le 2{,}86$$
$$7^\circ \le \beta \le 25^\circ$$
$$0 \le x/D \le 12$$

JET SPREADING ANGLE α

$\alpha = f(Ma_\infty, p_{tj}/p_\infty, T_{tj}/T_\infty)$ — β = const.

(5.1.1)

$$\alpha = \sum_{i=j=k=0}^{i=j=1,\ k=2} a_{ijk} (Ma_\infty)^i (T_{tj}/T_\infty)^j (p_{tj}/p_\infty)^k$$

	j=0			j=1		
	k=0	k=1	k=2	k=0	k=1	k=2
i=0	-10,13	14,14	-3,195	4,23	-1,847	0,5843
i=1	-5,415	-4,646	1,48	-6,83	5,181	-1,369

$\alpha = f(Ma_\infty, p_{tj}/p_\infty, \beta)$ — T_{tj}/T_∞ = const.

(5.1.2)

$$\alpha = \sum_{i=j=k=0}^{i=j=1,\ k=2} a_{ijk} (Ma_\infty)^i (\beta)^j (p_{tj}/p_\infty)^k$$

	j=0			j=1		
	k=0	k=1	k=2	k=0	k=1	k=2
i=0	-4,784	10,44	-2,213	0,1927	-0,1235	0,03674
i=1	-4,635	-5,998	1,606	-1,0	0,878	-0,2049

$\alpha = f(Ma_\infty, p_{tj}/p_\infty, T_{tj}/T_\infty, \beta)$

GRADIENT OF MASS FLOW INCREASE OF JET b'

$b' = f(Ma_\infty, p_{tj}/p_\infty, T_{tj}/T_\infty)$ — β = const.

(5.1.3)

$$b' = 10^{-3} \sum_{i=j=k=0}^{i=1,\ j=k=2} a_{ijk} (Ma_\infty)^i (\beta)^j (p_{tj}/p_\infty)^k$$

with a_{ijk}

	j=0			j=1			j=2		
	k=0	k=1	k=2	k=0	k=1	k=2	k=0	k=1	k=2
i=0	70,91	-60,67	13,52	-124,5	118,9	-26,35	38,02	-33,03	7,329
i=1	1,749	-16,88	5,895	6,925	-9,263	3,452	-9,951	7,627	-2,107

$b' = f(Ma_\infty, p_{tj}/p_\infty, \beta)$ — T_{tj}/T_∞ = const.

(5.1.4)

$$b' = 10^{-3} \sum_{i=j=k=0}^{j=1,\ j=k=2} a_{ijk} (Ma_\infty)^i (T_{tj}/T_\infty)^j (p_{tj}/p_\infty)^k$$

with a_{ijk}

	j=0			j=1			j=2		
	k=0	k=1	k=2	k=0	k=1	k=2	k=0	k=1	k=2
i=0	-12,81	9,322	-1,271	-,3654	2,488	-,6685	-,01141	-,07098	-,01953
i=1	-34,88	36,29	-7,743	6,046	-94,57	2,235	0,7311	-,3262	-,07661

$b' = f(Ma_\infty, p_{tj}/p_\infty, T_{tj}/T_\infty, \beta)$

If α and b' are substituted into equation (4.1.6), this yields the velocity distribution of the jet sink w_r^* for all parameters.

Fig. 13 is a comparison between the jet spreading angles which were experimentally determined and those of the interpolation polynomials.

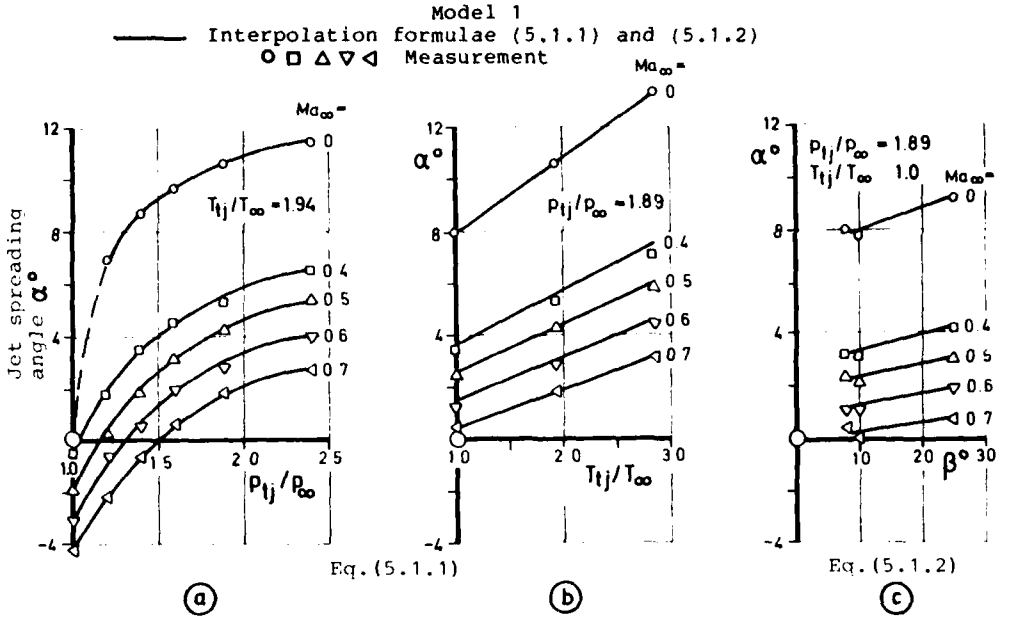

Fig. 13: Jet spreading angle α as a function of:
a) the nozzle pressure ratio, b) the jet temperature ratio, c) the afterbody angle; comparison between measurement and equations (5.1.1) and (5.1.2)

In Fig. 13a the jet spreading angle α is plotted vs the nozzle pressure ratio p_{tj}/p_∞ and in Fig. 13b vs the jet temperature ratio T_{tj}/T_∞, both for various Mach numbers Ma_∞; it was then compared with the calculated results of interpolation formulae (5.1.1). The result shows a very good agreement.

The trivial case $\alpha = 0$ for $Ma_\infty = 0.0$, $p_{tj}/p_\infty = 1.0$ and $T_{tj}/T_\infty = 1.0$ was not taken into account for the determination of the interpolation formulae in favour of a high accuracy of approximation in the remaining parameter variations, (see chain line in Fig. 13a)

Fig. 13c shows the experimental results and the curves from equation (5.1.2) for the jet spreading angle α plotted vs the afterbody angle ß with Ma_∞ as a parameter.

When the equations (5.1.1) thru (5.1.4) are substituted into equation (4.1.6) and when the quantities $\dot{m}_{jo}$ and D as well as the density of the free stream ρ_∞ are taken into account, then equation (4.1.6) yields a general relation which indicates the intensity of the jet entrainment velocity with downstream distance as a function of the parameters Ma_∞, p_{tj}/p_∞, T_{tj}/T_∞ and ß. Fig. 14 gives a representative comparison between the curves calculated from equation (4.1.6) and the experimental results. The good agreement between calculated and measured values is a result between the high accuracy required for the determination of the empirical equations (5.1.1) to (5.1.4).

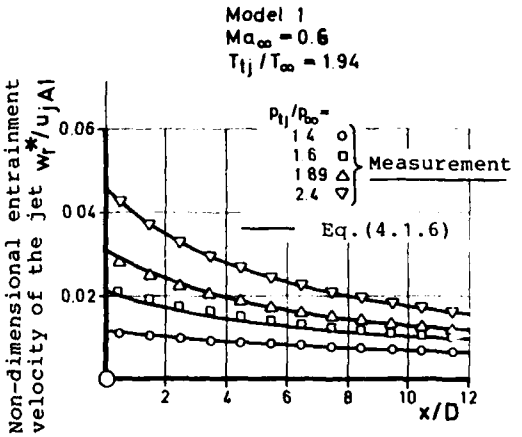

Fig. 14: Non dimensional entrainment velocity of the jet w_r^* / u_{jA1}; comparison between measurement and equation 4.1.6 (u_{jA1} at x/D = 1)

5.2 Afterbody Pressure Drag

The most important geometrical parameters of a rotationally symmetric afterbody are: angle ß, maximum diameter D_0, basic diameter D_b and length L. The definition of the boattail geometric parameters $\lambda_1 = L/D_0$ (fineness ratio) and $\lambda_2 = D_b/D_0$ (closure ratio) enables a general graphic representation of the afterbody geometry to be made. From the many results of this examination, the relationship between the pressure drag coefficient and the afterbody geometry can be derived taking the jet parameters and the free stream Mach number into consideration.

In Fig. 15 the pressure drag coefficients c_{DP} are plotted vs λ_2 and β for $Ma_\infty = 0.6$, $p_{tj}/p_\infty = 1.89$ and $T_{tj}/T_\infty = 1.0$.

The following relationship can be derived by means of the c_{DP} values of models 2 and 3 and those of Ref. 38 ($\lambda_2 = 0.415$ = constant for all three models) and considering the natural boundary value $c_{DP} = 0$ at $\lambda_2 = 1$ ($\hat{=}\ \beta = 0$, cylindrical afterbody in axial flow)

$$c_{DP} = C_3 \frac{1 - \lambda_2}{\lambda_1} \qquad (5.2.1)$$

Constant C_3 has been approximated as a function of the flow and jet parameters.

$$C_3 = f(Ma_\infty, p_{tj}/p_\infty, T_{tj}/T_\infty)$$

in the form of

$$C_3 = \frac{\eta}{(T_{tj}/T_\infty)^{0,2}} \qquad (5.2.1a)$$

where

$$\eta = \sum_{i=j=0}^{\substack{j=2 \\ i=2}} a_{ij} (Ma_\infty)^i (p_{tj}/p_\infty)^j \qquad (5.2.1b)$$

and a_{ij}

j \ i	0	1	2
0	0.0723585	-0.2341466	0.33113
1	0.0294628	0.0205799	-0.099855
2	-0.022101	0.0595517	-0.0371399

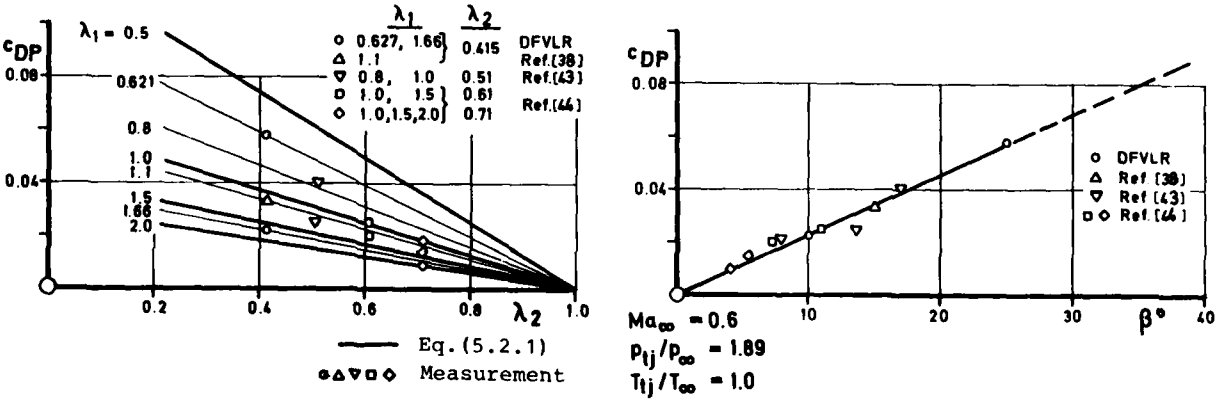

Fig. 15: Pressure drag coefficient c_{DP} as a function of the geometrical parameters λ_1, λ_2 and the afterbody angle β

From equation (5.2.1) and with respect to the relation $\tan \beta = (D_0 - D_b)/2L$ it follows that the coefficient of pressure drag is proportional to the afterbody angle β, $c_{DP} \sim \beta$. This is illustrated in Fig. 15 and confirmed by the test results of Ref. 38 , 43 and 44 .

Equation (5.2.1) is not applicable to the case where $p_{tj}/p_\infty = 1.0$, i.e. jet-off case. To be able to consider this case too, it is necessary to carry out systematic investigations of the afterbody base pressure distribution.

Summarizing the results it will be noted that the pressure drag of a rotationally symmetric afterbody of circular-arc shape provided with propulsion is proportional to the afterbody angle β and that λ_2 is inversely proportional to λ_1. The results show that for minimum afterbody pressure drag coefficient the closure ratio should be $\lambda_2 = 1.0$ (cylindrical afterbody). If the afterbody is to be optimized as regards the total drag, the friction drag W_{DF} must be taken into account. For a short afterbody, small λ_1, W_{DF} is also small ($W_{DF} = 0$ for $\lambda_1 = 0$), it, however, assumes larger values in the case of slim and long afterbodies. If, in addition to equation (5.2.1), an empirical equation could be derived for the friction drag coefficient c_{DF} in the form of

$c_{DF} = f(\lambda_1, \lambda_2)$, then provided one of the two geometric parameters λ_1, or λ_2 is given the remaining geometric parameter can be determined in such a way that

$$c_{DP} + c_{DF} = \text{Minimum}$$

In other words, the total afterbody drag coefficient is a minimum.

In this way, the optimum afterbody configuration with installed engine is defined for the respective operational spectrum.

6. THEORETICAL EVALUATION AND COMPARISON

The afterbody pressure distribution was calculated by means of the finite-element method and a potential-theoretical model set-up to simulate the jet effects. The results concerning the afterbody pressure drag have been compared with the test results. The potential-theoretical model entails that the plume effect of the jet is simulated by a solid truncated cone whose aperture angle is the same as the jet spreading angle α, as determined from equations (4.2.1) and (4.2.2), whereas the entrainment effect is simulated by the entrainment velocity w_r^*, as determined from equation (4.1.6).

In the last measuring plane (x/D = 12), u_n equals u_∞ of the respective translation velocity.

Fig. 16 shows the positive x-r plane and the arrangement of the area in finite elements.

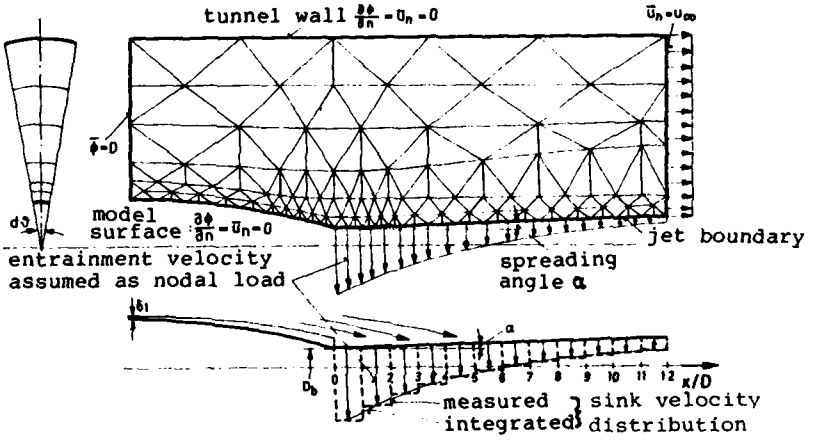

Fig. 16: Potential flow model, finite-element arrangement, sink distribution for rotationally symmetric jets

Because of the rotationally symmetric condition, calculations are made for one radial plane only.

Triangular elements with constant velocity distribution have been selected. The potential $\phi^{(e)}(x,r)$ in the elements is linearly approximated in x and r.

$$\phi^{(e)}(x,r) = \alpha_1 + \alpha_2 x + \alpha_3 r \qquad (6.1)$$

(e) The calculation by means of the finite-element method to determine the potential $\phi^{(e)}(x,r)$ at the elements of the model surface has been described indetail in Ref. 45 to 53 ; the description will therefore not be repeated here.

With the potential values in the nodes yield the velocity components in the element for

$$u_x = \frac{\partial \phi^{(e)}(x,r)}{\partial x} \qquad u_r = \frac{\partial \phi^{(e)}(x,r)}{\partial r} \qquad (6.2)$$

To obtain considerably improved results, the tangential velocity u_t on the afterbody contour has been determined according to Ref. 46 by the integration of the tangential velocity along the sides of three adjoining elements, see Fig. 17c.

From the tangential velocity u_t on the model surface, the pressure distribution c_p is calculated:

$$c_p = 1 - \left(\frac{u_t}{u_\infty}\right)^2 \qquad (6.2)$$

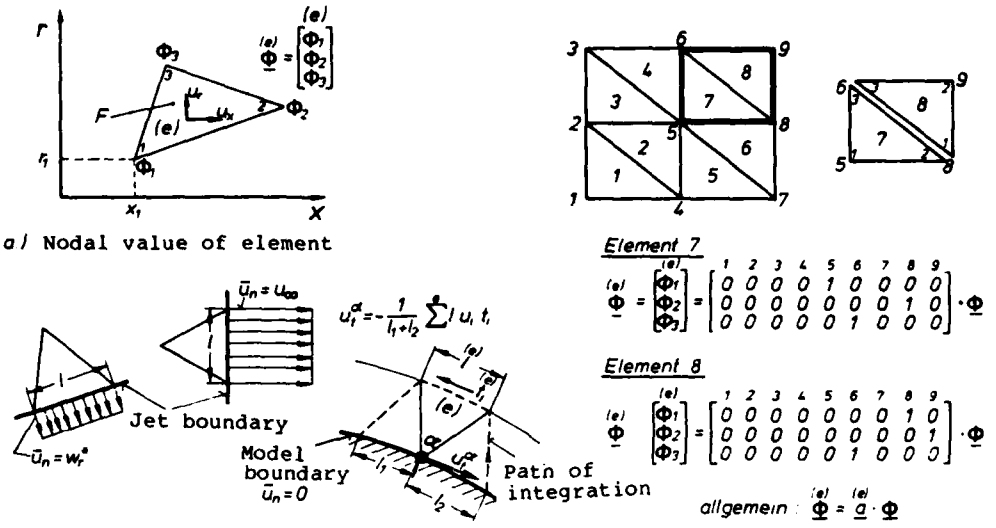

Fig. 17: Partition into finite elements; boundary conditions

The boundary layer thickness has been determined from boundary layer measurements. From this, the displacement thickness δ_1 is determined for incompressible flow from

$$\delta_1 = \int_0^{\delta} \left(1 - \frac{u}{u_\infty}\right)\left(1 + \frac{\Delta r}{r}\right) \cdot dr \qquad (6.3)$$

and for compressible flow from

$$\delta_{1k} = \int_0^{\delta} \left(1 - \frac{\rho \cdot u}{\rho_\infty \cdot u_\infty}\right)\left(1 + \frac{\Delta r}{r}\right) \cdot dr \qquad (6.4)$$

using $(1 + \Delta r/r)$ 1. The pressure distribution c_p is recalculated taking into account the displacement thickness in the form of the changed body contour, see Fig. 16b.

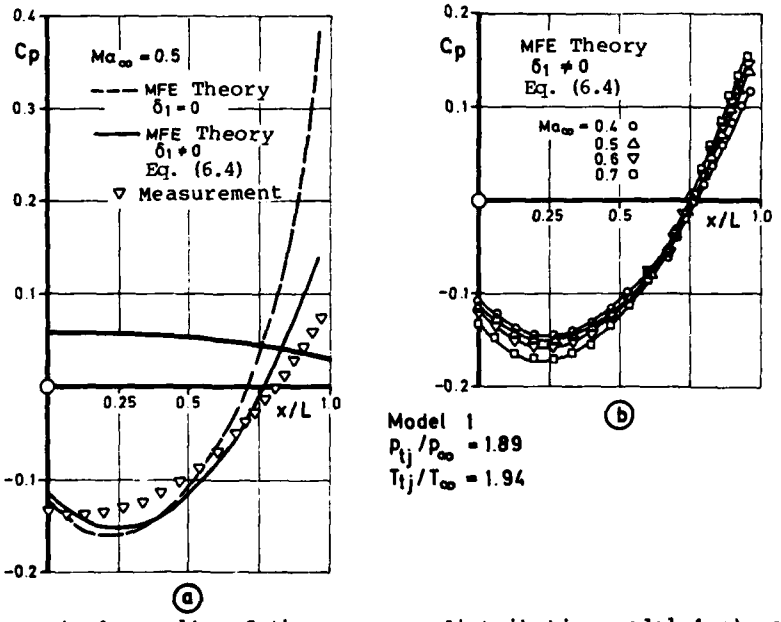

Fig. 18: Theoretical results of the pressure distribution model 1 a) comparison with the test results b) influence of the free stream Mach number

In Fig. 18a, the measured values are compared with the calculated ones with and without considering the boundary layer displacement thickness δ_1. The results will be considerably improved when δ_1 is taken into account. In this conjunction, the following must be explained: the substitute contour of the model was assumed to have a circular-

arc shape like the original model, with an exact boundary layer displacement thickness only at the forward (x/L = 0) and aft end (x/L = 1) of the model. If boundary layer measurements of higher accuracy were available, it would be possible to determine the exact substitute contour by several boundary layer measurements along the model surface and those would provide an even better agreement between the theoretical and measured pressure distributions. It is, however, the main objective of the theoretical computations to demonstrate the feasibility of the jet simulation model using the finite-element method. When comparing the theoretical results of the pressure distribution at various free stream Mach numbers, as shown in Fig. 18b, with the experimental results of Fig. 14a, the trend indicates a definite agreement between theory and measurement.

Fig. 19 shows the theoretically and experimentally determined coefficient of pressure drag c_{DP} for $p_{tj}/p_\infty = 1.89$ and $T_{tj}/T_\infty = 1.94$ is plotted representatively for all nozzle pressure and temperature ratios vs the Mach number Ma_∞. Without considering the displacement thickness δ_1, the theoretical method yields negative c_{DP} values. The mean deviation of the values from those determined by experiments is -133.6 %. Taking δ_{1ik} of equation (6.3) into account the mean deviation of the theoretical value from the experimental c_{DP} value is +11.9 % when plotted vs the Mach number (Fig. 19a), +7.4 % when plotted vs the jet temperature ratio T_{tj}/T_∞ (Fig. 19b) and 7.5 % when plotted vs the nozzle pressure ratio p_{tj}/p_∞ (Fig. 19c). The result is a mean deviation of Δc_{DP} = 8.9 % when plotted vs the parameters Ma_∞, p_{tj}/p_∞ and T_{tj}/T_∞.

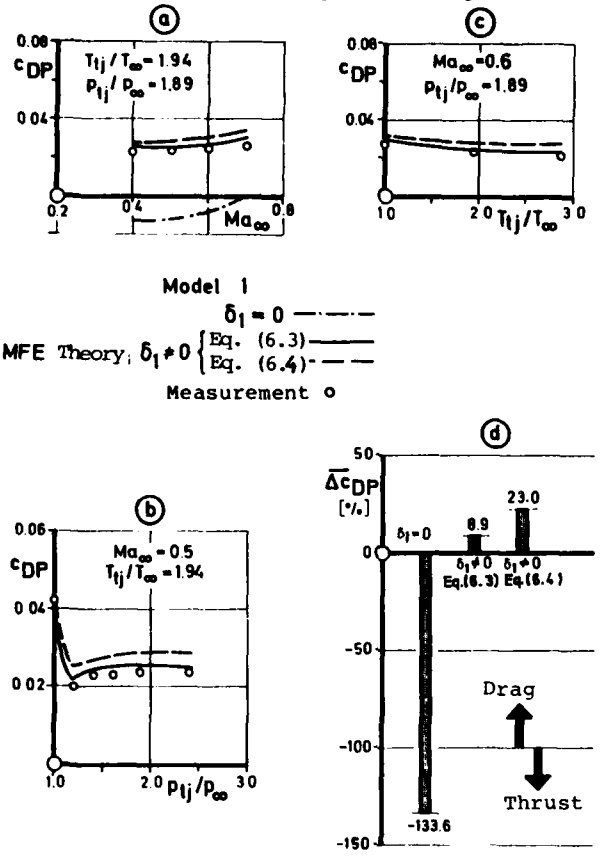

Fig. 19: Coefficient of pressure drag c_{DP} vs a) the free stream Mach number, b) the nozzle pressure ratio, c) the jet temperature ratio; comparison between theory and measurements, d) mean deviation in percent $\overline{\Delta c_{DP}}$ between the experimentally and theoretically determined coefficient of drag

Apart from the amount of deviation, the trends and variations of the pressure drag coefficients when plotted vs. the three parameters agree very well thus proving that the potential flow model as described in this chapter agrees quite well with the physical phenomena.

If δ_1 is evaluated for compressible flow, equation (6.4) yields a 6.5 % thicker displacement thickness:

$$\delta_{1\,k} = \delta_{1\,ik} + 6.5\ \%.$$

The evaluation with δ_{1k} yields a higher pressure drag coefficient c_{DP} as compared with the theoretical value Δc_{DP} = 11.1 % calculated with $\delta_{1\,ik}$:

$$c_{DP\,k} = c_{DP\,ik} + 11.1\ \%.$$

The absolute mean deviation of all experimentally determined c_{DP} values is now Δc_{DP} = 23.0 %, see Fig. 19d.

An even better quantitative agreement between theory and test can certainly be obtained on the one hand by more accurate boundary layer measurements, by the employment of the finite-element method for compressible flows on the other hand by equations of a higher order for the local approximation of the potential $\Phi^{(e)}$ and by other element forms and larger numbers of elements.

It was the objective of this study to describe the interaction of entrainment and plume effects of the jet in terms of theory and thus to demonstrate the established potential flow model. This has been confirmed by the results.

To demonstrate the jet effects tests on a typical combat aircraft model F-16 have been carried out in the MBB water tunnel Fig. 20 gives a qualitative survey over the jet effects on the adjacent aircraft components and the environment for various jet velocity ratios.

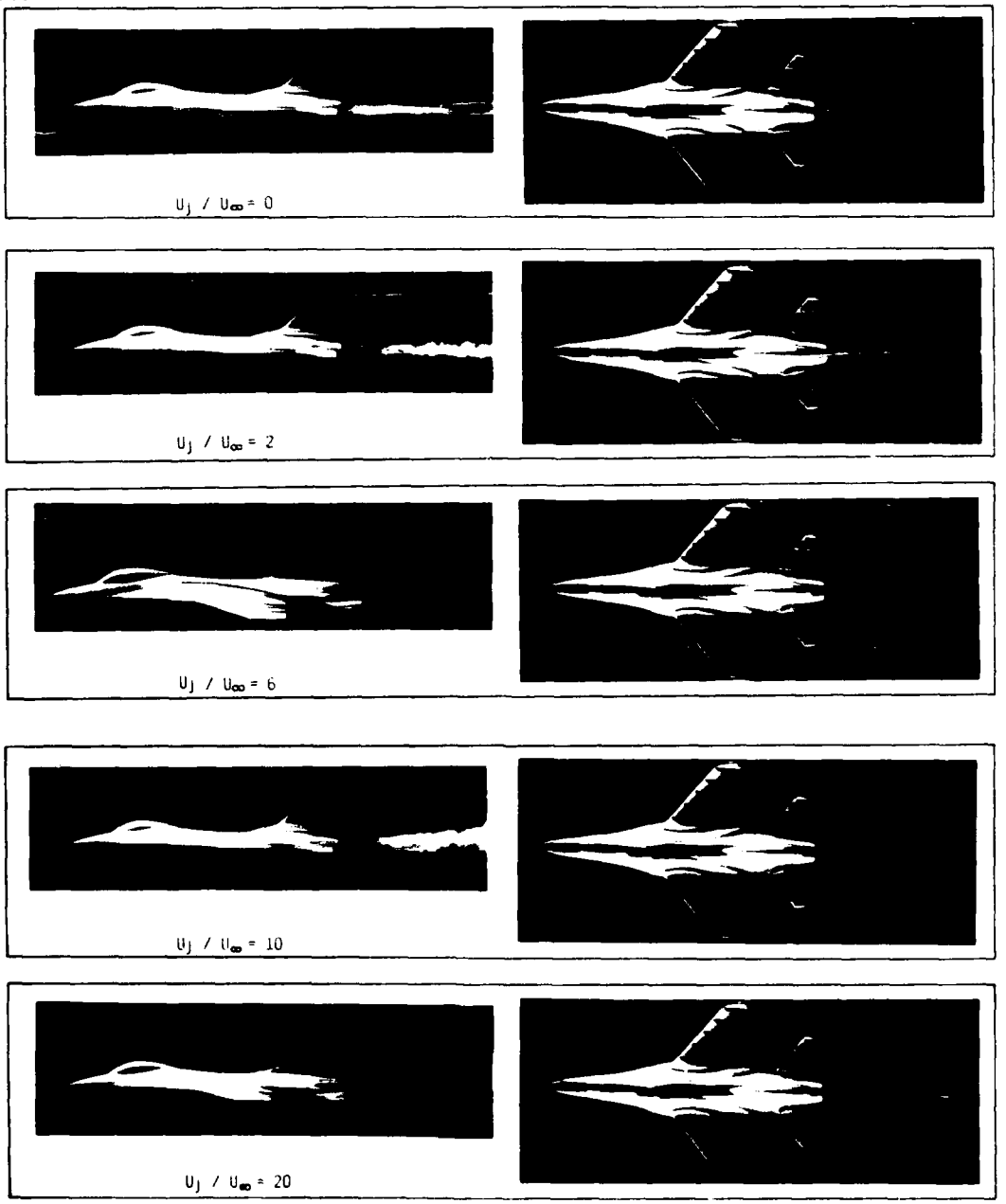

Fig. 20: Jet simulation in the MBB water tunnel on F-16 model , jet spreading, plume and entrainment effects of the engine jet.

7. CONCLUSIONS

It was the purpose of this study to find out the influence of entrainment and plume effects of the jet on the afterbody pressure distribution and pressure drag by extensive experimental testing. Based on the experimental results, the relationship between the coefficient of pressure drag and, in a wider sense, between the pressure drag of rotationally symmetric circular-arc afterbodies and their geometrical parameters in the examined Mach number, jet pressure and jet temperature ranges has been determined. The jet spreading angle and the jet entrainment velocity vertical to the jet boundary as a function of the parameters in the investigated range have been covered in the form of empirical formulae. In general, a potential flow model was set up which constitutes a procedure to describe, by means of the finite-element method, the flow behaviour around the afterbody taking into account the jet effect and thus enables the prediction of the afterbody pressure drag to be made.

The following results have been obtained from the investigations:

The jet spreading angle α increases with increasing nozzle pressure ratio p_{tj}/p_∞, temperature ratio T_{tj}/T_∞ of the jet and with afterbody angle β. It is, however, reduced with increasing free stream Mach number Ma_∞. This behaviour is described by equations (4.2.1) and (4.2.2).

The entrainment velocity w_r^* vertically to the jet boundary increases with the nozzle pressure ratio p_{tj}/p_∞ and the afterbody angle β. Furthermore, it depends on the jet temperature, i.e. the velocity increases as the jet temperature rises. However, it decreases more rapidly in axial direction when the jet is heated than with a cold jet. The entrainment velocity of the jet drops with increasing free stream Mach number. Taking into account the equations (4.2.1) and (4.2.4), these relationships are given in equation (4.1.6).

When the plume effect of the jet is simulated in the form of a solid truncated cone with the semi apex angle being equal to the jet spreading angle α and with the entrainment effect being assumed to be given by the entrainment velocity w_r^* vertically to the jet boundary, the equations (4.1.6), (4.2.1) and (4.2.2) yield the boundary conditions which the design engineer can use to make an allowance for the jet effect.

At lower free stream Mach numbers and smaller nozzle pressure ratios the flow around the afterbody is affected mainly by the entrainment effect of the jet. A balance is reached between the entrainment and plume effects of the jet when the nozzle pressure ratio increases. From $p_{tj}/p_\infty > 2.4$ upwards, the plume effect predominates, Ref. 42 . The entrainment effect decreases as the free stream Mach number increases, the jet affecting the environment by its plume effect. If the jet temperature rises, the influence of the plume effect becomes greater although the sink intensity is higher.

The pressure drag coefficient c_{DP} of rotationally symmetric afterbodies is proportional to the afterbody angle β and closure ratio $\lambda_2 = D_b/D_0$ and is inversely proportional to fineness ratio $\lambda_1 = L/D_0$. In the case of a thermal-insulated model surface, the engine jet heated by 500° C yields a 15 % lower pressure drag coefficient as compared with the value obtained with an unheated jet. Previous investigations without thermal insulation of the model surface, Ref. 37 have yielded pressure drag coefficients which were greater by approximately the same percentage. The design engineer can now derive the afterbody pressure drag to be expected using equation (5.2.1). When establishing a relationship with the frictional drag coefficient c_{DF} in the same manner as for the pressure drag coefficient c_{DP} in equation (5.2.1), it is possible to determine an optimum single-engine afterbody in respect of the total drag provided that $c_{DP} + c_{DF}$ = minimum.

The physical proposition of the model theory set up in this study of the simulation of the jet effects has been confirmed by the theoretical calculations. The discrepancies can still be reduced when the laws of compressible aerodynamics are applied, on the one hand, and measuring techniques are used, on the other hand, which permit a complete coverage of the flow events in such complex fields, thus yielding better boundary conditions in terms of quality.

The finite-element method has proved to be a rather flexible and not very time-consuming procedure for the evaluation of flow problems.

8. References

1 SALMI, R.J. Experimental Investigation of Drag of Afterbodies with Existing Jet at High Subsonic Mach Numbers. NACA RM E 54113, 1954.

2 CUBBAGE, J.M., Jr. Jet Effects on Base and Afterbody Pressures of a Cylindrical Afterbody at Transonic Speeds. NACA RM L 56C21, 1956.

3 MIGDAL, D.
GREATHOUSE, W.K. Optimizing Exhaust Nozzle/Airframe Thrust minus Drag. SAE Paper No. 680294, 1968.

4 MIGDAL, D.
MILLER, E.H.
SCHNELL, W.C.
An Experimental Evaluation of Exhaust Nozzle/Airframe Interference. AIAA Pager No. 69-430, 1969.

5 CHAMBERLAIN, D.
Measurement of Drag from Interaction of Jet Exhaust and Airframe.
Journal of Aircraft, Vol. 6, No. 2, 1969.

6 MILLER, E.H.
MIGDAL, D.
Subsonic Interference Characteristics of Single and Twin Jet Afterbodies.
Journal of Aircraft, Vol. 7, No. 3, May-June 1970.

7 RUNCKEL, J.F.
Aerodynamic Interference between Exhaust Systems and Airframe.
AGARD-CP-71, 1970.

8 BERGMANN, D.
Effects of Engine Exhaust Flow on Boattail Drag.
Journal of Aircraft, Vol. 8, No. 6, June 1971.

9 BERGMANN, D.
Exhaust Nozzle Drag: Engine vs Airplane Force Model.
Journal of Aircraft, Vol. 8, No. 10, October 1971.

10 COMPTON III, W.B.
An Experimental Study of Jet Exhaust Simulation.
AGARD-CP-150, 1975.

11 ROBINSON, C.E.
HIGH, M.D.
THOMPSON, E.R.
Exhaust Plume Temperature Effects on Nozzle Afterbody Performance over the Transonic Mach Number Range.
AGARD-CP-150, 1975.

12 AULEHLA, F.
LOTTER, K.
Nozzle/Airframe Interference and Interaction.
AGARD-LS-53, May 1972.

13 JAARSMA, F.
Experimental Determination of Nozzle Characteristics and Nozzle Airframe Interference. AGARD-LS-53, May 1972.

14 MIKKELSON, D.C.
BLAHA, B.J.
Flight and Wind Tunnel Investigation of Installation Effects on Underwing Supersonic Cruise Exhaust Nozzles at Transonic Speeds.
AGARD-CP-71-71.

15 WALKER, S.C.
Isolating Nozzle-Afterbody Interaction Parameters and Side Effects - A New Approach. AGARD-CP-150, 1975.

16 WILCOX, F.A.
CHAMBERLAIN, R.
Reynolds Number Effects on Boattail Drag of Exhaust Nozzle from Wind Tunnel and Flight Tests. AGARD-CP-150, 1975.

17 TOLLMIEN, W.
Berechnung turbulenter Ausbreitungsvorgänge.
ZAMM, Bd. 6 (1926), S. 468-478.

18 REICHARDT, H.
Gesetzmäßigkeiten der freien Turbulenz.
VDI-Forschungsheft 44, 2. Aufl., Berlin 1951.

19 FÖRTHMANN, E.
Über turbulente Strahlausbreitung.
Ing. Archiv, Bd. V, 1 (1934), S. 42-54.

20 CORRSIN, S.
ÜBEROI, M.
Further Experiments on the Flow and Heat Transfer in a Heated Turbulent Jet. NACA-Report 998, 1950.

21 LAURENCE, J.
Intensity, Scale and Spectra of Turbulence in the Mixing Region of a Free Subsonic Jet. NACA Report 1292 (1956).

22 WILLE, H.
Beiträge zur Phänomenologie der Freistrahlen.
Atg. f. Flugwissenschaften, 11, 1963, Heft 6.

23 SCHWANTES, E.
Das Rezirkulationsströmungsfeld eines VTOL-Hubtriebwerkes.
DLR-FB 72-50, 1972.

24 SQUIRE, H.B.
TROUNCER, H.
Round Jets in a General Stream. ARC, R & M 1974, 1944.

25 SZABLEWSKI, W.
Turbulente Ausbreitung runder Heißluftstrahlen in bewegter Luft.
Ing. Archiv 26 (1958), S. 368-377.

26 REICHARDT, H.
Turbulente Strahlausbreitung in gleichgerichteter Grundströmung.
Forsch. i. Ing.-Wesen 30 (1964), S. 133-139.

27 REICHARDT, H.
Zur Problematik der turbulenten Strahlausbreitung in gleichgerichteter Grundströmung.
Mitt. MPI f. Strömungsforschung Nr. 35, Göttingen 1965.

28 ROTTA, J.
Turbulente Strömungen. Teubner-Verlag, 1972.

29 PAI, S.I.
HSIEH, T.
Numerical Solution of Laminar Jet Mixing with and without Free Stream. Applied Scientific Research, Vol. 27, p. 39-62, Oct. 1972.

30 PAI, S.I.
Two-Dimensional Jet Mixing of a Compressible Fluid. Journal of the Aeronautical Sciences, August 1949.

31 DUGGINS, R.K.
The mixing of a Jet with a Parallel Stream Fluid Mechanics of Mixing.
Proceedings of the Joint Meeting, Atlanta, Ca, June 20-22, 1973 (A73-35501, 1973), New York, American Society of Mechanical Eng., 1973, p. 167-172.

32 SCHLICHTING, H.
Grenzschichttheorie. Verlag G. Braun, Karlsruhe, 5. Aufl.

33 FIEDLER, H.
Theoretische und experimentelle Analyse des statischen Druckes im ebenen turbulenten Freistrahl bei kleiner Machzahl. Deutsche Luft- und Raumfahrt, DLR-FB 67-04, 1967.

34 LOVE, E.S.
Experimental and Theoretical Studies of Axisymmetric Free Jets. NASA TR R-6, 1959.

35 ABRAMOVITSCH, G.N.
Turbulent Jets of Air, Plasma, and Real Gas. New York, 1969, Consultants Bureau.

36 ZACHARIAS, A.
Der Strahlinduktionskanal des Instituts für Entwurfsaerodynamik der DVLR Braunschweig (SIB), IB 129-81/13

37 DISSEN, H.
ZACHARIAS, A.
An Experimental Study of the Influence of the Jet Parameters on the Afterbody Drag of a Jet Engine Nacelle Scale Model. AGARDograph No. 208 on Improved Nozzle Testing Techniques in Transonic Flow, Oct. 1975.

38 EMUNDS, H.
RIEDEL, H.
Contribution of the Institute für Angewandte Gasdynamik of the DFVLR, Porz-Wahn. AGARDograph No. 208 on Improved Nozzle Testing Techniques in Transonic Flow, Oct. 1975.

39 COMPTON III, W.B.
RUNCKEL, J.F.
Contribution of the National Aeronautics and Space Administration Langley Research Center.
AGARDograph No. 208 ön "Improved Nozzle Testing Techniques in Transonic Flow", Oct. 1975.

40 COMPTON III, W.B.
An Experimental Study of Jet Exhaust Simulation.
AGARD Conference Proceedings No. 150 on Airframe/Propulsion Interference, AGARD-CP-150, 1974.

41 MECHIN, B.
HARDY, J.M.
Influence du Taux de Détente du Jet sur les Coefficients de Performance d'un Arrière-Corps Monoflux AGARD de Mach 0.6 a Mach 0.95.
AGARDograph No. 208 on "Improved Nozzle Testing Techniques in Transonic Flow", Oct. 1975.

42 ZACHARIAS, A.
Experimentelle Untersuchungen an einem AGARD-Heckmodell in einer geschlossenen Windkanalmeßstrecke und Vergleich mit Meßergebnissen in einer offenen Meßstrecke. DFVLR, IB 151 - 76/8, 1976.

43 REUBUSH, D.E.
RUNCKEL, J.F.
Effect of Fineness Ratio on Boattail Drag of Circular-Arc Afterbodies having Closure Ratios of 0.5. with Jet Exhaust at Mach Numbers up to 1.30. NASA TN D-7192, May 1973.

44 REUBUSH, D.E.
Effects of Fineness and Closure Ratios on Boattail Drag of Circular-Arc Afterbody Models with Jet Exhaust at Mach Numbers up to 1.3. NASA TN D-7163, May 1973.

45 ZIENKIEWICZ, O.C.
The Finite-Element Method in Engineering Science. McCraw-Hill Book Co., London 1971.

46 SCHMID, G.
Die Methode der Finiten Elemente angewandt auf Strömungsprobleme.
Ruhr-Universität Bochum, Inst. f. Konstruktiven Ingenieurbau.

47 ARGIRIS, J.H.
MARACZEK, G.
Potential Flow Analysis by Finite Elements.
Ingenieur-Archiv 41 (1972), S. 1-25, Springer Verlag 1972.

48 ODEN, J.T.
WELLFORD, L.C.
Analysis of Viscous Fluids by the Finite-Element Method.
AIAA Journal, Vol. 10, No. 12, Dec. 1972.

49 PERIAUX, J.
Three Dimensional Analysis of Compressible Potential Flows with the Finite-Element Method.
International Journal for Numerical Methods in Engineering, Vol. 9, 775-831, 1975.

50 SHEN, S.F.
HABASHI, W.
Local Linearization of the Finite-Element Method and its Applications to Compressible Flows.
International Journal for Numerical Methods in Engineering, Vol. 10, 565-577, 1976.

51 BAKER, A.J.
Finite Element Solution Theory for Three-dimensional Boundary Flows.
Computer Methods in Applied Mechanics and Engineering 4, 367-386, 1974.

52 BERNDT, P.
Bedeutung der Variationsrechnung in der Strömungsmechanik und ihre Anwendung bei kompressiblen Potentialströmungen.
Von der Fakultät für Maschinenwesen und Elektrotechnik der Technischen Universität München zur Erlangung der Würde eines Doktor-Ingenieurs genehmigte Dissertation, 1973.

53 SCHMID, G.
Incompressible Flow in Multiply Connected Regions.
International Conference on Numerical Methods in Fluid Dynamics, Southampton University, September 26-28, 1973.

STRUCTURE AND DEVELOPMENT OF TURBULENT JETS

by
J. Mathieu and G. Charnay
Laboratoire de Mécanique des Fluides
de l'Ecole Centrale de Lyon
36, avenue Guy de Collongue
69130 Ecully - France

SUMMARY

This survey paper provides information on the behaviour and on the modelling of turbulent jet flow. The essential ideas are discussed in connection with industrial and aeronautical applications. After an introduction of the quasi-equilibrium state related to the length and time scales, we analyze the coherent structures and spreading processes. Specific topics are considered such as the intermittency in the axial region, the characteristics of the production centers of the turbulent kinetic energy, the round and plane jet, the acoustic properties with their interactions with the turbulent structure, the initial conditions, and the phenomena in the stagnation region of an impinging jet. A general review of modelling methods precedes examination of computations carried out in physical space and of the large eddy simulation approach.

1. INTRODUCTION

The scientific and technical literature on jets is so abundant that it is pratically impossible to present an exhaustive overview. There have been approximately 30 articles published in the Journal of Fluid Mechanics on turbulent jets during the last two years. Within the context of this meeting it will be important to discuss the essential ideas, to specify the points that merit further development and if possible to relate this to industrial applications.

The practical applications of jets are numerous ; only the most evident will be cited. The hot jet with a high turbine nozzle velocity can be considered from an aerodynamic point of view but should be especially considered from an acoustic point of view. Systems with complex geometries are often employed. For example, turbines in civil aviation with double "flux" are used because of their relative quietness for a given thrust. Jet-engines for vertical take off and for short take off require study of the jet-wall interaction. The induced speed by the jet in the region near aircraft wings also needs to be considered. The problems concerning cooling of turbine blades downstream of the combustion chamber need to be investigated for various configurations. The injection of the cooling air transverse to the wall requires the examination of a jet transverse to a flow. These turbine applications include the problems of multi-jets. The largest part of industrial combustion operations have to do with diffusion phenomena. The classic burner is essentially a jet which must provide good mixing between combustants and air. The distribution of the stochiometric surface approximately determines the position of the flame. Often the burner operates in the interior of a small volume which complicates the initial problems with recirculation zones.

On could multiply the examples ; perhaps it is most important to consider the various complex geometries confronting the engineer, which, without doubt, have not been extensively studied.

2. CLASSICAL BEHAVIOUR OF FREE FLOWS

2.1. The quasi-equilibrium state

Let us consider a free jet impinging normally on a flat plate, the overall behaviour of this flow is illustrated in the definition sketch (fig. 1). In this rather complex case we can identify three regions :

. The first zone corresponds to a mixing layer (ref. 1 - 7 and fig. 2).

. The second one is related to a classical free jet (ref. 8 - 17 and fig. 3).

. The third one exhibits all the characteristics of a wall jet (ref. 18 - 24 and fig. 4).

Restricted areas are incorporated between two successive zones. In the mixing region a potential core can be identified. In this core the mean velocity is not altered by the turbulent diffusion process, and it does not extend further than $X_1/d_o = 5$ downstream from the nozzle exit. As far as only the mean velocity profiles are concerned, the jet region can be detected further than $X_1/d_o = 10$. If the jet is 2 δ in width at the last section where aerodynamic properties are not disturbed by the flat plate, a quasi equilibrium state for the wall jet can be found further than $\frac{X_2}{\delta} = 4$, with the origin of the axis taken at the impinging point (25). If all the properties of the flow, such as the turbulent characteristics, are considered in order to define a quasi equilibrium state, the previous values should be multiplied by a factor of about two (26).

Disregarding mathematical simplifications which can be introduced where equilibrium states are concerned, these states can be considered as the asymptotic behaviour of flows (laminar or turbulent) which develop in a defined environment ; they have clearly been identified in the previous sketches. With the developments of modelling methods in the last decade, transitional zones can be treated except for very specific properties such as the entrainment rate.

At first we can recall what are the characteristic properties of these equilibrium flows. For detailed information many authors are referenced here (mixing layers (27, 28, 29), free jets (8, 9, 30, 31, 32), wall jets (18, 21, 33) but an extensive overview of these problems has been given by Townsend (34).

For the case under consideration the turbulent flow develops along the two axes but we can imagine more complex configurations such as two or three dimensional turbulent jets in cross flows and the jet centerline (which may be defined as the locus of the momentum centers of cross sections) defines a curved axis of coordinates "s". With confined jets recirculation phenomena take place and the momentum equations must be considered in a general form

$$\frac{\partial U_i}{\partial t} + U_j \frac{\partial U_i}{\partial X_j} = - \frac{1}{\rho} \frac{\partial P}{\partial X_i} + \nu \frac{\partial^2 U_i}{\partial X_j^2}$$

$$\frac{\partial U_j}{\partial X_j} = 0$$

The pressure term is connected with the whole velocity field :

$$\frac{1}{\rho} \Delta P = \frac{\partial^2}{\partial X_i \partial X_j} [U_i U_j]$$

In this general form the problem is very complicated even though computing methods are available to treat the Navier-Stokes equations through adequate numerical schemes. The turbulent scales being much larger than the characteristic scales of the molecular interactions responsible for the viscosity, the Navier-Stokes equations may be used for any turbulent structures to be considered. The instantaneous properties of the flow U_i and P can be split into two : their mean and fluctuating parts

$$U_i = \overline{U_i} + u_i$$

$$P = \bar{P} + p$$

which emphasizes the role played by both mean and turbulent motions. Turbulence properties can only be accounted for in complex configurations in an unsophisticated way. For the three flow patterns (mixing zone, jet, and wall jet) boundary layer assumptions may be introduced (appendix 1) so that the momentum equation becomes :

$$\frac{\partial \overline{U_1}}{\partial t} + \overline{U_1} \frac{\partial \overline{U_1}}{\partial X_1} + \overline{U_2} \frac{\partial \overline{U_2}}{\partial X_2} = - \frac{1}{\rho} \frac{\partial \bar{P}}{\partial X_2} + \frac{\partial}{\partial X_2} (T_{12})$$

with $T_{12} = - \overline{u_1 u_2} + \nu \frac{\partial \overline{U_1}}{\partial X_2}$; $\frac{\partial \bar{P}}{\partial X_2} = 0$

It is supplemented by the continuity equation which can be written for the mean flow as :

$$\frac{\partial \overline{U_1}}{\partial X_1} + \frac{\partial \overline{U_2}}{\partial X_2} = 0$$

With this approximation, the pressure is a defined quantity ; at a given station it is the same inside as outside the turbulent zone. Accordingly the relation, which exists, between both the pressure field and the velocity distribution through Poisson's equation is not required to treat the problem. As for the stress, the shear stresses prevail over the normal stresses so that we can take :

$$\frac{\partial}{\partial X_1} \overline{u_1^2} << \frac{\partial}{\partial X_2} \overline{u_1 u_2}$$

Boundary layer assumptions having been introduced, a quasi-equilibrium state now may be characterized in a simple way. By proper scaling any properties of the fluid should satisfactorily be represented irrespective of the station considered. Thus time and length scales or length and velocity scales must be introduced. Where mean velocity and shear stress are concerned this leads to

$$\frac{\overline{U_1}[X_1, X_2]}{U^*[X_1]} = f \left[\frac{X_2}{X^*_2(X_1)}\right]$$

and $\frac{\tau}{\tau^*} = g \left[\frac{X_2}{X^*_2(X_1)}\right]$

If such a representation is successfull a complete description of the aerodynamic field also requires additional information about the longitudinal evolution of the two scales $U^{\ddagger}(X_1)$ and $X_2^{\ddagger}(X_1)$. Moreover by using the same parameters one should also be able to satisfactorily correlate turbulent results for a given flow pattern irrespective of the station considered. However several authors have criticized so large an extension of the concept of the quasi-equilibrium state even for the case of a free jet (1). For these researchers, the enlarged form of this concept is principally accepted because of its mathematical consequences : the flexibility of treating the problem through ordinary differential equations.

In fact, this concept would be completely valid if the behaviour of the phenomena was controlled by two mechanisms whose scales are sufficiently different from one another. If such a separation exists the micro-mechanism can be considered as instantaneously adjustable to the macro-mechanism, and thus, at any time, the micro-mechanism is in an equilibrium state. If we conjecture that the turbulence field is composed of two classes of structures exhibiting two different characteristic times, the first one related to the range of structures which contribute to the turbulent kinetic energy and the second one related to the spreading of the jet, the former's characteristic times should rigourously be in an equilibrium state. This situation is not supported by experimental investigations, however. Turbulence spectra are continuous (†), so that the structures which significantly contribute to the components of the Reynolds stress tensor are not drastically different from those which control the spreading of the jet although a typical role can preferentially be assigned to each range of the spectrum. We can conjecture that the largest eddies are specially responsible for the spreading of the jet. If so, the largest structures should be suspected no to be in an equilibrium state (††). From this point of view the evolution of the intermittency factor should be very significant (†††). The intermittency factor may be considered as a convenient parameter to specify the evolution of these largest structures, using the same scaling $U^{\ddagger}$ and $X^{\ddagger}$. It is shown in figure 5, that the intermittency profile is dependent on the section considered ; as we go downstream the indentations of the moving frontiers grow more rapidly than the characteristic width of the jet $X_2^{\ddagger}$ so that the flow tends to evolue into turbulent puffs separated from each other (24, 36). These large structures contribute only for a small amount to the components of the Reynolds stress tensor ; on the contrary the contribution of the mean structures to the Reynolds stresses is determinant so that an equilibrium state may be supposed. However, from very accurate comparisons of the dimensionless profile, a slight evolution can even be detected (19 and fig. 6).

From a fundamental point of view the equilibrium state assumption cannot be supported for patterns of flows exhibiting two regions. In a restricted area the turbulent eddies are directly subjected to the action of viscosity, whereas in most extended zones this action is restricted to the smallest structures responsible for the dissipation (18).

The turbulent behaviour of a free jet has been considered for a long while as a rather simple case. As a general rule, symmetrical flows have not seemed very complex. This opinion was partially supported by primitive assumptions based on an assumed local relation between the velocity fluctuation correlation and the mean velocity gradient at a given point through an eddy viscosity coefficient ν_T.

$$\overline{u_1 u_2}\ (\vec{X},t) = \nu_T(\vec{X},t)\ \frac{\partial \overline{U_i}}{\partial X_2}(\vec{X},t)$$

In fact, turbulence structures are unable to adapt themselves to local gradients at any point, although for a weak evolution of the mean flow this phenomenon can be ignored in a rough estimate. Anyway, a coherent theory has to introduce the memory of the turbulence structures which may be adequately represented by the second order

---

(τ) Except for very a typical circumstances which are encountered in meteorological problems but even in this case discussion is open.

(††) A fact which has also been emphasized for isotropic turbulence by Comte-Bellot and Corrsin (35).

(†††) The intermittency phenomenum has been first detected by Corrsin (30) at the edge of a turbulent zone. In this form, this concept characterizes the indentations of the turbulent zone, at a fixed point ; it is defined as the ratio of the time when the turbulent field intersects a sensing device, to the total time. This concept can easily be enlarged. If a typical event has to be emphasized, it can be useful to characterize its extension in time by means of a similar ratio (38). This event develops in a surrounding field whose properties must be detected at the appropriated times ; accordingly this selection method directly leads to conditional averages (53).

moments (†). The rate equation for the turbulent kinetic energy is written :

$$\overline{U_1}\,\frac{\partial \overline{q^2/2}}{\partial X_1} + \overline{U_2}\,\frac{\partial \overline{q^2/2}}{\partial X_2} = \overline{u_1 u_2}\,\frac{\partial \overline{U_1}}{\partial X_2} + \frac{\partial}{\partial X_2}\left[\overline{u_2 p} + \overline{\frac{u_2 q^2}{2}}\right] + \bar{\varepsilon}$$

In its contracted form the evolution of the Reynolds stress tensor can be easily interpreted : the turbulent kinetic energy is advected by the mean field, it is fed from an interaction between the shear stress and the mean velocity gradient, and it is dissipated by viscosity acting on small structures. Pressure and velocity fluctuations are responsible for turbulent diffusion. This equation displays the existence of production centers whose roles have been clarified (20, 37). For a free jet two turbulent centers feed the fluctuating flow with energy, they are approximately located at the inflexion points of the mean velocity profile. If only the energy production is considered, the region closed to the axis of the jet is not active ; it is fed with energy from the two symmetrical centers, with diffusion terms playing a determinant role. For lack of local production the amount of energy on the axis of the jet is slightly smaller than at the two inflexion points (28,30 and fig. 7), a fact which is reinforced where two dimensional jets are concerned. Turbulent structures issued from A and B interfere on the axis (a similar mechanism also exists in pipe flows, 38, 39). These structures can be identified by using an electronic gate which is triggered by the sign of u_2. On the axis successive events marked by the sign of $\overline{u_1 u_2}$ can also be detected (40). A statistical balance leads to $\overline{u_1 u_2} = 0$. During these periods of activity a significant contribution is brought to the shear stress $\overline{u_1 u_2}$; between these periods no important contribution to $\overline{u_1 u_2}$ is detected a fact which can be a consequence of the age of the structures under consideration (for old structures successively subjected to mean velocity gradients opposite in sign a statistical balance operates). On the other hand we can conjecture that more or less extended areas exist within turbulent fields similar to those encountered in wakes (the velocity of coherent structures travelling inside the flow may be different from the local velocity ; this relative speed could induce a wake pattern).

In fact, mixing zones are not so complex because they are fed from a unique turbulent center. The transverse position of these mixing zones cannot be deduced from symmetry arguments, the momentum equation must be applied with respect to the axis X_1 and X_2. For the X_2 component all the terms are of an order of magnitude ε, so boundary conditions have to be introduced very carefully (28 and fig. 8).

Wall jets exhibit strong asymmetrical behaviour due to the boundary conditions. In the wall region viscosity plays a direct role in the velocity distribution. Owing to the presence of the wall the large structure are limited in extent ; on the other hand, their dynamic behaviour is hampered by a fine grained turbulence located in the wall region. Wall jets have been thoroughly investigated and complex geometries have been examined (plane wall jet, concave and convex wall jets, jets with tailored walls) (18, 33, 41, 42, 43). Comparison made between the mean velocity profile and the shear stress profile invalidates a first gradient assumption ; in fact, a displacement between the zeroes of the gradient of the mean velocity and the shear stress term has been observed (††). Twenty years ago it was conjectured that such a displacement is the consequence of the turbulence memory (18) and an accurate explanation was given more than ten years ago (37) which underlines the memory effect in connection with the role played by advective terms. Prediction models given by Launder (44) supported by Lumley (45) and by Jeandel (46) are consistant with these findings. The energy budget also brings to light the strong asymmetry of the flow. Two turbulent centers exist but a large amount of energy originates from the jet production center ($\frac{P_{jet}}{P_{wall}} = 15$, fig. 9) so that the wall region is significantly altered farther than $\frac{X_2 U_f}{\nu} = 50$. This action of the jet region is appreciable even close to the wall. The connection between the skin friction coefficient and the Reynolds number $R\delta = \frac{U_m \delta}{\nu}$ (fig. 4) is slightly modify

$$C_f \sim R_\delta^{-0,18}$$

and the dependence between C_f and R_δ is somewhat smaller than in the case of a boundary layer along a flate plate (47).

The role played by the shape of the wall on the overall properties of the flow such as the spreading of the jet or the intermittency factor must be underlined (28, 41, 48 and fig. 10). These comparisons display the influence of large structures whose dynamic behaviour could probably be connected with quasi-linear theories of hydrodynamic stability (49, 50). These eddies, of course, do not participate in the quasi equilibrium state, their characteristic times being of the same order of magnitude as the spreading of the jet which is under their control. The complex shape of the turbulent frontier, in particular the size of the indentations of this frontier, does not determine the capability

---

(†) The dynamic behaviour or any turbulent structure is controled by the Navier-Stokes equation. Introducing the usual splitting into a mean field and a fluctuating field, information is extracted from the basic equation by averaging. An hierarchy of moments about mean values is introduced, and partial differential equations govern their evolutions which can also be interpreted in functional form.

(††) This situation has been observed in most turbulent shear flows in which there exists an asymmetry in the mean profile. If this effect becomes significantly large the turbulent production will be negative.

of a flow for entrainment. The engulfing mechanism is linked to the dynamic properties of the flow in a more intricate way ; however, a dependance can be pointed out where similar flow patterns are considered (37). The engulfment of external fluid by the turbulent flow and its contamination by turbulence through a "nibbling" process is not yet understood and one can regret that the effort made during the last decade (2, 28, 51 - 55) have somewhat receded. All these attempts have not been successfull in spite of more and more sophisticated means of investigation, and the spreading of the initial turbulent region remains one of the most challenging problem for scientists and engineers.

2.2. Some typical problems

2.2.1. Coherent structures and the spreading process.

In the last section general properties of free flows such as mixing zone free jets and wall jets have been examined. From an overall view of the technical literature we can conclude that two dimensional and round jets have been extensively investigated at a given stage of their development. In such circumstances the flow perperties may be precisely defined and are independent of initial conditions.

In the mixing zone, close to the exit nozzle, several researchers have detected coherent structures. This fact has led them to fundamentally reexamine the problem of the turbulence. In their opinion a turbulent field is not so randomized as had previously been imagined ; its behaviour is more or less dominated by large organized structures. In fact, however, these conclusions have been extracted from particular situations (56), and a more general review of this problem exhibits some real difficulties. Investigators operate in a large range of Reynolds numbers, starting conditions are often unknown and it is often difficult to detect the nature of the initial boundary layer (laminar or turbulent). In any case, the existence of coherent structures cannot be denied and the industrial importance of the flow in the region close to the exit where these structures are most clearly seen is evident (jet engines, ground effects for vertical take off and landing (VTOL) or for short take off and landing (STOL), burners...), therefore it would be very usefull to analyze investigations dealing with this problem especially examining some relevant experimental situations such as :

- the Reynolds number at the exit nozzle ;
- the nature and the thikness of the initial boundary layer ;
- the turbulence level at the starting section ;
- the spectrum in the free flow at the exit nozzle in order to detect typical frequencies in connection with the facility drawing.

We present information, previously quoted in Madrid conference (56), which emphasizes the large range of investigations even though the Reynolds number is choosen as a unique parameter :

Kinds of flows	Reynolds number	Location of the test section with respect to the starting section
Jet (round and plane).	$U_o d/\gamma$ = 300 to 300 000	15 to 100 d_o
Mixing zone of jet with or without excitation.	$U_o d/\gamma$ = 100 to 370 000	0 to 16 d_o

Where asymptotic behaviour is concerned the turbulent characteristics of the flow must be independant of initial conditions, a situation which is extremely difficult to manage for mixing zones. Recent works (57 - 60) examine the role played by the initial condition. If we admit that mixing zones are very sensitive to any external disturbances, the nature (laminar or turbulent) of the starting flow should be taken into account.

For lack of a general theory we must examine the development of coherent structures in *different types of flows*. At *first, the geometry* of the flow plays a role. For example Sunyach (28) has shown that the turbulence spectrum in a round jet exhibits a peak which reveals the existence of ordered structures, but this peak is not so apparent in a plane jet. By using hot wire rakes these large structures can also be detected. A circular geometry certainly reinforces the existence of stable toroidal structures the existence of which can easily be emphasized, especially using a Lagrangian frame. Acoustical disturbances (61) may also reinforce and control this phenomenon. An attempt has been made by the constructors to initiate a spanwise break up of these rolling structures and thus the nozzle exit of jet engines can exhibit a complex shape. With regard to the entrainment process, information is given by the transfer terms weighted by an intermittency factor. These equations have been derived by Dopazo (54). Estimation of these transfer terms by measurements carried out inside or outside the frontier are consistent with each other, for a wall jet, it has been made by Alcaraz (24 and fig. 11). However for purposes of this review it will be impossible to examine all the details ; we must concentrate on the most enlightening features.

Typical contributions to the problem of coherent structures presented at Southampton (March 1974) have been excellently reviewed by POAL Davies and AJ Yule (62). A more recent synthesis has been made by J. Mathieu and G. Charnay in Madrid (56). A general definition of coherent structures has been proposed by Yule : "Large eddies which may be repetitive in structure, remain coherent for significant downstream distances and which may be quasi-deterministic with birth-life-death cycles" (15). The existence of organized structures has been suspected as early as 1948. Dryden wrote "It is necessary to separate the random processes from the random elements", and many scientists have taken a great interest in this sort of investigations (63, 64, 65, ...). One should notice that most of this work for mixing zones has been carried out at moderate Reynolds numbers, the detection of coherent structure becoming more and more difficult as the velocity increases. In spite of some evidence the problem is open to debate. For instance, Bradshaw (66) concluded that "Experiments in plane mixing layers and the foregoing review of recent papers suggest that the two dimensional vortex-roll disturbances arise in the transition region and would appear only in plane mixing layers with laminar boundary layers at the nozzle exit and low turbulence in the external flow". This opinion agrees with the received view that mixing layers become unstable, at very low values of the Reynolds number based on local thickness, to two dimensional or axisymmetric disturbances. Accordingly these vortex rolls could be some sequels of linear transition instabilities.

However, the two dimensional "vortex roll" disturbances which are the eigenmodes of instability of a laminar mixing layer would become persistent under typical circumstances. These disturbances could grow and pair once, twice or even more often before appreciable three dimensionality appears. From a spectral analysis the pairing process could be considered as a reverse cascade, small structures being capable of becoming large structures. Anyway, this kind of mechanism can be detected even where homogeneous flows are concerned. With a view of a best understanding of the phenomena, the role played by the quoted parameters should be brought to light ; for example, we may easily understand how important the influence of fine grained turbulence acting as an additional viscosity could be ; it could be capable inhibiting the two dimensional instabilities from breaking up.

At this time the discussion is not supported by accurate enough experimental investigations which include all the parameters, so that it is not possible to give final conclusions about the role and importance of these structures. To a large extent, the answer depends on the definition which is accepted for turbulence. If we admit that turbulence is typically a three dimensional phenomenum including also a stretching process of the vortex lines by the velocity field itself, structures like vortex-rolls whose axes are perpendicular to the velocity are not concerned. This stretching mechanism is controled by the Helmholtz equation :

$$\frac{\partial \xi_i}{\partial t} + U_j \frac{\partial \xi_i}{\partial X_j} = \xi_j \frac{\partial U_i}{\partial X_j} + \mu \frac{\partial^2 \xi_i}{\partial X_j^2}$$

For two dimensional fields $\xi_j \frac{\partial U_i}{\partial X_j}$ is null. The evolution of ξ_i is determined by a balance between advective and diffusive terms only.

Even though we adopt this restrictive definition the presence of more complex ordered structures is not eliminated. The new basic problem still remains that of how typical structures could be selected and reinforced. Except for the isotropic turbulence which is only subjected to its own influence, most flow patterns are subjected to external forces the role of which can be more or less predominant. Disregarding initial conditions which could generate, under typical circumstances, turbulent structures directly marked by transitional modes, we must wonder whether the final state of a turbulent flow is still dominated by large organized structures. Coriolis, buoyancy or acoustical forces can also influence the development of turbulent fields (67, 68, 69, 61). It is even known that driving forces generated by the rotation of the frame can increase so much as to cancel randomizing effects. The action of a mean velocity gradient on a turbulent field is perhaps not so effective as the previous effects but it is the only mechanism capable of orienting turbulent structures during all the final stages of the flow development through the typical role of the stretching process (37). As a first simple case for consideration we can start with a basic model of an homogeneous shear flow. Except for the role played by initial conditions (70, 71, 72), it retains some of the main features encountered in mixing zones, jets and so on. Frontier effects are eliminated, but the turbulent field can be subjected to very strong external influences since the mean velocity gradient is not generated by the development of the turbulence field itself but is imposed from external boundary conditions. However, we can conjecture that the development of large eddies is subjected to a selection mechanism. Eddies, the axis of which coïncide with that of the stretching of the main flow, will be tracked and strongly amplified (†) (71 and fig. 12). Gence examined how much the turbulence is dependant on the relative position of principal axes of the strain with respect to those of the Reynolds stress tensor. In the case under consideration, the angle α which characterizes the relative position of these axes can be adjusted experimentally. A reversed energy cascade can occur for suitable values of α ; and such "pathological cases" have experimentally been detected (73, 74). Where shear effects exit, straining and rotating processes are mingled, so that the behaviour of turbulent structures is somewhat difficult to determine. Accounting the foregoing results it is possible to qualitatively combine a rotation of the straining axis with a rotation of the frame ; the relative position of the principal axes of the Reynolds stress tensor with respect to the principal axes of the straining process (associated with the mean velocity field) can be qualitatively predicted.

(†) On the contrary, the intensity of eddies whose axes coïncide with the contraction axes strongly decreases.

In all practical cases, the turbulent field is limited in extent. Surrounding regions are contaminated by the turbulent flow in a very complex way. The previous considerations have to be supplemented by a most challenging problem which concerns the entrainment process. At first, we must remark that it cannot be easily understood from a global analysis of the Reynolds stress tensor. Irrespective of the mechanical behaviour of the phenomena, computing methods use a matching process. Outside turbulent zones we can assume :

$$\overline{U_1}\ \frac{\partial \overline{U_1}}{\partial X_1} = -\frac{1}{\rho}\ \frac{\partial \bar{P}}{\partial X_1}$$

whereas just inside turbulent areas we write :

$$\overline{U_1}\ \frac{\partial \overline{U_1}}{\partial X_1} + \overline{U_2}\ \frac{\partial \overline{U_1}}{\partial X_2} = -\frac{1}{\rho}\ \frac{\partial \bar{P}}{\partial X_1} + \frac{\partial \tau}{\partial X_2}$$

Accounting for the order of magnitude of these quantities, it is found that :

$$\left|\overline{U_2}\ \frac{\partial \overline{U_1}}{\partial X_2}\right|_\delta \sim \left|\frac{\partial \tau}{\partial X_2}\right|_\delta$$

Accordingly, the rate equations for the tensor components $\overline{u_i u_j}$ are supplemented with the previous conditions given at the limiting value $X_2 = \delta$.(†)

With modeling methods delicate adjustments are made according to the shape of the jet (two dimensional jets or circular jets). This difficulty can easily be understood from these remarks. In section III, the flexibility of modelling methods will be reexamined briefly.

2.2.2. Some industrial consequences.

Where multi-jets are concerned the entrainment process becomes predominant. The stability of the system is rather poor and is probably controled by many types of entrainment processes and the jets tend to coalesce. Experimental investigations are difficult and rare (ref. 75 - 78) and prediction methods collapse. Flapping phenomena have also been detected (ref. 79).

The sensitivity of the flow, at the exit of the nozzle, to disturbances have been brought to light by using periodic sources located, for instance, in the settling chamber of a wind tunnel (61). We must also point out some recent findings related to the dynamics of an impinging jet (80). An impinging jet can be viewed as a synthesis of diverse flow patterns, namely a mixing zone, a free turbulent jet, a stagnation region surrounded by an area within strong streamline curvature which generates severe vortex stretching (81), Kestin and Mader), and finally a wall jet. Recently some researchers have detected a feedback phenomenon which underlines the sensitivity of the upstream flow to small disturbances. In a high-speed subsonic jet impinging on a flat plate, the surface pressure fluctuations exhibit a broad spectrum owing to the turbulent nature of the high Reynolds number jet. These pressure fluctuations suddenly change their pattern into almost periodic waves if the plate is placed close to the nozzle ($X_Q/d_o < 7.5$). Experimental data support the hypothesis that a feedback mechanism is responsible for the sudden change observed in the pressure fluctuations at the onset of resonance. One can conjecture that the feedback loop is associated with two mechanisms ; the downstream convected coherent structures and an upstream propagation pressure wave (like acoustic waves) generated by the impingement of the coherent structures on the plate. The upstream propagating waves are phase locked at the nozzle exit. For convenient conditions, these upstream propagating waves excite the thin layer near the nozzle lip and reinforce them. Thereby an instability process occurs which at least depends on the convection speed of coherent structures, the speed of the upstream propagating waves and the distance between the nozzle and the plate. This "collective interaction" is roughly described in the figure 13. We must remark that "the shear layer oscillating at a frequency much lower than its intrinsic unstable frequency undergoes a collective interaction in which many small vortices merge together to form a large coherent structure". The capability of a non-linear system in generating upper as well as lower frequencies with respect to a forcing frequency probably occurs through a somewhat more complex mechanism than the one proposed in the previous sketch. As the resonance is detected, the shear layer rapidly grows within a short distance of the nozzle. In this research the plate was placed perpendicularly to the axis of the jet. What happens for inclined plates (82) ? Is the resonance as sharp or is a larger range of frequencies concerned in the foregoing phenomenon ?

The role played by coherent structures in the spreading of the jet has been discussed. The turbulent mixing of a circular jet in cross flow is also of significant importance in emphasizing the role of deterministic structures on the development of the jet. This

---

(†) Through an averaging process and accounting for second order moments only information are most compressed, so that phenomena linked to the entrainment are partially oblitered.

configuration has been analyzed in several papers (83 - 87) and prediction methods have been developed. In order to reduce the computing time typical integral methods have been introduced based on two integral momentum equations. Where a plane jet is concerned mean vortex lines are normal to the direction of the mean flow (profile A) and no stretching process can take place where the mean flow is concerned only. With a circular jet a pair of vortices are generated through a stretching process of the initial vortex lines which coalesce (fig. 14.a) ; in fact, for the transverse profile B, the mean vortex lines and the mean velocity are colinear. The development of jet cross sections downstream along its centre-line are shown in figure 14.b. The phenomenum is not fundamentally different from the passage flow within a blade cascade. An explanation can be given starting from the vortex lines : a component in the streamline direction appears as the jet flow is bent. It is also possible to explain these deterministic structures accounting for small transverse inhomogeneities of the pressure field linked to the curvature of the streamlines. Scientists who are dealing with this problem have to consider a typical entrainment rate equation. The spreading of the jet is determined as the linear combination of a modified straight jet entrainment and the entrainment by a vortex pair and the problems of similarity and cross section shape in the curved jet has to be associated with entrainment. The role played by the mean and turbulent characteristics of the cross flow should also be examined. Where cooling effects of turbine blades are concerned the dynamic properties of the jet must be considered in connection with the overall aerodynamic field within the passage. The induced vorticity determines a pressure field with a low pressure region which could engulf the coalescent jets.

Two industrial consequences of specific development of jet flows have been underlined, namely coupling mechanisms for impinging jets and typical entrainment process for turbulent jet in cross flow. The noise generation of jets is also to be considered, taking into account the foregoing mechanisms.

The location of noise sources can be obtained through causality methods (to this end correlations between source terms in Lighthill's theory and the acoustic pressure in the far field are detected) or more recently by means of purely acoustical methods (reflecting telescope, elliptic mirror). From these investigations the role played by the aerodynamic field just downstream of the exit nozzle (88, 89, 90) should be predominant. When structures like rolling vortices exist, "vortex pairing" could be responsible for a large part of the noise generation (88). So far, this assumption which is utterly plausible has not yet been demonstrated. In fact,

. The jet noise does not significantly exceed the exit noise except for high speed jets, but in this situation the "pairing vortex" is not clearly detected.

. Investigations carried out at several points by means of a hot wire anemometer can disturb acoustical fields.

However Laufer's assumption is supported by several arguments :

- The acoustical field originating from a fixed point within the jet is discontinuous ; periods of intense activity alternate with silent periods.

- Excitation tends to reinforce a phenomenon similar to "pairing" which can be detected in the potential core by a subharmonic component in the spectrum. A theoretical analysis of this phenomenon has been presented by Kelly (91) who explains at first the linear development of the fundamental disturbance. For a given threshold the perturbation interacts with the mean field. Small disturbances imbedded in the flow are subjected to a parametric amplification which exhibits a resonance for a subharmonic value of the fundamental tone. Moreover it seems that such a mechanism can be detected in all the kinds of jet flows (92, 93, 94) ; this general feature also supports this explanation.

However, this theory fails to explain the development of the broad range noise. We can suspect that the underlying turbulence acts on the amplitude and the phase of the generated noise through a scattering process ; the noise generation by a break-up process of these organized structures can also be conjectured.

3. MODELLING METHODS

3.1. General view

We do not intend to give an overview of predictive methods which are to be treated in next section. Moreover an overall survey has been presented at several congresses and meetings (95, 96). Disregarding numerical simulations of the Reynolds equations with a view to predicting the overall turbulence field (†), we can classify these modelling methods into four groups. The first group examines the turbulence properties working in physical space ; a spectral equilibrium is implicitly assumed. For the second one an attempt is made to predict the role of the structures as a function of their sizes. For the third group a typical splitting of the field is proposed ; large structures of the

---

(†) This method requires very large computing time, it has extensively been developed for isotropic flow at moderate turbulent Reynolds numbers. The simulation of the smallest scales of turbulence determines the net sizes.

turbulence are treated in a deterministic way, the influence of the smallest ones being treated with a statistical approach. We must also mention probabilistic approaches which deal with a probability density function. This method is especially effective when some properties of the turbulent field (for example the concentration of chemical species with chemical reaction) do not follow a normal law. This method, currently being developed, is not sufficiently supported by mathematical developments and experimental data.

Only the first and the third methods will be further discussed they have close connection with our problem.

3.2. Modelling methods carried out in physical space

These methods assume a spectral equilibrium roughly characterized by the capability of defining three classes of turbulence structures. The largest eddies are strongly marked by the mean flow, feeding with energy the inertial range which is dominated by a constant energy flux travelling from the largest structures to the smallest ones. In this range of the spectrum the action of viscosity is supposed to be negligible ; as for the third part of the spectrum it is dominated by viscous effects which transform the mechanical energy of these fine grained structures into heat. Accordingly all the parts of the spectrum are linked to each other through this energy flux which is not altered within the inertial range. Turbulence characteristics are also defined by a simple scaling, the macroscales and the microscales being connected with each other through the turbulence Reynolds number. The amount of dissipative energy results from interactions between the mean field and turbulence structures responsible for $\overline{u_1 u_2}$. The smallest structures have to be adapted in order to dissipate an energy flux whose amount is fixed by larger structures.

With this method we essentially have to predict the evolution of both the mean field $\bar{U}_i$, $\bar{P}$ and the Reynolds stress components (†).

In fact this method which starts from correlations at a unique point does not fix the turbulence scaling, therefore the previous equations must be supplemented by the rate equation for $\bar{\varepsilon}$ or $\overline{q^2}L$ (46, 98). Where boundary layers assumptions are valid one must consider a differential system for the five components $\bar{U}_1$, $\bar{U}_2$, $\overline{q^2}$, $\overline{u_1 u_2}$ and $\bar{\varepsilon}$. For a steady and homogeneous shear flow, they are :

$$\bar{U}_1 \frac{\partial \bar{U}_1}{\partial X_1} + \bar{U}_2 \frac{\partial \bar{U}_1}{\partial X_2} = - \frac{1}{\rho} \frac{\partial \bar{P}}{\partial X_1} - \frac{\partial \overline{u_1 u_2}}{\partial X_2}$$

$$\frac{\partial \bar{U}_1}{\partial X_1} + \frac{\partial \bar{U}_2}{\partial X_2} = 0$$

$$\bar{U}_1 \frac{\partial \overline{q^2}/2}{\partial X_1} + \bar{U}_2 \frac{\overline{q^2}/2}{\partial X_2} = \overline{u_1 u_2} \frac{\partial \bar{U}_1}{\partial X_2} + \frac{\partial}{\partial X_2} \left[\overline{u_2 p} + \frac{\overline{u_2 q^2}}{2} \right] + \bar{\varepsilon}$$

$$\bar{U}_1 \frac{\partial \overline{u_1 u_2}}{\partial X_1} + \bar{U}_2 \frac{\partial \overline{u_1 u_2}}{\partial X_2} = \frac{\partial \bar{U}_1}{\partial X_2} \overline{u_2^2} + \overline{p \left[\frac{\partial u_1}{\partial X_2} + \frac{\partial u_2}{\partial X_1} \right]}$$

$$\bar{U}_1 \frac{\partial \bar{\varepsilon}}{\partial X_1} + \bar{U}_2 \frac{\partial \bar{\varepsilon}}{\partial X_2} + \frac{\partial \overline{u_1 \varepsilon}}{\partial X_1} + \frac{\partial \overline{u_2 \varepsilon}}{\partial X_2} = - 2\nu \overline{\left(\frac{\partial u_i}{\partial X_k} \frac{\partial u_j}{\partial X_k} \frac{\partial u_i}{\partial X_j} \right)} - 2\nu^2 \overline{\frac{\partial^2 u_i}{\partial X_k \partial X_j} \frac{\partial^2 u_i}{\partial X_k \partial X_j}}$$

The role played by the pressure is complex ; it is a consequence of linear and non-linear effects. The correlation term $\overline{u_1 u_2}$ grows up as both the mean velocity gradient and the transverse velocity fluctuations increase ; it is refrained by the rate of strain pressure correlation as seen in figure 15 (37).

The inhomogeneity of the field is taken into account by additional terms which are roughly evaluated. Where spreading flows are concerned, the entrainment process is not determined by the previous system. For lack of information other considerations are required. At the present time the treatment of both weak or strong inhomogenity and entrainment processes are in progress.

3.3. Large eddy simulation approach

If the largest structures are responsible for the rate of entrainment we cannot expect a fundamental improvement from methods which globally consider the fluctuating motions about the mean motion ; in other words, the usual splitting into mean and turbulent flow $U_i = \bar{U}_i + u_i$ may not be very adequate.

(†) In a first attempt introduced by Bradshaw (97) unique information has been used with the contraction $\overline{q^2} = \Sigma \overline{u_i u_j}$ for $i = j$ and a simple connection between $\overline{q^2}$ and $\overline{u_1 u_2}$ has been conjectured for a specific pattern of flow.

If the largest eddies are considered as deterministic structures substantial improvements might be made. The history of these structures should be considered in a Lagrangian frame and their entrainment capability might be reexamined through both an engulfing and a nibbling process. The method is briefly recalled.

Leonard (99) separates the velocity field $U_i(\vec{X},t)$ into a grid scale component $\hat{u}_i(\vec{X},t)$ and a subgrid component $u_i'(\vec{X},t)$ by using a weighing function $G(X/X')$

$$\hat{U}_i(\vec{X},t) = \int G[\vec{X}/\vec{X}'] \, U_i(\vec{X}',t) d\vec{X}'$$

$$U_i = \hat{u}_i + u'_i \quad ; \quad \int G[\vec{X}/\vec{X}']d\vec{X}' = 1$$

The filtering operation is of course different from an averaging process which has a statistical meaning. A filtered quantity has to be considered as a typical event which can occur under any circumstances. This event, when it happens, develops in an environment the properties of which have to be considered in connection with the existence of the principal event. This should lead to conditional samplings supplemented by averaging operations.

If the physical properties of the fluid are constant the result of filtering the Navier-Stokes equation is :

$$\frac{\partial \hat{u}_i}{\partial t} + \frac{\partial}{\partial X_j} \widehat{\hat{u}_i \hat{u}_j} = - \frac{1}{\rho} \frac{\partial \hat{p}}{\partial X_i} + \nu \nabla^2 \hat{u}_i$$

This equation is supplemented by the continuity equation :

$$\frac{\partial \hat{u}_j}{\partial X_j} = 0$$

For the advection term it is found that :

$$\widehat{\hat{u}_i \hat{u}_j} = \widehat{\hat{u}_i \hat{u}_j} + \widehat{u'_i \hat{u}_j} + \widehat{\hat{u}_i u'_j} + \widehat{u'_i u'_j}$$

By using a series expansion it is found that :

$$\frac{\partial}{\partial X_j} \widehat{\hat{u}_i \hat{u}_j} = \frac{\partial}{\partial X_j} [\hat{u}_i \hat{u}_j] + \frac{\partial}{\partial X_j} [\frac{\Delta^2}{\gamma} \frac{\partial}{\partial X_k} \frac{\partial}{\partial X_k} \hat{u}_i \hat{u}_j]$$

The Leonard term can be written

$$L_{ij} = \widehat{\hat{u}_i \hat{u}_j} - \hat{u}_i \hat{u}_j$$

The product of filtered quantities is considered with or without additional filtering.

The "cross term"

$$C_{ij} = \widehat{\hat{u}_i u'_j} + \widehat{u'_i \hat{u}_j}$$

represents interactions between the residual field and the filtered field. "A priori" this sort of interaction should not be located in spectral space.

On the other hand, the subgrid Reynolds tensor $R_{ij} = \widehat{u'_i u'_j}$ emphasizes the role of small structures only. However, it can be proved that such interactions can occasionally generate structures far outside the subgrid scale from a triadic analysis.

We set $T_{ij} = R_{ij} + C_{ij}$

and introduce the deviatoric tensor : $\tau_{ij} = T_{ij} - \frac{1}{3} T_{kk} \delta_{ij}$

On the other hand we write :

$$\bar{p} = \frac{\hat{p}}{\rho} + \frac{1}{3} T_{kk}$$

Finally we have :

$$\frac{\partial \hat{u}_i}{\partial t} + \frac{\partial}{\partial X_j} \hat{u}_i \hat{u}_j = - \frac{\partial \bar{p}}{\partial X} - \frac{\partial}{\partial X_j} . [L_{ij} + \tau_{ij}]$$

Subsequent workers have followed Smagorinski (100) and write

$$\tau_{ij} = - \nu_N \left[\frac{\partial \tilde{u}_i}{\partial X_j} + \frac{\partial \tilde{u}_j}{\partial X_j} \right]$$

for the "subgrid term".

Such an assumption gives rise to several remarks. For sake of brievety we will emphasize some difficulties probably originating from Smagorinsky's assumption. Non-linear interactions between turbulence structures are very complex ; reverse cascades of energy can occur. For these exchanges energy comes from structures belonging to the subgrid structures and goes to structures belonging to the filtered field. Gence has shown that these exchanges essentially depend on the relative position of the principal axes of the mean field (with respect to the principal axes of the Reynolds stress tensor). In the case under consideration a feedback mechanism can take place for adequate relative positions of the principal axes of the filtered field with respect to those of the subgrid field. Introducing a crude hypothesis through a turbulent eddy viscosity, Smagorinsky eliminated this "back scattering". Comparisons which have been made with an extended EDQNM method support this assumption (101, 102).

In spite of this difficulty computing times are very large. Nevertheless we can expect some illuminating information provided that an adequate numerical scheme is introduced.

We previously indicated that complex flows such as impinging jets can be viewed as a synthesis of diverse flow modulus. Where modelling methods are concerned we could develop some typical approaches concerning the impinging area. In fact, this region can be considered as preferentially marked by a strong curvature of the mean streamlines associated with a strong straining process. We just recall that Coriolis effects have recently been analyzed by spectral methods (68), theoretical results being in good agreement with more or less empirical relations (48). As for the rapid distorsion which is imposed on the turbulent field, it can be treated as a linear problem the characteristic time of the turbulence being rather large in comparison with the residence term (the time taken by a turbulent structure to travel from E to F, fig. 1). Strong curvatures effects probably restrain instabilities so that the entrainment is rather weak in this region, a fact which is connected with curved wall jet development (concave wall). A relative stability of the flow can also be detected in the near region downstream of the impinging zone.

4. CONCLUSION

The turbulent mechanisms inherent in the development of free turbulent flows are not completely understood. Homogeneous flows have been thoroughly analyzed and information is available ; on the contrary the contamination of the non-turbulent region by turbulent flows remains a challenging problem in spite of vigorous efforts : sophisticated investigations by means of hot wire or laser anemometers have been carried out and many experiments data are available. For lack of adequate theory, the entrainment process exhibits many aspects, the dynamic of large structures being probably a relevant parameter. The existence and the shape of these structures probably depends on the overall field. Under some circumstances they have a deterministic origin ; in other cases they can be considered as belonging to either a deterministic process or a statistical one. We can conjecture that in typical configurations, such as mixing zones, they are a sequel of a transition phenomenon which prevails even far from the exit nozzle. In the near future it will be very useful to carry out careful investigations in order to clarify these questions.

APPENDIX

In order to understand the role played by the pressure field we examine the partial differential system :

$$U_1 \frac{\partial U_1}{\partial X_1} + U_2 \frac{\partial U_1}{\partial X_2} = - \frac{1}{\rho} \frac{\partial P}{\partial X_1}$$

$$U_1 \frac{\partial U_2}{\partial X_1} + U_2 \frac{\partial U_2}{\partial X_2} = - \frac{1}{\rho} \frac{\partial P}{\partial X_2}$$

$$\frac{\partial U_1}{\partial X_1} + \frac{\partial U_2}{\partial X_2} = 0$$

In the momentum equation the viscous terms have been dropped. With these terms second derivatives appear which obliterate the role of the pressure and velocity field. Anyway, for incompressible fluids, viscous terms do not play a direct role in Poisson's equation ; they intervene through the velocity field only. A singular perturbation problem appears if these second order terms tend to zero.

In its complete form the system gives rise to a complex set of characteristic lines.

. Imaginary roots correspond to an elliptic behaviour of the system strictly linked to the role of the pressure terms. All the parts of the flow are closely connected with each other through this pressure term.

. The real root corresponds to an hyperbolic behaviour of the system. The characteristic curves are the streamlines, and disturbances can be propagated along these streamlines.

By introducing Prandtl's assumption the system takes a simpler form

$$U_1 \frac{\partial U_1}{\partial X_1} + U_2 \frac{\partial U_1}{\partial X_2} = - \frac{1}{\rho} \frac{\partial P}{\partial X_1}$$

$$\frac{\partial P}{\partial X_2} = 0$$

$$\frac{\partial U_1}{\partial X_1} + \frac{\partial U_2}{\partial X_2} = 0$$

The characteristic system is composed of :

. streamlines in connection with a real root ;

. normal lines to the mean velocity U_1 (double real roots). Disturbances can be propagated normally to the streamlines

$$(\frac{\partial P}{\partial X_2} = 0),$$

and the pressure field becomes a given external force which has the same value at any point of the normal characteristic line.

BIBLIOGRAPHY

(1) M. SUNYACH & J. MATHIEU, Zone de mélange d'un jet plan : fluctuations induites dans le cône à potentiel, intermittence. Int. J. Heat and Mass Trans., vol. 12, 1969, p. 1679-1697.

(2) I. WIGNANSKY and H.E. FIEDLER, The two dimensional mixing region. J. Fluid Mech., vol. 41, part 2, 1970, p. 327-361.

(3) G.L. BROWN and A. ROSHKO, On density effects and large structure in turbulent mixing layer. J. Fluid Mech., vol. 64, part 4, 1974, p. 775-816.

(4) F.H. CHAMPAGNE, Y.H. PAO & I.J. WYGNANSKI, On the two dimensional mixing region. J. Fluid Mech., vol. 74, part 2, 1976, p. 209-250.

(5) C. BEGUIER, L. FULACHIER & J.F. KEFFER, The turbulent mixing layer with an asymmetrical distribution of temperature. J.F.M., vol. 89, part 3, 1978, p. 561-587.

(6) V.K. PUI & I.S. GARTSHORE, Measurement of the growth rate and structure in plane turbulent mixing layers. J.F.M., vol. 91, part 1, 1979, p. 111-130.

(7) S.P. RAJAGOPALAN & R.A. ANTONIA, Properties of the large structure in a slightly heated turbulent mixing layer of a plane jet. J.F.M., vol. 105, 1981, p. 261-281.

(8) L.J.S. BRADBURY, The structure of a self-preserving turbulent plane jet. J.F.M., vol. 23, part 1, 1965, p. 31-64.

(9) G. HESKESTAD, Hot wire measurements in a radial turbulent jet. Trans. of ASME, E, vol. 33, 1966, p. 417-424.

(10) I. WYGNANSKI & H.E. FIEDLER, Some measurements in the self-preserving jet. J.F.M., vol. 38, part 3, 1969, p. 577-612.

(11) M.M. RIBEIRO & J.H. WHITELAW, Statistical characteristics of a turbulent jet. J.F.M., vol. 70, part 1, 1975, p. 1-15.

(12) A.E. DAVIES, J.F. KEFFER & W.D. BAINES, "Spread of a heated plane turbulent jet. Physics of Fluids, vol. 18, n° 7, 1975, p. 770-775.

(13) P. CHASSAING & A. CLARIA, Transfert de masse dans des jets turbulents de révolution en milieu non homogène. Int. J. Heat and Mass Transfer, vol. 19, 1976, p. 249-258.

(14) H.H. BRUUN, A time domain analysis of the large-scale flow structure in a circular jet. Part 1 : moderate Reynolds number. J.F.M., vol. 83, part 4, 1977, p. 641-671.

(15) A.J. YULE, Large-scale structure in the mixing layer of a round jet. J.F.M., vol. 89, part 3, 1978, p. 413-432.

(16) J. TSO, L.S.G. KOVASZNAY & A.K.M.F. HUSSAIN, Search for large-scale coherent structures in the nearly self-preserving region of an axisymmetric turbulent jet. AIAA paper, n° 80-1355, 1980.

(17) J.C. LAU, Effects of exit Mach number and temperature on mean flow and turbulence characteristics in round jets. J.F.M., vol. 105, 1981, p. 193-218.

(18) J. MATHIEU, Contribution à l'étude aérothermique d'un jet plan évoluant en présence d'une paroi. Pub. Scien. Tech. Min. Air, n° 374, 1959.

(19) A. TAILLAND & J. MATHIEU, Jet pariétal. Journal de Mécanique, vol. 6, n° 1, 1967, p. 103-131.

(20) F. SPETTEL, J. MATHIEU & J.F. BRISON, Tension de Reynolds et production d'énergie cinétique turbulente dans les jets pariétaux sur paroi plane et concave. Journal de Mécanique, vol. 11, n° 3, 1972, p. 403-425.

(21) H.P.A.H. IRWIN, Measurements in a self-preserving plane wall jet in a positive pressure gradient. J.F.M., vol. 61, part 1, 1973, p. 33-64.

(22) R.A. BAJURA & M.R. CATALANO, Transition in a two dimensional plane wall jet. J.F.M., vol. 70, part 4, 1975, p. 773-799.

(23) N.V. CHANDRASEKHARA SWAHY & P. BANDYOPADHYAY, Mean and turbulence characteristics of three-dimensional wall jets. J.F.M., vol. 71, part 3, 1975, p. 541-562.

(24) E. ALCARAZ, G. CHARNAY & J. MATHIEU, Measurements in a wall jet over a convex surface. Physics of Fluids, vol. 20, n° 2, 1977, p. 203-210.

(25) S. BELTAOS & N. RAJARATNAM, Plane turbulent impinging jet. J. of Hydrau. Res., vol. 11, n° 1, 1973, p. 29-59.

(26) C.D. DONALDSON & R.S. SNEDEKER, A study of free jet impingement. J. Fluid Mech., vol. 45, part 3, 1971, p. 477-512.

(27) H.W. LIEPMANN & J. LAUFER, Investigation of free turbulent mixing. NACA Tech., note 1257, 1947.

(28) M. SUNYACH, Contribution à l'étude des frontières d'écoulements libres. Thèse Université Lyon I, n° 37, 1971.

(29) A.K.M.F. HUSSAIN & Z.D. HUSAIN, Turbulence structure in the axisymmetric free mixing layer.

(30) S. CORRSIN, Investigation of flow in an axially symmetrical heated jet of air. NACA Report 3L23, 1943.

(31) R. CURTET & F.P. RICOU, On the tendency to self-preservation in axisymmetric ducted jets. Trans. of A.S.M.E., B. Eng., 1964, p. 765-776.

(32) K.W. EVERITT & A.G. ROBINS, The development and structure of turbulent plane jets. J. Fluid Mech., vol. 88, part 3, 1978, p. 563-583.

(33) B. BRADSHAW & M.T. GEE, Turbulent wall jets with and without an external stream. Rep. and Mem. n° 3252, 1960.

(34) A.A. TOWNSEND, The structure of turbulent shear flow. Cambridge University Press, Cambridge, England, 1956.

(35) G. COMTE-BELLOT & S. CORRSIN, Simple Eulerian time correlation of full and narrow-band velocity signals in grid-generated isotropic turbulence. J. Fluid Mech., vol. 48, part 2, 1971, p. 273-337.

(36) M. SUNYACH & J. MATHIEU, Zone de mélange d'un jet plan. C.R.A.S. Paris, t. 268, 1969, p. 655-658.

(37) J. MATHIEU, Remarks on turbulent flows with free stream boundaries. Von Karman Lecture Series, n° 36, 1971.

(38) J. SABOT, G. CHARNAY & G. COMTE-BELLOT, Intermittent phenomena in turbulent shear flows, Euromech 63, Denmark, 1975.

(39) J. SABOT & G. COMTE-BELLOT, Intermittency of coherent structures in the core region of fully developed turbulent pipe flow. J. Fluid Mech., vol. 74, part 4, 1976, p. 767-796.

(40) J.M. WALLACE, H. ECKELMANN & R.S. BRODKEY, The wall region in turbulent shear flow. J. Fluid Mech., vol. 54, part 1, 1972, p. 39-48.

(41) S. ESKINAZI & V. KRUKA, The wall jet in a moving stream. Syr. Univ. Res. Inst., Rep. ME 937-6309, 1963.

(42) D.E. GUITTON, Some contributions of the study of equilibrium and non equilibrium turbulent wall jet over curved surface. Thesis Mc Gill Univ., 1970.

(43) S.C. KACKER & J.H. WHITELAW, An experimental investigation of the influence of slot-lip thickness on the impervious-wall effectiveness of the uniform density two dimensional wall jet. Int. Jour. of Heat and Mass Trans., vol. 12, n° 9, 1969, p. 1196-1201.

(44) K. HANJALIC & B.E. LAUNDER, A Reynolds stress model of turbulence and its application to thin shear flow. J. Fluid Mech., vol. 52, part 4, 1972, p. 609-638.

(45) J. LUMLEY, Prediction methods for turbulent flows. Von Karman Lecture series, 1976.

(46) J. MATHIEU & D. JEANDEL, Prediction methods for turbulent flows. Von karman Lecture Series n° 76, 1975.

(47) E. ALCARAZ, G. GUILLERMET & J. MATHIEU, Mesure de coefficients de frottements pariétaux à l'aide de tube de preston. C.R.A.S. Paris, A, 1968, p. 432-434.

(48) P. BRADSHAW, Effects of streamlines curvature on turbulent flow. NATO, AGARDOGRAPH n° 169, 1973.

(49) W.C. REYNOLDS & M.C. POTTER, Finite amplitude instability of parallel shear flow. J. Fluid Mech., vol. 27, part 3, 1967, p. 465-492.

(50) P.G. SAFFMAN, Theoretical survey of coherent structures in turbulent flows. Proceedings of the role of coherent structure in modelling turbulence and mixing (Madrid 1980). Lecture Notes in Physics n° 136, Springer Verlag.

(51) L.S.G. KOVASZNAY, V. KIBENS & R.F. BLACKWELDER, Large-scale motion in the intermittent region of a turbulent boundary layer. J. Fluid Mech., vol. 41, part 2, 1970, p. 283-325.

(52) R.A. ANTONIA, A. PRABHU & S.E.STEPHENSON, Conditionnally sampled measurements in a heated turbulent jet. J. Fluid Mech., vol. 72, part 3, 1975, p. 455-480.

(53) G. CHARNAY, J. MATHIEU & G. COMTE-BELLOT, Response of turbulent boundary layer to random fluctuation in the external stream. Physics of Fluids, vol. 19, 1976, p. 1261-1272.

(54) C. DOPAZO, On conditioned averages for intermittent turbulent flows. J. Fluid Mech., vol. 81, part 3, 1977, p. 433-438.

(55) H. ECKELMANN & J.M. WALLACE, A comparison between pattern recognition methods and the VITA detection scheme in wall bounded turbulent shear flow. Proceedings of the role of coherent structure in modelling turbulence and mixing (Madrid 1980), Lecture Notes in Physics, n° 136, Springer Verlag.

(56) J. MATHIEU & G. CHARNAY, Experimental methods in turbulent structure research. Proceedings of the role of coherent structure in modelling turbulence and mixing (Madrid 1980), Lecture Notes in Physics n° 136, Springer Verlag.

(57) W.G. HILL & R.C. JENKINS, Effects of the initial boundary layer state on turbulent jet mixing. AIAA Journal, vol. 14, n° 11, 1976, p. 1513-1514.

(58) D. OSTER, B. DIOMBA, H. FIEDLER & I. WYGNANSKI, On the effect of initial conditions on the two dimensional turbulent mixing layer. Structure and Mechanism of turbulence I, edited by H. FIEDLER, Springer, New York, 1978, p. 48-64.

(59) L. BOGUSZAWSKI & G. POPIEL, Flow structure of the free round turbulent jet in the initial region. J. Fluid Mech., vol. 90, part 3, 1979, p. 531-539.

(60) Z.D. HUSAIN & A.K.M.F. HUSSAIN, Axisymmetric mixing layer : influence of the initial and boundary conditions. AIAA Journal, vol. 17, n° 1, 1979, p. 48-55.

(61) S.C. CROW & F.H. CHAMPAGNE, Orderly structure in jet turbulence. J. Fluid Mech., vol. 48, part 3, 1971, p. 547-591.

(62) P.O.A.L. DAVIES & A.J. YULE, Coherent structures in turbulence. J. Fluid Mech., vol. 69, part 3, 1975, p. 513-537.

(63) J. LAUFER, New bends in experimental turbulence research. An. Rev. of Fluid Mech., vol. 7, 1975, p. 307-326.

(64) P.G. SAFFMAN, The number of waves on unstable vortex rings. J. Fluid Mech., vol. 84, part 4, 1978, p. 625-639.

(65) A. ROSHKO, The plane mixing layer flow visualization results and three dimensional effects. Proceedings of the role of coherent structure in modelling turbulence and mixing (Madrid 1980), Lecture Notes in Physics n° 136, Springer Verlag.

(66) C.C. CHANDRSUDA, R.D. MEHTA, A.D. WEIR & P. BRADSHAW, Effect of free-stream turbulence on large structures in turbulent mixing layers. J.F.M., vol. 85, part 4, 1972, p. 693-704.

(67) J.P. BERTOGLIO, G. CHARNAY & J. MATHIEU, Effects de la rotation sur un champ turbulent cisaillé : application au cas des turbomachines. Journal de Mécanique, vol. 4, n° 4, 1980, p. 421-443.

(68) J.P. BERTOGLIO, Homogeneous turbulent field within a rotating frame. 13th AIAA Conference, Snowmass - Colorado, 1980.

(69) J.P. SCHON, J. MATHIEU, A. BAILLE, J. SOLAL & G. COMTE-BELLOT, Experimental study of diffusion processes in unstable stratified boundary layers. Advances in Geophysics, vol. 18, B, 1974, p. 265-272.

(70) A. CRAYA, Contribution à l'analyse de la turbulence associée à des vitesses moyennes. Pub. Sci. et Tech. Min. Air, n° 345, 1958.

(71) F.H. CHAMPAGNE, V.G. HARRIS & S. CORRSIN, Experiments on nearly homogeneous turbulent shear flow. J. Fluid Mech. , vol. 41, part 1, 1970, p. 81-139.

(72) J.N. GENCE, Action de deux déformations pures planes successives sur une turbulence homogène et isotrope. Thèse de Doctorat d'Etat, Université Claude Bernard, Lyon I, 1979.

(73) J.N. GENCE & J. MATHIEU, The return to isotropy of an homogeneous turbulence having been submitted to two successive plane strains. J.F.M., vol. 101, part 3, 1980, p. 555-566.

(74) J. MATHIEU & D. JEANDEL, Pathological cases in turbulent field and spectral approach. I.V.K. Lecture Series 1979-2, Prediction methods for turbulent flows, January 15-19, 1979.

(75) S. CORRSIN, Investigation of the behaviour of Parall, two dimensional air jets. NACA W 90, 1944.

(76) D.F. DURAO & J.H. WHITELAW, Turbulent mixing in the developing region of coaxial jets. Trans. A.S.M.E., Fluid Eng., vol. 95, n° 3, 1973, p. 467.

(77) J.H. WHITELAW & M.M. RIBEIRO, Turbulent mixing of co-axial jets with particular reference to the near exit region. Imp. Coll. of Sce and Techn. Report N 74 15966, 1973.

(78) A. KROTHAPALLI, D. BAGANOFF & K. KARAMCHETI, Development and structure of a rectangular jet in a multiple jet configuration. AIAA Journal, vol. 18, n° 8, 1980, p. 945-950.

(79) V.W. GOLDSCHMIDT & P. BRADSHAW, Flapping of a plane jet. Physics of Fluids, vol. 16, n° 3, 1973, p. 354-355.

(80) C.M. HO & N.S. NOSSEIR, Dynamics of an impinging jet. Part 1 : the feedback phenomenon. J. Fluid Mech., vol. 105, 1981, p. 119-142.

(81) J. KESTIN & R.T. WOOD, On the stability of two dimensional stagnation flow. J. Fluid Mech., vol. 44, part 3, 1970, p. 461-479.

(82) P.J. LAMONT & B.L. HUNT, The impingement of under expanded axisymmetric jets on perpendicular and inclined flat paltes. J. Fluid Mech., vol. 100, part 3, 1980, p. 471-511.

(83) H.M. Mc MAHON, D.D. HESTER & J.G. PALFERY, Vortex shedding from a turbulent jet in a cross-wind. J. Fluid Mech., vol. 48, part 1, 1971, p. 73-80.

(84) J.F. CAMPBELL & J.A. SCHETZ, Analysis of the injection of a heated turbulent jet into a cross-flow. NASA TR R-413, 1974.

(85) Z.M. MOUSSA, J.W. TRISCHKA & S. ESKINAZI, The near field in the mixing of a round jet with a cross-stream. J. Fluid Mech. , vol. 80, part 1, 1977, p. 49-80.

(86) D. ADLER & A. BARON, Prediction of a three dimensional circular turbulent jet in cross-flow. AIAA Journal, vol. 17, n° 2, 1978, p. 168-173.

(87) E. LE GRIVES, Mixing process induced by the vorticity associated with the penetration of a jet into a cross-flow. Trans. A.S.M.E., Jour. of Eng. for Power, vol. 100, n° 3, 1978, p. 465-475.

(88) R.A. PETERSEN, R.E. KAPLAN & J. LAUFER, Ordered structure and jet noise. NASA Contractor, Rep. 134733, 1974.

(89) C.J. MOORE, The role of shear-layer instability waves in jet exhaust noise. J. Fluid Mech., vol. 80, part 2, 1977, p. 321-367.

(90) D. JUVE, M. SUNYACH & G. COMTE-BELLOT, Intermittency of the noise emission in subsonic cold jets. J. Sound Vib., vol. 71, n° 3, 1980, p. 319-332.

(91) R.E. KELLY, On the stability of an inviscid shear layer which is periodic in space and time. J. Fluid Mech., vol. 27, part 4, 1967, p. 657-689.

(92) C.J. MOORE, The effect of shear layer instability on jet exhaust noise. Structure and Mechanisms of Turbulence, Berlin, 1977.

(93) P. DENEUVILLE & J. JACQUES, Jet noise amplification : a practically important problem. AIAA, 4th Aeroacoustics Conf., Atlanta, Georgia, 3-5 octobre, 1977.

(94) D. JUVE & M. SUNYACH, Radiation properties of a turbulent jet excited by a sinusoïdal acoustic disturbance. International Symposium on the Mechanics of Sound Generation in Flows, Göttingen, 1979.

(95) J. MATHIEU, Idées actuelles sur la turbulence. CANCAM 79, Sherbrooke, ter, 1979, p. 465-502.

(96) C. BRAUNER, D. JEANDEL & J. MATHIEU, Some approaches to turbulence problems. Non linear problems : present and future. Center for non linear studies, Los Alamos, New Mexico, March 2-6, 1981.

(97) P. BRADSHAW, D.H. FERRIS & N.P. ATWELL, Calculation of boundary layer development using the turbulent energy equation. J.F.M., vol. 28, part 3, March 3rd, 1967, p. 593-616.

(98) D. JEANDEL, J.F. BRISON & J. MATHIEU, Modelling methods in physical and spectral space. Physics of Fluids, vol. 21, n° 2, February, 1978, p. 169-182.

(99) A. LEONARD, Energy cascade in large-eddy simulations of turbulent fluid flows. Adv. in Geophys, 1974.

(100) J.S. SMAGORINSKY, General circulation experiments with the primitive equations, I : the basic experiment, Mon. Weath. Rev., 91, 1963, p. 99.

(101) D.C. LESLIE, Developments in the theory of turbulence, Clarendon Press, Oxford, 1973.

(102) C. CAMBON, D. JEANDEL & J. MATHIEU, Spectral modelling of homogeneous non isotropic turbulence. J. Fluid Mech., vol. 104, 1981, p. 247-262.

ACKNOWLEDGEMENTS

We are very indebted to Professor J. WALLACE for his comments and helpful assistance. We should like to thank M. SUNYACH and E. ALCARAZ for their contributions and C. BURNET, J. KREISS and O. PERRONNET for their technical support.

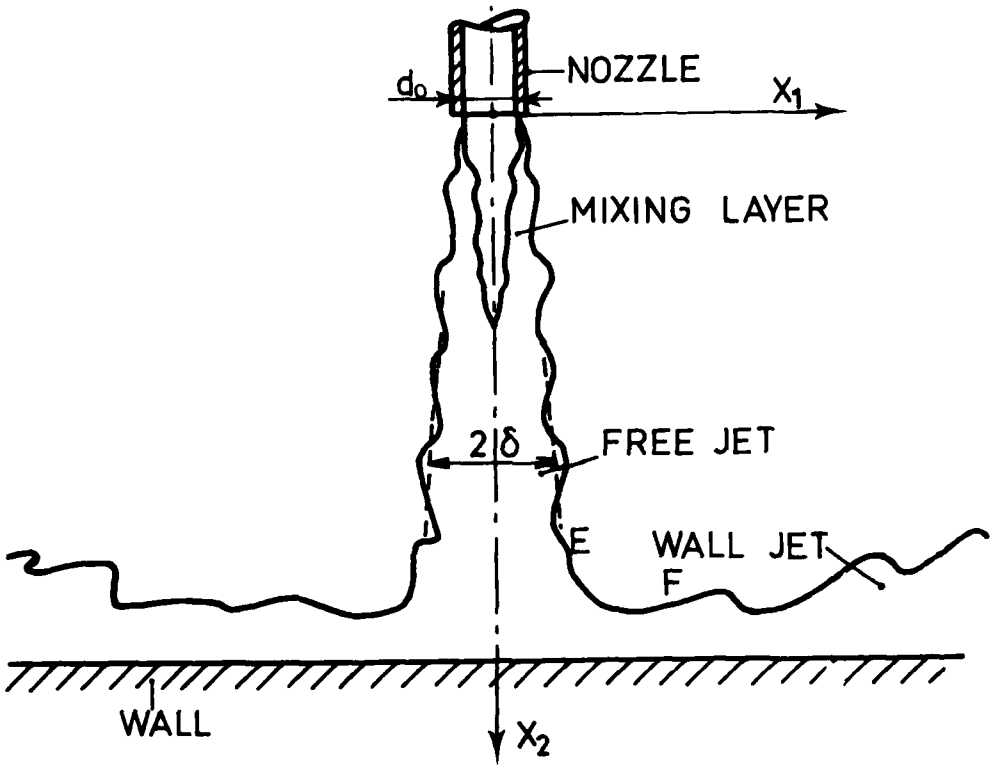

FIG. 1 - SKETCH OF AN IMPINGING JET.

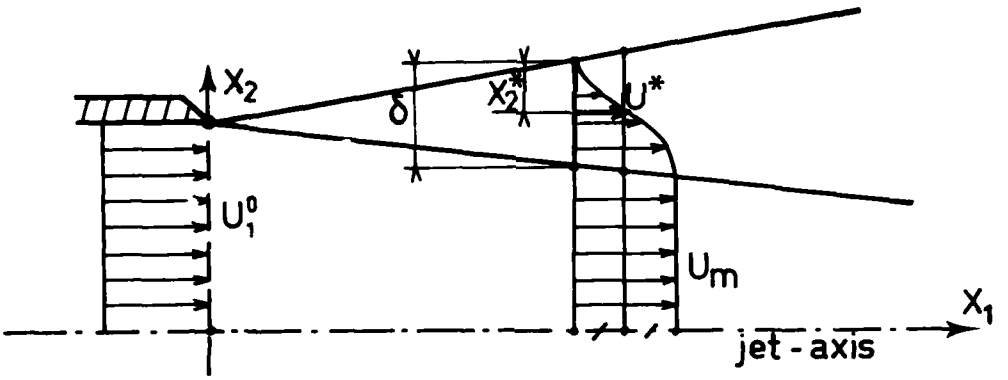

FIG. 2 - EQUILIBRIUM PROFILES OF VELOCITY IN A MIXING LAYER.

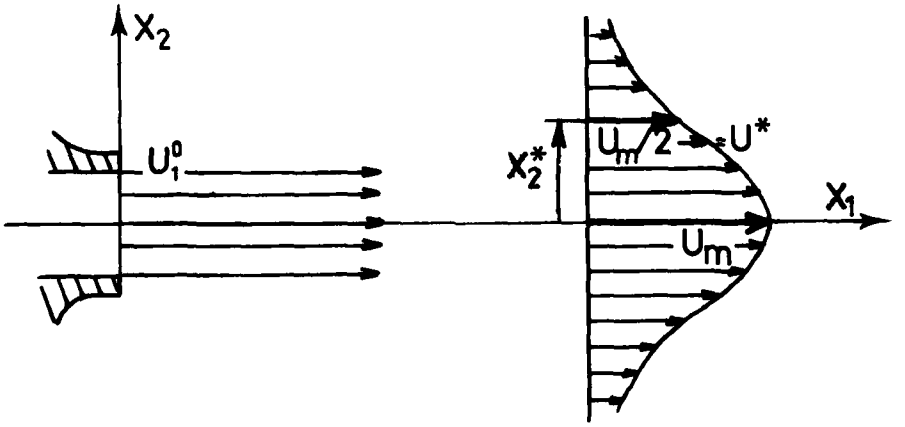

FIG. 3 - EQUILIBRIUM PROFILES OF VELOCITY IN A FREE JET.

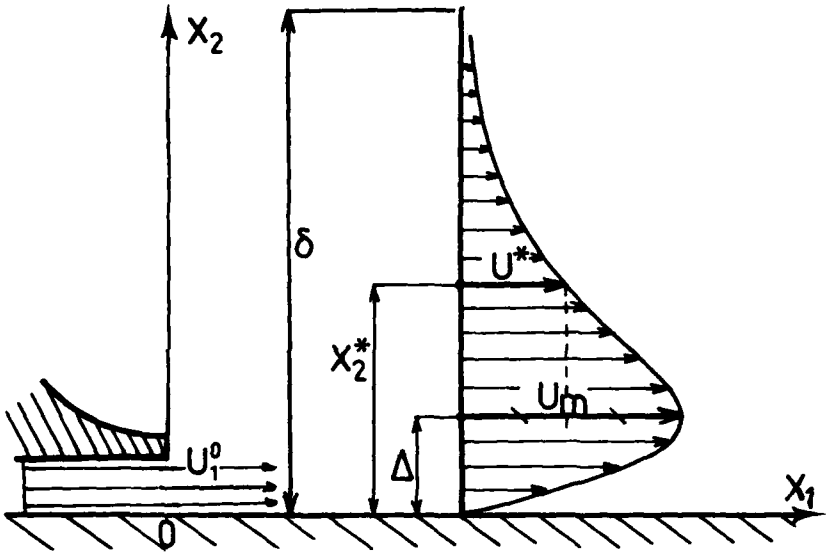

FIG. 4 - EQUILIBRIUM PROFILES OF VELOCITY IN A WALL JET.

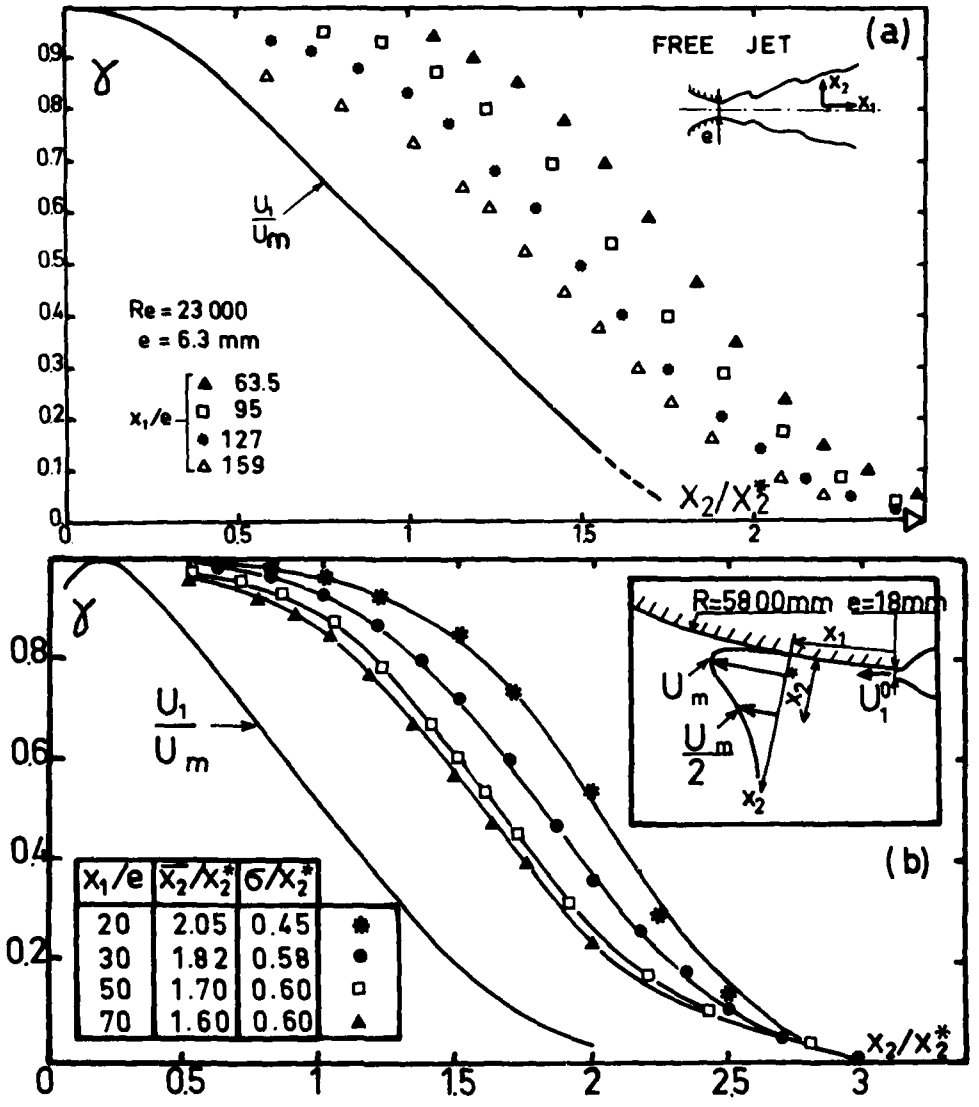

FIG. 5 - AXIAL EVOLUTION OF THE INTERMITTENCY FACTOR PROFILES.
A) FREE JET (SUNYACH, 28).
B) WALL JET (ALCARAZ, CHARNAY AND MATHIEU, 24).

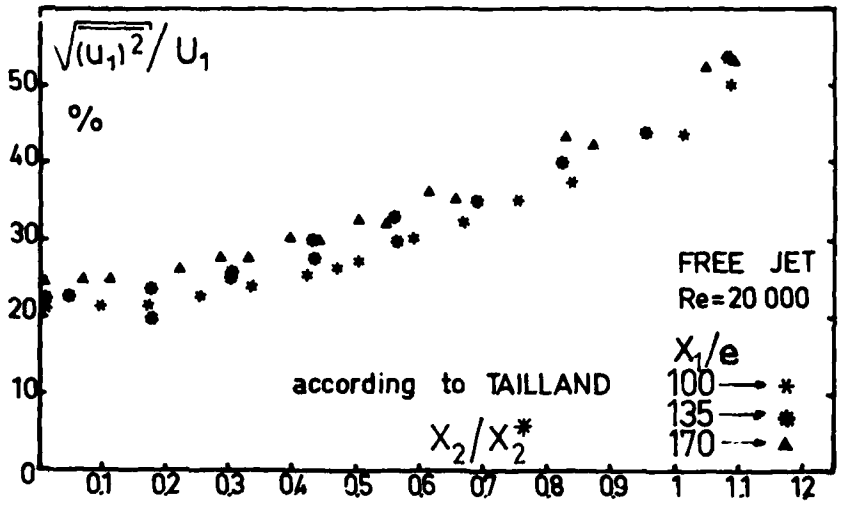

FIG. 6 - AXIAL EVOLUTION OF THE TURBULENT INTENSITY ALONG A FREE JET (TAILLAND AND MATHIEU, 18).

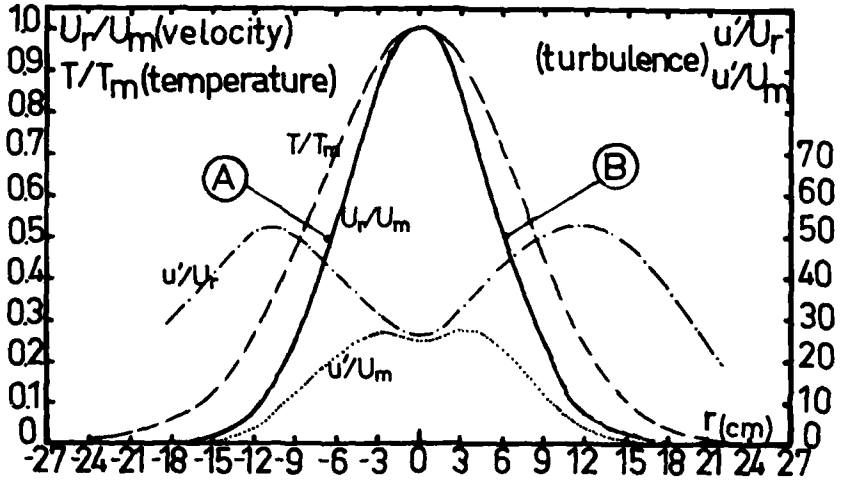

FIG. 7 - TRANSVERSE DISTRIBUTION OF THE TURBULENT INTENSITY ACROSS A FREE JET (CORRSIN, 30).

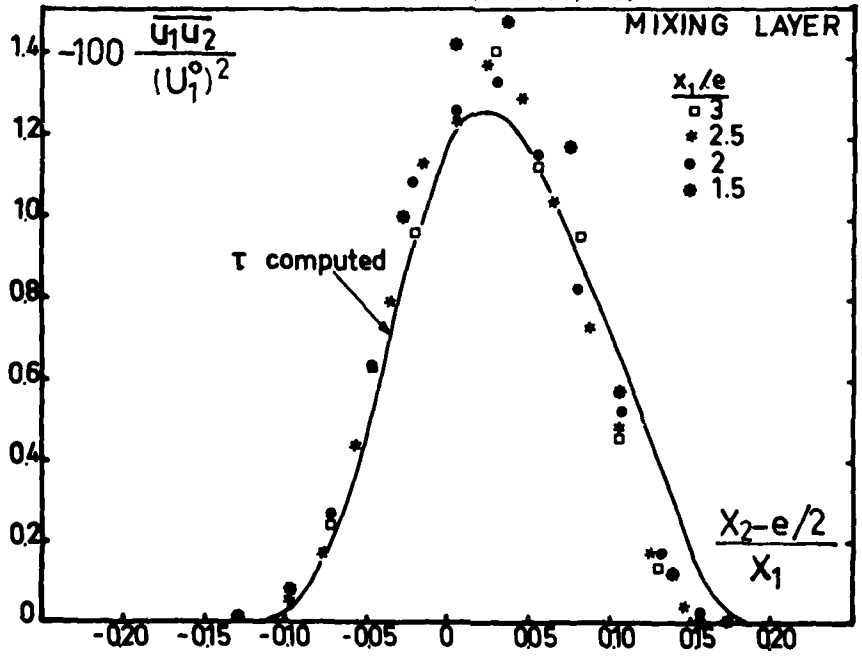

FIG. 8 - REYNOLDS SHEAR STRESS IN A MIXING LAYER (SUNYACH AND MATHIEU, 36).

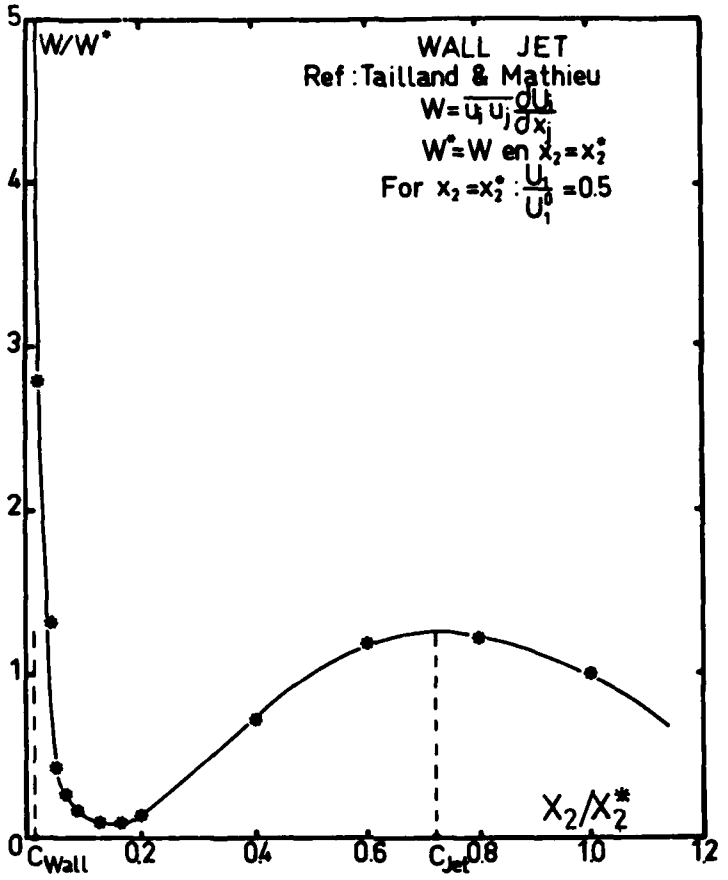

FIG. 9 - PRODUCTION OF KINETIC ENERGY $\overline{q^2}$ IN A WALL JET (TAILLAND AND MATHIEU, 18).

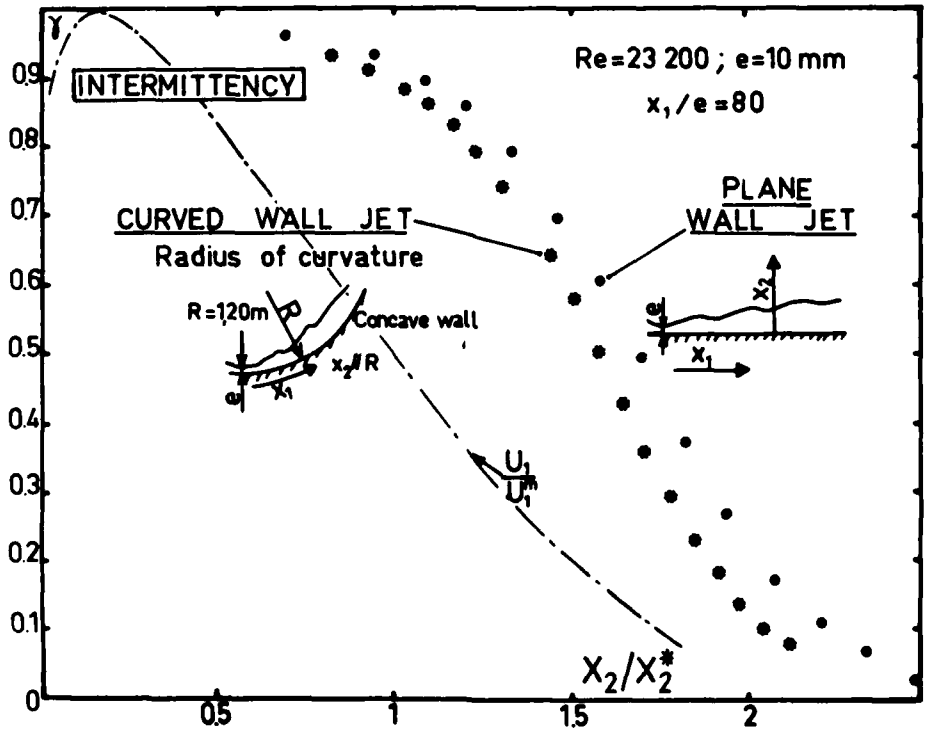

FIG. 10 - EFFECT OF CURVATURE ON THE INTERMITTENCY FACTOR IN A WALL JET (SUNYACH, 28).

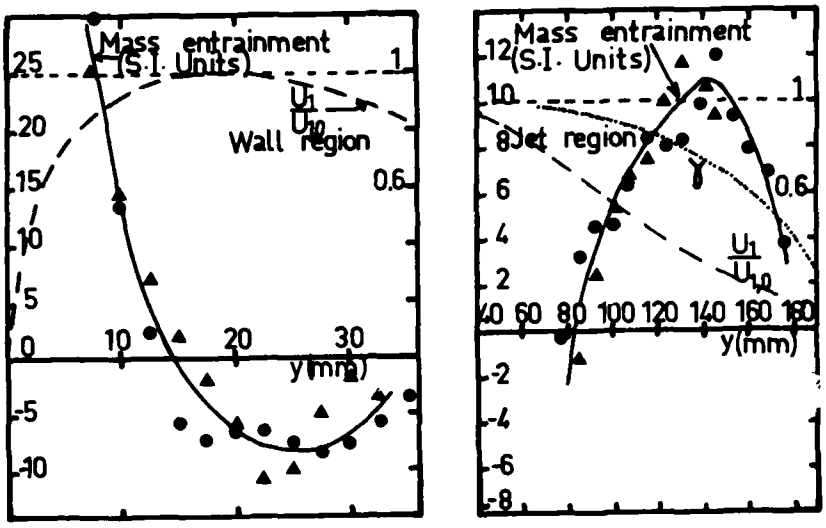

FIG. 11 - TERMS OF MASS ENTRAINMENT IN CONDITIONED EQUATIONS : $\partial(1-\gamma)U^e/\partial X + \partial(1-\gamma)V^e/\partial y$ WALL JET (ALCARAZ & AL, 24).

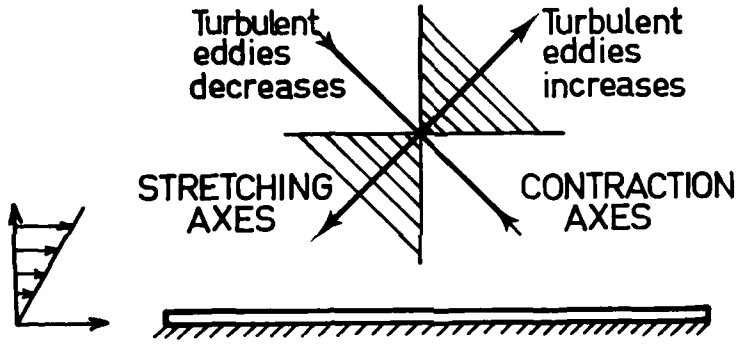

FIG. 12.a - DIRECTION OF AMPLIFICATION AND OF CONTRACTION OF THE TURBULENT EDDIES IN A SHEAR FLOW.

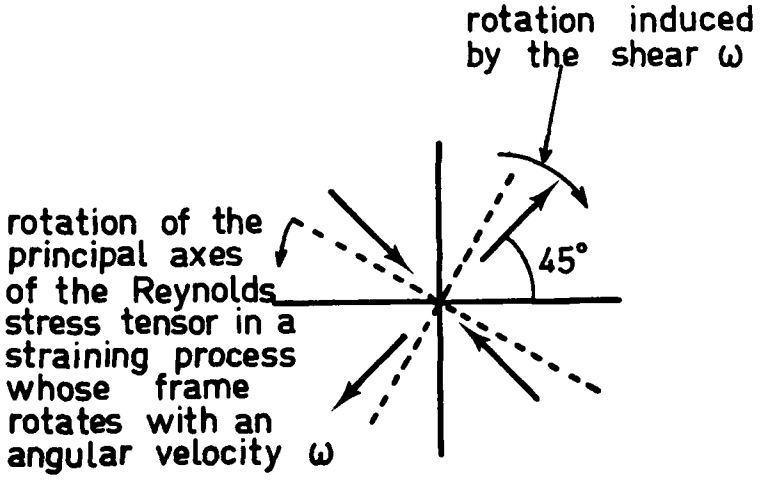

FIG. 12.b - ROTATION OF PRINCIPAL AXES OF THE REYNOLDS STRESS TENSOR AS OPPOSITE TO THE MEAN ROTATION ASSOCIATED WITH THE SHEAR.

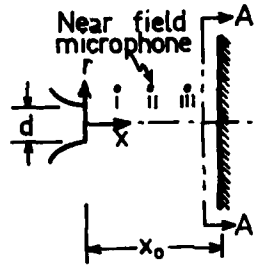

Schematic diagram of the impinging jet.

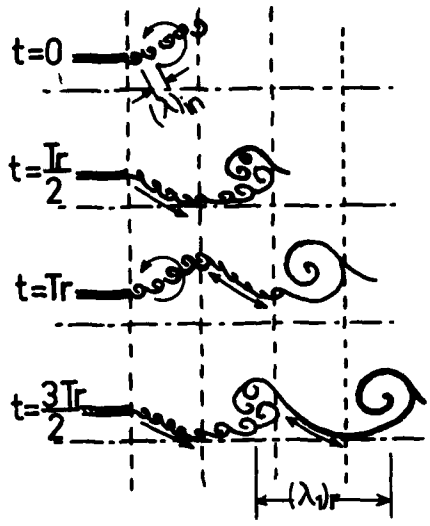

FIG. 13 - COLLECTIVE INTERACTION IN AN IMPINGING JET (HO AND NOSSEIR, 80) (HIGH SPEED SUBSONIC JET, X PLATE/d_o < 7.5).

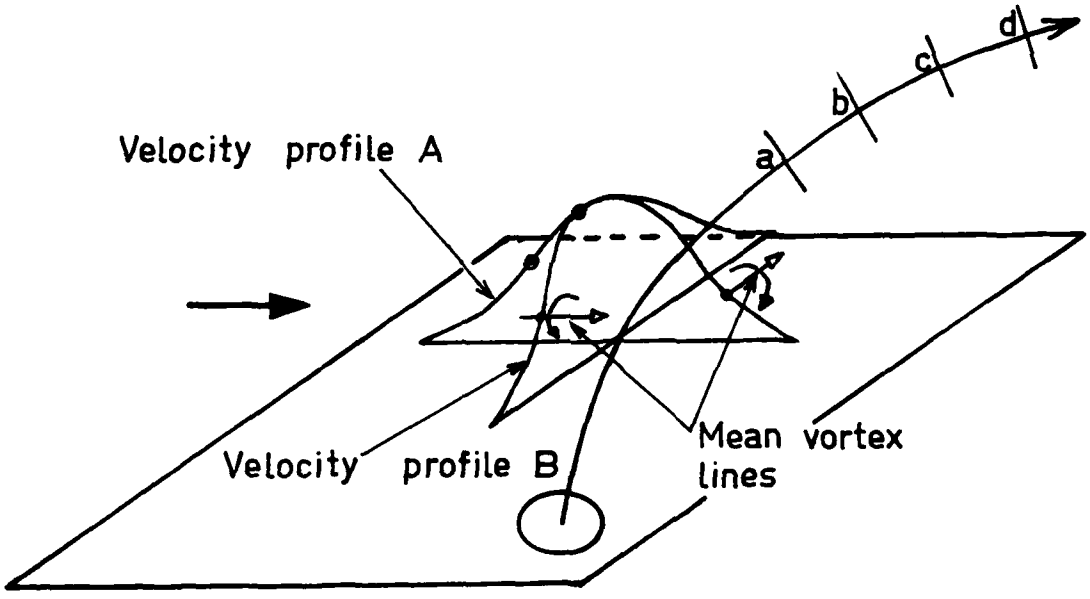

FIG. 14.a - SKETCH OF THE CENTRE-LINE OF JET IN CROSS-FLOW.

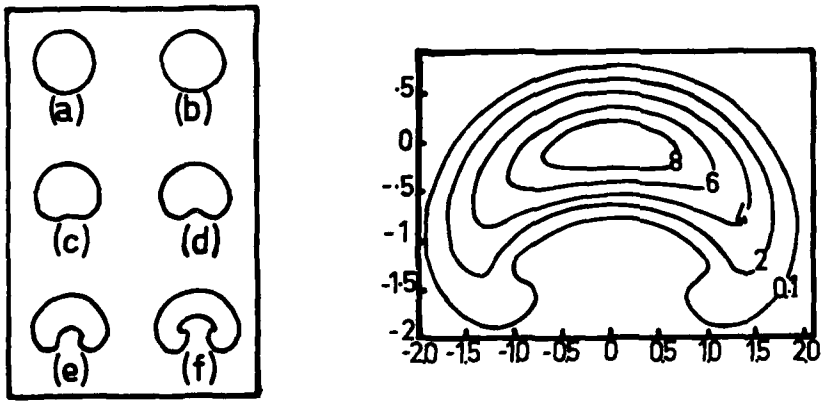

FIG. 14.b - DEVELOPMENT OF JET CROSS SECTIONS DOWNSTREAM ALONG ITS CENTRE-LINE AND LINE OF CONSTANT VELOCITY (ADLER AND BARON, 86).

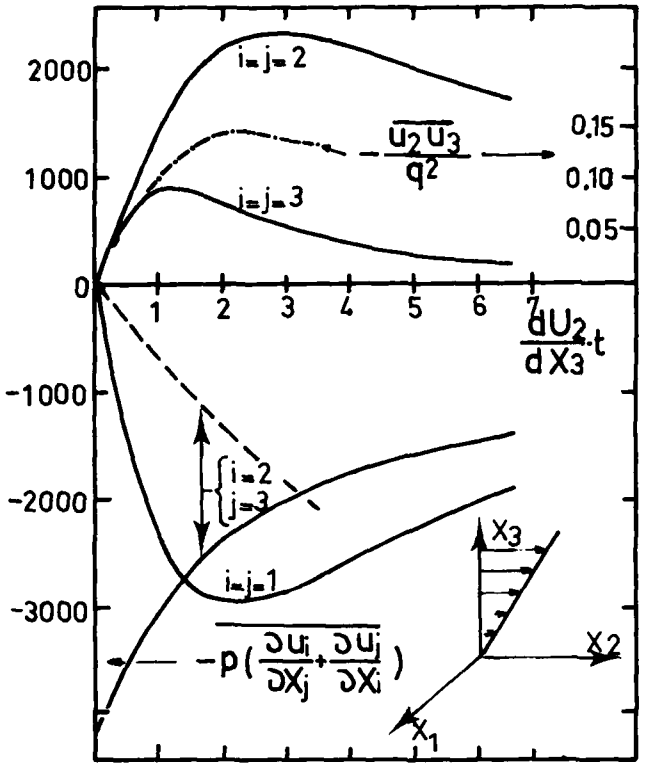

FIG. 15 - SHEAR STRESS AND VELOCITY PRESSURE CORRELATION
IN A UNIFORM SHEAR FLOW
— LINEAR COMPUTATION (WITHOUT TRIPLE CORRELATION)
--- APPROXIMATIVE SHAPE OF THE NON LINEAR PART OF THE VELOCITY PRESSURE CORRELATION.

A ROW OF JETS IN A CROSSFLOW

by

Z.A. Khan, J.J. McGuirk and J.H. Whitelaw

IMPERIAL COLLEGE OF SCIENCE AND TECHNOLOGY
Department of Mechanical Engineering
Fluids Section, London SW7 2BX

SUMMARY

Measurements and calculations are reported for the flow downstream of a single row of round jets discharging vertically into a confined horizontal cross-stream. The measurements include mean axial velocity and scalar concentration distributions, for pitch-to-diameter ratios (S/D) of 2 and 4, tunnel heights (H) of 4 and 8 jet diameters and a jet-to-mainstream velocity ratio of 2.3. Experimental results show that no impingement of the jets occurs on the upper wall even for the larger S/D and smaller H/D values. When S/D is reduced the jets quickly coalesce laterally and this trend towards two-dimensional flow inhibits impingement by acting to depress jet trajectories. Although jet spreading rates are similar for both pitch-to-diameter ratios, the rapid loss of individual jet identity for the smaller value, is clearly illustrated by qualitative differences in the measured velocity contour shapes on the furthest downstream cross-plane.

The calculated results were obtained by solving the steady three-dimensional elliptic form of the Reynolds equations with a two-equation model of turbulence. The effect of grid-refinement is examined and it is shown that numerical errors are still evident even for the finest grid used (20x20x30 nodes), but are not dominant and do not alter the general characteristics of the predicted flow behaviour. The effect of the boundary conditions in the plane of the jet exit are investigated and the results for the lower pitch-to-diameter ratio are shown to be sensitive to changes in these conditions. Comparison with the measured data shows good agreement for the larger pitch-to-diameter ratio, but only certain features are well predicted for the lower value. Finally, calculations are presented outside the range of measurements to quantify the influence of the blockage parameter on the flow development.

INTRODUCTION

The single jet in crossflow has been examined by many investigators and a review of previous work, as well as new measurements, is presented in reference 1. The properties of the flow in and around a row of jets in crossflow has received less attention with references 2 and 3 reporting some of the small number of measurements. Like the opposed rows of jets studied in reference 4, the emphasis of these previous multiple-jet investigations has been on characteristics relevant to gas-turbine dilution systems.

The results presented here relate to a single row of jets in crossflow with pitch-to-diameter ratios of 2 and 4, distances from the jet exit to wind-tunnel roof of 4 and 8 jet diameters and a jet-to-mainstream velocity ratio of 2.3. Measurements of mean flow properties were obtained with these arrangements and used to assess the accuracy of predictions obtained with a mathematical model of the flow which was subsequently used to extend the range of variables investigated experimentally.

The calculation method was based on the numerical solution of the steady, three dimensional elliptic form of the Reynolds equations and made use of the same computer program previously used in reference 5 to calculate the properties of a single jet in confined crossflow. The turbulence was represented by the two-equation model of reference 6. It is clear from the previous investigations of references 5, 7 and 8 that the number and location of grid nodes is limited by the finite computer storage available and can introduce significant numerical errors. As will be shown, the general characteristics of the flow are essentially grid independent and are in good agreement with measurement except for the lower pitch-to-diameter ratio case where the turbulence model does not reproduce the differring rates of vertical and lateral mixing observed in the measurements. The quality of the agreement is, however, sufficiently good to warrant the use of the method to investigate the influence of boundary conditions outside the range of the measurements.

The remainder of the paper is presented in four sections. The following section describes the experimental arrangement and presents the measured results. The calculation method, with preliminary grid-dependency tests and other computational details, is described in the third section and the calculated results are presented and compared with measurements in the fourth. A summary of the more important conclusions is presented in the final section.

FLOW CONFIGURATIONS AND MEASUREMENTS

The wind tunnel has a working section of 300 mm width and 200 mm height with five 25.4 mm holes located across the span of the floor with their centres separated by 50.8 mm. The holes were connected to 0.76 m long tubes which ensured fully-developed flow and

were located with their centre-lines 0.30 m downstream of a sandpaper trip. The arrangement is shown on figure 1 which also indicates the co-ordinate system and some of the symbols used below. The tunnel was operated with a mean velocity which was uniform over 90% of the inlet area of the tunnel and equal to 10.8 m/s. The average velocity in each pipe was 24.9 m/s, corresponding to a Reynolds number of 4.24×10^4.

The flow to the five holes, or three when a pitch-to-diameter ratio of four was required, was generated by a fan which passed the air to a plenum chamber and, through flexible piping, to the tubes connected to the holes. In the absence of cross-stream flow, mean velocity profiles obtained across two orthogonal diameters in the exit plane of each hole revealed maximum discrepancies in the flow rates obtained by integration of each of the twenty profiles of less than 1%. Comparison of the profiles revealed local discrepancies of not more than 6% of the maximum velocity value. In all cases, the exit profile conformed to fully developed turbulent pipe flow.

Measurements of mean velocity were obtained with an impact probe of external and internal diameters 1.1 and 0.61 mm respectively. A transducer and time-averaging voltmeter allowed reproducibility of pressure measurement of better than $\pm$ 1% for all measurements and considerably better at the higher velocities.

The local concentrations of a trace of helium gas, injected into the supply tube of the central jet upstream of the jet exit, was used to determine the location of jet fluid and was measured by sampling through the impact probe used for velocity measurements. Values of concentration were subsequently determined with a thermal conductivity cell. Further details of the main stream and jet flows, and of the measurement systems can be found in references 4 and 9.

Mean velocity and concentration contours, obtained by interpolation from a matrix of individual measurements are shown on figures 2 to 5 for ratios of duct height to hole diameter of 8 and 4 and for pitch-to-diameter ratios of 2 and 4. In each of the four cases, contours are presented at locations four and eight diameters downstream of the vertical plane containing the hole centre-lines. The axial velocity measurements are made non-dimensional with the upstream free stream velocity U_∞ and the concentration data are normalised to give datum valves of unity in the jet exit and zero in the free stream .

Inspection of figure 2 shows that, as has been observed before, the maximum velocity region is not coincident with the maximum concentration. At 4D, the near-wall velocity contours show the individual nature of the wakes behind the jets but this is no longer evident at 8D. Comparison of figures 2 and 3 shows that, with the present velocity ratio, the jet penetrates slightly further into the freestream with the larger duct height but, by the 8D location, and for both H/D values, has been turned parallel to the wall without impingement of the core of the jet fluid. Otherwise the two flows are similar and in considerable contrast with those obtained with a pitch-to-diameter ratio of 4, figures 4 and 5, where the individual nature of the jets is apparent both at 4D and 8D and the jet penetration, due to the reduced lateral mixing, is somewhat greater. The velocity maximum still tends to be associated with acceleration of the freestream rather than with the jet fluid. Superposition of tracer gas from each jet would, as expected, lead to regions of low concentrations in the gap between the holes only for the higher pitch-to-diameter case, further illustrating the ability of the free stream to penetrate between the jets in the S/D=4 case, but not for S/D=2.

CALCULATION METHOD AND COMPUTATIONAL DETAILS

The time-averaged forms of the equations of continuity and momentum have been solved, with the Reynolds stresses calculated using a two-equation turbulence model involving equations for turbulence energy k and dissipation rate ε. The equations may be written in the following form valid for steady, constant density flow :

$$\frac{\partial \bar{\rho}\,\bar{U}_i}{\partial x_i} = 0$$

$$\bar{\rho}\,\bar{U}_j \frac{\partial \bar{U}_i}{\partial x_j} = -\frac{\partial \bar{P}}{\partial x_i} - \frac{\partial}{\partial x_j}\left(\bar{\rho}\,\overline{u_i u_j}\right)$$

$$\bar{\rho}\,\bar{U}_j \frac{\partial k}{\partial x_j} = \frac{\partial}{\partial x_j}\left(\frac{\mu_t}{\sigma_k}\frac{\partial k}{\partial x_j}\right) - \bar{\rho}\,\overline{u_i u_j}\frac{\partial \bar{U}_i}{\partial x_j} - \bar{\rho}\varepsilon$$

$$\bar{\rho}\,\bar{U}_j \frac{\partial \varepsilon}{\partial x_j} = \frac{\partial}{\partial x_j}\left(\frac{\mu_t}{\sigma_\varepsilon}\frac{\partial \varepsilon}{\partial x_j}\right) - C_1 \frac{\varepsilon}{k}\bar{\rho}\,\overline{u_i u_j}\frac{\partial \bar{U}_i}{\partial x_j} - C_2 \bar{\rho}\frac{\varepsilon^2}{k}$$

with $$\bar{\rho}\,\overline{u_i u_j} = \frac{2}{3}\delta_{ij}k - \mu_t\left(\frac{\partial \bar{U}_i}{\partial x_j} + \frac{\partial \bar{U}_j}{\partial x_i}\right)$$

$$\mu_t = C_\mu \bar{\rho}\,k^2/\varepsilon$$

and $C_\mu = 0.09$, $C_1 = 1.44$, $C_2 = 1.92$, $\sigma_k = 1.0$ and $\sigma_\varepsilon = 1.3$.

The numerical scheme previously employed in reference 5 and described in greater detail in reference 10 was used to solve the three-dimensional forms of the above six coupled partial differential equations. The finite-difference formulation comprises a linearised, implicit, conservative scheme using central differencing except in regions where mean-flow convective fluxes dominate diffusive processes where upwind differencing is used. The method is formulated in terms of velocity and pressure, with a staggered grid arrangement and a guess and correct procedure to obtain the correct pressure field.

The solution domain for the present problem may be represented by a rectangular box whose upper and lower walls coincide with the roof and floor of the wind tunnel, boundary conditions along these solid walls employed the usual wall-function approach, see Launder and Spalding, reference 11. Assuming an infinitely long row of holes, the flow is symmetric about vertical planes through a hole centre (hereafter referred to as the centre-plane) and through the line bisecting the space between two holes (hereafter called the mid-plane): the second symmetry boundary condition is in contrast to that for a single jet in cross flow. The upstream boundary condition corresponded to the measured mean axial velocity profile at X/D=-5.5 with the cross-stream velocity components presumed zero and k and ε determined assuming a turbulence intensity of one per cent and a length scale equal to the duct height, the results obtained here were found by numerical experiment, to be insensitive to these assumptions and the location of the upstream plane. A similar approach was taken with the downstream boundary condition where the axial gradients of the five dependent variables were assumed zero, the influence of the position where this assumption was imposed was evaluated by comparing results for the downstream boundary located progressively further away from the jets. This boundary condition was eventually assigned at X/D=12.5 and had no influence on the results presented.

The final boundary condition which needs to be described here is that imposed over the jet exit plane. Apart from some special treatment necessary in the regions where the semi-circular hole boundary bisected the rectangular finite-difference control volume surface areas, two types of boundary conditions were tested. The first, and simplest, form assumed the efflux velocity ($\bar{V}_J$) to be constant over the hole, with zero U and W velocities and k and ε calculated from a turbulence intensity of one per cent and a length scale equal to the jet diameter. Since it is known (see, for example references 12, 13) that the flow within the hole is distorted due to the strong pressure gradients which are set up over the jet exit plane, the constant velocity type of boundary condition is unnecessarily crude and an alternative condition was also tested by invoking the assumption that the velocity profile across the injection hole is consistent with a constant total pressure condition, a feature of jets in crossflow which was noticed by Bergeles (reference 12) in his experiments at low velocity ratios where the distortion is strongest. Starting a calculation with zero static pressures everywhere within the flow field and a constant jet velocity ($\bar{V}_J$) enables the total pressure to be calculated initially ($P_{tot}=\frac{1}{2}\rho\bar{V}_J^2$), on subsequent iteration cycles, the static pressure over the hole has changed and this then enables the vertical velocity profile within the hole to be updated, using the equation :

$$P_{tot} = P_{stat} + 1/2\ \rho V^2$$

An additional constraint is that the total mass flow from the hole should be the same as in the constant velocity case.

The velocity profile produced using this treatment over the jet exit is compared on the centre-plane for S/D=2, H/D=4 in figure 6 to the profile measured by Andreopoulos (reference 13). The data of reference 13 were not taken in exactly the same configuration, but were measured in a single jet in crossflow at a slightly lower velocity ratio of 2.0 and with a jet fed from a plenum chamber rather than through long supply tubes. Nevertheless the qualitative trend is reproduced of a low velocity at the front of the jet and a higher than bulk mean velocity at the rear edge, the predicted shape is not in good agreement showing the maximum velocity too near the rear of the hole, however this boundary condition certainly produces a profile closer to the measured shape than a constant velocity condition. For the other variables in this second type of boundary condition, U and W were still set to zero (as implied by the above equation), but the boundary conditions on the turbulence quantities were made more realistic since it was known that the length of the jet supply pipes allowed fully-developed flow to form, accordingly the turbulence intensity level which fixed the k value in the jet exit was raised to 7 per cent a value representing the area averaged turbulence level in fully developed pipe-flow, the jet diameter was still used as the length scale in calculating ε.

In the next section results will be presented which were obtained with a finite-difference grid consisting of 20x20x30 nodes (in the y, z, x directions respectively). Non-uniform spacing was used in an attempt to cluster grid nodes in regions where rapid variations were expected. Because of the relatively small dimensions of the solution domain in the y-z plane, it was decided to use uniform spacing in these directions but finer grid spacing was adopted in the axial direction near the hole and increased geometrically in the up-and downstream directions; for the S/D=4 calculation, a total of 16 nodes lay within the half-hole inside the solution domain and this number increased to 35 for S/D=2. Because of the complex three-dimensional flow field and the use of upwind differencing, which is known to introduce numerical diffusion errors on coarse grids, it is necessary to investigate how grid independent are the solutions to be presented. The grid-dependence results are shown on figure 7 in the form of axial velocity profiles on the centre-plane for S/D=4, H/D=4. It can be seen that the solutions are particularly sensitive to changes in the grid size in the close to discharge region, this is most apparent in the growth of the wake region behind the jet. This does not extend to the X/D=4 location in the coarse grid case but shows an appreciable negative velocity region with the finest grid run. In addition, noticeable peaks in the maximum axial velocities

at X/D=2,4 start to appear as the grid is refined. Both these features are symptomatic of a reduction in numerical diffusion which tends to smear out peaked profiles and leads to additional diffusion of momentum from high momentum to low momentum regions and thus causes a "filling in" of wake regions. Although it can be presumed, on the evidence of figure 7, that the addition of extra nodes in the near discharge region would have brought about still further changes in the profiles, it can also be seen from figure 7 that the solutions downstream of X/D=4 are not very dependent on the grid size, so that trends observed in the results at these locations are not strongly influenced by numerical errors. Further grid refinement was impossible as the 20x20x30 calculation employed the maximum accessible core-store on the IBM 360/195 machine used. A typical calculation involved 300 iterations to converge using 1200 K bytes of core store and about 80 minutes CPU time.

Figure 8 indicates that the two jet exit boundary conditions yield very similar results for the S/D=4, H/D=4 configuration. The distortion of the exit velocity produced in the constant total pressure case was such that the jet velocity was decreased at the leading edge and in the front portion of the hole by about 20% from its mean value (lowest velocity ≈ 20 m/s and increased at the edge of the hole and towards the rear by about the same amount (maximum velocity ≈ 30 m/s). This distorted profile produces different values of the local strain rates which were observed to be higher in the constant total pressure case; these larger velocity gradients generate more turbulence and hence lead to larger values of the turbulent viscosity than in the solution assuming constant jet velocity. Consequently the axial velocity profiles show a smaller wake region and a slightly decreased penetration of the jet (more rapid diffusion of the vertical momentum) for the constant total pressure condition.

It was also confirmed that the higher levels of turbulence energy are produced predominantly by this extra generation effect described above and not due to the increased level of turbulence energy in the jet used in the constant total pressure condition. The same observations hold for the changes produced by altering the jet exit conditions for the case of a pitch-to-diameter ratio of 2, but now the effects are larger. Figure 9a presents the axial velocity profiles at four locations downstream of the discharge plane for the centre-plane and figure 9b similar results for the mid-plane conditions. In the case of constant jet velocity, the lateral mixing is not rapid enough to prevent the free-stream penetrating between the jets, although some distortion of the profile can be observed in the appearance of wake-regions on the mid-plane at X/D=4 and 8; the centre-plane profiles exhibit however the same inverted S-shape as was observed in the S/D=4 calculations. The imposition of the constant total pressure condition produces a markedly different behaviour. The increased strain-rates induced by the distorted jet exit profile (the efflux velocity variations are approximately the same) are enhanced now by the proximity of the jets. The additional mixing enables the jets to coalesce rapidly in the lateral direction as can be seen from the nearly identical shapes of the profiles at X/D=4 on centre-plane and mid-plane. This trend towards a two-dimensional jet implies that the free-stream can no longer penetrate the gaps between the holes and must be accelerated over the jets, causing the maximum axial velocity to lie nearer the upper wall in the constant total pressure case. The additional turbulent mixing has also caused the wake region behind the jets to become very much smaller (it lies completely upstream of X/D=2) and the inverted S-shape profile is no longer observed. The sensitivity of the calculations to the usually unknown profiles at the jet exit for low values of the pitch to diameter ratio is an undesirable feature which will be returned to in a later section.

It must be stressed however that these changes in the solution have not been brought about due to any change in the effective momentum flux ratio or velocity ratio (jet to freestream) implied by the switch from one boundary condition to the other. An evaluation of the momentum mean velocity in the jet using the constant total pressure condition ($\int_{Jet}\rho V^2 dA / \int_{Jet}\rho V dA$) showed that the effective velocity ratio had only increased by about one per cent from the value of 2.3 used in the constant velocity boundary condition calculation.

COMPARISON WITH MEASUREMENTS

Figures 10 to 12 present comparisons between predicted and measured axial velocity profiles on the centre-plane for four cross-stream planes X/D=4, 6, 8 and 10 and for three combinations of duct height to diameter and pitch-to-diameter ratios; at two planes, X/D=4 and 8, a comparison is also presented for the profiles on the mid-plane. The results in all cases were obtained with the constant total pressure boundary conditions In figure 10 the case of S/D=2, H/D=4 shows the worst agreement in that the shape of the profile is incorrectly predicted at X/D=4, although the close to two-dimensionality of the flow is correctly predicted. The measurements still exhibit the inverted S-shape at X/D=4, although in this low pitch-to-diameter ratio case this has all but disappeared by X/D=8; it persists in the other cases at the furthest downstream stations (see figures 11, 12). The increased rate of mixing in the calculations is unlikely to be caused predominantly by numerical diffusion since it was brought about by a change in boundary conditions with a fixed grid. It is more probable then that the turbulence model has merely overestimated the level of mixing causing one beneficial effect (stronger lateral mixing produces a jet coalescence and two-dimensional flow as in the measurements) and one negative effect (stronger vertical mixing causes the wake region to shrink and the inverted S-shape profile to disappear much more rapidly than in the measurements). It is impossible to separate these two effects with the present level of turbulence closure which uses a scalar eddy viscosity and hence increased lateral mixing must be accompanied by increased vertical mixing. It must also be said, however, that the sensitivity to the

jet exit boundary conditions for this case calls into question the validity of the assumptions made in implementing the constant total pressure condition (particularly the assumption that the U and W velocities are both zero). It would be interesting to undertake a more accurate treatment of the exit profile specification by performing also a calculation of the flow within the jet supply pipe which could interact with the jets in crossflow solution to produce (after several repeated, linked calculations) a set of conditions at the jet exit plane (which would be common to both calculations) consistent with the approaching jet flow distorting in response to the conditions in the wind-tunnel, but without some of the simplifications used in the present work. This technique has been used successfully in reference 8 for a single jet in crossflow but is obviously more necessary in the case considered in figure 10 as the discussion in the last section on sensitivity to jet boundary conditions indicated. Examination of the profiles for S/D=2, H/D=4 reveals a discrepancy in mass flow rates between measurements and calculations (seen most clearly at X/D=8). This is due to the assumed value of free-stream velocity used in the calculations; subsequent checks indicated that for this flow U_∞ had been somewhat lower, and hence the velocity ratio had assumed a slightly higher value of 2.6. Thus, in this case, it may also be noted that the lack of correspondence between measurements and calculations at the downstream stations (but not upstream) is almost entirely due to this mass-flow discrepancy; fortunately this did not occur in the other cases measured where the free-stream velocity was confirmed to be constant at 10.8 m/s.

The effect of increasing jet spacing is shown in figure 11 and the agreement between predictions and calculations is satisfactory. The free-stream penetration through the gaps can be clearly seen in both predicted and measured mid-plane profiles on X/D=4 and 8 and the shape of the centre-plane profile is predicted correctly. This inverted S-shape is typical of the strongly three-dimensional flow generated by rows of jets in confined cross flow; the vertical flow structure takes on a three-layered nature with the acceleration of the free-stream causing the upper velocity peak, the wake behind the jets causing the central low velocity region and the re-developing boundary layer on the bottom wall representing the fluid sucked into the low pressure region behind the holes but not totally entrained by the jets themselves. The peak in velocity caused by free-stream acceleration is underpredicted at X/D=4. It is possible that this local peak has been smeared out by numerical diffusion errors in the upstream, near-discharge region, although it is believed that the general shape of the profile is not adversely affected by this problem. The rate at which the profile flattens out in the vertical direction as we proceed from X/D=4 to 10 is well predicted, being if anything slightly too slow.

Figure 12 allows comparisons for the case where H/D is increased to 8 at a constant pitch-to-diameter ratio of 4. Once again, the inability to resolve local peaks can be identified at X/D=4 and 6 and this is almost definitely due to numerical diffusion errors since a uniform grid distribution in the vertical direction with only 20 points is certainly not suitable for this flow which remains within Y/D=4 over the whole downstream distance. A comparison of the location of the velocity maxima with figure 10 indicates slightly greater jet penetration which is to be expected for an increase in H/D. Once more the overall rate of smoothing out of the vertical profiles with increasing downstream distance is fairly well predicted.

Finally, on figures 13a and 13b the effect of decreasing the tunnel height to an H/D value of 2 is quantified using calculated results. The profiles on the centre-plane may be compared, figure 13a, with the predicted results for H/D=4 and figure 13b compares the same two configurations for the profiles at an off centre-plane location (Z/D=S/4). That impingement has occurred can be clearly seen at X/D=2 where the maximum velocity has risen above the Y/D=2 level in the case of H/D=4, but this is of course impossible when the tunnel roof is brought down to H/D=2. Jet bifurcation occurs when the wake region itself impinges on the upper wall downstream of X/D=4 causing an enhancement of the secondary flow in the cross-stream plane which results in a stronger tendency to two dimensionality in the case of H/D=2 and the maximum velocities to lie near the bottom wall and at off centre-plane locations. At a velocity ratio of 2.3 however, even with the upper wall at 2D distance impingement occurs some distance downstream of the discharge plane and is not strong enough to cause backflow velocities near the upper wall as observed in the single jet case of references 3 and 5 at higher velocity ratios.

CONCLUSIONS

The main conclusions drawn from the present work are as follows :

1) Measurements of a single row of jets in confined crossflow indicated that for a velocity ratio of 2.3 no impingement occurs for duct heights of 8D and 4D, even for a pitch-to-diameter spacing of 4D.

2) The effect of reducing S/D from 4 to 2 could be clearly identified in the measurements by a rapid lateral coalescence, loss of individual jet identity and the appearance of a practically two-dimensional flow.

3) Calculations using a 20x20x30 finite-difference grid and a two-equation turbulence model were found not to be grid-independent in the near-discharge region ($0 \leq X/D \leq 4$) but results further downstream were not strongly affected by numerical errors.

4) The rapid jet coalescence and trend toward two-dimensional flow behaviour were pre-

dicted in the lower pitch-to-diameter ratio case only when a constant total pressure boundary condition was used at the jet exit. In this calculation it is also believed that the turbulence model, which uses a scalar eddy viscosity, was overestimating the rate of mixing in the vertical direction causing the profile shapes in the near-field to be wrongly predicted.

5) The calculation for the S/D=2 flow was shown to be very sensitive to the boundary conditions at the jet exit and more work is required here to investigate a method for calculating these boundary conditions more accurately.

6) The calculated results for the larger pitch-to-diameter ratio case were in good agreement with the measurements for both H/D ratios measured, apart from the failure to resolve the locally peaked shape of the velocity profile in the near-field that was probably mainly due to numerical diffusion problems.

7) A lowering of the tunnel roof to a height of 2 jet diameters produced impingement of the jets which could be clearly identified in the calculated results. The impingement even at this H/D value was however fairly far downstream and the solution indicated no region of reverse flow near the tunnel roof.

REFERENCES

1 Crabb, D., Durão, D.F.G., and Whitelaw, J.H., "A Round Jet Normal to a Crossflow", ASME, J. Fluids Eng., 103, 142, 1981.

2 Walker, R.E., and Kors, D.L., "Multiple Jet Study," NASA CR-121217, 1973.

3 Kamotani, Y., and Greber, I., "Experiments in Confined Turbulent Jets in Crossflow," NASA CR-2392, 1974.

4 Atkinson, K., Khan, Z.A., and Whitelaw, J.H., "Experimental Investigation of Opposed Jets Discharging Normally into a Cross-Stream," J. Fluid Mech., to be published, 1981.

5 Jones, W.P., and McGuirk, J.J., "Computation of a Round Turbulent Jet Discharging into a Confined Crossflow," Turbulent Shear Flows, 2, 233. Springer Verlag, 1980.

6 Jones, W.P., and Launder, B.E., "The Prediction of Laminarisation with a two Equation Model of Turbulence," Int. J. Heat Mass Transfer, 15, 301, 1972.

7 Crabb, D., "Jets in Crossflow," Ph.D. Thesis, Imperial College, London University, 1979.

8 White, A.J., "The Prediction of the Flow and Heat Transfer in the Vicinity of a Jet in Crossflow," ASME paper 80-WA/HT-26, 1980.

9 Khan, Z., and Whitelaw, J.H., "Vector and Scalar Characteristics of Opposing Jets Discharging Normally into a Cross-Stream," Int. J. Heat Mass Transfer, 23, 1673, 1980.

10 Jones, W.P., "PACE: A Computer Program for Solving Three-Dimensional Flow Problems," Rolls-Royce Internal Report, 1975.

11 Launder, B.E., and Spalding, D.B., "The Numerical Computation of Turbulent Flows," Computer Methods in Applied Mechanics and Engineering, 3, 269, 1974.

12 Bergeles, G., "Three-Dimensional Discrete-Hole Cooling Processes, an Experimental and Theoretical Study," Ph.D. Thesis, Imperial College, London University, 1976.

13 Andreopoulos, J., "Measurements in a Pipe-Flow Issuing Perpendicularly into a Cross-Stream," ASME Paper 80-WA/HT-24, 1980.

ACKNOWLEDGEMENTS

The authors gratefully acknowledge financial support from the Science Research Council (ZAK) and Rolls-Royce Ltd (JJM). Computing facilities were provided by the Science and Engineering Council Rutherford Computing Laboratory.

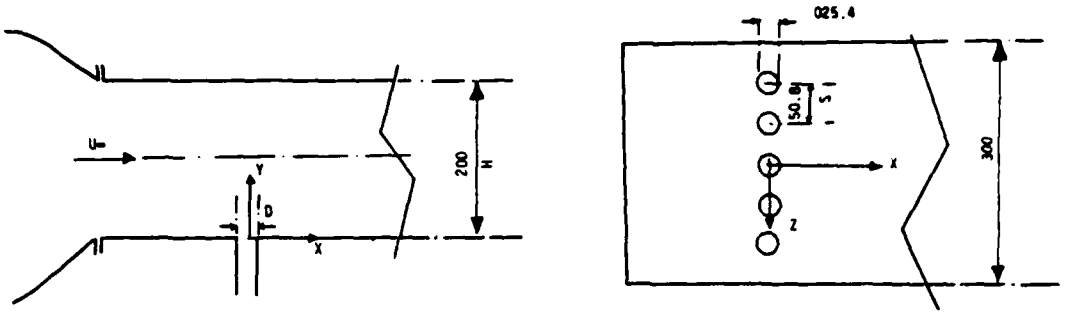

Figure 1 Schematic of multiple jets (dimensions in mm)

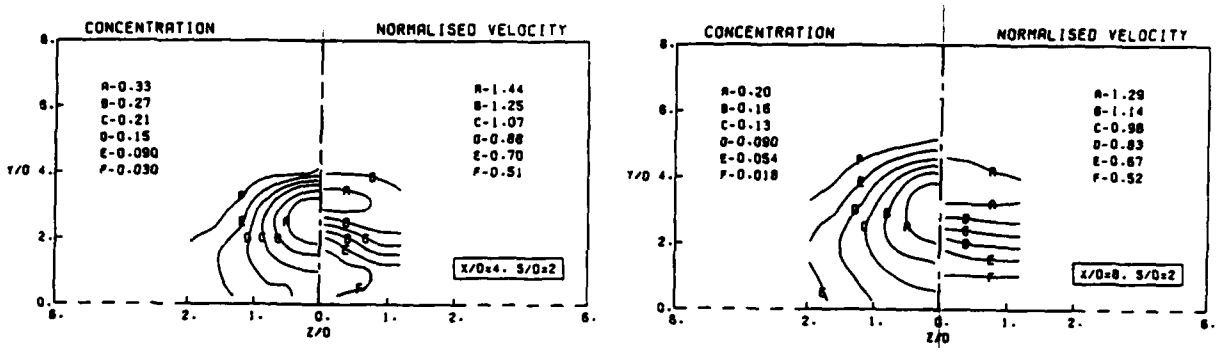

Figure 2 Velocity and concentration contours at two downstream positions for duct height 8D and a pitch-to-diameter ratio of two

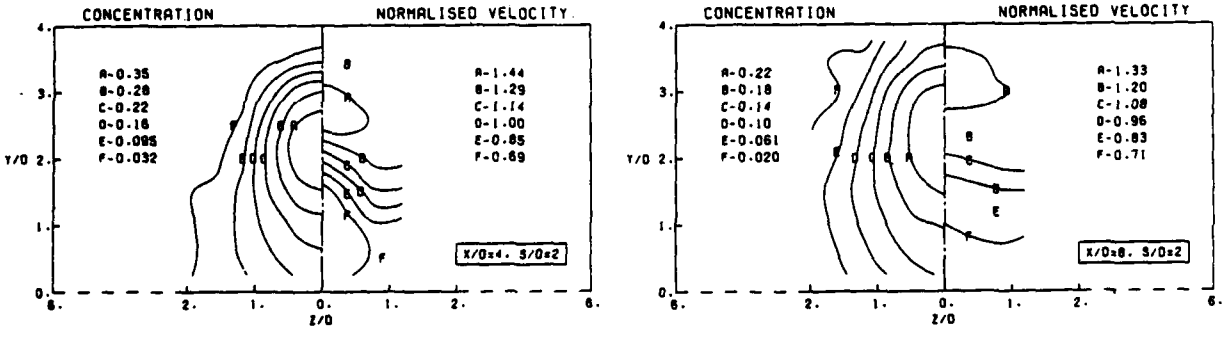

Figure 3 Velocity and concentration contours at two downstream positions for duct height 4D and pitch-to-diameter ratio of two

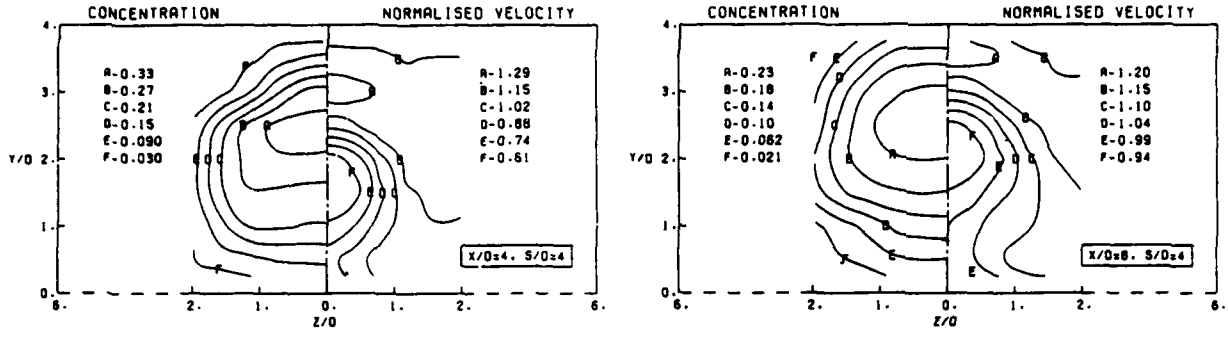

Figure 4 Velocity and concentration contours at two downstream positions for fuct height 4D and pitch-to-diameter ratio of four

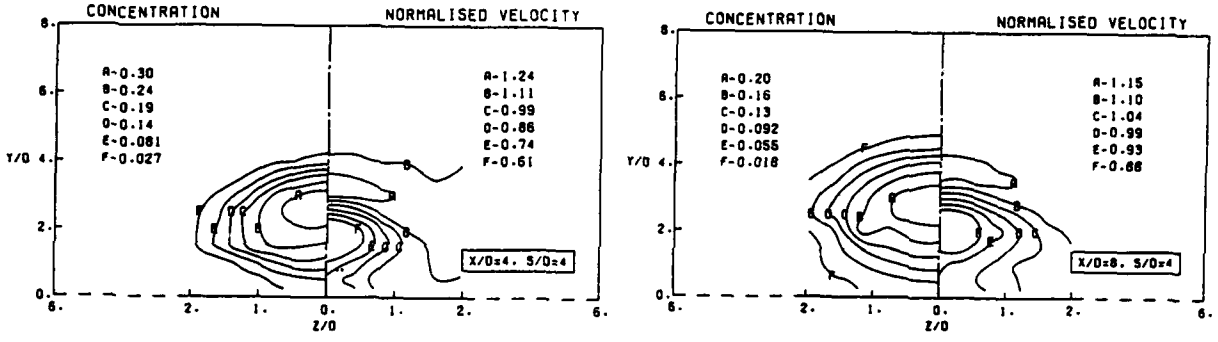

Figure 5 Velocity and concentration contours at two downstream positions for duct height 8D and pitch-to-diameter ratio of four

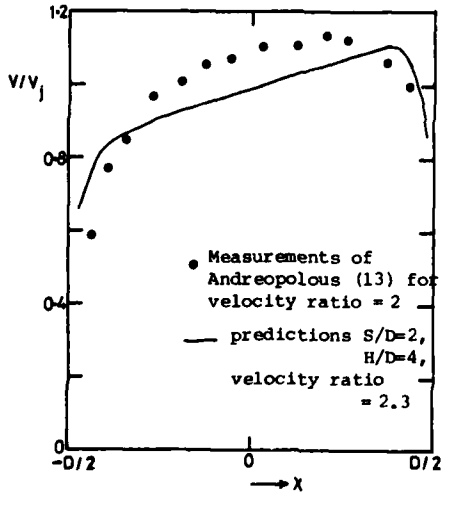

Figure 6 Jet exit velocity profile on centre-plane using constant total pressure condition

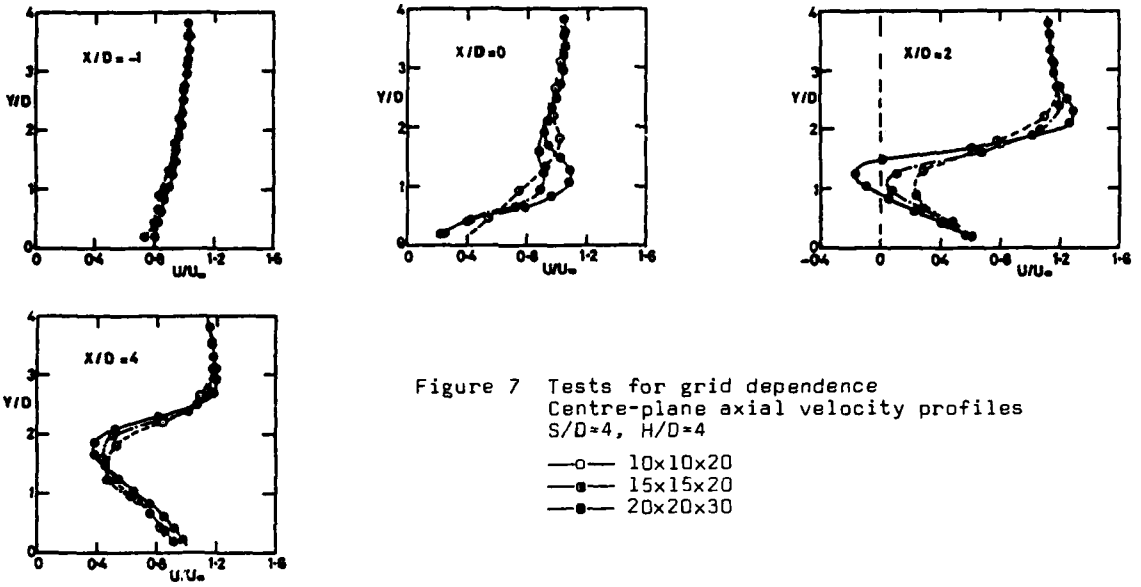

Figure 7 Tests for grid dependence
Centre-plane axial velocity profiles
S/D=4, H/D=4

—o— 10x10x20
—■— 15x15x20
—■— 20x20x30

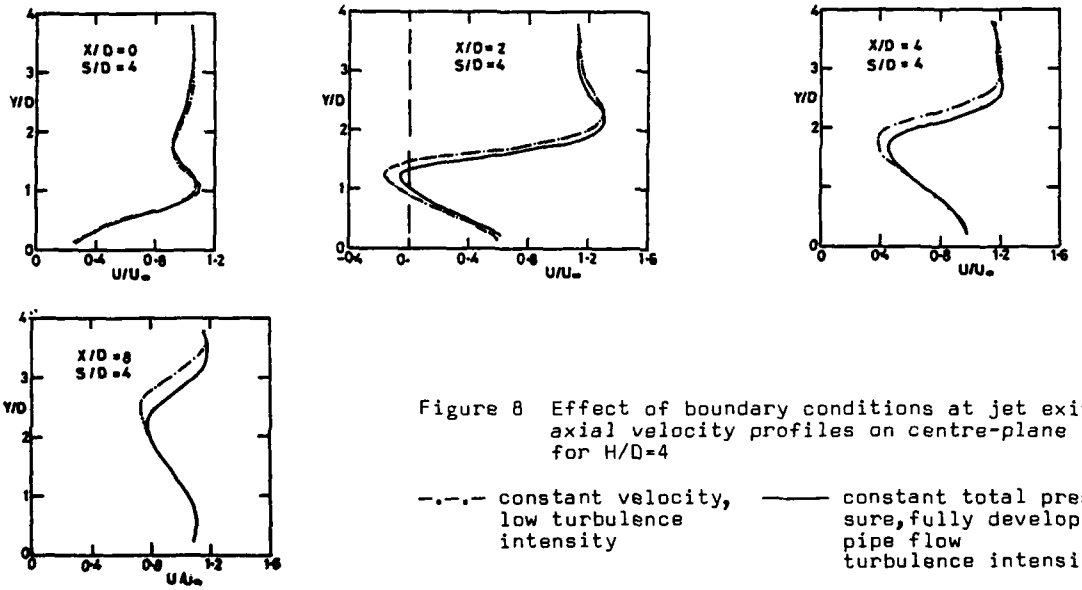

Figure 8 Effect of boundary conditions at jet exit, axial velocity profiles on centre-plane for H/D=4

-.-.- constant velocity, low turbulence intensity

——— constant total pressure, fully developed pipe flow turbulence intensity

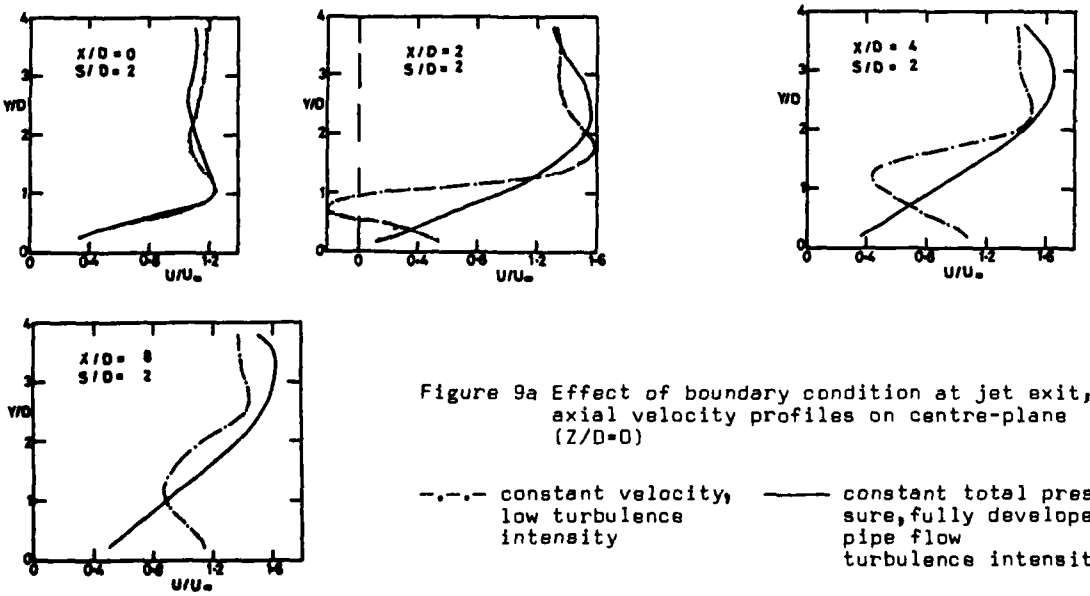

Figure 9a Effect of boundary condition at jet exit, axial velocity profiles on centre-plane (Z/D=0)

-.-.- constant velocity, low turbulence intensity

——— constant total pressure, fully developed pipe flow turbulence intensity

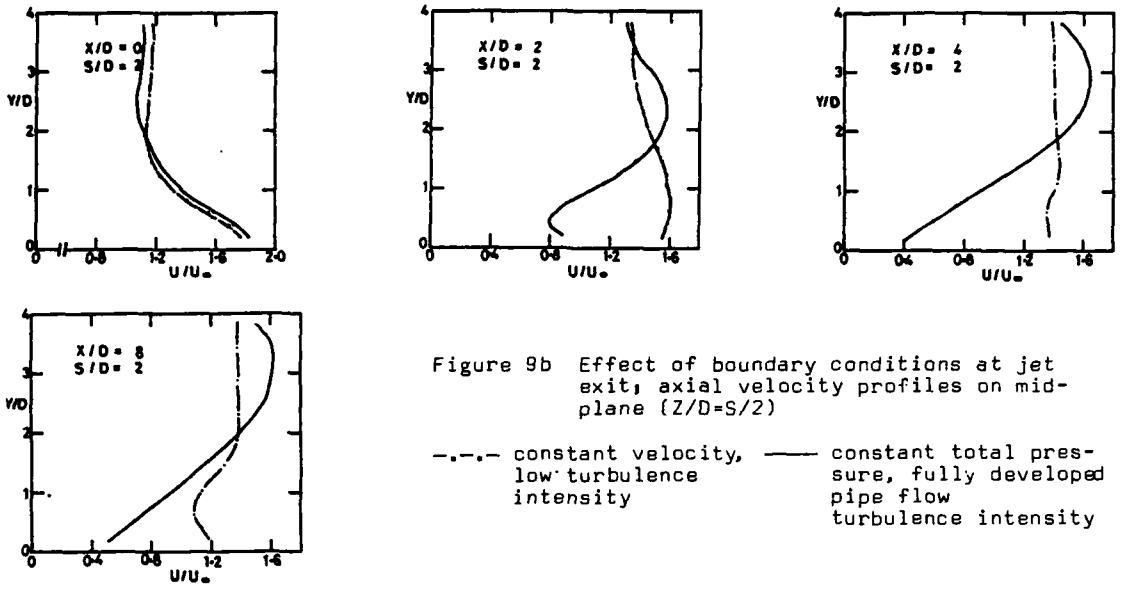

Figure 9b Effect of boundary conditions at jet exit; axial velocity profiles on mid-plane (Z/D=S/2)

-.-.- constant velocity, low turbulence intensity

—— constant total pressure, fully developed pipe flow turbulence intensity

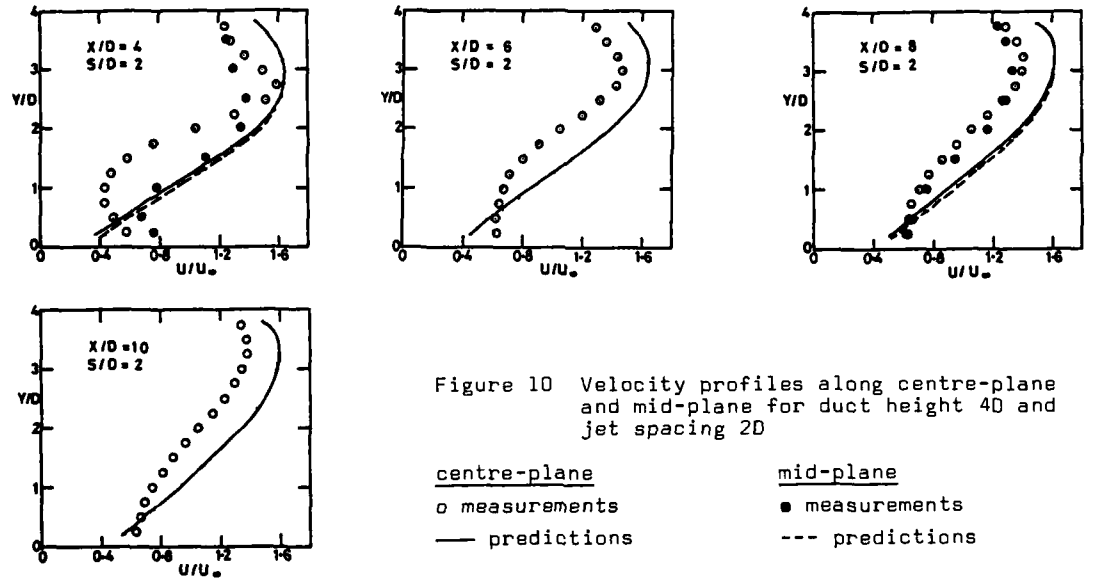

Figure 10 Velocity profiles along centre-plane and mid-plane for duct height 4D and jet spacing 2D

centre-plane
o measurements
—— predictions

mid-plane
• measurements
--- predictions

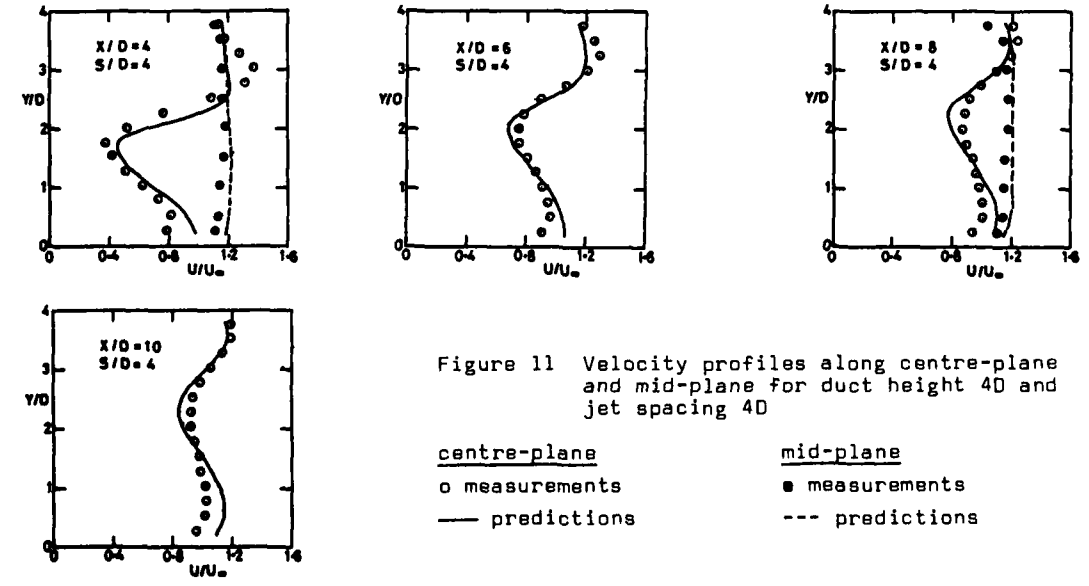

Figure 11 Velocity profiles along centre-plane and mid-plane for duct height 4D and jet spacing 4D

centre-plane
o measurements
—— predictions

mid-plane
• measurements
--- predictions

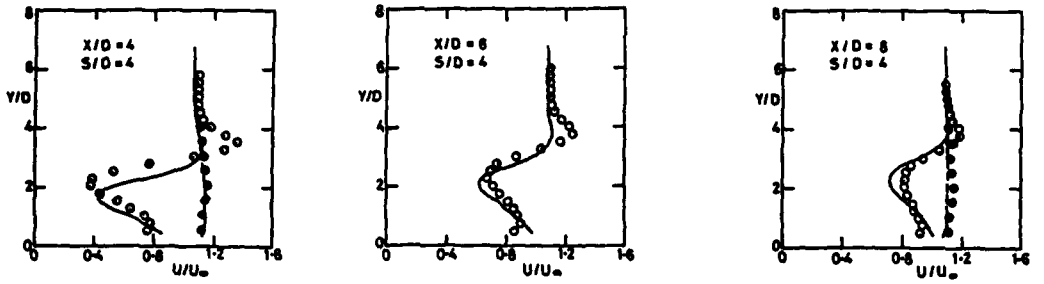

Figure 12 Velocity profiles along centre-plane and mid-plane for duct height 8D and jet spacing 4D

centre-plane
o measurements
—— predictions

mid-plane
• measurements
--- predictions

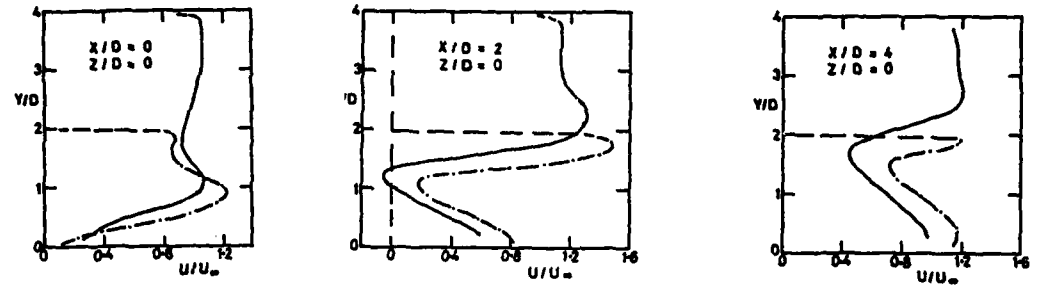

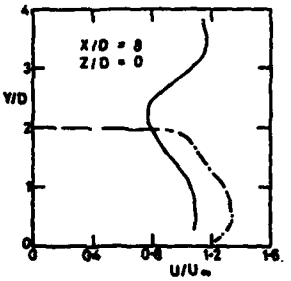

Figure 13a Axial velocity profiles on centre-plane for blockage ratios of 4 and 2
S/D=4 (—— H/D=4, -.- H/D=2)

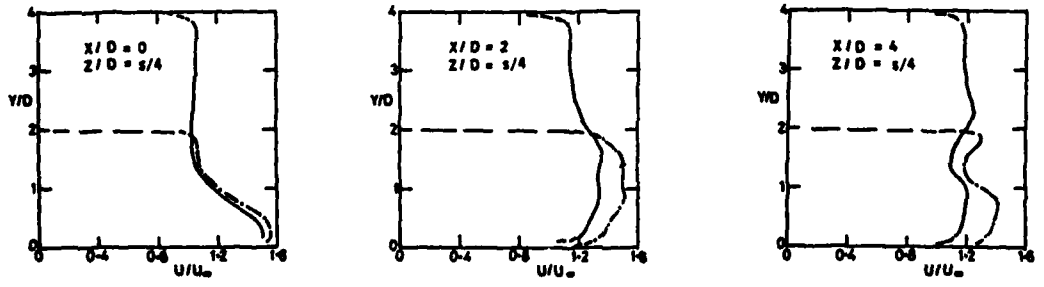

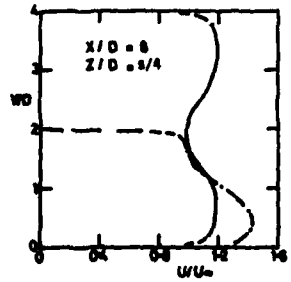

Figure 13b Axial velocity profile along Z/D=S/4 for blockage ratios of 4 and 2 with S/D=4
(—— H/D=4, -.- H/D = 2)

EXPERIMENTAL INVESTIGATION OF INITIALLY PLANAR JETS INCLINED TO AN EXTERNAL FLOW

by

Y. Pontikis*, R.A. Feik+, and A.D. Young
Queen Mary College,
(University of London),
Mile End Road,
London, E1 4NS,
England.

SUMMARY

The first part of the investigation was concerned with the development of a jet emerging from a full span narrow slit at the trailing edge of a thin aerofoil in a wind tunnel. The jet could therefore be regarded as two-dimensional. Three angles of jet inclination to the main flow were tested (10°, 20° and 30°) and two values of the ratio of the undisturbed stream velocity to the jet exit velocity (0.21 and (0.33). For the second part, half the slit was blocked resulting in a finite span jet with a streamwise edge, and the development and 'rolling up' of the edge region was studied for a jet inclination angle of 30°. The measurements covered mean flow and turbulence characteristics.

The mean velocity distributions in the two-dimensional jets showed a ready tendency to similarity with distance downstream from the jet exit, but the turbulence characteristics in the upper and lower halves showed significant differences consistent with the known effects of streamline curvature. The finite jet assumed a dumb-bell shape in section, the edge region growing inwards with distance downstream. There were significant differences between the mean velocity and streamwise vorticity distributions and their peaks followed markedly different loci.

1. INTRODUCTION

Over a period of nearly two decades investigations have been made into the characteristics of planar or 'two-dimensional' turbulent jets in a co-flowing stream at Queen Mary College, London, beginning with the work of Bradbury. The earlier work was concerned with the case where the jet was directed parallel to the direction of the undisturbed external airstream, and this work has been described in Ref. 1, 2, 3 and 4. More recently we have directed our attention to the case where the jet is initially at an angle (θ) to the undisturbed external stream direction. Feik (Ref. 5) examined the jet flow development with $\theta = 10^\circ$ and 20°, and later Pontikis (Ref. 6) investigated the flow with $\theta = 30^\circ$. Further, by blocking part of the slit from which the jet emerged at the rear of a thin aerofoil Pontikis extended his investigation to the streamwise edge region of the jet with $\theta = 30^\circ$.

This work on inclined jets is the subject of this paper. Its practical interest lies in the use of jet flaps and blown flaps for STOL applications, but it also presents features of fundamental fluid dynamic interest, not least being the effects of streamwise curvature on the turbulence characteristics of the jet. In what follows we find it convenient to refer to the unblocked jet as the 'two-dimensional jet' and the partially blocked jet as the 'three-dimensional jet'. Except where otherwise indicated, the results for $\theta = 30^\circ$ are used to illustrate the main features of the deflected jet flow where they are similar for all three deflection angles tested.

2. EXPERIMENTAL DETAILS

2.1 The two-dimensional jet.

The experiments were made in a wind tunnel of working section 1.24 m x 1.00 m in which the free stream turbulence level was 0.03%. The model is illustrated in Fig. 1. It consisted of a thin hollow wing of chord 71 cm spanning the tunnel with a nozzle along its trailing edge between two false side-walls 46 cm apart. Air passed from a blower into a settling chamber and thence into the wing where it was turned by guide vanes to emerge from the trailing edge nozzle as a planar jet. The initial deflection relative to the main stream direction was achieved by suitably shaping the nozzle. For deflection angles of 10° and 20° single stage nozzles were used but for the deflection of 30° it was found desirable to use a two stage nozzle ($10^\circ + 20^\circ$), see Fig. 1. This was done to minimise the extent of flow separation from the upper surface of the nozzle and to ease the milling of the nozzle contours. The final slot width varied slightly between 0.307 cm and 0.318 cm over the span. To avoid a leading edge separation bubble associated with the 30° jet deflection the nose of the wing was drooped as illustrated in Fig. 1. The droop required was estimated by means of the jet flap theory of Spence (Ref. 7) and its effectiveness was confirmed by the observed behaviour of wing surface tufts.

The undisturbed free stream velocity (U_∞) used for these tests was 12 m/s and two jet exit velocities (U_j) were tested corresponding to values of $U_\infty/U_j = 0.21$ and 0.33. Initial calibration tests showed the velocity in the jet at the nozzle exit to be uniform with a turbulence intensity of 0.01% over about 2/3 of the nozzle width (h), the remaining third being occupied by the internal boundary layers of the nozzle. Along the span the total pressure was found to be uniform apart from the internal boundary layers.

* Now in the Department of Aeronautics, Imperial College, University of London.

+ Now in the Aerodynamics Division, Aeronautical Research Laboratories, Melbourne, Victoria, Australia.

All the measurements were otherwise made in the mid-span longitudinal plane in the form of vertical traverses across the jet and surrounding free stream at stations from near the jet exit to about 120 nozzle widths downstream. Quantities measured were total and dynamic pressures, using pitot and static probes, mean velocity components (U,V) and the three Reynolds stresses $\overline{u^2}$, $\overline{v^2}$ and $\overline{uv}$ using single and cross hot wires. To minimise alignment errors the traversing probes were set parallel to the direction of the maximum velocity locus in the jet for each station. This locus was determined in preliminary tests. The notation used is illustrated in Fig. 2.

2.2 The three-dimensional jet.

The model was that of the two-dimensional tests with the deflection angle $\theta = 30^\circ$ but with the nozzle exit blocked over half its span, see Fig. 3. In this case, therefore, the exit slot had an aspect ratio (span/width) of about 72. The spanwise position of any traverse is denoted by S, where S is non-dimensional in terms of the open exit span (usually quoted as a percentage), thus S = 100% denotes the position where the blockage started and the jet ended.

Only one jet velocity was tested corresponding to $U_\infty/U_j = 0.21$. The traverses were made with the same probes as before and provided the total and dynamic pressures, the mean velocity components (U,V,W) and the five turbulent Reynolds stresses, namely $\overline{u^2}$, $\overline{v^2}$, $\overline{w^2}$, $\overline{uv}$ and $\overline{uw}$ (the Z axis lies parallel to the trailing edge, see Fig. 3). As before the measurements were made for a series of streamwise stations (X) ranging from close to the nozzle exit to 120 nozzle widths downstream, but in each traverses were made for values of S ranging from about 20% to about 100%.

3. RESULTS AND DISCUSSION

3.1 The two-dimensional jet. Mean quantities.

3.1.1 Velocities, jet thicknesses and momentum flux.

The maximum velocity loci which define the shapes of the centre-lines of the jets are shown in Fig. 4 for the combinations of θ and U_∞/U_j tested. Not unexpectedly, the loci curve more readily back towards the main stream direction with increase in U_∞/U_j.

Fig. 5 shows the velocity traverses adjacent to the jet at various streamwise stations for $\theta = 30^\circ$ and the two values of U_∞/U_j tested. U_{res} is the resultant velocity at a point and U_{ref} is the value of U_{res} for the particular profile at large negative values of Y_L/δ. Y_L is the vertical distance (positive upwards) from the jet centre-line (see Fig. 2), δ is a measure of the jet thickness and its definition is also illustrated in Fig. 2. Thus, the local free stream velocities just above and below the jet are denoted by U_{e1}, U_{e2} respectively, and the maximum velocity in the jet is denoted by U_m. We then write

$$U_{01} = U_m - U_{e1}, \quad U_{02} = U_m - U_{e2}. \tag{1}$$

For the upper half of the jet we write

$$\delta_1 = \text{value of } Y_L \text{ where } U - U_{e1} = U_{01}/2, \tag{2}$$

and for the lower half of the jet

$$\delta_2 = \text{value of } -Y_L \text{ where } U - U_{e2} = U_{02}/2, \tag{3}$$

and we define

$$2\delta = \delta_1 + \delta_2. \tag{4}$$

We see in Fig. 5 evidence of the wakes of the boundary layers from the upper and lower wing surfaces adjacent to the jet. The wake from the upper surface is quite strong initially as a result of some flow separation over the convex upper surface of the nozzle. However, for X/h = 37.5 and beyond this wake has been absorbed in mixing with the jet when $U_\infty/U_j = 0.21$. For the lower surface the boundary layer wake is much smaller and is more rapidly absorbed. With $U_\infty/U_j = 0.33$ the jet is relatively weaker and the upper surface separation is more marked, some evidence of the wake is still to be seen at X/h = 57.8 and the lower surface wake is also slower in being absorbed.

Fig. 6 presents normalised forms of the velocity profiles for $\theta = 30^\circ$, i.e. $(U - U_{en})/U_{0n}$ as a function of y/δ, where y is the distance normal to the maximum velocity locus and n = 1,2 for the upper and lower halves of the jet, respectively. The corresponding profile for Bradbury's undeflected jet is shown for comparison by the solid line. We note the remarkable tendency towards similarity in spite of the jet inclination even for traverses quite close to the jet exit where there is still evidence of the unabsorbed wing surface wakes. However, we must bear in mind the differences between U_{e1} and U_{e2} as well as between δ_1 and δ_2 and these are illustrated in Fig. 7 and 8 for $\theta = 30^\circ$ as functions of s/h, where s is the distance along the jet centre-line from the nozzle exit. The facts that initially $U_{e2} > U_{e1}$ and $\delta_1 > \delta_2$ result from the strong wing upper surface wake associated with the flow separation over the nozzle, but further downstream $U_{e2} < U_{e1}$, as might be expected, and $\delta_2 > \delta_1$, the reason for which we will discuss later.

The results for $\theta = 10^\circ$ and 20° show the same readiness to similarity when normalised, and the differences between U_{e1} and U_{e2} as well as between δ_1 and δ_2 decrease with reduction in θ.

We define jet momentum flux coefficients for the upper and lower halves of the jet at any station X/h as

$$J_1/h = \int_0^\infty U(U - U_{e1}).dy \;/\; U_{e1}^2.h, \tag{5}$$

and

$$J_2/h = \int_{-\infty}^0 U(U - U_{e2}).dy \;/\; U_{e2}^2.h, \text{ respectively,} \tag{6}$$

and write

$$J = J_1 + J_2. \tag{7}$$

Fig. 9 shows J/h as a function of X/h for the values of θ and U_∞/U_j investigated. As might be expected, far downstream where the factors that can influence momentum flux have largely disappeared (e.g. pressure gradients and normal Reynolds stresses) J/h tends to a constant value which decreases with increase of θ and of U_∞/U_j.

It has been suggested by Bradbury and Riley (Ref. 2) that the far downstream value of J is a more fundamental length scale than say h. We have accordingly taken $J_{ref.}$ as the value at the last downstream position and Fig. 10 and 11 show plots of $(U_e/U_0)^2$ and δ/J_{ref} as functions of s/J_{ref}. Here $U_e=(U_{e1} + U_{e2})/2$ and $U_0 = \frac{U_{01} + U_{02}}{2}$. For $U_\infty/U_j = 0.21$ there is an encouraging measure of collapse of the results consistent with undeflected jet data (Ref. 3 and 9) but for $U_\infty/U_j = 0.33$ the collapse is not quite so good, perhaps because of the stronger initial disturbances.

3.1.2 Entrainment rates and flow directions.

If we write $\dot{m}_1$ and $\dot{m}_2$ as the rates of mass flux across a section of the upper and lower halves of the jet then the corresponding volume entrainment rates are

$$E_1 = (d\dot{m}_1/ds)/\rho \quad \text{and} \quad E_2 = (d\dot{m}_2/ds)/\rho \; . \tag{8}$$

The total entrainment rate is

$$E = E_1 + E_2 \; . \tag{9}$$

Fig. 12 shows $E/U_\infty h$ and $(E_2 - E_1)/U_\infty h$ as functions of s/h for $U_\infty/U_j = 0.21$ and $\theta = 30^\circ$, and it also shows

$$\lambda = E_2/E_1 \quad \text{as a function of s/h for } \theta = 20^\circ \text{ and } 30^\circ. \tag{10}$$

It is evident that there is continuous entrainment into the jet, as one might expect, but the entrainment for the lower half of the jet is significantly greater than for the upper, almost twice as great by s/h = 120. Qualitatively similar results were obtained for both $\theta = 10^\circ$ and 20° and we see that λ is almost the same function of s/h for $\theta = 20^\circ$ as for $\theta = 30^\circ$.

Measurements of the flow inclination angles across the jets at various stations downstream from the nozzle also reflect the greater entrainment rate into the lower half of each jet as compared with the upper half, although the effects of the initial flow separation over the upper surface of the nozzle tend to mask this close to the nozzle. However, one can deduce from these measurements the angle between the flow direction on the centre line and the local tangent to the centre line. This angle was found to be positive, i.e. there was a flow across the centre line from the lower half of the jet to the upper, and for $\theta = 30^\circ$, $U_\infty/U_j = .21$, it varied from 1.85° for s/h = 18 to 0.3° for s/h = 125. The corresponding values of the velocity component normal to the centre line varied from about 0.11 U_∞ to 0.01 U_∞. This flow evidently helps to preserve the overall symmetry of the normalised velocity profile.

3.1.3 Turbulence quantities. Curvature effects.

Fig. 13a, b, c, show the distributions of $\overline{u^2}/U^2$, $\overline{v^2}/U^2$, and $\overline{uv}\;/\;U^2$ as functions of $\eta = y/\delta$ for the three stations X/h = 9.1, 57.8 and 120, for $\theta = 30^\circ$ and $U_\infty/U_j = 0.21$. Initially these turbulent stresses attain relatively greater values in the upper half of the jet than in the lower but they decrease more rapidly with X, so that further downstream (beyond about X/h = 40) they are somewhat smaller in the upper half than in the lower. Similar results were obtained for $\theta = 10^\circ$ and 20° and for $U_\infty/U_j = 0.33$.

A plausible explanation for these results can be sought in the longitudinal curvature of the jets. It was demonstrated by Bradshaw (Ref. 8) that streamline curvature has a large effect on the turbulence structure in turbulent shear flow, tending to enhance the larger eddies and the associated mixing process when the centre of curvature is in the direction of positive mean shear. This occurs for a turbulent boundary layer on a concave surface; conversely over a convex surface, there is enhanced damping of the turbulence due to the curvature. Hence, we may expect the lower half of our test jet to have its turbulence enhanced by the curvature induced by the main stream whilst that of the upper half would be reduced with consequent effects on the mixing rates.

This conclusion accords well with our results after allowance is made for the initial but generally localised effects of the flow separation over the upper surface of the nozzle.

Bradshaw suggested that there was an analogy between curvature and buoyancy effects and a form of Richardson number could be invoked to quantify curvature effects. In its simplest form for a thin shear layer of small curvature this Richardson number is

$$R_i = \frac{2U}{R} \;/\; (\partial U/\partial y) \tag{11}$$

where R is the local radius of streamline curvature, positive if the radial direction from the centre of curvature is in a positive sense. Bradshaw suggested that the curvature effect can be represented by a correction factor to a typical turbulent length scale (e.g. mixing length) of the form

$$F = 1 - C.R_i \qquad (12)$$

where C is of the order of 5-10.

Typical values of C derived from our measurements for $\eta = 1.0$ are:

U_∞/U_j	X/h =	57.8	98.3	120	159.1
.21	$\theta = 20^\circ$	8.1	5.1		6.2
.21	$\theta = 30^\circ$	7.8	12.1	14.7	
.33	$\theta = 30^\circ$	2.6	11.0	10.2	

These values of C are of the same order as predicted by Bradshaw but indicate some dependence on flow history. The low value for X/h = 57.8 when $U_\infty/U_j = .33$ and $\theta = 30^\circ$ is probably due to the effects of the initial flow separation which had not been completely absorbed by then. The measured values of δ/R and R_i at $\eta = 1.0$ are illustrated in Fig. 14a and b. These values are small but not insignificant.

Because of the asymmetry of the turbulence structure and the longitudinally varying curvature one cannot expect clear evidence of its self-preservation at some stage. However, plots of $\overline{u^2}/u_\xi^2$, $\overline{u^2}/U_0$, $\overline{v^2}/U_\delta^2$ and $\overline{uv}/U_\delta^2$ against η showed relatively little change with X/h beyond X/h = 60, suggesting some measure of self-preservation by then. We recall Bradbury (Ref.1,2) found self-preservation after X/h = 30 for a non-inclined jet. We also note that a plot of u_ξ^2/U_0^2 as a function of U_e/U_0 (Fig.15) shows reasonable agreement with the results for an undeflected jet due to Bradbury and Riley (Ref.3) except for the cases when $U_\infty/U_j = .33$ and $\theta = 20^\circ$ and 30°. In the latter cases the stronger effects of the initial flow separation evidently augment the turbulence level on the centre line in a way that persists far downstream.

3.3 The three-dimensional jet. Mean quantities.

3.3.1 Velocities.

Fig. 16 shows the spanwise distribution of mean velocity contours in a number of planes at various stations downstream of the nozzle exit. Y_E denotes the vertical distance below the horizontal plane through the nozzle exit. We see that we can regard the jet development as made up of two parts, an inner region (which we call the jet region), in which the flow details are broadly similar to those of the two-dimensional jet, and an outer region (the edge region), in which the flow is complex and determined by the interaction of the jet and its streamline edge to the external flow including the wake from the adjacent blocked part of the wing.

In the jet region we find the same ready tendency to similarity of the normalised transverse velocity profiles to a symmetrical form as in two dimensions. The maximum velocity as a function of X/h is slightly higher than in two dimensions and its locus lies somewhat lower than in two dimensions; this is presumably due to the downwash induced by the trailing vorticity that develops in the edge region. We shall return to this later, but it will be clear that since lift is generated on the wing, largely because of the jet, trailing vorticity must be present in the jet which is mainly concentrated in the edge region as for a wing of finite span.

Reverting to Fig. 16 we see that the edge region is initially marked by its extension in the transverse direction normal to the jet plane. However, as it develops downstream it tends to spread spanwise, so that its shape tends to become near-circular in section. By about X/h = 120 the edge region extends over almost all the jet span. We may also note that the maximum velocity (as well as maximum total pressure) for any value of X/h downstream of X/h > 10 occurs in the edge region and not in the jet region. This suggests that the mixing in the inner part of the edge region is somewhat less vigorous than in the jet region. It is noteworthy that the maximum velocity loci in the inner and outer regions move downwards together with downstream distance, - the velocity contours do not reflect the curling upwards of the edge region that one associates with the trailing vortex wake from a wing of finite span.

3.3.2 Vorticity.

The transverse components of the mean velocity have been plotted as vectors for different X/h stations and some of the results are illustrated in Fig. 17a and b. The vortex-like character of the flow in the edge region is now clearly visible as is the expected spanwise flow component outwards below the jet and inwards above it. There is also evidence of a weak vortex of opposite sign to the main one in the upper half of the jet just inboard of the main vortex.

To examine this in more detail the distribution of the streamwise vorticity component ξ in a given plane X/h = const. was determined from the data and the equation:

$$\frac{\xi h}{U_\infty} = \frac{\partial(W/U_\infty)}{\partial(Y_E/h)} - \frac{\partial(V/U_\infty)}{\partial(Z/h)} \qquad (13)$$

where W and V are the lateral and transverse mean velocity components, respectively. Fig. 18a and b shows the resulting iso-vorticity lines for X/h = 17.2 and 98.3. No great accuracy can be claimed for these results but they show clearly the presence of two secondary regions of vorticity on the inner periphery of the main one, the lower one is in the same sense as the main one but the upper one is of opposite sense.

If we define the centre of the vortex pattern as the position of maximum vorticity then we find that its locus is well above the locus of maximum velocity and it does not move markedly inwards with distance downstream as does the latter locus. The difference between the two loci is illustrated in Fig. 19.

It is of interest to note that the maximum velocity position for any downstream station lies in the region between the main region of vorticity and the secondary regions. It seems plausible that in this somewhat quiescent region the mixing is less vigorous than in neighbouring regions and hence a higher total pressure and velocity persist there.

3.3.3 Turbulent stresses.

Fig. 20a, b, c, show distributions of the five Reynolds stresses measured for S = 46% at the stations X/h = 17.2, 57.8 and 120. We can again note the somewhat higher values in the lower half of the jet region than in the upper half, as in two dimensions, to be ascribed to the effects of curvature.

The distribution of the stress $\overline{uw}$ reflects the spanwise variation of U with Z, which after the initial disturbances have died out tends to develop a positive gradient consistent with the maximum velocity occurring in the edge region.

Fig. 21a, b, c, show the corresponding distributions for S = 90%. Here we are in the edge region and the curves differ markedly from those of the jet region. We note the greater transverse extent of the region in which the stresses are of significant magnitude, and we also note the larger magnitudes in the lower half of the region. The position of the peaks is in the region of maximum streamwise vorticity.

4. CONCLUSIONS

Two-dimensional deflected jet.

1) Initial disturbances with $U_\infty/U_j = .21$ were readily absorbed by about 40h downstream of the jet exit. But with $U_\infty/U_j = .33$ and $\theta = 20^\circ$ and 30° the initial disturbances were stronger due to flow separation from the nozzle upper surface, complete absorption then required a distance of about 60h (Fig. 5).

2) However, the normalised mean velocity distribution across the jet attained similarity in all the cases tested by about 20h (Fig. 6).

3) The turbulence characteristics and associated entrainment rates showed significant differences between the upper and lower halves of the jet which can be plausibly explained in terms of longitudinal curvature effects (Fig. 12, 13, 14).

4) There was a flow across the jet centre line from the lower to the upper half.

5) The jet momentum thickness far downstream provides a useful reference length in collapsing the data in non-dimensional form for jet thickness and maximum velocity as functions of downstream distance (Fig. 10, 11).

Three-dimensional deflected jet of finite span.

6) The development of the inner, or jet, region was much the same as for the two-dimensional jet, but its spanwise extent decreased with downstream distance.

7) The outer, or edge region, grew at the expense of the inner region and its iso-velocity contours changed from being elongated transversely to a near-circular shape with distance downstream (Fig. 16).

8) The maximum velocity locus moved inwards with distance downstream but was located in the edge region at much the same height as the peak velocity in the jet region (Fig. 16).

9) A strong streamwise vorticity component developed in the edge region similar to that in the vortex wake of a lifting wing. However, there were two weaker secondary regions of streamwise vorticity inboard of the main one, one in the upper half of the jet and of opposite sense to the main one and the other in the lower half and of the same sense as the main one (Fig. 17 & 18).

10) The locus of peak streamwise vorticity lay above the level of that of maximum velocity and its spanwise position changed little with distance downstream (Fig. 19).

11) The position of peak turbulence intensity coincided roughly with that of maximum streamwise vorticity in the edge region.

12) These results present an interesting if severe test case for those attempting to model three-dimensional turbulent shear flows.

REFERENCES

1. Bradbury, L.J.S. An investigation into the structure of a turbulent plane jet. Ph.D Thesis, Univ. of London (1963).
2. Bradbury, L.J.S. The structure of a self-preserving turbulent plane jet. JFM, 23, Pt.1, 31-64 (1965).
3. Bradbury, L.J.S. & Riley, M.J. The spread of a turbulent plane jet issuing into a parallel moving airstream. JFM, 27, Pt.2, 381-394 (1967).
4. Riley, M.J. Plane turbulent jet flow in a favourable pressure gradient. ARC CP No.1236 (1973).
5. Feik, R.A. The structure and development of a two-dimensional jet inclined to a streamwise flow. Queen Mary College, ER 1001 (1973).
6. Pontikis, Y. An investigation of a two-dimensional jet and a jet of finite span inclined to a streamwise flow. Ph.D Thesis, Univ. of London (1979).
7. Spence, D.A. The lift coefficient of a thin jet-flapped wing. Proc.Roy.Soc.,A,251,407-425 (1956).
8. Bradshaw, P. Effects of streamline curvature on turbulent flow. AGARDograph No.169 (1973).
9. Everitt, K.W. The spread of turbulent jets and wakes. Ph.D Thesis, Univ. of London (1972).

DETAILS OF JET MODEL

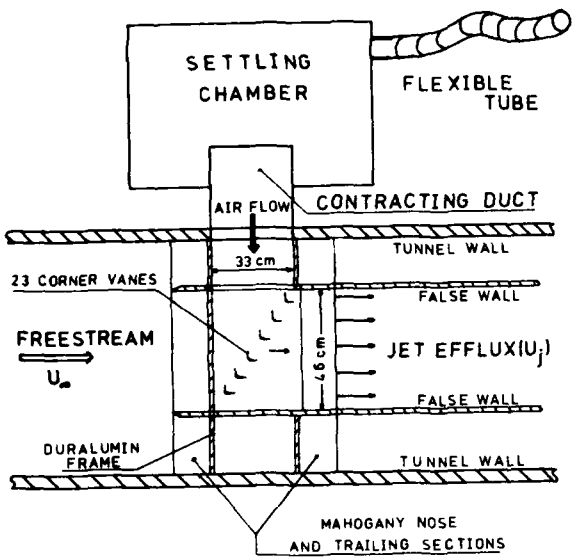

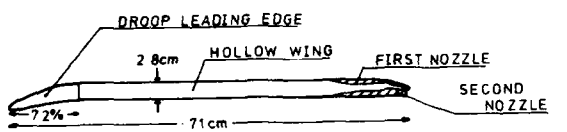

WING SECTION THRO' CENTRE LINE

FIGURE 1

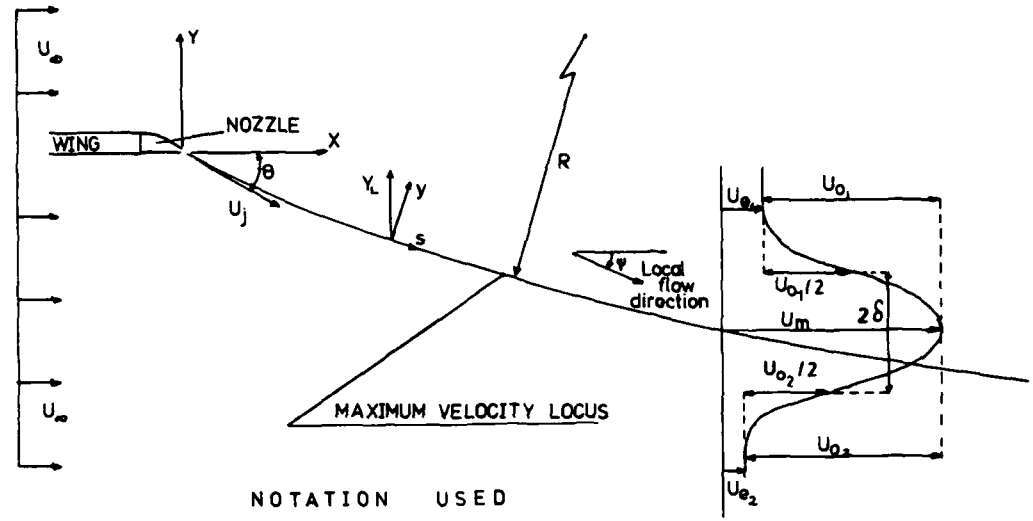

NOTATION USED

FIGURE 2

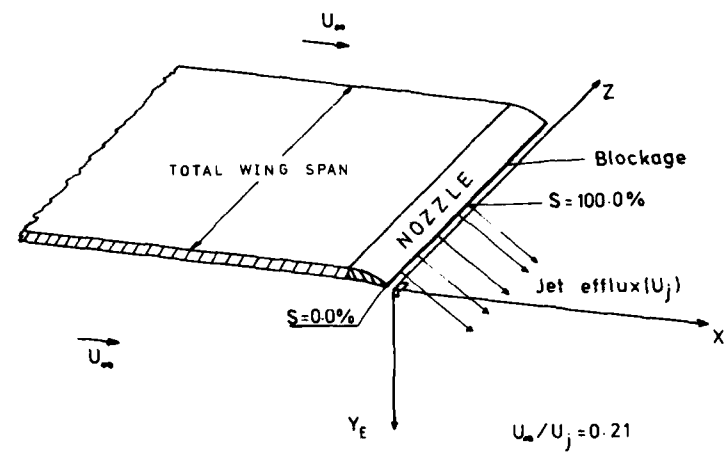

SCHEMATIC REPRESENTATION OF THE 3-D. JET

FIGURE 3

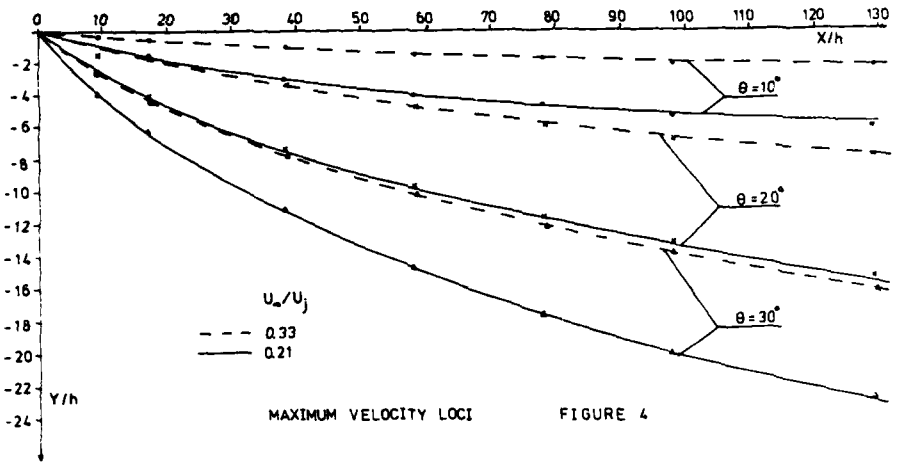

MAXIMUM VELOCITY LOCI FIGURE 4

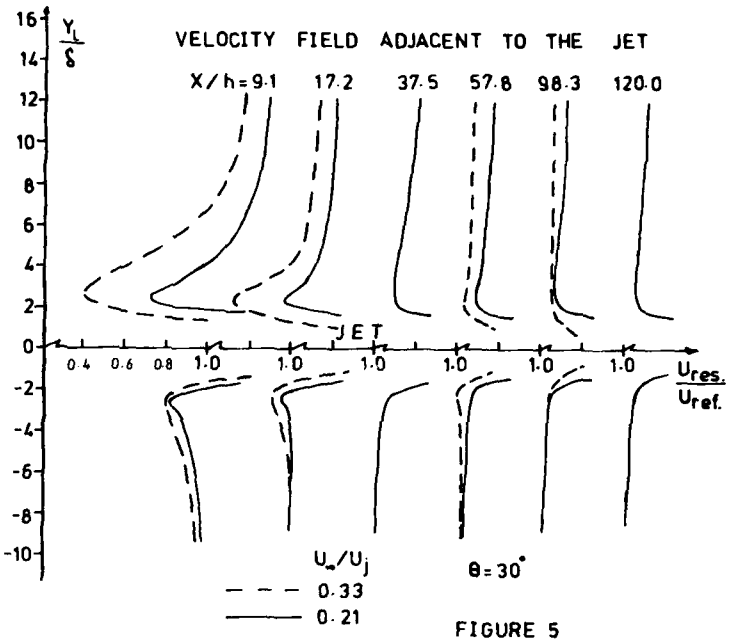

FIGURE 5

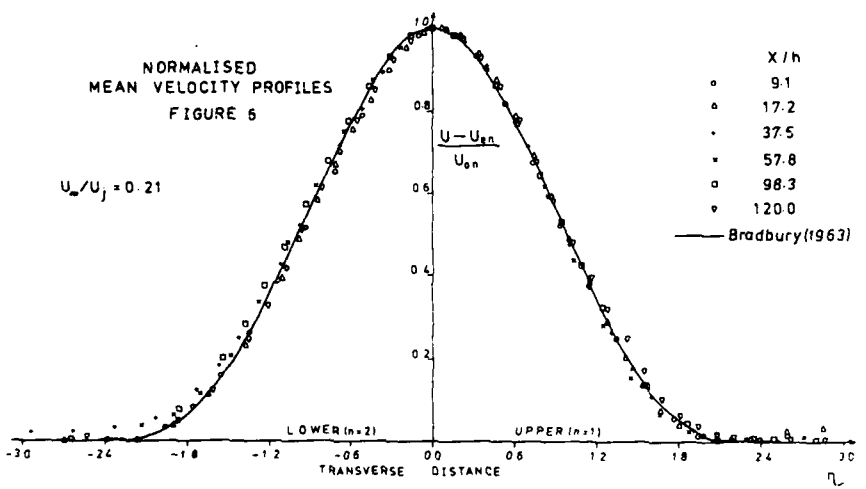

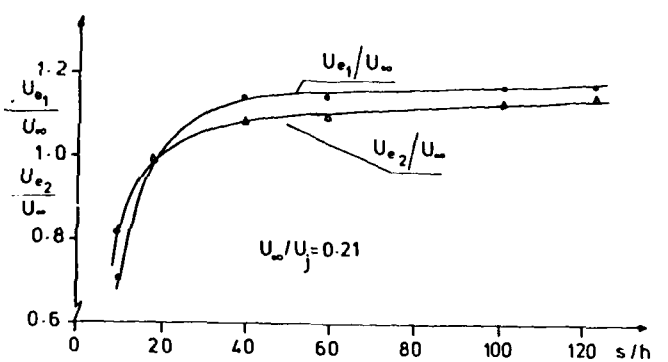

EDGE VELOCITIES
FIGURE 7

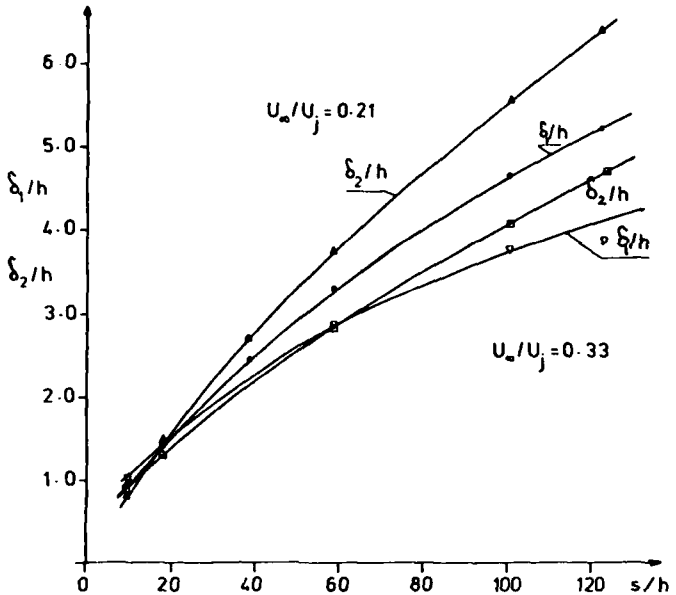

UPPER & LOWER HALF WIDTHS
FIGURE 8

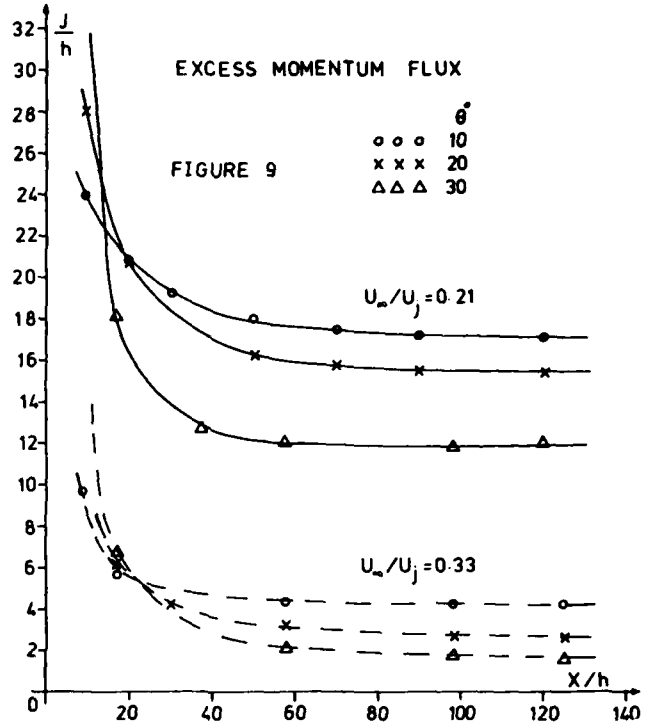

FIGURE 9

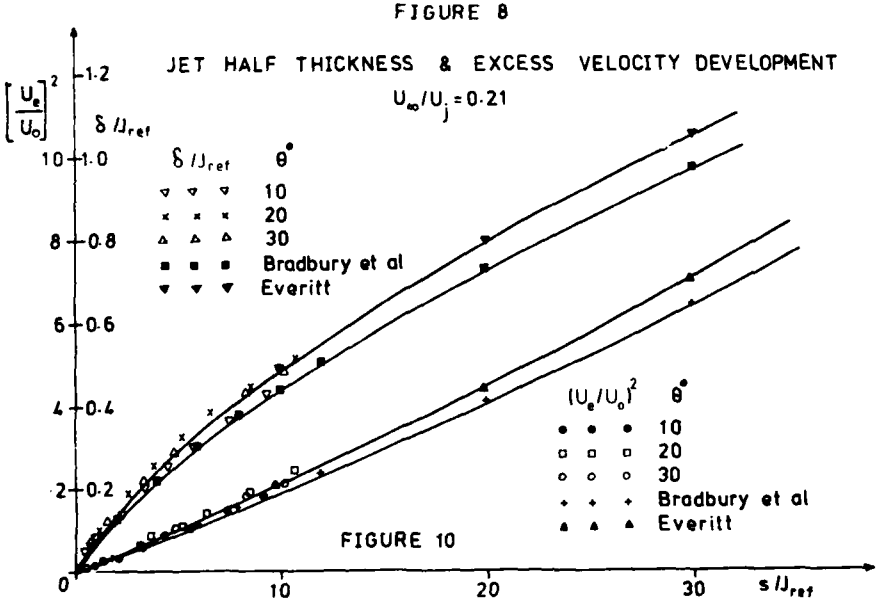

FIGURE 10

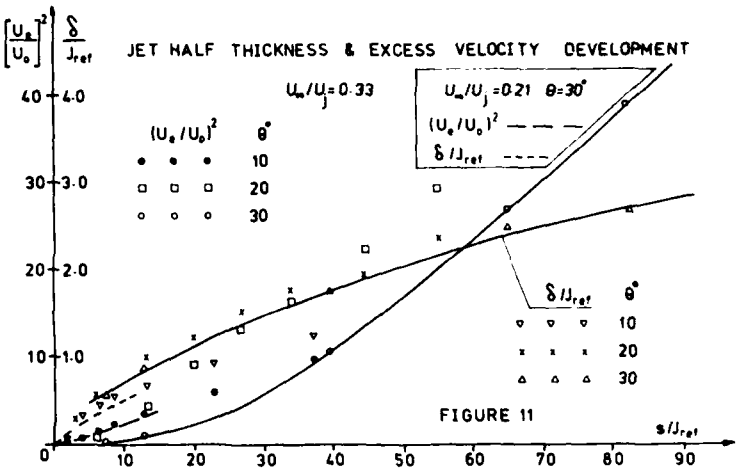

FIGURE 11

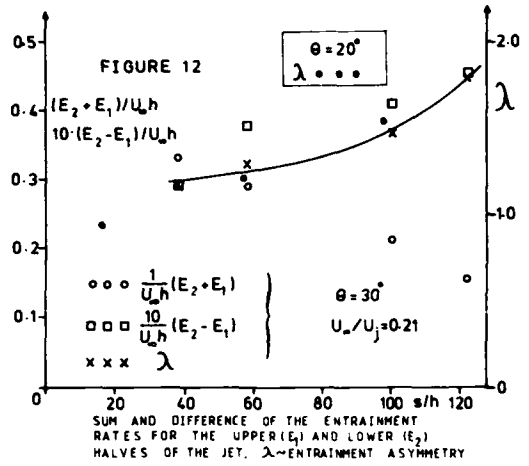

SUM AND DIFFERENCE OF THE ENTRAINMENT RATES FOR THE UPPER (E_1) AND LOWER (E_2) HALVES OF THE JET. λ~ENTRAINMENT ASYMMETRY

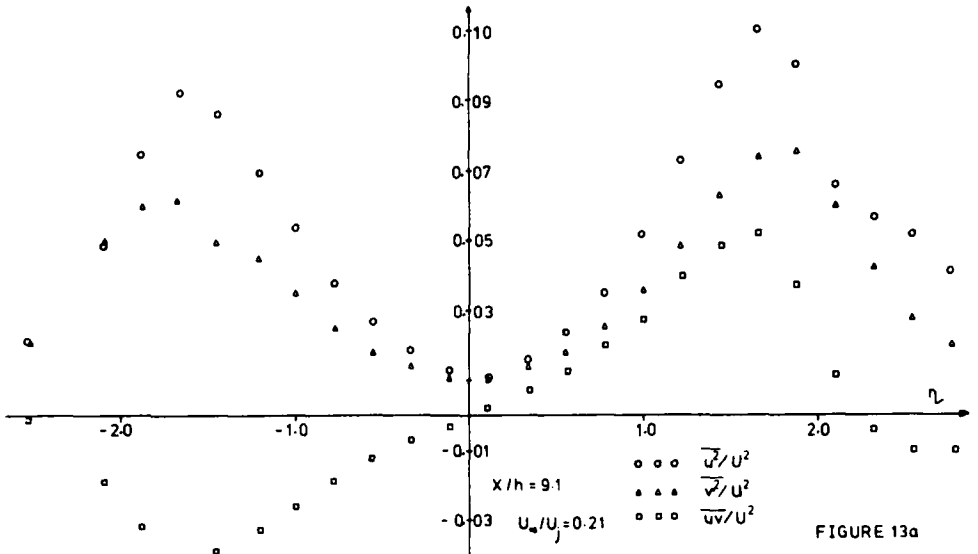

FIGURE 13a

TURBULENCE MEASUREMENTS

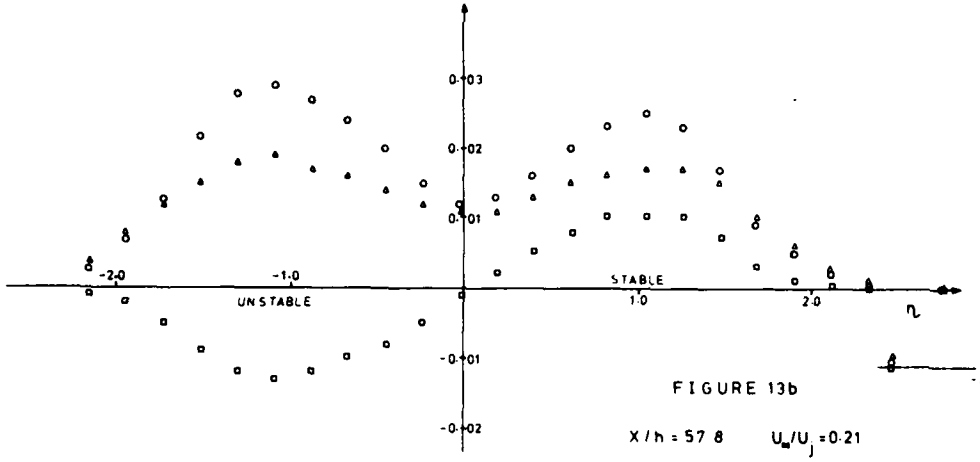

FIGURE 13b

X/h = 57·8 U_∞/U_j = 0·21

TURBULENCE MEASUREMENTS

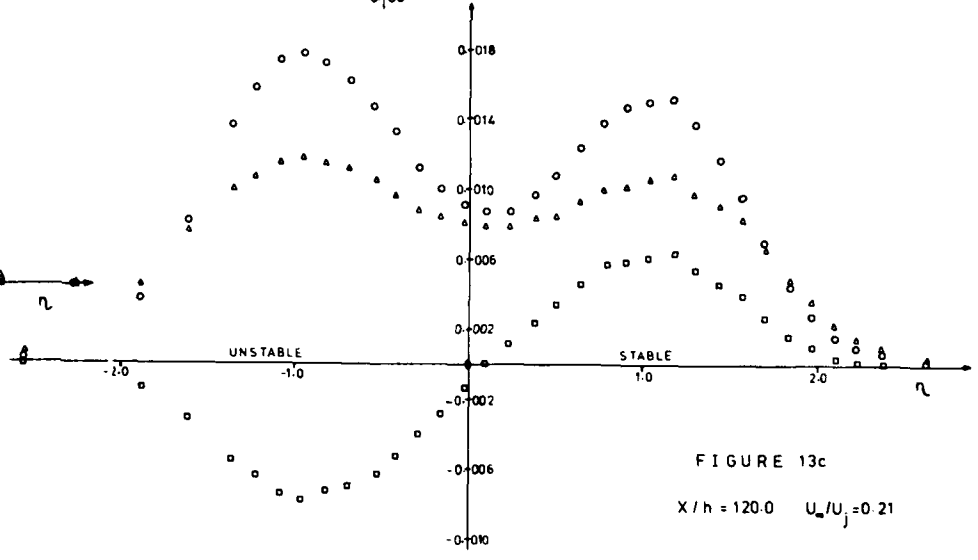

FIGURE 13c

X/h = 120·0 U_∞/U_j = 0·21

TURBULENCE MEASUREMENTS

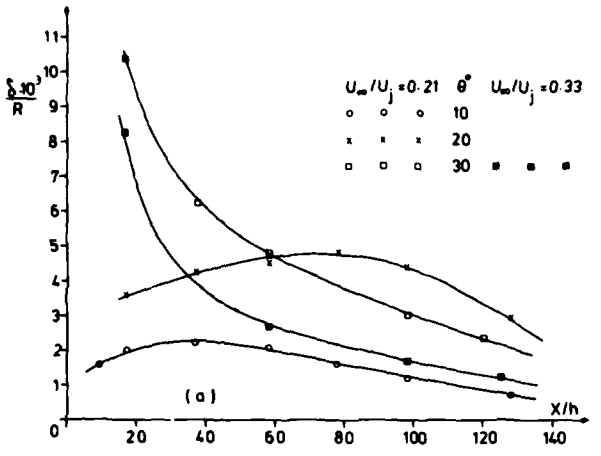

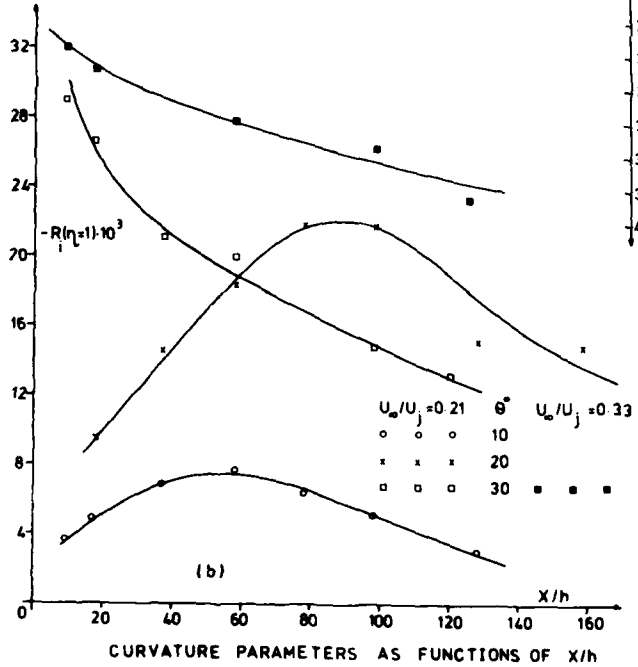

CURVATURE PARAMETERS AS FUNCTIONS OF X/h

FIGURE 14

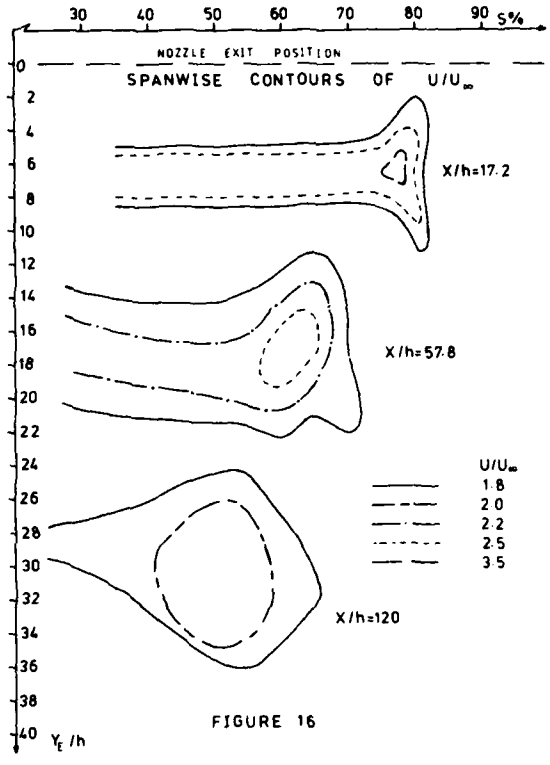

FIGURE 16

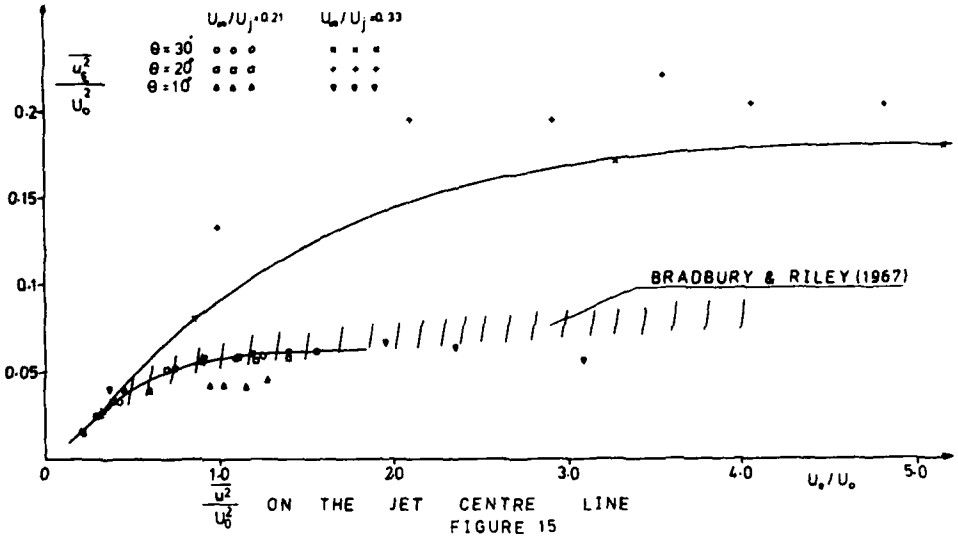

$\frac{u^2}{U_0^2}$ ON THE JET CENTRE LINE

FIGURE 15

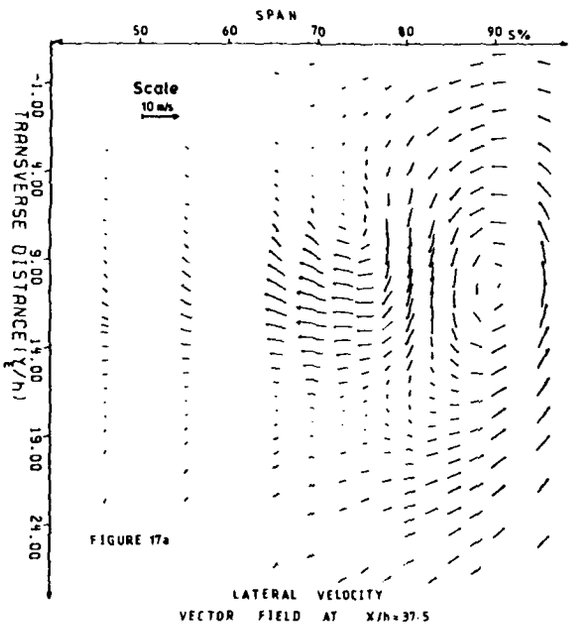

FIGURE 17a

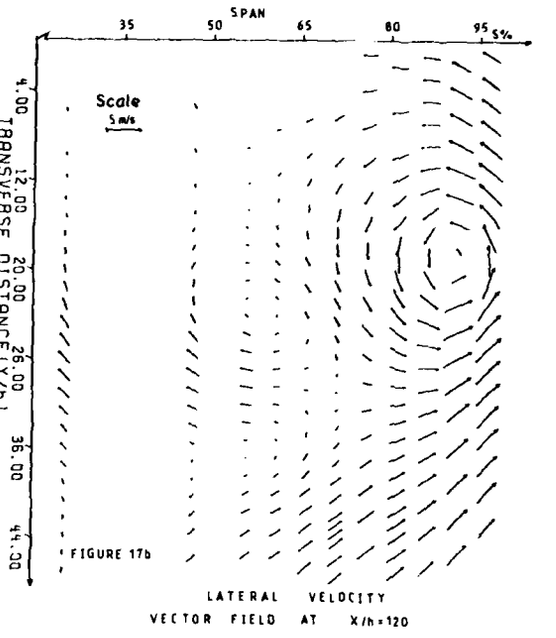

FIGURE 17b

SPANWISE DISTRIBUTION OF STREAMWISE COMPONENT OF VORTICITY (X/h = 17.2)

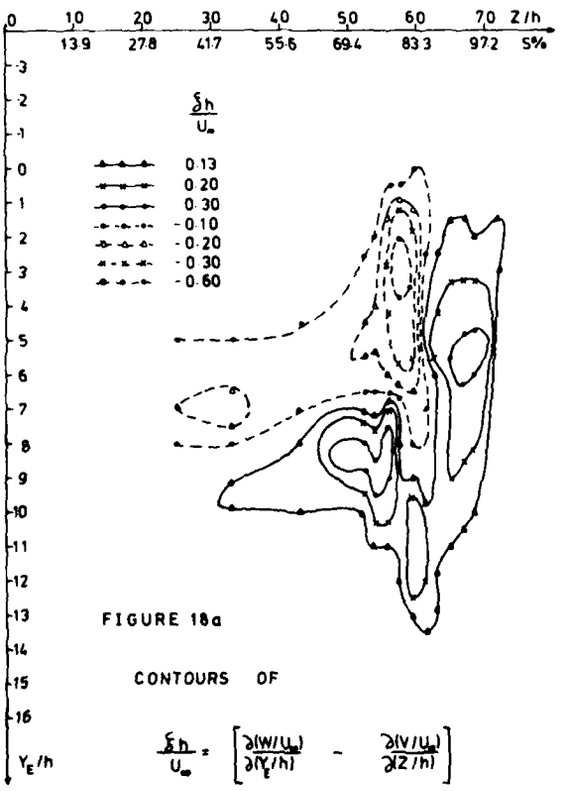

FIGURE 18a

CONTOURS OF

$$\frac{\xi h}{U_\infty} = \left[\frac{\partial(W/U_\infty)}{\partial(Y_E/h)} - \frac{\partial(V/U_\infty)}{\partial(Z/h)}\right]$$

SPANWISE DISTRIBUTION OF STREAMWISE COMPONENT OF VORTICITY (X/h = 98.3)

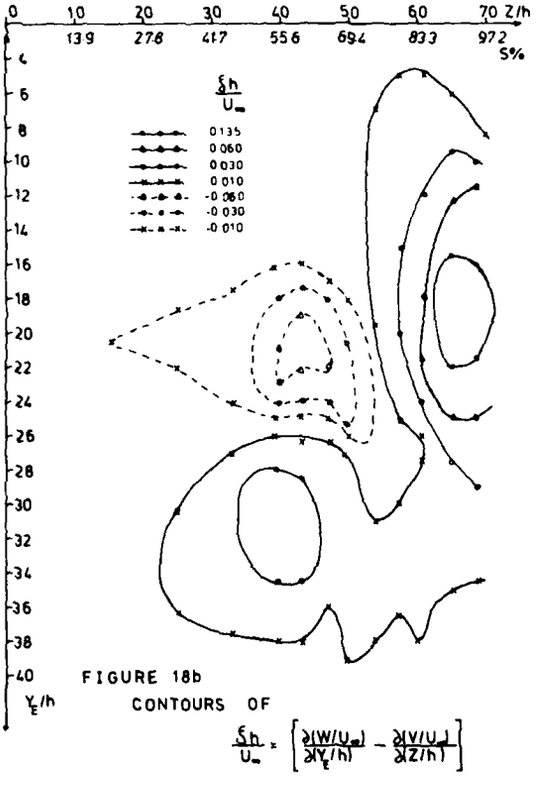

FIGURE 18b

CONTOURS OF

$$\frac{\xi h}{U_\infty} = \left[\frac{\partial(W/U_\infty)}{\partial(Y_E/h)} - \frac{\partial(V/U_\infty)}{\partial(Z/h)}\right]$$

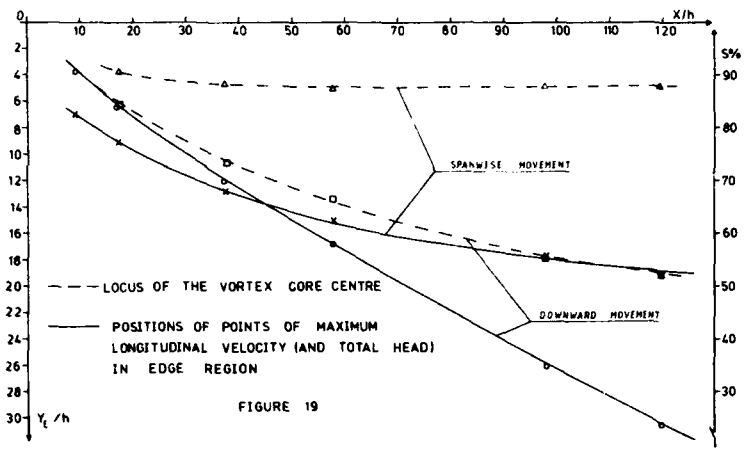

FIGURE 19

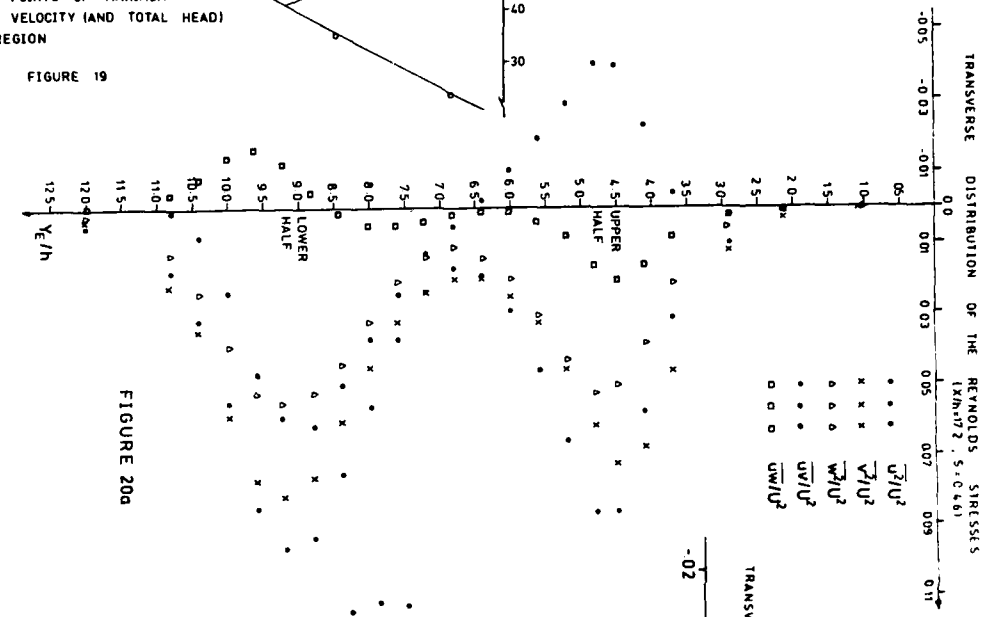

FIGURE 20a

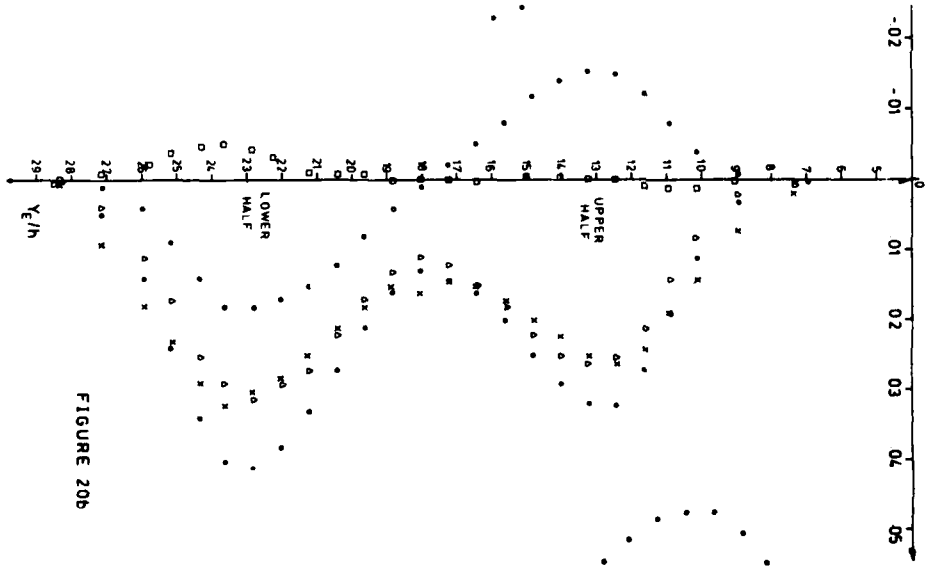

FIGURE 20b

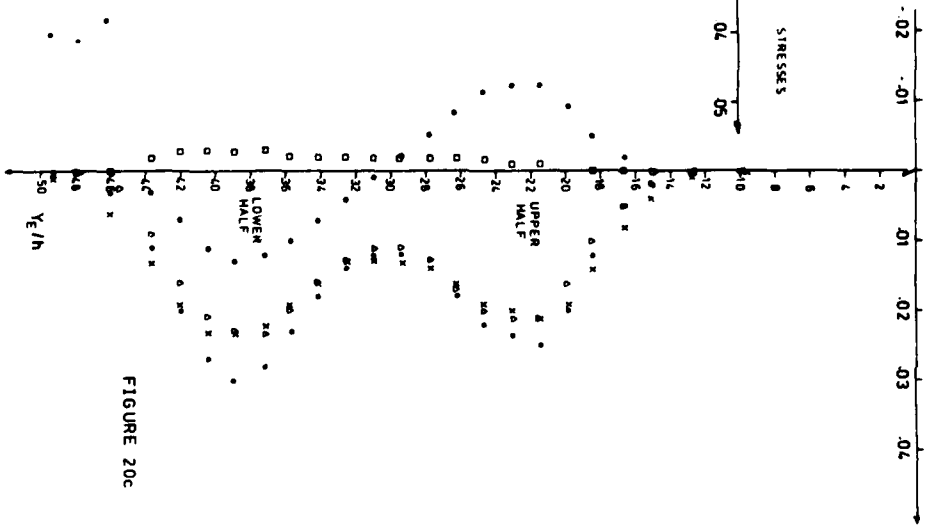

FIGURE 20c

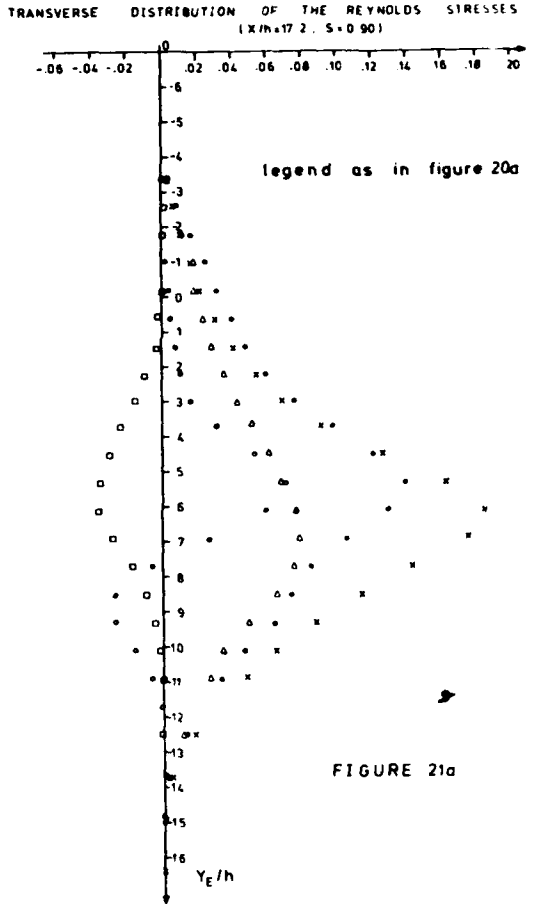

FIGURE 21a

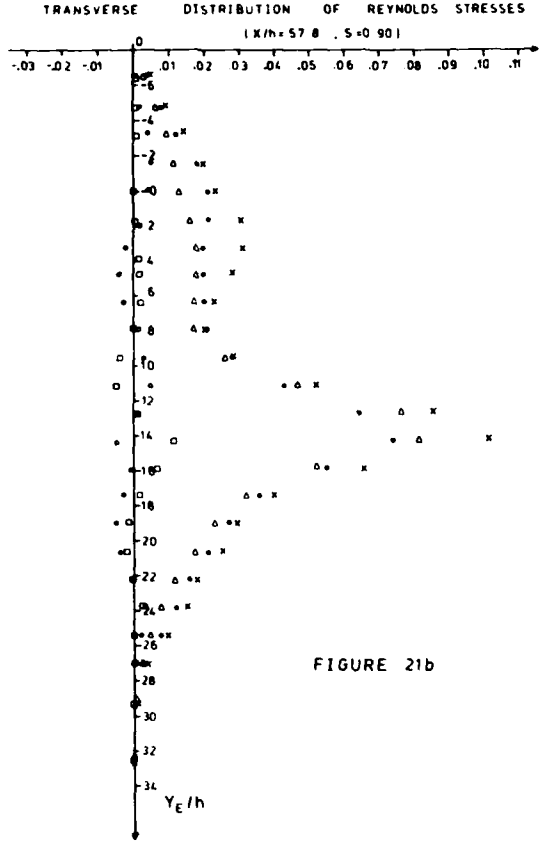

FIGURE 21b

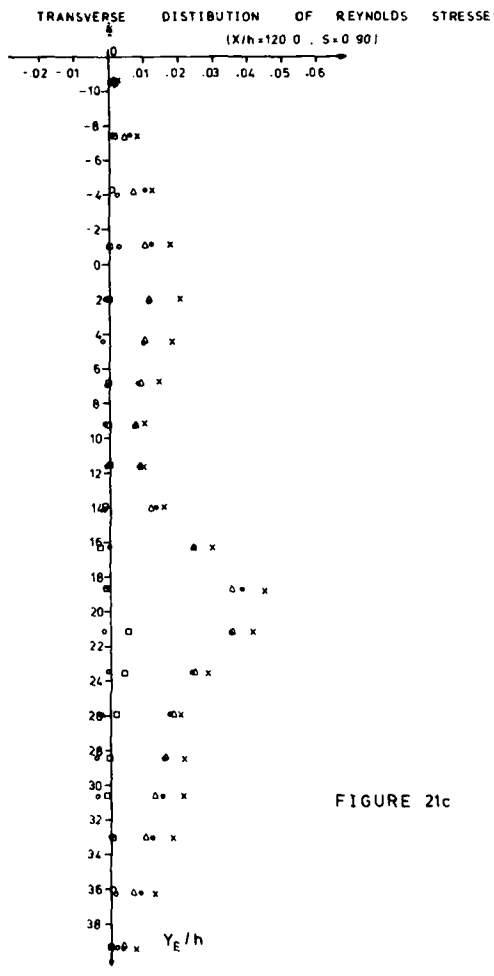

FIGURE 21c

RESONANT ENTRAINMENT OF A CONFINED PULSED JET

Pradip G. Parikh*

Jet Propulsion Laboratory
California Institute of Technology
Pasadena, California 91103, USA

Abstract

This paper reports the discovery of a new resonant entrainment phenomenon associated with a confined, pulsed jet flow. It was found that a confined jet, when pulsed at an organ-pipe resonant frequency of the confinement tube, experiences greatly enhanced entrainment and mixing near the exit end of the confinement tube. Both visual and quantitative evidence of this phenomenon is presented. The new effect should be of considerable interest in ejector and combustor design, both of which benefit from any enhancement in mixing between a primary and a secondary flow.

Introduction

Rapid mixing of a primary jet flow with entrained or a coaxially flowing secondary flow is of great importance in many applications as diverse as ejectors, combustors, and chemical lasers. The importance of increasing the mixing rate between primary jet flow and entrained flow in a thrust-augmenting ejector was stressed by Quinn [1], who showed that the thrust augmentation was directly proportional to the degree of mixing attained at the ejector exit. In an industrial burner utilizing gaseous, liquid, or particulate fuel, rapid mixing in the reaction zone is of utmost importance for compactness, high combustion efficiency, and improved homogeneity which is beneficial for control of pollutant formation [2].

Several investigators have used deliberately introduced unsteadiness to improve the mixing rate of jets. In an investigation primarily aimed at study of large-scale orderly structures in a turbulent jet, Crow and Champagne [3] found that, even at amplitudes of excitation as low as 2%, the entrainment rate in the first six diameters from the jet exit plane increased by 20% over the unforced case. Binder and Favre-Marinet [4] used a spinning butterfly valve upstream of a nozzle to produce amplitudes of pulsations up to 40% of mean velocity. Both the decay of the centerline velocity and the spreading distance of the jet were strongly affected by pulsations. Their co-workers Curtet and Girard [5] conducted a visualization study of pulsed jets and provided smoke and Schlieren pictures of puff formation. Bremhorst and co-workers [6,7] studied both fully pulsed and pulsed-core jets and attributed the increased entrainment of pulsed jets to their inherently larger entrainment interface structure. They also found lesser entrainment rates for pulsed-core jets as compared to a fully pulsed jet [7]. Viets [8] utilized a feedback fluidic loop to produce a flapping two-dimensional jet nozzle for V/STOL application and reported marked influence of this introduction of oscillating transverse velocity component on jet spreading rates.

During the course of their investigation of jet mixing rates, Hill and Greene [9] discovered the phenomenon of a "whistler nozzle," in which a step change in the area of an extended nozzle resulted in self-excited acoustic oscillations of the jet and led to significantly improved mixing rates, as evidenced by a rapid decay of the centerline velocity.

Recently, Habib and Whitelaw [10] reported measurements on velocity characteristics of a confined coaxial jet and found that confinement has beneficial effects on the mixing rate of coaxial jets.

The present study describes a new method of greatly enhancing entrainment and mixing rates of jets using both confinement and pulsing. It is shown that a confined jet exhibits a spectacular resonant entrainment behavior when pulsed at frequencies coinciding with the organ-pipe frequencies of the confining tube.

---

*Member of Technical Staff

Resonant Entrainment Phenomenon

The resonant entrainment phenomenon was observed during the course of an investigation to study effects of high-frequency pulsations on stagnation-point heat transfer. A schematic of the experiment is shown in Fig. 1. The supply air is filtered, metered by means of a laminar flow element, and delivered to a pulsing rotor device after passage through a settling chamber.

The details of the pulsing rotor device are shown in Fig. 2. The 0.318 cm (1/8 in.) diameter (d) opening at the base of the 1.143 cm (0.45 in.) diameter (D) confinement tube is opened and closed at high frequencies (up to 7.5 kHz) by means of a pulsing rotor. The rotor has eighteen 0.318 cm (1/8 in.) diameter holes and is driven by a Variac-controlled motor up to speeds of 25,000 rpm. The motor speed was measured directly by means of a photoelectric transducer.

The device thus produces a pulsed jet issuing from a 0.318 cm (1/8 in.) diameter orifice, whose pulsing frequency may be varied in the range 0 to 7.5 kHz.

The maximum jet velocity was attained, obviously, when the rotor was in fully open position and minimum when the rotor was in fully closed position. Due to the clearance between the rotor and the casing, the minimum jet velocity (or flow rate) was non-zero. For a fixed upstream pressure, the ratio of the flow rates for fully open position of the rotor to that at fully closed position (under stationary condition) was approximately 2.2. For the same upstream pressure, the flow rate under rotor spinning condition was approximately the average of the flow rates for fully open and fully closed stationary positions. From these stationary measurements, the amplitude of the velocity pulsations of the jet issuing from the orifice was estimated to be 37.5% of the mean velocity. This pulsed jet is confined by a confinement tube of diameter $D = 1.143$ cm (0.45 in.) and length $L = 11.1$ cm (4.37 in.) before issuing out into the ambient air. The region of interest is immediately downstream of the confinement tube exit plane.

Hot-wire measurements at the jet centerline, one diameter downstream of the confinement tube exit plane, showed that the mean velocity there increased sharply in the neighborhood of certain characteristic resonant pulsing frequencies. The peak velocities attained, together with corresponding resonant pulsing frequencies, are plotted in Fig. 3. The peak velocities are normalized with respect to U_{ave}, where

$$U_{ave} = \frac{\bar{\dot{m}}}{\rho_e A_2} \tag{1}$$

Here $\bar{\dot{m}}$ is the time-averaged mass flow rate as measured by the laminar flow meter (Fig. 1), ρ_e is the exit plane density, and A_2 is the confinement tube cross-sectional area. $\bar{\dot{m}}$ was maintained nearly constant during measurements at all frequencies. At the flow rates employed, U_{ave} was approximately 10 m/s (33 ft/sec).

The horizontal dashed line in Fig. 3 shows the normalized centerline velocity value (1.37) for an unpulsed jet for the same flow rate. This value was determined experimentally with the rotor stationary and in the fully open position. It may be seen that the augmentation in the centerline velocity at some resonant frequencies over the stationary value is up to 200%!

To provide an estimate of the half-width of this resonant behavior, measurements of centerline mean velocity one diameter downstream from the confinement tube exit plane were taken in the vicinity of the $\nu_p = 2241$ Hz resonance (Fig. 4). The vertical dashed lines denote the location and the magnitude of the normalized peak mean velocity for adjacent resonances. The horizontal dashed line denotes the experimental $(\bar{u}_{CL}/u_{ave})_{x=D}$ value for the unpulsed jet at the same mean primary mass flow rate. Notice that the half-width is approximately 100 Hz and that the normalized mean velocity between resonances remains substantially higher than the unpulsed value of 1.37.

Significance of the Resonant Frequencies

The frequencies at which a local maximum in the centerline velocity was observed (Fig. 3) were compared with the resonant frequencies of an open/ closed-ended organ pipe of the same length as the confinement tube. The resonant organ pipe frequencies are given from [11] as

$$\nu_{n,o-c} = (2n-1)\frac{C}{4L}, \quad n = 1,2,3,\ldots, \tag{2}$$

Here L' is the corrected length given by

$$L' = L + 0.3\,D \tag{3}$$

where L is the actual length and D is the pipe diameter [11].

Using the discharge tube dimensions of $L = 11.1$ cm and $D = 1.143$ cm (0.45 in.), together with the speed of sound $C = 344$ m/s at 21°C,

$$\nu_{1,o\text{-}c} = \frac{C}{4L'} = 751.6 \text{ Hz} \quad .$$

The measured resonant frequencies for the resonant entrainment phenomenon are tabulated in Table I and are normalized with the $\nu_{1,o\text{-}c}$ value determined above. Notice that strong resonances are observed when

$$(\nu_p/\nu_{1,o\text{-}c}) = 1,\ 3,\ 5,\ 7,\ 9 \quad ,$$

while weak resonances are observed when

$$(\nu_p/\nu_{1,o\text{-}c}) = \frac{1}{2}\ ,\ \frac{3}{2}\ ,\ \frac{5}{2}\ ,\ \text{etc.}$$

To ascertain that the "resonant" frequencies were indeed the organ-pipe resonant frequencies of the confinement tube, different tube lengths ranging from 6 to 24 cm were employed. In all cases the phenomenon was found to scale on the organ-pipe resonant frequency based on the tube length employed.

Radial Profiles and Centerline Velocity Decay

Radial traverse of the jet one diameter downstream from the exit plane with hot wire showed that high mean velocities persisted a considerable distance from the centerline. Figure 5 shows a comparison between the unpulsed confined jet and the confined jet pulsed at the resonant frequency, $f = C/4L'$ at the same mean flow rate. Note that, under resonant pulsing, not only are the mean velocities substantially larger, but so is the spreading distance. As the primary flow rate is the same for the two cases, the substantially higher volume flow rate for the pulsed jet must result from increased entrainment. This increased entrainment occurs only in the vicinity of the organ-pipe resonant frequencies of the confinement tube; hence the phenomenon will be termed resonant entrainment.

The question now arises as to where the large increase in the momentum of the jet comes from during resonant pulsing. To answer this question, we consider the unpulsed confined jet, as shown in Fig. 6. In this case, the high momentum of the small jet (of diameter d) is reduced considerably as the jet attaches to the confinement tube wall and the mean velocity decreases to satisfy continuity. If we assume an incompressible, one-dimensional flow at inlet and exit and neglect wall friction, a control volume analysis shows that

$$u_o = \frac{A_1}{A_2}\,u_1 = \left(\frac{d}{D}\right)^2 u_1 \tag{4}$$

$$\rho u_o^2 A_2 = \frac{A_1}{A_2}\,\rho u_1^2 A_1 = \left(\frac{d}{D}\right)^2 \rho u_1^2 A_1 \tag{5}$$

and

$$p_{2,s} - p_{1,s} = \rho u_1^2 \left(\frac{d}{D}\right)^2 \left[1 - \left(\frac{d}{D}\right)^2\right] \tag{6}$$

Also, for steady flow,

$$p_{2,s} = p_a \tag{7}$$

Thus, we see from Eq. (5) above that, under steady flow conditions, the momentum of the primary jet is larger than that of the jet issuing at the exit of the confinement tube by a factor of $(D/d)^2$. Furthermore, the decrease in the momentum is accompanied by an increase in the pressure from $p_{1,s}$ to $p_{2,s} = p_a$, as shown by Eqs. (6) and (7) above.

We shall next show that the momentum of the resonantly pulsed confined jet at the confinement tube exit is comparable to that of an unconfined pulsed jet of diameter d at the same mean flow rate. However, the spreading rate and centerline velocity decay for the resonantly pulsed confined jet are much more rapid.

The confinement tube of diameter D was replaced by a tube of the same length L but of a diameter d, i.e., the same as that of the orifice. Radial profiles of velocity were measured at two axial locations $x/d = 24$ and 48, where x was measured from the exit plane of the tube. The results are shown in Figs. 7(a) and (b). The mean flow rate in all cases was maintained at the same value. Note that the maximum spreading rate and centerline velocity decay are attained with case (iii), the resonantly pulsed confined jet.

The centerline velocity decay measurements are further shown in Fig. 8. It may be seen that, for a fixed mean flow rate, the initial decay $(x/d < 25)$ of centerline velocity for the resonantly pulsed confined jet is considerably more than that for either pulsed or unpulsed unconfined jet. At larger axial distances, the centerline velocity values for the two pulsed cases approach the same value.

Direct Measurements of Total Entrainment

In an effort to estimate the augmentation in the total entrainment rate during resonances, the pulsed jet was used in an ejector configuration (Fig. 9). The confinement tube was placed at the entrance end of a 15.24 cm (6 in.) diameter duct of 1.067 m (3-1/2 ft) length. The sum of the primary and the entrained flow rates was measured at the exit end of the duct by means of a rotating vane anemometer. The latter was calibrated in a wind tunnel for a relationship between the rotational speed and the flow rate.

The total flow rate through the rotating vane anemometer, normalized with the time-averaged primary flow rate, is shown in Fig. 10 for the resonant frequencies. The lower dashed line shows experimentally measured (Q_{total}/Q_p) value for the unpulsed jet with $D/d = 3.6$, while the upper dashed line shows this ratio for the case of $D/d = 1.0$ and $f = 0$. The primary flow rates in all cases are the same.

Comparing the two unpulsed cases at the same primary flow rate, the (Q_{total}/Q_p) ratio for the $D/d = 1.0$ case is considerably higher due to the higher momentum of the primary flow (see Eq. (5)).

Notice that, under resonant pulsing conditions, the (Q_{total}/Q_p) ratio for the $D/d = 3.6$ configuration approaches and even exceeds the unpulsed jet with $D/d = 1.0$. For a fixed geometry, $D/d = 3.6$, the augmentation in (Q_{total}/Q_p) ratio at some pulsing frequencies is more than 200% over the unpulsed value.

The effect of varying Q_p on the (Q_{total}/Q_p) ratio is shown in Fig. 11. The data points represented by circles are for the $D/d = 3.6$ configuration, while those represented by triangles are for the $D/d = 1.0$ configuration. In both cases the upper curve represents flow pulsed at a resonant frequency $\nu_p = C/4L'$, while the lower curve represents unpulsed flow.

In both cases of unpulsed flow, the (Q_{total}/Q_p) ratio levels off as Q_p is increased, while both cases of pulsed flow attain a maximum in the (Q_{total}/Q_p) ratio. The augmentation in total entrainment during resonant pulsing over the unpulsed value is only slight for the $D/d = 1.0$ case. This may be partially accounted for by the difference in the initial momentum between a steady and an unsteady jet at the same mean flow rate and the same diameter. For an unsteady jet, we may represent the phase-averaged velocity as

$$\langle u \rangle = \bar{u} + \tilde{u} \tag{8}$$

where $\bar{u}$ is the mean and $\tilde{u}$ is the periodic component of velocity $(\overline{\tilde{u}} = 0)$. Then it may be shown that the ratio of the time-averaged momentum of an unsteady jet to that of a steady jet with the same mean velocity $\bar{u}$ may be expressed as

$$\frac{\rho \langle u \rangle^2}{\rho \bar{u}^2} = 1 + \frac{\overline{\tilde{u}^2}}{\bar{u}^2} \tag{9}$$

which is always greater than unity. The increase in total entrainment at resonant pulsing over the unpulsed value for the $D/d = 1.0$ case is about 20% at $Q_p = 1.0$ scfm. However, for the $D/d = 3.6$ case, resonant pulsing augments the (Q_{total}/Q_p) ratio by 375% over the unpulsed value at $Q_p = 0.8$ scfm.

Finally, comparing the two pulsed cases, both with resonant pulsing at $f = C/4L'$, the case of $D/d = 3.6$ results in total entrainment rates higher than those for the $D/d = 1.0$ case over most of the flow rate range. More significantly, this enhanced entrainment occurs in a much shorter distance from the confinement tube exit plane, as shown by the radial profiles in Fig. 7(a),(b), the centerline velocity decay behavior, Fig. 8, and confirmed by flow-visualization studies discussed below.

Flow-Visualization Experiments

The vane anemometer measurements showed that the total entrainment of the confined pulsed jet ($D/d = 3.6$) approaches and even exceeds that of the unconfined pulsed jet ($D/d = 1.0$). What is more important, however, is that the local entrainment and mixing rates immediately downstream of the confinement tube exit are several times larger for the $D/d = 3.6$ case under resonant pulsing, as seen from the radial profiles and centerline velocity decay behavior.

The dramatically enhanced entrainment and mixing rates immediately downstream of the confinement tube exit were visualized by two methods: (i) methane flame and (ii) smoke injection.

(i) Methane flame. Methane gas was introduced as the primary fluid and burned at the exit end of the confinement tube ($D/d = 3.6$). Under resonant pulsing, the entrainment of ambient air was too excessive to maintain the fuel/air ratio above the lean flammability limit, and it was necessary to curtail the entrainment by means of a shallow can mounted at the exit end of the confinement tube. Photographs of the flame under no pulsing and resonant pulsing conditions are shown in Fig. 12. Fig. 12(a) shows unpulsed methane jet burning freely in air. Fig. 12(b) shows the flame for the same mean flow rate of methane, but pulsed at the resonant frequency $\nu_{1,o-c}$. Notice the considerably shortened flame length and the absence of soot-particle radiation, both of which are demonstrative of enhanced mixing and lean combustion.

(ii) Smoke injection. Smoke was introduced through a ring placed around the confinement tube, slightly below the exit plane. The objective was to trace the ambient air entrained by the jet issuing from the confinement tube. The smoke was made visible by a strobe light source, which was pulsed in synchronization with the pulsing rotor. Strong vortex interaction between the jet flow and the entrained flow was revealed under resonant pulsing. Fig. 13 shows a photograph of the large vortices at the exit from the confinement tube. No such large-scale vortex interaction could be detected under no pulsing and off-resonant-pulsing conditions.

Mean Pressure Measurements

Recall that, under steady flow conditions, the pressure $p_{1,s}$ at the base of the confinement tube ($D/d = 3.6$) is lower than that ($p_{2,s}$) at the exit, as shown by Eq. (6). Furthermore, the pressure $p_{2,s}$ at the exit is the same as the ambient pressure p_a. A few preliminary measurements were made to determine how this mean pressure distribution is affected by resonant pulsing. These measurements showed that, as the fundamental resonant frequency was approached, the pressure distribution along the confinement tube was markedly affected.

Under resonant pulsing, the mean pressure p_2 at the confinement tube exit approached the value $p_{1,s}$, while the mean pressure p_1 at the confinement tube base approached p_a. This means that the mean pressure near the exit of the confinement tube drops significantly below the ambient pressure p_a, causing a large quantity of ambient air to be drawn into the confinement tube. Furthermore, the jet issuing from the orifice at the base does not seem to attach to the walls of the confinement tube and appears at the exit as a small-diameter jet. Vigorous mixing between the jet and the entrained ambient air takes place near the exit end of the confinement tube through a strong vortex interaction. These observations are supported by the smoke-strobe visualization of the flow field shown in Fig. 13.

Conclusions

The investigation reported here has revealed the existence of a resonant entrainment phenomenon for a confined pulsed jet. The enhancement in entrainment and mixing achieved with resonant pulsing are impressive. The phenomenon should be of considerable interest in ejector and burner design, both of which benefit from any enhancement in mixing between a primary and a secondary flow.

From the foregoing presentation of measurements on the resonant entrainment phenomenon, it appears that the following two requirements need to be met for the phenomenon to occur.

1) The primary flow must be pulsed at frequencies which are equal to (or one-half of) the organ-pipe natural frequencies $\nu_{n,o-c}$ of the confinement tube.

2) The diameter D of the confinement tube must be larger than the diameter d of the primary jet orifice.

Evidently the augmentation in entrainment achieved under resonant pulsing will depend upon several parameters, namely, the D/d ratio, the discharge tube length L, and the primary jet flow rate Q_p. This opens up the possibility of optimizing the entrainment by proper selection of these parameters.

The mechanism responsible for the resonant entrainment phenomenon appears to be twofold:

1) Under resonant pulsing, there appears a low mean pressure region near the exit end of the confinement tube, which causes a large quantity of ambient air to be drawn in.

2) The resonantly pulsed confined jet does not attach to the wall of the confinement tube and mixes vigorously with the entrained flow through a strong vortex interaction.

Clearly, more detailed phase-averaged hot-wire and pressure measurements, together with flow-visualization techniques, will be necessary to uncover the underlying mechanism. Such an understanding will then lead to quantitative estimation of augmentation in entrainment rates under the resonant pulsing condition.

The amplitude of pulsation in the present investigation was approximately 37.5% of the mean velocity, which results in the sound level approaching that of a siren. It would be of interest to explore the minimum pulsation amplitude necessary to achieve resonant entrainment.

Table I

Q_p = 2.250 scfm , $\nu_{1,0-c}$ = 751.6 Hz

ν_p	$(\overline{u}_{CL}/u_{ave})_{x=D}$	$\nu_p/\nu_{1,o-c}$
Hz	----	----
378	2.17	0.503 ≈ 1/2
747	3.93	0.994 ≈ 1
1132	2.67	1.506 ≈ 3/2
1896	2.58	1.523 ≈ 5/2
2241	4.08	2.982 ≈ 3
2667	2.37	3.548 ≈ 7/2
3448	2.61	4.588 ≈ 9/2
3772	4.23	5.019 ≈ 5
5336	3.71	7.100 ≈ 7
6860	2.97	9.127 ≈ 9

Nomenclature

A_1	Cross-sectional area of the jet orifice (see Fig. 6).
A_2	Cross-sectional area of the confinement tube.
C	Speed of sound.
d	Diameter of the jet orifice.
D	Diameter of the confinement tube.
f	Pulsing frequency.
L	Confinement tube length.
$\bar{\dot{m}}$	Time-averaged primary mass flow rate.
p_1	Mean pressure at the confinement tube base under resonant pulsing.
p_2	Mean pressure near the confinement tube exit under resonant pulsing.
$p_{1,s}$	Pressure at the confinement tube base, steady flow.
$p_{2,s}$	Pressure near the confinement tube exit, steady flow.
p_a	Ambient pressure.
Q_p	Primary volume flow rate.
Q_{total}	Primary + entrained volume flow rate.
r	Radial coordinate.
r_o	radius o f the jet orifice.
R	Radius of the confinement tube.
u_o	Jet velocity at orifice exit (see Fig. 6).
u_1	Uniform jet velocity at confinement tube exit (see Fig. 6).
ρ	Density
ν_p	Pulsing frequency.
$\nu_{n,o-c}$	Resonant frequency of an organ pipe with one end open, the other closed.

References

1. Quinn, B., "A Simple Estimate of the Effect of Ejector Length on Thrust Autmentation," Journal of Aircraft, 10, No. 5, 313-314 (May 1973).

2. Parikh, P. G., R. F. Sawyer, and A. L. London, "Pollutants from Methane-Fueled Gas Turbine Combustion," Trans. ASME, Journal of Engrg. for Power, 95, Series A, No. 2 (April 1973).

3. Crow, S. C., and F. H. Champagne, "Orderly Structures in Jet Turbulence," Jour. of Fluid Mech., 48, Part 3, 547-591 (1971).

4. Binder, G., and M. Favre-Marinet, "Mixing Improvement in Pulsating Turbulent Jets," ASME Symposium on Fluid Mechanics of Mixing (June 1973).

5. Curtet, R. M., and J. P. Girard, "Visualization of a Pulsating Jet," ASME Symposium on Fluid Mechanics of Mixing (June 1973).

6. Bremhorst, K., and W. H. Harch, "Near-Field Velocity Measurements in a Fully Pulsed Subsonic Air Jet," Turbulent Shear Flows - I, (eds. F. Durst et al.), Springer-Verlag, 1979.

7. Bremhorst, K., and R. D. Watson, "Velocity Field and Entrainment of a Pulsed-Core Jet," paper submitted for publication in Journal of Fluids Engineering, ASME, 1980.

8. Viets, H., "Oscillating Jet Nozzles for V/STOL Application," AIAA Paper No. 74-1189 presented at AIAA/SAE 10th Propulsion Conference, October 1974.

9. Hill, W. G., and P. R. Greene, "Increased Turbulent Jet Mixing Rates Obtained by Self-Excited Acoustic Oscillations," ASME Paper No. 77-FE-18 presented at ASME Fluids Engineering Conference, June 1977.

10. Habib, M. A., and J. H. Whitelaw, "Velocity Characteristics of a Confined Coaxial Jet," Journal of Fluids Engineering, Dec. 1979, p. 521.

11. Stephens, R. W., and A. E. Bate, Acoustics and Vibrational Physics, Edward Arnold Publishers (1966), pp. 174-175.

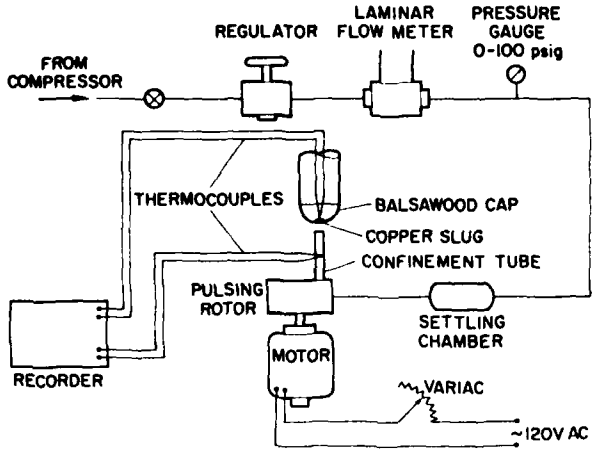

Fig. 1. Schematic of heat transfer experiment.

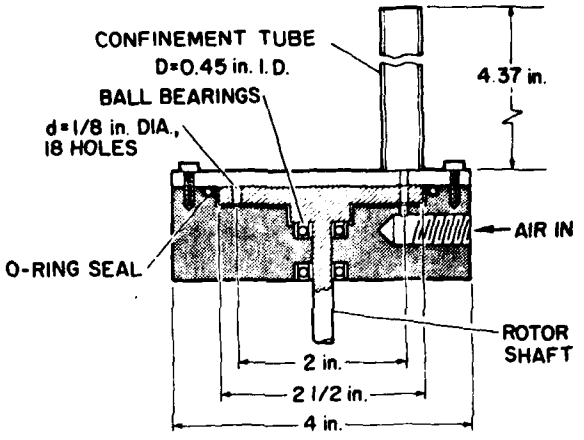

Fig. 2. Pulsing rotor.

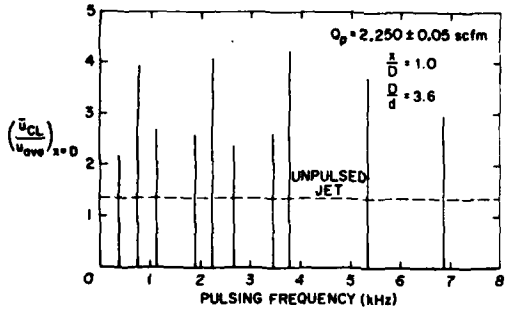

Fig. 3. Augmentation in centerline velocity under resonant pulsing.

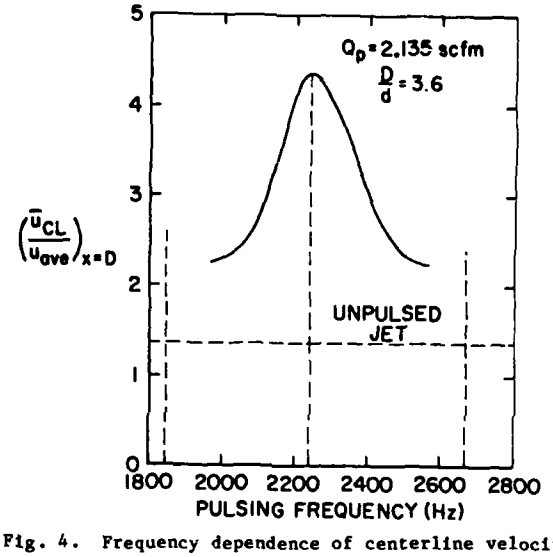

Fig. 4. Frequency dependence of centerline velocity

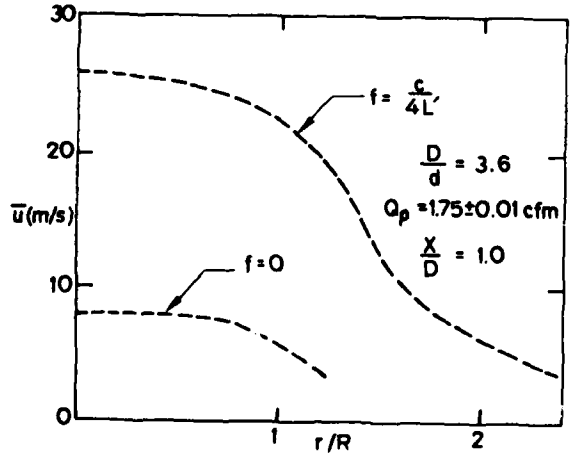

Fig. 5. Radial profiles of velocity at x/D = 1.0.

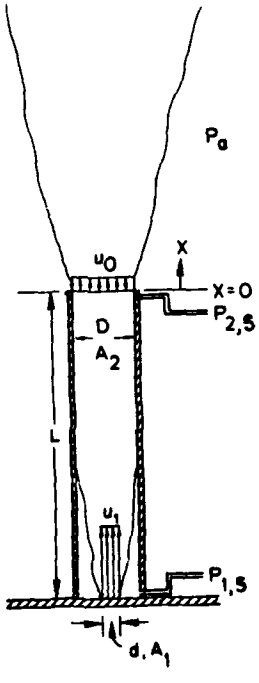

Fig. 6. Schematic of unpulsed confined jet.

AD-A113 907 ADVISORY GROUP FOR AEROSPACE RESEARCH AND DEVELOPMENT--ETC F/G 20/4
FLUID DYNAMICS OF JETS WITH APPLICATIONS TO V/STOL.(U)
JAN 82
UNCLASSIFIED AGARD-CP-308 NL

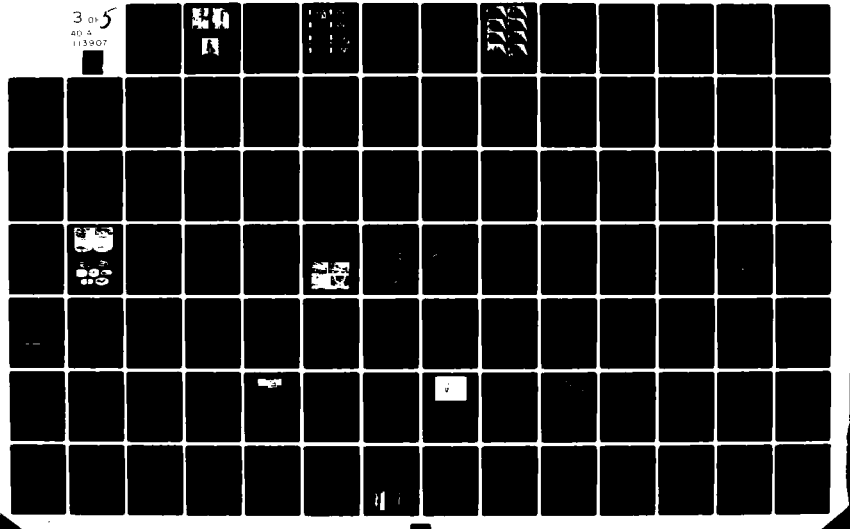

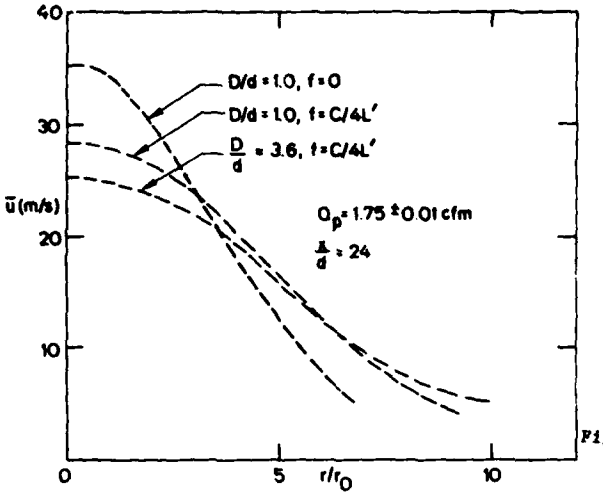

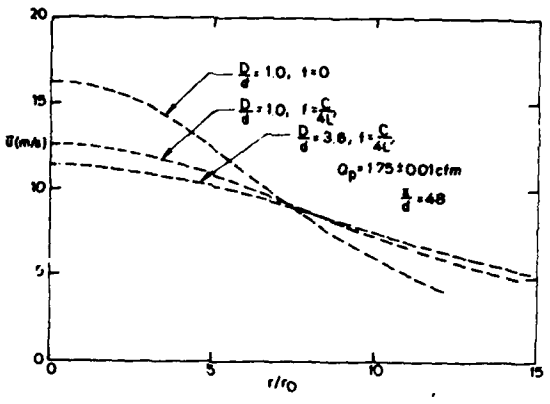

Fig. 7(a),(b) Radial profiles of velocity at x/d = 24, 48.

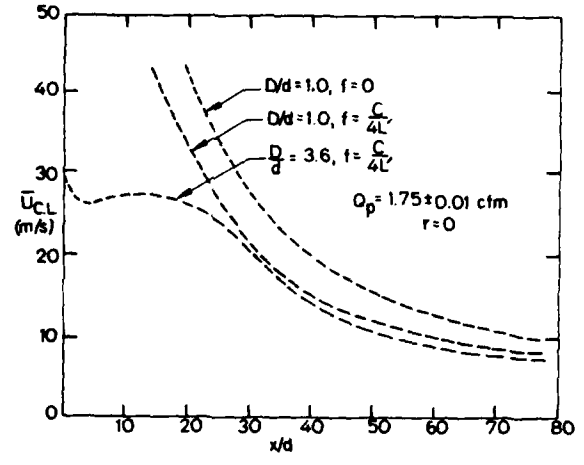

Fig. 8. Axial profiles of centerline velocity.

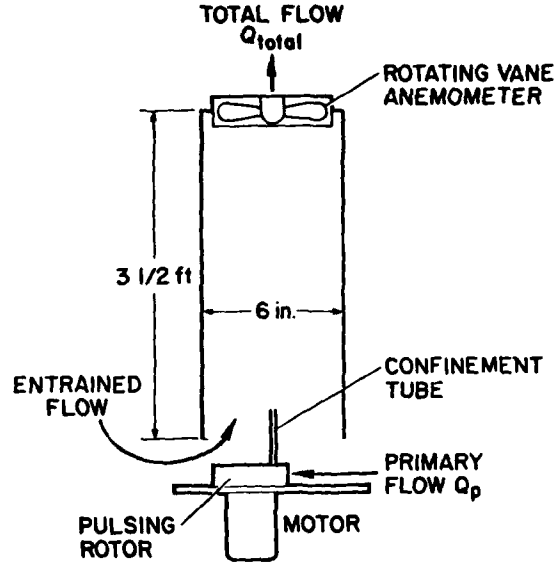

Fig. 9. Apparatus for direct measurement of total entrainment.

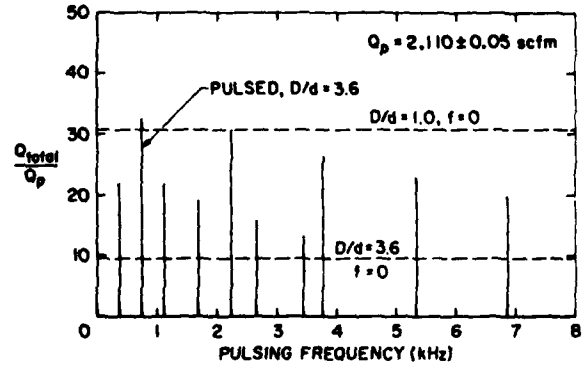

Fig. 10. Augmentation in total entrainment under resonant pulsing.

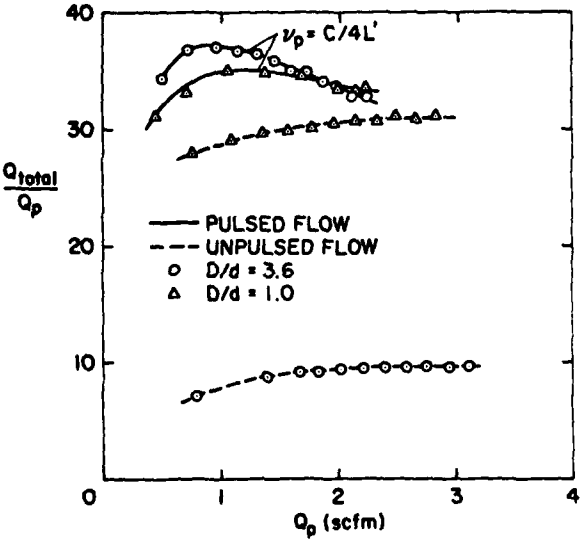

Fig. 11. Variation of total entrainment with primary flow rate.

Fig. 12(a). Unpulsed burning methane jet (D/d = 3.6)

Fig. 12(b). Burning methane jet under resonant pulsing (D/d = 3.6)

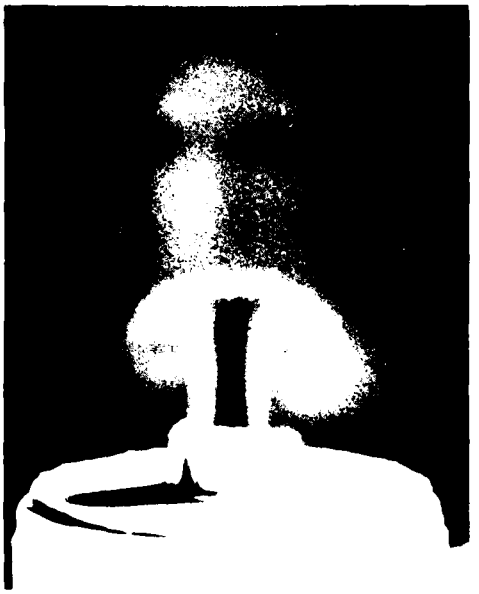

Fig. 13. Smoke-strobe visualization of confined pulsed jet at resonance

Flowfield and Noise Sources of Jet Impingement on Flaps and Ground Surface.

Dr.-Ing. Günther Neuwerth, Institut für Luft- und Raumfahrt der RWTH Aachen, Wüllnerstr. 7, 5100 Aachen FRG

Summary

On the basis of experimental results it is shown that, in an undisturbed free jet of high subsonic speed as well as in a jet deflected by externally blown flaps (EBF), there are ordered turbulence structures. First, a feedback mechanism which develops at small distances between nozzle and stagnation point on the flaps and which amplifies the turbulence structures is explained. It is subsequently shown, that the interaction of the jets and EBF generates a strong noise. Even without feedback both the undisturbed free jet and the jet deflected by EBF have the maximum levels in the noise spectrum at the Strouhal numbers of the natural ordered turbulence structures.

Introduction

When a subsonic free jet impinges on the ground (VTOL-aircraft) or on externally blown flaps (STOL-aircrafts) an interacting mechanism takes place. One of the consequences of this interaction is the radiation of noise with a special spectrum shape at high intensity. This paper will give a contribution to the understanding of the flowfield interaction and the mechanism of noise generation.

Natural ordered turbulence structures of free jets

Many authors, e.g. S. C. Crow and F. H. Champagne /1/ as well as H. Fuchs /2/, observed in turbulent free jet boundary layers ordered turbulence structures up to a distance of about 6 nozzle diameters downstream of the orifice. These experiments were performed in the Mach-number range $Ma < 0.2$ H. Fuchs found at a Strouhal number $S_d \approx 0.5$ strongly distinct axisymmetrical oscillations. This led to the assumption that the natural free jet turbulence is not completely homogenious but seems to have ordered wave structures.

As these macroscopic structures are coherent sound sources, they are effective and important for noise generation. Furthermore, these turbulence structures will have an influence on the noise generating mechanism when the free jet is interfering with solid bodies. At the Institute for Aerospace Engineering at the Technical University Aachen the turbulence structure of free jets has been investigated optically in the high subsonic Mach-number range which is of interest for aircraft engines /3/.

Free jet streams with nozzle exit diameters between 7 mm $\leq d \leq$ 21 mm were blown into an anechoic chamber. Spark Schlieren photographs were taken using the Cranz-Schardin-method of cold air jets at Reynolds numbers $Re = 10^6$ in a Mach-number range $0.5 \leq Ma \leq 1$. Because of the short exposure time of about $2 \cdot 10^{-7}$ seconds ordered macrostructures were distinctly visible. Figure 1 shows an example of such structures /3/. A series of photographs have been taken with a time difference between exposures of about $\Delta t = 20 \cdot 10^{-6}$ s. In these series of pictures the structures can be clearly seen as they are convected downstream.

In Figure 1a axisymmetric periodic structures can be recognized travelling downstream with a phase velocity $c_{St} = 0.63 \quad v_z$ (v_z = jet exit velocity). The jet exit Mach-number is Ma = 0.5.

The wavelength of the structures was $\lambda_{St} = 1.18 \cdot d$ and the Strouhal number $S_d = 0.54$. The measured Strouhal numbers are varying around a mean value. In Figure 2 such values taken from many exposures are plotted against the Mach-number. A further turbulence mode, the first azimuthal mode which has been predicted theoretically by Michalke /4/, can be recognized distinctly only for Mach-number $Ma > 0.8$ (see Figure 1b). This may be caused, however, by the limited sensitivity of the optical apparatus. Here the ordered turbulence structure surrounds the jet in form of a spiral. At these Mach-numbers such modes appear to be alternatively amplified.

Both the slow decrease of the Strouhal numbers with increasing Mach-numbers and the absolute values of the phase velocity agree well with the theoretical results of Michalke /4/. Figure 2 indicates that the axisymmetric turbulence mode shows clearly a findamental oscillation as well as a first harmonic. At some intervals of time only the fundamental can be observed, at others only the first harmonic oscillation.

Summarizing, it can be said that the free jet shows distinct structures in the range of high subsonic exit velocities which have special importance for the generation of noise caused by interference with externally blown flaps (EBF).

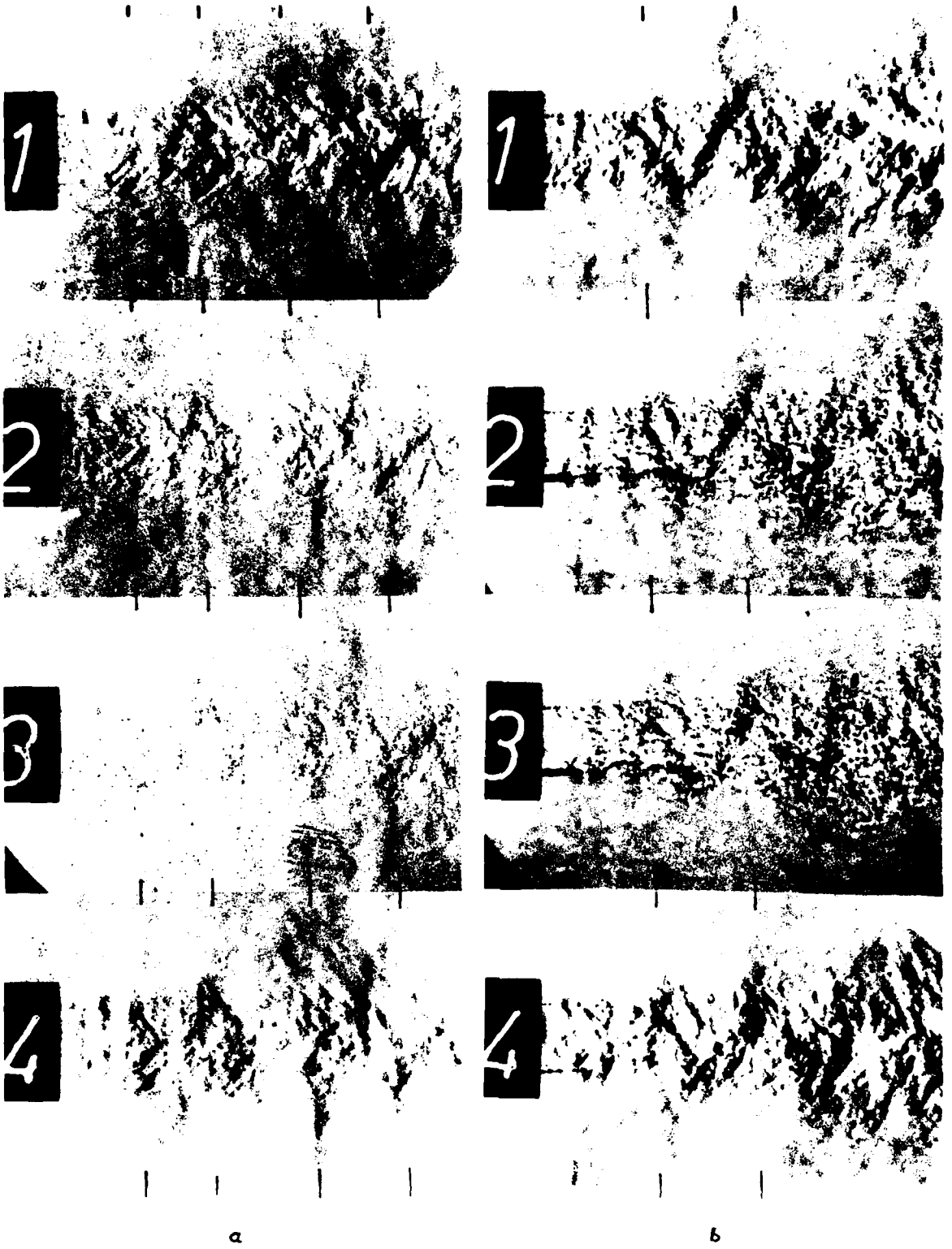

Figure 1 Natural ordered structures of a free jet /3/
a: axisymmetric structures Ma = 0.5, $S_d \approx 0.54$
b: azimuthal structures Ma = 0.9, $S_d \approx 0.33$
The dashes indicate the downstream convection of the structures.
Schlieren flash-light photographs $\Delta t = 20$ µs.

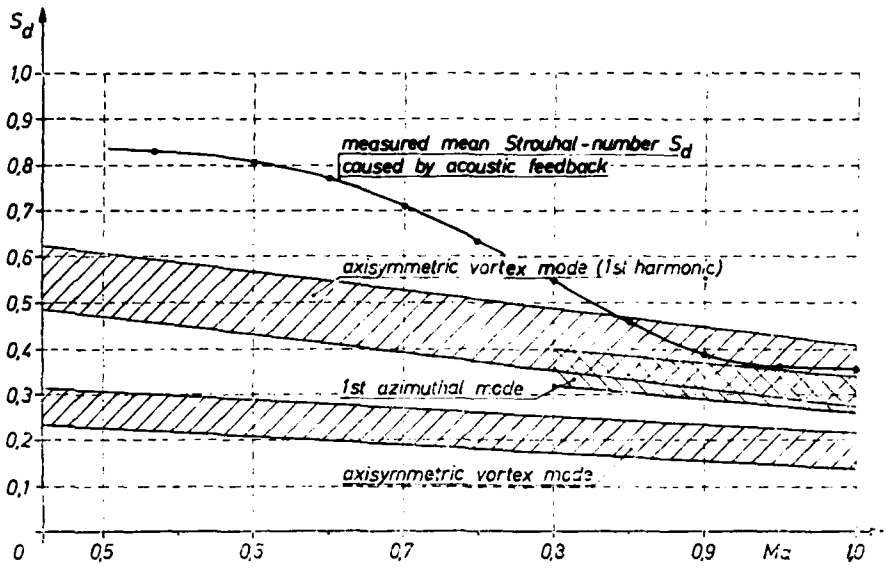

Figure 2 Strouhal number of the natural ordered turbulence structures as a function of Mach-number

Interaction between jets and externally blown flaps (EBF)

Investigations made by other authors, e.g., /6/, /7/, as well as the results reported in the present paper show a considerable increase of the sound pressure level from EBF compared to a free jet.

Herein the following phenomena appear:

1. During their deflection by the flaps, the turbulence structures are exposed to unstationary forces which cause the sound radiation.
2. As explained later, this effect can be reinforced by feedback at small distances between nozzle exit and stagnation point of the flap.
3. The system of wing and flaps reflects a portion of the sound waves which result from the interaction.
4. The turbulence generated in the boundary layer of the flaps and by the steep velocity gradient in the flap wake yields trailing edge noise.
5. By tangential interference between jet and flaps the scrubbing effect appears.

The experiments described in the following will show the significance of the natural ordered jet turbulence for noise generation.

Figure 3 shows the experimental equipment. Nozzle of different diameters could be moved in the axial (h) and vertical (a) directions.

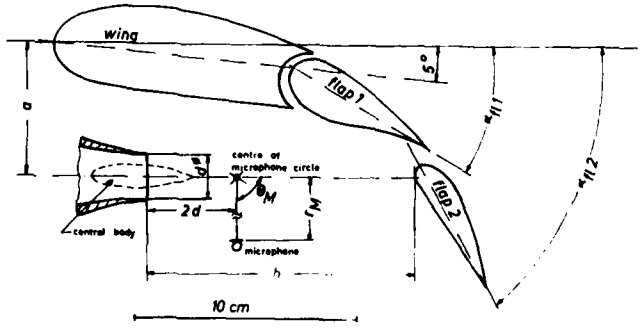

Figure 3 Blown flaps geometry

During some experiments a central body was placed in the jet exit in order to muffle the noise. The wing was equipped with two flaps whose angles of attack a_{fl} could be varied. The whole flap system had a span of 200 mm. The turning point of the microphone outrigger was placed at an axial distance of 2 . d downstream of the nozzle exit. The length of the outrigger was r_M = 800 mm.

In order to investigate the influence of the flaps on jet noise numerous frequency spectra were measured. Figure 4 shows, for instance, the sound pressure level SPL of a jet deflected by EBF (h/d = 7) as a function of the Strouhal number. For comparison, the SPL of an equivalent undisturbed jet is plotted. At the Strouhal number of the first harmonic axisymmetric turbulence mode of the jet - in this case at S_d = 0.38 - a level maximum is recognizable for the undisturbed free jet. The flaps deflecting the jet involve an increase of SPL over the total frequency spectrum compared with the free jet, the increase being greatest (namely about 20 dB), however, in the range of this first harmonic. It is, therefore, concluded that the turbulence structures have an important influence on the generation of noise.

Such structures can be recognized clearly in Figure 5 for a Mach-number Ma = 1. It shows eight Schlieren flash-light exposures of a jet deflected by EBF which have been taken with a time difference of Δt = 20 µs. The wavelenght of the structures λ_{St} and the distance Δl_{St} which the down-stream-moving structures covered during Δt can be measured. This, in turn, permits the calculation of the phase velocity c_{St} and the Strouhal number S_d of the turbulence structure. A physical interpretation of the SPL increase caused by EBF can be given by the deflection of the turbulence structures at the flaps. In that way fluctuating forces are generated resulting in strong sound sources.

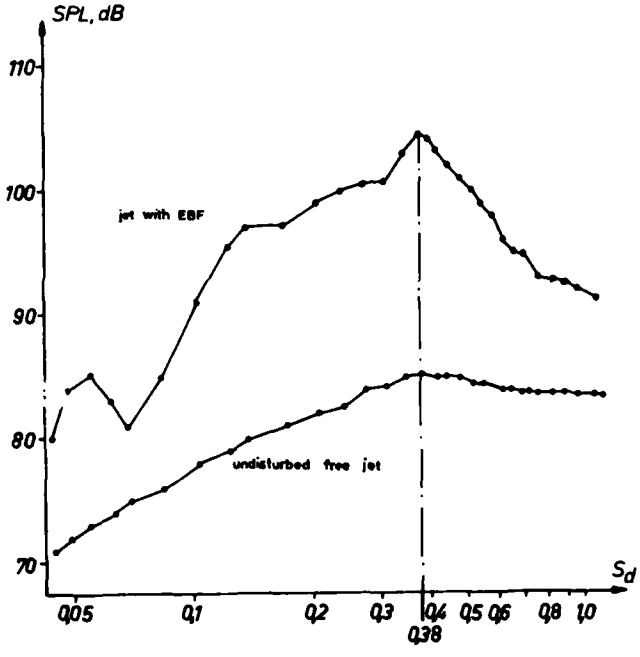

Figure 4 Spectral distribution of SPL at undisturbed free jet and at deflected EBF

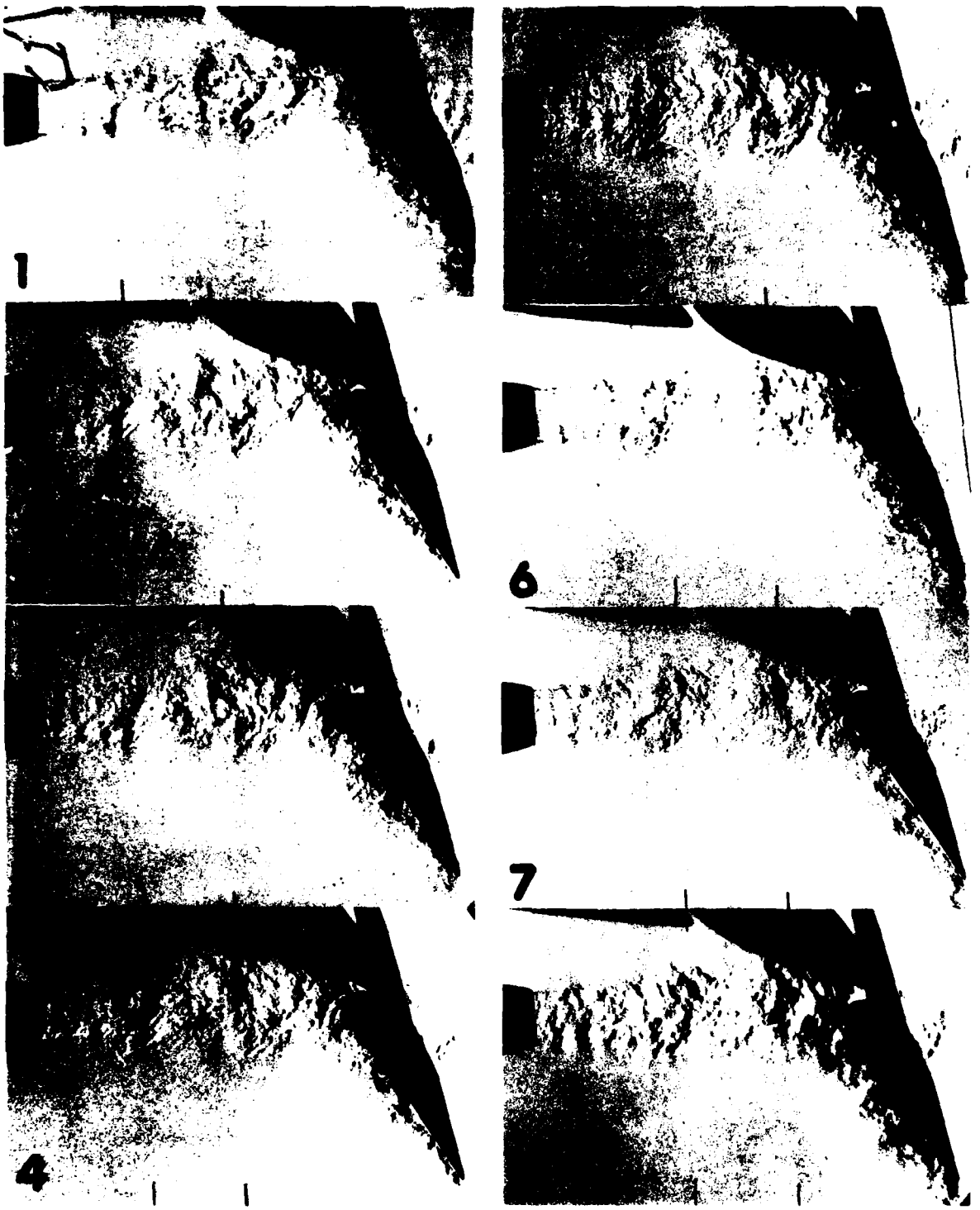

Figure 5 Ordered turbulence structures of an air jet deflected by EBF
Schlieren flash-light photographs Δt = 20 µs

Ma = 1 h/d = 6 α_{fl} = 30°
d = 15 mm a/d = 2.9 α_{fl_2} = 60°

The dashes indicate the downstream convection of the structures.

Reinforcement of the natural ordered turbulence structures by acoustic feedback

In earlier investigations /3/ it was pointed out that an acoustic feedback can occur if a jet impinges the ground in certain ranges of the distance h between the ground and the nozzle exit leading to noise with a markedly increased intensity. Using this arrangement the flowfield, the noise source intensity and the noise radiation into the farfield was computed /5/. This feedback effect was found as well in the EBF case. It is apparently sufficient for the formation of feedback that a solid body with a certain area (the lower flap) is situated in the jet. Feedback occurs if the distance between the leading edge of the lower flap and the nozzle exit is smaller than 6 d.

Figure 6 indicates a frequency spectrum for Ma = 0.8, d = 20 mm, α_{fl1} = 30°, α_{fl2} = 60° and h/d = 4 showing distinct peaks at four frequencies. The inherent Strouhal numbers S_{d1} = 0.24 and S_{d2} = 0.32 correspond to the axisymmetric and azimuthal fundamental oscillation of the free jet structures. The Strouhal numbers S_{d3} = 0.56 and S_{d4} = 1.12 represent the acoustic feedback frequency and its first harmonic (see Figure 2). As can be seen, the total noise level is dominated by the narrow band noise caused by feedback (S_{d3}) because it surpasses significantly the general level and can be heard as a strong single tone.

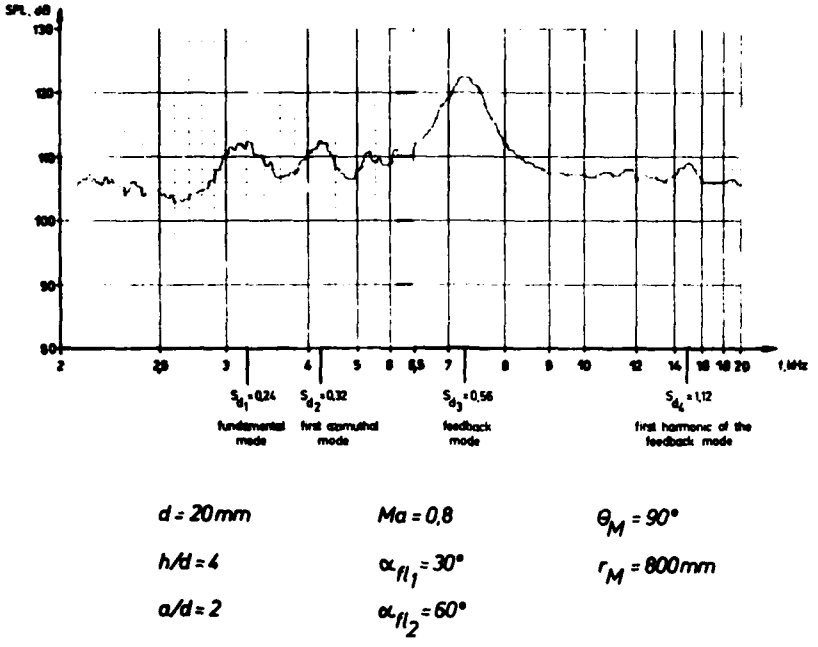

Figure 6 Frequency spectrum at appearance of acoustic feedback and natural structures simultaneously

As is explained in detail in Reference /3/, feedback develops due to the jet structures - deflected at the stagnation point of the flap - originating soundwaves. A part of these soundwaves is travelling upstream in the jet as in a channel and reinforces the natural turbulence structures considerably. They are then convected downstream to the flaps as distinctly visible vortices.

Conclusions

It was shown that an undisturbed free jet of high subsonic Mach-numbers always has ordered turbulence structures. These structures are very important with respect to the generation of noise by interference with externally-blown flaps. Additionally, the discrete vortices arising from the turbulence structures, in case of acoustic feedback, result in considerable increase of noise. However, the acoustic feedback can be suppressed by simple means.

On the other hand, no successful method could be found at this time to destroy the natural ordered structures but this is quite likely a necessity for the suppression of noise.

REFERENCES

1. Crow, S. C. and Champagne, F. H.:
"Orderly Structure in Jet Turbulence", Boeing Sci. Res. Lab. Doc., D1-82-0991, 1970.

2. Fuchs, H.:
"Space Correlations of the Fluctuating Pressure in Subsonic Turbulent Jets", DLR-FB 72-07, 1972.

3. Neuwerth, G.:
"Acoustic Feedback Phenomena of the Subsonic and Hypersonic Free Jet Impinging on a Foreign Body",
NASA TTF-15719, 1974.

4. Michalke, A.:
"Instabilität eines kompressiblen runden Freistrahls unter Berücksichtigung des Einflusses der Strahlgrenzschichtdicke", ZFW 19, 1971, H. 8/9, S. 319 - 328.

5. Klöppel, V.:
"Strahllärm von Triebwerken durch akustische Rückkopplung", Forschungsbericht des Landes NRW Nr. 2653,
Westdeutscher Verlag.

6. Dorsch, R. G., Kreim, W. J. and Olsen, W. A.:
"Externally-Blown-Flap Noise" NASA Lewis Research Center, Cleveland, Ohio, AIAA Paper No. 72-129.

7. Olsen, W. A., Dorsch, R. G. and Miles, J. H.:
"Noise Produced by a Small-Scale, Externally-Blown-Flap", NASA TN D-6636.

THE NEAR FIELD OF A PLANE TURBULENT JET

by

Leif N. Persen
Full Professor
Institutt for mekanikk
Universitetet i Trondheim
N.T.H. 7034 Trondheim
Norway

Abstract.

The paper presents a series of experiments done in the near field of the nozzle producing a plane turbulent jet. The jet opening is varied in size and geometry, the exit velocity is varied and the measuring device is varied from an ordinary pitot tube to the more sophisticated double hot-wire anemometer whereby also the Reynolds' stresses could be measured. The results are taken from a series of investigations which are being steadily continued.

The experimental data are considered in the light of theoretical considerations which start out with an examination of the classical boundary layer approach. The discrepancies between this approach and the far field have been touched upon by several authors, and the conclusion is drawn that information must be extracted from the complete set of equations governing the problem. For this purpose the NEUBER "three function approach", successfully applied to the study of notches, is applied to gain insight into the relations governing the Reynolds' stresses. The concept of self-similarity is discussed and it is shown why the concept used by Townsend applies only in the far field of the jet. The concept introduced by Bradbury and Riley of two different regions of similarity is not supported by the present approach. It is shown that the data in the near field suggest a correlation which has the linear spreading of the jet as an asymptotic behaviour. It is shown that this similarity concept applies only to the mean velocities in the near field, that the Reynolds' stresses behave differently, the theoretical deductions show why, and a new concept of propagation of disturbances can be applied to the distribution of the Reynolds' stresses. These results apply to all the jets investigated so far, and are also supported by experiments of water-in-water jets.

List of symbols.

x, y, z	space coordinates
x_o	apparent origin of the jet
u, v, w	components in the x-, y- and z-direction respectively of the velocity $\vec{v}$
$\vec{v}$	the velocity of the fluid
u', v', w'	velocity fluctuations
$\overline{u}$, $\overline{v}$, $\overline{w}$	mean velocity components
p	pressure
p_∞	pressure at infinity
$f(\eta)$	dimensionless velocity profile of the jet [$f(o) = 1$]
η	dimensionless coordinate perpendicular to the jet axis
$b_{\frac{1}{2}}$	half width of the jet
$b_{\frac{1}{2}}^{(o)}$	half width of the jet at $x = x_o$
$U_c(x)$	centerline velocity
U_o	exit velocity of the jet or $U_o = U_c(x_o)$
C	(with any index) = constant of integration
$\overline{v}_\infty$	velocity (at infinity) perpendicular to the jet axis
$\alpha, \beta, \lambda, \gamma, \kappa$	constants

σ_x, σ_y, σ_z — normal stresses (mean values with bar: $\bar{\sigma}_x$, ..)

τ_{xy}, τ_{yz}, τ_{zx} — shear stresses (mean values with bar: $\bar{\tau}_{xy}$,..)

Φ_i — (i = 1,2,3) potential functions

ψ — stress function

$Q(x)$ — mass flow through a plane perpendicular to the jet axis

μ — viscosity of the fluid

ρ — density of the fluid

$\nabla^2 \equiv \partial^2/\partial x^2 + \partial^2/\partial y^2 + \partial^2/\partial z^2$ = Laplace operator

$\nabla_i^2 \equiv \partial^2/\partial x^2 + \partial^2/\partial y^2$ = two-dimensional Laplace operator

F_i — (i = 1,2,3) potential functions

ξ — dimensionless x-coordinate

a, b, c — constants

N — jet parameter

1. Introduction.

The study of the flow will be based on the socalled REYNOLDS' equations (1894) for the mean velocity components $(\bar{u},\bar{v},\bar{w})$ of the turbulent flow field.

$$\left.\begin{aligned}
\rho \frac{D\bar{u}}{Dt} &= -\frac{\partial \bar{p}}{\partial x} + \frac{\partial}{\partial x}(\bar{\sigma}_x - \rho\overline{u'u'}) + \frac{\partial}{\partial y}(\bar{\tau}_{xy} - \rho\overline{u'v'}) + \frac{\partial}{\partial z}(\bar{\tau}_{xz} - \rho\overline{u'w'}) \\
\rho \frac{D\bar{v}}{Dt} &= -\frac{\partial \bar{p}}{\partial y} + \frac{\partial}{\partial x}(\bar{\tau}_{xy} - \rho\overline{u'v'}) + \frac{\partial}{\partial y}(\bar{\sigma}_y - \rho\overline{v'v'}) + \frac{\partial}{\partial z}(\bar{\tau}_{yz} - \rho\overline{v'w'}) \\
\rho \frac{D\bar{w}}{Dt} &= -\frac{\partial \bar{p}}{\partial z} + \frac{\partial}{\partial x}(\bar{\tau}_{xz} - \rho\overline{u'w'}) + \frac{\partial}{\partial y}(\bar{\tau}_{yz} - \rho\overline{v'w'}) + \frac{\partial}{\partial z}(\bar{\sigma}_z - \rho\overline{w'w'})
\end{aligned}\right\} \qquad (1.1)$$

In the form presented here the STOKES' hypothesis (1845) connecting the stresses with the gradients of the flow field has not yet been introduced. This means that the question of whether or not the NAVIER-STOKES' equations apply to turbulent flows does not have to be contemplated at the present stage. Equations (1.1) are valid for turbulent flow provided the REYNOLDS' rules for taking averages apply.

With the usually accepted assumption that the STOKES' hypothesis apply also in the turbulent case, the stresses may be given as the sum of a "laminar" and a "turbulent" contribution, the latter called the Reynolds' stresses:

$$\left.\begin{aligned}
\sigma_x &= \bar{\sigma}_x - \rho\overline{u'u'} = 2\mu\frac{\partial \bar{u}}{\partial x} - \rho\overline{u'u'} \\
\sigma_y &= \bar{\sigma}_y - \rho\overline{v'v'} = 2\mu\frac{\partial \bar{v}}{\partial y} - \rho\overline{v'v'} \\
\sigma_z &= \bar{\sigma}_z - \rho\overline{w'w'} = 2\mu\frac{\partial \bar{w}}{\partial z} - \rho\overline{w'w'}
\end{aligned}\right\} \qquad (1.2)$$

and

$$\left.\begin{aligned}
\tau_{xy} &= \bar{\tau}_{xy} - \rho\overline{u'v'} = \mu\left(\frac{\partial \bar{u}}{\partial y} + \frac{\partial \bar{v}}{\partial x}\right) - \rho\overline{u'v'} \\
\tau_{yz} &= \bar{\tau}_{yz} - \rho\overline{v'w'} = \mu\left(\frac{\partial \bar{v}}{\partial z} + \frac{\partial \bar{w}}{\partial y}\right) - \rho\overline{v'w'} \\
\tau_{zx} &= \bar{\tau}_{zx} - \rho\overline{w'u'} = \mu\left(\frac{\partial \bar{w}}{\partial x} + \frac{\partial \bar{u}}{\partial z}\right) - \rho\overline{w'u'}
\end{aligned}\right\} \qquad (1.3)$$

The theoretical treatment suggested for the study of the plane turbulent jet will be based on these equations and the assumptions they imply.

2. An examination of the boundary layer approach

The plane turbulent jet has been subjected to investigation by a number of authors of whom only a few will be referenced here. TOLLMIEN (1926) was the first one who established a solution based on Prandtl's mixing length theory by assuming the flow to be of the boundary layer type. This last assumption seems to have found recognition by later authors, and is one of the conclusions which will be challenged subsequently. TOWNSEND (1956) undertook extensive experimental investigations of the closely related wake flow and gave a survey of it in his book. Some of his conclusions it is hoped will be put in a different perspective. REICHARDT (1942) made an attempt to start on a different basis than TOLLMIEN (1926), but although his approach bears resemblance to the present line of reasoning, they differ in physical concepts. VAN DER HEGGE ZIJNEN (1947), seems to have made the most reliable measurements and included both heat and mass transfer in his investigation. More recently BRADBURY and RILEY (1967) examined the jet and drew conclusions which will be commented on later.

The basic equations of the problem are obtained from (1.1) by assuming:

$$\left.\begin{aligned} &1)\ \text{The flow is two-dimensional; } \bar{w} = 0\ ,\ \frac{\partial}{\partial z} = 0. \\ &2)\ \partial \sigma_x/\partial x \ll \partial \tau_{xy}/\partial y \\ &3)\ \bar{p} = \text{constant} \end{aligned}\right\} \qquad (2.1)$$

where σ_x and τ_{xy} represent the sum of "laminar" and "turbulent" contributions as given in (1.2) and (1.3). The first assumption (2.1) leads to neglection of the third equation (1.1), the third assumption (2.1) leads to the neglection of the second equation (1.1) and the second assumption (2.1) leads to the following simplification of the first equation (1.1):

$$\left.\begin{aligned} \rho\left(\bar{u}\,\frac{\partial \bar{u}}{\partial x} + \bar{v}\,\frac{\partial \bar{u}}{\partial y}\right) &= \frac{\partial \tau_{xy}}{\partial y} \\ \frac{\partial \bar{u}}{\partial x} + \frac{\partial \bar{v}}{\partial y} &= 0 \end{aligned}\right\} \qquad (2.2)$$

where the equation of continuity has been added. In order to close this system a phenomenological relationship of some sort is needed. TOLLMIEN (1926) used Prandtl's mixing length at this point. However, the attention will here be fixed on the one common feature of all investigations mentioned above: the experimentally recognized existence of a universal velocity profile. This profile will exist with or without a moving secondary flow, and may be expressed as follows:

If U_∞ is the velocity of the mowing secondary flow and U_c is the centerline velocity of the jet, then the velocity profile is given as

$$\frac{\bar{u} - U_\infty}{U_c - U_\infty} = f(\eta) \text{ where } \eta = y/b_{\frac{1}{2}}(x) \qquad (2.3)$$

where η represents a non-dimensional transverse distance where $b_{\frac{1}{2}}(x)$ is the socalled "half width", i.e. the value of y for which $\bar{u}$ is equal to $U_c/2$. This special form is adopted here to facilitate the application to experimental evidence.

This experimentally observed "universal velocity profile" seems to be in fact the only consistent phenomenological relationship which may be extracted from the experimental evidence presently known. The question of "selfpreservation" discussed by TOWNSEND (1956) as well as by BRADBURY and RILEY (1967) will enter the problem at a later stage, but does not change the statement in (2.3).

The universal velocity profile will here be used in the form

$$\bar{u} = U_c(x) f(\eta) \qquad (2.4)$$

where x is the coordinate along the axis of the jet and y is the transverse coordinate. The function $f(\eta)$ is a "bell-shaped" curve, which so far remains unspecified, but which for computational purposes later may be assumed given as

$$f(\eta) = e^{-\eta^2} \qquad (2.5)$$

in accordance with REICHARDT's approach.

With the acceptance of (2.4), it immediately follows from the continuity equation that the transverse velocity $\bar{v}$ must be given as

$$\bar{v} = -\frac{d}{dx}[U_e(x)\, b_{\frac{1}{2}}(x)] \int_0^\eta f(s)ds + U_e(x)\frac{db_{\frac{1}{2}}}{dx}\,\eta\, f(\eta) \tag{2.6}$$

One finds from this expression that the velocity $\bar{v}$ does not vanish when $\eta \to \infty$, a fact that will be of physical significance in conclusions to be drawn. The fact that the introduction of a universal velocity profile (2.4) determines $\bar{u}$ and $\bar{v}$ will now in view of (2.2) lead to the following expression for $\partial\tau_{xy}/\partial y$

$$\frac{1}{\rho}\frac{\partial\tau_{xy}}{\partial y} = U_e\frac{dU_e}{dx}f^2(\eta) - \frac{U_e(x)}{b_{\frac{1}{2}}(x)}\frac{d}{dx}[U_e(x)\, b_{\frac{1}{2}}(x)]f'(\eta)\int_0^\eta f(s)ds \tag{2.7}$$

This expression may in view of (2.3) be integrated once:

$$\left.\begin{aligned}\frac{1}{\rho}\tau_{xy} = {} & U_e(x)\left\{b_{\frac{1}{2}}(x)\frac{dU_e}{dx} + \frac{d}{dx}[U_e(x)\, b_{\frac{1}{2}}(x)]\right\}\int_0^\eta f^2(s)ds - \\ & U_e\frac{d}{dx}[U_e(x)\, b_{\frac{1}{2}}(x)]\, f(\eta)\int_0^\eta f(s)ds\end{aligned}\right\} \tag{2.8}$$

It is a matter of routine algebra to show that the condition of vanishing shear stress τ_{xy} at $\eta = \infty$ may be expressed as:

$$b_{\frac{1}{2}}(x) = cU_e^{-2}(x) \tag{2.9}$$

This is in complete agreement with the generally accepted behaviour of a plane jet where the centerline velocity $U_e \sim x^{-\frac{1}{2}}$ and the half widt $b_{\frac{1}{2}} \sim x$. Even so, certain further consequences of the similarity concept must be explored.

Introduction of (2.9) into (2.6) gives the following expression for $\bar{v}$:

$$\bar{v} = cU_e^{-2}(x)\frac{dU_e}{dx}\left\{\int_0^\eta f(s)ds - 2\eta f(\eta)\right\} \tag{2.10}$$

At $\eta = \infty$ one will thus have a velocity $\bar{v}_\infty$ which is given by

$$\bar{v}_\infty = cU_e^{-2}(x)\frac{dU_e}{dx}\int_0^\infty f(s)ds \tag{2.11}$$

The magnitude of this influx velocity depends thus on the centerline velocity and on the form of the non-dimensional velocity profile $f(\eta)$.

At this point one may for a moment re-examine the basic assumptions (2.1) and conclude that if the boundary layer concept is excluded but the assumptions in (2.1) are maintained, the equations of motion will reduce to:

$$\left.\begin{aligned}\rho[\bar{u}\frac{\partial\bar{u}}{\partial x} + \bar{v}\frac{\partial\bar{u}}{\partial y}] &= \frac{\partial\tau_{xy}}{\partial y} \\ \rho[\bar{u}\frac{\partial\bar{v}}{\partial x} + \bar{v}\frac{\partial\bar{v}}{\partial y}] &= \frac{\partial\tau_{xy}}{\partial x}\end{aligned}\right\} \tag{2.12}$$

The first one of these equations is identical to (2.2) already used to obtain the results (2.10) and (2.8). A proper combination of these latter equations combined with (2.9) leaves:

$$\frac{1}{\rho}\tau_{xy} = \bar{u}\bar{b} + \frac{C}{U_e}\frac{dU_e}{dx}2\eta f^2(\eta) \tag{2.13}$$

Now, the second equation (2.12) is reformulated by means of the continuity equation leaving

$$\frac{\partial\tau_{xy}}{\partial x} = \rho\frac{\partial}{\partial x}(\bar{u}\bar{v}) + \rho\frac{\partial}{\partial y}(\bar{v}^2) \tag{2.14}$$

For the previously established expression (2.13) for the shear stress τ_{xy} to be compatible with this equation, the following condition must be satisfied:

$$\frac{\partial}{\partial x}\left[\frac{C}{U_e}\frac{dU_e}{dx}2\eta\, f^2(\eta)\right] = \frac{\partial}{\partial y}(\bar{v}^2) \tag{2.15}$$

Introduction of the expression (2.10) for $\bar{v}$ into this equation will split it into the following two equations:

$$\frac{d}{dx}\left[\frac{1}{U_e}\frac{dU_e}{dx}\right] = \beta\frac{2}{U_e^2}\left(\frac{dU_e}{dx}\right)^2 \tag{2.16}$$

$$2\beta\eta f'^2(\eta) + f(\eta)\int_0^\eta f(s)ds + 2\eta f'(\eta)\int_0^\eta f(s)ds = 0 \tag{2.17}$$

where β is an arbitrary constant. One has thus found two equations for the determination of the two unknown functions $U_e(x)$ and $f(\eta)$. The solution of (2.16) may be expressed as

$$U_e(x) = U_o\left[1 + 2\frac{\lambda}{U_o}\beta(x-x_o)\right]^{-1/2\beta} \tag{2.18}$$

where

$$\left.\begin{aligned} &x = x_o \text{ is the distance downstream of the jet orifice at which location the velocity profile is fully developed} \\ &U_o = U_e(x_o) \text{ is the centerline velocity at } x = x_o \\ &-\lambda = \left.\frac{dU_e}{dx}\right|_{x=x_o} \text{ is the slope at } x = x_o \text{ of the curve } U_e(x) \end{aligned}\right\} \tag{2.19}$$

It is noted that the value $\beta = 1$ corresponds to the experimentally accepted decay of the centerline velocity U_e with increasing values of x. With this value of β the solution to (2.17) is easily found by introduction of the function $F(\eta)$ defined by:

$$F(\eta) = \int_0^\eta f(s)ds \quad , \quad F'(\eta) = f(\eta) \tag{2.20}$$

which transforms (2.19) into

$$FF' + 2\eta F'^2 + 2\eta FF'' = 0 \tag{2.21}$$

with the solution

$$F = C_1\left[\eta^{\frac{3}{2}} + \eta_o^{\frac{3}{2}}\right]^{\frac{1}{3}} \tag{2.22}$$

Here C_1 and η_o are constants of integration and β has been put equal to 1. The universal velocity profile is then determined from (2.20):

$$f(\eta) = \frac{dF}{d\eta} = \frac{1}{4}C_1\left[\eta^{3/2} + \eta\eta_o^{\frac{1}{2}}\right]^{-\frac{1}{3}} \tag{2.23}$$

This result does in no way resemble the bell-shaped velocity distribution known from experiments. It fails completely at $\eta = 0$, and even for large values of η its validity as an asymptotic expression must be further examined. One may therefore return to the basic equations (2.12) and conclude that the neglection of normal stresses leading to these equations was not a warranted assumption.

The expression (2.18) for the centerline velocity is, with $\beta = 1$, in complete agreement with experimental evidence, it introduces an origin of the independant variable in the streamwise direction which is determined by the conditions set by the jet orifice and it allows for a correct slope at this point of the function $U_e(x)$ giving the centerline velocity. This agrees very well with the considerations of ABRAMOVICH (1963) and conforms well with observations by ZIJNEN (1947/49). One may however contemplate the fact that this agreement is found in spite of the unwarranted assumptions being made.

At this point it is perhaps convenient to call attention again to the investigation by JOHNSON and WEINSTEIN (1963). The authors find here departure from the accepted relationship $U_e(x) \sim x^{-\frac{1}{2}}$, and proceed to look for explanations to this discrepancy. If one, however, applies the result of the careful study made by ZIJNEN [(1947)p. 264] on the conditions for the two-dimensionality of the experimental jet to be maintained, one will find that the authors' own experimental data support the $x^{-\frac{1}{2}}$-law in the region where this conditions is met. Their discrepancy occurs outside this region where consequently the two-dimensionality of the jet is in doubt.

The investigations by BRADBURY and RILEY (1967) indicate a change in the jet spreading and the centerline velocity with increasing distance along the jet. Thus two different regions of self-preserving flow are suggested. This contention will be examined at a later stage. The conclusion for the moment seems to be that an investigation based on the complete set of equations is inevitable.

3. The basic equations for two-dimensional turbulent flow.

The deductions so far has led to the need for an approach to two-dimensional turbulent flow, in which the basic equations are used without serious simplifications being introduced.

Following PERSEN (1976) one will find that (1.1) may be rearranged as follows:

$$\left.\begin{aligned}
&\frac{\partial}{\partial x}[\bar{\sigma}_x-\bar{p}-\rho\overline{u'u'}-\rho\bar{u}^2] + \frac{\partial}{\partial y}[\bar{\tau}_{xy}-\rho\overline{u'v'}-\rho\bar{u}\bar{v}] + \frac{\partial}{\partial z}[\bar{\tau}_{xz}-\rho\overline{u'w'}-\rho\bar{u}\bar{w}] = 0\\
&\frac{\partial}{\partial x}[\bar{\tau}_{xy}-\rho\overline{u'v'}-\rho\bar{u}\bar{v}] + \frac{\partial}{\partial y}[\bar{\sigma}_y-\bar{p}-\rho\overline{v'v'}-\rho\bar{v}^2] + \frac{\partial}{\partial z}[\bar{\tau}_{yz}-\rho\overline{v'w'}-\rho\bar{v}\bar{w}] = 0\\
&\frac{\partial}{\partial x}[\bar{\tau}_{xz}-\rho\overline{u'w'}-\rho\bar{u}\bar{w}] + \frac{\partial}{\partial y}[\bar{\tau}_{yz}-\rho\overline{v'w'}-\rho\bar{v}\bar{w}] + \frac{\partial}{\partial z}[\bar{\sigma}_z-\bar{p}-\rho\overline{w'w'}-\rho\bar{w}^2] = 0
\end{aligned}\right\} \qquad (3.1)$$

These are the equations of dynamic equilibrium in the d'Alembert's sense, where the terms of the type $\rho\bar{u}^2$, etc. represent the inertia forces which here appear as stresses. These equations of dynamic equilibrium will be identically satisfied if one introduces the flow function ψ and the 3 potential functions ϕ_1, ϕ_2 and ϕ_3 such that:

$$\left.\begin{aligned}
\bar{\sigma}_x - \bar{p} - \rho\overline{u'u'} - \rho\bar{u}^2 &= \frac{\partial^2\psi}{\partial y^2} + \frac{\partial^2\psi}{\partial z^2} + \alpha\left(\frac{\partial\phi_1}{\partial x} - \frac{\partial\phi_2}{\partial y} - \frac{\partial\phi_3}{\partial z}\right)\\
\bar{\sigma}_y - \bar{p} - \rho\overline{v'v'} - \rho\bar{v}^2 &= \frac{\partial^2\psi}{\partial z^2} + \frac{\partial^2\psi}{\partial x^2} + \alpha\left(\frac{\partial\phi_2}{\partial y} - \frac{\partial\phi_3}{\partial z} - \frac{\partial\phi_1}{\partial x}\right)\\
\bar{\sigma}_z - \bar{p} - \rho\overline{w'w'} - \rho\bar{w}^2 &= \frac{\partial^2\psi}{\partial x^2} + \frac{\partial^2\psi}{\partial y^2} + \alpha\left(\frac{\partial\phi_3}{\partial z} - \frac{\partial\phi_1}{\partial x} - \frac{\partial\phi_2}{\partial y}\right)
\end{aligned}\right\} \qquad (3.2)$$

and

$$\left.\begin{aligned}
\bar{\tau}_{xy} - \rho\overline{u'v'} - \rho\bar{u}\bar{v} &= -\frac{\partial^2\psi}{\partial x\partial y} + \alpha\left(\frac{\partial\phi_1}{\partial y} + \frac{\partial\phi_2}{\partial x}\right)\\
\bar{\tau}_{yz} - \rho\overline{v'w'} - \rho\bar{v}\bar{w} &= -\frac{\partial^2\psi}{\partial y\partial z} + \alpha\left(\frac{\partial\phi_2}{\partial z} + \frac{\partial\phi_3}{\partial y}\right)\\
\bar{\tau}_{zx} - \rho\overline{u'w'} - \rho\bar{u}\bar{w} &= -\frac{\partial^2\psi}{\partial x\partial z} + \alpha\left(\frac{\partial\phi_3}{\partial x} + \frac{\partial\phi_1}{\partial z}\right)
\end{aligned}\right\} \qquad (3.3)$$

This is in complete accordance with what NEUBER (1958) calls "his three-functions-approach", and it is easily shown that if (3.2) and (3.3) are satisfied, the 3 equations of dynamic equilibrium are identically satisfied provided

$$\nabla^2\phi_1 = 0 \ , \ \nabla^2\phi_2 = 0 \ , \ \nabla^2\phi_3 = 0 \qquad (3.4)$$

One may now use this approach to investigate the two-dimensional case in which $\bar{w} \equiv 0$ and $\partial\bar{u}/\partial z = \partial\bar{v}/\partial z \equiv 0$. According to (1.2) and (1.3) the situation will then be such that the only mean stress components which are different from zero will be $\bar{\sigma}_x$, $\bar{\sigma}_y$ and $\bar{\tau}_{xy}$. Thus one will have the following expressions for the Reynolds' apparent stresses:

$$\left.\begin{aligned}
-\rho\overline{u'u'} &= \rho\bar{u}^2 - 2\mu\frac{\partial\bar{u}}{\partial x} + \bar{p} + \frac{\partial^2\psi}{\partial y^2} + \frac{\partial^2\psi}{\partial z^2} + \alpha\left(\frac{\partial\phi_1}{\partial x} - \frac{\partial\phi_2}{\partial y} - \frac{\partial\phi_3}{\partial z}\right)\\
-\rho\overline{v'v'} &= \rho\bar{v}^2 - 2\mu\frac{\partial\bar{v}}{\partial y} + \bar{p} + \frac{\partial^2\psi}{\partial z^2} + \frac{\partial^2\psi}{\partial x^2} + \alpha\left(\frac{\partial\phi_2}{\partial y} - \frac{\partial\phi_3}{\partial z} - \frac{\partial\phi_1}{\partial x}\right)\\
-\rho\overline{w'w'} &= \qquad + \bar{p} + \frac{\partial^2\psi}{\partial x^2} + \frac{\partial^2\psi}{\partial y^2} + \alpha\left(\frac{\partial\phi_3}{\partial z} - \frac{\partial\phi_1}{\partial x} - \frac{\partial\phi_2}{\partial y}\right)
\end{aligned}\right\} \qquad (3.5)$$

and

$$
\left.
\begin{aligned}
-\rho\overline{u'v'} &= \rho\bar{u}\bar{v} - \mu\left(\frac{\partial\bar{u}}{\partial y} + \frac{\partial\bar{v}}{\partial x}\right) - \frac{\partial^2\psi}{\partial x\partial y} + \alpha\left(\frac{\partial\phi_1}{\partial y} + \frac{\partial\phi_2}{\partial x}\right)\\
-\rho\overline{v'w'} &= - \frac{\partial^2\psi}{\partial y\partial z} + \alpha\left(\frac{\partial\phi_2}{\partial z} + \frac{\partial\phi_3}{\partial y}\right)\\
-\rho\overline{w'u'} &= - \frac{\partial^2\psi}{\partial x\partial z} + \alpha\left(\frac{\partial\phi_3}{\partial x} + \frac{\partial\phi_1}{\partial z}\right)
\end{aligned}
\right\} \qquad (3.6)
$$

These equations reveal how the Reynolds stresses $\rho\overline{w'w'}$, $\rho\overline{v'w'}$ and $\rho\overline{u'w'}$ may vary with the space coordinates (x,y,z) even in a situation which offhand seems to be purely two-dimensional. If one adds the condition, that all derivatives with respect to z vanish, one obtains the following expressions for the Reynolds' stresses usually considered in a two-dimensional case

$$
\left.
\begin{aligned}
-\rho\overline{u'u'} &= \rho\bar{u}^2 - 2\mu\frac{\partial\bar{u}}{\partial x} + \bar{p} + \frac{\partial^2\psi}{\partial y^2} + \alpha\left(\frac{\partial\phi_1}{\partial x} - \frac{\partial\phi_2}{\partial y}\right)\\
-\rho\overline{v'v'} &= \rho\bar{v}^2 - 2\mu\frac{\partial\bar{v}}{\partial y} + \bar{p} + \frac{\partial^2\psi}{\partial x^2} + \alpha\left(\frac{\partial\phi_2}{\partial y} - \frac{\partial\phi_1}{\partial x}\right)\\
-\rho\overline{u'v'} &= \rho\bar{u}\bar{v} - \mu\left(\frac{\partial\bar{u}}{\partial y} + \frac{\partial\bar{v}}{\partial x}\right) - \frac{\partial^2\psi}{\partial x\partial y} + \alpha\left(\frac{\partial\phi_1}{\partial y} + \frac{\partial\phi_2}{\partial x}\right)
\end{aligned}
\right\} \qquad (3.7)
$$

One is here in the position to conceive of the flow function ψ as a modified Airy's stress function for the Reynolds apparent stresses in a two-dimensional turbulent flow. One of the main objectives of the flow function ψ and the potentials ϕ_1 and ϕ_2 is to satisfy the boundary conditions. Eqs. (3.7) thus indicate why it is not conceivable within the present approach to relate the Reynolds stresses exclusively to the mean velocity field without interference from the boundaries. On the other hand it may be regarded as a step forward that this interference is now singled out and expressed through the flow function ψ.

4. The plane turbulent jet.

With the results obtained in the preceding section, the problem of the plane turbulent jet is again to be considered. It should, however, be noted, that although the ultimate aim is to use these results to establish expressions for the Reynolds stresses which agree with experimental evidence, several previous considerations will have to be reexamined before any conclusions can be drawn. For that purpose the steps of Sec. 2 will be retraced.

The first assumption of a universal velocity profile given in the selfpreserving form (2.3) is so well founded on experimental evidence that it must be accepted. As a consequence of the continuity equation, the transverse velocity component $\bar{v}$ will then be given as (2.6), from which it follows that this velocity component at $\eta \to \infty$ will have the value $\bar{v}_\infty$, where

$$
\bar{v}_\infty = - \frac{d}{dx}[U_c(x)\ b_{\frac{1}{2}}(x)] \int_0^\infty f(s)ds \qquad (4.1)
$$

Here it has been assumed that $\lim_{\eta\to\infty} [\eta f(\eta)] = 0$

The next step in the previous deduction was to compute the shear stress from the simplified equation of motion. Demanding that this shear stress vanish as $\eta \to \infty$, one was led to the relation (2.9) between $U_c(x)$ and $b_{\frac{1}{2}}(x)$, which was stated to be in agreement with experimental evidence.

This latter line of reasoning cannot be used in the present case where the complete equations are to be used and τ_{xy} thus cannot be found. One may however pursue the following line of reasoning:

The full equations of motion will be given as

$$
\left.
\begin{aligned}
\rho\left[\bar{u}\frac{\partial u}{\partial x} + \bar{v}\frac{\partial\bar{u}}{\partial y}\right] &= - \frac{\partial\bar{p}}{\partial x} + \frac{\partial\sigma_x}{\partial x} + \frac{\partial\tau_{xy}}{\partial y}\\
\rho\left[\bar{u}\frac{\partial\bar{v}}{\partial x} + \bar{v}\frac{\partial\bar{v}}{\partial y}\right] &= - \frac{\partial\bar{p}}{\partial y} + \frac{\partial\tau_{xy}}{\partial x} + \frac{\partial\sigma_y}{\partial y}
\end{aligned}
\right\} \qquad (4.2)
$$

where the stress components are given in (1.2) and (1.3). The lefthand sides of these equations are now expressible in terms of $U_c(x)$ and $b_{\frac{1}{2}}(x)$ as well as $f(\eta)$ and its derivatives. It is then possible to draw the following conclusions:

1.) If the terms appearing on the lefthand side of the equations are not of equal importance, one has found a proper way of simplifying the equation.

2.) If the terms are of equal importance this leads to conditions which may be stated as

$$\left.\begin{aligned} b_{\frac{1}{2}}(x) &= C^{*}[U_c(x)]^{\gamma-1} \\ U_c(x) &= (C_1 x + C_1)^{-\gamma+\frac{1}{\alpha}} \end{aligned}\right\} \qquad (4.3)$$

where $C^{*}, C_1, C_{,}, \alpha$ and γ are constants. With the proper choice of these constants a complete agreement with the results (2.9) and (2.18) of the simplified approach is obtained. The justification, however, is changed.

For the further deductions $U_c(x)$ will be used in the form (2.18) with $\beta = 1$.

$$U_c(x) = U_o\left[1 + \frac{2\lambda}{U_o}(x-x_o)\right]^{-\frac{1}{2}} \qquad (4.4)$$

The half width $b_{\frac{1}{2}}$ will then accordingly be expressed as:

$$b_{\frac{1}{2}}(x) = b_{\frac{1}{2}}^{(o)}\left[1 + \frac{2\lambda}{U_o}(x-x_o)\right] \qquad (4.5)$$

where $b_{\frac{1}{2}}^{(o)}$ is the value of $b_{\frac{1}{2}}$ at $x = x_o$.

The function $f(\eta)$ is supposed to be normalized such that $f(0) = 1$ thus leaving $U_c(x)$ as the centerline velocity. The "half width" $b_{\frac{1}{2}}$ of the jet is supposed to be that value of y for which the velocity $\bar{u} = U_c/2$.

One will further find in view of (2.4) and (2.10)

$$\left.\begin{aligned} \bar{u} &= U_o\left[1 + \frac{2\lambda}{U_o}(x-x_o)\right]^{-\frac{1}{2}} f(\eta) \\ \bar{v} &= -\lambda b_{\frac{1}{2}}^{(o)}\left[1 + \frac{2\lambda}{U_o}(x-x_o)\right]^{-\frac{1}{2}}\left\{\int_o^{\eta} f(s)ds - 2\eta f(\eta)\right\} \end{aligned}\right\} \qquad (4.6)$$

5. The boundary conditions.

Having more or less exhausted the information inherent in the similarity concept in view of the basic equations, the boundary conditions are drawn to attention.

1.) From the definition of η (2.4) and of (4.5) one finds that

$$\left.\begin{aligned} &\eta \to 0 \text{ for } x \to \infty \text{ (with fixed value of } y) \\ &\left.\begin{aligned} \eta &\to 0 \text{ for } y = 0 \\ \eta &\to \infty \text{ for } y \to \infty \end{aligned}\right\} \text{(with fixed value for } x \text{)} \end{aligned}\right\} \qquad (5.1)$$

2.) The non-dimensional velocity component $\bar{u}$ is given by the function $f(\eta)$ which so far is unknown. It satisfies the following boundary conditions

$$\left.\begin{aligned} f(0) &= 1 \text{ (at either } y = 0 \text{ or } x = \infty) \\ f(\infty) &= 0 \text{ (at } y = \infty) \end{aligned}\right\} \qquad (5.2)$$

As shown already (eq.(4.1)) its behaviour for large values of the argument is assumed such that

$$\lim_{\eta\to\infty}(\eta f(\eta)) = 0 \qquad (5.3)$$

Finally

$$\int_o^{\infty} f(\eta)d\eta = \kappa \qquad (5.4)$$

where κ is a constant which may be zero or finite.

3.) The mass flow $Q(x)$ through a plane perpendicular to the jet centerline at an arbitrary position x may be expressed as

$$Q(x) = 2\int_o^{\infty} \bar{u}dy = 2U_c(x)\, b_{\frac{1}{2}}(x) \int_o^{\infty} f(\eta)d\eta \qquad (5.5)$$

With the expressions (4.4) and (4.5) this may be reformulated as

$$Q_x = 2U_o\, b_{\frac{1}{2}}^{(o)} \left[1 + \frac{2\lambda}{U_o}(x-x_o)\right]^{\frac{1}{2}\kappa} \tag{5.6}$$

and it is observed that even though the mass flow at $x=x_o$ is finite and equal to

$$Q(x_o) = 2U_o\, b_{\frac{1}{2}}^{(o)} \cdot \kappa \tag{5.7}$$

the mass flow $Q(x)$ tends to infinity as $x\to\infty$. This implies that an infinite amount of fluid is drawn in at $y = \pm\infty$ and discharged at $x = \infty$ through the action of the jet. This is an inescapable conclusion as long as the relations (4.4) and (4.5) for $U_c(x)$ and $b_{\frac{1}{2}}(x)$ are upheld.

Since this result seems somewhat unacceptable on physical grounds, two different approaches seem open for a resolution of the problem:

a.) One may assume κ in (5.4) to be equal to zero. This means assuming a recirculating flow with no fluid entering or leaving through the boundaries $x = x_o$, $x = \infty$, $y = \pm\infty$, and $Q(x) \equiv 0$ at any value of x.

b.) In accordance with the contentions of BRADBURY and RILEY (1967) one may assume two regions of similarity, each with different relations between $U_c(x)$ and $b_{\frac{1}{2}}(x)$

The subsequent deductions will however be carried out assuming only case a) above. Appropriate comments on case b) will be given later as will the comments by KOTSOVINOS (1978a,b)

6. The similarity regions.

If one assumes the similarity of the flow to be governed exclusively by (4.4) and (4.5), it follows that κ in (5.4) must be equal to zero. A recirculating flow will be the consequence and the non-dimensional velocity $f(\eta)$ may then be given as sketched in Fig.1.

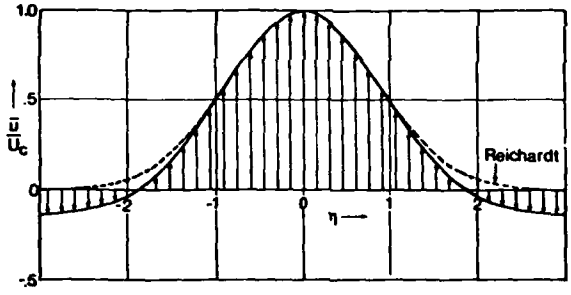

Fig. 1 Sketch of the velocity profile with recirculation

The following non-dimensional distance along the jet axis is now introduced

$$\xi = \frac{2\lambda}{U_o}(x-x_o) \tag{6.1}$$

The centerline velocity, the half width and the velocity components are then expressed as

$$\left.\begin{aligned} b_{\frac{1}{2}}(\xi) &= b_{\frac{1}{2}}^{(o)}\,(1+\xi) \\ U_c(\xi) &= U_o(1+\xi)^{-\frac{1}{2}} \\ \tilde{u} &= U_o(1+\xi)^{-\frac{1}{2}} f(\xi) \\ \tilde{v} &= -\lambda b_{\frac{1}{2}}^{(o)}\,(1+\xi)^{-\frac{1}{2}} \left\{\int_o^{\eta} f(s)ds - 2\eta f(\eta)\right\} \end{aligned}\right\} \tag{6.2}$$

The assumption is furthermore that

$$\int_o^{\infty} f(s)ds = 0 \tag{6.3}$$

This represents the basic similarity conditions and consequently the "laminar" stresses of the flow field will be:

$$\left.\begin{aligned}
\bar{\sigma}_x &= 2\mu\frac{\partial\bar{u}}{\partial x} = -2\mu\lambda[1+\xi]^{-3/2}\{f(\eta)+2\eta f'(\eta)\}\\
\bar{\sigma}_y &= 2\mu\frac{\partial\bar{v}}{\partial y} = +2\mu\lambda[1+\xi]^{-3/2}\{f(\eta)+2\eta f'(\eta)\}\\
\bar{\tau}_{xy} &= \mu(\frac{\partial\bar{u}}{\partial y}+\frac{\partial\bar{v}}{\partial x}) = \frac{\mu\lambda}{N}[1+\xi]^{-3/2}\{f'(\eta)-2\kappa^2[2\eta f(\eta)+2\eta^2 f'(\eta)-\tfrac{1}{2}\int_o^\eta f(s)ds]\}
\end{aligned}\right\} \quad (6.4)$$

where the parameter N has been introduced. It characterizes the jet at $x = x_o$ ($\xi = 0$) and is defined as

$$N = \lambda b_{\frac{1}{2}}^{(0)}/U_o \quad (6.5)$$

It is realized that these stresses decay with increasing values of ξ according to the -3/2 law. The way in which the Reynolds stresses decay may now be deduced by means of the results in Sec. 3.

One may start with assuming ψ, Φ_1, Φ_2 and Φ_3 to be independent of z, and continue by subtracting the last of eqs. (3.5) from the first ones. Thus:

$$\left.\begin{aligned}
-\rho\overline{u'u'}+\rho\overline{w'w'} &= \rho\bar{u}^2 - 2\mu\frac{\partial\bar{u}}{\partial x} - \frac{\partial^2\psi}{\partial x^2} + 2\alpha\frac{\partial\Phi_1}{\partial x}\\
-\rho\overline{v'v'}+\rho\overline{w'w'} &= \rho\bar{v}^2 - 2\mu\frac{\partial\bar{v}}{\partial y} - \frac{\partial^2\psi}{\partial y^2} + 2\alpha\frac{\partial\Phi_2}{\partial y}\\
-\rho\overline{u'v'} &= \rho\bar{u}\bar{v} - \mu(\frac{\partial\bar{u}}{\partial y}+\frac{\partial\bar{v}}{\partial x}) - \frac{\partial^2\psi}{\partial x\partial y} + \alpha(\frac{\partial\Phi_1}{\partial y}+\frac{\partial\Phi_2}{\partial x})
\end{aligned}\right\} \quad (6.6)$$

where the last equation is a reproduction from (3.7). Since the velocities as well as the mean stresses have been shown to be of the similarity type it seems a reasonable assumption that this holds also for the functions Φ_1 and Φ_2, and it may even be extended to apply to Φ_3:

$$\Phi_i = (1+\xi)^{-\beta}F_i(\eta) \quad (6.7)$$

Realizing that Φ_i are potential functions satisfying (3.4), it is easily shown that $F(\eta)$ consequently must be determined by the differential equation:

$$(\eta^2+\eta_o^2)\frac{d^2F_i}{d\eta^2} + 2(\beta+1)\frac{dF_i}{d\eta} + \beta(\beta+1)F_i = 0 \quad (6.8)$$

where

$$\eta_o = 1/2N \quad (6.9)$$

The differential equation (6.8) is closely related to the differential equation for the Legendre functions. However, the solution to this equation in general will not be pursued here, and only the following remark will be made at present. For $\beta = 0$ the equation is simplified and the following solution is found:

$$F^{(o)} = B_1 + B_2\ arctan\ (\eta/\eta_o) \quad (6.10)$$

Here B_1 and B_2 are constants of integration and F has been given a superscript to indicate the value of β for which it is valid. From (6.7) and (6.10) one will find that in this case

$$\left.\begin{aligned}
\frac{\partial\Phi_i^{(o)}}{\partial x} &= -\frac{2\lambda B_2}{U_o}(1+\xi)^{-1}\frac{\eta/\eta_o}{1+(\eta/\eta_o)^2}\\
\frac{\partial\Phi_i^{(o)}}{\partial y} &= +\frac{2\lambda B_2}{U_o}(1+\xi)^{-1}\frac{1}{1+(\eta/\eta_o)^2}
\end{aligned}\right\} \quad (6.11)$$

At this point the necessary preparations have been made to draw some conclusions. The attention is fixed on the way in which the terms in the expressions for the Reynolds' stresses decay with increasing distance downstreams (increasing values of ξ).

One observes first that the normal Reynolds' stresses $\rho\overline{u'u'}$, $\rho\overline{v'v'}$ and $\rho\overline{w'w'}$ must decay in the same way with distance downstreams since any other assumption would lead to the conclusion that regions of plane stress occur. The two first equations of (6.6) may then be used to contemplate how these Reynolds' stresses decay. Because of the initial

assumption that the mean velocity profile exhibits self-similarity, the way in which the terms on the right-hand side of (6.6) decay is known except for the function ψ. It is easily shown that the terms $\rho\bar{u}^2$, $\rho\bar{v}^2$, $\partial\phi_i/\partial x$ and $\partial\phi_i/\partial y$ decay with $(1+\xi)^{-1}$. Furthermore the viscous stresses have been shown in (6.4) to decay with $(1+\xi)^{3/2}$. Even though the decay of the function ψ is not known one may conclude that:

> the Reynolds' stresses are expressed through terms which decay at different rates with increasing values of ξ. Thus, if one is looking for the type of "self-similarity" that TOWNSEND (1956) is considering, one will have to proceed so far downstream that the viscous stresses have become insignificant compared with the other terms that decay more slowly. This shows also up in the results obtained by HESKESTAD (1965).

A final remark ought to be made with respect to the second region of similarity introduced by BRADBURY and RILEY (1967). The deduction of the differential equation (6.8) utilizes the relation between $b_{\frac{1}{2}}(x)$ and $U_c(x)$ as expressed in (6.2). This is changed in the second region and consequently a self-similar solution for Φ_i is not feasible in this region. This is here used as a justification for disregarding it for the time being.

7. The near-field of a plane jet, evaluation of experimental data.

The experimental set-up used in all cases to be referred to here is schematically shown in Fig.2.

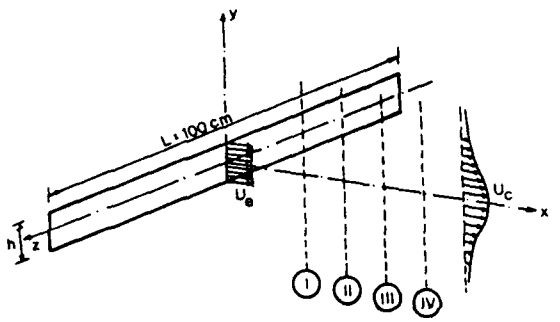

Fig. 2. Schematical exposition of the experimental set-up.

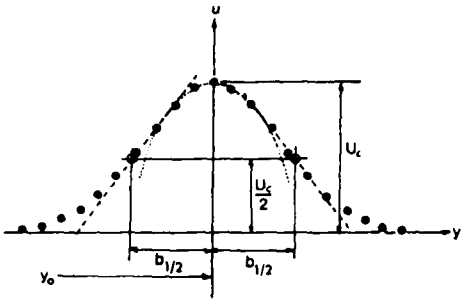

Fig. 3. Velocity profile (●) with the parabola and the straight lines determining U_c and $b_{\frac{1}{2}}$ respectively.

The plane jet is produced by a slit of height h and length $L=100$ cm through which a jet of air is produced. The exit velocity U_e of the jet is assumed evenly distributed over the slit height. The geometry of the slit is either characterized through sharp- or rounded edges. This will presumably influence the Reynolds' stresses and hopefully give rise to a methodical characterization of the jet.

The profiles are traversed at I, II, a.s.o. and the following quantities are measured at each station: $\bar{u}$, $\bar{v}$, $\overline{u'u'}$, $\overline{v'v'}$ and $\overline{u'v'}$. Based on the dimensions h and L of the slit, ZIJNEN (1947) gives the limits within which the flow will remain two-dimensional, and the position of the profiles were chosen accordingly. The experimental evidence to be presented here is obtained in a series of experiments in which values of the slit height, exit velocity and orifice geometry were varied.

The measurements will give velocity profiles as sketched in Fig.3. (● Data points). Through the data points a parabola is fitted using only the points in the neighborhood of the maximum. The best fit will give the constants U_c, y_o and y_* of the parabola:

$$\frac{\bar{u}}{U_c} = \frac{(y - y_o)^2}{y_*^2} + 1 \qquad (7.1)$$

where U_c is the centerline velocity, y_o is the position of the centerline and y_* is the length with which the y-coordinate is made dimensionless.

Knowing now the maximum amplitude U_c of the velocity profile, one may proceed to determine $b_{\frac{1}{2}}$, i.e. the width at which the profile exhibits half its maximum value. This is done by fitting straight lines though the data points close to this value as shown in Fig.3. From each velocity profile then, the following data will be available:

x , the position downstream where the profile has been obtained

y_o, the position of the centerline

y_*, the characteristic length of the profile

U_c, the centerline velocity

$b_{\frac{1}{2}}$, the half-width of the profile

These quantities are now to be considered the "data" of one experiment.

It is accepted that the velocity profiles are presumably self-similar, although a generally valid form for these self-similar profiles has not emerged. REICHARDT (1942) has proposed the following expression

$$\left.\begin{aligned} \bar{u}(x,y) &= U_c(x)\exp(-\alpha\eta^2) \\ \alpha\eta^2 &= 0.693(y/b_{\frac{1}{2}})^2 \end{aligned}\right\} \qquad (7.2)$$

This implies that the characteristic length y_* (used to non-dimensionalize the y-coordinate) is proportional to $b_{\frac{1}{2}}$ or

$$b_{\frac{1}{2}}/y_* = \sqrt{\ln 2} = 0.83255 \qquad (7.3)$$

Since both $b_{\frac{1}{2}}$ and y_* have been obtained from the velocity profiles, their ratio is computed and the agreement with the value of (7.3) is rather good. This may be interpreted as an indication that the Reichardt expression (7.2) may be used as an approximation when needed. The test indicates a fair agreement irrespective of opening heights, exit velocities or orifice geometry, and is based on the average value of the ratio for all profiles in each series.

The next step one can take is to examine the more or less generally accepted x-dependence of $b_{\frac{1}{2}}$ and U_c, expressed as

$$b_{\frac{1}{2}} \sim x \quad , \quad U_c \sim x^{-\frac{1}{2}} \qquad (7.4)$$

This means that the product $b_{\frac{1}{2}}U_c^2$ ought to be a constant, and for all profiles this product is, within the accuracy of the experiment, indeed a constant. This does not necessarily mean that the relations (7.4) are true, but one can note as a first result of these experiments:

$$\left.\begin{aligned} &\textit{The relationship} \\ &U_c \sim 1/\sqrt{b_{\frac{1}{2}}} \\ &\textit{seems to have found experimental support (See Eq.(2.11) even for the near field of the jet.} \end{aligned}\right\} \qquad (7.5)$$

Further investigations of the experimental evidence indicates that the relations (7.4) as well as the assymptotically valid expression (4.10) must be replaced by a more complex expression in the near field. The expression to be proposed as a fair representation of experimental evidence is given as

$$\frac{b_{\frac{1}{2}}^{\ 2}}{b_{\frac{1}{2}}^{(o)2}} = \frac{(x - x_o)^2}{L_{char}^2} + 1 \qquad (7.6)$$

where $b_{\frac{1}{2}}^{(o)}$ is the half width at $x = x_o$, i.e. at the location nearest to the orifice where (7.6) may be applied. For $x < x_o$ the jet is still so much influenced by the orifice geometry, that no general feature can be expected. For $x > x_o$ it is hoped, that the expression (7.6) can be used irrespective of orifice geometry, exit velocity or slit height, and that consequently the influence of these factors can be expressed through the three constants of the expression, x_o, L_{char} and $b_{\frac{1}{2}}^{(o)}$. This idea is in keeping with the ideas brought forward by BRADBURY and RILEY (1967), but it carries one step further, because of the implications of the attempt to express the influence of the factors mentioned above through 3 constants.

At this point experimental evidence is conveniently drawn to attention. The degree to which the u-component satisfies the similarity property is extremely good and even in water the results are satisfactory in this respect.

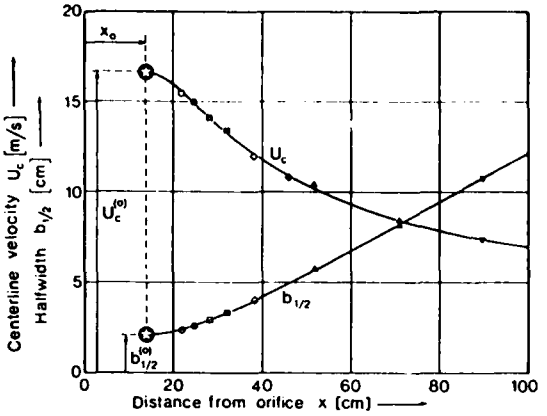

Fig. 4. The centerline velocity U_c and the half width $b_{\frac{1}{2}}$ as a function of the distance x from the orifice (obtained in an air jet)

Fig.4. reveals how the data obtained in one series of experiments with an air jet conform with the expression (7.6). In addition the variation of the centerline velocity U_c with the downstream distance x is shown [See (7.8)].

The classical result that the parameters of the jet do not seem to correlate with the jet Reynolds number $Re = U_e h/\nu$ is verified (U_e = exit velocity in the jet orifice and h = slit height). This indicate that all data ought to be correlated through the geometry of the jet orifice. The result of such a correlation is shown in Fig. 5. It reveals how the three parameters x_o, L_{char} and $b_{\frac{1}{2}}^{(o)}$ are all proportional to h and the constants

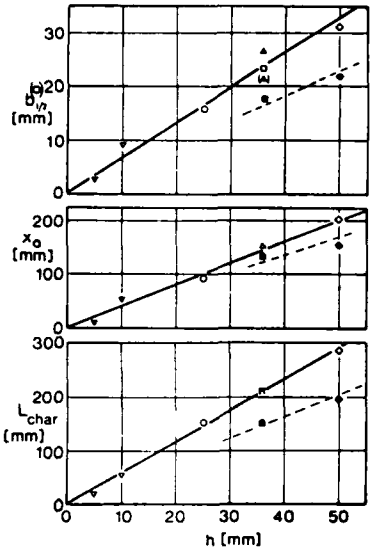

Fig.5. The constants $b_{\frac{1}{2}}^{(o)}$, x_o and L_{char} as functions of the slit height h.

of proportionality depend of the shape of the orifice. The actual numbers are given in (7.7)

$$\left.\begin{aligned} L_{char} &= 5.82\ h \quad \text{(rounded edge)} \\ L_{char} &= 4.11\ h \quad \text{(sharp edge)} \\ b_{\frac{1}{2}}^{(o)} &= 0.660\ h \quad \text{(rounded edge)} \\ b_{\frac{1}{2}}^{(o)} &= 0.457\ h \quad \text{(sharp edge)} \\ x_o &= 4.02\ h \quad \text{(rounded edge)} \\ x_o &= 3.41\ h \quad \text{(sharp edge)} \end{aligned}\right\} \quad (7.7)$$

The correlation (7.6) has now been verified experimentally and as a cosequence of (7.5) one obtains

$$U_c = U_c^{(o)}(1+\xi^2)^{-1/4} \qquad (7.8)$$

where

$$\xi = \frac{x-x_o}{L_{char}} \qquad (7.9)$$

This means that the expression for the velocity component $\bar{u}$ may be expressed as

$$\bar{u} = U_c^{(o)}(1+\xi^2)^{-1/4}\ f(\eta) \qquad (7.10)$$

where $f(\eta)$ is an unknown function and η a non-dimensional distance normal to the jet axis:

$$\eta = y/b_{\frac{1}{2}} \qquad (7.11)$$

The lateral velocity component $\bar{v}$ will in view of the continuity equation be expressed as:

$$\bar{v} = U_c^{(o)}\ \frac{b_{\frac{1}{2}}^{(o)}}{L_{char}}\ \xi(1+\xi^2)^{-3/4}\left\{\eta f(\eta) - \tfrac{1}{4}\int_o^\eta f(s)\,ds\right\} \qquad (7.12)$$

It is noticed that the ratio $b_{\frac{1}{2}}^{(o)}/L_{chqr}$ occurs in this expression as a jet parameter. This ratio is computed for each series of experiments and the result is remarkably constant, a verification of the dependence on h shown in Fig.5.

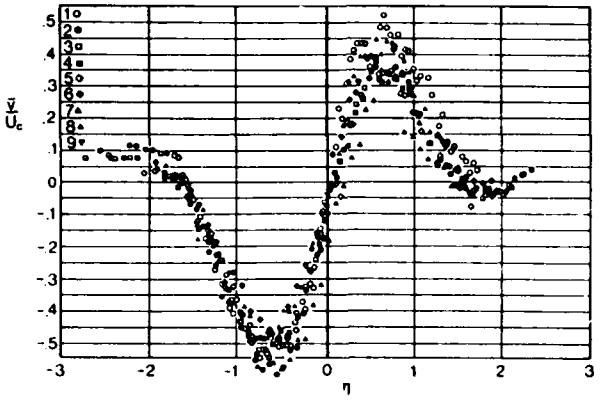

Fig. 6. The velocity component $\bar{v}$ plotted to exhibit the similarity predicted by (7.12).

Since now the jet parameters have been determined, the variation in space of the $\bar{v}$-component of the velocity is known. When plotted as $\bar{v}/U_q$ against η one must obtain one curve only. To what extent this is verified by experimental evidence is shown in Fig. 6. It should be observed that measurement of this velocity component is rather uncertain because of its small mean value as compared with the velocity fluctuations.

8. Evaluation of the $\overline{u'u'}$- and $\overline{v'v'}$- data in the near field.

The theoretical approach to the problem has indicated a certain behaviour to be expected of the $\overline{u'u'}$- and the $\overline{v'v'}$-data. First it is observed that the transverse coordinate appropriate for correlating the data may be the similarity variable η defined in the treatment of the velocity profile [Eq. (7.11)]. Second it is noticed that whereas $\bar{u}$ is of the form $U_q(x)$ times $f(\eta)$, a similar simple similarity property cannot be expected for the $\overline{u'u'}$ and $\overline{v'v'}$ profiles. The more general form to be adopted here is suggested by the theoretical considerations and may be expressed as

$$\left.\begin{matrix}\sqrt{\overline{u'u'}} \\ \sqrt{\overline{v'v'}}\end{matrix}\right\} = B(x)\,F(\eta) + A(x)G(\eta) \qquad (8.1)$$

where all functions so far are considered as unknown. One might draw upon the theoretical deductions to extract the specific forms of $B(x)$ and $A(x)$ by identifying one part as the one caused by viscous action and the other as the one caused by the fluctuations alone, but presently an approach via a propagation hypothesis for turbulent fluctuations is preferred.

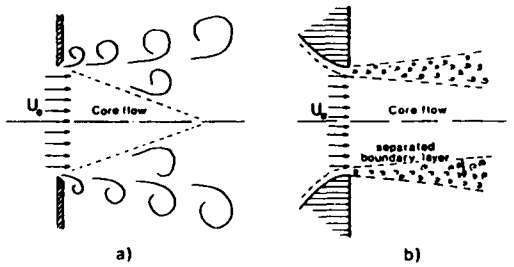

Fig. 7. Sketch of the two nozzles, sharp(a) and rounded (b)

When contemplating the origin of the Reynolds' stresses $\rho\overline{u'u'}$ and $\rho\overline{v'v'}$ one is led to the conclusion that the fluctuations causing these stresses originate in part from the boundary of the nozzle and in part from the core flow. The two different geometries of the nozzle used in this investigation are sketched in Fig. 7. It is indicated how the rounded nozzle is shedding the boundary layer in the nozzle whereby high vorticity is being concentrated in two narrow regions. The sharp edged nozzle is creating larger eddies and the more violent mixing action leads to a much shorter distance to the end of the core flow than in the rounded case. This observation is confirmed by the fact that the x_o (the position of the "origin") is larger for the rounded than for the sharp-edged nozzle.

The fluctuations may now be conceived of as small "jets" in a moving flow. Since it has been established that jets seem uninfluenced by viscosity (Re-number independent) this modelling of a fluctuation conforms with the idea that turbulent energy is passed on from larger to smaller "eddies". If the larger fluctuations are identified as the socalled coherent structures in turbulence, the jet model predicts the propagation properties of such structures (Bursts and Sweeps). However, the model also indicates how the Reynolds stresses will behave. The integrated action of such a concept will lead to the assumption for $\sqrt{\overline{u'u'}}_-$ and $\sqrt{\overline{v'v'}}_-$ profiles which may be expressed as:

$$\left.\begin{matrix}\sqrt{\overline{u'u'}} \\ \sqrt{\overline{v'v'}}\end{matrix}\right\} = B(x)\ exp\left[-D\eta^2\right] + A(x)\left\{exp\left[-C(\eta-\eta_o)^2\right] + exp\left[-C(\eta+\eta_o)^2\right]\right\} \qquad (8.2)$$

Here Reichardt's proposed velocity profile in the form of Gaussian hat curve has been adopted as approximations to the functions $F(\eta)$ and $G(\eta)$ in (8.1). The constants D, C and η_o are all to be determined such that the adopted expressions best possibly reflects experimental evidence. It turns out that for the $\overline{u'u'}$-data, the following values seem satisfactory:

$$D = 0.5, \quad \eta_o = 1.0, \quad C = 0.9 \qquad (8.3)$$

One may then use a best fit procedure to determine the values of $B(x)$ and $A(x)$ for each profile (given x-values) whereupon these functions can be analysed. Fig. 8. shows examples of how this procedure predicts the $\overline{u'u'}$-profile for the case of a rounded nozzle. For

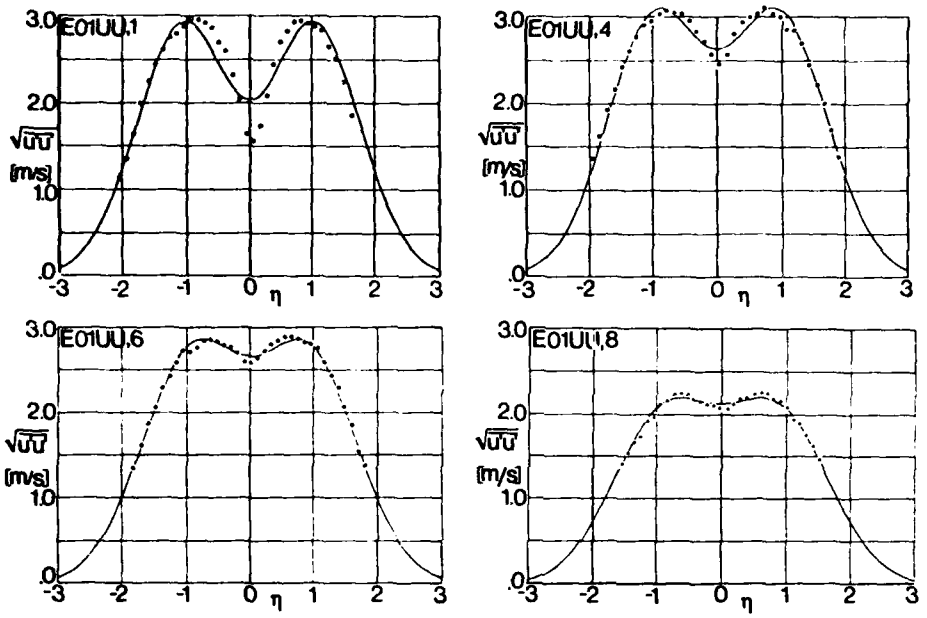

Fig. 8. $\sqrt{\overline{u'u'}}$- profiles in the case of a rounded edge.

cases with the sharp edged nozzle the agreement is even better. The same values as given in (8.3) apply indicating their relative independence on the nozzle geometry. For the $\overline{v'v'}$-data, however, the constants to be used are

$$D = 0.7, \quad \eta_o = 0.8, \quad C = 1.1 \qquad (8.4)$$

Fig. 9. shows how extremely well the adopted form in (8.1) for the normal Reynolds stresses predicts their development with increasing downstream distance. If however this result is to be given any significance, the functions $A(x)$ and $B(x)$ must conform with the theoretical considerations of Sec. 7. This means that if the propagation theory for large scale turbulent structures is correct the function $A(x)$ ought to be given as

$$A(x) = A_o\ (1+\xi^2)^{-1/4} \qquad (8.5)$$

where x has been replaced by ξ according to (7.9).

In Fig. 10. the functions $A(x)$ for both nozzle geometries are computed. The earlier argumentation on the length x_o from the nozzle to the point of "origin" is supported by the experimental data. Thus, the "normal" behaviour of the decay functions $A(x)$ can in the case of a rounded nozzle be expected for values of $\xi > 1$. The best fit procedure of $A(x)$ to the remaining data give expressions for A_o as shown in the figure. It is remarkable how the values obtained in the two cases conforms with each other, an additional sign that the contentions behind the results have now been given substance by experimental support. It is however stressed that further experimentation is needed and is at the moment in progress.

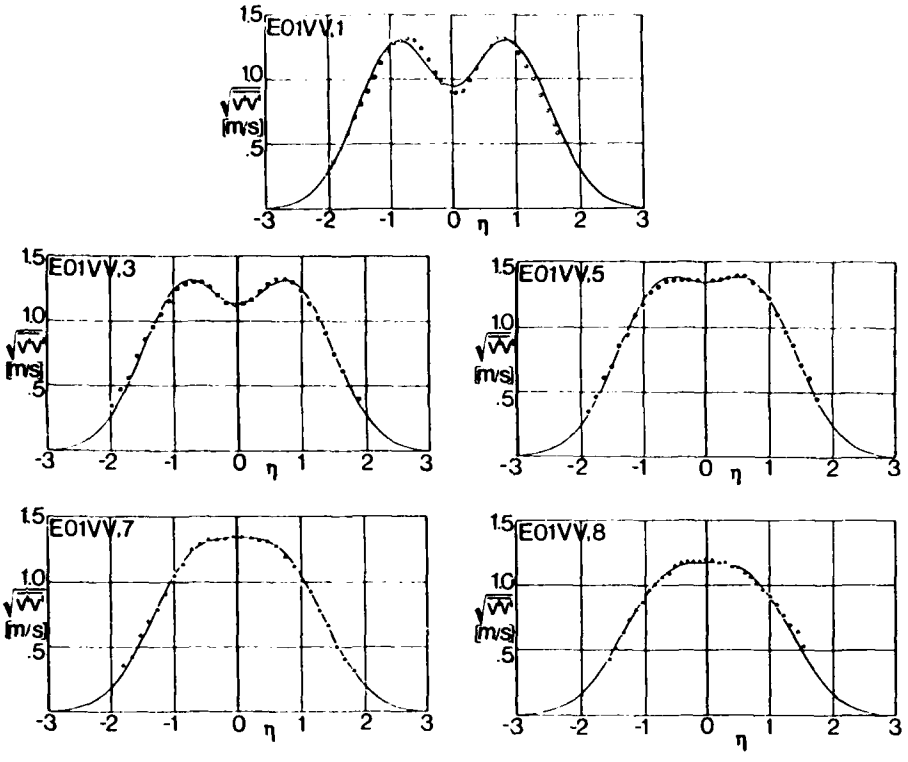

Fig. 9. $\sqrt{v'v'}$*-profiles in the case of a rounded nozzle.*

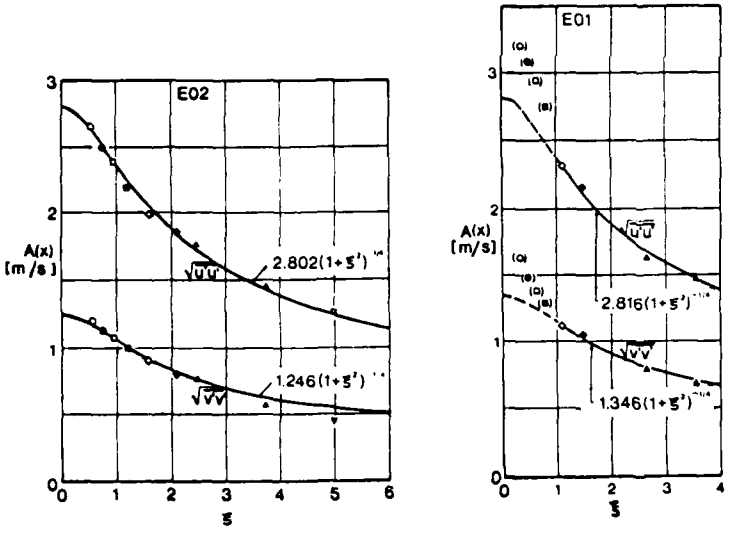

Fig. 10. The function A(x) in (8.5) determined for the rounded edge (E01) and the sharp edge (E02)

Fig. 11 shows the values of $B(x)$ corresponding to the $A(x)$-values given in Fig. 10 to be increasing at first and are then starting to decrease. This means that the data of the series of experiments do not allow an assymptotic behaviour of $B(x)$ to be determined. However, the values obtained for $\overline{u'v'}$ seem to be interesting in the sense that they shed light on the similarity aspect of the flow. From the theoretical deductions one observes that $\overline{u'v'}$ seem to decay as uv. This means that $\overline{u'v'}$-data ought to exhibit similarity if they are normalized by the factor $\xi/(1+\xi^2)$. Fig. 12 shows how well this is satisfied for the two cases of nozzle geometry. It is however even more remarkable that the actual values in the two cases differ so little from each other in spite of the great difference in geometry. The results obtained so far must however be considered inconclusive since they have raised questions which necessitates further experimentation. This is the case for the functions $A(x)$ and $B(x)$ as well.

Conclusions.

In spite of the fact that certain results in this series of experiments need further verification, a number of conclusions may still be drawn. The near field of the jet is here indicated by the positions x/h at which profiles were taken, i.e. the range $4.4 < x/h < 36.0$. The hotwire measurements were made in the region $6.3 < x/h < 25.7$.

1.) Self-similarity of the $\bar{u}$-velocity profiles is to an astonishing degree exhibited in the near field, and is consequently not only an assymptotic property of the

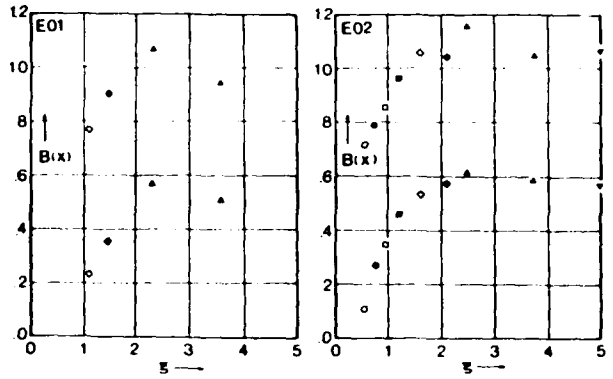

Fig. 11 The function B(x) in (8.5) determined for the rounded edge (E01) and the sharp edge (E02).

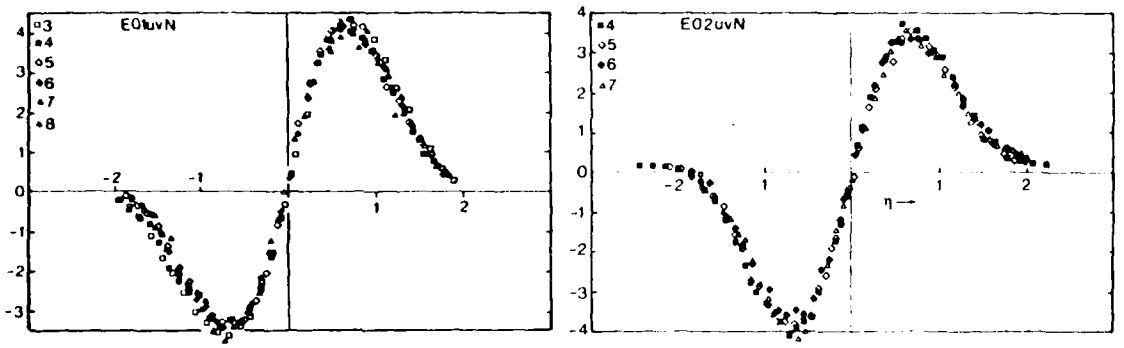

Fig. 12 The $\overline{u'v'}$- data normalized through $\xi/(1+\xi^2)$ for the rounded edge (E01) and the sharp edge (E02).

profile. This conclusion has the support of BRADBURY and RILEY (1967) but is here extended to include the profiles at very small values of x/h.

2.) Evidence seems also to support the conclusion that the self-similar measured $\bar{u}$-profile may seem insensitive to changes in the boundary conditions which greatly influences other quantities. The discussion given in Sec. 2 conforms very well with the remarks of KOTSOVINOS (1978a,b) and draws the attention to the boundary induced recirculation. This may occur in the outer part of the jet and not cause significant enough influence on the measured values in the central part of the jet.

3.) The experimentally supported decay function introduced in (7.8) is also supported by the results of HUSSAIN and CLARK (1977) which exhibit results in complete agreement with Fig. 4. The fact that the same decay function seems to apply in a logical manner to the development of the Reynolds stresses with increasing downstream distance gives further support to it. It should be noted that the decay function is such that it has the linear spread of the jet as an assymptotic behaviour.

4.) The introduction of the stress functions in Sec. 3 shows why the similarity concept of TOWNSEND (1956), where all quantities of the basic equations decay similarly, only can be expected to apply in the far field of the jet. The examination of the basic equation which led to the introduction of these functions and which also led to the conclusion that TOLLMIEN's original boundary layer approach could not be upheld, is supported also by the conclusions of MILLER and COMINGS (1957).

5.) HUSSAIN and CLARK (1977) find a strong influence on "the mean and turbulence quantities in the near field" of the corresponding "characteristics of the initial (upstream) flow". It ought to be noticed that several of their measurements were made in the immediate negihborhood of the jet exit, where the potential core region is still present. In the region downstream of x_o however their results may be said to be complemented by the presented hypothesis on the downstream development of the Reynolds stresses. Their representation of the variation of the centerline turbulence intensity may thus have been put in a different

perspective.

6.) No analytic expression for the similarity profile for $\bar{u}$ is suggested. This reflects the contention that boundary conditions will influence the recirculating motion and thus change the profile in the outer region of the jet where measurements are difficult to make.

7.) The contention of the similarity property of the fluctuations leading to the contended transport theory for the Reynolds' stresses is in complete accordance with the von Kármán concept.

8.) All conclusions drawn here are supported by data obtained so far in the water-in-water jet. These data, obtained by hot-wire anemometry, are however steadily being extended and will be reported on elsewhere.

Acknowledgement.

The author is indepted to Mr. Jan A. Skaug and Mr. Lars Sætran at the Institutt for Mekanikk, NTH, Trondheim who performed the experiments with great care. The financial support of NTNF (Royal Norwegian Council for Scientific and Industrial Research) under contract B 0601.10883 is also gratefully acknowledged.

REFERENCES

ABRAMOVICH G.N.: *The Theory of Turbulent Jets*, MIT Press (1963).

BRADBURY L.J.S. and J. RILEY: *The Spread of a Turbulent Plane Jet issuing into a Parallel Mowing Stream*, J. Fluid Mech. (1967), vol.27 part 2 pp. 381-394.

HESKESTAD G.: *Hot Wire Measurements in a Plane Turbulent Jet*, Journ. Appl. Mech. Dec. (1965) pp. 721-734.

HUSSAIN A.K.M.F. and A. RAY CLARK: *Upstream Influence on the Near Field of a Plane Turbulent Jet*, Phys. of Fluids, vol.20, No.9, (1977).

JOHNSON N.R. and A.S. WEINSTEIN: *Simultaneous Diffusion of Momentum and Energy*, Devel. in Mech., vol.2, part 1, Proc. Eight Midwestern Conference Apr. 1-3, (1963) Pergamon Press.

KOTSOVINOS N.E.: *A Note on the Conservation of the Volume Flux in free Turbulence*, J. Fluid Mech. (1978a) vol.86, part 1, pp. 201-203.

KOTSOVINOS N.E.: *A Note on the Conservation of the Axial Momentum of a Turbulent Jet*, J. Fluid Mech.,(1978b), vol.87, part 1, pp. 55-63.

MILLER D.R. and E.W. COMINGS: *Static Pressure Distribution in the Free Turbulent Jet*, J. Fluid Mech., vol.3 (1957/58) pp. 1-16.

NEUBER H.: *Kerbspannungslehre*, Springer Verlag (1958) 2nd ed.

PERSEN L.N.: *A Short Note on Turbulent Flows*, DKNVS Skrifter No.2 (1976) Universitetsforlaget, Oslo.

REICHARDT H.: *Gesetzmässigkeiten der freien Turbulenz*, VDI - Forschungsheft 414 (1942).

REYNOLDS O.: *On the Dynamical Theory of Incompressible Fluids and the Determination of the Criterion*, Phil. Trans. A, CL XXXVI, 123 (1894).

STOKES G.G.: *On the Theories of the Internal Friction of Fluids in Motion*, Camb, Trams. VIII, 287 (1845).

TOLLMIEN W.: *Berechnung turbulenter Ausbreitungsvorgänge*, ZAMM 6, 468-478 (1926) NACA TM 1085 (1945).

TOWNSEND A.A.: *The Structure of Turbulent Shear Flow*, Camb. Univ. Press, (1956), (2nd ed. 1976).

ZIJNEN B.G. van der HEGGE: *Measurements of the Velocity Distribution in a Plane Turbulent Jet of Air*, Appl. Sci. Res., Sec. A, vol.7, pp. 256-313 (1947/49).

JET V/STOL WIND-TUNNEL SIMULATION AND GROUNDPLANE EFFECTS

Richard J. Margason
Head, Subsonic Aerodynamics Branch
NASA Langley Research Center
Hampton, Virginia 23665

SUMMARY

Low-speed wind-tunnel testing of V/STOL aircraft concepts to determine the aerodynamic-propulsion interaction effects during the transition between hover and wing-borne flight is a necessary step in the development cycle of this type of aircraft. Powered models are normally used to determine the aerodynamic performance characteristics. This paper examines some of the pretest preparation necessary to define the objectives of an appropriate investigation. Several factors which influence the selection of the model concept and the engine simulator are discussed. In addition, some of the test techniques important for this class of aircraft model are examined. Finally, the paper reviews some of the wind-tunnel wall effects important to this type of aircraft testing with special emphasis on groundplane effects.

SYMBOLS

A	area, m^2 (ft^2) or aspect ratio, b^2/S
A_e, A_j	engine exit cross-sectional area, m^2 (ft^2)
A_i	engine inlet cross-sectional area, m^2 (ft^2)
b	wing span, m (ft)
c	chord, m (ft)
C_D	drag coefficient, $Drag/q_\infty/S$
C_L	lift coefficient, $Lift/q_\infty S$
$C_{L,\infty}$	lift coefficient out of ground effect
$C_{N,T}$	tail normal-force coefficient, $N_T/q_\infty S_T$
C_T	thrust coefficient, $T/(q_\infty S)$
D, D_n	jet diameter, m (ft)
D_e	equivalent exit diameter, the diameter of a circle whose area equals the sum of the areas of all the engine exits, m (ft)
h	height of jet above ground, m (ft)
ℓ	length, m (ft)
L	lift, N (lb)
N_T	tail normal force, N (lb)
P	pressure, Pa (lb/ft^2)
q_∞	free-stream dynamic pressure, Pa (lb/ft^2)
q_{max}	maximum dynamic pressure at jet exit plane, N (lb/ft^2)
$q(z)$	maximum dynamic pressure at distance z from the jet exit plane, N (lb/ft^2)
S	wing area, m^2 (ft^2)
S_T	tail area, m^2 (ft^2)
T	static thrust, N (lb)
V, V_∞	free-stream velocity, m/sec (ft/sec)
V_b, V_G	ground belt velocity, m/sec (ft/sec)
V_e	effective velocity ratio, $\sqrt{q_\infty/(T/2A_e)}$
V_e'	effective velocity ratio at which jet impinges on floor, $1.31\ D_e/h$
$V_{e,min}$	minimum effective velocity ratio for which data can be corrected to free air conditions, $0.65\ V_e'$
V_j	jet velocity, m/sec (ft/sec)

$\dot{w}$ inlet weight flow, N/sec (lb/sec)

$\dot{w}_p$ drive weight flow, N/sec (lb/sec)

x,y,z distance along X, Y, or Z axis, respectively, m (ft)

X,Y,Z Cartesian coordinates

α angle of attack, deg

δ_f flap deflection angle, deg

δ_j jet deflection angle, deg

ΔL induced lift increment, N (lb)

$\Delta\alpha$ change in angle of attack due to wall effects, deg

η flap turning efficiency, Resultant force/static thrust

$\Lambda_{c/4}$ sweep angle of the wing quarter chord, deg

Notation:

CL conventional landing

CTO conventional takeoff

OGE out of ground effect

RVTO rolling vertical takeoff

STO short takeoff

VTO vertical takeoff

1.0 INTRODUCTION

V/STOL aircraft frequently experience considerable refinement as the design passes from the conceptual development phase through the preliminary design and final configuration definition process. These refinements are usually a result of compromises in performance requirements which occur as a result of the extreme variety flight conditions imposed upon these types of aircraft. While a V/STOL aircraft design must achieve efficient performance throughout the entire mission, particular emphasis must be given to performance in the low-speed transition between hover and wingborne flight.

The propulsion systems of V/STOL aircraft must be designed to generate both the thrust needed for conventional flight and the lift force needed for hover and the additional force components necessary for control purposes during hover and transition flight. This multi-function character of the V/STOL propulsion system requires design features which makes it significantly different from conventional aircraft propulsion systems. For example, in most aircraft configurations, the lifting force for hover is provided at two or more locations in order to provide moment trim and control about all three axes.

The lift jet exhaust issuing from the aircraft mix with the external flow field to generate an extremely complicated three-dimensional flow. In general, the jet-induced effects cause additional forces and moments on the aircraft both statically and dynamically. The character and magnitude of these jet-induced effects are influenced by the flight regime as well as by the specific aircraft configuration. Several authors have surveyed and described these V/STOL propulsion-induced effects (see refs. 1 to 4).

In the low-speed flight regime, these effects are present in several areas: (1) the performance losses sustained while hovering out-of-ground effect; (2) the performance changes and hot-gas ingestion problems occurring while hovering in-ground effect; and (3) the induced aerodynamic effects in transition flight from hover to wingborne flight (out-of-ground effect and in-ground effect) during a horizontal flight mode. Resolution of the conflicts which arise from the design requirements imposed by these different modes of flight present a significant challenge to the aircraft designer. Satisfactory solution is essential in order to provide the necessary lift forces as well as adequate control power for low-speed flight.

The designer must be able to estimate the performance of the aircraft in this low-speed flight regime. Since very few proven prediction methods are available (ref. 5), extensive wind-tunnel investigations must be conducted to verify the performance estimates. The results of these investigations are used to refine the configuration while the design process continues through prototype flight to production.

Techniques for low-speed wind-tunnel tests of conventional aircraft configurations are fairly well established (ref. 6); however, additional factors must be considered when testing V/STOL configurations. Although V/STOL aircraft include a very large variety of configurations, they may be conveniently grouped into two broad categories: those having very low disk loading and those having high disk loading. The most common category is the low-disk loading rotorcraft. Examples of powered rotorcraft models (fig. 1) are the AH-1G (ref. 7), the ABC (advanced blade concept) (ref. 8), the RSRA (rotor systems research aircraft) (ref. 9), and the tilt-proprotor configuration (ref. 10). These models typically use electric motors, gear boxes, rotating shafts, and variable pitch rotors to provide their powered lift. As a class, rotorcraft models are very complex mechanically, especially with regard to the dynamic modeling requirements. For example, the general rotor model system (GRMS) (ref. 11) used for the AH-1G (ref. 7) and RSRA (ref. 9) models is an extremely complex piece of equipment. Detailed discussion of the complexities of such rotorcraft models will not be attempted within the scope of the present paper. The GRMS is discussed in detail in reference 11, and a broader look at rotorcraft models is presented in reference 12.

The second major category of V/STOL aircraft configurations is the high-disk loading vehicles as illustrated in figure 2. Examples of STOL aircraft models include externally blown flap (EBF) (ref. 13), upper-surface blown (USB) flap (ref. 14), and internally blown jet flap (IBF) (ref. 15). An examination of propulsive-lift aerodynamic theories pertinent to STOL aircraft is presented in reference 16 in which many methods are discussed, ranging from Spence's two-dimensional jet-flap procedure to recent three-dimensional theories which require large, complex computer programs. Some of these methods are effective means of estimating gross performance for STOL configurations. Examples of V/STOL aircraft models include lift-jet plus lift-cruise (ref. 17), deflected thrust (ref. 18), augmentor (ref. 19), and lift fan (ref. 20).

Despite many conferences (such as ref. 2) and publications concerning V/STOL aero/propulsion interaction, there has been a limited documentation of V/STOL model test techniques. In the 1960's, John Williams and associates published several very useful reports (e.g. ref. 21) which provided detailed information of specific test techniques such as strain-gage balances with air lines for propulsion power, model scale simulation of jet engines, and groundplane effects. Recently, several papers (refs. 22 to 25) have been published with descriptions of more recent model methods. The material from reference 25 by Nark has been especially useful for the present paper.

Since the configurations involving jet V/STOL aircraft concepts have more demanding test requirements than the STOL configurations, the present paper will emphasize factors which influence wind-tunnel tests of high-disk loading V/STOL aircraft. These factors will be discussed in three sections: (1) Pretest Preparation; (2) Test Techniques; and (3) Tunnel and Groundplane Effects.

2.0 PRETEST PREPARATION

2.1 Define Investigation Objectives

The first step in planning a jet V/STOL wind-tunnel investigation is a definition of the test objectives. Generally, this will require measurement of the aerodynamic forces and moments for longitudinal performance characteristics and, occasionally, for lateral-directional characteristics as well. These aerodynamic characteristics must include the aerodynamic propulsion-induced effects for transition flight, that is, between hover and wingborne flight. This usually includes vertical takeoff and landing as well as short takeoff and landing characteristics. The flight envelope must be defined in sufficient detail so that the test parameters can provide adequate definition of the thrust effects. The configuration variables must be identified and the model so constructed that significant variables, such as flap deflection, tail incidence, nozzle deflection, control surface deflection, external stores, landing gear, and other perturbations and protrusions may be evaluated.

The first, and most obvious, requirement in evaluating the performance of flight vehicles using wind-tunnel data is that the flight aircraft must be faithfully duplicated in the wind-tunnel model. Unfortunately, this duplication is seldom achieved in practice and for many reasons. Often power-train components cannot be obtained in physical sizes that permit direct scaling. The wind-tunnel tests are accomplished before flight, and changes are usually incorporated in the aircraft as a result of the wind-tunnel tests. Often the cost of a completely scaled model is prohibitive in relation to the purposes of a particular test. In any event, complete model-scale duplication of the flight aircraft is seldom accomplished, and it then becomes important to reduce the significance of the differences by careful representation of the actual aircraft and by careful testing techniques.

When designing a wind-tunnel model to represent a powered V/STOL configuration, there are a number of significant factors to be considered. Some of the major factors requiring attention are: engine device selection for best simulation, model scale size for maximum model construction efficiency, model scale size to tunnel size ratio for minimum wall-induced interference, engine-inlet mass-flow simulation (critical to V/STOL concepts), and drive-air mass-flow requirements as related to available high pressure air supply.

Experience over many years with powered model testing has shown that attention to detail is much more critical for this class of models than for conventional aerodynamic testing. Faithful reproduction of the various details of the model are necessary, and some of these factors will be discussed in more detail in subsequent sections. Further, good advanced planning pays off in making the data from the tests far more useful. Finally, because of the increased number of model variables and test condition variables, this type of testing requires many more runs than a conventional model; hence the tunnel entries tend to be rather lengthy. Careful planning is required to arrange the run schedule in such a way that proper power-off conditions are obtained for use with the power-on data so that proper data correlation can be accomplished.

2.2 Select Model Concept

Proper selection of the model concept involves several factors which will be discussed in the following sections. One of the first decisions is a determination of whether to use a full-span configuration or a semispan configuration. Next, the balance concept must be selected. Whether to include the thrust forces on the balance or to measure the aerodynamic forces separately is the fundamental choice. The third area deals with the propulsion factors and their influence on the aerodynamics. A few examples of the significance of model details on the aero/propulsion induced effects will be illustrated to identify the significance of small configuration changes.

2.2.1 Semispan Versus Complete Configuration

The choice between a full-span or a semispan model is often dictated by the availability of wind-tunnel facilities. An example of this choice was described by Zierten and Rettie (fig. 3, see ref. 23) where a semispan C-14 model was tested in a 2.7- by 2.7-m (9- by 9-ft) tunnel, and later a full-span model was developed for tests in a 6.1- by 6.1-m (20- by 20-ft) wind tunnel. The results showed very good comparison between the two concepts for the longitudinal aerodynamic data, but unsatisfactory comparisons for some of the lateral-directional data.

The results of some tests conducted in Germany by Hertel on a two-nozzle configuration (ref. 26) are presented in figure 4. The sketch shows the two nozzles exhausting near the ground with an upflow. Starting at the centerline between the two jets, the velocity of the upflow was measured with both jets operating; the results are indicated by the circles. There was a gradual dropoff in the upflow velocity as the probe was moved toward the jet centerline from the line of symmetry. With a reflection plane at the plane of symmetry, there was an increased upflow velocity at the line of symmetry which drops off more rapidly than the data without the plane of symmetry. The use of a vertical reflection plane is not appropriate for measuring data with jets in ground effect. Further, the results show that there is not a true line of symmetry; instead, there is quite a bit of mixing and interaction between the upflows from the two jets. Even with a fully three-dimensional model, asymmetries can occur. The model jet deflections and pressure ratios must be carefully balanced to accurately describe the actual configuration. For example, Hall (ref. 27) showed that major asymmetry occurs with twin jets which have either different pressure ratios or different deflection angles.

The reflection plane also has an adverse effect on the inlet temperature rise. Data obtained by Ryan, Heim, and Cosgrave (ref. 28) with a small-scale hot-gas ingestion model are presented in figure 5 to show this effect. The two jets, impinging on the ground with an interference fountain between them, are moved from a height of 2 diameters above the ground to a height of 10 diameters above the ground. When no reflection plane is located between the two jets, there is a large inlet temperature rise at height of 2 diameters. The inlet temperature rise decreases sharply and then approaches zero at heights above 10 diameters. With the reflection plane, however, there is a temperature rise of only about 30°F (17°C) close to the ground, and the inlet temperatures increase steadily as the nozzles are moved away from the ground. When the nozzles are close to the ground, high velocities on the reflection plane carry the gases up above the inlet and disperse them away from the inlet. Consequently, inlets near the ground are not influenced by the hot gases when the reflection plane is in place. As the nozzles are moved away from the ground, with a reflection plane being present, the inlets gradually move into a region where the hot gases tend to congregate, furnishing results in sharp contrast to the data without the reflection plane. The data in figures 4 and 5 indicate the importance of the modeling techniques used in investigating aerodynamic/propulsion interaction problems.

2.2.2 Balance Selection

An important factor in defining the model concept is selection of the best means of force and moment measurement. Most modern tunnel facilities utilize internal strain-gage balances to measure the forces and moments, but there are certain constraints on the proper selection of such balances. Transition tests of jet V/STOL aircraft occur at low free-stream dynamic pressures which lead to small aerodynamic forces. As a result, it is important to keep the model weight low so that the balance can have adequate sensitivity for the low forces and moments generated aerodynamically. Another important aspect of sizing the balance is a determination of whether to make the thrust forces metric or nonmetric. An illustration of the impact of this is presented in figure 6 which shows a typical lift-drag polar for a powered-lift model. The curve in the upper left shows the results of a model with metric thrust forces. The lift coefficients are greater than 7 and large thrust forces (drag coefficients less than -2) are experienced.

The balance must be sized to handle the large forces generated by the engines at large negative drag coefficients. Generally, better overall aerodynamic data information is possible with a metric engine-thrust installation. Nonmetric designs typically generate ambiguous data when airframe balance results are combined with thrust forces.

The data on the right hand portion of figure 6 illustrate the airframe forces that would be measured by a nonmetric thrust balance installation. The lift coefficients get as high as 5 and the drag coefficients range from 0 to 1; therefore, a more sensitive balance can be selected for the nonmetric case, especially in the axial force component. An excellent discussion of the merits of nonmetric thrust installation (fig. 7) were presented by Knott (ref. 22). One of the most important benefits includes avoiding crossing the balance with the high pressure air for the thrust simulator. Obtaining a precise thrust value is less critical for high quality aerodynamic interference data since it can be measured directly. However, fouling between the propulsive side of the model and the aerodynamic side of the model is difficult to avoid and requires considerable attention to detail. Precise measurement of thrust-induced force increments can be obtained betweenusing such a nonmetric engine thrust installation.

2.2.3 Propulsion Factors

One particularly important aspect of V/STOL model testing is the need to describe a "power-off reference configuration" for each power-on configuration tested. These data are used to determine the interference of the lifting jets on the transition flight aerodynamic characteristics. One method of evaluating induced power effects is given by equation (1):

$$\frac{\Delta L}{T} = \left(\frac{L}{T}\right)_{\text{power on}} - \frac{C_{L,\text{power off}}}{2} \frac{S}{A_e} V_e^2 + \sin(\alpha + \delta_j) \qquad (1)$$

When a model has a flow-through nacelle for the cruise configuration, it provides the least restriction to air flow and, as a result, the lowest interference drag force. When an engine simulator is installed, it provides a restriction to the flow when it is unpowered. As a result, an increased interference drag force occurs and the inlet-mass flow is reduced. When either the nacelle exit or the entire nacelle is deflected, the flow interference increases and becomes more complex producing larger effects on the model aerodynamic performance. In the case of an augmentor configuration the wing surface deflects to form a nonaerodynamic shape which produces largely separated flow and results in completely ambiguous aerodynamic data.

Previous work (refs. 29 to 31) has shown that the effect of engine inlet flow can be significant even when the engine simulator is not powered. An example of these effects are presented in figure 8 for a subsonic, vectored-thrust V/STOL configuration with the nozzles deflected 90°. Longitudinal aerodynamic performance characteristics are presented for the model with inlets either open or closed for identical operating conditions. Ejectors similar to those described in reference 32 were used in the wind-tunnel model. Without thrust, the inlet weight flow measured was dependent on the free-stream dynamic pressure. With thrust, the inlet weight flow measured was nearly independent of free-stream dynamic pressure and thrust level because of choking near the ejector primary nozzles. Data were also taken with the inlets closed. By using the inlet weight flow rate and the free-stream density, the increment in lift due to the inlet flow was calculated to be significantly less than the measured lift increment. A comparison of wing pressure data (ref. 31) without power for the inlets open and inlets closed for the front vectored thrust configurations helps explain part of this difference. These data show that closing the inlets induced a downwash on the wing which decreased local angle of attack between 1° and 2°. Fuselage and nacelle pressure data indicate that opening the inlets produced flow changes similar to those associated with the jet-exit interference effect at high effective velocity ratios. These results are discussed in detail in reference 29 and indicate that the inlet effect is largely caused by the nozzle efflux.

Several experimental investigations (ref. 33 to 36) have demonstrated that the turbulence and/or decay of jet dynamic pressure with increasing distance from the jet exit has a significant impact on the jet-induced loads. An example (ref. 36) of these results is shown in figure 9 where the decay of the jet dynamic pressure is plotted as a function of distance downstream from the jet for hover. The jet with the slowest rate of dynamic pressure decay is deemed to have the longest potential core in the jet, approximately 6 diameters. With a plug representing an engine centerbody inserted flush with the exit, the dynamic pressure drops somewhat more rapidly. As the round plug, simulating the centerbody, is moved inside the jet, away from the exit plane, further reductions in dynamic pressure are noted. Using these jet configurations, data (fig. 10) were obtained with the jet mounted in a flat plate to determine the hover lift losses. The data show that the lift losses obtained are proportional to the rate of decay of the jet shown in figure 9; that is, the jet with the least turbulence has the least lift loss. The jets with the highest levels of turbulence have the highest lift loss. Work (ref. 34) was done with the same hardware to determine the influence of the centerbody on the jet turbulence for lift loss at transition flight speeds. An apparent contrasting trend was found; that is, there is a crossover at a low forward velocity ratio (approximately 0.10) as transition speeds approaching wingborne flight are obtained, the greatest lift losses are obtained with the jet having the least turbulence in hover. However, jet decay data in reference 34 show that as the crossflow increases, the jet decay occurs more rapidly. These results show that the presence of a centerbody

in the nozzle of the jet significantly influences the jet-induced interference effects. Jet V/STOL models should duplicate, as closely as possible, the anticipated jet exhaust conditions. It further appears that previous model studies which have nad uniform jet velocity profiles may have significantly overestimated the jet-induced lift losses in transition flight.

2.2.4 Model Detail

A number of investigations have shown the importance of modeling even minute details in the model construction techniques. Perhaps one of the most interesting results (ref. 37) obtained shows the effect on induced lift of a systematic variation of fuselage bottom edge radii. Figure 12 shows that a flat fuselage bottom with sharp edges produces a positive induced lift. This induced lift decreases rapidly with small increases in edge radius, and especially at low heights; it could be concluded that the action of the fountain upwash on the fuselage is the principal cause.

An investigation (ref. 38) was conducted with simplified EBF wind-tunnel models to obtain information on the effect of wing sweep. One of the models was unswept with a rectangular planform and the other had 27° sweep with a taper ratio of 0.3. Both models were tested with a flap deflection of 60°. A comparison of these swept- and unswept-wing EBF model data with YC-15 flight data obtained in steady flight at various values of h/c is shown in figure 13. The unswept-wing model data are in good agreement with the flight data, indicating that wing sweep may be an important factor determining the ground effects of powered-lift STOL aircraft. The close quantitative agreement between the model and airplane results is probably fortuitous since there are a number of differences between the two configurations, such as flap deflection and wing taper ratio. However, it would be expected that wind-tunnel tests of an exact model of the YC-15 airplane would produce positive lift increments in ground effect generally similar to those observed on the airplane. The conclusion can then be drawn that the apparent discrepancy between YC-15 flight ground effects and the early EBF model ground effects can be explained by differences in configuration such as wing sweep and flap deflection.

2.3 Engine Simulator Selection

Since propulsion effects are the most critical factor in the transition regime of V/STOL concepts, the most important model design decision should be the engine simulator selection. Several concepts for thrust simulation are available to the model designer. A brief summary of these concepts is provided in Table 2 (taken from ref. 25). The simplest concept, the flow-through nacelle for unpowered wind-tunnel models, is relatively simple to design and build, and quite adequate for aerodynamic drag studies where propulsion induced effects are not a significant factor. A second approach is a jet powered by compressed air from a plenum chamber. This concept provides a very simple operation for test purposes while maintaining a generally good representation of the exit geometry and jet pressure ratio. It can be used for both hot and cold jets. The one deficiency in this arrangement is that the inlet flow is not simulated. A third concept is the jet ejector, which does provide both inlet and exhaust flow simulation. However, it is difficult to achieve a scaled inlet flow rate when the exhaust thrust is simulated. The final approach is the turbine powered simulator which is the most complex and, for low pressure ratio applications, provides a very fine simulation tool. It is, however, quite expensive, difficult to calibrate, and subject to problems of equipment reliability.

2.3.1 Simulator Concept

To illustrate the simulator concept selection process, a specific example based on the model in reference 40 will be used. A comparison of a full-scale fan configuration and three available simulators is presented in figure 14. The physical descriptions and calibration data have been published for the 14-cm (5.5 in.) diameter fan (ref. 39) and for the small ejector (ref. 32). The model scale will be determined by the ratio of simulator diameter to full-scale diameter; therefore, once an existing simulator has been chosen, the model size is fixed. For the example model, three model scales were possible: the 14-cm (5.5-in.) diameter fan would provide an 8.6-percent scaled model, the lift-fan ejector (11.3 cm diameter) model scale would be 7.4 percent, and the ejector (5.1 cm diameter) model scale would be 3.4 percent. Model size alone cannot be used as the yardstick for selection of the 14-cm (5.5-in.) diameter fan or the lift-fan ejector. However, the ejector simulator results in such a small model that it would be difficult to install the necessary instrumentation. Figure 15 presents a comparison of the installation of each of these simulators in a proposed scale model of a tandem lift-fan pod. The front fan was facing forward with side deflector nozzles and the aft fan was mounted horizontally for lift.

2.3.2 Inlet-Flow Simulation

The positions of the engine inlets in V/STOL aircraft configurations can strongly influence the external flow over nearby surfaces. The inlets of lifting engines are frequently located on the upper surface of the fuselage, wing, or a pod. The engines must operate efficiently with the inlet-flow distortion caused by the external flow over the upper surfaces. These factors, peculiar to many V/STOL concepts, require that the engine inlet flow be simulated properly. Figure 16 presents a comparison of inlet mass flow of three engine simulators with that of the full-scale engine. The inlet mass flow is ratioed to the exit cross-sectional area. This figure indicates that the 14-cm (5.5-in.) diameter fan simulates the full-scale article very

well, while the ejector simulator provides only about half of the scaled inlet flow. In the case of the 14-cm (5.5-in.) diameter fan, if the exit-flow characteristics are simulated properly, the inlet-flow characteristics will also be simulated properly.

2.3.3 Drive Air Requirements

After evaluating the adequacy of each engine simulator for use in an investigation, it must be determined if the needed compressed air to drive the simulators is available. A comparison of the drive air required to operate these simulators is presented in figure 17. The scale on the right indicates that the thrust required is a direct function of the model scale factor squared. The total scaled thrust required to simulate aircraft operating conditions through transition is presented as a function of required drive air mass flow and effective velocity ratio defined as $V_e = \sqrt{q_\infty/(T/2A_e)}$. The determination of required thrust at particular effective velocity ratios will be described later.

The thrust versus drive-air mass flow curves (shown in fig. 17) indicate the thrust required to properly operate the simulators. The curve does not indicate the maximum thrust available from the simulators, but does indicate the amount of compressed air needed to operate these simulators. Figure 17 indicates that the lift-fan ejector simulators will require a maximum of 44 N/sec (10 lb/sec). However, plumbing bends, unions, and valves could possibly increase line loss to a value which might make it difficult to deliver full flow to the model simulators unless a very high supply pressure is available. It was concluded after review of the advantages and disadvantages of each engine simulator that the most appropriate simulation system for this particular example should be the 14-cm (5.5-in.) diameter fans.

2.3.4 Static Thrust Calibration

For most aerodynamic testing, the primary variables that must be properly simulated are the jet thrust exit area and inlet mass flow. It has been shown and discussed previously in figures 9 to 11 that the exit dynamic pressure decay can be a significant factor in the simulation of aero/propulsion interference effects. Part of the calibration should include a documentation of the dynamic pressure decay for the device used in the model.

Proper calibration of inlet flow involves the use of specific facilities such as those shown in figures 18 and 19 and described in references 41 and 42, respectively. These facilities used either a vacuum tank on the exit (fig. 18) or a pressure tank on the inlet (fig. 19) to simulate the nozzle pressure ratio. Briefly, the powered model static test stand (fig. 19, ref. 42) allows direct reading of two force components and the moment in the nozzle plane of symmetry. The apparatus consists of a metric platform supported by four pads floating in mercury. The platform is restrained by load cells which provide the force and moment measurements. Each of the load cells can be loaded for calibrations with a special screw jack and reference load cell. High pressure air is supplied to the platform through a flexible hose cross-over system. The cross-over hoses terminate in the plenum chamber. The models attach to the apparatus at this point. Proper simulation of the nozzle pressure ratios encountered in the wind tunnel was accomplished by pressurizing the fan airflow to a total pressure of nearly 1.9 atmospheres. At the highest pressure ratio setting and highest inlet total pressure setting, nozzle pressure ratios were on the order of 2.7. Both the fan flow rate and turbine flow rate were measured using standard flow meters. These flow meters were installed in the air supply lines upstream of the thrust stand.

The fundamental parameters calibrated were the fan weight flow and the nozzle gross thrust. The fan weight flow calibration is based upon measured inlet flow conditions. The gross thrust calibration is determined from measured fan and turbine discharge characteristics and from local flow conditions external to the nozzle exit. The pressure data were recorded using instrumentation in the engine simulator. The thrust was measured by the powered model test stand. The instrumentation used in the powered nacelles was sufficiently redundant to provide different methods of calibration for both weight flow and thrust. The following discussion describes the version of fan weight flow and gross thrust calibrations that were used for the wind-tunnel testing. The selected methods of calibration provide the most accurate and straightforward results.

The pretest thrust calibration procedure should include measurement of the inlet weight flow, the total resultant thrust force, the deflection angle of the efflux and dynamic pressure decay. These calibrations preferably should be done both for the isolated simulator device, and for the simulator device assembled in the complete airplane configuration. The pretest calibration curves should be checked as part of the wind-tunnel investigation for each model configuration. This check is necessary to calculate the induced effects of thrust on the aerodynamic data. The importance of checking the thrust calibrations during the tunnel entry should be emphasized as a major way of achieving confidence in the accuracy of the results.

3.0 TEST TECHNIQUES

V/STOL test techniques involve considerable attention to model detail to be sure that the test configuration represents the desired configuration. Examples of the significance of these details has been shown in figures 12 and 13. The model must

accurately represent the airplane. Part of good test technique is the checking or rerunning the static calibration in the wind tunnel as discussed in the previous section. The establishment of a good test program is essential to the acquisition of the necessary data. Several factors involved in test program development will be discussed in the next few sections.

3.1 V/STOL Transition Flight Representation

The estimated operating conditions of the full-scale aircraft configuration through the transition flight regime are needed before a useful test plan can be developed. An example of the V/STOL regime for the AV-8B aircraft (ref. 24) is illustrated in figure 20 where the relationship between air speed and the engine nozzle angle for level flight is shown. Examination of the shaded portion and the light portion of the plot shows that a large number of potential test conditions can be eliminated and a more directed test program can be established. Another example of the V/STOL flight regime for a transport type V/STOL (ref. 40) is presented in figure 21 for the configuration in the takeoff and in the landing conversions. The required percentage of installed thrust and the resultant forward speed for equilibrium flight through transition is shown in figure 21. The curves presented in figure 22 indicate the relationship between thrust deflection and forward speed, and are plotted as a function of the jet deflection angle for the landing and takeoff conversions. One way to keep the length of the tunnel entry to a minimum is to obtain aerodynamic data only near the estimated operational effective velocity ratios and the full-scale dynamic pressure shown by the shaded regions. For example, detailed aerodynamic performance testing of the configuration with a jet deflection of 0° at very low velocity ratios or with a jet deflection of 90° at very high velocity ratios would be unreasonable. The flight vehicle could not operate under these conditions and the data generated would not be representative of a realistic flight envelope.

3.2 Aerodynamic Data Nondimensionalization

The data from several V/STOL configurations (fig. 23, refs. 30, 18, 17, and 43 clockwise from upper left photograph) that have been tested in the Langley 4- by 7-Meter (V/STOL) Tunnel and in the 300-MPH 7- by 10-Foot Low-Speed Tunnel have been analyzed to determine jet-induced interference effects. Configurations with the rear nozzles at the wing trailing edge show beneficial jet interference at transition velocity ratios. This is illustrated by a wing-canard configuration in figure 24 along with data for the Harrier-type configuration showing the detrimental jet interference typical of configurations having nozzles under the wing. In order to directly compare one configuration with another, figure 25 presents L/T versus V_e for several configurations. From this more traditional approach, it would appear that the wing-canard configuration would be the superior configuration. However, this approach does not account for wing or jet areas that may be different on each configuration.

If, however, equation (1) is rearranged, the data can be compared as $(L/T)\ (A_j/S)$ versus $(V_e)^2$, a different conclusion may be evident

$$\frac{L}{T}\frac{A_j}{S} = \frac{C_{L,\text{power off}}}{2}(V_e{}^2) + \frac{A_j}{S}\sin(\alpha + \delta_j) \tag{2}$$

where the first term on the right hand side of the equation is the slope and is a function of the power-off configuration C_L, and the second term is the intercept and is a function of jet area. Therefore, the higher the power-off C_L, the better the configuration should be in transition; the larger the disk or jet area, and hence lower disk loading, the better the configuration should be in hover. Several points can be noted: (1) the $(L/T)\ (A_j/S)$ parameter is nearly linear with $(V_e)^2$; (2) the slope of the parameter is indicative of the configuration aerodynamic lift coefficient and is thus a measure of how well it might perform in transition flight; (3) the value of the parameter at the intercept when $V_e = 0$ is indicative of how well the configuration can hover; and (4) any difference between the data and the plot of calculated $(L/T)\ (A_j/S)$ is an indication of the interference present. The data in figure 26 show the same interference trends for the wing-canard configuration and the Harrier-type configuration as in figure 25. Where the data of figure 25 show the wing-canard configuration to be superior, in figure 26, it is shown to have inferior hover performance because it is a higher pressure ratio concept. These configurations are compared at several angles of attack and nozzle deflections in reference 44.

Several general trends can be noted. Those configurations with nozzles at or near the wing trailing-edge flaps have high slopes and generally beneficial interference effects indicating potentially good transition characteristics. However, these configurations tend to have small nozzle areas and a resultant high thrust loading which make them poor hovering configurations. The Harrier-type configuration with nozzles below the wing has detrimental interference effects indicating poorer transition characteristics. However, this configuration had a larger jet area and showed better hovering characteristics. While many other data nondimensionalization formats could be used, these data analyses are intended to illustrate the importance of the format selection when evaluating data from a particular V/STOL aircraft or when comparing several V/STOL aircraft.

4.0 WIND-TUNNEL WALL AND GROUNDPLANE EFFECTS

4.1 Wind-Tunnel Wall Effects

The primary work on wind-tunnel wall effects and their corrections for V/STOL configurations was done by Heyson (refs. 45 to 47). This work differs from classicial corrections (ref. 48) because it eliminates the small angle assumption for the change in angle of attack due to wall effects. It was shown that theoretical correction is effective if the magnitude of wall interference is kept within reasonable bounds. The wall interference tends to be proportional to lift coefficient. As a result, it is quite large for V/STOL configurations where the lift coefficient approaches infinity as the forward speed approaches zero.

The character of the flow distortion caused by the presence of the walls is typified by nonuniform interference as illustrated in figure 27. Variations of flow angularity occur across the span of the test section and affects the wind-tunnel model as a wash-in twist distribution (local α increase from wing root to wing tip). Proper correction requires that the wing spanload distribution be corrected to the uniform free-air flow angle. Variations of flow angularity along the length of the test section due to wall interference can present a more serious problem. Over the length of the vehicle, the distortion can be large enough to provide an aerodynamic change in both tail incidence and height. Effectively, the model is distorted from the configuration which it was originally intended to represent. Corrections for these longitudinal angularity variations are most difficult as shown below.

A systematic investigation (ref. 49) of the wind-tunnel wall effects was conducted in several different wind-tunnel test sections using the model shown in figure 28. The fan-in-wing model used a 20-cm (8-in.) diameter fan mounted in each side of a low-aspect-ratio wing. The wing-fuselage was mounted on a strain-gage balance with the horizontal tail mounted on a separate strain-gage balance. A sample of the data obtained on the wing-fuselage at an angle of attack of 16° is presented in figure 29. Without corrections, the lift-thrust ratio appears to be inversely proportional to the cross-sectional area of the test section. With corrections, excellent correlation of the wing lift parameter is achieved throughout the range of effective velocity ratio. This indicates that the chordwise and spanwise variations of flow angularity at the wing due to wall interference have been properly accounted for.

A sample of the data obtained on the tail at an angle of attack of only 0° is presented in figure 30. Without corrections, the tail normal-force coefficient shows considered scatter at the low velocity ratios. There are no discernable trends with change in test section cross-sectional area. With corrections, there is a change in local angle of attack especially at the low velocity ratios as shown by the more negative tail normal force coefficients. However, the corrections are not effective in reducing the data scatter and providing consistent experimental results. These data show that there is a limit to which these corrections can be applied.

This limit was experimentally investigated in detail by Tyler and Williamson (ref. 50) and was found to be a function of the jet height above the tunnel floor and the effective diameter of the jets. (See fig. 31.) The effective velocity ratio (for a configuration with two laterally spread jets) at which the jet exhaust impinged on the floor was experimentally determined to be:

$$V_e' = 1.31\, D_e/h \qquad (3)$$

Assuming a D_e/h of 0.143 for a typical model (ref. 40) which is mounted 7 effective diameters above the floor, V_e' becomes 0.187. It was found, based on data taken with a model in various tunnel sizes, that the effect of the walls could be corrected to free air with an effective velocity ratio of 65 percent of the stagnation point velocity ratio V_e'. For D_e/h of 0.143, this $V_{e,min}$ becomes 0.121. Using the correction technique described in references 45 and 46 and keeping the maximum correction to angle of attack $\Delta\alpha$ at the tail to 5°, resulted in a $V_{e,min}$ of 0.125. Testing below this minimum velocity ratio would cause a vortex to be formed ahead of the model (as shown in fig. 31) which would encircle the model inducing flow patterns inconsistent with the free-air condition. Another suggestion (ref. 51) for a limiting test condition is to terminate testing when the deflected lifting wake impinges 2.5 wing spans downstream from the model. This is consistent with Turner's criteria for use of a moving-belt groundplane which will be discussed in Section 4.3.

4.2 Conventional Groundplane

The effect of the boundary layer developed on a conventional groundboard was studied in reference 52 to identify expected adverse effects. The experiments were made using a carriage to move a model through still air over the ground in the same fashion as an airplane landing or taking off. This same model was then tested over a conventional fixed groundboard in a wind tunnel. The lift-loss increment over the fixed groundboard was much greater than that experienced with the moving model technique which represents the true loss in lift that this type of configuration would experience in ground effect. There is an additional lift loss for the wind-tunnel results caused by the boundary layer on the conventional fixed groundboard. Figure 32 shows schematically the type of flow that has been observed conventional groundboard tests with only the air

moving and in moving model tests as observed in O.N.E.R.A. water-tunnel flow visualization experiments (ref. 53). The top sketch shows the flow pattern around the model moving at free-stream velocity with no boundary-layer induced velocity reduction as illustrated by the vector sketch on the left. The jet sheet from the model impinges on the groundboard with some of the sheet attempting to flow forward under the model. This forward flow can penetrate the high energy free-stream air only a short distance. The bottom sketch shows the flow field around the model over a fixed groundboard with the velocity profile at the left showing the loss in velocity in the boundary layer on the groundboard. The jet sheet impinges as before but the part of the sheet that flows forward under the model nearest the groundboard can penetrate farther upstream because of the lower energy of the airstream in the boundary layer; this upstream penetration by the jet sheet can separate the boundary layer even upstream of the model. This boundary-layer separation results in an appreciable alteration of the flow field in the vicinity of the model as indicated by the relocation of the stagnation streamline. It is apparent that the boundary layer on the groundboard must be eliminated for proper ground simulation.

4.3 Moving-Belt Groundplane

Several research organizations have developed moving-belt groundplanes to better simulate the ground effect and eliminate the boundary layer found in wind tunnels. A sketch of one of the first moving-belt groundplanes developed (ref. 54) is presented in figure 33. This elaborate moving-belt groundplane was developed at the Royal Aircraft Establishment for tests with speeds up to 27.4 m/sec (90.0 ft/sec). The lower part of the figure shows the effectiveness of the belt in removing the ground boundary layer and achieving an approximately uniform velocity profile down to the groundplane surface. Turner (ref. 52) developed several moving-belt groundplanes at the NASA Langley Research Center. A variety of aircraft configurations have been tested over these moving-belt groundplanes. In general, configurations which operate at high circulation lift coefficients such as a tilt wing, jet flap and in some cases, unpowered double-slotted flap configurations, require the belt. A correlation of conditions requiring the moving belt groundplane is presented in figure 34 for combinations of lift coefficient and configuration height to span ratio for conditions which do or do not require the moving-belt groundplane. Above the correlation line lie the combinations of lift coefficients and height ratios where a conventional groundplane is adequate. Below the correlation line lie the combinations where a moving belt is required. Near the correlation line is a series of symbols for three different aircraft configurations. The sketch at the right side of the figure illustrates the meaning of the symbols. Data were taken with a conventional groundplane (dashed line) and with a moving-belt groundplane (solid line). When the curves were different, the difference showed a reduction in lift-curve slope at some lift coefficient for the data taken with a conventional groundplane as illustrated in figure 34. This condition identified a maximum lift coefficient at a given ground height when the conventional groundplane no longer provided a simulation of ground height consistent with that provided by the moving-belt groundplane. The symbols on figure 34 thus identify a number of test conditions where Turner (ref. 52) showed the moving belt was needed to obtain a valid simulation of ground effect. The correlation line in figure 34 corresponds to the height above the ground computed by assuming that the effective wake for the lifting surface impinges on the ground at a distance of 2.5 spans downstream from the model. This wake deflection angle is related to the wake skew angle described by Heyson in reference 51. The agreement between the plotted points and the solid line or boundary is apparently significant. It is interesting to note that the downstream distance of 2.5 spans is almost the same as the impingement distance at which recirculation effects in the wind tunnel begin to produce the limiting test condition (section 4.1) effects on the data as shown by Heyson (ref. 55). The conventional groundplane is adequate for those combinations of lift and height occurring at conditions which are above the boundaries shown by the solid line. For those combinations falling below the boundaries shown, the moving belt is required.

Results are presented in figure 35 for a powered low-aspect-ratio wing in ground effect (ref. 55) showing the effect of the moving belt on the ground effect. The lift and drag coefficients are presented as a function of height for this configuration with a 20° flap deflection, a 24° nacelle deflection and an angle of attack of 0°. In all cases, the boundary layer was removed ahead of the model. A residual boundary layer approximately 2.5 cm (1.0 in.) thick developed between the upstream location of the boundary-layer removal section and the location of the model. On the curve of lift coefficient as a function of height, the shaded region in the upper left-hand corner represents the region determined by Turner (ref. 53) and presented in figure 34 where the moving belt was needed to get the correct lift on the model. The data presented in figure 34 for a powered wing-in-ground effect (ref. 55) includes results with the moving belt stopped and with the moving belt at free-stream velocity. The lift coefficient data for the power-off condition shows essentially no difference due to the belt. The two power-on curves show only a moderate difference at the lowest height for the data presented. It is suggested that for this low-aspect-ratio configuration, the removal of the boundary layer was sufficient to obtain an appropriate groundplane simulations over the range of lift and height considered. In general, other tests (ref. 52) have shown that configurations in which the lift is concentrated in discrete jets such as direct jet V/STOL or tilt-up or nacelle configurations do not require the belt.

5.0 CONCLUDING REMARKS

The present paper has looked at some of the critical considerations for wind-tunnel investigations of jet V/STOL aircraft configurations. Aspects ranging from model design to test techniques and data presentation have been considered. Possible problems can be anticipated and corrected. For example, semispan models may be useful for measurement of STOL longitudinal aerodynamic characteristics. They are usually unsatisfactory for lateral-directional aerodynamic characteristics and are definitely unsatisfactory for ground effects.

The areas discussed emphasized the need for thorough pretest preparation starting with a clear definition of the investigation objectives, careful selection of model concepts, and the engine simulator device. While metric engine simulations require detailed attention to air line interference effects, they can provide the better representation of overall aerodynamics. Nonmetric engine simulators require careful design attention to avoid balance fouling; however, they provide the most precise measurement of thrust induced effects. Once the model is put together, a complete pretest static calibration and checkout and fitting of all the parts and configurations is essential.

In planning the test program, a first essential is limiting the tests to only those aspects of the flight envelope that relate to the transition flight regime. Some thoughts are suggested on forms for nondimensionalizing aerodynamic data to clearly assess the interference effects. A new data nondimensionalization format is suggested. At zero flight velocity, the format provides a value which is indicative of hover efficiency. At transition flight speeds, the format is linear with respect to flight velocity and provides a direction indication of aero/propulsion interference on aircraft performance.

Finally, the wind-tunnel wall effects are discussed with emphasis on groundplane effects. Wind-tunnel wall corrections by Heyson are effective for conditions ranging from cruise down into the transition speed regime. It is recommended that this method be used to correct for wall effects and to assess validity of transition test results. The Tyler and Williamson expression for the minimum effective velocity condition for data which can be corrected to free-air conditions should be used when planning a test of V/STOL aerodynamic transition characteristics. It is concluded that for configurations having the lift spread over the span of the wing, the moving-belt groundplane technique may be essential; for jet-lift configurations with discrete jets, the moving belt is of lesser importance.

REFERENCES

1. Barche, J.: Jet Lift Problems of V/STOL Aircraft. AGARD CP-143, V/STOL Aerodynamics, 1974, pp. 16-1 - 16-18.

2. Hickey, D. H.: V/STOL Aerodynamics: A Review of the Technology. AGARD CP-143, V/STOL Aerodynamics, 1974, 1-1 - 1-13.

3. Anon: Military Applications of V/STOL Aircraft. AGARD CP-126, 1972.

4. Margason, R. J.: Review of Propulsion Induced Effects on Aerodynamics of Jet V/STOL Aircraft. NASA TN D-5617, 1970.

5. Platzer, M. F.; and Margason, R. J.: Prediction Methods for Jet V/STOL Propulsion Aerodynamics. J. Aircraft, vol. 15, no. 2, February 1978, pp. 69-77.

6. Pope, A.; and Harper, J. J.: Low-Speed Wind Tunnel Testing. John Wiley & Sons, Inc., New York, 1966.

7. Freeman, C. E.; Phelps, A. E. III, and Mineck, R. E.: Aerodynamic Characteristics of a 1/4-Scale Powered Helicopter Model With a V-Type Empennage. NASA TM 74033, 1978.

8. Phelps, A. E.; and Mineck, R. E.: Aerodynamic Characteristics of a Counter-Rotating, Coaxial, Hingeless Rotor Helicopter Model With Auxiliary propulsion. NASA TM 78705, 1978.

9. Mineck, R. E.; and Freeman, C. E.: Aerodynamic Characteristics of a 1/6-Scale Powered Model of the Rotor Systems Research Aircraft. NASA TM X-3489, 1977.

10. Wilson, J. C.; Mineck, R. E.; and Freeman, C. E.: Aerodynamic Characteristics of a Powered Tilt-Proprotor Wind-Tunnel Model. NASA TM X-72818, 1976.

11. Wilson, J. C.: A General Rotor Model System for Wind-Tunnel Investigations. J. Aircraft, vol. 14, no. 7, July 1977, pp. 639-643.

12. Harris, F. D.: Aerodynamic and Dynamic Rotary Wing Model Testing in Wind Tunnels and Other Facilities. AGARD/Von Karman Institute Lecture Series No. 63, Helicopter Aerodynamics and Dynamics, April 2-6, 1973.

13. Johnson, W. G.: Aerodynamic Characteristics of a Powered, Externally Blown Flap STOL Transport Model With Two Engine Simulator Sizes. NASA TN D-8057, 1975.

14. Phelps, A. E. III; Johnson, J. L., Jr.; and Margason, R. J.: Summary of Low-Speed Aerodynamic Characteristics of Upper-Surface-Blown Jet-Flap Configurations. NASA SP-406, 1976, pp. 63-88.

15. Vogler, R. D.: Wind-Tunnel Investigation of Internally Blown Jet-Flap STOL Airplane Model. NASA TN D-8309, 1976.

16. Margason, R. J.; Yip, L. P.; and Gainer, T. G.: Recent Developments in Propulsive-Lift Aerodynamic Theory. NASA SP-347, Aerodynamic Analyses Requiring Advanced Computers, Pt. II, 1975, pp. 871-896.

17. Wooten, W. H.; and Hoff, G. E.: Deflected Exhaust Jet Effects on V/STOL Fighter Performance. General Electric Rep. R73AEG279, July 1973.

18. Margason, R. J.; Vogler, R. D.; and Winston, M. M.: Wind-Tunnel Investigation at Low Speeds of a Model of the Kestrel (XV-6A) Vectored-Thrust V/STOL Airplane. NASA TN D-6826, 1972.

19. Anon: Conceptual Design Study of a Military Ejector Augmented Wing V/STOL Aircraft. NASA CR-137516, May 1974.

20. Lampkin, Bedford A.; Staff of the Lift-Fan Research Aircraft Project Office, Ames Research Center; and Staff of the Propulsion Systems Project Office, Lewis Research Center: An Analysis of Propulsion Concepts for V/STOL Lift-Cruise Fan Research and Technology Aircraft. NASA TM X-73,237, April 1977.

21. Williams, J.; and Butler, S. F. J.: Further Developments in Low-Speed Wind-Tunnel Techniques for V/STOL and High-Lift Model Testing. Roy. Aircraft Establishment Tech. Note AERO 2944, January 1964.

22. Knott, P. G.: V/STOL Aerodynamic Testing Techniques at British Aircraft Corporation. AIAA Paper 77-584, June 1977.

23. Zierton, T.; and Rettie, I.: Wind Tunnel Test Techniques for Powered Lift Airplanes. AIAA Paper 77-888, July 1977.

24. Johnson, D. B.; Lacey, T. R.; and Voda, J. J.: Powered Wind Tunnel Testing of the AV-8B; A Straightforward Approach Pays Off. AIAA Paper 79-0333, January 1979.

25. Nark, T.: Powered Lift Testing. Presented at AIAA First Atlantic Aeronautical Conference, Williamsburg, Virginia, March 26-28, 1979.

26. Hertel, H.: Wandstromungen und Aufstrome aus der Umlenkung von Freistrahlgruppen (Wall Flows and Up-Streams Due to the Diversion of Free Jet Groups). Fortschritt Berichte VDI Zeitschrift Fortschr., vol. 12, no. 11, pp. 1-72, July 1966.

27. Hall, G. R.; and Rogers, K. H.: Recirculation Effects Produced by a Pair of Heated Jets Impinging on a Ground Plane. NASA CR-1307, 1969.

28. Ryan, P. E.; Heim, R. J.; and Cosgrove, W. J.: A Generalized Experimental Investigation of Hot Gas Recirculation and Ingestion for Jet VTOL Aircraft. NASA CR-1147, 1968.

29. Wooler, P. T.; Kao, H. C.; Schwendemann, M. F.; Wasson, H. R.; and Ziegler, H.: V/STOL Aircraft Aerodynamic Prediction Methods Investigation. U.S. Air Force AFFDL-TR-72-26, vols. I-IV, 1972.

30. Mineck, R. E.; and Schwendemann, M. F.: Aerodynamic Characteristics of a Vectored-Thrust V/STOL Fighter in the Transition-Speed Range. NASA TN D-7191, 1973.

31. Mineck, R. E.; and Margason, R. J.: Pressure Distribution on a Vectored-Thrust V/STOL Fighter in the Transition-Speed Range. NASA TN D-2867, 1974.

32. Margson, R. J.; and Gentry, G. L.: Static Calibration of an Ejector Unit for Simulation of Jet Engines in Small-Scale Wind-Tunnel Models. NASA TN D-3867, 1967.

33. Gentry, G. L.; and Margason, R. J.: Jet-Induced Lift Loses on VTOL Configurations Hovering In and Out of Ground Effect. NASA TN D-3166, 1966.

34. Kuhlman, J. M.; Ousterhout, D. S.; and Warcup, R. W.: Experimental Investigation of Effect of Jet Decay Rate on Jet-Induced Pressures on a Flat Plate. NASA CR-2979, 1978.

35. Kuhlman, J. M.; and Warcup, R. W.: Jet Decay Rate Effects on Hover Jet-Induced Loads. J. Aircraft, vol. 17, no. 8, August 1980, p. 605.

36. Kuhlman, J. M.; and Warcup, R. W.: Effects of Jet Decay Rate on Jet-Induced Loads on a Flat Plate. J. Aircraft, no. 15, no. 5, May 1978, pp. 293-297.

37. Wohllebe, F. A.; and Migdal, D.: Some Basic Test Results of V/STOL Jet-Induced Lift Effects in Hover. AIAA Paper 79-0339, January 1979.

38. Campbell, J. P.; Hassell, J. L.; and Thomas, J. L.: Ground Effects on Lift for Turbofan Powered-Lift STOL Aircraft. J. Aircraft, no. 15, no. 2, Feb. 1978, pp. 78-84.

39. Lowe, W. H.; and Sanger, R. W.: Static Performance of a 13.97-cm (5.5-In.) Diameter Model Lift Fan. NASA CR-2051, 1972.

40. Hoad, D. R.; and Gentry, G. L., Jr.: Longitudinal Aerodynamic Characteritics of a Low-Wing Lift-Fan Transport Including Hover Characteristics In and Out of Ground Effect. NASA TM X-3420, 1977.

41. Hunt, D. N.: Experimental Techniques Used to Evaluate Propulsion System Interference Effects on the Cruise Configuration of the Boeing C-14. AIAA Paper 79-0335, January 1979.

42. Wells, O. D.; Lopez, M. L.; Welge, H. R.; Henne, P. A.; and Sewell, A. E.: Wind Tunnel and Analytical Investigation of Over-The-Wing Propulsion/Air Frame Interferences for a Short-Haul Aircraft at Mach Numbers From 0.6 to 0.78. NASA CR-2905, 1977.

43. Winston, M. M.: Induced Interference Effects on the Aerodynamic Characteristics of a 0.16-Scale Six-Jet V/STOL Model in Transition. NASA TN D-5727, 1970.

44. Paulson, J. W., Jr.; Thomas, J. L.; and Winston, M. M.: Transition Aerodynamics for Close-Coupled Wing-Canard Configuration. AIAA Paper 79-0336, January 1979.

45. Heyson, H. H.: Linearized Theory of Wind-Tunnel Jet-Boundary Corrections and Ground Effect for VTOL-STOL Aircraft. NASA TR R-124, 1962.

46. Heyson, H. H.: Use of Superposition in Digital Computers to Obtain Wind-Tunnel Interference Factors for Arbitrary Configurtions, With Particular Reference to V/STOL Models. NASA TR R-302, 1969.

47. Heyson, H. H.: Wind-Tunnel Testing of VTOL and STOL Aircraft. NASA TM -78750, 1978.

48. Glauert, H.: The Inteference of Wind Channel Walls on the Aerodynamic Characteristics of an Aerofoil. British A.R.C. R&M No. 867, 1923.

49. Heyson, H. H.: The Effect of Wind-Tunnel Wall-Interference on the Performance of a Fan-In-Wing VTOL Model. NASA TN D-7518, 1974.

50. Tyler, R. A.; and Williamson, R. G.: Experience With the NRC 10 Ft. x 20 Ft. V/STOL Engine Model Testing. Canadian Aeronautics and Space Journal, no. 10, no. 9, September 1972, pp. 191-199

51. Anon: Conference on V/STOL and STOL Aircraft. NASA SP-116, April 1966.

52. Turner, T. R.: A Moving-Belt Ground-Plane for Wind-Tunnel Ground Simulation and Results for Two Jet-Flap Configurations. NASA TN D-4228, 1967.

53. Werle, Henri: Simulation de L'Effet de Sol au Tunnel Hydrodynamique (Ground-Effect Simulation at the Water-Tunnel). La Rech. Aerospatiale, no. 95, July-August 1963, pp. 7-15.

54. Butler, S. F. J.; Moy, B. A.; and Hutchins, G. D.: Low-Speed Tunnel Tests of an A.R.9 Jet-Flap Model, With Ground Simulation by Moving-Belt Rig. Roy. Aircraft Establishment Tech. Note AERO 2957, April 1964.

55. Thomas, J. L.; Paulson, J. W., Jr.; and Margason, R. J.: Powered Low-Aspect-Ratio Wing In Ground Effect (WIG) Aerodynamic Characteristics. NASA TM 78793, July 1979.

TABLE 1. THRUST INDUCED EFFECTS

	Thrust On Balance	Thrust Off Balance
High pressure air	Must cross balance	Does not cross balance
Direct thrust effects	On balance	Obtained from calibration
Thrust-induced effects	On balance	Almost but not all on balance
Forces induced on nacelle installations	Included in force data	Obtained by analysis
Balance design	Critical in design of support system	Standard technique
Model fouling	No problem	Critical in design of support system
Thrust calibration	Essential	Necessary but not critical
Pressure tares	Balance design must ensure pressures tares are low compared with forces being measured	Not critical

TABLE 2.- THRUST SIMULATION

Nacelle type	Air Supply Requirement	Principal Simulations	Other Simulation Capabilities	Comment
Flow	None	o Inlet geometry o Inlet V_i/V_∞ at one mach	o Dual flow	o Simple o Good for aerodynamic drag studies
Blown Jet	Large	o Exhaust nozle geometry o Gross thrust	o Dual flow o Hot gas	o Simple operation o Erroneous inlet contribution
Ejector	Moderate	o Inlet geometry/or o Exhaust nozzle geometry/and o Gross thrust	o Dual flow	o Inlet and exhaust flow not simulated simultaneously
Turbine Powered	Small	o Inlet geometry and/or exhaust nozzle geometry o Inlet V_i/V_∞ and not gross thrust o Gross thrust and not inlet V_i/V_∞		o Sensitive mechanism o Difficult to simulate inlet and exhaust flow simultaneously

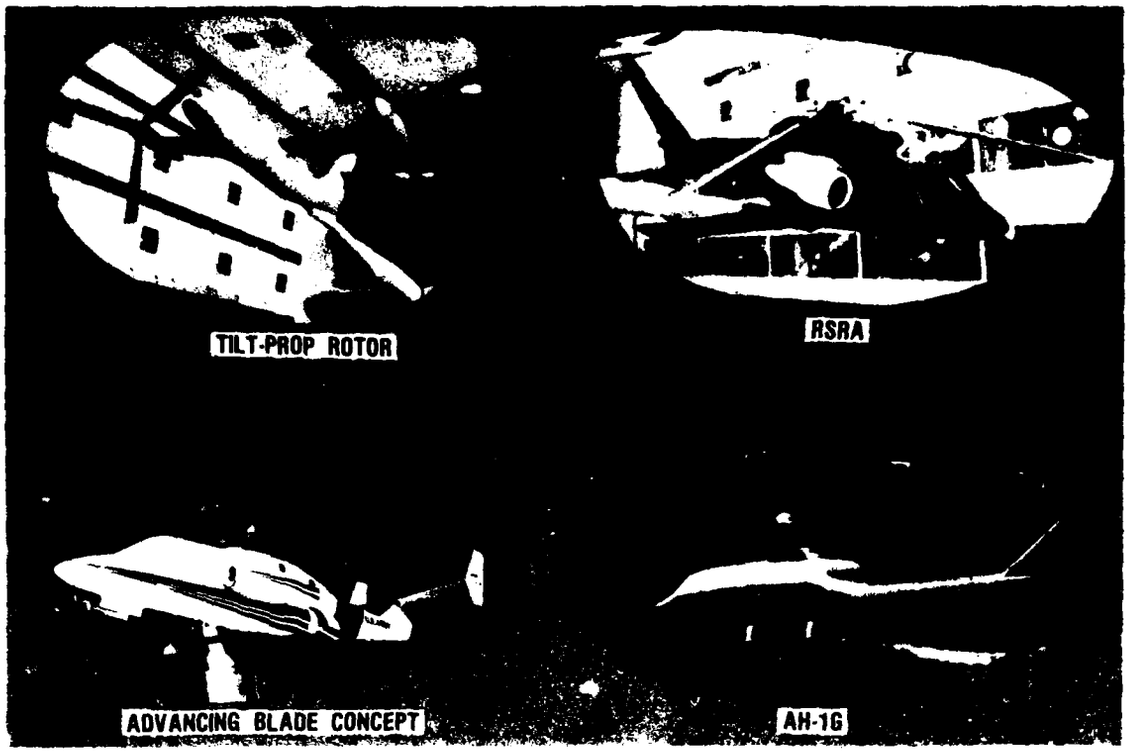

Figure 1.- Examples of several complex rotor models.

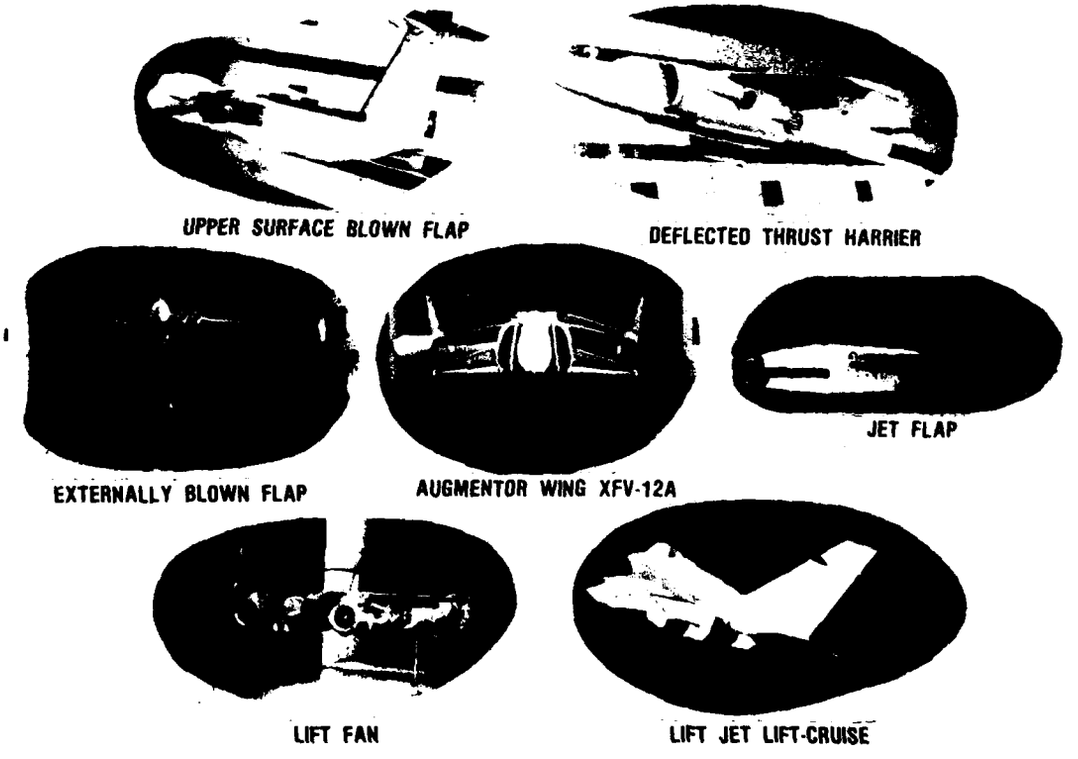

Figure 2.- Examples of several complex STOL and V/STOL models.

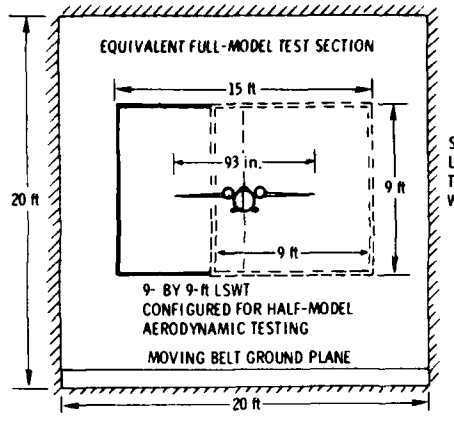

Figure 3.- Geometry relationship of a semi-span model and of a full-span model of the C-14 in two wind-tunnel test sections (ref. 23).

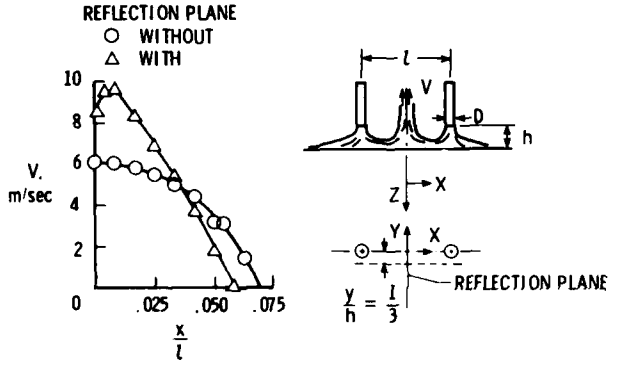

Figure 4.- Effect of a reflection plane on the measured upflow velocities in the fountain flow caused by two jets exiting vertically near the ground. The nozzles were at a height (h/D) of 3 and the upflow velocities were measured in the nozzle exit plane at a lateral distance (y/h) of 1/3 (ref. 27).

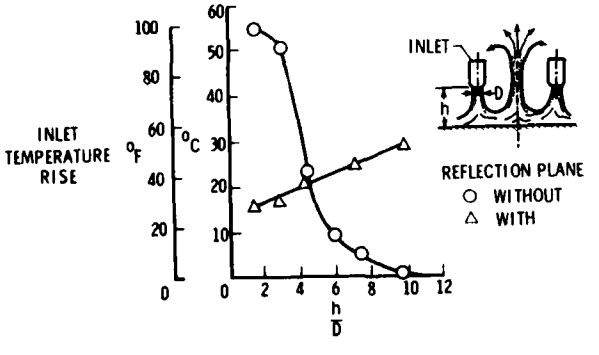

Figure 5.- Effect of a reflection plane on the measured inlet air temperature rise resulting from the fountain flow caused by two jets exiting vertically near the ground (ref. 29).

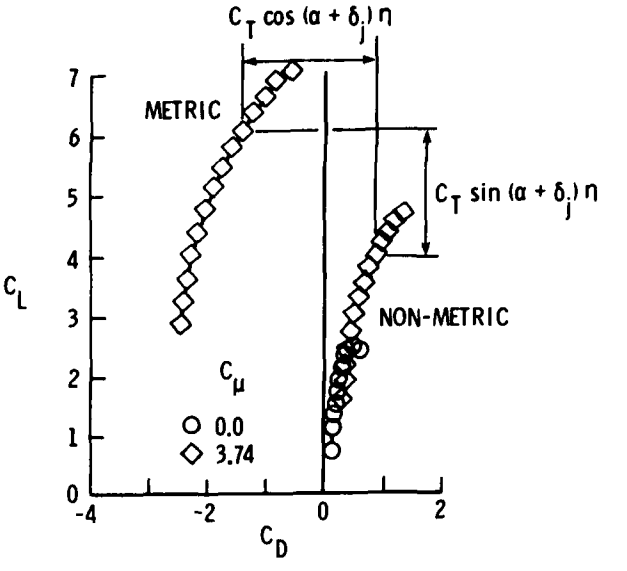

Figure 6.- Effect of thrust on balance (metric or nonmetric) data for a typical powered-lift configuration.

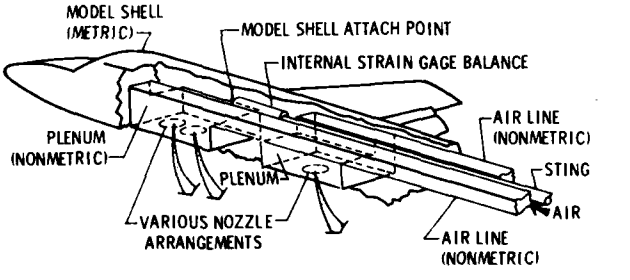

Figure 7.- Model concept for aero/propulsion interaction measurement with a nonmetric balance (from ref. 22).

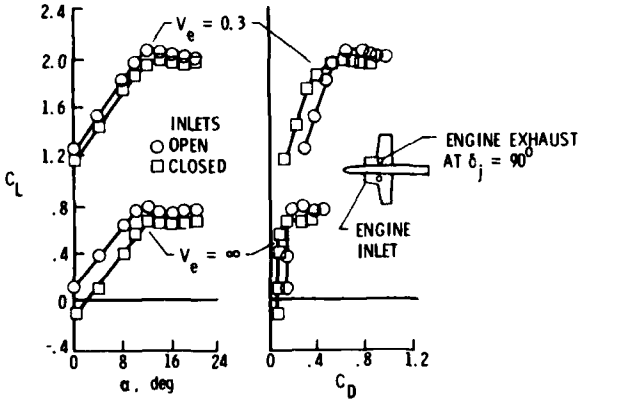

Figure 8.- Effect of inlet-weight flow on the longitudinal aerodynamic characteristics of a subsonic, vectored-thrust V/STOL configuration (ref. 30).

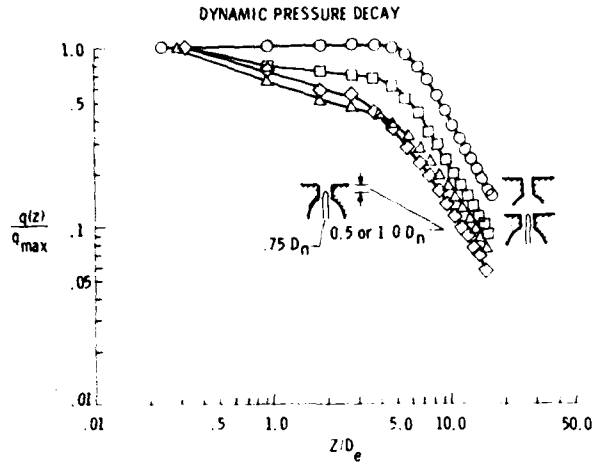

Figure 9.- Effect of plug tip location on jet centerline dynamic pressure decay in hover (ref. 34).

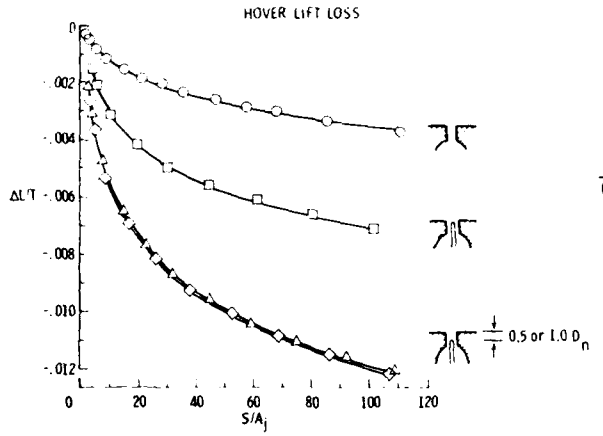

Figure 10.- Nondimensional hover lift loss for a simple jet and a jet with several plug tip locations (ref. 35).

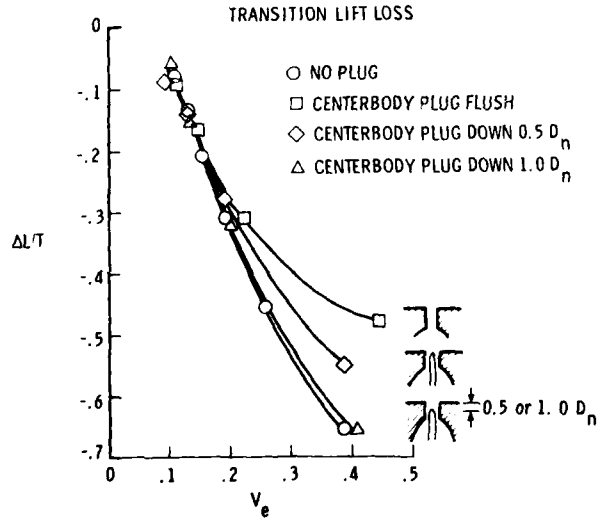

Figure 11.- Nondimensional transition flight lift loss for a simple jet and a jet with several plug tip locations (ref. 36).

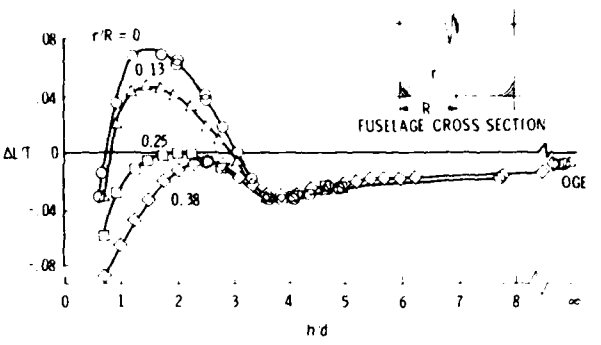

Figure 12.- Influence of fuselage bottom edge radius on induced lift of a lift-jet configuration in ground effect (ref. 37).

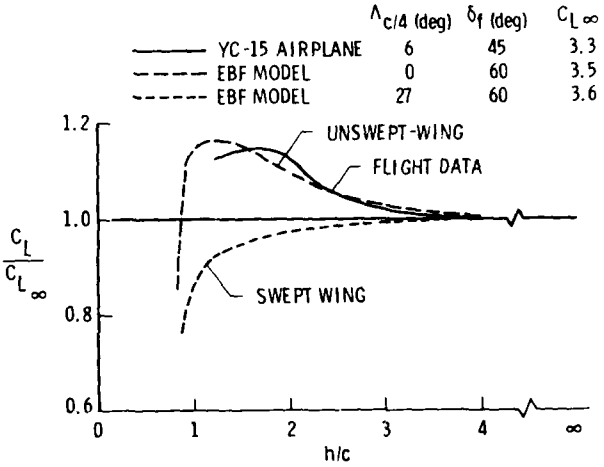

Figure 13.- Effect of wing sweep on two aspect-ratio-7 externally blown flap configuration compared with YC-15 flight data (ref. 38).

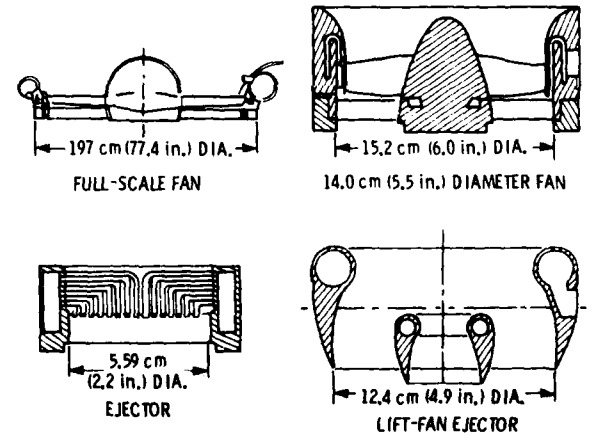

Figure 14.- Example of a full-scale lift-fan configuration and three simulators which can be used in a powered wind-tunnel model.

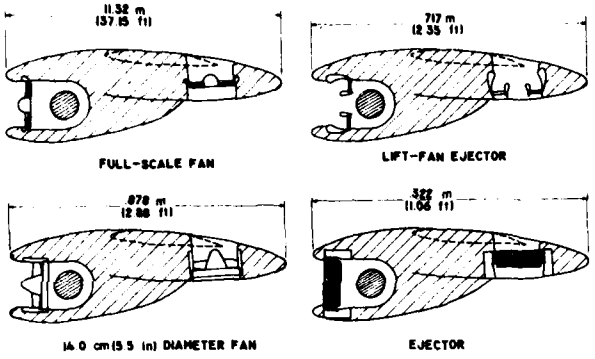

Figure 15.- Examples of lift-fan and of several model simulators installed in a hypothetical two-fan nacelle.

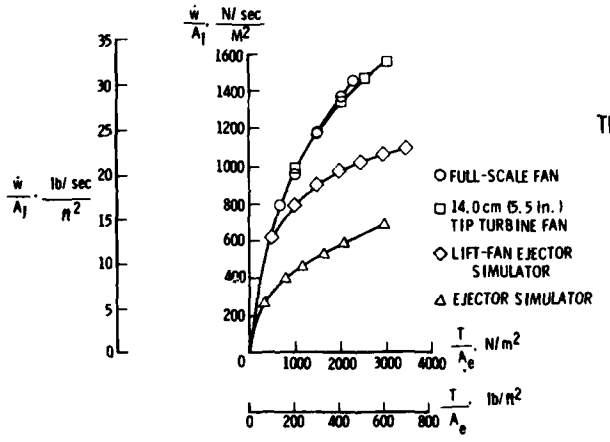

Figure 16.- Comparison of inlet-weight flow for the fan and model simulators.

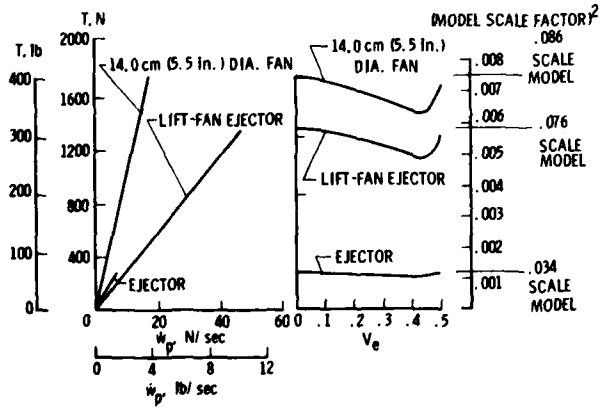

Figure 17.- Comparison of high pressure drive air required to power the model simulators.

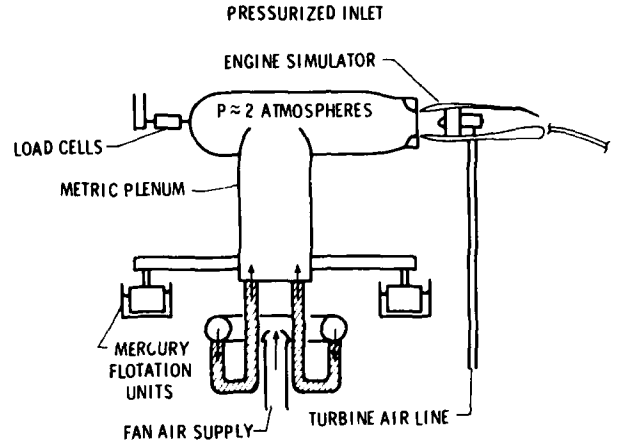

Figure 18.- Powered nacelle installation in vacuum type static calibration facility (ref. 41).

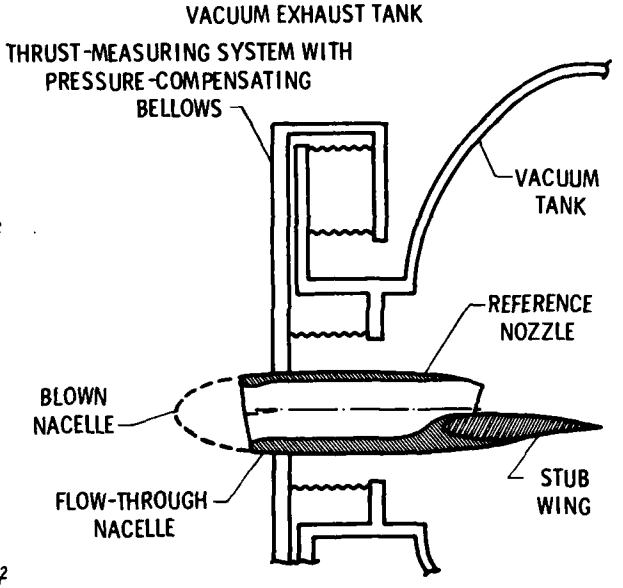

Figure 19.- Powered nacelle installation in a pressure type static calibration facility (ref. 42).

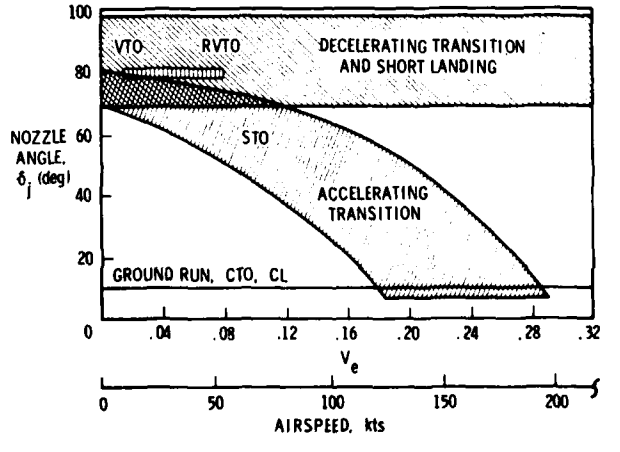

Figure 20.- AV-8 V/STOL flight operations envelope (ref. 24).

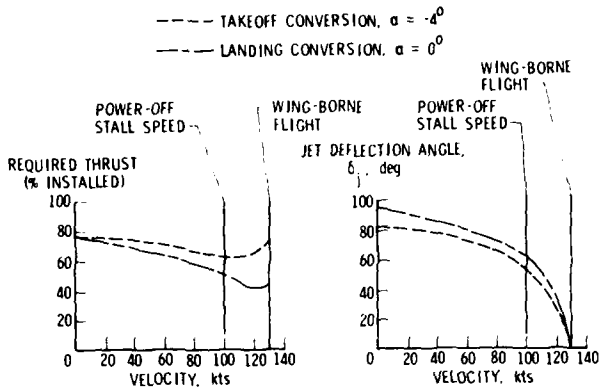

Figure 21.- Estimated requirements for installed thrust and jet deflection through the transition-flight regime.

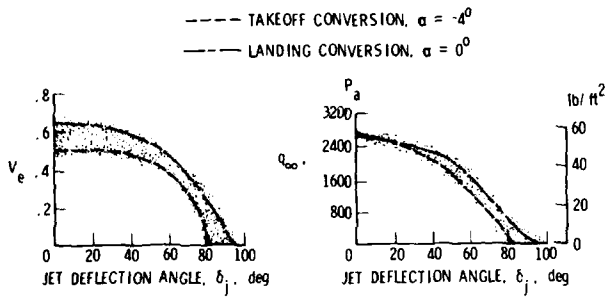

Figure 22.- Powered wind-tunnel model operating conditions required to represent transition flight.

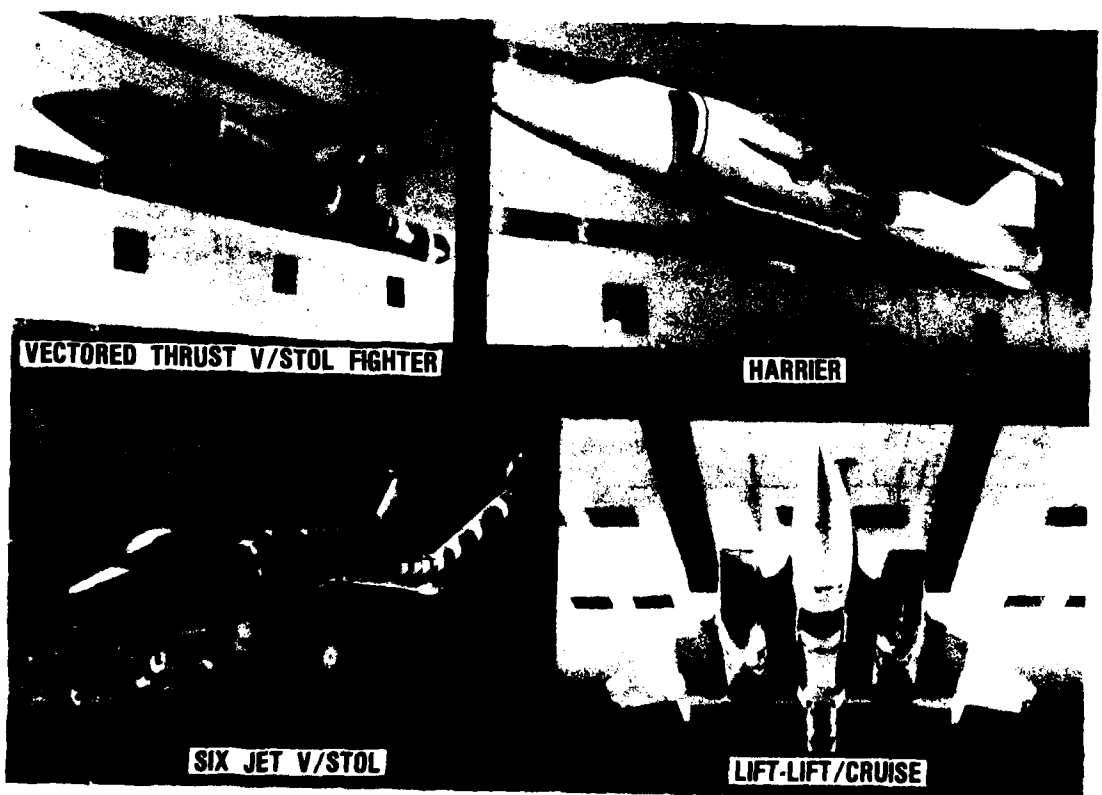

Figure 23.- Several V/STOL configurations installed in the NASA Langley 4- by 7-Meter (V/STOL) Tunnel: vectored thrust (ref. 30); Kestrel (ref. 18); six-jet V/STOL (ref. 43); and lift-lift/cruise (ref. 44).

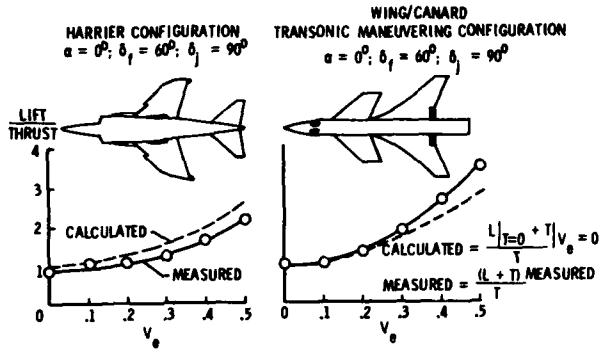

Figure 24.- Interference effects in hover and transition.

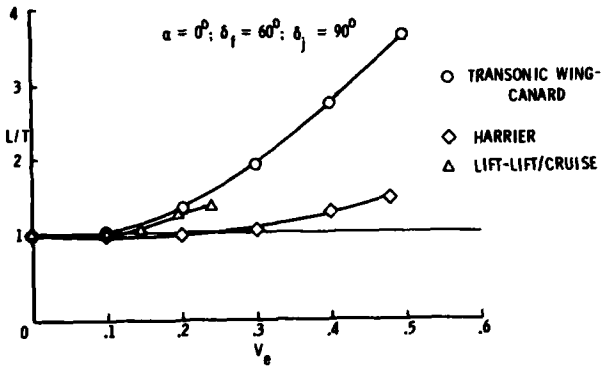

Figure 25.- Traditional transition performance parameter.

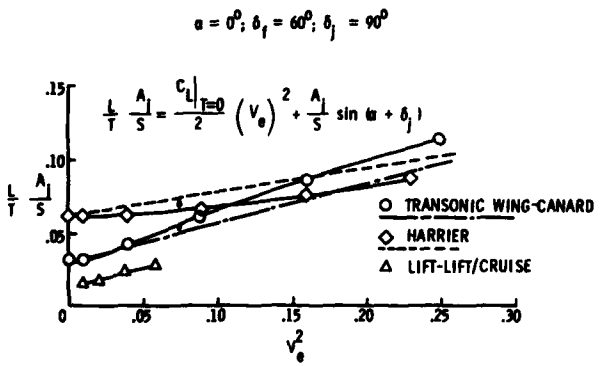

Figure 26.- Revised transition performance parameter.

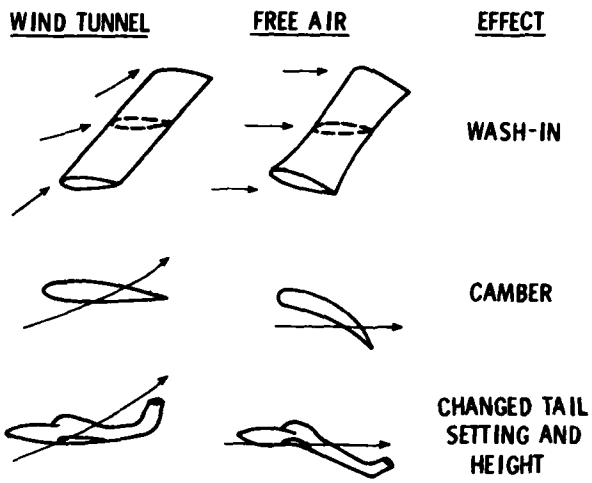

Figure 27.- Nonuniform flow interference on wind-tunnel models which represent an effective distortion of the corresponding vehicle in free air (ref. 47).

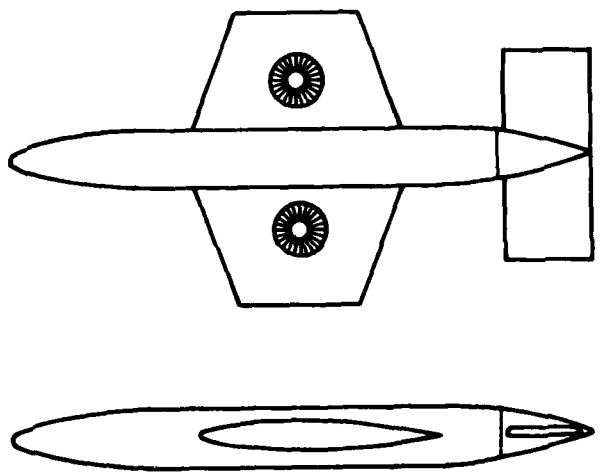

Figure 28.- Fan-in-wing wind-tunnel model used to investigate wind-tunnel wall effects (ref. 49).

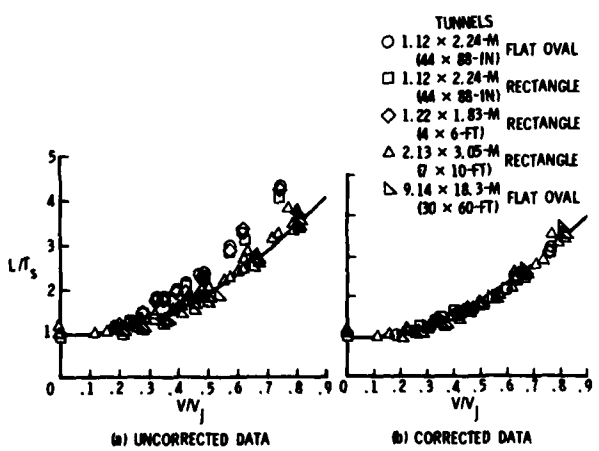

Figure 29.- Sample of wind-tunnel wall effects showing the effect of test section size and the effect of wall correction theory on wing lift at an angle of attack of 16° (ref. 49).

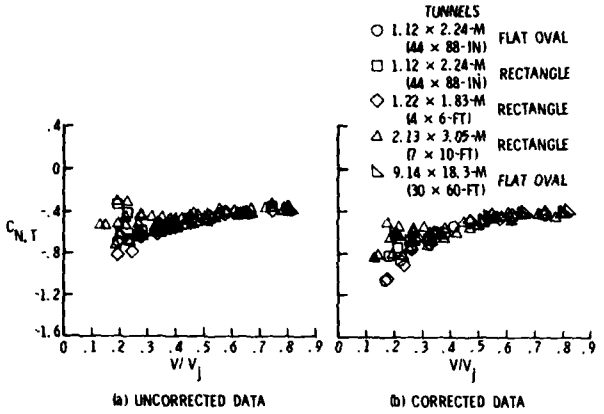

Figure 30.- Sample of wind-tunnel wall effects showing the effect of test section size and the effect of wall correction theory on tail normal force at an angle of attack of 0° (ref. 49).

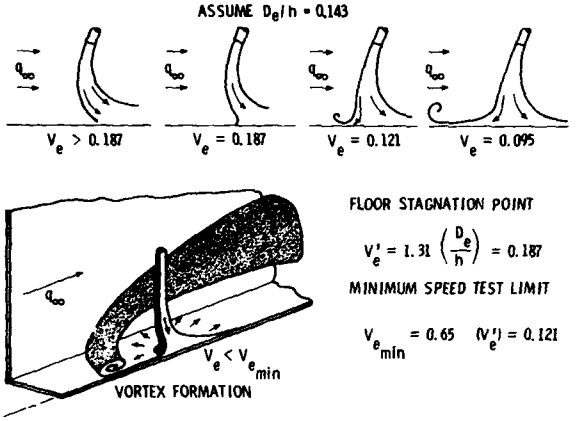

Figure 31.- Minimum speed testing limit for a configuration with two side-by-side lifting jets at h/D_e = 7 (ref. 50).

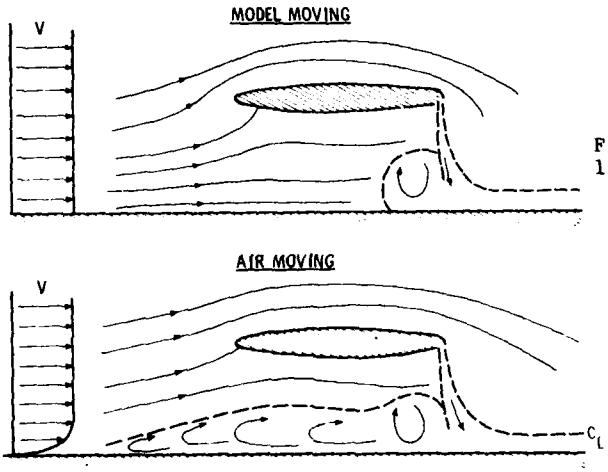

Figure 32.- Sketches of flow over a ground-plane for both the case with the model moving and the case with only air moving (ref. 53).

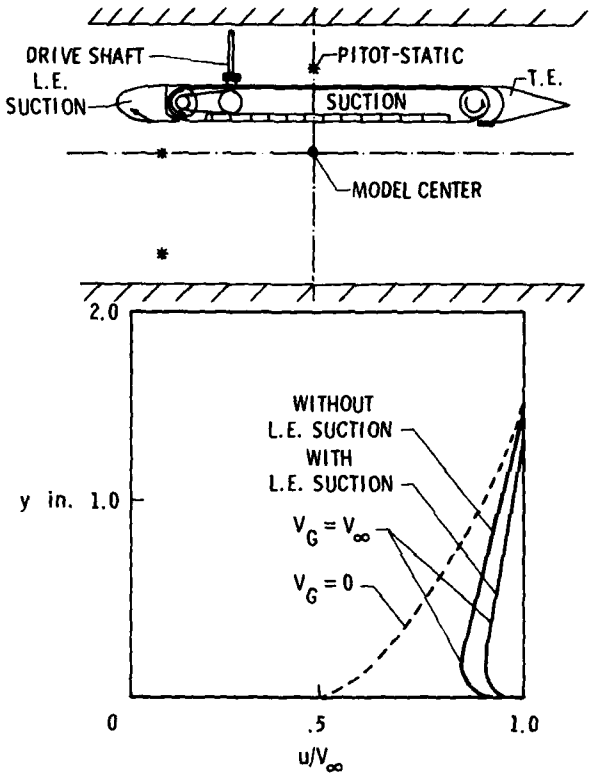

Figure 33.- Early moving-belt groundplane developed by RAE (ref. 54) including the effects of belt velocity and boundary-layer suction on the ground boundary-layer profiles on the moving belt.

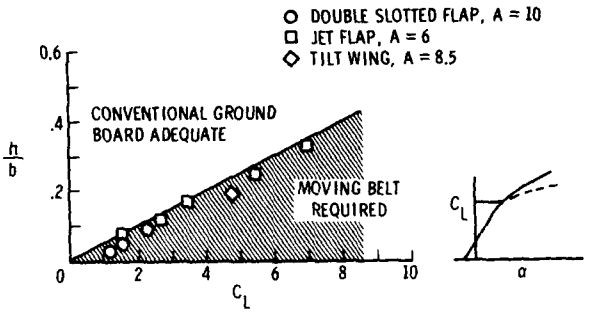

Figure 34.- Correlation of combinations of lift coefficient and configuration height to span ratio to show which combinations require use of moving belt of which combinations allow use of conventional ground plane (ref. 52).

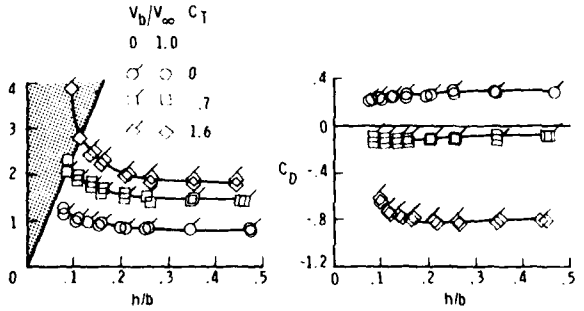

Figure 35.- The effect of the moving ground belt on the powered wing-in-ground effect with the ground boundary-layer removal compressor on and both with and without the moving belt operating (ref. 55). The shaded part of the C_L-h/b plot illustrates the Turner criteria (ref. 53).

*The Modelling and Prediction Of Multiple Jet VTOL Aircraft Flow Fields in Ground Effect

+Donald R. Kotansky

McDonnell Aircraft Co.

McDonnell Douglas Corporation

St. Louis, MO, USA

SUMMARY

An engineering methodology based on an empirical data base and analytical fluid dynamic models has been developed for the prediction of propulsive lift system induced aerodynamic effects for multiple lift jet VTOL aircraft operating in the hover mode in and out of ground effect. The methodology takes into account the effects of aircraft geometry, aircraft orientation (pitch, roll) as well as height above ground. Lift jet vector and splay directions with respect to the airframe, lift jet exit flow conditions, and both axisymmetric and rectangular nozzle exit geometry are also accommodated. The methodology has been embodied in a computer code which accommodates configurations with up to six lift jets.

In ground effect, the prediction methodology proceeds logically from the aircraft lift jet exits through the free jets, jet impingement points, wall jets, fountain bases (stagnation lines) and fountain upwash flow and impact on the airframe undersurface. The induced suckdown flows are computed from the potential flowfield induced by the turbulent entrainment of both the free jets and wall jets in ground effect and from the free jets alone out of ground effect. Key elements of this methodology including geometric considerations, computation of stagnation lines and fountain upwash inclination, fountain upwash formation and development, and fountain impingement on the airframe are emphasized in this paper.

NOMENCLATURE

A	Area
AR	Aspect ratio
D	Jet exit diameter (circular nozzle), nozzle exit width (rectangular nozzle)
$f(\phi)$	Radial momentum flux distribution about jet impingement point (normalized)
H	Nozzle exit height above ground plane measured perpendicular to ground plane
L	Nozzle exit length (rectangular nozzle)
$\dot{m}$	Mass flow
$\dot{M}$	Momentum flux
N	Normal distance above ground plane in wall jet, number of jets in idealized lift system
NPR	Nozzle pressure ratio
R	Radial distance
S	Nozzle exit centerline spacing
S'	Distance between jet impingement points on ground plane

*Portions of this work were supported by the Naval Air Development Center (contract N62269-76-C-0086), the NASA Ames Research Center (contracts NAS2-9646 and NAS2-10184), the Office of Naval Research (contract N00014-79-C-0130) and McDonnell Aircraft Company Independent Research and Development resources.

+Branch Chief-Technology, Aerodynamics

$s_{V/2}$ Velocity profile width at point in profile where $V = \frac{V_{max}}{2}$

U Wall jet velocity

V Jet or fountain velocity

X,Y,Z Cartesian coordinates with Z normal to the ground plane

α Jet impingement angle measured from ground plane

γ Momentum normalization correction

ϕ Stagnation line slope in ground plane

κ Fountain sidewash angle measured from the ground plane

λ_M^* Momentum flux magnitude recovery (conservation) factor

ρ Density

ϕ Azimuthal angle in ground plane; $\phi = 0°$ in direction of the horizontal component of free jet mean velocity in oblique impingement situations

ϕ' Computational polar angle measured in the ground plane about a jet impingement point referenced to the line joining the jet impingement points

ω Fountain upwash inclination measured from the ground plane

Subscripts

1,2 Jet designation

f Fountain, final

fI Fountain impingement

j Jet

je Jet exit

max Maximum

min Minimum

N Normal

o Initial

R Radial

TH Theoretical

wj Wall jet

INTRODUCTION

The design of successful high performance military VTOL aircraft requires a critical blend of new propulsive lift system technology with tried and proven CTOL high speed aircraft characteristics. The VTOL aircraft configuration analyst is beset with a myriad of performance requirements, airframe configuration variables and propulsive lift system options; yet there is a dearth of useful vehicle performance prediction methods to aid in the identification of promising vehicle configurations. This, in combination with the many physical variables involved can result in a largely subjective and empirical approach to vehicle configuration definition based on past experience. The unique operational requirements of VTOL aircraft that are responsible for this complex design dilemma are, of course, the vertical and transition flight requirements. These flight modes necessitate a knowledge of forces and moments on the vehicle which are unfamiliar to the CTOL aircraft designer. These flowfield effects are characteristically dependent on the selected propulsive lift system and its physical integration into the airframe due to the interactive nature of the lift jet induced aerodynamics on the airframe. These jet induced flowfield interactions occur in the transition and in the hover flight modes both in and out of ground effect. A purpose of this paper is to provide an insight and quantitative basis for the modelling and prediction of multiple jet induced flowfields and the resulting aerodynamic forces and moments on the airframe in ground effect. A propulsion system designed without taking into account the induced forces may not provide sufficient thrust for an adequately controlled takeoff without a reduction in payload. In addition to these induced net loads, situations are encountered where unfavorable moments

are produced on the airframe, resulting in significant stability and control problems. Until accurate, general purpose flowfield prediction techniques become available for these complicated viscous flowfields, dependence on wind tunnel testing for design and performance verification will be relatively high.

The induced forces (and moments) in and out of ground effect usually result from one of two reasonably well understood flow phenomena. These are jet entrainment and the formation of jet flow fountains. Jet entrainment causes otherwise static air to be set into motion, resulting in locally reduced static pressures on nearby airframe undersurfaces thus introducing negative aerodynamic loads. The jet entrainment effect occurs both in and out of regions influenced by the presence of the ground but is frequently accentuated as the distance between the nozzle exit and the ground is reduced. This is attributable to the proximity of the additional entrainment resulting from the ground wall jets. The flowfield about a VTOL aircraft hovering in ground effect is shown schematically in Figure 1.

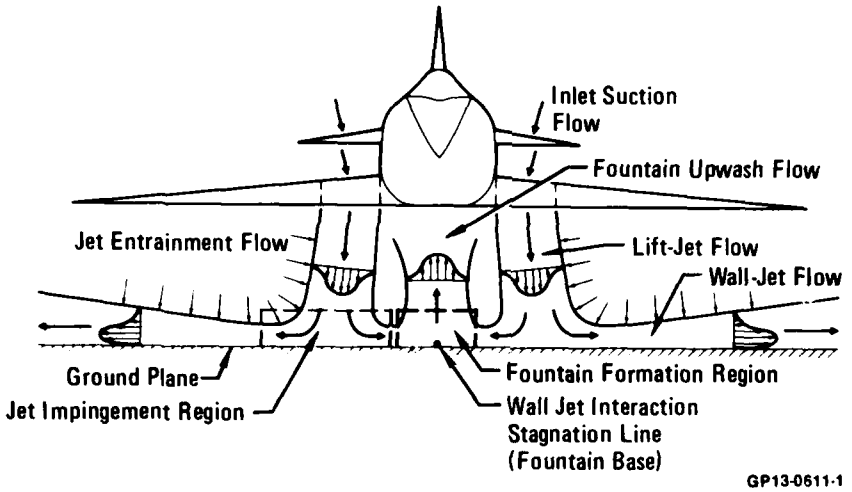

Fig. 1 Flowfield About a VTOL Aircraft Hovering in Ground Effect

The formation of jet flow fountains requires the impingement of the jets on the ground or shipboard landing pad and, therefore, is peculiar to operation close to the ground. The formation of fountains is configuration dependent in that multiple jets are required. The jet impingement points, relative strengths of the jets, and jet impingement angles influence the characteristics of the fountain. The upward convection of jet flow in the fountains usually results in a positive aerodynamic lift, caused by the positive pressurization of airframe undersurfaces containing and deflecting the fountain flow. Because of the upward convection of the lift jet flow in the fountains, a degradation of propulsion system performance may result from exhaust gas ingestion. In this respect, fountains can also be detrimental to VTOL aircraft performance in proximity to the ground. Significant VTOL hover flowfield interactions and their resulting effects on vehicle performance in ground effect are summarized in Figure 2.

The following sections of this paper will outline the empirically based methodology developed by the McDonnell Aircraft Company (MCAIR) for the modelling and prediction of multiple jet V/STOL aircraft flowfields in ground effect. This methodology was developed during the period from 1975 through 1980. The reader will be referred to appropriate published references for detailed mathematical developments and thorough documentation of experimental data. Key elements in the development of the methodology will be emphasized in this paper.

• Lift Loss (Suck-Down)	→ Turbulent Jet Entrainment
• Lift and Moment Sensitivity to Pitch and Roll	→ Deflection of Fountains
• Lift and Moment Sensitivity to Cross-Winds	→ Deflection of Jets and Fountains by Cross-Winds and Cross-Wind Induced Aerodynamic Loads
• Engine Thrust Loss from Exhaust Gas Ingestion	→ Fountain, Cross-Wind and Buoyant Convection of Hot Exhaust Gas

GP13-0611-2

Fig. 2 VTOL Flowfield Interactions in Ground Effect

GEOMETRIC CONSIDERATIONS

The viscous (turbulent) flowfield between a multiple jet VTOL aircraft and the ground is strongly dependent on many geometric factors related to the geometry of the airframe, integration of the propulsive lift system including the geometry of the nozzle exits and the spacial relationship of the airframe to the ground plane. The significant jet mean flow geometry and overall flowfield geometry includes:

- o Lift jet system arrangement including the number of jets, jet exit spacings and jet exit orientation with respect to the aircraft axes (including longitudinal "vector" and lateral "splay" angles),
- o Nozzle exit shape and mean velocity distribution at the nozzle exit, and
- o Aircraft surface geometry, orientation and height above ground.

Most of the above geometric variables were taken into account in the initial development of a ground flow field prediction computer program by MCAIR which is described in detail in Reference 1. This work was based on the fundamental free jet flow development and impingement characteristics of round jets which, for the most part, were available in the published literature. Specifically, the free jet entrainment data of Kleis and Foss (Reference 2) and the geometric and kinematic properties of free and impinging round jets established by Donaldson and Snedeker (Reference 3) were used extensively. The data of Donaldson and Snedeker were also used to determine analytical expressions for wall jet entrainment.

A key element in the modelling of the ground surface flow field below a hovering V/STOL aircraft is the local distribution of radial momentum flux about the individual jet impingement points on the ground plane. This distribution is largely dependent on the exit shape of the jet nozzle (for low values of H/D) and the local impingement angle of the jet on the ground plane. The data of Donaldson and Snedeker in Figure 3 show that for a round turbulent jet this distribution is sensitive to the local jet impingement angle and relatively insensitive to the ratio of height above ground to nozzle exit diameter (H/D). These distributions of momentum flux together with the magnitudes of the total momentum fluxes emanating from the nozzle exits establish the location and (momentum) strength of the fountains in the flow field below the aircraft.

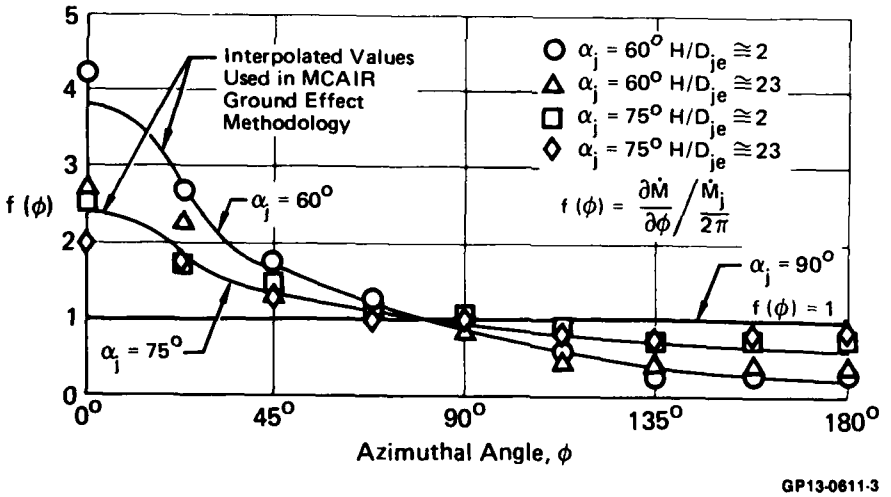

Fig. 3 Azimuthal Distribution of Wall Jet Radial Momentum Flux for an Impinging Round Jet
From Reference 3

Another significant geometric consideration is the number and arrangement of the propulsive lift jets in the aircraft lift system. Figure 4 shows a generic idealized multiple lift jet arrangement spaced symmetrically about a hypothetical center of gravity. The octagonal central area circumscribed by the lines connecting the eight lift jet centerlines represents an idealized inner region. All area outside of this region extending to infinity constitutes the idealized outer region. The interaction lines of the wall jets resulting from the ground impingement of the lift jet pairs are shown as the dashed lines in Figure 4. These lines indicate the ideal locations of the wall jet stagnation lines which form in both the inner and outer regions. A stagnation line pattern as

shown in Figure 4 would result from the ideal vertical impingement of round jets producing a $f(\phi) = 1$ distribution of wall jet radial momentum flux (see Figure 3). Figure 5 shows the maximum available fountain force as a function of the number of lift jets in an ideal multiple lift jet system. The lower curve in Figure 5 shows the maximum fountain force F_F available from the inner region only,

$$F_F(\text{inner region}) = (\tfrac{1}{2} - \tfrac{1}{N})\, F_T \qquad (1)$$

where F_T is the total lift system thrust and N is the number of jets in the idealized lift system.

It should be noted that a two jet lift system has no inner region, by definition, and, therefore, all fountain force obtained from a two jet fountain is outer region force. The result shown in equation (1) is predicated on the assumption that all lift jet momentum flux that enters a volume below the aircraft whose planform is the inner region eventually is turned vertically and imparts this vertical momentum to the airframe. The upper curve in Figure 5 indicates the total available ideal fountain force including contributions from both the inner and outer regions. The lift jet momentum flux entering the outer region volume is assumed to impinge on the airframe with an ideal sidewash angle of incidence resulting from the turning of the flow in an upward direction at the stagnation lines. Performing an integration of the vertical component of the outer region momentum flux and adding the result to the force from the inner region,

$$F_F(\text{outer region + inner region}) = (\tfrac{1}{2} - \tfrac{1}{N} + \tfrac{1}{\pi})\, F_T \qquad (2)$$

The potential benefits to be gained from additional fountain force resulting from the use of increasing numbers of jets up to six or even eight is obvious, but it must be realized that actual fountain forces produced on the airframe undersurface are much less than the ideal values shown in Figure 5 by a factor of one third to one quarter based on the ideal inner plus outer region values. (The reasons for this are discussed later in this paper.) Limited data on experimentally measured values of fountain force are shown in Figure 5 for two and four jet configurations. These data were recorded on experimental configurations for which jet entrainment induced suckdown effects were minimal.

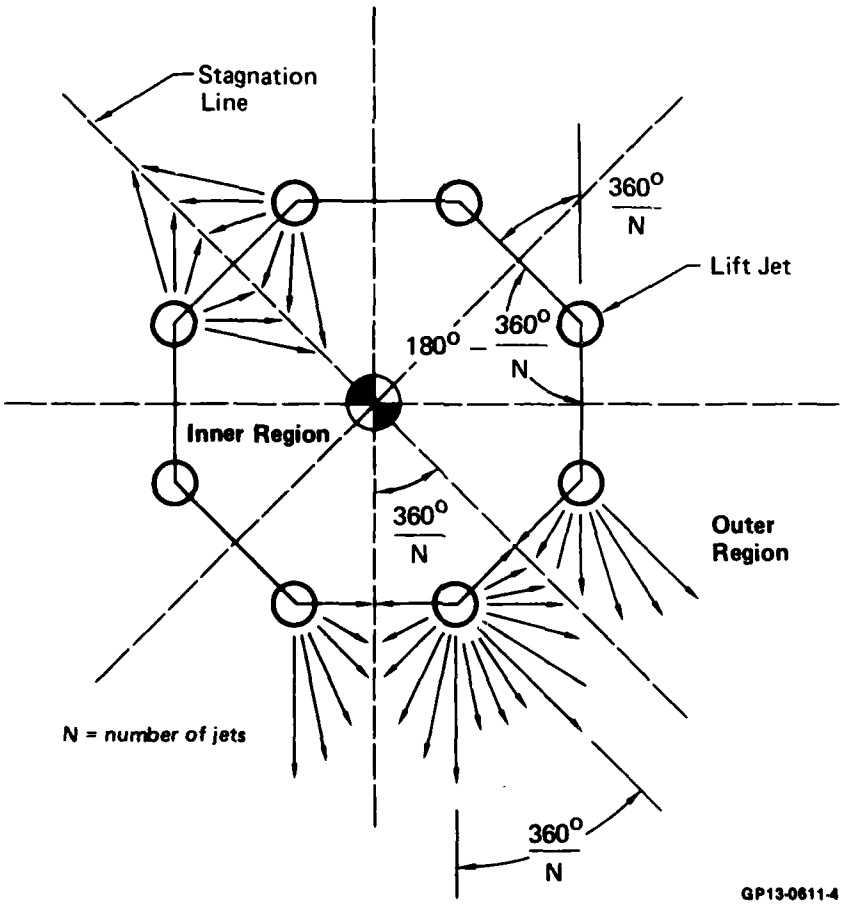

Fig. 4 Idealized 8-Jet Lift System Impinging on a Ground Plane

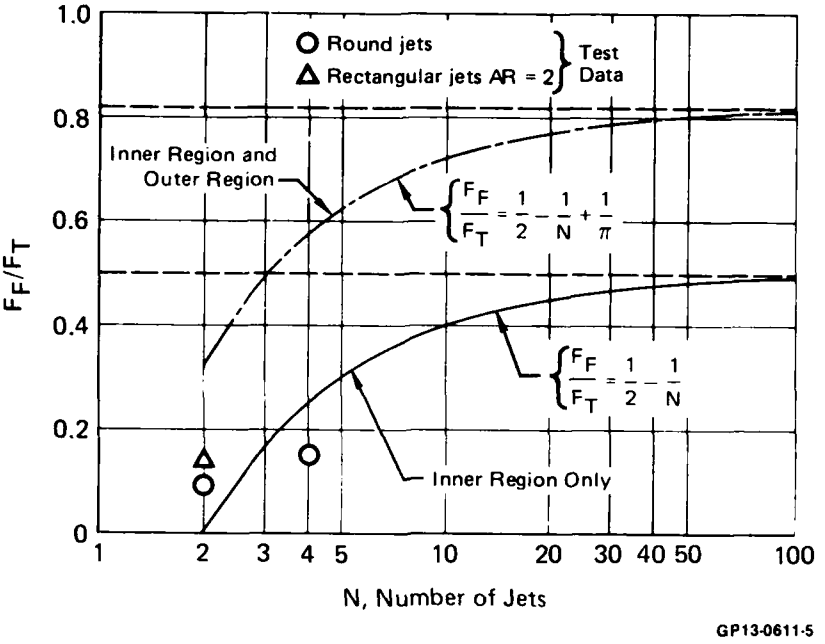

Fig. 5 Variation of Maximum Ideal Fountain Force with Number of Round Jets

Recent interest in certain VTOL and STOL propulsive lift systems, such as thrust augmenting ejector systems and other concepts employing non-circular nozzles, has revealed a need for the understanding of the basic free jet and jet impingement characteristics of jets emanating from rectangular exit area nozzles. Consequently, two experimental programs (References 4 and 5) were undertaken to investigate the wall jet characteristics produced by the impingement on a ground plane of jets emanating from low and high aspect ratio rectangular exit area nozzles. The primary purpose of these studies was to experimentally determine the azimuthal distributions of wall jet radial momentum flux about the impingement points of these jets for rectangular nozzles with exit area aspect ratios (L/D) of one, two, three, four, six and eight for both vertical and oblique impingement.

The high aspect ratio rectangular nozzle data ($4 \leq L/D \leq 8$) obtained in the first investigation (for low nozzle pressure ratios only) (Reference 4) indicated that, unlike axisymmetric jets, the wall jet radial momentum flux distributions for vertical impingement are highly directional, even for the aspect ratio four (L/D = 4) nozzle at heights above ground as great as sixteen nozzle widths. Consequently, the second study (Reference 5) was undertaken to extend the data base to include rectangular nozzles with exit area aspect ratios of one, two and three. Wall jet velocity profiles were obtained for the three low aspect ratio nozzles as a function of jet impingement angle, nozzle exit height above ground and nozzle pressure ratio which included choked and under-expanded nozzle exit flow conditions. The ground flow field computer program originally developed in Reference 1 was updated to include the impingement data obtained for both high and low aspect ratio rectangular nozzles.

Figure 6 presents a qualitative view of the wall jet radial momentum flux distributions associated with impinging jets issuing from both axisymmetric and rectangular nozzles. The axisymmetric nozzle produces a uniform distribution in vertical impingement $f(\phi)$ = const. ($\alpha_j = 90°$). In oblique impingement, a peak occurs in the distribution in the $\phi = 0°$ direction with the relative magnitude of the peak increasing with decreasing impingement angle. The rectangular nozzles in vertical impingement, on the other hand, produce a prominent peak of the momentum flux distribution in a direction normal to the long sides of the nozzle exit, as indicated in Figure 6 by the L/D = 4 nozzle at $\alpha_j = 90°$. The primary effect of oblique impingement of the rectangular nozzle in pitch (rotation about the nozzle exit minor axis) is to shift the peak to an azimuthal location approximately coincident with the magnitude of the impingement angle. The L/D = 1 (square) nozzle exhibits characteristics similar to that of the axisymmetric nozzle at low pressure ratios. At high pressure ratios, however, the square nozzle exhibits characteristics common to both axisymmetric and rectangular nozzles with a primary peak occurring at $\phi = 0°$, as with axisymmetric nozzles, and a secondary peak occurring at an azimuthal angle approximately coincident with the jet impingement angle, as exhibited by rectangular nozzles.

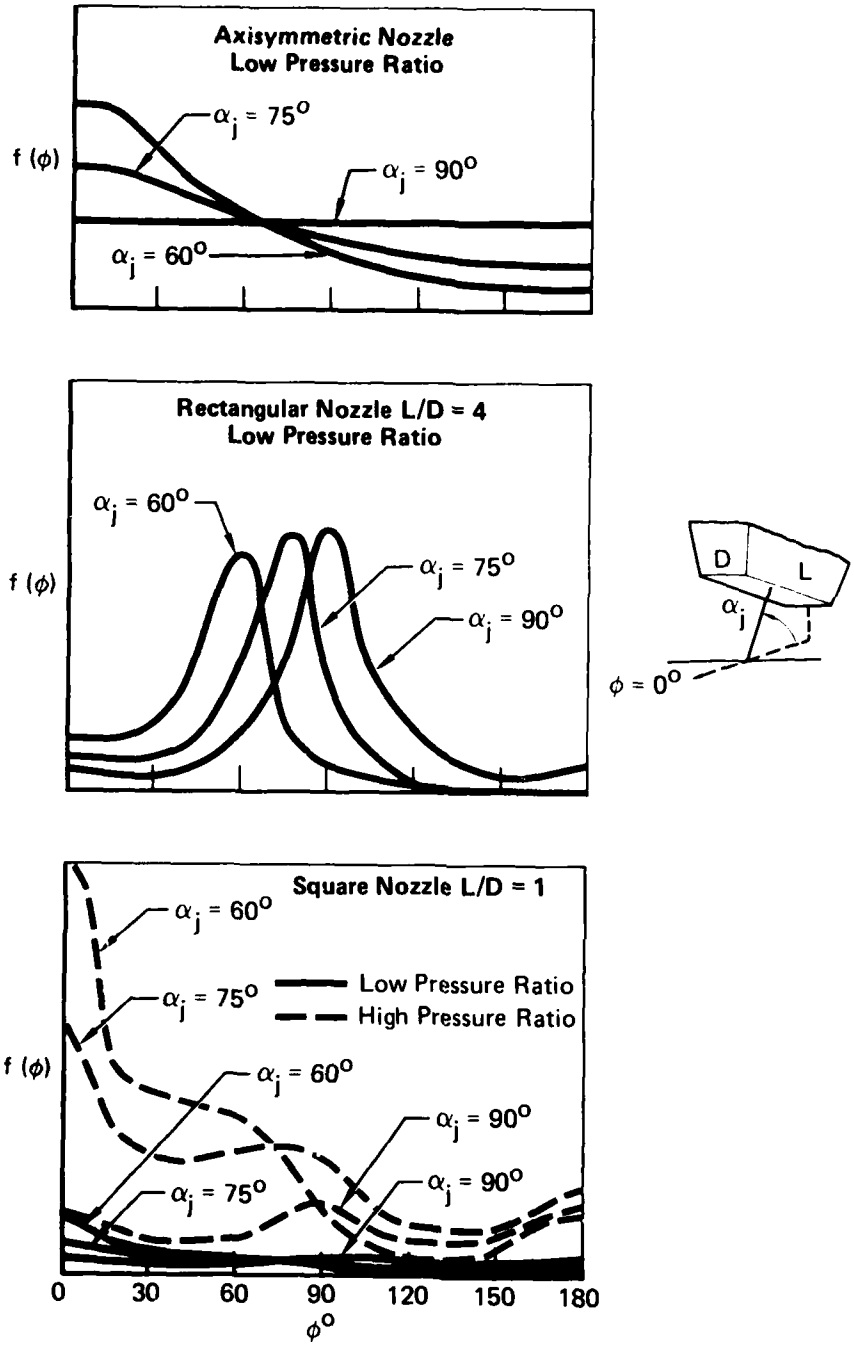

Fig. 6 Jet Impingement Radial Momentum Flux Distributions

The azimuthal distributions of wall jet radial momentum flux were determined by hot film anemometer surveys for each of the six single rectangular nozzle configurations and are presented in entirety in References 4 and 5. This work is also summarized in Reference 6. Selected results are presented herein for an aspect ratio two nozzle for vertical impingement (Figure 7) and for oblique impingement in pitch (Figure 8) (rotation about the nozzle exit minor axis). The abscissa on each graph is the integral of the wall jet velocity squared, multiplied by the radial distance, R, from the jet impingement point to the point of measurement and is representative of the magnitude of the wall jet radial momentum flux. The radial distance, R, is included in order to account for the increase in area with radial distance. This allows comparison of data recorded at different radial stations. In vertical impingement, the wall jet radial momentum flux was measured over one quarter of the periphery of the impingement region from $\phi = 0°$, corresponding to a direction perpendicular to the nozzle minor axis, to $\phi = 90°$ corresponding to a direction perpendicular to the nozzle exit major axis. In oblique impingement the wall jet radial momentum flux was measured over one half of the periphery of the impingement region from $\phi = 0°$ (corresponding to the direction of the horizontal component of the free jet mean flow) to $\phi = 180°$.

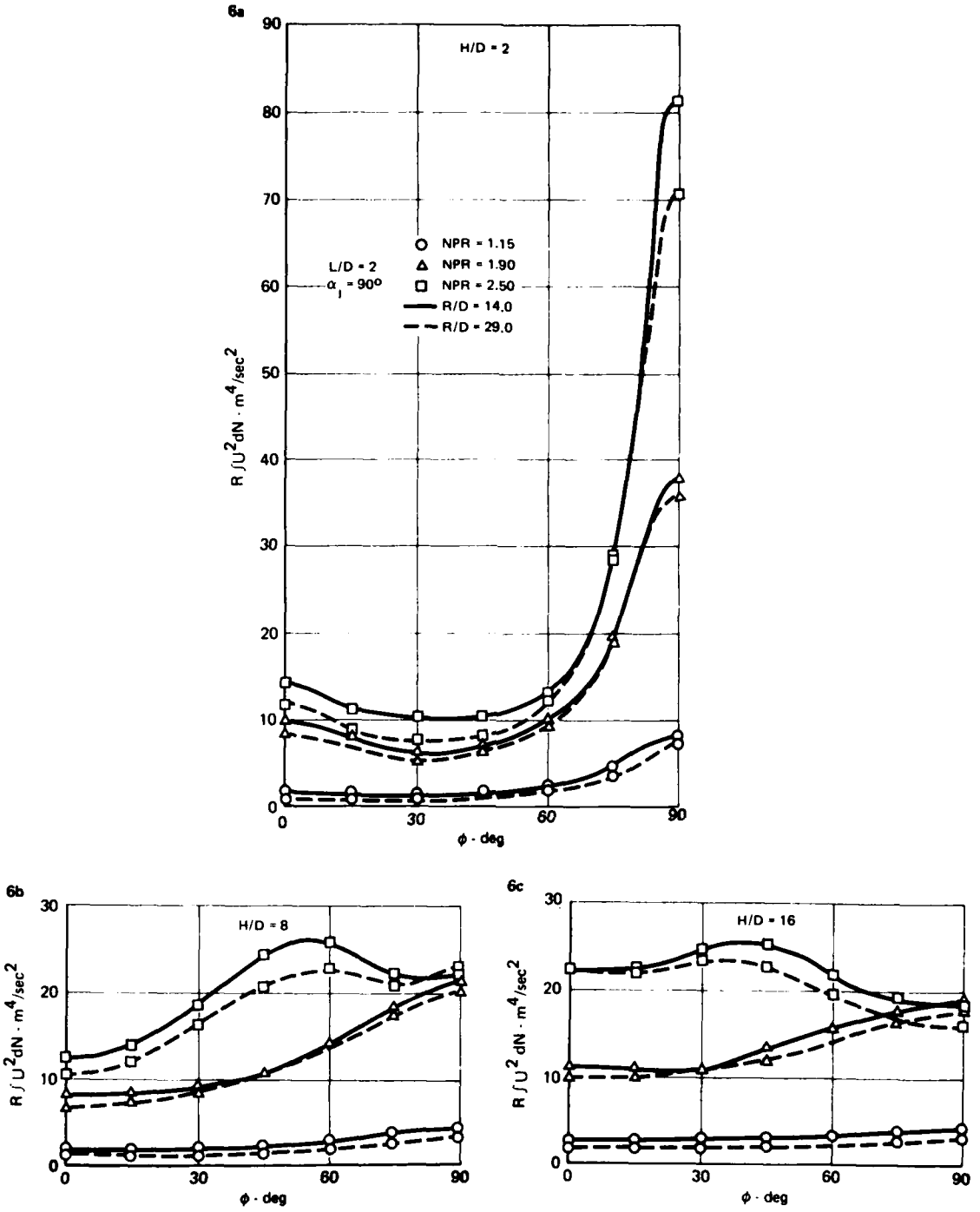

Fig. 7 Azimuthal Distribution of Wall Jet Radial Momentum Flux
L/D = 2 Nozzle Vertical Impingement

In vertical impingement, the momentum flux distributions for the higher aspect ratio nozzles ($2 \leq L/D \leq 8$) all exhibited similar characteristics at low nozzle pressure ratios with a peak at $\phi = 90°$ (perpendicular to the nozzle exit major axis) as exemplified by the aspect ratio two nozzle results shown in Figure 7. However, at NPR = 2.50, although the aspect ratio two (and three) nozzles displayed the characteristic peak at $\phi = 90°$ for H/D = 2; at H/D = 8 the momentum flux distribution peak became broader and shifted to approximately $\phi = 60°$; and at H/D = 16, the peak shifted to approximately $\phi = 45°$. A minor peak is exhibited at $\phi = 0°$ (perpendicular to the nozzle exit minor axis) for the higher pressure ratios at H/D = 2, but vanishes at H/D = 8.

For oblique impingement in pitch, at low nozzle pressure ratios, the occurrence of a peak in the distribution of momentum flux at an azimuthal angle approximately coincident with the magnitude of the pitch angle is characteristic of rectangular nozzles (L/D > 1) and is exhibited by the L/D = 2 nozzle in Figure 8. The data in Figure 8 for the aspect ratio two nozzle indicate a broadening and a shift of the location of the momentum flux peak toward $\phi = 0°$ at the higher H/Ds for a nozzle pressure ratio of 2.50. Similar behavior was observed for the aspect ratio three nozzle. These data indicate the sensitivity of the jet impingement flow field to nozzle exit area shape and, additionally, nozzle pressure ratio. Data for oblique impingement in roll (rotation about the nozzle exit major axis) for all nozzles may be found in References 4 and 5.

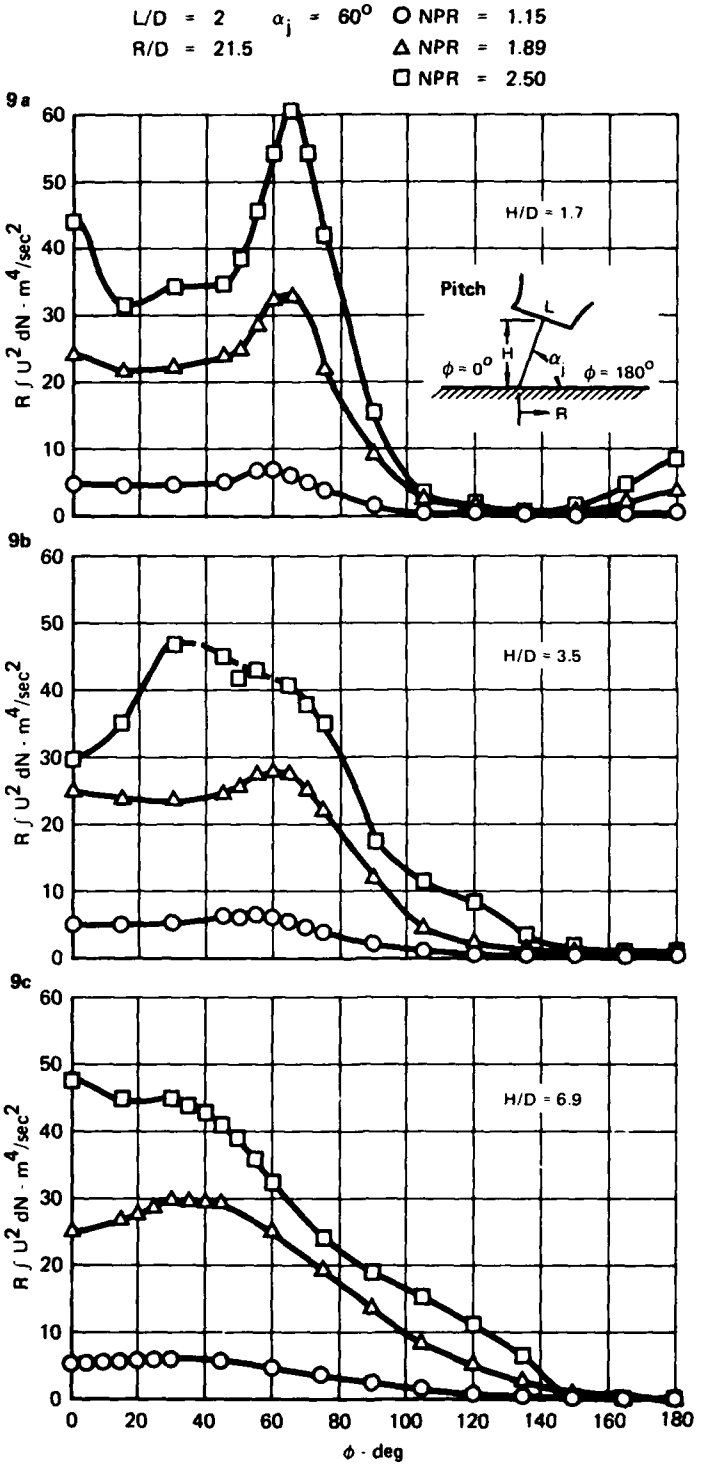

Fig. 8 Azimuthal Distribution of Wall Jet Radial Momentum Flux

L/D = 2 Nozzle Oblique Impingement - Pitch

COMPUTATION OF STAGNATION LINES AND FOUNTAIN UPWASH INCLINATION

In Reference 1, an analytical model was developed for the computation of wall jet stagnation lines formed between any pair of impinging jets for completely arbitrary conditions. Required input for these computations is simply the jet thrust scaled azimuthal distributions of radial momentum flux (as given in Figures 3, 7 or 8 for example). The model developed in Reference 1 is termed the "Momentum Flux Method".

The Momentum Flux Method establishes the location of the stagnation line between two jet impingement points by balancing the total momentum flux in the wall jets in a direction normal to the stagnation line in the ground plane. As a result of the requirement of a total momentum flux balance (normal to the stagnation line), the upward direction of the fountain in a vertical plane normal to stagnation line must itself be vertical, although a non-vertical sidewash component is allowed.

Green, Reference 7, has modified the criterion for determination of the location of the stagnation line by requiring a balance of wall jet momentum flux per unit area of the wall jet at the stagnation line. The balance of momentum flux per unit area is imposed in a direction normal to the stagnation line in the ground plane. Imposition of this criterion results in an imbalance of total wall jet momentum flux at the stagnation line in a direction normal to the stagnation line in the ground plane and, also, allows a non-vertical trajectory of the fountain upwash flow in a vertical plane normal to the stagnation line. This model for the determination of the stagnation line location is denoted as the "Momentum Flux Density Method". The basic equations for the "Momentum Flux Method" (MFM) and the "Momentum Flux Density Method" (MFDM) models are compared in Table 1 (see Figure 9 for nomenclature definition).

Computation of wall jet stagnation lines using the "Momentum Flux Method" and the "Momentum Flux Density Method" were recently compared with actual stagnation line locations obtained experimentally through flow visualization techniques, and the results were presented in Reference 5. Based on these and other comparisons, the "Momentum Flux

Table 1. Two Methods for the Computation of Stagnation Line Location

Momentum Flux Method (MFM)	Momentum Flux Density Method (MFDM)
Stagnation Line Slope:	
$\tan\theta = \dfrac{\beta \sin\phi'_2}{1+\beta\cos\phi'_2}$	$\tan\theta = \dfrac{\beta \sin\phi'_2}{1+\beta\cos\phi'_2}$
where	where
$\beta = \dfrac{R_1}{S'}\sqrt{\dfrac{\gamma_2 f_2(\phi_2)\dot{M}_{je2}/\gamma_1 f_1(\phi_1)\dot{M}_{je1}}{R_2/R_1}} + \dfrac{R_2}{S'}$	$\beta = \dfrac{R_1}{S'}\left[\dfrac{\gamma_2 f_2(\phi_2)\dot{M}_{je2}/\gamma_1 f_1(\phi_1)\dot{M}_{je1}}{R_2^2/R_1^2}\right] + \dfrac{R_2}{S'}$
On the Line Joining the Jet Impingement Points:	
$\dfrac{R_2}{R_1} = \dfrac{\dot{M}_{je2} f_2(\phi_2)\gamma_2}{\dot{M}_{je1} f_1(\phi_1)\gamma_1}$	$\dfrac{R_2}{R_1} = \sqrt{\dfrac{\dot{M}_{je2} f_2(\phi_2)\gamma_2}{\dot{M}_{je1} f_1(\phi_1)\gamma_1}}$

GP13-0611-17

Density Method" was found to give a more accurate prediction of wall jet stagnation line location. Utilizing the nomenclature of Reference 1 as shown in Figure 9, the equations for the slope of the stagnation line in the ground plane for the MFDM is the following:

$$\tan\theta = \frac{\beta \sin\phi'_2}{1+\beta\cos\phi'_2} \qquad (3)$$

where

$$\beta = \frac{R_1}{S'}\left[\frac{\gamma_2 f_2(\phi_2)\dot{M}_{je_2}/\gamma_1 f_1(\phi_1)\dot{M}_{je_1}}{R_2^2/R_1^2}\right] + \frac{R_2}{S'} \qquad (4)$$

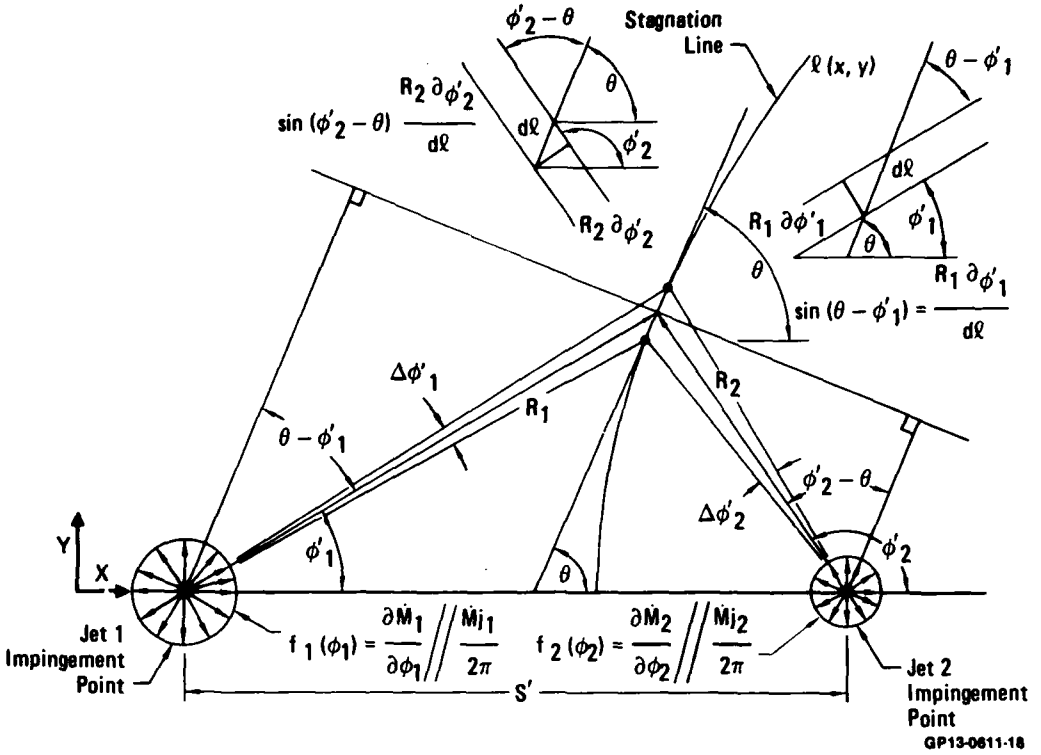

Fig. 9 Wall Jet Interaction Geometry

and, at the line joining the jet impingement points in the ground plane,

$$\frac{R_2}{R_1} = \sqrt{\frac{\dot{M}_{je_2} f_2(\phi_2)\gamma_2}{\dot{M}_{je_1} f_1(\phi_1)\gamma_1}} \qquad (5)$$

Through the use of a control volume located on the stagnation line and a total momentum flux balance in a direction normal to the stagnation line in the ground plane, a relation between the momentum flux quantities in the two interacting wall jets and the horizontal component of momentum flux exiting the control vclume in the fountain upwash is obtained (for negligible sidewash):

$$\frac{\gamma_1 f_1 \dot{M}_{je_1}}{2\pi} \sin(\theta - \phi'_1)\, \partial\phi'_1 - \frac{\gamma_2 f_2 \dot{M}_{je_2}}{2\pi} \sin(\phi'_2 - \theta)\, \partial\phi'_2 + \rho V_f \cos\omega [U_{R_1} R_1 \partial\phi'_1 + U_{R_2} R_2 \partial\phi'_2] h = 0 \qquad (6)$$

where V_f is the fountain upwash velocity, ω is the fountain inclination angle and h is the wall jet height. Assuming a total momentum flux magnitude conservation factor λ_M in the fountain formation region:

$$\rho V_f [U_{R_1} R_1 \partial\phi'_1 + U_{R_2} R_2 \partial\phi'_2] h = \lambda_M [\gamma_1 f_1 \dot{M}_{je_1} \frac{\partial\phi'_1}{2\pi} + \gamma_2 f_2 \dot{M}_{je_2} \frac{\partial\phi'_2}{2\pi}] \qquad (7)$$

Substituting equation (7) in equation (6) and solving for $\lambda_{\dot{M}} \cos \omega$ the following general result is obtained for any location on the stagnation line:

$$\lambda_{\dot{M}} \cos \omega = \frac{\frac{\gamma_2 f_2 \dot{M}_{je_2}}{R_2} \sin^2 (\phi'_2 - \theta)}{\frac{\gamma_2 f_2 \dot{M}_{je_2}}{R_2} \sin (\phi'_2 - \theta)} \qquad (8)$$

$$- \frac{\frac{\gamma_1 f_1 \dot{M}_{je_1}}{R_1} \sin^2 (\theta - \phi'_1)}{+ \frac{\gamma_1 f_1 \dot{M}_{je_1}}{R_1} \sin (\theta - \phi'_1)}$$

For the special case of two round jets impinging vertically, on the line joining the jet impingement points,

$$\lambda_{\dot{M}} \cos \omega = \frac{1 - \sqrt{\dot{M}_{je_1}/\dot{M}_{je_2}}}{1 + \sqrt{\dot{M}_{je_1}/\dot{M}_{je_2}}} \qquad (9)$$

Figure 10 demonstrates the relation between ω and the impinging jet pair momentum flux ratio as obtained from equation (9) with $\lambda_{\dot{M}}$ as a parameter. The validity of this model of fountain upwash flow inclination was investigated with experimental data from the test program described in Reference 8 and is summarized briefly in the paragraphs following.

An analytical model for the fountain sidewash inclination was presented in Reference 1. The result is

$$\tan \kappa = \frac{2}{\cot (\theta - \phi'_1) + \cot (\phi'_2 - \theta)} \qquad (10)$$

where κ is the fountain sidewash inclination angle and the other symbols are defined in Figure 9.

FOUNTAIN UPWASH FORMATION AND DEVELOPMENT

It has been observed consistently that fountain forces are substantially smaller than conservatively estimated values based on lift jet thrust and momentum conservation. This is demonstrated quantitatively by the experimental data shown in Figure 5. For this reason, a thorough investigation of the fountain upwash formation and development process was conducted by MCAIR for fountains formed by two impinging round jets for a wide range of parametric test conditions. These results are reported in entirety in Reference 8. An important result of this investigation was the quantification of a fountain formation upwash normal momentum flux recovery coefficient, $\lambda_{\dot{M}N}$.

The fountain upwash normal momentum flux recovery factor ($\lambda_{\dot{M}N}$) is defined as the ratio of the fountain normal momentum flux exiting the fountain formation region to the total wall jet radial momentum flux entering the fountain formation region (see Figure 1). In this investigation, the flow through the fountain formation region was incompressible (ρ = constant), and the fountain formation region was assumed to be small so that radial area change effects were negligible (dR ≅ 0), thus

$$\lambda_{\dot{M}N} = \frac{\left(\int_{X_o}^{X_f} V_N^2 \, dX\right)_f}{\left(\int_0^{N_1} U_R^2 \, dN\right)_{wj(1+2)}} \qquad (11)$$

where $\left(\int_{X_o}^{X_f} V_N^2 dX\right)_f$ is representative of the fountain normal momentum flux at Z/D = 1.0 and $\left(\int_0^{N_1} U_R^2 dN\right)_{wj(1+2)}$ is representative of the sum of the local wall jet radial momentum

flux produced by the impinging jets in the system. A typical set of wall jet and fountain upwash flow mean velocity surveys for one test condition are shown in Figure 11. The surveys were obtained with a hot film anemometer. Since the local velocity ratios, V_{min}/V_{max}, for the fountain velocity profiles were considerably higher than those determined for the wall jet velocity profiles, the following procedure was established to define the limits of integration and to lend consistency to the calculation process.

The upper limits of integration of the wall jet velocity profiles were established for each case by the normal distance, N_1, corresponding to the larger velocity ratio, U_{min}/U_{max}, of the two wall jet velocity profiles. The wall jet velocity and velocity squared profiles for jet 1 and jet 2 were then integrated and summed to yield $(\int_0^{N_1} U_R\, dN)_{wj}$ and $(\int_0^{N_1} U_R^2 dN)_{wj}$. Now, since the fountain formation region is assumed to be small, with little exposed jet area available for mass entrainment, conservation of mass was assumed throughout the fountain formation region to yield

$$(\int_{X_o}^{X_f} V_N\, dX)_{\substack{f \\ Z/D=1}} = (\int_0^{N_1} U_R\, dN)_{wj(1+2)} \qquad (12)$$

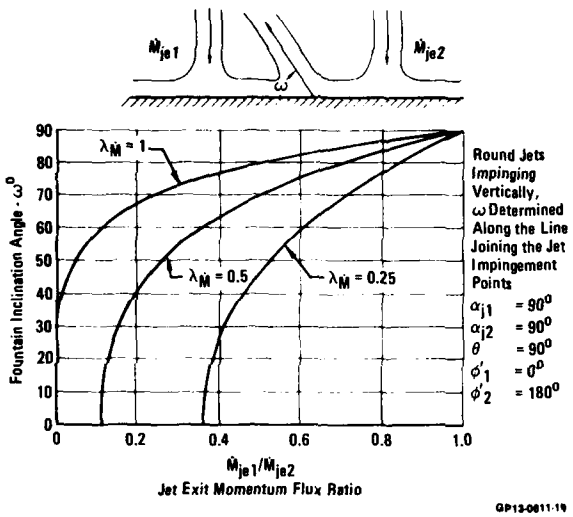

Fig. 10 Fountain Inclination Angle

Thus, the initial and final limits of integration (X_o, X_f) for the fountain velocity and velocity squared profiles were determined such that equation (12) was satisfied.

Figure 12 presents the fountain normal momentum flux recovery factor, $\lambda_{\dot{M}N}$ as a function of the jet exit momentum flux ratio, $\dot{M}je_{LOW}/\dot{M}je_{HIGH}$, for the data of Reference 8. The data indicate a general decrease in the fountain momentum flux recovery with a decrease in the nozzle thrust bias (increased $\dot{M}je_{LOW}/\dot{M}je_{HIGH}$). In addition, a slight increase in $\lambda_{\dot{M}N}$ is shown in the presence of a nozzle exit plane plate over that found without the plate. A polynomial curve-fit (also shown in Figure 12) was determined for the data and is given approximately by the following expression:

$$\lambda_{\dot{M}N} = 1.0 - 1.5\,(\frac{\dot{M}je_{LOW}}{\dot{M}je_{HIGH}}) + 1.5\,(\frac{\dot{M}je_{LOW}}{\dot{M}je_{HIGH}})^2 - 0.5\,(\frac{\dot{M}je_{LOW}}{\dot{M}je_{HIGH}})^3 \qquad (13)$$

Fig. 11(a) Wall Jet Velocity Profiles

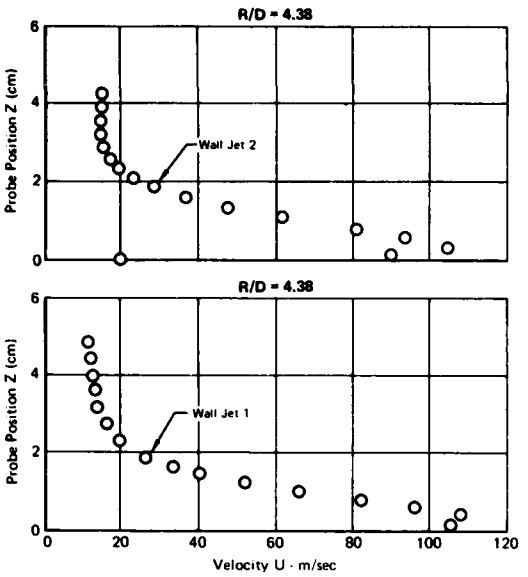

Fig. 11(b) Fountain Velocity Profiles

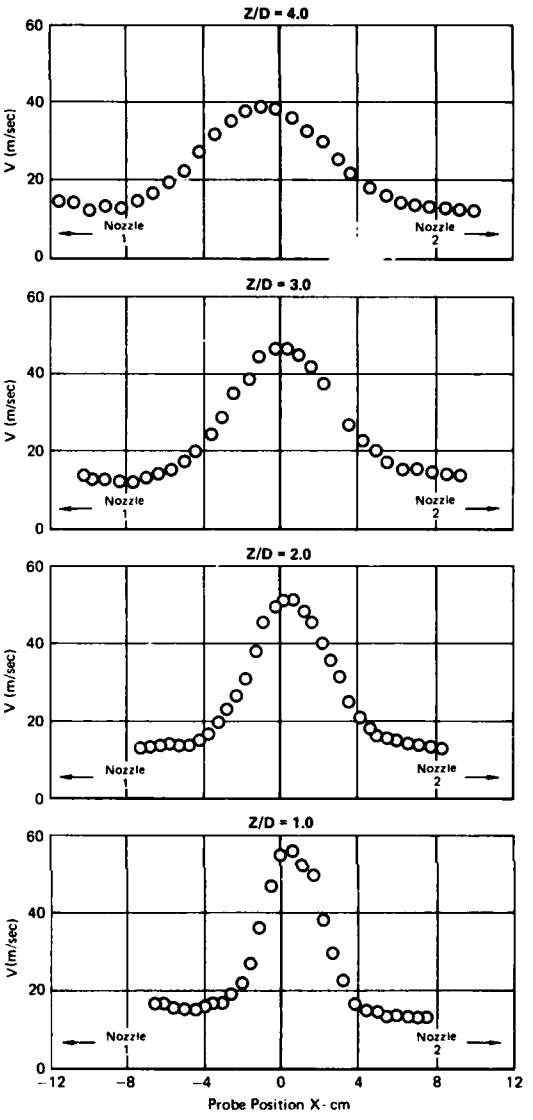

Fig. 11 Symmetrical Two Jet Fountain

$H/D = 5.0 \quad S/D = 12.80 \quad NPR = 1.89 \quad \alpha_{j1} = \alpha_{j2} = 90°$

The behavior of the normal momentum flux recovery factor with the jet exit momentum flux ratio is not surprising. The strongest wall jet interaction and associated loss of mean flow energy or momentum occurs with two equal strength impinging jets. As one of the impinging jets becomes weaker (increased thrust bias), the wall jet interaction becomes weaker. For a high thrust bias, the weaker wall jet simply tends to deflect the stronger jet with an attendant reduction in mixing and loss of mean flow energy.

Fountain geometric spreading characteristics and fountain mass flow were determined from the fountain upwash velocity profile data for all of the cases investigated in Reference 8. For the data of Figure 11, the fountain spreading characteristics and mass flow are shown in Figure 13.

Fountain upwash trajectories were also determined for all of the cases investigated. The trajectories were defined as the loci of the maximum velocity points as determined from the fountain upwash velocity profiles. The fountain upwash inclination, ω, was determined as the angle between the ground plane and a straight line connecting the fountain base and the fountain upwash trajectory at Z/D = 3. The fountain upwash inclination for the data of Reference 8, is plotted as the function of the jet exit momentum flux ratio ($M_{je_{LOW}}/M_{je_{HIGH}}$) for the fountain inclination at Z/D = 3 in Figure 14. Also shown in the figure are the theoretical values of the fountain inclination, ω_{TH}, based on equation (9). Figure 14 indicates that for a fountain inclination determined at Z/D = 3, a momentum flux recovery factor, $\lambda_{\dot{M}}$, of approximately 0.65 results in a reasonable fit to the experimental data.

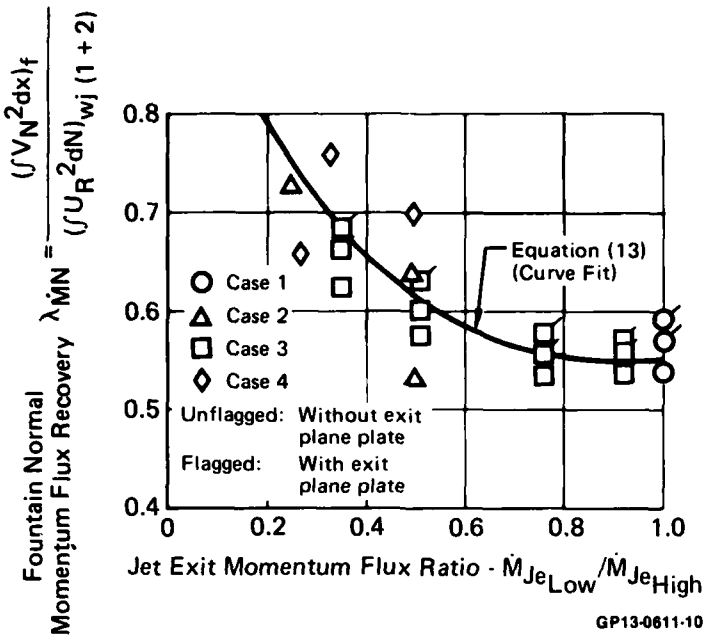

Fig. 12 Fountain Normal Momentum Flux Recovery Based on Conservation of Mass Flux Through the Fountain Formation Region

FOUNTAIN IMPINGEMENT ON THE AIRFRAME

The establishment of the above ground flow field modelling elements, together with recent improvements made to three dimensional panel methods for the determination of jet entrainment induced suckdown, leaves only one empirical element remaining to complete the prediction methodology for a wide range of V/STOL aircraft configurations. This remaining element is the quantification of the amount of momentum flux transferred to the airframe undersurface from the upwash momentum flux in the fountain. This quantity, λ_{fI}, is termed the fountain upwash momentum flux transfer coefficient. λ_{fI} is expected to be strongly dependent on airframe undersurface shape, but only weakly dependent on aircraft height above ground, H/D, when fountain spreading characteristics are accurately accounted for in application of the overall prediction methodology.

To demonstrate the usefulness of the existing methodology, fountain impingement forces were determined and compared with experimental data for simple bodies and planforms for which λ_{fI} was expected to be approximately unity and for which suckdown forces were expected to be insignificant. Results are shown in Figure 15 and are very encouraging. The deviations between the predictions and the data at H/Ds of 1 and under are, most likely, beyond the ability of the prediction methodology due to the basic changes in the flow structure beneath a body at these low H/Ds. That is, distinct regions of free jet flow, jet impingement, wall jets, fountain formation, and fountain upwash most likely do not exist at these conditions. A study is currently underway at MCAIR to determine λ_{fI} for two, three and four jet VTOL aircraft configurations from analytical computations and the net forces measured on the vehicles in static wind tunnel tests.

Fountain impingement forces measured on a swept low wing/ fuselage combination are shown in Figure 16. The data shown here were produced by the impingement of single and multiple radial jets simulating fountain upwash flows produced by the vertical impingement on a ground plane of two and four round jets all with equal thrust. The normal force data shown has been non-dimensionalized on the total thrust of the simulated jet lift system. In the two jet case, the plane of the radial jet was perpendicular to the aircraft longitudinal axis, and in the simulated four jet case, the radial jet planes were mutually orthogonal and aligned parallel to the aircraft longitudinal and lateral axes. The data in Figure 16 show the variation in net fountain force with longitudinal location of the center of the fountain as the fountain impingement region was moved from the forward fuselage to aft of the wing trailing edge. As would be expected, the maximum fountain force results when the lateral fountain legs impinge on the widest portion of the wing. A noticeable drop in fountain force magnitude occurs when the lateral fountain legs are moved aft of the wing trailing edge. These data also indicate the relative magnitudes of two versus four jet fountains. The maximum points on these curves have been plotted in Figure 5 for comparison with the theoretical maximum fountain force. The indicated increase in fountain force with increasing H/D for the two jet fountain is due to variation of fountain induced suckdown which decreases as the aircraft rises above the ground. The comparative decrease in fountain force with H/D produced by the four jet fountain is characteristic of fountains with three or more jets which form a central core of upwash flow.

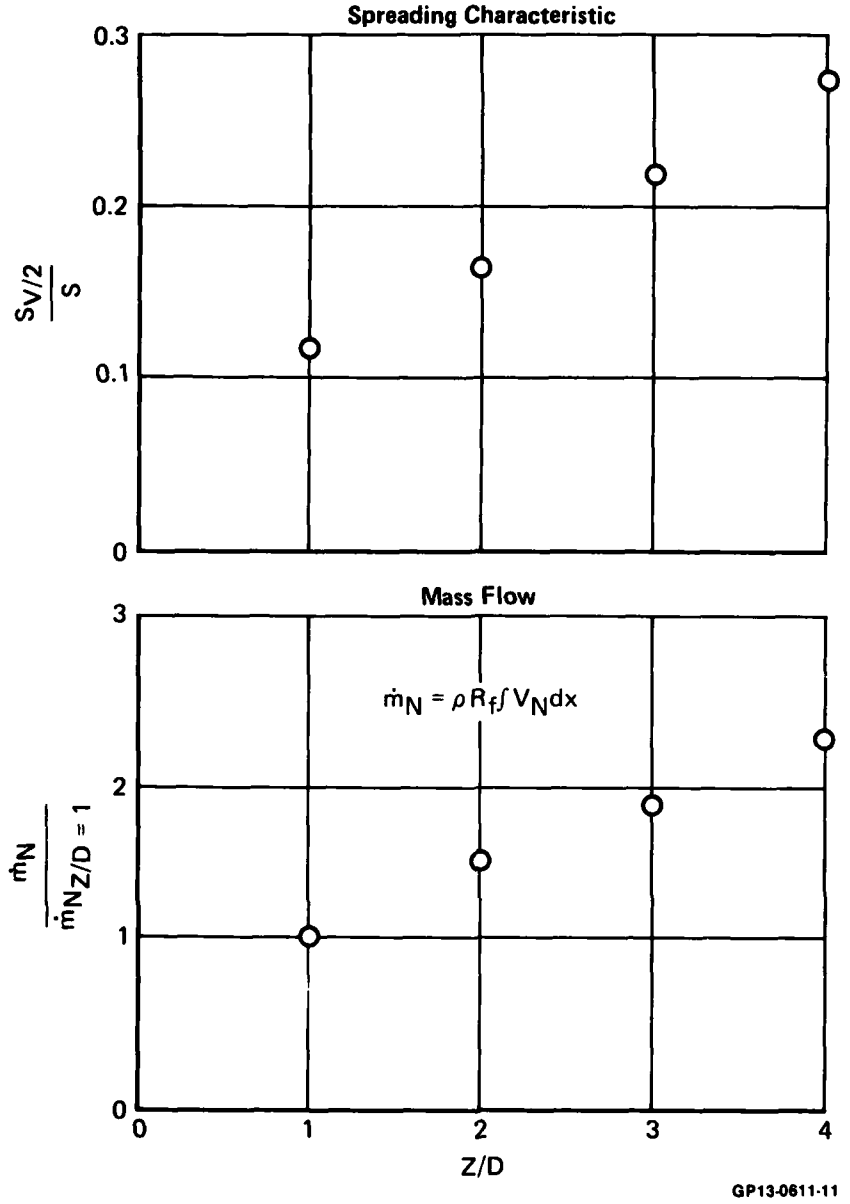

Fig. 13 Fountain Upwash Characteristics

Additional lift may be obtained from fountain upwash impingement through the use of airframe undersurface protuberances in the form of fences or strakes which tend to capture the fountain upwash flow. The confining surfaces should extend through 360° of azimuth in an undersurface plane roughly parallel to the ground plane with the aircraft in the proper pitch and zero roll attitude for vertical translation. Permanently fixed surfaces suitable for high speed flight such as longitudinal axes strakes and/or pods can be utilized for this purpose, but lateral axis devices should be retractable. The confined under-surface area should be large enough to "capture" the central core of a multi-jet fountain including any fountain impact area translation on the airframe undersurface due to nominal aircraft pitch and roll excursions during hover. Sensitivities of lift improvement device related forces and moments to larger excursions in pitch and roll with and without cross winds should be investigated to assure adequate stability and control margins. This currently must be accomplished through wind tunnel testing of powered aircraft models in ground effect. Tests of this nature require accurate modelling of full scale airframe surface geometry including all undersurface contour details and protuberances. It is also desirable that full scale jet exit conditions in terms of nozzle exit geometry, nozzle exit velocity profiles and jet vector and splay angles be simulated carefully in the reduced scale tests.

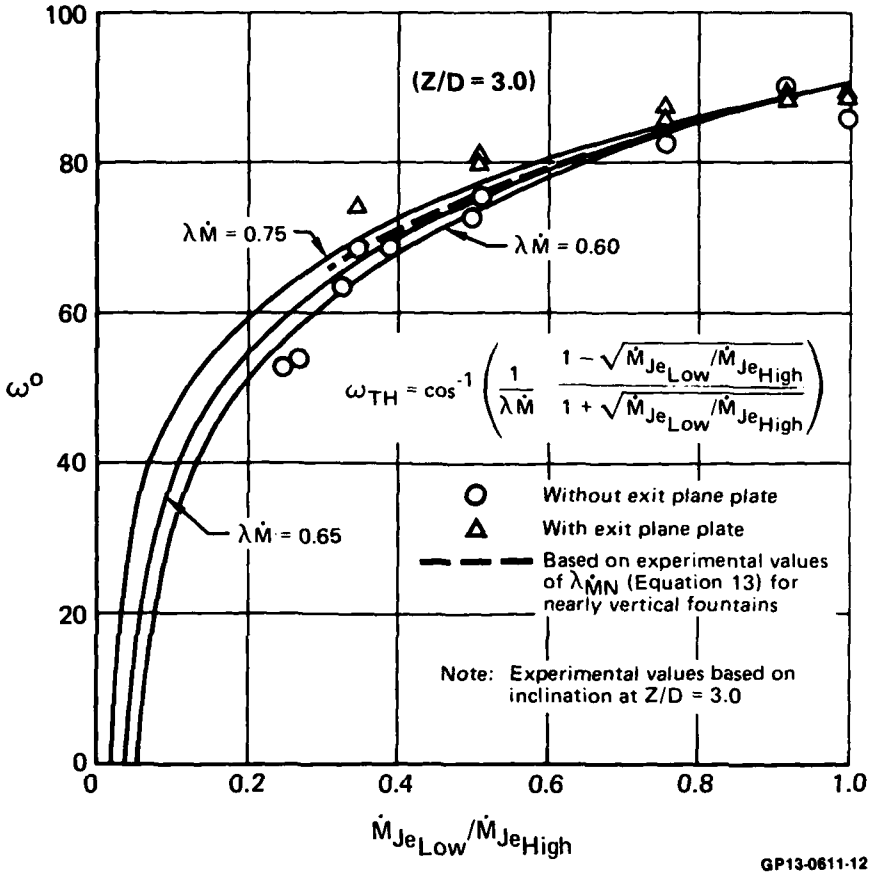

Fig. 14 Two-Jet Fountain Inclination - Vertical Impingement

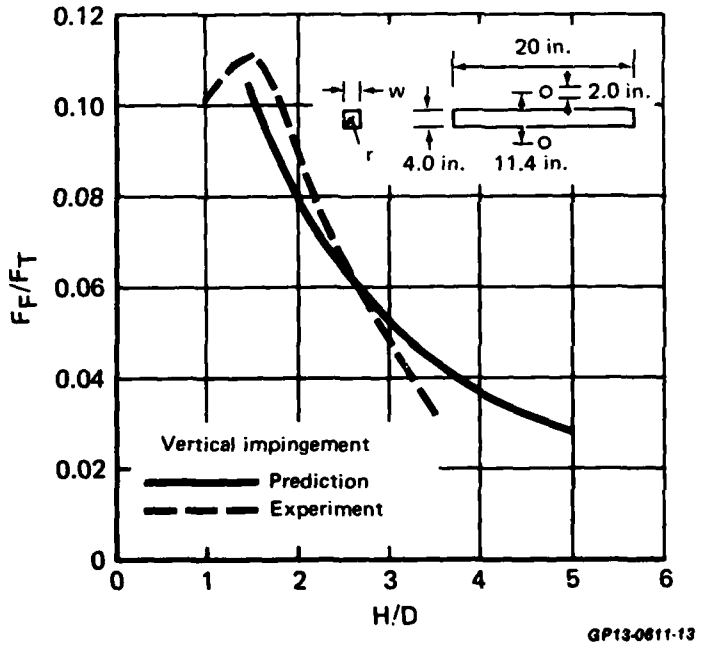

Fig. 15 Accuracy of Two-Jet Fountain Impingement Force Prediction

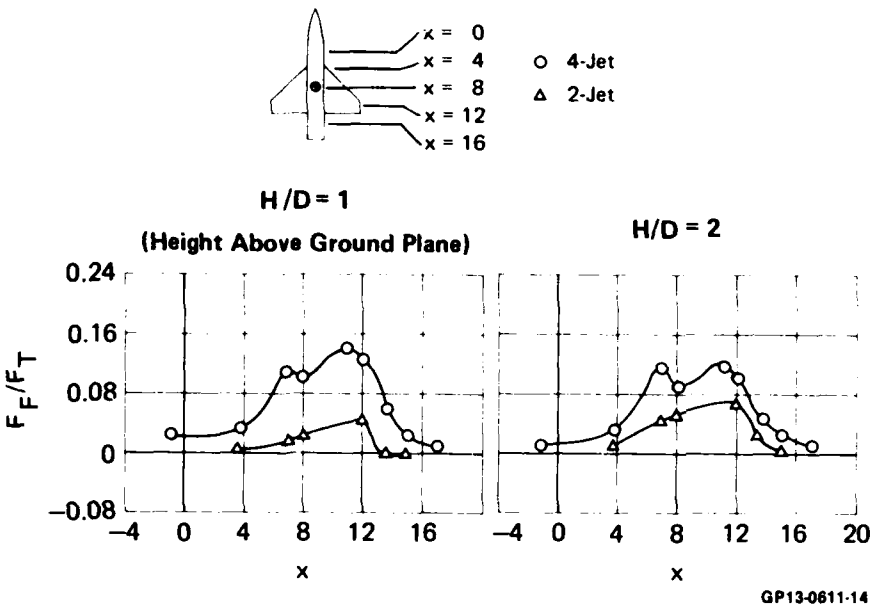

Fig. 16 Fountain Impingement Test
2 and 4-Jet Fountain Impingement on a Fuselage/Wing

The beneficial effect of passive lift improvement devices is demonstrated by the induced lift increment (ΔL) data shown in Figure 17 which was measured in ground effect tests performed with a 15% scale powered model of the AV-8A. The data in Figure 17 indicate the positive lift increments obtained through the addition of gun pod strakes and a forward fence to the baseline vehicle which included gun pods. The data shown were obtained with all four lift jets vectored perpendicularly to the ground plane, however, the nozzles were splayed outward in the nominal splay position (5° forward nozzles, 11.2° aft nozzles). The sensitivity of the fountain forces to changes in nozzle splay angle (or vector) is demonstrated by the data presented in Figure 18 which shows the additional positive lift increment gained by reducing the outward splay angle of all nozzles on the model to 0°. Similar positive lift increments have been measured on models of other aircraft configurations, and in some cases, positive lift improvement can be obtained by simply deflecting existing flaps on the baseline aircraft. Caution must be used to verify that local upwash flowfield changes caused by lift improvement devices do not result in lift engine hot exhaust gas ingestion.

The mechanism for the increase in fountain lift force due to the use of lift improvement devices (LIDs) appears to be a combination of two effects, (1) the confining surfaces form a concavity which is pressurized at some pressure increment less than or equal to the maximum dynamic pressure in the fountain upwash flow, and (2) the concavity or portions thereof act as turning vanes and increase the local turning of the impinged upwash flow beyond what would normally be obtained by undersurface impingement without the lift improvement devices. In the latter case, an ideally designed LID would double the beneficial force increment obtained by ideal fountain impingement on a flat airframe undersurface parallel to the ground. In the former case, the LID acts like the skirt on a typical ground effect machine. Both mechanisms are theoretically very sensitive to H/D in all multi-jet fountain situations, and the data in Figure 17 and 18 and other data tend to confirm this.

CLOSING REMARKS

This paper has emphasized empirical and analytical descriptions of certain key elements of multiple jet viscous flow fields below VTOL aircraft hovering in ground effect. In the actual flowfield below the VTOL vehicle, these flow phenomena occur elliptically, and interactions may occur which can alter the induced effects significantly from the physical descriptions presented herein. Two frequently occurring and strongly influential additional factors are strong cross-winds and aircraft transient motions whose frequency is high enough to preclude quasi-steady analysis based on steady state characteristics. The development of accurate prediction techniques for cross-wind effects on fountain upwash development is extremely complicated, although very important to the identification of both stability and control and exhaust gas ingestion problems.

Predictions of three dimensional (and time dependent) viscous flows of this nature will not be available soon. It is likely that strong dependence on wind tunnel testing will be required for the foreseeable future in the vehicle design and development process. However, as discussed in the previous sections, the configuration analyst can utilize existing data and prediction techniques to guide the configuration synthesis process and to avoid serious problem areas. Reference 9 summarized the current approaches to V/STOL aircraft flowfield prediction in ground effect and included projections on future prediction technique development.

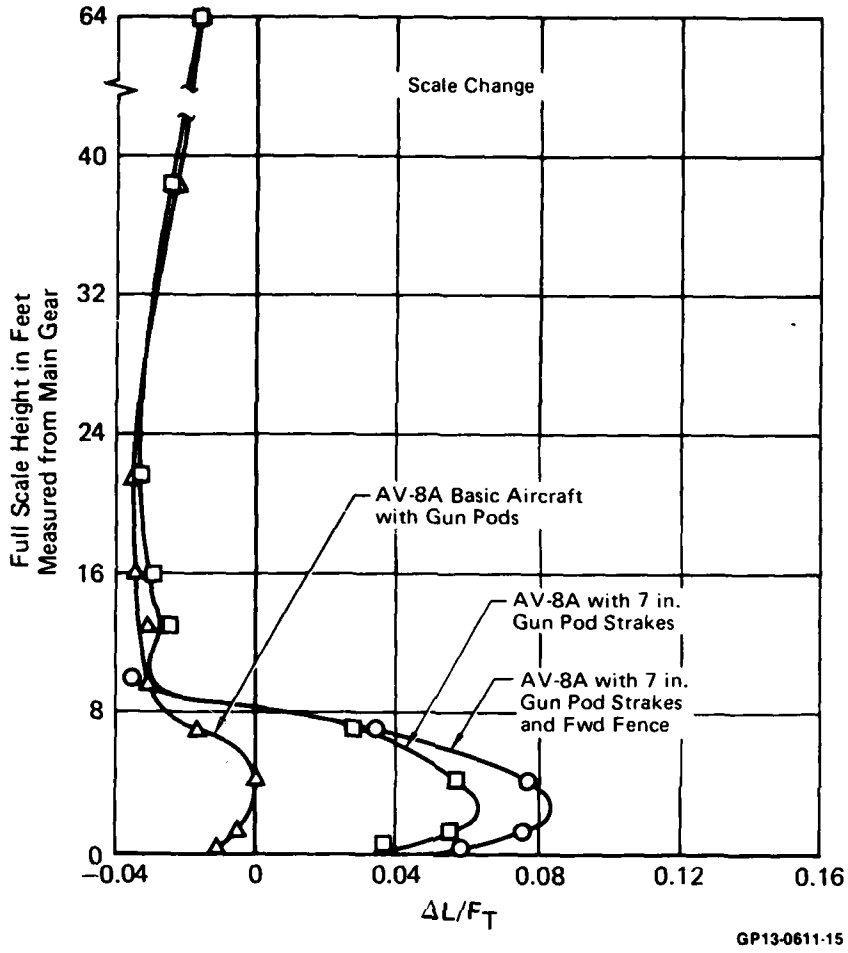

Fig. 17 Fountain Capture with Lift Improvement Devices

In view of the frequent necessity for investigation of V/STOL aircraft jet induced effects through wind tunnel tests of small scale powered models in ground effect, it is productive to comment on the basic requirements of fluid dynamic similarity for the purpose of model testing. The first of these is simply exact, detailed scaling of the small scale model from the full-scale vehicle including all major protuberances, stores, and landing gear. Kinematic scaling of external and internal flows requires that primary velocity ratios (free stream to jet) be correctly simulated, and this would be accounted for automatically if ideal Reynolds number and Mach number simulation were achieved. However, in reality, Reynolds number and Mach number simulation are rarely achieved; in lieu of these, further application of kinematic scaling is desirable. For example, just as airframe undersurface geometry and nozzle exit geometry should be scaled directly, the nozzle exit flow velocity profiles should be representative of what might be expected from the full scale vehicle. This has a direct influence on jet entrainment induced suckdown and fountain formation and development. Kinematic scaling or simulation of jet exit velocity profiles in this manner may be thought of as a pseudo-Reynolds number and internal geometric simulation. Additionally, inlet suction flows should be included in the small scale model simulation in terms of primary velocity ratio based on jet exit and/or free stream velocity. Nozzle exit Mach number simulation should be achieved if nozzle exits are significantly under-expanded as shown dramatically by the data of Figures 7 and 8.

REFERENCES

1. Kotansky, D.R., Durando, N.A., Bristow, D.R., and Saunders, P.W., "Multi Jet Induced Forces and Moments on VTOL Aircraft Hovering In and Out of Ground Effect", Final Technical Report, Naval Air Development Center, NADC Report No. 77-229-30, June 1977.

2. Kleis, S.J., and Foss, J.F., "The Effect of Exit Conditions on the Development of an Axisymmetric Turbulent Free Jet", Third Year Technical Report, NASA Grant NGR 23-004-068, Michigan State University, 15 May 1974.

3. Donaldson, C. du P., and Snedeker, R.S., "A Study of Free Jet Impingement, Part I - Mean Properties of Free and Impinging Jets", Journal of Fluid Mechanics, Vol. 45, Part 2, pp 281-319, 1971.

4. Kotansky, D.R., and Glaze, L.W., "Investigation of Impingement Region and Wall Jets Formed by the Interaction of High Aspect Ratio Lift Jets and a Ground Plane", Report No. NASA CR152174, Ames Research Center, September 1978.

5. Kotansky, D.R., and Glaze, L.W., "Investigation of the Interaction of Lift Jets and a Ground Plane", Report No. NASA CR 152343, Ames Research Center, April 1980.

6. Kotansky, D.R., and Glaze, L.W., "Characteristics of Wall Jets Produced by the Impingement on a Ground Plane of Rectangular Jets of Aspect Ratio One through Eight", AIAA Paper No. 81-0012 presented at the AIAA 19th Aerospace Sciences Meeting, St. Louis, Mo., 12-15 January, 1981.

7. Private Correspondence, K.A. Green, Naval Air Development Center to D.R. Kotansky, 24 August 1978.

8. Kotansky, D.R., and Glaze, L.W., "Investigation of the Effects of Ground Wall Jet Characteristics on Fountain Upwash Flow Formation and Development," Report No. ONR-CR-212-261- IF, Office of Naval Research, June 1980; Also AIAA Paper No. 81-1294, AIAA 14th Fluid and Plasma Dynamics Conference, Palo Alto, Cal., 23-25 June 1981.

9. Kotansky, D.R., and Bower, W.W., "Forces and Moments Produced on a Two-Dimensional Body in a Strong Lift-Jet/Airframe/ Ground Interaction", Presented at the Workshop on "Prediction Methods for Jet V/STOL Propulsion Aerodynamics", Naval Air Systems Command, Arlington, Virginia, 28-31 July 1975, Volume 1, pp. 288-303.

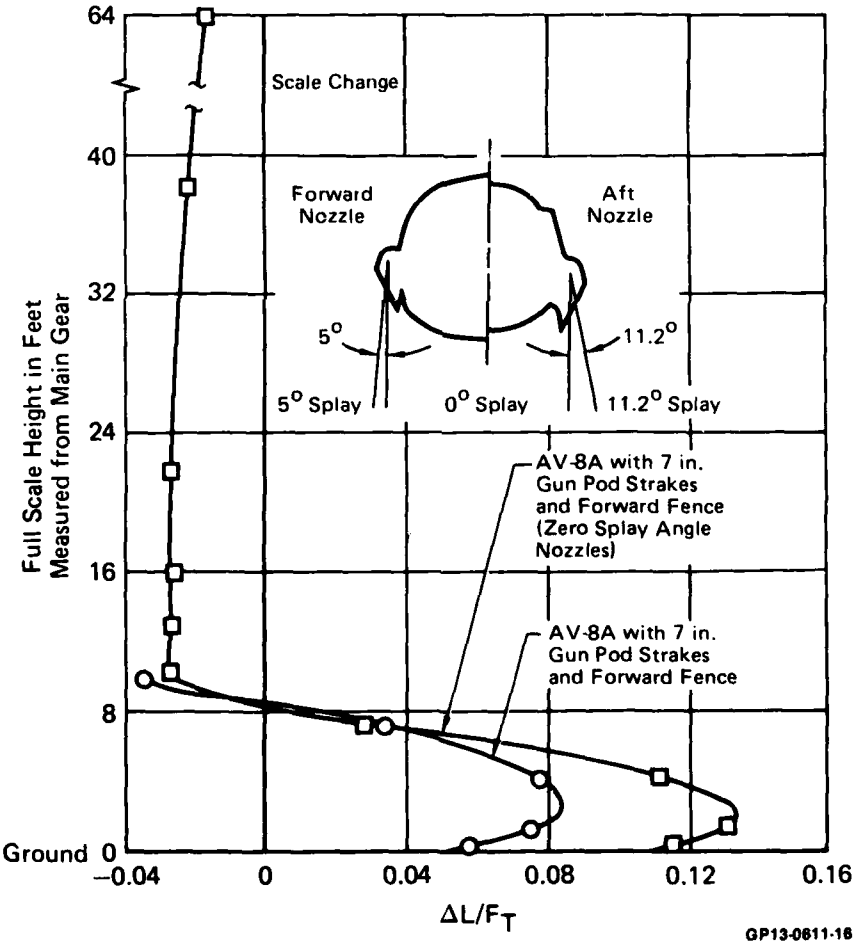

Fig. 18 Effect of Changing Nozzle Splay Angle

EVALUATION OF THE EFFECTS OF MODEL SCALE AND TEST TECHNIQUE ON JET-INDUCED EFFECTS

by
Stanley G. Kalemaris
V/STOL Project Engineer
Grumman Aerospace Corporation
Bethpage, New York 11714
USA

SUMMARY

The effects of model scale and test technique on the jet-induced lift of a twin-turbofan V/STOL aircraft were evaluated experimentally. The smallest model was 2.1% as large as the full-scale model. The two most important items to be modeled were found to be fuselage shape and the coannular nature of a typical turbofan exhaust. Lift-enhancing strakes were found to be effective in enhancing the ground cushion and eliminating a possible source of scale effect.

LIST OF SYMBOLS

D Inside diameter of fan nozzle
h Height above ground measured to bottom of fuselage at center of vertical thrust
ΔL Jet-induced lift
NPR Nozzle Pressure Ratio, Nozzle Total Pressure/Ambient Pressure
P Pressure
T Gross thrust (total per aircraft) or Temperature

SUBSCRIPTS

a Ambient
C Core
F Fan
J Jet
T Total

INTRODUCTION

The importance of jet-induced effects to the design and operation of V/STOL aircraft is well established and needs no amplification in this paper. The program manager seeks two things from jet-effects testing:

- The results must predict full-scale characteristics well enough to protect against building another unsuccessful V/STOL
- The facilities and hardware must be simple enough that the test program does not consume all of the time and funds available for development.

The contradictory nature of these requirements prompted the investigation discussed in this paper. In the early phases of a program, testing is confined to small, simple models because results can be obtained quickly, many configurations may be tested, fixes can be evaluated easily, and the program budget is too small to do anything better. As the program progresses, larger and more elaborate models are built; in a few cases, full-scale models with real engines are built, but by the time the program reaches this phase the configuration is usually frozen. Ironically, the most faithful test is undoubtedly one performed using the aircraft itself; however, in the case of CTOL aircraft, this is most often done with unsuccessful designs.

Grumman is fortunate to have had the opportunity to test a full-scale model of its proposed V/STOL demonstrator (Fig. 1). The existence of test data from smaller models of the same configuration permitted us to evaluate the reliability of small-scale data. The nozzle diameter ranged from 2.5 cm for the smallest model to 118.9 cm for the full-scale model.

DISCUSSION

The concept which evolved into Grumman Design 698 was first tested in 1976 at the Grumman Research Lab. The model was hand carved from wood and used 2.5-cm diameter, low (1.016) pressure ratio circular nozzles exhausting normal to the ground. Induced lift measured on this model is presented as a function height in Figure 2. Results are shown for the model both with and without lift-enhancing longitudinal strakes extending vertically below the fuselage chines. The two significant items to be noted are the ground cushion at intermediate height for the basic airframe and the ability of the strakes to strengthen this cushion and extend it to lower heights.

The next tests were conducted by the project at the Grumman Farmingdale Test Center in 1977. The model for these tests was machined from metal in accordance with the preliminary design drawings of the full-scale aircraft and was twice as large (5.1-cm nozzle diameter) as the model tested in the Research Lab. The nozzle pressure ratio was higher (1.13) and the jets were splayed out 7° in the y-z plane. The results of these tests are summarized in Figure 3.

By comparing Figures 2 and 3, one can see that the larger model confirmed the effectiveness of the strake in enhancing the ground cushion. If both tests have been conducted only with strakes, this paper would probably never have been written. However, the large differences in the strakes-off data from the two tests were the cause of great concern, as the ground cushion which existed with the smaller model was not present with the larger model.

By the time these results were available, the baseline aircraft configuration included strakes. Because of this, it was tempting to accept the results of the larger model as confirming the effectiveness of the strakes and proceed with the design. However, the qualitative difference between the two sets of strake-off data suggested that there might be fundamental differences in the flows around the two models. If this were true, it was important to understand these differences and determine whether further increases in size or nozzle pressure ratio (up to full scale) could cause a qualitative change in the strake-on induced lift characteristics.

The first step was to measure the induced lift with only one jet operating to verify that it followed the trends established by other investigations (e.g., NASA TND-5617 and TND-3166). As can be seen in Figure 4, the larger and smaller models exhibit the expected characteristics.

Once the similarity of the single-jet flows had been established, the investigation turned to the formation of the upwash flow between the nozzles and its interaction with the aircraft. The first variables to be investigated were nozzle pressure ratio, jet splay angle, and model size.

Figure 5 summarizes the results of varying nozzle pressure ratio for the larger and smaller models. There is a noticeable variation in the level of induced lift for both models at very low nozzle pressure ratios, which suggests that the choice of nozzle pressure ratio for the smaller model was ill-advised. In no case, however, does the character of the data change; that is, the sign of $\Delta L/T$ does not change with pressure ratio. This indicated to us that the qualitative change in $\Delta L/T$ between the two models could not be accounted for by differences in pressure ratio. Both this conclusion and the asymptotic character of the curves of Figure 5 with increasing pressure ratio strongly suggest that any differences in nozzle pressure ratio between small-scale models and full-scale aircraft will not significantly affect the jet-induced characteristics (at least for subsonic jets).

Figure 6 shows the results of varying jet splay angle. Nozzle splay does change the level of induced lift, but does not eliminate the ground cushion.*

To check scale effect, a mold was made from the larger model. The mold was used to make a plastic casting, which was tested in the Research Lab with 5.1-cm diameter nozzles. Figure 7 shows that the results for the larger model were essentially the same at both facilities, which suggested that there was a significant scale effect without strakes.

If this was the case, did it imply that there was also a scale effect with strakes at some larger model size? Or was some other factor responsible? A close examination of the model revealed one other possibility. The smaller model was carved from a rectangular block of wood and the chines were rounded with a file. The larger model, however, had 5.5-mm radius chines. Figure 8 shows the effect of using clay to simulate the square chines of the smaller model. There is excellent qualitative agreement between the two sets of data, and no apparent scale effect, although some effect of nozzle pressure ratio is evident. The flow patterns thought to be responsible for this effect are illustrated in Figure 9.

A larger model (Fig. 10) of Design 698 was built and tested by British Aerospace. The wing and fuselage geometries of this model were identical to the larger of the two models previously discussed. This was the first model in which inlet flow and separate core and fan flows were simulated; the smaller models had used uniform circular jets. The fan nozzles were 27.9-cm in diameter and the maximum fan pressure ratio simulated was 1.25. Ejectors were used for both the fan and core simulators.

Figure 11 shows the results of the tests at British Aerospace. As can be seen by comparing Figures 3 and 11, the results obtained at BAe agree with those obtained with 5.1-cm uniform jets at Grumman. This indicates that there is no effect of model size and no effect of simulating the engine core. This latter result is not confirmed by later testing of a slightly different configuration at Grumman.

*Other work indicates that excessive toe <u>in</u> can eliminate the ground cushion, but that is beyond the scope of this investigation.

Since the testing discussed above was completed, the aircraft configuration has evolved to incorporate a rounder fuselage with strakes and a higher (~1.5) fan pressure ratio. This is the configuration of the full-scale model of Figure 1, and of a 1/24 scale model (5.0-cm nozzle diameter) tested at Grumman. Both of these models were built and tested with support from agencies of the United States government. The small-scale model was built as an exact replica of the full-scale model. The test apparatus provide the capability to vary jet temperature and pressure and to simulate both uniform and coannular jets. For the coannular jets, fan and core temperature and pressure could be varied independently.

While the primary purpose of building and testing the small-scale model was to acquire data for use in developing a computerized prediction methodology for jet flow near the ground, it provided an excellent opportunity to evaluate scale effect and determine which variables had the greatest effect on small-to-full-scale correlation. The variables considered were nozzle pressure ratio, jet temperature, and type of flow (uniform or coannular).

Figure 12 shows the effect of varying jet total pressure for uniform, room-temperature jets. With strakes extending 15° below the horizontal, there is only a small effect of jet total pressure and no clear trend of induced force with nozzle pressure ratio.

Figure 13 illustrates the effect of temperature for the same configuration. These tests were performed at the highest nozzle pressure ratio, shown in Figure 12, so that forces and balance sensitivity would be high. Jet temperature has only a small effect on induced forces and there is no apparent trend with temperature near the ground.

Figure 14 shows the effect of core temperature for the same aircraft configuration, but with proper simulation of the core and fan flows. As in the case of a uniform jet, temperature has little effect on induced lift. More importantly, a comparison of Figure 14 with Figures 12 and 13 shows a significantly lower level of ground cushion with a coannular jet than with a uniform jet.

Figure 15, which is for a slightly different configuration (strakes extending 45° below the horizontal), shows that while it is important to simulate coannular flow, it is less important to have an exact simulation of each of the two flows. The test condition, $(P_{Fan} - P_a)/(P_{Core} - P_a) = 1.76$, which is closest to the full scale conditions does not have a significantly different level of $\Delta L/T$ than any other combination of fan and core pressures, including the case where core pressure is higher than fan pressure.

Figure 16 compares the results of testing the small-scale model (with coannular flow) and the data from the full-scale model. Three things are apparent from this figure:

- Deflecting the strakes farther below the horizontal increases the peak level of the ground cushion and reduces the height at which it occurs
- There is excellent correlation between the small-scale and full-scale test results
- There is considerable scatter in the full-scale data.

The first result is not unexpected, and is consistent with scale model testing of a configuration with a square fuselage. See, for example, Figure 2, where vertical strakes enhanced the ground cushion which existed for the basic aircraft. Strakes at 45° and 15° can be considered intermediate cases between the two extremes of Figure 7.

The second result is the most important one, and has significant implications for future V/STOL testing. It is, in fact, the major conclusion of this investigation.

The third result is due to the data acquisition system used for the full-scale model. Induced lift is a small number calculated from three large numbers; namely, power-on balance reading, power-off balance reading, and thrust (calculated from exit rakes). Since the accuracy of these various items is of the same order of magnitude as the induced lift, a significant amount of scatter was inevitable. Induced lift on the small-scale models was measured by separate airframe balances, which is an inherently more precise test technique.

CONCLUSIONS

For aircraft of the class considered, scale effects are small. Details of the airframe must be simulated accurately; coannular jets must also be simulated. As long as these items are modelled properly, differences in jet temperature and nozzle pressure ratio will not cause significant differences in jet-induced lift between the model and the full-scale aircraft.

It is suggested that all V/STOL aircraft should have lift-enhancing strakes for the following reasons:

- They work
- By assuring flow separation at the chines of the fuselage, and fixing the location of this separation, they eliminate a possible source of scale effect.

ACKNOWLEDGEMENTS

The tests which provide the basis of this paper could not have been performed without the efforts of Drs. W. Hill and R. Jenkins and Messrs. R. Rice and F. Wohllebe of Grumman Aerospace, Messrs. M. Falarski and M. Dudley of NASA and Messrs P. Knott and J. Porter of British Aerospace.

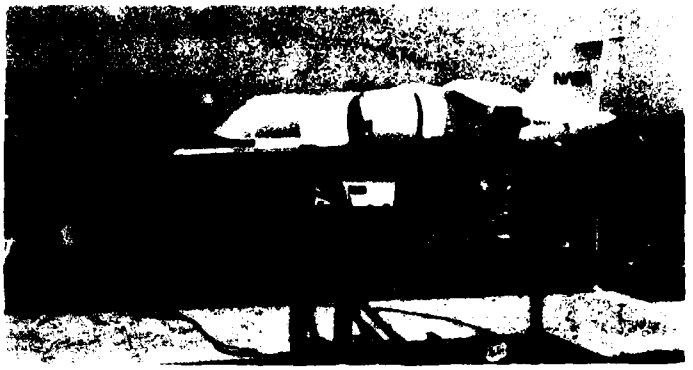

Fig. 1. Full Scale Model of Design 698 at NASA Ames

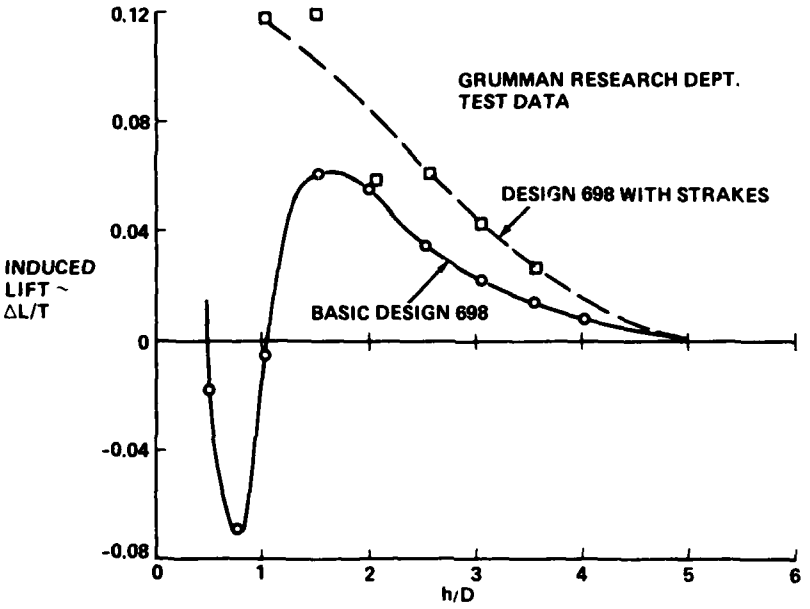

Fig. 2. Results of First Suckdown Tests of Grumman Design 698

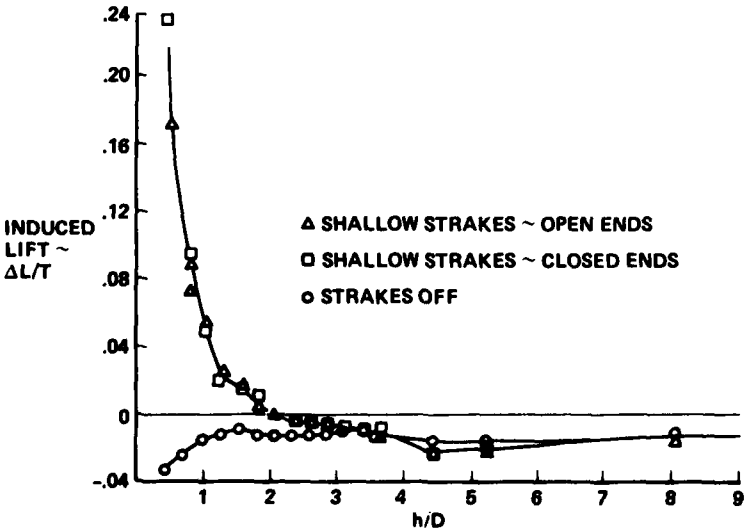

Fig. 3. Results of Second Suckdown Tests of Grumman Design 698

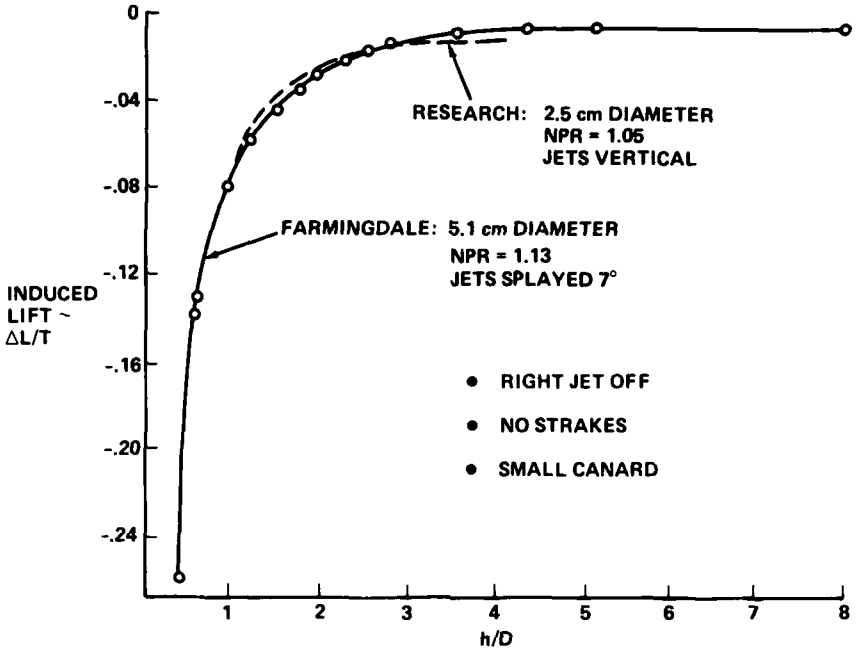

Fig. 4. Effect of Single-Jet Operation on the Induced Lift

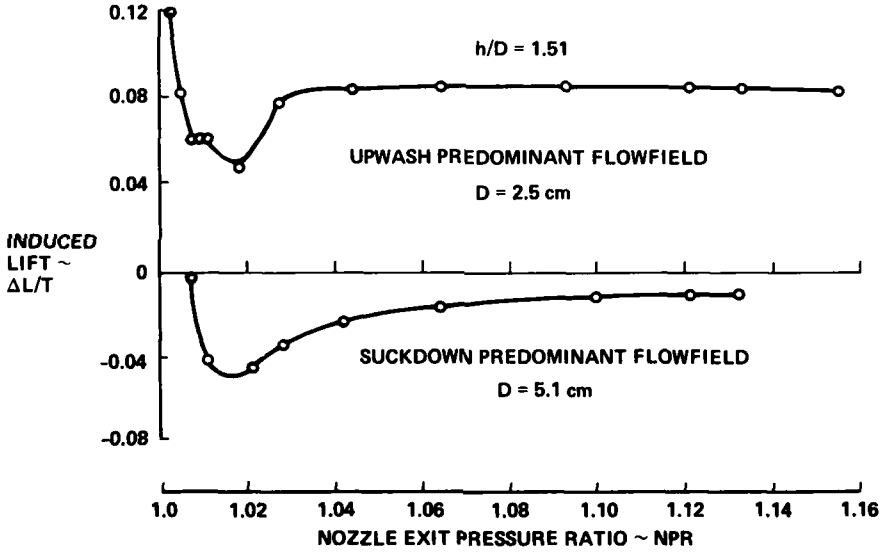

Fig. 5. Effect of Nozzle Exit Pressure Ratio on Induced Lift

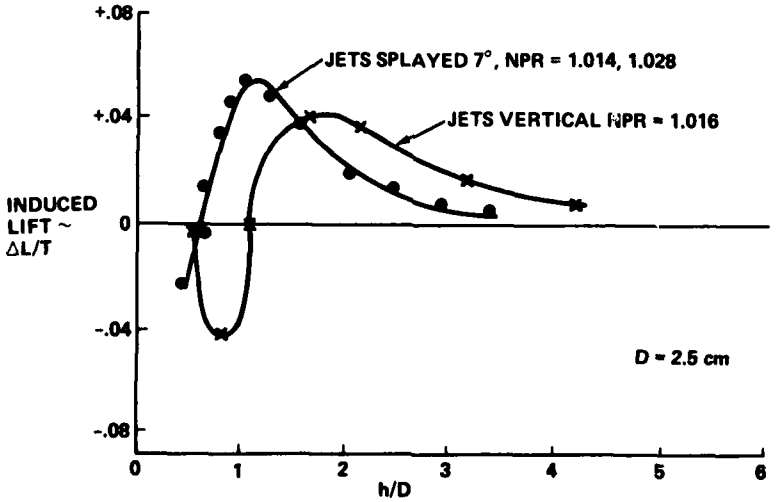

Fig. 6. Effect of Jet Splay on Induced Lift

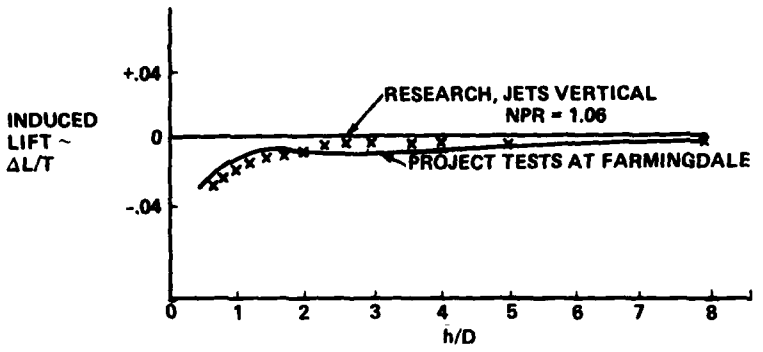

Fig. 7. Comparison of Identical Models Tested at Two Facilities

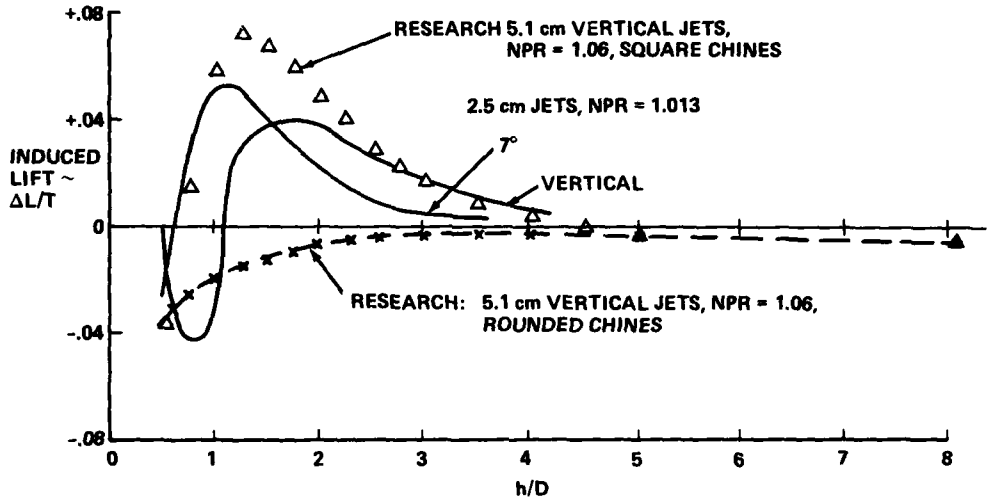

Fig. 8. Fuselage Shape was the Predominant Factor

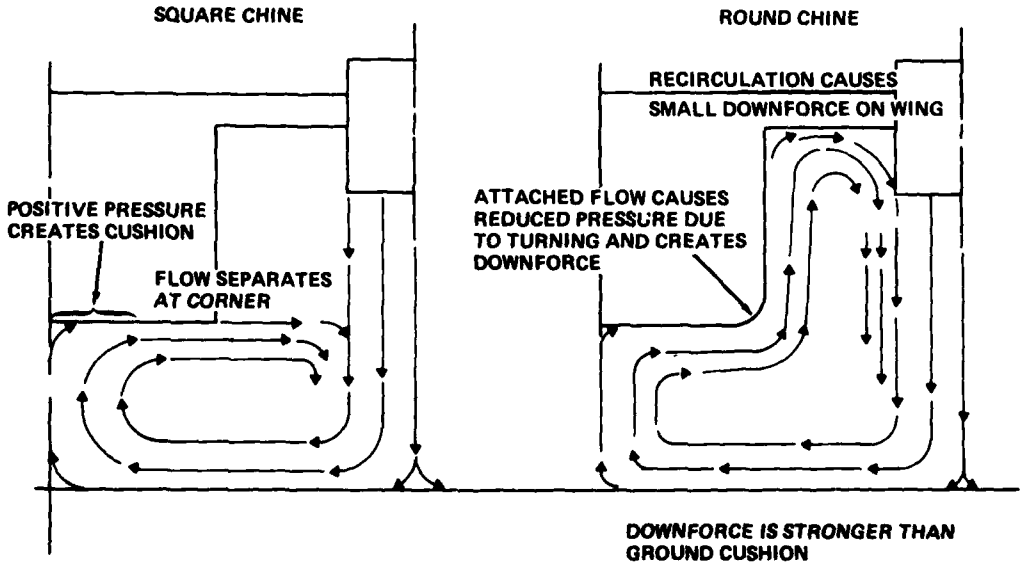

Fig. 9. Effect of Chine Shape on Flow Field

Fig. 10. BAe Model of Design 698 in BAe V/STOL Tunnel

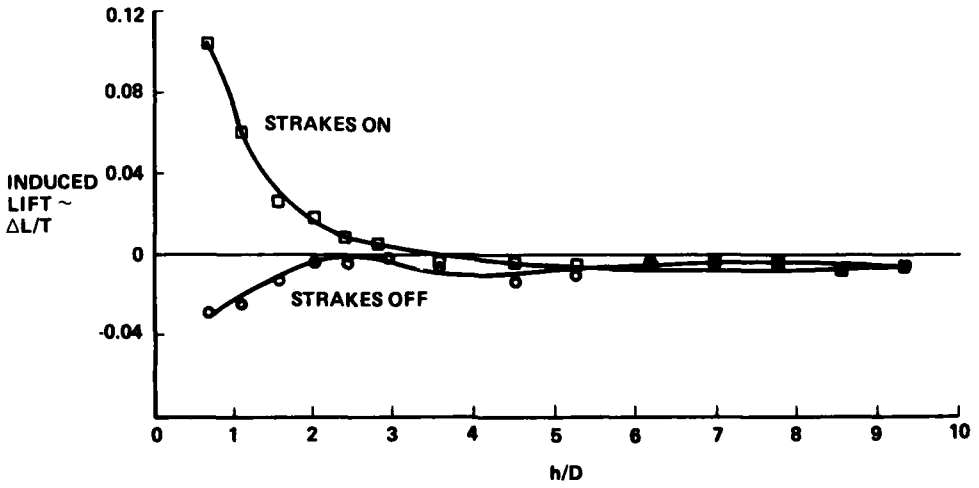

Fig. 11. Results of Suckdown Tests at British Aerospace

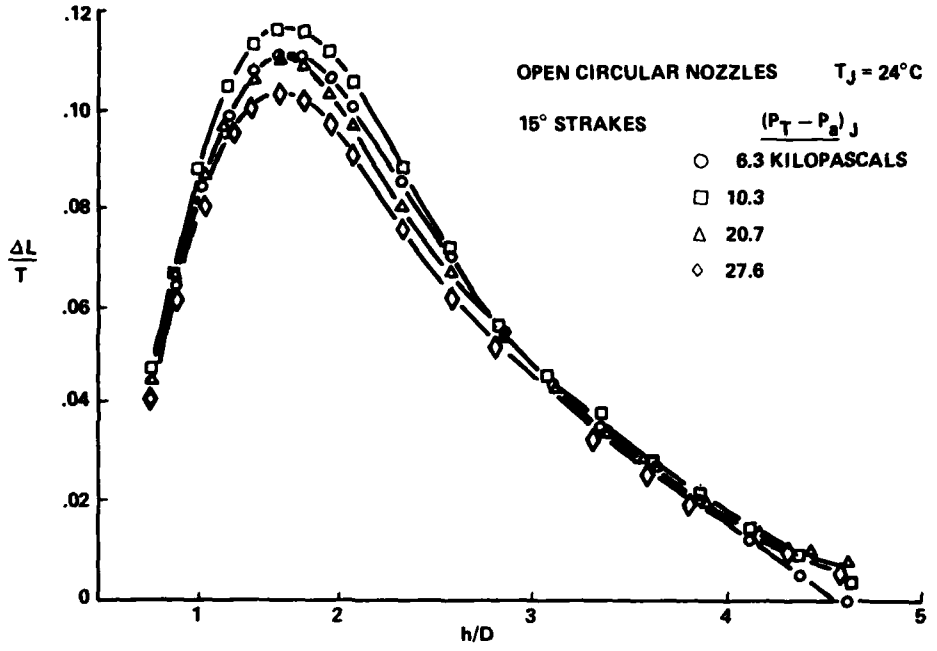

Fig. 12. Effect of Nozzle Stagnation Pressure on Induced Lift

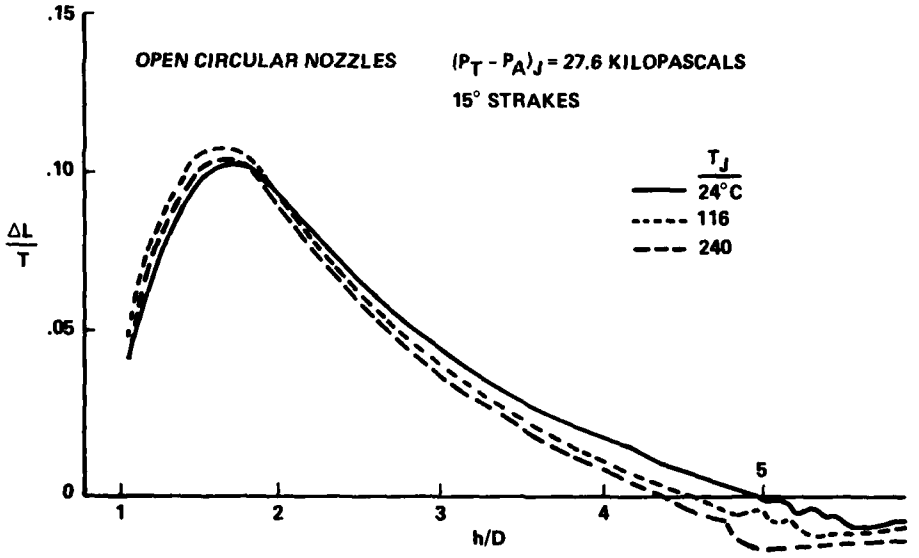

Fig. 13. Effect of Nozzle Exit Temperature on Induced Lift

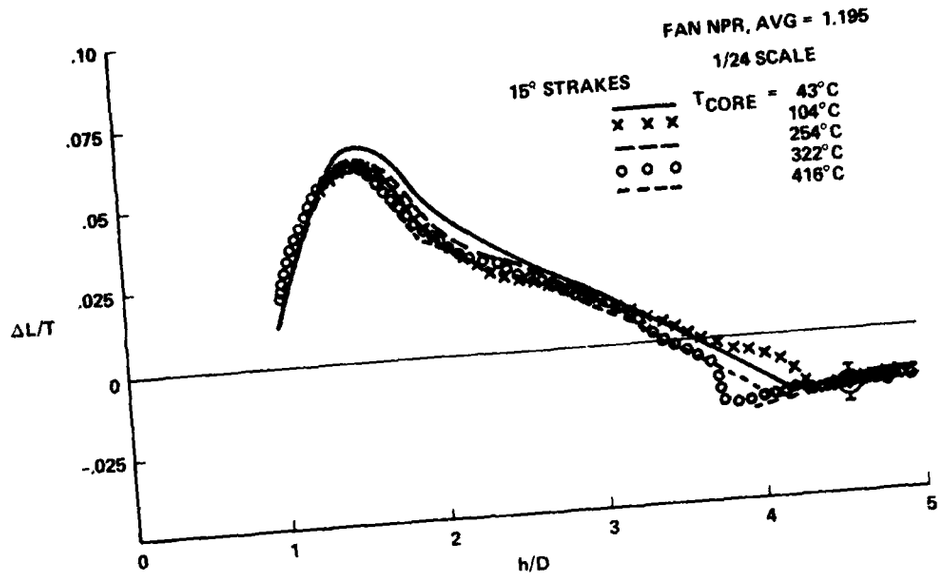

Fig. 14. Effect of Core Temperature on Interference Forces

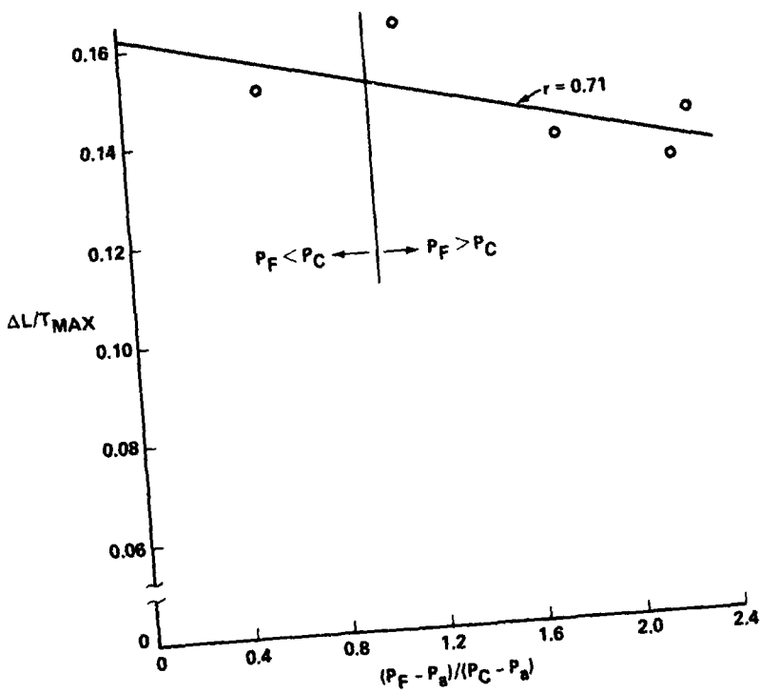

Fig. 15. Effect of Variations in Core and Fan Pressure on Induced Lift

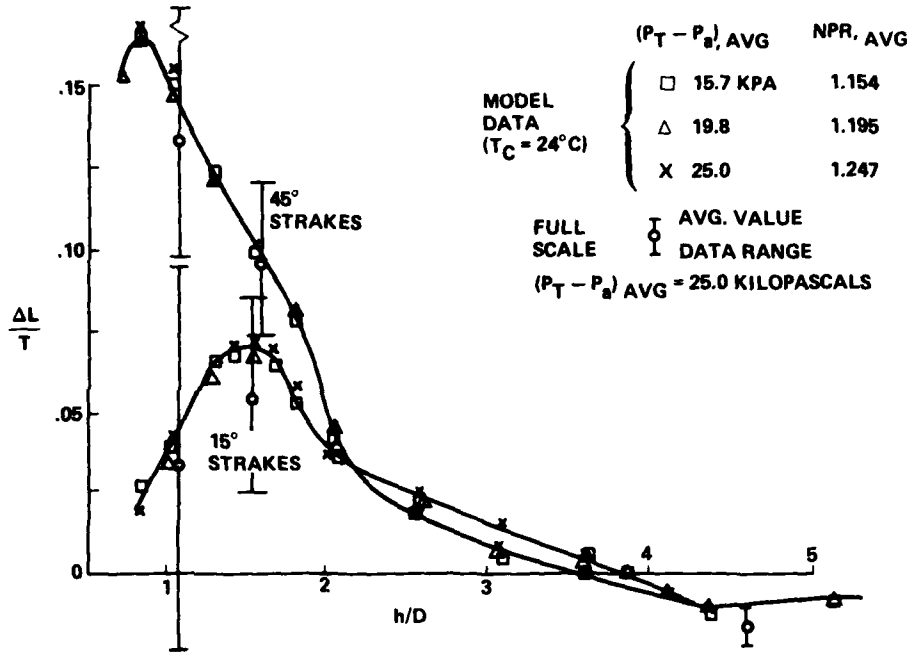

Fig. 16. Effect of Fan Nozzle Pressure on Induced Lift

JET EFFECTS ON FORCES AND MOMENTS OF A VSTOL FIGHTER TYPE AIRCRAFT

by

B. Haftmann

Vereinigte Flugtechnische Werke GmbH
2800 Bremen 1, Hünefeldstraße 1-5, Germany

SUMMARY

This report is a compilation of significant results classified as "Jet Effects on Forces and Moments of the VAK-191 B".

The basis of the report are the flight tests carried out by VFW and the US-Navy.

The jet induced effects were investigated during the Vertical/Short Take-Off and Landing (VSTOL) mode in and out of ground effect, in yawed flight, during hover and transition right up to aerodynamic flight.

The flight test results were compared with wind tunnel measurements performed during the VAK-191 B development phase and used for preparation of simulation and Automatic Flight Control System development.

Trends and deviations between aircraft and model test results were verified, analysed and corrected if necessary. Compared to conventional aerodynamics there was considerably questioned the adequacy of wind tunnel data preparation.

The practicability of wind tunnel data for the assessment of VSTOL aircraft design and determination of flight characteristics and performances are discussed and evaluated. Finally, recommendations for the measurements of jet induced forces and moments on VSTOL aircraft are outlined.

SYMBOLS

A_e	jet exit area
b	wing span
$\bar{c}$	mean aerodynamic chord (m.a.c.)
D_e	jet exit diameter
e	index for "experimental system"
H,h	center of gravity height over ground
L	lift
ΔL	jet induced lift loss
l	rolling moment
M_∞	flight Mach number
Δm	jet induced pitching moment
N	normal force
n	yawing moment
P_T/P_∞	nozzle pressure ratio
q_x/q_e	jet streamwise local dynamic pressure ratio
s	halfspan
T	thrust
T_n, T_z	normal thrust
T_e	jet exit temperature
V_∞	aircraft forward speed
V_j	jet exit velocity
W	weight
x	jet streamwise station
α	angle of attack
β	angle of yaw
ϑ_f	flap angle
ϑ_e	elevator angle
σ	nozzle swivel angle

1. INTRODUCTION

VFW-FOKKER and the US Navy have participated in a joint flight test program for the VAK-191 B (Fig. 1) between June 1974 and October 1975. A significant portion of the flight tests was devoted to determining the propulsion induced forces and moments on the aircraft. The experimental program included vertical and short take-offs and landings and hover flights in and out of ground effect (IGE and OGE) as well as transitions to full wingborne flight.

The program objectives to be fulfilled by these flight tests were as follows:

- Measurement of the propulsion-induced forces and moments on the VAK-191 B aircraft during various flight conditions.
- Comparison of flight test results with existing model and prediction data.
- Evaluation of the effectivness and applicability of utilizing scale model tests to predict aircraft flight characteristics.
- Recommendations for future V/STOL induced forces and moments testing and data reduction techniques.

2. OVERVIEW ON THE PROPULSION-INDUCED FORCES AND MOMENTS

Besides some intake influences the changes in forces and moments are basically due to suction forces caused, IGE and OGE, by flow entrained into the jets and by the fountain phenomena of vertically blowing groups of nozzles near the ground. Therefore the jet induced effects mainly depend on the position of the engines relative to the aircraft surfaces and to strength and direction of the propulsion efflux.

Regarding the lift loss it can generally be said that a nozzle position near the wing leading edge causes more suck-down than a position near the wing trailing edge.

Much more difficult to evaluate are the jet induced moments. The change in pitching moment is primarily initiated by jet induced downwash at the elevator and depends mainly on the nozzle swivel angle. Increasing the latter leads to an increase in pitchup moment although the jet axis drifts away from the elevator. Besides this it was observed that on the VAK-191 B the cruise engine contributes more to the jet induced downwash than the lift engines, probably because its efflux influences a broader region of the wing span.

Regarding the side slip the jet induced downwash is increased substantially leeward the nozzles resulting in higher suck down forces on the leeside wing half and inducing a rolling moment out of the wind direction. The forward lift engine and the two forward cold nozzles of the cruise engine are particularly responsable for this phenomena on the VAK-191 B.

In contrary the rear lift engine and the two hot rear nozzles of the cruise engine have a considerable influence on sidewash induction on the fin, thereby affecting the yawing moment. Strong suction occurs in the jet wake and reinforces the natural crosswind on the fin, thus increasing the directional stability.

Another influence on aircrafts lateral moments arises from the engine intakes. Due to the symmetrical positioning of the lift engines relative to the center of gravity, the lift engine intakes only contribute to the rolling moments. The cruise engine intake, however, destabilizes the yawing moment. This leads in total to a destabilizing increment from engine effect in a region up to 15kts where the intake influence is stronger than the jet induced moment on the fin.

3. FLIGHT TESTS

The flight test program comprised the whole pattern of vertical and short take-off (VTO, STO), vertical and short landing (VL, SL) and hover flight, each in and out of ground effect, and the transition up to aerodynamic flight. The flight data was transmitted via telemetry to a ground station with provision for continuous real time taping of the selected aerodynamic parameters.

During the long test period the flight test program -originally resulting from simulation based on W/T results- was steadily improved by pilots' experiences and introduction of new flight test techniques for different test areas.

Figures (2) and (3) summarize the procedures the pilots used for aircraft stabilization or steady movement to produce data on jet induced forces and moments.

In fig. (2), left hand side, test objectives are defined: take-off, short take-off and hovering out of ground effect (OGE), landing and short landing and hovering in ground effect (IGE). For example during take-off, time $t - \Delta t$ the aircraft is at preconditions with engines idle, nozzle angle 45 deg, attitude preselected. At time t pilots input is: engine full power, main engine nozzle angle swivelled between 80 and 100 deg. At time $t + \Delta t$ aircraft reacts first by increasing height in ground effects and then gaining altitude out of ground effect. The STO and hovering OGE begins with increasing height IGE. Pilots input is to reduce thrust and to adjust nozzle angle and attitude as required. The aircraft then follows on with OGE stabilization.

Landing is performed vice versa, whereby short landing leads to hovering IGE as can be seen in the last line of figure (2).

The next fig. (3) outlines two special techniques to measure OGE and IGE jet induced effects with throttle pulse and step down method, respectively. Throttle pulse input used

at low forward speeds to produce data out of ground effect, step down technique aimed at aircraft stabilization at constant height in ground effect with throttle manipulation for constant height steps.

To obtain the effect of (V_∞ / V_j) during transition flight it was aimed to keep nozzle angle and thrust constant and increase aircraft speed by changing pitch attitude only. However, the usefullness of this method was limited by the descent rate which quickly built up to extreme values. Therefore it was necessary to vary the cruise engine thrust as an addition parameter with corresponding uncomfortable data reduction.

Wingborne flight, outlined in the last line,was performed by stabilizing the aircraft in different configurations, for instance, flap setting, angle of attack or velocity.

4. MODEL TESTS

The windtunnel tests for the VAK-191 B started in 1963 and the final tests were performed in August 1970 at the beginning of the flight test program. About 3000 hours were spend to investigate jet induced effects in and out of ground effect. The relevant wind tunnel tests with engine jet simulation were carried out in the DFVLR low speed tunnel Porz Wahn near Cologne.

4.1 Model Description

The design prinziple of the model is shown in fig. (4). A three tube support sting was mounted in the wind tunnel test section by a wire suspension. Compressed air was fed through this sting to the engine nozzles, which were mounted at the front end of the sting. The upper tube led the air to the rotary cruise engine nozzles, whilst the two lower tubes fed the lift engine ones.

The complete hull of the model encased the sting-nozzle arrangement without touching it. The hull was connected to the sting via a six component strain gauge balance. The gaps between hull and nozzles were sealed by a thin rubber foil.

In this arrangement the strain gauge balance measures the aerodynamic forces acting on the hull, while the sting directly carries the thrust load of the jets. So it is possible to study the influence of the jets on the external flow around the model without interaction of the jet momentum force.

Due to the wind tunnel equipment and the simple model design the use of real jet temperatures was not possible. In fact all tests were performed simply with cold compressed air.

Suggestions for the best scaling of nozzle exit velocities necessary for nozzle pressure ratios are outlined in chapter 8.

4.2 Range of Model Tests

Jet effects were determined using models with and without ground simulations, with a continuously adjustable plate beneath the model in flight attitude.
Following procedures were simulated:

- Conventional take-off and landing with lift engines off, cruise engines nozzles swivelled back (σ = 5°), for speed up to 120kts and angle of attack 0 to 12 deg.
- Short take-off and landing with lift engines running, at speeds up to 170kts and swivel angles 5 to 90 deg.
- Transition, with speed and angle of attack up to 240kts and -6 to 30°, respectively. The swivel angle varied between 5 and 90 deg.

Furthermore the following variations were tested:

- Cruise engine running, lift engines off
- Cruise engine off, lift engines running
- Cruise and lift engine running

4.3 Typical Model Data

The next fig. (5) shows results from suck down wind tunnel tests out of ground effect. Jet induced lift loss referred to the normal thrust component $(\Delta L/Tz)e$ is plotted against velocity ratio $(V_\infty / V_j)e$ for two angles of attack α with nozzles swivel angle as parameter, flap angle ϑ_f and elevator angle ϑe equal zero.

Similar diagrams are plotted for pitching moments fig. (6)

For purpose of quick and effective model data application also crossplots were made, such as lift loss against angle off attack with velocity ratio as parameter etc. All

aerodynamic data for jet induced effects were stored in punch cards which can be interpolated and calculated for arbitrary configurations.

5. MODEL TO FLIGHT COMPARISON

The jet induced components are defined as the difference between the forces and moments on an aircraft configuration with engine on and off, respectively.

The establishing of the jet effects therefore requires further testing with an engine-off configuration for which corresponding wind tunnel data were used.

These data, depending on angle of attack, flap and trim angle, were subtracted from the forces and moments of the flight configuration and thus led under consideration of thrust forces and moments to the jet induced effects.

The results were then plotted in a computer output together with the wind tunnel based jet induced effects of the same configuration.

6. ANALYSIS

This chapter contains flight test evaluation results compared and analysed with wind tunnel data.

Evaluated flight tests are outlined in fig. (7). The number of flights and range of used parameters are plotted for different flight modes. A total of 80 flights were analysed including 31 take-offs and landings, 5 step down, 5 hovering, 4 transition and 5 wingborne flights.

The next diagrams display the results. Though the number of plots is limited because of the brief character of this report, they are as well representative as they cover the whole field of flight tests and include results of satisfying to good agreement between wind tunnel and flight test data.

6.1 Test Data in Ground Effect

The diagram in fig. (8) presents a landing in ground effect. Lift to normal thrust component is plotted against h/b, h being the height of aircraft center of gravity over ground and b the wing span.

The diagram shows a vertical landing, zero forward speed with nozzle swivelled to σ = 100 deg. To avoid angles of attack and sideslip of $\pm$ 180 deg the forces are referred to the earth coordinate system. Undercarriage touch is at h/b = .35.

The curves show for model and flight test the same trend in ground effect but the absolute value is nearly 2% different. Typical for vertical landing is the increasing suck down with decreasing height which is, however strongly reduced directly over ground by so called fountain effects.

Fig. (9) shows the lift loss for a short landing in ground effect. The data is taken from two flights at aircraft speed of 39kts and 57kts, respectively. The lift loss level at the lower speed lies between 6% and 10% of normal thrust. Increasing the aircraft velocity to 57 kts leads to an increasing lift loss of about 14%.
Once more the dependence from height over ground compare well for flight and model test, but showing a constant difference of nearly 4%.

The next fig. (10) presents the jet-induced change of pitching moment for the same two flights, 39kts and 57kts in the upper and lower diagram, respectively. A phase shift of 0.2 to 0.4 h/b is noticeable in the upper graph, possibly caused by dynamic effects on the aircraft. The lower diagram shows a jet influence of about 2% thrust times m.a.c. without a clear trend correlation in the plots. These 2% thrust times m.a.c. is equivalent to 0.4 mkp in model tests or 5% of a lift engine moment. This will be detailed in chapter 7.

A comparable set of flight test data was evaluated for take-off in ground effect.

Diagram (11) shows the suck-down for a vertical take-off. The picture is similar to the vertical landing one but shows in contrary to this a phase shift off about 3% height to wing span. Taking this into account the lift loss difference between flight and model test is in the order of 1%.

The next diagram (12), presenting a short take off, outlines once more a rather good agreement in height dependence between flight and model test. The absolute values, however, differ in the same order of magnitude (4%) as observed in the short landing case.

The corresponding changes in pitching moment are shown in the next fig. (13). Even here the similarity to the short landing case is obvious. Differences in trend and absolute values are nearly the same.

Generally can be said that there is no remarkable difference in test data quality between take-off and landing flight technique.

After having presented typical forces and moments comparisons and discussed trends and discrepancies, the influence of main parameters on jet-induced effects will now be outlined.

Velocity Effects

Aircraft velocity influence on lift loss is illustrated in fig. (14) for a take-off example.

- aircraft speed between 0 kts and 70 kts causes increasing lift loss in flight test results
  - hovering produces 2% - 4% referred to normal thrust, whereas forward speed gives 6% to 12%
  - lift loss difference between flight and model tests for VTOL and STOL up to 70 kts is 2% and 4% - 6%, respectively.

Regarding pitching moments an increase in nose up pitching moment of the order of 4% normal thrust times m.a.c. was observed between hover and 70 kts in ground effect.

Effect of Nozzle Angle

Nozzle angle was varied between 85 and 100 deg during in ground effect flight tests, but no effect on lift or pitching moment was observed.

Effect of Aircraft Height above Ground

In vertical take-off and vertical landing mode an immediate increase of lift loss was observed during ground clearance up to heights of about .8 and .6 wing span, respectively, there after decreasing continuously to 3% normal thrust loss.

In short take-off and short landing mode with forward speeds above 30 kts, height influence on suck down forces and moments is less pronounced and rather erratic.

6.2 Test Data out of Ground Effect

Coming to heights where ground effect no longer exists, the main deciding parameter becomes the free stream to jet velocity ratio. Fig. (15) shows the lift loss for a transition flight with σ = 100,5 deg. The jet induced forces increase strongly with increasing forward speed and are of a much higher amount than observed in the in ground effect tests. The trends of model and flight tests compare very well but a difference in the absolute value of 3% to 4% remains. Fig. (16) presents the same data of a transition flight with σ = 80 deg. The symbols belong to the different flights from which the curve's slope is produced. The input point for zero forward speed was taken as a mean value from several hovering tests. Again the model tests are similar in trend but lower in level.

Corresponding jet-induced pitching moments are to be seen in fig. (17). Here the difference lies between 6% to 8% normal thrust times m.a.c.

The jet-induced pitching moments for the σ = 100,5 deg flight is plotted in fig. (18). In comparison to the previous diagram the curve's slope at velocity ratios above .15 is much smaller here what leads to smaller absolute values at higher forward speeds. At .25 we find, for instance, a change in pitching moment of 12% compared with 24% in the 80^{o} case.

After presenting typical force and moment comparisons and discussing trends and discrepancies, the influence of main parameters will now be outlined.

Velocity effects

The crossplot in fig. (19) shows the important influence of the freestream to jet velocity ratio on the jet induced lift loss. The data are derived from 6 flights. It can bee seen that tripling the velocity ratio increases the lift loss by a factor of about 3.5.

Effect of Nozzle Angle

Compared to velocity ratio the influence of cruise engine swivel angle is relatively small. This result confirms that lift loss versus normal thrust component plot is reasonable. It is to be noticed, however, that the normal thrust component of the cruise engine decreases considerably with nozzle swivel angle and that a referring to total thrust would lead to a much stronger dependence.

7. CONCLUSION

7.1 Overall Conclusions

Some items must be emphasized before discussing the applicability of data.

- The high order of magnitude of jet-induced effects compared with other forces and moments acting on the aircraft, namely bleed control forces and moments and aerodynamic forces and moments.
- The problem of correlation between wind tunnel and flight test results, and the assessment and prediction of aircraft handling and flight characteristics as well as engine overpower for compensation of jet induced lift losses.

7.1.1 Meeting the jet-induced Forces and Moments

In the VTOL and hovering mode where no primary aerodynamic lift acts on the aircraft a lift loss in order of 5% thrust due to jet-induced effect occurs. This is in the same order of magnitude as the thrust surplus referred to aircraft weight should be for acceptable vertical acceleration.

Jet induced pitching moments are about 2% total thrust times m.a.c., which is small compared to one lift engine pitching moment of 15 to 20 times in magnitude and to thrust modulation and bleed control which are 12 and 8 times, respectively.

Raising the aircrafts forward speed increases the jet induced effects rapidly, as shown in fig. (20) derived from wind tunnel test results.

To counterbalance the aircraft weight during transition the normal force N, the sum of lift, normal thrust component T_z and jet induced lift loss must equalize the weight W. In the diagram a typical variation of these forces is plotted versus Mach number for constant angle of attack and variable swivel angle. The shaded curve shows the resulting lift loss when the total normal force is equal to the aircraft weight. The figure shows that with increasing aerodynamic lift and thereby reduced normal thrust component jet lift loss increases and after reaching a maximum decreases to a small value at the end of transition. Notice the lift loss in this diagram is referred to the constant weight and not to normal thrust, therefore varying strongly with swivel angle.

As a thumb rule the maximum normally lies between half and three quarters of the aircrafts minimum aerodynamic flight speed reaching the order of 30% to 50% of the aircraft weight.

Besides the lift loss considerable changes on pitch, yaw and rolling moment occur, resulting from wing and especially from jet-tail interference. Pitching moment is altered by about 30% thrust times m.a.c. influencing strongly the aircraft flight characteristics during transition.

7.1.2 Applicability of Data

Coming to the problem of wind tunnel-flight test data correlation and prediction of aircraft flight characteristics.

Bleed nozzle and flight control system design as well as their adjustment in the aircraft were realized on the basis of wind tunnel results and were never changed during the whole flight test period. This implied that the aerodynamics departments engagement during flight tests was small, to meet with any urgent situation on the aircraft, except on two occasions occuring at the beginning of the transition flight test phase. These incidents important for model data applicability will be discussed in the following.

The first occuring in longitudinal motion, when the pilot increased forward speed from hovering. Nose-up pitching moments produced commanded an earlier lift engine thrust modulation than predicted by flight test simulation. This increased thrust induced additional suck-down on the horizontal tail keeping aircraft further nose-up, resulting in unacceptable handling qualities.

At that time we recognized, that jet-induced nose-up pitching moments were higher on the aircraft than derived from wind tunnel results.

We succeeded by changing the zero tail setting by 3.5 deg aircraft nose down, linearizing elevator characteristics and in addition shifting the starting point of lift engine thrust modulation. No further changes then were necessary until the end of the flight tests.

Evaluating the pitching moments from flight tests confirmed that they were large compared to wind tunnel test data, remember fig. (17).

The thick support sting at the rear of the fuselage is the cause of the small measured nose-up pitching moments in model tests. It decreases the downwash thus producing nose down moments which do not exist on the aircraft. Theoretical calculations using the panel method for wing-body including jets confirmed the effects of a rear mounted sting. These calculations were performed together with Grumman Aerospace Corporation for Naval Air Propultion Test Center.

The second incident occured in side slip. In spite of good model to flight data correlation, it was more problematic and dangerous for the safety of pilots and aircraft. The main features are explained in fig. (21), which presents jet and intake influences on lateral motion.

Yawing moment referred to thrust and wing half span is plotted against effective velocity ratio which is about equal to Mach number. The cruise engine intake is destabilizing in yaw, whereas the "basic" aircraft and jet influences are stabilizing.

The destabilizing intake moment for a fixed yaw angle, being roughly a linear function of flight Mach number equalizes the stabilizing parabolic yawing moment at a certain speed (see detail A). From hovering up to this limiting speed of about 15 kts (marked by the dashed line) the aircraft is unstable in yaw motion. On the right hand side rolling moment is plotted against effective velocity ratio. Lift engine intakes as well as jet influences are destabilizing in roll. This delicate problem was foreseen when roll control was limited in speed and side slip angle. However, as the limiting speed "B" was well within the boundary for full roll control we assumed that no safety problem would arise, on condition the pilot was "off" the rudder pedals. Caution was necessary because wind tunnel tests predicted higher jet-induced effects for increasing angle of attack.

The aircraft had to be kept within the boundaries shown in fig. (22), where the rolling moment in steady sideslip is plotted, comparing wind tunnel based simulation with flight test data. The curves were taken from simulation tests holding constant angle of sideslip for different angles of attack and aircraft speed with 50% of full roll control power. Two points marked by full circle and triangle are evaluated from flight tests with approximately comparable conditions. It indicates satisfactory agreement to the simulated characteristic within a range of about $\pm$ 5% deviation of the needed roll control power.

Concluding, the prediction of flight characteristics based on wind tunnel results was representative even in the case of unconventional and critical motion caused by sideslip. Thus model data applicability for prediction of aircraft flight characteristics was adequate in longitudinal, directional and lateral motion.

7.1.3 Model versus Flight Test Correlation

The prediction inadequacies of wind tunnel jet-induced aerodynamic data are summarized.

Jet-induced lift loss is higher on the aircraft than on the model.

- about 2% to 4% of normal thrust component in ground effect
- about 4% to 10% of normal thrust component out of ground effect
- about 2% to 3% of normal thrust component during hover flight

Jet-induced pitching moments differ both in nose-up and nose-down direction in ground effect, the discrepancies being about 3% thrust times m.a.c.

In transition out of ground effect the flight test nose-up pitching moments are 5% to 8% higher than in wind tunnel tests. The explanation for this deviation was given in the previous chapter. Thus the outstanding discrepances between wind tunnel and flight test results concentrate mainly on jet induced lift losses during transition.

7.2 Problem Areas

7.2.1 Discrepancies between Windtunnel Model and real Aircraft

One reason for the differences in wind tunnel and flight test results is found in more or less important discrepances between model and full scale aircraft, such as nozzle geometry, exit momentum, jet quality and failure in measurement of thrust, velocity, angle of attack and normal acceleration etc.

The next two figures give an example of the influence of nozzle geometry on jet decay and induced forces. They are taken from earlier measurements of Kuhn and Williams. Fig. (23) compares jet decay that means the decrease of axis dynamic pressure of three different

nozzles, each for a cold and hot jet. The nozzles' exits are different in shape but equal in area. The great advantage of the circular nozzle is clearly shown, followed by the quadratic and then by the rectangular one. At a distance of 4 diameters behind the nozzle for instance the decay of the rectangular jet has already taken place to an amount of 70% whereas the circular jet decay is not yet noticeable. Using hot air, however, leads, especially for the circular jet to earlier decay.

Fig. 24 compares two nozzles with same exit geometry but with different pressure chambers. The lower diagram shows the jet decay as function of distance behind nozzle. Nozzle 1 with a circular pressure chamber proves to be far more resistant, because of lower turbulences than nozzle 2 with a long rectangular pressure chamber. In the upper diagram the lift loss is plotted produced on a circular flat disk by nozzles 1 and 2 blowing through a hole in the plate's center. It is to be seen that the later decaying jet 1 induces much less lift loss than the higher turbulent jet 2 with its rapid decay.

The figure shows that double magnitude of suckdown and an increase of 3% thrust is easily possible.

7.2.2 Measurement Accuracy

The engine thrust determination could be another source for discrepancies during flight tests.

Thrust calculation based on compressor speed of rotation gives higher thrust when accelerating the engine and lower thrust during deceleration leading to higher evaluated lift losses for take-off compared to landing. Error in thrust determination is of the order of ± 3% to ± 7%, whereby 3% more thrust shifts the flight test data close to the model data for most flights in ground effect. Furthermore inaccuracy and nonregistering of velocity and acceleration inputs could contribute to the observed discrepances.

8. RECOMMENDATIONS

From the experience gained during the aerodynamic development, wind tunnel and flight tests on the VAK-191B, together with the associated problems, such as jet to airframe interference, recommendations are made to encourage future VSTOL development.

8.1 Critical Model Test Parameters

This is one field of importance for future model design and testing. Besides angle of attack the main parameters used in longitudinal motion tests were:

- effective velocity ratio $(V_\infty / V_j)e$
- nozzle swivel angle

While the nozzle swivel angle mainly influences the induced pitching moments by causing a downwash field at the tail, the effective velocity ratio reveals to be strongly involved in all problems of jet-induced forces and moments on the aircraft. So it becomes the most important parameter whose physical background has to be studied carefully.

8.2 Scaling for Future Models

Considering the critical parameter of effective velocity ratio, it is recommended that a better jet mixing with real temperature (hot gas) and turbulent efflux should be utilized for model simulation.

To circumvent the difficulties of hot gas simulation - data input is laborous and expensive and turbulent engine efflux difficult to achieve - the following stepwise method is recommended:

- simulate effective velocity ratio with cold jets
- design nozzles for homogenous low turbulent flow
- provide individual massflow at each nozzle; pairwise in the case of nozzles symmetrical to the fuselage center line
- conduct measurements in rough program under these conditions
- assume jet induced effects obtained 5% to 10% higher than measured
- increase jet turbulence in some incremental steps with vortex generators at the nozzle exit near the jet boundary
- obtain real engine flow characteristics from manufacturer, correlate turbulence and evaluate lift losses
- conduct the complete model test program on the basis of correlated engine to model jet turbulence
- if engine flow characteristics are not available, impute jet-induced lift losses by data measured from assumed jet turbulence with tolerances of ± 5% of normal thrust component.

Measuring jet induced pitching moments special attention must be paid to sting correction, because a fuselage tail support sting causes aircraft nose-down pitching moments. To

improve model jet-induced pitching moment simulation, higher downwash must be achieved with turbulence generators in the jet boundary as described above.

8.3 Improved Test Technique

The VAK-191 B model technique proved successfull especially in model size (1:10) and design. Intake blocking as in the VAK-191 B depends on aircraft layout, normally intake effects are measured seperately.

Great accuracy is necessary for model design, with complete knowledge of jet efflux produced. Provision should be made for variable jet turbulence with vortex generators ets. in the nozzle exit. The low turbulent jet condition requires a large air chamber to allow homogeneous flow to the nozzles. Valve tapped ducts for seperate nozzle air flow should be used.

Referring to flight test techniques there is hardly any difference in data quality in the various methods used. To avoid velocity ratio fluctuations, the thrust should be kept constant within a short time interval, resulting in step down throttle pulse input methods for data evaluation. The disadvantages of these methods are:

- rapid thrust alteration leads to inaccuracy and failures in thrust calculation
- attitude stabilization is difficult after dynamic thrust alteration
- data information is limited to few height inputs per flight

On the other hand a more steady flight with a lot of small time intervals of aircraft stabilization produces good results. This method was preferred for test evaluation and is proposed for future flight testing on VTOL-aircraft.

8.4 Improved Instrumentation

The basic instrumentation of VAK model tests was sufficient, although further equipment will be necessary to extend measurements on jet quality. The aim is to measure jet turbulence as reference for the jet mixing intensity and this necessitates the measurement of jet intermittancy in the neighbourhood of the jet boundary with, for instance, a hot wire instrument.

For flight tests the jet-induced effects call for exact measurements of velocity and thrust. Velocity is checked and corrected in the low speed region by different methods, measurement of thrust, however, is insure as its calculation is based on compressor speed of rotation, intake temperature and engine characteristics. A more exact thrust determination can be obtained by measurement of engine exit characteristics. This method is proposed for future flight tests.

9. REFERENCES

1. Williams, J., Wood, M.N., "Aerodynamic Interference Effects with Jet Lift Schemes on V/STOL Aircraft at Forward Speeds", AGARDograph 103, Par 2, 1965
2. Williams, J., Wood, M.N., "Aerodynamic Interference Effects with Jet Lift V/STCL Aircraft under Static and Forward-Speed Conditions", Zeitschrift für Flugwissenschaften, Juli 67
3. Kuhn, R.E., "NASA Research on the Aerodynamics of Jet VTOL Engine Installations", AGARDograph 103, Part 2, 1965
4. Vogler, R.D., "Interference Effects of Single and Multiple Round or Slotted Jets on a VTOL Model in Transition", NASA TN D-2380, 1064.
5. Vogler, R.D., "Ground Effects on Single and Multiple Jet VTOL Models at Transition Speeds over Stationary and Moving Ground Planes", NASA TND-3213, 1966
6. Otis, J.H.Jr., "Induced Interference Effects on a Four-Jet VTOL Configuration with Various Wing Planforms in the Transition Speed Range", NASA TN D-1400, 1962.
7. Chinn, H.W.," Results of Flight Tests on the Short SC1 VTOL Research Aircraft with Particular Reference to Handling Qualities in the Hover and Transition", AGARD Report 527, 1966
8. G. Krenz, J. Barche, "Jet Influence on V/STOL-Aircraft in the Transitional and High Speed Flight Regime", AGARD Conference Proceedings No. 27, 1967

Fig.1 VAK 191 B during Vertical Take Off

TEST TECHNIC	A/C PRECONDITIONS	PILOT INPUT	A/C REACTION
TAKE OFF	ME, LE } idle σ 45 deg ϑ pre-selection	ME, LE } full power σ 80÷100 deg	H increased IGE → OGE
HOVERING / STO (OGE)	increasing height IGE→OGE	ME, LE } reduce thrust σ } adjust as ϑ } required	A/C OGE stabilisation
LANDING	hovering OGE or retransition	ME, LE } constant thrust power setting σ, ϑ } pre-selected v constant	A/C constant rate of descent OGE variable rate of descent IGE
HOVERING / SL (IGE)	hovering OGE	ME, LE thrust for const. height steps	A/C stab. in different heights IGE

Fig.2 Flight test objectives

TEST TECHNIC	A/C PRECONDITIONS	PILOT INPUT	A/C REACTION
THROTTLE PULSE INPUT	A/C steady jet-borne flight condition v 0÷40 kts	ME, LE } throttle pulse input (+/-)	A/C climb / descent OGE
STEP DOWN METHOD	A/C steady flight condition v 20÷80 kts	ME, LE } throttle manipulation for const. H steps	A/C quasi stabilized at const. heights IGE
TRANSITION	ME, LE } as required σ } constant v 120÷180 kts	ϑ input (+/-)	v decreased increased
WING BORNE FLIGHT	A/C steady level flight	v, α, σ } selected ME thrust adjusted for steady level flight at selected flight condition	A/C stabilized in different configurations at different flight conditions.

Fig.3 Flight test techniques

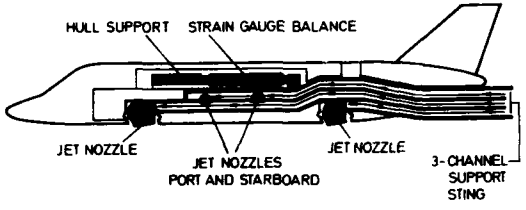

Fig.4 Wind tunnel model special designed for engine efflux interference tests

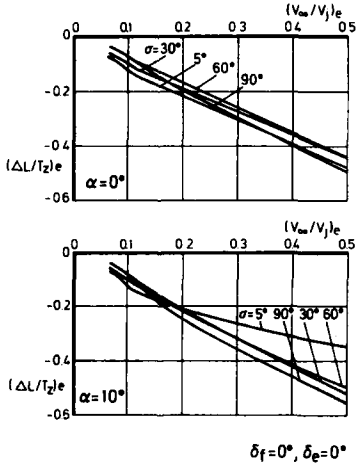

Fig.5 Jet induced lift loss out, of ground effect obtained form model tests

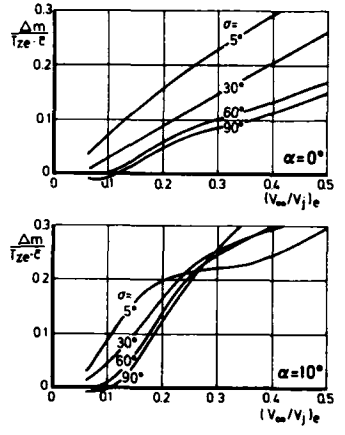

Fig.6 Jet induced pitching moments corresponding to the lift loss shown in fig. 5

Flight-Technic		Number of Flights	Parameter Range σ (deg)	Parameter Range v (kts)
IGE	Take-off	31	85 — 100	0 — 66
	Landing	31	90 — 100	0 — 68
	Step down	5	87 — 100	0 — 40
OGE	Hovering	5	90 — 100	0 — 10
	Transition	4	29 — 100	20 — 200
	Wing-Borne	5	9	220 — 310

LANDING

TAKE OFF

Fig.7 Evaluated flight tests

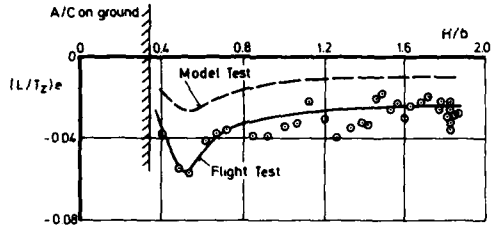

Fig.8 Jet induced lift loss as function of ground clearance for vertical landing with $\sigma = 100^{\circ}$ nozzle swivel angle

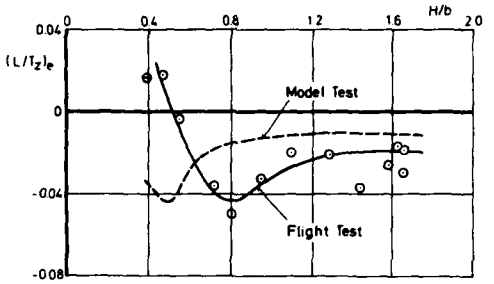

Fig.11 Jet induced lift loss as a function of ground clearance for vertical take-off with $\sigma = 90^{\circ}$ nozzle swivel angle

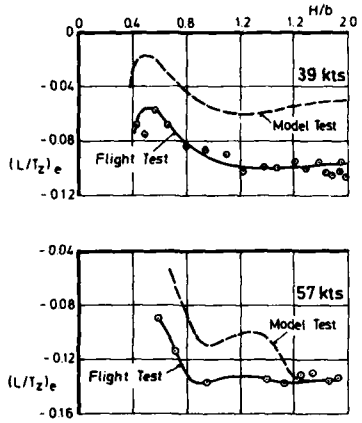

Fig.9 Jet induced lift loss as a function of ground clearance for short landing with $\sigma = 90^{\circ}$ nozzle swivel angle and forward speeds of 39 and 57 kts

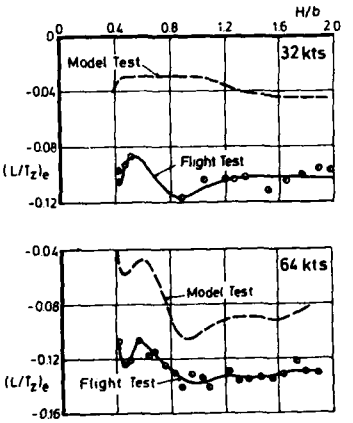

Fig.12 Jet induced lift loss as a function of ground clearance for short take-off with $\sigma = 90^{\circ}$ swivel angle and speeds of 32 and 64 kts

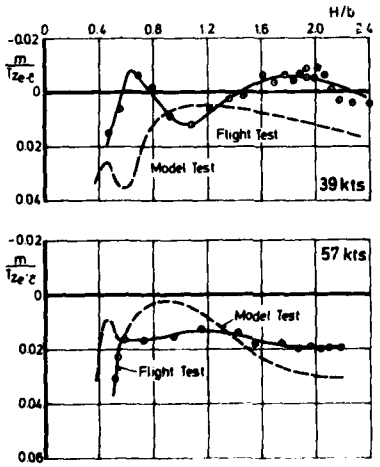

Fig.10 Jet induced pitching moments corresponding to the lift losses shown in fig. 9

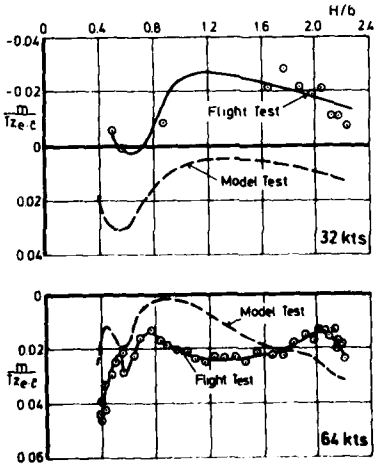

Fig.13 Jet induced pitching moments corresponding to the liftlosses shown in fig. 12

TAKE OFF

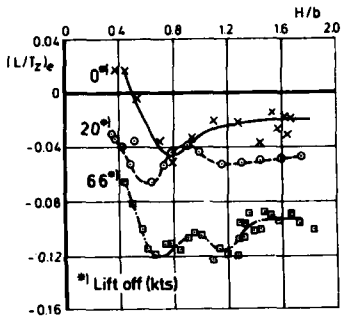

Fig.14 Effect of forward speed in ground effect on jet induced lift loss for take-off with $\sigma = 90^{\circ}$ nozzle swivel angle

TRANSITION

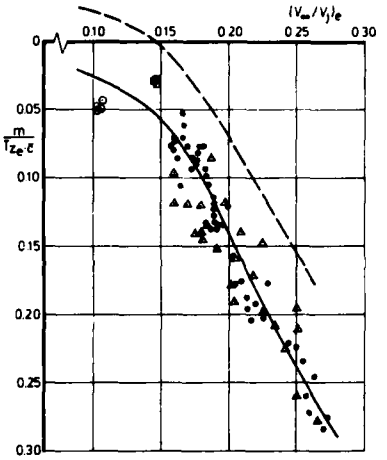

Fig.17 Effect of forward speed out of ground effect on jet induced pitching moments with $\sigma = 80^{\circ}$ nozzle swivel angle

TRANSITION

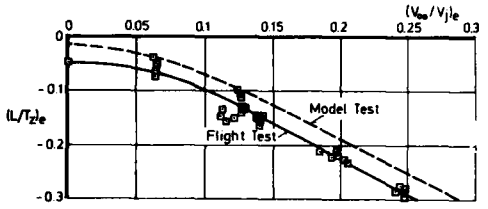

Fig.15 Effect of forward speed out of ground effect on jet induced lift loss with $\sigma = 100,5^{\circ}$ swivel angle

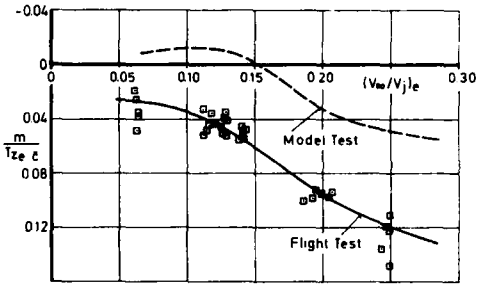

Fig.18 Effect of forward speed out of ground effect on jet induced pitching moments with $\sigma = 100,5^{\circ}$ nozzle swivel angle

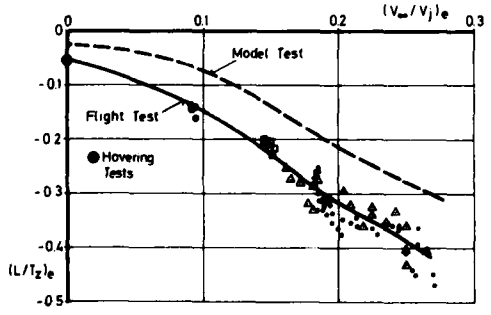

Fig.16 Effect of forward speed out of ground effect on jet induced lift loss with $\sigma = 80^{\circ}$ nozzle swivel angle

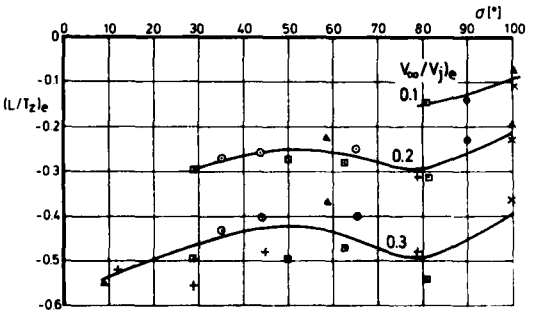

Fig.19 Effect of nozzle swivel angle on jet induced lift loss at various forward speeds out of ground effect

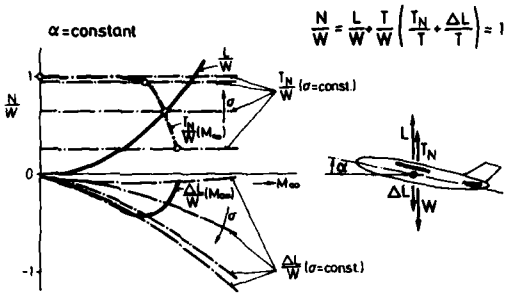

Fig.20 Development of vertical force components from jetborne to wingborne flight derived from wind tunnel tests

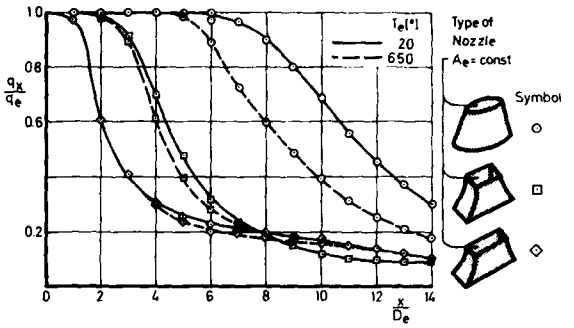

Fig.23 Effect of nozzle exit type on jet decay

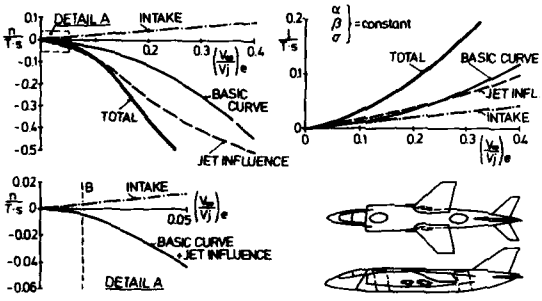

Fig.21 Development of yawing and rolling moments as function of forward speed derived from wind tunnel tests

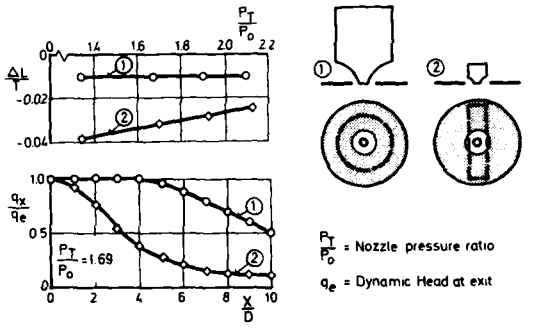

Fig.24 Connection between jet decay and jet induced lift loss

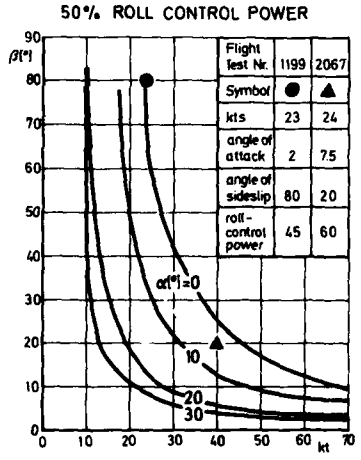

Fig.22 Boundaries of steady sideslip flight conditions estimated for the use of 50% roll control power compared with flight test results

Thrust Augmenting Ejectors:
A Review of the Application of Jet Mechanics to V/STOL Aircraft Propulsion

by

Brian Quinn
President
Aeronautical Research Associates of Princeton, Inc.
P.O. Box 2229, 50 Washington Road
Princeton, New Jersey 08540
USA

SUMMARY

This paper reviews the fundamental role played by the fluid dynamics of jets within thrust augmenting ejectors that are designed as propulsive units for V/STOL aircraft. It begins with a general discussion that deals with the question of energy transfer efficiency and its impact on the production of thrust. It explains why propellor-like devices more effectively convert available energy to thrust and cautions that overall ejector performance is very sensitive to losses sustained by individual components. Stipulating that the most important loss mechanism is incomplete mixing between the ejector's primary and entrained streams, the paper then reviews an experimental data base that provides insight into interactions between turbulent mixing and other factors and also provides direction toward improving mixing and ejector performance. The paper contrasts free mixing and mixing in a confined environment and concludes that the development of theoretical methods that successfully predict the performance of V/STOL ejectors must await the results of new experiments that measure turbulence intensities and Reynolds stresses in confined regions.

NOMENCLATURE

A	cross sectional area
$\bar{C}_L$	mean lift coefficient on blade, Equation (1)
D	diameter of axisymmetric duct or breadth of "two-dimensional" channel
F_{isen}	thrust produced by isentropic expansion
H	enthalpy or half-width of "two dimensional" channel
L	length of mixing duct
M	Mach number or momentum flux, Equation (7) et seq.
m	M/U^2, Equation (9)
$\dot{m}$	mass flow
P,p	mean pressure, pressure at a point
$\Delta q/q_{IDEAL}$	measure of duct-diffuser losses in an ejector
S	frequency x nozzle diameter/jet velocity
T	thrust
U	mass averaged velocity in duct
u,v,w	components of velocity at a point
V	mean velocity
x,y,z	coordinates in direction (x) and transverse (y,z) to flow
$Y_{1/2}$	half-velocity width of jet
β	flow skewness, Equation (4)
ε	drag-lift coefficient, Equation (1)
η_N	primary nozzle thrust efficiency, T/F_{isen}
θ	primary stagnation temperature/ambient temperature
ζ	inlet loss coefficient
π	primary stagnation pressure/ambient pressure
ρ	density
σ	solidity, Equation (1)
τ_{ij}	shear stress
φ	T/F_{isen}
ψ	$\theta^{-1/2}\ \dot{m}/\dot{m}_0$

Subscripts

0,1,2,3	relating to primary, secondary, fully mixed, diffuser exit

1. INTRODUCTION

The fluid dynamics of jets plays a key role in several technologies applicable to V/STOL aircraft. Propulsion is one of these and has proven especially troublesome to designers because of the great difference in power required for cruise, on the one hand, and for vertical takeoff, on the other. One proposed solution to this problem has been to use the energetic exhaust gases from engines designed to certain cruise specifications by ducting them to ejectors which simultaneously "augment" and rotate the direction of the engine's thrust vector.

Ejectors are purely pneumatic devices but have factors in common, as well as in contrast, with such mechanical devices as propellors and rotors. Like the mechanical devices, ejectors transfer available energy and impart motion to large quantities of ambient air. In both cases, the momentum of the resultant motion is equivalent to the thrust produced by either device. Unlike the mechanical systems which transfer energy through normal stresses acting on the solid surfaces of rotating blades, conventional ejectors transfer energy through shear stresses acting on the fluid surfaces of jets. Opponents of ejectors correctly point out that the latter mechanism is inherently less efficient than the former while proponents recite a littany of advantages that accrue to ejectors and question if efficiency is really a germane issue.

This paper begins with a general discussion that deals with the question of energy transfer efficiency and its impact on the production of thrust. It quantifies the degree to which propellor-like devices more effectively produce thrust from available energy than do ejectors, but suggests that the difference in effectiveness is not so large as to warrant altogether discounting ejectors. There then follows a discussion of the role played by the fluid dynamics of jets within ejectors. Within this framework, recent experiments demonstrate how high primary temperatures and pressures impact ejector performance through their effects on turbulent mixing. Curiously, these temperature effects are either favorable or not, accordingly, as the ejector is either short or long. The experiments also explain why most theoretical analyses fail to predict the favorable effect of temperature. On the other hand, an example illustrates how one analysis provides *a posteriori* assistance in explaining an unexpected experimental result, very rapid mixing associated with acoustic resonance. Accelerating mixing beyond the rate associated with normal turbulent processes is key to the successful application of ejectors to V/STOL aircraft. The paper discusses several schemes for accelerating turbulent mixing before reviewing what is known of mixing in a confined environment. Following a discussion of methods available to analyze ejector flows, the last section summarizes the paper's principal conclusions.

2. THE PRODUCTION OF THRUST

Every ejector consists of one or more primary nozzles which discharge jets of high energy fluid into a duct. It also has an inlet which directs a lower energy secondary stream of fluid into the same duct where the two streams mix. An adjunct to mixing the primary jet and the secondary stream in a confined region is a reduction in mean pressure from ambient which, in turn, maintains the flow of the secondary stream through the inlet. Under normal circumstances, the secondary flow rate increases when a diffuser is used to raise the pressure of the mixing streams to the level at the ejector's exhaust plane. References 1, 2 and 3 provide explicit descriptions of the ejector process.

Expelling fluid through the primary jets produces useful thrust which in a sense characterizes the source of energy. Useful thrust is also produced by the reduced pressures acting on the upstream surfaces of the inlet, and it is this contribution which "augments" the primary propulsive force. The ratio of the force produced by the entire ejector system, F, to the force produced by isentropically expanding the primary mass flow to ambient pressure, $F_{isen} = \dot{m}_0 V_{isen}$, is called the thrust augmentation ratio, φ .

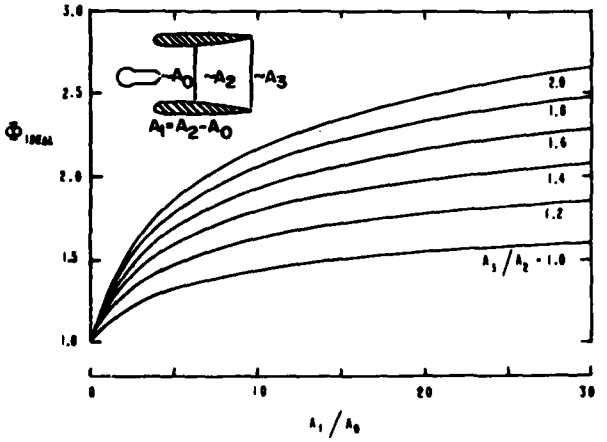

Figure 1. Ideal thrust augmentations for ejectors with constant area mixing tubes.

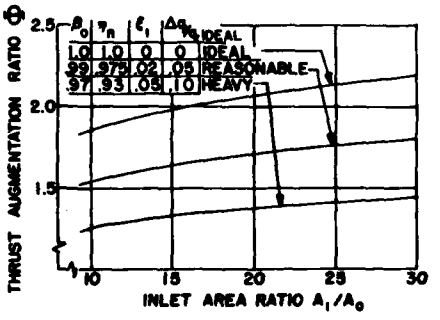

Figure 2. The effect of losses on the thrust augmentation of ejectors. $A_3/A_2 = 1.5$. From Reference 1.

Ideal ejectors transfer energy from the primary jets to the secondary stream in a mixing duct which is maintained either at constant pressure or at constant cross-sectional area. Under these conditions, together with the assumptions that the two incompressible flows completely mix, that there are no pressure gradients normal to the mean flow direction, and that there are no inlet, nozzle or friction losses, one can algebraically solve the equations expressing conservation of mass and momentum within the mixing duct. The results of such a solution for constant area mixing appear in Figure 1 and show that specifying ideal ejector performance requires two, independent geometric parameters. This point deserves emphasis in view of the tendency in recent articles to relate φ to just one parameter, usually A_3/A_0 . Traditionally, one relates performance to the inlet area ratio, A_1/A_0 , and the diffuser area ratio, A_3/A_2 , and increasing each parameter increases performance.

While Figure 1 suggests the potential of ejectors to double the thrust of a prime mover, one must keep in mind the ideal nature of the assumptions underlying the calculation. Earlier papers [1,4] examine

those assumptions and, through control volume methods which allow somewhat more complicated but still algebraic solutions, they assess the effect of nonuniform velocity profiles, nozzle losses, inlet losses and wall friction. Thus, for $A_1/A_0 = 20$, $A_3/A_2 = 1.5$ so $\varphi_{IDEAL} = 2.069$, a five percent increase in either η_N, β_0, or ζ, results in a five percent reduction in φ while a five percent increase in $\Delta q/q_{IDEAL}$ results in a twelve percent reduction in φ. The situation is worse when losses are considered to be acting together, as must be the case in a functioning ejector. This state of affairs, Figure 2, represents a much more reasonable estimate of what might be expected from thrust augmenting ejectors. While a doubling of thrust still appears to be within reach, the calculation shows that achieving such a goal demands extreme caution in identifying and controlling loss mechanisms. If not, ejectors lose their appeal for application to V/STOL aircraft simply because propellors of any variety are better thrust augmentors.

Figure 3 clearly states the case and deserves discussion since one rarely considers the thrust augmentation performance of propellors. By definition, ψ is the ratio of thrust produced by a propulsive device to the thrust produced by an isentropically expanded jet of equivalent energy. Following McCormick's [5] discussion of modified blade element theory, the power required of a propellor producing a thrust, T, is

$$P = \left[1.15 + \frac{3\varepsilon}{4}\left(\frac{12}{\sigma\bar{C}_L}\right)\right]^{1/2}\left[\frac{T^3}{2\rho A_3}\right]^{1/2} \tag{1}$$

where ε is a drag-lift ratio, σ is a solidity, $\bar{C}_L$ is the average lift coefficient along the span of the blade, and A_3 is the area swept by the blade. On the other hand, the jet from an ideal nozzle produces thrust

$$F_{isen} = \rho A_0 V_{isen}^2$$

with kinetic energy flux

$$P = \frac{1}{2}\rho A_0 V_{isen}^3$$

$$= \frac{1}{2}\left(F_{isen}^3/\rho A_0\right)^{1/2} \tag{2}$$

Equating (1) and (2) eventually gives a relation for the system's thrust augmentation ratio

$$\varphi = \frac{T}{F_{isen}} = \left(\frac{A_3}{A_0}\right)^{1/3}\left[\frac{0.707}{1.15 + (3\varepsilon/4)(12/\sigma\bar{C}_L)^{1/2}}\right]^{2/3} \tag{3}$$

Typically, $0.05 \leq \sigma \leq 0.12$ for helicopter rotors, $0.2 \leq \sigma \leq 0.4$ for propellors, and $2 \leq \sigma \leq 5$ for ducted fans. These values, together with $\varepsilon = 0.03$ and $\bar{C}_L = 0.5$, give the associated regions in Figure 3. The region labeled "ejectors" in the figure represents the envelope of performance of all ejectors with the "reasonable" losses discussed in connection with Figure 2. The performance curve of any particular ejector (defined, for example by its inlet area ratio A_1/A_0) with "reasonable" losses rests within this region. Three examples are given, $A_1/A_0 = 10$, 16, and 25. It is clear from these results that quite apart from performance, designers have other factors in mind when they choose ejectors for V/STOL aircraft propulsion systems. These factors are discussed in a number of earlier papers [1,2,3] and include favorable flight-lift characteristics, low downwash velocities and temperatures in hover, low noise production, a general advantage due to the lack of rotating machinery and circular planforms, and compatability with modern turbine engines.

Propellor devices and ejectors all produce thrust by transferring energy into a stream whose momentum flux represents the force produced by the device. In view of Figure 3, the essential difference between the two systems is that propellors impart more momentum per unit of available energy. The reason for this is that propellors transfer energy through normal stresses while ejectors rely on shear stresses for energy transfer. Several years ago it was thought that the use of high temperature and moderately high pressure engine effluents in the primary flow would further degrade energy transfer efficiency in ejectors. A number of independent calculations [6,7,8] support this concern. Figure 4, for example, was adapted from Reference 9 and clearly predicts the adverse effect on thrust augmentation of increasing the temperature of the primary gas of an inlet area ratio 15 ejector operating at a primary pressure ratio of 2.5. However, this calculation and, to the best of our knowledge, all other control volume methods that include the effects of primary gas temperature and pressure, fail to account for the interaction between such state variables and the heart of the ejector process, turbulent mixing. Even those analyses that attempt to account for friction and other losses through the use of descriptive parameters have no *a priori* means of relating those parameters to state variables. In which case, compressible flow control volume analyses serve only as guidelines to the thermodynamic limits of ejector performance and contrary

to the intention of Figure 4, they can predict neither the performance nor the mechanics of a specific ejector operating under different primary temperatures and pressures. There is, however, a set of experimental data that sheds light on the interplay between the mechanics and the thermodynamics of ejectors.

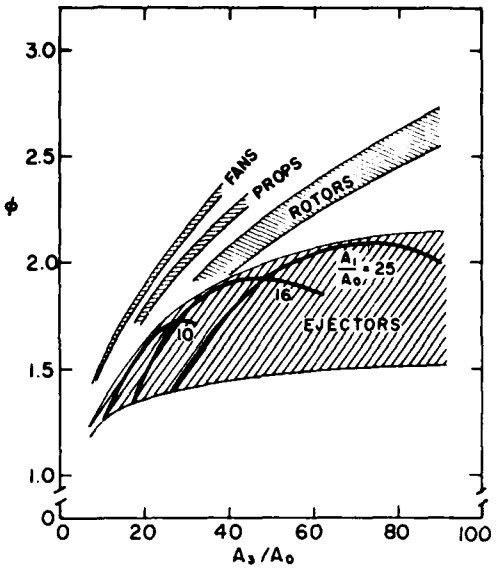

Figure 3. Propellors and similar devices are better thrust augmentors than ejectors, but their swept areas must be circular.

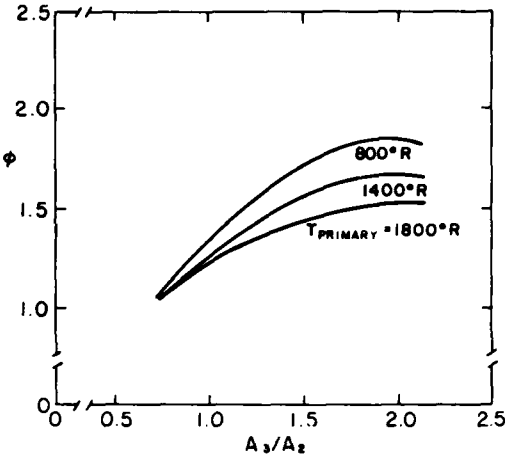

Figure 4. The effect of heating the primary fluid on the performance of an A_1/A_0 = 15 ejector operating at π = 2.5 as computed by the control volume approach of Reference 6. Figure adapted from Reference 9.

3. THE MECHANICS AND THERMODYNAMICS OF NON-IDEAL EJECTORS

References 7, 10, and 11 report experiments with a simple, well calibrated, A_1/A_0 = 25.8 ejector consisting of a convergent primary nozzle and a constant area mixing duct smoothly mated to a bellmouth inlet. Because of this simple configuration, one can see clearly those interactions between primary state variables and performance that are usually overpowered and masked by events arising in diffusers and other components. In each of the experiments, the ejector entrains its secondary air and exhausts its efflux to the atmosphere. Reference 11 reports distributions of the pressure along the wall of the mixing tube and surveys of the temperature and pressure in the ejector's exhaust plane. Primary temperature and pressure ratios vary throughout the ranges $1.0 \leq \theta \leq 2.7$ and $1.7 \leq \pi \leq 6.6$, respectively, while the length-diameter ratio of the mixing duct spans the range $3.5 < L/D < 12.5$. The shapes of the pressure and temperature surveys in the exhaust plane provide a graphic indication of how completely primary and entrained flows mix. These observations are quantified by the skewness ratio, β_3, which is a shape parameter associated with mass and momentum distributions at the exit plane of the ejector, i.e.

$$\beta_3 = \frac{\int \rho u^2 \cdot d(a/A_3)}{\int \rho \cdot d(a/A_3) \cdot \left[\int u \cdot d(a/A_3)\right]^2} \qquad (4)$$

$\beta_3 = 1$ results from the perfectly uniform profiles characteristic of completely mixed flows, whereas $\beta_3 = 1.5$ indicates very scant mixing between primary and secondary streams. Figure 5 presents selective but representative results from Reference 11 and shows the more complete mixing, i.e. a monotonically decreasing β_3, afforded by longer mixing ducts. As a consequence of Figure 5, There would appear to be no appreciable benefit to be gained from increasing L/D beyond eight, although this would not be the case for ejectors with inlet area ratios, A_1/A_0, greater than 25.8. It is also very important to observe in Figure 5 that the two flows more completely mix when the primary stream is hot, and that this effect becomes more pronounced as the length of the mixing duct diminishes. The reason for this is that a hotter flow at a given stagnation pressure expands to a higher velocity, and this gives rise to a more intensive shear layer that more rapidly mixes the attendant jet.

Reference 7 describes experiments in which the mass entrainment performance of the ejector was measured over the same range of primary state variables and length-diameter ratios. Four representative sets of data appear in Figure 6 which support the contention that mixing is complete and performance maximizes at $L/D \approx 8$ for this ejector. Increasing the mixing duct length beyond eight diameters actually degrades performance because the velocities at the edge of the boundary layer are higher when the flow is well mixed, and the resulting friction losses become more pronounced. Apart from this, the data at $L/D > 8$ appear to have reached levels consistent with thermodynamic limits, that is, increasing pressure and temperature of the primary flow reduces performance. On the other hand, where the two streams have not mixed well, say $L/D < 5$, the data also show that the favorable mixing effect of higher temperature compensates the adverse thermodynamic effect of higher temperature. So much so, in fact, that at the higher pressure, $\pi = 3.1$, raising the primary flow stagnation temperature from $\theta = 1.0$ to $\theta = 2.7$ actually increases the performance of the ejector.

AD-A113 907 ADVISORY GROUP FOR AEROSPACE RESEARCH AND DEVELOPMENT--ETC F/G 20/4
FLUID DYNAMICS OF JETS WITH APPLICATIONS TO V/STOL.(U)
JAN 82
UNCLASSIFIED AGARD-CP-308 NL

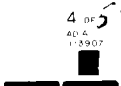

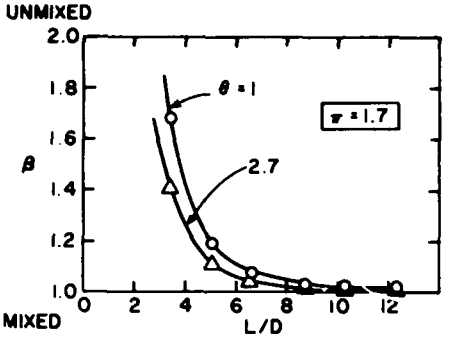

Figure 5. Flow skewness at the end of a family of constant area mixing tube ejectors. A_1/A_o = 25.8 . Primary and entrained streams mix faster (decreasing β) when the primary stream is heated. From Reference 11.

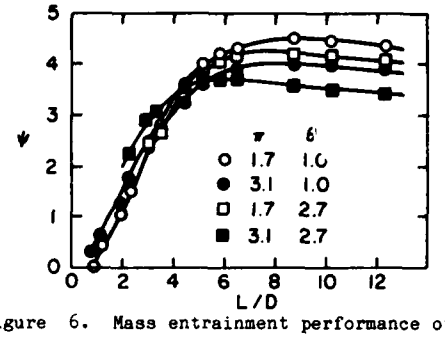

Figure 6. Mass entrainment performance of a family of constant area mixing tube ejectors, A_1/A_o = 25.8 , operating at various primary pressure and temperature ratios. From Reference 7.

Finally, Figure 7 shows representative thrust augmentation measurements obtained under the conditions θ = 1 , 1.7 $\leq \pi \leq$ 6.6, and 0 $\leq$ L/D $\leq$ 11.2 as extracted from Reference 11. As in the preceeding figure, performance increases with the length of the duct, achieves a maximum as β_3 approaches unity at L/D $\approx$ 8, and thereafter decreases as friction losses take their toll. These data are especially interesting because in marked contrast to the predictions of most analyses, the performance of this simple ejector actually improves over the entire range of L/D as the pressure ratio increases from 1.7 to 3.1. The reason for this apparent conflict is that Φ depends linearly on the primary nozzle's thrust efficiency, η_N (but it can be shown that Ψ is almost independent of η_N) and for this particular nozzle, η_N = 0.91 at π = 1.7, whereas η_N = 0.955 at π = 3.1 . These efficiencies, of course, are the values of Φ in Figure 7 with the mixing duct removed from the ejector, i.e., L/D = 0. The performance of the ejector at π = 3.8 is quite another matter. While the nozzle efficiency differs little from that at π = 3.1 , the data obtained at the higher pressure yield a higher level of performance so long as L/D remains less than 6. Thereafter, performance is better at π = 3.1. A negligible difference in nozzle efficiency does not explain this observation but an increase in the rate of turbulent mixing does. Thus, with accelerated mixing between primary and entrained streams, short ejectors show an improvement in performance. On the other hand, long ejectors show a reduction in performance because accelerated mixing quickly produces a more uniform profile within the duct which, in turn, leads to higher velocities on the

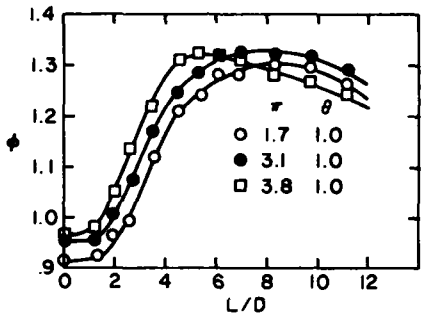

Figure 7. Thrust augmentation performance of a family of constant area mixing tube ejectors, A_1/A_o = 25.8 , operating at the indicated primary pressure ratios. The nozzle's thrust efficiency at these pressure ratios is given by the data at L/D = 0. From Reference 11.

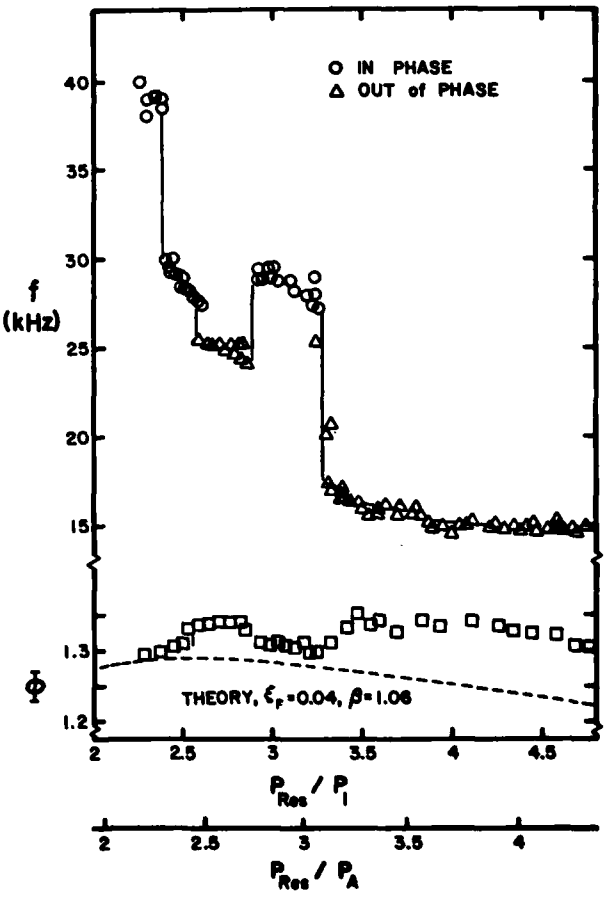

Figure 8. Direct association of improved mixing and higher thrust augmentation with the existence of axisymmetric screech tone resonance in a constant area mixing tube ejector, A_1/A_o = 25.8 , θ = 1.0. From Reference 11.

walls of the duct and larger friction losses. To explain the source of accelerated mixing at x = 3.8 , it is reasonable to look for mechanisms that alter eddy size or structure. One such mechanism is the resonant coupling of transverse acoustic waves to screech tones.

It is well known (Reference 12 and other references cited at Reference 11) that underexpanded jets from convergent nozzles emit loud, usually high pitched tones. These are screech tones which derive from the intensification and phase ordering of eddies in the jet's shear layer by pressure waves resulting from the interaction of preceeding eddies with shock cells in the jet. Ordering occurs both in the direction of the flow and circumferentially around the jet. Two circumferential modes have been observed: symmetric, with signals at diametrically opposed locations in phase and asymetric, with opposed locations also opposed in phase. The experiments of Reference 11 indicate that screech tones from jets issuing into ducts selectively tune in frequency and phase to certain resonant transverse acoustic modes of the duct. Moreover, the rate at which the jet mixes with its surroundings is considerably faster in the asymmetric modes. Figure 8 clearly associates the abrupt changes in screech frequency with equally abrupt changes in the performance of an L/D = 5.1 ejector. The dashed line, a calculation that follows the procedure outlined in the Appendix of Reference 7, serves only as a line of reference and describes performance under conditions of constant friction factor and flow skewness. Departure of the data from the calculation underscores that neither the friction factor nor the skewness ratio remain constant and, in fact, change with a favorable impact on performance whenever the mixing mode becomes asymmetric. Pressure and temperature surveys [7] taken at the exhaust plane confirm the accelerated mixing associated with transverse modes.

The experiments discussed in connection with Figures 5, 6, and 7 permit a reasonable response to the question "what are the effect of elevated temperatures and pressures on ejector performance?" The answer, quite simply, depends somewhat upon the reaction of the ejector's components to temperature and pressure but mostly upon whether or not the ejector is long enough to assure nearly complete mixing. Insofar as ejectors viewed as lift and thrust augmentors for V/STOL aircraft are rather short, it would seem that the effects of elevated primary temperatures are at worst negligible and at best favorable. Aside from the influence elevated pressures have on component efficiencies (which most likely relate to Reynolds number), experiments suggest a negligible effect of pressure on the performance of short ejectors unless, of course, through some combination of events, elevated pressures trigger mechanisms that accelerate mixing. In this case, higher primary pressures improve the performance of short ejectors. In the general case, all practical ejectors show improvements in performance when means are found to accelerate mixing.

4. ACCELERATED MIXING

The very short overall lengths typically imposed on ejectors by V/STOL applications encourage designers to decrease the length required to transfer energy from primary to secondary streams. The most obvious solution to this design problem looks at mixing as a surface or interface phenomenon and consists of injecting the primary flow through a number of nozzles rather than just one nozzle. Unfortunately, the benefits from this solution diminish rapidly because inlet lossses due to skin friction increase along with the increasing number of primary nozzles. A related solution provides the primary jet with an increased mixing surface by expelling it through a nozzle with a number of lobes or geometric irregularities. These too tend to promote inlet losses due to friction, or even local separation, in the entrained streams flowing over their external surfaces. The complete solution to the problem of reducing the length of ejectors without sacrificing performance includes devising means to accelerate mixing between the primary and entrained streams. The literature reports a number of techniques that are operationally different but conceptually similar in that they somehow alter the large scale turbulent structure of shear layers.

Such structures, or eddies, in a free planar jet may be imagined as irregular, fluid logs with a diameter approximately half the thickness of the jet rolling in the direction of flow around axes that span the breadth of the jet. They are characterized by length and velocity scales equal to the jet thickness and the velocity difference between the centerline of the jet and its edge. The real free jet is not nearly so anisotropic and includes eddys with axes normal to the larger and more intense log-like eddies. The latter, however, are the agents principally responsible for mixing the planar jet with its surroundings. Hypermixing nozzles [1,4,13,14] accelerate mixing by providing the jet with a second set of intense eddies which, along with the log-like eddies, mix the jet with its surroundings. This is accomplished by dividing a planar nozzle into relatively small spanwise segments. Adjacent segments alternately incline the jet slightly from its mean flow direction, thereby assigning length (the segment's dimension) and velocity (twice the inclination angle) scales to eddies with axes aligned with the mean flow direction. Figure 9 contrasts the development of planar and hypermixing free jets. Initially the streamwise eddies of the hypermixing jet nearly double the mixing rate, but as they grow in their downstream development, a destructive interference occurs, and the hypermixing jet's rate of spreading, $dY_{1/2}/dx$, returns to that of the planar jet. In References 13 and 14, Bevilaqua discusses hypermixing jets in some detail.

One very attractive feature of hypermixing jets is their efficiency. Most hypermixing nozzles develop thrust efficiencies around 96 percent. This is around two percent less than the thrust efficiiency of plain convergent nozzles and is a small price to pay for doubling the rate of mixing.

While the literature reports no direct measurements, acoustic stimulation of jets also appears to be an efficient means of accelerating mixing. Sato's [15] study of stability and transition of a free planar jet, for example, provides early indication that external sound increases the width of the mean flow profile. The effect, he reports, is consistently observed at two different sound frequencies at around 38 db above background noise. Roffman and Toda [16] also report experiments on planar jets that are most sensitive to sound at acoustic Strouhal numbers (based on nozzle slot width), S, of 0.14. They present mean flow data at Strouhal numbers of 0.0 (no sound), 0.109 and 0.055 and these signals clearly have a marked effect on jet spreading. Fifteen slot widths downstream, for example, the jet bathed in sound at S = 0.109 has a mean half-velocity width more than 40 percent wider than a similar jet with no applied sound. Other investigators observe like effects with axisymmetric jets. Becker and Massaro [17] claim that at a certain critical frequency, the jet flares near its root and "the initial angle of spread as

much as doubled...". Hill [18] describes the "Whistler", a nozzle that develops a controllable, self-excited tone. Oscillating at a Strouhal number of 0.315, the mean half-velocity width of the jet exceeds that of a non-oscillating jet by 50 percent at ten nozzle diameters downstream.

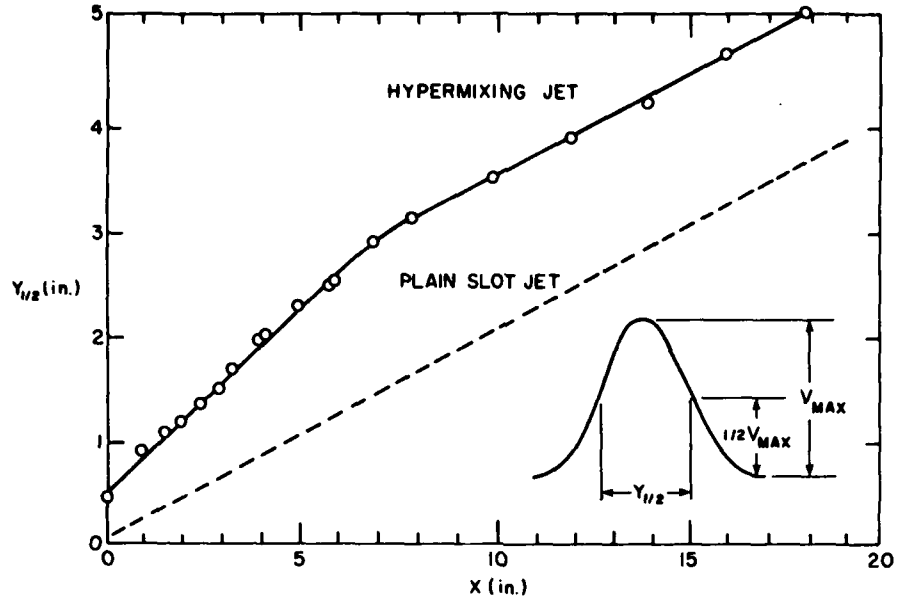

Figure 9. Accelerated spreading and mixing provided by streamwise vortices (0 < x < 7 inches) in a hypermixing free jet.

Similar effects occur at relatively high subsonic jet Mach numbers. Over the range $0.15 \leq M \leq 0.9$, Borisov and Gynkina [19] describe measurements of jets subject to intense acoustic tones focused at the nozzle's exit plane. Typical results showing the increased half-velocity widths of free jets subject to acoustic radiation appear in Figure 10, while Figure 11 indicates the dependence of the jet's width on Strouhal number. There are two peaks in this curve, indicating that the jet is sensitive to acoustic stimulation at a fundamental tone (approximately equal to Sato's S = 0.24 for symmetric disturbances in a planar jet) and its harmonic. A very thorough investigation of the response of axisymmetric jets to acoustic signals is described by Crow and Champagne [20]. Here, too, sensitivity of the jet's mean flow properties to stimulation at a fundamental tone (S = 0.3) and its harmonic (S = 0.6) is evident. Some of their results appear in Figure 12 and curiously suggest a moderately faster decay rate of the centerline velocity for the harmonic stimulation. Fiedler and Kroschelt's [21] results add to the data in support of enhanced jet mixing in the presence of acoustic stimulation. In addition, their work expressly relates the enhancement to an intensification of the large scale eddies in the mixing layer.

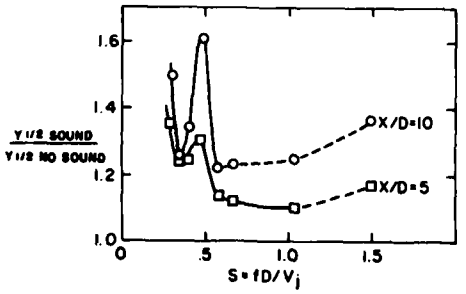

Figure 10. Relative half-width at two downstream locations of an axisymmetric jet subject to acoustic radiation at various frequencies. From Reference 19.

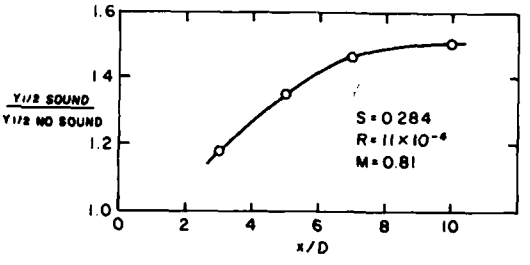

Figure 11. Relative half width development of an axisymmetric jet subject to acoustic radiation. From Reference 19.

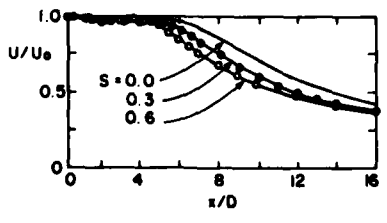

Figure 12. Decay of maximum velocity in an axisymmetric jet subject to acoustic radiation. From Reference 20.

Glass [22] observes very rapid spreading from highly underexpanded free jets (stagnation pressure ratios around 5 to 15) whenever disturbances impinge on shock cells and create self-sustained screech tones. It is exactly this phenomenon [11] operating in a confined flow environment that brings about the remarkable improvement in the performance of compact ejectors which we discussed in preceeding paragraphs: resonance within the mixing duct intensifies shear layer eddies and accelerates mixing.

It is unlikely however, that resonant stimulation of the primary jet is of importance in practical ejector applications. The necessary condition is that a resonant frequency of the mixing tube differs little from a sensitive frequency of the jet. Restricting attention to planar configurations, this condition may be written as follows:

$$\frac{f_{res}\, D}{a} = \frac{f_{jet}\, t}{V_{jet}} \quad \frac{D}{t} \quad \frac{V_{jet}}{a} \tag{5}$$

Taking $k_n = (f_{res}D/a) = (n/2)$ and $S_m = (f_{jet}t/V_{jet}) = m/4$, where n and m are integers, the condition for resonant stimulation of mixing in an ejector becomes, roughly,

$$\frac{A_1}{A_0} = \frac{2n}{m} \quad \frac{1}{M_{jet}} - 1 \tag{6}$$

and it is easy to show by substitution that no reasonably small integers n and m can balance this equation within such practical limits as $M_{jet} \approx 0.6$ and $20 \leq (A_1/A_0) \leq 7.5$. It is necessary to find other means than duct resonance if one wishes to accelerate mixing through acoustic stimulation in practical applications.

One step beyond stimulating jets with the small disturbances of acoustic waves is exciting large disturbances in unsteady jets. Techniques for creating the unsteady jet appear to fall into two categories depending on whether the jet issues from axisymmetric or planar nozzles. In the axisymmetric case, the jets are pulsed by some technique that renders the driving pressure a function of time. Curtet and Girard's [23] photographs show that pulsed jets consist of vortex rings surrounding the body of the jet, while Binder and Favre-Marinet [24] discuss the sensitivity of the spreading and decay of pulsed jets to the amplitude and frequency of pulsation. Spreading increases with frequency up to a saturation frequency, afterwhich it is no longer sensitive. Even after saturation, however, the jet remains sensitive to amplitude and spreads faster as amplitude increases. Bremhorst and Harch [25] present data at two frequencies, 10 and 25 Hz, and also show mixing increasing with frequency. They conclude that the mean velocity properties of steady and pulsed jets are functionally equivalent, the effect of pulsation being to move the virtual origin of the jet far upstream. Entrainment substantially increases with pulsation. In fact, they measure four times the entrainment of a steady jet at eleven nozzle diameters downstream.

Viets [26] discusses experiments with aspect ratio 10 planar nozzles that produce unsteady jets through fluidic means. These jets spread 2 to 5 times faster than steady jets although usually at a large (20-30 %) cost in thrust efficiency. Moreover, to accommodate the fluidic coupling tubes, such nozzles presently require a bulk that would seriously degrade the inlet performance of any ejector. However, this fault must be considered as amenable to creative design techniques and the nozzles not discarded as a viable means to accelerate mixing and reduce the lengths ejectors need for high performance.

5. CONFINED MIXING

Mixing jets in a confined environment imposes complications that are absent in an unbounded environment. Free jet mixing occurs at constant pressure, and the flux of momentum at any stage of the jet's development remains invariant. The jet spreads almost linearly and beyond the potential core, roughly ten nozzle dimensions from the nozzle's exit plane, the peak velocity in the jet decays according to an inverse power of distance. Also beyond the potential core, the mean properties of the jet become nearly self-preserving and scale with a local characteristic dimension of the jet, although Wygnanski and Fiedler's [27] measurements suggest that true self-preservation in an axisymmetric jet develops not less than 70 diameters downstream.

Confined mixing usually occurs in a strong adverse pressure gradient in the flow direction. The curvature of the flow near the inlets of certain practical ejectors may also produce transverse pressure gradients that can become quite large. Tailoring the cross-sectional area of the duct may also produce zero or favorable pressure gradients in the flow direction, but such configurations have little bearing on V/STOL applications wherein one seeks to increase pressure as rapidly as possible. In any event, mixing in a confined region conserves total impulse (momentum plus pressure) rather than momentum flux. In addition and in contrast to the free jet whose mass continuously increases with its development, the confined jet develops in such a way that the mass flowing through any section of the mixing tube remains constant. Curtet [28] defines a similitude parameter, m, that expresses the constancy of both total impulse and mass flowing within a constant area mixing duct. Thus, for an ejector that entrains and exhausts air to the atmosphere, and with

$$M = V_1^2 \frac{A_1}{A_2} + V_0^2 \frac{A_0}{A_2} - \frac{1}{2} V_1^2 \tag{7}$$

and

$$\overline{U} = V_0 \frac{A_1}{A_2} + V_1 \frac{A_1}{A_2} \tag{8}$$

Curtet's parameter becomes

$$m = \frac{M}{\overline{U}^2} - \frac{1}{2} \tag{9}$$

It can be shown that for high performance ejectors

$$\frac{M}{\overline{U}^2} \approx 1 - \frac{P_\infty - P_2}{\rho \overline{U}^2} \tag{10}$$

where $(p_\infty - p_2)$ is the pressure rise through a diffuser. Thus, ideally,

$$m = \frac{1}{2} \left(\frac{A_2}{A_3}\right)^2 \tag{11}$$

and values of m of interest to the thrust augmentation problem lie within the range $0.15 \leq m \leq 0.6$. Curtet's [28] experiments with two-dimensional confined jets amply cover this range and provide the foundation necessary for understanding mixing in a constant area duct. Some of his results appear in Figure 13 which shows the decay of velocity along the centerline of the duct. The data bear a resemblance to the decay of maximum velocity in free jets, but there are also some marked differences at certain downstream locations. Hill [29] classifies these locations as the four distinct regions sketched in Figure 14. These are:

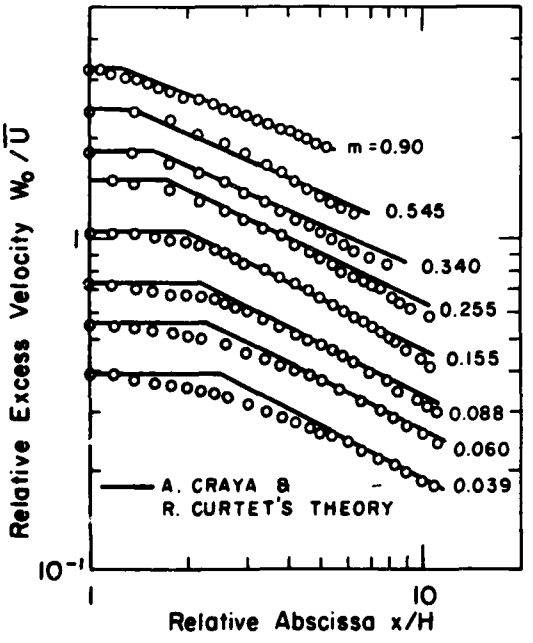

Figure 13. Decay of the excess velocity in a jet mixing with a secondary stream in a two-dimensional duct of width 2H at several of Curtet's similarity parameters, m . From Reference 28.

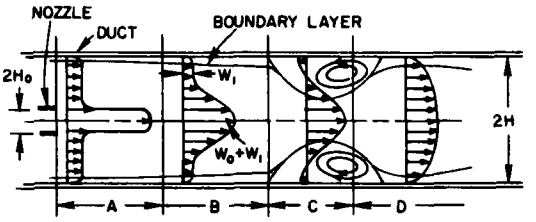

Figure 14. Schematic diagram of jet mixing in a constant area duct. Adapted from Reference 29.

(A) A potential core region, akin to the initial region of a free jet in which the central irrotational part of the jet maintains its Bernoulli constant. However, in contrast to the constant pressure free jet, the pressure is rising so the velocity on the centerline of the jet decreases. This effect is quite pronounced in Curtet's [28] data obtained in a two-dimensional duct (Figure 13). In this region, the secondary stream remains potential beyond the wall boundary layer and also decreases in velocity downstream due to the rising pressure. Curtet's data suggest that the potential core region ends at a distance L_A given approximately by $L_A/2H \approx 0.645m^{-0.22}$.

(B) A developing region wherein the jet profile assumes a rounded appearance and spreads out toward the boundary layer on the duct's wall. The secondary stream between the boundary layer and the jet remains irrotational. Hill [29] examines the conditions under which such jet profiles might be self-preserving and concludes that $W_1/W_0 \ll 1$ (see Figure 14) is necessary. Typically one expects to find $0.3 \leq W_1/W_0 \leq 0.9$ in high performance ejectors. Apparently (and surprisingly) this range of W_1/W_0 satisfies Hill's condition because Curtet's [28] experiments indicate that "...downstream of the potential core and upstream of the point at which it (the jet) reaches the walls, the curve $W/W_0 = f(y/\ell)$ becomes practically independent of x." ℓ is approximately equal to the half-velocity width of the jet and is defined by $2W_0\ell = \int_H^H W\, dy$. While Curtet's paper contains no profiles that allow the reader to test the accuracy of his claim, Razinsky and Brighton [30] do provide such a figure of data obtained at $W_1/W_0 = 0.5$ in an axisymmetric test rig. In their case, the function $W/W_0 = (1 - \varsigma^{3/2})^2$, where ς = (radial position/jet width), describes well data measured throughout the inner 60% of the jet. Beyond that radial position, data obtained near the potential core lie somewhat above, and data obtained closer to the end of the regime lie somewhat below the function. If one ignores the boundary layers on the duct's walls and assumes the validity of the similarity profile, the skewness factor, Eq. (4), at the end of this region is $\varphi_B = 1.012$ for $m = 0.15$ and $\varphi_B = 1.188$ for $m = 0.6$. The first of these is a respectable value, and increasing the length of the ejector beyond the end of region B gains little in φ. The second value of φ_B urges increasing the length of the mixing tube. To a very rough approximation, the end of region B appears to follow the relation $L_B/2H = 2.35m^{-0.77}$ for two-dimensional ducts.

(C) If the jet entrains all of the secondary stream before spreading to the walls of the duct, a recirculation region develops. Curtet [28] indicates that his similarity parameter, m, must exceed 0.93 for this situation to occur. In the ideal case this corresponds to a diffuser area ratio $A_3/A_2 = 0.73$, an unlikely situation for ejectors that augment thrust. Within the present context, this region therefore has limited interest.

(D) At the beginning of the final region, the jet merges with the boundary layers on the walls of the duct. The flow is everywhere rotational and not at all self-preserving. It is amusing, however, that in this region, as well as in region C, one can find a length scale δ that suitably fits experimental velocity profiles to the function $W/W_{max} = [1 - (r/\delta)^{3/2}]^2$.

Hill [31] concludes that a similar set of four flow regions characterizes the development of jets in axisymmetric ducts whose diameters vary in the stream direction. Figure 15, for example, shows that within region B, before the jet reaches the wall, velocity profiles measured at four downstream locations appear similar, notwithstanding the fact that over these locations the duct's area changes by almost a factor of two. This is an encouraging result. It not only supports Curtet's [28] and Razinsky and Brighton's [30] observations on self-preservation, it also suggests a lack of essential difference between the development of jets in either constant or varying diameter ducts. But, in fact, there may well be essential differences that for the present remain unknown because the literature contains scant measurements of turbulence intensities and Reynolds stresses for confined mixing. Razinsky and Brighton [30] report some measurements of turbulence in constant area, axisymmetric mixing ducts. Unfortunately, there appear to be no corresponding measurements in the literature that allow one to look for the influence of changes in the duct geometry on turbulent scales and mixing rates. It is also not clear if such effects could be seen in axisymmetric flows although experiments suggest they may exist in two-dimensional flows.

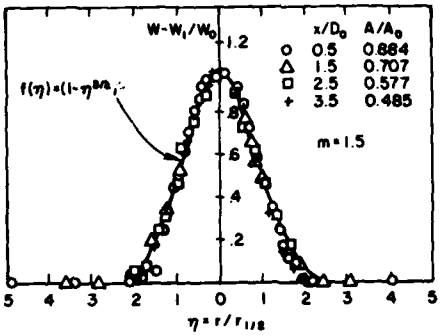

Figure 15. Nearly self-similar velocity profiles occuring in a convergent duct. From Reference 31.

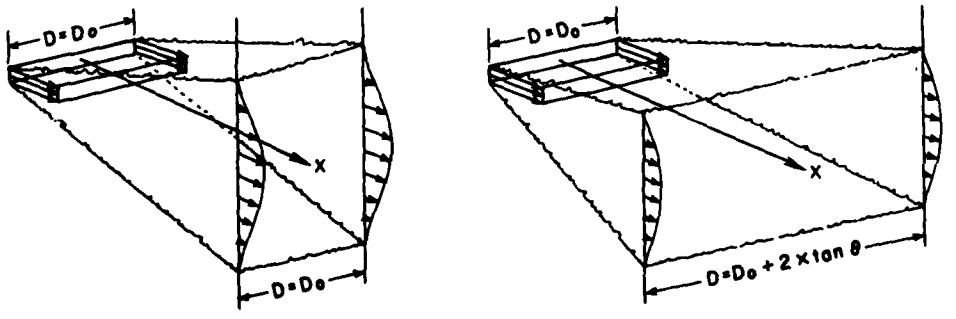

(a) Unstrained (b) Strained

Figure 16. (a) Unstrained mixing in a duct whose sidewalls remain parallel and (b) strained mixing in a duct whose sidewalls diverge.

Reference 32 reports the results of experiments with two ejector configurations, A_1/A_0 = 39 and 116, tested over a range of diffuser area ratios. The primary nozzles of both configurations are simple slots that span the square entrance plane of an L/D_0 = 3 diffuser. Air is entrained from the atmosphere through an efficient inlet, and the mixing flow exhausts to the atmosphere through a straight-wall diffuser. Two opposing sidewalls of the diffuser remain parallel and the remaining two walls diverge. The objective of the experiment is to assess the effect on ejector performance of positioning the primary nozzles so that they span either the parallel or the diverging walls of the diffuser. In the latter case, the principal vortices in the primary jet are stretched or strained as they flow through the diffuser (Figure 16). The implication is that a strained vortex filament produces higher Reynolds stresses and more rapid mixing as a consequence of the conservation of its angular momentum. Figure 17 presents results of the experiment and shows the higher entrainment velocities associated with the strained mixing. It is not clear from these data however, whether the improved performance is due to better mixing, to better diffusion, or to both. Pitot surveys of the flow within the diffuser support the more rapid mixing theory, but in the absence of accurate turbulence measurements, the reason for improved performance from strained mixing remains speculative.

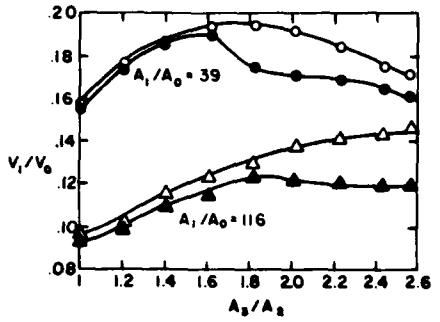

Figure 17. Entrainment velocity ratios achieved in two diverging wall ejectors under strained (open symbols) and unstrained (solid symbols) mixing conditions.

Some words of caution are in order. Their application to V/STOL aircraft imposes on ejectors a severe constraint on overall length that encourages abandoning a dedicated mixing duct in favor of mixing in a diffuser. Typically, one sees length-to-throat ratios on the order of two or three. The pressure gradients within such high performance devices are thus very strong and require the use of sophisticated techniques to prevent flow separation. In contrast, laboratory experiments concerned with confined mixing normally employ length-to-diameter ratios on the order of five to fifteen, and their pressure gradients are relatively smaller. Thus, in a realistic ejector, the four regions discussed above may become confused or altogether unidentifiable as strong pressure gradients interact with turbulent mechanisms. The use of accelerated mixing devices certainly compounds the problem. Finally, it is somewhat ironic that what we know least about in physics is what we are most sure of in practical ejectors: the flow is turbulent and three-dimensional.

6. ANALYSIS METHODS

Both conditions, turbulence and three-dimensionality, make analysis of flows within ejectors very difficult. In principle, one would like to solve the following set of equations:

State: $$\bar{P} = \rho RT$$

Continuity: $$\frac{\partial}{\partial x}(\rho u) + \frac{\partial}{\partial y}(\rho v) + \frac{\partial}{\partial z}(\rho w) = 0$$

Momentum: $$\frac{\partial}{\partial x}(\rho u^2) + \frac{\partial}{\partial y}(\rho uv) + \frac{\partial}{\partial z}(\rho uw) = -\frac{\partial \bar{p}}{\partial x} + \frac{\partial \tau_{yx}}{\partial y} + \frac{\partial \tau_{zx}}{\partial z}$$

$$\frac{\partial}{\partial x}(\rho uv) + \frac{\partial}{\partial y}(\rho v^2) + \frac{\partial}{\partial z}(\rho vw) = -\frac{\partial p}{\partial y} + \frac{\partial \tau_{yy}}{\partial y} + \frac{\partial \tau_{zy}}{\partial z}$$

$$\frac{\partial}{\partial x}(\rho uw) + \frac{\partial}{\partial y}(\rho vw) + \frac{\partial}{\partial z}(\rho w^2) = -\frac{\partial p}{\partial z} + \frac{\partial \tau_{yz}}{\partial y} + \frac{\partial \tau_{zz}}{\partial w}$$

Energy: $$\frac{\partial}{\partial x}(\rho uH) + \frac{\partial}{\partial y}(\rho vH) + \frac{\partial}{\partial z}(\rho wH) = \frac{\partial}{\partial y}\left(\frac{\mu_t}{Pr}\frac{\partial H}{\partial y}\right) + \frac{\partial}{\partial z}\left(\frac{\mu_t}{Pr}\frac{\partial H}{\partial z}\right)$$

subject to the appropriate wall boundary conditions and initial conditions. The problem is elliptic, however, and at least one of the initial conditions, usually the pressure, remains as an iteration parameter. Only one value, the correct value, of this parameter will bring the mixing flow to its correct, pre-specified pressure at the ejector's exit plane. To the best of our knowledge, the literature reports no attempt to solve this complete set of equations. A few authors solve simplified equations.

Hedges and Hill [33] consider two-dimensional, compressible boundary layer-like equations and use several different mixing lengths in an eddy viscosity model to represent shear stresses within the duct's different flow regions. Thus, prior to spreading to the duct's boundary layer, the mixing length in the jet's shear layer is proportional to the width of the shear layer, while the mixing length in the boundary layer is proportional to a boundary layer Reynolds number. An altogether different mixing length is used after the jet and the duct boundary layer merge. The calculations compare reasonably well with data obtained from an ejector with a non-constant area mixing duct, except in those regions of strong pressure gradient. This is not surprising since eddy viscosity models are really appropriate only when equilibrium exists between the mean flow gradient and the eddy viscosity.

DeJoode and Patanker [34] circumvent this problem by using the Launder-Spalding two equation k-ε model to describe turbulent viscosity in their analysis of three-dimensional, incompressible mixing within an ejector. The model differs from eddy viscosity models such as that used by Hedges and Hill in that differential equations, rather than algebraic equations or constants, describe key features of turbulence. The k-ε model produces satisfactory results in certain complex flows and succeeds in DeJoode and Patankar's work in delineating the streamwise vortex structure that develops in hypermixing jets. It also does a creditable job in describing the downstream development of the very irregular hypermixing jet velocity profiles. When compared to measurements of the pressure rise through an L/D ≈ 1.3, A_1/A_0 = 21.5, A_3/A_2 = 1.9 ejector however, the theory falls about 7% below experimental data. The authors suggest that this is due to their neglect of effects produced by wall jets and friction on the walls of the diffuser. While this is no doubt true, another and more important reason is that their computational domain excludes the ejector's end walls where three-dimensional effects dominate the flow pattern. Other works [35,36] use the same or similar k-ε turbulence procedures to compute thrust augmentation performance of ejectors. In general, the calculations do not compare very well with experimental data, and we suspect the cause is the three-dimensionality of the flow throughout the entire ejector. Our search of the literature fails to identify any successful effort to compute a fully three-dimensional ejector flowfield with an advanced turbulence model.

In those select cases where the flow remains two-dimensional, where pressure gradients are not too severe and, especially, where velocity profiles are reasonably self-similar, integral methods afford a fairly accurate and timely computational approach. Hill [31] describes an incompressible flow method which reduces the six equations of motion to a continuity equation and three moments of the x-momentum equation. Their simultaneous solution describes the development of the mean pressure, the primary and secondary flow velocities and the spreading width of the primary jet. The pressure distribution Hill computes fairly well agrees with pressures measured on the wall of an axisymmetric ejector of variable cross-sectional area. In principle, then, one should be able to predict the ejector's thrust augmentation with almost the same accuracy, although this has yet to be done. Whether or not such predictions would be useful to V/STOL applications remains doubtful, however, in view of the severe restrictions that identify the validity of the method.

One-dimensional control volume methods provide the most simple analyses. Their shortcoming is their inability to describe physical events in explicit terms. In a sense, this is also their principal strength since the details of turbulent mixing and other three-dimensional physical processes occurring in ejectors remain ill-defined at the present time. In this regard, certain parameters may succinctly express the combined effects on performance of one or more of the physical processes. The flow skewness, β, for example conveniently integrates the effects of mixing, wall friction, and flow separation within the entire, three-dimensional flow domain. Unfortunately, assigning numerical values to such parameters presumes access to a broad data base that reflects experience with many configurations. At the present time, a designer equipped with such a data base may use any number of incompressible [1,37] or compressible [6,7,38] control volume analyses to estimate the effect of geometric and fluid dynamic parameters on performance. That he may do so with more accuracy and with less resort to art or intuition than would be required should he attempt the numerical solution of equations employing sophisticated models of turbulent transport, serves as an indictment of the meager progress we have made in developing theoretical methods of analyzing ejector performance.

7. CLOSURE

Two other types of ejectors deserve mention. Foa [39] discusses a mechanism for inducing a flow into a duct through the action of pressure waves established by rotating jets. Alperin [40] uses a control volume approach to analyze the compressible flow of an ejector at high pressures and directs attention to the "second solution" in which the mixed flow exhausts from the ejector at supersonic speeds. While both technologies are important each lies beyond the scope of this work: the first because pressure, rather than shear stresses, transfer energy and the second because such an ejector concept remains to be experimentally realized. Consistent with the theme of this AGARD Fluid Dynamics Panel Symposium, our interests concern the fluid dynamics of jets within thrust augmenting ejectors for V/STOL aircraft.

There must be compelling design reasons for this application of ejector technology since the energy available from aircraft engines could produce more thrust if it were applied to the shaft of a propellor. Admitting such a compelling reason, perhaps a rectangular planform required for the propulsive unit, the V/STOL aircraft application imposes a severe length constraint on the ejector. Reducing the length of an ejector normally reduces its performance because there is less opportunity for the primary jet to transfer its energy and momentum to the entrained stream. Accelerating the rate of mixing solves the problem. One method of accelerating mixing is to heat the primary jet. This also has the adverse effect of decreasing the density and momentum of the mixed flow but the more uniform distribution of momentum due to increased mixing produces a net positive result in short ejectors. Other methods of accelerating mixing act on the turbulent structure of the jet. These include hypermixing, which amplifies streamwise vortex structures and unsteady jets which also amplify lateral vortex structures and may also lead to pressure-driven energy exchanges.

Knowledge of the fluid dynamics of jets mixing in a confined region is poor. The experimental data base consists mostly of wall pressure measurements and mean velocity profiles at selected stations within a constant diameter, axisymmetric duct. There are some mean flow data taken in convergent-divergent

axisymmetric ducts, and in constant area, rectangular ducts. In general, however, experiments described in the literature involve long axisymmetric mixing ducts and relatively mild pressure gradients. In contrast, high performance V/STOL ejectors are short, two-dimensional planforms with very large pressure gradients. To understand the mechanics of mixing within them requires new experiments that measure turbulence intensities and Reynolds stresses, in addition to mean flow properties, within similar, two-dimensional planforms. Equipped with this information, we might then expect a substantial improvement in the accuracy with which theoretical analyses predict the performance of thrust augmenting ejectors.

REFERENCES

1. Quinn, B., "Recent Developments in Large Area Ratio Thrust Augmentors", AIAA Paper No. 72-1174, 1972.

2. Viets, H., "Thrust Augmenting Ejectors", 1968-1969 Von Karman Institute Lecture Series published as Aerospace Research Laboratories Report 75-0224, Wright Patterson Air Force Base, Ohio, 1975.

3. Porter, J. L. and Squyers, R. A., "A Summary/Overview of Ejector Augmentor Theory and Performance", Vols. I, II, Vought Corporation, ATC Report R-91100-9CR-47, 1981.

4. Quinn, B., "Compact Ejector Thrust Augmentation", J. of Aircraft, 10, 8 August 1973, pp. 481-486.

5. McCormick, B. W., Aerodynamics of V/STOL Flight, Academic Press, New York, 1967, p. 99.

6. Nagaraja, K. S., Hammond, D. L. and Graetch, J. E., "One-Dimensional Compressible Ejector Flows", AIAA Paper 73-1184, 1973.

7. Quinn, B., "Ejector Performance at High Temperatures and Pressures", J. of Aircraft, 13, 12, Dec. 1976, pp. 948-954.

8. Hasinger, S., "Performance Characteristics of Ejector Devices", Aerospace Research Laboratories Report TR-75-0205, Wright-Patterson Air Force Base, Ohio, 1975.

9. Nagaraja, K. S., "Recent Developments in Ejector Technology in the Air Force: An Overiew", Proceedings of a Workshop on Thrust Augmentation, NASA CP 2093, September 1979.

10. Quinn, B., "Mixing Duct Pressure Distributions and Exhaust Flow Characteristics of a High Temperature and Pressure Cylindrical Ejector", Aerospace Research Laboratories Report TR-75-0227, Wright-Patterson Air Force Base, Ohio, 1975.

11. Quinn, B., "Interactions Between Screech Tones and Ejector Performance", J. of Aircraft, 14, 5, May 1977, pp. 467-473.

12. Powell, A., "On the Mechanism of Choked Jet Noise", Proceedings of the Physical Society, Vol. 866, 1953, pp. 1039-1056.

13. Bevilaqua, P. M., "Evaluation of Hypermixing for Thrust Augmenting Ejectors", J. of Aircraft, Vol. II, No. 6, June 1974, pp. 348-354.

14. Bevilaqua, P. M., "An Analytic Description of Hypermixing and Tests of an Improved Nozzle", AIAA/SAW 10th Propulsion Conference, Paper No. 74-1190, Oct. 1974.

15. Sato, H., "The Stability and Transition of a Two Dimensional Jet", J. of Fluid Mechanics, Vol. 7, 1960, p. 53.

16. Roffman, G. L. and Toda, K., "A Discussion of the Effects of Sounds on Jets and Flueric Devices", ASME J. of Engineering for Industry, Nov. 1969, p. 1161.

17. Becker, H. A. and Massaro, T. A., "Vortex Evolution in a Round Jet", J. of Fluid Mechanics, Vol. 31, Part 3, 1968, p. 435.

18. Hill, G. W., "Self-Excited Super Turbulence: The Whistler Nozzle", Grumman Aerospace Corp., Report RE-488, Oct. 1974.

19. Borisov, Y. Y. and Gynkina, N. M., "Acoustic Excitatiton of High Velocity Jets", Sov. Phys. Acoust., Vol. 21, No. 3, 1975, p. 30.

20. Crow, S. C. and Champagne, F. W., "Orderly Structure in Jet Turbulence", J. of Fluid Mechanics, Vol. 48, Part 3, p. 547.

21. Fiedler, H. and Korschelt, D., "The Two Dimensional Jet with Periodic Initial Condition", Proceedings of the Second Symposium on Turbulent Shear Flows, Imperial College, London, July, 1979, pp. 8.18-8.23.

22. Glass, D. R., "The Effects of Acoustic Feedback on the Spread and Decay of Supersonic Jets", AIAA Paper No. 68-80, January 1968.

23. Curtet, R. M. and Girard, J. P., "Visualization of a Pulsating Jet", Fluid Mechanics of Mixing, ASME, New York, 1973, pp. 173-180.

24. Binder, G. and Favre-Marinet, M., "Mixing Improvements in Pulsating Turbulent Jets", Fluid Mechanics of Mixing, ASME, New York, 1973, pp. 167-172.

25. Bremhorst, K. and Harch, W. H., "Near Field Velocity Measurements in a Fully Pulsed Subsonic Air jet", Symposium on Turbulent Shear Flows, University Park, Pennsylvania, April 1977, pp. 2.41-2.50.

26. Viets, H., "Flip-Flop Jet Nozzle", AIAA Journal, Vol. 13, No. 10, Oct. 1975, pp. 1375-1379.

27. Wygnanski, I. and Fiedler, H., "Some Measurements on the Self Preserving Jet", J. of Fluid Mechanics, Vol. 38, Part 3, 1969.

28. Curtet, R., "Confined Jets and Recirculation Phenomena with Cold Air", Combustion and Flame, Vol. 2, No. 4, December 1958, pp. 383-411.

29. Hill, P. G. "Turbulent Jets in Ducted Streams", J. of Fluid Mechanics, Vol. 22, Part 1, 1965, pp. 161-186.

30. Razinsky and Brighton, J. A., "Confined Jet Mixing for Nonseparating Conditions", J. of Basic Engineering, Vol. 94, Series D, September 1972, pp. 551-558.

31. Hill, P. G., "Incompressible Jet Mixing in Converging-Diverging Axisymmetric Ducts", ASME J. of Basic Engineering, March 1967, pp. 210-220.

32. Viets, H. and Quinn, B., "Concurrent Mixing and Diffusion in Three Dimensions", *AIAA Paper No.* 75-873, June 1975.

33. Hedges, K. R. and Hill, P. G., "Compressible Flow Ejectors, Part I - Development of a Finite-Difference Flow Model", Transactions of the ASME, J. Fluids Engineering, Series I, 96, 3, September 1974, pp. 272-281.

34. DeJoode, A. D. and Patankar, S. V., "Prediction of Three-Dimensional Turbulent Mixing in an Ejector", AIAA J., Vol. 16, No. 12, February 1978, pp. 145-150.

35. Bevilaqua, P. M. and DeJoode, A. D., "Viscid/Inviscid Interaction Analysis of Thrust Augmenting Ejectors", Workshop on Thrust Augmentating Ejectors, NASA/Ames Research Center, California, NASA CP 2093, September 1979, pp. 71-84.

36. Schum, E. F. and Deltart, J. H., "Ejector Nozzle Developments", to be published in the Proceedings of the Ejector Workshop for Aerospace Applications, Dayton, Ohio, August 1981.

37. Kentfield, J. A. C., "Prediction of Performance of Low-Pressure-Ratio Thrust-Augmenter Ejectors", Journal or Aircraft, Vol. 15, No. 12, December 1978, pp. 849-856.

38. Dutton, J. C., "Investigations of the Supersonic-Supersonic Ejector", to be published in the Proceedings of the Ejector Workshop for Aerospace Applications, Dayton, Ohio, August 1981.

39. Foa, J. V., "A Vaneless Turbopump", AIAA Journal, Vol. 1, No. 2, February 1963, pp. 466-467.

40. Alperin, M. and Wu, J. J., "Thrust Augmenting Ejectors", to be published in the Proceedings of the Ejector Workshop for Aerospace Applications, Dayton, Ohio, August 1981.

OPTIMISATION THÉORIQUE ET CONTRÔLE EXPERIMENTAL D'UN INJECTEUR

A. Mignosi

Département d'Aérothermodynamique

ONERA, Centre d'Etudes et de Recherches de Toulouse

31055 - TOULOUSE, FRANCE

RESUME

Une modélisation de systèmes injecteurs, permettant d'augmenter la poussée, ou pouvant constituer un dispositif d'entraînement de fluide, est proposée, en vue d'évaluer et d'optimiser les performances qu'on peut en attendre dans le cas d'un régime stationnaire.

Un schéma simple, faisant l'hypothèse d'un mélange rapide des écoulements, permet d'exprimer à partir des équations de base, l'influence des différents paramètres caractéristiques de la trompe. Son contrôle expérimental est effectué à partir de résultats obtenus dans l'étude et la mise au point d'une soufflerie à induction.

On examine ainsi l'influence des différents paramètres : rapport des sections de l'injection et du fluide entraîné, nombres de Mach et rapports de pression, rapport des températures.

La configuration même de l'injecteur apparaît également comme très importante, notamment en ce qui concerne les fluctuations de pression et le bruit aérodynamique qui en résultent.

SUMMARY : *Theoretical Optimisation and Experimental Verification of an Ejector*

A modelisation of induction systems, which could be used for thrust augmentation or more generally constitute a fluid drive system, is proposed for the steady regime case. A simple scheme in which a rapid mixing of the flows is assumed, allows to solve the basic equations and express the main parameters influence.

Its verification is effected, using a set of experimental data obtained during the study of an induction driven wind-tunnel. Various parameters (area ratio between injected and driven flows, Mach number, pressure and temperature ratios) are studied. The injector configuration also appears to be very important, in particular as to pressure fluctuations produced at injection and the corresponding aerodynamic noise in the wind tunnel.

NOTATIONS PRINCIPALES

a	vitesse du son	S	section
u	vitesse de l'écoulement	λ	rapport des sections
M	nombre de Mach	Q	débit
ρ	masse volumique	q	pression dynamique
p	pression statique		
p_i	pression totale		
T	température		
T_i	température totale		
h_i	enthalpie totale		
t	rapport de températures		
f	fréquence		
H	hauteur		
L	largeur		

Indices

j	injection
m	mélange
v	veine d'essai
1	écoulement entraîné

1. INTRODUCTION.

L'utilisation d'injecteurs constituant le moteur d'une soufflerie a été le point de départ de nombreuses études effectuées à l'ONERA.

Une solution de ce type avait été en particulier proposée, sous l'impulsion de Mr P. Carriere, pour réaliser une soufflerie européenne à grand nombre de Reynolds (Projet LEHRT, Large European High Reynolds Wind Tunnel). Cette soufflerie devait fonctionner par courtes rafales, à température ambiante, avec une veine de 20 m2 de section.

Des études théoriques et expérimentales sur des installations à échelle réduite, visant d'une part à optimiser les performances du système injecteur et à prouver d'autre part que les qualités de l'écoulement peuvent être bonnes malgré le bruit engendré par les jets moteurs, ont donc été effectuées. On analyse ici les principaux aspects de ces études.

Après une présentation des équations de base schématisant le fonctionnement de l'injecteur, on discute les résultats principaux concernant son optimisation théorique et expérimentale, ainsi que les mesures caractérisant la qualité de l'écoulement, en s'intéressant particulièrement au bruit aérodynamique provenant des fluctuations de pression.

2. THEORIE DE L'INJECTEUR.

2.1. Modélisation mono-dimensionnelle stationnaire.

Considérant un écoulement ne présentant pas d'effets de courbure accentués, nous définissons comme "écoulement moyen" l'écoulement uniforme qui transporte les mêmes débits de masse, de dynalpie ($p + \rho u^2$) et d'enthalpie. Cet écoulement (m) est celui qui se réaliserait à l'extrémité d'un canal cylindrique prolongeant la section considérée, et dans lequel aurait lieu un mélange idéal sans effets pariétaux de viscosité et de conductibilité thermique [1].

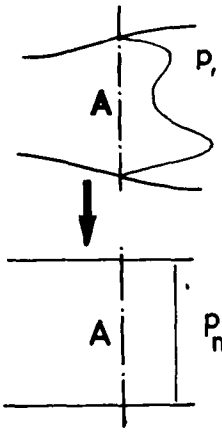

$p, \rho, u, M(x,y,z)\ldots$

p_m, ρ_m, u_m
$M_m \ldots$

$$(1)\quad \int_A \rho u\, dS = \rho_m u_m A$$

$$(2)\quad \int_A (p + \rho u^2) dS = (p_m + \rho_m u_m^2) A = (1 + \gamma M_m^2)\, p_m A$$

$$(3)\quad \int_A \rho u h_i\, dS = \rho_m u_m h_{im} A$$

Si nous prenons comme variables principales la vitesse, la densité et la pression moyennes, la température, l'enthalpie totale et le nombre de Mach moyens s'en déduisent par les relations :

$$p_m / \rho_m = r T_m \; ; \quad M_m = u_m / a_m \; ; \quad a_m = \sqrt{\gamma r T_m} \; ; \quad h_{im} = C_p T_m + u_m^2/2 = C_p T_{im}$$

Nous disposons ainsi de 3 équations pour 3 inconnues, ce qui permet de définir l'état moyen.

On a été amené à mettre en oeuvre dans les études expérimentales effectuées deux types d'injection : injection périphérique au travers de fentes aménagées aux parois, injection répartie par une série d'injecteurs bidimensionnels placés au sein de l'écoulement.

Les principaux aspects en sont schématisés figure 1 : l'injection périphérique donne lieu à des survitesses près des parois, leur amortissement et en conséquence le mélange avec l'écoulement entraîné s'effectuant sur une grande distance ; l'injection répartie au sein de l'écoulement donne un mélange plus rapide et des frottements aux parois plus faibles ; il faut cependant y ajouter les pertes de charge propres aux aubages au bord de fuite desquels est effectuée l'injection.

La modélisation utilisée pour l'analyse des paramètres de la trompe suppose qu'une discontinuité des caractéristiques a lieu au niveau du plan d'injection, faisant passer brutalement des caractéristiques notées (1) pour l'écoulement entraîné et notées (j) pour l'écoulement moteur, aux caractéristiques (m) du mélange. Les écoulements (1) et (j), aussi bien que l'écoulement moyen (m) qui en résulte, sont supposés stationnaires et uniformes.

L'écoulement moyen peut alors être calculé facilement, à partir des équations de base qui expriment la conservation de la masse, de la dynalpie et de l'énergie, équations écrites figure 2.

En se servant des relations classiques des écoulements isentropiques, on peut transformer les équations initiales en un système explicite de 3 équations à 8 inconnues, en y faisant apparaître des formes adimensionnelles. Si l'on se donne 5 paramètres caractéristiques des écoulements, on peut alors calculer les autres ; par exemple $\lambda = S_m / S_j$; M_1 ; M_j ; p_{ij} / p_{i1} et T_{ij} / T_{i1} paramètres de l'injecteur et de l'écoulement entrainé, permettent de définir :

- Q_1 / Q_j : rapport de débit massique
- p_{im} / p_{i1} : rapport de pression réalisé par l'injecteur
- T_{im} / T_{i1} : rapport de température
- M_m : nombre de Mach de l'écoulement après mélange.

On peut aussi se fixer λ ; M_1 ; M_j ; T_{ij} / T_{i1} et p_{im} / p_{i1} la perte de charge étant imposée par le circuit ; on calcule alors :

$$p_{ij} / p_{i1} \; ; \; Q_1 / Q_j \; ; \; T_{im} / T_{i1} \; ; \; M_m$$

De l'analyse de ces paramètres, il est possible de choisir parmi les différentes solutions un compromis entre les meilleures performances aérodynamiques des injecteurs et les contraintes technologiques.

Une telle discussion, effectuée d'abord pour le cas d'écoulements moteur et entrainé à même température totale (égale à l'ambiante), a permis de définir les principales caractéristiques de la solution proposée par l'ONERA pour le projet LERHT[2] . La soufflerie transsonique T2 du Centre de Recherches de Toulouse, qui est sensiblement l'échelle 1/10 du projet européen proposé, ainsi qu'une petite installation pilote T'2, définies de la même manière, sont les deux installations dans lesquelles a été mis au point et optimisé le fonctionnement de la soufflerie à induction.

Leur adaptation pour un fonctionnement permettant d'accroître le nombre de Reynolds par une diminution sensible de la température de l'écoulement, a conduit ensuite à étendre l'analyse à des cas où la température totale des jets moteurs est sensiblement différente de celle de l'écoulement entraîné.

2.2. Trompe utilisée pour augmenter la poussée des jets - critère de performance.

Afin d'illustrer les possibilités de cette modélisation dans le cas d'un augmenteur de poussée, on peut choisir un critère simple d'augmentation de poussée ne prenant pas en compte pour cette première analyse, les effets de perte de charge. La trompe sera schématisée d'une manière identique à celle proposée par B. QUINN, REF. 7.

Si l'on suppose que la trompe entraine un écoulement qui se détend après mélange, isentropiquement à la pression atmosphérique, on peut exprimer la poussée $\bar{F}$ de cet ensemble en fonction des grandeurs moyennes (m).

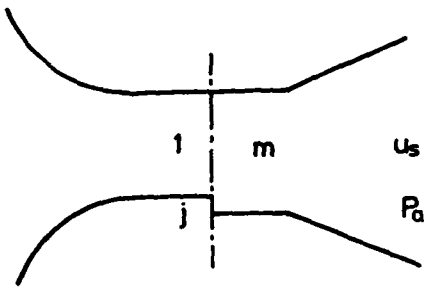

$$\bar{F} = q_m u_{ms} = q_m \sqrt{2C_p} \sqrt{T_{im}} \sqrt{1-\left(\frac{P_a}{P_{im}}\right)^{\frac{\gamma-1}{\gamma}}}$$

$$F_j = q_j u_{js} = q_j \sqrt{2C_p} \sqrt{T_{ij}} \sqrt{1-\left(\frac{P_a}{P_{ij}}\right)^{\frac{\gamma-1}{\gamma}}}$$

$$\psi = \frac{\bar{F}}{F_j} = \left(1+\frac{q_1}{q_j}\right)\sqrt{\frac{T_{im}}{T_{ij}}} \sqrt{\frac{1-(P_a/P_{im})^{\frac{\gamma-1}{\gamma}}}{1-(P_a/P_{ij})^{\frac{\gamma-1}{\gamma}}}}$$

Cette poussée $\bar{F}$ est proportionnelle au produit $q_m\sqrt{T_{im}}$ et fait intervenir la pression d'arrêt Pim. Si l'on définit alors la poussée conventionnelle du jet Fj de la même manière, on peut alors exprimer le rapport d'augmentation de poussée ψ qui ne dépend plus que des paramètres caractéristiques de la trompe.

2.3. Optimisation théorique de l'injecteur augmenteur de poussée.

L'optimisation du fonctionnement de la trompe peut être effectuée en analysant l'influence de chaque paramètre, en les faisant varier à tour de rôle, les autres étant gardés constants (voir PL.3.1).

On s'intéressera au rapport d'augemntation de poussée ψ et au rapport d'entrainement Q1/Qj. Le cas considéré correspond à :

Pij/Pil = 1,15 ; Tij/Til = 1 ; Mj = 0,3 ; Ml = 0,1 ; λ = 25

On observe d'abord que les deux critères d'optimisation vont dans le même sens pour tous les paramètres sauf pour la température. Si l'on augmente le rapport de température, on ne constate pas d'effet sensible sur l'augmentation de poussée alors que le rapport d'entrainement subit une grande augmentation.

Le rapport de pression Pij/Pil qui est lié au nombre de Mach du jet lorsque celui-ci est subsonique, fait diminuer les performances de la trompe lorsqu'il augmente. Il en est de même du nombre de Mach Mj du jet dans le cas d'un jet subsonique, alors que la tendance est inverse pour un jet supersonique. En effet le débit Qj passe par un maximum pour Mj = 1.

L'effet du Mach Ml semble naturel.

L'effet de λ conduit à choisir des rapports de section élevés. Nous allons maintenant présenter l'application que nous avons faite d'un injecteur en l'utilisant comme moteur d'une soufflerie à induction.

2.4. Optimisation théorique de l'injecteur. Cas d'une soufflerie.

Constituant le moteur de la soufflerie, l'injecteur utilise l'énergie stockée dans un réservoir sous pression, pour entraîner par des jets l'écoulement principal.

Il doit compenser les pertes de charge du circuit et son optimisation est, bien évidemment, liée étroitement à ces pertes de charge. Le but recherché est de minimiser le débit d'air injecté nécessaire à la réalisation d'un écoulement donné dans la veine d'essai, tout en y assurant de bonnes qualités d'écoulement.

Considérant le fonctionnement de la soufflerie T2 pour un nombre de Mach dans la veine de l'ordre de 0,9, soit une perte de charge de l'ordre de 10 %, les caractéristiques retenues pour l'injection sont les suivantes :

Mj = 1,6 ; Ml = 0,6 ; λ (rapport des sections) = 20 à 40.

La résolution des équations de la trompe permet alors de calculer le rapport des débits Qj/Qv en fonction de l'un des 4 paramètres précédents, les 3 autres étant tenus constants. Les résultats obtenus sont tracés figure 3.2.

On observera l'influence essentielle du rapport des températures, t = Tij/Til ; on a clairement intérêt à injecter de l'air chaud dans de l'air froid puisque le rapport d'entraînement Ql/Qj augmente très sensiblement avec le rapport des températures, se trouvant pratiquement doublé entre t = 1 (Tij = Tl = 300°K) et t = 2,5 (Tij = 120°, Til = 300°). C'est bien cette propriété qui nous a conduit à retenir un fonctionnement cryogénique pour lequel l'air moteur est injecté à température ambiante, le refroidissement de l'écoulement étant assuré ensuite par injection d'azote liquide dans le circuit.

En ce qui concerne Mj, l'effet est bien plus faible et ceci reste vrai même pour un rapport t de l'ordre de 2,5. De plus, il est difficile d'amorçer correctement des tuyères lorsque le nombre de Mach de sortie est grand, si l'on ne dispose pas d'une pression de stockage élevée.

Le nombre de Mach Ml de l'écoulement entraîné doit être choisi le plus élevé possible, mais le gain est faible et nous sommes limités par la technologie de l'injecteur qui bloque l'écoulement pour Ml = 0,66.

On note aussi l'importance du rapport section mélangeur-injecteur λ = Sm/Sj et l'intérêt d'utiliser un λ élevé. A l'augmentation du λ correspond cependant une augmentation du Pij/Pil, donc une élévation de la pression de stockage et des efforts aux lèvres des tuyères (figure 4). Ce rapport λ est variable à T2, l'ensemble de l'injecteur étant divisé en 7 x 14 tuyères supersoniques à Mj = 1,6, qui sont alimentées par groupes de 6 ou 8 tuyères ; le λ minimum pour T2 est de 20.

Les calculs effectués avec les données actuelles de T2 (Ml = 0,6, Mj = 1,6), et pour deux valeurs de λ (20 et 40), montrent l'apport de pression d'arrêt réalisé par l'injecteur en fonction du rapport de débit Qj/Ql (voir figure 4).

Le diagramme calculé pour λ = 20 et différents rapports t indique que l'apport de pression ΔPi/Pi reste sensiblement constant, quel que soit le rapport de température, lorsque l'on s'est fixé le rapport des pressions. La perte de charge du circuit variant assez peu avec la température, mais dépendant du Mach, permet en première analyse de dire que le nombre de Mach de la soufflerie en fonctionnement, non bloqué par un col, dépend essentiellement du rapport Pij/Pil, quelle que soit la température.

On note aussi l'intérêt d'avoir un λ élevé, puisque pour une perte de charge donnée, Qj/Ql décroît lorsque λ augmente.

Sur la figure 5 on a représenté le domaine d'utilisation prévu pour la soufflerie T2 en fonctionnement cryogénique, pour une perte de charge estimée de 8 %, correspondant à un nombre de Mach veine de 0,8. On constate l'intérêt d'avoir un λ élevé, et l'on observe que l'on peut atteindre un rapport d'entraînement Ql/Qj supérieur à dix pour Tij/Til = 2,5.

2.5. Pertes de charge liées au système injecteur.

La détermination de la perte de charge dans la zone de l'injecteur est délicate, pour la raison évidente qu'il est difficile de la dissocier de celle du circuit.

On reviendra plus loin à l'optimisation expérimentale de cette perte de charge ; on peut cependant faire déjà quelques observations :

L'injection périphérique est simple à réaliser et l'on peut facilement faire varier la section d'injection par le calage des deux lèvres. Il existe vraisemblablement un angle optimum d'injection, permettant d'assurer avec un mélange assez rapide des deux écoulements une diminution des frottements aux parois, ceci sans trop perdre sur la vitesse axiale d'entrainement des jets (α de 5 à 10°).
Le jet à la paroi transforme complètement la couche limite venant d'amont ; on crée au niveau de l'injecteur une nouvelle couche limite de très faible épaisseur initiale, avec un maximum de vitesse qui décroît très vite suivant l'abscisse, tout en s'éloignant de la paroi (voir figure 1).

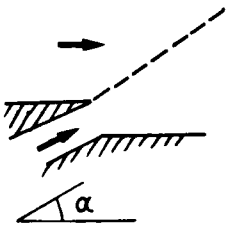

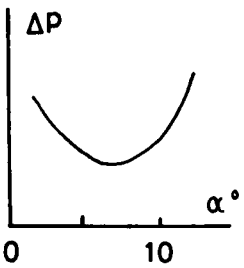

Pour l'injection répartie, le mélange s'effectue plus rapidement; le calcul de la perte de charge propre aux aubages est possible si l'on néglige les effets latéraux. L'estimation de ces effets latéraux (effet de coin avec couches limites tridimensionnelles) est malheureusement pratiquement impossible, en particulier dans le cas étudié ici, pour lequel les jets se situent au bord de fuite des aubages du premier coude.

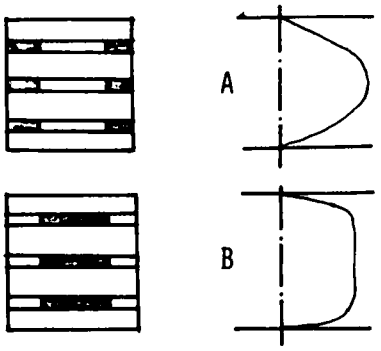

Il est possible également de faire varier la surface d'injection et la disposition des jets, la solution retenue étant de compartimenter l'intérieur de chaque aubage. On peut agir ainsi sur le profil des vitesses après mélange, et attaquer le diffuseur aval avec un profil de vitesse réduisant les risques de décollement dans le diffuseur.

A - Alimentation par la partie centrale

B - Alimentation par les parties latérales

3. CONTROLE EXPERIMENTAL : CAS D'UNE SOUFFLERIE A INDUCTION.

3.1. Installations T'2 et T2.

Une petite installation, représentant l'échelle 1/4 de la soufflerie T2, et ayant donc une veine de 10 x 10 cm^2 a d'abord été construite, en vue d'étudier et d'optimiser le fonctionnement de la soufflerie à induction et d'aboutir ainsi à la meilleure définition de la soufflerie T2.

Cette installation pilote T'2 comporte un circuit à retour qui peut être pressurisé jusqu'à 5 bars. Différents injecteurs : injecteurs périphériques, coudes injecteurs à 2 et 3 aubes y ont été essayés. On a pu y analyser commodément et systématiquement l'influence des différents paramètres : longueur du mélangeur, position de l'évacuation, géométrie de l'injection, etc .....

Plus récemment la soufflerie pilote T'2 a permis d'étudier et d'optimiser un fonctionnement à basse température ; le circuit a simplement été isolé thermiquement par une mince couche de liège recouvrant tout l'intérieur du circuit ; le refroidissement de l'écoulement est effectué par une injection rapide d'azote liquide dans un élément situé immédiatement après le mélangeur.

La soufflerie T2 qui représente donc sensiblement l'échelle 1/10 du projet proposé pour la grande soufflerie européenne, a une veine de 40 x 40 cm^2 ; un schéma en est donné figure 6.

L'injection de l'air moteur est faite par le bord de fuite des aubes du premier coude ; ce coude comporte 7 aubes, dont la forme a été particulièrement soignée, en utilisant notamment une méthode de calcul de grilles d'aubes et de couches limites, ayant permis d'obtenir des distributions de pression pour lesquelles il n'y a pas de décollement.

Chaque aube comporte à son bord de fuite 14 tuyères d'injection à Mj = 1,6 ; chacune est compartimentée intérieurement de façon à pouvoir faire varier la section d'injection et le rapport de sections λ (figure 7).

3.2. Optimisation du mélangeur.

C'est à partir d'essais systématiques effectués dans l'installation pilote T'2 qu'ont été déterminés la configuration et le choix des paramètres, à retenir pour l'injecteur de la soufflerie à induction.

Les paramètres généraux (Mj, λ, Pij/Pil) étant définis par les équations de la trompe, un problème pratique important reste celui du mélangeur et de son optimisation. Le choix d'une injection périphérique, ou d'une injection répartie, effectuée alors par le bord de fuite des aubages du premier coude, y apparaît comme essentiel.

Ceci est bien mis en évidence sur la figure 8, où l'on montre une comparaison entre les meilleures performances obtenues avec une injection périphérique et avec une injection par les trois aubages du coude (il s'agissait alors d'une injection sonique, Mj = 1).

Dans les deux cas, on observe une longueur optimale, celle pour laquelle est obtenu dans la veine d'essai le nombre de Mach le plus élevé. Il est clair que l'injection par les aubages du coude est optimale pour une longueur de mélangeur nettement plus faible que pour l'injection périphérique ; le rapport de la longueur optimale à la hauteur du mélangeur est de l'ordre de 6 pour l'injection périphérique, et de l'ordre de 2 pour l'injection répartie ; c'est en fait le rapport à la distance entre deux fentes d'injection qui est devenu le paramètre déterminant.

Notons que cette diminution de la longueur du mélangeur a certainement contribué assez sensiblement à un gain appréciable sur le débit injecté, observé dans ces expériences.

3.3. Effet de la section d'injection.

L'influence de la section d'injection a été étudiée de manière systématique à la soufflerie T2, en faisant varier le nombre et la disposition des tuyères du coude injecteur.

Le nombre de Mach de l'écoulement dans la veine a été fixé par l'amorçage contrôlé d'un second col, réalisant un petit domaine supersonique à M < 1,2.

Chaque aubage comprend 14 tuyères et peut être alimenté soit dans sa partie centrale (8 tuyères), soit latéralement (3 tuyères de chaque côté).

On peut, bien entendu, réaliser plusieurs configurations de jets donnant une même valeur de λ = Sm/Sj ; certaines configurations conduisent à un mauvais fonctionnement aérodynamique ; d'autres, assez satisfaisantes, permettent de garder une perte de charge quasi-constante et de contrôler l'augmentation de Qv/Qj en fonction du λ (voir le haut de la figure 9).

Un optimum apparaît pour λ = 29 qui correspond aussi au régime adapté (égalité entre la pression statique du jet et celle de l'écoulement entraîné).

Pour les deux cas λ = 29 et λ = 20, nous avons tracé les rapports Qv/Qj et Pij/Piv en fonction du nombre de Mach veine. Le rapport des débits Qv/Qj peut atteindre 8 pour λ = 29, alors qu'il est de 7 pour λ = 20.

3.4. Effet du rapport de température des jets.

L'effet de ce paramètre a été contrôlé expérimentalement à la soufflerie T'2(veine de 10x10 cm^2) lors d'essais cryogéniques sans amorçage de col ; la température d'arrêt des jets moteurs est voisine de la température ambiante (Tij = 283°K ; λ = 20 ; Mj = 1,6) ; la température génératrice de l'écoulement entraîné Til varie de 283°K à 120°K grâce à une injection d'azote liquide effectuée après le mélangeur [3,4].

Précédemment, nous avions constaté que pour un nombre de Mach Ml donné et un rapport Pij/Pil fixé, l'apport de pression d'arrêt (Pim-Pil)/Pil dépendait peu du rapport de température (voir figure 4). Comme la perte de charge totale du circuit ne dépend principalement que du nombre de Mach, on doit en déduire que le nombre de Mach veine reste sensiblement constant, quel que soit le rapport Tij/Til et n'est lié qu'à Pij/Pil.

Les résultats expérimentaux confirment cette prédiction, comme le montre la figure 10 pour des essais sans col effectués pour deux rapports de pression Pij/Pil et pour Piv ≈ 1,2 bar.

Si nous traçons le rapport des débits Qv/Qj pour cet ensemble d'essais, nous observons figure 10 la décroissance de ce rapport lorsque Tij/Til augmente ; ceci provient essentiellement de l'augmentation du débit massique dans la veine, en raison de l'augmentation de la densité du gaz entraîné lorsque celui-ci est refroidi.

Un calcul de trompe effectué de manière à recouper le cas à température ambiante, restitue correctement cette tendance.

4. CARACTERISATION DES QUALITES DE L'ECOULEMENT.

4.0. Outre les performances qu'on y réalise et les nombres de Reynolds qu'on y atteint, un aspect essentiel d'une soufflerie transsonique moderne est la qualité de l'écoulement dans la veine, dont il convient de réduire au plus faible niveau possible les fluctuations. On s'intéresse ici spécialement aux fluctuations de la pression et de la vitesse.

Les exigences relatives au projet LEHRT étaient de ce point de vue très sévères [5] ; elles correspondaient au spectre réduit de fluctuations de pression statique présenté figure 14. Des essais systématiques d'optimisation de la qualité de l'écoulement ont dû ainsi être effectués, afin d'obtenir que le bruit provenant essentiellement des jets moteurs soit suffisamment faible, ceci dans une gamme de fréquences pouvant s'étendre jusqu'à 40 KHz.

4.1. Techniques de mesure mises en oeuvre.

Avant d'analyser les résultats expérimentaux obtenus, il est utile de donner quelques précisions sur les montages et les capteurs utilisés.

Un certain nombre de difficultés expérimentales qui sont apparues dans la mesure des fluctuations de pression, concernent principalement les aspects suivants :

- Nécessité de disposer de capteurs insensibles aux vibrations.
- Nécessité d'avoir un élément de mesure de faible dimension, afin d'éviter d'intégrer les fluctuations sur une surface trop importante.
- Obtention d'une grande bande passante (40 KHz) ; nécessité d'une calibration en fonction de l'angle de propagation et de la fréquence.

Les détails de l'étude étant donnés dans une publication antérieure [6], on en présente ici les aspects principaux.

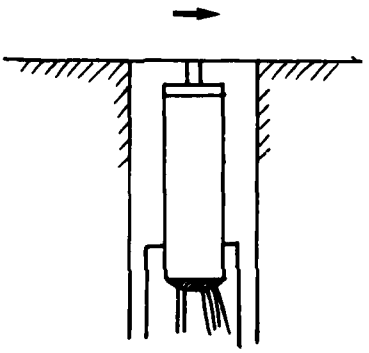

On a été amené à utiliser des capteurs Kulite miniaturisés, de 2 mm de diamètre, montés derrière un petit orifice (d = 0,4 mm) à la paroi, avec un volume minimum entre l'orifice et la membrane du capteur.

Le signal est numérisé à une cadence $N = 2{,}5\ f_{max}$, une transformée de Fourier rapide permettant d'obtenir ensuite l'énergie F par bande de fréquence Δf .

On utilise pour la représentation les variables réduites

$$n = fH/U \quad \text{et} \quad \sqrt{n\,F(n)}\ ;$$

F (n) est définie par $\int_B F(n)\,dn = \overline{p'^2}/q^2$

(H hauteur de la veine ; U vitesse ; q pression dynamique dans la veine d'essai).

4.2. Analyse des fluctuations de pression et optimisation des qualités de l'écoulement.

Les premières mesures ont eu pour but de déterminer les principales sources de bruit, et la façon dont ce bruit se propage et s'atténue le long du circuit.

On a représenté figure 11 la variation du niveau RMS de la fluctuation de pression en fonction de la position depuis la veine et jusqu'au mélangeur (le niveau RMS est relatif à une gamme de fréquence allant jusqu'à 40 KHz).

Cet exemple typique, mesuré à T'2 avec une injection périphérique, montre que la principale source de bruit est évidemment la trompe d'injection. La fluctuation de pression qu'elle produit s'atténue rapidement vers l'aval, et plus rapidement encore vers l'amont. Le bruit des jets subit un effet directionnel qui doit être d'autant plus marqué que la vitesse de l'écoulement est plus importante.

Les mesures ont consisté d'autre part à relever le niveau moyen de fluctuation dans la veine de T'2 en fonction de la pression d'injection, et pour différentes valeurs du rapport des sections λ. Les résultats présentés figure 12 sont relatifs à une injection par les aubes du coude ; la pression totale de l'écoulement dans la veine est Pil = 1,2 bar.

Notons que le nombre de Mach veine augmente pour un λ donné avec la pression d'injection Pij, et qu'il est d'autant plus élevé que λ est plus petit.

On remarque qu'une pointe de bruit se produit dans tous les cas pour Pij = 3 bars ; cette valeur critique correspond en fait à l'amorçage des tuyères de jets, auquel correspond un régime instable à fortes fluctuations.

Lorsque les tuyères sont amorcées, on note encore une augmentation du niveau de bruit avec la pression du jet ; le cas λ = 20 donne une fluctuation plus faible, ceci étant lié probablement à une atténuation des ondes remontantes avec l'augmentation du nombre de Mach.

La droite de la figure 12 donne la variation du niveau de bruit avec le nombre de Mach ; la pointe de bruit observée à gauche pour λ = 40 et Pij = 3 bars apparaît à Mv = 0,4 ; pour λ = 20, elle apparaît à Mv = 0,55.

Afin de mieux caractériser le phénomène, une série de spectres de la fluctuation de pression ont été effectués, dans les deux configurations λ = 20 et λ = 40 ; on donne figure 13 les spectres obtenus à λ = 40, pour 3 valeurs du nombre de Mach veine : 0,4, 0,55 et 0,65.

On observe qu'ils présentent a priori une même allure générale, à savoir un maximum à basse fréquence, suivi d'un plateau qui se termine par la coupure liée au filtre.

Cependant, une pointe de bruit à haute fréquence vient se superposer très nettement à Mv = 0,4, c'est-à-dire à Pij = 3 bars, mettant ainsi clairement en évidence l'instabilité liée à l'amorçage des tuyères de jets.

Des analyses expérimentales systématiques de la fluctuation de pression ont également été effectuées pour l'écoulement dans la soufflerie T2, complétées par la mesure des fluctuations de la pression totale, de la direction de l'écoulement, et des composantes u' et v' de la fluctuation de la vitesse.

Les spectres de la fluctuation de pression correspondant à différentes configurations et présentés figure 14, appellent les commentaires suivants :

Les spectres obtenus à trois nombres de Mach pour un rapport de section λ = 20, et sans amorçage d'un col sonique en sortie de veine, sont donnés d'abord en haut de la figure 14.

On y voit nettement deux régions à fluctuations de pression élevée :

- à haute fréquence (n > 1 ; f > 500 Hz), l'augmentation du niveau de la fluctuation est classique, et provient du bruit engendré par les couches limites turbulentes des parois ;
- à basse fréquence ($n < 4.10^{-2}$; f < 20 Hz), apparaît de plus une augmentation importante du niveau de la fluctuation de pression :

Deux moyens ont alors été mis en oeuvre successivement, pour réduire ce bruit à basse fréquence.

Dans une première opération, la veine a été équipée d'un col aval, soigneusement étudié pour amorcer un écoulement modérément supersonique, n'augmentant que faiblement la perte de charge, tout en interdisant aux ondes acoustiques en provenance de l'injection de se propager jusqu'à la veine d'essai. Le résultat obtenu est déjà assez spectaculaire, les courbes du milieu de la figure 14 montrant que la "bosse" à basse fréquence se trouve réduite de moitié. On notera que le niveau à haute fréquence n'est pas modifié, ceci confirmant qu'il s'agit à haute fréquence du bruit de couche limite.

Dans une seconde opération, conservant le second col, on s'est attaché à améliorer le fonctionnement de l'injecteur du point de vue des fluctuations de pression qu'il produit. Il est apparu que le rapport des sections λ était un paramètre essentiel. Un rapport λ = 29, qui permet de réduire encore de moitié le bruit à basse fréquence, a finalement été retenu. Il représente en fin de compte un compromis satisfaisant, permettant d'obtenir une performance élevée avec de faibles fluctuations de pression ; celles-ci demeurent en fait pratiquement comprises dans la zone ombrée qui correspond aux spécifications énoncées pour le projet de grande soufflerie européenne.

La figure 15 donne finalement, en fonction du nombre de Mach veine, la composante longitudinale de la fluctuation de la vitesse, mesurée au fil chaud dans la chambre de tranquillisation et au film chaud dans la veine d'essai. On voit que les améliorations apportées aux fluctuations de pression,ont permis d'obtenir un taux de turbulence inférieur à 1% dans la chambre de tranquillisation. Le rapport de contraction conduit alors à un taux de turbulence de l'ordre du millième dans la veine d'essai.

REFERENCES

1. Carrière P. — *The Injector Driven Tunnel*
AGARD Lecture Series on Large Transonic Wind Tunnels ; AGARD Report R-600, 1973.

2. Carrière P. — *Sur quelques problèmes fondamentaux relatifs à un projet de soufflerie transsonique à induction*
Abhandl. aus dem Aerodynamischen Institut der Rhein-Westf. Techn. Hochschule, Aachen H, 22, 1975.

3. Michel R. — *The Development of a Cryogenic Wind Tunnel Driven by Induction : Flow Control and Instrumentation Studies in a Pilot Facility at ONERA/CERT*
AGARD Lecture Series N° 111, Cryogenic Wind Tunnels, 1980.

4. Michel R. — *A Cryogenic Transonic Intermittent Tunnel Project : The Induced Flow Cryogenic Wind Tunnel T2 at ONERA/CERT*
AGARD Lecture Series N° 111, Cryogenic Wind Tunnels, 1980.

5. Hartzuiker J.P., Pugh P.G., Lorenz-Meyer, Fasso G.E. — *On the Flow Quality Necessary for the Large European High Reynolds Number Transonic Wind Tunnel LEHRT*
AGARD Report R 644, March 1976.

6. Quémard C., Mignosi A. — *Definition of a High Flow Quality Injector Driven Tunnel : The Pressurised Transonic Wind Tunnel T2 of ONERA/CERT*
18ème Conférence Israëlienne Annuelle sur l'Aviation et l'Astronautique
Haïfa, Mai 1976.

7. QUINN B. — *Compact Ejector Thrust Augmentation.*
Extrait du JOurnal of Aircraft, Vol. 10, n° 8, Août 1973.

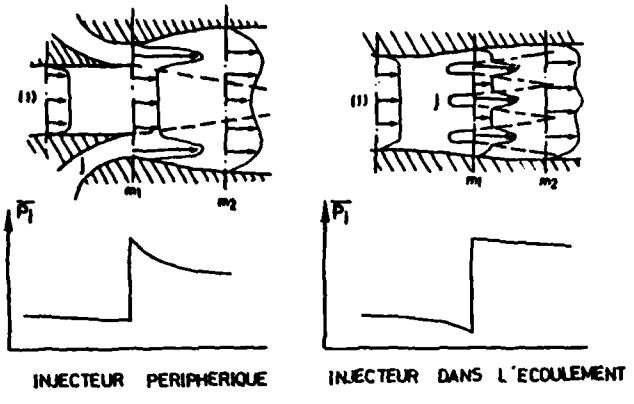

FIG. 1 : Injection périphérique et intérieure

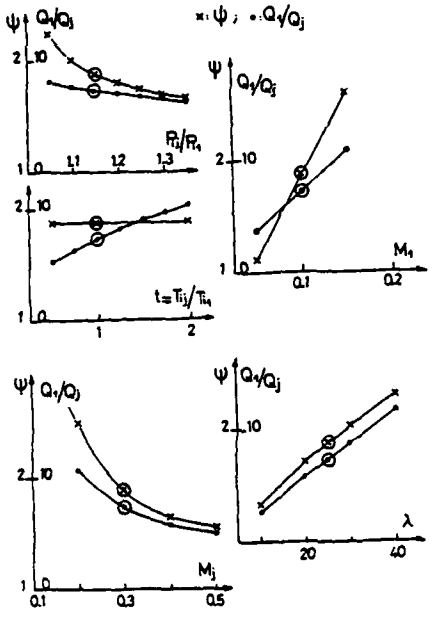

FIG. 3.1 : Effet des 5 paramètres Pij/Pi1, Tij/Ti1, M1, Mj, λ

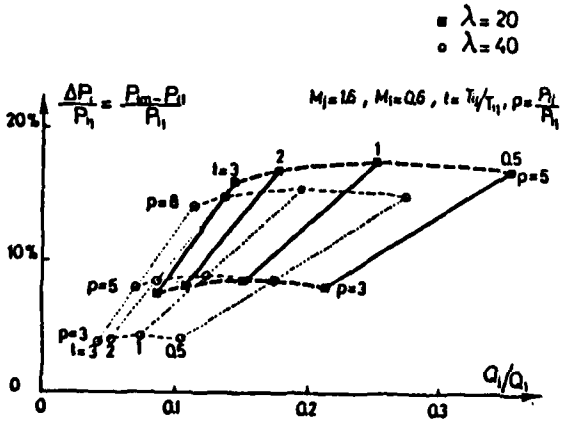

Parametres.

$\lambda = \frac{S_m}{S_j}$, M_1 , M_j , $\frac{P_{ij}}{P_{i_1}}$, $\frac{T_{ij}}{T_{i_1}}$.

Equations de base.

Masse $\rho_1 u_1 S_1 + \rho_j u_j S_j = \rho_m u_m S_m$

Dynalpie $(p+\rho u^2)_1 S_1 + (p+\rho u^2)_j S_j = (p+\rho u^2)_m S_m$

Energie $Q_1 H_{i_1} + Q_j H_{ij} = Q_m H_{i_m}$

Variables caractéristiques de la trompe.

(1) $\alpha = \frac{Q_j}{Q_1} = \frac{P_{ij}/P_{i_1}}{(\lambda-1)\sqrt{T_{ij}/T_{i_1}}} \frac{\Sigma_1}{\Sigma_j}$

(2) $\frac{T_{im}}{T_{ij}} = \frac{1+\alpha(T_{ij}/T_{i_1})}{1+\alpha}$

(3) M_m calculé par $\Phi_m = \sqrt{\frac{T_{i_1}}{T_{im}}} \frac{\Phi_1 + \alpha\Phi_j\sqrt{T_{ij}/T_{i_1}}}{1+\alpha}$

(4) $\frac{P_m}{P_{i_1}} = \sqrt{T_{im}/T_{i_1}} \left(\frac{\lambda-1}{\lambda}\right)(1+\alpha)\frac{\Sigma_m}{\Sigma_1}$

EFFICACITE . $E_p = \frac{(P_m - P_1)/P_{i_1}}{\alpha}$ (à maximiser)

avec . $\bar{Q} = P/P_i(M)$, $\Sigma = A/A_c(M)$; $\Phi = \bar{Q}\Sigma(1+\gamma M^2)$

FIG. 2 : Equations de la trompe

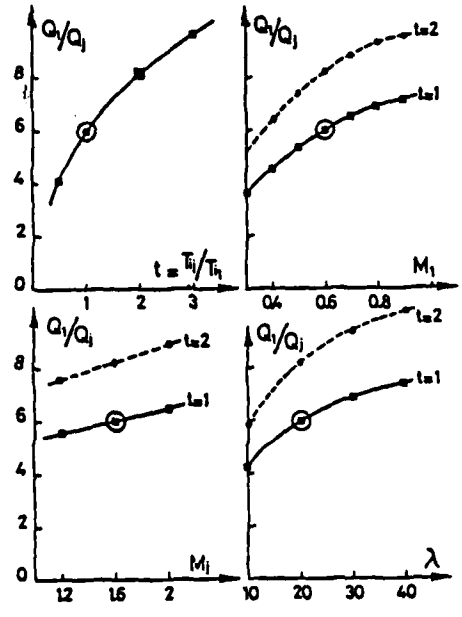

FIG. 3.2. : Effet des 4 paramètres M1, Mj, λ, Tij/Ti1

FIG. 4 : Diagramme de fonctionnement

ΔPi/Pi en fonction de Qj/Q1

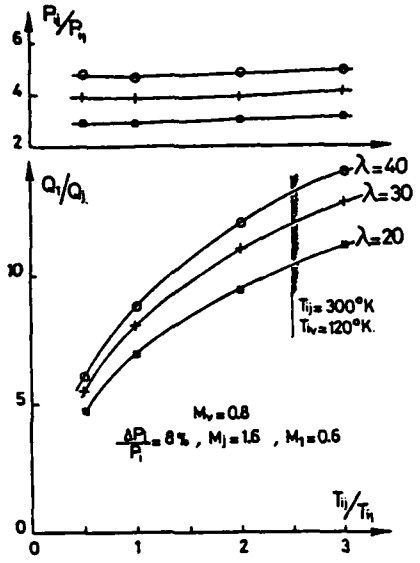

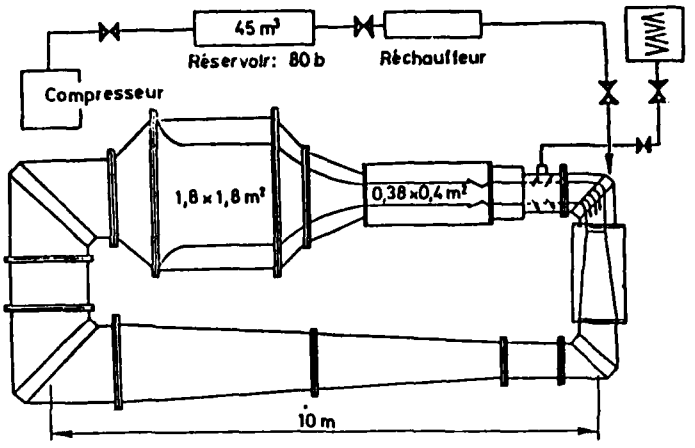

FIG. 5 : Diagramme prévu pour T2 à Mv = 0,8

FIG. 6 : Schéma de la soufflerie T2

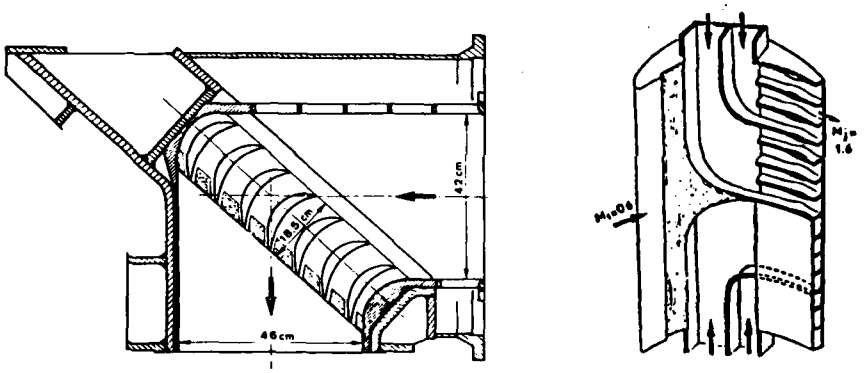

FIG. 7 : Coude injecteur

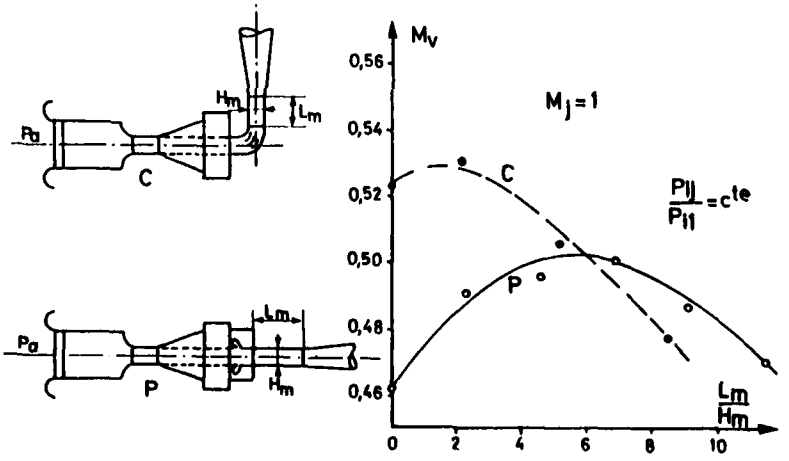

FIG. 8 : Influence de la longueur du mélangeur

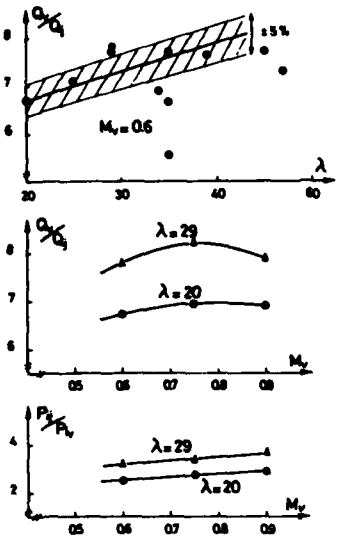

FIG. 9 : Effet du λ et de la configuration des jets sur les performances de la soufflerie T2.

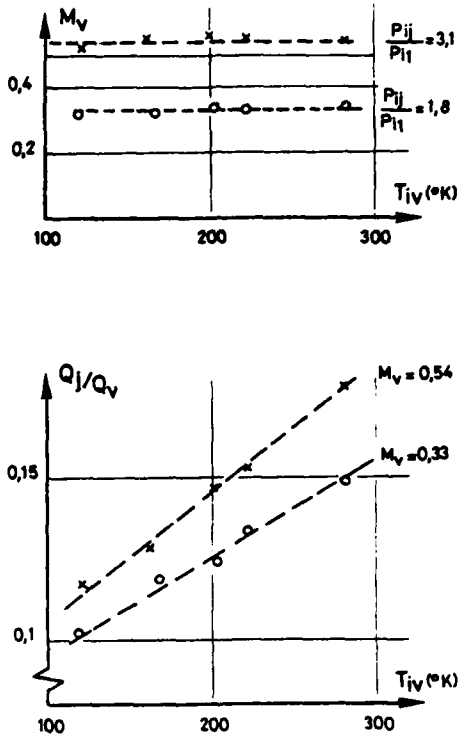

*FIG. 10 : Effet du Tiv sur le Mach **veine** et sur Qj/Qv.*
Tij = 280°k , Piv = 1,2 b.

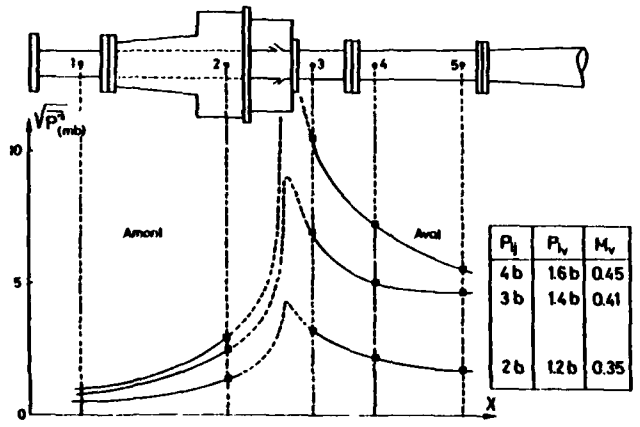

P_{ij}	P_{iv}	M_v
4 b	1.6 b	0.45
3 b	1.4 b	0.41
2 b	1.2 b	0.35

FIG. 11 : Niveau du bruit le long du circuit

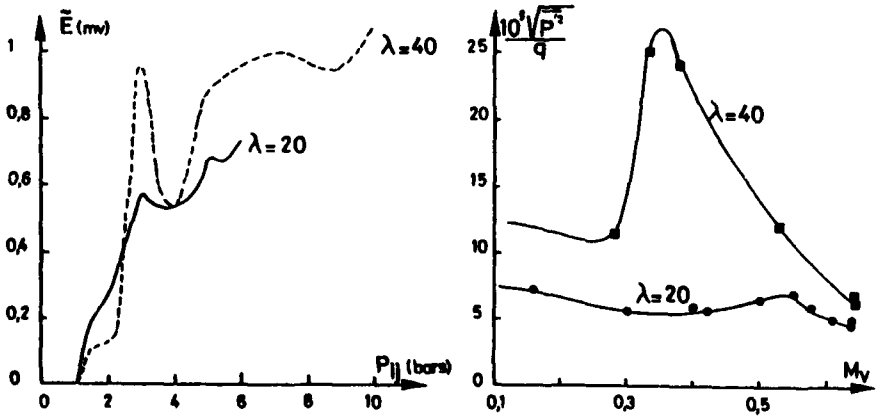

*FIG. 12 : Bruit dans la **veine** de T'2 : effet de Pij et λ*

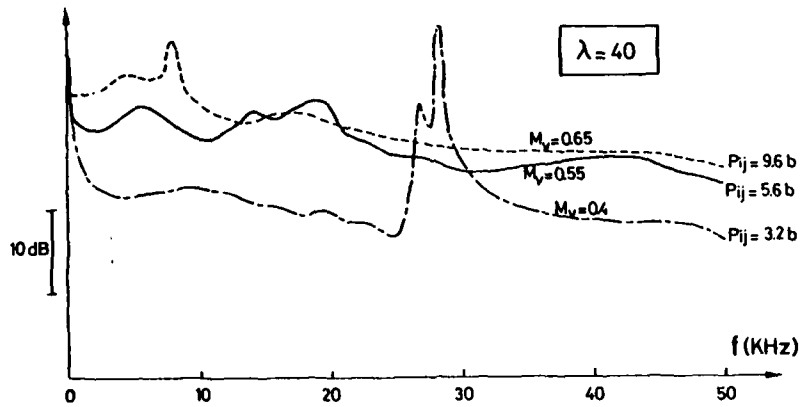

FIG. 13 : Spectres de fluctuation de pression à T'2

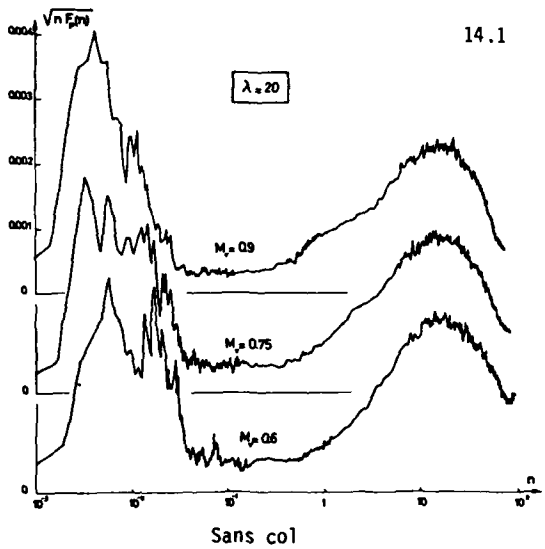

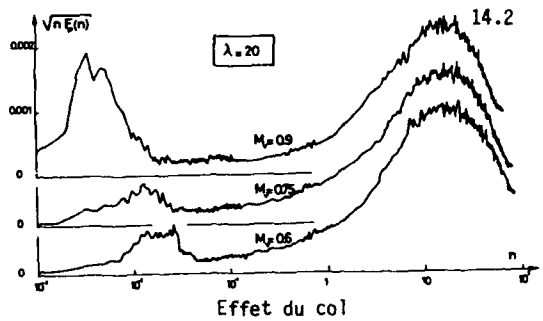

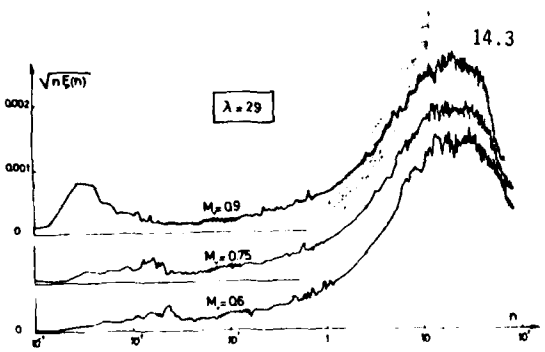

FIG. 14 : Spectres de fluctuation de pression dans la veine de la soufflerie T2.

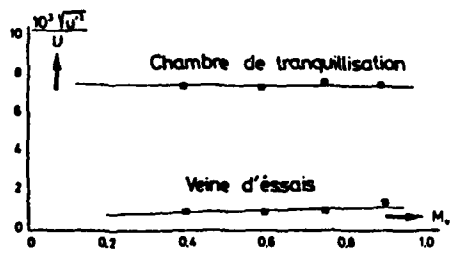

FIG. 15 : Soufflerie T2 : Intensité de turbulence.

UNSTEADY EJECTORS

Hermann Viets
Associate Dean and Professor
College of Engineering
West Virginia University
Morgantown, WV 26506
U.S.A.

SUMMARY

Ejectors are examined from the point of view of introducing a time dependency into the flow to increase the mixing rate and hence improve the performance of very short devices. Some past studies of unsteady flows related to ejectors are reviewed and a device proposed which has the potential of increasing the mixing by means of both an unsteady flow and also an acoustic interaction between the frequencies generated by the jet and the ejector shroud. Standing acoustic waves are identified in the ejector and, even for a nozzle geometry which is not optimized, the short unsteady ejector performance is superior to that of a slot jet geometry.

1. INTRODUCTION

The use of unsteady flow to enhance ejector performance has been pursued by various investigators operating from different points of view. Much of the effort has centered on creating a time dependent primary flow to the secondary flow by normal (pressure) forces rather than tangential (shear) forces. Such a transfer would be more efficient and could be accomplished in a shorter streamwise distance. A secondary objective, still of interest even if the primary objective is not attained, is to increase the mixing rate of the primary jet so that relatively complete mixing is accomplished in a short streamwise distance. The advantage of complete mixing has been described by Quinn,[1] Bevilaqua[2] and others. The mixing increase must be achieved, however, without an exorbitant increase in primary nozzle losses. A comprehensive review of ejectors has recently been completed by Porter and Squyers.[3]

The objective of the present paper is to outline briefly some of the past efforts in unsteady ejectors and to highlight some current work on unsteady ejector components.

2. SOME PAST UNSTEADY EXPERIMENTS

An early experiment on unsteady ejectors was performed by Lockwood[4] employing a pulsejet combustor similar to those used in German aircraft in the mid 1940's. The pulse consisted of a slug of air which passed through the ejector shroud in the manner of a piston. An analysis of such a system where the primary flow (when it is on) completely fills the ejector shroud has been performed by Johnson and Yang[5] by the method of characteristics. These results are in reasonable agreement with the results of an accompanying experiment and suggest the existence of an optimum frequency.

Although the concept of filling the ejector completely with a slug of fluid is enticing, it is not entirely suitable for higher area ratio ejectors. For such cases, Foa[6] proposed a rotary primary jet where the components of the rotating nozzle were pictured to act like vanes of an impeller. The rotary jet has been analyzed by Hohenemser and Porter[7] and further tested for application by Maise.[8]

Various investigators have examined different ways of generating a time dependency in the primary nozzle flow. McCormack, Cochran and Crane[9] vibrated the jet nozzle in a transverse direction. Binder and Favre-Marinet[10] employed a rotating butterfly valve upstream to generate a pulsing flow at the exit of an axisymmetric nozzle. Flow visualization studies by Curtet and Girard[11] verified this structure and showed that the pulsating flow resulted in a series of vortex rings. This pulsating jet was subsequently applied in an ejector configuration[12] and indicated an improvement in thrust augmentation, especially for short ejectors. Unfortunately, the thrust augmentation in this case was defined as the Ejector Thrust/Nozzle Thrust with a fixed total pressure. This definition does not take into account the nozzle thrust efficiency nor any changes in primary mass flow between the two conditions.

A fluidically controlled rectangular nozzle which produces a flapping jet was developed by Viets[13] and exhibited a rapid half width growth. The advantages of the fluidic control are the lack of moving parts and fluid control lines. Detailed investigations of this jet[14,15] showed strong vortex interactions leading to the mixing improvements. Vortex growth in driven unsteady jets at low Reynolds Numbers has been shown by Rockwell.[16] Another nozzle employing a fluidic instability was developed by Hill and Green[17] and consists of a rapid expansion section in a round duct.

Simmons, Platzer and Smith[18] have examined the unsteady jet flowfield produced by an angular oscillation of the jet nozzle itself and have recently studied a jet driven by an embedded oscillating vane.[19]

In addition to the emphasis on the primary jet itself, some recent effort has been directed at the control of wall boundary layers by unsteady stimulation[20,21] which has application to the ejector problem. Again the aim is to create vortex structures to improve mixing and energize the lower part of the boundary layer.

3. ACOUSTIC EFFECTS

Most of the unsteady primary nozzles described above have considered the performance advantage of such

nozzles to be basically due to the improved mixing rate thereby produced. This is valid providing the thrust efficiencies of the unsteady nozzles are high enough to make them competitive with nozzles such as the hypermixing type.[1,2] If the thrust efficiencies are not sufficiently high, the loss in the primary nozzle cannot be overcome by a viscous mixing improvement. There is, however, an alternate phenomenon which can be employed to improve the mixing by transferring the energy through normal (pressure) forces rather than tangential (viscous) forces as discussed in Section 1. The mixing can be accomplished by an acoustic interaction between the primary jet and the ejector shroud, as demonstrated by Quinn.[22] His configuration consisted of an axisymmetric duct and a choked primary jet, which produces a strong screech tone as shown by Powell[23] and recently studied by Krothapall;, Baganoff, Hsia and Karamcheti.[24]

The acoustic interaction is most effective when the acoustic frequency available from the primary jet is well matched with the fundamental natural modes in the duct shroud. As demonstrated by Viets, Campbell and Korkan,[25] a substantial difference in frequency between the jet and the fundamental modes greatly reduces the acoustic effect and the resultant mixing improvement. For a rectangular ejector with a rectangular primary nozzle, matching the acoustic frequencies becomes a problem if one simultaneously desires a reasonable high secondary to primary flow area ratio on the order of 20 - 30. In addition, for jet flows of less than unit mach number at the exit, there is no distinct frequency generated but rather a broad band noise. Therefore, under conditions of an unchoked primary jet or a choked primary in conjunction with a larger ejector area ratio, an alternate acoustic generator is required if an acoustic interaction is to be provoked.

One possibility for use as an unsteady primary jet under these conditions is the "whistler nozzle" described in Reference 17, since it can operate at subsonic mach numbers. The acoustic feedback fluidic jet[13] is also a possibility if sufficiently high frequency can be generated. A rotor jet based on the mechanical devices described in Refs. 20 and 21 is also a possible choice for a primary and offers the additional advantage of allowing a number of primary nozzles to have not only the same frequency but also a fixed phase relationship and is currently being studied. This is also true of a modified version of the acoustic feedback jet nozzle[13] described in Ref. 26 as a gust tunnel application.

4. A SUBSONIC ACOUSTIC GENERATOR

Still another nozzle which offers the required acoustic properties at subsonic exit velocities was originally developed as a two phase injector,[27] operating with a liquid primary into a gaseous secondary. The nozzle has the advantage of no moving parts and hence high reliability. Operating in a single phase condition in air, the nozzle produces distinct frequencies which can be tuned both by changes in the nozzle geometry and by the operating conditions. The nozzle schematic is shown in Figure 1. The nozzle operation simply requires that the jet attach to one wall within the nozzle body. Then part of the jet is scooped off, fed back and impressed on the jet flow just downstream of the contraction. This causes the jet to attach to the opposite wall and the process begins anew. The strongly unsteady quasi-sinusoidal flowfield is clear in Figure 2 which illustrates the two phase operation of water flow into air.

The remainder of this paper will consider the flowfield generated by this nozzle and its acoustic interaction with the ejector shroud. If the acoustic interaction is substantial, then the nozzle can be optimized in terms of scale, frequency and spreading rate relative to a particular ejector shroud geometry.

The acoustic interactions observed by Quinn[22,28] were attributed to standing transverse waves in the ejector shroud due to a tuning of the screech tones produced by the choked jet to the transverse dimension. This interaction probably causes the jet itself to oscillate. In the present case, the jet is driven unsteady even without an acoustic interaction. Thus the effect of the acoustics on the jet may be rather small.

5. FREE JET ACOUSTICS

Three unsteady jets and one slot jet were investigated in this program. Two of the unsteady nozzle designs are shown in Figure 3. The primary difference between the two designs is the length of the feedback loop. The different designs lead to a frequency difference of roughly a factor of three at nozzle stagnation pressure ratios of about 1.15 based on ambient pressure. Nozzle 3 is essentially the same design as Nozzle 2 except for a somewhat shorter feedback loop which increases the frequency by about 20%.

In order to correlate the flow inside the oscillating jet with the acoustic structure outside, hot wire measurements within the jet were compared with pressure transducer measurements and microphone measurements taken outside the jet. A Flow Corp. (now Datametrics) Model 900 constant temperature hot wire anemometer was employed inside the jet and an Endevco Model 8506-2 high frequency response pressure transducer as well as a B&K Model 4136 microphone and amplifier system were employed outside the jet. The output from each of the systems was input to a Hewlett-Packard Model 3582A spectrum analyzer which yields the magnitude as a function of frequency. Thus the dominant frequencies present in any signal could be easily determined. A typical spectral output for Nozzle #2 at a stagnation pressure ratio of 1.17 is shown in Figure 4 as determined with the Endevco pressure transducers.

The two lowest frequency modes present in the flowfield of Nozzle #2 are compared in Figure 5 as they are determined both in the jet (hot wire) and out of the jet (microphone and pressure transducer). The apparent frequency steps in the hot wire case are only caused by the finite bandwidth employed by the spectrum analyzer. The conditions inside and outside the jet flow clearly indicate the same frequency content. The pressure is non-dimensionalized with the ambient pressure while the frequency is reduced to a Strouhal number form by V/D (exit velocity/exit dimension).

The dominant frequencies outside the jet flow are compared in Figure 6 for the microphone and pressure transducer results. In each case the instrument is located in the exit plane of the jet and at a distance equal to half the major dimension of the ejector shroud (in other words, located at the same position as the shroud wall, when the shroud is mounted.)

Each of the frequency modes A-G can be identified and explained. Mode A is the driving mode of the jet oscillation. Mode B is the second harmonic, being double the frequency of Mode A. Mode C is very weak. In some of the spectra it hardly appears. The fourth harmonic is Mode E, while Modes F and G are again only multiples of Modes E and F respectively. The intermediate Mode D can be explained based on the nozzle scale. The nozzle is 5 cm deep and the duct mode based on this dimension and a speed of sound of 335 m/sec results in 3311 Hz, which is the Mode D. Since the Mode D, based on the nozzle scale is so close to Mode C, the third harmonic of the driving motion, the energy from Mode C appears to be contributing to Mode D and thereby reducing its own amplitude.

The frequency of Nozzle #3 is increased over that of Nozzle #2 as shown by Figure 7. The first harmonic exists at approximately 1300 Hz or a Strouhal number of .059. At higher pressures, the second harmonic clearly exists at approximately 2600 Hz (i.e. curve B) and the third harmonic at curve D. The intermediate mode, curve C is caused by the duct mode based on the depth of the rectangular nozzle, 5.08 cm. as was the case in Nozzle #2.

As the pressure is lowered, the frequency of Mode B rises while the frequency of the duct Mode C decreases. The two modes coalesce by $\bar{P}$ = 1.08. At higher pressures a third harmonic (Mode D) is evident but weak, while at lower pressures a higher frequency value appears. The fourth harmonic exists at low pressures while at higher values Mode E appears to be the multiple of the average of Modes B & C.

6. FREE JET FLOWFIELDS

As might be expected based on previous flapping free jet experiments (Refs. 13, 15, 18 & 27), the unsteady jet mixes more rapidly with the ambient fluid than jets without a time dependent driver. The centerline velocity decay and the half width growth of Nozzles 1 & 2 are shown in Figures 8 and 9 respectively and are compared to the two dimensional slot jet value. Based on the velocity decay, Figure 8, there appears to be a small frequency dependence showing improved mixing (decay) as the frequency decreases. This result is opposed to that of Reference 19 which found a mixing improvement with frequency.

The two apparently conflicting results can fit into a coherent picture of the vortex growth in the unsteady jet. As clearly shown by Brown[29] and others, a forced unsteady jet leads to large vortex formations. For the case of the flapping jet, these vortices have been found by both flow visualization and by conditioned sampling with a hot wire anemometer.[15] For low frequencies, these vortices would be widely spaced and weak and exert little influence on the entrainment. Under these conditions, an increase in frequency would improve the mixing properties. On the other hand, at higher frequencies there is little to be gained by having the vortices even more closely spaced.

The effect of vortex growth may also be seen in the half width growth results of Figure 9. For each frequency, there appears to be a plateau or leveling of the half width growth at a different streamwise location. The most obvious case is the frequency of 980 Hz and occurs at approximately 13 nozzle width downstream. For higher frequencies, this occurs progressively farther downstream and for f = 3500 Hz the plateau is twice as far downstream as for 980 Hz. Apparently the near field entrainment depends upon the frequency. Brown has observed that the vortices entrain in the near field but do not entrain external fluid farther downstream. Thus the plateaus may reflect the end of the near field entrainment caused by the vortex structure.

7. DUCT ACOUSTICS

A rectangular duct was chosen as the ejector shroud as shown in the schematic of Figure 10. The inside dimensions of the duct are 5.1 cm by 17.8 cm. The duct length was varied during the experiment. The longer transverse dimension of the duct was chosen to achieve resonance with a driving frequency of approximately 1000 Hz.

As described by Succi, et al.[30] and employed by Viets et al.,[25] the frequencies of the modes corresponding to resonant transverse waves are related to the speed of sound C_o and the duct dimensions b and d by

$$F_{m,n} = \frac{C_o}{2}\sqrt{(m/b)^2 + (n/d)^2}$$

where m and n are integer values.

If the speed of sound is assumed to be 335 m/sec (1100 ft/sec), then the frequencies corresponding to some particular resonant modes are shown below for duct dimensions 5.1 cm by 17.8 cm.

m	n	F(Hz)
1	0	946
2	0	1887
3	0	2833
0	1	3289
0	2	6578
1	1	3422
2	1	3791

It should be noted that these values do not take into account the flow in the duct nor any real fluid or real wall effects. Actual resonant frequencies are expected to approximate these values but are not precisely equal to them.

In order to test the duct acoustics, white noise (produced by a General Radio Type 1390 A Random Noise Generator) was introduced at the duct inlet and the resulting acoustic levels measured at the exit plane of the duct (located at L/D = 6.1). A typical spectrum of the acoustic output on the duct exit centerline is shown in Figure 11a. The clearly defined peaks indicate a response of the duct to those frequencies. Calibration of the level of the white noise source shows that the peaks between 150 and 400 Hz are exaggerated out of proportion due to the fact that the input levels are high. The lowest transverse resonant frequency was shown to be approximately 946 Hz. The peaks between 400 Hz and the lowest transverse frequency are attributed to the organ pipe modes described by Morse and Ingard,[31] which have a lowest mode of 150 Hz (for this length).

If the acoustic measurements are taken off the duct centerline, even to the point of reaching the far wall location, the peaks between 400 and 900 Hz are not greatly affected as seen in Fig. 11b. This is consistant with their dependence on the duct length. However, the modes near the 1000 Hz transverse resonance value do vary with transverse position as might be expected.

To test the longitudinal modes, the end of the duct is filled with sound absorbing foam which should eliminate the organ pipe mode by not allowing reflections of the waves. That this is accomplished is seen in Figure 11c (with the microphone inserted through the foam) especially in comparison with Figure 11a. It is interesting that there remains a small peak at 990 Hz (remember that the apparent low frequency modes are caused by the input signal.

8. TRANSVERSE WAVES

The overall objective of the oscillatory duct flow is to examine the transverse wave structure to see if such waves are actually generated. High frequency response Endevco transducers are mounted in the duct walls at a streamwise position equal to two duct dimensions (35.6 cm). The output signals are fed to a Hewlett-Packard Model 3582A Spectrum Analyzer which decomposes the signal into its frequency components.

(a) Resonance in a long duct, X/D = 6.1, Nozzle #2

The variation of each component magnitude across the duct is shown in Figure 12 for Nozzle #2, having a lowest harmonic frequency approximately equal to the anticipated transverse resonant duct frequency. The first harmonic, 1060 Hz, produces a standing wave of a half wavelength with a node at the center. The second harmonic yields an entire wave with two node points. The third and fourth harmonics are very consistant with 1 1/2 and two waves respectively.

The same procedure applied across the short side of the rectangular duct yields the result of Figure 13 which clearly shows that the standing wave structure is not a function of that direction.

Taking the same pressure measurements at an upstream position, X = .28 (near the ejector inlet), and decomposing the signals into their frequency components results in Figures 14 and 15. The structure of the first, second and fourth modes are similar to the downstream structure (Figures 12 and 13) except for several data points near the center of the duct. This discrepancy is caused by the primary jet, which has a high velocity at that streamwise location and interferes with the pressure measurement. An additional discrepency between the upstream and downstream modes is shown in the two third (3200 Hz) modes. The problem is resolved by the fact that 3200 Hz is the transverse duct mode corresponding to the nozzle depth as was discussed in relation to the free jet modes, Figures 6 and 7.

(b) Resonance in long duct, X/D = 6.1, Nozzle #1

The spectra developed by the pressure traverse of the duct at S/D = 2 downstream exhibit a strong peak at the primary frequency of Nozzle #1, 3300 Hz, as shown in Figure 16. Based on the results of Figure 12, a waveform of 1 1/2 waves is expected at the 3300 Hz frequency. However, only a full wave is found. There may be an effect due to the nozzle duct frequency which is almost equal.

The next substantial wave structure, at 7800 Hz, shows no definite pattern. However, if the resonant frequency of the longer transverse dimension of the duct is 1060 Hz (from Figure 12), a corresponding resonance in the short duct dimension is 3700 Hz. The 7800 Hz frequency is roughly double that value, so one might expect a waveform similar to that of the 2120 Hz case in Figure 12, but in the short dimension. That is indeed a possible waveform as seen in Figure 17.

At frequencies of 10,300 and 15,500 Hz, higher order mode shapes are possible. The former could, for example, correspond to the mode M = 5, n = 2 while the latter may correspond to M > 5, n = 2. Of course as the order of the modes increases, it is more difficult to determine the precise modes since the spectrum becomes very crowded with possible modes. From the point of view of the unsteady ejector, the higher order modes are really of less interest because they are expected to contain less energy.

(c) Resonance in long duct X/D = 6.1, Nozzle #3

The lowest dominant frequency for this nozzle, 1300 Hz, effectively produces resonance in the duct according to Figure 18 and verified by the uniform magnitude in the other direction, Figure 19.

The next appreciable wave is at 4640 Hz and is not a harmonic of the first mode but is related to both duct dimensions. From Figures 18 and 19, M = 2 and n = 1. The calculated frequency for this mode structure is 3791 Hz, which is, of course, for the zero flow condition.

The 6000 Hz case does not indicate a clear wave shape. It is a mixed mode depending on both transverse dimensions and is almost a combination of the lower frequencies. It may be a result of an oscillation among several modes which exist near this frequency. Additional minor mode peaks exist at higher frequencies and there it becomes increasingly difficult to distinguish between modes.

Thus, when the forced oscillation is near the resonant frequency, it achieves a manner of resonance which is not as strong as it would be if the frequency were better matched. It does, however, produce similar pressure waves.

(d) Resonance in shorter ducts

The standing waves described above appear even for very short ejector shrouds. The transverse waves in an ejector of length equal to its major width, i.e. L/D = 1, are shown in Figure 20 driven by nozzle #2. The mode structure is essentially the same as in Figure 12 and shows the same primary nozzle interference as in Figure 14.

9. MASS AUGMENTATION

In order to examine the overall performance of the ejector, the mass augmentation of the device was determined by integrating the exit velocity profiles and dividing by the primary mass flow as determined by the venturi measurement. The mass flow ratios are shown in Figure 21 as a function of ejector length for the slot nozzle and three different oscillating nozzles. The actual levels of mass augmentation are not significant because the nozzles have not been optimized in terms of thrust efficiency and spreading rate relative to the duct size.

The trends in mass flow ratio show that for a long ejector the use of unsteady flow in general and acoustic interaction in particular is not warranted. The loss in nozzle thrust efficiency suffered by the unsteady jets has overpowered any mixing and acoustic advantages. However, for shorter ejectors, the performance does not deteriorate as rapidly with length for the oscillating jets as compared to the slot jet. It is for these very short ejectors that the unsteady effects discussed here are expected to be of significance.

The monotonic decrease in performance with decreasing length is only interrupted at a length of 2.1 shroud widths. This position will be examined in greater detail but the preliminary indications are that there is no strong streamwise organ type of resonance. That is, there is a coherent streamwise wave but it is not greater in magnitude than the wave which exists for a duct length of L/D = 3.

10. CONCLUSIONS

Unsteady ejectors clearly exhibit some performance advantages which make them attractive for very short duct geometries. The basic problems are to design the primary nozzles with small losses in thrust efficiency while retaining high reliability.

In terms of the driven acoustic interaction experiment, the results are encouraging. Standing transverse waves can be created in the ejector duct with a subsonic primary jet. The performance of such a device remains to be optimized. In particular, the design of the nozzle geometry must take into account not only the matching of the duct geometry to the frequency but also simultaneously matching the spreading rate to the duct geometry. In order to accomplish this result, preliminary nozzle experiments are required to determine the frequencies and spreading rates of a number of various designs. From these a design can be chosen which satisfies both the acoustic and mixing requirements.

11. REFERENCES

1. Quinn, B., "Compact Ejector Thrust Augmentation," J. Aircraft, Vol. 10, No. 8, Aug. 1973, pp. 481-486.

2. Bevilaqua, P.M., "Evaluation of Hypermixing for Thrust Augmenting Ejectors," J. Aircraft, Vol. 11, No. 6, June 1974, pp. 348-354.

3. Porter, J.L. and Squyers, R.A., "A Summary/Overview of Ejector Augmentor Theory and Performance," Vought Corp., ATC Report No. R-91100-9CR-47, April 1981.

4. Lockwood, R.M., "Investigation of the Process of Energy Transfer from an Intermittent Jet to a Secondary Fluid in an Ejector-Type Thrust Augmenter," Hiller Aircraft Corp. Report No. APR-64-4, March 1964.

5. Johnson, W.S. and Yang, T., "A Mathematical Model for the Prediction of the Induced Flow in a Pulsejet Ejector with Experimental Verification," ASME Paper WA/FE-33, 1968.

6. Foa, J.V., "A Vaneless Turbopump," AIAA Journal, Vol. 1, No. 2, Feb. 1963, pp. 466-7.

7. Hohenemser, K.H. and Porter, J.L., "Contributions to the Theory of Rotary Jet Flow Induction," J. Aircraft, Vol. 3, No. 4, 1966, pp. 339-46.

8. Maise, G., "Effects of Shroud Design on the Performance of Rotary-Flow Augmentors," Grumman Aerospace Corp. Report. PXP-001-38, June 1974.

9. McCormack, P.P.; Cockran, D. and Crane, L., "Periodic Vorticity and its Effect on Jet Mixing", Physics of Fluids, Vol. 9, No. 8, Aug. 1966, pp. 1550-60.

10. Binder, G. and Favre-Marinet, M., "Mixing Improvement in Pulsating Turbulent Jets," Symposium on Fluid Mechanics of Mixing, ASME, 1973.

11. Curtet, R.M. and Girard, J.P., "Visualization of a Pulsating Jet," Symposium on Fluid Mechanics of Mixing, ASME, 1973.

12. Binder, G. and Didelle, H., "Improvement of Ejector Thrust Augmentation by Pulsating on Flapping Jets", Symposium of Jet Pumps & Ejectors and Gas Lift Techniques, Cambridge, England, 1975. (Published by BHRA Fluid Engineering, Cranfield, Bedford, England).

13. Viets, H., "Flip Flop Jet Nozzle," AIAA Journal, Vol. 13, No. 10, Oct. 1975, p. 1375. (Also AIAA Paper No. 74-1189, AIAA 10th Propulsion Conf., San Diego, Calif., Oct. 1974.)

14. Piatt, M. and Viets, H., "Conditioned Sampling in an Unsteady Jet," AIAA Paper No. 79-1857, AIAA Aircraft Systems and Technology Mtg., New York, Aug. 1979.

15. Viets, H., "Coherent Structures in Time Dependent Flow," Proceedings of the NATO/AGARD Specialists Meeting on Turbulent Boundary Layers, The Hague, Netherlands, CP-271, Sept. 1979.

16. Rockwell, D.O., "External Excitation of Planar Jets", J. Applied Mech., Dec. 1972, pp. 883-890.

17. Hill, W.G. and Green, P.R., "Increased Turbulent Jet Mixing Rates Obtained by Self Excited Acoustic Oscillations", J. Fluids Engin., Vol. 99, No. 3, 1977, pp. 520-525.

18. Simmons, J.M.; Platzer, M.F. and Smith, T.C., "Velocity Measurements in an Oscillating Plane Jet Issuing into a Moving Air Stream", J.F.M., Vol. 84, Part 1, 1978, pp. 33-53.

19. Collins, D.J.; Platzer, M.F.; Lai, J.C.S. and Simmons, J.M., "Experimental Investigation of Oscillating Subsonic Jets", Symposium on Numerical and Physical Aspects of Aerodynamic Flows, Calif. State Univ., Long Beach, Calif., Jan. 1981.

20. Viets, H.; Piatt, M. and Ball, M., "Boundary Layer Control by Unsteady Vortex Generation," Journal of Wind Eng. and Ind. Aero., Vol. 7, 1981, pp. 135-144.

21. Viets, H.; Ball, M. and Bouginé, D., "Performance of Forced Unsteady Diffusers," AIAA Paper No. 81-0154, AIAA Aerospace Sciences Mtg., St. Louis, Mo., Jan. 1981.

22. Quinn, B., "Effect of Acoustic Interactions on Ejector Performance," J. Aircraft, Vol. 12, No. 11, Nov. 1975, pp. 914-916.

23. Powell, A., "On the Mechanism of Choked Jet Noise," Proc. Phys. Soc., Vol. B66, 1953, p. 1039.

24. Krothapalli, A; Baganoff, D.; Hsia, Y. and Karamcheti, K., "Some Features of Tones Generated by an Underexpanded Rectangular Jet", AIAA Paper 81-0060, Aerospace Sciences Mtg., St. Louis, Mo. Jan. 1981.

25. Viets, H.; Campbell, J. and Korkan, K., "Acoustic Interactions in Ejectors", AIAA Paper No. 81-2045, AIAA 7th Aeroacoustics Conf., Palo Alto, Calif., Oct. 1981.

26. Viets, H.; Ball, M. and Piatt, M., "Experiments in a Subscale Pilot Gust Tunnel," AIAA Journal, Vol. 19, No. 6, June 1981, pp. 820-822.

27. Viets, H.; Balster, D. and Toms, H.L. Jr., "Time Dependent Fuel Injectors," AIAA Paper No. 75-1305, AIAA Propulsion Mtg., Oct. 1975.

28. Quinn, B., "Interactions Between Screech Tones and Ejector Performance," J. Aircraft, Vol. 14, No. 5, May 1977, pp. 467-473.

29. Brown, G.B., "On Vortex Motion in Gaseous Jets and the Origin of Their Sensitivity to Sound", Physical Society, Vol. 47, Pt. 4, 1935, pp. 703-732.

30. Succi, G.P. Baumeister, K.J. and Ingard, K.V., "Interaction of a Turbulent Jet Noise Source with Transverse Modes in a Rectangular Duct", NASA Technical Paper 1248, June 1978.

31. Morse, P.M. and Ingard, K.V., Theoretical Acoustics, McGraw-Hill, 1968, p. 474.

12. ACKNOWLEDGMENT

The support of the U.S. Air Force Office of Scientific Research under Grant 81-0025 monitored by Capt. (Dr.) M.S. Francis is much appreciated. In addition, the able assistance of Mont Ball in the construction and testing of the apparatus is gratefully appreciated.

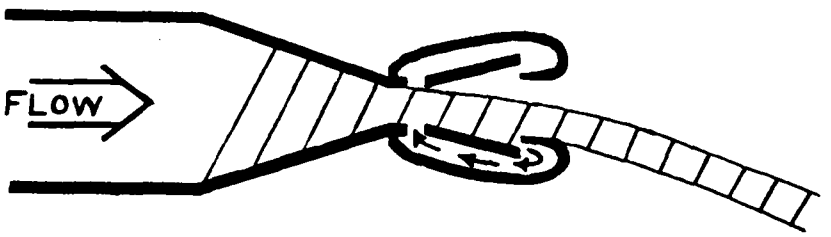

Figure 1. Schematic of the nozzle operation.

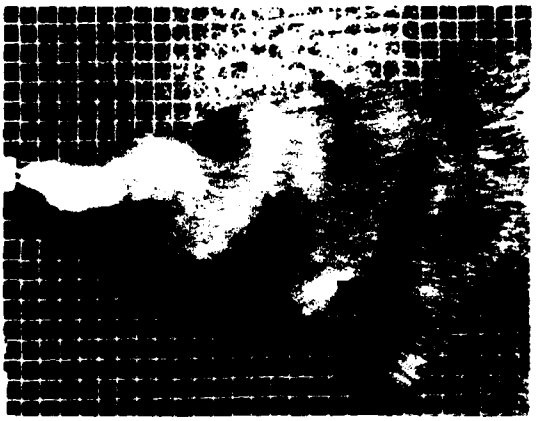

Figure 2. Two phase operation of Nozzle 1, water flow into air.

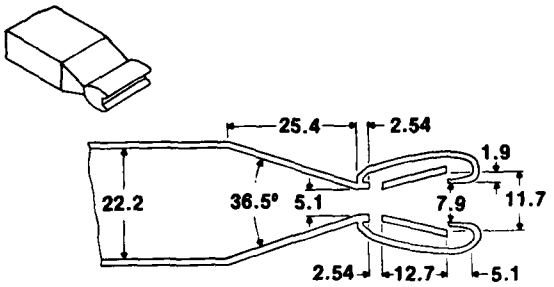

Figure 3a. Geometry of Nozzle 1.

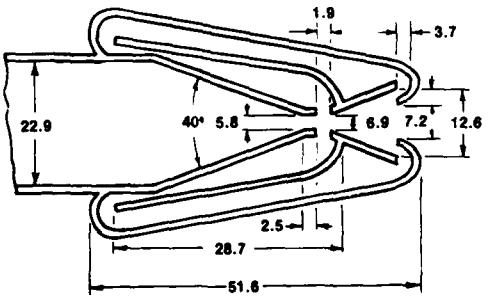

Nozzle 2 dimensions in millimeters

Figure 3b. Geometry of Nozzle 2.

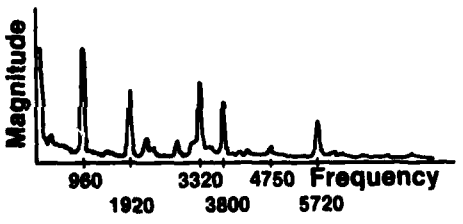

Figure 4. Frequency spectrum of Nozzle 2.

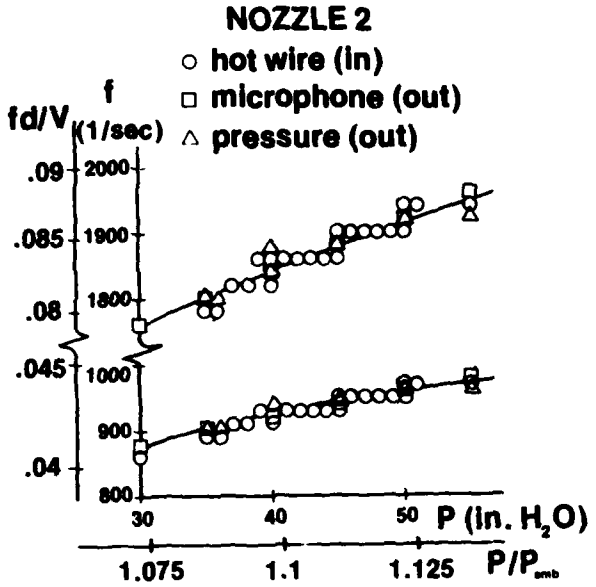

Figure 5. Frequency variation with pressure level for Nozzle 2 by three different methods.

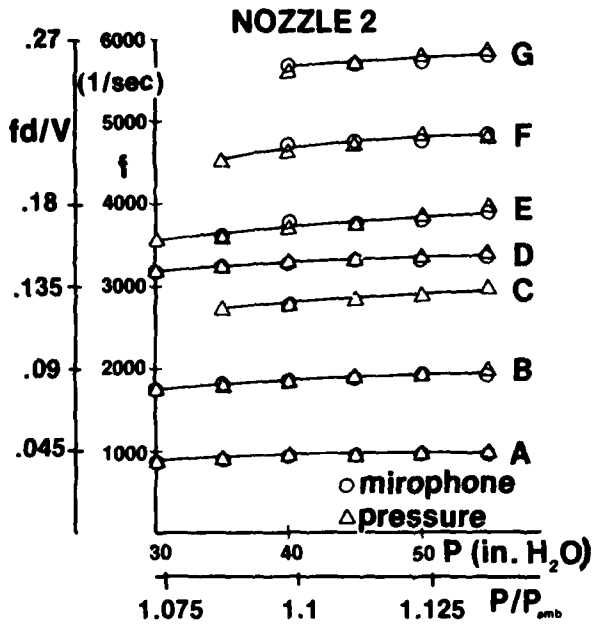

Figure 6. Frequency modes with pressure for Nozzle 2.

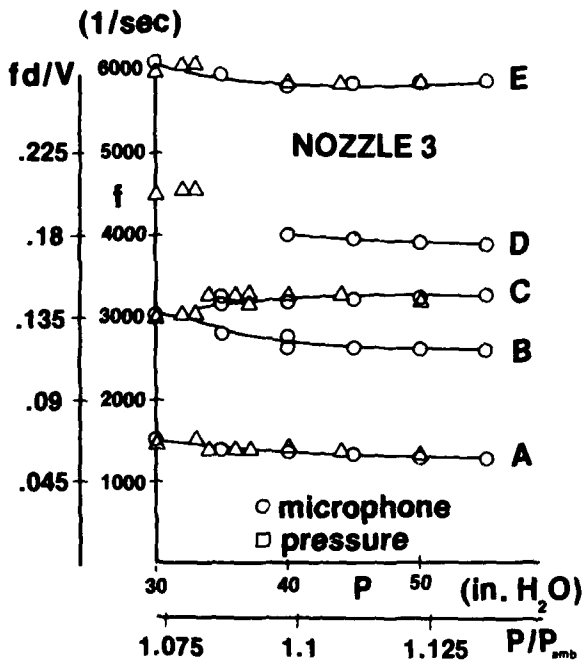

Figure 7. Frequency modes with pressure for Nozzle 3.

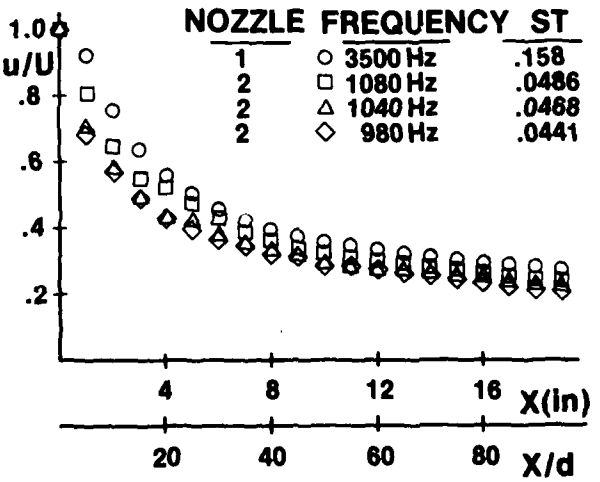

Figure 8. Velocity decay for unsteady jet flows.

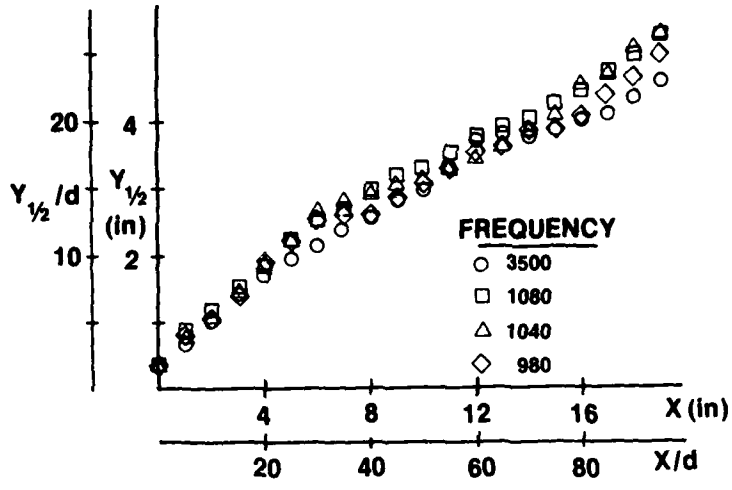

Figure 9. Half width growths for unsteady jet flows.

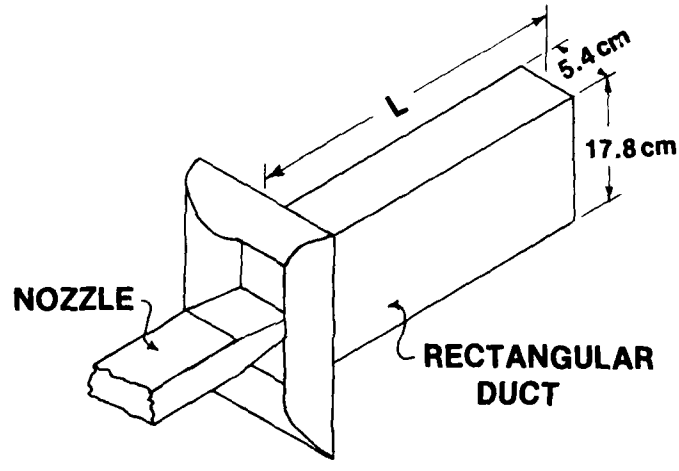

Figure 10. Schematic of the acoustic ejector experiment.

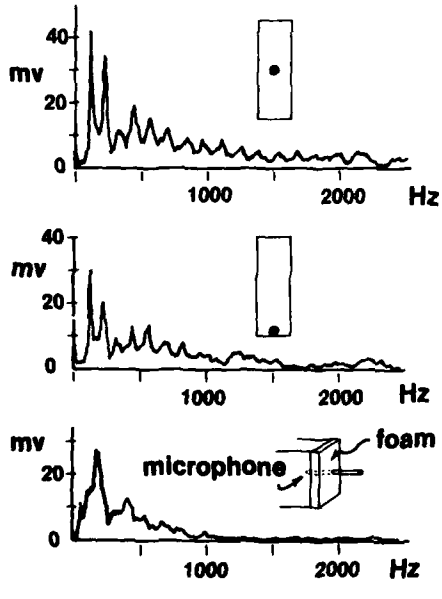

Figure 11. Frequency spectra with the microphone at two locations at the duct exit and with foam at the exit plane.

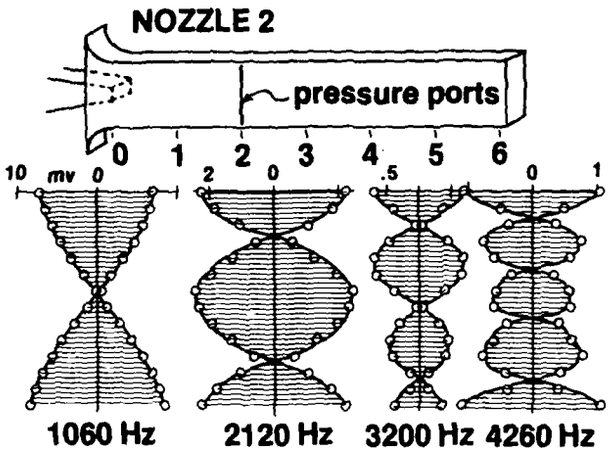

Figure 12. Pressure level distributions of the lower frequency components (taken at X/D = 2, across the longer duct width), Nozzle 2, L/D = 6.1.

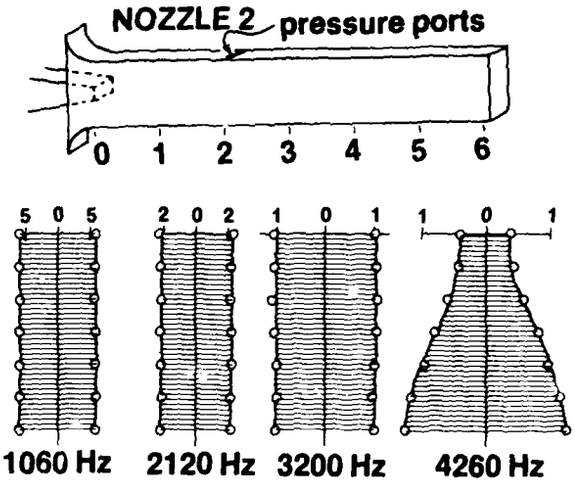

Figure 13. Pressure level distributions of the lower frequency components (taken at X/D = 2, across the shorter duct width), Nozzle 2, L/D = 6.1.

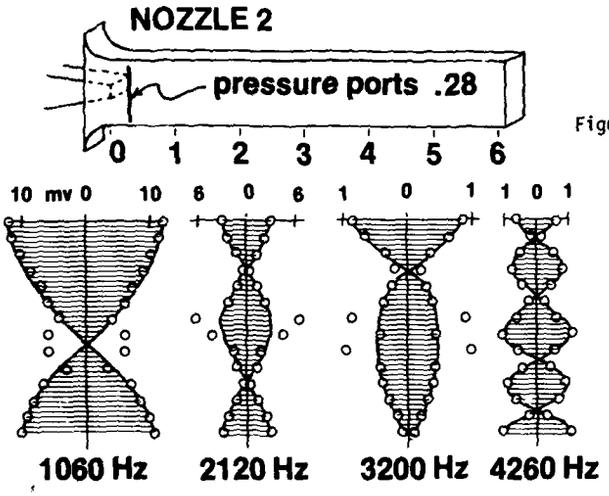

Figure 14.

Pressure level distributions of the lower frequency components (taken at X/D = .28, across the longer duct width), Nozzle 2 L/D = 6.1.

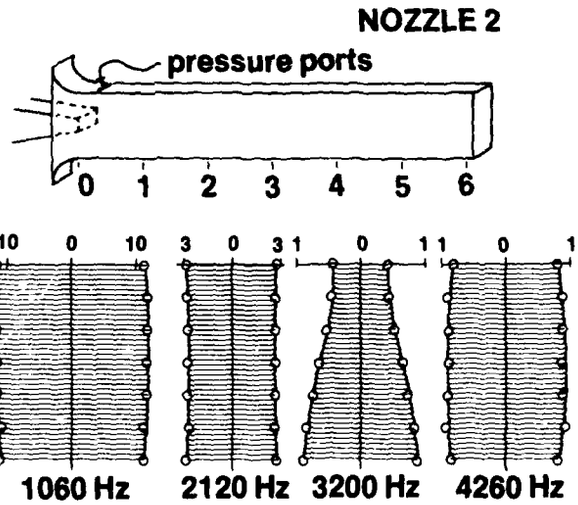

Figure 15. Pressure level distributions of the lower frequency components (taken at X/D = .28, across the shorter duct width), Nozzle 2, L/D = 6.1.

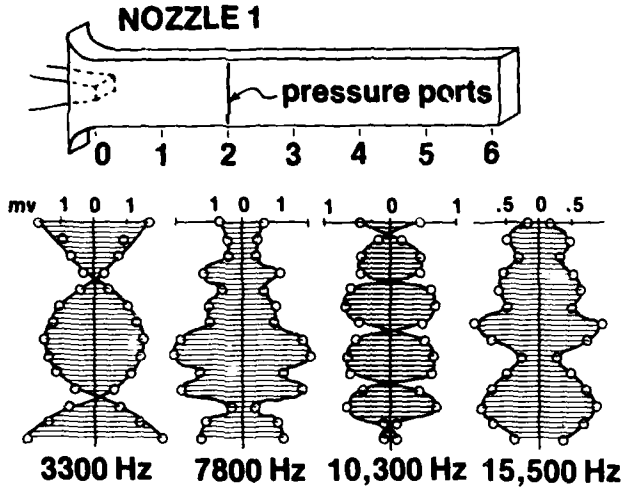

Figure 16. Pressure level distributions of the lower frequency components (taken at X/D = 2, across the longer duct width), Nozzle 1, L/D = 6.1.

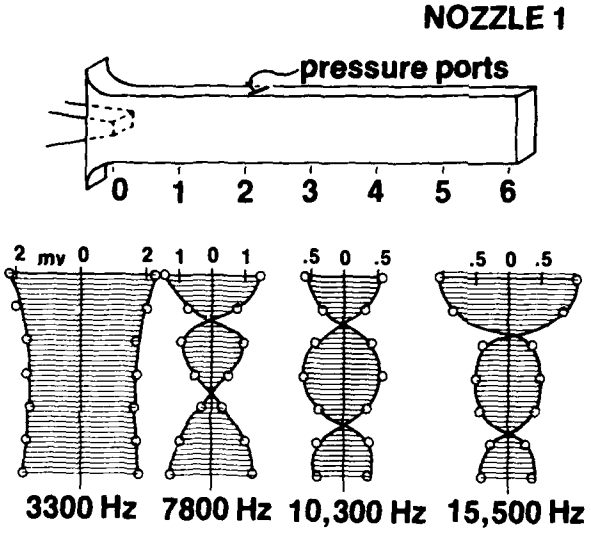

Figure 17. Pressure level distributions of the lower frequency components (taken at X/D = 2, across the shorter duct width), Nozzle 1, L/D = 6.1

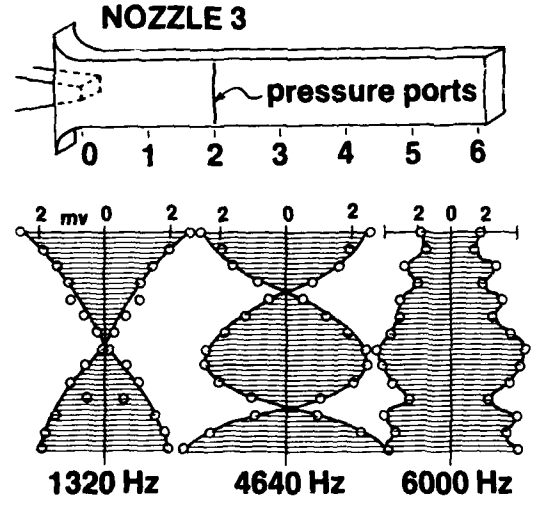

Figure 18. Pressure level distributions of the lower frequency components (taken at X/D = 2, across the longer duct width), Nozzle 3, L/D = 6.1.

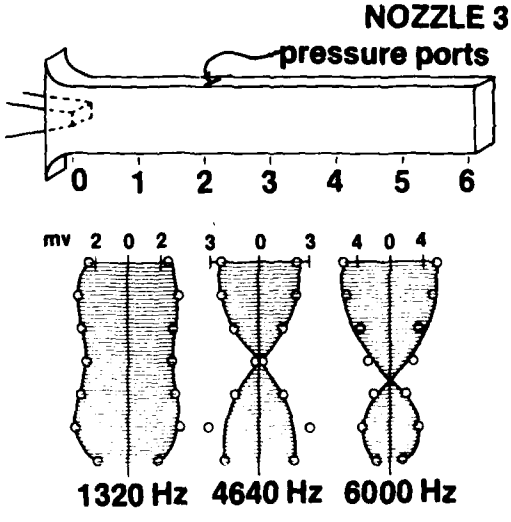

Figure 19. Pressure level distributions of the lower frequency components (taken at X/D = 2, across the shorter duct width), Nozzle 3, L/D = 6.1.

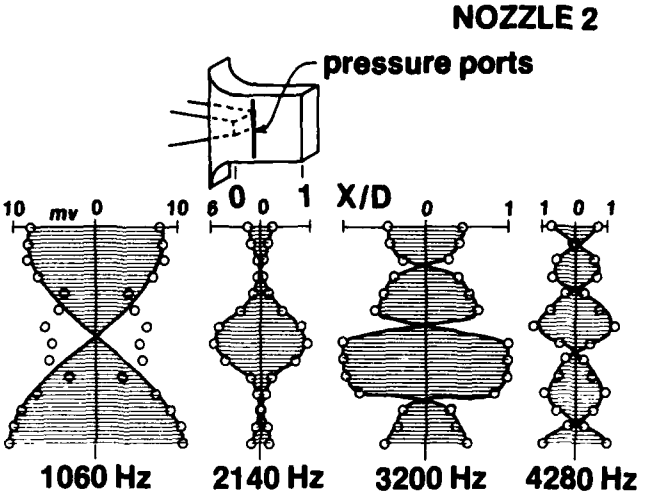

Figure 20. Pressure level distributions of the lower frequency components (taken at X/D = .28, across the longer duct width), Nozzle 2, L/D = 1.

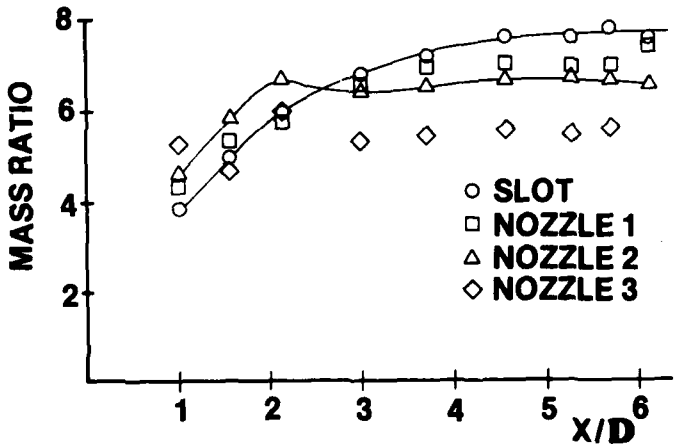

Figure 21. Mass ratio = exit mass flow/primary mass flow, as a function of duct length.

IMPROVEMENT OF EJECTOR THRUST AUGMENTATION BY PULSATING OR FLAPPING JETS

by

G. BINDER and H. DIDELLE
INSTITUT DE MECANIQUE
Associé au Centre National de la Recherche Scientifique
Université Scientifique et Médicale de Grenoble
B.P. 53, 38041 GRENOBLE CEDEX
FRANCE

SUMMARY

The influence of pulsating or flapping motions forced on the primary jet on the performance of thrust augmenting ejectors has been investigated experimentally. The effect of the frequency and the amplitude of the forced perturbations was determined for various mixing duct lengths and diffusor geometries. The mixing duct to jet area ratios were 9 and 20 in the pulsating and flapping case respectively.

In constant area ejectors the improvement in thrust augmentation ϕ over the performance obtained with a steady jet in the same geometry increases with decreasing duct length. Thus, with a total length of only ONE duct width $\phi = 1.2$ could be obtained with unsteady jets whereas $\phi = 1$ in the steady case. ϕ was further improved by the gain in diffusor pressure recovery produced by the unsteady jets. Maximum augmentations of 1.9 and 1.65 were obtained with pulsating and flapping jets respectively as compared to 1.35 and 1.5 in the steady case.

These improvements in ejector performance are mainly due to the faster mixing produced by these jets.

NOMENCLATURE

A	flapping angle
$a = \sqrt{\overline{u_j^2}}/\overline{V_j}$	pulsating amplitude
$C_p = p_b/p_j$	blowing pressure ratio (Fig.2)
D	diameter or width
e	diffusor effectiveness
f	frequency
L	length
p	pressure
R	radius
Re	Reynolds number
S	area $\quad A = S_i/S_j$
$St = \frac{Dj.f}{\overline{V}j}$	Strouhal number
T	thrust
u	velocity fluctuation
V	velocity
α	angular deflection of jet
ϕ	thrust augmentation ratio
ρ	density
η_a	overall efficiency
Ψ	ratio of total to primary mass flow rate
τ	TE/Tj

Subscripts

j	jet
ja	jet discharging into ambiant
m	mixing duct
d	diffusor
E	ejector
t	total
1	mixing duct entrance

Superscript

$(\overline{\ })$	space-time average

1. INTRODUCTION

Reduction in take-off and landing distances of aircraft requires larger thrust to weight ratio in order to increase respectively acceleration and deceleration during these stages of flight. Since ejectors are simple and rugged devices which permit to augment the thrust produced by a given power plant, especially at low forward speed, their application to V/STOL is very appealing. Unfortunately thrust augmenting ejectors tend to be cumbersome which is a major handicap for aeronautical applications. There is, however, no inherrent theoretical impossibility which precludes reduction in size or better performance or even both together. The search for such improvements has motivated a number of investigations and in particular the present work.

Ejectors are also quite interesting from a basic point of view because of the essential role played by turbulent mixing and entrainment. In the ideal case of uniform velocity distributions in the primary, secondary and exit streams the thrust augmentation ϕ may simply be expressed in terms of the mass flow ratio ψ and the energy efficiency η_e by $\phi = \sqrt{\psi \eta_e}$

$(1 - \eta_e)$ is the percentage of kinetic energy dissipated into heat in the apparatus. The thrust augmentation ϕ is defined here as the ratio of the total thrust of the ejector divided by the thrust of the jet discharging into the atmosphere, the generating pressure head of the jet being kept constant.This relationship although only qualitatively correct underscores the necessity to maximize the entrainment and to minimize the dissipation in order to produce better thrust augmentation. How these mechanisms can both be affected in the desired direction by manipulating the turbulence is by any means a trivial question. Neither do we know the answer to the question : what is the optimal entrainment-dissipation within certain size restrictions ? Moreover, at the present time there exists no theory either which could provide reliable guidance towards this goal.

In the work presented here, we have attempted to manipulate the turbulence by forcing time-dependent perturbations on the main jet and we have explored the effects on thrust augmentation.

2. THE DOUBLE ROLE OF MIXING RATE ON THRUST AUGMENTATION

In ejectors composed of a constant area mixing chamber followed by a diffusor the mixing rate between the primary jet and the secondary stream plays an essential role in both ducts. The secondary flow is sucked into the ejector because of the depression in the entrance section. The flow rate of the secondary stream ($\psi - 1$) and therefore the thrust augmentation ϕ depend also directly upon this depression which results from the turbulent mixing in the constant area duct and from the pressure recovery in the diffusor.

The integrated momentum equation shows that in the constant area duct the downstream pressure-rise and the wall friction force are balanced by the momentum loss. Such a loss at constant mass flow can only result from the diminishing non-uniformity of the transverse velocity profile also from the turbulent mixing of the jet. As the jet spreads further into the secondary stream with distance downstream the profile becomes more uniform and the friction force increases. After the jet has spread to the duct wall the gain in profile uniformity is slower and smaller and the momentum loss is not even sufficient to compensate the increase of the friction force. This occurs for a length of approximately 5 Dm for a steady core jet (Fig. 1). For a constant area ejector driven by such a jet the maximum depression at the inlet and, therefore, the maximum thrust augmentation is consequently obtained for a duct length of about 5 Dm. This optimal length can be reduced if the mixing rate can be enhanced and simultaneously ϕ may be slightly improved due to a smaller value of the friction force.

It may be useful to recall some quantitative results of constant area ejectors. The largest possible thrust augmentation given by one dimensionel calculations is $\phi = 2$ for an infinitly large area ratio if there is perfect mixing and no friction. For an area ratio of $\lambda = 10$ the calculated value is $\phi = 1.47$ and measured values are between 1.3 and 1.4 (1).

The general purpose of a diffusor is to produce a pressure rise as efficiently as possible. If a diffusor is fixed behind the mixing duct of an ejector its pressure recovery is added to the depression generated by the mixing. ψ and ϕ are therefore increased. The gain is even more important than the one resulting from the simple addition of the separate pressure recoveries because there is also less dissipation due to the smaller velocity difference between the primary and secondary streams. Contrary to the result for the constant area ejector, there is no upper limit for the computed value of ϕ for an ejector with diffusor provided the diffusor effectiveness e - ratio of the actual to the ideal pressure recovery - remains high at large values of the diffusor outlet to inlet area ratio. The beneficial effect of the diffusor on ϕ falls off rapidly to zero as e decreases from 1 to 0.5. For instance for an ejector with an overall area ratio of 10 ϕ drops from 2.38 to 1.88 to 1.47 (value for the constant area ejector) when e decreases from 0.95 to 0.90 to 0.5. Very high values of ϕ , say $\phi > 2$, can therefore only be produced with excellent diffusors.

A necessary condition for high diffusor effectiveness is the absence of separation. Diffusor stall is very sensitive to the shape of entrance velocity profile especially to low velocities near the wall. But this is precisely what occurs in an ejector with a core jet when the flow at the end of the constant area duct is not completely mixed. Thorough mixing between the primary and secondary stream is, therefore, also crucial for good diffusor performance.

Diffusor effectiveness incorporates not only effects of kinetre energy dissipation but also of velocity non-uniformities. High effectiveness requires furthermore a high degree of uniformity in the exit velocity profile. The figures quoted above indicate that such uniformity should be realized and not only unseparated flow if thrust augmentations larger than two are pursued. However, a positive pressure gradient acts in the opposite sens since it accentuates velocity differences. In order to maintain good homogeneity of the velocity in the diffusor against the action of the pressure gradient turbulent mixing must be maintained therein. It has recently been demonstrated (2) that free stream turbulence of a *minimum* scale and intensity improves diffusor performance. One way to maintain active turbulent mixing in the case of the diffusor is to have an entrance profile with sufficiently steep gradients to sustain intense turbulence production.

But with a central jet this would mean low velocities near the wall and therefore separation. The avoidance of separation and the production of persistant mixing in the ejector diffusor lead also to conflicting requirements.

The recognition that mixing plays a crucial role in ejector performance has lead several investigators to manipulate the turbulence in order to enhance the mixing rate. This has effectively been tried by use of multiple jets (3) , swirl (4) , hypermixing nozzles (5) or a combination of these in particular multiple hypermixing nozzles (6). BERTIN (7) and FOA (8) pointed out that turbulent entrainment is inherently a very dissipative process and attempted to produce entrainment by normal pressure forces rather than by the turbulent shear-stress, the former by compression waves and the latter by swirling fluid sheets ("vaneless turbopump"). The first idea is, of course, only applicable in high speed compressible flow. The second one seems to suffer from the large turbulent production produced by swirl.

The objective of the present research was to investigate the effect on thrust augmentation of unsteadiness forced on the jet such as pulsations or flapping. The investigation of free pulsating or flapping jets undertaken simultaneously in our laboratory showed that they spread faster than steady jets (9, 10, 11). A beneficial effects of unsteadiness on ejector performance could thus be expected. Since quantitative predictions of such turbulent flows are presently beyond reach the extend of these effects could only be ascertained experimentally.

3. APPARATUS. FLOW CHARACTERISTICS. EXPERIMENTAL PROCEDURE

3.1 Flow Loop.

The jets were generated with the following set-up :

- an inlet caisson with dust filtres and cooling radiators designed to maintain the jet temperature equal to ambiant temperature to $\pm$ 0.5°C. The purpose of these provisions was to facilitate the measurement with hot wire anemometers.
- a centrifugal blower giving 0.5 m^3 discharge with a head of 80 mm of water
- control valves
- a settling caisson (cross-section 60 x 60 cm) with grids and a honey comb to produce uniform flow
- a terminal contraction.

3.2 Ejectors.

The geometric characteristics of the jets and ejectors tested are summarized on Fig. 1.

3.3 Pulsating jet.

A pulsating jet may be defined by a velocity at the nozzle exit having a fixed direction and a modulus varying periodically in time. Such a jet was generated by a butterfly valve inserted between the caisson and the nozzle. There is a 4 : 1 contraction between the caisson and the pulsator and between the pulsator (dia. 160 mm) and the terminal nozzle (dia. 80 mm). This valve is driven by a variable speed motor which imposes the frequency.

Typical flow conditions were :

jet mean velocity : $5 \leqslant \bar{V}_j \leqslant 20$ m/s Reynolds number : $Re = \dfrac{\bar{V}_j D_j}{\nu} > 3.10^4$

jet pulsations
r.m.s. relative amplitude : $a = \sqrt{\overline{u^2}}/\bar{V}_j \simeq 60\%$

frequency : $10 \leqslant f \leqslant 50$ hz Strouhal number : $St = \dfrac{fD_j}{\bar{V}_j}$: $0 \leqslant St \leqslant 0.6$

St = 0 evidently corresponds to the steady jet.

3.4 Flapping jet.

A flapping jet is characterized by an exit velocity V_j having a constant modulus and a direction varying periodically about the mean flow direction Ox. If α is the angle between V_j and Ox, then for instance : $\alpha = A \sin(2\pi ft)$. We call the amplitude A the flapping angle.

The flapping motion is produced by making use of the COANDA effect as in fluidic switching amplifiers. Essential in the design of nozzle (Fig. 2) are the two cylindrical surfaces to which the jet may attach producing thus an angular deflection. If the radius of curvature of these surfaces is approximatly equal to the width of the jet it may be blown off from the surface to which it is attached by a small control jet. Since the main jet cannot stay in the middle it flips over to the other surface. The same process repeated alternatively on each cylinder produces the flapping. Alternate periodic blowing is generated with a cylindrical double valve (Fig. 2) in which one port is open while the other one is blocked. This valve is driven by a variable speed motor. The flapping angle A increases with the ratio $C_p = p_b/p_j$. The influence of various geometrical and dynamical parameters on the flapping angle is described in (12).

Typical flow conditions are :

jet mean velocity $\bar{V}_j = 23$ m/s Reynolds number $Re \simeq 1.6.10^4$

flapping motion
optimum blowing pressure $1 \leqslant C_p \leqslant 2$ optimum frequency $f \simeq 20$ hz, $St \simeq 10^{-2}$
angle $4 \leqslant A \leqslant 8°$ blowing discharge/main jet discharge 4 to 8 %

3.5 Measurements of thrust augmentation

Thrust augmentation is defined as

$$\Phi = \frac{\text{total thrust}}{(\text{thrust of jet})_a} = \frac{Tt}{T_{ja}} \qquad (1)$$

The index a specifying that the jet exhausts into the ambiant air. This may also be written :

$$\Phi = \frac{(\text{thrust on ejector}) + (\text{thrust of jet})}{(\text{thrust of jet})_a} = \frac{T_E + T_j}{T_{ja}} \qquad (2)$$

Now : $T_{ja} = Sj\ \overline{V_{ja}^2}$ and $T_j = S_j\ (\overline{V_j^2} + \overline{p_1})$

p_1 being the pressure in the ejector inlet section,

and $\frac{\overline{V_{ja}^2}}{2} + \frac{\overline{p_1}}{\rho} = \frac{\overline{V_j^2}}{2} - \frac{\overline{V_s^2}}{2}$ since : $\frac{\overline{V1^2}}{2} + \frac{\overline{p_1}}{\rho} = 0 \qquad (3)$

Φ may, therefore, be written in the form

$$\Phi - 1 = \sigma + (\sigma + \tfrac{1}{2})(\overline{V_s^2}/\overline{V_{ja}^2}) \qquad (4)$$

where $\sigma = T_E/T_j$. This relationship shows clearly the contribution of the thrust exerted on the ejector to the thrust increase ($\Phi - 1$). Since $\overline{V^2} < \overline{V_{ja}^2}$, and even $\overline{V_s^2} < \overline{V_{ja}^2}/10$ in most practical situations - this was the case in all the present experiments - it is seen that the dominant contribution to ($\Phi - 1$) comes from the force exerted on the ejector. The second term in (4) is only a correction to σ - at most equal to $\sigma/4$ - due to the increase in mass flow of the primary jet.

This relationship was also useful in the present work because it shows that Φ may be entirely determined from the measurement of the thrust on the ejector and the velocities of the jet blowing into the mixing duct V_j and of the secondary stream V_1 according to equations (3). No measurements are also needed of the jet discharging into the ambiant atmosphere. This proved especially convenient with the pulsating jet because it would have been difficult to obtain the same pulsation amplitude with and without the ejector.

In the pulsating case T_E was measured directly on the thrust bench, the ejector duct being fixed to the floating beam (see below) ; $\overline{V_j^2}$ and $\overline{V_1^2}$ were measured with a hot wire anemometer. Traverses provided the data for space averaging and time averaging was performed with an integrating voltmeter. It should be emphasized that because of the large pulsation amplitudes : $\overline{V_j^2} = \overline{V_j^2} + \overline{u_j^2} \neq \overline{V_j^2}$, typically $\overline{V_j^2} \simeq 1.3\ \overline{V_j}^2$. $\overline{V_j^2}$ was determined by measuring $\overline{V}_j$ and $\overline{u_j^2}$.

The thrust bench (Fig. 3) consists of a floating beam supported at both ends by two steel foils fixed to a rigid frame. The elastic deflection of these foils is proportional to the force applied to the beam ; it was about 0.1 mm/N and was optically amplified 4000 times to facilitate the measurements.

Independent checks made by measuring the momentum flux at the ejector exit showed that the preceeding method gave values of $\Phi - 1$ about 8 to 10 % too low. The results reported here are also rather underestimated values of Φ.

With the flapping jet ejector the above procedure gave poor results because of non uniformity in the spanwise direction and because of the unknown pressure distribution on the nozzle. The total thrust was then measured directly by the force exerted by the exhausting momentum flux on a plate perpendicular to the ejector axis. The plate (1.80 x 2.20 mm) was fixed to the beam of the thrust bench. T_{ja} and T_t were both measured in this way. The presence of the mixing duct did not appreciably affect the flapping so that the same conditions were easily maintained with or without ejector.

The measurement of the deflection produced by the force on the thrust bench was improved by using a capacitive displacement transducer (sensibility better than 1 μm). The electrical transducer output also facilitated the time averaging of thrust which fluctuates considerably especially when the ejector has a diffusor.

4. RESULTS AND DISCUSSION

4.1 Pulsating jet ejectors

Tests were performed for different mixing duct length Lm = 1 to 9 Dm, with six different conical diffusors (see Fig. 1) and for different frequencies of pulsation. In order to limit the number of test cases the measurements for a given Lm were begun with the constant area ejector and then diffusors of increasing area ratio were added. The sequence was stopped once Φ decreased with respect to the previous

geometry since the optimum value was passed. The detailed results for the ejectors Lm = 5 and 1 Dm only are presented here (Fig. 4 and 5) but they are the most significant. Augmentations for Lm > 5 Dm were smaller than for Lm = 5 Dm in any case. On Fig. 4 and 5 Φ is plotted vs Strouhal number for various diffusor geometries, the first number in the bracket on each curve indicating the value of the half angle and the second one the length L_D/R_m (R_m is used as length scale for the diffusor to conform to common usage). Values of Φ on the ordinate axis correspond to the steady state case.

It should be stressed that Φ is the thrust ratio due to jets produced by the same head and with identical pulsation frequency and amplitude. The reference value of Φ with a pulsating jet is also the thrust of the corresponding free pulsating jet and NOT that of the steady jet. Otherwise the comparison would have been unfair since $\overline{V_j^2}$ is appreciably larger than $\overline{V}_j^2$ when the amplitude is large.

4.1.1. Ejectors Lm = 5 Dm

It is observed on Fig. 4 that Φ of the constant area ejector Lm = 5 Dm (symbol : +) increases from 1.32 to 1.45 when the jet is pulsating at frequencies corresponding to Strouhal numbers between 0.05 and 0.35. The decrease in Φ at higher frequencies is due to a decrease in amplitude. This gain in Φ is solely due to the faster mixing produced by the forced pulsations as expected from the previous measurements in free jets (9). Φ = 1.45 is close to maximum value quoted above for constant area ejectors with λ = 9.

Diffusors added to the mixing duct produce a decrease in Φ from 1.35 to 1.28. This proves that the flow separates in the diffusors. There is a loss in Φ because there is a slight pressure drop in the diffusor necessary to push the flow through it. This result was not surprizing since the selected diffusor geometries were at the limit or in the region of stall on the performance chart for even smaller profile non-uniformities than the one reached at the end of a 5 Dm mixing duct (13)

The most spectacular result of Fig. 4 is the jump of Φ from 1.28 to values between 1.7 and 1.88 with the diffusor (5,8) when the frequency of pulsation is increased from 0 to St = 0.05. Several tests at different velocities have been performed with this geometry (circled values indicate the velocity). The longer diffusor with the same angle gave augmentations of about 1.60 and the 7° diffusors gave augmentations between 1.60 and 1.70. Since the performances with other mixing ducts were smaller, the geometry Lm = 5 Dm with a diffusor (5,8) is thus not far from optimal. An independant check of Φ was performed with this geometry by measuring the exit velocity profile along four diameters and by computing the momentum flux therefrom. The integration yielded Φ = 2.02 also a value somewhat higher than the one obtained from direct thrust measurements.

It is remarkable that the maximum effect of the pulsation is obtained at a Strouhal number of only 0.05. Indeed, the results with free pulsating jets (9) show the maximum effect on the mixing rate is produced at St = 0.2 - 0.3. This difference in behaviour is, however, not contradictory if the life time of the pulsation is taken into consideration. This time or the distance downstream over which the forced perturbation subsists increases with decreasing frequency. For St $\simeq$ 0.3 this distance is about 12 Dj or 4 Dm. At a frequency St = 0.05 there must hence subsist an appreciable pulsation amplitude at the diffusor entrance which is able to maintain active mixing therein. This argument is also consistent with the observed fact that the largest gain in Φ due to the pulsations comes from the improvement of the diffusor pressure recovery.

4.1.2. Ejectors Lm = Dm

With a very short mixing duct Lm = 1 Dm the thrust augmentation is 1 whatever the diffusor (Fig. 5) when the jet is steady. This duct is too short to allow any significant entrainment to be produced inside and the diffusors are attacked by pure jet flow which fully separates. By contrast the performances with the pulsating jet are quite remarkable. Not only is there an augmentation of 1.18 reached with just the mixing duct - with a total length=ONE diameter ! - but the diffusors improve the performance to Φ = 1.42. To obtain appreciable pressure recovery in the diffusors after such a short mixing duct was quite unexpected. These thrust augmentation results prove that separation is delayed by the vigorous turbulence produced by the forced pulsations.

It is observed that the 5° - diffusors perform better than the 7° - ones and that the shorter ones do better than the longer ones. This shows that 7° is more of an angle than the pulsating jet can fill. Furthermore it shows that the diffusors (5,6) and (7,3) are at the limit of stall or partially stalled since added length deteriorates the performance. It would have been interesting to test shorter 5°-diffusors or diffusors with smaller divergence angles in order to find the optimal geometry but this would have required other ducts which unfortunately were not available.

Contrary to the behaviour of Φ with Lm = 5 Dm, here it increases monotonically with Strouhal number. This may be explained by the increased influence of pulsation with Strouhal number on the initial development of the jet.

4.1.3. Best performances vs total length

The best thrust augmentations vs total length L_t -for all geometries tested are summarized on Fig.6 - Comparison of the results obtained with steady and pulsating jets in constant area ejectors show that forced pulsations :

- increase the maximum value of $\emptyset$ from 1.33 to 1.46
- improve $\emptyset$ for any duct length but especially in short geometries. Thus the thrust gain due to the ejector ($\emptyset$ - 1) passes from 0 to 0.16, 0.05 to 0.29, 0.17 to 0.38 for the respective lengths of 1, 2 and 3 Dm.

It may also be noted that the 2 Dm long pulsed ejector produces almost the same $\emptyset$ as the 5 Dm.long steady one, $\emptyset$ = 1.29 as compared to 1.33.

Diffusors improved performance only when the jet was pulsed except for a slight gain in the steady

case for Lm - 9 Dm. The gain in thrust due to pulsation for a given length is approximately 0.2 for L_t up to 5 Dm. There after this gain grows since ϕ decreases in the steady case while it increases with length in the unsteady case up to L_t = 9 Dm where ϕ reaches the highest value of about 1.9.

4.2. Flapping jet ejectors

The improved and simplified measurement technique developed for the flapping jet ejectors allowed the gathering of more extensive data. With the two-dimensional geometry it was on the other hand also possible to vary the diffusor angle continuously so that for every mixing duct and diffusor length the optimum angle could be determined exactly. Moreover the flapping angle could be varied very easily by adjusting the blowing pressure (12). For each geometry the optimal flapping motion was then determined.

Preliminary tests showed that the best thrust augmentations were obtained at rather low frequencies of 10-20 hz and low blowing pressures except with wide angle diffusors so that only a limited range of frequencies and blowing pressures had to be explored in order to find the optimal conditions.

Fig. 7 and 8 show the thrust augmentations for total ejector lengths of 7 and 3 Dm vs diffusor divergence angle. In each case several combinations of mixing duct and diffusor lengths were tested. The first number in the bracket corresponds to the length of the constant area mixing duct and the second one to the length of the diffusor. The points on the ordinate axis are, of course, those of the constant area ejector Lm = L_t . The representation ϕ vs θ has the advantage of showing the optimal diffusor angle for a given combination of Lm and L_d as may clearly be seen on Fig. 7 and 8.

4.2.1. Ejectors L_t = 7 Dm

The most striking result of Fig. 7 is the improvement of thrust augmentation due to the forced flapping of the jet. The best results in the steady and unsteady cases are respectively 1.48 and 1.65. Actually for any given geometry ϕ is always higher with the flapping jet.

The gain in ϕ is mainly due to the better efficiency of the diffusor since for the constant area ejector ϕ rises only from 1.42 to 1.45 when jet is forced.

The maximum ϕ in either steady or unsteady case are nearly independent of the (Lm, L_d) combination and are reached for rather low values of θ . Even the ejectors with no constant area mixing duct yield a maximum ϕ comparable with the others. Actually it is the largest value in the steady case. Hence, there must be active turbulent momentum mixing in these diffusors. The sharp distinction between mixing duct and diffusor which was stressed in the introductory remarks on mixing is also rather artificial although convenient for the sake of clarity. There is a pressure rise due to mixing in both but in the diffusor there is an additional pressure rise induced by the diverging geometry. Since in the steady case there is only a slight gain in ϕ (from 1.42 to 1.45 and 1.48) produced by the diffusors it may be concluded that the divergence pressure recovery contributes very little to the total pressure rise.

ϕ = 1.65 is the largest thrust augmentation obtained. The corresponding flapping motion was A = 3.5° f = 20 hz ; the blowing pressure was p_s = 32 mm (≙ generating pressure of main jet) and the mass flow of the blowing was 4 % of the main jet flow.

4.2.2. Ejectors L_t = 3 Dm

The improvement in ϕ due to the forced flapping is here again quite striking. The maximum value rises from 1.35 to 1.57. This latter value compares very favorably with the maximum ϕ = 1.65 obtained for L_t = 7 Dm with an ejector which is more than twice in length. The forced flapping is also quite interesting for the short geometries.

Comparison between the steady and unsteady results shows a large gain already for the constant area ejectors (ϕ increases from 1.35 to 1.49) due to the faster mixing produced by the flapping according to expectations from the free jet behaviour (11). In the steady case there is no pressure recovery gained by the divergence as proven by the nearly monotonic deterioration of ϕ with θ for the three geometries. When the jet is forced there is a modest gain in ϕ when the ejector has at least a short constant area duct.

4.2.3. Best performances vs total length

For constant area ejectors the maximum value of ϕ is only increased from 1.45 to 1.49 by the forced flapping (Fig. 9) but the length is reduced by 50 % (3 Dm instead of 6 Dm) an important factor in aeronautical applications.

In this geometry thanks to the possibility to increase the diffusor angle continuously, it was possible to observe a gain in ϕ due to the diffusors with the steady jets. But this gain is only appreciable for long ejectors $L_t \geq$ 6 Dm. When the jet is forced diffusors improve ϕ as soon as $L_t >$ 2 Dm. The maximum ϕ observed is 1.65 also lower than with the pulsating jet despite a larger area ratio (λ = 20 as compared to 9.15).

Particularly interesting is the good performance obtained with short geometries. Thus for L_t = 3 Dm ϕ reaches already a value of 1.56 while doubling the length produces only a increase to 1.65.

Comparison with the pulsating case shows that ϕ grows faster with L_t and is higher up to L_t = 5 Dm when the jet is subjected to forced flapping but then it levels off rapidly. The performance of the pulsating ejector on the contrary continues to increase up to L_t = 9 Dm.

5. CONCLUDING REMARKS

These experiments show that manipulations of jet turbulence and mixing rate by forced pulsations or flapping motions produce important improvements in ejector thrust augmentations. Gains with respect to steady jet performances are especially remarkable in short geometries and with diffusors. Only in the forced cases is there an appreciable or even large pressure recovery produced by the diffusor divergence.

The thrust augmentations considered here do not take into account losses or power requirements of the unsteady jet generation and should therefore not be confused with overall efficiency. It is not claimed that pulsating or flapping jet ejectors produce higher thrust for given total power. It is only shown that the forcing produces faster and more energetic mixing and permits to recover at least some of the potential pressure rise of the diffusor divergence. These improvements are a necessary but, of course, not a sufficient condition for practical applications.

The valve used to create the pulsating jet was certainly very inefficient. Moreover, the kinetic energy of the pulsating jet is larger than that of the steady jet with the same mean velocity. The evaluation of the overall energy efficiency is not even attempted in this case.

The cost of the flapping generation is approximately the flow bleeded from the main jet for the control blowing. This was about 4 % of the main jet discharge for typical optimal flapping motions ($p_s = p_j$). For the L_t = 3 Dm case, ϕ increases from 1.38 to 1.56. With $\Delta T_{ja}/T_{ij}$ = - 0.04 and $\Delta\phi$ = + 0,18 the relationship $T_t = \phi T_{ja}$ yields upon differentiation $\Delta T_t/T_{ja}$ = + 0,12. There is also a 12 % overall gain in thrust for the same power input.

In this investigation no effort was devoted to the development of more efficient generating devices which of course does not preclude the possibility of more efficient designs based on other ideas. Resonnance effects could for instance be used to produce pulsations and, on the other hand, the generation of self flapping jets by using feedback as in fluidic oscillators is a real possibility (14, 15).

Acknowledgements

Financial support of the Direction des Recherches, Etudes et Techniques from the Ministère de la Défense is gratefully acknowledged.

REFERENCES

1. DIDELLE, H. and BINDER, G., Institut de Mécanique, Université Scientifique et Médicale de Grenoble. Jets Instationnaires. L'Augmentation de Poussée des Trompes à Jets Pulsants ou Battants, 1976 - 249 p.

2. HOFFMANN J.A., "Effects of Free-Stream Turbulence on diffusor Performance" - J. Fluids Engineering Vol. 103, Sept. 1981, pp. 385-390.

3. BERTIN J. and LE NABOUR M., "Contribution to the development of ejectors and jet pumps" Contribution à l'étude des trompes et éjecteurs . Techniques et Sciences Aéronautiques, n° 2, pp. 127-138, (1959).

4. HOHENEMSER K.H. and PORTER J.L., "Contribution to the theory of rotary jet flow induction". J. of Aircraft, 3, 4, pp. 339-346, (July - AUG. 1966).

5. FANCHER R.B., "Low-area ratio thrust augmenting ejectors". J. of Aircraft, 9, 3, pp. 243-248, (March 1972).

6. QUINN B., "Compact ejector thrust augmentation", J. of Aircraft, 10, 8, pp. 481-486, (August 1973).

7. BERTIN J., "Dilution pulsatoire sur réacteur", Compte Rendus à l'Académie des Sciences, vol 240, 1955, pp. 18-22.

8. FOA J.V., "A Vaneless Turbopump, A.I.A.A. Journal vol. 12, n° 2, 1963, pp. 466-467.

9. FAVRE-MARINET M. and BINDER G., "Structure des Jets Pulsants", Journal de Mécanique, vol. 18, N° 12, (1979), pp. 355-394.

10. BINDER G. and FAVRE-MARINET M., "Flapping jets". Flow-induced structural vibrations, pp. 57-62, (Springer Verlag, 1974). I.U.T.A.M. - I.A.H.R. Symp., Karlsruhe, (Aug. 14-16, 1972).

11. SOUTIF, M., FAVRE-MARINET M., and BINDER G., Institut de Mécanique, Université Scientifique et Médicale de Grenoble, "Diffusion et Structure des Jets Battants", 1977, 202 p.

12. FAVRE-MARINET M., BINDER G., and Te V. HAC, "Generation of Oscillating Jets, to be published in J. Fluids Engr.

13. COCANOWER J.B., KLINE S.J. and JOHNSTON J.P. : "A unified method for predicting the performance of subsonic diffusors of several geometries". Thermosciences Div., Dpt Mechanical Engn., Stanford Univ., California, 94 p.,(May 1965).

14. QUINN B., "Effects of Acoustic Interactions on Ejector Performance" J. Aircraft, Vol 12 n° 11, 1975, pp. 914-916.

15. VIETS H., "Flip-Flop Jet Nozzle", A.I.A.A. Journal vol 13, n° 10, 1975, pp. 1375-1379.

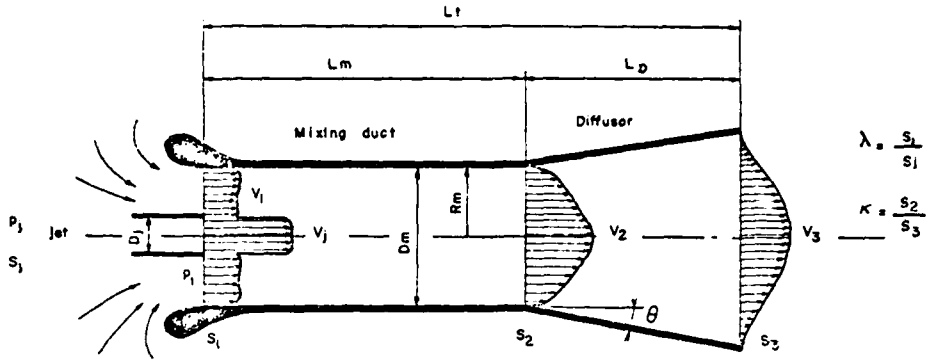

	PULSATING JET EJECTOR		FLAPPING JET EJECTOR
GEOMETRY	axisymmetric		two - dimensional
JET Dj	60 mm		10 mm } hight 500 mm
MIXING DUCT Dm	242 mm		200 mm } hight 500 mm
area ratio λ	9.15		20
length	$1 \leqslant Lm/Dm \leqslant 9$		$0 \leqslant Lm/Dm \leqslant 9$
DIFFUSOR θ	5°	7°	continuously variable
length LD	LD/Rm = 6,8,10	LD/Rm = 3,4,6	$0 \leqslant Lm/Dm \leqslant 9$
area ratio	$2.4 < 1/\kappa < 3.6$	$1.9 < 1/\kappa < 3.1$	continuously variable

FIG.1 DEFINITION SKETCH AND GEOMETRIC CHARACTERISTICS OF EJECTORS

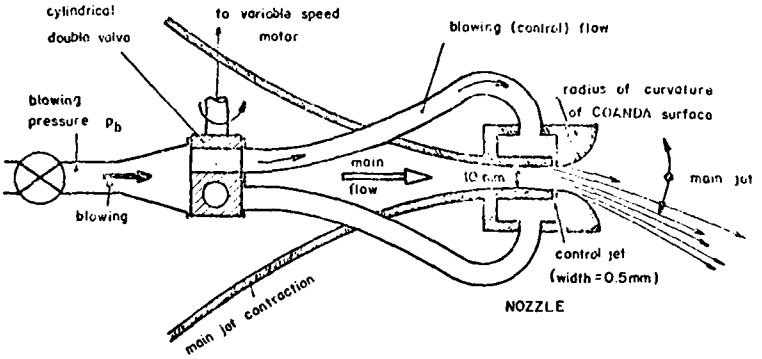

FIG.2 - FLAPPING JET NOZZLE.

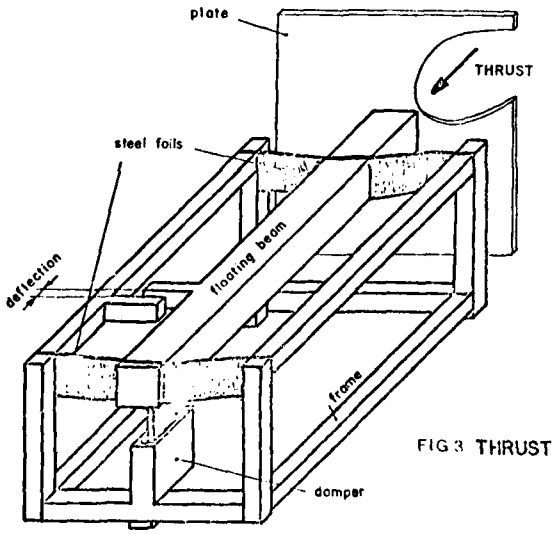

FIG.3 THRUST BENCH.

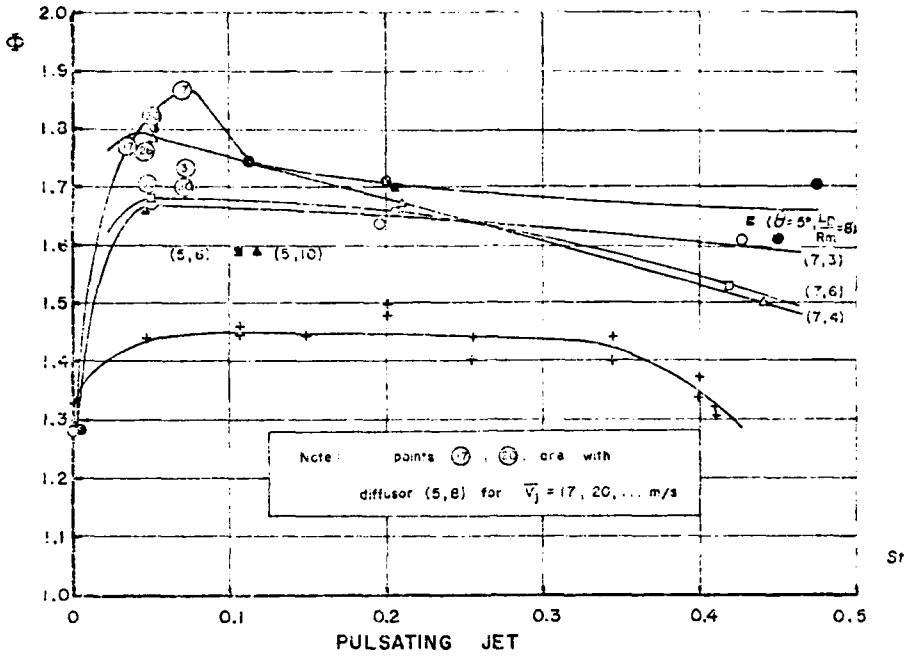

FIG.4 THRUST AUGMENTATION OF EJECTORS Lm = 5 Dm

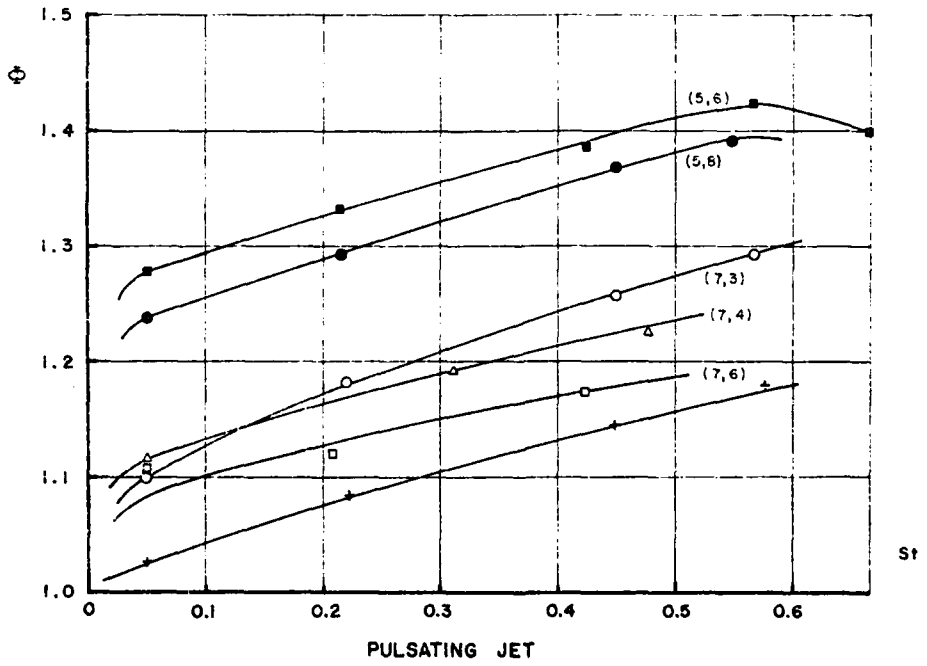

FIG.5 THRUST AUGMENTATION OF EJECTORS Lm = 1 Dm

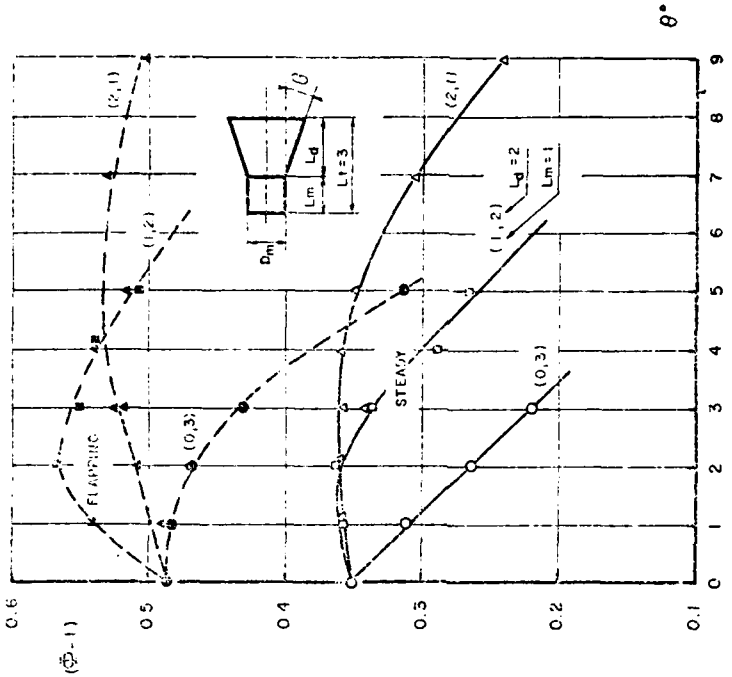

FIG.8 THRUST AUGMENTATION OF EJECTORS Lt = $3D_m$

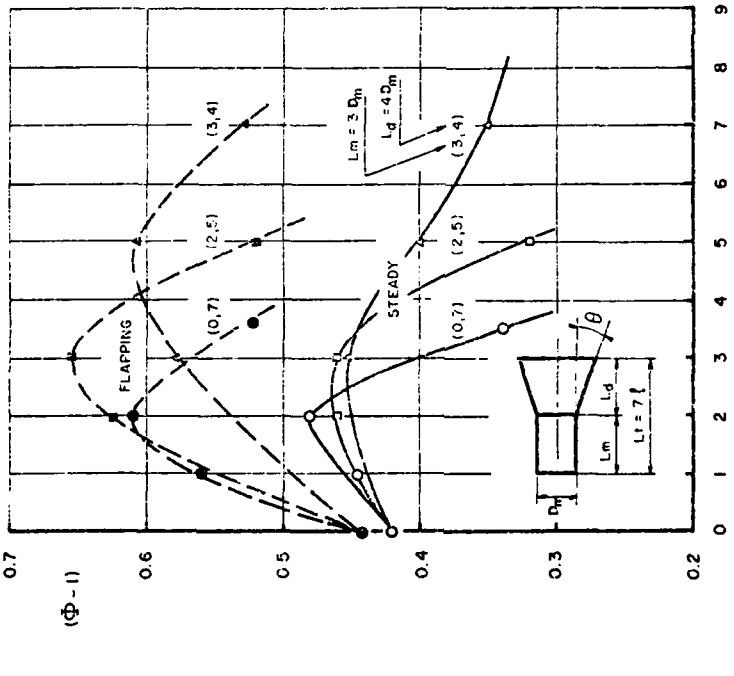

FIG.7 THRUST AUGMENTATION OF EJECTORS Lt = $7D_m$

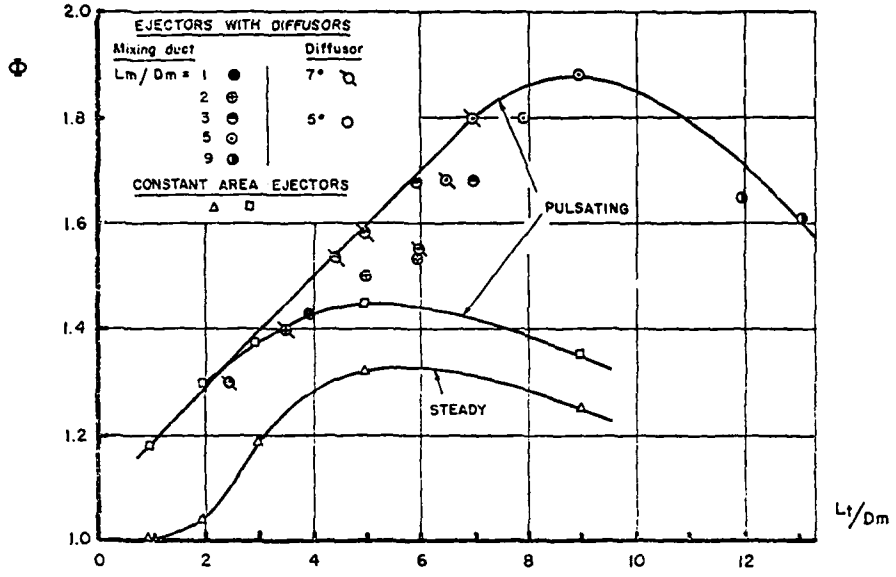

FIG.6 BEST THRUST AUGMENTATIONS VS TOTAL LENGTH WITH PULSATING AND STEADY JET. (Axisymmetric ejector $\lambda = 9.15$).

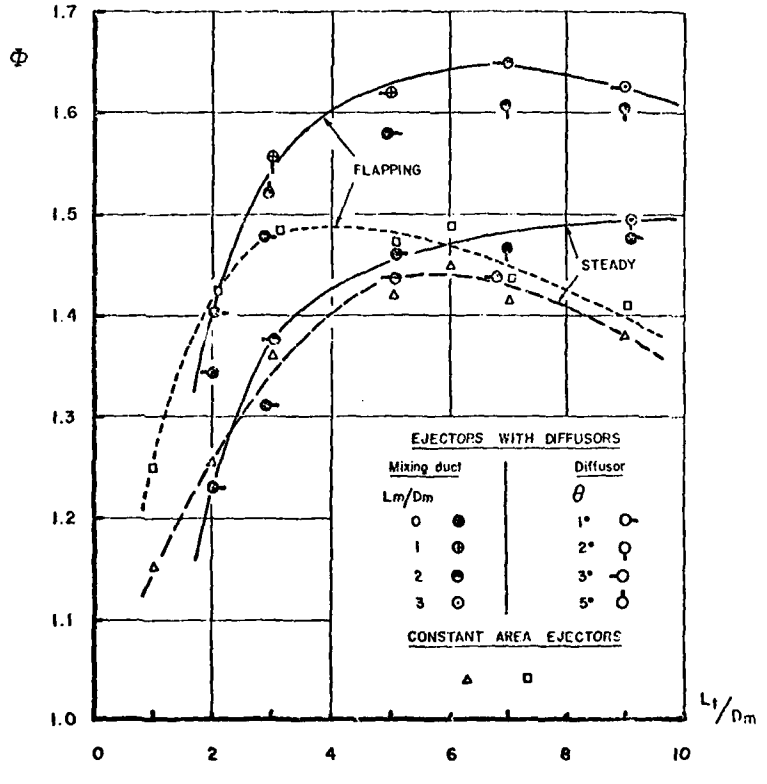

FIG.9 BEST THRUST AUGMENTATIONS VS TOTAL LENGTH WITH FLAPPING AND STEADY JET.
(two-dimensional ejector $\lambda = 20$).

ETUDE EXPERIMENTALE D'UN DEVIATEUR DE JET

M. LEPRETRE C. PORTIER

Société BERTIN, BP 3, PLAISIR 78370 Fr.

RESUME

Un modèle probatoire de dispositif aérodynamique d'orientation du vecteur poussée d'un réacteur a été mis au point en exploitant les propriétés de recollement d'un jet sonique ou faiblement supersonique sur une surface déviatrice plane ou courbe convenablement disposée en aval du plan de sortie de la tuyère.

L'étude paramétrique effectuée a fourni des résultats très encourageants montrant qu'il était possible, avec des solutions simples, d'obtenir des taux de déviation importants sans perte exagérée de la poussée résultante ; un tel système peut être mis à profit soit pour améliorer la maniabilité en combat soit pour réaliser un appareil STOL.

Le dispositif ainsi défini se caractérise par une grande simplicité, le recollement du jet s'avérant spontané et stable dans tout le domaine exploré, sans requérir la mise en oeuvre de systèmes annexes tels que soufflage ou aspiration.

SUMMARY

An aerodynamical device of a jet engine thrust vectoring has been developed on a probatory model.

For that purpose, a sonic or slightly supersonic jet is reattached on a reverser surface, plane or curved, suitably placed downwards a nozzle outlet.

A parametric study has been made. Important reverse rates can be obtained without a drastic loss of the resultant thrust. Such a device can be used to improve the manoeuvrability in fight or to realize a STOL aircraft.

Defined in that way, this device is very simple :
in fact the jet reattachment is spontaneous and stable all over the explored domain and does not need any extra system such as blowing or suction.

NOTATIONS

Paramètres géométriques :

D_c	diamètre au col de la tuyère
D	diamètre en sortie de tuyère
L	longueur du déviateur
R	rayon de courbure du déviateur
X	marche longitudinale entre déviateur et plan de sortie tuyère
Y	marche transversale
H	hauteur de la cavité
l	longueur du flasque
d	écart entre limite supérieure du flasque et axe tuyère
J	jeu longitudinal entre flasque et plan de sortie tuyère
e	jeu radial du flasque par rapport au diamètre de sortie tuyère
α_o	angle d'attaque du déviateur

Paramètres physiques :

M	nombre de Mach en sortie de tuyère
V	vitesse locale de l'écoulement
ρ	masse spécifique locale
p	pression statique locale
p_o	pression génératrice de l'écoulement
p_a	pression atmosphérique
γ	coefficient polytropique des gaz
r	courbure locale de l'écoulement

Performances :

F_x	poussée axiale
F_y	poussée latérale
F_{xo}	poussée axiale sans déviation

1 - INTRODUCTION

Parmi les qualités demandées aux avions de combat des nouvelles générations, la manoeuvrabilité en combat et la capacité de décollage et d'atterrissage court figurent en bonne place. La mise au point d'un système adéquat d'orientation du vecteur poussée constitue, de ce fait, un objectif privilégié.

Dans le premier cas, il s'agit de fournir à l'appareil les moments de manoeuvre complémentaires nécessaires à son évolution à forte incidence, configuration dans laquelle cette fonction ne peut être assurée par la seule aérodynamique externe ; dans le second, on demande au système de délivrer, à basse vitesse, une part significative des efforts de portance requis pour le décollage ou l'atterrissage sur des plateformes de dimensions restreintes : terrain sommairement aménagé ou porte-avions.

L'étude exploratoire présentée ici avait pour but la réalisation d'un modèle simple de déviateur permettant d'orienter la poussée en exploitant les propriétés du recollement d'un jet sur une paroi courbe et en s'attachant à conserver la géométrie des tuyères de révolution à section variable actuellement développées.

Le dispositif préconisé permet donc de s'affranchir des problèmes posés par l'emploi de tuyères aplaties dont le jet bidimensionnel se prête bien à la déviation mais qui impliquent, du fait de leur complexité, des coûts de développement considérables.

Les essais, effectués au point fixe sur des maquette à échelle réduite, ont permis de vérifier la faisabilité du principe et de s'assurer du réalisme de la solution tant sur le plan fonctionnel que technologique, le recollement étant spontané et stable et l'architecture extrêmement rustique.

Les niveaux de poussée latérale fixés par les spécifications étaient de 15 % de la poussée axiale nominale dans la première application (manoeuvrabilité) et de 60 % dans la seconde (STOL) ; dans le premier cas, la perte de poussée résultante maximale était fixée à 5 %.

2 - PRINCIPE DE FONCTIONNEMENT

Le principe mis en oeuvre résulte de l'adaptation au cas particulier des réacteurs d'avion de travaux de recherche entrepris depuis de longues années à la Société BERTIN & Cie sur les problèmes de recollement de jets supersoniques et qui ont abouti notamment, en collaboration avec la Société des Engins MATRA, à la conception d'un système de pilotage original applicable à des petits missiles (Ref. 1).

Le dispositif est représenté schématiquement sur la Figure 1.

Il comporte principalement une surface déflectrice dénommée déviateur, disposée en aval du plan de sortie de la tuyère de manière à ménager, par rapport à celui-ci, une marche descendante dans le sens de l'écoulement, de largeur X et de hauteur Y ; à ce déviateur sont associés, de part et d'autre, deux flasques latéraux de forme et de dimensions appropriées formant avec lui un canal bidimensionnel ouvert, au sein duquel s'organise l'écoulement.

Lors de la mise en route apparaît un régime transitoire au cours duquel le jet provoque, par entraînement visqueux, une dépression au niveau de la marche ; de ce fait, un déséquilibre se trouve créé entre les pressions régnant de part et d'autre de l'écoulement par ailleurs canalisé par les flasques.

Il en résulte un basculement du jet ; celui-ci recolle sur le déviateur, entretenant ainsi la dépression initiale dans la zone morte qui s'établit à l'aplomb de la marche où règne un courant de recirculation.

Pour que le phénomène soit stable, il importe alors que l'angle d'attaque du jet sur le déviateur et la courbure de celui-ci soient convenablement choisis, de manière à éviter le décollement au point d'impact lié à l'interaction onde de choc - couche limite et à assurer tout le long du déviateur l'équilibre centrifuge du jet.

Cette condition d'équilibre centrifuge est approchée théoriquement à partir de la relation :

$$\frac{dp}{dr} = \frac{\rho V^2}{r} \rightarrow R = \frac{D}{\sqrt{\frac{u_1^n(u_2^n - 1)}{u_2^n(u_1^n - 1)}} - 1}$$

expression dans laquelle les indices 1 et 2 correspondent respectivement aux limites extérieure et intérieure du jet, avec :

$$u = \frac{p}{p_o}$$

$$n = \frac{1}{\gamma} - 1$$

Ce rayon est ensuite optimisé par des essais sur des déviateurs encadrant la valeur nominale.

L'angle d'attaque, pour sa part, est déterminé de manière empirique en faisant varier pas à pas le paramètre α_o.

3 - MOYENS D'ESSAIS

Les essais sont réalisés en deux étapes : dans un premier temps, on optimise le rayon et l'angle d'attaque du déviateur à l'aide d'essais fonctionnels au cours desquels on évalue la stabilité du recollement par des relevés de pression sur des prises régulièrement réparties dans le plan de symetrie du système ; ensuite, on procède à l'optimisation des autres paramètres au moyen d'essais de performances sur une balance à deux composantes.

Dans chacun des cas, les essais sont réalisés au point fixe, en gaz froids, par raffales et sans écoulement externe.

Le schéma de principe de la balance utilisée est représenté Figure 2.

L'ensemble pesé se compose d'une bouteille en alliage léger fretté (40 dm^3/200 bar), d'une électro-vanne et d'un détendeur à dôme pilotable à distance raccordé directement à la maquette ; il est suspendu au châssis au moyen de deux câbles autorisant le libre déplacement longitudinal et transversal.

La bouteille est remplie préalablement à l'essai à partir d'un cadre d'azote. L'électro-vanne (2 voies) montée sur la bouteille assure l'isolement après remplissage alors que l'électro-vanne (3 voies) placée sur le bâti permet à la fois de fermer le circuit de remplissage et de mettre le flexible de liaison à l'air libre, évitant ainsi toute réaction parasite.

De son côté, le circuit de pilotage comprend un détendeur pilote et une électro-vanne 3 voies raccordée au dôme du détendeur principal par une tuyauterie flexible n'introduisant qu'une faible interaction.

La mesure des poussées axiale et latérale est réalisée à l'aide de capteurs piezo-résistifs travaillant suivant le cas en compression ou en traction, la liaison entre bouteille et bâti étant assurée par des adaptateurs équipés de doubles cardans destinés à éliminer les interactions résultant des défauts d'alignement.

4 - DESCRIPTION DES MAQUETTES

Les différentes maquettes, quelles qu'en soient les dimensions, sont toutes conçues selon un schéma simple permettant de procéder aisément à des modifications ou des réglages en cours de mise au point.

L'architecture générale de la maquette est représentée Figure 3.

Un corps en alliage léger supporte au moyen d'usinages appropriés les différents éléments du montage ; il est muni d'un adaptateur équipé d'une bride tournante permettant un positionnement aisé et rigoureux de la maquette sur la balance.

La tuyère, rapportée sur le corps, est alimentée suivant le cas à travers un dispositif de tranquillisation (nid d'abeille) ou de mise en rotation simulant les conditions d'écoulement en sortie du réacteur. La pression génératrice est mesurée en aval de ce dispositif, dans une chambre où la vitesse de circulation des gaz est faible.

Enfin, des cales de réglage et des boutonnières sont prévues pour l'ajustement des paramètres fonctionnels X et Y et de la position des flasques latéraux.

Deux séries de maquette associées aux deux séries d'expériences décrites dans le programme d'étude ci-après ont été construites ; les premières se rapportent aux essais en écoulement supersonique, les secondes aux essais en écoulement sonique.

Dans le premier cas, afin de balayer le taux de détente entre 2 et 4, à pression de sortie donnée (détente à l'atmosphère), trois tuyères correspondant à des Mach en sortie de 1,04, 1,36, et 1,54 ont été réalisées.

Le dimensionnement des maquettes, effectué en tenant compte des contraintes imposées par le matériel existant (balance et circuit de soufflage) nous a conduit à retenir les valeurs suivantes :

. en écoulement supersonique au Mach moyen de 1,36 :

- en configuration monotuyère : D_c = 17,8 mm
  D = 18,7 mm
  F_x ∿ 70 N (pour p_o = 3 bars)
- en configuration bi-tuyère : D_e = 12,6 mm
  D = 13,2 mm
  écartement entre divergents à la sortie = 3 mm

. en écoulement sonique :

$D_e = D$ = 24 mm

F_x ∿ 70 N (pour p_o = 2 bars)

A titre indicatif, ces valeurs conduisent à des durées pratiques de raffales supérieures à 10 secondes et à des Nombre de Reynolds moyens en sortie de tuyère de l'ordre de 10^6.

5 - PROGRAMME D'ETUDE

Le programme expérimental est mené schématiquement en deux temps :

- une étude comparative sommaire du comportement du dispositif dans les deux configurations mono et bi-tuyères, sur une plage relativement étendue du nombre de Mach (M compris entre 1 et 1,6) ;

- une étude paramétrique approfondie sur un arrière-corps monotuyère en régime sonique destinée à cerner les problèmes d'avionnabilité du système.

5.1 - Essais préliminaires

En premier lieu, on procède sur banc statique à la détermination des paramètres nominaux ; pour celà, on met à profit les différents moyens de réglage prévus sur les maquettes et l'on évalue la stabilité du recollement à partir de l'évolution des pressions statiques à la paroi du déviateur (Figures 4 et 5) ; cette opération, effectuée au Mach moyen de 1,36, en configuration monotuyère est répétée, au même Mach, sur la configuration bi-tuyère ; les réglages retenus pour les divers paramètres géométriques sont en définitive les suivants :

	Monotuyère	bituyère
rayon de courbure du déviateur : R	100 mm	60 mm
angle d'attaque : α_o	ajustable entre 0 et 10 degrés	ajustable entre 0 et 10 degrés
longueur du déviateur : L	ajustable entre 31 et 60 mm	ajustable entre 22 et 48 mm
jeu entre divergent et flasque : e	0,65 mm	0,9 mm
hauteur de cavité : H	10 mm	10 mm

marche longitudinale	: X	2 mm	2 mm
marche transversale	: Y	3 mm	3,2 mm

Les mêmes essais effectués aux deux Mach extrêmes 1,04 et 1,56 permettent de confirmer la validité de ces réglages dans la totalité du domaine des taux de détente envisagés.

Une fois terminée cette étude qualitative de la stabilité du recollement, on procède avec les principaux réglages retenus, à une analyse quantitative des performances en fonction des paramètres ajustables, notamment l'angle d'attaque du déviateur, sa longueur et le taux d'adaptation de la tuyère.

Ces essais se terminent par un examen du comportement et de l'efficacité d'un déviateur plan de faible longueur, en vue de simplifier le système et d'en limiter l'encombrement, dans le cadre d'application aux faibles déviations.

5.2 - Etude paramétrique approfondie

Cette étude est menée en écoulement sonique sur une maquette à échelle sensiblement plus grande afin d'ajuster plus finement les paramètres géométriques et de réaliser l'intégration d'une motorisation simplifiée avec un minimum de sujétions.

Comme précédemment, une première étape au banc statique permet d'ajuster les paramètres de réglage de la marche X et Y.

Les essais effectués sur trois formes de déviateur (deux déviateurs plan - un déviateur courbe) conduisent au choix de la configuration nominale :

X = 2 mm

Y = 2,5 mm

On note toutefois qu'un accroissement de la hauteur de marche ne serait pas préjudiciable à la stabilité et que le fonctionnement reste possible avec une largeur de marche nulle (valeur qui sera retenue ultérieurement sur déviateur plan).

Ces valeurs étant définies, on procède à une étude systématique au banc de poussée portant sur les différents paramètres géométriques et physiques.

On vérifie dans cette configuration le caractère spontané du recollement permettant de s'affranchir de tout artifice aérodynamique tel que soufflage ou aspiration.

6 - RESULTATS D'ESSAIS ET DISCUSSION

6.1 - Essais préliminaires

L'influence de la longueur du déviateur sur les performances apparaît Figures 6 et 7 où sont indiquées, en fonction du taux d'adaptation, l'efficacité latérale et la perte de poussée axiale ; on constate ainsi qu'il est possible sur un monotuyère légèrement supersonique, de réaliser avec un déviateur courbe de dimensions suffisantes ($L \sim 2,5\ D$) des poussées latérales dépassant 30 % de la poussée axiale sans déviation. Dans ces conditions, la perte de poussée varie entre 5 et 10 % selon le taux d'adaptation.

D'un autre côté, les caractéristiques du système évoluent avec l'angle d'attaque du déviateur comme indiqué sur les Figures 8 et 9 correspondant à une configuration bi-tuyère pour laquelle on observe un accroissement corrélatif des pertes (> 15 % F_{yo}). et de l'efficacité latérale qui avoisine 60 % aux niveaux de pression génératrice les plus bas.

Il est donc clair dès ces premiers essais que des déviations très importantes sont réalisables avec des déviateurs courbes correctement réglés et cela particulièrement sur un bi-réacteur ; des perspectives d'utilisation STOL paraissent ainsi ouvertes à un tel dispositif moyennant une optimisation des paramètres.

Pour les applications correspondant à des poussées latérales plus modestes (manoeuvrabilité), il ressort qu'une géométrie plane de faible longueur doit être satisfaisante ; des essais partiels effectués tant en mono qu'en bi-tuyère le confirment et un programme d'analyse paramétrique détaillé est donc lancé dans la configuration monotuyère sonique, dont nous allons commenter les résultats.

6.2 - Etude paramétrique approfondie

6.2.1 - Influence de la longueur du déviateur

L'évolution des caractéristiques est indiquée Figures 10 et 11 en fonction de l'allongement (rapport L/D entre la longueur du déviateur et le diamètre en sortie de tuyère) ; on met en évidence que pour la configuration étudiée (déviateur plan en écoulement sonique) il existe un optimum au voisinage de la valeur L/D = 1,25 ; au-dessous, le dispositif s'avère instable au-delà d'un certain rapport de pression (p_o/p_a = 2,25 pour L/D = 1) ; au-dessus, la stabilité est satisfaisante mais les performances diminuent en raison d'un décollement prématuré.

Il convient toutefois de noter que l'optimum ainsi défini correspond à un réglage donné des autres paramètres et qu'on doit s'attendre à des modifications de celui-ci lorsque les réglages changent. Seule une investigation très complète permettrait d'apprécier l'amplitude de ces variations mais, d'ores et déjà, les valeurs obtenues apparaissent technologiquement viables.

6.2.2 - Influence de la longueur des flasques

Les dispositifs de confinement de l'écoulement constituent évidemment des éléments fonctionnels essentiels du système dans la mesure où ils participent à la stabilité du recollement. Par contre, leur présence est contraignante, tant du point de vue de l'aérodynamique externe en accroissant la traînée de l'arrière-corps que de la technologie en compliquant le mécanisme de rétraction. L'un des principaux objectifs de l'étude paramétrique réside donc dans l'optimisation de leur encombrement ; en particulier, on recherchera pour une longueur de déviateur donnée, la longueur minimale de flasque compatible avec le respect des performances.

Les courbes caractéristiques correspondant à différentes longueurs de flasques sont portées sur les Figures 12 et 13 où l'on observe une chute brutale de la poussée latérale pour un allongement l/D voisin de 2/3 ; on notera que, d'une manière analogue à ce qu'on observe pour le paramètre précédent, cette chute de performance s'accompagne corrélativement d'une réduction des pertes de poussée axiale.

6.2.3 - Influence de la hauteur des flasques

Dans le même ordre d'idée, la réduction de l'encombrement en hauteur doit être recherchée ; toutefois, l'examen des courbes des Figures 14 et 15 montre qu'il ne faut pas attendre de gains spectaculaires de ce côté, une réduction significative de l'efficacité latérale apparaissant dès que la limite supérieure du flasque affleure le plan de symétrie horizontal de la tuyère ; on constate parallèlement que cette disposition particulière (d = o) conduit à la perte de poussée axiale maximale. On s'en tiendra avantageusement à un dépassement relatif d/D de l'ordre de 10 %.

D'une manière plus générale, l'étude des deux derniers paramètres met en évidence l'impossibilité de supprimer les dispositifs de confinement ; seule, une réduction de leurs dimensions peut être envisagée.

6.2.4 - Influence de l'écartement des flasques

La position des pétales de la tuyère propulsive n'est pas figée et dépend des conditions de vol ; l'adaptation du dispositif de pilotage nécessite donc l'étude du comportement de la bascule en présence d'un écartement des flasques variable (jeu radial e).

La variation de ce paramètre est obtenue sur maquette au moyen de cales d'épaisseur dans une plage de réglage comprise entre 0,5 et 5,5 mm (soit environ 2 à 20 % du diamètre de sortie tuyère).

Les Figures 16 et 17 représentent la variation de l'efficacité latérale et de la perte de poussée axiale paramétrée en rapport de pression ; on note que les performances sont très affectées par la position transversale des flasques, particulièrement au-delà d'un espacement e voisin de 10 % du diamètre D ; toutefois, la stabilité du recollement ne semble pas remise en cause par ces réglages.

Des essais complémentaires ont permis de constater par ailleurs qu'un ajustement de l'incidence du déviateur ne permettait pas d'accroître sensiblement la poussée latérale.

Ces résultats suggèrent en pratique l'intégration d'un dispositif d'articulation des flasques permettant de s'adapter aux variations du col de tuyère.

6.2.5 - Influence du jeu longitudinal entre flasque et tuyère

L'analyse de ce paramètre vise à s'assurer que la solution étudiée est compatible avec les exigences fonctionnelles sur avion tant au plan thermique (tenue des composants en présence de gaz chauds) que mécanique (positionnement par rapport à la tuyère, compensation des dilatations).

Dans la plage de variation comprise entre 0 et 1,5 mm, on a pu mettre en évidence une évolution sensible des performances ; les Figures 18 et 19 récapitulent les résultats obtenus. On y observe une inflexion de l'efficacité au voisinage du rapport de pression $p_0/p_a = 2$; par contre, au plan fonctionnel, le recollement est peu perturbé par l'aspiration au niveau de la fente et l'effet trompe qui s'ensuit se traduit par un gain notable des performances axiales.

Le comportement global du système vis-à-vis de ce paramètre paraît satisfaisant et permet d'envisager favorablement un refroidissement naturel des éléments les plus sollicités thermiquement.

6.2.6 - Influence d'une réalimentation de la marche

L'étude des fuites entre déviateur et plan de sortie tuyère, entraînant une réalimentation de la marche, répond au même souci que précédemment ; les résultats présentés Figures 20 et 21 montrent une sensibilité plus grande du dispositif vis-à-vis de ce paramètre, le débit secondaire aspiré entraînant un épaississement de la couche limite qui affecte les conditions de recollement.

Une vérification globale du fonctionnement en présence de jeux représentatifs d'une configuration réelle a été effectuée en associant sur la même maquette une fente de réalimentation et un jeu entre flasque et tuyère de même valeur (1 mm soit 5 % de D); la caractéristique correspondante illustre bien l'intérêt du confinement et montre qu'il sera nécessaire de trouver un compromis entre une simplification extrême associée à des jeux importants et une définition plus performante mais très sophistiquée.

6.2.7 - Influence des défauts locaux

Différents défauts géométriques ont été simulés sur maquette en tenant compte, de façon aussi réaliste que possible, des problèmes de conception et de fabrication : bord d'attaque du déviateur sans arête vive (différents rayons ont été testés), présence d'obstacles singuliers à la surface (rivets représentés ici par des vis tête fraisée à dépassement contrôlé).

Par ailleurs, des essais ont été réalisés avec un écoulement tournant représentatif des conditions de sortie réacteur.

Dans tous les cas, les pertes d'efficacité enregistrées n'ont pas dépassé 1 % de F_{x_0} ; on peut donc considérer que ces défauts constituent un problème marginal de la mise au point d'un déviateur réel.

6.2.8 - Influence du taux d'adaptation

Les différentes caractéristiques présentées étant paramétrées en p_0/p_a ont déjà permis d'évaluer l'allure des variations de performances en fonction du taux d'adaptation ; les Figures 22 et 23 précisent cette influence pour une géométrie donnée et dans un domaine de pression élargi.

On note une perte d'efficacité latérale continue mais faible à mesure que croît la pression génératrice et, qualitativement, le dispositif de pilotage couvre la totalité du domaine d'utilisation envisagé sans modification significative de la stabilité de recollement.

7 - CONCLUSION

La présente étude a montré qu'il était possible d'obtenir le recollement d'un jet sonique ou faiblement supersonique sur une paroi plane ou profilée dans une plage de pression génératrice correspondant au domaine de vol généralement envisagé pour les avions de combat.

On est parvenu, dans la version nominale retenue, à réaliser des taux de déviation répondant aux spécifications visées (jusqu'à 60 % de la poussée axiale nominale) sans pertes exagérées.

Les essais systématiques d'optimisation des réglages fonctionnels ont permis de définir les limites d'utilisation et de vérifier notamment la nécessité de mettre en oeuvre des moyens de confinement ajustables.

On a vu égalementqu'on pouvait envisager le refroidissement, total ou partiel, des différents composants en ménageant des fentes de réalimentation correctement dimensionnées dans les zones les plus sollicitées.

Le dispositif reste simple sur le plan des formes et de la technologie et ne nécessite pas d'organes annexes d'aspiration ou de soufflage pour favoriser le recollement ; plus particulièrement, il ne remet pas en cause la conception des tuyères de révolution actuellement développées.

8 - REMERCIEMENTS

Cette étude a été réalisée sous contrat de la Direction des Recherches, Etudes et Techniques de la Délégation Générale pour l'Armement.

9 - REFERENCES

(1) - CONTROLE DU VECTEUR POUSSEE D'UNE TUYERE PAR RECOLLEMENT SUR PAROI COURBE
R. KATZ - M. LEPRETRE
11ème Colloque d'Aérodynamique Appliquée 6-7-8 Novembre 74 Bordeaux

(2) - USE OR THE COANDA EFFECT FOR OBTAINING JET DEFLECTION AND LIFT WITH A SINGLE FLAT-PLATE DEFLECTION SURFACE
UWE H. VON GLAHN
Naca Technical Note 4272 (1958)

(3) - USE OF THE COANDA EFFECT FOR JET DEFLECTION AND VERTICAL LIFT WITH MULTIPLE-FLAT-PLATE AND CURVED PLATE DEFLECTION SURFACES
UWE H. VON GLAHN
Naca Technical Note 4377 (1958

(4) USE OF COANDA EFFECT FOR THE DEFLECTION OF JET SHEETS OVER SMOOTHLY CURVED SURFACES. Part. 1
A.B. BAILEY
Utia Technical Note n° 4950 (1961)

(5) - USE OF THE COANDA EFFECT FOR THE DEFLECTION OF JET SHEETS OVER SMOOTHLY CURVED SURFACES Part. 2
W.E.B. Roderick
Utia Technical Note n° 51 (1961)

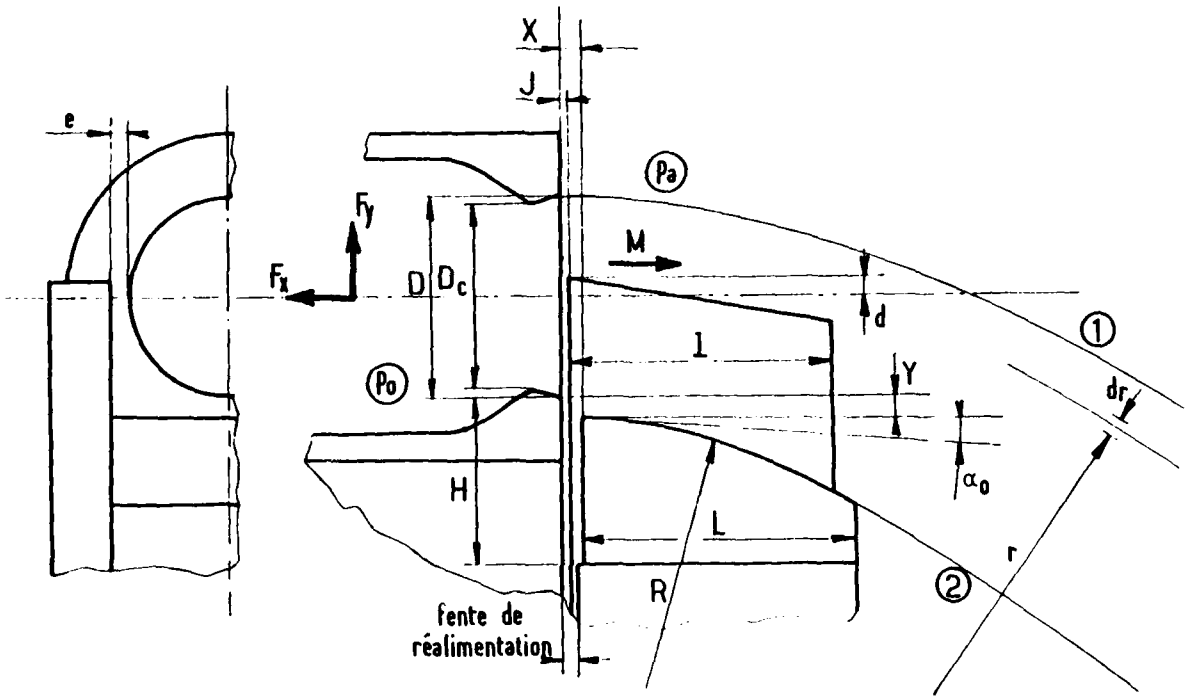

Fig. 1 Schéma de principe

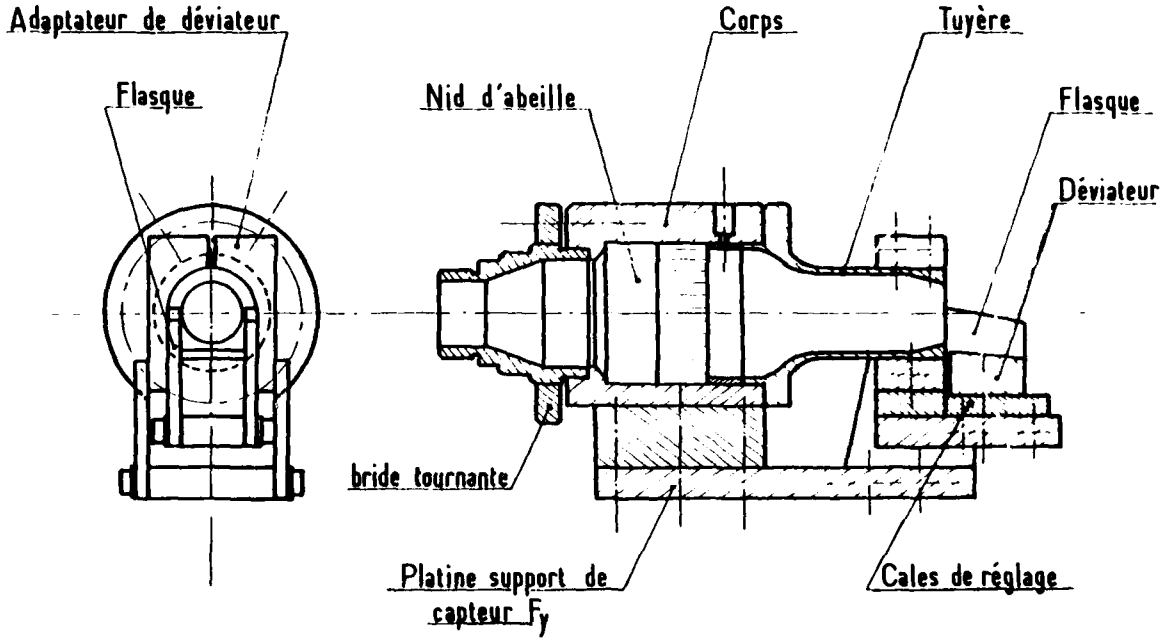

Fig. 2 Schéma du moyen d'essais

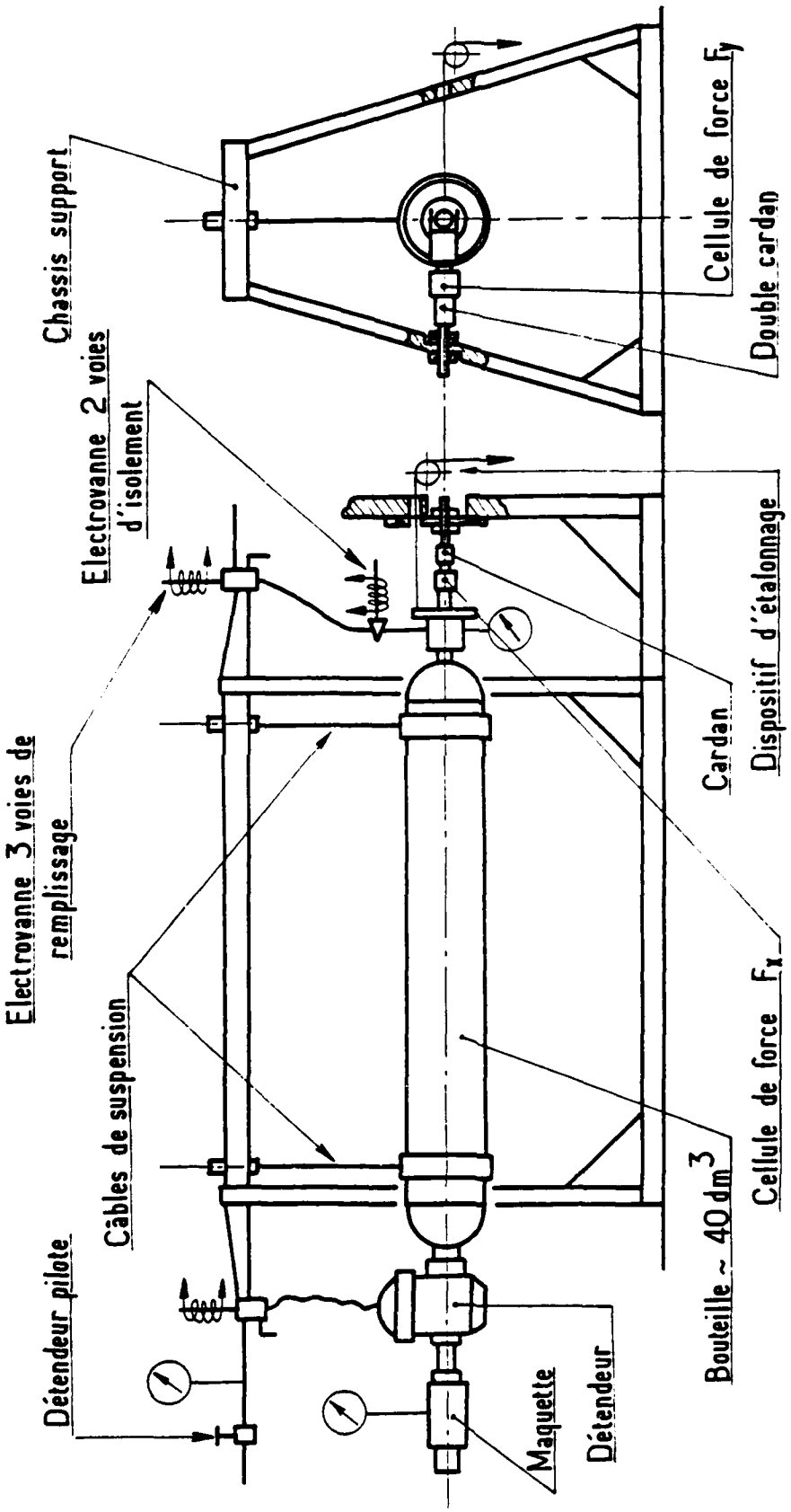

Fig. 3 Architecture de la maquette

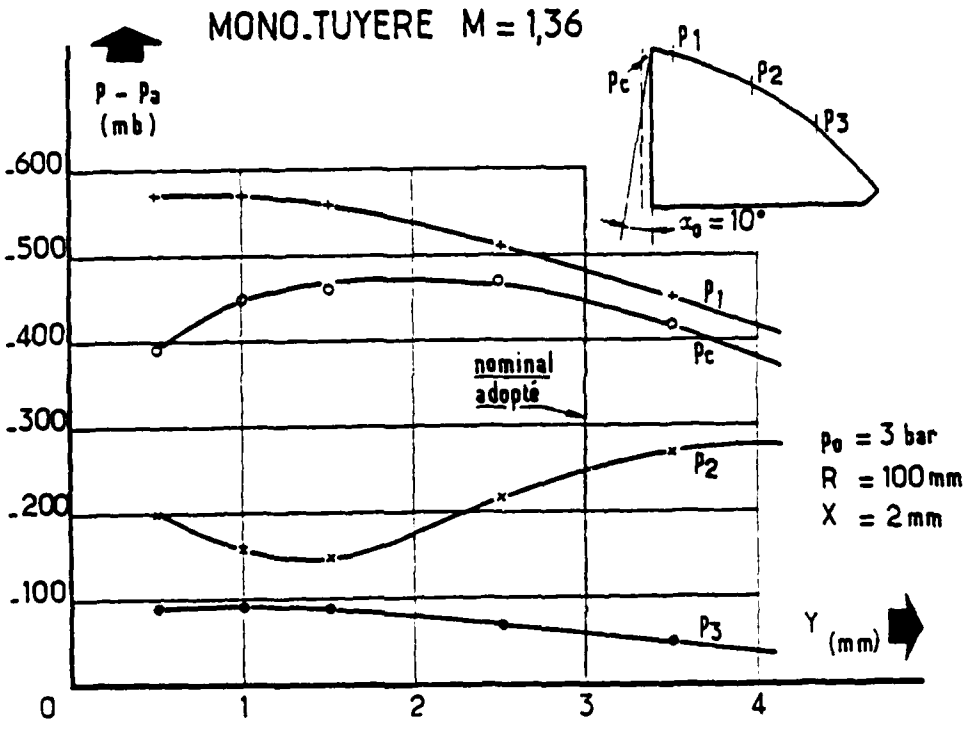

Fig. 4 Evolution des pressions pariétales en fonction de la marche TRANSVERSALE

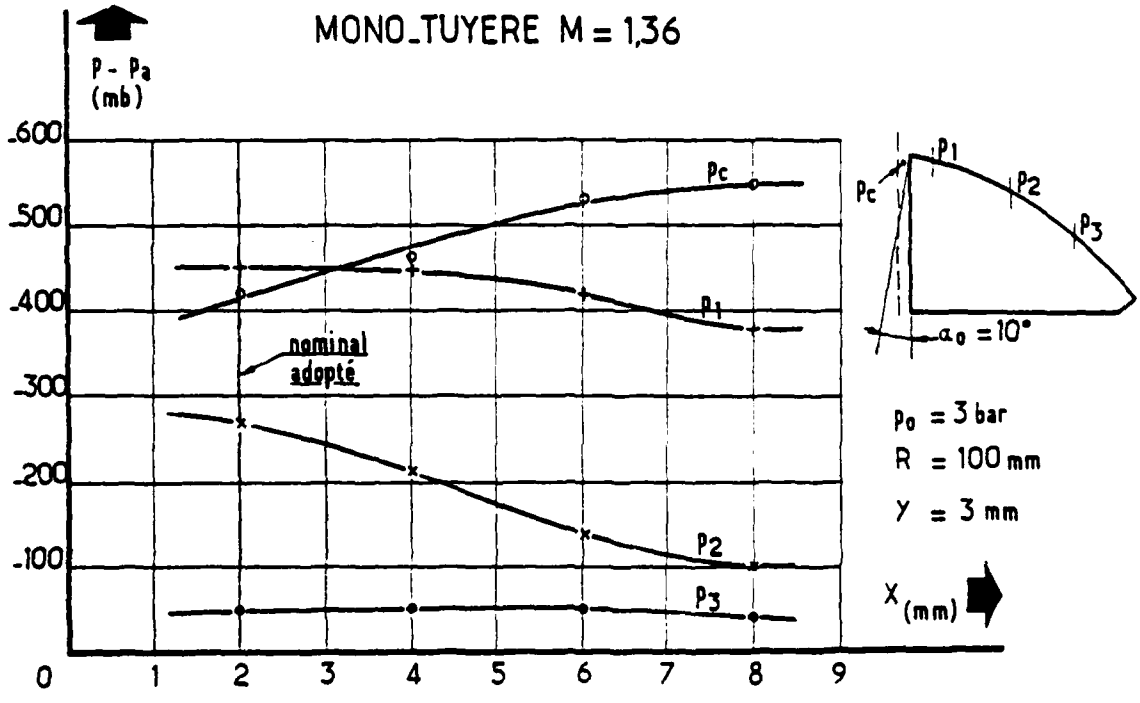

Fig. 5 Evolution des pressions pariétales en fonction de la marche LONGITUDINALE

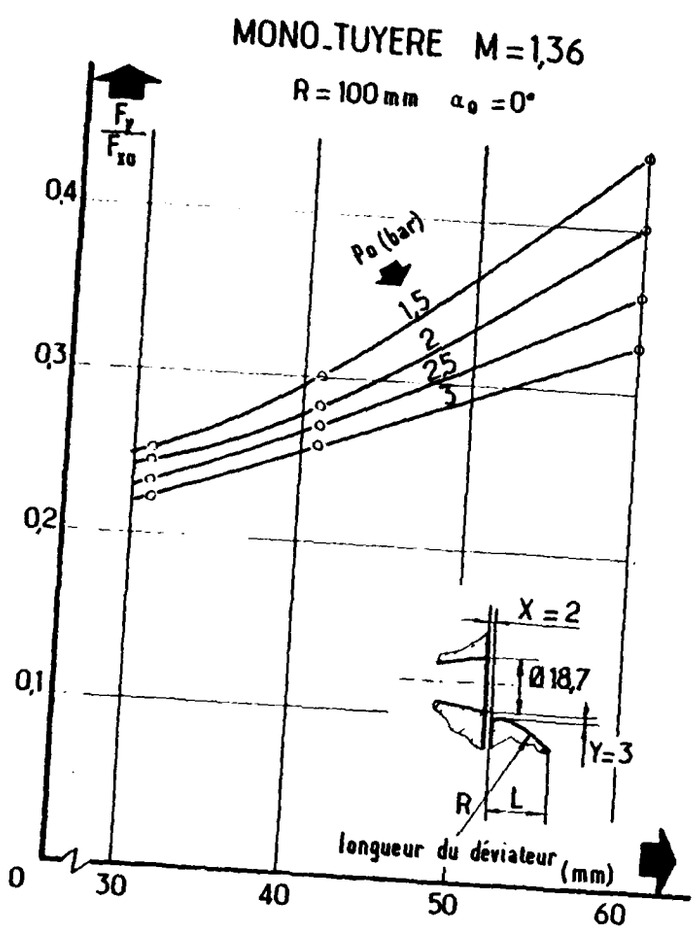

Fig. 6 Influence de la longueur du déviateur sur l'efficacité latérale (M = 1,36)

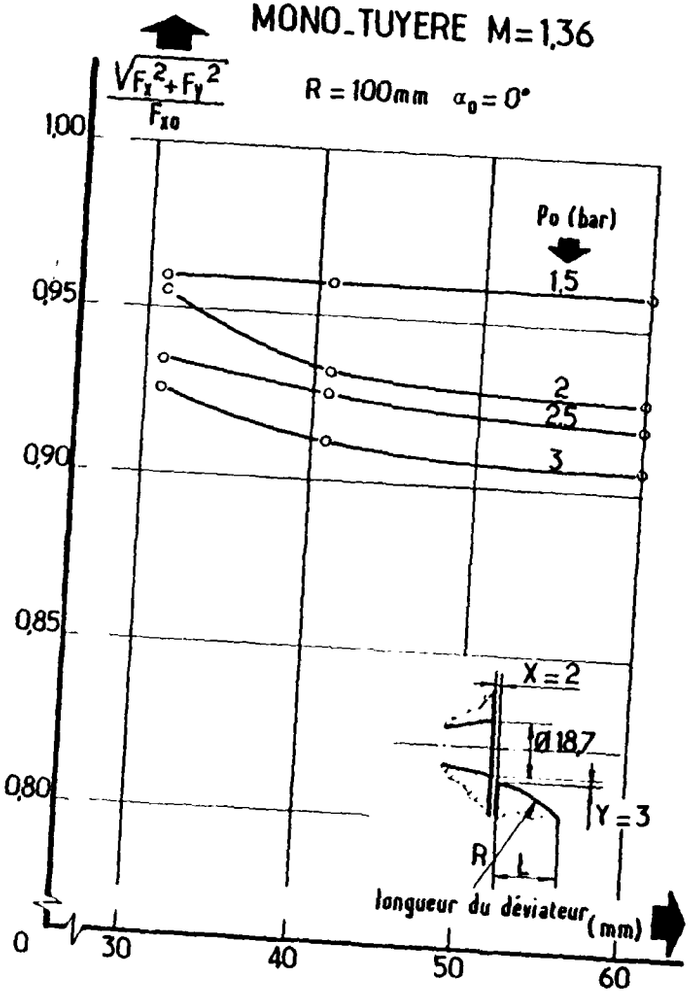

Fig. 7 Influence de la longueur du déviateur sur les pertes de poussée (M = 1,36)

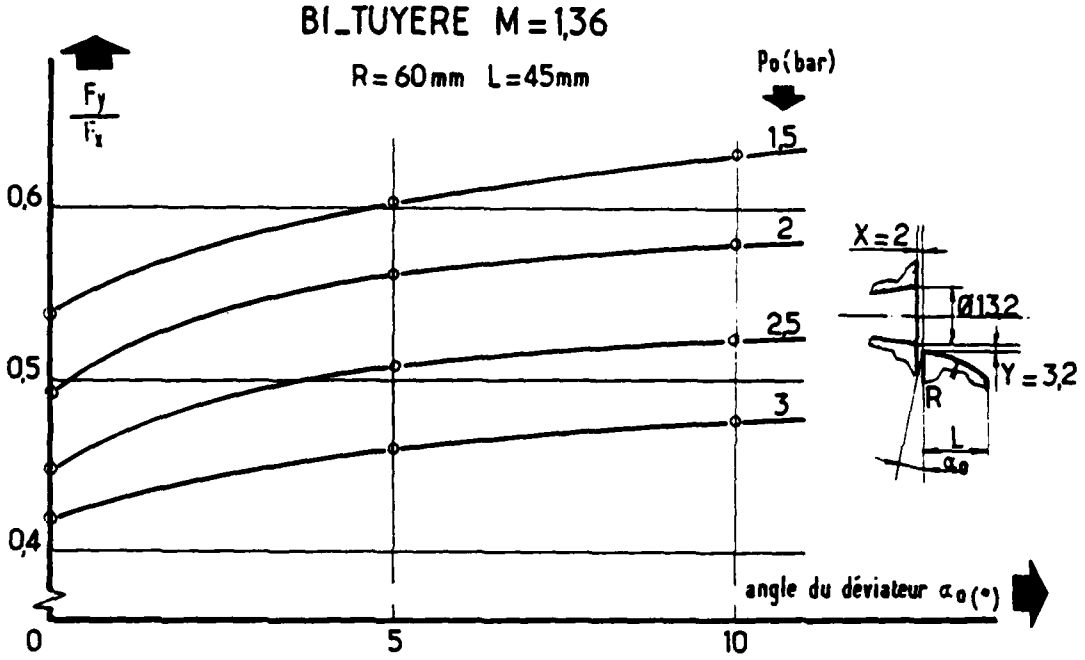

Fig. 8 Influence de l'angle d'attaque sur l'efficacité latérale

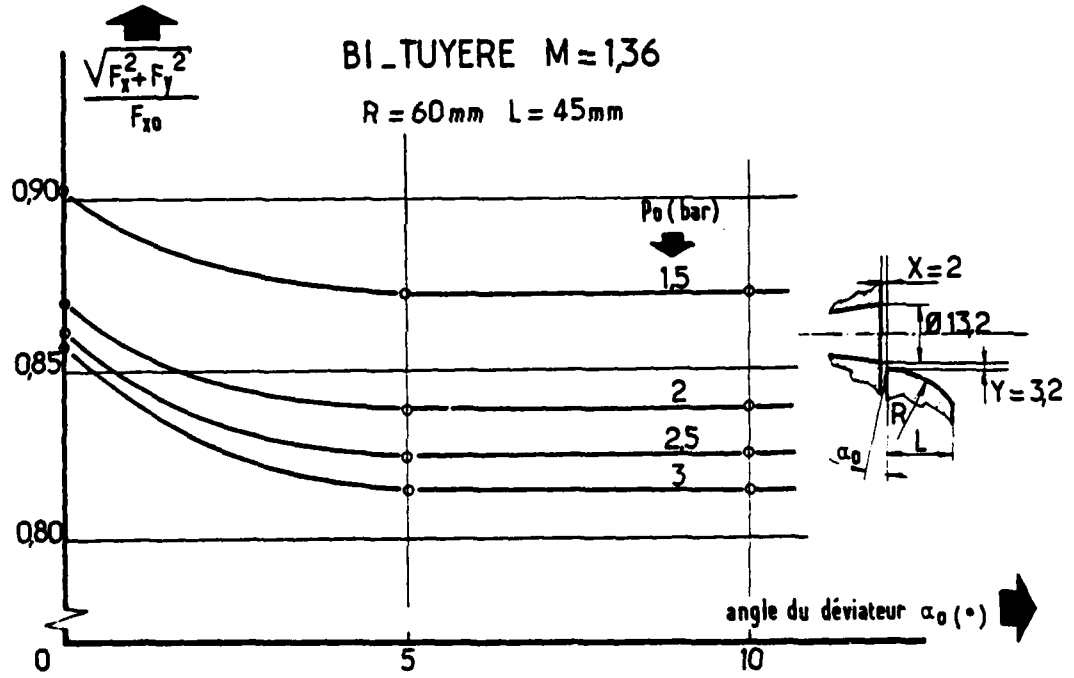

Fig. 9 Influence de l'angle d'attaque sur les pertes de poussée

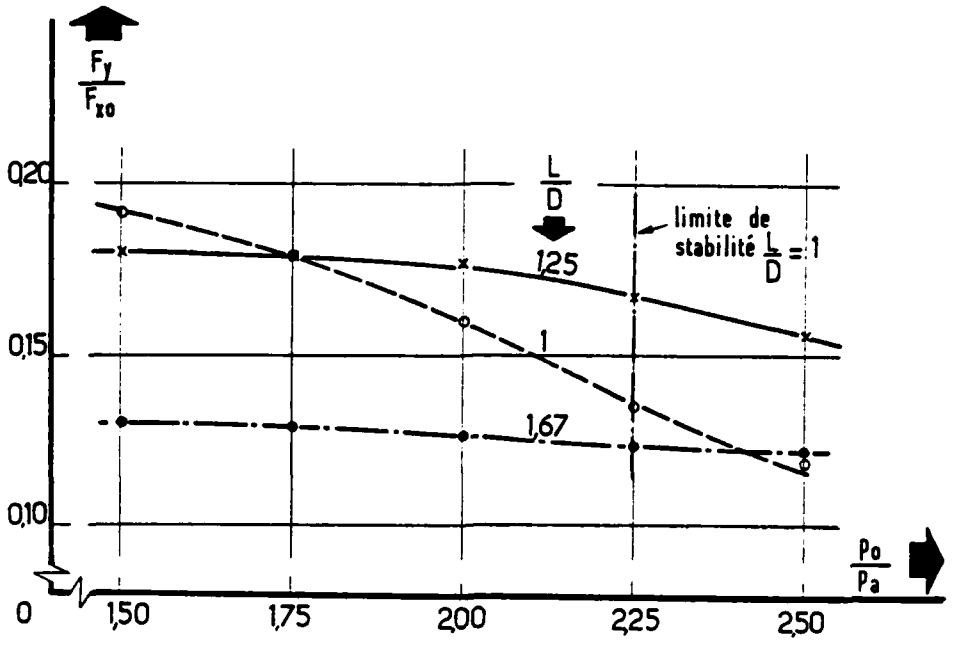

Fig. 10 Influence de la longueur du déviateur sur l'efficacité latérale (M = 1)

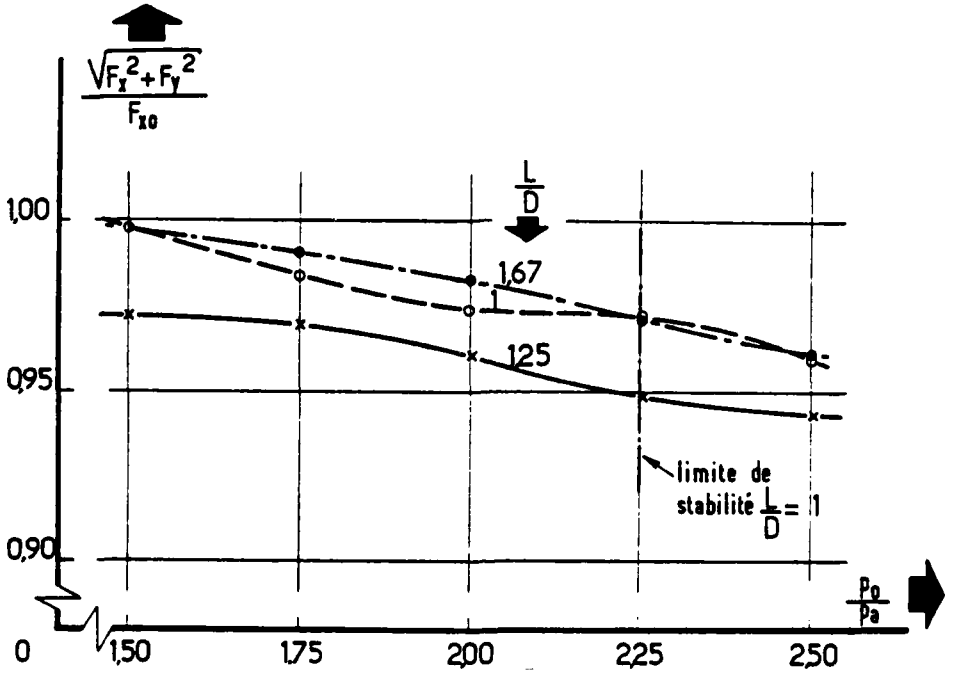

Fig. 11 Influence de la longueur du déviateur sur les pertes de poussée (M = 1)

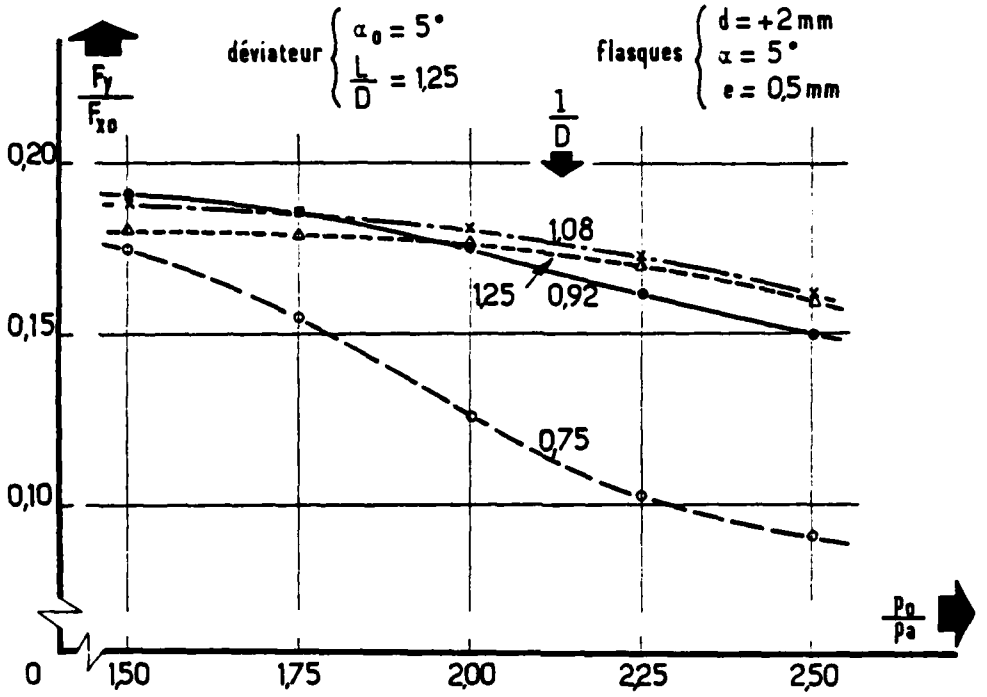

Fig. 12 Influence de la longueur des flasques sur l'efficacité latérale

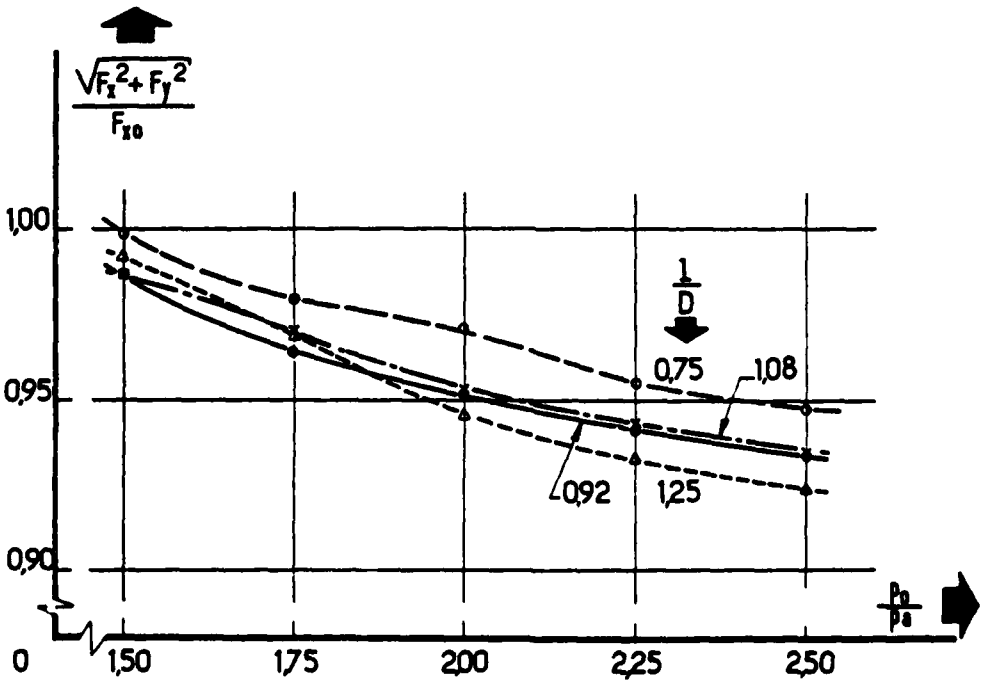

Fig. 13 Influence de la longueur des flasques sur les pertes de poussée

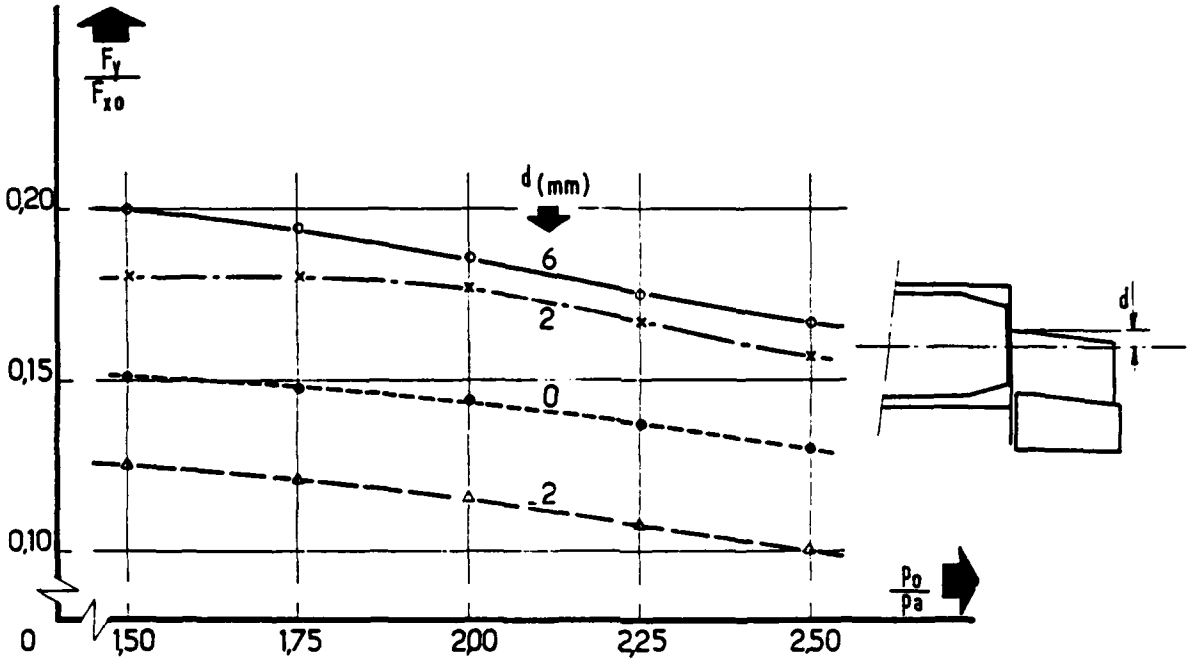

Fig. 14 Influence de la hauteur des flasques sur l'efficacité latérale

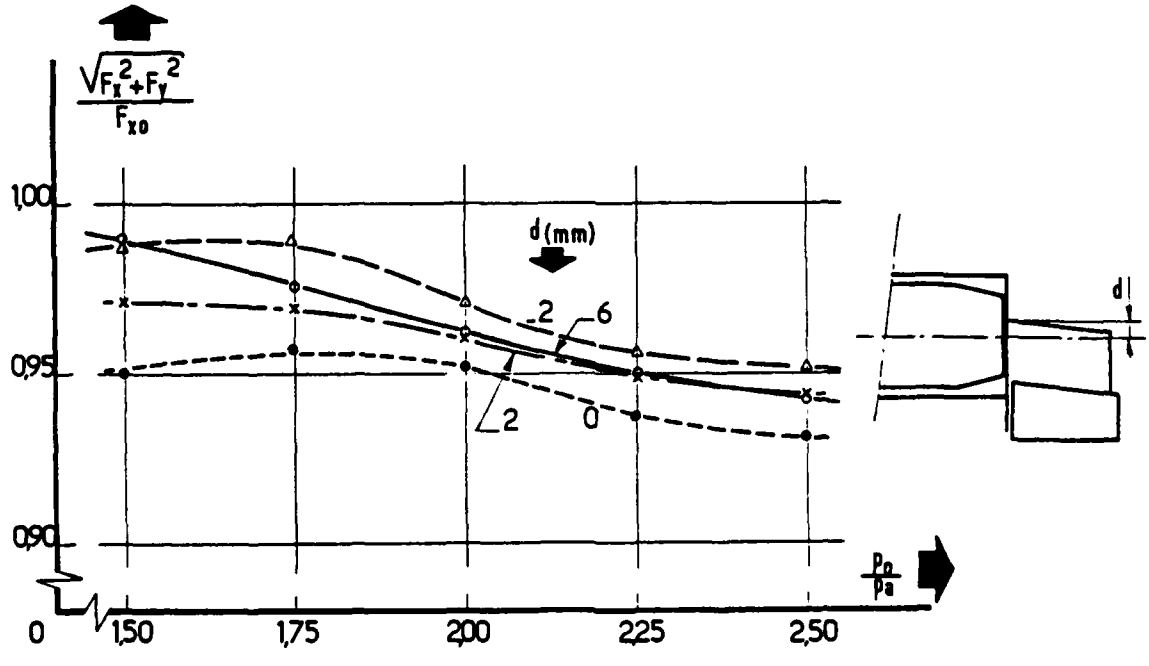

Fig. 15 Influence de la hauteur des flasques sur les pertes de poussée

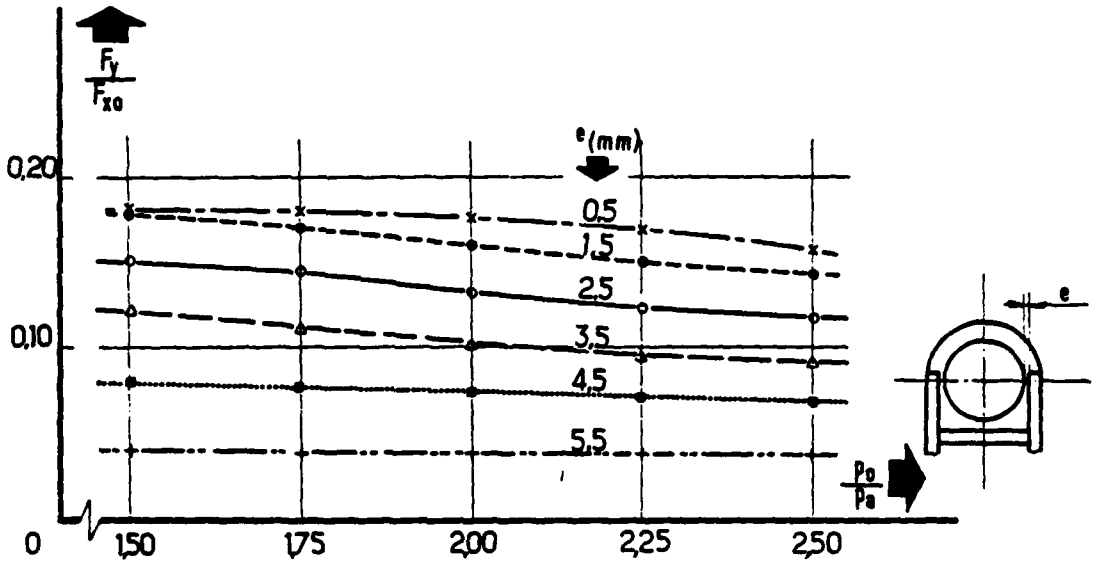

Fig. 16 Influence de l'écartement des flasques sur l'efficacité latérale

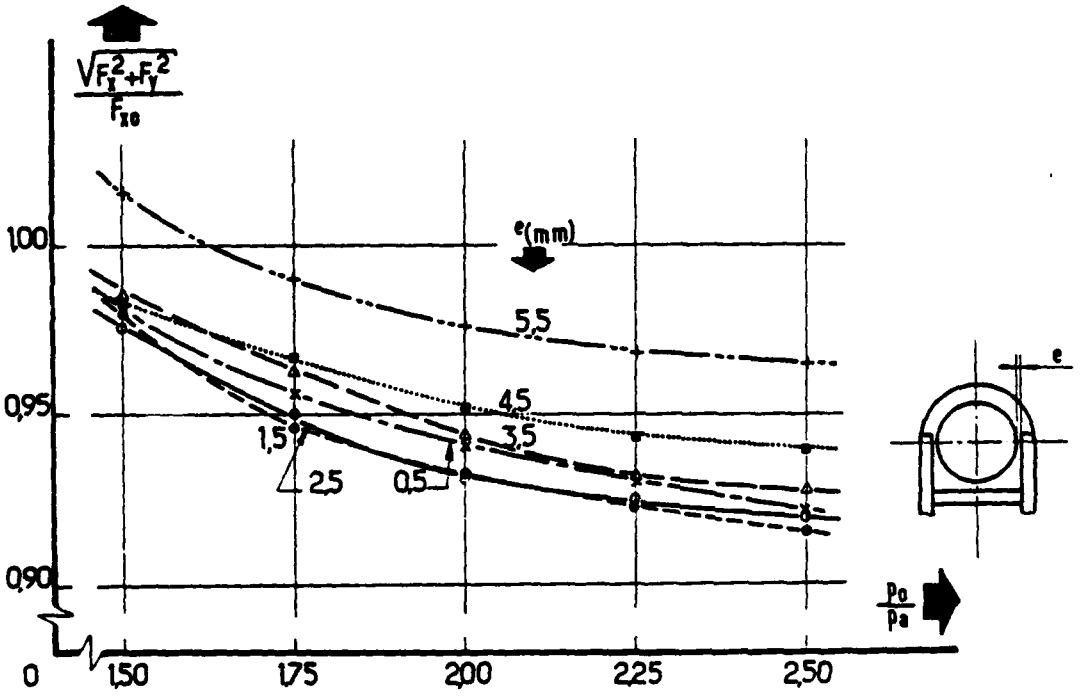

Fig. 17 Influence de l'écartement des flasques sur les pertes de poussée

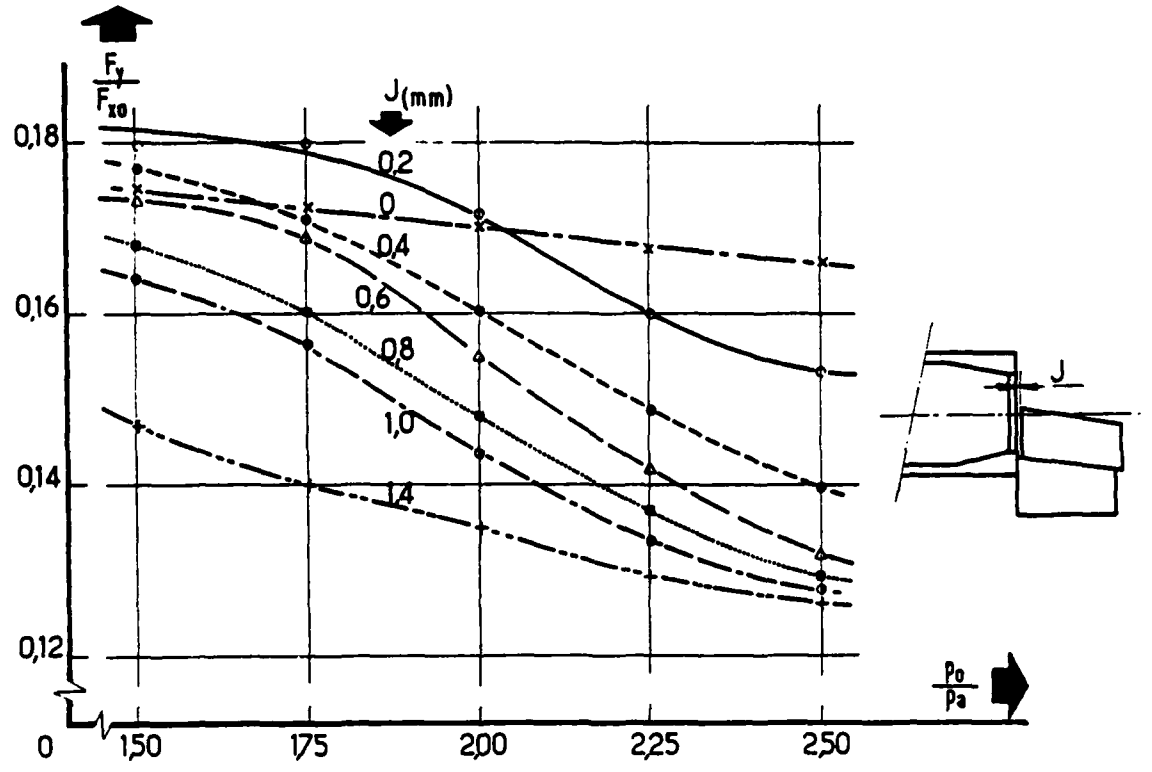

Fig. 18 Influence du jeu longitudinal des flasques sur l'efficacité latérale

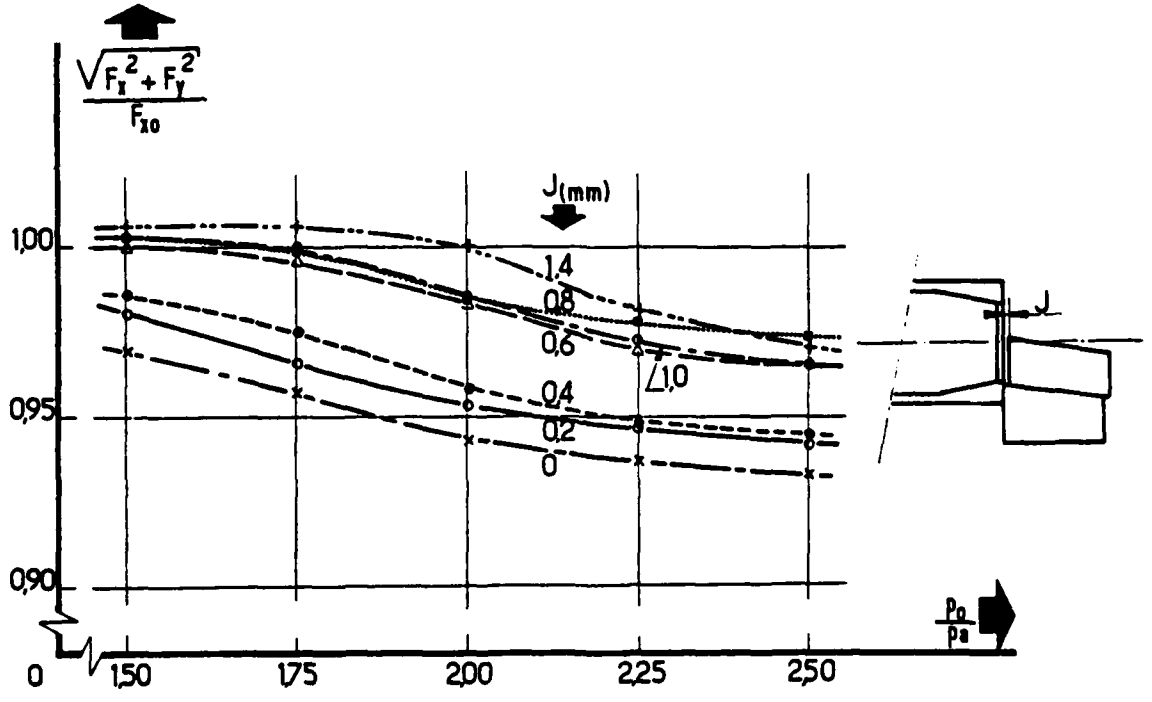

Fig 19 Influence du jeu longitudinal des flasques sur les pertes de poussée

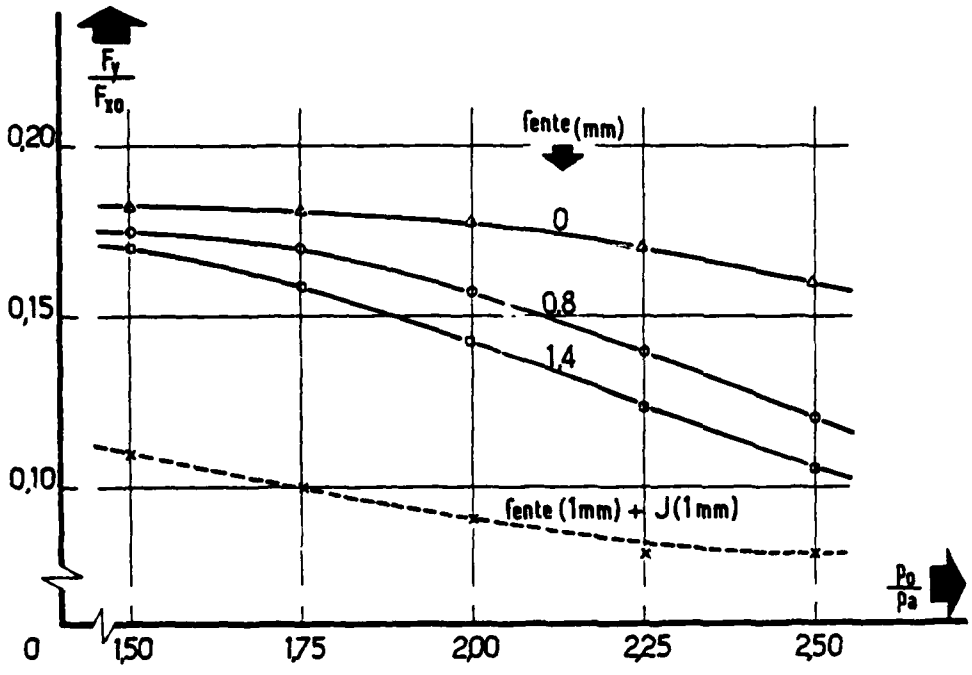

Fig. 20 Influence d'une réalimentation de la marche sur l'efficacité latérale

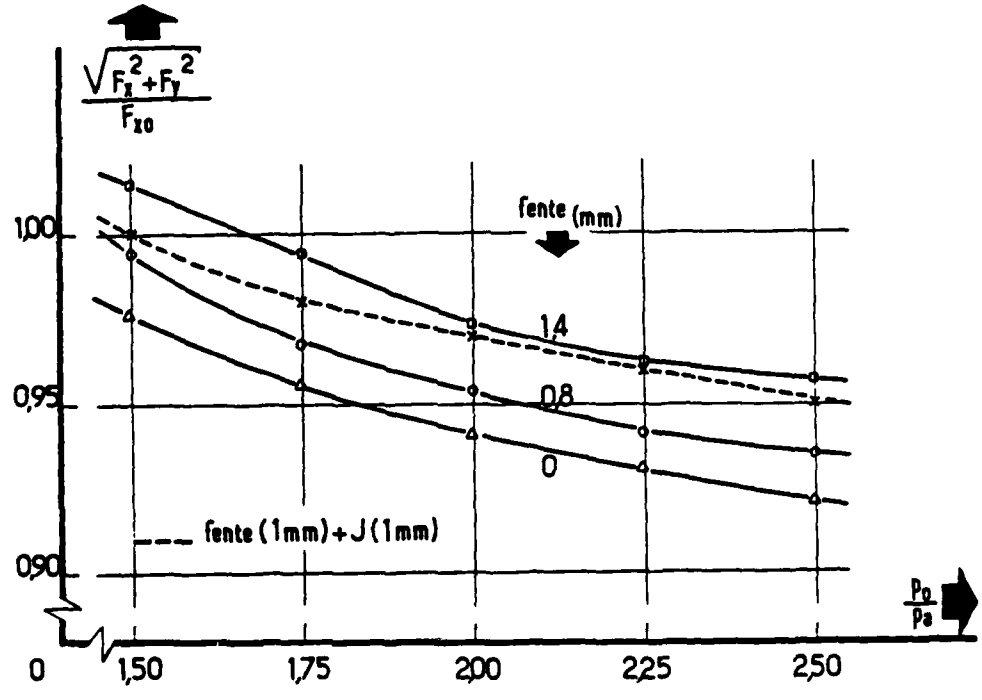

Fig. 21 Influence d'une réalimentation de la marche sur les pertes de poussée

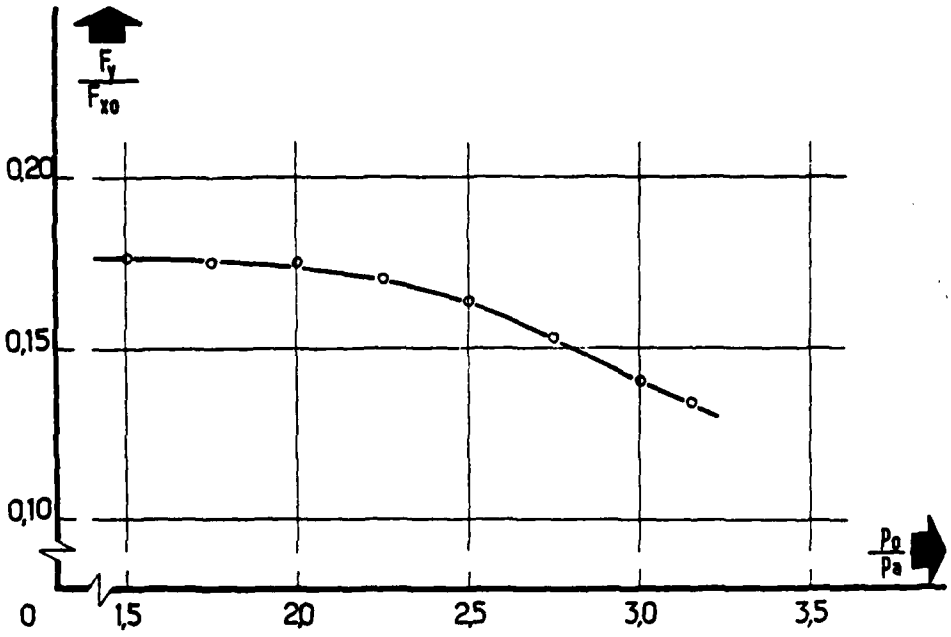

Fig. 22 Influence du taux d'adaptation sur l'efficacité latérale

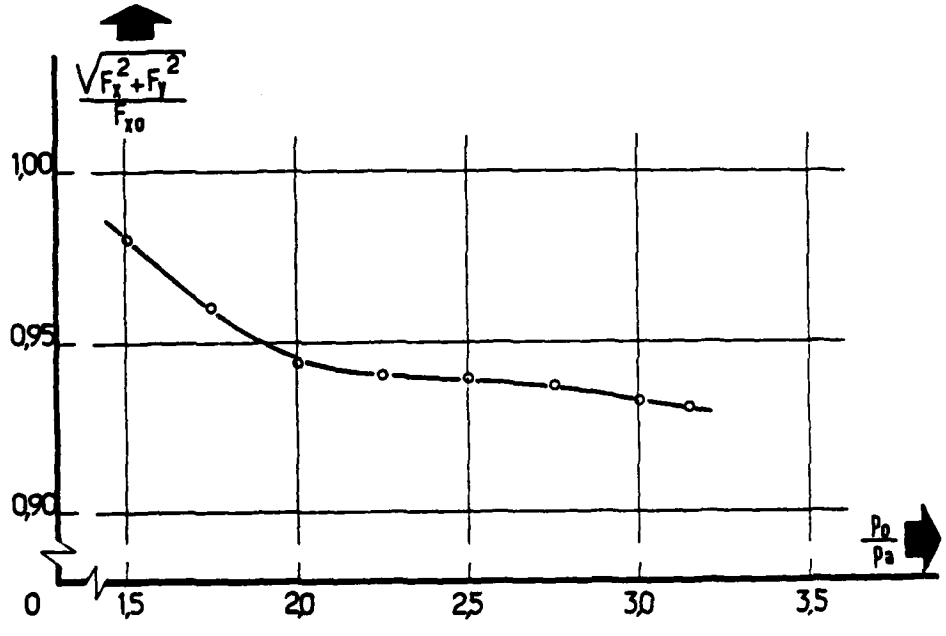

Fig. 23 Influence du taux d'adaptation sur les pertes de poussée

TURBOPROP AND TURBOJET EJECTOR OPTIMISATION

by

V.P.RIVIELLO and A.MUROLO
Alfa Romeo Avio S.p.A.
Pomigliano d'Arco Napoli
Italia

and

G.TORELLA
Italian Air Force Academy
Pozzuoli Napoli
Italia

SUMMARY

The off-design performance of turboprop and turbojet engine with ejector exhaust ducts have been investigated at Alfa Romeo Avio during AR 318 turboprop engine (and its derived versions) development and certification program.

The optimisation of the matching between engine and exhaust duct system has been developed along the following line.

A theoretical approach has been used by introducing in a Synthesis programme the appropriate numerical simulation of the ejector, both in the case of subsonic condition at the engine exhaust station and in the case of sonic station, with supersonic development of the flow through the ejector.

Then a lot of experimental tests has been carried out on the AR 318 facilities,to compare the results in the case of subsonic engine exit.

In order to study the supersonic flow through the ejector a set of available experimental results has been examinated so that the reliability of theoretical methods to evaluate the secondary flow, for cold condition, has also been verified.

For hot conditions experimental tests have been performed at Alfa Romeo facilities and results are shown compared with theoretical calculations.

Next step has concerned the installation of a suitable ejector system on the AR 180.10 turbojet engine, which is a derived version of the AR 318 turboprop.

LIST OF SIMBOLS

A	Area
H	Enthalpy
M	Mach number
P	Pressure
ϱ	Density
R	Gas constant
T	Temperature
V	Velocity
W	Mass flow rate

SUBSCRIPTS

c	Cold or secondary flow
E	Main flow
S	Static
T	Total
U	Ejector exit section

1. INTRODUCTION

This paper deals with two problems proceeded during the AR 318 turboprop engine and its derived versions development and certification program:

1) An ejector system at the exhaust duct of the AR 318 engine was required, so that a cooling secondary flow through the nacelle is obtained and the flow rate is governed by the engine ratings.

2) In order to increase the thrust of the AR 180.10 turbojet engine, designed for low speed aircraft, it was decided to study a suitable ejector system.

Therefore the job has been divided in two parts: one for the turboprop engine, dealing with the AR 318 engine, the other one for the supersonic ejector, studied on the Alfa Romeo Avio test facilities.

2. TURBOPROP ENGINE

2.1 The Engine

The AR 318 turboprop engine is the first engine designed and developed by Alfa Romeo Avio after World War II.

It is a low cost 600 SHP engine for commercial and commuter aircraft with up to 10000 LBS take-off weight, and for turbo-trainer aircraft with installed power from 350 to 600 SHP.

The AR 318 is a very simple engine, as fig. 1 shows. Its basic components are designed for easy maintenance. The engine main modules are the following:

- -epicycloidal gearbox which includes the axial lobe air intake;
- -single stage high pressure ratio centrifugal compressor;
- -high efficiency, low pollution reverse flow combustor;
- -integral casting two stage turbine.

Since the first run, on September 1977, testings totalled over 1500 hours on test bed and 150 flying hours on a Beechcraft A90 KING AIR aircraft.

2.2 Ejector System Requirements

Studing with an airframe company the installation of the AR 318, for a practical application on a single engine turbo-trainer aircraft, it was discussed the possibility to use an ejector system for the aircraft exit duct.

Such a system was required for the following reasons:

- -a very easy installation is got because the exhaust duct has not to be build and stripped with the engine;
- -a cooling secondary flow is directed through the nacelle; this flow is controlled by the engine rating and it is particularly necessary for aircraft operating in the hot zones of the world;
- -a reduction of static pressure at the engine exit station is obtained so that the pressure losses in the aircraft exhaust duct are balanced by different enthalpic drop through the turbine.

A possible configuration of the installation on an aircraft is shown in fig. 2

2.3 Numerical Simulation

A reliable computer programme for off-design engine performance prediction, and for different engine configurations, is already available at Alfa Romeo Avio and at IAF Academy, (1). This programme had been prepared on the ground of the 'state vector' theory (2), (3),(4). The number and the kind of parameters in the state vector is strictly depending on engine configuration.

The choice of the parameters used as components may be the widest one, (5), and the computer program calculates them by using the condition of constant mass flow rate in a number of engine stations. A set of equations, whose number is equal to the number of vector state components, can be obtained and solved by an iterative method.

One of the control station used to write the set of equations is the engine exhaust, so that the mathematical model of the ejector becomes an important and essential part of the iterative method for engine performance evaluation.

For both subsonic and supersonic ejector performance prediction many mathematical models are available in literature (6),(7),(8),(9),(10),(11).

The main aim of this paper is to find out a simple model suitable for integration with Synthesis computer program. In fact, as previously stated, the aim is to obtain a digital computer programme fit to study the engine-ejector all together, in any working condition. This is also the philosophy of the Synthesis programme, which studies the behaviour of the engine as a whole without considering the particular flow type in the turbomachine.

The subsonic ejector model is based upon the following considerations.

As previously stated the ejector installation modifies the engine thermodynamic cycle because the static pressure at the engine exit station is lower than the atmospheric pressure. This causes a variation of enthalpic drop through the turbine.

The numerical simulation of the ejector has been developed with the condition that secondary flow must provide an equilibrium pressure at the engine exit station between the static pressures of engine exhaust gas and the same secondary flow.

A flow chart of the numerical method used is shown in fig. 3

The iterative calculation model of the ejector has been inserted in the iterative Synthesis programme; the analysis of the installation effect starts when the Synthesis has already evaluated the exhaust stream parameters. In this way the static temperature, gas velocity and geometrical properties of engine exhaust jet are known.

The first calculation step is devoted to guess the value of the ratio between secondary flow rate and main flow rate (W_f/W_E, fig. 4).

Furthermore, with the hypothesis of complete mixing, the enthalpy and the total temperature at the ejector final station(A_U) are computed. Using isentropical flow, thermodynamic state and mass conservation equations, gas velocity, static temperature and density at A_U station are also obtained.

Then from the value of secondary mass flow and A_c area (see fig. 4), it is possible to evaluate all parameters for the cold secondary inlet station (i.e. P_{Sc}, T_{Sc}, V_c).

At station 3 there is the equality of static pressures so $P_{Sc}=P_{SE}$.

The value of P_{SE} and the exhaust engine geometry determines the static temperature and velocity of hot stream. Thus from momentum equation between station 2 and A_U a new value of static pressure at station 3 can be calculated.

The value of static pressure from step 5 (fig. 3) is compared with the value of the same parameter calculated in step 7. This comparison is the end of first step of ejector effet iterative calculation. If the difference between the two values of static pressure in station 3 is greater then the prefixed tolerance the iteration goes on restarting from step 1 (fig. 3). Otherwise the iterative calculation for state vector components goes on.

The modified Synthesis programme has been used to carry out several calculations for different engine working conditions. Some of these results are shown in fig. 5,6,7; they are obtained for the same engine ratings (i.e. engine speed and fuel flow).

The results show the effect of an ejector system on the performance of AR 318-052, compared with the behaviour of the engine without the ejector exit duct.

Fig. 5 shows the variation of secondary mass flow rate and residual thrust for different ejector area ratio at fixed flight conditions (design-point of version 052 of the AR 318 engine).

Fig. 6 and 7 show the variation of shaft power and equivalent power in the same conditions of fig. 5. The most important result is that any variation in power is very low and to show them a large scale plotting has been used. In these figures the x-axis has a double scale. This is the result of the study carried out in order to evaluate the ejector installation effect on a turboprop engine. The ejector improves power because it increase enthalpic drop in turbine. The same effect can be obtained increasing the exhaust area of the engine. The most important difference between the two methods is that the ejector increases residual thrust, while the larger exhaust area decreases this parameter. The final effect is a different equivalent power behaviour in the two different cases (fig. 7)

2.4 Experimental Tests

The experimental tests have been carried out at Alfa Romeo Avio AR 318 hangar test bed in Pomigliano d'Arco(Naples).

These tests have been performed in order to prove the reliability of the numerical method outlined in the previous section.

Ejector dimension have been chosen to test the system without creating any interference with AR 318 certification program. So an area ratio that did not cause a large change in engine behaviour has been chosen by the Synthesis programme.

To evaluate a suitable lenght of the ejector a program from theory of ref. (11), was developed. So with Synthesis area and mass flow ratio the ejector lenght has been calculated. Practically this phisical parameter affects the mixing between main and secondary flow.

In order to consider the influence of lenght on ejector performance and to choice geometrical dimensions near required conditions, the small numerical programme has been used in a parametric study. Briefly the best value of ejector lengt to diameter ratio is about 3.5, ref.12. This value puts in agreement several oppositing requirements (i.e. weight, secondary flow rate and internal frictional losses).

As previously stated the main aim of experimental tests is to evaluate the secondary mass flow rate so the model instrumentation is sketched in fig. 4. The truncated cone shaped inlet has been chosen in order to evaluate the relative position engine-ejector on system performance.

The most significative results are plotted in fig. 8,9,10. Engine global performance (i.e. power, S.F.C.) change are not plotted because, as calculated by the appropriate computer program, see ref. 13,the differences measured during the tests have been very small as stated in ejector dimensions choice.

Plotted results show the good agreement betweem theoretical and experimental data concerning main to secondary mass flow ratio and exhaust gas temperature.

Fig. 10 shows the standard deviation of measured exhaust temperature, that is:

$$S.D._{EGT} = \sqrt{\frac{\sum_{i=1}^{N} (T_i - T_m)^2}{N-1}}$$

where: T_i is the value measured at the i-th thermocouple;
T_m is the mean exhaust gas temperature;
N is the number of the thermocouples.

This parameter has been chosen to get some informations about the degree of mixing for the three different positions in fig. 4. The first result is that the best mixing is achieved at the position A of fig.4.

3. TURBOJET ENGINE

3.1 The Engine

The use of ejector system for thrust augmentation is actually widely diffused particularly for V/STOL during take-off/landing operations.

The purpose of present study is to use an ejector system to increase thrust of the AR 180.10 turbojet engine for an application on a low speed aircraft.

The layout of the engine is shown in fig.11. The core engine is the same of the AR318 without the turbine second stage. The air intake is modified from the lobe to an axial one since there is no gearbox soace problem. The engine so obtained is a 400 LBS take-off turbojet engine already tested on the Alfa Romeo Avio test facilities.

3.2 Ejector System Requirements

In that case the ejector system requirements is the optimisation of secondary mass flow rate so that maximum thrust augmentation is obtained from static to maximum forward speed conditions.

Numerical simulation of engine-ejector system has been carried out to have a computer programme to evaluate the complete performance all over the operative field of the engine. Confirmation of theoretical results has been obtained by a set of cold and hot tests performed on a scaled down ejector model.

3.3 Numerical Simulation

The main difference between turboprop and turbojet ejector system application is the engine exhaust station condition. In fact while for turboprop engine the flow is always subsonic at the engine exhaust station, for turbojet engine, at high rating conditions, the flow becomes sonic, when there is a simple convergent exhaust duct, or supersonic in the case of convergent-divergent diffuser.

Many studies deal with such a problem and a wide analysis may be found in ref. (8).

As already pointed out in the turboprop section, the main purpose of this job was to test a mathematical model to be matched with Synthesis computer programme. So only one-dimensional theories have been treated for the two essentially different conditions:

-supersonic regime

-mixed flow regime

and assumptions and development of equations are available in ref. (8).

The main difference is that while in ref. (8) the theories are applied to determine operative conditions of the ejector system to achieve a forecast secondary to main mass flow ratio, in the case under examination the aim is to know the behaviour of the system for assigned external conditions.

So for the supersonic regime a computer program has been prepared where the primary flow has been calculated by the one-dimensional theory of convergent-divergent diffusers and secondary flow is evaluated by the assumption of chocking condition at a certain position along the ejector and by the balance of momentum in the section.

Results obtained for assigned geometry, ambient and primary flow conditions are shown compared with the experimental tests of ref. (8), see fig. 12.

After the programme has been modified to evaluate also the development of the two flows through the ejector in the case of different stagnation temperature by balancing total energy at inlet and outlet of the ejector.

Results have shown that the high secondary to external pressure ratio stated for the supersonic regime, leads this model to be not suitable for the aim of this study.

So the mixed flow regime has been treated and matched with the Synthesis computer programme to evaluate the complete system performance. The flow chart is shown in fig. 13.

In that case the engine thermodinamic cycle is evaluated without ejector effect because of sonic or supersonic engine exit station. So the iterative scheme is divided in two parts:

-one for the calculation of state vector for engine thermodynamic cycle;

-the other one for the evaluation of the secondary mass flow by continuity, momentum and energy balance between inlet and outlet of ejector system.

3.4 Experimental Tests

To have a confirmation of reliability of theoretical calculation for the AR 180.10 turbojet exhaust gas conditions, a scaled down ejector system has been prepared and tested at Alfa Romeo Avio facilities. The layout is shown in fig. 14.

By this facility a maximum primary pressure of about 600 kPa and a total temperature of 1000 K are available and those values include the AR 180.10 exhaust gas conditions.

Temperature and pressure modulations are obtained respectively by fuel control and by an actuator system. So the primary mass flow rate is fixed by temperature and pressure condition while secondary flow starts from ambient conditions, as on a turbojet engine at sea level static.

Some preliminary tests have been carried out with convergent-divergent diffuser and with a simple convergent diffuser. The primary to secondary area ratio (A_E/A_c) during

those first tests was about 1/12.

The instrumentation has been chosen to have an accurate evaluation of the secondary mass flow rate and of the development of the mixed flow through the ejector with some information about the exit gas temperature distribution.

Some of the preliminary results are shown in fig. 15 and 16, compared with theoretical calculations. During these tests a convergent-divergent diffuser with A_U/A_* (diffuser exit station-chocking station area ratio) equal to about 2.5 was used.

Results show the accurancy of theoretical calculations particularly at low primary total temperature and high pressure, while increasing temperature and decreasing pressure the difference goes up til 5÷6 % in the worst conditions, see fig15.

Fig. 16 shows exhaust gas temperature versus total temperature of the primary flow. Temperature distribution is very flat with maximum difference at high temperature of about 5 K. In the same diagram is plotted the exit temperature calculated with the assumption of full mixing between primary and secondary measured mass flow rate, using their measured inlet total temperature (i.e. controlled total temperature for the primary flow and ambient temperature for the secondary flow).

Results show, with a maximum difference of 4 K, that full mixing assumption is nearly to be fully verified.

Following this comment, the difference between experimental and calculated temperature derives from the difference on mass flow ratio.

The experimentation is not finished yet and during the next tests different primary to secondary area ratio shall be tested while a build of the AR 180.10 turbojet engine has been already prepared with an ejector system where a primary to secondary area ratio of about 1/6 is obtained.

Fig. 17 and 18 show theoretical results obtained for the AR 180.10 - ejector configuration prepared for experimental tests. The value of A_E/A_c has been chosen in order to obtain thrust augmentation till 150 m/s forward speed.

4. CONCLUSION

Synthesis performance prediction programme and ejector simulation matching has been obtained for both turboprop and turbojet engine.

The accurancy of the complete system performance prediction has been shown to be very high for turboprop engine.

For turbojet engine satisfactory results have been obtained but AR 180.10 test bed results will represent the most significative confirmation of theoretical and experimental tests already carried out.

REFERENCES

1. RIVIELLO V.P., TORELLA G. :"Programma ARP002 - Manuale d'uso - Aggiornamento 4" Report Alfa Romeo Avio, 1980
2. SARAVANAMUTTOO H.I.H. , FAWKE A.J. :"Simulation of Gas Turbine Dynamic Performance" ASME Paper 70-GT-23, 1970
3. FAWKE A.J., SARAVANAMUTTOO H.I.H :"Digital Computer Methods for Prediction of Gas Turbine Dynamic Response" SAE Trans. 1971
4. COHEN H., ROGERS G.F.C., SARAVANAMUTTOO H.I.H. :"Gas Turbine Theory" - pp. 241-296 - Longman, London, 1972
5. TORELLA G., RUSSO A., COLANTONIO A., BOTTARI E. :"Calcolo delle Prestazioni Stazionarie di un Turbomotore Monoalbero: Rapporto fra Risultati Teorici e Sperimentali" - l'Aerotecnica Missili e Spazio, n. 2, Giugno 1980
6. MANGANIELLO E.J., BOGATOSKY D. :"Investigation of Rectangular Exhaust-Gas Ejector Appliable for Engine Cooling" - NACA Report 818,1945
7. ZANETTI L. :"Studio Unidimensionale di Eiettori a Flusso Motore Supersonico e Flusso Secondario Subsonico" - l'Aerotecnica Missili e Spazio - Ottobre 1973
8. UEBELHACK H.T. :"One Dimensional Inviscid Analysis of Supersonic Ejectors" - AGARDograph 163, pp. 5-16, November 1972
9. ADDY A.L. :"The Analysis of Supersonic Ejector Systems" - AGARDograph 163, pp. 39-103 November 1972
10. TAYLOR D. :"Ejector Design for a Variety of Applications" - AGARDograph 163, pp. 103-163, November 1972
11. SAE Aerospace Information Report AIR 1191 :"Performance of Low Pressure Ratio Ejector for Engine Nacelle Cooling" - November 1971
12. RIVIELLO V.P., MUROLO A;, BRUNO F., TORELLA G. :"Ottimizzazione del Progetto di Eiettori per Motori Turboelica" VI° Congresso A.I.D.A.A. , Roma 5-9 Giugno 1981

13. RIVIELLO V.P. :"Programma ARPO04/D - Manuale d'uso" - Report Alfa Romeo Avio 1979

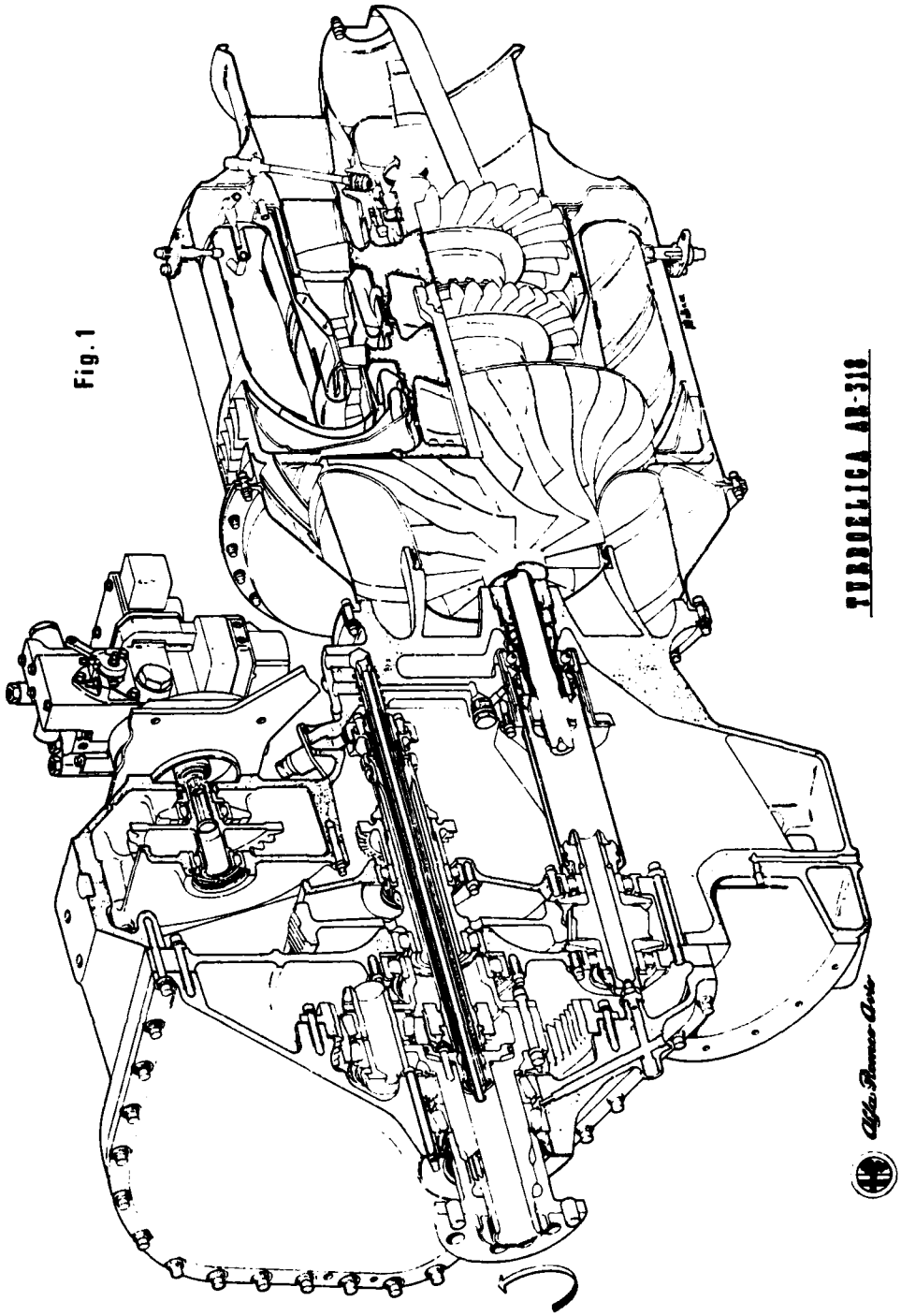

Fig. 1

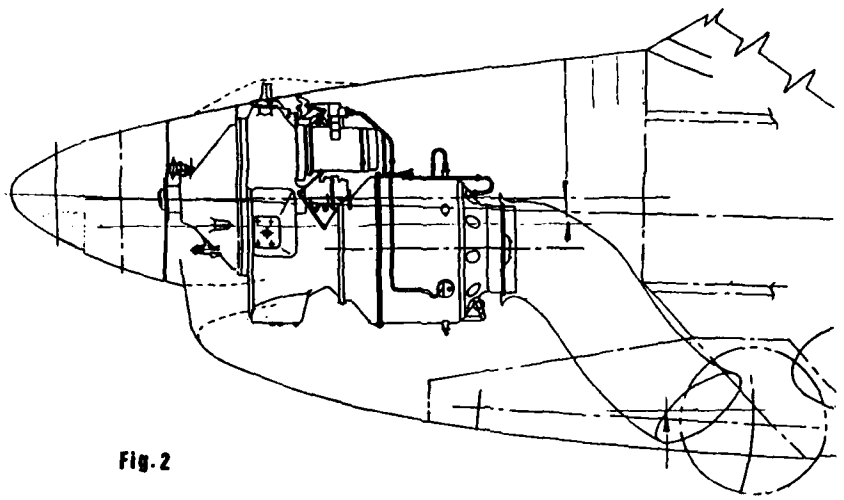

Fig. 2

FIG. 3

FLOW CHART FOR SECONDARY FLOW CALCULATION

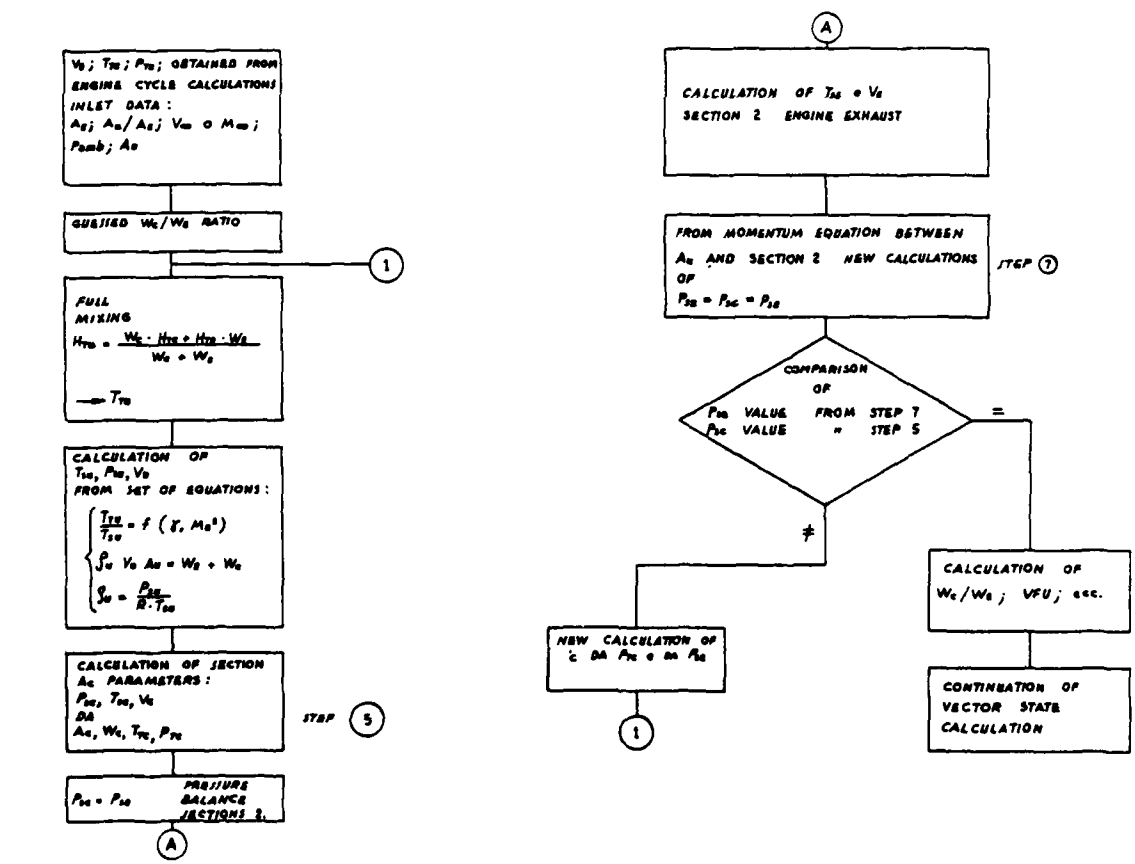

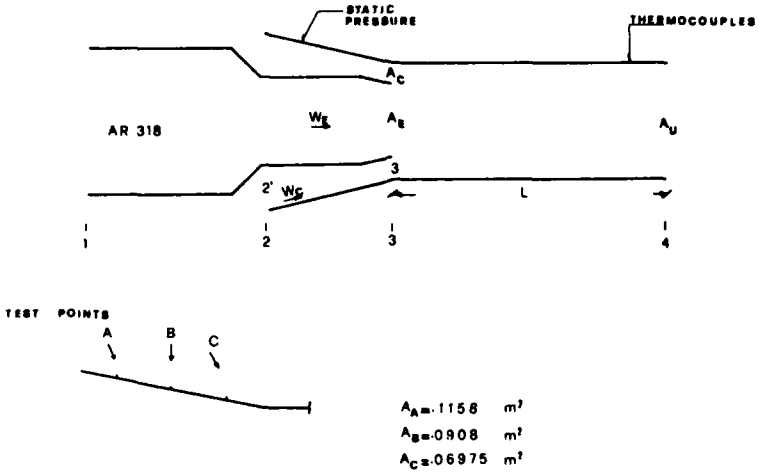

Fig. 4

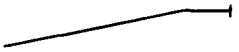

12000 ft 125 ft/s = 250 kts

AR 318 – 052

FIG. 5

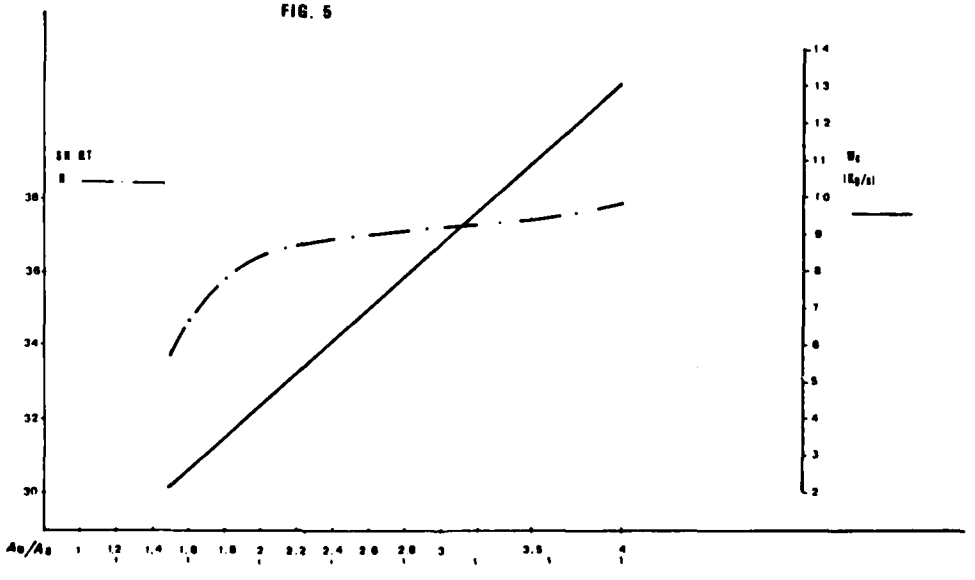

FIG. 6

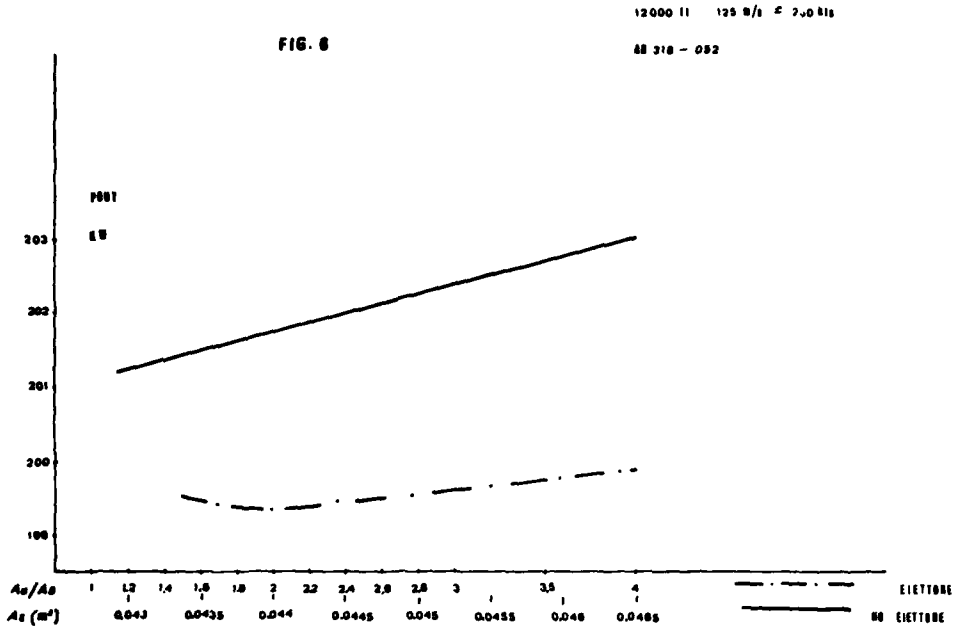
PORT
203
202
201
200
199
As/As
As (m²)
EIETTORE
NO EIETTORE

FIG. 7

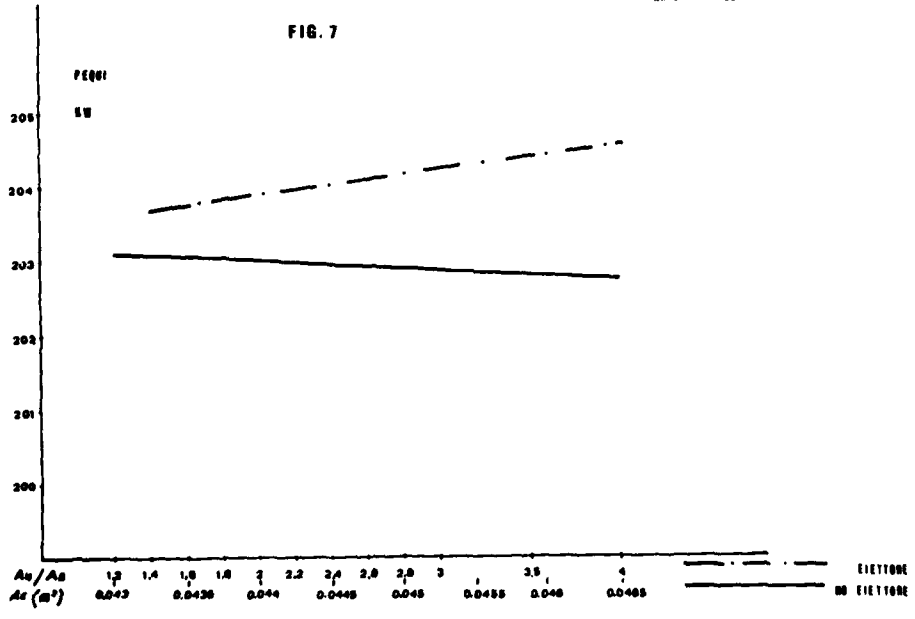
PEGGI
205
204
203
202
201
200
As/As
As (m²)
EIETTORE
NO EIETTORE

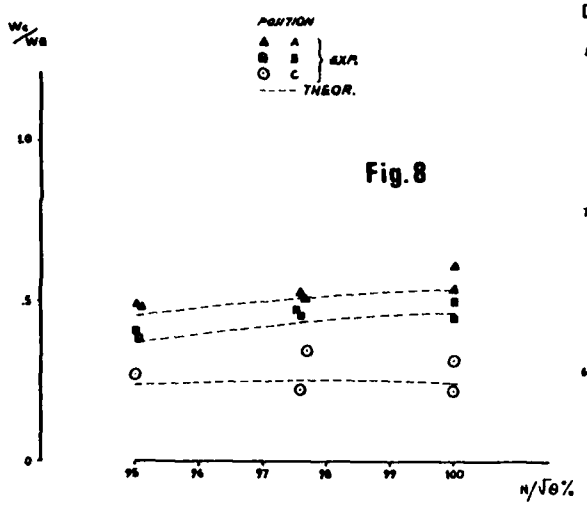

Fig.8

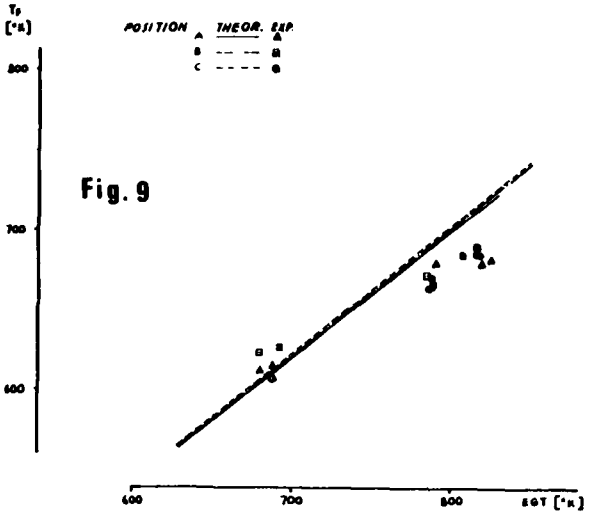

Fig. 9

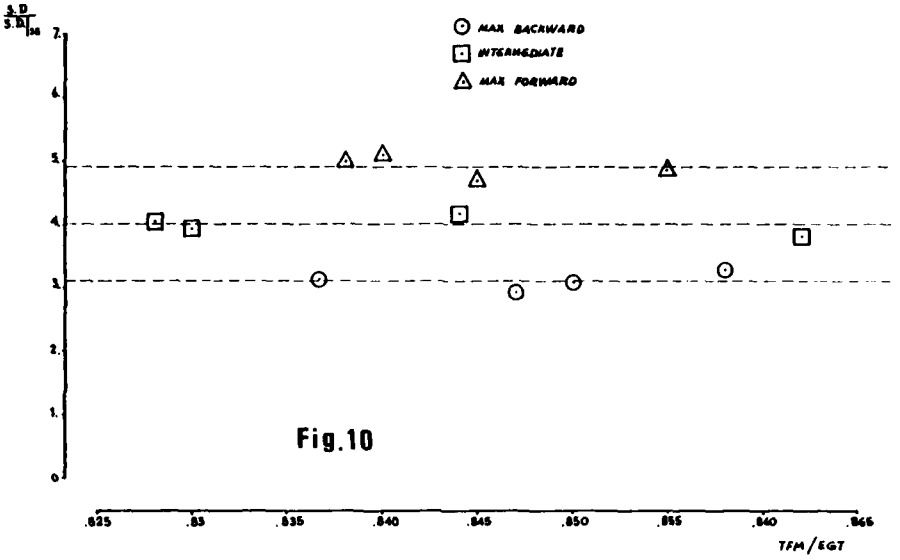

Fig.10

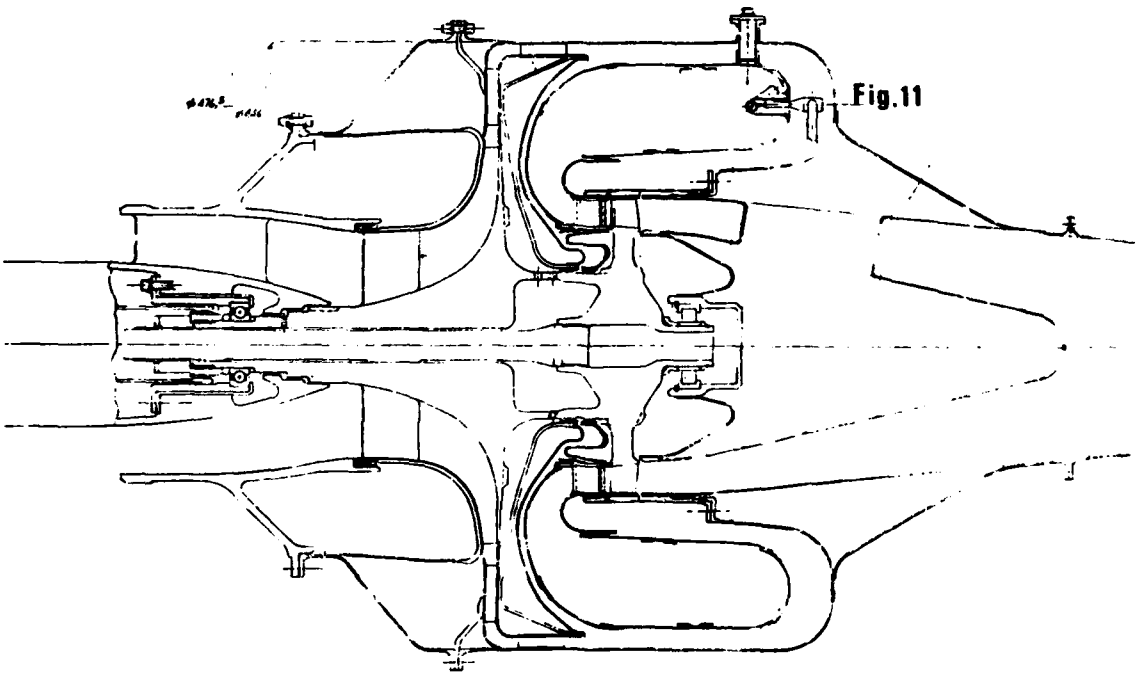

Fig.11

Fig.12

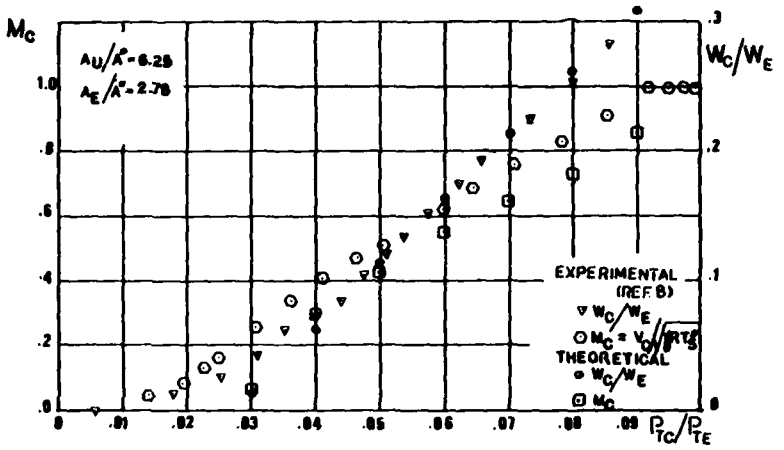

SONIC SUPERSONIC EXIT STATIONS

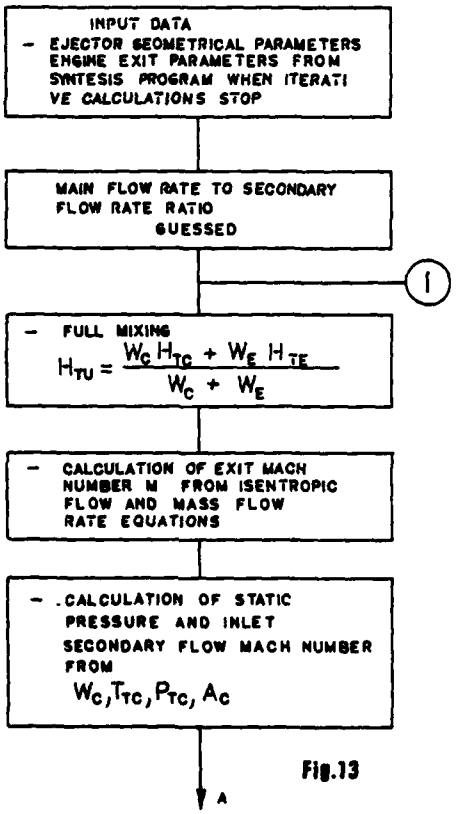

Fig.13

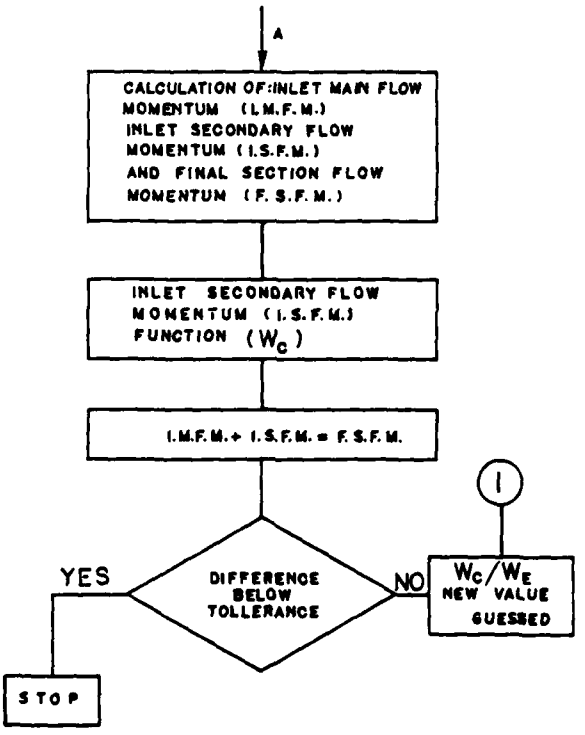

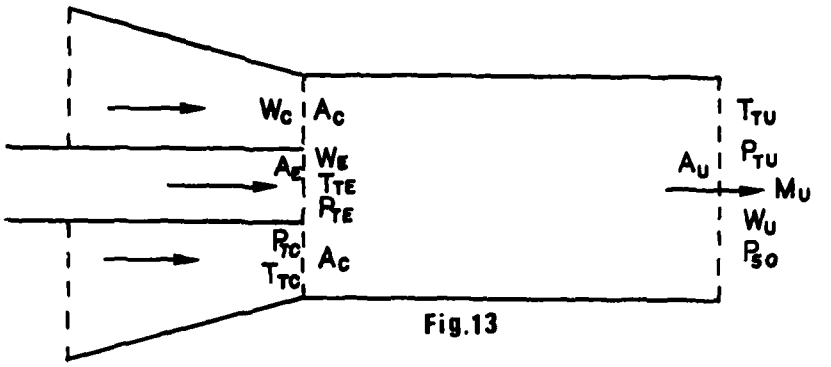

Fig.13

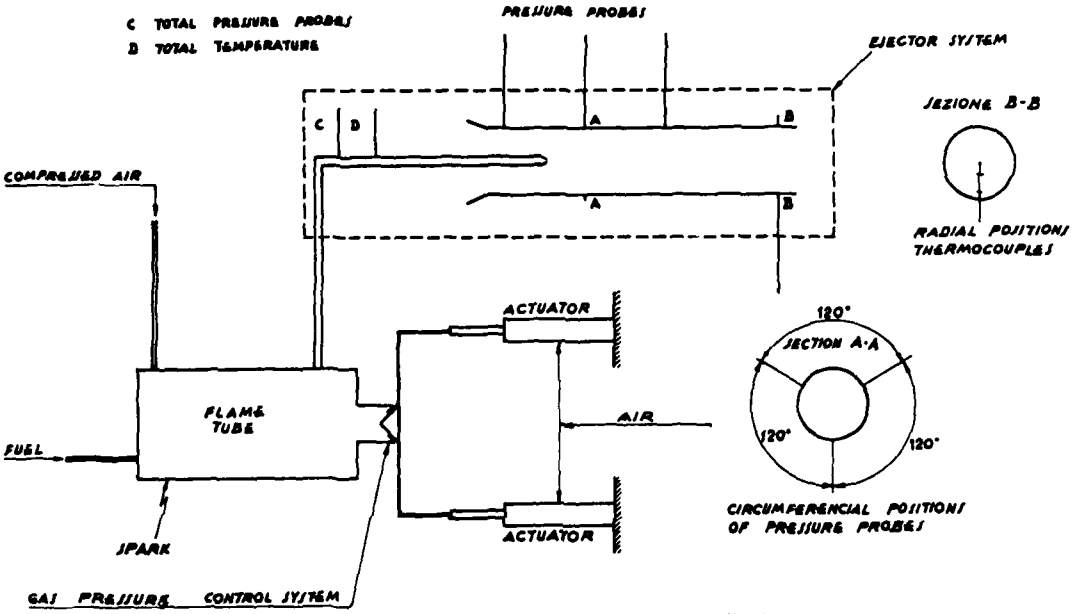

COLD AND HOT TESTS FACILITY

FIG. 14

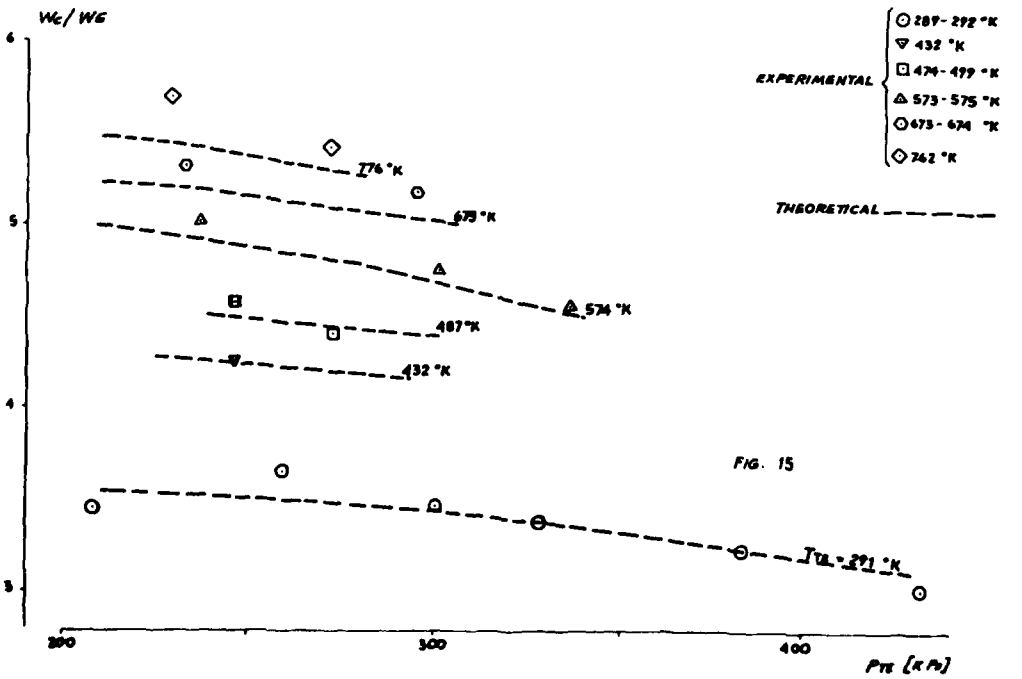

FIG. 15

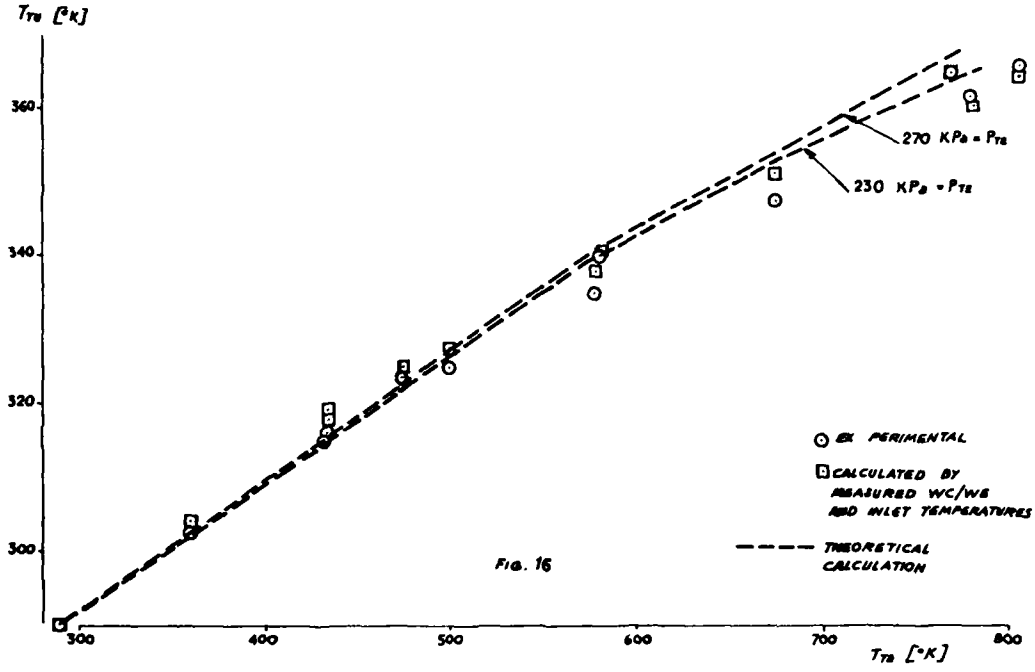

FIG. 16

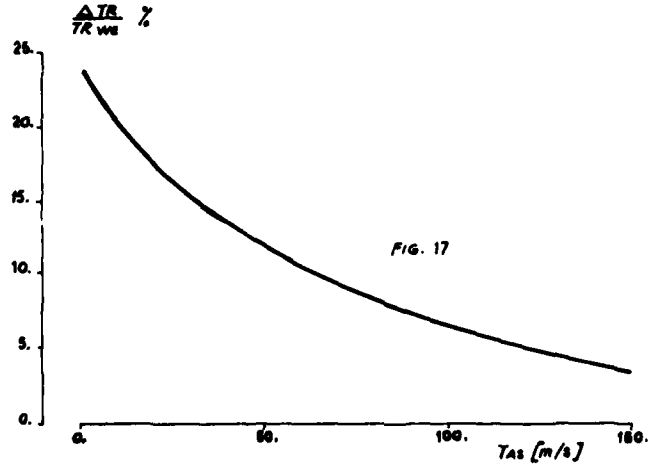

FIG. 17

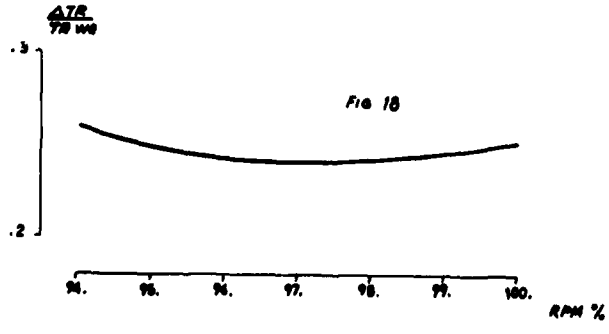

FIG 18

ON THE INCLUSION OF INFORMATION ON EDDY STRUCTURE IN SECOND-ORDER-CLOSURE MODELS OF TURBULENT FLOWS

Coleman duP. Donaldson
Aeronautical Research Associates of Princeton, Inc.
1800 Old Meadow Road, Suite 114
McLean, Virginia 22102

and

Guido Sandri
Aeronautical Research Associates of Princeton, Inc.
50 Washington Road, P.O. Box 2229
Princeton, New Jersey 08540

SUMMARY

A brief review of some of the difficulties inherent in second-order-closure modeling is given. In particular, the impropriety of using "universal" single-scale equations in closing the equations is discussed. The results of defining a simple tensor scale and deriving equations for its components from a moment expansion of the two-point correlation tensor equation are discussed. These results are compared with experimental data from nearly homogeneous shearing flows, and suggestions for further research are put forward.

INTRODUCTION

Over the past fifteen years, advances in computer technology have been such that it is now practical to use second-order-closure methods for calculating turbulent flows on many engineering problems. Since such calculations give more information than the older eddy viscosity methods, they are starting to be used widely by the engineering community. These methods are not universally loved and admired. Indeed, there is a very articulate group of experimentalists who maintain that the methods are invalid in principle because, according to these experimentalists, they take no account of the rather orderly procession of structures that are found in turbulent flows.

In view of this split in the turbulence community, the authors would like, in what follows, to review briefly the nature of second-order turbulence models, discuss some of the shortcomings of various levels of closure, present some ideas as to how eddy structure might be considered within a second-order-closure method, and give some examples of how the inclusion of such information affects the outcome of calculations for homogeneous shear flows.

1. MODELING AND THE APPEARANCE OF SCALES

The authors will assume that the readers are, in general, familiar with second-order turbulence calculations and know that equations for the mean flow and some second-order turbulent correlations are solved simultaneously to predict a given flow. In what follows, we will assume that a full closure is considered and that we are required to model certain terms that appear in the equations for the Reynolds stress correlation

$$\frac{D\langle u_i u_j\rangle}{Dt} = -\langle u_i u^k\rangle U_{j,k} - \langle u_j u^k\rangle U_{i,k} - \langle u_i u_j u^k\rangle_{,k}$$
$$- \rho^{-1}\langle p u_i\rangle_{,j} - \rho^{-1}\langle p u_j\rangle_{,i} + \rho^{-1}\langle p(u_{i,j} + u_{j,i})\rangle$$
$$+ \nu g^{mn}\langle u_i u_j\rangle_{,mn} - 2\nu g^{mn}\langle u_{i,m} u_{j,n}\rangle \qquad (1.1)$$

Let us consider here the modeling of several terms. We start with the third-order velocity correlation $\langle u_i u_j u_k\rangle$. The simplest way to make a third-order covariant tensor out of the second-order covariant tensor $\langle u_i u_j\rangle$ is to take a covariant derivative of this quantity. If we do this and note that $\langle u_i u_j u_k\rangle$ is symmetric in all three indices, we can write

$$\langle u_i u_j u_k\rangle \sim \langle u_i u_j\rangle_{,k} + \langle u_k u_i\rangle_{,j} + \langle u_j u_k\rangle_{,i} \qquad (1.2)$$

The quantity on the right-hand side of this expression has all the tensor and symmetry properties we require, but it does not have the right dimensions. We can remedy this by multiplying by a scalar formed from a length and a velocity. We choose a length, say Λ_U, and take as our velocity

$$q = \langle u^i u_i\rangle^{\frac{1}{2}} \qquad (1.3)$$

and thus write

$$\langle u_i u_j u_k\rangle = \Lambda_U\left(q\langle u_i u_j\rangle_{,k} + q\langle u_k u_i\rangle_{,j} + q\langle u_j u_k\rangle_{,i}\right) \qquad (1.4)$$

This is a model of the velocity diffusion correlation. It is certainly not the only one we can write. But let us note here that a major assumption has been made if we assume this model, or for that matter any model that changes only the quantity inside the parentheses on the right-hand side of Eq. (1.4). The tacit assumption that we have made is that, although we know that the scales of turbulence are not the same in all directions, one scale alone is sufficient to describe the diffusion of turbulent correlations by the action of the turbulent environment. As we will see, this assumption of scalar scale prevails in most of the second-order-closure modeling that has been done to date.

Let us consider the modeling of another term, namely,

$$\rho^{-1}\left\langle p\left(u_{i,j}+u_{j,i}\right)\right\rangle \tag{1.5}$$

The tensor and symmetry character we need is contained in $\langle u_i u_j\rangle$ itself. However, continuity requires that the term we are modeling becomes zero if contracted, so we write

$$\rho^{-1}\left\langle p\left(u_{i,j}+u_{j,i}\right)\right\rangle \sim u_i u_j - g_{ij}\frac{q^2}{3} \tag{1.6}$$

The dimensions are not correct and we fix this by multiplying by a scalar formed from a length Λ_I and the velocity q ; thus,

$$\rho^{-1}\left\langle p\left(u_{i,j}+u_{j,i}\right)\right\rangle = \frac{q}{\Lambda_I}\left(u_i u_j - g_{ij}\frac{q^2}{3}\right) \tag{1.7}$$

Note again that in proceeding as we have, we have assumed that all components of turbulent energy always approach $q^2/3$ and do so at the same rate. This is certainly not true for certain stratified flows. Nevertheless, it is inherent in our choice of the single scale Λ_I .

Let us consider one more example of modeling. Let us model the dissipation term

$$2\nu g^{mn}\left\langle u_{i,m}u_{j,n}\right\rangle \tag{1.8}$$

The tensor and symmetry characteristics we require are contained in $\langle u_i u_j\rangle$ so we might be inclined to write

$$2\nu g^{mn}\left\langle u_{i,m}u_{j,n}\right\rangle = 2\nu\,\frac{\left\langle u_i u_j\right\rangle}{\Lambda_D^2} \tag{1.9}$$

This is not so bad at low Reynolds numbers but at high Reynolds numbers we know that dissipation is roughly isotropic, so a more useful model is

$$2\nu g^{mn}\left\langle u_{i,m}u_{j,n}\right\rangle = 2\nu g_{ij}\frac{q^2}{3\lambda^2} \tag{1.10}$$

Let us assume, for the time being, that we choose as our models Eqs. (1.4), (1.7) and (1.10). The problems which now face us are still formidable. The following questions arise:

a) Can one choose a universal relationship between the Λs and λ ?

b) Assuming one can accomplish this task, for example, let us set (see Ref. 1)

$$\Lambda_I \equiv \Lambda \tag{1.11}$$

$$\Lambda_U = k_U\Lambda \tag{1.12}$$

and

$$\lambda^2 = \Lambda^2 \Big/ (a + b\,q\Lambda/\nu) \tag{1.13}$$

Then is it possible to find a universal equation for Λ ?

(c) If one cannot find a universal equation for Λ , can one find a single equation valid for a restricted set of flows – nonstratified, nonswirling shear flows for example?

(d) Even for a restricted class of flows, will more than one equation be necessary to adequately describe the behavior of the scale of turbulence?

These are some of the questions we would like to address in what follows. Before discussing the problem of scales, it might be helpful in this brief review to make some comments regarding complete versus partial second-order closure.

2. PARTIAL VERSUS COMPLETE CLOSURE

In the world of engineering at the present time, partial second-order-closure methods predominate over complete closure methods by a significant margin. It is important to

know what information is lost in going to a partial closure. In many cases, the information lost is recovered by use of equilibrium nondiffusive or algebraic stress modeling. In these methods, the dynamic equations are used to solve for the turbulent energy q^2 and a scale Λ and then the equilibrium values of the other correlations are computed from the equilibrium values of $\langle u_i u_j \rangle / q^2$. This does not always give a proper picture of the physics. To examine this point, let us consider two restricted cases of flow: a two-dimensional shear layer and a two-dimensional axisymmetric flow. We will consider only the production terms in the equations so that the phenomena we will demonstrate have nothing to do with modeling.

2.1 Two-Dimensional Shear Flow

The appropriate equations for the substantive derivative of the pertinent second-order correlations are

Streamwise fluctuations
$$\frac{Duu}{Dt} = -2\langle uv \rangle \frac{\partial U}{\partial y} \tag{2.1}$$

Fluctuations in the direction of mean vorticity
$$\frac{Dww}{Dt} = 0 \tag{2.2}$$

Normal fluctuations
$$\frac{Dvv}{Dt} = 0 \tag{2.3}$$

Momentum transport
$$\frac{Duv}{Dt} = -\langle vv \rangle \frac{\partial U}{\partial y} \tag{2.4}$$

We can see a characteristic of the behavior of the solution by writing

$$\frac{Dq^2}{Dt} = -2\langle uv \rangle \frac{\partial U}{\partial y} \tag{2.5}$$

Using the operator D/Dt on this expression, under the assumption that $\langle uv \rangle$ changes far more rapidly than $\partial U/\partial y$, we have

$$\frac{D^2 q^2}{Dt^2} = -2 \frac{\partial U}{\partial y} \frac{D}{Dt} \langle uv \rangle \tag{2.6}$$

Substituting Eq. (2.4) into (2.6) yields

$$\frac{D^2 q^2}{Dt^2} = 2 \langle vv \rangle \left(\frac{\partial U}{\partial y} \right)^2 \tag{2.7}$$

We can see from Eq. (2.7) the form of the exponential instability caused by the production terms in two-dimensional shear flows. Let us take $\langle vv \rangle$ proportional to q^2 , say $\langle vv \rangle = q^2/3$; then

$$q^2 = q_0^2 \, e^{\sqrt{2/3}\,|\partial U/\partial y|\,t} \tag{2.8}$$

2.2 Two-Dimensional Axisymmetric Flow

The appropriate equations for this case are

Streamwise fluctuations
$$\frac{D\langle vv \rangle}{Dt} = -2\langle uv \rangle \frac{1}{r} \frac{\partial}{\partial r} (rV) \tag{2.9}$$

Fluctuations in the direction of mean vorticity
$$\frac{D\langle ww \rangle}{Dt} = 0 \tag{2.10}$$

Normal fluctuations
$$\frac{D\langle uu \rangle}{Dt} = 4 \langle uv \rangle \frac{V}{r} \tag{2.11}$$

Momentum transport
$$\frac{D\langle uv \rangle}{Dt} = -\langle uu \rangle \frac{1}{r} \frac{\partial}{\partial r} (rV) + 2\langle vv \rangle \frac{V}{r} \tag{2.12}$$

Consider now an approach using q^2:

$$\frac{Dq^2}{Dt} = -2\langle uv \rangle \left(\frac{\partial V}{\partial r} - \frac{V}{r} \right) \tag{2.13}$$

This looks very much like Eq. (2.5). We get, upon operating as before and substitution of Eq. (2.12)

$$\frac{D^2q^2}{Dt^2} = 2\left(\frac{\partial V}{\partial r} - \frac{V}{r}\right)\left[\langle uu\rangle\left(\frac{\partial V}{\partial r} + \frac{V}{r}\right) - 2\langle vv\rangle\frac{V}{r}\right] \tag{2.14}$$

We might be inclined again to put (as before) $\langle uu\rangle = \langle vv\rangle = q^2/3$ in which case we would get

$$q^2 = q_0^2\, e^{\sqrt{2/3}\,|(\partial V/\partial r) - V/r|t} \tag{2.15}$$

which is just like Eq. (2.8) with the deformation rate $\partial U/\partial y$ replaced by the deformation rate $\partial V/\partial r - V/r$. But this result is incorrect, as can be demonstrated by operating on Eq. (2.12) with D/Dt and substituting Eq. (2.9) and Eq. (2.11) for $D\langle vv\rangle/Dt$ and $D\langle uu\rangle/Dt$. If these operations are carried out, one obtains

$$\frac{D^2\langle uv\rangle}{Dt^2} = -8\,\frac{V}{r}\,\frac{\partial}{\partial r}\,(rV)\langle uv\rangle \tag{2.16}$$

If we write V in terms of the circulation, that is

$$V = \Gamma/2\pi r \tag{2.17}$$

then Eq. (2.16) becomes

$$\frac{D^2\langle uv\rangle}{Dt^2} = -\frac{1}{\pi^2}\,\frac{1}{r^3}\,\frac{\partial\Gamma^2}{\partial r}\langle uv\rangle \tag{2.18}$$

From Eq. (2.18) we see that the character of turbulent production is markedly different depending on whether $\partial\Gamma^2/\partial r$ is positive or negative. If $\partial\Gamma^2/\partial r > 0$ in a free vortex, the flow tends to be stable. If $\partial\Gamma^2/\partial r < 0$ in a free flow (the edge of a propeller wake), the flow tends to have Taylor-like vortical instabilities.

The purpose of the above discussion is to warn the engineer unfamiliar with second-order-closure methods concerning the use of these techniques whenever the unmodeled production terms tend to admit oscillatory solutions for the transport correlation.

3. SCALE MODELS

We should point out again that the discussion in Section 2 was independent of modeling although the exact details of a given solution do depend on the details of the model used. In general, models today have an equation for q^2 or for all the independent components of $\langle u_iu_j\rangle$ and an equation for the scale Λ or for the dissipation ε which at high Reynolds number is proportional to q^3/Λ (as may be seen by combining Eq. (1.10) with (1.13)).

We would now like to address the question of whether or not it is possible to construct a single universal scale equation. Intuitively, one might guess that this would be impossible, and computationally one finds that the "constants" in the scale equations that are used can be adjusted to give better results if a certain set of constants is used for, say, two-dimensional jet flows and another set is used for axisymmetric jet flows. There are a number of ways in which this problem might be addressed but, for the present, we will consider what can be learned from the use of a very simple tensor scale Λ_{ij} that can be obtained from a model of the equation for the two-point correlation tensor R_{ij}:

$$R_{ij}(\underline{x},\underline{y}) = \left\langle u_i(\underline{x})u_j(\underline{y})\right\rangle \tag{3.1}$$

with

$$R_{ij}(\underline{x},\underline{x}) = \left\langle u_iu_j\right\rangle \tag{3.2}$$

The scale that we shall consider is

$$\Lambda_{ij}(\underline{x}_c) = \frac{3}{q^2}\int \frac{R_{ij}(x_c,r)}{4\pi r^2}\,d\underline{r} \tag{3.3}$$

Here, $\underline{r} = \underline{y} - \underline{x}$ and $\underline{x}_c = (\underline{x} + \underline{y})/2$. This definition is by no means ideal for describing the structure of an eddy, but it does give some information about the structure of a turbulent flow and, as we shall see, will help make specific some of the shortcomings of a single universal scale equation.

To obtain a differential equation for Λ_{ij}, we take three steps:

a) Develop a closure model for the R_{ij} equation so that when $\underline{y} \to \underline{x}$, we obtain our standard $\langle u_iu_j\rangle$ equation.

b) Substitute into the closed R_{ij} equation the moment expansion

$$R_{ij}(\underline{x}_c,\underline{r}) = M^o_{ij}4\pi r^2\delta(\underline{r}) - M^1_{ijk}4\pi r^2\frac{\partial}{\partial r_k}\delta(r) + \ldots \tag{3.4}$$

Note that by integrating over all $\underline{r}$, one finds

$$M^o_{ij} = \frac{q^2}{3}\Lambda_{ij} \tag{3.5}$$

c) Integrate term by term over all $\underline{r}$ in the modeled R_{ij} equation.

A simple choice for a modeled R_{ij} equation with which we have some experience (Ref. 2) yields

$$\frac{\partial}{\partial t}\left(q^2\Lambda_{ij}\right) + U_k\frac{\partial}{\partial x_k}\left(q^2\Lambda_{ij}\right) + q^2\left(\Lambda_{ik}\frac{\partial U_j}{\partial x_k} + \Lambda_{jk}\frac{\partial U_k}{\partial x_k}\right) =$$

$$= v_{c_1}\frac{\partial}{\partial x_k}\left[(q\Lambda)\frac{\partial}{\partial x_k}\left(q^2\Lambda_{ij}\right)\right] + v_{c_2}\frac{q^3}{\Lambda}\Lambda_{ij} +$$

$$- \frac{q^3}{\Lambda}\left(\Lambda_{ij} - \delta_{ij}\frac{\Lambda_{kk}}{3}\right) - 2bq^3\delta_{ij} \tag{3.6}$$

where Λ is the single scale utilized in the standard model and in the universal scale equation. We identify Λ as follows:

$$\Lambda = \frac{1}{3}\Lambda_{kk} \tag{3.7}$$

because for locally isotropic turbulence, $\Lambda = 2L_f/3$ where L_f is the Taylor longitudinal scale, a relation supported by analysis of a number of flows. Taking the trace of Eq. (3.6) and subtracting the equation for q^2, we find the rate equation for Λ, *namely*,

$$\frac{\partial\Lambda}{\partial t} + U_k\frac{\partial}{\partial x_k}\Lambda + \underline{2\Lambda\left(\frac{\Lambda_{ij}}{3\Lambda} - \frac{\langle u_iu_j\rangle}{q^2}\right)\frac{\partial U_i}{\partial x_j}} = \frac{v_{c_1}}{q^2}\left\{\frac{\partial}{\partial x_k}\left[q\Lambda\frac{\partial}{\partial x_k}(q^2\Lambda)\right] - \Lambda\frac{\partial}{\partial x_k}\left[q\Lambda\frac{\partial q^2}{\partial x_k}\right]\right\} + v_{c_2}q \tag{3.8}$$

Here we note that the coefficient of the production term, which is underlined in the above equation and which, by the way, is <u>not</u> a modeled term, is not a constant as has been assumed in many of the universal scale equation models.

To cast Eq. (3.8) into a form more like one of the universal scale equations in use today, we will assume that the structure of Λ_{ij} depends linearly on the anisotropy of the turbulence through a parameter σ. This is a very restrictive assumption but, as we shall see, some interesting results can be gleaned from its use. Substituting

$$\Lambda_{ij} = \Lambda\left[\delta_{ij} + \sigma\left(\frac{\langle u_iu_j\rangle}{q^2} - \frac{\delta_{ij}}{3}\right)\right] \tag{3.9}$$

into Eq. (3.8), we obtain

$$\frac{\partial\Lambda}{\partial t} + U_k\frac{\partial\Lambda}{\partial x_k} = -2\left(\frac{\sigma}{3} - 1\right)\frac{\langle u_iu_j\rangle}{q^2}\frac{\partial U_i}{\partial x_j} + \frac{v_{c_1}}{q}\left\{\frac{\partial}{\partial x_k}\left[q\Lambda\frac{\partial}{\partial x_k}(q^2\Lambda)\right] - \Lambda\frac{\partial}{\partial x_k}\left[q\Lambda\frac{\partial q^2}{\partial x_k}\right]\right\} +$$

$$+ v_{c_2}q \tag{3.10}$$

We may also obtain an equation for σ from Eqs. (3.6) and (3.8). It is

$$\frac{\partial\sigma}{\partial t} + U_k\frac{\partial\sigma}{\partial x_k} = 2\left(\frac{\sigma}{3} - 1\right)\left(\sigma + \frac{q^4}{\langle u_iu_j\rangle\langle u_iu_j\rangle - q^4/3}\right)\frac{\langle u_mu_n\rangle}{q^2}\frac{\partial U_m}{\partial x_n} +$$

$$+ \frac{v_{c_1}}{\Lambda}\left\{\frac{\partial}{\partial x_k}\left[q\Lambda\frac{\partial}{\partial x_k}(\sigma\Lambda)\right] - \sigma\frac{\partial}{\partial x_k}\left[q\Lambda\frac{\partial\Lambda}{\partial x_k}\right]\right\} \tag{3.11}$$

A lesson to be learned from Eqs. (3.10) and (3.11) is that the structure of turbulent [illegible] in different types of mean flow mitigates against the use of a universal scale [illegible] and that, at the very least, a second equation is needed to determine the [illegible] that appears in the Λ equation; i.e., the factor $-2|(\sigma/3) - 1|$. It is not [illegible] to proceed in this approximate manner, however, since Eq. (3.6) is a perfectly [illegible] for all components of the tensor Λ_{ij}.

[illegible] lesson to be learned from Eqs. (3.10) and (3.11) is that there can be no [illegible] equilibrium solutions to the equation for Λ. This seems reasonable since

Λ grows at the rate of development of the mean flow, and this time scale is slow so that equilibrium solutions are not, in general, possible. On the other hand, there is a non-diffusive equilibrium solution to the σ equation for any given type of flow. We interpret this to mean that the structure is able to quickly distinguish what it ought to be for a given type of flow, while the actual scale is only determined by the development of the particular mean motion.

It is instructive to examine our equation for σ somewhat further, although it should be remembered that this approximate equation can give only a qualitative picture of the real physics. Let us ask for the equilibrium, nondiffusive solution of Eq. (3.11) for the case of equilibrium, nondiffusive Couette flow as determined from the high Reynolds number form of the equations for the components of the one-point correlation tensor $\langle u_i u_j \rangle$, namely,

$$\frac{\partial}{\partial t}\langle u_i u_j \rangle + U_k \frac{\partial \langle u_i u_j \rangle}{\partial x_k} = - (u_i u_j) \frac{\partial U_j}{\partial x_k} - (u_j u_k) \frac{\partial U_i}{\partial x_k} - \frac{\partial}{\partial x_k}\langle u_i u_j u_k \rangle +$$

$$- \rho^{-1}\left[\langle p u_i \rangle_{,j} + \langle p u_j \rangle_{,i} \right] - \frac{q}{\Lambda}\left[\langle u_i u_j \rangle - \frac{\delta_{ij}}{3} q^2 \right] - \frac{2b}{3} \delta_{ij} \frac{q^3}{\Lambda} \qquad (3.12)$$

The equilibrium, nondiffusive solutions are (for $b = 1/8$)

$$\frac{\langle uu \rangle}{q^2} = \frac{1 + 4b}{3} = 0.50 \qquad (3.13)$$

$$\frac{\langle vv \rangle}{q^2} = \frac{\langle ww \rangle}{q^2} = \frac{1 - 2b}{3} = 0.25 \qquad (3.14)$$

$$\frac{\langle uv \rangle}{q^2} = b\sqrt{\frac{1 - 2b}{3b}} = 0.177 \qquad (3.15)$$

and

$$\frac{q}{\Lambda(\partial U/\partial y)} = \frac{1 - 2b}{3b} = 2 \qquad (3.16)$$

Since the term

$$\frac{q^4}{\langle u_i u_j \rangle \langle u_i u_j \rangle - q^4/3}$$

in Eq. (3.11) turns out to be positive when it is evaluated using Eqs. (3.13)-(3.15), the only non-negative solution for σ permitted in this case is $\sigma = 3$. Thus, for homogeneous shear flows, we might expect the term in front of the production term in the scale equation, Eq. (3.10), to be zero. In actual practice, the term $-2(\sigma/3 - 1)$ is taken equal to 0.35 for two-dimensional shear layers. This implies a σ of 2.48. In the section which follows, we will show that indeed the correct value of σ for a developing homogeneous shear flow is 3. What, according to Eq. (3.11), is the cause for the lowered value of σ generally used in nonhomogeneous flows? It appears that a principal contribution to the value of σ is the diffusion term. It is not surprising then that, if one were to consider a two-dimensional and an axisymmetric jet, one would expect to use a different σ in the two cases. This is because the effect of diffusion is quite different in these two cases.

4. HOMOGENEOUS FLOWS WITH COUPLED STRESS AND TENSOR SCALE EQUATIONS

In this section, we give two analytic solutions to the coupled equations for the stress tensor and scale tensor equations. The second solution will be compared in some detail with experimental results as well as results obtained using more conventional approaches.

4.1 Equations in Standard Coordinates

The centroid vector and mean velocity vector are taken to have components

$$(x,y,z) \ , \ (U(y),0,0)$$

with $\partial U/\partial y = U' =$ constant. The relevant components of the Reynolds stress equations are obtained from Eq. (3.12). There is a useful form for numerical integration in which $\langle u_1^2 \rangle$ and Λ_{11} are calculated from

$$\langle u_1^2 \rangle = q^2 - \langle u_2^2 \rangle - \langle u_3^2 \rangle \qquad (4.1)$$

$$\Lambda_{11} = 3\Lambda - \Lambda_{22} - \Lambda_{33} \qquad (4.2)$$

The other relevant components of the stress and energy equations are

$$\frac{\partial}{\partial t}\left\langle u_2^2\right\rangle = \frac{1}{3}(1-2b)\frac{q^3}{\Lambda} - \frac{q}{\Lambda}\left\langle u_2^2\right\rangle \tag{4.3}$$

$$\frac{\partial}{\partial t}\left\langle u_3^2\right\rangle = \frac{1}{3}(1-2b)\frac{q^2}{\Lambda} - \frac{q}{\Lambda}\left\langle u_3^2\right\rangle \tag{4.4}$$

$$\frac{\partial}{\partial t}\left\langle u_1u_2\right\rangle = -u_2^2U' - \frac{q}{\Lambda}\left\langle u_1u_2\right\rangle \tag{4.5}$$

$$\frac{\partial q}{\partial t} = -\frac{\left\langle u_1u_2\right\rangle}{q}U' - b\frac{q^2}{\Lambda} \tag{4.6}$$

For the tensor scale components, we obtain, using Eqs. (3.6), (3.10) and (3.12),

$$\frac{\partial}{\partial t}\Lambda_{22} = -\frac{1}{T}\Lambda_{22} + (1-2b)q \tag{4.7}$$

$$\frac{\partial}{\partial t}\Lambda_{33} = -\frac{1}{T}\Lambda_{33} + (1-2b)q \tag{4.8}$$

$$\frac{\partial}{\partial t}\Lambda_{12} = -\frac{1}{T}\Lambda_{12} - U'\Lambda_{22} \tag{4.9}$$

$$\frac{\partial}{\partial t}\Lambda = 2\frac{\left\langle u_1u_2\right\rangle}{q^2}U'\Lambda - \frac{2}{3}\Lambda_{12}U' + v'q \tag{4.10}$$

where

$$\frac{1}{T} = -2\frac{\left\langle u_1u_2\right\rangle}{q^2}U' + \frac{q}{\Lambda}(1-2b-v') \tag{4.11}$$

and we have shortened our notation by writing $v_{c_2} = v'$.

4.2 Solution of the Shearless Equations

Setting $U' = 0$, we see that equations for q and Λ decouple from the tensor components. Introducing the deviators

$$d_{ij} = \left\langle u_iu_j\right\rangle - \frac{1}{3}\delta_{ij}q^2 \tag{4.12}$$

$$D_{ij} = \Lambda_{ij} - \frac{1}{3}\delta_{ij}\Lambda_{kk} \tag{4.13}$$

and the time

$$\tau = \frac{\Lambda}{q} \tag{4.14}$$

we have the set

$$\frac{\partial}{\partial t}q = -\frac{b}{\tau}q \ , \ \frac{\partial}{\partial t} = \frac{v'}{\tau}\Lambda \tag{4.15}$$

$$\frac{\partial}{\partial t}d_{ij} = -\frac{b}{\tau}d_{ij} \ , \ \frac{\partial}{\partial t}D_{ij} = -\frac{1-2b-v'}{\tau}D_{ij} \tag{4.16}$$

$$\frac{\partial}{\partial t}\tau = b + v' \tag{4.17}$$

Integrating Eq. (4.17) as

$$\tau = (b+v')(t-t_0) + \frac{\Lambda_0}{q_0} \tag{4.18}$$

we see that q , Λ , d_{ij} and D_{ij} are suitable powers of $(q_0/T_0)\tau$; for example,

$$q = q_0\left[(b+v')\frac{q_0}{\Lambda_0}(t-t_0) + 1\right]^{-b/(b+v')} \tag{4.19}$$

$$d_{ij} = d_{ij_0}\left[(b + v')\frac{q_0}{\Lambda_0}(t - t_0) + 1\right]^{-1/(b+v')} \tag{4.20}$$

$$\Lambda = \Lambda_0\left[(b + v')\frac{q_0}{\Lambda_0}(t - t_0) + 1\right]^{-v'/(b+v')} \tag{4.21}$$

A good fit to experimental data on the decay of turbulent energy and the growth of eddy size for grid turbulence is obtained if one chooses

$$b \approx 1/8 \ , \ v' \approx 0.075 \tag{4.22}$$

We then see that for large times

$$q^2 \sim q_0^2\left[\cdot\ 2\frac{q_0}{\Lambda_0}t\right]^{-5/4} \tag{4.23}$$

$$d_{ij} \sim d_{ij_0}\left[\cdot\ 2\frac{q_0}{\Lambda_0}t\right]^{-5} \tag{4.24}$$

which shows that the deviator decays with a power about four times larger than the energy. This substantial difference may eventually be checked in our anisotropic grid flow.

4.3 An Exact Solution of the Equations with Shear

To obtain a solution of the equations with shear that is an asymptotic solution valid at times when initializing transients have disappeared, we let

$$\begin{aligned} q &= V\, e^{aU't} & \Lambda &= L\, e^{aU't} \\ \langle u_1^2\rangle &= W_1\, e^{2aU't} & \Lambda_{11} &= L_1\, e^{aU't} \\ \langle u_2^2\rangle &= W_2\, e^{2aU't} & \Lambda_{22} &= L_2\, e^{aU't} \\ \langle u_3^2\rangle &= W_3\, e^{2aU't} & \Lambda_{33} &= L_3\, e^{aU't} \\ \langle u_1u_2\rangle &= W_4\, e^{2aU't} & \Lambda_{12} &= L_4\, e^{aU't} \end{aligned} \tag{4.25}$$

Substituting these forms into the appropriate differential equations, we find that the exponentials cancel and that an algebraic set of equations for the amplitudes is obtained. It is possible, with some algebra, to solve the amplitude equations explicitly in terms of the parameters b and v'. The energy components are (with $b = 0.125$ and $v' = 0.075$)

$$\frac{\langle u_1^2\rangle}{q^2} = \frac{1 + 6v' + 4b}{3(1 + 2v')} = 0.565 \tag{4.26}$$

$$\frac{\langle u_2^2\rangle}{q^2} = \frac{\langle u_3^2\rangle}{q^2} = \frac{1 - 2b}{3}\frac{1}{1 + 2v'} = 0.217 \tag{4.27}$$

The scale components are

$$\frac{\Lambda_{11}}{\Lambda} = \frac{1 + 6v' + 4b}{1 + 2v'} = 1.696 \tag{4.28}$$

$$\frac{\Lambda_{22}}{\Lambda} = \frac{\Lambda_{33}}{\Lambda} = \frac{1 - 2b}{1 + 2v'} = 0.652 \tag{4.29}$$

We see that

$$\frac{\Lambda_{11}}{\Lambda_{22}} = \frac{\langle u_1^2\rangle}{\langle u_2^2\rangle} = \frac{1 + 6v' + 4b}{1 - 2b} = 2.60 \tag{4.30}$$

The off-diagonal components are

$$Br = \frac{-\langle u_1u_2\rangle}{q^2} = -\frac{1}{1 + 2v'}\sqrt{\frac{(1 - 2b)(b + v')}{3}} = 0.194 \tag{4.31}$$

$$\frac{\Lambda_{12}}{\Lambda} = -\frac{1}{1+2v'}\sqrt{3(1-2b)(b+v')} = -0.194 \tag{4.32}$$

The Corrsin parameter is

$$Co \equiv \frac{-\langle u_1 u_2\rangle}{\sqrt{\langle u_1^2\rangle\langle u_2^2\rangle}} = \sqrt{\frac{3(b+v')}{1+4b+6v'}} = 0.55 \tag{4.33}$$

The ratio of the two times is

$$\frac{1}{\alpha} = \frac{q}{U'\Lambda} = \frac{1}{1+2v'}\sqrt{\frac{1-2b}{3(b+v')}} = 0.972 \tag{4.34}$$

and the growth rate, a, is

$$a = v'\frac{1}{\alpha} = \frac{v'}{1+2v'}\sqrt{\frac{1-2b}{3(b+v')}} = 0.073 \tag{4.35}$$

We notice two additional interesting parameters:

$$\frac{\langle u_1 u_2\rangle}{q^2}\frac{U'\Lambda}{q} = \alpha \cdot Br = b + v' = 0.200 \tag{4.36}$$

$$\frac{\Lambda_{ij}}{\Lambda} - \delta_{ij} = 3\left(\frac{\langle u_i u_j\rangle}{q^2} - \frac{1}{3}\delta_{ij}\right) \tag{4.37}$$

As we have noted in the previous section, this last condition is equivalent to $\sigma = 3$. Also note that for this coupled, asymptotic, convective solution that ratios of $\langle u_i u_j\rangle/q^2$ and the Bradshaw number $\langle u_1 u_2\rangle/q^2$ and the value of $q/(\Lambda\partial U/\partial y)$ have been modified slightly.

4.4 Comparison with Experimental Results

It is now appropriate that we consider the agreement between these theoretical results just obtained and experimental measurements. The measurements we will make use of are those of Harris, Graham and Corrsin (Ref. 3). Figure 4.1 is Figure 3 from Reference 3. It shows the growth in $\langle u_1^2\rangle$, $\langle u_2^2\rangle$ and $\langle u_3^2\rangle$ in a constant shear flow. For these measurements, U_c was 1240 cm/sec, $U' = \partial U/\partial y = 48$ sec^{-1} and $h = 30.48$ cm. Also shown in the figure is the behavior of the Corrsin number

$$-\langle u_1 u_2\rangle \Big/ \sqrt{\langle u_1^2\rangle\langle u_2^2\rangle}$$

Since we expect, after an initial transient, that the flow adjusts to an exponential solution with certain parameters constant, we plot faired results from Figure 4.1 in semi-logarithmic form in Figure 4.2. It is apparent from Figure 4.2 that an exponential solution has been reached at an x/h of approximately 8. We note that the growth rates in terms of x/h may be written

$$\langle u_1^2\rangle \,,\ \langle u_2^2\rangle \,,\ \langle u_3^2\rangle \sim e^{2a_c x/h}$$

On the figure we have indicated the a_c's that best fit each curve. An average of these values gives $a_c = 0.087$ or, let us say, $a_c = 0.09$. To compare these results with the theoretical results just given, we must multiply a_c by $U_c/hU' = 0.848$ which gives $a = 0.076$. This is not in bad agreement with the theoretical value of 0.0729.

A program has been written to solve the full set of coupled $\langle u_i u_j\rangle$ and Λ_{ij} equations, namely, Eqs. (4.1) through (4.18) and the result of a computation of q versus both dimensional time and nondimensional time

$$U'\Delta t = \left(\frac{x}{h} - \left(\frac{x}{h}\right)_0\right)\frac{hU'}{U_c} \tag{4.38}$$

is given in Figure 4.3. It is seen that although the growth rate of q is well predicted the actual values of q are some 20% in error and remain so in the asymptotic region of the solution. This is not good but we will discuss a possible cause of this error after we have exhibited the agreement between experimental results and all the parameters we have derived for the exponential behavior of a homogeneous shear flow. These comparisons are shown in the second, third and fourth columns of Table 4.1.

It is not difficult to show that other simpler, second-order models of turbulent flow have exponential asymptotic solutions in the case of homogeneous shear flow. In Table 4.1 we also show the theoretical results for the following models:

a) A full closure in the case of the $\langle u_i u_j \rangle$ tensor and the single scale equation

$$\frac{d\Lambda}{dt} = 0.35 \frac{\Lambda}{q^2} \langle uv \rangle U' + v'q \tag{4.39}$$

b) A q - Λ model constructed from

$$\frac{dq}{dt} = - \frac{\langle uv \rangle}{q} U' - \frac{bq^2}{\Lambda} \tag{4.40}$$

$$\frac{d\Lambda}{dt} = 0.35 \frac{\Lambda}{q^2} \langle uv \rangle U' + v'q \tag{4.41}$$

together with the assumption that

$$\langle uv \rangle = -0.33 q \Lambda U' \tag{4.42}$$

Table 4.1 Comparison of Theoretical Predictions and Experimental Results for the Asymptotic Solution of Homogeneous Shear Flow

Parameter	Experiment (x/h = 11)	Theory: Full Closure Tensor Scale	Diff. %	Theory: Full Closure Single Scale	Diff. %	Theory: q - Λ Model	Diff. %
$Br = - \frac{\langle uv \rangle}{q^2}$	.149	.1944	25%	.1839	19%	.221	33%
$Co = \frac{- \langle uv \rangle}{\sqrt{\langle uu \rangle \langle vv \rangle}}$	.47	.5547	16	.5207	10	NA	-
$q/\Lambda U'$	.67	.972	35	1.242	46	1.492	55
a	.076	.0729	4	.0287	165	.0345	120
$\langle uu \rangle / q^2$	.502	.5652	11	.5220	4	NA	-
$\langle vv \rangle / q^2$	.199	.2174	8	.2390	17	NA	-
$\langle ww \rangle / q^2$	.299	.2174	38	.2390	25	NA	-
$\frac{\langle vv \rangle + \langle ww \rangle}{q^2}$	.498	.4348	14	.4780	4	NA	-

4.5 Discussion of Results

An examination of Table 4.1 is instructive. First of all, the tensor scale model, with only two adjustable constants which were set from an experiment on grid turbulence, seems to do the best overall job. It gives by far and away the best prediction of asymptotic growth rate. The single scale model as normally used (which has the added parameter $c = 0.35$) is pretty good on all quantities except $q/\Lambda U'$ and the growth rate, where it is very poor indeed. The approximate q - Λ model which has still another adjustable parameter does least well for the parameters chosen which are typical of those boundary-layer-like flows.

A most interesting result is found if we make the assumption that, as indicated by the theoretical developments we have presented, the "constant" in the simple scale equation should be zero and not equal to 0.35 for homogeneous shear flows. If we do assume $c = 0$ in this formulation and find the asymptotic values of the basic parameters for homogeneous shear flow, we obtain almost the same values of the parameters that were obtained using the tensor scale equation. This is not surprising since the two formulations are now very similar. However, it must be remembered that it was the tensor scale equation which, when solved for homogeneous shear flow, showed that the production term should disappear from the scale equation.

If one puts $c = 0$ in the q - Λ model we have concocted, the growth rate and the Bradshaw number become too large (0.0963 and 0.257, respectively) while the parameter $q/\Lambda U'$ drops to 1.284 (which is not a great improvement).

What we really don't like about the present theoretical results are the disagreements between the theoretical and experimental values of the Bradshaw number and $q/\Lambda U'$. In addition, the improper partitioning of the energies is bothersome. We believe the two problems are closely related and that a tendency-towards-isotropy that consists of more than the Rotta tensor that was used in these calculations is essential. It is clear that the asymptotic solutions of the coupled full closure and tensor scale equations, together with experimental data such as that we have just been using, provide an excellent framework within which to study this problem.

5. CONCLUSIONS AND RECOMMENDATIONS

In the previous sections we have reviewed some of the characteristics of second-order modeling as it is currently used. One of the primary criticisms of these methods has been that they take no account of the structure that can be found in turbulent fields by modern instrumentation. We have given an outline of how, by the use of a simple definition of tensor scale, second-order-closure models might be extended to take account of information on structure that can be gleaned from the two-point correlation equations. The tensor scale used is certainly not ideal for this purpose, but it was used not only because we are familiar with it but also it illustrates many features that will be exhibited by any other definition of tensor scale.

We believe we have demonstrated two things in the results presented.

First, we believe we have shown that there really cannot be such a thing as a universal scalar scale equation. Hence, we believe that any steps taken to improve second-order-closure methods in the future must include, among other things, the derivation from appropriate models of the two-point correlation tensor equations multiple scales which will give some indication of the structure of the turbulent eddies that exist in a given mean flow. The method we have used here defines a tensor scale and uses a moment expansion to look at some general features of the structure problem that can be derived from a particular definition of tensor scale. The method is a good approximation for homogeneous flows. It is less justifiable for nonhomogeneous flows. However, we believe that, at the present time, it bears a relation to a more complete formulation much like eddy viscosity methods bear to more complete formulation for calculating the Reynolds stress correlation $\langle u_i u_j \rangle$.

Second, we believe that we have shown that the homogeneous shear experiments are very powerful tools for the modeler. We believe that they do indeed have asymptotic solutions that are exponential and that when the asymptotic state is reached certain nondimensional parameters become constant. Since the asymptotic value of these parameters can be computed from a given model (see Eqs. (4.31) through (4.37), the experimental results are an extremely useful tool for the development of valid models. One reason the measured values of these parameters are so useful is that they are independent of initial conditions and, in the past, arguments over initial conditions have been used to cover a multitude of modeling sins. On the other hand, with homogeneous flows, the modeler may be able to help the experimentalist. If one looks at the data for the longitudinal integral scale L_f in Ref. 3, one is hard pressed to fit an exponential growth rate derived from that appropriate for all the other measured variables to these data. It is hard to conceive of a solution that is linear in L_f and exponential in all other quantities except the microscale which should (according to theory) be constant and according to experiment is almost so. Therefore, one can pose the question, "Are the reported scale data really correct?"

Perhaps, having posed this question, we should bring this discussion to a close on the well-known basis that it is alright for an experimentalist to question a modeler, but it is not appropriate for a modeler to question an experimentalist. Our own feelings are that there should be more cooperation between modelers and experimentalists than is evident at present. Be that as it may, we cannot bring this paper to a close without a plea to those who would support experimental work to continue to support detailed studies of homogeneous shear flows both in unstratified and stratified media. We believe that such studies, when combined with efforts to calculate such flows, will rapidly advance our understanding of turbulent shear flows and our ability to handle these flows computationally.

6. REFERENCES

1. Rotta, J.: Statistische Theorie nichthomogener Turbulenz, Z. Physik 129, 547 (1951).

2. Sandri, G. and Cerasoli, C.: Aeronautical Research Associates of Princeton, Inc., Fundamental Research in Turbulent Modeling, 1981, A.R.A.P. Report No. 438.

3. Harris, V.G., Graham, J.A.H. and Corrsin, S.: Further Experiments in Nearly Homogeneous Turbulent Shear Flow, J. Fluid Mechanics 81, pp. 657-687 (1977).

7. ACKNOWLEDGEMENTS

The work described herein was supported by the Air Force Office of Scientific Research under Contract F44620-76-C-0048. The authors wish to acknowledge the assistance of Dr. Carmen Cerasoli of A.R.A.P. who is responsible for the experimental results noted here.

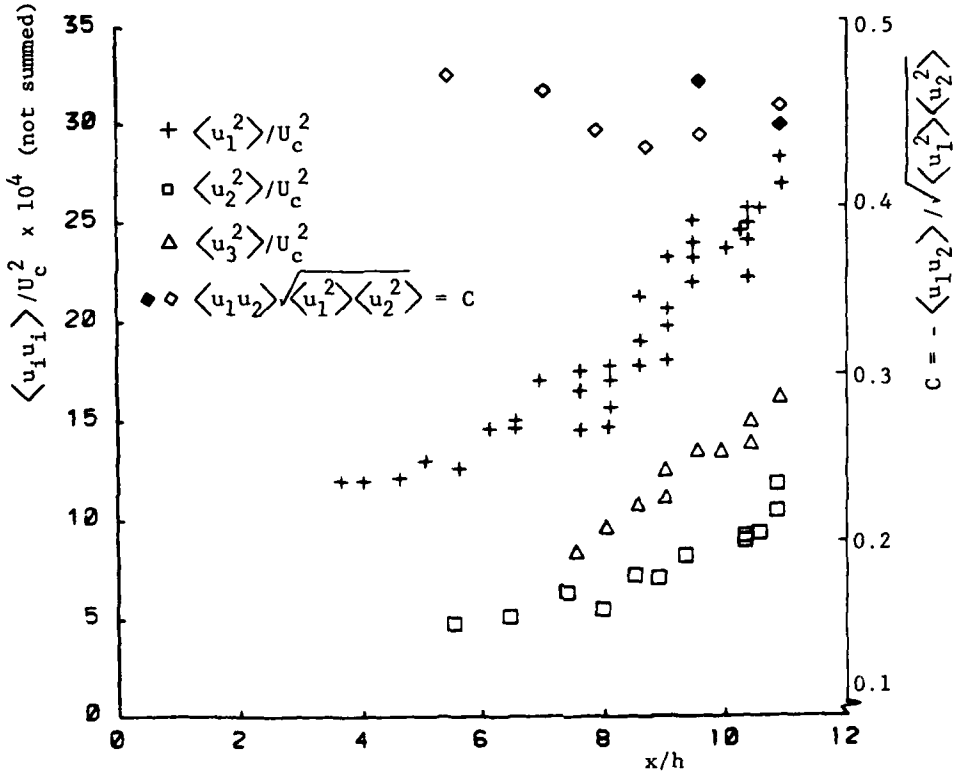

Figure 4.1 Downstream development of turbulent component energies and shear-stress correlation coefficient along tunnel centerline in a uniform shear (taken from Ref. 3)

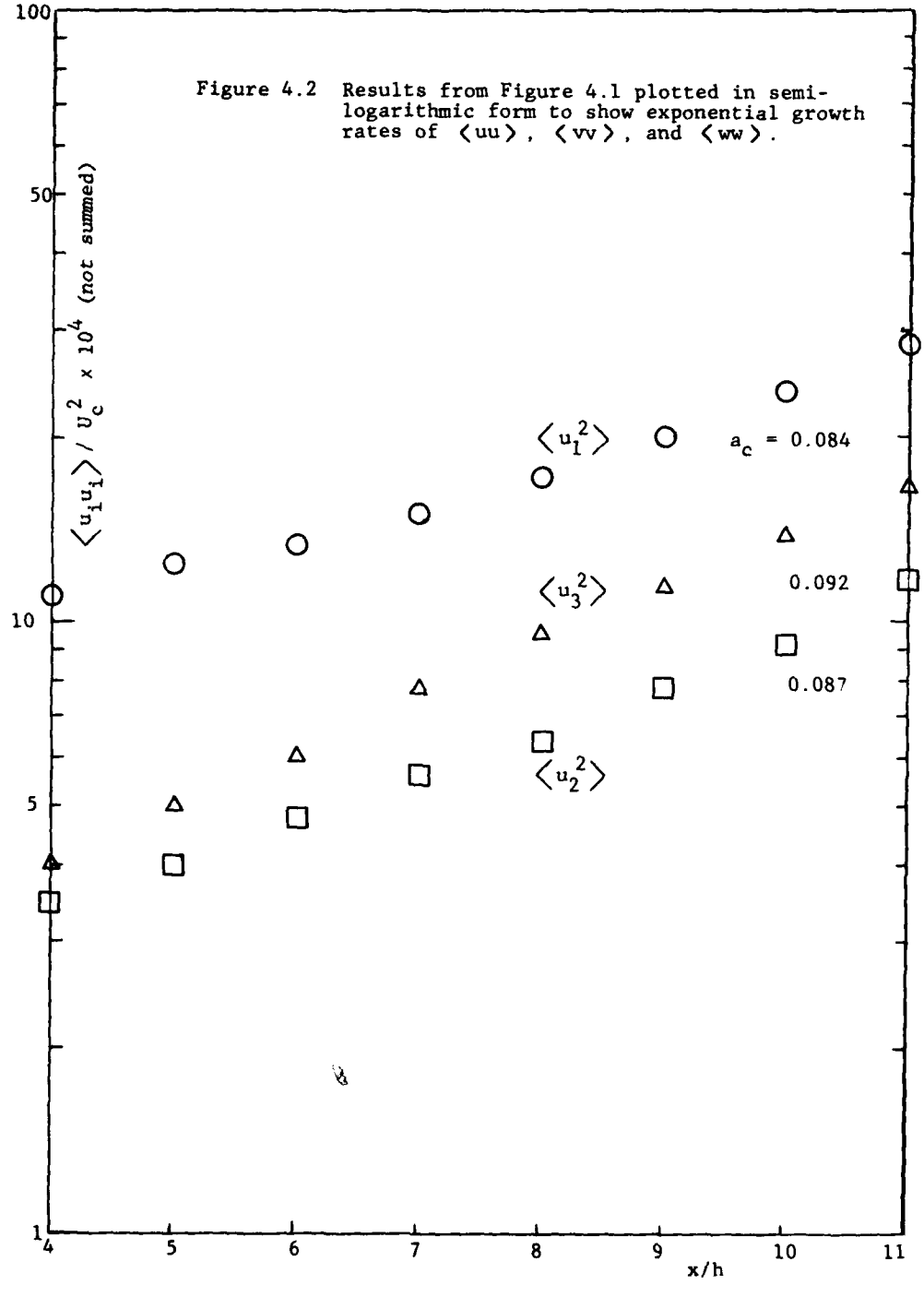

Figure 4.2 Results from Figure 4.1 plotted in semi-logarithmic form to show exponential growth rates of $\langle uu \rangle$, $\langle vv \rangle$, and $\langle ww \rangle$.

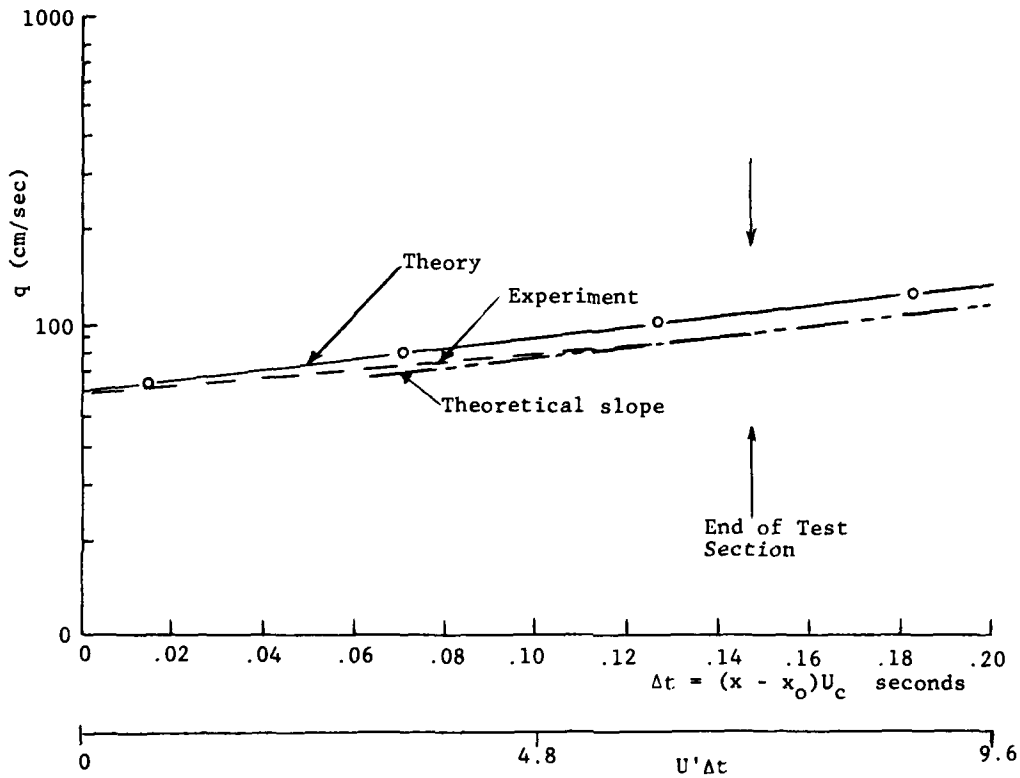

Figure 4.3 Computations of q compared with experimental results and the theoretical asymptotic slope for homogeneous shear flow.

"A THREE-DIMENSIONAL FINITE ELEMENT ALGORITHM FOR PREDICTION OF V/STOL JET-INDUCED FLOWFIELDS"

By

A. J. Baker
Professor of Engineering Science & Mechanics
University of Tennessee, Knoxville, TN 37916, USA

P. D. Manhardt and J. A. Orzechowski
Principal Consultants, Computational Mechanics Consultants, Inc.
3601A Chapman Hwy., Knoxville, TN 37920, USA

and K. T. Yen
Aerospace Engineer, U. S. Naval Air Development Center
Warminster, PA 18974, USA

SUMMARY

A three-dimensional mathematical model of the basic V/STOL jet, and the flow in the associated near-field, is constructed using a formal order-of-magnitude analysis. This produces a parabolized approximation to the steady, time-averaged, three-dimensional Navier-Stokes equations for a turbulent subsonic flow. A continuity-constraint finite element numerical solution algorithm is identified, which independently enforces ordered phenomena for solution of the equation system including transport equations for turbulence kinetic energy and dissipation parameters. The numerical solution of the established equation system yields prediction of core vortex roll-up, far-field deflection of the cross-flow, near-field entrainment of the cross-flow into the jet, and wake flow reversal with additional entrainment into the jet core. The primary causal mechanism is computationally assessed to be the turbulence interaction on the upstream face of the jet, as verified by results from a range of computational experiments. The results of these computational studies, and the associated algorithm procedures are summarized in this paper.

1. INTRODUCTION

The injection of a high-velocity jet of exhaust (or air), at essentially right angles to the aerodynamic surface and to the cross-flow induced by the aircraft forward flight, produces an extremely complicated three-dimensional flow-field which can significantly impact aerodynamic performance. The transverse jet is fundamental to many physical processes, including V/STOL aircraft, and has been the subject of wide-ranging experimentation and linearized theoretical analyses. The premier theoretical study was reported in the dissertation of Chang [1], who employed potential flow theory and bound vortex filament concepts to predict the shape of the separation boundary between a uniform onset flow perpendicular to a cylindrical jet. The basic concept of viscous-corrected potential flow theory has been extended and refined to a great extent, c.f., [2,3]. Jordinson [4] conducted pioneering experiments on a cold, circular V/STOL jet that confirmed the horse-shoe cross-section contours predicted by the potential flow models. However, his results also confirmed that the V/STOL jet entrained portions of the injection plane boundary layer into the wake region behind the jet. This is not characteristic of a jet issued from an isolated orifice [5], and is perhaps the consequential contributor to alterations of V/STOL aerodynamic characteristics.

The observations from Jordinson's data prompted considerable additional experimentation, c.f., [6-12]. McMahon and Mosher [8] obtained oil flow streaklines on the injection plate that graphically illustrated the pronounced difference between a circular V/STOL jet and the equivalent-diameter solid blockage. For the latter, the upstream and downstream center-line stagnation points are connected by an apparent inviscid flow streamline. The exterior flow is blockage deflected, while the flow interior to this streamline forms a closed recirculation zone. The streaklines for the V/STOL jet exhibited detailed and significant differences, except in the upstream stagnation region (indicating blockage-dominance). Past mid-jet, the V/STOL surface flow is directed almost radially inwards. Downstream of mid-jet, two streamlines are symmetrically oriented separating the complex wake interior flow from the deflected free-stream. The incoming streamlines, which divide the the flow region into entrained or deflected segments, intersect the downstream-dividing streamlines symmetrically, and a weak stagnation line appears to connect these two points. Figure 1, from [9], clearly delineates the near wake streakline pattern.

Pitot-static pressure measurement of the basic V/STOL jet three-dimensional flowfield has yielded mean flow characterization well downstream of the plane of injection, c.f., [10-12]. Figure 2 illustrates the essential geometry and coordinate system descriptions, and "far-field" is nominally the region $X_1/D \geq 5$, where D is the jet original diameter. Mosher [10] concludes, for an incompressible circular jet, that entrainment is the principle jet bending mechanism as the velocity ratio $\lambda = \rho_j U_j^2/\rho_\infty U_\infty^2$ increases. For the $\lambda = 8$ circular jet, Kamotani and Greber [11] determined the locus of planes with unit normal parallel to X_1. Resolution of the local velocity vector into scalar components in the local X_i coordinate system renders visible the jet cross-section shape and the transverse counter-rotating vortex. Figure 3, from [11] shows the symmetric half-plane distribution of axial velocity for the $\lambda = 8$ circular jet at stations $X_1/D = 7$ and $X_1/D = 23$, illustrating the hallmark "kidney" shape. Since the jet orifice is axisymmetric, a characteristic of the V/STOL jet in cross-flow appears as a preferential erosion of the potential core in the near wake region, producing an off-plane double maxima. Figure 3c) shows the transverse plane velocity vector distribution at $X_1/D = 23$; the vortex center is coincident with the extremum axial velocity, Figure 3b). Additional data [12] for the $\lambda = 8$ circular jet confirms the centered double-vortex structure as near to the plane of injection as $X_1/D = 5.2$.

These far-field data have been examined for similitude [12]; the definition of jet far-field centerline trajectory over a range of velocity ratios is well correlated.

The physical size of the pitot-static apparatus has generally precluded data acquisition closer to the injection plane than $X_1/D \approx 5$, although it has been attempted [13]. Additional experimental characterization of the basic V/STOL jet has thus been limited to measurement of pressure distributions on the plate forming the injection plane [10-12, 14-15]. Generally, the upstream pressure distribution appears analogous to potential flow about a solid cylinder, confirming the oil-flow streakline data. However, an extensive low pressure region, downstream and aft of mid-jet is a persistent characteristic of the flat-plate V/STOL jet, yielding a (the) significant aerodynamic influence, since in reality the injection plane is an aerodynamic surface. Alternative jet cross-sections and shapes modify the details of the associated pressure distribution [15], but do not alter the basic characterization.

A computational experiment [16], has assessed the key causal mechanism of the low pressure region. A porous aerodynamic contour was assumed to exist, surrounding the jet and separating the region of transverse flow affected primarily by blockage from that dominantly influenced by entrainment. Computational experiments were conducted to optimize agreement of computed surface pressure coefficient with experimental data on the airfoil image on the injection plate. The computational experiments confirmed that the large low pressure region was the direct consequence of the entrainment character of the V/STOL jet.

Fundamental insight into the dominant fluid dynamic mechanisms of the V/STOL jet in cross-flow can (only) be gained by advanced theoretical and computational (as a sub-classification of theoretical) analyses. The experimental data have provided a basic characterization. The farfield velocity measurements confirm the preferential wake erosion of the initially-circular jet cross-section, and the formation of a vortex pair. The axial velocity contours flatten broadside to the onset flow to produce a bluff rather than aerodynamic cross-section. The action of the jet is to induce entrainment of the injection surface boundary layer flow, producing a large region of low pressure downstream of mid-jet. However, while these data provide a rather substantial mean flow characterization of the basic jet, the dominant causal mechanisms remain little better defined than being an interaction between the jet and the cross-flow.

This paper summarizes a theoretical model of the basic turbulent V/STOL jet in cross-flow geometry. The resulting, highly non-linear system of three-dimensional partial differential equations, is amenable to numerical solution using present-day computer hardware/firmware systems. A finite element algorithm is utilized, which ensures consistent enforcement of the consequences of the mathematical assumptions and simplifications. Numerical results are presented, confirming the robustness of the developed analysis procedure in predicting each of the characterizations documented by the physical experiments for the basic V/STOL jet.

2. THOERETICAL MODEL

The V/STOL jet in cross-flow configuration is a completely three-dimensional, turbulent problem specification. No lower dimensional or non-turbulent analysis can yield a significant prediction of the complex associated flowfield interaction. Therefore, there are only two choices for governing differential equation systems: 1) the steady-flow three-dimensional parabolic Navier-Stokes equations, and 2) the steady or unsteady flow three-dimensional complete Navier-Stokes system. Solution of the complete Navier-Stokes system for a general turbulent aerodynamic flow, using adequate grid resolution, is beyond the capability of present-day computer hardware/firmware systems. However, the parabolic Navier-Stokes partial differential equation system, for nominally directed, turbulent three-dimensional aerodynamic flow, is solvable on current computer equipment. This equation set is derived as a simplification of the steady, three-dimensional time-averaged Navier-Stokes equations, which in Cartesian tensor notation $1 \le (i,j) \le 3$, and employing superscript tilde and bar to denote mass-weighted and conventional time-averaging, respectively [17], are

$$L(\bar{\rho}) = \frac{\partial}{\partial x_j}\left[\bar{\rho}\tilde{u}_j\right] = 0 \tag{1}$$

$$L(\bar{\rho}\tilde{u}_i) = \frac{\partial}{\partial x_j}\left[\bar{\rho}\tilde{u}_i\tilde{u}_j + \bar{p}\delta_{ij} + \bar{\rho}\widetilde{u_i''u_j''} - \bar{\sigma}_{ij}\right] = 0 \tag{2}$$

$$L(\bar{\rho}\tilde{H}) = \frac{\partial}{\partial x_j}\left[\bar{\rho}\tilde{H}\tilde{u}_j - \tilde{u}_i\bar{\sigma}_{ij} + \bar{\rho}\widetilde{H''u_j''} - \overline{u_i''\sigma_{ij}''} + \bar{q}_j\right] = 0 \tag{3}$$

$$L(\bar{\rho}k) = \frac{\partial}{\partial x_j}\left[\bar{\rho}\tilde{u}_j k + (C_k\frac{k}{\varepsilon}\bar{\rho}\overline{u_i''u_j''} - \bar{\mu}\delta_{ij})\frac{\partial k}{\partial x_i}\right] + \bar{\rho}\overline{u_i''u_j''}\frac{\partial\tilde{u}_i}{\partial x_j} + \bar{\rho}\varepsilon = 0 \tag{4}$$

$$L(\bar{\rho}\varepsilon) = \frac{\partial}{\partial x_j}\left[\bar{\rho}\tilde{u}_j\varepsilon + C_\varepsilon\frac{k}{\varepsilon}\bar{\rho}\overline{u_i''u_j''}\frac{\partial\varepsilon}{\partial x_j}\right] + C_\varepsilon^1\bar{\rho}\overline{u_i''u_j''}\frac{\varepsilon}{k}\frac{\partial\tilde{u}_i}{\partial x_j} + C_\varepsilon^2\bar{\rho}\frac{\varepsilon^2}{k} = 0 \tag{5}$$

In equation 1-5, $\bar{\rho}$ is density, $\tilde{u}_i$ is the mean velocity vector, $\bar{p}$ is pressure, δ_{ij} is the Kronecker delta, and $\tilde{H}$ is stagnation enthalpy. The Stokes stress tensor $\bar{\sigma}_{ij}$ and heat flux vector $\bar{q}_j$ are defined as

$$\bar{\sigma}_{ij} = \bar{\rho}\bar{\nu}(E_{ij} - \frac{2}{3}\delta_{ij}\tilde{E}_{kk})/Re \tag{6}$$

$$\bar{q}_i = \bar{\kappa}\frac{\partial H}{\partial x_j} \tag{7}$$

and $\overline{\rho u_i' u_j'}$ is the Reynolds stress tensor. The fluid kinematic viscosity and heat conductivity are $\bar{\nu}$ and $\bar{\kappa}$, and $\tilde{E}_{ij}$ is the mean flow strain rate tensor

$$\tilde{E}_{ij} \equiv \frac{\partial \tilde{u}_i}{\partial x_j} + \frac{\partial \tilde{u}_j}{\partial x_i} \tag{8}$$

Equations 4-5 are the transport equations for the turbulent kinetic energy and isotropic dissipation function, as obtained using the closure model of Launder, Reece and Rodi [18] for the pressure-strain and triple correlations. The various coefficients C_β^α are model constants, Hanjalic and Launder [19], and

$$k \equiv \tfrac{1}{2}\overline{u_i' u_i'} \tag{9}$$

$$\varepsilon \equiv \frac{2\bar{\nu}}{3}\overline{\left[\frac{\partial u_i'}{\partial x_j}\frac{\partial u_i'}{\partial x_k}\right]}\delta_{jk} \tag{10}$$

The parabolic Navier-Stokes equation set (3DPNS) is derived from equations 1-10 assuming the ratio of extremum mean cross-flow velocity component to axial (jet) component is a number less than unity, and further assuming that:

1. the velocity component of the jet, parallel to the jet path, suffers no reversal,
2. diffusive transport processes in the direction parallel to the jet path are higher-order, hence negligible, and
3. the overall elliptic character of the parent three-dimensional Navier-Stokes equations is enforcable through (iterative) construction of a suitable pressure field.

Viewing Figure 2, for the V/STOL jet, the x_1 (curvilinear) coordinate defines the jet path mean flow direction with scalar velocity component $\tilde{u}_1$ of order unity, i.e., $O(1)$. Hence, in terms of order of magnitude, $O(\tilde{u}_2) \equiv O(\delta) \equiv O(\tilde{u}_3)$ and $O(\delta) \leq O(1)$. Then, the continuity equation 1 ensures that the variation in $\tilde{u}_1$ on x_1 must be the order of transverse plane variations of $\tilde{u}_2$ and $\tilde{u}_3$; hence, for $\frac{\partial}{\partial x_1} \equiv O(1)$, $\frac{\partial}{\partial x_2} \approx O(\delta^{-1}) \approx \frac{\partial}{\partial x_3}$. The order of terms in the momentum equations 2 can then be determined. For the $\tilde{u}_1$ equation, since $O(\bar{\rho}\overline{u_i' u_j'})$ must be $O(\delta)$, the term $\frac{\partial}{\partial x_1}(\bar{\rho}\overline{u_1' u_1'})$ is higher order and discarded. The assumption that x_1-diffusion is negligible permits setting $\frac{\partial}{\partial x_1}(E_{11}) \equiv 0$, hence $O(Re) < O(\delta^{-1})$. Therefore, the terms in $\bar{\sigma}_{12}$ and $\bar{\sigma}_{13}$ involving $\tilde{u}_2$ and $\tilde{u}_3$, i.e., $\frac{\partial}{\partial x_2}\left(\frac{\partial \tilde{u}_2}{\partial x_1}\right)$ and $\frac{\partial}{\partial x_3}\left(\frac{\partial \tilde{u}_3}{\partial x_1}\right)$, are both $O(\delta)$ and negligible.

Deletion of these terms is the fundamental step in the parabolic approximation, since their elimination removes the elliptic boundary value character in the direction parallel to the jet path. The existence of $\frac{\partial}{\partial x_1}(\bar{\rho}\tilde{u}_i\tilde{u}_i)$, which is $O(1)$, instills the initial value form for the resultant equation, hence permits marching the solution for $\tilde{u}_1$ parallel to the jet path direction. Therefore, the 3DPNS form, denoted $L^P(\cdot)$, for the $\tilde{u}_1$ momentum equation, is

$$L^P(\bar{\rho}\tilde{u}_1) \equiv \frac{\partial}{\partial x_1}(\bar{\rho}\tilde{u}_1 u_1) + \frac{\partial \bar{p}}{\partial x_1} + \frac{\partial}{\partial x_2}\left[\bar{\rho}\overline{u_1' u_2'} - \bar{\sigma}_{12}\right] + \frac{\partial}{\partial x_3}\left[\bar{\rho}\overline{u_1' u_3'} - \bar{\sigma}_{13}\right] = 0 \tag{11}$$

In instances of interest to the V/STOL problem, x_1 corresponds to a curvilinear coordinate. Therefore, the derivatives expressed in equation 11 are the co-variant derivative, with the corresponding handling of unit vector variation. The 3DPNS form for the energy equations is constructed in the same manner, yielding

$$L^P(\bar{\rho}\tilde{H}) = \frac{\partial}{\partial x_1}(\bar{\rho}\tilde{u}_1\tilde{H}) + \frac{\partial}{\partial x_\ell}\left[\bar{\rho}\tilde{H}\tilde{u}_\ell - \tilde{u}_i\bar{\sigma}_{i\ell} + \overline{\rho H' u_\ell'} - \overline{u_i'\sigma_{i\ell}'} + \bar{q}_\ell\right] = 0 \tag{12}$$

Equation 12 introduces the 3DPNS limited index summation convention, $1 \leq (i,j) \leq 3$ and $2 \leq \ell \leq 3$.

For the ordering analysis applied to the $\tilde{u}_2$ and $\tilde{u}_3$ momentum equations 2, pressure variations in the transverse plane must balance the dominant order terms. Each transverse derivative of $\bar{\rho}\overline{u_2' u_j'}$ and $\bar{\rho}\overline{u_3' u_j'}$ is $O(1)$, while all other terms are $O(\delta)$ and higher. Hence, in the primitive form, equation 2 for $\tilde{u}_\ell$ is an initial-value description on transverse pressure gradient. The solution of these equations is made tractible by forming the divergence of $L(\bar{\rho}\tilde{u}_\ell)$. Retaining the $O(\delta)$ convection and $O(\delta^2)$ laminar diffusion terms for generality, the 3DPNS equivalent of the transverse momentumequations $L(\bar{\rho}\tilde{u}_\ell)$ is [20]

$$L^P(\bar{p}) = \frac{\partial^2 \bar{p}}{\partial x_\ell^2} + \frac{\partial^2}{\partial x_j \partial x_\ell}\left[\bar{\rho}\tilde{u}_\ell\tilde{u}_j + \bar{\rho}\overline{u_\ell' u_j'} - \bar{\sigma}_{\ell j}\right] = 0 \tag{13}$$

Equation 13 defines an elliptic boundary value problem for determination of pressure distribution in the transverse plane. The pressure field that satisfies this Poisson equation consists of complementary and particular solutions.

$$\bar{p}(x_i) = p_c(x_i) + p_p(x_i) \tag{14}$$

The complementary solution is assumed to satisfy the $O(\delta)$ inviscid flow phenomena,

$$L(p_c) = \frac{\partial^2 p_c}{\partial x_\ell^2} + \frac{\partial^2(\bar{\rho}\tilde{u}_\ell\tilde{u}_j)}{\partial x_j \partial x_\ell} = 0 \tag{15}$$

subject to the Dirichlet boundary conditions known for $p(x_1,x_\ell)$. Elsewhere, an appropriate boundary condition for p_C is homogeneous Neumann. The particular pressure p_p satisfies equation 13, less the convection term,

$$L(p_p) = \frac{\partial^2 p_p}{\partial x_\ell^2} + \frac{\partial^2}{\partial x_j \partial x_\ell}\left[\bar{\rho}\,\overline{u_\ell' u_j'} - \bar{\sigma}_{\ell j}\right] = 0 \tag{16}$$

subject to homogeneous Dirichlet boundary conditions on boundary segments where p_C is known.

The critical aspect affecting application of the 3DPNS equation set, to analysis of the V/STOL jet, is knowledge of the boundary values for $\bar{p}(x_1,x_\ell)$, as required via assumption 3 of the 3DPNS argument. Viewing Figure 2 the V/STOL jet is a fully three-dimensional problem with elliptic coupling throughout in its entirety. However, if the "computational box" surrounding the jet and the near field flow is sufficiently large in lateral (X,Y) extent, it is fair to assume that a potential flow pressure exists on segments of the box boundaries. Therefore, the validity of the 3DPNS analysis is expected to be limited to a region "close" to the injection plate surface, eg., $0 < x_1/D < 4$, provided the lateral boundaries are sufficiently remote. For the reported analyses, the boundaries of the 3DPNS simulation were placed at $|x_\ell|/D \approx 3$. The associated complementary pressure boundary condition $\bar{p}$, on the upstream and lateral side boundaries, were set by the farfield potential solution for flow about a cylinder. The complementary pressure $\bar{p}_C$ at the downstream transverse outflow boundary was determined using Bernoulli's equation, which admitted reversal of the transverse flow and was compatible with the lateral farfield potential solution.

A closure model for the kinematic Reynolds stress $\overline{u_i' u_j'}$ appearing in equations 2-5 is required to complete the 3DPNS order analysis. For a stress-strain rate constitutive equation [21], the lead terms of the kinematic form have been determined [20,22] as

$$-\overline{u_i' u_j'} = -k\alpha_{ij} + C_4\frac{k^2}{\varepsilon}\tilde{E}_{ij} + C_2 C_4 \frac{k^2}{\varepsilon^2}\tilde{E}_{ik}\tilde{E}_{kj} + \ldots \tag{17}$$

$\tilde{E}_{ij}$ remains the symmetric mean flow strain-rate tensor, equation 8, and α_{ij} is a diagonal tensor in principal coordinates.

$$\alpha_{ij} \equiv \frac{1}{3k}(\overline{u_k' u_k'})a_{\underline{i}}\delta_{ij} \tag{18}$$

The $a_{\underline{i}}$ are coefficients admitting anisotropy, where $a_1 \equiv C_1$, and $a_2 \equiv C_3 \equiv a_3$, and the C_α are defined by Launder et. al. [18]. In rectangular Cartesian coordinate coordinates, the expansion and ordering of equation 17 yields

$$\begin{aligned}
-\overline{u_1' u_1'} &= C_1 k - C_2 C_4 \frac{k^3}{\varepsilon^2}\left[\left(\frac{\partial \tilde{u}_1}{\partial x_2}\right)^2 + \left(\frac{\partial \tilde{u}_1}{\partial x_3}\right)^2\right] - 2C_4\frac{k^2}{\varepsilon}\left[\frac{\partial \tilde{u}_1}{\partial x_1}\right] \\
-\overline{u_2' u_2'} &= C_3 k - C_2 C_4 \frac{k^3}{\varepsilon^2}\left[\frac{\partial \tilde{u}_1}{\partial x_2}\right]^2 - 2C_4\frac{k^2}{\varepsilon}\left[\frac{\partial \tilde{u}_2}{\partial x_2}\right] \\
-\overline{u_3' u_3'} &= C_3 k - C_2 C_4 \frac{k^3}{\varepsilon^2}\left[\frac{\partial \tilde{u}_1}{\partial x_3}\right]^2 - 2C_4\frac{k^2}{\varepsilon}\left[\frac{\partial \tilde{u}_3}{\partial x_3}\right] \\
-\overline{u_1' u_2'} &= -C_4\frac{k^2}{\varepsilon}\left[\frac{\partial \tilde{u}_1}{\partial x_2}\right] - C_2 C_4 \frac{k^3}{\varepsilon^2}\left[\frac{\partial \tilde{u}_1}{\partial x_3}\left(\frac{\partial \tilde{u}_2}{\partial x_3} + \frac{\partial \tilde{u}_3}{\partial x_2}\right)\right. \\
&\qquad \left. + 2\frac{\partial \tilde{u}_1}{\partial x_2}\left(\frac{\partial \tilde{u}_1}{\partial x_1} + \frac{\partial \tilde{u}_2}{\partial x_2}\right)\right] \\
-\overline{u_1' u_3'} &= -C_4\frac{k^2}{\varepsilon}\left[\frac{\partial \tilde{u}_1}{\partial x_1}\right] - C_2 C_4 \frac{k^3}{\varepsilon^2}\left[\frac{\partial \tilde{u}_1}{\partial x_2}\left(\frac{\partial \tilde{u}_2}{\partial x_3} + \frac{\partial u_3}{\partial x_2}\right)\right. \\
&\qquad \left. + 2\frac{\partial \tilde{u}_1}{\partial x_3}\left(\frac{\partial \tilde{u}_1}{\partial x_1} + \frac{\partial \tilde{u}_3}{\partial x_3}\right)\right] \\
-\overline{u_2' u_3'} &= -C_2 C_4 \frac{k^3}{\varepsilon^2}\left[\frac{\partial \tilde{u}_1}{\partial x_2}\frac{\partial \tilde{u}_1}{\partial x_1}\right] - C_4\frac{k^2}{\varepsilon}\left[\frac{\partial \tilde{u}_2}{\partial x_3} + \frac{\partial \tilde{u}_3}{\partial x_2}\right]
\end{aligned} \tag{19}$$

Thereupon, recalling the index convection, $1 \le i \le 3$ and $2 \le j < 3$ the 3DPNS forms for equations 4-5 are

AD-A113 907 ADVISORY GROUP FOR AEROSPACE RESEARCH AND DEVELOPMENT--ETC F/G 20/4
FLUID DYNAMICS OF JETS WITH APPLICATIONS TO V/STOL.(U)
JAN 82
UNCLASSIFIED AGARD-CP-308 NL

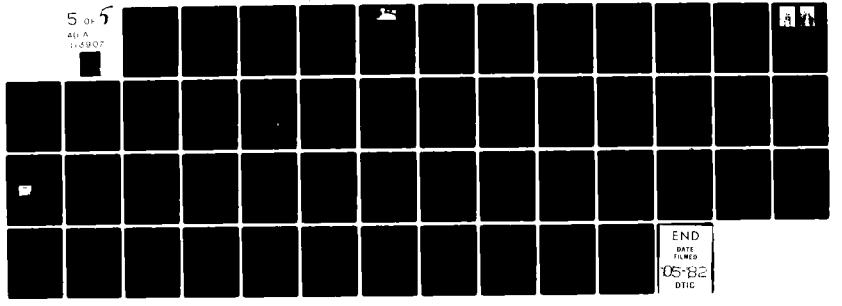

$$L^P(k) = \frac{\partial}{\partial x_i}(\bar{\rho}\tilde{u}_i k) + \frac{\partial}{\partial x_i}\left[\bar{\rho}(C_k \frac{k}{\varepsilon}\overline{u_i'u_\ell'} - \bar{\nu}\delta_{i\ell})\frac{\partial k}{\partial x_\ell}\right] + \bar{\rho}\,\overline{u_i'u_\ell'}\frac{\partial \tilde{u}_i}{\partial x_\ell} + \bar{\rho}\varepsilon = 0 \qquad (20)$$

$$L^P(\varepsilon) = \frac{\partial}{\partial x_i}(\rho\tilde{u}_i\varepsilon) + \frac{\partial}{\partial x_i}\left[C_\varepsilon \frac{k}{\varepsilon}\overline{u_i'u_\ell'}\frac{\partial \varepsilon}{\partial x_\ell}\right] + C_\varepsilon^1\,\overline{\rho u_i'u_\ell'}\frac{\varepsilon}{k}\frac{\partial \tilde{u}_i}{\partial x_\ell} + C_\varepsilon^2\frac{\varepsilon^2}{k} = 0 \qquad (21)$$

Upon assessment, the established 3DPNS equation set 11-21 numbers one less than the number of dependent variables defined. Therefore, equations governing higher order phenomena must be included in the system. Since the 3DPNS momentum equation 11 is written on u_1 only, both components of $\tilde{u}_\ell \equiv \{\tilde{u}_2, \tilde{u}_3\}$ are required determined subject to the constraint of equation 1. The finite element algorithm accomplishes this by enforcing a measure of the continuity equation (error) on the solution of the $O(\delta)$ 3DPNS approximation to the momentum equations 2 written on $\tilde{u}_\ell$. Retaining the first two orders of terms, the 3DPNS transverse momentum equations are

$$L^P(\rho\tilde{u}_\ell) = \frac{\partial}{\partial x_1}\left[\rho\tilde{u}_1\tilde{u}_\ell + \overline{\rho u_1'u_\ell'}\right] + \frac{\partial}{\partial x_k}\left[\bar{\rho}\tilde{u}_\ell\tilde{u}_k + \overline{\rho u_\ell'u_k'} + \bar{p}\delta_{k\ell} - \bar{\sigma}_{k\ell}\right] = 0 \qquad (22)$$

Equation 22 is of the form of equation 11 and employs the additional limited index $2 \le k \le 3$. The middle two terms in the second bracket are $O(1)$, while the remaining terms are all $O(\delta)$ or smaller.

3. FINITE ELEMENT SOLUTION ALGORITHM

The theoretical model of the flowfield description of the turbulent V/STOL jet in a cross-flow has been constructed as the 3DPNS equation system 11-22. The members of this set whose solutions are marched parallel to the jet path (x_1, Figure 2) include equations 11, 12, 20-22. The remainder are constitutive or elliptic equations, which are solved at each transverse plane and contain parametric dependence on x_1. The general form for the space-marched system is

$$L^P(q_j) = \frac{\partial}{\partial x_1}(\bar{\rho}\tilde{u}_1 q_j) + \frac{\partial}{\partial x_\ell}\left[\rho\tilde{u}_\ell q_j + f_{\ell j}\right] + s_j = 0 \qquad (23)$$

where $f_{\ell j}$ and s_j are specified non-linear functions of their arguments (on index j). The solution domain Ω for equation 23 is the product of R^2 and x_1, for all elements of $x_1 \ge x_1^0$, and for R^2 spanned by the $x_\ell = \{x_2, x_3\}$ coordinate system, Figure 2. The generalized differential boundary condition on $\partial\Omega = \partial R \times x_1$ is

$$\ell(q_j) = a_1 q_j + a_2 \frac{\partial}{\partial x_i} q_j \hat{n}_i + a_3 = 0 \qquad (24)$$

where the a_i are specified coefficients and $\hat{n}_i$ is the outwards pointing unit normal vector. The initial distribution for q_j on $\Omega_0 \equiv R^2 \times x_1^0$ is

$$q_j(x_\ell, x_1) \equiv q_j^0(x_\ell) \qquad (25)$$

The finite element numerical solution algorithm defines the approximation $q_j^h(x_\ell, x_1)$ to the (unknown) exact solution $q_j(x_\ell, x_1)$ to equations 23-25 as

$$q_j(x_\ell, x_1) \approx q_j^h(x_\ell, x_1) \equiv \sum_{e=1}^{M} q_j^e(x_\ell, x_1) \qquad (26)$$

where the summation $1 \le e \le M$ is over the finite element domains R_e^2 forming the (spatial) discretization of R^2. The elemental approximation is

$$q_j^e(x_\ell, x_1) \equiv \{N_k(x_\ell)\}^T \{QJ(x_1)\}_e \qquad (27)$$

where j(J) is a free index denoting members of the column matrix $\{q^h\}$, and sub- or superscript e denotes pertaining to the $e^{\underline{th}}$ finite element. The elements of the row matrix $\{N_k(x_\ell)\}^T$ are the $k^{\underline{th}}$ degree cardinal basis polynomials written on x_ℓ, $2 \le \ell \le 3$.

The functional requirement of any numerical algorithm is to minimize the error in q_j^h in some norm. This is accomplished using finite element theory by requiring: 1) the gen-

erated errors $L^p(q_j^h)$ and $\ell(q_j^h)$ to be orthogonal to the function space employed to define q_j^h, and, 2) the error in the discrete approximation $L^p(\tilde{\rho}^n)$ to satisfaction of continuity, equation 1, be enforced as a differential constraint. These conditions are combined [20], using a multiplier set $\vec{\beta}$, to form the theoretical statement of the finite element algorithm as

$$\int_{R^2}\{N_k\}L^p(q_j^h)d\vec{x}+\beta_1\int_{\partial R}\{N_k\}\ell(q_j^h)d\vec{x}+\vec{\beta}_2\cdot\int_{R^2}\nabla\{N_k\}L^p(\tilde{\rho}^h)d\vec{x} \equiv \{0\} \tag{28}$$

Equation 28 defines a system of ordinary differential equations written on the coordinate x_1, parallel to the jet path, Figure 2, in the form

$$[C]\{QJ\}' + [U]\{QJ\} + [FLJ]\{QL\} + \{SJ\} = \{0\} \tag{29}$$

Using the trapezoidal integration rule, and substituting equation (29) yields,

$$\{FJ\} \equiv \{QJ\}_{j+1} - \{QJ\}_j - \frac{\Delta x_1}{2}[\{QJ\}'_{j+1} + \{QJ\}'_j] \equiv \{0\} \tag{30}$$

which defines a system of non-linear algebraic equations for determination of the elements of $\{QJ(x_1)\}$. The Newton iteration algorithm for equation 30 is

$$[J(FJ)]^p_{j+1}\{\delta QJ\}^{p+1}_{j+1} = -\{FJ\}^p_{j+1} \tag{31}$$

written on the iteration vector $\{\delta QJ\}$, where

$$\{QJ\}^{p+1}_{j+1} \equiv \{QJ\}^p_{j+1} + \{\delta QJ\}^{p+1}_{j+1} \tag{32}$$

For the elements $\{\tilde{u}_2,\tilde{u}_3\}$ of q_j^h in equation 28, $\vec{\beta}_2 \equiv \Delta x_1(\hat{j} + \hat{k})$, and a measure of the continuity equation (solution) becomes applied as the differential constraint. This measure, that spans R^2 and vanishes as continuity becomes satisfied, is the harmonic solution $\phi(x_\ell)$ to the Poisson equation

$$L^p(\phi) \equiv \frac{\partial^2\phi}{\partial x_\ell^2} - \frac{\partial}{\partial x_i}(\tilde{\rho}\tilde{u}_i) \equiv 0 \tag{33}$$

The boundary conditions for ϕ are homogeneous Dirichlet everywhere at farfield. Equation 33 becomes homogeneous as the error in the continuity equation 1 becomes negligibly small, and ϕ becomes null as a consequence of the boundary condition specifications. A detailed discussion of the algorithmic embodiment of the differential constraint concept is given by Baker [23].

4. RESULTS AND DISCUSSION

The principal requirements of the 3DPNS theoretical (and computational) model of the V/STOL jet is to assess fluid dynamic factors dominating formation of the counter-rotating axial vortex pair and entrainment of the cross-flow into the jet. For the reported results, the 3DPNS solution domain R^2 was defined as the symmetric half-plane, with the circular jet located mid-domain, Figure 4a). For reference, Figure 4b) graphs the transverse plane potential velocity vector distribution used to initialize $\tilde{u}_\ell(x_1^0,x_\ell)$ at the nodes of $\Omega(0)$. The tail of each vector is at a node, and the non-uniform discretization is constituted of $M = 576$ triangular finite element domians R^2_e spanned by the linear basis $\{N_1(x_\ell)\}$. The computation simulation requires solution of a non-linear system of ordinary differential equations. Hence, the members $\tilde{u}_1$, $\tilde{u}_\ell$, $\tilde{H}$, k and ε, must be initialized at the nodes of $\Omega(0)$. Secondly, since the finite element algorithm statement has transformed the elliptic boundary value character of the 3DPNS equations, boundary conditions on all members of $\{QJ(x_1)\}$ are required specified everywhere on $\partial\Omega = \partial R^2 \times x_1$. Basically, see Figure 4a), line AB is a symmetry plane, CDA is the farfield potential boundary, and BC is inflow/outflow with vanishing normal derivatives.

The specification of suitable initial-conditions $\{QJ(0)\}$ is in itself a problem, since little data are available for guidance. For the present simulation, the initial jet was assumed to be of circular cross-section, with constant axial velocity (distribution) $\tilde{u}_1(x_1^0) \equiv U_j$. The initial $\tilde{u}_1$ distribution exterior to the initial jet cross-section was assumed constant, at a level smaller than the initial jet velocity U_j. This constant is required non-zero, to prevent the 3DPNS equation set from becoming singular, dependent upon the imposed cross-flow velocity level U_∞ (cf., the order of magnitude analysis). Both the jet and cross-flow were assumed constant density and isoenergetic. Hence, $\tilde{H}(x_1) =$ constant, and the V/STOL jet velocity ratio is thereby $\lambda = U_j/U_\infty$. With non-zero cross-flow, and following considerable numerical experimentation, the cylinder potential flow

field shown in Figure 4b) defines $\tilde{u}_\ell(0)$ outside the initial jet, and inside the initial jet $\tilde{u}_\ell(0) \equiv 0$. Thus, Bernoulli's equation yields the corresponding initial distribution of p_c on $\Omega(0)$.

Defining suitable initial distributions for turbulent kinetic energy and dissipation function is even more perplexing, since the interaction on the upstream face of the jet is extremely complicated. In the total absence of data, a step distribution in turbulence levels was assumed appropriate. The initial level of turbulent kinetic energy k was assumed a distinct constant inside and outside the jet over $\Omega(0)$. The initial dissipation was also specified unique constants, to produce desired levels of turbulent kinematic viscosity ($\nu^t \equiv C_\mu k^2/\varepsilon$) inside and outside the jet, eg., $\nu_j^t \neq \nu_\infty^t$, within the constraint $1 < \nu_j^t/\nu_\infty^t < 10^2$. For $\nu_\infty^t \approx 10^2$, suitable levels were determined as $k(0) = 0.0005$ and $\varepsilon(0) = 0.0012$ inside the jet.

Several validation test cases were executed for zero crossflow, $U_\infty \equiv 0$, to firmly quantify algorithm performance with regards to symmetries and robust conservation of mass. The latter is particularly critical, since the sole mechanism for generation of $u_\ell \neq 0$ is through continuity, which is employed only as the differential constraint on equation 22, that otherwise exhibits a null solution. The results of these tests are reported in [24] and strongly confirmed algorithm viability.

The principal subject is analysis of a circular cross-section, subsonic V/STOL jet, issued perpendicular to a flat plate into a subsonic crossflow at velocity ratio $\lambda = U_j/U_\infty = 10$. The results of the validation test cases, and additional numerical experiments, provided the initialization procedure. The initial plateau distributions of axial velocity $\tilde{u}_1(0)$ inside and outside the initial jet, and the reference crossflow velocity were set at $U_j : U_j : U_\infty = 1.0/0.2/0.1$, with $U_j = 36.6$ m/s (120f/s). The initial distribution for transverse velocity $\tilde{u}_\ell(0)$ is potential flow about a cylinder, Figure 4b). The initial levels for turbulence kinetic energy $k(0) \geq 0.0005$ and dissipation $\varepsilon(0) \geq 0.0012$ were set at distinct constants, inside/outside the initial jet, to produce the desired initial levels of $1 < \nu^t < 100$. The reference Reynolds number based on jet orifice diameter was $Re = 0.6 \times 10^6$.

Figure 5 summarizes the 3DPNS algorithm solution in terms of the computed evolution of the transverse velocity field on $0 < x_1/D \leq 1.25$, for the initially-circular, turbulent V/STOL jet in cross-flow, $U_j : U_j : U_\infty = 1.0/0.2/0.1$. The non-dimensional (on U_j) extremum tranverse scalar component, upon which each figure is scaled, is noted in each legend as $\tilde{u}_\ell^m$. Figure 4b) is the initial condition, and $\tilde{u}_\ell^m = 0.174$. The blockage effect of the jet becomes almost immediately evident, Figure 5a), as is the beginning of entrainment in the lateral (top) farfield. The transverse velocity field begins to penetrate the downstream interface of the jet by $x_1/D = 0.5$, Figure 5b), and a decrease in the outflow in the wake region is evident. This becomes considerably pronounced by $x_1/D = 0.75$, Figure 5c), where wake flow reversal has begun. The entrainment from the lateral farfield has also become stronger with penetration on the lee side of the jet. The vortex structure interior to the initial jet becomes fully developed by $x_1/D = 1.0$, Figure 5d). The combined actions of blockage, entrainment, wake flow reversal and axial vortex are each matured and clearly evident in the solution at $x_1/D = 1.25$, Figure 5e).

The results of Figure 5 indicate the 3DPNS analysis procedure exhibits potential for prediction of the near-field essential characteristic action of the elementary V/STOL jet in cross-flow. In particular, the region of reversed flow and angle of the wake streamline, Figure 5e), are in qualitative agreement with the oilflow streakline experimental results, Figure 1. The generation of the axial vortex (pair) is in qualitative agreement with farfield data, Figure 3. The jet boundary is not impervious to the cross-flow, and the intrusion of entrainment is predicted on the downstream face of the jet. These results are certainly influenced by the many decisions and compromise required to complete the mathematical specification, in particular the initial conditions and size and refinement of the computational solution domain. However, the impetus to attack these detailed aspects is hopefully enhanced by these encouraging results.

Additional computational experiments were conducted to quantize the influence of gross turbulence factor modifications. Figure 6 summarizes the results for the circular V/STOL jet specification. Figures 6a)-b) show the transverse velocity field $\tilde{u}_\ell$ on $0.5 \leq x_1/D \leq 1.0$, is computed holding $\nu^t \equiv 10$ a constant throughout the entire solution domain. Some farfield entrainment action occurs, but the nearfield crossflow appears almost negligibly deflected. Figure 6c) shows the comparison solution at $x_1/D = 0.5$, for the constant ν^t but with $\nu_j^t \equiv 100$. The jet is considerably more impervious to the crossflow. In comparison to Figure 5b), a somewhat greater deflection of the upstream farfield has occured, and downstream penetration is essentially absent. For the complete 3DPNS simulation, Figure 5, the extremum $\nu^t \approx 160$ was computed on the jet upstream boundary at $x_1/D = 0.5$. Clearly, the turbulence phenomena exerts a predominant influence on the predicted results.

5. SUMMARY AND CONCLUSIONS

A mathematical model has been constructed for analysis of the near-field evolution of the V/STOL jet in subsonic crossflow. The results of the computational simulations of a circular V/STOL jet have yielded results of technical interest and anticipated merit. Without initial-condition generated bias, and using the most elementary solution starting conditions, the 3DPNS solution predicted the essential evolution character in substantial completeness. In particular, the simulation predicted lateral entrainment, axial vortex-pair initiation and inducement of the wake flow into the jet region, antiparallel to the initialized potential crossflow direction. These experimental documented features of the V/STOL jet were generally lost when the turbulence field was artificially constrained, indicating that the characteristic action is a turbulence-dominated effect.

It should be emphasized as well that none of the flow characteristics were consequentially captured without robust enforcement of the (non-parabolic) continuity equation. The developed constraint algorithm met the detailed mathematical requirements and accurately enforced solution aspects related to the 3DPNS ordering analysis. In particular, the finite element based algorithm maintained the (energy norm) error in exact satisfaction of continuity at $E(\phi,\phi) \leq 6. \times 10^{-5}$ for algorithm convergence set at $\epsilon = 10^{-4}$. The 3DPNS algorithm averaged four iterations per step for convergence, following a few extra iterations to homogenize the initial condition specifications. The solution on $0 \leq x_1/D \leq 1.25$ required less than 10 CPU minutes to execute, on a CDC CYBER/203 computer, using 200K single precision words of central memory.

6. ACKNOWLEDGMENTS

This work was principally supported under U.S. Navy contracts N62269-77-C-0491 and N62269-79-C-0295, to Computational Mechanics Consultants, Inc., and administered through the Naval Air Development Center, Warminster, PA. Modest additional support was provided under the U.S. Navy contract N62269-80-M-3026 to University of Tennessee.

7. REFERENCES

1. Chang, H. C., "The Roll-Up Of A Cylindrical Jet In A Cross-Flow," United States Air Force Technical Report ARL 73-0131, 1973.

2. Wooler, P. T., "Development Of An Analytical Model For The Flow Of A Jet Into A Subsonic Cross-Wind," NASA SP-218, 1968, p. 101-118.

3. Schmidt, H., "Deflection Of A Round Turbulent Jet In A Cross-Wind," Arch Mech., Vo' 26, Pt. 5, 1974, p. 849-859.

4. Jordinson, R., "Flow In A Jet Directed Normal To The Wind," ARC Report And Memoranda No. 3074, 1956.

5. Moussa, A. F., Trischka, J. W. and Eskinazi, F., "The Near Field In The Mixing Of A Round Jet With A Cross-Stream," J. Flu. Mech., Vol. 80, Pt. 1, 1977, p. 49-80.

6. Vogler, R. D., "Surface Pressure Distributions Induced On A Flat Plate By A Cold Air Jet Issuing Perpendicularly From The Plate And Normal To A Low-Speed Free Stream Flow," NASA TN D-1629, 1963.

7. Bradbury, L. J. S. and Wood, M. N., "The Static Pressure Distribution Around A Circular Jet Exhausting Normally From A Plane Wall Into An Airstream," C. P. No. 822, 1965, British Aero. Res. Council.

8. McMahon, H. M. and Mosher, D. K., "Experimental Investigation Of Pressures Induced On A Flate Plate By A Jet Issuing Into A Subsonic Crosswind," NASA SP-218, 1968, p. 49-62.

9. Margason, R. J. and Fearn, R., "Jet-Wake Characteristics And Their Induced Aerodynamic Effects On V/STOL Aircraft In Transition Flight," NASA SP-218, 1968, p. 1-18.

10. Mosher, D. K., "An Experimental Invistigation Of A Turbulent Jet In A Cross-Flow," Aerospace Engineering Report No. 70-7, Georgia Institute Of Technology, 1970.

11. Kamotani, Y. and Greber, I., "Experiments On A Turbulent Jet In A Cross-Flow," AIAA J., Vol. 10, No. 11, 1972, P 1425-29.

12. Fearn, R. and Weston, R. P., "Vorticity Associated With A Jet In A Cross-Flow," AIAA J., Vol. 12, No. 12, 1974, p. 1666-1671.

13. Fearn, R. L. and Benson, J. P., "Velocity Field Near The Jet Orifice Of A Round Jet In A Cross-Flow," NASA Report CR-152353, 1979.

14. Fearn, R. L. and Weston, R. P., "Induced Pressure Distributions Of A Jet In A Cross-Flow," NASA TN-D-7916, 1976.

15. Thames, F. C. and Weston, R. P., "Proper es Of Aspect-Ratio 4.0 Rectangular Jets In A Subsonic Cross-Flow," AIAA Paper No. 78-1508, 1978.

16. Baker, A. J., Manhardt, P. D., and Yen, K. T., "A Numerical Interaction Algorithm For Prediction of V/STOL Jet-Induced Flowfields," Proceedings, V/STOL Aircraft Aerodynamics, Vol. 1, 1979, pp. 204-227.

17. Cebeci, T. and Smith, A. M. O, Analysis Of Turbulent Boundary Layers, Academic Press, New York, 1974.

18. Launder, B. E., Reece, G. J. and Rodi, W., "Progress In The Development Of A Reynolds-Stress Turbulence Closure," J. Flu. Mech., V. 68, Pt. 3, 1975, pp. 537-566.

19. Hanjalic, K. and Launder. B. E., "A Reynolds Stress Model Of Turbulence And Its Application To Thin Shear Flows," J. Flu. Mech., V. 52, Pt. 4, 1972, pp. 609-638.

20. Baker, A. J. and Orzechowski, J. A., "A Continuity Constraint Finite Element Algorithm For Three-Dimensional Parabolic Flow Prediction," ASME Winter Annual Meeting, Nov. 1981.

21. Lumley, J. L., "Toward A Turbulent Constitutive Relation," J. Fluid Mech., V. 41, Pt. 2, 1970, pp. 413-434.

22. Baker, A. J., Yu, J. C., Orzechowski, J. A., and Gatski, T. B., "Prediction And Measurement Of Turbulent Aerodynamic Trailing Edge Flows," Technical Paper AIAA-80-1395, 1980, to appear in AIAA Journal, 1981.

23. Baker, A. J., "Research On Numerical Algorithms For Three-Dimensional Navier-Stokes Equations, II. Dissipative Finite Element," U. S. Air Force Technical Report AFWAL-TR-80-3157, 1981.

24. Baker, A. J., Orzechowski, J. A. and Manhardt, P. D., "A Numerical Three-Dimensional Turbulent Simulation Of A Subsonic V/STOL Jet In Cross-Flow Using A Finite Element Algorithm," U.S. Navy Report NADC-79021-60, 1981.

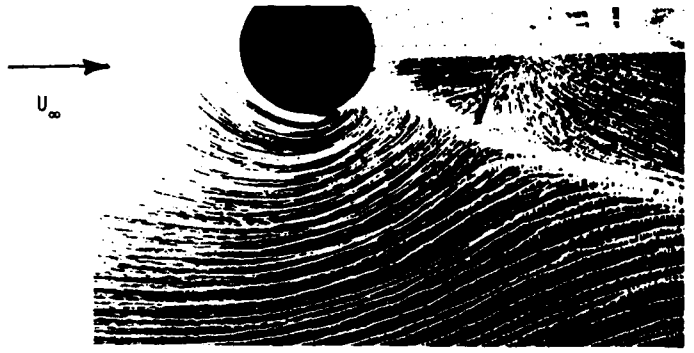

Figure 1 Oil Flow Streaklines For A Circular V/STOL Jet, From Margason And Fearn [9].

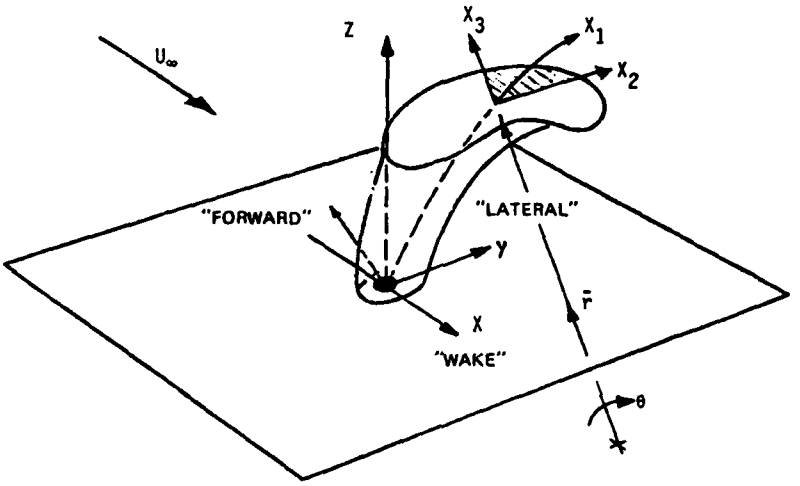

Figure 2 Coordinate Description For V/STOL Jet In A Cross-Flow.

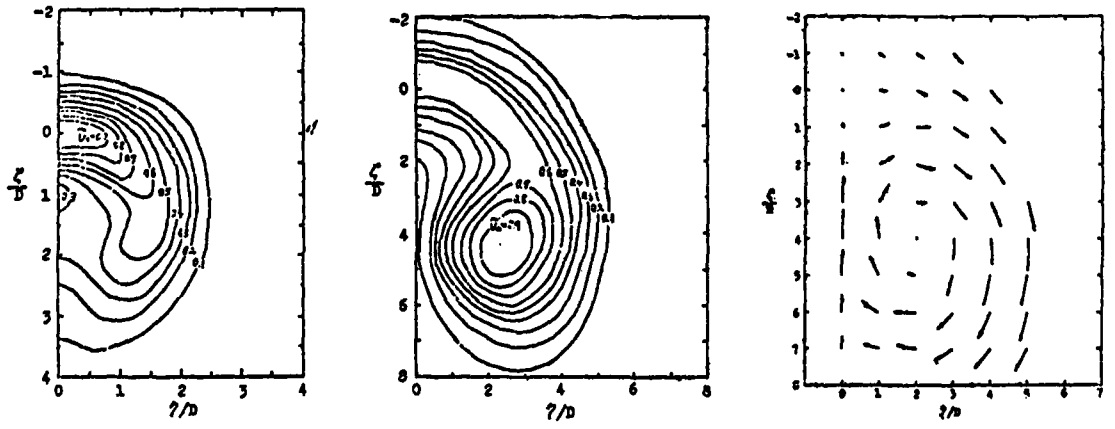

a) Axial Isovels, $x_1/D = 7.0$

b) Axial Isovels, $x_1/D = 23$

c) Transverse Plane Velocity Distribution, $x_1/D = 23$

Figure 3 Experimental Velocity Distributions, Circular Cross-Section Jet, $\lambda = 8$, From Kamotani and Greber [11].

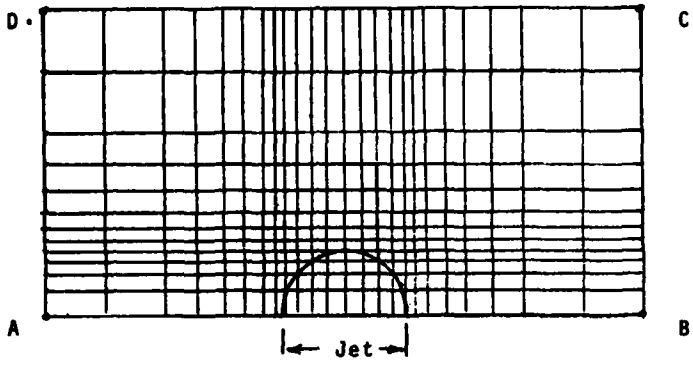

a) Transverse Solution Domain Discretization

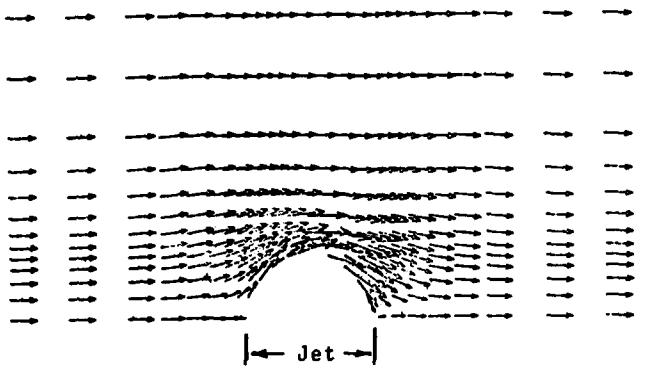

b) Transverse Velocity Initialization $\tilde{u}_\ell(0)$

Figure 4 3DPNS Discretization Information For V/STOL Jet Simulation

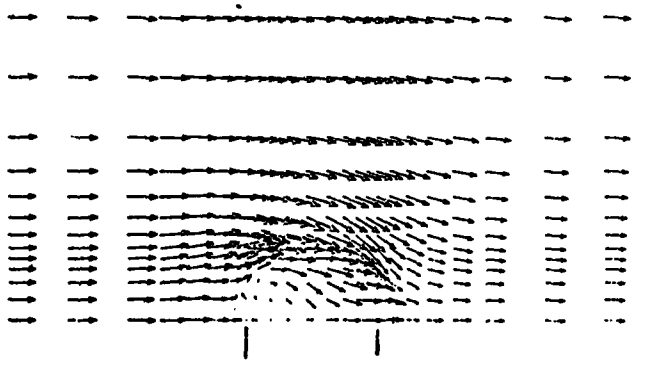

a) $x_1/D = 0.25$
$\tilde{u}_\ell^m = 0.176$

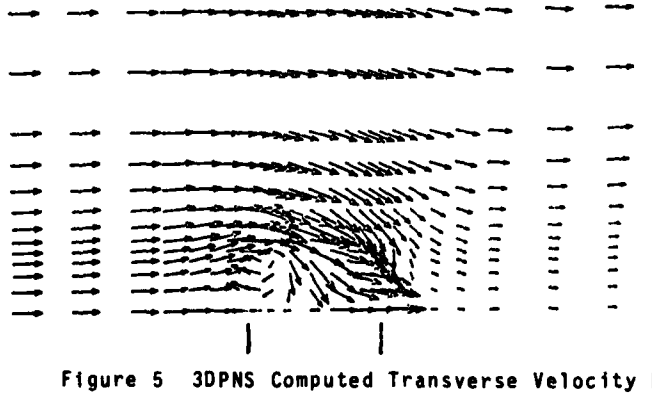

b) $x_1/D = 0.50$
$\tilde{u}_\ell^m = 0.160$

Figure 5 3DPNS Computed Transverse Velocity Distributions, Circular V/STOL Jet, $U_j:\bar{U}_j:U_\infty = 1.0/0.2/0.1$, Turbulent.

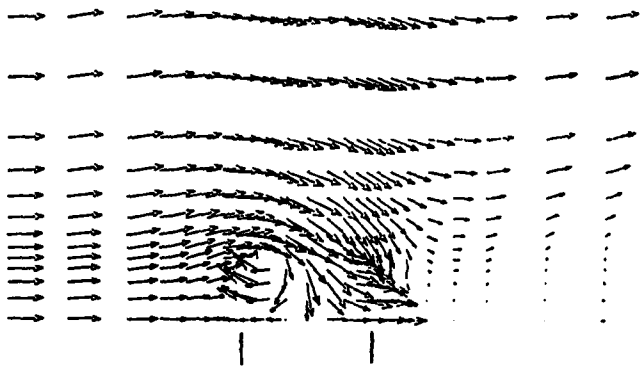

c) $x_1/D = 0.75$
$\tilde{u}_\ell^m = 0.136$

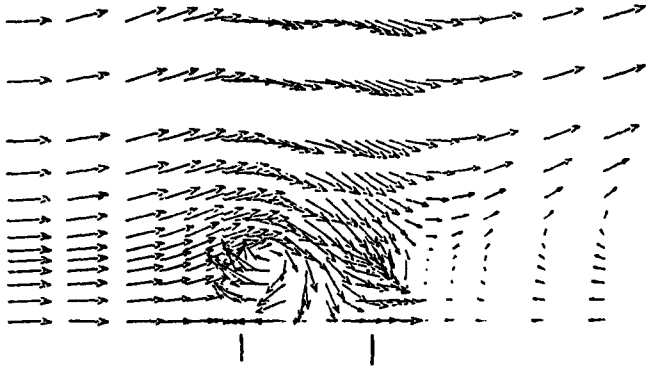

d) $x_1/D = 1.0$
$\tilde{u}_\ell^m = 0.110$

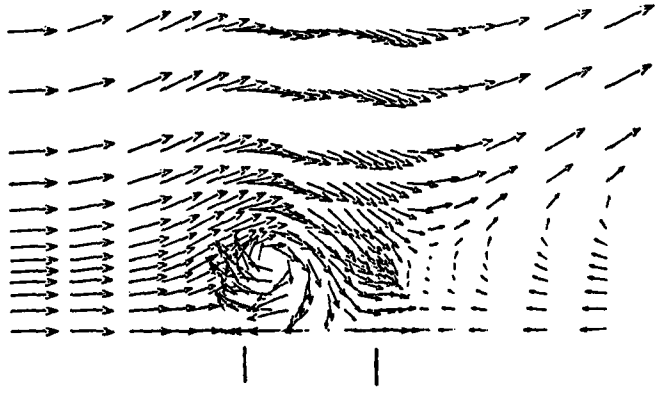

e) $x_1/D = 1.25$
$\tilde{u}_\ell^m = 0.102$

Figure 5 3DPNS Computed Transverse Velocity Distributions, Circular V/STOL Jet, $U_j:\tilde{U}_j:U_\infty$ = 1.0/0.2/0.1, Turbulent, Concluded.

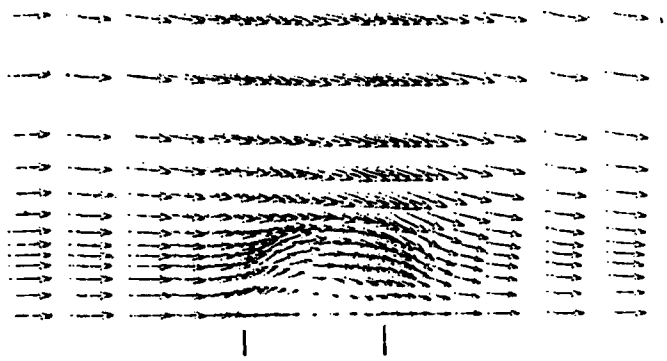

a) x_1/D = 0.5
ν^t = 10/10
$\tilde{u}^m_\ell$ = 0.107

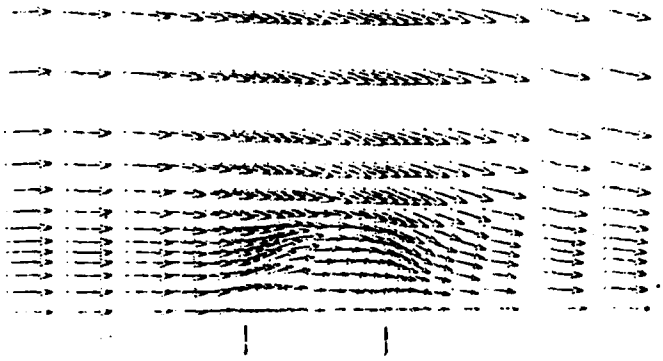

b) x_1/D = 1.0
ν^t = 10/10
$\tilde{u}^m_\ell$ = 0.109

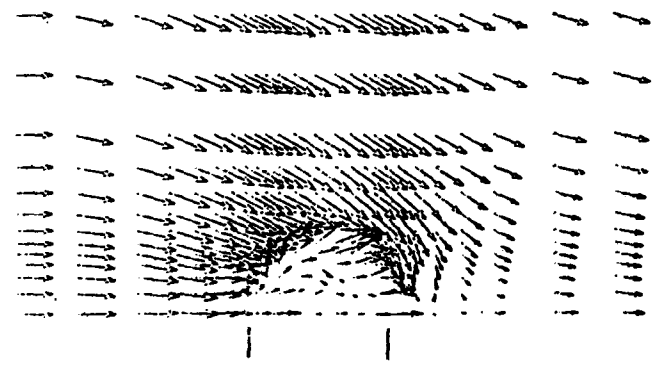

c) x_1/D = 1.0
ν^t = 100/10
$\tilde{u}^m_\ell$ = 0.139

Figure 6 3DPNS Assessment of Gross Turbulence Modifications, Circular V/STOL Jet, U_j:U_j:U_∞ = 1.0/0.2/0.1.

PREDICTION OF PROPULSION INDUCED EFFECTS IN TRANSITION USING A MODIFIED JET WAKE MODEL

by

M. M. Walters and K. T. Yen
Aircraft and Crew Systems Technology Directorate
Naval Air Development Center
Warminster, Pennsylvania 18974
United States of America

SUMMARY

The prediction of V/STOL propulsion induced aerodynamics associated with the transition flight regime by computational methods has been characterized by the inability to accurately account for the negative pressures generated in the wake area behind the jet. For those configurations which include surface area immediately behind the jet, the inaccuracies generated in the prediction of the surface pressures in this wake area dominate to the extent that gross errors result in the prediction of the induced effects for the entire configuration.

This paper presents the results of a study undertaken to improve the prediction of the induced surface pressures in the wake area without altering the existing accuracy for the area ahead of the jet. Two short-lived, low strength vortices were incorporated into the wake area of the existing Wooler jet model, with the location and strength determined from experimental data. The prediction of the induced surface pressures on a flat plate resulting from the modified Wooler model improved the accuracy of the existing model for a range of velocity ratios. The modified model resulted in significant improvement in the prediction of the induced lift on a complete V/STOL configuration.

LIST OF SYMBOLS

a	Distance from center of jet to location of wake vortex.
b	Distance from center of jet to location of image vortex of wake vortex.
c, d, e	Vortex filament length components
C_p	Surface pressure coefficient
D	Jet diameter
E_1, E_2, E_3	Entrainment coefficients used in Wooler's jet model
ΔL	Induced lift increment
r	Radial distance from center of jet
R	Jet radius
S	Length of vortex filament
T	Jet thrust
x, y, z	Cartesian coordinates
u, v, w	Velocity components
U_∞	Freestream velocity
V	Velocity
V_e	Effective velocity ratio, $\frac{V_\infty}{V_j}$
γ	Vortex strength
θ	Meridional jet angle

Subscripts

j	Jet
p	Panel control point
v	Vortex

INTRODUCTION

The V/STOL propulsion induced aerodynamics associated with the transition flight regime have a major influence on aerodynamic characteristics resulting in large forces and moments being induced on the aircraft. These jet induced effects involve the interaction of the jet and freestream flow and are primarily the result of four viscous flow phenomena: jet blockage, wake separation, entrainment, and vortex generation. Due to the complex interaction of these four phenomena, the individual effect of each component has not been separated, making analytical and/or numerical prediction difficult.

Current existing prediction techniques applicable to the transition flight regime, references (1) through (3), consist largely of potential flow computational programs with empirically derived jet models to account for the viscous interactions which characterize transition aerodynamics. These techniques model the jet quite differently dependent upon the approach taken by the developer.

One of the first methods, developed by Wooler in reference (1), combines distributions of sinks and doublets along the calculated jet path to obtain the velocity field due to the jet interference. As shown in Figure 1, the sinks are uniformly distributed along an axis normal to the freestream and account for the entrainment characteristics of the jet. Their strength, which varies with the distance along the jet, is dependent upon three empirically derived coefficients whose values were chosen to result in good coorelation between experimentally and theoretically determined jet centerlines. The doublets are distributed along the jet centerline and account for the jet blockage effect by creating a flow past an equivalent circular cylinder. This model is effective in predicting the induced effects for aircraft configurations which do not include surface area behind the jet. However, for those configurations which include surface area behind the jet, this model, along with the other jet models for transition analysis, results in predictions which underestimate the negative pressure experienced in the jet wake region.

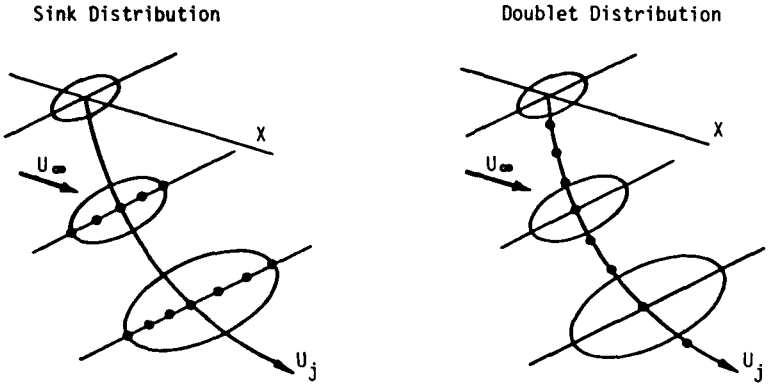

Figure 1. Wooler Transition Jet Model

An alternative jet model was proposed by Fearn, reference (2), which involves a completely different approach. Fearn's model assumes the two contrarotating vortices to be the dominant characteristic of the transition jet and thus bases his model on the strength and location of these vortices. An extensive series of tests were conducted to measure the strength and location of these vortices as a function of velocity ratio and jet injection angle. The resulting data were then used to generate the equations defining the strength and location of the two vortices. The prediction capability of this model has only been compared to data representing the surface pressure coefficients for a flat plate, with results indicating the same underestimation of the negative pressure coefficients in the wake area.

Beatty, in reference (3), developed the most recent prediction methodology for transition analysis which enables the use of either the Wooler or Fearn jet model in combination with the Hess potential flow analysis. The capability to predict the induced effects, however, has not been improved since no wake modifications were made to either jet model.

As a result of the common deficiency demonstrated by each of these methods, this study was initiated with the objective of modifying an existing jet wake model through an improved representation of the physical flow process (as opposed to an additive or multiplicative empirical correction which has been previously attempted). Wooler's jet model was selected as the basic model to be modified because of its increased capability, being applicable to multiple jets and including sideslip effects.

APPROACH

The literature concerning the basic flow processes associated with a jet in a crossflow was reviewed to determine possible areas of Wooler's jet model which could be modified to more closely represent the physical flow situation. Three areas were found in which modifications were warranted which could improve the prediction of the negative pressure coefficients in the jet wake region.

Jordinson, in reference (4), presents pressure coefficient contours measured at various locations along the jet centerline for three different velocity ratios. These contour maps, a sample of which is shown in Figure 2, indicate the presence of a pair of short-lived vortices in the wake region for each velocity ratio in addition to the well established pair of contrarotating vortices associated with a jet in a crossflow. The existence of these vortices has not been directly dealt with in transition jet models and since their presence would increase the local entrainment in the wake, incorporating these vortices was a first step in the approach to modify Wooler's model. The initial location of vortices was determined from these maps with the path of the vortices established from data of subsequent measurements taken further down the jet centerline for the same velocity ratio.

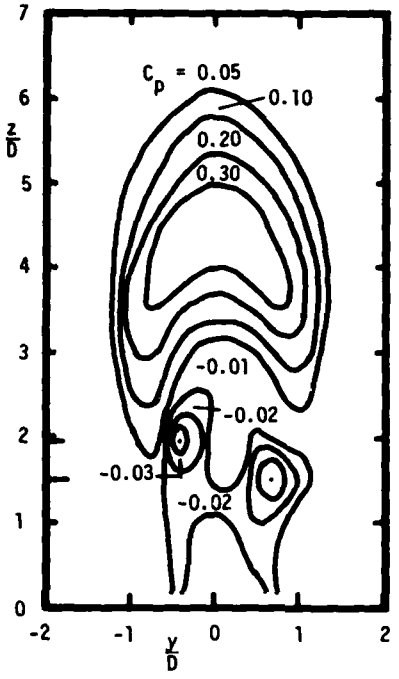

Figure 2. Pressure Coefficient Contour Map, V_e = 0.125

Having established the location and path of these vortices, their initial strength was determined using the experimental data obtained by Mosher, reference (5). This data defines the location of a stagnation point at the rear of the jet created by the interaction of the freestream flow and the wake region of the jet, as indicated in Figure 3. The two vortices were combined with Wooler's doublet model of the jet to calculate a vortex strength which resulted in a stagnation point location and a streamline flow similar to Figure 3. This initial vortex strength was then allowed to decay to reflect Jordinson's data which indicates the absence of these vortices beyond a height above the flat plate of 4.5 jet diameters. Fearn's equations for vortex strength, reference (2), were used to calculate the variation of strength with distance along the vortex trajectory, with modifications to account for the faster decay of the short-lived vortices indicated by Jordinson's data. Velocities induced by these additional vortices were then calculated using the Biot-Savart Law. The development of these resulting velocity equations is presented in the following section.

The second area of modification resulted from a review of the oil film flow studies conducted by Mosher in reference (5). Figure 3 shows two representative photographs of the flow variation with velocity ratio which resulted from this study. These photographs indicate an aft movement of the separation point around the jet as the velocity ratio is increased, and a change in the streamline pattern indicating that entrainment is related to velocity ratio. A plot of the separation point movement with velocity ratio is contained in Figure 4, and forms the basis for the second modification to the Wooler jet model.

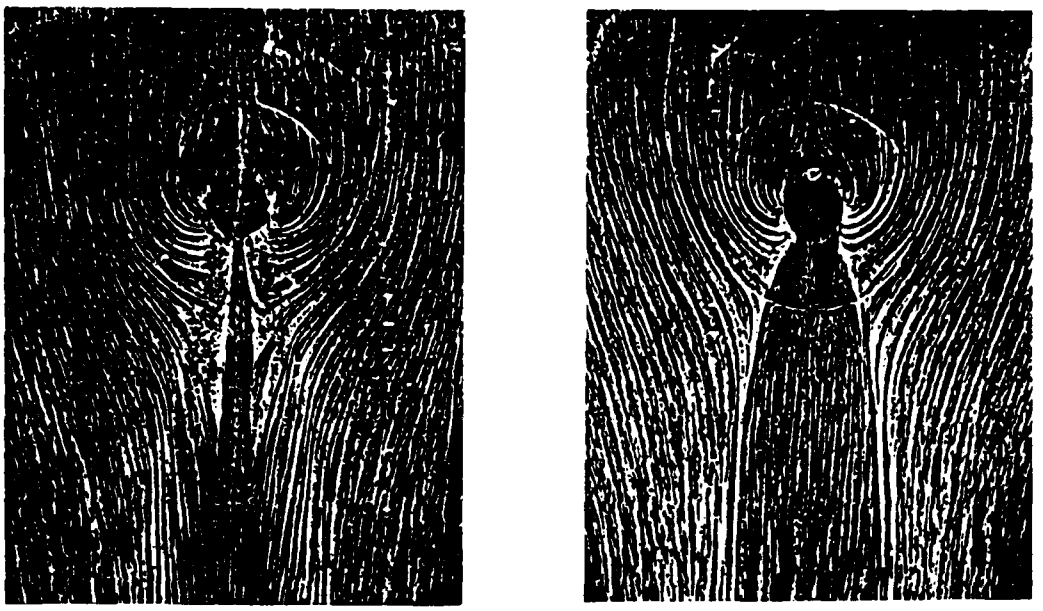

(a) $V_e \approx 0.25$ (b) $V_e = 0.125$

Figure 3. Oil Film Studies of Streamline Pattern Variation With Velocity Ratio

A uniform distribution of sinks along an axis normal to the freestream flow, as shown in Figure 1, is used in the Wooler model to account for the entrainment of the jet. To enable a variation of entrainment characteristics with velocity ratio, and to reflect the movement of the separation point, the present invariant sink distribution is varied by locating the two end points of the distribution line at the separation points around the jet as illustrated in Figure 5. This will tend to localize the entrainment in the wake region as the velocity ratio increases, reflecting the changing streamline pattern as shown in Figure 3.

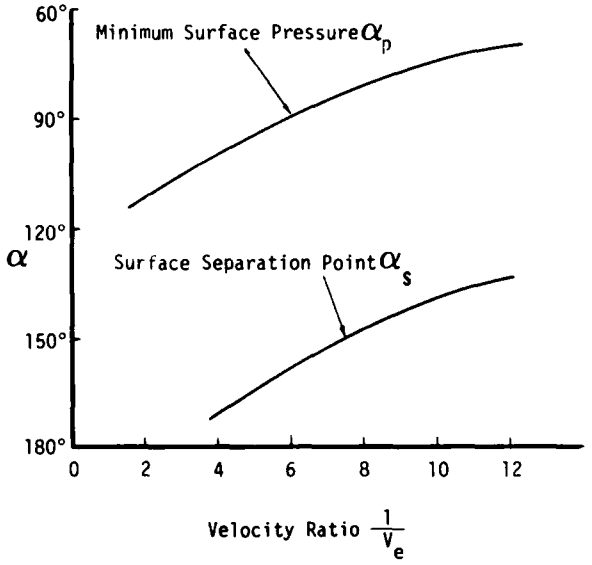

Figure 4. Location of Minimum Pressure Point and Separation Point Versus Velocity Ratio, $\frac{1}{V_e}$

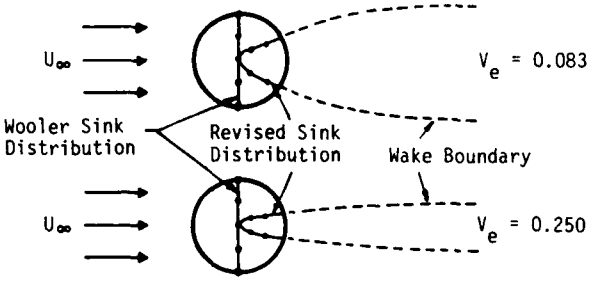

Figure 5. Jet Sink Distribution Models

The third modification was indicated from a review of the work by Kamotani and Greber, reference (6). Three entrainment coefficients, E_1, E_2, and E_3 used in Wooler's jet model account for the crossjet entrainment and parallel-jet entrainment. Experimental entrainment data for a free jet in hover flight was used to determine E_2, with E_1 and E_3 being chosen to result in good correlation between experimentally and theoretically determined jet centerlines and induced surface pressures. Figure 6, from reference (7), indicates the relative insensitivity of these coefficients to velocity ratio. Kamotani and Greber have experimentally determined directly that the coefficients vary significantly with velocity ratio and should be a magnitude greater than those used by Wooler. Modification of the entrainment coefficients to reflect the findings of Kamotani and Greber will also result in increased entrainment and constitute the third of the three steps in the overall approach to obtain an improved jet model. Since the original entrainment coefficients are in the form of constraints these can be replaced simply by expressions as a function of velocity ratio to reflect the variation shown in Figure 6.

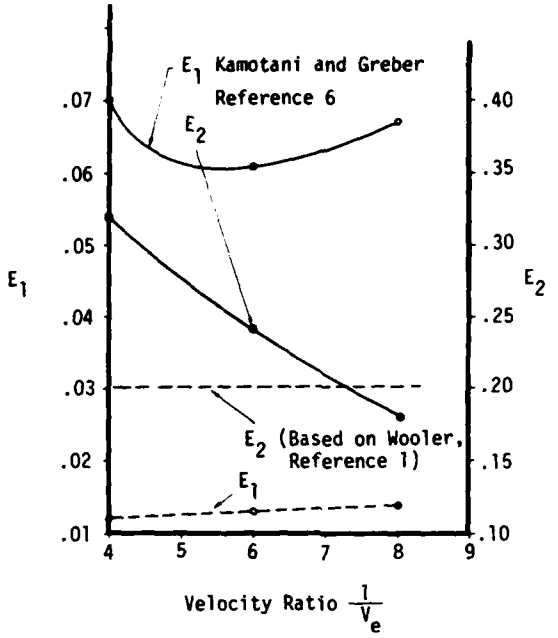

Figure 6. Variation of Entrainment Coefficients With Velocity Ratio

METHOD DEVELOPMENT

The development of the equations to calculate the induced velocities resulting from the two wake vortices began with the use of the method of images to locate two image vortices inside the jet. These image vortices maintained the circular jet blockage effect created by Wooler when the two wake vortices were incorporated into the model. An illustration of the orientation of these vortices relative to the jet is contained in Figure 7 along with a definition of the terms to be used in the equations that follow. The trajectory and strength variation of these image vortices are calculated using the same procedure as the wake vortices discussed in the previous section. Referring to Figure 7, the induced velocity equations were derived by transforming the coordinates of vortices B, C, and D in terms of vortex A through the relations

$$x_{v_B} = \frac{b}{a} x_{v_A} \qquad x_{v_C} = x_{v_A} \qquad x_{v_D} = \frac{b}{a} x_{v_A}$$

$$y_{v_B} = \frac{b}{a} y_{v_A} \qquad y_{v_C} = -y_{v_A} \qquad y_{v_D} = \frac{-b}{a} y_{v_A}$$

$$z_{v_B} = z_{v_A} \qquad z_{v_C} = z_{v_A} \qquad z_{v_D} = z_{v_A}$$

Using the data of Jordinson to determine the path of the vortices, the vortex strength was then allowed to decay to reflect the dissipation of the vortex indicated also by Jordinson's data. Fearn's equation, reference (2), for calculating the vortex strength variation is

$$\gamma = \frac{0.72}{V_e} \text{ erf } \left\{ 4.304 \frac{\left(1 - e^{-\frac{S}{D} V_e}\right)}{\sqrt{S/D}} \right\}$$

and was used as a basis with the constants adjusted to reflect the increased dissipation of the wake vortices.

Having determined the location, path, and strength variation of the wake vortices, the induced velocity from each vortex was calculated using the Biot-Savart Law, resulting in

$$\Delta V_{v_A} = \frac{\gamma}{4\pi} \frac{\left[(y_v - y_p)e-(z_v+z_p)d\right]\bar{i} + \left[(z_v + z_p)c-(x_v - x_p)e\right]\bar{j} + \left[(x_v - x_p)d-(y_v - y_p)c\right]\bar{k}}{\left[(x_v - x_p)^2 + (y_v - y_p)^2 + (z_v + z_p)^2\right]^{3/2}}$$

$$\Delta V_{v_B} = -\frac{\gamma}{4\pi} \frac{\left[(\frac{b}{a} y_v - y_p)e-(z_v + z_p)\frac{b}{a}d\right]\bar{i} + \left[(z_v + z_p)\frac{b}{a}c-(\frac{b}{a} x_v - x_p)e\right]\bar{j} + \left[(\frac{b}{a} x_v - x_p)\frac{b}{a}d-(\frac{b}{a} y_v - y_p)\frac{b}{a}c\right]\bar{k}}{\left[(\frac{b}{a} x_v - x_p)^2 + (\frac{b}{a} y_v - y_p)^2 + (z_v + z_p)^2\right]^{3/2}}$$

$$\Delta V_{v_C} = -\frac{\gamma}{4\pi} \frac{\left[-(y_v + y_p)e+(z_v + z_p)d\right]\bar{i} + \left[(z_v + z_p)c-(x_v - x_p)e\right]\bar{j} + \left[-(x_v - x_p)d + (y_v + y_p)c\right]\bar{k}}{\left[(x_v - x_p)^2 - (y_v - y_p)^2 + (z_v + z_p)^2\right]^{3/2}}$$

$$\Delta V_{v_D} = \frac{\gamma}{4\pi} \frac{\left[-(\frac{b}{a} y_v + y_p)e+(z_v + z_p)\frac{b}{a}d\right]\bar{i} + \left[(z_v + z_p)\frac{b}{a}c-(\frac{b}{a} x_v - x_p)e\right]\bar{j} + \left[-(\frac{b}{a} x_v - x_p)\frac{b}{a}d+(\frac{b}{a} y_v + y_p)\frac{b}{a}c\right]\bar{k}}{\left[(\frac{b}{a} x_v - x_p)^2 - (\frac{b}{a} y_v + y_p)^2 + (z_v + z_p)^2\right]^{3/2}}$$

where (x_v, y_v, z_v) are the coordinates of the vortex, (x_p, y_p, z_p) the coordinates of the panel control point, and (c, d, e) the lengths of the vortex filament segments. Rearranging the terms of the equations to obtain the total (u, v, w) components of velocity induced by the total vortex system and substituting $\frac{R^2}{a^2}$ for $\frac{b}{a}$ from the method of images relationship, $ab = R^2$, results in

$$u_v = \frac{\gamma}{4\pi} \left\{ \frac{(y_v - y_p)e-(z_v + z_p)d}{\left[(x_v - x_p)^2+(y_v - y_p)^2+(z_v + z_p)^2\right]^{3/2}} - \frac{(\frac{R^2}{a^2} y_v - y_p)e-(z_v + z_p)\frac{R^2}{a^2}d}{\left[(\frac{R^2}{a^2} x_v - x_p)^2+(\frac{R^2}{a^2} y_v - y_p)^2+(z_v + z_p)^2\right]^{3/2}} \right.$$
$$\left. - \frac{-(y_v + y_p)e+(z_v + z_p)d}{\left[(x_v - x_p)^2-(y_v + y_p)^2+(z_v + z_p)^2\right]^{3/2}} + \frac{-(\frac{R^2}{a^2} y_v + y_p)e+(z_v + z_p)\frac{R^2}{a^2}d}{\left[(\frac{R^2}{a^2} x_v - x_p)^2-(\frac{R^2}{a^2} y_v + y_p)^2+(z_v + z_p)^2\right]^{3/2}} \right\}$$

$$v_v = \frac{\gamma}{4\pi} \left\{ \frac{(z_v + z_p)c-(x_v - x_p)e}{\left[(x_v - x_p)^2+(y_v + y_p)^2+(z_v + z_p)^2\right]^{3/2}} - \frac{(z_v + z_p)\frac{R^2}{a^2}c-(\frac{R^2}{a^2} x_v - x_p)e}{\left[(\frac{R^2}{a^2} x_v - x_p)^2+(\frac{R^2}{a^2} y_v - y_p)^2+(z_v + z_p)^2\right]^{3/2}} \right.$$
$$\left. - \frac{(z_v + z_p)c-(x_v - x_p)e}{\left[(x_v - x_p)^2-(y_v + y_p)^2+(z_v + z_p)^2\right]^{3/2}} + \frac{(z_v + z_p)\frac{R^2}{a^2}c-(\frac{R^2}{a^2} x_v - x_p)e}{\left[(\frac{R^2}{a^2} x_v - x_p)^2-(\frac{R^2}{a^2} y_v - y_p)^2+(z_v + z_p)^2\right]^{3/2}} \right\}$$

$$w_v = \frac{\gamma}{4\pi} \left\{ \frac{(x_v - x_p)d-(y_v - y_p)c}{\left[(x_v - x_p)^2+(y_v - y_p)^2+(z_v + z_p)^2\right]^{3/2}} - \frac{(\frac{R^2}{a^2} x_v - x_p)\frac{R^2}{a^2}d-(\frac{R^2}{a^2} y_v - y_p)\frac{R^2}{a^2}c}{\left[(\frac{R^2}{a^2} x_v - x_p)+(\frac{R^2}{a^2} y_v - y_p)+(z_v + z_p)^2\right]^{3/2}} \right.$$
$$\left. - \frac{-(x_v - x_p)d+(y_v + y_p)c}{\left[(x_v - x_p)^2-(-y_v + y_p)^2+(z_v + z_p)^2\right]^{3/2}} + \frac{(\frac{R^2}{a^2} x_v - x_p)\frac{R^2}{a^2}d+(\frac{R^2}{a^2} y_v + y_p)\frac{R^2}{a^2}c}{\left[(\frac{R^2}{a^2} x_v - x_p)^2-(\frac{R^2}{a^2} y_v + y_p)^2+(z_v + z_p)^2\right]^{3/2}} \right\}$$

These components are simply added to the induced velocity components calculated by Wooler's model to obtain the total velocity induced by the jet.

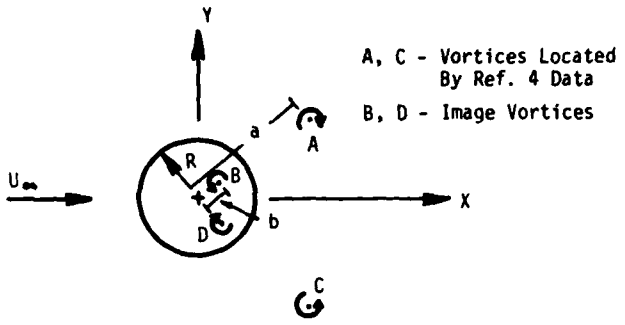

Figure 7. Schematic of Jet Wake Modification

RESULTS AND CONCLUSIONS

The resulting modified jet model was used to calculate the surface pressure coefficients induced on a flat plate and the lift induced on a complete V/STOL configuration to determine the extent of improvement in prediction capability over the original Wooler jet model. Surface pressure coefficients were calculated for three velocity ratios (V_e = 0.10, 0.167, 0.20). Typical comparisons are presented in Figure 8 for the velocity ratio, V_e = 0.167. In this figure, the pressure coefficient predictions of the modified Wooler model are compared with those of the unmodified Wooler model and also with the wind tunnel test data of reference (8). The comparisons are presented for radial locations at several meridional jet angles beginning with θ = 0° the location directly upstream of the jet. Results indicate a significant improvement in the calculation of the pressure coefficients for all velocity ratios when compared with the unmodified model predictions. In addition, excellent agreement is shown between the modified model predictions and the test data for each meridional angle with the exception of θ = 180°. Along this radial, the highly negative pressure coefficients near the jet are not properly accounted for by the modified model, even though a small improvement is shown over the unmodified predictions. These results are identical for the two other velocity ratios calculated indicating an effective cancellation of the induced velocity by the vortex system at the θ = 180° radial.

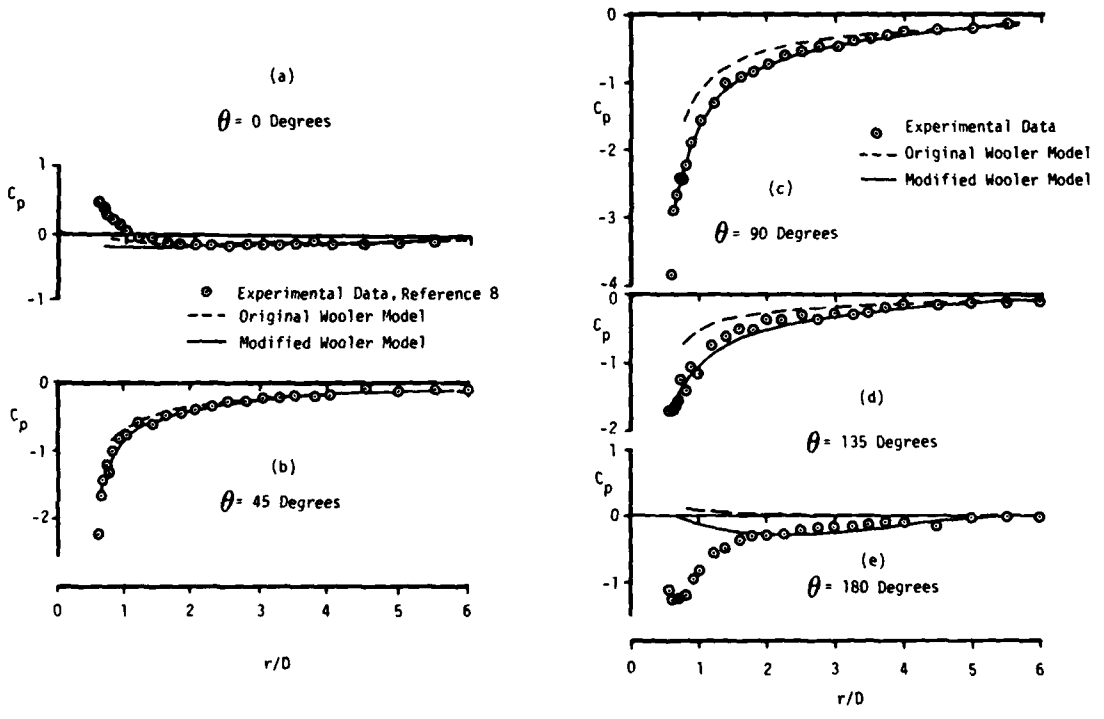

Figure 8. Comparison of Predicted Results from Wooler Jet Model and Modified Wooler Jet Model to Experimental Data for Flat Plate Configuration

The modified model was also used to predict the induced lift of a V/STOL configuration used in the wing tunnel test program of reference (9). This configuration, shown in Figure 9, is a clipped delta, supersonic aircraft with a single jet located in the fuselage. The induced lift was calculated for five velocity ratios, V_e, ranging from 0.05 to 0.25 with the results compared in Figure 9 with predictions from the unmodified Wooler model and the test data of reference (9). A significant improvement is indicated over the unmodified model with excellent agreement shown with the test data except for an extraneous data point at $V_e = 0.167$.

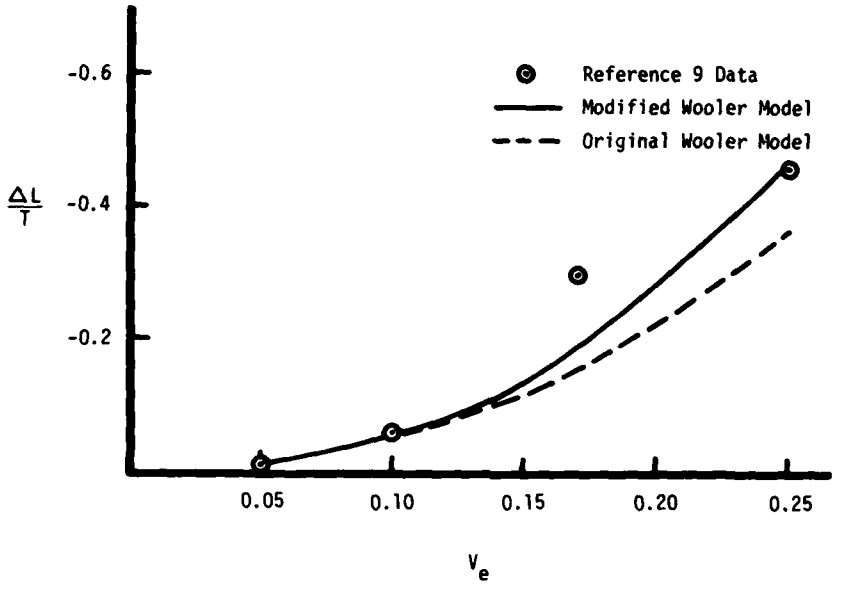

Figure 9. Comparison of Predicted Results from Wooler Jet Model and Modified Wooler Jet Model to Experimental Data for Supersonic V/STOL Configuration

CONCLUSIONS

The increased accuracy of predicting the induced lift with the modified Wooler model indicates the incorporation of the two wake vortices to be a significant improvement. This improvement is tempered however by the discrepancy shown in the region immediately behind and near the jet, indicating the need for continued effort in localizing increased entrainment in that area. It is anticipated that a further modification of adjusting the sink distribution, as previously discussed, to reflect the increased entrainment with velocity ratio in the area aft of the jet will improve the prediction in this region.

REFERENCES

1. Wooler, P. T., Kao, H. C., Schwendemann, M. F., et. al.; V/STOL Aircraft Aerodynamic Prediction Methods Investigation, AFFDL-TR-72-26, January, 1972.

2. Fearn, R. and Weston, R. P.; A Description of the Vortex Pair Associated with a Jet in a Crossflow, Prediction Methods for Jet V/STOL Propulsion Aerodynamics, Proceedings of Workshop held in Arlington, VA, July, 1975.

3. Beatty, T. D. and Kress, S. S.; Prediction Methodology for Propulsive Induced Forces and Moments of V/STOL Aircraft in Transition/STOL Flight, NADC-77119-30, July, 1979.

4. Jordinson, R.; Flow in a Jet Directed Normal to the Wind, R&M 3074, Aeronautical Research Council, 1958.

5. Mosher, D. K.; An Experimental Investigation of a Turbulent Jet in a Crossflow, Ph.D. Thesis, Georgia Institute of Technology, 1970.

6. Kamotani, Y. and Greber, I.; Experiments on a Turbulent Jet in a Crossflow, Report FTAS/TR-71-62, Case Western Reserve University (NASA CR-72893), 1971.

7. Yen, K. T.; The Aerodynamics of a Jet in a Crossflow, NADC-78291-60, December, 1978.

8. Fearn, R.; Induced Pressure Distribution of a Jet in a Crossflow, NASA TN D-7916. July, 1975.

9. Vogler, R. D.; Interference Effects of Single and Multiple Round or Slotted Jets on a VTOL Model in Transition, NASA TN D-2380, August, 1964.

EFFECTS OF BUOYANCY AND ENTRAINMENT ON HOT FREE JETS AND WALL JETS

BY

K. Gersten, F.v. Schulz-Hausmann, S. Schilawa

University Bochum, Federal Republic of Germany

SUMMARY

The flows of hot exhaust-gas jets are strongly influenced by buoyancy forces as well as by entrainment effects which in turn depend on the location of the jets with respect to the ground or other geometrical boundaries. When the hot jets impinge the ground, hot wall jets develop along the ground, again under the influence of buoyancy and entrainment effects.

The present work is a theoretical investigation of two-dimensional hot free jets and wall jets including buoyancy and entrainment effects.

1. INTRODUCTION

During take-off and hovering of a VTOL aircraft the development of the hot exhaust-gas jet flow is strongly influenced by buoyancy forces. In Fig. 1 two typical situations are shown where buoyancy forces have a strong influence on the flow development of the jets.

According to Fig. 1a the path of the free hot jet is strongly affected by the buoyancy forces. In a first approximation it can be assumed that the environment of the jet is still air. In reality, however, the entrainment induces some flow in the neighborhood of the jet. Hence, the path of the hot jet is the result of the mutual interaction between the viscous flow within the jet and the induced flow field outside of the jet. The latter depends on geometrical boundaries such as a ground plane or walls.

An integral method will be presented to predict the development of hot jets including buoyancy and entrainment effects.

When the hot jet impinges the ground, as shown in Fig. 1b, a hot wall jet developes along the ground. In this case, the buoyancy forces are directed perpendicularly to the main horizontal flow of the wall jet. Prandtl's boundary-layer theory fails to predict buoyancy effects on horizontal hot wall jets since forces perpendicular to the wall are usually neglected in this theory. By using higher-order boundary-layer theory the buoyancy effects can be taken into account. Experimental results show that horizontal hot wall jets finally separate and leave the ground. This phenomenon of the so-called thermal ground effect will also be discussed from point of view of higher-order boundary-layer theory.

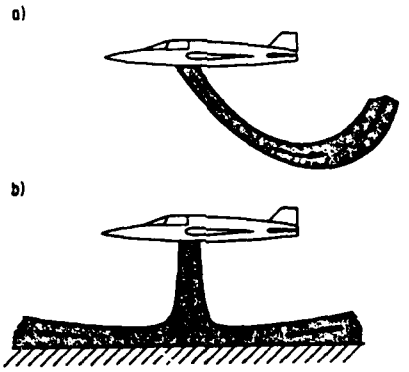

Fig. 1
Hot Free Jet and Wall Jet

2. BASIC EQUATIONS

Two-dimensional hot free jets and wall jets will be considered. The so-called Boussinesq approximation is being used which means that in the flow equations the density is equal to density at the reference temperature T_∞ except in the terms of the buoyancy forces, where the density is assumed to be a linear function of temperature.

Using a coordinate system according to Fig. 2 the basic equations are:

$$\frac{\partial u}{\partial x} + \frac{\partial}{\partial y}[(1 + ky)v] = 0 \qquad (1)$$

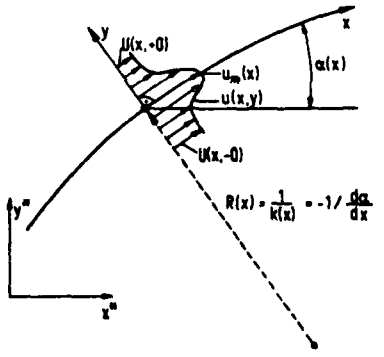

Fig. 2 Coordinate System

$$u\frac{\partial u}{\partial x} + (1 + ky)v\frac{\partial u}{\partial y} + k\,u\,v =$$

$$-\frac{1}{\rho}\frac{\partial p}{\partial x} + g\beta_\infty(1 + ky)(T - T_\infty)\sin\alpha + \frac{\partial}{\partial y}[(\nu_\infty + \nu_t)(1 + ky)\frac{\partial u}{\partial y}] \qquad (2)$$

$$u\frac{\partial v}{\partial x} + (1 + ky)v\frac{\partial v}{\partial y} - k\,u^2 =$$

$$-(1 + ky)\frac{1}{\rho}\frac{\partial p}{\partial y} + g\beta_\infty(1 + ky)(T - T_\infty)\cos\alpha + (1 + ky)\frac{\partial}{\partial y}[(\nu_\infty + \nu_t)\frac{\partial v}{\partial y}]$$

$$u\frac{\partial T}{\partial x} + (1 + ky)v\frac{\partial T}{\partial y} = \frac{\partial}{\partial y}\left[\left(\frac{\nu_\infty}{Pr} + \frac{\nu_t}{Pr_t}\right)(1 + ky)\frac{\partial T}{\partial y}\right] \qquad (4)$$

These are the Navier-Stokes equations for this coordinate system reduced by those terms which are negligible within a second-order boundary-layer theory for laminar flow. Beside the Boussinesq approximation, the buoyancy-force terms are completely taken into account. The pressure is due to the flow, i.e. the difference against the static pressure field, see refs. 1 and 2.

3. INTEGRAL METHOD FOR HOT FREE JETS

3.1. Integral Equations

Integration of the basic equations with respect to y leads tothe following integral equations:

Momentum-integral equation

$$\frac{d}{dx}\left[\int_{-\infty}^{0}(1 + ky)u(1 - U(x, -0))dy + \int_{0}^{\infty}(1 + ky)u(u - U(x, +0))dy\right]$$

$$+\frac{dU(x,-0)}{dx}\int_{-\infty}^{0}[u - U(x, -0)]dy + \frac{dU(x,+0)}{dx}\int_{0}^{\infty}[u - U(x, +0)]dy =$$

$$g\beta_\infty \sin\alpha \int_{-\infty}^{+\infty}(1 + ky)\quad(T - T_\infty)dy \qquad (5)$$

Energy-integral equation

$$\frac{d}{dx}\left[\int_{-\infty}^{0}(1 + ky)\frac{1}{2}u\,(u^2 - U^2(x, -0))dy + \int_{0}^{\infty}(1 + ky)\frac{1}{2}u(u^2 - U^2(x, +0))dy\right] =$$

$$= g\beta_\infty \sin\alpha \int_{-\infty}^{+\infty}(1 + ky)^2 u(T - T_\infty)dy - \int_{-\infty}^{+\infty}(\nu_\infty + \nu_t)(1 + ky)\frac{\partial u}{\partial y}\frac{\partial}{\partial y}[(1 + ky)u]dy \qquad (6)$$

Thermal-energy integral equation

$$\frac{d}{dx}\left[\int_{-\infty}^{+\infty}u(T - T_\infty)dy\right] = 0 \qquad (7)$$

Thermal-moment integral equation

$$\frac{d}{dx}\left[\int_{-\infty}^{+\infty}u\left(\int_{y}^{+\infty}u(T - T_\infty)dy\right)dy\right] = -\int_{-\infty}^{+\infty}\left(\frac{\nu_\infty}{Pr} + \frac{\nu_t}{Pr_t}\right)(1 + ky)u\frac{\partial T}{\partial y}\,dy \qquad (8)$$

This equation was derived by integrating Equ.(4) with respect to y from y to + ∞ followed by multiplication of u and a second integration with respect to y from - ∞ to + ∞ .

Normal-momentum integral equation

$$\frac{d\alpha}{dx}\{\int_{-\infty}^{0}[u^2 - U^2(x, -0)]dy + \int_{0}^{\infty}[u^2 - U^2(x, +0)]dy\} =$$

$$g\beta_\infty \cos\alpha \int_{-\infty}^{+\infty}(1 + ky)(T - T_\infty)dy + \frac{P(x, -0) - P(x, +0)}{\rho} \tag{9}$$

3.2. Outer Flow Field

The jet induces an outer flow, which is inviscid and irrotational, i.e. a potential flow field. The entrainment leads to the matching conditions:

$$V(x, -0) = \frac{d}{dx}[\int_{-\infty}^{0}(u - U(x, -0))dy] \tag{10a}$$

$$V(x, +0) = -\frac{d}{dx}[\int_{0}^{\infty}(u - U(x, +0))dy] \tag{10b}$$

Bernoulli equation connects velocity components and pressure in the outer flow field at the outer edge of the viscous jet region

$$P(x, -0) + \frac{\rho}{2}[U^2(x, -0) + V^2(x, -0)] = 0 \tag{11a}$$

$$P(x, +0) + \frac{\rho}{2}[U^2(x, +0) + V^2(x, +0)] = 0 \tag{11b}$$

3.3. Distribution of Velocity and Temperature Within the Jet

The following distributions of the velocity component in main flow direction have been used:

$$\frac{u(x,y)}{u_m(x)} = F_u(\eta_u, \frac{U(x, -0)}{u_m(x)}, \frac{U(x, +0)}{u_m(x)}), \quad \eta_u = \frac{y}{\delta_u(x)} \tag{12}$$

where $u_m(x)$ is the local maximum velocity in the jet and $\delta_u(x)$ characterizes the jet width (see Fig.2). It is assumed that the points with the velocities $1/2(u_m + U(x, -0))$ and $1/2(u_m + U(x, +0))$ have the same distance δ_u from the (curved) axis of the jet.

The function $F_u(\eta_u)$ has the form

$$F_u = \frac{U(x, -0)}{u_m(x)} + [1 - \frac{U(x, -0)}{u_m(x)}][1 - \tanh^2(0.8814\,\eta_u)] \qquad \eta_u \leq 0$$

$$= \frac{U(x, +0)}{u_m(x)} + [1 - \frac{U(x, +0)}{u_m(x)}][1 - \tanh^2(0.8814\,\eta_u)] \qquad \eta_u \geq 0 \tag{13}$$

The temperature distribution is given in a similar way

$$\frac{T(x,y) - T_\infty}{T_m(x) - T_\infty} = F_T(\eta_T) = [1 - \tanh^2(B(Pr)\eta_T)]^{Pr} \tag{14}$$

where

$$\eta_T = \frac{y}{\delta_T(x)}, \quad B(Pr) = \operatorname{arctanh}[(1 - 0.5^{1/Pr})^{1/2}] \tag{15}$$

For turbulent flow Pr is replaced by Pr_t.

3.4. System of Ordinary Differential Equations

Using the distribution for the velocity and temperature in the integral relations of Sec. 3.1. leads to the system of equations:

$$\frac{d}{dx}\left[u_m^2(x)\delta_u(x)A_2 \right] + \frac{dU(x, -0)}{dx} u_m(x)\delta_u(x)A_9 + \frac{dU(x, +0)}{dx} u_m(x)\delta_u(x)A_{10} =$$

$$= g\,\beta_\infty(\sin\alpha)(T_m(x) - T_\infty)\delta_T(x)\,A_1 \tag{16}$$

$$\frac{d}{dx}\left[\frac{1}{2} u_m^3\,\delta_u(x)A_3 \right] = g\beta_\infty(\sin\alpha)\, u_m(T_m(x) - T_\infty)\delta_T(x)A_4 - (\nu_\infty + \nu_t)\frac{u_m^2(x)}{\delta_u(x)} A_5 \tag{17}$$

$$\frac{d}{dx}\left[u_m(x)(T_m(x) - T_\infty)\,\delta_T(x)A_{11} \right] = 0 \tag{18}$$

$$\frac{d}{dx}\left[u_m^2(x)(T_m(x) - T\,)\delta_T(x)A_7 \right] = -\left(\frac{\nu_\infty}{Pr} + \frac{\nu_t}{Pr_t} \right) u_m(x)(T_m(x) - T_\infty)A_6 \tag{19}$$

$$\frac{d\alpha}{dx}\left[u_m^2(x)\delta_u(x)A_{12} \right] = g\beta_\infty(\cos\alpha)(T_m(x) - T_\infty)\delta_T(x) \cdot A_{13} + \frac{P(x, -0) - P(x, +0)}{\rho} \tag{20}$$

The shape parameters A_1 to A_{13} are in general functions of $\Delta = \delta_T(x)/\delta_u(x)$, $U(x, -0)/u_m(x)$, $U(x, +0)/u_m(x)$ and $k(x)\delta_u(x)$. Some shape parameters are special cases of others, for example:

$$A_{11} = \lim_{k\delta_u \to 0} A_4$$

The values of the shape parameters for $U(x, -0) = U(x, +0) = k(x)\delta(x) = 0$ are given in ref. 3.

This system of five ordinary differential equations has to be satisfied by the five unknown functions

$$\delta_u(x), \quad \Delta(x), \quad u_m(x), \quad T_m(x) - T_\infty, \quad \alpha(x),$$

whereas the values of the potential flow field $U(x, -0)$, $U(x, +0)$, $P(x, -0)$, $P(x, +0)$ are considered to be given.

The matching between the jet flow and the outer flow field is done by an iteration process. The calculation starts by guessing the five unknown functions, as well as the entrainment velocities $V(x, -0)$ and $V(x, +0)$. Then potential theory yields $U(x, -0)$, $U(x, +0)$ and hence $P(x, -0)$ and $P(x, +0)$, respectively. Now all shape parameters can be determined. The system of differential equations can be solved to get a new set of five functions. The cycle is repeated until convergence is reached.

For laminar flows the eddy viscosity vanishes, $\nu_t = 0$, whereas for turbulent flows the molecular viscosity can be neglected, $\nu_\infty = 0$, compared to the eddy viscosity, which is assumed to be a function of y only.

As turbulence model the eddy viscosity ν_t is connected with the jet width as

$$\nu_t = \kappa\,[u_m(x) - U(x, -0)]\delta_u \qquad y < 0 \tag{21a}$$

$$\nu_t = \kappa\,[u_m(x) - U(x, +0)]\delta_u \qquad y > 0 \tag{21b}$$

where κ and Pr_t are functions of the local Archimedes number defined by

$$Ar(x) = \frac{g\,\beta_\infty\,E_T\,Q^3(x)}{K^3(x)} \tag{22}$$

Here the following abbreviations have been used:

$$E_T = \int_{-\infty}^{+\infty} u(T - T_\infty)dy \tag{23}$$

$$Q(x) = \int_{-\infty}^{0} [u - U(x, -0)]dy + \int_{0}^{\infty} [u - U(x, +0)]dy \tag{24}$$

$$K(x) = \int_{-\infty}^{0} (1 + ky)u(u - U(x, -0))dy + \int_{0}^{\infty} (1 + ky)u(u - U(x, +0))dy \tag{25}$$

The relations derived in ref. 3 can be applied:

$$\kappa = 0.035\ (1 + 1.64\ Ar(x)) \tag{26}$$

$$Pr_t = 0.5\ (1 + 1.02\ Ar(x))\ . \tag{27}$$

4. RESULTS FOR HOT FREE JETS

4.1. First Order Approximation

In a first approach the entrainment and hence the potential flow can be neglected. This has been done in ref. 3. A proper selection of reference values permitted the characteristics of the jet flow to be expressed as universal function, in which - in case of turbulent flow - the initial jet orientation is the only input parameter. When the local volume flow, the momentum and the thermal energy are given , the characteristic parameter is the local Archimedes number Ar(x), defined in Eq.(22).

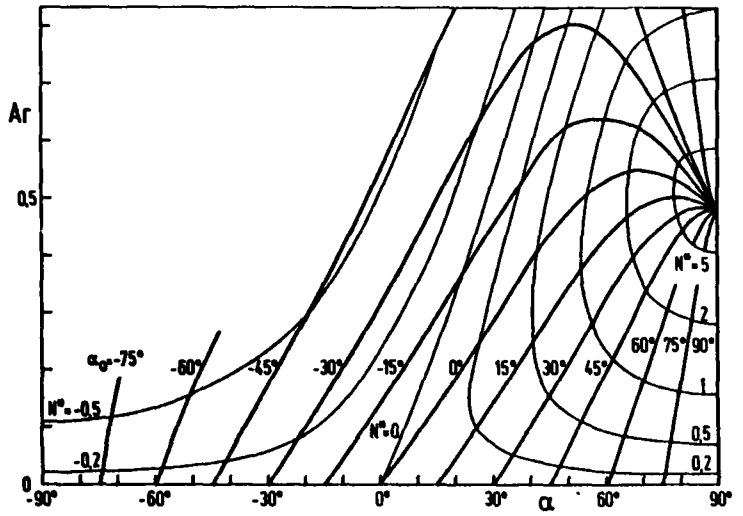

Fig. 3 Turbulent Hot Free Jets
Archimedes Number Ar(α,α) and Ar(N*,α)

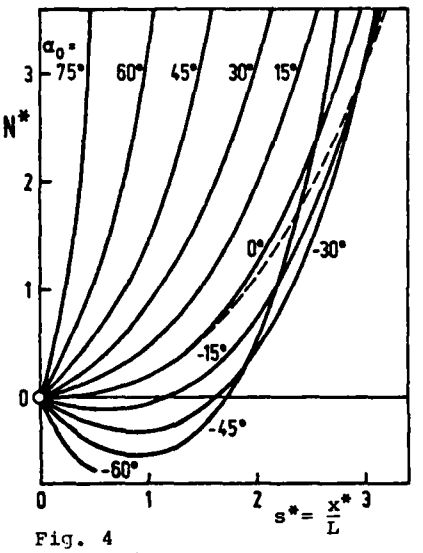

Fig. 4
Paths of Turbulent Hot Free Jet

Fig. 3 shows such a universal diagram, which covers all possible turbulent hot free jets. The curves α_o = const represent jets which have the shape angle α_o in their virtual origin (Q = 0). The curves show the dependence of the local Archimedes number Ar(x) on the local slope angle α(x). All curves end up at Ar = 0.47 , α = 90° corresponding to the vertical plume. Moreover, the diagram contains the dimensionless local vertical position of the jet with respect to the virtual origin (see Fig. 2):

$$N^* = \frac{Y^*}{L} = \frac{Y^*}{K_o (E_T\ g\beta_\infty)^{-2/3}}\ , \tag{28}$$

Having this information it is possible to determine the complete path of each individual jet. The result is given in Fig. 4. It represents the paths of all possible turbulent jets.

If the initial volume flow is already non-zero then the initial slope angle α_o in the virtual origin of this jet has to be found via Fig. 3. All other parameters of the flow can also be determined by further universal diagrams. As an example Fig. 5 shows the dimensionless maximum velocities

$$U_m = \frac{u_m(x)}{U_o} = \left(Ar\ \frac{A_2}{A_8} \right)^{-1/3} \tag{29}$$

as function of the dimensionless coordinate along the jet path

$$s = \frac{x}{L} \tag{30}$$

where $U_o = (E_T\ g\beta_\infty)^{1/3}$ (31)

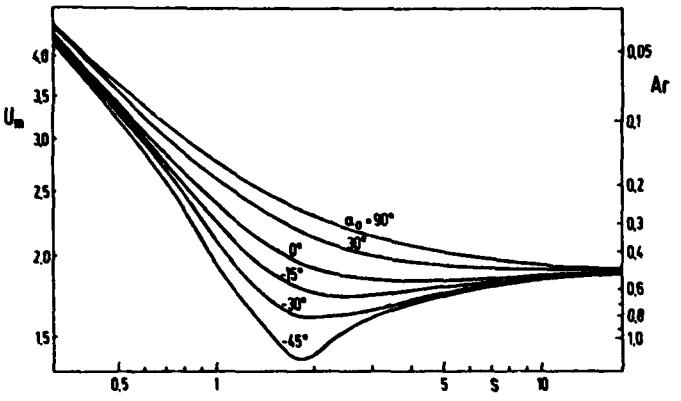

Fig. 5 Turbulent Hot Free Jets
Maximum Velocity $U_m(s,\alpha_o)$

In Fig. 6 the maximum velocities, maximum temperatures and the slope angles as function of the coordinate along the jet path are shown for the initial slope angle $\alpha_1 = 0$. Parameter is the Archimedes number Ar_1 at the initial station. The effect of the buoyancy forces can be seem quite clearly, in particular at the development of the maximum velocity. The maximum velocity of the isothermal jet ($Ar_1 = 0$) is decreasing monotonically whereas the non-isothermal jet will first follow the curve of the isothermal jet, but deviates further downstream to higher maximum velocities, which for high enough Archimedes numbers will even increase until it reaches its final constant value corresponding to the vertical plume.

The theoretical results have been compared with experiments showing quite satisfactory agreement.

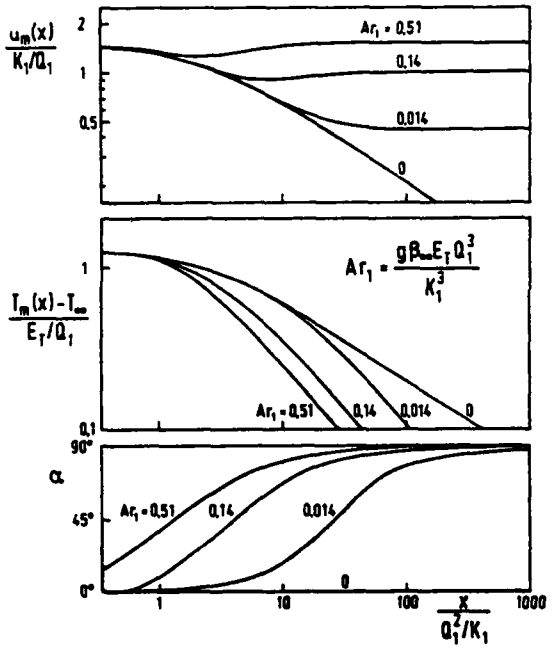

Fig. 6 Influence of Initial Archimedes Number Ar_1 on Turbulent Hot Jets

4.2. Entrainment Effects

The entrainment effects on the path of a turbulent jet with arbitrary Archimedes number Ar_1 and an initial slope $\alpha_1 = 0$ are shown in Fig. 7. The dotted lines in this figure are the results of the first order approximation. The solid lines show the calculated path considering the induced outer flow field. The general effect is a more bent path of the jet, which is mainly influenced by the induced pressure difference.

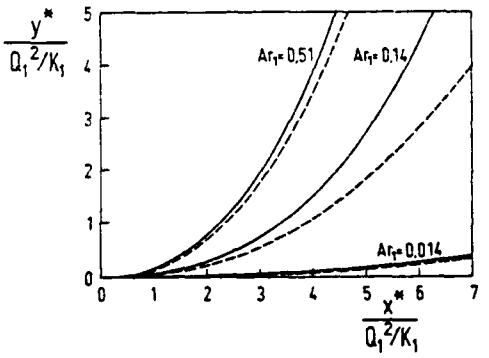

Fig. 7
Paths of Turbulent Hot Free Jets
----- outer flow neglected
——— outer flow included

5. HIGHER ORDER BOUNDARY LAYER THEORY FOR HORIZONTAL LAMINAR HOT WALL JETS

5.1 Basic Equations

A cartesian coordinate system according to Fig. 8 is used. In order to get a solution of the system, Eqns. (1) to (4), for large Reynolds numbers the method of matched asymptotic expansions can be applied. The whole flow field is divided into two fields, the outer region (potential flow) and the inner or boundary layer region.

When $\varepsilon = \frac{1}{\sqrt{Re}} = \frac{1}{\sqrt{U_R L/\nu}}$ is used as perturbation parameter and

$$N = \frac{1}{\varepsilon}\frac{y}{L} = \frac{\bar{y}}{\varepsilon} \quad , \quad s = \frac{x}{L}$$

as new variables, the asymtotic series for the inner solution (wall jet) are:

$$\frac{u(x,y)}{U_R} = u_1(s,N) + \varepsilon\, u_2(s,N) + \ldots$$

$$\frac{v(x,y)}{U_R} = \varepsilon v_1(s,N) + \varepsilon^2 v_2(s,N) + \ldots \qquad (32)$$

$$\frac{p(x,y)}{\rho U_R^2} = p_1(s,N) + \varepsilon\, p_2(s,N) + \ldots$$

$$\frac{T(x,y)-T_\infty}{T_R} = \theta_1(s,N) + \varepsilon\, \theta_2(s,N) + \ldots$$

The resulting differential equations for first and second order boundary layer are:
First order:

$$\frac{\partial u_1}{\partial s} + \frac{\partial v_1}{\partial N} = o \qquad (33)$$

$$u_1\frac{\partial u_1}{\partial s} + v_1\frac{\partial u_1}{\partial N} = -\frac{\partial p_1}{\partial s} + \frac{\partial^2 u_1}{\partial N^2} \qquad (34)$$

$$\frac{\partial p_1}{\partial N} = Ar^*\,\theta_1 \qquad (35)$$

$$u_1\frac{\partial \theta_1}{\partial s} + v_1\frac{\partial \theta_1}{\partial N} = \frac{1}{Pr}\frac{\partial^2 \theta_1}{\partial N^2} \qquad (36)$$

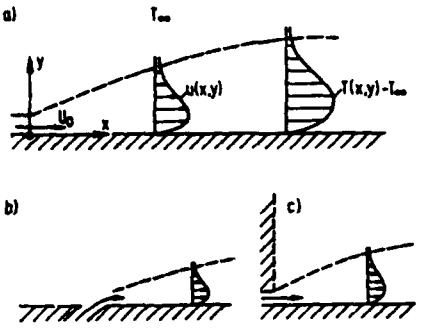

Fig. 8
Horizontal Hot Wall Jet
a) Coordinate System
b) Wall Jet Along Ground
c) Wall Jet in a Quater Plane

with the boundary conditions:

$N = o$: $u_1 = o$, $v_1 = o$, $\theta_1 = o$
$N \to \infty$: $u_1 = o$, $\theta_1 = o$.

From the solution we get the entrainment velocity:

$$V_2(s,o) = -\frac{d}{ds}\int_o^\infty u_1(s,N)\, dN \qquad (37)$$

Second order:

$$\frac{\partial u_2}{\partial s} + \frac{\partial v_2}{\partial N} = o \qquad (38)$$

$$u_1\frac{\partial u_2}{\partial s} + u_2\frac{\partial u_1}{\partial s} + v_1\frac{\partial u_2}{\partial N} + v_2\frac{\partial u_1}{\partial N} = -\frac{\partial p_2}{\partial s} + \frac{\partial^2 u_2}{\partial N^2} \qquad (39)$$

$$\frac{\partial p_2}{\partial N} = Ar^*\theta_2 \qquad (40)$$

$$u_1\frac{\partial \theta_2}{\partial s} + u_2\frac{\partial \theta_1}{\partial s} + v_1\frac{\partial \theta_2}{\partial N} + v_2\frac{\partial \theta_1}{\partial N} = \frac{1}{Pr}\frac{\partial^2 \theta_2}{\partial N^2} \qquad (41)$$

with the boundary conditions:

$N = o$: $u_2 = v_2 = \theta_2 = o$
$N \to \infty$: $u_2 = U_2(s,o)$, $\theta_2 = o$, $p_2 = o$.

The outer solution has the asymptotic series

$$\frac{u(x,y)}{U_R} = U_2(s,\bar{y}) + \ldots$$

$$\frac{v(x,y)}{U_R} = V_2(s,\bar{y}) + \ldots \qquad (42)$$

$$\frac{p(x,y)}{\rho U_R^2} = P_2(s,\bar{y}) + \ldots$$

$$\frac{T(x,y)-T_\infty}{T_R} = o$$

$U_2(s,\bar{y})$, $V_2(s,\bar{y})$ belong to a solution of the Laplace equation (potential flow).

The most important parameter of the problem is the modified Archimedes number

$$Ar^* = \frac{g\beta_\infty T_B L^{\frac{1}{2}} \nu^{\frac{1}{2}}}{U_R^{5/2}} = \frac{g\,L}{U_R^2}\,\beta_\infty T_B\,\frac{1}{\sqrt{Re}} \qquad (43)$$

where

$$T_B = \frac{E_T}{U_R\,L} = \frac{\int_0^\infty u(o,y)\,[T(o,y)-T_\infty]\,dy}{U_R\,L}$$

$$U_R^2 = \frac{1}{\nu L}\int_0^\infty u(o,y)\,dy \int_0^\infty u^2(o,y)\,dy$$

For a finite value of Ar^* the reference temperature, i.e. the thermal energy in the wall jet, has to be much larger then the kinetic energy represented by U_R^2 when the limiting case of high Reynolds numbers is considered. Only under this condition the buoyancy term remains in the first order equation.

5.2. Result of First Order Solution

From the momentum equation in y-direction it can be seen that the pressure within the hot wall jet is lower than the outer pressure. Therefore, the wall pressure p_w is decreasing at first, with a minimum at $x/L = 0.025 \cdot Ar^{*0.836}$. The pressure at that point is about

$$\frac{p_{wmin}}{\rho U_R^2} = -\,0.75\,Ar^{*0.836} \qquad (44)$$

This lower pressure has also been found in experiments, see refs. 5, 6. Beyond that point the pressure is increasing monotonically reaching zero again for $x \to \infty$. The friction coefficient

$c_f = \tau_w/\frac{\rho}{2} U_R^2$ as function of the coordinate x is shown in Fig. 9. The modified Archimedes number Ar^* is parameter. The curve $Ar^* = 0$ corresponds to the classical wall jet solution without buoyancy forces. It turns out that the buoyancy forces lead to an increase of the shear stress. By choosing suitable reference values it is possible to reduce the infinite number of curves in Fig. 9 to just one single curve, which is given in Fig. 10 ($Re \to \infty$).
The following new variables have been used:

$$c_f^* = Ar^{*-1.045}\,c_f\,\sqrt{Re} \qquad (45)$$

$$x^* = Ar^{*\,0.836}\,\frac{x}{L} \qquad (46)$$

As a result from first order theory the shear stress increases due to buoyancy forces and therefore the danger of flow separation is even less than without buoyancy forces.

5.3. Results of Second Order Solution

The outer flow induced by the wall jet is always such that the x-component of the velocity at the outer edge of the wall jet is opposite to the main flow of the wall jet. Surprisingly, this negative outer flow velocity leads to an increase of the shear stress when buoyancy forces are absent. This tendency is reduced by buoyancy forces, but not sufficient to reach flow separation.

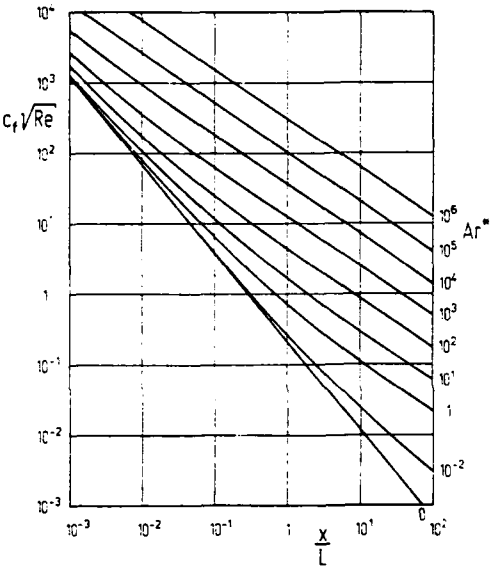

Fig. 9 Horizontal Wall Jets

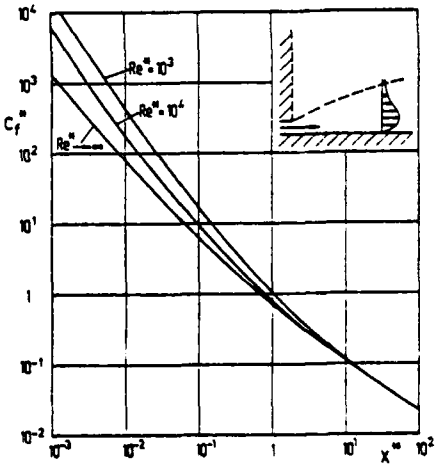

Fig. 10 Horizontal Hot Wall Jet (Pr = 0.7)

REFERENCES

[1] Gersten, K.,d'Avila, J.S.: Higher order boundary layer effects in combined free and forced convection. ESA-TT-498 (1979), 122-131, also: DLR-FB-77-16(1977),122-131.

[2] Gersten, K.,Gross, J.F.: Higher-order boundary-layer theory. Fluid Dynamics Transactions Vol. 7, Pt. II (1974), 7-36.

[3] Gersten, K., Schilawa, S., v. Schulz-Hausmann, F.K.: Nichtisotherme ebene Freistrahlen unter Schwerkrafteinfluß. Wärme- und Stoffübertragung 13 (1980), 145-162.

[4] Gersten, K., Schilawa, S.: Buoyancy effects on forced-convection heat transfer in horizontal boundary layers. Proceedings of the International Heat Transfer Conference Toronto, 1978, MC 13, 73-78.

[5] Cox, M., Abbott, W.A.: Studies of the flow fields created by single vertical jets directed downwards upon a horizontal surface. ARC CP 912,1964.

[6] Schwantes, E.,: Rezirkulationsfeld eines VTOL-Hubtriebwerkes. DLR-FB-72-50, 1972.

[7] Turner, J.S.:Buoyancy Effects in Fluids. Cambridge University Press 1973.

V/STOL AIRCRAFT AND FLUID DYNAMICS

by

Leonard Roberts
Stanford University, Stanford, California U.S.A.

and

Seth B. Anderson
Ames Research Center, NASA, Moffett Field, California, U.S.A.

SUMMARY

A recent AGARD Flight Mechanics Panel Symposium on the "Impact of Military Applications on Rotorcraft and V/STOL Aircraft Design" (Paris, April 1981) is summarized with respect to fixed-wing aircraft. The influence of the mission needs on the configurational design of V/STOL aircraft, the implications regarding some problems in fluid dynamics relating to propulsive flows, and their interaction with the aircraft and the ground plane, are summarized.

1. INTRODUCTION

A recent AGARD Flight Mechanics Panel (FMP) Symposium on the "Impact of Military Applications on Rotorcraft and V/STOL Aircraft Design" (April 1981) summarized the military mission needs and their influence on the configurational aspects of V/STOL aircraft design; identified several classes of V/STOL aircraft that are in various phases of research and development; and recognized that, with projected advances in technology, a number of practical V/STOL aircraft now appear feasible.

To achieve the desired performance of the V/STOL aircraft under consideration requires further progress in several technical disciplines including structures, materials, controls, propulsion, and aerodynamics. Of particular interest to this symposium is how the fluid-dynamical aspects of propulsive flows interact with aircraft surfaces and with the ground plane, thereby affecting performance.

It is the purpose of these remarks to summarize some of the conclusions of the previous symposium and to discuss areas of additional research in fluid dynamics that can contribute to an improvement in performance of V/STOL aircraft.

2. MISSION NEEDS

The need for military V/STOL aircraft results primarily from the potential vulnerability to enemy attack of main airbases in Europe and elsewhere, and of large aircraft carriers at sea. In the event of such attacks, V/STOL aircraft could conceivably operate from damaged runways or damaged carrier decks while continuing to utilize the logistics and support capabilities of those major assets. Alternatively, with the introduction of dispersed operations on land and at sea, V/STOL aircraft could operate without the necessity for long runways or large ships.

With respect to land-based aircraft it is argued that the dispersed site operational capability of V/STOL aircraft provides the advantage of quick response to requests for close air support with higher sortie rates, lower detectability on the ground, and a lower probability of concentrated attack. It is important here t distinguish between the need for improvements in short landing as opposed to short take-off capability. Most modern fighter aircraft, by virtue of their high thrust-to-weight ratio, already have the capability of taking off in relatively short distances (say 2,000 ft), whereas, landing on a 2,000 ft runway is a much more difficult problem, given the allowable errors in touchdown point and a limited means of reducing touchdown speed of conventional fighters. Also, for transport aircraft, the need is for shorter landing capability at dispersed destination points (long runways are generally available at the major supply points and the return takeoff is generally easier after the cargo delivery has been completed, since the aircraft is then lightly loaded).

With this emphasis, STOL, in some applications, can be refined to CTOSL; i.e., conventional takeoff and short landing. It may be feasible to design such CTOSL aircraft with essentially the same thrust-to-weight ratio as their conventional counterparts (i.e., T/W ~ 0.9 for fighters and T/W ~ 0.3 for transports), thus avoiding the engine-weight penalty usually associated with high T/W STOL aircraft. The technical challenge is to find ways of using propulsion-induced flow to augment aerodynamic lift, thereby reducing landing speed and obtaining good flightpath control to assure minimum touchdown dispersion.

In the event that operation from very short runways is required (say, 500 to 1,000 ft), thrust-to-weight ratios higher than those for conventional aircraft become necessary and landing speeds become sufficiently low that special consideration must be given to aircraft stability, control, and handling qualities. The resulting configuration effectively has all the essential characteristics required for vertical landing (i.e., high T/W and a control system integrated with, and dependent on, the propulsion system). Again, the landing task places the greatest demands on the design; as a result, the best compromise to satisfy mission needs may be a STOVL aircraft (short takeoff and vertical landing) rather than a VTOL aircraft. Payload and fuel-load capabilities of such an aircraft for short takeoff will be substantially better than for vertical takeoff.

For sea-based operations, V/STOL eliminates the need for catapult and arresting gear and allows greater flexibility in ship operations obviating the need to steam into the wind; e.g., during launch and recovery of aircraft. The more compelling reasons for V/STOL, however, is the concern regarding the vulnerability of large carriers to the threat of long range missiles. V/STOL aircraft would permit the smaller, less vulnerable ships to be deployed as a distributed force. The optimum size and number of such ships is the subject of

much study but there appears to be a growing belief that a new generation of aircraft carriers having deck lengths of approximately 600 to 800 ft would be a logical complement to, and ultimately substitution for, the current generation of large carriers.

For the present generation carriers and a next generation smaller carrier, the STOVL aircraft may be the correct choice. Such aircraft would have substantial payload and fuel-load capability by virtue of short takeoff (rather than vertical takeoff) and would permit greater flexibility in ship operation through vertical landing (at the reduced weight associated with mission return). Although several types of STOVL and VTOL naval air missions are currently under study, including carrier-onboard-delivery, close support/attack, and supersonic interception, no formal V/STOL aircraft requirement within the U.S. Navy has yet emerged. It seems likely that such a requirement will evolve, in conjunction with new weapon and ship requirements, as part of an integrated systems approach that addresses the problem of replacing the current generation of large aircraft carriers.

3. V/STOL AIRCRAFT CONFIGURATIONS

A number of fixed-wing V/STOL aircraft configurations were reviewed at the FMP Symposium. Those selected here for discussion are (a) the upper surface blowing (USB) STOL aircraft, (b) the turbofan subsonic V/STOL aircraft, and (c) the direct jet-lift supersonic V/STOL interceptor. They represent a broad range of aircraft concepts covering CTOSL, STOL, STOVL, and VTOL. They also incorporate the use of propulsive flows in a variety of ways. Therefore, they form a good basis for the subsequent discussion of several areas in fluid dynamics which need to be better understood with a view to optimize proulsive induced-flow effects.

3.1 Upper Surface Blowing (USB)

The upper-surface blowing concept uses the engine exhaust, usually from a high-bypass-ratio engine, in conjunction with a trailing-edge flap to improve the wing lift through Coanda flow turning and increased wing circulation. The schematic engine-wing-flap geometry for a recent demonstration program (the Quiet Short-Haul Research Aircraft program conducted by NASA and Boeing) is shown in Fig. 1. Maximum lift coefficients above 10 have been demonstrated in flight, compared with lift coefficients of the order of 2 that are usually achieved by aerodynamic means on a typical transport aircraft wing-flap combination. With various flight safety margins, values of C_L and the corresponding low approach speeds (60 knots) and landing distances (500 ft) for moderate thrust-to-weight ratios (~0.5) clearly indicate the value of incorporating the propulsive-aerodynamic interactions into the design of STOL aircraft.

(a) Quiet STOL Research Aircraft with Upper Surface Blowing (NASA-Boeing).

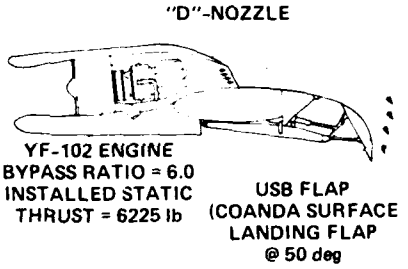

(b) Engine-Wing Schematic.

Figure 1. Upper Surface Blowing.

This work is now being extended to examine configurations of conventional thrust-to-weight ratios ($T/W = 0.3$) – characteristic of military transport aircraft – and to determine whether effective flow turning can be maintained under these lower thrust conditions. The high speed (transonic) characteristics of this engine-wing combination are also being investigated to determine whether positive interference between the wing and the exhaust flow can be realized that will lead to improved cruise efficiency. These results will have important implications regarding the questions of whether CTOL aircraft can achieve short landing performance (i.e., CTOSL aircraft) simply by changing the engine placement and flap design. Several fluid dynamic areas are of interest for this concept.

3.2 Vectored Turbofan

This STOVL or VTOL concept has also been the subject of extensive research (by Grumman and NASA), including full-scale static- and wind-tunnel tests, and small-scale model flight tests in transition and hover. It employs two high-bypass-ratio engines (which can be tilted to change the thrust vector) integrated with controllable inlet guide vanes and a system of control vanes in the engine exhaust flow (Fig. 2). The effectiveness of these vanes in deflecting the exhaust flow to provide control moments in hover and transition is of particular interest. The vane pitching moment was found to be linear over a deflection-angle range of $\pm 20°$, whereas only $\pm 5°$ of deflection was required to provide trim moment for the aircraft. Evidently, substantial margin remained for maneuvering and gust compensation.

The influence of the ground plane on aircraft lift is also of extreme interest. Aircraft lift for a given thrust was found to depend on aircraft height above ground because of the exhaust impingement and the resulting fountain effect. Ground effect was positive (i.e., lift/thrust > 1) and increased typically to a maximum of about 1.08 at a height equal to twice the engine inlet diameter. However, substantial changes in lift associated with meandering of the fountain were observed. Further research is needed for this unsteady phenomenon to be fully understood.

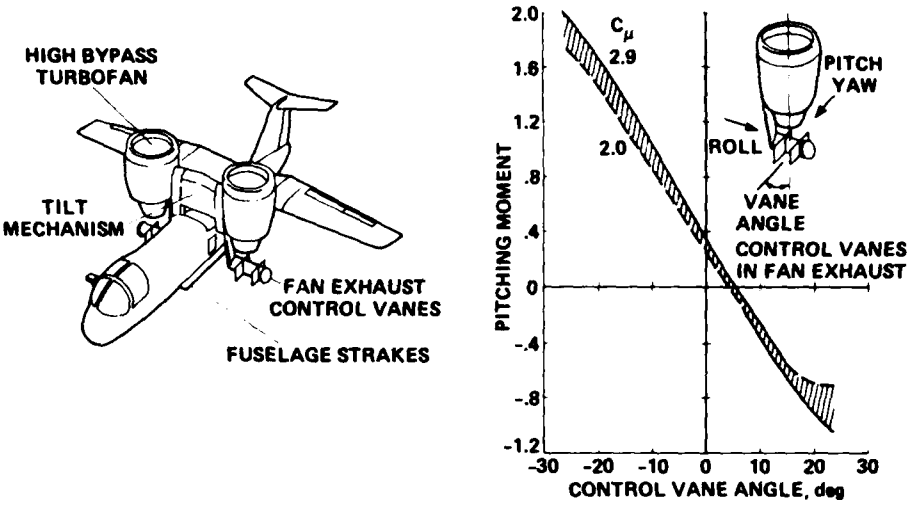

(a) Tilting Turbofan VTOL Aircraft (NASA-Grumman).

(b) Variation of Pitching Moment with Control Vane Angles.

Figure 2. Vector Turbojet.

3.3 Direct Jet Lift

Direct jet lift has been successfully applied to the Harrier VTOL aircraft and is now being considered for application to supersonic fighter and interceptor aircraft. The Harrier aircraft employs a "four poster" Pegasus engine in which four rotatable nozzles direct the flow downward for vertical flight. The two forward nozzle exhausts are relatively cool since they use by-pass air, whereas the two rear exhausts are hot. In some applications it is necessary to maintain a nominal aircraft forward speed in order to avoid damage to the ground plane due to excessive heating. Despite the exhaust impingement problem, the Harrier has operated successfully from various ground surfaces including road segments, grass fields, dirt strips, and aluminum matting. It is therefore natural to seek ways of adapting this successful form of propulsion to supersonic aircraft.

Two general variants of the Pegasus approach to direct jet lift applicable to STOVL and VTOL are currently under study (by BAE and Rolls Royce). The first of these (Fig. 3) adds plenum chamber burning (PCB) to the two front nozzles to increase the thrust and combines the two rear nozzles (to reduce supersonic drag) into a single nozzle which also rotates into a vertical thrust position. While extensive testing has been conducted to prove the PCB concept, questions remain regarding the effects of the three hot exhausts on the ground plane and on the underside of the aircraft. Also the fountain produced by the three exhaust streams may be less stable than that of the more symmetric four-poster configuration of the Harrier and may produce adverse effects from hot-gas ingestion into the engine.

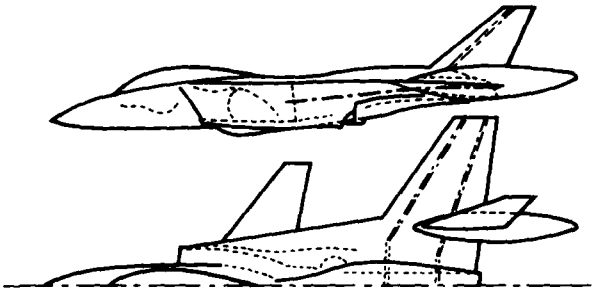

Figure 3. Supersonic VTOL Configuration with Plenum Chamber Burning (Rolls Royce).

The second broad variant of the Pegasus approach (under investigation by de Havilland of Canada) is to augment the thrust of the forward nozzles by using ejectors located in the fuselage (Fig. 4). This has the advantage of retaining the cold front exhausts (thus avoiding the adverse effects of hot gas ingestion) and providing a relatively low impingement velocity on the ground plane. The two rear hot nozzles are again combined into a single nozzle as in the previous discussion. Uncertainties that remain to be resolved include (a) the extent to which thrust can be improved by cold flow augmentation within the geometrical constraints of a practical supersonic aircraft design, and (b) the effect of the fountain caused by the impingement of exhaust flows (in this case heating effects should not be a problem due to extensive use of cold air; however, the fountain may cause upset moments on the wing and fuselage).

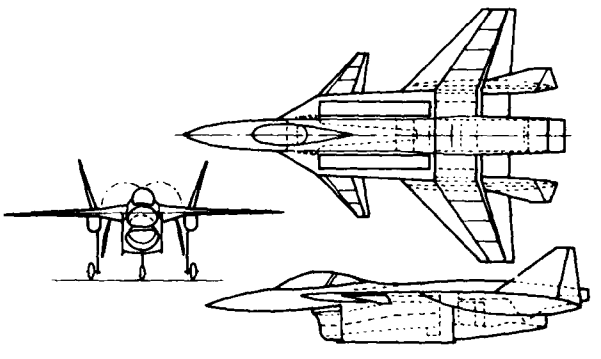

Figure 4. Supersonic VTOL Configuration with Fuselage Thrust Augmentor (de Havilland).

4. PROBLEMS IN FLUID DYNAMICS

The practical problems touched upon in the previous discussion represent only a limited cross-section of those that fall within the scope of this symposium on the "Fluid Dynamics of Jets with Application to V/STOL." Two general areas of interest to fluid dynamics seem to occur and recur whenever V/STOL aircraft configurations are discussed, namely: (1) the mixing between a propulsive stream and a parallel flow in producing thrust and lift, and (2) propulsive flows issuing from, and impinging upon, neighboring surfaces.

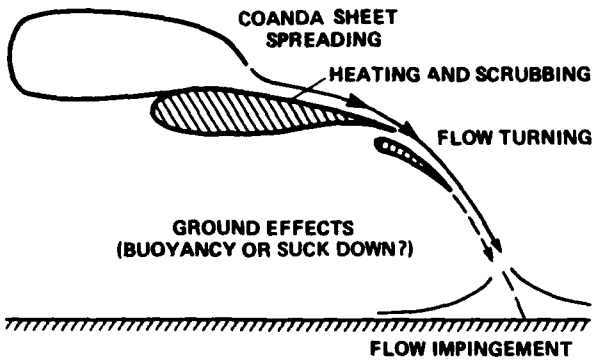

Figure 5. STOL Fluid Dynamics Phenomena.

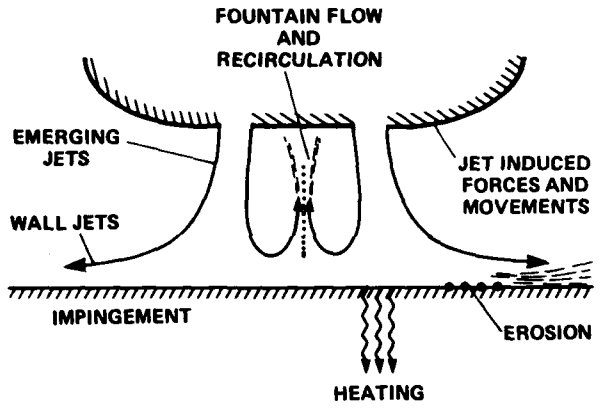

Figure 6. VTOL Fluid Dynamics Phenomena.

First, with respect to the mixing of the propulsive flow with a near parallel stream (Fig. 5), although there is extensive analytical and experimental work reported in the technical literature, additional work is required on the lateral spreading of jet flows over curved surfaces (e.g., the upper surface of a wing) and on the subsequent turning from the stream direction of Coanda surfaces. Such redirection of the flow is, in principle, one of the simplest ways of increasing wing lift without attendant duct losses and without complex mechanical devices. The application of this principle to increasing or controlling the circulation around wings and other lifting devices is receiving attention in both the fixed-wing aircraft and helicopter industries, although the basic phenomena are not yet fully understood.

Second, regarding propulsive flows issuing from, or impinging upon, neighboring surfaces (Fig. 6), a wide variety of fluid dynamical phenomena in two and three dimensions remain to be fully explored and explained. These include: augmentor mixing, internal vorticity within jets in a crossflow, the influence of a closely placed ground plane on the thrust performance of augmentors and jets, flow spreading over the ground plane, stability of fountain flows in the presence of neighboring surfaces, etc. In contrast to the near-parallel flows discussed earlier, this class of flows may be characterized by convection and the generation of shear stress in several directions so that thin layer approximations to the flow are not valid. There has been some progress through the use of computer models of the flow, but these invariably depend on assumptions relating to the nature of turbulent transport of momentum and energy which are not generally based on definitive experiments that pertain to the particular geometry in question. A concentrated effort is needed to combine careful experimental measurement with intelligent computer modelling in order to gain a better understanding of some of the controlling phenomena in V/STOL related fluid dynamics.

5. CONCLUDING REMARKS

The mission needs for V/STOL aircraft are again receiving critical attention for both land-based and sea-based forces. The traditional disadvantages of V/STOL aircraft in terms of payload and range are now being reduced by advances in technology and offset by the introduction of new operational modes for the deployment of these aircraft. The successful operational experience of the Harrier lends credibility to the mission value of V/STOL aircraft.

Improvements in the use of propulsive forces, involving the engine airflow and its interaction with the aircraft aerodynamic flow, are evolving as the critical element in many of the V/STOL aircraft configurations under consideration. In particular, for CTOSL and STOL aircraft, it appears that substantial reductions in takeoff and landing speeds and resulting field lengths can be achieved by placement of the engine exhaust above the wing (upper-surface blowing) without the necessity for increasing the installed thrust of the aircraft. For VTOL aircraft new developments in thrust augmentation (plenum chamber burning or the use of cold-flow ejectors) now permit the consideration of STOVL supersonic fighter/interceptor configurations having little penalty in propulsion system weight when compared to their CTOL counterparts.

The performance and operational effectiveness of these configurations, however, will depend on the successful integration of propulsion and aerodynamics; i.e., a more complete understanding of the fluid dynamics of the propulsive flow and its interaction with the airframe and the ground plane. It seems most likely that this improved understanding, when applied to the most promising configurational concepts, will result in a new generation of V/STOL aircraft that will add a new dimension to the development of air defense forces.

ADDITIONAL READING

The papers below were presented at the AGARD FMP Symposium on the Impact of Military Applications on Rotorcraft and V/STOL Aircraft Design; Paris, France, April 6, 1981.

Andrews, D. R., "Is it Worth Providing Military Aircraft with a V/STOL Capability?" Defense Operational Analysis Establishment, U.K.

Hazen, David C. (Executive Director), "U.S. Military V/STOL; Who Needs It? Wants It? Can Afford It?" Assembly of Engineering, National Research Council, Washington, D.C.

Lewis, W. J. and Simpkin, P., "Multi-Mission STOVL with Vectored Thrust Engines." Rolls Royce Ltd.

Roberts, L., Deckert, W., and Hickey, D., "Recent Progress in V/STOL Aircraft Technology," NASA-Ames Research Center, Moffett Field, California.

Whitley, D. C., "V/STOL Aircraft Technology in Canada," de Havilland Aircraft of Canada.

Investigation of Wall Jets

E. Krause, D. Hänel, N.I.I. Hewedy
Aerodynamisches Institut
RWTH Aachen
Germany

The interaction between wall jets and the main flow is presently being studied by means of experimental and numerical investigations. The following jet-configurations are considered: Tangential injection of a jet through a slot in a forward facing step into a boundary layer, which is tripped at the leading edge, and tangential and slightly inclined injection of a jet through a slot in a rearward facing step. In the following the aims, means of investigations, and results are briefly described.

Tangential injection through a slot in a forward facing step

An incompressible two-dimensional flow, generated in the closed low-speed wind tunnel of the Aerodynamisches Institut was tripped at the leading edge of a flat plate mounted tangentially on the bottom of the test section (Fig. 1). About 1 m downstream from the leading edge a forward facing step with a slot was mounted on the plate. Both, slot height and the height of the step could be varied. The aim of this investigation is to study the deflection of the jet issuing through the slot by the main flow, the wall pressure and shear distribution upstream of the step, the variation of the location of the separation point as a function of Reynolds number, slot- and step height, velocity ratio u_{jet}/u_∞, and the time averaged velocity profiles, and Reynolds stresses upstream of the separation point [1] . The measured velocity profiles are to be compared with predictions obtained through finite-difference approximations of the boundary layer equations, which were closed with simple assumptions for the Reynolds stresses.

The wall pressures were measured through 62 holes (with diameter 0,6 mm) along the center line of the plate with a micromanometer and two-Betz-manometers. Hot-wire anemometers were used for measuring profiles of main velocity and the Reynolds stresses. A pulsed wire-anemometer was used in the separated region flow. The wall shear was determined with a Preston tube.

The experimental results show that the wall pressure distribution is strongly influenced by the slot height and the velocity ratio u_{jet}/u_∞. It was found that all wall pressures can be correlated through similarity parameters (Fig. 2). A rough correlation of the wall shear distribution is also possible. Relatively close agreement is obtained in a comparison of the experimental data with predictions of the separation point (Fig. 3). The comparison of the numerical predictions with the measured velocity profiles revealed, that overall agreement is good, except for the region close to the separation point (Fig. 4). Velocity profiles measured in the separated flow region with a pulsed wire-anemometer (see for example Fig. 5) are presently being used to model closure assumption for the flow in the immediate vicinity of the jet.

Injection through a slot in rearward facing step

In the second part of the investigation the influence of tangential slot injection in an attached boundary layer on the surface pressure distribution has been studied numerically, while experiments are presently being prepared.

The flow has been determined by matching finite-difference solutions of the potential equation and the boundary layer equations for two-dimensional, steady, compressible turbulent flow.

For the solution of the potential equation, relaxation techniques are being employed. The boundary-layer equations are solved by implicit finite-difference techniques. The boundary conditions on the surface are defined either by the no-slip conditions or in the case of injection by prescribed values of velocity and temperature or heat flux. For inclined injection, also the normal velocity at the wall can be prescribed, but it is restricted in its magnitude through the boundary-layer approximation. The matching of the solutions for the inviscid flow and the boundary-layer equations is carried out iteratively. The normal velocity at the outer edge of the boundary layer provides the boundary condition for the solution of the inviscid flow on the surface, and inversely, the outer boundary conditions for the boundary layer are taken from the iterated solution for the inviscid flow. The results obtained so far show that, if the interaction of the boundary layer with the inviscid flow is taken into account, the displacement effect becomes an important factor. Its influence was studied by varying the strength and the position of the injection with respect to the leading edge. Some results are shown here [2] , as an example, for a viscous transonic flow over a 6 percent parabolic airfoil. In Fig. 6 the pressure coefficient of the profile at zero angle of attack is plotted for vanishing injection rate. The inviscid solution clearly shows the shock wave and the past-shock expansion. In the viscous flow the shock is smeared out by viscous effects. The influence of injection immediately upstream of the shock is shown in Fig. 7. The solid curve corresponds to the viscous pressure distribution in Fig. 6. The other curves indicate various injection rates. The pressure distribution with injection shows larger expansions and steeper adverse pressure gradients. This behaviour of the flow can be explained by the variation of the displacement thickness shown in Fig. 8. In the case of injection the displacement thickness decreases near the slot and causes there an additional expansion followed by the recompression shock which moves further upstream. The influence of injection in the supersonic region upstream of the shock is shown in Fig. 9. The pressure distribution is changed significantly by the additional expansion and recompression waves. Similar results were obtained for lifting airfoils. Presently the solution is extended to large injection rates, but restricted to subsonic outer flow [3].

Such a injection was simulated by blowing through a backward facing step. In the slot fully developed flow was assumed. The profile in the inlet was held fixed, but the upstream influence in the boundary layer is considered. Near the slot, strong normal gradients of the tangential velocity cause a large variation of the normal velocity, which can exceed the limit of Prandtl's boundary-layer theory. These phenomena restricted investigations to moderate injection rates in calculation mentioned before, in which iterative coupling of a boundary-layer solution and a potential flow solution was used. The strong interaction between a compressible, laminar or turbulent boundary layer and a jet, was investigated by direct coupling of the numerical solution of the boundary-layer equations and one for the potential equation.

In the vicinity of the injection region the pressure is not prescribed as in Prandtl's theory, but is computed as part of the solution by coupling the boundary layer with the outer potential flow through the displacement thickness. The pressure is split up into one part which is obtained from the solution for the inviscid flow about the body contour and into a second part, calculated from a solution of the small perturbation potential equation (e.g. the Hilbert integral), which takes into account the displacement through the boundary layer. Its discretized form results in a quasi-linear relation between displacement thickness and pressure.

A second relation is obtained for the displacement thickness and the pressure from the boundary-layer equations. When discretized with an implicit finite-difference scheme, they yield a system of linear equations with a tridiagonal matric structure. The recursion relation is used to eliminate u in the expression for the displacement thickness, so that similar to an inverse boundary-layer method, the pressure is given as function of the displacement thickness. This relation is coupled with the relation obtained from the potential equation, and the pressure is updated during the boundary-layer calculation. A global iteration over the length of the interaction region is necessary in order to determine the upstream influence on the pressure. The iteration can be accelerated by overrelaxing the displacement thickness during the iteration.

The coupling was facilitated in the following way: Assume that the compressible flow in the boundary layer can be described by Prandtl's boundary-layer equations, i.e.

$$(\rho u)_x + (\rho v)_y = 0 \tag{1}$$

$$\rho u u_x + \rho v u_y + p_x = (\mu u_y)_y \tag{2}$$

$$\rho u h_x + \rho v h_y - u p_x = (\lambda T_y)_y + \mu (u_y)^2 \tag{3}$$

On the outer edge of the boundary layer the flow is governed by the Euler equations

$$\rho_e u_e u_{ex} + p_x = 0 \tag{4}$$

$$h_e + u_e^2/2 = h_{t\infty} \tag{5}$$

The pressure can be thought of as consisting of one part due to the inviscid flow field $p_o(x)$ and one part due to viscous displacement of the inviscid flow $p_\delta(x)$, so that

$$p(x) = p_o(x) + p_\delta(x) \tag{6}$$

The pressure due to viscous displacement can be determined in the frame of small perturbation theory for subsonic flow, hence

$$p_\delta(x) = -\frac{2}{\pi\sqrt{1-Ma_\infty^2}} \int_{x_o}^{x_1} \frac{1}{\rho_e(\xi)} \frac{dA(\xi)}{d\xi} \frac{1}{(x-\xi)}\, d\xi \tag{7}$$

where A(x) is the mass flux displaced by the boundary layer

$$A(x) = \int_o^\delta (\rho_e u_e - \rho u)\, dy \tag{8}$$

The pressure $p_\delta(x)$ takes into account the displacement upstream from the position x.

The numerical solution can be obtained with an implicit formulation, in which the recursion relation can be written as

$$u_{m,n} = E_{m,n}\, u_{m+1,n} + F_{m,n} + G_{m,n}\, u_{en} \tag{9}$$

The indices m and n count the steps in the directions normally and tangentially to the wall. The quantity u_{en} is the unknown external velocity. The integral for the mass flux can be replaced by a sum in finite-difference formulation, i.e.

$$A_n = \sum_{m=1}^{M} \beta_m\, u_{m,n} + \beta_e\, u_{e,n} \tag{10}$$

The last two equations can be combined to yield

$$A_n = \beta_{1,n}\, u_{e,n} + \beta_{2,n} \tag{11}$$

The coefficients β_1 and β_2 are functions of the recursion coefficients E,F, and G and of the density of the outer edge of the boundary layer. Now, since p_δ is related to u_e, the expression for p_δ can be written as

$$p_{\delta,n} = -\frac{2}{\pi\sqrt{1-Ma_\infty^2}}\left[\sum_{k=1}^{n-1} \alpha_{n,k} A_k + \alpha_{n,n} A_n + \sum_{k=n+1}^{N} \alpha_{n,k} A_k\right] \qquad (12)$$

The value of A_K upstream of the location $x = (n-1)\Delta x$ are taken from the last iteration and the downstream values from the forelast one. If $p_{\delta,n}$ is replaced through the Euler-equation (4), there is obtained

$$u_{e,n} = \alpha_{1,n} A_n + \alpha_{2,n} \qquad (13)$$

so that from eq. (11) and (13) the final result is given by

$$u_{e,n} = (\alpha_{1,n} \beta_{1,n} + \alpha_{2,n})/(1 - \beta_{1,n}) \qquad (14)$$

The calculation is repeated until convergence is obtained. This method of solution can be incorporated into the numerical solution of the boundary-layer equations without effort.

Figs. 10 and 11 show some results obtained for tangential slot injection into a subsonic boundary layer over a flat plate. In Fig. 10a, b, c the velocity profiles near the slot, the displacement thickness and the pressure disturbances through the interaction are shown as a function of the streamwise coordinate. For laminar flow a parabolic velocity profile was assumed for the flow in the slot. The slot is positioned at $x/L = 1$ and strong interaction was considered between $x/L = .3$ and 2. If the blowing rate $\dot{m}_{BL}/(\delta_\infty u_\infty H)$ is greater one, as in this case, the displacement thickness decreases near the slot. The pressure shows a rapid variation near the slot and increases finally in the mixing region downstream from the slot. The opposite behaviour is observed for slot injection with $\dot{m}_{BL}/(\delta_\infty u_\infty H) < 1$ in Figs. 11a, b and c. In this case the displacement thickness increases continously and the pressure increases slightly upstream from the slot and after a relatively small decrease remains constant.

These results show that the boundary-layer can substantially be influenced through the blowing rate, in particular, if the displacement thickness is affected. Small changes in the thickness distribution can cause relatively large changes in the pressure. The method is at the present time being extended to the calculation of transonic boundary layers.

References:

[1] N.I.I. Hewedy: Untersuchung eines ebenen tangential ausgeblasenen Gegenstroms. Thesis at the RWTH Aachen, 1980.

[2] D. Hänel, H. Henke, A. Merten: Transonic flow over airfoils with tangential injection. Proc. of 3. GAMM Conf. on Num. Meth. in Fluid Mech., in Notes on Num. Fluid Mech., 2, Vieweg-Verlag Braunschweig, 1980.

[3] D. Hänel: Laminare Grenzschichtströmung mit Ablösung. Paper on the Jahrestagung der DGLR, 1981, Jahrbuch der DGLR, 1981.

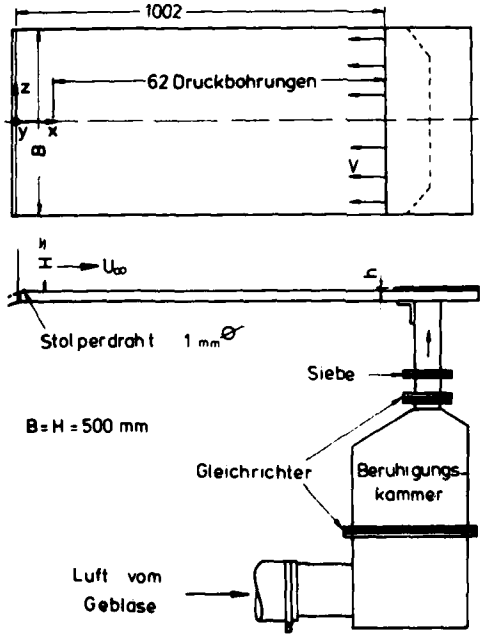

Fig. 1: Experimental set up for tangential injection through a slot in a forward facing step.

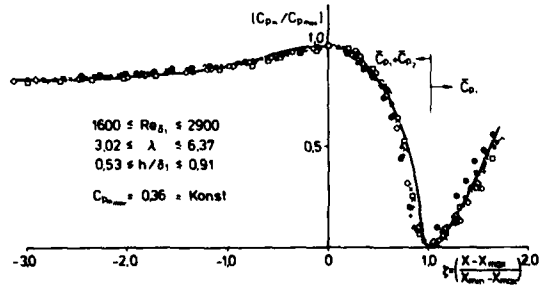

Fig. 2: Wall pressure distribution measured upstream of the slot shown in Fig. 1.

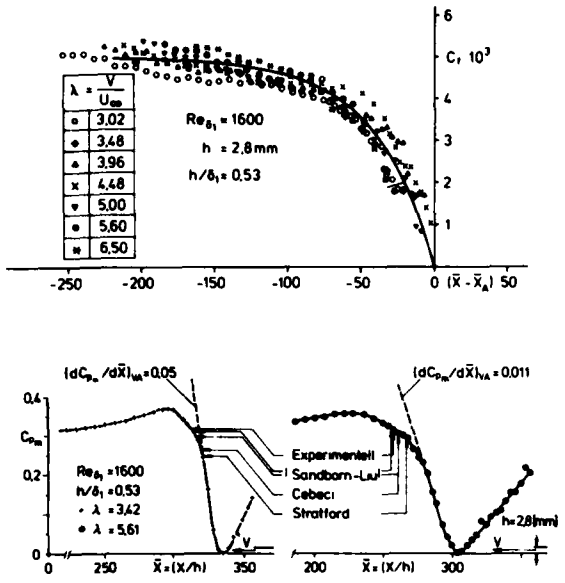

Fig. 3: Wall shear distribution measured upstream of the slot shown in Fig. 1. Comparison with predicted separation points.

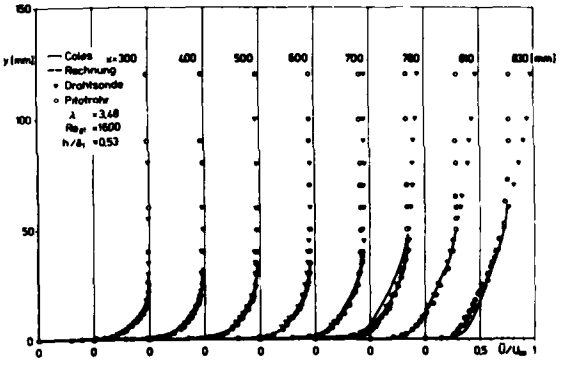

Fig. 4: Time averaged velocity profiles measured upstream of the separation point. Comparison with numerically predicted data.

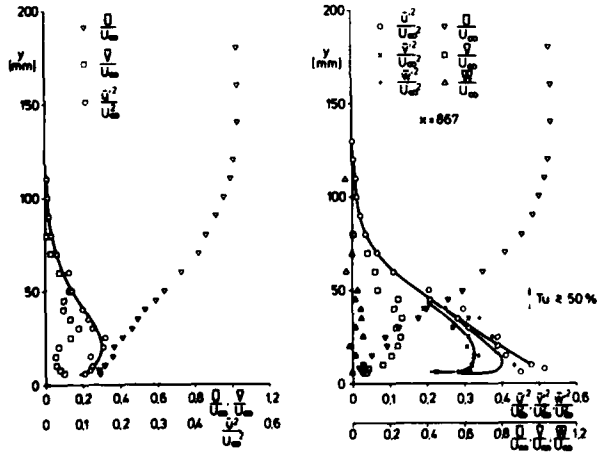

Fig. 5: Measured velocity profiles in the separated region.

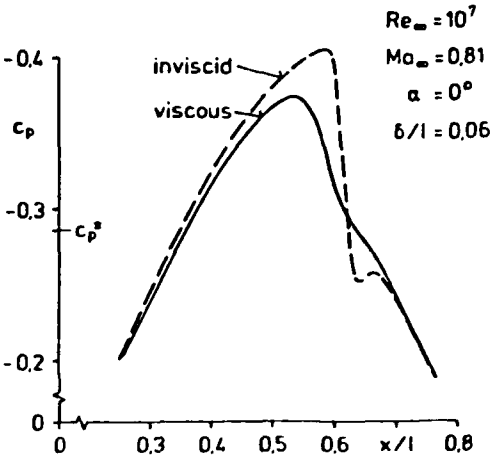

Fig. 6: Pressure distribution without injection for a 6 percent parabolic airfoil.

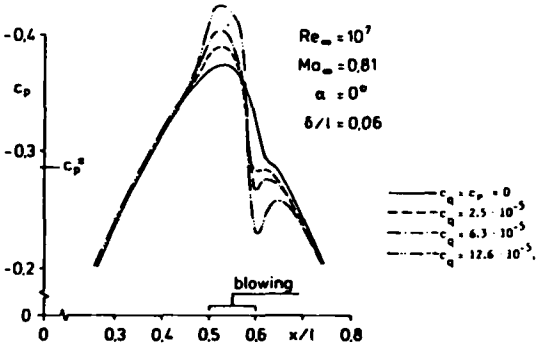

Fig. 7: Pressure distribution with injection on a 6 percent parabolic airfoil.

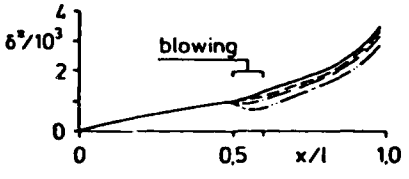

Fig. 8: Displacement thickness for injection rates given in Fig. 7.

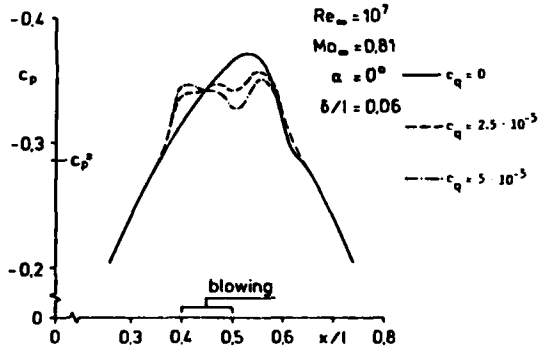

Fig. 9: Pressure distribution for a 6 percent parabolic airfoil.

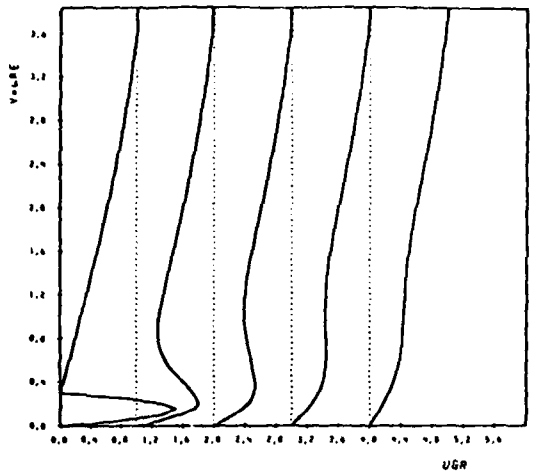

Fig. 10a: Development of the velocity profiles in the boundary layer near the slot.
$Re_\infty \approx 10^5$; $Ma_\infty = .1$; $H/L = 10^{-3}$; $\frac{\dot{m}_{BL}}{\rho_\infty u_\infty H} = 1{,}2$.

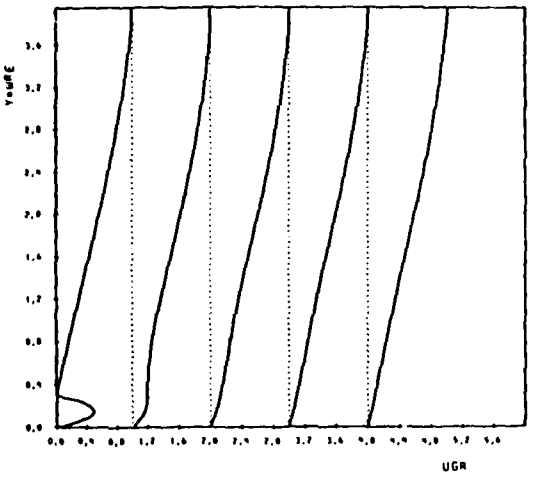

Fig. 11a: Development of the velocity profiles in the boundary layer near the slot.
$Re = 10^5$; $Ma = 0.1$; $H/L = 10^{-3}$; $\frac{\dot{m}_{BL}}{\rho_\infty u_\infty H} = 0.4$.

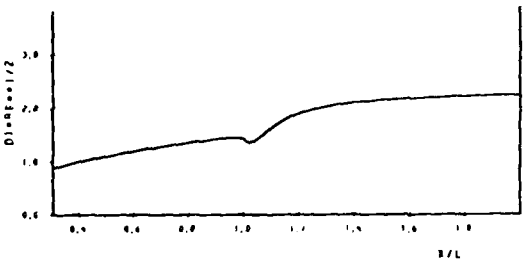

Fig. 10b: Displacement thickness as function of x.

Fig. 11b: Displacement thickness as function of x.

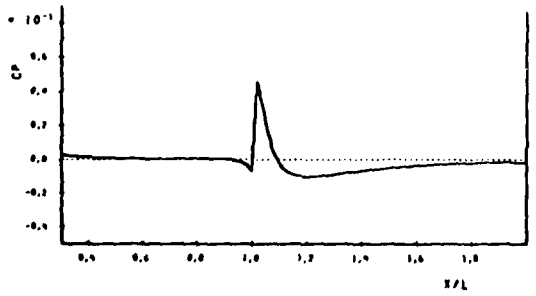

Fig. 10c: Induced pressure as function of x.

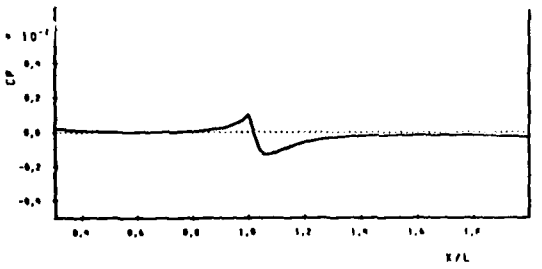

Fig. 11c: Induced pressure as function of x.

THE CALCULATION OF JET INTERFERENCE PRESSURE DISTRIBUTION USING INTEGRAL AND NUMERICAL METHODS BASED ON ACTUAL MEASUREMENTS OF ENTRAINMENT

by

Philip E. C. Ransom[1] and John H. Barnes[2]
School of Mechanical, Aeronautical and Production Engineering
Kingston Polytechnic, Kingston Upon Thames
Surrey KT2 6LA, England

SUMMARY

A discussion of factors influencing interference effects on aerodynamic surfaces surrounding jets is used to introduce a tracer gas method for the measurement of jet entrainment. The application of this technique to the study of axisymmetric free jets is described. A numerical method is developed which employs measured values of entrainment to compute the interference pressure distribution over a flat surface surrounding the jet. Comparisons are made with theory to show that computational inaccuracies may be reduced to required values. Examples are quoted which show that there is good agreement between measured and computed surface pressure distributions.

NOMENCLATURE

B_1, B_2	entrainment coefficients
C	concentration of tracer gas
C_0	concentration of tracer gas at nozzle exit
C_1	concentration of tracer gas in atmosphere
F	interference force
l	length
$\dot{m}_2$	mass flow rate of air leaving nozzle
$\dot{m}_e$	mass flow rate of entrained air
$\dot{m}_g$	mass flow rate of tracer gas
n	positive integer
P	pressure
Q	sink strength
R	radius measured from sink to plane surface
r	horizontal radius from nozzle centre line
r_j	nozzle radius
r_0	surface radius
T	jet thrust
v_j	jet velocity
V_R	radial velocity towards sink
V_r	radial velocity parallel to surface
W	mass fraction of tracer gas in jet at nozzle exit
W_m	bulk mean mass fraction of tracer gas in air
z	axial distance from nozzle exit
θ	angle subtended at jet axis
ρ	density

1. INTRODUCTION

The phenomena of the entrainment of surrounding fluid into a freely emanating jet is well known and this has been utilized for pumping in both high and low pressure applications such as injectors and vacuum pumps. Generally it has been adequate to know the order of total entrainment achieved by a jet stream but now in this era of jet lift aircraft it is of increasing importance to gain as much quantitative data as possible about the variation of entrainment along jet trajectories.

The reason for this need for an extension in knowledge is because of the significance of jet entrainment in the stimulation of static pressure interference on surfaces adjacent to the jet. Entrainment is however, only one aspect of the total flow field which causes loss of lift on the aerodynamic surfaces of jet lift aircraft. A review of a large number of reports (1) attempted to correlate data from different sources but found that there was no large measure of agreement. Furthermore certain aspects of the subject could be seen to have been rather neglected. This was principally due to the fact that in jet aerodynamics there are a large number of variables involved, many of which are mutually independent.

It has been suggested (1) that consideration of the phenomena could be simplified by recognising that it is the flow field, created by the interaction of jet and cross flow, which is responsible for the pressure distribution over the associated aerodynamic surface. This is illustrated in Fig. 1.

The flow field is created by the interaction of many independent variables broadly grouped into two main categories, Geometric and Fluid Dynamic.

The Geometric variables relate to both the nozzle (for example: shape, interior surface, number, size, inclination etc.) and the parts of air frame with which it is associated (for example: main plane, fuselage, tail assembly etc.). The fluid dynamic variables relate to the properties of the jet, and the cross flow, fluids.

Two basic parameters may be used to describe the flow field, created by the above interactions, namely entrainment and blockage. Entrainment is that mass of fluid drawn from the surroundings into the jet. In the case of the free jet this process occurs as a result of turbulent mixing only, but when cross flow is superimposed the deflected jet forms the familiar pattern consisting of two contra rotating vortices which draw additional fluid into the plume. Blockage is the obstruction to the cross flow created by a solid body which has the same geometrical shape as the jet plume developing from the nozzle exit.

The flow field in turn is considered to be responsible for the generation of surface effects such as pressure distributions, interference forces and moments etc.

The emphasis in this study is a closer examination of the flow field, in particular the entrainment into the jet plume and the relationship of this with the induced pressure field. In order to simplify the experimental work, only the case of an axisymmetric jet discharging into stationary surroundings has been examined at this stage. This has had the effect of reducing the number of variables involved and allowing the flow field to be specified solely in terms of entrainment.

Prediction of surface pressure variations have been made by assuming that, for entrainment, the jet can be mathematically modelled on the basis of a line sink sitting along its axial centre line. Using the philosophy that an axisymmetric jet comprises a potential core length followed by a fully mixed development

[1] Senior Lecturer in Aircraft Propulsion
[2] Ph.D.(Eng) Principal Lecturer in Thermofluids & Aerodynamics

it is possible to argue that the sink can consist of two sections one after each other each having its own separate (but constant) radial strength. The basic method of calculation of interference pressure is shown in section 5 and can be seen to have a serious limitation as it leads to the prognosis of an infinite pressure force on an infinite surrounding plane surface.

Surprisingly enough, improvements to this rather basic calculation method have not been possible up to now because of a scarcity of data on how entrainment varies along the axes of jets (1, 2) and indeed how this affects the flow path.

It is worth re-stating at this point that another aspect of jet trajectory and interference is that of blockage. The method of allowing for this as well as entrainment has been referred to by Dr. Bradbury in the general review where by the jet is modelled on the basis of a line doublet but possibly having sinks and sources of unequal strengths.

The difficulty detailed in this introduction led to the aims of this particular investigation.

2. AIMS

The purpose of the investigation was two fold:–

(a) to correct the serious deficiency in entrainment for axisymmetric free jets, including investigating effects on entrainment of independent variables such as flow velocity temperature etc. and geometric configurations.

(b) to improve pressure distribution prediction methods so that it can make use of improved entrainment data. Numerical methods are devised so as to be able to accommodate any pattern of entrainment along the jet trajectory.

3. EXPERIMENTAL TECHNIQUE

The determination of the radially induced entrainment into an axisymmetric free jet was accomplished by adding tracer gas to the jet fluid far upstream of the nozzle, and measuring the decay of tracer concentration in the jet plume.

Air from a compressor was supplied to a plenum chamber where it was mixed with the tracer gas (argon) to produce a gas mixture containing 10% by volume of argon. The mixture was directed through the plenum chamber which contained heaters capable of raising the gas temperature by 500°C, at entry to the convergent nozzle. (Fig. 2) On leaving the nozzle at high subsonic velocity the air/gas mixture was diluted by air entrained into the jet plume. Samples of this air/argon mixture were drawn from the plume through a suction probe attached to a rotary vacuum pump. The probe, which was mounted on to a 3 axis traversing gear, could be positioned at any station up to 120 nozzle radii downstream from the nozzle and up to 20 nozzle radii from the nozzle axis.

Analysis of the gas mixture was carried out using a quadrupole mass spectrometer (3, 4) allowing the concentration of the argon to be measured throughout the jet plume. Typical concentration curves are shown in Fig. 3. The dilution of the tracer gas enabled entrainment at each axial station to be determined.

If tests are carried out with a Schmidt No. of around unity experience has shown that the turbulent Schmidt No. is also of the same order. The consequence of this is that both hydrodynamic and concentration radial profiles are very similar. This is of course very useful when a concentration profile can be obtained more easily than a velocity profile.

4. MEASUREMENT OF ENTRAINMENT

Entrainment into a free jet has been measured many times, usually by mapping the velocity profile in the jet at various stations downstream of the nozzle. From this an estimate of flow in the plume may be made. The variation of velocity in the fully developed part of the jet follows a Gaussian type distribution, so that at the edge of the plume the jet velocity is similar to that of the surrounding fluid and this fact makes it difficult to define the jet boundary with certainty. Since a large proportion of the flow occurs in the low velocity region, accurate determination of entrainment is difficult.

Alternative methods have been attempted but the results are somewhat contradictory (1).

In order to overcome these objections, a flow tracing system in which the jet fluid is doped with a small volume of tracer gas is being developed. This system permits the jet boundary to be determined with greater certainty, and consequently a better measurement of entrainment to be made.

Flow tracing techniques are attractive in the study of complicated flow systems, particularly where analysis has proved to be impossible. For applications in air such tracers as smoke, water droplets, and tufts have been used, but the full benefit is gained only if the tracer faithfully follows the flow pattern dictated by the fluid under examination, if it can be detected and (where necessary) measured accurately and the presence of the tracer does not modify the fluid properties to an unacceptable degree.

Most tracers are unable to satisfy these requirements entirely so it is important to establish limitations before results from a given flow system are of use.

In the past tracer systems have been detected visually and recorded by a photographic process. The development of relatively cheap mass spectrometers and other systems now permits rapid chemical analysis, so that non-visual tracers may be employed.

The tracer gases used in this work have similar mass numbers, similar densities, and similar molecule sizes to that of the fluid being traced. Thus the tracer will follow the trajectory of an air flow much more faithfully than will smoke particles, dust particles or water spray, where particle sizes are many orders of magnitude larger than the molecules of nitrogen and oxygen. With a tracer gas even large accelerations of the flow may be followed accurately.

The detection and measurement is by mass spectrometer (3, 4) which has sufficient sensitivity to detect the presence of the tracer better than 100 parts per million. In addition the proportion of gas in air by volume or by mass may be determined as well as the concentration, i.e. the partial density.

The entrainment between the nozzle exit station and any parallel axial station may be obtained as follows:–

Let mass flow rate of air through the nozzle he $\dot{m}_a$, let the mass flow rate of tracer gas through the nozzle be $\dot{m}_g$ and let the mass flow rate of entrained air, drawn into the jet between the nozzle and plane Z – Z distance z from nozzle be $\dot{m}_e$.

Total mass flow at nozzle exit = $\dot{m}_a + \dot{m}_g$ (4.1)

Total mass flow at any station Z – Z = $\dot{m}_a + \dot{m}_g + \dot{m}_e$ (4.2)

let W be the mass fraction of tracer gas in the jet at nozzle exit

$$\therefore \quad W = \frac{\dot{m}_g}{\dot{m}_a + \dot{m}_g} \tag{4.3}$$

let W_m be the bulk mean mass fraction of tracer gas in the jet at axial station Z – Z

$$\therefore \quad W_m = \frac{\dot{m}_g}{\dot{m}_a + \dot{m}_g + \dot{m}_e} \tag{4.4}$$

divide 16 by 17

$$\frac{W}{W_m} = \frac{\dot{m}_a + \dot{m}_g + \dot{m}_e}{\dot{m}_a + \dot{m}_g} \tag{4.5}$$

$$\therefore\ W(\dot{m}_a + \dot{m}_g) - W_m(\dot{m}_a + \dot{m}_g) = W_m\dot{m}_e$$

$$\text{Whence } \dot{m}_e = \left(\frac{W}{W_m} - 1\right)\left(\dot{m}_a + \dot{m}_g\right) \tag{4.6}$$

For a given experimental condition, the values of $\dot{m}_a$, $\dot{m}_g$ and W will be known. Thus it is necessary to measure W across the jet and determine from this the bulk mean value of W_m for a particular axial station in order to obtain the entrainment.

5. ENTRAINMENT IN AN AXISYMMETRIC JET

As a jet discharges into a body of initially stagnant fluid, it induces the surrounding fluid to flow radially inwards, and this effect increases the mass flow in the jet as the distance increases from the nozzle. Theory assumes that the entrainment process occurs at constant pressure, but clearly there must be small but significant pressure differences to establish the movement of surrounding fluid into the jet stream. G. I. Taylor established a technique for determining the streamline pattern by replacing the jet with a sink. This approach has been used by Wygnanski (5) and is developed further here to compute the pressure distribution on a flat surface.

When discharging into still air jets comprise two distinct regions. During the first few jet diameters downstream from the nozzle the jet possesses a potential core, that is a zone in which the fluid velocity remains, unaffected by and unmixed with, surrounding fluid. Within the potential core the velocity remains unchanged from its magnitude in the plane of the nozzle exit. With increasing distance downstream, the cross sectional area of the potential core decreases as the thickness of the mixing layers increase until they reach to a maximum at the end of the potential core.

At this point the jet is said to be fully developed.

5.1 *Integral Method*

5.1.1 RADIAL VELOCITY CALCULATION

Consider an elemental length of line sink d_z at vertical distance z as shown in Fig. 4. The Velocity at point P along R due to a sink strength Q per unit length is given by:

$$V_R = -\frac{Qd_z}{4\pi R^2} \tag{5.1}$$

Now the horizontal component of velocity (V_r) at point P is $-V_R \sin\theta$

$$\therefore\ V_R = -\frac{Qd_z \sin\theta}{4\pi R^2} \tag{5.2}$$

To obtain the effect of an impervious surface, OP, the well known method of mirror images is used by introducing a line sink of strength Q going in the minus Z direction. Consideration of an elemental section length d_z distance $-z$ completes the procedure and it can be seen that the velocity along the surface is then effectively doubled since two sinks now induce the flow.

$$\text{Thus}\quad V_r = -\frac{2Qd_z \sin\theta}{4\pi R^2} \tag{5.3}$$

The inflow velocity at P due to a line sink extending from the origin O to infinity is given by:–

$$V_r = -\int_{z=0}^{z=\infty} \frac{Qd_z}{2\pi R^2}\, \sin\theta \tag{5.4}$$

$$= -\int_{\theta=\pi/2}^{\theta=0} \frac{Q \sin\theta\, d\theta}{2\pi r} \tag{5.5}$$

Clearly it can be seen that the velocity, V_r, at any radius r, and hence the pressure distribution over a flat surface, depends upon the assumptions made concerning the entrainment rates both in the potential core and the fully developed region.

5.1.2 POTENTIAL CORE REGION

It is assumed that the potential core region has a length equal to n x r_j where $0 < n < 12$ and the volumetric entrainment rate is given by $2\pi B_1 r_j v_j$ where B_1 is a constant independent of length v_j is the jet velocity and r_j is the jet radius.

From Fig. 2.:–

$$z = n.r_j,\ \theta = \tan^{-1}\frac{r}{n r_j}$$

$$\theta = \mathrm{Tan}^{-1}\, r/nr_j$$

$$\therefore\quad V_r = -\int_{\theta=\pi/2} \frac{2\pi B_1 r_j v_j}{2\pi r} \cdot \sin\theta\, d\theta$$

$$= \frac{B_1 r_j v_j}{r}\left\{\frac{1}{(1 + \frac{r^2}{(nr_j)^2})^{1/2}}\right\} \tag{5.6}$$

5.1.3 FULLY DEVELOPED REGION

Beyond the potential core region it is assumed that the entrainment is given by:–

$$Q = 2\pi B_2 r_j v_j$$

$$\therefore \quad V_r = -\int_{\theta=\tan^{-1}\frac{r}{nr_j}}^{\theta=0} \frac{B_2 2\pi r_j v_j \sin\theta}{2\pi r} d\theta$$

$$= \frac{B_2 r_j v_j}{r}\left\{1 - \frac{1}{(1+\frac{r^2}{(nr_j)^2})^{\frac{1}{2}}}\right\} \qquad (5.7)$$

5.1.4 COMBINED REGION

The horizontal or surface velocity due to entrainment along the complete jet paths is given by the addition of equations 5.6 and 5.7

$$V_r = \frac{r_j v_j}{r}\left\{B_2 - \frac{B_2 - B_1}{(1+\frac{r^2}{(nr_j)^2})^{\frac{1}{2}}}\right\} \qquad (5.8)$$

by substituting the values given by Wygnanski (5)

i.e. $B_1 = .032$, $B_2 = .114$

a particular equation for V_r is obtained, that is,

$$V_r = \frac{r_j v_j}{2\pi r}\left\{0.716 - \frac{0.515}{(1+\frac{r^2}{(nr_j)^2})^{\frac{1}{2}}}\right\} \qquad (5.9)$$

5.1.5 PRESSURE DISTRIBUTION OVER A PLANE SURFACE

For incompressible flow conditions the pressure distribution over a plane surface is given by:–

$$P_s = \tfrac{1}{2}\rho_0 V_r^2 \qquad (5.10)$$

where the density ρ_0 is constant

Substituting from equation (5.8)

$$P_s = \tfrac{1}{2}\rho_0 \frac{r_j^2 v_j^2}{r^2}\left\{B_2 - \frac{B_2 - B_1}{(1+(\frac{r}{nr_j})^2)^{\frac{1}{2}}}\right\}^2 \qquad (5.11)$$

5.1.6 INTERFERENCE FORCE CALCULATIONS

The force on an elemental ring is given by:–

$$dF = 2\pi r dr.\, P$$

where P is the suction pressure acting on the surface at radius r.

Hence the total suction force on a defined circular area is:–

$$F = -\int_{r_j}^{r_0} 2\pi\rho_0 \frac{V_1}{2}^2 r\, dr \qquad (5.12)$$

by substitution of the expression for V_r in equation (5.11) and integrating the following force equation is obtained:–

$$F = \pi\rho_0 r_j^2 v_j^2\left\{B_2^2 \log_e\frac{r_0}{r_j} - (2B_2(B_1 - B_2))\log_e\left\{\frac{\sqrt{1+n^2 r_j^2/r_0^2} - n\, r_j/r_0}{\sqrt{n^2+1} - n}\right\} + (B_2 - B_1)^2 \log_e\left\{\frac{\sqrt{n^2+1}}{\sqrt{1+n^2 r_j^2/r_0^2}}\right\}\right\} \qquad (5.13)$$

It is useful to non dimensionalise by dividng by the jet thrust T, giving the ratio

$$\frac{F}{T} = \left\{B_2^2 \log_e\frac{r_0}{r_j} - (2B_2(B_1 - B_2))\log_e\left\{\frac{\sqrt{1+n^2 r_j^2/r_0^2} - n\, r_j/r_0}{\sqrt{n^2+1} - n}\right\} + (B_2 - B_1)^2 \log_e\left\{\frac{\sqrt{n^2+1}}{\sqrt{1+n^2 r_j^2/r_0^2}}\right\}\right\} \qquad (5.14)$$

where $T = \rho_0 \pi r_j^2 v_j^2$

Using the values of B_1 and B_2 suggested by Wygnanski for potential core lengths from 0.5 to 6 jet diameters ($1 < n < 12$), Fig. 5, was plotted for values of plate radius up to 8 jet radii. Measurements reported in Ref. 6 have been added to the graph.

The discrepancy between theory and practical results indicates the need for a closer examination of the entrainment into the jet.

It is to be expected that at large values of plate radius r_0, a limiting value of suction force would be reached. However it is of significance that the theory does not comply with this basic premise. Equation (5.14) shows that the suction force/jet thrust increases continuously with plate radius which suggests that the assumptions regarding entrainment must be inadequate.

5.2 Numerical Technique

5.2.1 SURFACE VELOCITIES

In this section a numerical method is described which can be used to evaluate surface pressure distributions. As a start it is assumed that the axial line sink system OZ (Fig. 4) comprises a number of finite cylindrical elements each having an individually assigned sink strength and, for example, each having the length of the initial jet radius r_j.

The strength of these individual sinks is taken to vary with axial distance, so that at distance z ($= n.r_j$) from the nozzle, the sink strength is written as Qn.

From equation (5.3) the surface velocity at point P (see Fig. 4), due to one sink of strength Qn at distance z from the nozzle, is given by:–

$$(\Delta V_r)_z = -\frac{Qn\, r_j}{2\pi R^2} \cdot \sin\theta \qquad (5.15)$$

$$= -\frac{Qn\, r_j \cdot r}{2\pi(r^2 + n^2 r_j^2)^{3/2}} \qquad (5.16)$$

where $\sin\theta = \frac{r}{R} = \frac{r}{\sqrt{r^2 + n^2 r_j^2}}$.

The summation of this equation for n 0 to ∞ permits the calculations of the surface velocity at point P due to a continuous line of finite sink elements extending to infinity.

That is:–

$$V_r = \frac{r_j r}{2\pi} \lesssim_{n=0}^{\infty} \frac{Qn}{(n^2 r_j^2 + r^2)^{3/2}} \qquad (5.17)$$

5.2.2 SURFACE PRESSURE DISTRIBUTION

Evaluation of the surface pressure distribution is obtained by substitution of (5.17) into (5.10) hence

$$P_s = \tfrac{1}{2}\rho_0 \frac{r_j^2 r^2}{4\pi^2} \left\{ \lesssim_{n=0}^{n=\infty} \frac{Qn}{(n^2 r_j^2 + r^2)^{3/2}} \right\}^2 \qquad (5.18)$$

5.2.3 ACCURACY OF THE NUMERICAL METHOD

Due to the natural decaying effect of a jet flowing into stagnant surroundings it is obvious that some finite axial distance of entrainment should be able to be used to determine pressure distributions within say 1%. Furthermore the length of sink element used in the calculations will also affect the accuracy of the pressure distribution prediction. Consequently an analysis has been made to find the optimum total entrainment axial distance, and the optimum axial sink element length.

This has been accomplished by comparing the results of the numerical method with analytical method using entrainment rates suggested by Wygnanski (5). The required degree of accuracy for pressure distribution over an area of 6 jet radii is obtained with an effective jet trajectory length of 120 jet radii. In addition each unit length of trajectory (length of one jet radius) is divided into 100 segments. Fig. 6 shows the effect of increasing the effective length of trajectory over which entrainment is considered to be active and the number of segments by which each unit of trajectory is divided during computation.

6. RESULTS

6.1 Concentration Profiles

Radial traverses of various axial stations downstream of the nozzle exit were made using the suction probe attached to the fast inlet system of the mass analyser. At each radial station measurements of tracer gas concentrations were made and Fig. 3 shows concentration distributions in a typical jet. It is possible to normalise these profiles with reference to the radius at which the concentration has fallen to one half the centreline value. These indicate that all radial distributions lie on a single curve.

6.2 Calculated Entrainment Values

Using the tracer gas technique measurements of the entrainment into the jet have been made. Fig. 7 shows the results of this integration for two jet conditions both at the same jet mach number but with differing initial jet temperatures. Both jets exhibit similar trends showing an almost linear increase of mass flow in the jet plume with axial distance from the nozzle exit. It is noticable that at axial distances greater than 40 jet radii the rate of entrainment tends to decrease

This effect contradicts data from another source (1) which suggested that entrainment increased linearly with axial distance from the nozzle. However it seems reasonable to suppose that at very large distances from the nozzle, where the jet velocity has virtually decayed to zero then the entrainment also should be zero.

The effect of enhanced jet temperature is to increase the rate of entrainment at least in the region closest to the nozzle exit. At large distances from the nozzle, where the temperatures of both plumes tend towards the same value, it is possible that entrainment rates may become similar. Further data is necessary before this can be confirmed.

6.3 Pressure Distributions

Using the measured values of entrainment shown in Fig. 7 the numerical technique described in section 5.2 was used to evaluate the surface pressure distribution over an infinite flat surface out to a radius equal to 6 jet radii. Comparison was made with predictions using constant entrainment rates (Section 5.1) and with values measured during the experiments (Figs. 8 and 9). It is encouraging to note that the predictions made with the numerical method using measured values of entrainment are in reasonable agreement with the measured pressure distribution for both test conditions.

7. CONCLUSIONS

The tracer technique is a useful method for the study of jet interferance phenomena including flow field and surface effects. The numerical method used to predict the surface pressure distributions over a flat surface shows that reliable entrainment data is required if accuracies are to be improved.

The data reported here is limited by the restrictions imposed by the measuring equipment. Clearly considerable improvements could be obtained if measurements of entrainment were taken at stations much further away from the nozzle exit plane.

8. REFERENCES

1. Ransom, E. C. P. & Wood, P. M. "Jet Interference Literature Survey and Critical Review.". Prepared for Procurement Executive, Ministry of Defence. Contract Number AT/2055/04SRA Kingston Polytechnic Report TFAR 75/1/ER, June 1975.

2. Smy ,J. R. & Ransom, E. C. P. "The Structure of Single Jets at Large Angles to a Cross Flow." Prepared for Procurement Executive, Ministry of Defence. Contract Number K/A72c/352 Hawker Siddeley Aviation Report HSA-KAD-R-GON-2288, June 1976.

3. Phipps, P.D. "An Investigation into Streamline Mixing into Constrained Laminar and Turbulent Axisymmetrical Flow using a Mass Spectrometer – Tracer Gas Analysis." M.Phil. Thesis, Kingston Polytechnic, June 1981.

4. Ransom, E. C. P., Barnes, J. H. & Phipps, P.D. "An experimental investigation of the disperson of a gas jet in a coflowing stream of air." Proceedings of the 2nd International Conference on Numerical Methods in Laminar and Turbulent flow, Venice. Pineridge Press, July 1981.

5. Wygnanski, I. "The flow induced by Two Dimensional and Axisymmetric Turbulent Jets issuing normally from an Infinite Plane Surface." The Aeronautical Quarterly, Vol. 15, p.373–380, 1964.

6. Mayson I, Ogilvie, F. B. & Harris, K. D. "An investigation under Static External Flow Conditions of the Axial Force Induced on Circular Flat Plates Surrounding Simple Uniform and Co-axial Jets Exhausting Normally to the Plates." Hawker Siddeley Aviation Ltd., Hatfield Research/1010/IM/FBO/DKS. December 1971.

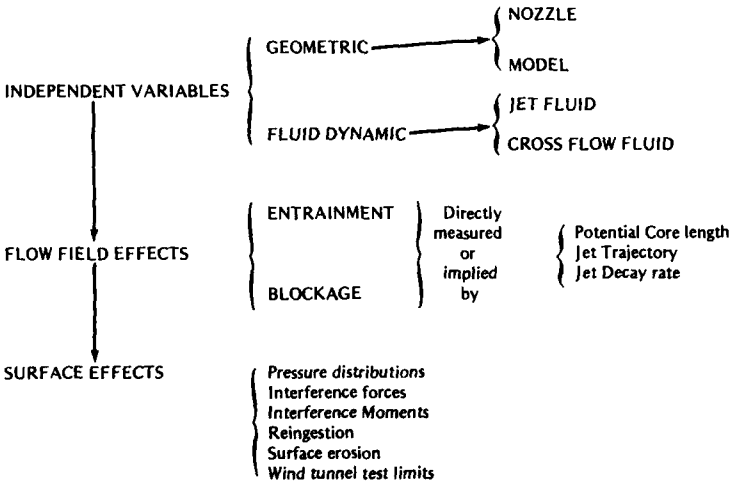

Fig. 1

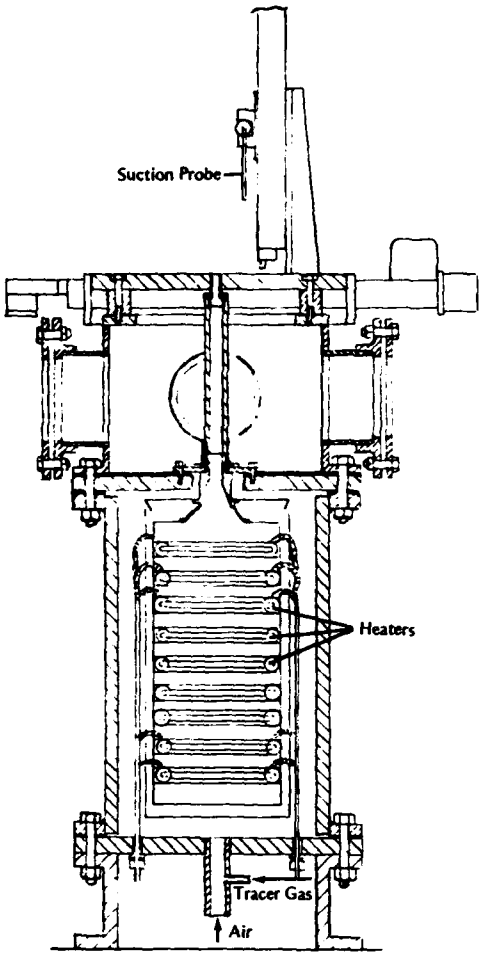

Fig. 2. Free Jet Rig

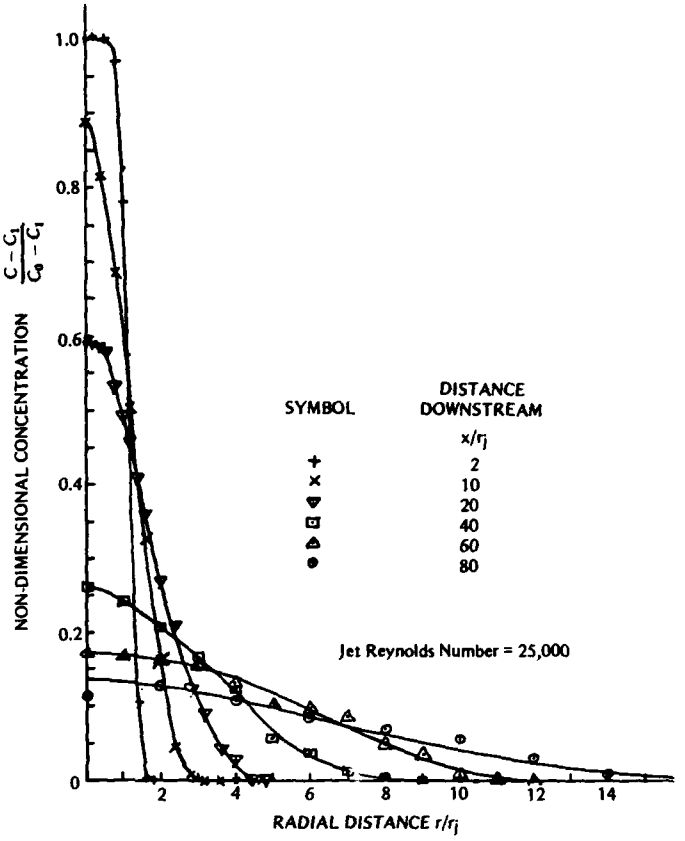

Fig. 3. Radial Decay of Concentration at various Downstream Stations

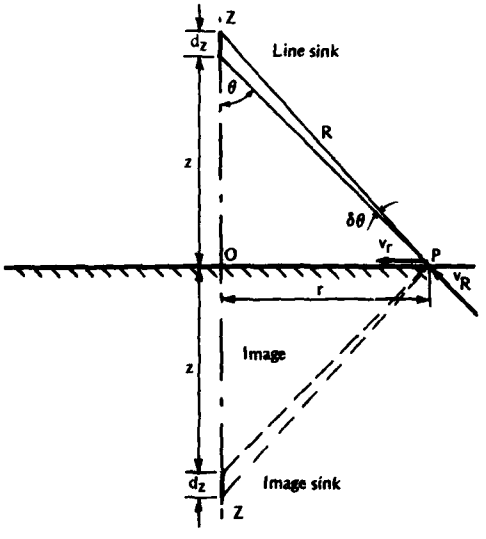

Fig. 4.

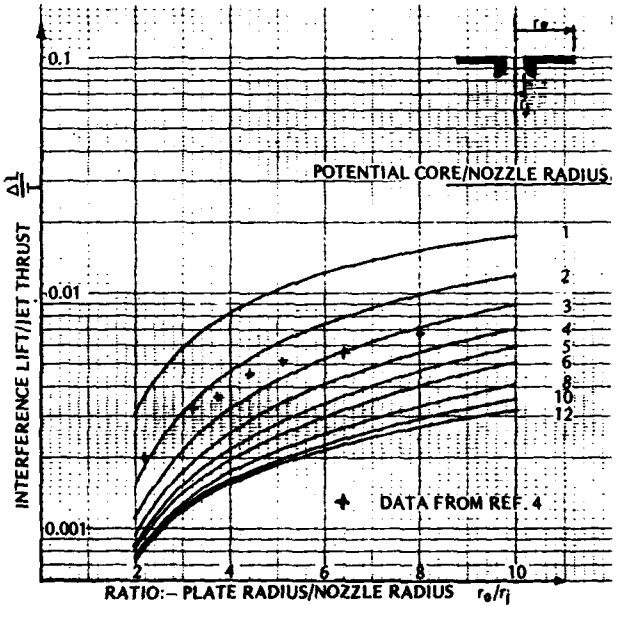

Fig. 5. Interference Lift/Jet Thrust against Plate Radius Ratio for Various Potential Core Lengths (Entrainment Coefficients Constant)

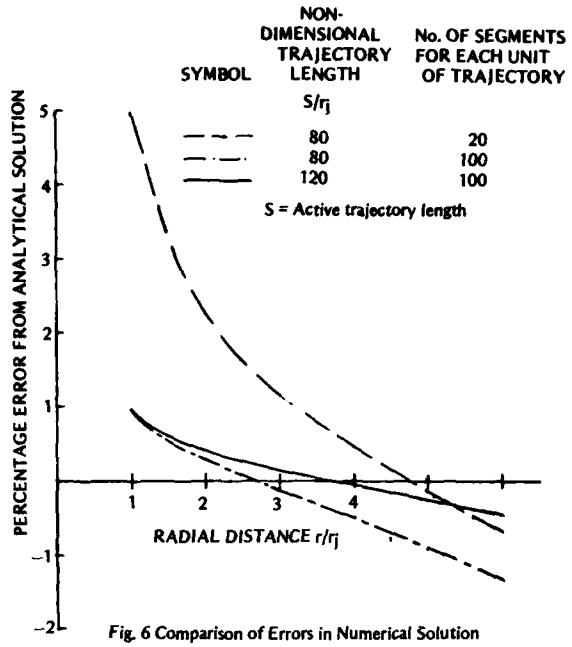

Fig. 6 Comparison of Errors in Numerical Solution

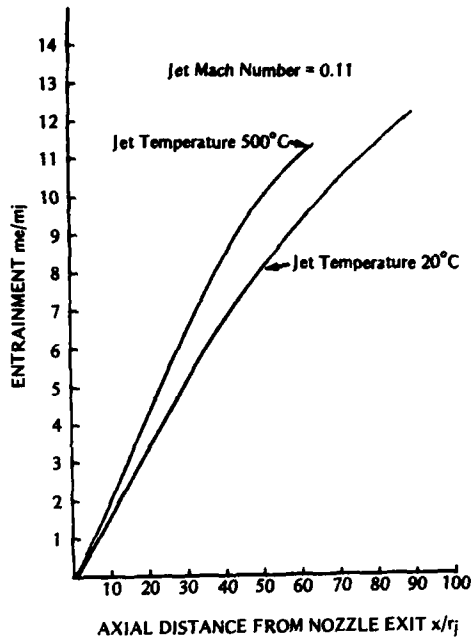

Fig. 7 Entrainment into an Axisymmetric Free Jet

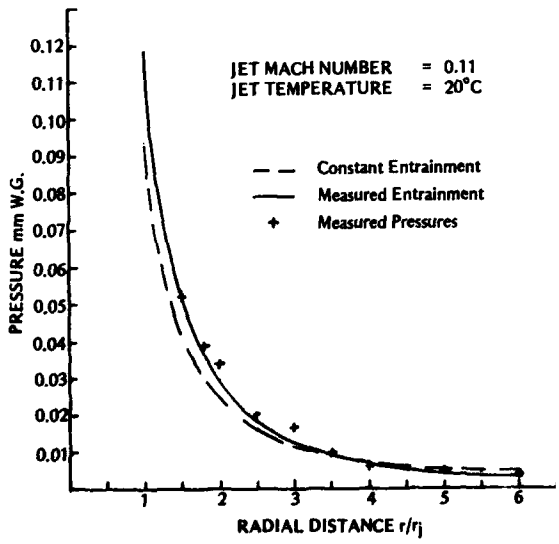

Fig. 8 Pressure Distribution Over Flat Surface

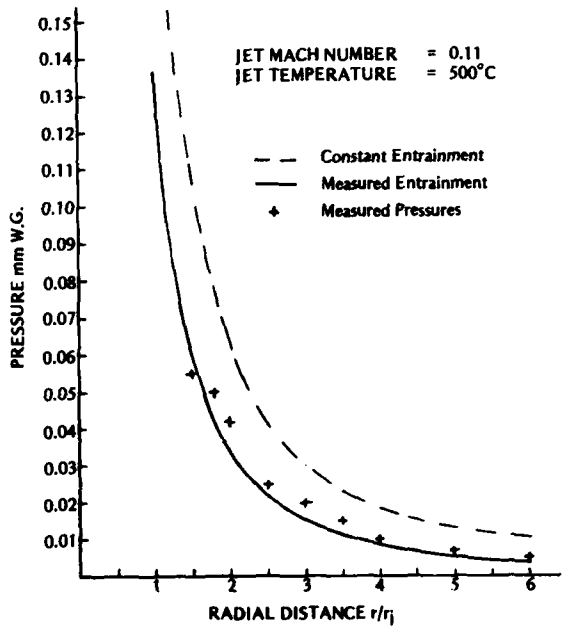

Fig. 9 Pressure Distribution Over Flat Surface

SUMMARY REMARKS

on the AGARD/FDP SYMPOSIUM

on the Fluid Dynamics of Jets

with Application to V/STOL

Dr. Ir. B.M. Spee
National Aerospace Laboratories (NLR)
Netherlands

It was about two years ago now that Alec Young and Brian Quinn, the co-chairmen of the programme committee of this symposium asked me to volunteer in writing the technical evaluation report of the meeting. Because I was the author of the TER of the last symposium of the Fluid Dynamics Panel on V/STOL aerodynamics in 1974, it would be easy for me to give a judgement on the progress in this area that has been made since then. Then during the last meeting of the FDP in Toulouse in the spring of this year, after the final decisions on the programme of this meeting had been made, Alec Young convinced me that since I, as the author of the TER had to sit down here all the time and to listen very attentively to all the presentations, I would be in an excellent position to make the closing remarks at the end of the meeting.

I accepted the invitation, and I really believed at that time that it would not be difficult to summarize the main conclusions from the papers that were to be presented this week. However, in the course of the symposium, listening to the authors and to the discussions after the papers, I realized that this was a complete mistake. I now think that it is quite difficult to draw conclusions immediately after a meeting like this one. I feel that I need, in fact, some more time to think over many points that have been discussed this week. Nevertheless, I will do the job that I have accepted, and I will give my personal feelings about what this symposium has put forward. But I would like to stress that it is to be considered as a first reaction only, and that it may be well possible that the final conclusions that will be given in the TER will be somewhat different.

Now to make this even more probable, I would like to ask you to give your reaction to these concluding remarks. I know that there will be no more time for further discussions at this meeting, because if that would be the case, my remarks would quite certainly not be the closing remarks. However, there always is the possibility of correspondence by letter, and I would appreciate to receive comments from you. It would certainly help me in writing a TER that really brings the message of the symposium to the attention of people that are responsible for research programmes and research budgets. This is, I think, the main purpose of a technical evaluation report.

First of all, an observation on the way this symposium has been organized. I found the formula that has been applied with a general review paper on the subject of the symposium and survey papers from experts on the different session topics of the meeting, very effective. I can say this although being a member of the programme committee because, as far as I remember, this formula has been proposed by the co-chairmen of the committee.

The general review paper by Bradbury, the survey paper by Barche on jet interaction with neighbouring surfaces, the survey paper by Mathieu on jet structure, the survey paper by Margason on windtunnel simulation, the survey paper by Quinn on injection and thrust augmentation and the survey paper by Donaldson on the modelling of turbulent flows, all gave an excellent view of the state of the art of the different aspects of jets and V/STOL aerodynamics, and they together form a framework that has been of much help to those of us that are not experts on all these subjects to put the different contributions in the right perspective.

A striking aspect of the programme to me as an experienced listener at FDP meetings, was the fact that so many of the papers presented described experimental investigations of an exploratory nature; that is, aiming at a better understanding of the different types of very complex three-dimensional turbulent flow phenomena that are in general associated with jets. Apart from the review and survey papers and the invited short contributions, there have been only four out of twenty one papers that reported in particular on activities in the field of the development of prediction methods. There was a paper by McQuirk on "a row of jets in a crossflow", a paper by Baker on "a three-dimensional interaction algorithm for numerical prediction of V/STOL jet-induced flows", a paper by Walters on a "method for the prediction of V/STOL propulsion induced aerodynamics", and a paper by Kotansky on "the modelling and prediction of multiple jet V/STOL aircraft flowfields in ground effects". I will come back to these papers in a moment.

In my opinion, it is not just accidental that the papers on experimental investigations are practically all from universities, and that the large national research institutes hardly contributed to the symposium. It is quite usual that the universities are engaged in this type of exploratory experiment which is relatively cheap. The national research institutes generally concentrate on experiments that are set up particularly as a check on theoretical prediction methods. This type of experiment usually asks for a lot of details and a very high accuracy, and they are consequently quite expensive in general.

Obviously, there is still a large need for such exploratory experimental investigations on V/STOL aerodynamics, because our knowledge of these flow phenomena is rather limited. It means that the progress on V/STOL aerodynamics has not been very impressive in the last ten years. Let me go back to that last meeting of the FDP on V/STOL aerodynamics in Delft in 1974. In the opening lecture of that symposium, David Hickey of Ames Research Center said that after twenty years of research the western world had only one operational V/STOL aircraft, the Hawker Siddeley Harrier. I have heard the same remark several times again at this meeting. Hickey said he found the failure to use V/STOL technology in civil transportation systems disappointing and suggested that improvements in aerodynamics could bring V/STOL aircraft in a better position in competition with conventional aircraft.

The general feeling at the 1974 meeting was that the situation in the field of research on V/STOL aerodynamics was far from promising. The majority of the papers at that symposium reported on research that was carried out quite some time before the meeting and on projects that had already been stopped at that time. It was stated that the basic flow phenomena were well understood, but that one was still far away from sufficiently accurate theoretical prediction methods.

Now, what happened since that meeting. The fuel crisis of 1974 almost completely killed the interest in civil V/STOL applications. Also, the activities on military V/STOL aircraft projects decreased further. In Europe only the United Kingdom kept some interest in military V/STOL aircraft, but I have the impression that much of the further development of the Harrier was left to McDonnell-Douglas. The activities in the United States were as well limited. Apart from the work on the Harrier, the only recent activity that resulted in real prototype aircraft was the STOL transport project, which as it looks now, will probably not have a further continuation. The main interest nowadays seems for V/STOL aircraft designed to operate from damaged runways and from smaller ships as was mentioned by Roberts.

The absence of V/STOL projects, of course, also decreased the budgets that had been made available for research in this field, and consequently, the extent of the research activities also in aerodynamics. This happened especially in Europe where, particularly in France and Germany, the research on V/STOL aerodynamics came to an almost complete standstill. What has been put forward at this symposium reflects this situation.

As was the case after the 1974 meeting, I think that it has to be said again that the progress on V/STOL aerodynamics is not very impressive. Our knowledge of the fluid dynamics of jets applied to V/STOL increased considerably, but it is still in an early stage. Fortunately, aircraft designers in general and designers of V/STOL aircraft in particular are obviously very intelligent people. They are able to make reasonably good aerodynamic designs with only a minimum of design tools; that means theoretical prediction methods and an experimental data base, in hand. One could say that aerodynamic design of V/STOL aircraft in a sense is more art than science today.

As far as the experimental data base is concerned, the problem is that the number of variables and options, and therefore the number of possible shapes and parameters in the aerodynamic design is so large that such an experimental data base with enough adequate information for the designer is very difficult to build up. The designer of V/STOL aircraft is also facing a lack of powerful theoretical prediction methods. Most of the prediction methods are based on potential flow methods using empirical input to represent the propulsive flow characteristics. The existing prediction methods are very limited in their range of valid application and in the extent of their verification with experimental results. The designer of V/STOL aircraft is obviously in a much less comfortable position than his colleague, the designer of conventional aircraft. The designer of conventional aircraft nowadays has very sophisticated prediction methods in hand; methods that are based on a combination of potential flow calculations and viscous flow boundary layer type calculations, with additional modelling of the interaction of these two. A very important aspect in the modern design procedures for conventional aircraft is the fact that some of the methods can be used in an inverse way, which makes it possible to find the aircraft geometry for a given desired pressure distribution, and consequently to really optimize the shape of the aircraft. I think that such inverse methods will be unattainable in the near future for V/STOL aircraft.

The paper by Kotansky on "the modelling and prediction of multiple jet V/STOL aircraft flow fields in ground effect" is typical for how the designer of V/STOL aircraft currently uses a mixture of empirical methods and potential flow methods for the engineering prediction of ground flow fields, induced suckdown and fountain formation for multiple jet aircraft. I think it is quite impressive as an engineering method, but still rather primitive compared with the sophisticated methods used nowadays to design conventional aircraft.

The absence of an adequate experimental data base and sophisticated theoretical prediction methods makes the designer of V/STOL aircraft very much dependent on wind tunnel testing. In using the wind tunnel, the designer of V/STOL aircraft is faced with another additional problem, and that is how to extrapolate the results of the tests to full scale, free flight conditions. It has to be realized that in the case of testing of conventional aircraft, the availability of calculation methods plays an important role in the interpretation of wind tunnel results and in the extrapolation of those results to full scale data. They are used rather intensively for the interpretation of differences between free flight test data and wind tunnel data. For V/STOL testing this can be quite a difficult problem as I understood from the paper by Haftmann on tests on a V/STOL fighter type aircraft.

Wind tunnel testing technique itself is rather complicated for V/STOL configurations, as was indicated by Margason. His paper has shown that relatively small variations in model geometry can have a large effect, and this indicates the need for testing on large models.

I was surprised that the problem of wall interference effects for V/STOL testing obtained hardly any attention at this symposium. This subject has been studied quite intensively during the fifties and sixties. The important phenomenon is the non-linear behaviour of the wall effect due to the influence of the tunnel walls on the position of the jets. I do not have the impression that the problem of wall interference for V/STOL testing is solved. In fact, there is quite some activity going on nowadays in the field of wall effects on CTOL testing, a problem that is relatively simple. The absence of activities on wall effects, I think, suggests that it is accepted that the testing of V/STOL aircraft in wind tunnels does not have the same quality as the testing of conventional aircraft.

Now, back to the point of prediction methods. For me the papers by McQuirk on "a row of jets in a crossflow" and by Baker on the development of "a three-dimensional interaction algorithm for numerical prediction of V/STOL jet induced flows" were two of the highlights of the symposium. These methods have at least the potential to bring the prediction methods for V/STOL aerodynamics to a more sophisticated level. Particularly Baker's investigation on the calculation of the jet in a cross flow, exhausting from a flat plate, using a parabolic approximation of the Navier Stokes equations for the turbulent jet can be considered, I think, as a first step to a more detailed and more accurate modelling of this important V/STOL flow problem. Of course, it has to be considered as a first step only. I think the method still gives a far from complete description of the flow field. In comparison with the potential flow methods using singularity distributions to represent the jet flow and its entrainment, Baker's method is able to give a detailed description of the flow inside the jet. This is important in particular in those cases where the jet impinges on a lifting surface. However, Baker's method, I think, does not necessarily give a better prediction, for instance, of the pressure distribution on the flat plate from which the jet is originating. The method will not, as far as I understood, be able to give an adequate description of the flow in the immediate vicinity of the orifice where the jet interacts with the boundary layer on the plate, because the assumptions underlying the parabolic approximation of the Navier Stokes equations, I think, are not fulfilled in this region. The interaction between the jet and the boundary layer on the plate from which the jet originates will probably be small for those cases where the angle of the jet with respect to the outer flow direction is large; that is, close to ninety degrees, and the ratio of the jet velocity and the free-stream velocity is large, but the effect may be large for smaller angles of the jet and/or smaller velocity ratios.

Another point that is not yet clear in my opinion is whether the turbulent jet model and a potential flow model for the outer flow can be coupled in an adequate way in general through an iteration process. It is to be expected that in many cases there will be only a weak interaction between the jet flow and the outer flow. In those cases the application of a simple boundary condition will probably be sufficient to obtain rapid convergence of such an iteration process. There may, however, be other flow conditions where there is a strong interaction between the jet flow and the outer flow. I was wondering whether in such cases the coupling between the two flow fields should not be performed in an interactive way through a type of boundary condition as used, for instance, for strong interaction problems between boundary layer and the outer potential flow around a lifting surface. For a flow with strong interactions such an interactive boundary condition may be a necessary condition to obtain convergence. Again, I suppose the flow condition at smaller jet angles and smaller velocity ratios may be expected to be a more critical one. Now these are problems for the future, of course. I mention them to indicate that I feel that there is still a long way to go.

It is evident that the method of Baker has its limitations and that even a relatively simple flow as the one considered in the paper can not be described in every detail. For the area close to the orifice maybe a less simplified version of the Navier Stokes equations has to be applied, such as the one used by McQuirk. If that is the case, three different flow regions described by different methods have to be coupled. This would be quite a difficult job indeed.

It is clear that the modelling of a much more complicated flow around practical V/STOL aircraft configurations using approximations of the Navier Stokes equations is not attainable in the near future, in spite of the rapid increase of available computing power. The development of adequate turbulence modelling is often mentioned also as one of the main problems for the calculation of the jet flow. This point was mentioned by McQuirk, and he concluded that in some of his calculations, the turbulence model was responsible for over-estimating the rate of mixing. Of course, accurate turbulence modelling is important for the calculation of turbulent flow. However, I think that the experience from boundary layer research shows that this point should not be over-emphasized. I have the feeling that sometimes it is used by the mathematicians as an explanation for discrepancies which can as well be due to the numerical treatment of the problem.

A last point that I would like to mention in relation with the method described by Baker is that, again from experience with the application of boundary layer prediction methods, it is known that finite difference and finite element methods may well give more details of the flow than integral methods, but that integral methods are generally preferred by the users of such prediction methods because they are so much easier to apply. It is not obvious, at least not to me, whether and how methods, such as the one developed by Baker, can be translated into an integral method.

The application of methods based on approximations of the Navier Stokes equations can also contribute much to the development of prediction methods for flows in ducts, including thrust augmenting ejectors, an area where, as I understood, one-dimensional methods are still the best that we have available. In some cases, however, particularly in the case of improvement of ejector thrust augmentation by pulsating or flapping jets, as described by Parikh, Viets and Binder, the flow cannot be considered as a steady flow. Quasi-steady theories and models of turbulence will quite certainly fail to predict such flows. This point has been indicated several times during the meeting as an area of further study.

In any event, a large effort on the development of methods of the type applied by Baker and McQuirk is of extreme importance in order to make progress in the field of V/STOL aerodynamics. However, as I already said, we have to accept that it will be a long and laborious process to come to a point where these methods can be used in the design of V/STOL aircraft.

In the meantime there is almost certainly room for a further development of the potential flow methods where the jets are represented by singularity distributions. They have to be considered as the main tool for the prediction of the performance of V/STOL aircraft in the years to come. I found it surprising that there has been only one paper on such methods, the paper by Walters. He modified the singularity distribution in Wooler's model in order to obtain a better agreement with the pressure distribution on the plate for a jet normal to the free stream.

It is important to keep in mind that the fact that the pressure distribution on the flat plate shows a better agreement does not necessarily mean that a method gives a better overall description of the flow field. The pressure distribution on the plate is influenced by the interaction between the jet and the boundary layer on the plate, so the pressure distribution on the plate is possibly not always the best yardstick. Also, it is to be realized that the singularity distribution is adjusted for the case of a jet perpendicular to the undisturbed flow. A further refinement will probably be necesary to give a better prediction of the flow for smaller jet angles.

During the symposium we heard the usual remarks on the importance of turbulence ranging from "turbulence is not important at all" to "the turbulence models that we are using are not good enough". I do not think that there has been a real controversy at the meeting on whether or not turbulence and entrainment are important. If we are interested in the details of the jet, we have to take into account viscous effects, that is, the turbulent shear stress. If we are interested only in the effect of the jet on the potential flow at some distance from the jet, details are not of interest. In that case, the deflection of the jet thrust which can be represented by a doublet distribution is the main effect, whatever the deflection mechanism may be, at least for a jet angle of ninety degrees. The entrainment to be represented by a sink distribution in that case has a smaller effect, but the addition of entrainment in the model can make the difference between reasonable agreement and good agreement.

Now, let me go back to the presentations on experimental investigations. I found it surprising that with so many papers on experiments, there were only, as far as I remember, two papers, one by Catalano and the by Durao, where the application of the laser doppler anemometer was described. I found this surprising because, in principle, this technique is the obvious one to investigate the flow in and around jets.

The application of conventional measuring techniques with hot wires and pressure probes and rakes has serious drawbacks for the types of flow under consideration, where one has to measure velocity and turbulence at relatively large distances from a surface. The presence of the probes or rakes will, in general, have an important effect in disturbing the flow that is to be investigated. This is possibly not unacceptable if one is mainly interested in a relatively rough description of the flow characteristics, but it is certainly not acceptable for experiments aiming at the very detailed and accurate description of the flow field that is used for the judgment on prediction methods. So, the fact that little attention was given to the application of the laser doppler technique can be due to the fact that, in most cases, only a rough description of the flow field was required. However, if it means that the development of this technique has not yet reached the point that the required detail and required high accuracy that is needed for test case experiments can be obtained, I think there is every reason to give much attention to a further development of this technique and to build up adequate experience with its application.

To conclude these closing remarks, I think we could say that the symposium demonstrated clearly that the situation in the area of V/STOL aerodynamics is characterized by two points:

a - the flow phenomena are of such a complexity that a very large research effort is required to increase our knowledge substantially

b - the short term interest in V/STOL application is limited, and therefore the budgets that are available for research in this area are relatively small

I think this means that, as it stands now, we will not be able to really optimize V/STOL aircraft from an aerodynamic point of view in a similar way as we do for conventional aircraft for a long period to come.

Nevertheless, the symposium made clear that there is high quality research going on at several places. I think AGARD has the responsibility to do whatever possible to increase cooperation and communication between those active in this field. We all know how important in both theoretical and experimental work it is to learn from the experiences from and the errors made by others. Finally, I apologize for having not mentioned in this short time all the excellent papers of the meeting. I will try to do better in the TER. I think we had an enjoyable and a fruitful symposium.

CLOSING REMARKS

Dr. QUINN

Dr. Spee, we thank you for your excellent comments in review of the symposium. I do know that there are about 31 people who would like to respond to those comments, those happen to be authors. I will not let that happen at this time, so that the closing technical remarks can be yours.

On behalf of my co-chairman, Prof. Young, and the other members of the Programme Committee, I will take this opportunity to give very special thanks to the authors whose efforts at writing and presenting their discussions is what this meeting is all about. I applaud you all, and I give you my personal thanks.

At this time I would like to turn the microphone over to the Chairman of the Fluid Dynamics Panel, Dr. Orlik-Rückemann.

Dr. ORLIK-RÜCKEMANN

I would like to join Dr. Quinn in congratulating Dr. Spee on his excellent,even if only preliminary, technical description and evaluation of this symposium. We will all be looking forward to seeing the final version of it. My job here is to thank all the people who have made this symposium possible. To start with, I think that we are really fortunate to have been invited to Portugal, and thanks are due to the Portuguese authorities for providing those splendid quarters for our meeting. We also owe a great deal to many people who are involved in the planning, preparing and conducting of this meeting. First, of course, Professor Young and Dr. Quinn and their programme committee for defining the topic of this symposium, the careful selection of all the papers, and in addition for chairing the various sessions.

Secondly, our Portuguese panel members, Professor Falcao, who together with the Panel Executive, Mr. Bob Rollins, and the Panel secretary, Mademoiselle Anne-Marie Rivault looked after all the local arrangements and ensured that all systems were functioning smoothly and on time. In this they were ably assisted by Miss Henriques. The interpretation was done by Mrs. Stuart, Mrs. Waudby and Monsieur de Liffiac, who not only did an excellent job, but also showed a great deal of patience and understanding when dealing with the customary technical and human imperfections. I am sure that you will all join me in this.

I have a few words about the future activities planned by our Panel. Knowing these plans in advance, you can start early on your own plans to participate and pass on this information to somebody in your organization. In December of this year, there will be a special course at VKI in Belgium on Modern Data Analysis Technique in Noise and Vibration Problems. In March of next year, we will have a lecture series on High Angle of Attack Aerodynamics, which will be presented in Belgium, Germany and the United States. In May, there will be two specialist Meetings in London; one on "Prediction of Aerodynamic Loads on Rotorcraft" and the second on "Wall Interference in Wind Tunnels". Finally, in September we will have a symposium on "Aerodynamics of Missiles", which will be held in Trondheim in Norway. We hope to see you again at some of these activities. I would like to remind the panel members that this afternoon, beginning at 2.30 in a room behind this one, our Portuguese colleagues will talk to us about their work, not only in fluid dynamics, but in the general field of applied mechanics. I am sure that the panel members will not want to miss this unique opportunity to find out a little bit more about the scientific activities in this country.

Thank you all for your participation, the meeting is now adjourned.

REPORT DOCUMENTATION PAGE

1. Recipient's Reference	2. Originator's Reference	3. Further Reference	4. Security Classification of Document
	AGARD-CP-308	ISBN 92-835-0308-2	UNCLASSIFIED

5. Originator Advisory Group for Aerospace Research and Development
North Atlantic Treaty Organization
7 rue Ancelle, 92200 Neuilly sur Seine, France

6. Title

FLUID DYNAMICS OF JETS WITH APPLICATIONS TO V/STOL

7. Presented at

the Fluid Dynamics Panel Symposium held at the Fundaçao Calouste Gulbenkian, Lisbon, Portugal, 2–5 November 1981.

8. Author(s)/Editor(s)	9. Date
Various	January 1982
10. Author's/Editor's Address	**11. Pages**
Various	446

12. Distribution Statement This document is distributed in accordance with AGARD policies and regulations, which are outlined on the Outside Back Covers of all AGARD publications.

13. Keywords/Descriptors

Jets	Short takeoff aircraft
Fluid dynamics	Thrust vector control
Vertical takeoff aircraft	Jet mixing flow

14. Abstract

This volume includes the thirty-one papers presented at the Symposium sponsored by the AGARD Fluid Dynamics Panel in Lisbon, Portugal, on 2–5 November 1981. In addition, a summary of important features of the meeting made by Dr Ir. B.M.Spee is included following the papers. A more comprehensive Technical Evaluation Report will be prepared for publication early in 1982.

AGARD *Conference Proceedings* No.308 Advisory Group for Aerospace Research and Development, NATO FLUID DYNAMICS OF JETS WITH APPLICATIONS TO V/STOL Published January 1982 446 pages This volume includes the thirty-one papers presented at the Symposium sponsored by the AGARD Fluid Dynamics Panel in Lisbon, Portugal, on 2–5 November 1981. In addition, a summary of important features of the meeting made by Dr Ir. B.M.Spee is included following the papers. A more comprehensive Technical Evaluation Report will be prepared for publication early in 1982. P.T.O.	AGARD-CP-308 Jets Fluid dynamics Vertical takeoff aircraft Short takeoff aircraft Thrust vector control Jet mixing flow	AGARD Conference Proceedings No.308 Advisory Group for Aerospace Research and Development, NATO FLUID DYNAMICS OF JETS WITH APPLICATIONS TO V/STOL Published January 1982 446 pages This volume includes the thirty-one papers presented at the Symposium sponsored by the AGARD Fluid Dynamics Panel in Lisbon, Portugal, on 2–5 November 1981. In addition, a summary of important features of the meeting made by Dr Ir. B.M.Spee is included following the papers. A more comprehensive Technical Evaluation Report will be prepared for publication early in 1982. P.T.O.	AGARD-CP-308 Jets Fluid dynamics Vertical takeoff aircraft Short takeoff aircraft Thrust vector control Jet mixing flow
AGARD Conference Proceedings No.308 Advisory Group for Aerospace Research and Development, NATO FLUID DYNAMICS OF JETS WITH APPLICATIONS TO V/STOL Published January 1982 446 pages This volume includes the thirty-one papers presented at the Symposium sponsored by the AGARD Fluid Dynamics Panel in Lisbon, Portugal, on 2–5 November 1981. In addition, a summary of important features of the meeting made by Dr Ir. B.M.Spee is included following the papers. A more comprehensive Technical Evaluation Report will be prepared for publication early in 1982. P.T.O.	AGARD-CP-308 Jets Fluid dynamics Vertical takeoff aircraft Short takeoff aircraft Thrust vector control Jet mixing flow	AGARD Conference Proceedings No.308 Advisory Group for Aerospace Research and Development, NATO FLUID DYNAMICS OF JETS WITH APPLICATIONS TO V/STOL Published January 1982 446 pages This volume includes the thirty-one papers presented at the Symposium sponsored by the AGARD Fluid Dynamics Panel in Lisbon, Portugal, on 2–5 November 1981. In addition, a summary of important features of the meeting made by Dr Ir. B.M.Spee is included following the papers. A more comprehensive Technical Evaluation Report will be prepared for publication early in 1982. P.T.O.	AGARD-CP-308 Jets Fluid dynamics Vertical takeoff aircraft Short takeoff aircraft Thrust vector control Jet mixing flow

Papers presented and discussions held at the Fluid Dynamics Panel Symposium held at the Fundaçao Calouste Gulbenkian, Lisbon, Portugal, 2–5 November 1981. ISBN 92-835-0308-2	Papers presented and discussions held at the Fluid Dynamics Panel Symposium held at the Fundaçao Calouste Gulbenkian, Lisbon, Portugal, 2–5 November 1981. ISBN 92-835-0308-2
Papers presented and discussions held at the Fluid Dynamics Panel Symposium held at the Fundaçao Calouste Gulbenkian, Lisbon, Portugal, 2–5 November 1981. ISBN 92-835-0308-2	Papers presented and discussions held at the Fluid Dynamics Panel Symposium held at the Fundaçao Calouste Gulbenkian, Lisbon, Portugal, 2–5 November 1981. ISBN 92-835-0308-2

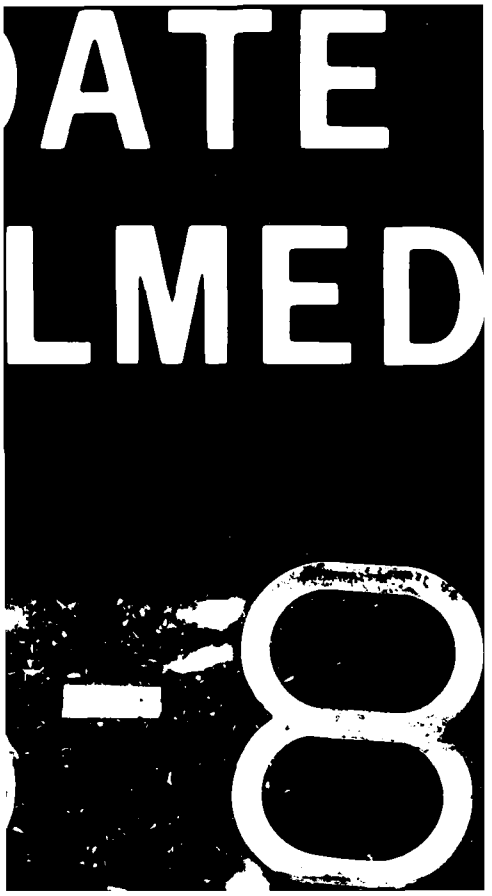
ATE
LMED
8